Bulgarian Chemical Communications, Volume 47, Special Issue B (pp. 5–5) 2015

PREFACE

The Bulgarian National Conference on Physics has been is reestablished following the proposal of the Sofia Branch of the Union of Physicists in Bulgaria (UPB). This came after some long period of organisation of targeted conferences. The national level conference covering all branches of physics was held between 10th and 12th October 2014 in the Paisii Hilendarski University of Plovdiv. The conference was organized by the Faculty of Physics of the University of Plovdiv together with the Sofia and Plovdiv branches of the UPB `http://plovdiv2014.bgphysics.eu/`.

Special thanks go to the chairperson, Professor Temenuzhka Yovcheva. Optimistically, we believe that this annual conference focused on the new scientific results of the Bulgarian as well as the international physics scholars will stimulate further development of physics research in Bulgaria and will establish new relations and collaborations between colleagues in Bulgaria and in international context.

Prof. Todor Mishonov, DSc.

Co-chair of the conference and editor of the present proceedings

St Clement of Ohrid University of Sofia

© 2015 Bulgarian Academy of Sciences, Union of Chemists in Bulgaria

PHOTONICS AND TELECOMMUNICATIONS

ФОТОННИ И ТЕЛЕКОМУНИКАЦИОННИ ТЕХНОЛОГИИ

Bulgarian Chemical Communications, Volume 47, Special Issue B (pp. 9–14) 2015

Analysis of fluorescence spectra of oxyfluoride compositions doped with samarium oxide (Sm_2O_3) and samarium fluoride (SmF_3)

T. Pashova[1]*, I. Kostova[2,3], T. Eftimov[1], D. Tonchev[2,3]

[1] *Faculty of Physics, Paisii Hilendarski University of Plovdiv, 24 Tsar Asen Str., BG-4000 Plovdiv, Bulgaria*
[2] *Faculty of Chemistry, Paisii Hilendarski University of Plovdiv, 24 Tsar Asen Str., BG-4000 Plovdiv, Bulgaria*
[3] *Laboratory for Electronic and Optic Materials, University of Saskachewan, 54 College Dr, Saskatoon, Canada*

ZnO-ZnF_2-P_2O_5-B_2O_3 compositions, doped with a varying quantity of samarium oxide (Sm_2O_3) and samarium fluoride (SmF_3) have been synthesized. The thermal properties of the obtained compositions have been measured using DSC analysis. Fluorescence spectra measured at different excitation wavelengths are shown. The fluorescence excitation efficiency for varying quantity of Samarium in the samples and the pumping wavelength has been studied. With optical pumping in the 370–490 nm range fluorescence spectra indicating the presence of Sm^{3+} have been obtained. The widening of the pumping range to higher wavelengths a new fluorescence peak was observed. The range in which the peak is observed was established from the performed analysis and the excitation wavelength of maximum efficiency was determined.

Key words: samarium, fluorescence, emission spectra, optical materials

INTRODUCTION

The interest towards luminescence properties of novel non-organic materials with rare earth elements has grown considerably during the last several years because of their possible applications in laser technologies, optoelectronics, eco-technologies and other developing areas [1].

This paper presents the optical properties of ZnO-ZnF_2-P_2O_5-B_2O_3: Sm_2O_3 and SmF_3 compositions. Several samples with this composition have been synthesized differing by the content of Sm_2O_3 and SmF_3, for $x = 0.025, 0.075, 0.125, 0.175$, and 0.25 mol%, correspondingly. After the samples were obtained their thermal properties were studied using DSC analysis, as well as their optical properties by excitation at the following wavelengths: 370, 395, 405, 410, 415, 425, 435, 450, 470, 490, 505, 515, 525, 535, 565, 572, 590, 605, 615, 632, 660, and 700 nm.

Spectral analysis shows that with excitation in the 370 to 500 nm range four characteristic peaks for Sm^{3+} [2, 3]. The study of the 500-600 nm excitation range exhibits a new fluorescence peak in the 670 - 680 nm range which suggests a Sm^{2+} ion [4].

EXPERIMENTAL PART

Synthesis

For the synthesis of ZnO-ZnF_2-P_2O_5-B_2O_3-Sm_2O_3-SmF_3 glasses the following reagents have been used: ZnO (Alfa Aesar, 99.9%), ZnF_2 (Alfa Aesar, 99%), P_2O_5 (Alfa Aesar, 98%), B_2O_3 (Alfa Aesar, 99.98%), Sm_2O_3 (Alfa Aesar, 99.99%), SmF_3 (Alfa Aesar, 99.99%). For the purpose of complete homogenization of the mixture, the synthesis was performed in a zirconium furnace Zircar 110 (temperature range from 0 to 1750°C) at a temperature of 950°C for a period of 3 h. The samples were cast at 1200°C and cooled at room temperature. Five compositions with different content of Sm_2O_3 and SmF_3 were obtained as is shown in Table 1.

Table 1. ZnO-ZnF_2-P_2O_5-B_2O_3-Sm_2O_3-SmF_3 copositions

Sample No	**ZnO,** mol%	**ZnF_2,** mol%	**P_2O_5,** mol%	**B_2O_3,** mol%	**Sm_2O_3,** mol%	**SmF_3,** mol%
1	36.23	36.23	9.69	18.00	0.025	0.025
2	36.13	36.13	9.69	18.00	0.075	0.075
3	36.03	36.03	9.69	18.00	0.125	0.125
4	35.93	35.93	9.69	18.00	0.175	0.175
5	35.78	35.78	9.69	18.00	0.25	0.25

The synthesis of the new compositions shows the optimum content of rare earth elements in so much as transparency is concerned. It is somewhat surprising that the optimum content is 0.125 mol% which neither the minimum, nor the maximum quantity of both dopants (sample 3). This is shown in Fig. 1. It can be seen that sample 3 is a transparent and gas bubbles free.

* To whom all correspondence should be sent:
teodora_pashova@abv.bg

© 2015 Bulgarian Academy of Sciences, Union of Chemists in Bulgaria



Fig. 1. A picture of the tested compositions.

Differential scanning calorimetry

The thermal properties of the obtained samples were measured using a Differential scanning calorimeter (TA Instrument DSC Q100) with a fast cooling system (FACS) for a heating rate of 2 K/min and modulation period of 60 s. The results of the analysis are processed using the TA Instruments Universal Analysis (UA) software.

Sample preparation

The glass samples obtained are in the form of round plates having a diameter of about 1 cm. To perform the optical measurements, a piece of the plate is taken and is ground to a fine homogeneous powder. A bowl and a pestle are used for the purpose.

Experimental optical set up

Figure 2 represents schematically the experimental set-up for the study of the optical properties of samples of the ZnO-ZnF_2-P_2O_5-B_2O_3:Sm_2O_3 and the SmF_3 compositions.

Light emitting diodes (LEDs) emitting in the spectral range from 370 nm to 700 nm were used to

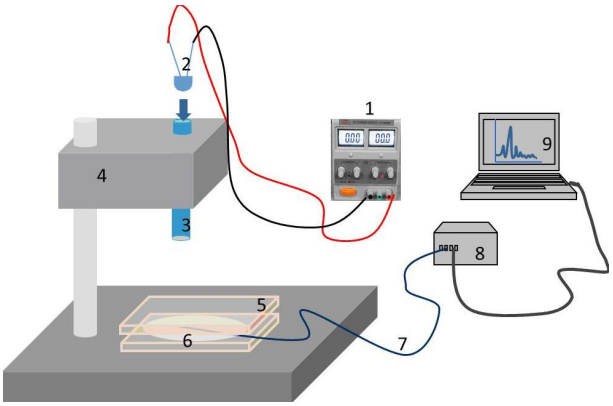


Fig. 2. Experimental set up: 1 – power supply, 2 – light source, 3 – a lens collimating system, 4 – holder of the light source, 5 – fused silica plates, 6 – powder sample of the studied material, 7 – a detecting optical fiber, 8 – Spectrometer, 9 – read and write software.

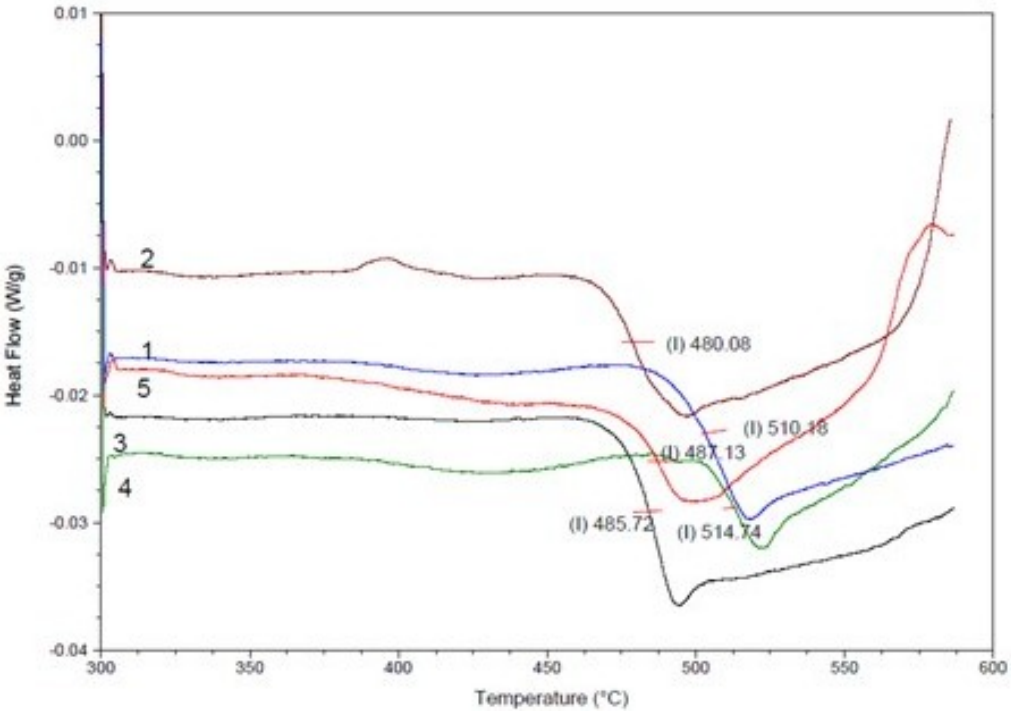


Fig. 3. Dependence of T_g on the content of Sm_2O_3 and SmF_3 in the composition.

directly excite the sample. A lens system was used to collimate the divergent light from the LEDs. The output light spot has a diameter of about 1–2 mm. The glass plates were used to position the samples and the detecting fiber and to ensure a uniform thickness of the layer. The detecting system consists of a detecting optical fiber (7), a fiber-optic spectrometer (8) (AvaSpec) in the 200 - 1160 nm spectral range, powered by a computer via a USB port, and using a specialized software AvaSoft-basic (9).

The purpose of the experimental set-up is to check the excitation efficiency of the ZnO-ZnF_2-P_2O_5-B_2O_3:Sm_2O_3 and SmF_3 compositions; to check if the quantity of Sm_2O_3 and SmF_3 produces an effect on the emission fluorescence spectra.

RESULTS AND ANALYSIS

Thermal analysis

The data from the DSC are presented in Fig. 3. As is seen, the glass transition temperature (T_g) is in the 485 to 514°C range and no linear dependence is observed on the content of the rare earth ions (Sm_2O_3 and SmF_3) in the composition.

Fluorescence analysis

Fluorescence spectra are taken after excitation of each of the samples with a collection of 22 LEDs in the range from 370 nm to 700 nm. The data obtained are summarized in three sub-ranges, namely: (1) [370–490 nm]; (2) [505–590 nm]; (3) [605–700 nm].

The resulting fluorescence spectra are presented after normalization to maximum intensity of the scattered excitation light.

1. Spectra in the 370 to 490 nm. Experimental data are shown graphically as presented in Fig. 4. A strong fluorescence typical for the Sm ions of third valency is seen from the graphs. Four peaks are observed at 564, 600, 645, and 704 nm [2, 3, 5].

The most intensive fluorescence spectrum is for excitation at 405 nm. As is seen form the graph, there is a tendency for the peaks to diminish in intensity as the excitation wavelength increases. The deviations are due to the different optical power launched in the samples under study and the imperfections in the experimental set up as the degree of collimation of the excitation light of LEDs, positioning of detecting optical fiber, stability of power unit and etc.

2. Spectra in the 505 to 590 nm range. Fig. 5 represents the fluorescence spectra in the 505 to 590 nm range. It is seen that for an excitation of 505 nm a fluorescence peak at 650 nm is observed although weak. It is further noticed that with the increase of the excitation wavelength a new peak around 670-680 nm appears, which is not characteristic for the Sm ion of third valency.

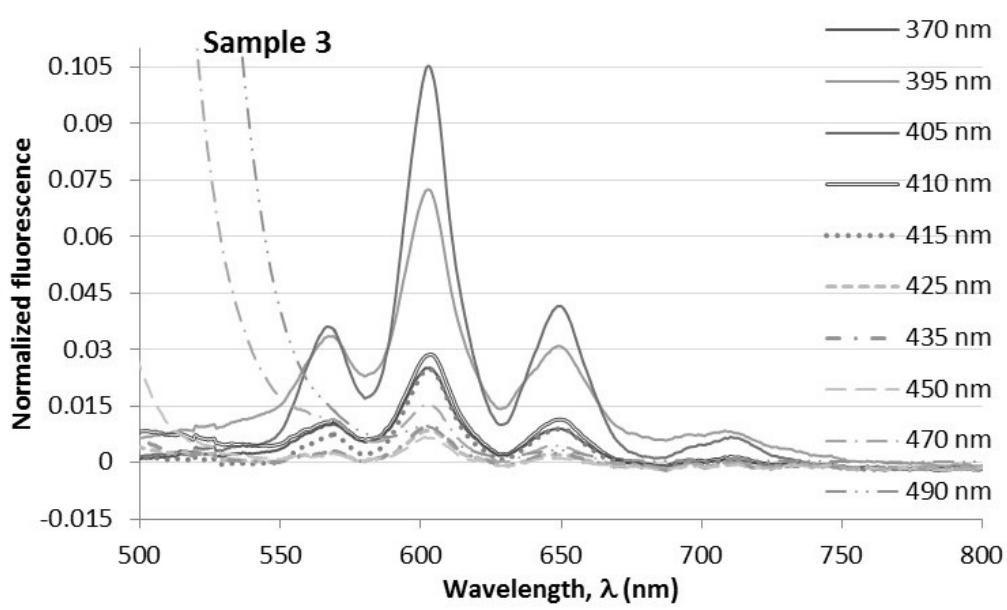


Fig. 4. Fluorescence spectra of ZnO-ZnF_2-P_2O_5-B_2O_3-Sm_2O_3-SmF_3 glasses normalized to the scattered excitation maximum intensity for excitation in the 370 nm - 490 nm range.

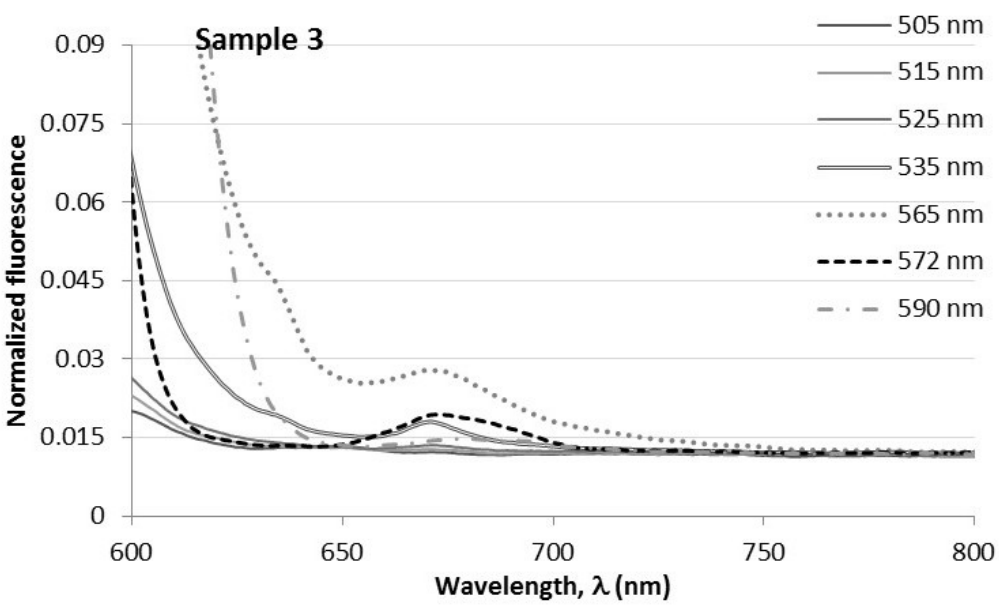


Fig. 5. Normalized fluorescence spectra of ZnO-ZnF_2-P_2O_5-B_2O_3-Sm_2O_3-SmF_3 glasses for excitation wavelengths in the 505 nm to 590 nm range.

From the literature it is known that this wavelength is situated in the region characterizing the fluorescence of the Sm ions from the second valency [4].

The new peak is most intense upon excitation of 565 nm, but the well-formed at 572 nm.

3. Spectra in the 605 to 700 nm range. The plots in Fig. 6 show that fluorescence is very weak in 605 to 700 nm range.

As is evidenced from Fig. 7, the most interesting range is the one from 370 nm to 500 nm.

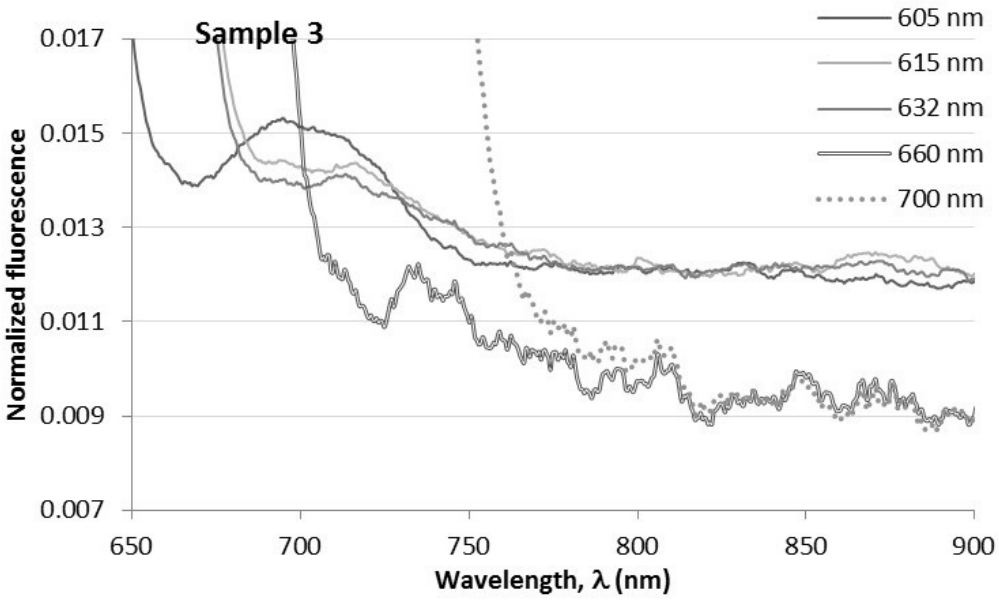


Fig. 6. Normalized fluorescence spectra of ZnO-ZnF_2-P_2O_5-B_2O_3-Sm_2O_3-SmF_3 glasses for excitation wavelengths in the 605 nm to 700 nm range.

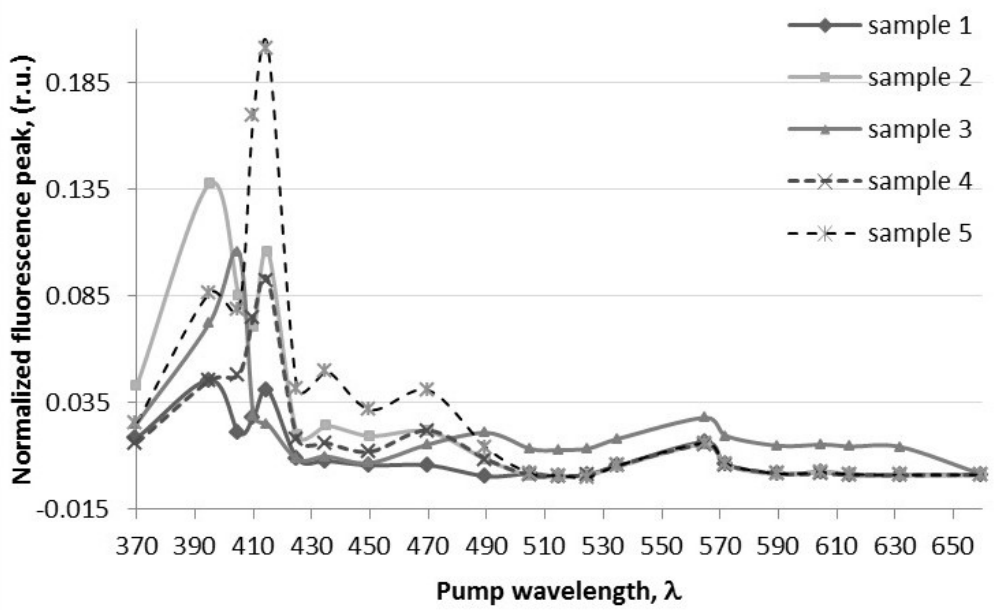


Fig. 7. Plot of the maximum of the fluorescence peak vs. the excitation wavelength.

In the opaque compositions containing Sm_2O_3 and SmF_3 under 0.12 mol%, a competition between the pumping sources at 395 nm and 415 nm causing a maximum fluorescence is observed. This competition is overcome for a content of Sm_2O_3 and SmF_3 above 0.13 mol%. This means that with the increase of the concentration of the rare earth ion in the composition the wavelength of the most efficient excitation source increases as well.

CONCLUSIONS

Five samples ZnO-ZnF_2-P_2O_5-B_2O_3-Sm_2O_3-SmF_3 with different content of Sm_2O_3 and SmF_3 have been synthesized. From the measurements made and the analyses performed, the following conclusions can be drawn::

1. The range of glass transition temperature is $T_g = [485–514]$ °C;
2. There is no linear dependence between T_g and the content of the rare earth ions (Sm_2O_3 and SmF_3) in the composition;
3. The intensity of the fluorescence spectrum of the synthesized compounds depends on the content of Sm_2O_3 and SmF_3;
4. The most efficient excitation is in the 390-420 nm range and depends on the concentration of the rare-earth ion.

REFERENCES

[1] Y. Deng, Sh. Yi, Y. Wang and J. Xian, *Opt. Mater.* **36**, 1378–1383 (2014).

[2] M. Jayasimhadri, L. R. Moorthy, S. A. Saleem and R. V. S. S. Ravikumar, *Spectrochim. Acta A* **64**, 939–944 (2006).

[3] T. Pashova, I. Kostova, T. Eftimov, D. Tonchev and G. Patronov, *Fundamental Sciences and Applications* **18**, 137–142 (2012).

[4] Y. Huang, K. Jang, W. Zhao, E. Cho, H. S. Lee, X. Wang, D. Qin, Y. Zhang, Ch. Jiang and H. J. Seo, *J. Solid State Chem.* **180**, 3325–3332 (2007).

[5] S. Arunkumar and K. Marimuthu, *J. Alloy Compd.* **565**, 104–114 (2013).

АНАЛИЗ НА ФЛУОРЕСЦЕНТНИ СПЕКТРИ НА ОКСИФЛУОРИДНИ КОМПОЗИЦИИ, ЛЕГИРАНИ СЪС САМАРИЕВ ОКИС (Sm_2O_3) И САМАРИЕВ ФЛУОРИД (SmF_3)

Т. Пашова[1], И. Костова[2], Т. Ефтимов[1], Д. Тончев[2]

[1] *Физически факултет, Пловдивски университет "Паисий Хилендарски", ул. "Цар Асен" №24, 4000 Пловдив, България*
[2] *Химически факултет, Пловдивски университет "Паисий Хилендарски", ул. "Цар Асен" №24, 4000 Пловдив, България*

(Резюме)

Синтезирани са $ZnO\text{-}ZnF_2\text{-}P_2O_5\text{-}B_2O_3$ стъкла, легирани с различно количество самариев окис (Sm_2O_3) и самариев флуорид (SmF_3). Представени са флуоресцентните спектри, снети за различни дължини на напомпване. Изследвана е ефективността на възбуждане на флуоресценция в зависимост от количественото съдържание на самарий в пробите и промяна в дължината на възбуждащия източник. При оптично напомпване в диапазона 370–490 nm се получават флуоресцентни спектри, характеризиращи наличие на Sm^{3+}. При разширяване на областта на напомпване, към по-големите дължини на вълните, се наблюдава поява на нов неизследван от нас флуоресцентен пик. От проведения анализ се установи областта, в която се получава пика и е определена най-ефективната дължина на възбуждане.

Bulgarian Chemical Communications, Volume 47, Special Issue B (pp. 15–20) 2015

Research of 16-channel fiber-optic (FO) system for measuring long period sensor networks (LPSN)

V. Plachkova[1*], P. Balzhiev[2], G. Dyankov[1], T. Eftimov[1], P. Petrov[1]

[1] *Faculty of Physics, Paisii Hilendarski University of Plovdiv, 24 Tsar Asen Str., BG-4000 Plovdiv, Bulgaria*
[2] *Faculty of Telecommunications, Technical University of Sofia, 8 Kl. Ohridski Blvd., 1000 Sofia, Bulgaria*

Progress in fiber optic technology offers great opportunities to develop a wide range of highly sensitive fiber-optic sensors in many new application areas. In the field of the sensors we witness an increased interest in the simultaneous measurement of two or more physical parameters [1,2]. These measurements are carried out with sensors based on a simple and effective detection of the signals by using a linear CCD photodiode matrix in combination with a diffraction grating to measure the spectral shifts, which are proportional to the phase change introduced into the sensing fiber. The resulting responses are linear [3].

The tested 16-channel system is compared to a single-channel spectrometer on the basis of a long period grating (LPG) with a photodiode.

The possibilities of the spectrometer based on linear CCD photodiode array in combination with diffraction grating for measuring single-channel and multi-channel measurement and simultaneous recording of data using software developed for this purpose were investigated.

The sensitivity of the 16-channel spectrometer was tested by measuring the change in the spectrum of LPG due to mechanical stress, change of the refractive index and the influence of temperature [4].

Key words: long period sensor, linear CCD photodiode matrix, long period grating, sensitivity of the 16-channel spectrometer

INTRODUCTION

The study of the behavior of any system is done most effectively by a comparison to some already tested analogous system. In our case it is an optical spectrum analyzer (OSA) AQ6331.

There has been no completely uniform appearance of the spectrum of choice for testing a LPG, the resulting spectrum of the 16-channel CCD-based OSA is wider, in contrast to that of AQ6331. This is due to the non-uniformity of the structure of the two spectral analyzer.

SENSITIVITY OF LPG TO TEMPERATURE, STRAIN, BENDING AND REFRACTIVE INDEX

- *Sensitivity to temperature*. The temperature sensitivity is expressed by the differential equation [4]

$$\frac{d\lambda}{dT} = \frac{d\lambda}{d(\delta n_{\text{eff}})}\left(\frac{dn_{\text{eff}}}{dT} - \frac{dn_{\text{cl}}}{dT}\right) + \Lambda\frac{d\lambda}{d\Lambda}\frac{1}{L}\frac{dL}{dT} \quad (1)$$

In the differential equation λ is the wavelength, T – the temperature, n_{eff} – the effective refractive index of the core, n_{cl} is the effective refractive index of the shell, $\delta n_{\text{eff}} f = n_{\text{core}} - n_{\text{cladd}}^{(m)}$, L is the length of the LPG and Λ its period.

- *Sensitivity to the refractive index*. Sensitivity of sensors based on LPG to the refractive index is given by [4]

$$\frac{d\lambda}{dn} = \frac{d\lambda}{dn_{\text{eff}}}\frac{dn_{\text{eff}}}{dn} \quad (2)$$

- *Sensitivity to stress*. The sensitivity of the sensors based on long period gratings (LPGs) to tensile is described by the differential equation [4]

$$\frac{d\lambda}{d\varepsilon} = \frac{d\lambda}{d(\delta n_{\text{eff}})}\left(\frac{dn_{\text{eff}}}{d\varepsilon} - \frac{dn_{\text{cl}}}{d\varepsilon}\right) + \Lambda\frac{d\lambda}{d\Lambda} \quad (3)$$

- *Sensitivity to bending*. Manifested in two ways: as a change in the central wavelength in the bands of attenuation ***or*** split in two of every one of the attenuation band.
- *Multiple sensitivity*. If the sensor is sensitive to n values $x_i (i = 1,\ldots,n)$, which in case of Δx_i result in changes of the center wavelength with $\Delta\lambda_i$, then these changes are described by a matrix [4]

$$\begin{pmatrix} \Delta\lambda_1 \\ \Delta\lambda_2 \\ \vdots \\ \Delta\lambda_n \end{pmatrix} = \begin{bmatrix} K_{11} & K_{12} & \ldots & K_{1n} \\ K_{21} & K_{22} & \ldots & \vdots \\ \vdots & \vdots & \ddots & \vdots \\ K_{nl} & \ldots & \ldots & K_{nn} \end{bmatrix} \begin{pmatrix} \Delta x_1 \\ \Delta x_2 \\ \vdots \\ \Delta x_n \end{pmatrix} \quad (4)$$

* To whom all correspondence should be sent:
vania_plachkova@abv.bg

© 2015 Bulgarian Academy of Sciences, Union of Chemists in Bulgaria

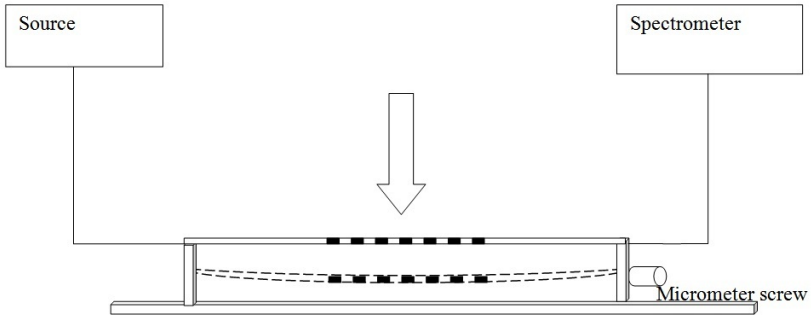


Fig. 1. Scheme of the experimental setup used to study the effects of bending on the optical fiber long period diffraction gratings.

Usually, however, it is preferred that the sensors are sensitive to only a couple of parameters, in principle they are sensitive to

- refractive index and temperature
- temperature and bending

STUDY OF THE SPECTRAL RESPONSE OF LONG PERIOD GRATINGS (LPG) UNDER BENDING STRESS

Scheme of the experimental setup used to study the effects of bending on the optical fiber long period gratings is presented in Fig. 1.

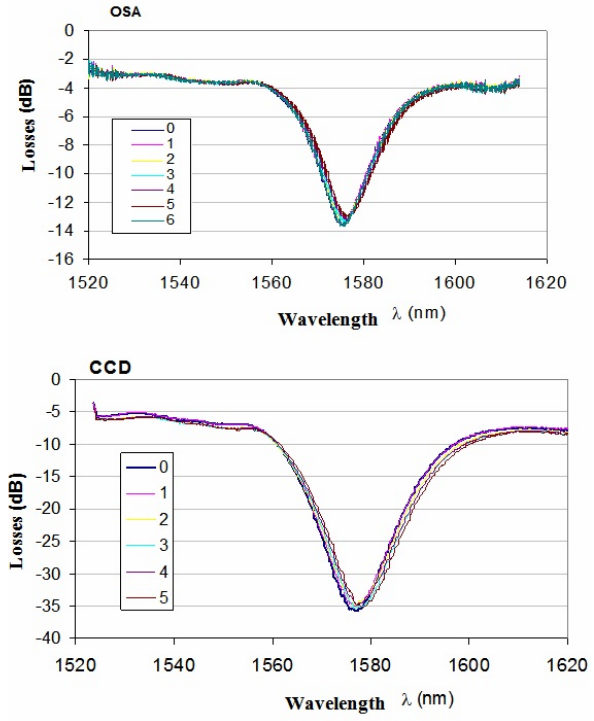


Fig. 2. Impact through pressure registered with OSA AQ6331 and CCD-based spectrometer.

The C + L broadband ASE source (1522–1622 nm) of 16-channel system was used as a light source for both the OSA and the CCD based spectrometer. Since the AQ6331 model does not allow processing software on a computer, it has built in specific software for operation.

Bending responses were recorded under the same conditions to investigate the granting of the long period grating in the experimental setup through 100 μm. The spectrum of the signal to both spectrum analyzers is the same.

The spectra of the LPG measured in parallel with both the AQ6331 OSA and the CCD-based spectrometer are shown in Fig. 2. The figure shows the effects by pressing a certain depth in μm recorded with SA AQ6331 and CCD-based spectrometer. Fig. 3 shows the spectral shift by means of the pressure $d\lambda/dx =$ 0.306 nm/OE. In Fig. 4 is a quadratic approximation around the minimum in a mechanical process.

Impact through pressure to the LPGs studied in parallel with CCD-based spectrometer and OSA AQ6331 indicates that both spectrum analyzers

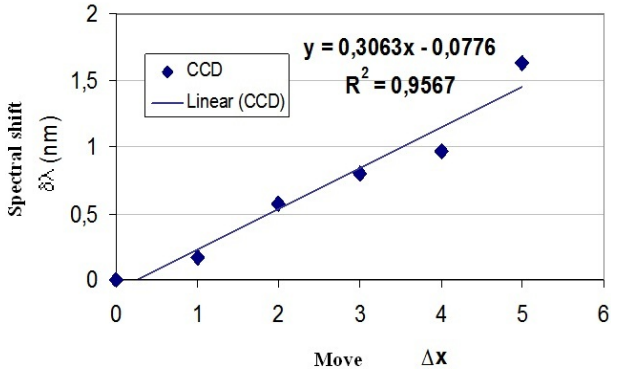


Fig. 3. Spectral shift by pressing with $d\lambda/dx =$ 0.306 nm/OE.

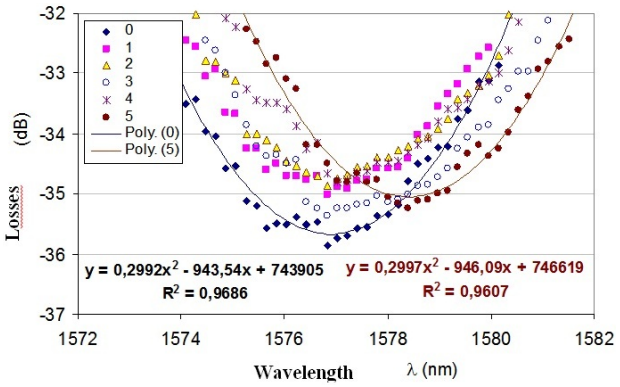


Fig. 4. Quadratic approximation around the minimum in mechanical impact.

have the same response to the minimum for the same depth pressure. This indicates that the CCD-based spectrometer in no way inferior to the most renown OSA AQ6331 and can also be used as effectively as it in the study of the responses of LPGs under pressure.

STUDY OF THE SPECTRAL RESPONSE OF LPGS TO SURROUNDING REFRACTIVE INDEX CHANGES

The scheme of the experimental set-up used for the recording of the response under the effect of a change in the refractive index is the same as in Fig. 1, the surface of the grating is wetted with water by means of a dispenser. Fig. 5 shows the impact by changing the refractive index of water recorded with an optical spectrum analyzer AQ6331 and CCD-based spectrometer again mentioned the shift of the minimum.

The spectrum of an LPG is changed by changing the refractive index of the surrounding medium in which the grating is located. The index of refraction depends on the content of the medium. In this case it is chosen to alter this parameter of the LPG with water (refractive index of water is 1.33). Thus, changing the environment of the LPG from air to water will cause a spectral shift.

This sensitivity of the LPGs is widely used in biosensimg for analyzing various fluids, solvents, solid materials, which are characterized by different refractive indices.

STUDY OF THE SPECTRAL RESPONSE OF LPGS TO TEMPERATURE CHANGES

The response of the LPG to temperature variations was determined only with CCD-based spectrometer, as it is the subject of research studies. Before we explore the LPG's response to controlled temperature

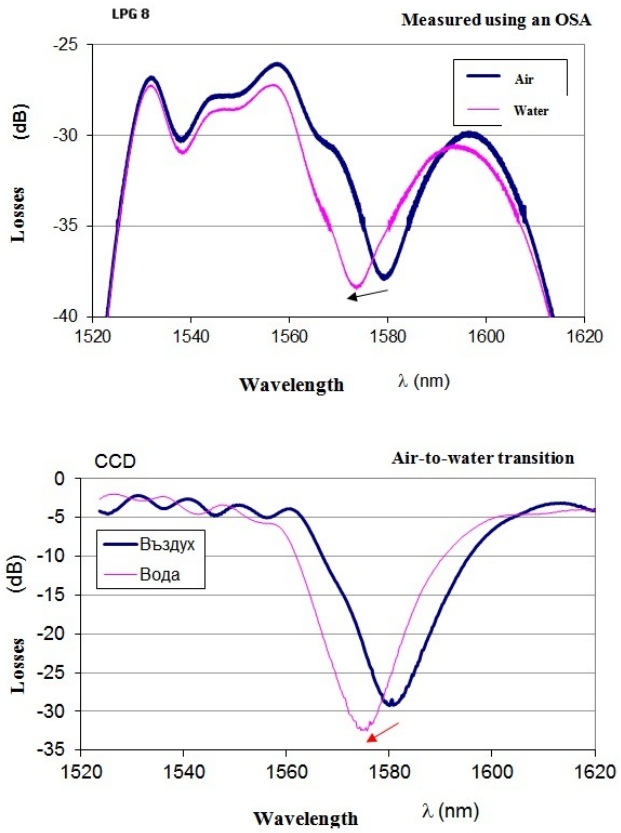


Fig. 5. Response to changes of the refractive index from air to water registered with AQ6331 OSA and CCD-based spectrometer: $d\lambda = -5.48$ nm

changes we record the stacked consecutive spectral responses caused by heating the grating with a solder (Fig. 6) during which the temperature cannot be controlled accurately. Measurements gave very good results, which provides grounds for further studies at higher temperatures than those used in this thesis.

The experimental setup used to determine the response of the spectrum of at lower temperatures of a Peltier cooler, power supply, temperature

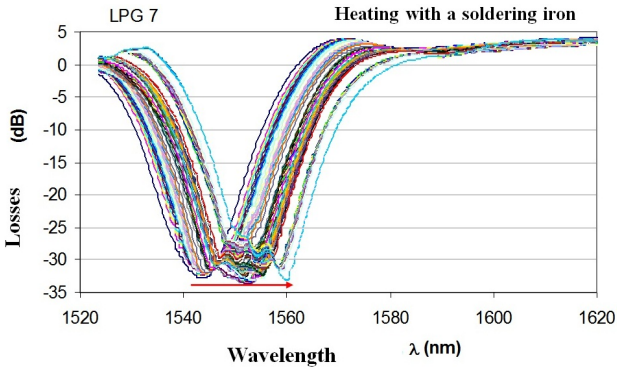


Fig. 6. Spectral shifts caused by heating with a solder.

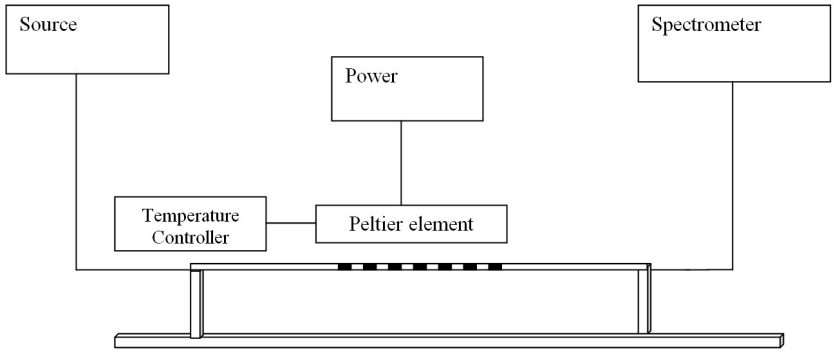


Fig. 7. Scheme of the experimental setup used to register the response under the influence of temperature changes (in average temperature intervals).

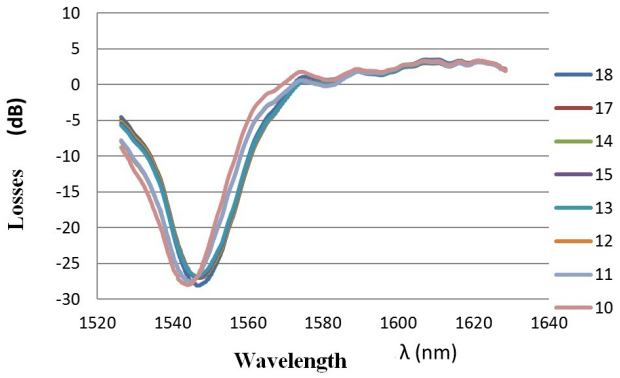


Fig. 8. Spectral shifts of a LPG as a result of heating with low temperatures.

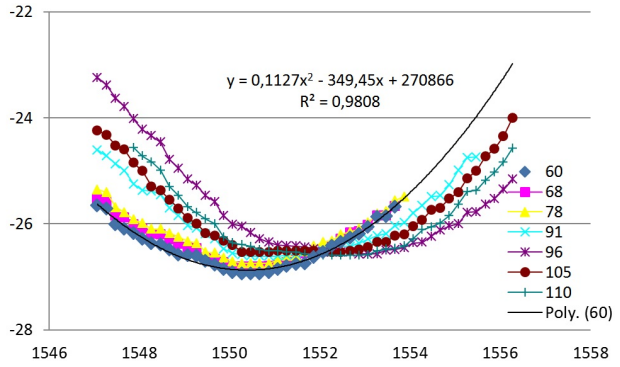


Fig. 9. Quadratic approximation around the minimum used to determine the resonance wavelenth.

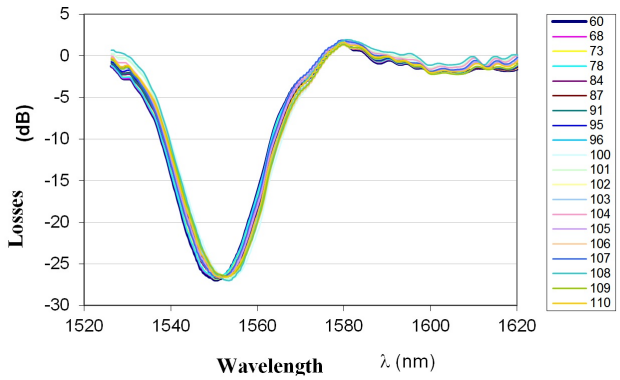


Fig. 10. Spectral responses of an LPG to heating from 60°C to 110°C.

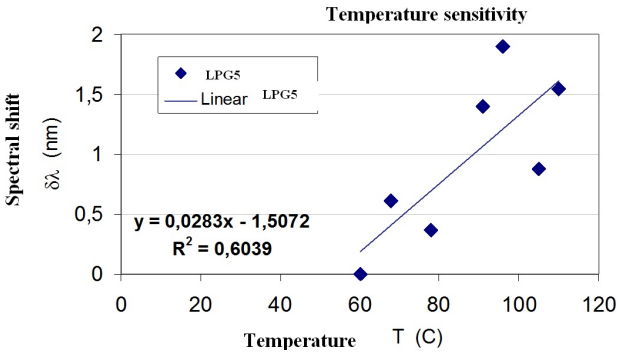


Fig. 11. Temperature sensitivity of a LPG.

controller for measuring the temperature, the CCD-based spectrometer and a computer. The response was recorded at room temperature of about 220°C, such as the grating is first heated and then cooled. Threshold of Peltier heating element reaches 490°C, and on cooling to 110°C. A flow chart of the experimental set-up used for the recording of the response under the effect of the change in temperature (temperature at average intervals) is shown in Fig. 7. Fig. 8 shows the observed spectral changes and Fig. 9 illustrates the quadratic fitting of the minimum used to determine the shifts. The responses are set to the minimum of a LPG as a result of heating and cooling to a lower temperature. Fig. 9 represents a quadratic

approximation around the minimum when heated at high temperatures.

The experimental setup used to determine the spectral response of a LPG under the influence of high temperatures is the same as in Fig. 10, except that polarity of the Peltier elements is reversed and it is used as heater, which reaches a high temperature range. The response was recorded from 60°C to 110°C. Fig. 10 presents the response of the minimum of the LPG due to heating it to higher temperature. Fig. 11 represents the temperature sensitivity of the LPG. As a whole the tested LPG is very weakly sensitive to temperature $S_T = 28.3$ pm/°C.

From the spectra for different levels of the temperature can be seen that the bars are sensitive to higher temperatures, it is of course quite by accident and has not been a major goal.

As described in section 2, this type of arrays are typically designed to be sensitive to the two mentioned parameters, i.e. those gratings used for the tests are not specifically designed to study the responses in temperature influence, and are specialized for the other two parameters, but however with them sufficiently gives the dependence of the temperature in the temperature range 10°C recorded by CCD-based 16-channel spectrophotometer.

CONCLUSIONS

- The 16-channel CCD - based spectrometer can analyze 16 different responses of long period gratings with the same signal quality for any channel number.
- The 16-channel CCD - based spectrometer provides the same sensitivity to spectral shifts as the standard AQ6331 OSA.
- 16-channel CCD - based spectrometer exhibited excellent repeatability of signals after multiple switching between channels.
- 16-channel CCD - based spectrometer has an extremely wide range of applications both in science and industry in areas such as: biosensing, temperature and strain sensing.

REFERENCES

[1] J. P. Carvalho, L. Coelho, J. M. Baptista, O. Frazao and J. L. Santos, *Meas. Sci. Technol* **22**, 065201 (2011).

[2] R. P. Murphy, S. W. James, and R. P. Tatam, *J. Lightwave Techn.* **25**, 825–829 (2007).

[3] P. Balzhiev, W. J. Bock, T. A. Eftimov, P. Mikulic, R. Arnaudov and V. Plachkova, "Multiplexed LPG sensor system using an InGaAs CCD linear array and optical switches" in Proc. of ... *Fellow IEEE*, (2013).

[4] S. W. James and R. P. Tatam, *Meas. Sci. Technol.* **14**, R49–R61 (2003).

ИЗСЛЕДВАНЕ НА 16-КАНАЛНА ВЛАКНЕСТО-ОПТИЧНА (ВО) СИСТЕМА ЗА ИЗМЕРВАНЕ НА ДЪЛГОПЕРИОДИЧНИ (ДПР) СЕНЗОРНИ МРЕЖИ

В. Плачкова[1], Пл. Балджиев[2], Г. Дянков[1], Т. Ефтимов[1]

[1] *Физически факултет, Пловдивски университет "Паисий Хилендарски", ул. "Цар Асен" №24, 4000 Пловдив, България*
[2] *Факултет по телекомуникации, Технически университет–София, бул. "Климент Охридски" №8, 1000, София, България*

(Резюме)

Прогресът във влакнесто-оптичните технологии предлага изключителни възможности за разработка на широк спектър от високо-чувствителни влакнесто-оптични сензори в много нови области на приложения. В областта на сензорите се прояви завишен интерес към измерване на два и повече физически параметъра едновременно. Тези измервания се извършват със сензори, основаващи се на проста и ефективна схема за детекция на сигналите, с използване на линейна фотодиодна CCD матрица в комбинация с дифракционна решетка, за да измери спектралните отместванията, които са пропорционални на фазовите промени, въведени в сензорното влакно. Получените отклици са линейни.

Изследваната 16-канална система е сравнена с едноканален спектрометър на основата на дългопериодична решетка с фотодиод.

Изследвани са възможностите на спектрометъра на основата на линейна фотодиодна CCD матрица в комбинация с дифракционна решетка за едноканално измерване и многоканално измерване, както и едновременното записване на данни посредством разаботен за целта софтуер.

Чувствителността на 16-каналения спектрометър е тествана чрез измерване промяната на спектъра на дългопериодични решетки, следствие въздействие на механично напрежение, промяна на показателя на пречупване и влияние на температурата.

Bulgarian Chemical Communications, Volume 47, Special Issue B (pp. 21–28) 2015

Calculations of photonic crystal fibers by the Galerkin method with sine functions without a refractive index approximation

E. Karakoleva, B. Zafirova*, A. Andreev

Georgi Nadjakov Institute of Solid State Physics, Bulgarian Academy of Sciences, 72 Tsarigradsko Chaussee Blvd., 1784 Sofia, Bulgaria

Results from the calculation of the basic characteristics of the photonic crystal fiber with two rings of holes are presented by the approach which takes into account the exact distribution of the refractive index over the cross section of the photonic crystal fiber. Formulae are theoretically derived for the calculation of holes with arbitrary shapes by dividing the material within them into rotated at different angles rectangles.

Key words: photonic crystal fibre, Galerkin method, a set of sine functions

INTRODUCTION

Photonic crystal fibers (*PCF*s) attract considerable attention since their waveguiding structure provides possibilities for creation of new or improved properties compared to that of the conventional optical fibers. They can be prepared in such a way that insures a single mode operation practically within the whole range of transparency of the material from which they are made (*endlessly single mode fibers*) at the same time with a very small change in the mode field diameter. The core diameter of the single mode fiber can be very high – 20–30 μm, which allows a transmission of high level optical power. Depending on the core diameter *PCF* can reveal very low or very high optical nonlinearity. Single mode fibers can be produced with unique dispersion properties – with an ultra flattened dispersion over very wide spectral range, a zero dispersion, realized at a chosen wavelength (even in the visible range), a zero dispersion in several chosen spectral ranges. The fibers can be easily prepared with very high birefringence - until one order higher than the birefringence, achieved by the standard anisotropic fibers by a suitable combination of the locations and the sizes of the holes [1–12].

The high refractive index contrast of the materials of the *PCF* requires full-vector methods [13] to model the fibers accurately. The most used numerical methods are a plane wave expansion method (*PWM*) [14–16], a localized function method (*LFM*) [17, 18], a beam propagation method (*BPM*) [19, 20], a finite-element method (*FEM*) [21, 22], a finite-difference method in the time domain (*FDTD*) [23], a finite-difference method in the frequency domain (*FDFD*) [24–31], a source-model technique (*SMT*) [13, 32, 33], and a highly accurate semi-analytical multipole method (*MM*) [34, 35]. A brief review of their merits and drawbacks is given in [24].

The approximation of the refractive index of the *PCF* is the major factor limiting the accuracy of the calculated data [13]. The description of the refractive index profile of the fine structure of interfaces between domains with high contrast in the refractive indices must be very precisely because the effective index of the mode critically depends on it. Another drawback [24] of the Galerkin method is the great number of double integrals which must be solved.

To overcome these drawbacks a development of the application of the Galerkin method for *PCF* is proposed. The main idea is presented in [36–38] together with results from a numerical calculation of the fiber with one ring of circular holes and a comparison of the values of the effective index of the fundamental mode received by it and another numerical methods. Here a numerical calculation is presented by the development for *PCF* with two rings of circular holes. More over, expressions are given for an analytical calculation of the double integrals of the elements of the matrices of the modes of the *PCF* with holes with square and rectangular shapes and *PCF* with holes with arbitrary shapes approximated by layers of parallel rectangles rotated at different angles.

The expressions are obtained by an approach which considerably reduced the number of the doubles integrals in the case of holes with symmetrical shapes. The main idea for the proposed approach is outlined in [36, 37]. To overcome the loss of accuracy

* To whom all correspondence should be sent:
blzaf@issp.bas.bg

© 2015 Bulgarian Academy of Sciences, Union of Chemists in Bulgaria

and to reduce the calculation time, all integrals in the proposed development are analytically calculated in the case of holes with circular, square and rectangular shapes.

FORMULATION OF THE PROBLEM

A translationally invariant *PCF* consisting of N_h holes located in an optical medium (a host medium) is considered. Monochromatic light with angular frequency ω and time dependence $\exp(i\omega t)$ propagates along *PCF* in the direction of the axis z. It is looked for transverse distributions of the electric and the magnetic fields of the mode with respect to a Cartesian coordinate system xOy with an origin at the lower left angle of a rectangular material domain with dimensions L_x $(0 \le x \le L_x)$ and L_y $(0 \le y \le L_y)$ comprising the cross-section of *PCF* with an arbitrary location of the holes. It is assumed that the electric and the magnetic fields are zero at the domain boundaries. With an appropriate choice of its dimensions this approximation is reasonable due to the abrupt drop of the fields of the guided modes outside the core.

The electric and the magnetic fields of the mode are solutions of the vector wave equations:

$$\nabla^2\vec{E} + \nabla\left[\vec{E}.\frac{\nabla n^2}{n^2}\right] + n^2k^2\vec{E} = 0 \qquad (1)$$

$$\nabla^2\vec{H} + \left[\frac{\nabla n^2}{n^2} \times \left(\nabla \times \vec{H}\right)\right] + n^2k^2\vec{H} = 0 \qquad (2)$$

In the Cartesian coordinate system the vector equations are decomposed into x, y and z components, where the fact that $\partial n/\partial z = 0$ is used. The dependence of the components of the fields on the coordinate z is assumed to be $\exp(i\beta z)$, where β is the longitudinal constant of propagation.

It is looked for solutions of the transverse components of the electric and magnetic fields in the form:

$$E_x(x,y) = \sum_{\mu=1}^{\infty}\sum_{\nu=1}^{\infty} A^E_{\mu\nu}\Phi_{\mu\nu}(x,y) \qquad (3)$$

$$E_y(x,y) = \sum_{\mu=1}^{\infty}\sum_{\nu=1}^{\infty} B^E_{\mu\nu}\Phi_{\mu\nu}(x,y) \qquad (4)$$

$$H_y(x,y) = \sum_{\mu=1}^{\infty}\sum_{\nu=1}^{\infty} A^H_{\mu\nu}\Phi_{\mu\nu}(x,y) \qquad (5)$$

$$H_x(x,y) = \sum_{\mu=1}^{\infty}\sum_{\nu=1}^{\infty} B^H_{\mu\nu}\Phi_{\mu\nu}(x,y) \qquad (6)$$

where,

$$\Phi_{\mu\nu}(x,y) = \left[\frac{2}{(L_xL_y)^{1/2}}\right]\sin(\sigma_\mu x)\sin(\rho_\nu y) \qquad (7)$$

is a complete orthonormal set of sine functions which are orthogonal over the finite rectangular domain:

$$\int_0^{L_x} dx \int_0^{L_y} dy \Phi_{\mu\nu}(x,y)\Phi_{\mu'\nu'}(x,y) = \delta_{\mu\mu'}\delta_{\nu\nu'} \qquad (8)$$

$\sigma_\mu = (\mu\pi/L_x)$; $\rho_\nu = (\nu\pi/L_y)$; μ, ν are integers; $A^E_{\mu\nu}$, $B^E_{\mu\nu}$, $A^H_{\mu\nu}$, $B^H_{\mu\nu}$ are unknown coefficients in the expansions of the E_x, E_y, H_y and H_x respectively.

Using the Galerkin method, the two systems of two partial differential equations are converted into two systems each of $2m_xm_y$ coupled linear algebraic equations (m_x and m_y are the numbers of members in the truncated sums over μ and ν) for the unknown coefficients $A^E_{\mu\nu}$, $B^E_{\mu\nu}$, $A^H_{\mu\nu}$, $B^H_{\mu\nu}$ [39]

$$\sum_{\mu=1}^{m_x}\sum_{\nu=1}^{m_y}(M^E_{\mu'\nu',\mu\nu}A^E_{\mu\nu} + N^E_{\mu'\nu',\mu\nu}B^E_{\mu\nu}) = (\beta/k)^2A^E_{\mu'\nu'} \qquad (9)$$

$$\sum_{\mu=1}^{m_x}\sum_{\nu=1}^{m_y}(R^E_{\mu'\nu',\mu\nu}A^E_{\mu\nu} + S^E_{\mu'\nu',\mu\nu}B^E_{\mu\nu}) = (\beta/k)^2B^E_{\mu'\nu'}, \qquad (10)$$

$$\mu' = 1,2,...,m_x, \quad \nu' = 1,2,...,m_y.$$

$$\sum_{\mu=1}^{m_x}\sum_{\nu=1}^{m_y}(M^H_{\mu'\nu',\mu\nu}A^H_{\mu\nu} + N^H_{\mu'\nu',\mu\nu}B^H_{\mu\nu}) = (\beta/k)^2A^H_{\mu'\nu'} \qquad (11)$$

$$\sum_{\mu=1}^{m_x}\sum_{\nu=1}^{m_y}(R^H_{\mu'\nu',\mu\nu}A^H_{\mu\nu} + S^H_{\mu'\nu',\mu\nu}B^H_{\mu\nu}) = (\beta/k)^2B^H_{\mu'\nu'}, \qquad (12)$$

$$\mu' = 1,2,...,m_x, \quad \nu' = 1,2,...,m_y,$$

where:

$$M^E_{\mu'\nu',\mu\nu} = \frac{4}{S}\int_0^{L_x}dx\int_0^{L_y}dy\Big[(n^2 - n^2_{\mu\nu})P_{ssss} + 2\frac{\sigma_{\mu'}}{k^2}\ln(n)\left(\sigma_\mu P_{ccss} - \sigma_{\mu'}P_{ssss}\right)\Big] \qquad (13)$$

$$N^E_{\mu'\nu',\mu\nu} = \frac{8}{S}\frac{\sigma_{\mu'}}{k^2}\int_0^{L_x}dx\int_0^{L_y}dy\ln(n) \times (\rho_\nu P_{sccs} + \rho_{\nu'}P_{scsc}) \qquad (14)$$

$$R^E_{\mu'\nu',\mu\nu} = \frac{8}{S}\frac{\rho_{\nu'}}{k^2}\int_0^{L_x}dx\int_0^{L_y}dy\ln(n) \times (\sigma_\mu P_{cssc} + \sigma_{\mu'}P_{scsc}) \qquad (15)$$

$$S^E_{\mu'\nu',\mu\nu} = \frac{4}{S}\int_0^{L_x} dx \int_0^{L_y} dy \Big[(n^2 - n^2_{\mu\nu})P_{ssss} + 2\frac{\rho_{\nu'}}{k^2}\ln(n)(\rho_\nu P_{sscc} - \rho_{\nu'} P_{ssss})\Big] \quad (16)$$

$$M^H_{\mu'\nu',\mu\nu} = \frac{4}{S}\int_0^{L_x} dx \int_0^{L_y} dy \Big[(n^2 - n^2_{\mu\nu})P_{ssss} + 2\frac{\sigma_{\mu}}{k^2}\ln(n)(\sigma_{\mu'} P_{ccss} - \sigma_\mu P_{ssss})\Big] \quad (17)$$

$$N^H_{\mu'\nu',\mu\nu} = -\frac{8}{S}\frac{\rho_\nu}{k^2}\int_0^{L_x} dx \int_0^{L_y} dy \ln(n) \times (\sigma_\mu P_{cscs} + \sigma_{\mu'} P_{sccs}) \quad (18)$$

$$R^H_{\mu'\nu',\mu\nu} = -\frac{8}{S}\frac{\sigma_\mu}{k^2}\int_0^{L_x} dx \int_0^{L_y} dy \ln(n) \times (\rho_\nu P_{cscs} + \rho_{\nu'} P_{cssc}) \quad (19)$$

$$S^H_{\mu'\nu',\mu\nu} = \frac{4}{S}\int_0^{L_x} dx \int_0^{L_y} dy \Big[(n^2 - n^2_{\mu\nu})P_{ssss} + 2\frac{\rho_\nu}{k^2}\ln(n)(\rho_{\nu'} P_{sscc} - \rho_\nu P_{ssss})\Big] \quad (20)$$

$$n \equiv n(x,y) = \begin{cases} n_i = \text{const}, & x,y \in S_i, \\ n_{\text{host}} = \text{const}, & x,y \notin S_i \quad i = 1,2,...,N_h \end{cases}$$

n_i is the constant refractive index of the ith hole with the surface S_i, n_{host} is the constant refractive index of the host medium, $n^2_{\mu\nu} \equiv (\sigma^2_\mu + \rho^2_\nu)/k^2$ is a dimensionless quantity,

$$\begin{aligned} P_{ssss} &\equiv P_{ssss}(x,y) \\ &= \sin(\sigma_\mu x)\sin(\sigma_{\mu'} x)\sin(\rho_\nu y)\sin(\rho_{\nu'} y), \\ P_{ccss} &\equiv P_{ccss}(x,y) \\ &= \cos(\sigma_\mu x)\cos(\sigma_{\mu'} x)\sin(\rho_\nu y)\sin(\rho_{\nu'} y). \end{aligned}$$

The definitions of the remaining products are analogous.

Here the main idea of the development is briefly presented. Each of the integrals in Eq. (13) – Eq. (20) is a sum of double integrals over the host medium and over the holes in it. In Eq. (13) – Eq. (20) integrals over the holes surfaces are added and subtracted in which the refractive indices are replaced by the refractive index of the host medium in order not to integrate over the host medium:

$$\int_0^{L_x}\int_0^{L_y} f(x,y;n(x,y))dxdy = \int_0^{L_x}\int_0^{L_y} f(x,y;n_{\text{host}})dxdy + \sum_{i=1}^{N_h}\iint_{S_i}[f(x,y;n_i) - f(x,y;n_{\text{host}})]dxdy \quad (21)$$

e.g. the double integral over the domain with N_h interfaces is replaced by a sum of a double integral over a homogeneous medium with a surface S and a refractive index n_{host} (where the orthogonality of the sine functions can be used) and N_h homogeneous media with surfaces S_i, $i = 1,2,...,N_h$ with changed refractive indices. That gives a possibility for the exact refractive index profile of the cross section of the *PCF* to be taken into account and for the double integrals to be analytically calculated in the case of circular, square and rectangular shapes of the holes.

Then the expressions Eq. (13) – Eq. (20) can be written as:

$$M^E_{\mu'\nu',\mu\nu} = \frac{4}{S}\sum_{i=1}^{N_h+1}\Big[n^i_s I^i_{ssss} + 2\frac{\sigma_{\mu'}}{k^2}\ln(n^i_d) \times (\sigma_\mu I^i_{ccss} - \sigma_{\mu'} I^i_{ssss})\Big] \quad (22)$$

$$N^E_{\mu'\nu',\mu\nu} = \frac{8}{S}\sum_{i=1}^{N_h+1}\frac{\sigma_{\mu'}}{k^2}\ln(n^i_d)(\rho_\nu I^i_{sccs} + \rho_{\nu'} I^i_{scsc}) \quad (23)$$

$$R^E_{\mu'\nu',\mu\nu} = \frac{8}{S}\sum_{i=1}^{N_h+1}\frac{\rho_{\nu'}}{k^2}\ln(n^i_d)(\sigma_\mu I^i_{cssc} + \sigma_{\mu'} I^i_{scsc}) \quad (24)$$

$$S^E_{\mu'\nu',\mu\nu} = \frac{4}{S}\sum_{i=1}^{N_h+1}\Big[n^i_s I^i_{ssss} + 2\frac{\rho_{\nu'}}{k^2}\ln(n^i_d) \times (\rho_\nu I^i_{sscc} - \rho_{\nu'} I^i_{ssss})\Big] \quad (25)$$

$$M^H_{\mu'\nu',\mu\nu} = \frac{4}{S}\sum_{i=1}^{N_h+1}\Big[n^i_s I^i_{ssss} + 2\frac{\sigma_\mu}{k^2}\ln(n^i_d) \times (\sigma_{\mu'} I^i_{ccss} - \sigma_\mu I^i_{ssss})\Big] \quad (26)$$

$$N^H_{\mu'\nu',\mu\nu} = -\frac{8}{S}\sum_{i=1}^{N_h+1}\frac{\rho_\nu}{k^2}\ln(n^i_d)(\sigma_\mu I^i_{cscs} + \sigma_{\mu'} I^i_{sccs}) \quad (27)$$

$$R^H_{\mu'\nu',\mu\nu} = -\frac{8}{S}\sum_{i=1}^{N_h+1}\frac{\sigma_\mu}{k^2}\ln(n^i_d)(\rho_\nu I^i_{cscs} + \rho_{\nu'} I^i_{cssc}) \quad (28)$$

$$S^H_{\mu'\nu',\mu\nu} = \frac{4}{S}\sum_{i=1}^{N_h+1}\Big[n^i_s I^i_{ssss} + 2\frac{\rho_\nu}{k^2}\ln(n^i_d) \times (\rho_{\nu'} I^i_{sscc} - \rho_\nu I^i_{ssss})\Big], \quad (29)$$

where:

$$n^i_s = \begin{cases} n^2_i - n^2_{\text{host}}, & i = 1,2,\ldots N_h \\ n^2_{\text{host}} - n^2_{\mu\nu}, & i = N_h + 1 \end{cases};$$

$$n^i_d = \begin{cases} n_i/n_{\text{host}}, & i = 1,2,\ldots N_h \\ n_{\text{host}}, & i = N_h + 1 \end{cases};$$

$$I^i_{ssss} = \begin{cases} I^{S_i}_{ssss} = \iint_{S_i} P_{ssss}(x,y)dxdy, & i = 1,2,\ldots N_h \\ I^S_{ssss} = \iint_S P_{ssss}(x,y)dxdy, & i = N_h + 1 \end{cases}.$$

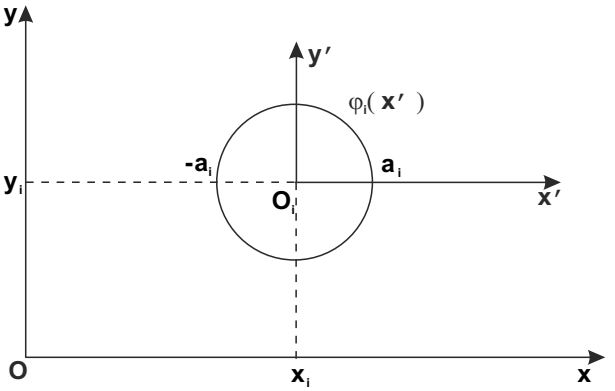


Fig. 1. A local coordinate system $x'O_iy'$ with an origin at the centre of the ith hole of the *PCF* and axes parallel to the axes of the global coordinate system xOy.

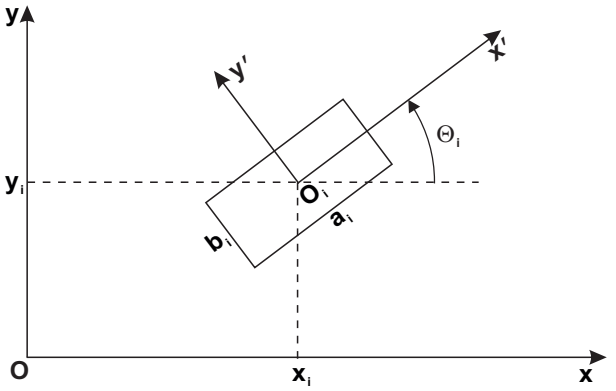


Fig. 2. A local coordinate system $x'O_iy'$ with an origin at the centre of the ith hole with a rectangular shape and axes rotated at an angle θ_i with respect to the axe x of the global coordinate system.

The number N_h+1 is referred to the material domain. The definitions of the remaining integrals are analogous.

Let us consider the ith hole. A local coordinate system is introduced with an origin at the centre of the ith hole and axes parallel to the axes of the global coordinate system xOy (Fig. 1) in the case of a circular hole and axes rotated at an angle θ_i with respect to the axe x of the global coordinate system (Fig. 2) in the case of a rectangular hole. It was shown in [36,37] that in the case of circular holes the double integrals in Eq. (22)-Eq. (29) can be reduced to four integrals I_{mm}, I_{mp}, I_{pm} and I_{pp}:

$$
\begin{aligned}
I^{S_i}_{ssss} &= (c_{mm}I_{mm} - c_{mp}I_{mp} - c_{pm}I_{pm} + c_{pp}I_{pp})/4\\
I^{S_i}_{ccss} &= (c_{mm}I_{mm} - c_{mp}I_{mp} + c_{pm}I_{pm} - c_{pp}I_{pp})/4\\
I^{S_i}_{sscc} &= (c_{mm}I_{mm} + c_{mp}I_{mp} - c_{pm}I_{pm} - c_{pp}I_{pp})/4\\
I^{S_i}_{sccs} &= (-s_{mm}I_{mm} + s_{mp}I_{mp} - s_{pm}I_{pm} + s_{pp}I_{pp})/4\\
I^{S_i}_{scsc} &= (s_{mm}I_{mm} + s_{mp}I_{mp} + s_{pm}I_{pm} + s_{pp}I_{pp})/4\\
I^{S_i}_{cssc} &= (-s_{mm}I_{mm} - s_{mp}I_{mp} + s_{pm}I_{pm} + s_{pp}I_{pp})/4\\
I^{S_i}_{cscs} &= (s_{mm}I_{mm} - s_{mp}I_{mp} - s_{pm}I_{pm} + s_{pp}I_{pp})/4
\end{aligned}
$$

where
$c_{jk} = \cos(\sigma_j x_i)\cos(\rho_k y_i)$, $s_{jk} = \sin(\sigma_j x_i)\sin(\rho_k y_i)$ are "address" functions depending only on the location of the holes with respect to the global coordinate system and

$$
I_{jk} = \int_{-a_i}^{a_i}\int_{-\varphi_i(x')}^{\varphi_i(x')} dx'dy' \cos(\sigma_j x')\cos(\rho_k y'),\ j,k = m,p
$$

are integrals which depend on the shape of the hole, but not on its location. Here x_i and y_i are the coordinates of the centre of the ith hole in the global coordinate system, a_i is its radius, $\varphi_i(x') = \sqrt{a_i^2 - (x')^2}$ and $\sigma_m \equiv \sigma_\mu - \sigma_{\mu'}$; $\sigma_p \equiv \sigma_\mu + \sigma_{\mu'}$; $\rho_m \equiv \rho_\nu - \rho_{\nu'}$; $\rho_p \equiv \rho_\nu + \rho_{\nu'}$. For all holes with identical shapes the four integrals can be solved only once. For completeness the expressions are given for an analytical calculation of the four integrals for circular holes:

$$
\begin{aligned}
I_{jk} &= \int_{-a_i}^{a_i}\int_{-\sqrt{a_i^2-(x')^2}}^{\sqrt{a_i^2-(x')^2}} dx'dy' \cos(\sigma_j x' + \rho_k y')\\
&= \frac{2\pi a_i}{\sqrt{\sigma_j^2+\rho_k^2}} J_1(a_i\sqrt{\sigma_j^2+\rho_k^2}) \quad j,k = m,p,
\end{aligned}
$$

where J_1 is the Bessel function of order 1. In the case of *PCF* with circular holes all integrals in the matrices elements are analytically solved.

When the hole is with square or rectangular shape or the arbitrary shape of the hole is approximated by a layer of parallel rectangles, rotated at an angle θ_i, then the double integrals in Eq. (22)-Eq. (29) are calculated by the following formulae:

$$
\begin{aligned}
I^{S_i}_{ssss} &= (u_{mm} - u_{mp} - u_{pm} + u_{pp})/2\\
I^{S_i}_{ccss} &= (u_{mm} - u_{mp} + u_{pm} - u_{pp})/2\\
I^{S_i}_{sscc} &= (u_{mm} + u_{mp} - u_{pm} - u_{pp})/2\\
I^{S_i}_{sccs} &= (-v_{mm} + v_{mp} - v_{pm} + v_{pp})/2\\
I^{S_i}_{scsc} &= (v_{mm} + v_{mp} + v_{pm} + v_{pp})/2\\
I^{S_i}_{cssc} &= (-v_{mm} - v_{mp} + v_{pm} + v_{pp})/2\\
I^{S_i}_{cscs} &= (v_{mm} - v_{mp} - v_{pm} + v_{pp})/2
\end{aligned}
$$

$$u_{jk} = c^{-}_{jk}A^{-}_{jk} + c^{+}_{jk}A^{+}_{jk}$$
$$v_{jk} = c^{-}_{jk}A^{-}_{jk} - c^{+}_{jk}A^{+}_{jk}$$
$$c^{\pm}_{jk} = \cos(\sigma_j x_i \pm \rho_k y_i)$$
$$A^{-}_{jk} = [\sin(p^{-}_{jk}a_i/2)/p^{-}_{jk}][\sin(q^{+}_{jk}b_i/2)/q^{+}_{jk}]$$
$$A^{+}_{jk} = [\sin(p^{+}_{jk}a_i/2)/p^{+}_{jk}][\sin(q^{-}_{jk}b_i/2)/q^{-}_{jk}]$$
$$p^{\pm}_{jk} = \sigma_j \cos\theta_i \pm \rho_k \sin\theta_i$$
$$q^{\pm}_{jk} = \sigma_j \sin\theta_i \pm \rho_k \cos\theta_i \quad j,k = m,p.$$

Here i is the successive number of the rectangle with dimensions a_i and b_i, rotated at an angle θ_i with respect to the axe x of the global coordinate system. When the holes with arbitrary shapes are approximated by layers of parallel rectangles all integrals are analytically solved with except of those referring to the rectangles comprising the irregular ends of the holes. There an averaging can be made over the parts of faces occupied by materials with different refractive indices before beginning of the calculations and the integrals can be analytically calculated for them. The systems of algebraic equations (9-12) are written in the form of matrix eigenvalue equations:

$$\widehat{C}^E\vec{X}^E = (\beta/k)^2\vec{X}^E; \quad \widehat{C}^H\vec{X}^H = (\beta/k)^2\vec{X}^H,$$

where

$$\widehat{C}^E \equiv \begin{pmatrix} \widehat{M}^E & \widehat{N}^E \\ \widehat{R}^E & \widehat{S}^E \end{pmatrix}; \quad \widehat{C}^H \equiv \begin{pmatrix} \widehat{M}^H & \widehat{N}^H \\ \widehat{R}^H & \widehat{S}^H \end{pmatrix};$$

$$\widehat{M}^E,\ \widehat{N}^E,\ \widehat{R}^E,\ \widehat{S}^E,\ \widehat{M}^H,\ \widehat{N}^H,\ \widehat{R}^H,\ \widehat{S}^H$$

are matrices consisting of the coefficients

$$M^E_{\mu'\nu',\mu\nu};\ N^E_{\mu'\nu',\mu\nu};\ R^E_{\mu'\nu',\mu\nu};\ S^E_{\mu'\nu',\mu\nu};$$

$$M^H_{\mu'\nu',\mu\nu};\ N^H_{\mu'\nu',\mu\nu};\ R^H_{\mu'\nu',\mu\nu};\ S^H_{\mu'\nu',\mu\nu};$$

$$\vec{X}^E = (\vec{A}^E, \vec{B}^E)^T \quad \text{and} \quad \vec{X}^H = (\vec{A}^H, \vec{B}^H)^T$$

are eigenvectors, consisting of the unknown coefficients $A^E_{\mu\nu}$; $B^E_{\mu\nu}$; $A^H_{\mu\nu}$; $B^H_{\mu\nu}$ and $(\beta/k)^2$ are unknown eigenvalues.

The method is reduced to a suitability for coding and is incorporated into a created single *Visual FORTRAN 6.5* code. It calculates matrices elements, modal effective indices and transverse components of both the electric and magnetic fields propagating along the *PCF*. *EISPACK* [40] is incorporated into the code and is used to solve the eigenvalue equations.

NUMERICAL RESULTS

The *PCF* under consideration consists of two rings of cylindrical air holes each with a diameter $d = 5.0\ \mu$m and a refractive index $n_i = 1.0\,(i = 1,2,\ldots,18)$, arranged in a hexagonal lattice with a constant (a pitch) $\Lambda = 6.75\ \mu$m within a host medium with a refractive index $n_{\text{host}} = 1.45$. The wavelength is $\lambda = 1.45\mu m$. The vector distribution of the transverse magnetic field

$$\vec{H}_t(x,y) = \vec{H}_x(x,y) + \vec{H}_y(x,y)$$

and the contour map of the magnetic field of the fundamental mode of the *PCF* with two rings of circular holes are shown in Fig. 3 and Fig. 4

The essential part of the results is shown in Table 1. It can be seen that the value of n_{eff} with smallest relative errors

$$\Delta_m = 3.1459 \times 10^{-8} \quad \text{and} \quad \Delta_L = -6.0466 \times 10^{-9}$$

Table 1. The convergence of the solution for n_{eff} of the fundamental mode of the *PCF* with two rings of holes

$\mathbf{L_x = L_y\,[\mu m]}$	$\mathbf{m_x = m_y}$	$\mathbf{n_{eff}}$	$\mathbf{\Delta_m}$	$\mathbf{\Delta_L}$
32.20	79	1.445396232634340	$1.1757E-08$	–
32.40	81	1.445396308797130	$2.1309E-08$	$5.2693E-08$
32.60	80	1.445396265103050	$3.5066E-08$	$-3.0230E-08$
32.80	81	1.445396247724620	$7.7172E-10$	$-1.2023E-08$
33.00	81	1.445396233574110	$1.0139E-08$	$-9.7901E-09$
33.20	81	1.445396224834410	$3.1459E-08$	$-6.0466E-09$
33.40	82	1.445396265177670	$3.4329E-08$	$2.7912E-08$
33.60	82	1.445396247763510	$3.2795E-08$	$-1.2048E-08$
33.80	82	1.445396221895270	$3.2206E-08$	$-1.7897E-08$
34.00	80	1.445395906427260	$4.0761E-08$	$-2.1826E-07$
34.20	80	1.445395820298730	$4.1892E-08$	$-5.9588E-08$

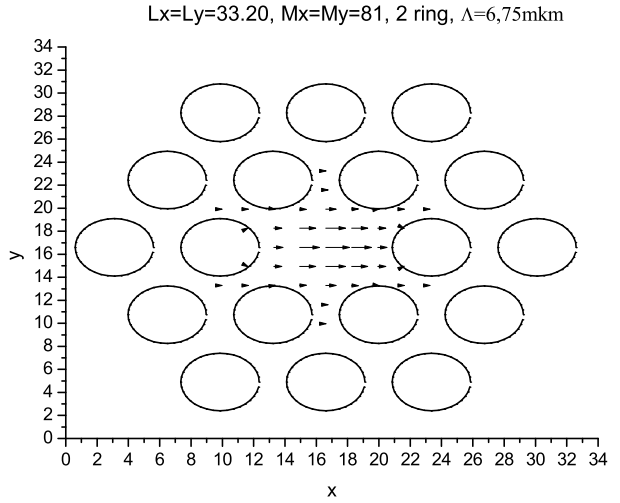


Fig. 3. The vector distribution of the transverse magnetic field $\vec{H}_t(x,y)$ (linearly polarized along the axe x) of the fundamental mode over the cross section of the *PCF* with two rings of holes.

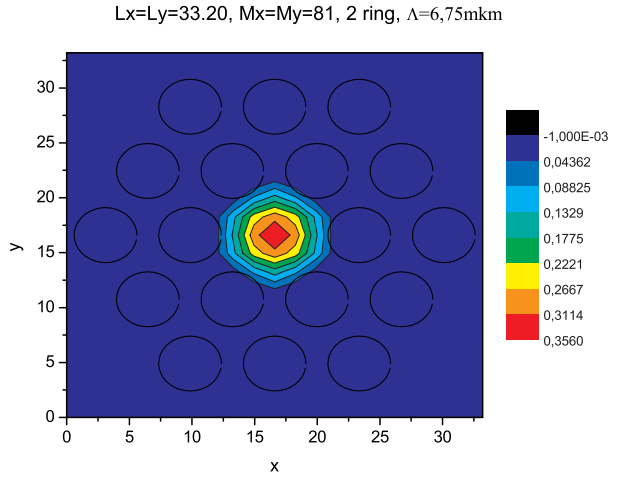


Fig. 4. A contour map of the magnetic field of the fundamental mode of the *PCF* with two rings of holes.

is a solution of the problem, $n_{\text{eff}} = 1.44539622$. Here Δ_m is the smallest relative error between two successive solutions with terms in their expansions which differs by 1 and Δ_L is the smallest relative error for two solutions at two successive values of the dimensions of the material domain which differs by 0.2 μm.

The three dimensional graphics of the magnetic field of the fundamental mode of the *PCF* with two rings of holes is shown on Figure 5.

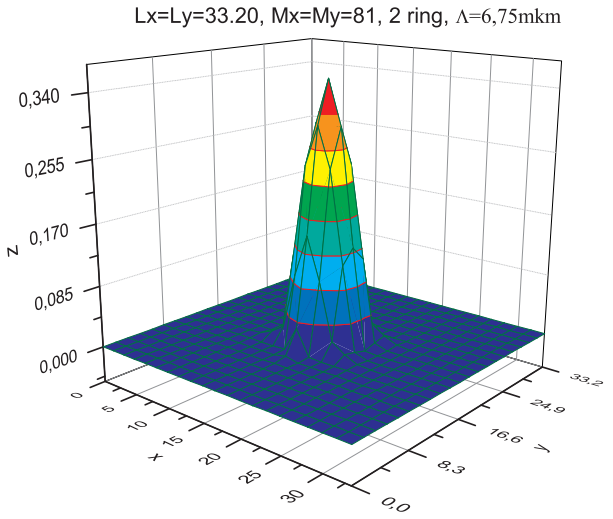


Fig. 5. The three dimensional graphics of the magnetic field of the fundamental mode of the *PCF* with two rings of holes.

The values of the effective refractive index of the fundamental mode of the *PCF* with one and two rings of holes, calculated by the proposed development, the *PWM* and the adjustable boundary condition method (*ABC*) are given in Table 2.

The effective index of the fundamental mode of the fiber with one ring of circular holes retains 7 digits when the number of the members in the expansions is changed by 1 and 11 digits when the dimensions of the material domain are changed in the process of the solution convergence. For the fiber with two rings the retained digits are 7 and 8 respectively. Taking into account the exact profile of the refractive index of the fiber and analytically calculating all integrals (i.e. the

Table 2. Comparison of the values of the effective index of the fundamental mode of the *PCF* under consideration

Method	Number of the rings	Reference	n_{eff}	Number of the members in the expansions	Relative Error in the solution convergence	Number of the retained digits
PWM	1	[16]	1.4453952	131072	10^{-6}-10^{-7}	
ABC	1	[41], [42]	1.445397228			7
Our Results	1	[38]	1.44539725467	68	$4\times10^{-8}/8\times10^{-12}$	7/11
	2		1.44539622	81	3×10^{-8}/-6×10^{-9}	7/8

matrices in the eigenvalue problems) the proposed development increases the accuracy of the calculation of the effective refractive index with one to two orders and reduces the number of the members in the expansions of the field with three orders in comparison with *PWM*.

The theoretical derived expressions for the holes with square or rectangular shapes are incorporated in the created code. Numerical calculations by this code both for entire holes and for parts of the holes will be the subject of future study.

CONCLUSION

It is presented a numerical calculation with the development of the Galerkin method in its application for modeling of *PCF*. The effective index of the fundamental mode of the fiber with two rings of holes with circular shape is calculated with a high accuracy: 7 digits retain when the number of the members in the expansion is changed by 1 and 8 digits retain when the dimensions of the material domain are changed in the process of the solution convergence. The relative error of the effective index of the fundamental mode of a *PCF* with two rings of holes is with less value than that of the effective index of the fundamental mode of a *PCF* with one ring of holes calculated by *PWM* with one to two orders and the number of the members of the expansions of the magnetic field in a *PCF* with two rings of holes is with less value than that in a *PCF* with one ring of holes used by *PWM* with three orders. It is shown also the vector distribution of the transverse magnetic field, its contour map and three-dimensional plot. The proposed expressions for an analytical calculation of the double integrals of the elements of the matrices of the modes of the *PCF* with holes with square or rectangular shapes and of the *PCF* with holes with arbitrary shapes approximated by layers of parallel rectangles rotated at different angles give a possibility for an accurate and fast calculation of the *PCF*. The high accuracy of the received results and the small number of members in the field expansion show that the proposed development can be successfully used for modeling of the *PCF*.

REFERENCES

[1] L. P. Shen, W. P. Huang and S. S. Jian, *IEEE Journal of Lightwave Technology* **21**, 1644–1651 (2003).

[2] R. K. Sinha and S. K. Varshney, *Microwave and Optical Technology Letters* **37**, 129–132 (2003).

[3] J. C. Knight, T. A. Birks, R. F. Cregan, P. S. J. Russell and J. P. de Sandro, *Electronics Letters* **34**, 1347–1348 (1998).

[4] M. Napierala, T. Nasilowski, E. Beres–Pawlik, F. Berghmans, J. Wojcik and H. Tienpont, *Optics Express* **18**, 15408–15418 (2010).

[5] J. Limpert, A. Liem, M. Reich, T. Schreiber, S. Nolte, H. Zellmer, A. Tiinnermann, J. Broeng, A. Peterson and C. Jakobsen, *Optics Express* **12**, 1313–1319 (2004).

[6] V. Tombelaine, A. Labruyere, J. Kobelke, K. Schuster, V. Reichel, P. Leproux, V. Couderc, R. Jamier and H. Bartelt, *Optics Express* **17**, 15392–15401 (2009).

[7] A. Ortigosa–Blanch, J. C. Knight, W. J. Wadsworth, J. Arriaga, B. J. Mangan,T. A. Birks and P. St. J. Russell, *Optics Letters* **25**, 1325–1327 (2000).

[8] T.P. Hansen, J. Broeng, E. Knudsen, A. Bjarklev, J. R. Jensen and H. Simonsen, *IEEE Photonics Technology Letters* **13**, 588–590 (2001).

[9] K. Suzuki, H. Kubota, S. Kawanishi, M. Tanaka and M. Fujita, *Optics Express* **9**, 676–680 (2001).

[10] Yi Ni, Lei Zhang, Liang An, Jiangde Peng and Ch. Fan, *IEEE Photonics Technology Letters* **16**, 1516–1518 (2004).

[11] M. D. Nilsen, C. Jacobsen, N. A. Mortensen, J. R. Folkenberg and H. R. Simonsen, *Optics Express* **12**, 1372–1376 (2004).

[12] W. J. Wodsworth, J. Knight and T. Birks, *Optics and Photonics News* **23**, 24–31 (2012).

[13] M. Szpulak, W. Urbanczyk, E. Serebryannikov, A. Zheltikov, A. Hochman, Y. Leviatan, R. Kotynski and K. Panajotov, *Optics Express* **14**, 5699–5714 (2006).

[14] Z. Zhu and T. G. Brown, *Optics Express* **8**, 547–554 (2001).

[15] A. Ferrando, E. Silvestre, J. J. Miret, M.V. Andrés and P. Andrés, *Optics Letters* **24**, 276–278 (1999).

[16] R. Kotynski, M. Dems and K. Panajotov, *Optical and Quantum Electronics* **39**, 469–479 (2007).

[17] A. Weisshaar, J. Li, R. L. Gallawa and I. C. Goyal, *IEEE J.of Lightwave Technology* **13**, 1795–1780 (1995).

[18] T. M. Monro, D. J. Richardson, N. G. R. Broderick and P. J. Bennett, *IEEE J.of Lightwave Technology* **18**, 50–56 (2000).

[19] M. Koshiba, Y. Tsuji and M. Hikari, *IEEE Transactions on Magnetics* **35**, 1482–1485 (1999).

[20] M. D. Feit and J. J. A. Fleck, *Applied Optics* **19**, 2240–2246 (1980).

[21] S. Guenneau, A. Nicolet, F. Zolla and S. Lasquellec, *Progress In Electromagnetics Research* **41**, 271–305 (2003).

[22] K. Saitoh, M. Koshiba, T. Hasegawa and E. Sasaoka, *Optics Express* **11**, 843–852 (2003).

[23] D. H. Choi and W. J. R. Hoefer, *IEEE Transactions on Microwave Theory and Techniques* **MTT-34**, 1464–1470 (1986).

[24] S. Guo, F. Wu, S. Albin, H. Tai and R. S. Rogowski, *Optics Express* **12**, 3341–3352 (2004).

[25] Z. Zhu and T. G. Brown, *Optics Express* **10**, 853–864 (2002).

[26] M. S. Stern, *IEE Proceedings J. Optoelectronics* **135**, 56–63 (1998).

[27] W.P. Huang and C.L. Xu, *IEEE J. Quantum Electronics* **29**, 2639–2649 (1993).

[28] K. Bierwirth, N. Schulz and F.Arndt, *IEEE Transactions of Microwave Theory and Technique* **34**, 1104–1113 (1986).

[29] H. Dong, A. Chronopoulos, J. Zou and A. Gopinath, *IEEE Journal of Lightwave Technology* **11**, 1559–1563 (1993).

[30] P. Lüsse, P. Stuwe, J. Schüle, and H. G. Unger, *Journal of Lightwave Technology* **12**, 487–493 (1994).

[31] K. S. Yee, *IEEE Transactions on Antennas and Propagation* **14**, 302–307 (1966).

[32] A. Hochman and Y. Leviatan, *JOSA A* **21**, 1073–1081 (2004).

[33] A. Hochman and Y. Leviatan, *JOSA B* **22**, 474–480 (2005).

[34] T. P. White, B. T. Kuhlmey, R. C. McPhedran, D. Maystre, G. Renversez, C. M. deSterke and L. C. Botten, *JOSA B* **19**, 2322–2330 (2002).

[35] B. T. Kuhlmey, T. P. White, G. Renversez, D. Maystre, L. C. Botten, C. Martijn de Sterke and R. C. McPhedran, *JOSA B* **19**, 2331–2340 (2002).

[36] E. Karakoleva, B. Zafirova and A. Andreev, *arXiv* 1302.250 [physics. optics] (2013).

[37] E. I. Karakoleva, B. S. Zafirova and A. T. Andreev, *Comptes rendus de l'Academie bulgare des Sciences* **66**, 667–678 (2013).

[38] E. I. Karakoleva, B. S. Zafirova and A. T. Andreev, *2nd National Congress on Physical Science* 25–29 September 2013, Sofia, Congress Proceedings, edited by T. M. Mishonov et al., Heron-Press, Sofia, 2014, Section: Physical Optics, Optical Methods, Optical Electronics, Article S065.

[39] D. Marcuse, *IEEE Journal of Quantum Electronics* **28**, 459–465 (1992).

[40] http://www.netlib.org/eispack/

[41] N. A. Issa and L. Poladian, *IEEE Journal of Lightwave Technology* **21**, 1005–1012 (2003).

[42] S. Campbell, R. C. McPhedran, C. M. deSterke and L. C. Botten, *JOSA B* **21**, 1919–1928 (2004).

ПРЕСМЯТАНЕ НА ФОТОННО-КРИСТАЛНИ ВЛАКНА С МЕТОДА НА ГАЛЕРКИН С РАЗЛОЖЕНИЕ ПО СИНУСОВИ ФУНКЦИИ БЕЗ АПРОКСИМАЦИЯ НА ПОКАЗАТЕЛЯ НА ПРЕЧУПВАНЕ

Е. Караколева, Бл. Зафирова, А. Андреев

Институт по физика на твърдото тяло "Акад. Г. Наджаков", Българска академия на науките, бул. "Цариградско шосе" №72, 1784 София, България

(Резюме)

Представени са резултати от пресмятане на основни характеристики на фотонно-кристално влакно с два пръстена от дупки с подход, който отчита точната зависимост на показателя на пречупване от напречните координати *x* и *y* на фотонно-кристално влакно. Теоретично са изведени формули за пресмятане на дупки с произволна форма чрез разделянето на материалната област в тях на правоъгълници, завъртяни на произволни ъгли спрямо глобална координатна система в равнината на напречното сечение на фотонно-кристалното влакно.

Bulgarian Chemical Communications, Volume 47, Special Issue B (pp. 29–34) 2015

Optical properties of thin PMMA films for sensor application

A. Lalova*, R. Todorov

Acad. J. Malinowski Institute of Optical Materials and Technologies, Bulgarian Academy of Sciences
Acad. G. Bonchev Str., BG-1113 Sofia, Bulgaria

In this paper we present results from the study of the optical properties of thin poly (methyl methacrylate) (PMMA) films deposited by conventional spin coating technique and their change during exposure to vapors of some solvents of PMMA, such as chloroform, acetone, methanol and ammonia. The optical constants (refractive index, n and extinction coefficient, k) and the thickness, d were calculated using the measured reflectance spectra, R of the thin films deposited on the Si wafer. The thickness dependence of the optical properties of the thin PMMA layers was investigated. The results for the optical constants showed that the refractive index of PMMA films thicker than 110 nm are independent of the film's thickness. The reflectance changes, $\Delta R/R$ of the thin films from poly (methyl methacrylate) following exposure to vapors of chloroform and methanol were investigated. The obtained results for $\Delta R/R$ were used to calculate the thickness changes of the thin PMMA films after exposure to vapors of different liquids. To explain the resulting change in the optical properties, the dissolution rate of PMMA film in different solutions (chloroform, acetone, methanol and ammonia) was investigated. It was found that the dissolution rate in chloroform and acetone was greater than 63 nm/s, while in methanol and ammonia, the thickness changes were within the experimental error for times greater than 60 min. On the basis of the results obtained the potential application of PMMA layers as building coatings in quarter wavelength optical stack working as optical sensor is discussed.

Key words: optical properties, thin films, PMMA, sensor properties

INTRODUCTION

The presence of volatile organic compounds (VOCs) in the environment as a result of their extensive use in industrial and commercial applications is not negligible. They are toxic and carcinogenic for human health. Detection of these vapors and gases in atmosphere has become an important environmental issue [1–3].

In gas sensing applications one of the most important parameters is the sensing layer which produces a signal during exposure to a toxic gas. In the last decade polymeric thin films have attracted interest for gas sensing applications because of their high sensitivity and selectivity [4, 5].

In terms of its gas sensing performance poly (methyl methacrylate) (PMMA) is a promising chemical material. It has recently been found that PMMA thin films obtained by spin coating and self-assembly are suitable candidates for the detection of several VOCs [6–8]. From the literature it is known that upon contact with chloroform thin PMMA films increase their thickness by $\Delta d = 13.6 - 19.7\%$ [6]. In previous works [9, 10] the possibility was shown for preparation of a Bragg stack from $As_{30}Ge_{10}S_{60}$/PMMA for the infrared spectral range and the potential for gas sensing application.

The subject of the investigation of the present work is to summarize the results of a study on the optical properties of PMMA and their changes during exposure to vapors of some liquids which are solvents of the PMMA such as chloroform, acetone, methanol and ammonia. The potential application as building coatings in 1D photonic crystal working as optical sensor was probed in a three-layered coating consisting from chalcogenide film/PMMA/chalcogenide film.

EXPERIMENTAL DETAILS

The stock solution of the polymer was prepared by dissolution of PMMA (Poly (methyl methacrylate)) in 20 ml of Dichloroethane (Aldrich) at ambient temperature using magnetic stirrer for accelerating the process. The polymer films with different thicknesses were obtained by the method of spin coating using the stock solution further diluted by adding dichloroethane. Polymer layers with thicknesses of 180 nm were obtained by dripping a drop of 0.3 ml of 3.2%w/v polymer solution on a preliminarily cleaned substrate. The speed and duration of spinning were 2500 rpm and 30 s. To remove the extra solvent the samples were annealed at 60 °C for 30 minutes.

The three-layered coatings consisting from chalcogenide film/PMMA/chalcogenide film were prepared by layer-by-layer deposition of As_2S_3 and PMMA. The bulk As_2S_3 glass was synthesized in

* To whom all correspondence should be sent:
alalova@iomt.bas.bg

© 2015 Bulgarian Academy of Sciences, Union of Chemists in Bulgaria

a quartz ampoule by the method of melt quenching from elements of purity 99.999% [11]. The chalcogenide layers were deposited by thermal evaporation at a deposition rate of 0.5–0.7 nm/s in vacuum of 10^{-3} Pa. The X-ray microanalysis shows that the film composition is close to that of the bulk samples. The thickness was controlled in situ by quartz oscillator monitoring and ex situ by optical and profiler measurements.

Transmittance, T and reflectance, R spectra of single layers and three-layered stacks were measured at normal and oblique incidence of light with a high precision UV-VIS-NIR spectrophotometer Cary 5E (the accuracy in T and R at normal incidence are 0.3% and 0.5%, respectively).

The spectrophotometer is equipped with a gas cell which allows in-situ measurements of the spectrophotometric quantities in the presence of a given gas.

RESULTS AND DISCUSSION

Reproducible deposition of the polymer layers by spin-coating technique necessary to create a calibration curve for the dependence of the thickness of the resulting layer on the concentration of the solution employed for the deposition. The knowledge of the optical parameters of the polymer films is very important for the adaptability of the material for different applications. The refractive index, n and extinction coefficient, k and the thickness, d of the spin-coated PMMA films deposited on Si wafer were determined through minimization of a function consisting of the discrepancies between measured and calculated R spectra using multi-wavelength nonlinear curve fitting [12]. For description of the refractive index the Sellmeier's equation was applied:

$$n^2(\lambda) = 1 + \frac{A_1\lambda^2}{\lambda^2 - A_2^2}, \qquad (1)$$

where A_1 and A_2 are the Sellmeier's coefficients. The dispersion of the extinction coefficient was described by the following exponential dependence:

$$k = B_1 \exp(B_2/\lambda), \qquad (2)$$

where B_1 and B_2 are dispersion coefficients The results for the calibration curve for the film's thickness are presented in Fig. 1. It is seen that the thickness of the spin-coated PMMA films depends on the concentration of the solution following a linear approximation.

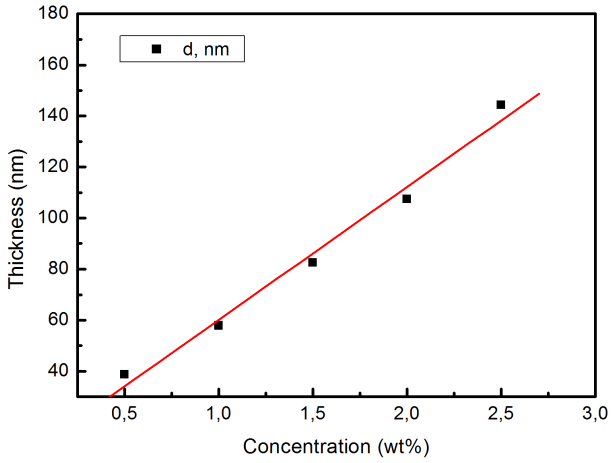


Fig. 1. Dependence of the thickness of the spin-coated PMMA film on the solution concentration.

The obtained dependence of the refractive index on the thickness of the polymer films is plotted in Fig. 2.

It is seen that the refractive index of thin PMMA films increase with the increasing of the thickness following an exponential low of the type $n = n_0 + A_1(1 - \exp(-d/d_1))$, where n_0 is the initial value of the refractive index, $A_1 = -0.90$ and $d_1 = 31.91$ are parameters. The values of the refractive index for films with thicknesses greater than 110 nm are close to that of the bulk material ($n_{\text{bulk}} \sim 1.49$) [13, 14]. It can be expected that with the increasing of the film's thickness the film's density increases, which is the most likely cause for the observed trend of the curve.

It is well known that PMMA swells when exposed to organic vapors [8, 15], which results in a shift of the reflection spectrum. Our next step was

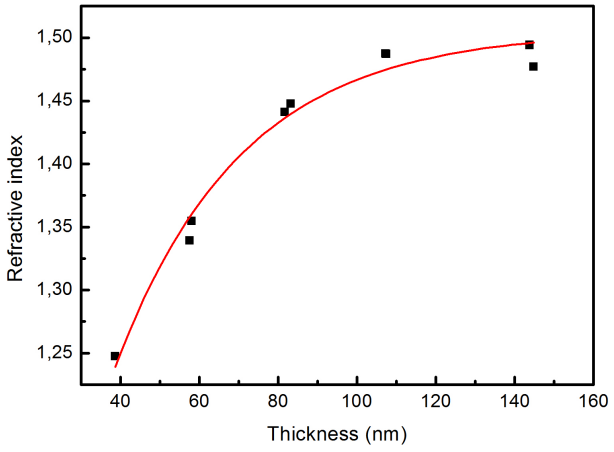


Fig. 2. Dependence of the refractive index on the thickness of thin spin-coated PMMA films at wavelength of 600 nm.

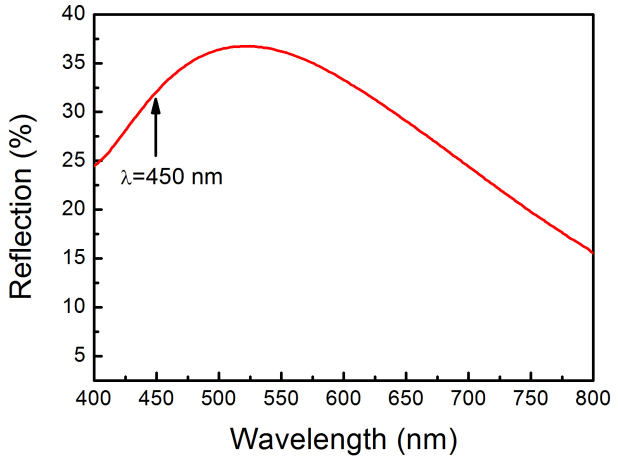


Fig. 3. Reflection spectra of a spin-coated PMMA film with thickness 180 nm on a glass substrate.

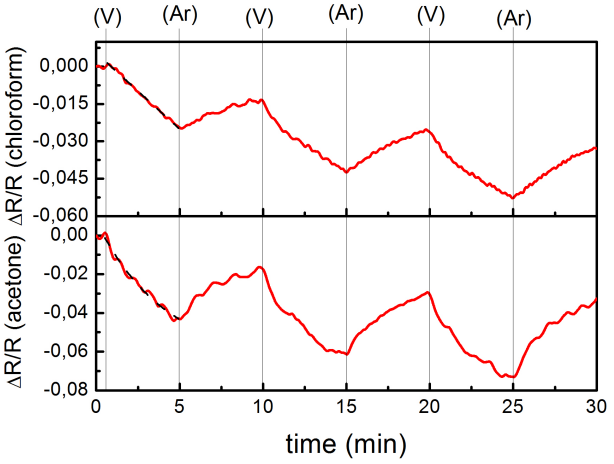


Fig. 4. Changes in the reflection at $\lambda = 450$ nm of a single PMMA film with thickness 180 nm exposed to methanol (a) and ammonia (b) vapors in argon atmosphere at temperature 0°C (V) and subsequent treatment with argon (Ar).

to investigate the changes of the optical properties of thin PMMA films during exposure to vapors of different substances in order to determine their ability for sensing of different vapors. We measured how the reflectance from PMMA films at a fixed wavelength changes as a result of the induced increasing of the thickness. The working wavelength was chosen to be in the steep part of the interference extreme where the value of the reflectance depend strongly on the wavelength and maximum changes in R can be expected (Fig. 3). We traced the change of the reflection at a wavelength of $\lambda = 450$ nm in dependence on the time of exposure to vapors. The reflectance measurement was performed in-situ, consecutively introducing vapors of liquid solvent putted at 0°C of the substance with argon and argon only in a gas cell for 5 minutes. We have performed three and more cycles for each substance. The results are plotted in Figs. 4 and 5.

It is seen in Fig. 4 that the time dependence of $\Delta R/R$ follows an exponential law of the type $y = y_0 + A_1 \exp(-x/t_1)$, where y_0 is the initial value of the reflectance, A_1 and t_1 are parameters. The determined values for A_1 were 0.072 and 0.020 for methanol and ammonia, respectively. The parameter t_1 has a physical meaning of diffusion coefficient of the vapors in the PMMA film. The values for t_1 were 0.64 min and 0.33 min for methanol and ammonia respectively.

After the third repetition of exposure to different vapors the changes in the reflection continued. The argon treatment following treatment with methanol Fig. 4 (a) and ammonia Fig. 4 (b) vapors is sufficient to restore the initial state of the reflectance spectra. From Fig. 4 it is seen that the changes in the reflection are $\Delta R/R = 3.7\%$ after exposure to methanol and $\Delta R/R = 1.3\%$ after exposure to ammonia.

The exposure of the PMMA films to the vapors of chloroform and acetone also leads to changes in the reflection (Fig. 5).

But in this case the argon treatment cannot restore the original state of the polymer film.

It is seen in Fig. 5 that the time dependence of $\Delta R/R$ follows again an exponential law of the type $y = y_0 + A_1 \exp(-x/t_1)$.

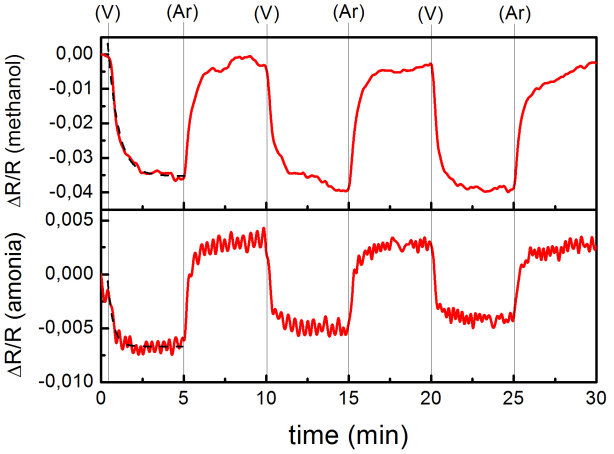


Fig. 5. Changes in the reflection at $\lambda = 450$ nm of a single PMMA film with thickness 180 nm exposed to chloroform (a) and acetone (b) vapors in argon atmosphere at temperature 0°C for 5 minutes (V) and subsequent treatment with argon for 5 minutes (Ar).

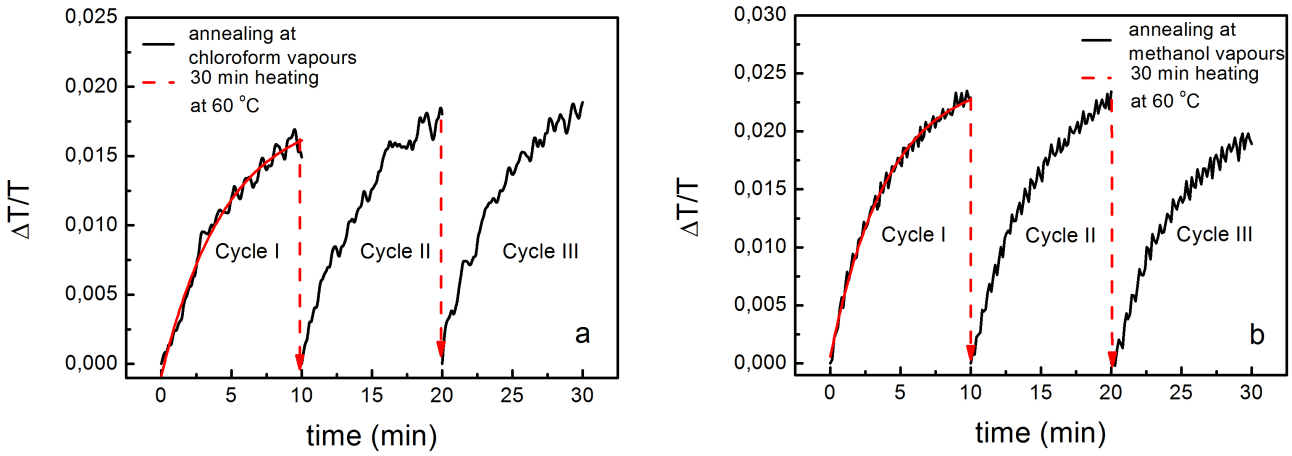


Fig. 6. Time dependence of the transmittance of three-layered coatings from As_2S_3 and PMMA with thicknesses 54 nm and 180 nm respectively exposed to chloroform (a) and methanol (b) vapors in argon atmosphere at 0°C. The annealing procedures at 60°C for 30 minutes are only signed with dot lines.

The determined values for A_1 were 0.32575 and 0.072 for chloroform and acetone, respectively. The diffusion parameter t_1 is estimated at 4.74 min and 4.13 min for chloroform and acetone respectively. The vapors of chloroform and acetone demonstrated significantly higher values for t_1 than those for methanol and ammonia.

The results plotted on Fig. 5 show changes in the reflection, $\Delta R/R$ of 2.5% at exposure to chloroform vapors (a) and $\Delta R/R = 4.5\%$ at exposure to acetone vapors (b). It is seen that the treatment with argon recovers about 50% of the initial state of the polymer film.

Considering the type of the curves following treatment two groups of reagents of the chosen substances may be distinguished. It is known that all of the investigated substances – methanol, ammonia, chloroform and acetone are solvents of PMMA. To determine how they reacted with the PMMA films we investigated the dissolution rate of 180 nm polymer film in liquid solvents. The experiment consists in immersing the film in a given solvent for an exact time. The reflection spectrum of treated film was collected afterwards and the thickness and optical constants were calculated by the above-described procedure. The dissolution rate was determined as:

$$V = |d_1 - d_0| / \tau, \qquad (3)$$

where d_0 and d_1 are the film's thicknesses before and after immersion in the solvent, respectively, τ is the duration of the treatment. For methanol and ammonia, we established that the thickness changes are within the experimental error for treatment longer than 60 min, while the dissolution rate of films from the second group (chloroform and acetone) is 63 nm/s.

In a prior work [16, 17] we demonstrated the potential application of the thin PMMA layers as building coatings in a quarter wavelength optical stack working as optical sensor and the permeability of the thin As_2S_3 film to chloroform. It is necessary to demonstrate a method to restores the original state of the structure. To this end, three-layer coatings consisting of As_2S_3/PMMA/As_2S_3/glass substrate were prepared. The relative changes of the transmittance in chloroform (a) and methanol (b) vapors are shown in Fig. 6. Since the presence of the As_2S_3 film delays the reaction of the PMMA [17], for removing the absorbed vapors we heated the structure at 60 degrees for 30 minutes.

It is seen in Fig. 6 that the time dependence of $\Delta T/T$ follows an exponential law of the type $y = y_0 + A_1 \exp(-x/t_1)$, where A_1 is -0.019 and -0.024 for chloroform and methanol respectively. The values for t_1 are 4.59 min for chloroform and $t_1 = 4.06$ min for methanol.

After exposure of the three-layer system to vapors it was found that the changes after the third iteration are similar for both kinds of vapor and also that the thermal treatment restores the original state of the coating. It is seen in Fig. 6 that the relative change of the transmittance is $\Delta T/T = 1.7\%$ after exposure to chloroform vapors and after exposure to methanol vapors – 2.2%.

CONCLUSIONS

In the present work the optical properties of thin PMMA films and their changes due to exposure to vapors of some solvents of PMMA are investigated. It was found that the refractive index is thickness dependent for values of $d < 110$ nm. For thin films with thickness greater than 110 nm the coatings possess refractive index close to that of the bulk. The changes of the optical properties during exposure to vapors of chloroform, acetone, methanol and ammonia were followed. When the thin polymer films were exposed to vapors of methanol or ammonia and subsequently treated in argon restoration of their initial state was observed for many cycles. In the case of treatment with chloroform or acetone, again cyclic changes were displayed but the treatment with argon restores only 50% from the initial state of the reflectance spectrum. The obtained changes in the reflectance spectrum were in the range of 1.3–4.5%. Maximal values were observed after exposure to vapors of methanol and acetone. The potential application of a three-layered coating consisting from chalcogenide film/PMMA/chalcogenide film as building stack for 1D photonic crystal working as optical sensor was probed. It was found that the changes after exposure of the multilayered coatings to the vapors of the chloroform and methanol showed good cyclic properties as the treated films must be annealed at 60°C for 30 minutes. The magnitude of the obtained changes observed in the reflectance of the three layered coatings was the similar (1.7–2.2%) to that of the single polymer films.

REFERENCES

[1] Y. Li, T. Zhang and P. Liang, *Anal. Chim. Acta* **536**, 245-249 (2005).

[2] A. Lua, J. Liu, D. Zhao, Y. Guo, Q. Li and N. Li, *Catal. Today* **90**, 337-342 (2004).

[3] M. H. China, C. C. Liu, T. C. Chou, *Biosens. Bioelectron.* **20**, 25-32 (2004).

[4] B. Adhikari and S. Majumdar, *Prog. Polym. Sci.* **29**, 699-766 (2004).

[5] D. N. Debarnot and F. P. Epaillard, *Anal. Chim. Acta* **475**, 1-15 (2003).

[6] R. Capan, A. K. Ray, A. K. Hassan and T. Tanrisever, *J. Phys. D: Appl. Phys.* **36**, 1115-1119 (2003).

[7] İ. Capan, C. Tarimci and T. Tanrisever, *Sensor Lett.* **5**, 533-537 (2007).

[8] İ. Capan, C. Tarimci, A. K. Hassan and T. Tanrisever, *Mater. Sci. Eng. C* **29**, 140-143 (2009).

[9] R. Todorov, J. Tasseva and Tz. Babeva, "Thin Chalcogenide Films For Photonic Applications" in *Photonic Crystals-Innovative Systems, Lasers and Waveguides*, edited by Dr. Eng. Alessandro Massaro, INTECH, Rijeka, Croatia, 2012, pp. 143-168.

[10] T. Babeva, G. Marinov, J. Tasseva, A. Lalova and R. Todorov, *J. Phys.: Conf. Ser.* **398**, art. num. 012025 (2012).

[11] R. Todorov and K. Petkov, *J. Optoelectron. Adv. Mater.* **3**, 311-317 (2001).

[12] T. Babeva, R. Todorov, S. Mintova, T. Yovcheva, I. Naydenova and V. Toal, *J. Opt. A: Pure Appl. Opt.* **11**, art. num. 024015 (8pp) (2009).

[13] C. B. Walsh and E. I. Franses, *Thin Solid Films* **347**, 167-177 (1999).

[14] C. B. Walsh and E. I. Franses, *Thin Solid Films* **429**, 71-76 (2003).

[15] I. Capan, C. Tarimci, M. Erdogan and A. K. Hassan, *Mat. Sci. Eng. C* **29**, 1114-1117 (2009).

[16] A. Lalova and R. Todorov, *Bulg. Chem. Commun.* **45**, 59-62 (2013).

[17] A. Lalova and R. Todorov, *J. Phys. Conf. Ser.* **514**, art. num. 012014 (2014).

ИЗСЛЕДВАНЕ НА ОПТИЧНИТЕ СВОЙСТВА НА ТЪНКИ PMMA СЛОЕВЕ ЗА ПРИЛОЖЕНИЕТО ИМ КАТО СЕНЗОРИ

А. Лалова, Р. Тодоров

Институт по оптически материали и технологии "Акад. Йордан Малиновски", Българска академия на науките, ул. "Акад. Г. Бончев" бл. 109, 1113 София, България

(Резюме)

В настоящата работа са представени резултати от изследването на оптичните свойства на тънки ценрофужно отложени тънки филми от poly (methyl methacrylate) (PMMA) и тяхната промяна при взаимодействие с пари на хлороформ и метанол. Оптичните константи (показател на пречупване, n и коефициент на поглъщане, k) и дебелината, d са изчислени от измерените спектри на отражение R, за слоеве, отложени върху силициева подложка. Резултатите показват, че показателят на пречупване за тънките филми с дебелина над 110 nm съвпада с този на обемния материал. Проследена е относителната промяната на коефициента на отражение $\Delta R/R$ при излагане на тънки филми от poly(methyl methacrylate) на пари на хлороформ и метанол. От получените резултати за $\Delta R/R$ са пресметнати промените в дебелината на тънките слоеве след третирането им. За да бъдат обяснени получените промени в оптичните свойства е изследвана скоростта на разтваряне на тънки слоеве от PMMA в различни разтворители (хлороформ, ацетон, метанол, амоняк). Установено е, че в хлороформ и ацетон скоростта на разтваряне на покритията е по-голяма от 63 nm/s, докато в метанол и амоняк промените в дебелината са в рамките на грешката за времена по-големи от 60 min. На основа на получените резултати е обсъдено потенциалното приложение на слоеве PMMA, като градивен елемент в четвърт вълнови оптични стекове, работещи като оптични сензори.

Bulgarian Chemical Communications, Volume 47, Special Issue B (pp. 35–39) 2015

Using double resonance long period gratings to measure refractive index of milk of varying fat content

E. V. Penchev[1]*, W. J. Bock[2], T. A. Eftimov[3], P. Mikulic[2]

[1] *University of Food Technology, BG-4000 Plovdiv, Bulgaria*
[2] *Photonic Research Center, Université du Québec en Outaouais, Gatineau, Canada*
[3] *Plovdiv University, BG-4000 Plovdiv, Bulgaria*

We have studied the possibility to measure the refractive index of milk using double resonance (DR) long period fiber grating (LPG) characterized by a higher refractometric sensitivity around water refractive index values. DR LPGs are characterized by a turning point beyond which the resonance minimum splits into two minima which shift in opposite directions for surrounding refractive index (SRI) changes to which they can be highly sensitive. Due to this DR LPGs are a promising platform for bacteria sensing that allows the implementation of lab-on-the-fiber concept. Similar application for milk analysis requires the measurement of milk refractive index for different fat content levels. We have applied direct center wavelength (CW) shift method and the differential signal method to track RI changes and compared the values obtained with a standard Abbe refractometer. CW shift as high as 5 nm were obtained for a fat content varying from 0.1% to 3.5%.

Key words: double resonance (DR) long period fiber grating (LPG), refractive index, sensors

INTRODUCTION

Fiber optic (FO) sensor technology has advanced dramatically in the area of biochemical sensing [1]. Among the variety of sensing transducer types are long period gratings (LPG) [2] because, similarly to core-cladding intermodal sensors [3, 4], they exhibit a very high sensitivity to surrounding refractive index (SRI) changes. Sensing the presence of bacteria such as *Escherichia Coli* and Staphilococcus then naturally becomes feasible and desirable with suitable FO sensors. In particular, the importance of sensing *E. Coli* bacteria in milk has been of interest worldwide for decades [5–7]. So far the method mostly employed for FO E-Coli sensors is based on fluorescence [8, 9]. However, the recently demonstrated sensitivity of about 2322 nm/r.i.u. with double resonance (DR) LPGs has enabled their successful application to bacteria in water [10] and it has been possible to measure bacteria concentration rather than just the detection of *E. Coli* presence [10]. With the far higher theoretically possible sensitivity to SRI, DR LPGs become a promising transducer for bacteria sensing in milk and dairy products. The principle for bacteria sensing is immobilization of phages on the surface of a double resonance LPG and when immersed in water infected with *E. Coli*, the latter are selectively captured by the phage. The accumulation of bacteria on the LPG surface changes the refractive index which in turn causes center wavelength down shifts of the LPG. The wavelength shifts are measured by an OSA and a spectrometer, and are a measure of the bacteria concentration. To achieve maximum sensitivity of the LPG it is made in a way that its turning point is around the refractive index of water in which the bacteria is to be detected. This is done by deliberate controlled etching of the LPG. However, if *E. Coli* is to be measured in milk, then it matters what the refractive index of milk is and how it varies with fat content.

The purpose of the present work is to measure refractive index changes of milk with varying fat content using the same type of DR LPGs as the ones used to sense the concentration of *E. Coli* [10].

EXPERIMENTAL SET-UP

The experimental set-up to take the measurements consists of a 16-channel LPG interrogation unit which uses an InGaAs CCD unit [11]. The two LPGs (LPG1 and LPG2) are connected to port 1 and 10 respectively, while Port 16 is used for taking a reference measurement with respect to the spectrum of the internal C+L (1522-1622 nm) band ASE broadband source.

The LPG spectrum is observed in a reflection mode using a fiber mirror deposited at one end of a tunable air-gap attenuator. In this way if the signal from the source is too strong it can be attenuated to

* To whom all correspondence should be sent:
emil.penchev@abv.bg

© 2015 Bulgarian Academy of Sciences, Union of Chemists in Bulgaria

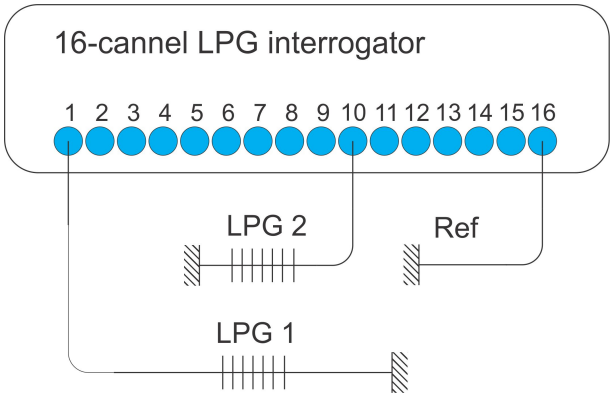


Fig. 1. Experimental set-up.

a desirable level. Before taking measurements, first a reference signal was taken through channel 16 using a fiber jumper. Next spectra of the double resonance LPGs were taken in air with an RI = 1. It is characteristic of this type of gratings to be observable after immersed in water or in a liquid with a higher RI.

The first thing we must do is to calibrate the LPG. To calibrate the LPG we measure its spectrum response to different surrounding refracting index (SRI) as it is shown in Fig. 2. In the spectral range only the left side of the double resonance is seen. The right side is beyond 1622 nm and is out of the range of the interrogator. The calibration is made using glycerin-water solutions with different concentration and correspondingly different refracting indices. What we can see in Fig. 2 is that the spectrum response of the LPG is shifting to smaller wavelengths when SRI increases. Then the spectral responses with increasing values of the RI were taken for each grating. To measure the spectral shifts we take the wavelengths at a given loss level for example -15 dB on either side of the minimum.

Having the spectral responses of the LPGs over a range of SRIs, we can determine the wavelength shifts at the level of -15 dB for the left and the right sides of the minimum and the average. As we can see in Fig. 3 when SRI is increasing the negative spectral shifts increase as well. The changes of the spectral shifts vs. SRI are linear for the both sides and their average (Fig. 3). It is evident that the spectral shifts are not symmetrical and the right side shifts more than the left side. This changes the shape and width of the DR LPG. For LPG1 the sensitivity to SRI of the right side is $S_n = -1530.7$ nm/r.i.u. and of the left side $S_n = -698.87$ nm/r.i.u. The average sensitivity is $S_{\text{avg}} = -1114.8$ nm/r.i.u. Since the LPG has two resonances, the minimum-to-minimum shifts is double i.e. -2229.6 nm/r.i.u. However, if the internal slopes' shifts of the double resonances are measured the sensitivity would be -3061.4 nm/r.i.u. With a resolution of 0.1 nm that is easily attainable by the LPG multichannel interrogator a sensitivity of around 3.3×10^{-5} r.i.u can be obtained for double resonance tracking or 6.6×10^{-5} r.i.u for single resonance tracking.

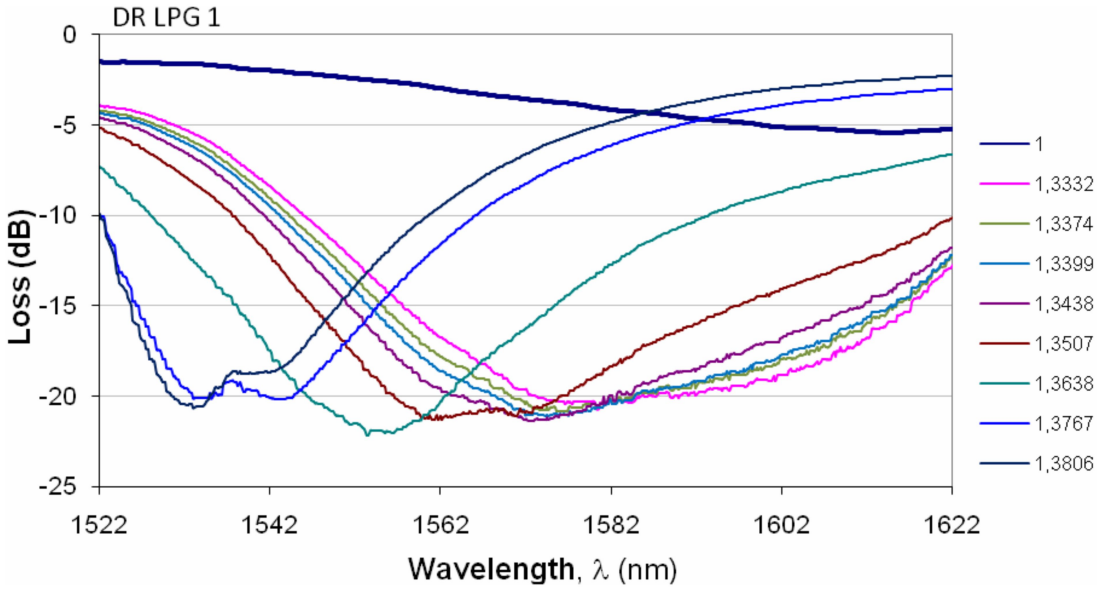


Fig. 2. Spectral response of DR LPG 1 over different SRI.

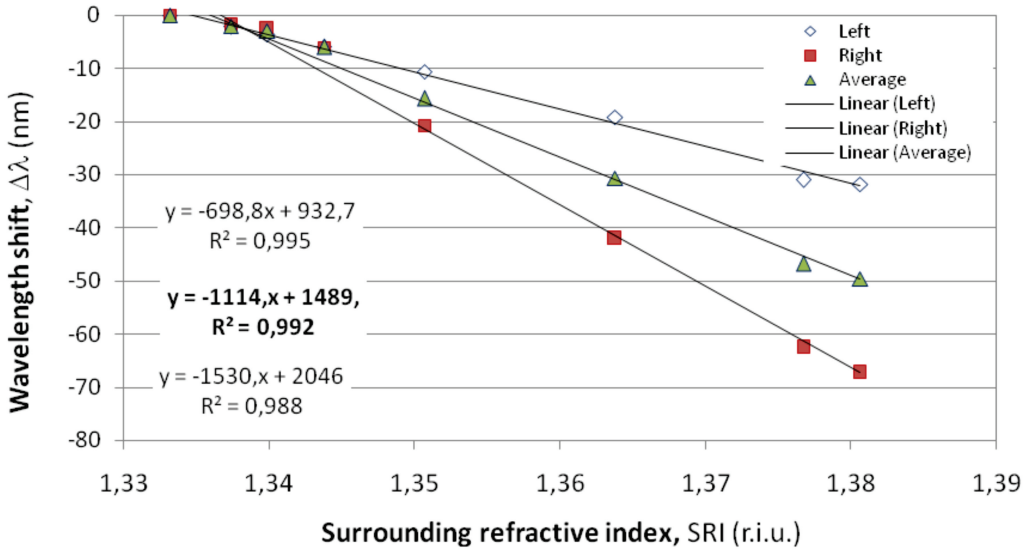


Fig. 3. Wavelength changes at -15 dB for the left and right sides of the minimum and their average for DR LPG 1.

Having determined the sensitivities of the LPG, we measure the spectral changes caused by water and four different fat contents namely 0.1%, 1%, 2% and 3.25%). All measurements were taken at room temperature.

We perform the same spectral measurements for milk with a different fat concentration levels. When the concentration of fat in milk increases the refractive index of the milk increases and the higher concentration, the higher refractive index. That can be seen in Fig. 3. Thus, when the concentration of fat in milk increases, the minimum of the spectral response shifts to smaller wavelengths. Also, the widths of the grating's spectrum become narrower, which means that the right side of the spectrum shifts at a higher rate.

In this case again we measure the wavelength shifts to the right and to the left of the minimum. Then we determine the corresponding refractive indices by placing the points on the Wavelength vs. SRI plots from Fig. 2. This is shown in Fig. 5. for the left and right side shifts. For greater accuracy the curve fitting is polynomial.

Fig. 6 shows the final dependence of the milk refractive index vs. the percentage of the fat contents for both LPGs.

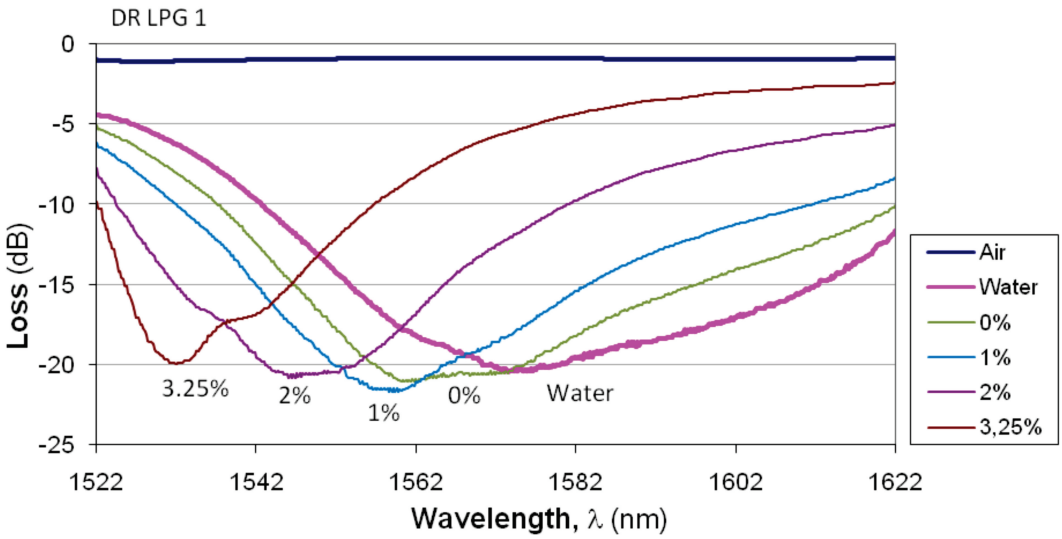


Fig. 4. Spectrum response of DR LPG 1 to milk with different fat concentrations.

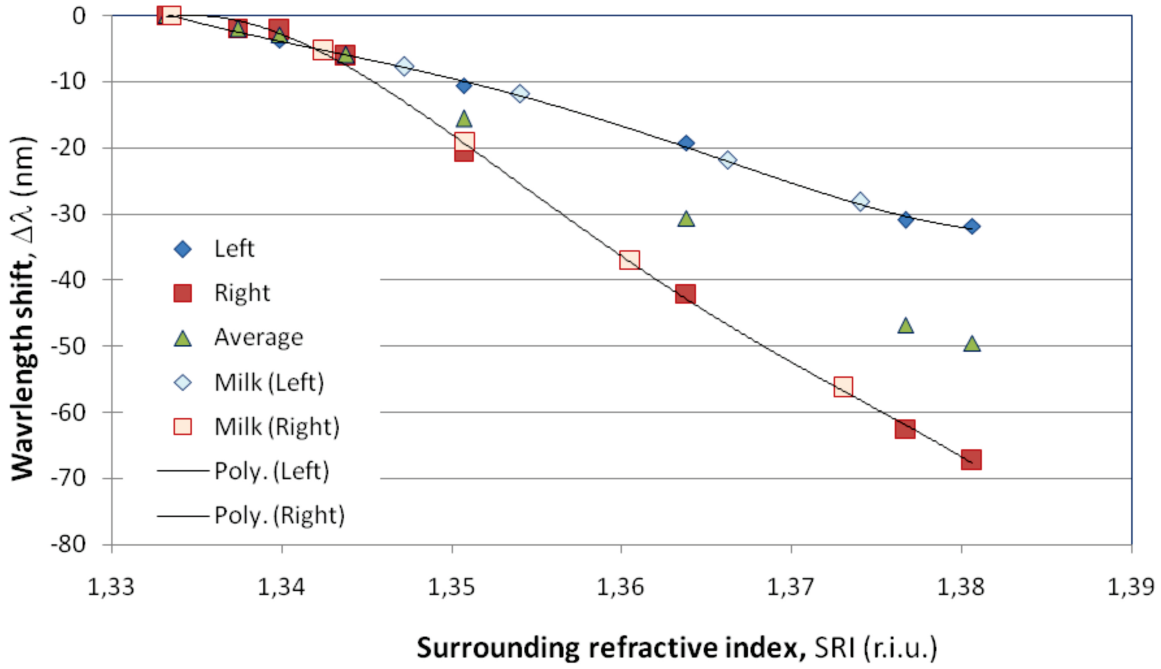


Fig. 5. Wavelength changes at -15 dB for the left and right sides of the minimum and their average for DR LPG 1 dipped in milk with different fat concentration.

For both gratings the dependence of the milk refractive index on the percentage of fat is linear and both gratings provide practically the same results.

These results are particularly important in view of the fact that milk is a turbid media and LPGs can be multiplexed spectrally and spatially as in this case which permits to track changes during different technological processes.

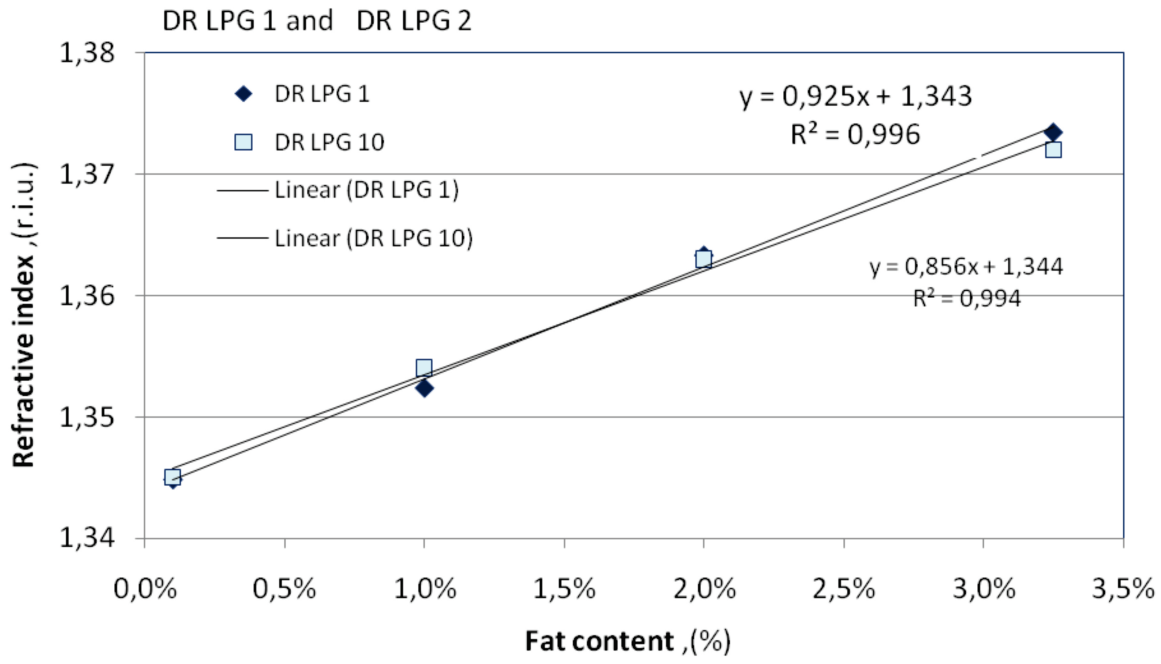


Fig. 6. Dependence of milk refractive index vs. fat content.

CONCLUSION

Our experiments allow the formulation of the following conclusions:

1. The refractive index of raw cow milk can successfully be measured making use of high SRI sensitivity double resonance LPGs
2. The increase of the fat content of raw milk causes a linear increase of the refractive index
3. To measure bacteria concentration in raw milk the DR LPGs must be manufactured with a maximum sensitivity around different refractive indices depending on the fat content.

REFERENCES

[1] D. J. Monk and D. R. Walt, *Anal. Bioanal. Chem.* **379**, 931–945 (2004).

[2] T. Eftimov, "Application of fiber gratings in Chemical and Biochemical Sensing" in *Optical Guided-wave Chemical and Biosensors II*, Vol. 8, edited by Mohammed Zourob and Akhlesh Lakhtakia, Springer Verlag, 2010, pp. 151–176.

[3] M. Smietana, D. Brabant, W. Bock, P. Mikulic and T.Eftimov, *J. Lightwave Techn.* **30**, 1185–1189 (2012).

[4] T. A. Eftimov, W. J. Bock, E. Penchev, "Bent fused fiber taper intermodal interferometer as a refractive index sensor" in *Proc. of 23rd Int. Conf. on Optical Fiber Sensors, OFS-23, Santander, Spain, 2–6 June 2014*, SPIE 9157, P27/Paper 9157 – 233.

[5] I. Gogol, *Vet. Med. Nauki.* **15**, 82–86 (1978).

[6] A. H. Soomro, M. A. Arain, M. Khaskheli and B. Bhutto, *Pakistan Journal of Nutrition* **1**, 151–152 (2002).

[7] R. Kumar and A. Prasad, *Veterinary World* **3**, 495–496 (2010).

[8] K. Miyajima, T. Koshida, T. Arakawa, H. Kudo, H. Saito, K. Yano and K. Mitsubayashi, *Anal. Bioanal. Chem.* **379**, 931–945 (2004).

[9] T. Geng, Joe Uknalis, S.-I Tu and A. K. Bhunia, *Biosensors* **3**, 120–131 (2013).

[10] S. M. Tripathia, W. J. Bock, P. Mikulic, R. Chinnappan, A. Ng, M. Tolba, M. Zourob, *Biosensors and Bioelectronics* **35**, 308–312 (2012).

[11] V. Plachkova, P. Balzhiev, G. Dyankov, T. Eftimov and P. Petrov, "Study of the performance of a 16-channel fiber-optic (FO) system for interrogation of long period gratins sensor networks (LPGSN)" in *Proc. National Conference in Physics 2014*, Plovdiv, Bulgaria.

ИЗПОЛЗВАНЕ НА ДЪЛГО-ПЕРИОДИЧНА РЕШЕТКА С ДВОЕН РЕЗОНАНС ЗА ИЗМЕРВАНЕ ПОКАЗАТЕЛЯ НА ПРЕЧУПВАНЕ НА МЛЕКА С РАЗЛИЧНО СЪДЪРЖАНИЕ НА МАЗНИНИ

Е. Пенчев[1], В. Бок[2], Т. Ефтимов[3], П. Микулич[2]

Стопански факултет, Университет по хранителни технологии, бул. "Марица" №26, 4002 Пловдив, България

[2] *Photonic Research Center, Université du Québec en Outaouais, Gatineau, Canada*

[3] *Физически факултет, Пловдивски университет "Паисий Хилендарски", ул. "Цар Асен" №24, 4000 Пловдив, България*

(Резюме)

В настоящата статия сме проучили възможността за измерване на коефициента на пречупване (RI) на мляко, като за целта сме използвали дълго-периодична решетка (LPG) с двоен резонанс (DR), която се характеризира с по-висока рефрактометрична чувствителност около коефициента на пречупване на вода. Дълго-периодичните решетки с двоен резонанс се характеризират с това, че при определена стойност на показателя на пречупване на околната среда резонансният минимум се разделя на два минимума, които се отместват в противоположни посоки с повишаване на показателя на пречупване, към който те могат да бъдат много чувствителни. Поради тази причина DR LPGs са подходящи за сензори за детектиране на бактерии. Подобни приложения за анализ на мляко изискват измерване на показателя на пречупване на млека с различно съдържание на мазнини. Използвали сме метода за директно следене на дължината на вълната при изместване на централния максимум (CW) и метода за диференциално следене на сигнал за проследяване на промени на RI. Получените резултати сме сравнили със стойностите, получени със стандартен *Abbe* рефрактометър. Установихме, че при промяна на съдържанието на мазнини от 0.1% до 3.5%, централният максимум се измества с около 5 nm.

Bulgarian Chemical Communications, Volume 47, Special Issue B (pp. 40–43) 2015

Optical properties of thin Ag/As-S-Ge films

R. Todorov*, A. Lalova, V. Lozanova

Acad. J. Malinowski Institute of Optical Materials and Technologies, Bulgarian Academy of Sciences
Acad. G. Bonchev Str., BG-1113 Sofia, Bulgaria

Subject of study of the present work are the optical properties of thin films of the system As-S-Ge and their changes after photo-diffusion of silver. For this purpose, thin chalcogenide layers were deposited on substrates of optical glass BK-7 and thin silver film was evaporated after by thermal evaporation. The dependence of the changes in the transmittance spectra, refractive index and optical band gap of the films on the time of illumination are traced. From the resulting dependencies conclusions are drawn about the mechanism of diffusion of silver in thin films of As-S-Ge. It was shown, that significant changes in their optical properties are observed after diffusion of the silver. For a thin film with a composition $As_{30}Ge_{10}S_{60}$ the refractive index increases from 2.64 to 2.98 at a wavelength of 488 nm after silver photo-doping. The possibility of relief diffraction grating recording with 0.7 *mu*m line width s is shown.

Key words: chalcogenide glass, silver diffusion coefficient, optical properties, refractive index, diffraction

INTRODUCTION

Diffusion of silver into thin chacogenide films is an interesting phenomenon resulting in a significant change in the films' optical band gap and, respectively, of their physical properties [1]. The compositional dependences of the photo-dissolved Ag in Ge_xS_{1-x} system were studied thoroughly by Kawaguchi and Maruno [2]. Their data show a high photo-diffusion rate of Ag in both S and Ge-rich glasses, with the minimum for the composition GeS_2. The authors found that the S and Ge-rich glasses adopt a relatively low amount of Ag, with the maximum being adopted namely by GeS_2.

How the mixed glassy network, consisting of different types of structural units (pyramids, tetrahedral or octahedral units), influences the ion mobility and particularly – the photo-diffusion of the silver, is an interesting problem [3]. The photo-diffusion in the ternary system As–S–Se, consisting from AsS_3 and $AsSe_3$ pyramids, has been a subject of numerous papers [4–6]. The silver photo-diffusion in mixed glassy network of the thin films built from different tetrahedral units of Ge-S-Ge system is investigated in [7]. The glassy network of thin As–S–Ge films is built from $AsS_{3/2}$ pyramidal and $GeS_{4/2}$ tetrahedral units [8]. The kinetics of the photo-dissolution of Ag into S-rich As–S–Ge glassy films of various compositions along the tie-line $(GeS_4)x(AsS_3)_{1-x}$ ($0 \leq x \leq 1$) was studied in [9]. The authors found that the photo-dissolution rate and the amount of adopted Ag (except for GeS_4) do not depend on the glass composition.

The aim of the present paper is to investigate the optical properties of thin films of the system $As_{40-x}Ge_xS_{60}$ at constant sulfur content (60 at%) and their changes after photo-diffusion of silver.

EXPERIMENTAL DETAILS

Thin As–S–Ge films were deposited on optical BK-7 glass substrates, in a high vacuum of 10^{-3} Pa by thermal evaporation of previously weighted quantities of the bulk materials. Thin films of compositions $As_{30}S_{60}Ge_{10}$ and $As_5S_{60}Ge_{35}$, and thickness of about 1.0 μm were deposited. To obtain thin films with uniform thickness, the substrates were rotated continuously during the processes of the thermal evaporation. The substrate holder is a dome-shaped calotte that can be considered as a segment of a sphere. The evaporation sources are located approximately at the geometric centre of that sphere. The ready chalcogenide coatings were immediately placed under vacuum and thin silver film with 50 nm thickness was evaporated on top of them.

The films were exposed to monochromatic light at $\lambda = 488$ nm (Ar^+-laser – 120 mW/cm^2). The transmittance, T and reflectance, R, were measured by UV-VIS-NIR spectrophotometer Cary 5E (Australia) in the region 400–2000 nm with an accuracy of $\pm 0.1\%$ and $\pm 0.5\%$, respectively. To prevent samples from oxidation and influence of dark mobility of silver in chalcogenide films the spectrophotomeric measurements were done immediately after film's deposition. The time for collecting of the spectrphotomeric measurements of virgin samples was approximately 20 minutes. A suitable lithographic mask was used for the diffraction gratings recording.

* To whom all correspondence should be sent:
rossen@iomt.bas.bg

© 2015 Bulgarian Academy of Sciences, Union of Chemists in Bulgaria

RESULTS AND DISCUSSION

The time dependence of the transmittance for $As_{30}Ge_{10}S_{60}$/Ag coating at $\lambda = 488$ nm is shown in Fig. 1. Prior to illumination of the samples the value of T is low $\sim 0\%$. As silver progresses into the chalcogenide film, the transmittance increases reaching maximal values of 5–6% after 15 minutes.

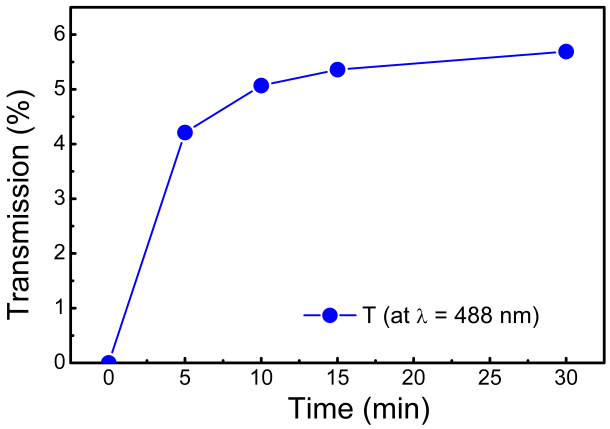


Fig. 1. Dependence of transmittance at $\lambda = 488$ nm of $As_{30}Ge_{10}S_{60}$/Ag coating on the time of irradiation with Ar-laser ($\lambda = 488$ nm).

The experimental results in Fig. 1 demonstrate that the transmittance changes more drastically in the first 10 minutes of the exposure to light. Bychkov et al. [10] found that the concentration profile of silver changes in time by the so called error function while in [11] it is demonstrated that the diffusion front possesses step-like profile due to the quick diffusion of mobile silver ions. Considering that the mass diffusion length is $L_d = 2\sqrt{Dt}$, we can make a rough calculation of the diffusion coefficient, D. Assuming that the time necessary for the silver to penetrate through a chalcogenide layer with thickness of 950 nm is approximately 600 s in this case, the silver diffusion coefficient is in the range of $D = 1.6 \times 10^{-14}$ cm^{2}s^{-1}. This value for the diffusion coefficient is lower in comparison with the one obtained in our previous work for As_2S_3 [12] and As–S–Se [5] films.

The refractive index, n and thickness, d of thin $As_{30}Ge_{10}S_{60}$ films were calculated from the interference extrema in the transmission spectra using Swanepoel's method [13, 14]. The program used to calculate n will determine it to an accuracy of $\pm 0.5\%$ for an error in the transmittance of $\pm 0.1\%$ [14]. The accuracy of the calculated thickness is 0.5-1%.

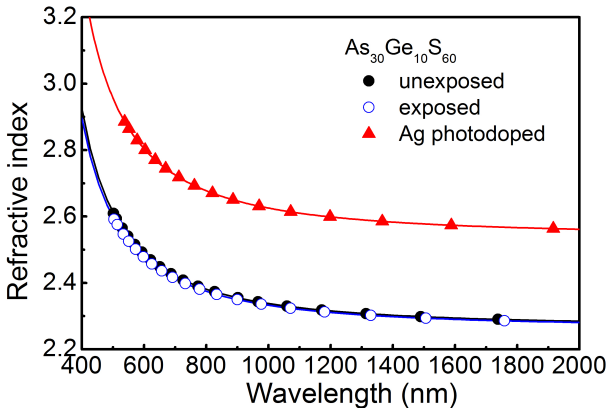


Fig. 2. Dispersion of the refractive index of the as-deposited thin $As_{30}Ge_{10}S_{60}$ film after illumination with Ar-laser and photo-doping with silver.

The calculated values for n were extrapolated by Sellmeier's equation:

$$n^2(\lambda) = 1 + \frac{A_1 \lambda^2}{\lambda^2 - A_2^2} \qquad (1)$$

where A_1 and A_2 are Sellmeier's coefficients. The coefficients obtained from Eq. (1) with λ written in nm are presented in Table 1. The dispersion of calculated refractive indices of unexposed exposed and silver photo-doped thin films is shown in Fig. 2. It is seen that the refractive index of thin $As_{30}Ge_{10}S_{60}$ film drastically increases after photo-doping with silver while the changes of the values of n after illumination of the as-deposited thin silver-free film are negligible.

Table 1. Optical parameter of silver doped thin As-Ge-S films.

Composition		d [nm]	n at $\lambda = 488$ nm	A_1	A_2 [nm]	E_g^{opt} [eV]	B cm$^{1/2}$eV$^{1/2}$
$As_{30}Ge_{10}S_{60}$	undoped	956	2.64	4.186	269.24	2.33	745
	Ag - doped	971	2.98	4.827	269.48	2.24	487
$As_5Ge_{35}S_{60}$	undoped	877	2.78	4.735	267.55	2.07	568
	Ag - doped	879	3.04	8.148	102.18	1.97	375

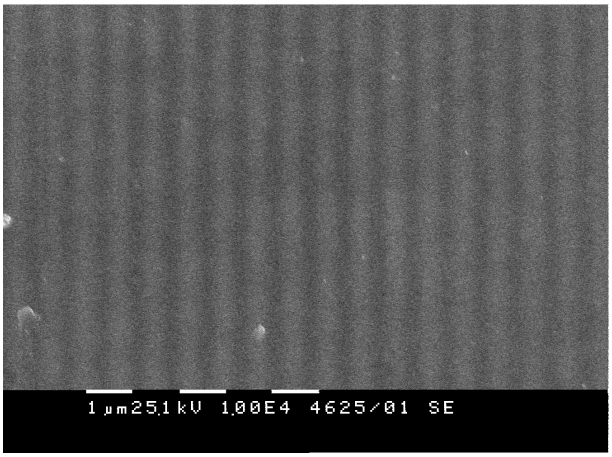


Fig. 3. SEM image of a diffraction grating recorded in thin $As_{30}Ge_{10}S_{60}$ film.

Comparison between the optical parameters of undoped and silver containing films with compositions $As_{30}Ge_{10}S_{60}$ and $As_5Ge_{35}S_{60}$ are given in Table 1. It is seen that the increase of the reflective index of the thin films after silver photo-diffusion in them is in the range of 0.26–0.34 at $\lambda = 488$ nm. The results for the thickness of the chalcogenide coatings show that the doping process leads to volume expansion.

The optical band gap of the thin films was determined from the absorption coefficient, α. It is known that at high values of the absorption coefficient, where the condition $\alpha d \geq 1$ is observed, α can be calculated from the equation:

$$T = (1-R)^2 \exp(-\alpha d), \qquad (2)$$

where T is transmittance, R is reflectance and d is thin film's thickness. Analysis of the strong absorption region ($10^4 \leq \alpha \leq 10^5$ cm^{-1}) has been carried out using the following well-known quadratic equation, often called Tauc's law [15]:

$$(\alpha h\nu)^{1/2} = B(h\nu - E_g^{\text{opt}}), \qquad (3)$$

where B is a substance parameter, which depends on the electronic transition probability, $(h\nu)$ is the photon energy and E_g^{opt} is the so-called Tauc's gap. The results for the optical gap of the thin films, E_g^{opt} and the slope parameter, B before and after silver photo-doping are given in Table 1. It is seen that the value of E_g decreases after photo-doping for both chalcogenide films. The slope parameter B in Eq. (3) is assumed to be an indicator for the degree of the structural randomness in the amorphous semiconductors and could be related to the localized-states tail width, ΔE ($B \sim 1/\Delta E$) [16]. The observed decrease of B for thin As–Ge–S films after photo-doping (see Table 1) suggests an increase of the localized-states tail in the band gap.

We used the results for the thickness changes to examine the possibility for thin As–Ge–S film to be used for recording of relief diffraction grating. We applied a simple copy technique of lithographic masks with 700 nm period to obtain a diffraction pattern in the thin film. The experiments were performed on thin films with composition $As_{30}Ge_{10}S_{60}$. The scanning electron microscopy image of the recorded diffraction pattern is clearly seen in Fig. 3.

CONCLUSIONS

The optical properties of thin films from the system As-S-Ge and their changes after photo-diffusion of silver were investigated in the present work. It was established that the silver doping of thin films from As-Ge-S system leads to a significant increase of the refractive index - 0.26–0.34 at $\lambda = 488$ nm. Due to the incorporation of silver atoms in the glassy network of the thin films, expansion of their thickness was observed. The obtained results were applied for recording of a relief diffraction gratings with 0.7 μm line width.

REFERENCES

[1] K. Shimakawa, A. Kolobov and S. R. Elliott, *Adv. Phys.* **44**, 475–588 (1995).

[2] T. Kawaguchi and S. Maruno, *J. Appl. Phys.* **71**, 2195–2201 (1992).

[3] A. Bolotov, E. Bychkov, Yu Grushko, A. Pradel, M. Ribes, V. Tsegelnik and Yu. Vlasov, *Solid State Ionics* **113-115**, 697–710 (1998).

[4] T. Wágner, A. Mackova, V. Perina, E. Rauhala, A. Seppala, S. O. Kasap, M. Frumar, Mir. Vlček and Mil. Vlček, *J. Non Cryst. Solids* **299-302**, 1028–1032 (2002).

[5] J. Tasseva, R. Todorov, Tz. Babeva and K. Petkov, *J. Opt.* **12**, art. num. 065601 (9pp) (2010).

[6] R. Todorov, A. Lalova, K. Petkov and J. Tasseva, *Semicond. Sci. Tech.* **27**(11), art. num. 115014 (2012).

[7] S. Valková, T. Wágner, M. Bartoš, M. Pavlišta, J. Přikryl, M. Vlček, B. Frumarová, L. Beneš and M. Frumar, *J. Optoelectron. Adv. Mater.* **13**, 1553–1558 (2012).

[8] K. Petkov and B. Dinev, *J. Mater. Sci.* **29**, 468–472 (1994).

[9] D. Tsiulyanu and I. Stratan, *Optoelectron. Adv. Mater. Rapid Commun.* **5**, 851–857 (2011).

[10] E. Bychkov, A. Bolotov, Yu. Grushko, Yu. Vlasov and G. Wortmann, *Solid State Ionics* **90**, 289–294 (1996).

[11] M. Frumar and T. Wagner, *Curr. Opin. Solid State Mater. Sci.* **7**, 117–126 (2003).

[12] S. Sainov, R. Todorov, I. Bodurov and T. Yovcheva, *J. Opt.* **15**, art. num. 105705 (2013).

[13] R. Swanepoel, *J. Phys. E. Sci. Instrum.* **16**, 1214–1222 (1983).

[14] R. Todorov, J. Tasseva, Tz. Babeva and K. Petkov, *J. Phys. D: Appl. Phys.* **43**, 505103 (2010).

[15] J. Tauc, in *Amorphous and liquid semiconductor*, edited by J. Tauc, Plenum. Press, London and New York, 1974, p. 159.

[16] N. F. Mott and E. A. Davis, *Electronic Processes in Non-Crystalline Materials*, Clarendon Press, Oxford, 1979, pp. 272–409.

ОПТИЧНИ СВОЙСТВА НА ТЪНКИ Ag/As-S-Ge СЛОЕВЕ

Р. Тодоров, А. Лалова, В. Лозанова

Институт по оптически материали и технологии "Акад. Йордан Малиновски", Българска академия на науките, ул. "Акад. Г. Бончев", бл. 109, 1113 София, България

(Резюме)

Обект на изследване на настоящата работа са оптичните свойства на тънки слоеве от системата As-S-Ge и техните промени след фотодифузия на сребро в тях. За тази цел тънките халкогенидни слоеве бяха отложени върху подложки от оптично стъкло ВК-7 с предварително нанесен чрез радио-честотно разпрашване сребърен филм. Проследени са в зависимост от времето на осветяване промените в спектрите на пропускане, показателя на пречупване и оптичната забранена зона на тънкослойните покрития. От получените зависимости са направени заключения за механизма на дифузия на сребро в тънки слоеве от As-S-Ge. Установено е, че след фотодифузия на сребро, в тънките слоеве се получават значителни промени в оптичните им свойства. За тънък слой със състав $As_{30}Ge_{10}S_{60}$ показателят на пречупване нараства от 2.32 до 2.61 за дължина на вълната 1060 nm. Показана е, възможността да бъдат записани релефни дифракционни решетки с ширина линията 0.7μm.

Bulgarian Chemical Communications, Volume 47, Special Issue B (pp. 44–54) 2015

Polymer materials in optical design

S. Kasarova[1]*, N. Sultanova[1], I. Nikolov[2]

[1] *Department of Mathematics and Physics, Prof. Assen Zlatarov University of Bourgas, 1 Prof. Yakimov Str., BG-8010 Bourgas, Bulgaria*
[2] *Department of Optics and Spectroscopy, Faculty of Physics, St. Kliment Ohridsky University of Sofia, 5 J. Bourchier Blvd., BG-1164 Sofia, Bulgaria*

Due to the low weight and cost polymer optical elements and systems appear in a wide spectrum of industrial, medical, scientific, military and consumer applications. Optical properties as transmission, refraction and dispersion of various types of polymers are studied. Extensive refractometric data obtained by different measuring methods is presented. Dispersion in the visible and near-infrared regions is examined. Some important material, mechanical and thermal characteristics have been also determined. Presented results are useful in the design of all-plastic or hybrid glass-plastic optics.

Key words: optical polymers, refractive indices, dispersion, elastic modulus, thermo-optic coefficients

INTRODUCTION

Polymer materials are presently used in the design and fabrication of consumer as well as precise optical elements and devices. In photonic applications, plastics offer key advantages over glasses as low cost and weight, high impact resistance, ability to integrate proper mechanical and optical features, flexibility, etc. Optical plastics are clear polymers that provide excellent light transmission in the visible (VIS) and near-infrared (NIR) regions. Polymer manufacturing includes lenses for video and still cameras, compact disk drives, light-emitting diodes, printers and bar-code readers, biomedical optics and ophthalmic lenses, light-guides, optical films, high-density optical storage media, diffractive optics, flat panel displays, metallised reflectors, optical fibers, couplers, power splitters, modulators, switches and connectors for optical communication networks [1, 2]. Great economies are possible through usage of moulded polymers for reproducing aspheric and other complex geometric surfaces, which are costly to produce in glass as well as in the production of miniature optical elements, necessary in the medical vision instruments, as laparoscopes, arthroscopes, cystoscopes, endoscopes, etc [3].

The principal optical polymers (OPs) are polymethyl methacrylate (PMMA), polystyrene (PS), polycarbonate (PC), methyl methacrylate styrene copolymer (NAS), styrene acrylonitrile (SAN), and methylpentene (TPX) [4]. Chemical companies produce various trade-marks of OPs as NAS–21 Novacor, CTE–Richardson, Zeonex (cyclo olefin polymers of Zeon Corporation), Optorez (alicyclic methacrylate copolymers of Hitachi Chemicals), Bayer, etc. and develop new types of polymer materials.

Application of polymer materials in optical design is determined not only by their optical but also by their mechanical, thermal and some physical characteristics. Because of some major drawbacks of OPs as temperature sensitivity, lower scratch resistance, higher water absorption and some other peculiarities in comparison to glasses, nowadays hybrid plastic and glass components are preferable. Incorporation of these materials may result in high quality optics taking the advantage of lower weight of plastics and thermal and chemical stability of glasses.

The aim of this paper is characterization of optical as well as some additional properties of OPs, important in the lens design. We have studied principal polymers, some trade-marks and materials produced by Eastman Chemical Company, USA (ECC). Transmittance, refraction and dispersion are investigated in the visible and near-infrared spectra. Extensive refractometric data of bulk polymers as well as thin films has been obtained by different measuring techniques. Normal dispersion of polymer materials is studied on base of Cauchy-Schott and Sellmeier's approximations. Important dispersive characteristics as principal, partial and first order dispersions, Abbe numbers, dispersion curves, etc. in the VIS and NIR regions have been obtained. Thermal instability of OPs is determined by their refractive

* To whom all correspondence should be sent:
kasarova_st@yahoo.com

© 2015 Bulgarian Academy of Sciences, Union of Chemists in Bulgaria

index dependence with temperature and dimensional changes which we analyse on base of measured refractometric data. We derive the thermo-optic coefficients as well as thermal expansion coefficients of OPs in the range between 10°C and 50°C. Elastic moduli have been investigated by ultrasonic measurements of polymers. Comparison to glasses of the obtained results is presented.

OPTICAL CHARACTERISTICS

Application of a given material in optical and photonic design requires precise data of its optical characteristics. Refraction, absorption, scattering of light are of great importance for transparent media. The first two are determined by average values of the material characteristics in volume samples, while scattering is due to local fluctuations of optical uniformity within the medium [5].

Transmission of optical polymers

Transmittance of the materials depends on their structure and sample thickness d. Most OPs are optically transparent in the VIS and NIR spectra, and consequently optical losses of polymer waveguides are low in the three telecommunication windows around 850, 1310 and 1550 nm. Tipically, they are totally opaque in the ultraviolet and infrared regions beyond 2100 nm, though there are weak absorption bands at about 900 nm, 1150 nm, 1350 nm and 1675 nm [1,6].

We used a UV-VIS-NIR spectrophotometer Varian Carry 5E and transmittances of thin polymer films of ECC materials were measured in the spectral range from 400 nm to 2500 nm. In Fig.1 transmission spectra of a polycarbonate film with $d = 35$ μm and a copolyester film with $d = 33$ μm are presented. Both polymer layers transmit well in the VIS and NIR regions up to 1700 nm. Presented spectra have weak absorption bands between 1660 and 1700 nm, due to the first overtone of the –CH group. A considerable transmission decrease is observed at wavelengths greater than 2200 nm where absorption of other C–H groups occurs. Similar results have been obtained for all other studied polymer films. Absorption bands can be shifted to the longer wavelength regions outside the telecommunication–spectral windows by replacing the lighter hydrogen atom in the C–H bonds with heavier ones such as deuterium and halogens [1]. Recently, low–loss fluorinated polymer materials in the NIR region have been synthesized and applied for producing of various functional optical devices [2].

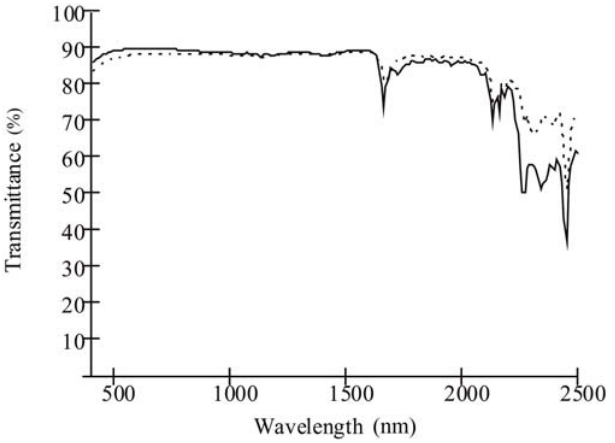


Fig. 1. Transmission spectra of a polycarbonate and a copolyester film with close thickness.

Refractive index measurement of OPs

We have investigated more than 20 types of OPs made in USA, Japan and Germany. Different methods and techniques were applied to measure refractive index values of bulk specimens [7] and thin polymer films [8,9].

Measurements of bulk polymer samples. A classical Pulfrich–Refractometer PR2 with its V–shaped SF3 glass prism (VoF3) has been used to determine refractive indices of volume polymer samples in the VIS spectrum. Measurements are based on the deviation angle method. Polymer plates with thickness varying from 2.5 mm to 5.5 mm and cubic specimens with two polished, mutually perpendicular faces have been prepared according to the requirements of the measuring method and the applied VoF3 prism [7]. Proper immersion emulsions with a suitable refractive index were used to ensure the optical contact between the plastic samples and the prism. Measuring temperature of 20°C was maintained and thermostatic regulation was possible with stability of 0.1°C. Refractive indices were measured at the emission wavelengths of the spectral lamps of the PR2 instrument in the VIS region: green e–line 546.07 nm and blue g–line 435.83 nm of the mercury source, yellow d–line 587.56 nm of the helium source, and blue F–line 486.13 nm as well as red C–line 656.27 nm of the hydrogen lamp. Measurement accuracy of the Pulfrich–Refractometer is 2×10^{-5} [10]. The V–type prism with its thermostatic housing is suitable to obtain precise refractometric data at varying temperature. Some of the polymers were measured in the range between 10 and 50°C using a MLW thermostat U4 with a water

bath, made in Germany. Thus, influence of temperature on refraction and dispersion of OPs was investigated.

Additional goniometric set-up with the same prism, a white lighting module (a 250 W halogen lamp and a condenser system) with interference filters (IFs) and a photo detector device has been assembled to obtain refractometric data in the entire VIS and NIR regions up to 1052 nm [7]. The amplitude transmittances of the IFs have been measured with the aid of a Varian Carry 5E VIS–NIR spectrophotometer and the wavelengths of maximal transmission have been determined as 548, 589, 597, 659, 703 and 752 nm for the VIS region, and 804, 833, 879 and 1052 nm for the NIR spectrum. A G5–LOMO goniometer with an accuracy of one arc second was used to measure the deviation angle. Comparison between the obtained results by the PR2 refractometer and the goniometric set–up in VIS light was possible. A number of polymer specimens have been measured with this goniometric set-up and a He–Ne laser emitting at 632.8 nm as a lighting module [11]. A detailed metrological analysis of the applied measuring techniques pointed out that our measurements of the refractive indices of bulk polymer samples guarantee accuracy better than ± 0.001 [12].

Measurements of thin films. Among studied OPs, films were possible to be obtained only for the ECC materials, which have been delivered in the form of pellets. Measured samples with varying thickness were prepared by casting of some amount of the polymer solutions on glass substrates. The pellets of polycarbonate, polyester, polyaryate, polyacrylate, and cellulose materials were dissolved in chloroform and the two types of copolyesters A and B – in 1,1,2,2–tetrachloroethane. Solutions of the first five materials were prepared with concentration of 10 wt% while the concentration of the copolyester solutions was 1 wt%. Higher refractive polymers were deposited on heavy TF4 glass plates. TK21 glass plates were used for the low refractive materials. The substrates were with surface areas of about 5 cm^2 or 8 cm^2. The obtained films were dried at temperature of 20°C for 48 hours and then were heated up to 60°C during 6 hours to evaporate the rest of the solvent. Film thickness d was measured by a digital micrometer (Mitutoyo Corporation) with an accuracy of ± 1 μm.

We have used the total internal reflection method to measure refractive indices of thin polymer films by means of laboratory assembled laser microrefractometers (LMR) with three [8] or four wavelength illumination [9]. Measuring principle is based on the critical angle determination by means of the diffraction pattern disappearance [13]. The experimental schemes in both cases differ in the illumination part. Measuring wavelengths in case of the three–wavelength LMR are 532, 632.8 and 790 nm, while for the four–wavelength LMR, they are 406, 656, 910 and 1320 nm. The examined samples are placed between a TF4 glass prism and a chromium diffraction grating with a 40 μm period. The optical contact between the measured film, prism and the grating is realised using methylene iodide with a measured refractive index value $n_{633} = 1.732$ for high index polymers and microscopic immersion oil with $n_d = 1.52$, in case of low refractive OPs. The prism unit with the sample is mounted on a rotary goniometric stage with resolution of 1 arcmin. At small angles of incidence, diffraction orders are observed in reflection on a screen. At the critical angle of the examined material, total internal reflection occurs at the interface prism – film, and the diffraction pattern disappears. The incident angle φ_c is then measured on the goniometric scale. An infrared beam–finder card, model IRC32R (Electrophysics), with peak emission at 655 nm and spectral range $800 \div 1700$ nm, was used to visualise the diffraction image in the infrared light.

The experimental uncertainty of the laser microrefractometric method depends mainly on the accuracy of evaluation of the angle of incidence when total internal reflection of studied polymers occurs. Extra noise, introduced by the multiple surface reflections in the film and the glass substrate, and light scattering in the polymer medium also influence on the reading value of the angle φ_c. The estimated standard uncertainty of the results was found to be ± 0.002, taking into account the maximal standard deviation of the mean refractive index, calculated on base of several measurements of each polymer film [12].

Refractive index results. Some of the obtained refractive indices of bulk polymer samples and thin films at selected wavelengths in VIS and NIR spectral regions are included in Table 1. Presented results for the volume specimens were obtained by the PR2 instrument and the goniometric set–up at measuring temperature of 20°C. In case of polymer films, the first four samples were measured at room temperature of 23°C by the three–wavelength LMR and the rest three – by both modifications of the LMR to obtain additional dispersion data.

Table 1. Measured refractive indices of bulk polymers and thin films

		Bulk OPs						
Polymer		n_g	n_F	n_d	n_{633}	n_{804}	n_{879}	n_{1052}
PMMA		1.5025	1.4973	1.4914	1.4890	1.4843	1.4835	1.4813
PS		1.6171	1.6056	1.5917	1.5872	1.5775	1.5756	1.5718
PC		1.6117	1.5994	1.5849	1.5802	1.5703	1.5683	1.5645
SAN		1.5882	1.5783	1.5667	1.5626	1.5543	1.5526	1.5496
Zeonex E48R		1.5431	1.5376	1.5309	1.5284	1.5234	1.5224	1.5204
Optorez 1330		1.5219	1.5163	1.5094	1.5075	1.5031	1.5021	1.4984
Cellulose		1.4804	1.4765	1.4706	1.4687	1.4639	1.4627	1.4608
Polyacrylate		1.5065	1.4995	1.4941	1.4924	1.4888	1.4880	1.4855
EBM copolyester		1.5861	1.5747	1.5613	1.5580	1.5493	1.5465	1.5449
		Thin polymer films						
		n_{406}	n_{532}	n_{633}	n_{656}	n_{790}	n_{910}	n_{1320}
Polyarylate	$d = 15\ \mu$m	–	1.656	1.642	–	1.639	–	–
Copolyester A	$d = 6\ \mu$m	–	1.537	1.525	–	1.514	–	–
Copolyester B	$d = 33\ \mu$m	–	1.647	1.632	–	1.619	–	–
Polycarbonate	$d = 35\ \mu$m	–	1.599	1.595	–	1.591	–	–
Polyacrylate	$d = 6\ \mu$m	1.501	1.490	1.485	1.484	–	1.478	1.476
Polyester A	$d = 40\ \mu$m	1.513	1.502	1.496	1.495	–	1.489	1.486
Cellulose	$d = 9\ \mu$m	1.493	1.473	1.467	1.466	–	1.460	1.457

Presented results of n_d of the examined OPs vary in an interval from 1.4706 for the cellulose material up to 1.5917 for the PS polymer. The comparison to optical glasses [14,15] reveals a much more restricted range of refractive index values of the polymer materials. Recently, MITSUI Chemicals offers special high refractive index optical polymers with $n_e = 1.74$, which are especially suitable for ophthalmic lenses [16].

Comparison between refraction of bulk samples and thin polymer films, prepared from one and the same material, is possible at 632.8 nm. As it is seen from Table 1, refraction of bulk PC material is lower than that of the ECC polycarbonate film. Opposite relation is observed for the ECC polyacrylate volume specimen and the thin polymer layer. Refractive indices of the cellulose bulk specimen and film are similar and values differ in the third decimal place. The established differences due to the fact that in case of bulk samples average volume refractive index is measured, while for thin polymer films, a local value of the index is registered. The latter is influenced by the polymer packing and nonuniformity near the film free surface at the place of the laser beam incidence [12]. For some of the thin polymer films refractive index dependence on the thickness of the polymer layer has been established [17]. In case of the polyarylate material, refractive index increases with the thickness diminishing of the film. This could be explained with the increased polymer packing near the surface. However, such dependence was not observed for all of the polymers. Obviously, refraction of thin films is influenced by the specific material structure. Similar results have been obtained by other authors, too [18]. Refractive index values depend also on the film quality and uniformity as well as on the adhesion and viscosity of the solutions and their hardening time [5].

Dispersive characteristics of OPs

Presented transmittance spectra in Fig. 1 as well as measured refractive indices of OPs (Table 1) confirm their normal dispersion in the regarded VIS and NIR spectral regions. There are several approximating dispersive equations in literature as Herzberger's, Hartmann's, Cauchy's and Sellmeier's formulae [7]. Only the last one, however, has physical ground. Usually, three terms in the Sellmeier's approximation are used to ensure sufficient precision over the wavelength range from the ultraviolet to the infrared area [14,19]. We have applied the Cauchy–Schott dispersion equation [7,20] which can be derived from the Sellmeier's formula. It is valid for transparent media in their region of normal dispersion. In case of bulk polymer samples and thin films, measured by both LMRs, we

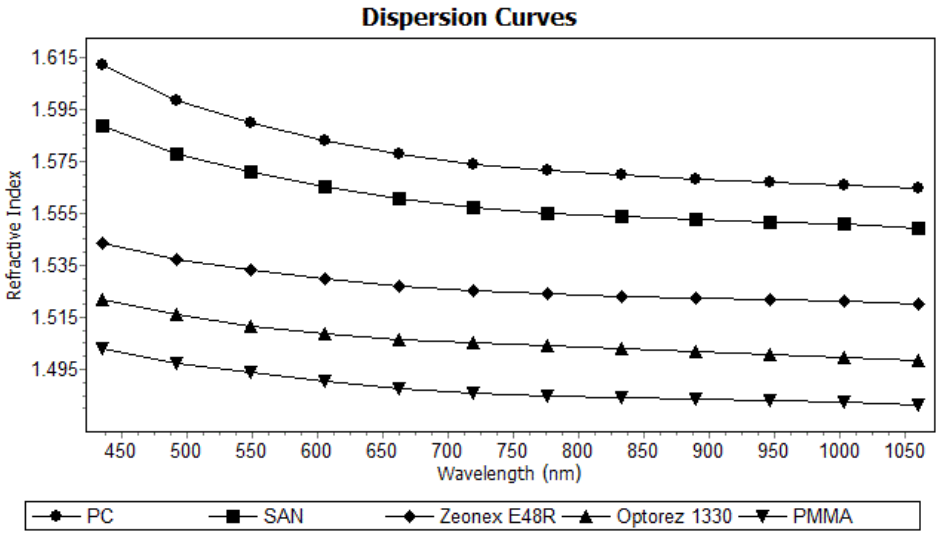


Fig. 2. Dispersion curves of bulk OPs.

have used six dispersion coefficients in the Cauchy–Schott approximation, as follows:

$$n^2 = A_1 + A_2\lambda^2 + \frac{A_3}{\lambda^2} + \frac{A_4}{\lambda^4} + \frac{A_5}{\lambda^6} + \frac{A_6}{\lambda^8}, \qquad (1)$$

where the wavelength λ is expressed in microns. Our analysis of Eq. (1) shows that the accuracy of the calculated refractive indices of optical glasses is better than $\pm 1 \times 10^{-4}$ in the entire VIS range and NIR spectrum up to 1060 nm and decreases to about $\pm 5 \times 10^{-4}$ at 1500 nm [12].

We have realised the program OptiColor on the base of Eq. (1) that allows us to obtain the dispersion coefficients from A_1 to A_6 using a system consisting of six linear equations. Other options of the program are calculation of dispersion curves, random refractive indices at selected wavelengths and Abbe numbers of the examined materials.

In Fig. 2 dispersion charts of some of the studied bulk polymers are presented while dispersion of thin films is illustrated in Fig. 3. Refraction of the polyacrylate, polyester A and cellulose films are measured by both modifications of LMR.

Presentation of several dispersion curves in one diagram makes possible the comparison between the values of refractive indices and dispersion behaviour of OPs. As it is seen in Fig. 2, the higher refractive PC and SAN materials show greater dispersion in the VIS region. For thin films in Fig. 3, this tendency is not observed. The least refractive cellulose film reveals highest dispersion in comparison to the polyester and polyacrylate films. In this case, however, broader wavelength interval is considered. In the NIR region, all studied OPs have lower dispersion which makes them useful materials for communication applications.

Dispersion curves of the polymer films, measured by the three-wavelength LMR, were calculated by the Cauchy-Schott Eq. (1) with three coefficients and Sellmeier's approximation with two terms in the series [8]. Similar calculation accuracy of the dispersion curves in both cases was established. Because of the restricted wavelength measuring range between 500 and 800 nm, the detailed analysis of the dispersion behavior of OPs is not efficient. Our investigations on thin polymer films with varying thickness show that their dispersive characteristics in the regarded spectral range are similar for one and the same material, though they differ in refraction [12, 17].

Dispersion behaviour of optical materials is usually evaluated by their principal dispersion $n_F - n_C$ and Abbe numbers ν_d or ν_e. A more accurate description of optical properties is achievable with the aid of the relative partial dispersions $P_{x,y}$ at selected wavelengths x and y, which is necessary in the design of high quality optics. We have introduced additional analogous parameters to characterize dispersive properties of OPs for the NIR measuring spectrum. Partial dispersions $\Delta n_{\mathrm{NIR}} = n_{804} - n_{1052}$ and Abbe numbers ν_{879}, defined as:

$$\nu_{879} = \frac{n_{879} - 1}{n_{804} - n_{1052}}, \qquad (2)$$

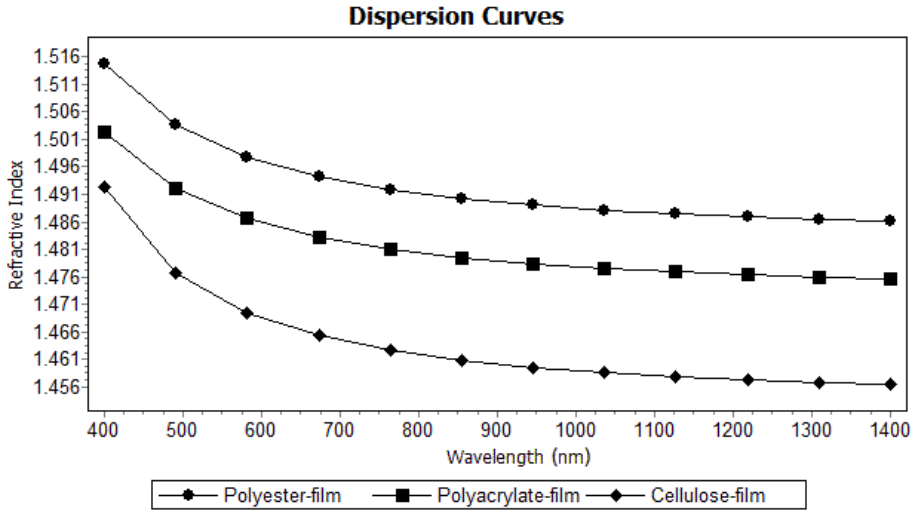


Fig. 3. Dispersion curves of thin polymer films.

are calculated for volume specimens. Estimation of ν_{879} is accomplished by substituting measured refractive indices at the wavelengths of maximal transmission of the applied NIR interference filters with the goniometric set-up. Principal and partial dispersions in VIS and NIR regions, as well as Abbe numbers ν_d and ν_{879} of some of the studied bulk polymers are included in Table 2.

Wavelength dependence of $dn/d\lambda$ assures more detailed examination of the dispersive properties of studied materials in various parts of the spectrum. In the region of normal dispersion obtained graphs of $|dn/d\lambda|$ versus λ should be smooth and monotonously decreasing for correctly measured refractive indices [12]. In Table 2 values of n_{850} and dispersion of first order $|dn/d\lambda|$ at d-line in VIS region and 850 nm for the data communication band are also included. Refraction and dispersion at 1310 and 1550 nm are not calculated, since these wavelengths do not lie in the measuring spectral interval of the bulk polymer samples. Polymers are set in order of decreasing values of ν_d which corresponds to growing principal $n_F - n_C$ and partial $n_g - n_F$ dispersions in the VIS region. Results show that greatest contribution to the principal dispersions is due to refractive index variations in the blue part of the spectrum. Partial dispersions in the measuring NIR area of the bulk OPs are with smaller values in respect to $n_F - n_C$ and $n_g - n_F$ and the rough estimation shows that Δn_{NIR} is of about one third from the principal dispersion for most of the polymers, included in Table 2. Comparison to Schott glass types with similar refractive index values (Table 3) shows that OPs are higher dispersive materials in the VIS light, especially in the blue part of the spectrum.

In the NIR region all of the presented materials (Tables 2 and 3) reveal lower dispersion, compared to VIS area. Abbe numbers ν_{879} of most OPs are

Table 2. Dispersive characteristics of bulk polymers

Characteristics	PMMA	Zeonex E48R	Optorez 1330	SAN	PS	PC
$n_F - n_C$	0.0083	0.0094	0.0098	0.0160	0.0194	0.0201
ν_d	59.2	56.5	52.0	35.4	30.5	29.1
$n_g - n_F$	0.0052	0.0055	0.0056	0.0099	0.0115	0.0123
$\lvert dn/d\lambda\rvert_d \times 10^{-5}$, nm^{-1}	5.75	6.06	4.74	10.13	11.04	11.59
Δn_{NIR}	0.0030	0.0030	0.0048	0.0047	0.0057	0.0058
ν_{879}	161.2	174.1	105.4	117.6	101.0	98.0
$\lvert dn/d\lambda\rvert_{850} \times 10^{-5}$, nm^{-1}	1.04	1.16	1.89	1.89	2.69	2.62
n_{850}	1.4837	1.5228	1.5023	1.5533	1.5762	1.5690

Table 3. Dispersive characteristics of Schott glasses

Characteristics	N-BK10	N-BK7	N-PSK3	N-BAK2	LF5	F5
n_d	1.49782	1.51680	1.55232	1.53996	1.58144	1.60342
$n_F - n_C$	0.00744	0.00805	0.00870	0.00904	0.01423	0.01587
ν_d	66.95	64.17	63.46	59.71	40.85	38.03
$n_g - n_F$	0.00394	0.00430	0.00467	0.00492	0.00818	0.00920
$\lvert dn/d\lambda\rvert_d \times 10^{-5}$, nm^{-1}	3.87	4.18	4.51	4.67	7.25	8.06
Δn_{NIR}	0.00375	0.00390	0.00412	0.00399	0.00539	0.00588
ν_{879}	131.0	130.5	132.1	133.3	105.6	100.4
$\lvert dn/d\lambda\rvert_{850} \times 10^{-5}$, nm^{-1}	1.69	1.77	1.88	1.85	2.58	2.82

with higher values in comparison to glass types with similar refraction. For example, the value of ν_{879} of PMMA (Table 2) is considerably greater than the respective Abbe number of the N-BK10 glass (Table 3), though their refractive indices are very close. The Zeonex E48R polymer is with similar refraction to the N-BK7 glass but it is considerably less dispersive material in the NIR region. In case of high refractive optical materials as flint types glass F5 or LF5 and PS or PC polymers, dispersion in NIR area is similar, regarding the ν_{879} and Δn_{NIR} values. However, among all of the examined materials the acrylic polymers and cyclo olefin trade-mark Zeonex E48R show lowest dispersion in this part of the spectrum. Obviously, these plastics seem to be the most suitable optical materials for night vision optics.

Comparison among values of first order dispersion $|dn/d\lambda|$ in the NIR region shows similarity for polymers and glasses. For all of the presented materials, $|dn/d\lambda|_{850} < 3 \times 10^{-5}$ nm^{-1}. In comparison to VIS area first order dispersion of OPs decrease about five times for most of the polymers. In case of presented glasses in Table 3, reduction of dispersion is less. However, results for the PMMA and Zeonex E48R materials confirm again their lowest dispersion in NIR spectrum.

ADDITIONAL CHARACTERISTICS OF POLYMERS IN OPTICAL DESIGN

Material, mechanical, thermal and environmental characteristics of polymers play an important role in the optical design, too. The use of plastic elements is preferable for the reduction of weight, due to the essentially smaller densities of the polymers. Generally, density ρ of the optical grade plastics is about 1 g/cm^3 and varies in the limits between $0.83 \div 1.4$ g/cm^3 [5, 12, 21]. In Table 4, values of ρ of some of the examined OPs at temperature of 20°C are included. Densities have been measured by the Archimedean immersion method and an uncertainty of the results is $\pm 1 \times 10^{-3}$ g/cm^3.

In addition to the optical requirements, plastics should be selected on the basis of their mechanical properties and environmental compatibility. Some of the considered mechanical characteristics of OPs in the design are elastic moduli, impact resistance I, in terms of the widely used Izod test, and Poisson's ratio μ. In Table 4 parameters I, μ and water absorption A_{H_2O} per 24 hours of the examined OPs, steeped in water, at temperature of 23°C in percents by weight, are given in accordance to literature data [22–25]. Ultrasonic measurements have been used to investigate elastic moduli of OPs. Influence of temperature on refraction and dimensional instability of polymers is evaluated on base of calculated thermo-optic coefficients $\Delta n_d/\Delta T$ and linear thermal expansion coefficients α.

In many applications polymer elements are subjected to various kinds of external forces that may cause them to deform or break. In such cases, polymer materials should have a sufficient degree of toughness and flexibility. Young's modulus E, also known as the tensile modulus, is a measure of the stiffness of an isotropic material. Poisson's ratio μ is another important material characteristic used in elastic analysis. Generally, "stiffer" materials will have lower Poisson's ratios than "softer" materials. There are other elastic moduli, such as bulk modulus and the shear modulus which are related to the values of E and μ.

Static and dynamic methods are usually applied for determination of the elastic moduli of solids. Experimental conditions such as magnitude of the external load as well as loading rate significantly affect the measuring accuracy of the results, obtained by static stress-strain measurements. The dynamic methods

Table 4. Some material characteristics of OPs

Optical Polymer	$\rho \times 10^3$ kg/m^3	E *GPa*	G *GPa*	μ	I J/m	$\Delta n_d/\Delta T$ $\times 10^{-4}, K^{-1}$	α $\times 10^{-5}, K^{-1}$	A_{H_2O}, %
PMMA	1.187	$4.17 \div 5.57$	$1.49 \div 2.06$	$0.35 \div 0.4$	$16 \div 32$	-1.30	7.5	0.3
PS	1.040	3.69	1.37	0.35	$19 \div 24$	-1.31	6	<0.1
PC	1.195	$2.78 \div 3.37$	$0.99 \div 1.23$	$0.37 \div 0.4$	$600 \div 850$	-1.00	4.7	0.2
SAN	1.160	4.30	1.57	0.37	$11 \div 21$	-1.10	5.3	0.28
Optorez 1330	1.202	4.76	2.29	0.37	-	-1.20	6.6	1
Zeonex E48R	1.007	3.66	1.34	0.37	21	-1.26	6.6	< 0.01
Bayer	1.204	2.98-3.53	1.07-1.30	0.36-0.39	850	-1.20	5.6	0.12

with a sinusoidal load are also applicable and are with a relatively high accuracy. According to the applied frequency range, the dynamic methods are classified as: acoustic (the frequency is below 10^4 Hz) and ultrasonic (the frequency is between 10^4 and 10^8 Hz). The dynamic methods are widely applied to study the elastic properties and determine the elastic moduli of glasses and glass-forming liquids. As it is known, velocity c_l of longitudinal acoustic waves depends on Young's modulus and Poisson's ratio, according to the relation:

$$c_l = \sqrt{\frac{E(1-\mu)}{\rho(1+\mu)(1-2\mu)}}. \qquad (3)$$

Velocity of shear (transverse) wave c_t is related to shear modulus G by:

$$c_t = \sqrt{\frac{G}{\rho}}. \qquad (4)$$

Equations (3) and (4) are valid for propagation of elastic waves in solid objects which transverse dimensions are much greater than the sound wavelength. Shear modulus G and bulk modulus K can be also calculated by the expressions:

$$G = \frac{E}{2(1+\mu)} \text{ and } K = \frac{E}{3(1-2\mu)}. \qquad (5)$$

We have measured velocity of the longitudinal ultrasonic waves of bulk polymer samples. A digital ultrasonic precision thickness gauge CL-104, produced by Krautkramer-Branson, has been applied. The operating principle is based on the measurement of the travel time of the propagated and reflected ultrasonic pulse on the back wall of the specimen. The ultrasonic gauge has an option to determine the velocity in the material, if thickness of the investigated sample is entered manually via keyboard. A single element contact transducer CLF 4 with a delay line at operating frequency of 15 MHz and measuring range from 0.18 to 25 mm was used. It is suitable for measuring of thin samples where separation of the excitation pulse recovery from backwall echoes is necessary. Thicknesses of the samples were determined by a Kinex-G633 micrometer with an instrumental error of ± 0.01 mm. Obtained values of c_l and ρ at 20°C were used to calculate the dynamic elastic moduli by Eqs. 3 and 5. Results for E and G moduli of some polymers are included in Table 4. Our comparison to the literature data of static elastic moduli of OPs reveals much higher values in case of dynamic measurements [12]. This is attributed to the high frequency of the ultrasonic waves. Since measurements from ultrasonic and from dynamic experiments depend on the frequency, the modulus of elasticity estimated by ultrasonic testing is compared with the storage modulus estimated by dynamic experiments [26]. Presented data of OPs gives the possibility for comparison to mechanical characteristics of optical glass types. Obtained values of E of OPs are about 20 to 30 times smaller in respect to Young's moduli of glasses which would result in easier deflection of plastic elements by external loading or intrinsic mass. However, glasses are fragile and with much lower impact resistance [14]. Obviously, unique priority of polymers over glass is safety which determines their only choice in medical applications.

Optical and mechanical properties of polymers may change as a function of temperature. Thermal stability of OPs is very important for their practical applications in systems and devices which operate in variable or extreme environmental conditions. Heating of polymers can cause undesirable transformations in their structure. Increase of maximal service temperature of optical systems can be achieved via

introduction of suitable substituents in polymers [1] or usage of hybrid glass-polymer optics [27]. On the other hand, large thermo-optic coefficients of polymers allow for their application in active photonic devices as switchers, attenuators, modulators, amplifiers, controllers, etc. Thermo-optic coefficients of studied OPs have been calculated on base of our refractometric measurements at various temperatures between 10 and 50°C. Some of the obtained results at d-line are included in Table 4. Values of $|\Delta n/\Delta T|$ of polymer materials are with about two orders of magnitude larger than those for optical glass [14, 15]. Some variations of the thermo-optic coefficients with temperature and wavelengths are observed [27]. Differentiation of the Lorentz-Lorenz equation with respect to temperature arrives at the following expression:

$$\frac{dn}{dT} = \frac{(n^2-1)(n^2+2)}{6n}(\Phi - 3\alpha), \qquad (6)$$

where Φ is the temperature coefficient of the molecular polarisability and α is the linear thermal expansion coefficient which is the fractional change in length per degree of temperature. Since for polymers the volume expansion coefficient β ($\beta \cong 3\alpha$) is always one or two orders of magnitude larger than Φ [28], polymers have negative thermo-optic coefficients. On base of our results on the temperature gradients of refractive indices, approximate values of α of studied OPs can be calculated by simplifying Eq. (6):

$$\alpha \approx \frac{2n}{(n^2-1)(n^2+2)}\frac{dn}{dT}. \qquad (7)$$

Obtained linear thermal expansion coefficients are included in Table 4. Plastic optical materials typically show 10 times higher α values than those of metals and 20 times higher than those of glasses [14]. Thermal expansion alters the geometric parameters of optical systems as focal lengths, radii of curvature of surfaces, lens thicknesses, air spaces, diameters, etc. Consequently, thermally-induced optical aberrations of polymer elements appear. At low temperatures, metal rings and housing elements subject to compression the assembled lenses and optical components, wherein internal stresses and birefringence arise and degrade the optical image. Among presented OPs in Table 4, the PC polymer shows greatest thermal stability as well as highest impact resistance. For this reason, safety glasses and systems requiring durability often are made from polycarbonate, though it is a relatively soft plastic.

Moisture absorption can change a component's optical geometry, increases refractive index slightly and causes optical nonhomogeneities. The PMMA polymer is the most moisture-sensitive material in Table 4. The Zeonex plastic has lowest water absorption value of less than 0.01% (compare to PC – 0.2% and PMMA – 0.3%). Moisture absorption affects not only the dimensions and densities but also the refractive index of plastic optical materials. Moist atmosphere with relative humidity above 85%, high temperatures over 40°C and acidity of the medium damage the polished surfaces of the optical elements, forming stains and deposits. Ultraviolet and ionizing radiations degrade optical properties of OPs, too.

SUMMARY AND CONCLUSIONS

In this report optical, some mechanical, thermal and environmental characteristics of polymer materials are presented which are useful in the design of optical elements and systems. Transmission, refraction and dispersion of bulk polymers as well as thin films are studied. Obtained spectra (Fig. 1) show that OPs transmit well in the VIS and NIR regions up to 2100 nm. Refractive index measurements at nineteen wavelengths of various bulk polymer samples and at seven wavelengths of thin polymer films are carried out. Results (Table 1) show that volume plastics and thin layers have some differences in refraction and should be studied separately. Software program OptiColor is realised on base of the Cauchy-Schott approximation to calculate dispersion curves, refractive indices and Abbe numbers in the VIS and NIR regions (Fig. 2 and Fig. 3, Table 2). Principal, partial dispersions and first order dispersions $|dn/d\lambda|$ at d-line and data communication wavelength 850 nm are determined. Comparison of studied polymer materials to some optical glasses with similar refraction (Table 3) shows that OPs are more dispersive in the VIS range. In the NIR spectrum, dispersion of all materials is lower but there are some polymers which are more efficient for application in night vision instruments and data communication systems than glasses. Results show that OPs complement available classes of optical media with lower refractive but higher dispersive materials and broaden their combinations in achromatic hybrid pairs.

Some physical, mechanical and thermal characteristics of OPs are presented, too. On base of measured density and ultrasonic velocity dynamic elastic moduli E and G are determined. Their values are lower

than for glasses but in combination with the high impact resistance, OPs are preferable materials in elements where flexibility and safety in usage are required. Thermal instability of OPs results primary in variation of refractive index and dimensional changes of optical elements, due to thermal expansion, playing a secondary role. Results on thermo-optic coefficients, linear thermal expansion coefficients, tensile and shear moduli, etc. are presented (Table 4). Measured and computed optical and material characteristics of OPs confirm their compatibility to glasses and may be useful in the design of all-plastic or hybrid glass-plastic optics.

Acknowledgments. *Investigations of properties of polymers are carried out with the financial support of the "Prof. Assen Zlatarov" University of Bourgas, Bulgaria, under research project NIH264.*

REFERENCES

[1] Al. Driessen *et al.*, "Polymer-Based Integrated Optics Devices" in *Polymer Optical Fibers*, edited by H. S. Nalwa, American Scientific Publishers, Los Angeles, 2004, pp. 73–101.

[2] M–C. Oh *et al.*, *Polymers* **3**, 975–997 (2011).

[3] P. Tolley, *Photon. Spectra* **10**, 76–79 (2003).

[4] D. F. Horne, *Optical production technology*, 2nd edition, Adam Hilger Ltd., Bristol, 1983.

[5] D. W. Van Krevelen, *Properties of polymers*, Elsevier, Amsterdam, 1990.

[6] J. Lytle, "Polymeric optics" in *Handbook of Optics*, Vol. 2, edited by M. Bass *et al.*, McGraw–Hill Inc., New York, 1995, pp. 34.1–34.21.

[7] N. Sultanova, C. Ivanov and I. Nikolov, *Opt. Quant. Electron.* **35**, 21–34 (2003).

[8] S. Kasarova *et al.*, *J. Optoelectron. Adv. Mater.* **11**, 1440–1443 (2009).

[9] S. Kasarova *et al.*, *Proc. of SPIE* **7501**, 75010P–75010P–8 (2009).

[10] Carl Zeiss JENA, *The manual of Pulfrich-Refraktometer PR2*, Jena D–77830, Germany, 1976.

[11] I. Nikolov, N. Sultanova and S. Kasarova, *Proc. of SPIE* **5830**, 511–515 (2005).

[12] N. Sultanova, S. Kasarova and I. Nikolov, *Refractive Index Metrology of Optical Polymers*, Lap Lambert Academic Publishing, Saarbrucken, 2014.

[13] S. Sainov, *Rev. Sci. Instrum.* **62**, 3106–3107 (1991).

[14] SCHOTT, *Glass Technologies*, available from: http://www.us.schott.com.

[15] HOYA Corporation USA, available from: http://www.hoyaoptics.com.

[16] MITSUI Chemicals Inc., available from: http://www.mitsuichem.com.

[17] N. Sultanova, S. Kasarova and I. Nikolov, *J. Phys.: Conf. Ser.* **514**, 012026 (2014).

[18] K. Petrova *et al.*, *J. Optoelectron. Adv. Mater.* **9**, 464–467 (2007).

[19] W. Tan *et al.*, "Fundamental Optical Properties of Materials I" in *Optical Properties of Condensed Matter and Applications*, edited by J. Singh, John Willey & Sons, New York, 2006, pp. 1–25.

[20] S. Kasarova, N. Sultanova, C. Ivanov and I. Nikolov, *Opt. Mater.* **29**, 1481–1490 (2007).

[21] *Materials Data Book*, Cambridge University Engineering Department, 2003.

[22] *Professional Plastics, Mechanical Properties of Plastic Materials*, available from: http://www.professionalplastics.com.

[23] J. T. Seitz, *J. Appl. Polym. Sci.* **49**, 1331–1351 (1993).

[24] *Material Property Data*, available from: http://www.matweb.com.

[25] *Properties of Optical Plastic Materials*, available from: http://www.sunex.com.

[26] G. Bourkas *et al.*, *Adv. Mater. Sci. Eng.* **2010**, 891824 (2010).

[27] N. Sultanova, S. Kasarova and I. Nikolov, *Opt. Quant. Electron* **45**, 221–232 (2013).

[28] K. Chen *et al.*, *Opt. Laser. Eng.* **47**, 708-711 (2009).

ПОЛИМЕРНИ МАТЕРИАЛИ ЗА ОПТИЧЕН ДИЗАЙН

Ст. Касърова[1], Н. Султанова[1], Ив. Николов[2]

[1] *Катедра "Математика и физика", Университет "Проф. д-р Асен Златаров", бул. "Проф. Якимов" №1, 8010 Бургас, България*
[2] *Физически факултет, Софийски университет "Св. Климент Охридски", бул. "Джеймс Баучър" №5, 1164 София, България*

(Резюме)

Безспорните предимства на полимерните материали като по-малка плътност, устойчивост на удар, ниска себестойност на оптичните изделия, безопасността им при работа и др. наложиха използването им не само в битовата, но и в прецизна оптика. Приложението им е свързано с определяне на техните оптични характеристики, както и на механичните и топлинните им свойства, устойчивост към ултравиолетови и йонизиращи лъчения, химична резистивност и др.

В предложения доклад са представени резултатите от изследване рефракцията и дисперсията на различни оптични полимерни материали във видимия и близък инфрачервен спектър. Използвани са подходящи методи за измерване показателите на пречупване на обемни и тънкослойни полимерни образци в различни спектрални интервали [1-3]. Определени са основни дисперсионни характеристики като числа на Аббе, средни дисперсии, относителни и относителни частни дисперсии за видимата област и са въведени аналогични за измервателния инфрачервен диапазон. Изследвано е влиянието на температурата върху рефрактометричните и дисперсионни свойства на полимерите.

Рефрактометричните данни на полимерите не са достатъчни за правилния избор на материала за конкретната оптична система. Необходимо е физикомеханично охарактеризиране на материалите като твърдост, якост, износоустойчивост, съпротивление на драскане и др. В настоящата работа са представени резултати за еластичните модули на изследваните полимери, получени от ултразвукови измервания. Получените стойности дават възможност за сравнителна характеристика на полимерите с оптичните стъкла. Голямата чувствителност на полимерите към температурата може да бъде преодоляна чрез комбинирането на полимерни материали с подходящи оптични стъкла за получаване на атермални и ахроматни оптични елементи [4].

1. N. Sultanova, C. Ivanov, I. Nikolov, *Opt. Quant. Electron.* **35** No 1 (2003) 21-34.
2. S. Kasarova, N. Sultanova, T. Petrova, V. Dragostinova, I. Nikolov, *J. Optoelectron. Adv. Mater.***11** Iss.10 (2009) 1440-1443.
3. S. Kasarova, N. Sultanova, C. Ivanov, I. Nikolov, *Opt. Mat.* **29** Iss. 11 (2007) 1481-1490.
4. N. Sultanova, S. Kasarova, I. Nikolov, *Opt. Quant. Electron.* **45** No 3 (2013) 221-232.

Bulgarian Chemical Communications, Volume 47, Special Issue B (pp. 55–59) 2015

Microstructure and optical properties of thermally evaporated very thin silver films

V. Lozanova*, R. Todorov

Acad. J. Malinowski Institute of Optical Materials and Technologies, Bulgarian Academy of Sciences
Acad. G. Bonchev Str., BG-1113 Sofia, Bulgaria

The present paper shows results for the optical properties of nanocrystalline silver thin films in attempt to understand the effects of the particle size. Ag-films with thickness from 10 nm to 20 nm were deposited on optical glass by thermal evaporation. Depending on the deposition rate, due to different sizes of the grains building the layers, it was observed variation in the color of the coatings from red to blue. The grain size was determined by X-ray diffraction from the formula of Debye-Scherrer. A strong absorption band due to surface plasmons was observed in the transmittance spectra of the films. The absorbance maximum is positioned in the spectral range 400–550 nm in dependence of the film's grains size. The evolution of the thin silver films during vacuum annealing was investigated. It was established that the heating of 25 nm films at 250°C leads to aggregation of the grains.

Key words: silver nanoparticles, very thin films, Debye-Scherrer formula, X-ray diffraction, grain size, optical properties

INTRODUCTION

Thin silver films have found many applications in different optical devices such as solar cells, light emitting diodes, to improve the properties of organic semiconductor materials and to launch new metamaterials [1–3].

It is well-known that the deposition conditions (deposition rate, vacuum pressure and substrate type and temperature) control the aggregation of the grains during the deposition of the thin metal films [4,5]. On its part, the size of the crystalline grains building the metal coatings affects the electrical and optical properties of the metals layers [6]. The thickness dependence of very thin silver films (with thickness up to 2.8) was investigated in [7]. The authors found that the refractive index of the thin films was significantly increased and the extinction coefficient is slightly increased compared with the bulk at visible and infrared wavelengths. They observed that with the increasing of the thin film thickness, the refractive index decreased, while the extinction coefficient and absorption increased. The influence of the deposition rate on the structure was investigated in [8]. The authors found that the deposition rate influences strongly the microstructure of thin silver films.

In our previous work we investigated thin silver films obtained by cathode sputtering [9]. We found that the deposition rate influences significantly the microstructure of the thin films and respectively – their optical properties. The object of investigation of the present work is the influence of the deposition rate and film's thickness on the optical properties of thin silver coatings obtained by thermal evaporation.

EXPERIMENTAL DETAILS

The films with thickness ranging in 10-25 nm were deposited by thermal evaporation in vacuum $\sim 1 \times 10^{-3}$ Pa on an optical glass and Si wafer. The thickness of the thin films was controlled after film deposition by profilemeter "Talystep". The annealing of the thin films at 200°C was performed in vacuum of 10^{-3} Pa for 1 hour.

The transmittance (T) and reflectance (R) were measured by a UV-VIS-NIR spectrophotometer Cary 5E (Australia) in the range 350-2000 nm to an accuracy of $\Delta T = \pm 0.1\%$ and $\Delta R = \pm 0.5\%$.

X-ray diffraction patterns were collected by X-ray diffractometer "Philips 1710" – with monochromatic Cu-Kα emission ($\lambda = 1.54056$)Å and Bragg-Brentano focusing geometry.

RESULTS AND DISCUSSION

The phase structure of the thin films deposited by thermal evaporation at deposition rates 0.03 and 0.1 nm/s was probed by X - ray diffraction (XRD). The XRD patterns of the thin silver films are shown in Fig. 1. For comparison the XRD pattern of a thin silver film deposited by radio-frequency (*rf*) sputtering is given. Peaks due to diffraction from the crystallographic planes (111) and (200) at $2\theta = 38^{\circ}$ and 44°, respectively are seen in the pattern. The diffraction pattern of the thin film deposited at 0.1 nm/s demonstrates the sharpest and most intensive diffraction peaks.

* To whom all correspondence should be sent:
vlozanova@iomt.bas.bg

© 2015 Bulgarian Academy of Sciences, Union of Chemists in Bulgaria

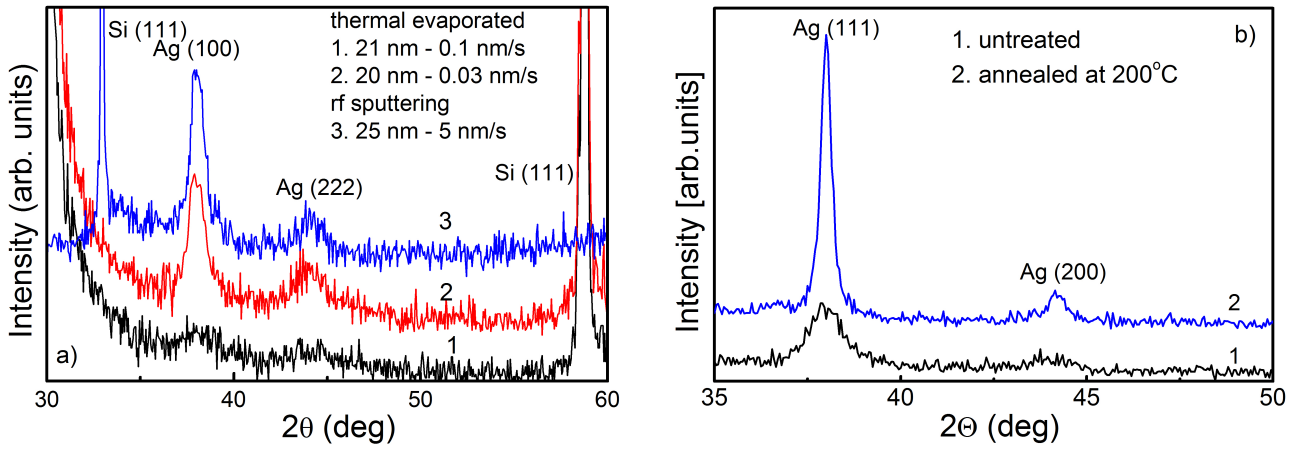


Fig. 1. X-ray diffraction patterns of thin silver films deposited by thermal evaporation on Si-wafer at deposition rates 0.03 and 0.1 nm/s and rf sputtering with thickness, $d \sim 0.02$ μm (a); X-ray diffraction patterns of a thin silver film deposited by thermal evaporation before and after annealing in vacuum ($\sim 10^{-3}$ Pa) at 200°C (b).

The microstructure of the thin silver films deposited by thermal evaporation at different rates in the range 0.04-0.44 nm/s is investigated in [8]. The authors found that silver shows a preferred orientation in (111) crystallographic plane. It was found that the average grain size and the intensity of X - ray diffraction peak, its width at half maximum (FWHM) depend on the deposition rate.

It is seen that the diffraction pattern of the thin film deposited by cathode sputtering demonstrates narrow peaks. It was determined that the temperature of the substrate during the sputtering process was arisen to 200°C. According to [10] the annealing temperature of very thin silver films is a key factor for the transformation of the size of the grains building the layer. Depending on the temperature, collision or separation can be observed. Therefore we annealed the thin silver film in vacuum ($\sim 10^{-3}$ Pa) at 200°C. In Fig. 1b the X-ray diffraction patterns before and after annealing are shown. It is seen that after annealing the diffraction peaks become narrower and possess higher intensity.

The Debye-Scherrer formula was applied for the calculation of the average crystallite size:

$$d_p = \frac{0.94\lambda}{\beta cos\Theta}, \qquad (1)$$

where β is the peak width, λ is wavelength of the X-rays (in the present study Cuα line was used and $\lambda = 1.54056$ Å).

The data from the XRD pattern and the results from the calculation of the grain size are summarized in Table 1. It is seen that the increase of the deposition rate in the thermal evaporation decreases the grain size of the thin films. The deposition of the thin films on the warm substrate, i.e. by sputtering leads to an increase of the size of the grains.

Table 1. The half-width (FWHM) of diffraction peak for Ag (111) and the grain size, d_g

Deposition rate, V [nm/s]	Peak half-width (FWHM) [rad]	Particle size, d_g [nm]
0.03	0.027	8.18
0.10	0.015	10.5
5 *(rf sputtering)*	10	11

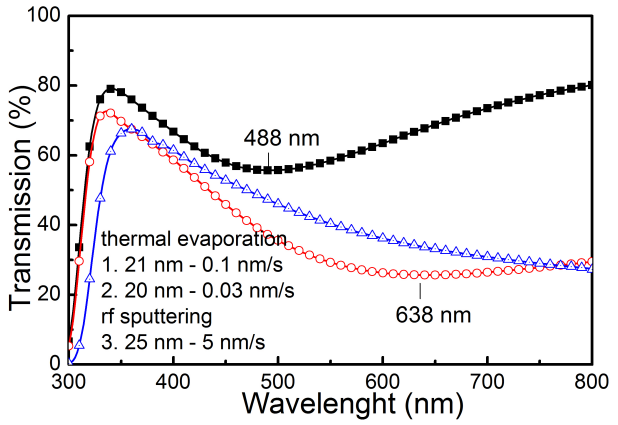


Fig. 2. Transmittance spectra of thin silver films deposited by thermal evaporation (deposition rates 0.03 and 0.1 nm/s) and *rf* sputtering.

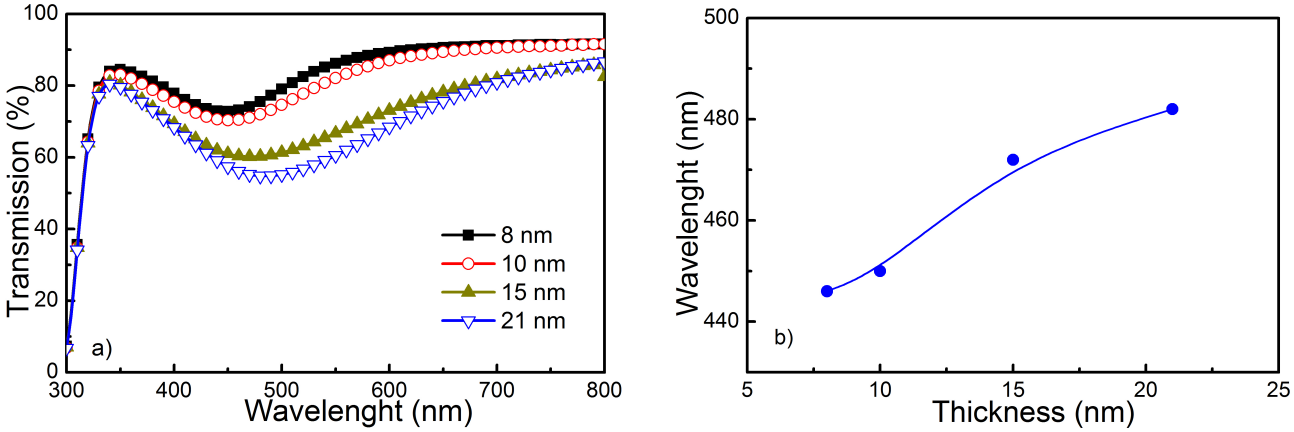


Fig. 3. Transmittance spectra of thin silver films deposited by thermal evaporation at 0.03 nm/s (a) and position of maximum absorption in dependence of the film's thickness (b).

The transmittance spectra of the same thin films in the spectral range 300-800 nm are shown in Fig. 2. A presence of absorption bands is seen in the spectra of the thin films deposited at the deposition rates 0.03 and 0.1 nm/s. It is seen that the increase of the size of the grains leads to a shift of the absorption band to longer wavelengths.

The transmittance spectra of thin silver films in the thickness range 8–21 nm and deposited with deposition rate 0.1 nm/s are given in Fig. 3a. It is seen that the position the absorbance band is varied from 448 to 488 nm. In the thickness range of 10–20 nm we can expect that the film is structured with discrete islands similar to nanoparticles [10]. According to [11] the small metal particles (with diameter < 40 nm) absorb energy through the following mechanisms: (i) Collective excitations of the "free" electrons, which give rise to surface modes or surface plasmon resonances that are determined by the particle shape and variations of the dielectric function; (ii) Electron transitions of bound electrons from occupied to empty bands of different index, also called interband transitions; (iii) Surface dispersion or scattering of the "free" electrons, when their mean free path is comparable with the size of nanoparticles. The resonance wavelength depends on the orientation of the electric field relative to the particle and the size and form of the nanoparticles. According to different literature sources [11,12], the maximum absorption of the silver nanoparticles is placed in the spectral range of 420-650 nm. The dependence of the position of maximum absorption on the film's thickness is shown in Fig. 3b. According to [10] with the increasing of the thin films the average size of grains which built the thin films increases

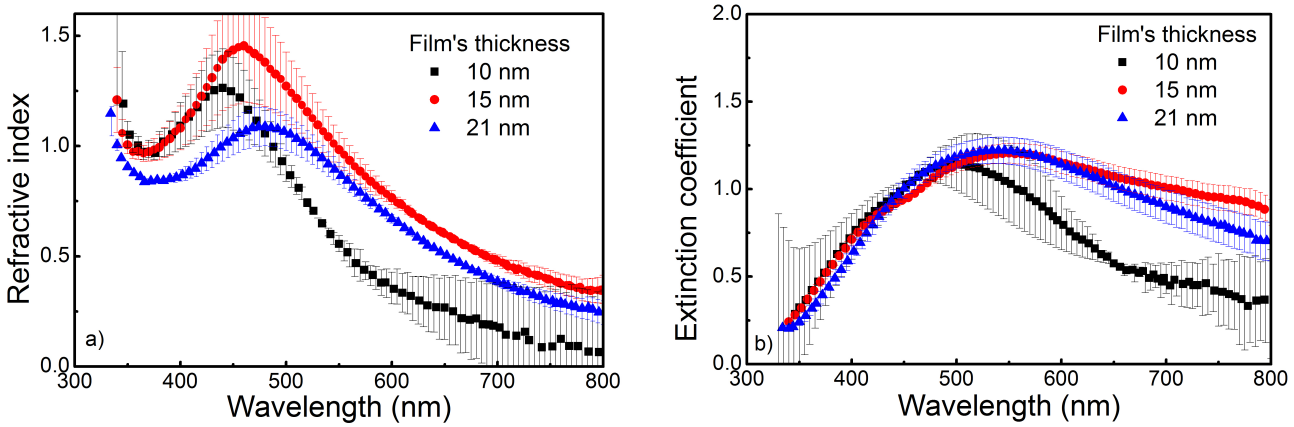


Fig. 4. Refractive index, n and extinction coefficient, k of thin silver films in the thickness range 10–21 nm.

and maximum scattering is expected to shift to longer wavelengths.

The optical constants (refractive index, n and extinction coefficient, k) of the thin films are given in Fig. 4. The calculation method is detailed in our previous work [9]. The maximal error is determined assuming ± 5 nm accuracy in the thickness determination. As expected, the experimental error for the refractive index is higher in the range of resonance wavelengths and it decreases for wavelengths longer than 550 nm for thin films with thicknesses 15 and 21 nm. It is seen that the thin film with thickness 10 nm possess smaller values for the refractive index and extinction coefficient in the spectral range 500–800 nm while the thin films with thicknesses 15 and 21 nm have nearly similar optical constants. The increase of the extinction coefficient with increase film's thickness can be explained with increasing of the number free electrons. Similar trend in thickness dependence of the extinction coefficient has been observed in [13]. It is seen that trough the variation of the thickness of the thin films we can varied the position of the absorption band in the visible spectral range.

CONCLUSIONS

The present paper is focused on the investigation of the optical properties of nanocrystalline silver thin films and attempts to understanding the effects related to the particle size. Ag-films were deposited by thermal evaporation on optical glass with thickness from 10 nm to 20 nm. The grain size, determined from the X-ray diffraction patterns applying the Debye-Scherrer's formula, was in the range of 2–10 nm.

It was found that the size of the grains building the thin films depends on the deposition condition and that the dimension of the particles governs the optical properties of the thin films. The present results can be used for modeling of metal-dielectric composite coatings for application as sun absorbers for photovoltaic elements.

REFERENCES

[1] Y-J. Jen, A. Lakhtakia, C-W. Yu and Ch-T. Lin, *Opt. Express* **17**, 7784–7789 (2009).

[2] C. Y. Chen, M. W. Tsai, T. H. Chuang, Y. T. Chang and S.C. Lee, *Appl. Phys. Lett.* **91**, 063108 (2007).

[3] B. T. Schwartz and R. Piestun, *J. Opt. Soc. Am. B* **20**, 2248–2253 (2003).

[4] T. Kawagoe and T. Mizoguchi, *Jpn. J. Appl. Phys.* **32**, 935–938 (1993).

[5] J. Lv, *Appl. Surf. Sci.* **273**, 215–219 (2013).

[6] D. P. Singh, P. Goel and J. P. Singh, *J. Appl. Phys.* **112**, 104324 (2012).

[7] W. Cai and V. Shalaev, *Optical Metamaterials, Fundamentals and Applications*, Chapters 1 and 2, Springer, NewYork, Dordrecht Heidelberg, London, 2010, pp. 1–36.

[8] L-P. Wang, P-D. Han, Z-X. Zhang, B-S. Xu, *J. Synthetic Cryst.* **43**, 99–103 (2014).

[9] V. Lozanova, J. Tasseva and R. Todorov, *Bulg. Chem. Commun.* **45**, 43–46 (2013).

[10] A. N. Belov, S. V. Bulyarsky, D. G. Gromov, L. M. Pavlova and O. V. Pyatilova, *CALPHAD: Computer Soupling of Phase Diagrams and Thermochemistry* **44**, 138–141 (2012).

[11] C. Nogues, *J. Phys. Chem. C* **111**, 3806–3819 (2007).

[12] D. Rajesh and C. S. Sunandana, *Appl. Surf. Sci.* **259**, 276–282 (2012).

[13] B. Lu, X. Xu, X. Yu and Z. Fan, *Acta Optica Sinica* **30**, 283–286 (2010).

МИКРОСТРУКТУРА И ОПТИЧНИ СВОЙСТВА НА МНОГО ТЪНКИ СРЕБЪРНИ СЛОЕВЕ ОТЛОЖЕНИ ЧРЕЗ ТЕРМИЧНО ИЗПАРЕНИЕ

В. Лозанова, Р. Тодоров

Институт по оптически материали и технологии "Акад. Йордан Малиновски", Българска академия на науките, ул. "Акад. Г. Бончев" бл. 109, 1113 София, България

(Резюме)

Настоящата работа показва резултати за изследване на оптичните свойства на тънки нанокристални сребърни филми с цел да се установи тяхната зависимост от размера на частиците (зърната) изграждащи слоевете. Тънки сребърни филми бяха отложени чрез термично изпарение върху подложки оптично стъкло и силиций с дебелина от 10 до 20 nm. В зависимост от скоростта на отлагане, поради различния размер на зърната изграждащи слоевете се наблюдаваше вариране на цвета на покритията от червен до син. Размера на зърната беше определен чрез рентгенова дифракция чрез формулата на Дебай-Шерер. В спектрите на коефициента на пропускане се наблюдаваше абсорбционна ивица дължаща се на повърхностните плазмони. В зависимост от размера на зърната максимума на поглъщането е в обхвата от 400 до 550 nm. Изследвано е влиянието на термично третиране във вакуум (10^{-3} Pa) върху размера на зърната. Установено е, че нагряването на филмите с дебелина 25 nm при температура 250°C води до агрегация на зърната.

CONDENSED MATTER PHYSICS

ФИЗИКА НА КОНДЕНЗИРАНАТА МАТЕРИЯ

Bulgarian Chemical Communications, Volume 47, Special Issue B (pp. 63–70) 2015

Silicon surface modified by H^+ ion plasma immersion implantation and thermal oxidation

S. Alexandrova[1*], A. Szekeres[2], E. Valcheva[3]

[1] *Department of Applied Physics, Technical University of Sofia, 8 Kl. Ohridski Blvd., 1797 Sofia, Bulgaria*
[2] *Institute of Solid State Physics, Bulgarian Academy of Sciences, 72 Tzarigradsko Chaussee Blvd., 1784 Sofia, Bulgaria*
[3] *Faculty of Physics, Department of Solid State Physics and Microelectronics, St. Kliment Ohridski University of Sofia, 5 James Bourchier Blvd., 1164 Sofia, Bulgaria*

In this contribution results on the study of modification of Si surface through shallow plasma immersion ion (PII) implantation of H^+ ions with energy of 2 keV and doses ranging from 10^{13} H^+/cm^2 to 10^{15} H^+/cm^2 are presented. The implantation was regarded to proceed into Si through native SiO_2 layer. The structure and the optical properties of thin hydrogenated Si layer are characterized using spectroscopic ellipsometry (SE) and simulation of the distributions of the ions and implantation induced defects. Two-layer optical models are applied for examination of the composition and dielectric function behavior of the formed structures. The native oxide is found to be 3 nm thick. The thickness of the Si modified layer ranged between 23 to 14 nm depending on ion fluence. After oxidation the formed SiO_x layers were characterized by optical spectroscopy methods. Observed variations in oxide composition and optical parameters are connected with the structure of the PII modified Si layer being oxidized, leading to lower intrinsic oxide stress (below $\sim 7 \times 10^8$ N/m^2) and smaller oxide refractive index as compared to the stoichiometric SiO_2. The built-in internal stress was evaluated from the displacements of the characteristic peaks at 3.4 eV of Si in the RS and ER spectra and from the refractive index gained by SE. The results indicate the possibility to obtain structures with reduced structural strains and low concentration of defects.

Key words: Hydrogen implantation, PIII Si Surface Modification, Stress

INTRODUCTION

Modification of surfaces has gained increasing importance for device fabrication in the next generation when the active regions are located in shallow surface layers. Incorporation of hydrogen into silicon offers the possibility to build very thin nanosized silicon oxide layers that can have different role in silicon based structures and devices.

However, incorporation of hydrogen in silicon device can have detrimental as well beneficial effects on device parameters. The purpose is to enhance beneficial and surpass detrimental. For that reason the role of hydrogen has been the subject to intensive investigations in the past decade. Among different beneficial effects stabilization of device characteristics through gettering of impurities and saturation of defects for future nanoelectronic applications, for exfoliation of silicon in smart cut process, increase carrier life time in solar cells, etc., can be stated. The detrimental effect appear mostly because the passivated through hydrogen saturation of dangling Si bonds defects can act as week Si-H states which have the tendency to disrupt and annihilate the pasivation effect upon external influence and long device exploitation. Several hydrogen related defects, i.e. Si-H bonds, hydrogen induced platelets, monatomic hydrogen, hydrogen molecules, and hydrogen-related complexes have been discussed in the literature [1,2]. The mechanisms that govern interactions of hydrogen-related species with silicon defects and their role in grown process are still under debate.

Future new developments require detailed studies of hydrogen behavior in semiconductors. Of special interest is the behavior of hydrogen on the silicon surface and its role in the oxide growth process. Hydrogen can easily be introduced into semiconductors through proper hydrogen containing environments. In Si technology hydrogenation is usually achieved by implantation process, either beam [1,3] or plasma ion implantation (PIII) [4,5]. In spite of the advantages (shallow implants and large implanted area) PIII technique still is related with formation of lattice defects induced by collisions of implanted ions with the surface and atoms of substrate material in addition to plasma radiation.

The present study is devoted to the mechanism of influence of hydrogen introduction in Si through ion implantation on the structure and optical properties of the nanoscaled surface layer. The impact was placed to the possibility to achieve control over the mechanical stress in the silicon oxide layers since this pa-

* To whom all correspondence should be sent:
salex@tu-sofia.bg

© 2015 Bulgarian Academy of Sciences, Union of Chemists in Bulgaria

rameter has an effect on overall characteristics of the devices including structural defects.

Hydrogenation of the surface region of c-Si substrates is achieved by shallow low energy plasma-beam H^+ ion immersion implantation with different fluences up to 10^{15} cm^{-2}. The study was performed using highly sensitive optical methods combined with modeling the distributions of the ions and implantation induced defects. The process-induced changes in the structure and optical properties of the thin hydrogenated Si layer and the SiO_x layer formed on it are studied.

EXPERIMENTAL DETAILS

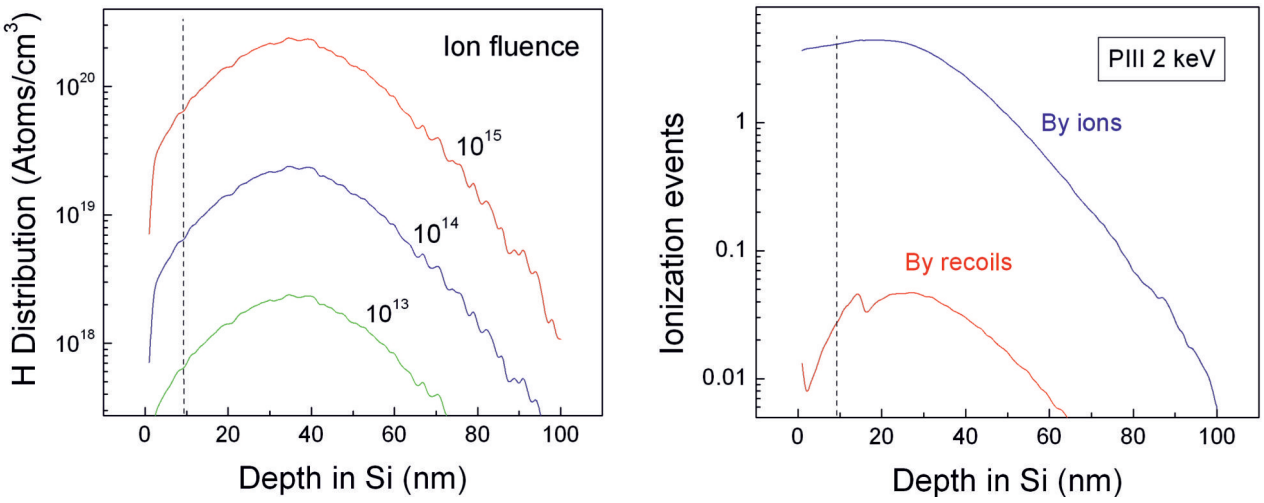
The wafers in this study were monocrystalline Si (c-Si), Cz-grown Wacker wafers with orientation Si(100) and Si(111) and resistivity ranging from 4 to 10 Ohm.cm. The c-Si surface was modified by plasma immersion ion (PII) implantation accomplished in a planar plasma reactor. No externally heating was applied to the substrates. The energy of H^+ implant was chosen as low as 2 keV, so that the projected H^+ implantation depth in Si substrate to be approximately within 20–30 nm inwards the Si surface. The H+ fluence varied from 10^{13} to 10^{15} H^+/cm^2. Before implantation the samples underwent a standard RCA cleaning procedure, while after implantation, possible surface contaminations were removed by a short dip in diluted HF.

Next very thin silicon oxide layers have been formed on the hydrogenated Si substrates through exposure to dry O_2 atmosphere at temperatures ranging from 700° to 850°C. The layers were characterized by micro-Raman spectroscopy (RS), spectroscopic ellipsometry (SE) in the VIS range and electroreflectance (ER) spectroscopy. The observed displacement of the characteristic peak at 3.4 eV of Si relative to unstressed situation in the SE and ER spectra is related to internal stress resulting from the technological processes. In the spectra RS the mechanical stress from the shift of the 520 cm^{-1} Si Raman phonon mode is known to be sensitive to lattice strain [6]. The Raman spectra were obtained by LabRAM HR micro-Raman spectrometer equipped with CCD detector at laser excitation wavelength of 632 nm. The peak position accuracy is below 0.05 cm^{-1}. Using ER and SE the mechanical stress in Si/oxide was determined from the shift of the energy position of the Si direct bandgap at 3.4 eV [7]. The ER spectra were measured recording the modulation of the reflectivity $\Delta R/R$ in response of an external modulating electric field applied to the sample in the photon energy region of 3.0–3.8 eV around the Si direct bandgap energy. The sensitivity in measuring $\Delta R/R$ was 1 ppm, and the accuracy of measuring the signal strength was 2%. The measurements were performed at room temperature in the low-field mode condition. The values of the direct transition E_g and broadening parameter Γ, were calculated from the analysis of the ER spectra line shape using the Aspnes three-point technique [8]. SE spectra were taken with a "Rudolph Research" variable-angle ellipsometer with polarizer-compensator-sample-analyzer configuration in the spectral range of 300–640 nm. The accuracy of the polarizer, analyzer and incidence angle was within $\pm 0.01^{\circ}$. The pseudo-dielectric function $\langle \varepsilon \rangle$ has been calculated following the procedure outlined elsewhere [9].

The depth profiles of the implanted ions and implantation induced defects were derived using the SRIM code based on a Monte-Carlo simulation method [10] for different ion fluences.

RESULTS AND DISCUSSION

Hydrogenation is known for its modification of Si surfaces [11], forming an overlayer which is less dense and contains voids and attached H-atoms and defect sites [12]. On one hand voids could mean smaller internal stress and subsequent oxidation of the modified surface can proceed faster. On the other hand, the transitional region between the oxide and the Si substrate can be located just in this modified layer. Hydrogenation induced defects are precursors of interface defect centers that appear at the interface after dry oxidation. Some defects remain in the Si substrate and some are incorporated into the oxide layer. Although implantation with the light H^+ ions is not expected to cause severe damage in the Si lattice, the ionization effects can be substantial. Simulation using SRIM code shows the hydrogen concentration profile ionization events in the Si subsurface region as displayed in Fig. 1. High hydrogen concentration in the Si subsurface region is evident from the results in Fig. 1a, which however, is not necessarily sufficient for complete hydrogen saturation of the dangling bonds at the interface. The ionization effects lead to defect generation in the Si subsurface region where the oxide layer will be displayed during oxidation. This region is marked in Fig. 1 by the dotted line.



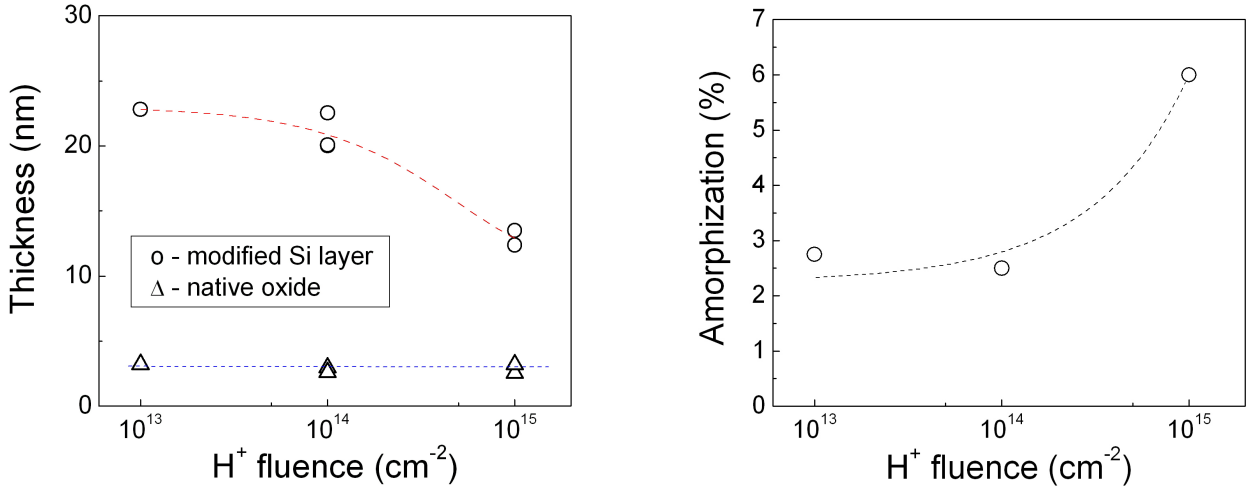
(a) (b)

Fig. 1. Ion (a) and vacancy (b) profiles for implantation with 2 keV H^+ into Si wafers.

From the ion distribution in Fig.1a it is evident that the maximum of the concentration is located at 36 nm. During subsequent oxidation when the hydrogenated Si wafer is subjected to elevated temperature this distribution will alter. Suggesting diffusion as a mechanism of migration of the H^+ ions the profile was modeled using standard diffusion equation with $D = D_0 \exp(-E_a/kT)$ diffusion coefficient $D_0 = 9.4 \times 10^{-3}$ cm^2/s and activation energy $E_a =$ 0.48 eV [13]. The ion distribution profile was flattened at a very low level. Such a low hydrogen concentration would have no influence on the oxidation process and on the optical and morphological properties of the hydrogenated Si surface. It can be suggested that possible anomalies in H^+ diffusion behavior in Si occur, which can be attributed to trapping of H at implantation induced defect centers. Support of this suggestion comes from modeling of the optical constants from data gained by the ellipsometric study. Performing the optical modeling results have been gained for the thickness of the layer being modified by the hydrogen implant and the alteration of its optical constants from those of unimplanted c-Si material. The optical modeling of the ellipsometric data (discussed in detail elsewhere [14] established a thin native oxide on the Si substrates with an average thickness of 3 nm (Fig. 2a). The thickness of the modified Si layer, given also in Fig. 2a, was found to be dependent on H^+ fluence. It can be seen that it shrinks with increasing the ion fluence. Most probably, higher H^+ fluence caused stronger lattice disorder and larger amount of defects in the Si surface region, being an impediment to the H motion inwards. The other reason for that could be the H solubility- related saturation of the Si surface, which additionally hinders the H implants motion [15,16]. Indirect evidence for the process induced damage was the presence of an amorphized Si phase in the Si surface layer. Depending on H+ fluence its volume fraction amounted to 2.4%, 2.7% and 5.8% for fluences of 10^{13}, 10^{14} and 10^{15} cm^{-2} H^+, respectively (Fig. 2b). Including voids fraction in the modeling of the effective medium composition gave unsatisfactory fitting results. This can be regarded as an indication that the voids, if present, bear a lower fraction than the one used in the modeling. This composition can be characterized as substoichiomertic SiO_x.

As next approximation SRIM simulation was performed for the implantation energy of 2 keV used, the implantation being taken to proceed into Si through the native SiO_2 with thickness of 3 nm as found from the SE data modeling. Fig. 3 shows the depth profiles of the implanted H^+ ions and the implantation generated defects (vacations created by incoming ions and recoils). From Fig. 2 it was inferred that the thickness of the H-modified Si region depends on ion fluence. The question is whether this dependence can be related to the profile of the implanted hydrogens since it is known that different fluences change only the intensity of peaks and not their position.

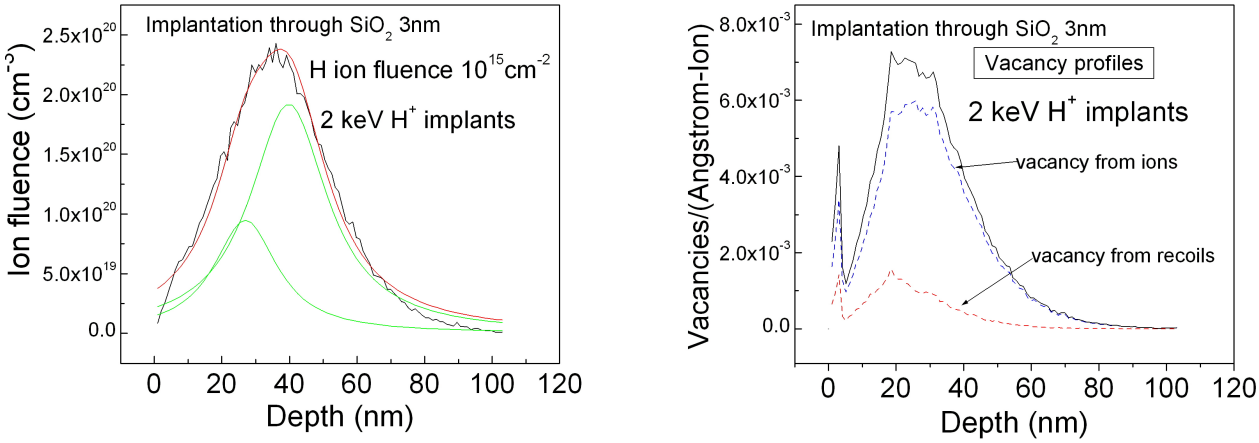
As seen in Fig. 3a, the deconvolution of the ion concentration spectrum resulted in two components, one expending deeper into the Si bulk. It could be expected that the shallower peak lies in the native oxide.



(a) (b)

Fig. 2. Thickness of the native oxide and the modified Si surface layer vs. H^+ fluence (a). Volume fraction of the amorphized Si in the modified Si layer (b).

However, this peak has its maximum at a much deeper position (∼20 nm) than the SiO_2 thickness (∼3 nm). Then it is reasonable to suggest that the modified Si region is related rather to defects created by the ion implantation process than the projected range of hydrogen ions. In Fig. 3b SRIM simulation data for vacations shows two defect regions that can be identified lying in the oxide and within the Si. The effect of the ion implantation fluence on the modified Si thickness is not obvious. However, it can be suggested that the highest fluence can have a more pronounced effect on the modification process. The implanted hydrogen atoms could be captured in the SiO_2 up to the peak of the defects in the bulk to form a region with high H-concentration similarly to the process by the Si exfoliation [17]. Taking in view that by PII not only H^+ but also H_2^+ and H_3^+ species are implanted, whose energies are 1/2 and 1/3 of the total implantation energy, respectively. The defect profiles for these species are shallower than for the H^+, filling the well between the SiO_2 and bulk peaks and forming a continuous defect region. Our fluences are well below the typically needed for film transfer process of mid-10^{16} atoms/cm^2 [11], so that no pile-up takes place, but the highly hydrogenated region can hinder further H-penetration into the Si bulk. The modified Si region



(a) (b)

Fig. 3. Ion (a) and defect (b) profiles for implantation with 2 keV H^+ through SiO_2 into Si wafer.

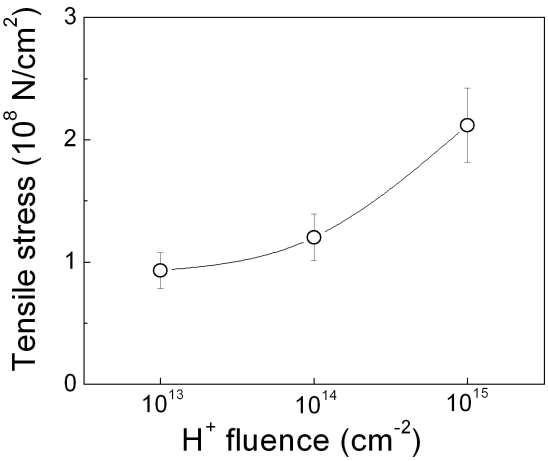


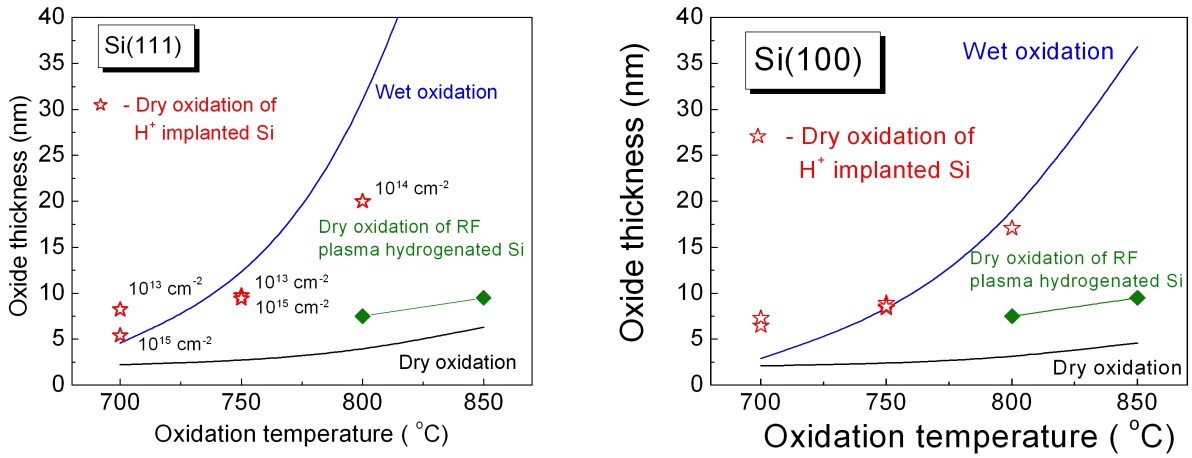
Fig. 4. H^+ implantation induced stress in the native oxide and the Si substrate as a function of H^+ fluence.

would then extent up to about 20 nm as seen by the position of the defect concentration peak in Fig. 3b, which correlates well with the thicknesses of the modified Si surface layer ranging 23-14 nm (Fig. 2a).

Modeling the dielectric function shifts of the critical energy points around ~3.4 and ~4.2 eV were observed. These were interpreted as due to the structural defects created by the ion implantation process, which in turn generates strains inside the silicon. Therefore, the shifts of the energy positions carry information about the internal stress in the modified layer. The evaluated tensile stress levels in Si as a function of H^+ fluence is presented in Fig. 4. Here the average shifts of the two energy peaks are taken for the stress calculation. Apparently, H+ implantation with lower fluences generated negligible structural strains in the implanted region and even at 10^{15} cm^{-2} it remains below 2.5×10^8 N/cm^2.

Modification of Si surface layer upon hydrogenation of the Si wafer influences the subsequent oxidation mechanism. The transitional region between the oxide and the Si substrate can be located just in this modified layer. It was established that oxidation rates increase up to values comparable those for wet oxidation and are orientation dependent. This is evident in Fig. 5, where comparative results on the oxidation rates are displayed for both Si(111) and Si(100).

Mechanical stress levels in the Si surfaces hydrogenated at different conditions were evaluated applying the three spectroscopic techniques SE, RS and ER. The refractive index as a function of wavelength gained from modeling of SE data is presented in Fig. 6a. Taking the values at 633 nm the stress was calculated. From the shifts of Si Raman mode (Fig. 6b) and Si direct energy gap in ER spectra (Fig. 6c) relative to unstressed positions also allow information on stress level to be extracted. The quantification to transfer the SE, RS and ER results into mechanical stress was assessed taking in view the strain coefficient corresponding to theoretically evaluated hydrostatic equivalence [18,19], assuming homogeneous structures and, consequently, uniaxial stress conditions. Evaluating the stress from ER and SE correlation coefficient was taken 2.09×10^7 N/m^2/meV [20]. Appling RS the value of 4.34×10^8N/m^2/cm^{-1} was used [21]. The results are summarized in Fig. 6d.



(a) (b)

Fig. 5. Oxidation rates for Si wafers hydrogenated with different H^+ fluences at oxidation temperatures from 700 to 850°C for Si(1110 (a) and Si(100) (b).

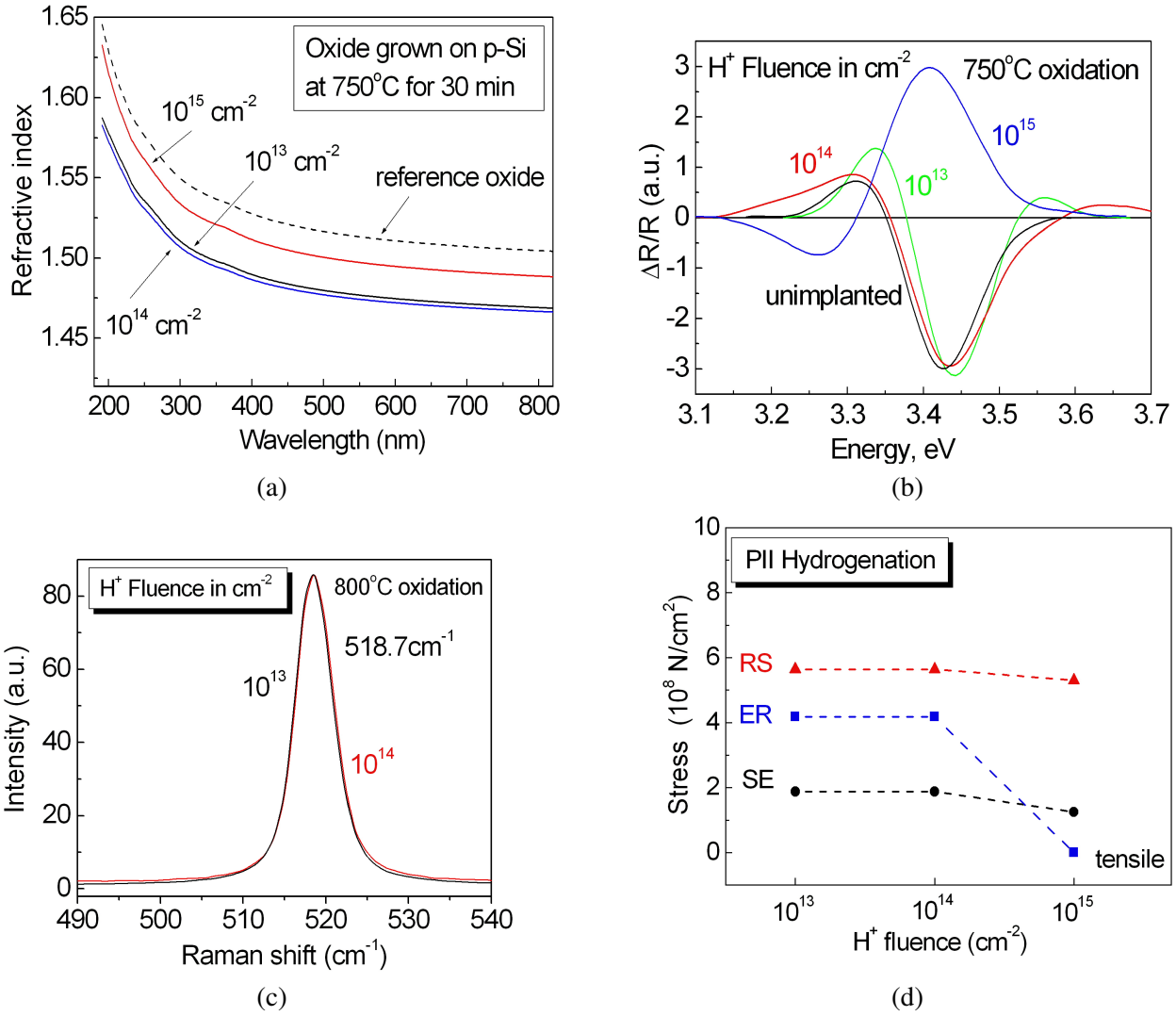


Fig. 6. a) SE spectra of the refractive index of the oxidized Si surface; b) Electroreflectance spectra of the oxidized Si surface for different H^+ implantation fluences; c) RS spectra for oxidized Si surface hydrogenated by RF hydrogen plasma; d) Mechanical stress in oxidized Si surface hydrogenated by PIII.

Additional conclusion from the results for the refractive index in Fig. 6a concerns the value at 633 nm, which is below the typical 1.46 for stoichiometric SiO_2. This supports the assumption that oxide composition is SiO_x, $x < 2$.

Although certain differences are observed in the results gained by the different measurement techniques, there are tendencies that are worth to notice. It is well documented that thermal oxidation of Si results in oxide in compressive stress and, consequently tensile in the underlying Si. The optical techniques applied in the present study probe the stress condition of the Si substrate. It is seen from Fig. 6d that hydrogenation results in low tensile stress of Si and low compressive stress in the oxide, i.e. leads to less strained oxide/Si structure in comparison to over 10^9 N/cm^2 for oxide on unhydrogenated Si [22]. Lower stress level is related to low defect densities.

Comparison with the stress level after PII hydrogenation (see Fig. 4) shows that oxidation process induces additional stress, which is due to the extension of the Si lattice parameter through the advent of the oxygen atoms. It is well established that this enlargement amounts to about 20% from the initial Si volume. In spite of the oxidation induced increase, the obtained stress levels show low levels taking in view that the oxidation temperature is low and no postoxidation annealing was applied. This beneficial effect is achieved through Si hydrogenation by PIII technology.

CONCLUSIONS

Application of PII implantation on Si wafers modifies the Si surface creating a 14-23 nm thick (varying with H^+ fluence) Si surface layer characterized by low degree of amorphization (up to 5.8 %), creation of structural defects and small degree of internal tensile stress. The modified Si region is related rather to defects created by the ion implantation process than the projected range of hydrogen ions. The subsequent oxidation at low temperatures below 800°C results in growing of substoihimetric SiO_x layer with low compressive stress. Oxidation rate is higher in comparison to dry Si oxidation approaching the value for wet oxidation. Modification of Si by PIII hydrogenation offers possibility of preparation of SiO_x layers on Si wafers at controllable mechanical stress at technologically reasonable oxidation rate.

REFERENCES

[1] O. Moutanabbir, B. Terreault and A. Giguére, *Phys. Stat. Sol. c* **6**, 1958-1963 (2009).

[2] M. Xu and X. Q. Feng, *Theoretical Appl. Fracture Mechanics* **42**, 295-301 (2004).

[3] C. Moulet and M. S. Goorsky, "Lattice Strain Measurements in Hydrogen Implanted Materials for Layer Transfer Processes" in *Ion Implantation*, edited by M. Goorsky, Rijeka, InTech, 2012, pp. 65-88.

[4] P. K. Chu, *J. Vac. Sci. Technol. B* **22**, 289-296 (2004).

[5] J. D. Bernstein, S. Qin, C. Chan and T. J. King, *IEEE Electron Device Lett.* **16**, 421-423 (1995).

[6] I. de Wolf, *Spectroscopy Europe* **15**, 6-13 (2003).

[7] J. W. Grover and P. Handler, *Phys. Rev. B* **9**, 2600-2006 (1974).

[8] J. Misiewicz, P. Sitapek and G. Sek, *Opto-Electron. Review* **8**, 1-24 (2000).

[9] A. Szekeres, A. Paneva and S. Alexandrova, *Vacuum* **343-344**, 8-12 (1999).

[10] J. F. Ziegler, J. P. Biersack and U. Littmark, *The Stopping and Range of Ions in Matter*, New York, Pergamon, 1985.

[11] A. Szekeres, P. Lytvyn and S. Alexandrova, *Appl. Surf. Sci.* **191**, 148-152 (2002).

[12] R. Job, Y. Ma and A. G. Ulyashin, *Mat. Res. Soc. Symp. Proc.* **788**, L3.34 (2004).

[13] A. Van Wieringen and N. Warmoltz, *Physica* **22**, 849-865 (1956).

[14] M. Anastasescu, M. Stoica, M. Gartner, S. Bakalova, A. Szekeres and S. Alexandrova, *Journal of Physics: Conf. Series* **514**, 012036 (2014).

[15] M. J. Binns, S. A. McQuaid, R. C. Newman and E. C. Lightowlers, *Semicond. Sci. Technol.* **8**, 1908-1911 (1993).

[16] M. Stavola, Chapter 9.8 in *Properties of Crystalline Silicon*, edited by R. Hull, London, INSPEC, 1997, pp. 511-519.

[17] R. Job, W. Düngen, Y. Ma, W. R. Fahrner, L. O. Keller, J. T. Horstmann and H. Fiedler, *ECS Transactions* **3**, 147-157 (2006).

[18] J. T. Fitch, C. H. Bjorhmann, G. Lucovsky, F. H. Pollak and X. Yin, *J. Vac. Sci. Technol. B* **7**, 775-781 (1989).

[19] A. B. Horsfall, J. M. M. dos Santos, S. M. Soare, N. G. Wright, A. G. O'Neill, S. J. Bull, A. J. Walton, A. M. Gundlach and J. T. M. Stevenson, *Semicond. Sci. Technol.* **18**, 992-996 (2003).

[20] T. Ya. Gorbach, G. Yu. Rudko, P. S. Smertenko, S. V. Svechnikov and M. Ya. Valakh, *Appl. Phys. A: Mater. Sci. & Process.* **58**, 183-186 (1994).

[21] E. Anastassakis, A. Cantarero and M. Cardona, *Phys. Rev. B* **41**, 7529–7535 (1990).

[22] G. Lucovski, `http://www.mdm.imm.cnr.it/sites/default/files/ESF/presentations/Lucovsky_inter_rev.pdf`

МОДИФИЦИРАНЕ НА Si ПОВЪРХНОСТ ЧРЕЗ ПЛАЗМЕНА ЙОННА ИМПЛАНТАЦИЯ НА H^+ И ТЕРМИЧНО ОКИСЛЕНИЕ

С. Александрова[1], А. Секереш[2], Е. Вълчева[3]

[1] *Департамент по приложна физика, Технически университет – София, бул. "Кл. Охридски" №8, 1000 София, България*
[2] *Институт по физика на твърдото тяло, Българска академия на науките, бул. "Цариградско шосе" №72, 1784 София, България*
[3] *Физически факултет, Софийски университет "Св. Кл. Охридски", бул. "Дж. Баучер" №5, 1164 София, България*

(Резюме)

Модификацията на полупроводникови повърхности представлява интерес за приборите от следваща генерация, при които активните области се разполагат в тънък приповърхностен слой. Включването на водород в силиций дава възможност за формиране на свръхтънки наноразмерни слоеве от силициев оксид, които могат да изпълняват различна роля в структури и прибори на базата на силиций.

В настоящата работа са представени резултати по изследване на оптичните свойства на окислена Si повърхност, модифицирана чрез хидрогениране на тънък приповърхностен слой. Хидрогенирането се извършва чрез плазмена йонна имплантация на H^+ йони с енергия 4 keV и дози от 10^{13} H^+/cm^2 до 10^{15} H^+/cm^2. Свръхтънки слоеве SiO_x се формират върху хидрогенираната Si повърхност чрез окисление в среда на сух O_2 при температури от 700°C до 850°C. Словете са характеризирани чрез микро-Раманова спектроскопия, спектрална елипсометрия във видимата област и електроотражение. Изследвани са пряката зона при 3.4 eV на Si от данните на спектрална елипсометрия и електроотражение, параметърът на уширение на пиковете на електроотражение и положенията на Рамановите линии и полуширините им. Отместванията на характеристичните пикове в изследваните спектри са пряко свързани с вътрешните механични напрежения в структурите. Резултатите показват, че върху хидрогенирана Si повърхност могат да се получават оксидни слоеве с понижени механични напрежения и високи концентрации на структурни дефекти.

При плазмената имплантация модифицираният слой е с дебелина от 14 до 23 nm в зависимост от H^+ доза и се характеризира с ниска степен на аморфизация (до 5.8%), генерация на структурни дефекти и ниски механични напрежения на разтягане. Параметрите на оксидните слоеве също показват зависимост от имплантационната доза, а също и от температурата на окисление. Вариациите в състава и оптичните параметри на слоевете са свързани със структурата на модифицирания при имплантацията Si слой. Процесът на окисление води до ниски механични напрежения на свиване (под $\sim 7 \times 10^8$ N/m^2) и показател на пречупване, по-нисък от този на стехиометричния SiO_2. Специално внимание е отделено на възможностите за контрол на механичните напрежения в слоевете, тъй като те влияят на структурните дефекти и по този начин определят крайните характеристики на приборите.

Bulgarian Chemical Communications, Volume 47, Special Issue B (pp. 71–75) 2015

Study of LPE grown dilute nitride GaInAsN layers with small concentration of Nitrogen by PL and Hall effect measurements

M. Milanova[1]*, P. Vitanov[2], P. Terziyska[3], G. Koleva[1], C. Barthou[4], B. Clerjaud[4]

[1] *Central Laboratory of Applied Physics, Bulgarian Academy of Sciences, 61 Sankt Peterburg Blvd., 4000 Plovdiv, Bulgaria*
[2] *Central Laboratory of Solar Energy and New Energy Sources, Bulgarian Academy of Sciences, 72 Tsarigradsko Chaussee Blvd., 1784 Sofia, Bulgaria*
[3] *Institute of Solid State Physics, Bulgarian Academy of Sciences, 72 Tsarigradsko Chaussee Blvd., 1784 Sofia, Bulgaria*
[4] *Université Pierre et Marie Curie, Institut des NanoSciences de Paris, rue de Lourmel 140, 75015 Paris, France*

In this paper electrical and optical properties of GaInAsN layers with small ($< 0.6\%$) nitrogen content have been studied by temperature dependent Hall effect and low-temperature photoluminescent measurements. Dilute nitride layers several microns thick have been grown by low-temperature liquid-phase epitaxy at different epitaxial temperatures. Polycrystalline GaN has been used as a source of nitrogen. The composition of the epitaxial GaInAsN layers has been determined by a combination of X-ray microanalysis and XRD measurements. Temperature dependences in the range 80–300 K of Hall free carrier concentrations and mobility have been analyzed. The effect of nitrogen on the electronic structure of the epitaxial layers have been studied from PL spectral features at 4.5 K.

Key words: dilute nitrides, InGaAsN, PL measurements, Hall effect measurements

INTRODUCTION

Dilute nitride alloys, such as GaInAsN, GaAsSbN, have recently attracted much attention as a potential materials for high-efficiency solar cells fabrication, due to their unique properties [1-3]. The incorporation of a small quantity of nitrogen into GaAs causes a dramatic reduction of the band gap and can be used for solar cells with extended long wavelength edge beyond the GaAs cut-off at 870 nm. Solar cells based on dilute nitride alloys are excellent suited for application in multijunction solar cells [4-6] and recently developed the spectral splitting concentrator photovoltaic system [7].

Unfortunately, the addition of small concentrations of nitrogen to GaAs layers results to a rapid reduction in bandgap energy with increasing of nitrogen concentration, but it also deteriorates the crystalline and optoelectronic properties of the dilute nitride materials, including reduction of the photoluminescence intensity and carrier lifetime, reduction of electron mobility and increase of the background carrier concentration. Near the critical composition the conduction band minimum is an "amalgamated state" form semi-localized and delocalized states of comparable energy and the duality of these states is responsible for many of the anomalous optical and electronic properties of dilute nitride alloys [8]. Technologically, the incorporation probability of nitrogen in GaAs is very small and strongly depends on the growth conditions The growth of dilute nitride alloys is difficult because of the wide immiscibility range, a large difference in the lattice constant value and very small atom radius of N atoms. Despite the progress in application of these materials in many optoelectronic devices based on quantum wells (QWs) structures, such as lasers at 1.3-1.5 μm and long-wavelength photodetectors, it remains difficult to obtain thick epitaxial layers with good crystalline quality [9]. The growth of thick epitaxial layers creates many problems which are absent in QWs structures.

In this paper we examine the electrical behavior of the liquid-phase epitaxy (LPE) grown thick GaInAsN layers with low nitrogen content grown at different technological conditions using Hall effect measurements and study the band gap formation of these dilute nitride layers by low-temperature photoluminescence (PL) measurements.

EXPERIMENT

A series of GaInAsN epitaxial layers have been grown on semi-insulating (100) GaAs substrates. The crystal growth was done in a horizontal quartz tube using a graphite boat designed for 10×15 mm^2 substrate. A flux of Pd-membrane purified hydrogen at atmospheric pressure was used for experiments. No

* To whom all correspondence should be sent:
milanovam@yahoo.com

© 2015 Bulgarian Academy of Sciences, Union of Chemists in Bulgaria

special baking of the system was done before epitaxy. Starting materials for the solutions consisted of 6N pure solvent metals Ga, In and of polycrystalline GaAs and GaN with purity of 5N. After the loading the charged boat was heated at 750°C for 1 h in a purified H^2 gas flow in order to dissolve the source materials and decrease the contaminants in the melt. Epitaxial GaInAsN layers 5–8 μm thick were prepared from In-rich solutions from two different initial epitaxy temperatures of 650 and 600°C. The crystallization was carried out from a melts containing 0.1 and 0.5 at.% nitrogen at a cooling rate of 1°C/min for 10 minutes. The composition of the epitaxial $Ga_{1-x}In_xAs_{1-y}N_y$ layers was determined by a combination of X-ray microanalysis and XRD measurements. The In content in the layers measured by X-ray microanalyses was between 2–2.2%. The N content was estimated from HR XRD curves using Vegard's law. The Hall mobility and carrier concentration in the layers were measured by the Van der Paw Hall technique on 5×5 mm^2 samples, with alloyed indium ohmic contacts. The photoluminescence (PL) spectra under excitation of 488 nm Coherent Argon laser were obtained at 4.5 K. They were analyzed with a Jobin-Yvon Spectrometer HR460 and a multichannel CCD detector.

RESULTS AND DISCUSSION

Four series of samples with different nitrogen content have been obtained. The incorporation of nitrogen into InGaAs strongly dependences on the growth temperature and nitrogen content in the growth melts. Samples E93 and E98 prepared from melts with 0.1% nitrogen content at two different temperature ranges of 650–640°C and 600–590°C contain 0.03 and 0.05% nitrogen, respectively. Nitrogen content in the samples E96 and E99 grown at the same temperature ranges from melts containing 0.5% nitrogen is 0.2 and 0.6%, respectively. Obviously the lowering the epitaxy temperatures and increase nitrogen content in the melt enhance the incorporation of nitrogen in the grown layers. Lattice-matched growth conditions have been established for layers containing 0.6% nitrogen. Since In and N have opposing strain effects on the lattice by adjusting the contents of In and N in quaternary InGaNAs alloy lattice-matched to GaAs dilute nitride layers have been grown. The lattice mismatch $\Delta a/a_0$ for sample E99 determined from the XRD spectrum was ~0.07%. The full width at half maximum (FWHM) of X-ray diffraction (XRD) $\omega/2\theta$ scan was 64 arc seconds for the 5.5 μm thick layer. The measured root mean-square (RMS) surface roughness by AFM method was 0.23 nm. The incorporation of lower N in the other three samples can't compensate the strain effect of In on the epitaxial growth. These samples have been grown metamorphic with rough surface and lower crystalline quality.

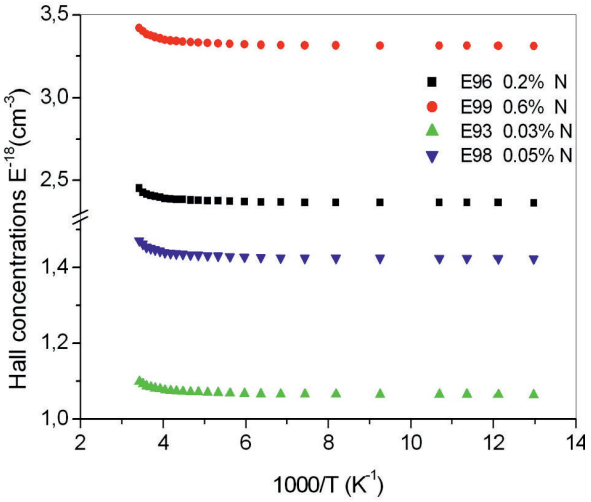


Fig. 1. Hall concentration as a function of inverse temperature for as grown InGaAsN layers with different N content.

In Fig. 1 are plotted the temperature dependences of Hall concentrations nH for the investigated four samples grown at different conditions.

All as grown InGaAsN layers are n-type and exhibit high free carrier concentration in the range (1–3) $\times$ 10^{18} cm^{-3}. These measured background doping densities of dilute nitride layers are more than one order of magnitude higher in comparison to GaInAs samples not containing nitrogen grown earlier at the same growth conditions in the growth ambient without nitrogen. It is seen that free carrier concentration increases with increase the nitrogen content in the layers. Two distinct temperature regimes with different temperature dependence of n_H are observed. The saturation of n_H at low temperatures ($T < 200$ K) is attributed to fully ionized shallow donors. At temperatures higher than 200 K a thermally activated increase in carrier concentration is observed, suggesting the presence of a deep donor level within the InGaAsN bandgap. The deep donors are likely related to the presence of N-related deep-level defects, typically associated with different N-N pair and N-cluster states [10]. The nitrogen pairs and clusters create the localized states near the conduction band edge.

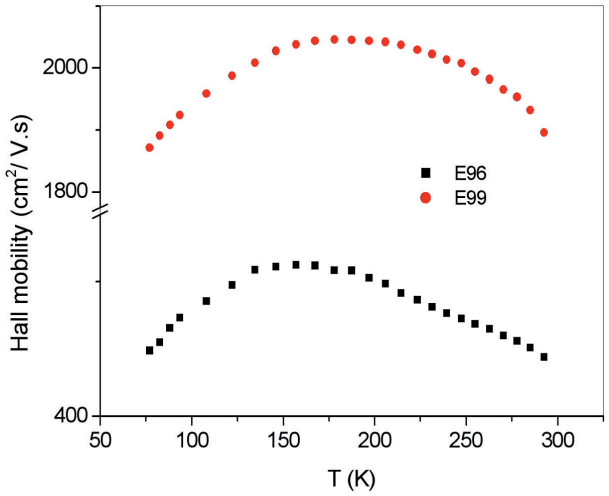


Fig. 2. Hall mobility as a function of temperature for metamorphic (E96) and lattice matched GaInAsN (E99) samples.

The activation energy of these states is much greater than the activation energy of the hydrogen-like shallow donor levels, suggesting the presence of a second deep donor level. The deep donors act as carrier trapping centers. Their activation energy decreases with increasing N composition which could be explained by the downward shift of the conduction band edge with increasing nitrogen content, while the N-related defect level remains unchanged.

Fig. 2 presents the temperature dependencies of the Hall-mobility for two of the samples. It is seen a well expressed low-temperature mobility decrease which suggests that the mobility is being limited by some kind of defect scattering and trapping. The mobility of the metamorphic GaInAsN sample E96 is low, down to 500 cm^2/V.s, since it possibly contains threading dislocations of high density and the latter causes relatively poor material quality. High values about 2000 cm^2/V.s for Hall mobility exhibits the lattice matched to GaAs substrate InGaAsN E99 sample. These values are about the theoretical limit predicted by Fahy and O'Reilly [11].

Low-temperature PL spectra of the investigated samples grown at different conditions are plotted in the Fig. 3. PL spectra recorded on samples E93 and E96 grown from an initial epitaxy temperature of 650°C from different melts are presented in the Fig. 3a. PL spectrum of E93, containing nitrogen at doping level of 0.03% dominates by sharp free exciton line at 1.484 eV. The peak at 1.45 eV is most probably due to an excitonic recombination on carbon acceptors; the carbon contamination probably comes from the graphite boat used in the LPE growth. A weaker structured emission band with two peaks around 1.370 and 1.405 eV localized far from band-gap edge is also observed. It is a nitrogen related band, associated with In-rich N-nanoclusters and different N-N pair. The similarly nitrogen related peaks we have observed for GaAs layers simultaneously doped with In and N, but they are absent for GaAs layer doped only with In [12]. In our previous work it was found a preferential formation of In-N bonds and the dominant local environment for N atoms was In-rich clusters [13]. The PL spectrum of sample E96 exhibits lower intensity and different shape compare

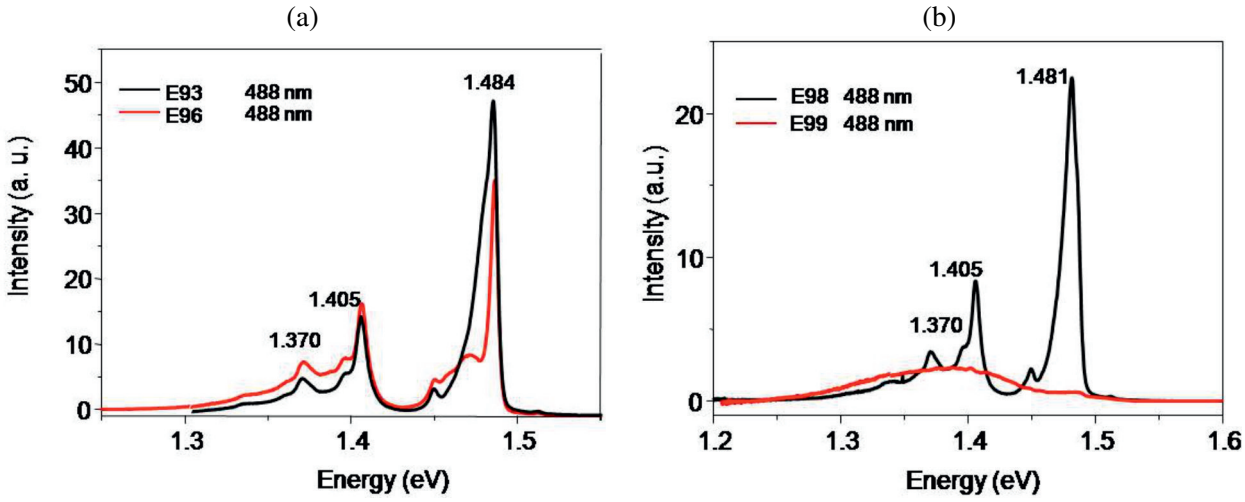


Fig. 3. PL spectra at 4.5K for samples grown from two different initial epitaxy temperatures of: a) 650°C; b) 600°C.

to PL spectrum of E93 sample. The effect of nitrogen in this layer containing 0.2% nitrogen in the solid is registered also additional wide peak at the low energy side of the free exciton line.

Sample E98 grown at the lower temperatures with 0.05% nitrogen content exhibits similar spectrum as those of E93 as it is seen from the Fig. 3b. A dramatic reduction in the PL intensity is observed for PL spectrum of the sample E99 containing 0.6% nitrogen in the layer presented at the same figure. It is dominated by wide emission band covering the peaks from nitrogen related clusters. This could be explained by pseudopotential theory of Kent et al [14]. According this theory the conduction band edge is formed from the delocalized and some localized cluster states. At the critical composition of N the deepest cluster states is overtaken by delocalized ones, since they are moving rapidly to the lower energies with increasing of N content in the alloy.

CONCLUSIONS

Four series of samples have been grown from melts with nitrogen content of 0.1 and 0.5 at.% from two different initial epitaxy temperatures. Nitrogen incorporation in the layers grown from melts with low nitrogen content of 0.1 at.% is in the range 0.03–0.05% and it acts as an isoelectronic impurity. The PL spectra consist of several peaks: sharp free exciton line; peak related to recombination on carbon acceptors and low energy peaks relating to the excitons bound to the N isoelectronic traps. Additional nitrogen related band appears at the law energy side of the sharp free exciton line of the alloy for sample E96 with 0.2% nitrogen content grown from 650°C. PL spectrum of sample E99 grown at lower temperatures containing 0.6% nitrogen in the solid exhibit wide emission band with low intensity due to the transition from nitrogen doping to alloy formation.

Hall effect measurements reveal sharp increase in the free background carrier concentrations up to (2–3) $\times 10^{18}$ cm^{-3} for all as grown GaInAsN samples which is about one order of magnitude higher in comparison with not containing nitrogen layers. The Hall electron mobility values about 2000 cm^2/V.s are measured for lattice matched to GaAs dilute nitride layers.

REFERENCES

[1] M. Weyeres, M. Sato and H. Ando, *Jap. J. Appl. Phys.* **31**, L853–L855 (1992).

[2] L. Bellaiche, S. H. Wei and A. Zunger, *Appl. Phys. Lett.* **70**, 3558–3560 (1997).

[3] W. Shan, W. Walukiewicz, J. W. Ager, E. E. Haller, J. F. Geisz, D. J. Friedman, J. M. Olson and S. R. Kurtz, *Phys. Rev. Lett.* **82**, 1221–1224 (1999).

[4] S. R. Kurtz, A. A. Allerman, E. D. Jones, J. M. Gee, J. J. Banas and B. E. Hammons, *Appl. Phys. Lett.* **74**, 729–731 (1999).

[5] A. J. Ptak, D. J. Friedman, S. Kurtz and J. Keihl, "Enhanced depletion width of GaInNAs solar cells grown by molecular beam epitaxy" in *Proceedings of 31IEEE PVSC*, Orlando, Florida, USA, January 3-7, 2005, 603–606.

[6] M. Yamaguchi, K. Nishimura, T. Sasaki, H. Suzuki, K. Arafune, N. Kojima, Y. Ohsita, Y. Okada, A. Yamamoto, T. Takamoto and K. Araki, *Solar Energy* **82**, 173–180 (2008).

[7] V. P. Khvostikov, S. V. Sorokina, N. S. Potapovich, V. I. Vasil'ev, A. S. Vlasov, M. Z. Shvarts, N. Kh. Timoshina and V. M. Andreev, "Single-junction solar cells for spectrum splitting PV system" in *Proceedings of the 25th EU PV Solar Energy Conference and Exhibition*, Valencia, Spain 6-10 September 2010.

[8] P. R. C. Kent and A. Zunger, *Phys. Rev. Lett.* **86**, 2613–2616 (2001).

[9] N. Tansu, J. Y. Yeh and L. J. Mawst, *Appl. Phys. Lett.* **83**, 2112–2114 (2003).

[10] S. B. Zang and S. H. Wei, *Phys. Rev. Lett.* **86**, 1789–1792 (2001).

[11] S. Fahy and E. P. O'Reilly, *Physica E: Low-dimensional systems and nanostructures* **21**, 881–885 (2004).

[12] M. Milanova, B. Arnaudov, S. Evtimova, Z. Alexieva, P. Vitanov, R. Kakanakov, E. Goranova, C. Barthou and B. Clerjaud, *J. Phys.: Conf. Ser.* **223**, 012016 (2010).

[13] M. Milanova, P. Vitanov, P. Terziyska, G. Koleva and G. Popov, *Phys. Stat. Sol. (c)* **10**, 597–600 (2013).

[14] P. R. C. Kent, L. Bellaiche and Al. Zunger, *Semiconductor Science and Technology* **17**, 851–859 (2002).

НОВИ МАТЕРИАЛИ ЗА ПРИЛОЖЕНИЕ В МНОГОПРЕХОДНИ СЛЪНЧЕВИ ЕЛЕМЕНТИ НА ОСНОВАТА НА A^3B^5 ХЕТЕРОСТРУКТУРИ

М. Миланова[1], П. Терзийска[2], П. Витанов[3], Г. Колева[1], К. Барту[4], Б. Клерио[4]

[1] *Централна лаборатория по приложна физика, Българска академия на науките, бул. "Санкт Петербург" №59, 4000 Пловдив, България*

[2] *Институт по физика на твърдото тяло, Българска академия на науките, бул. "Цариградско шосе" №72, 1784 София, България*

[3] *Централна лаборатория по слънчева енергия и нови енергийни източници, Българска академия на науките, бул. "Цариградско шосе" №72, 1784 София, България*

[4] *Университет "Мария и Пиер Кюри", Институт по нанонауки – Париж, ул. "де Лурмел" №140, 75015 Париж, Франция*

(Резюме)

Създаването на нова генерация многопреходни слънчеви елементи (СЕ), които използват целия слънчев спектър, води до значително повишаване ефективността на СЕ. Изборът на подходяща комбинация от материали за изготвяне на многопреходните СЕ е определящ за увеличаване ефективността на преобразуване на слънчевата радиация над 40%. Рекордната стойност от 41% за ефективността на преобразуване на концентрирано слънчево излъчване в трипреходни СЕ, разработени от Spectrolab, САЩ, дава надежда за практическа реализация на значително по-висока ефективност при увеличаване броя на СЕ в каскадата. Тези очаквания могат да се реализират, ако бъдат намерени нови материали, подходящи за използването им в многопреходните СЕ.

Твърдите разтвори от разредени нитриди са ключов нов материал за приложение в многопреходните СЕ и дават възможност за „инженеринг" на забранените зони и константите на решетката на материалите.

В настоящата работа е демонстрирана възможността за израстване на разредени нитриди GaAsN, InGaAsN върху подложки от GaAs от течна фаза. Израснатите структури са с добро кристалографско качество. Нелегираните слоеве са с n-тип проводимост. Установена е аномална промяна на концентрацията на свободните токови носители в сравнение с конвенционалните III-V съединения. Измерените стойности на подвижността на Хол в слоевете е ~ 2000 $cm^2/V.s$.

Изследван е механизмът на включване на азотните атоми в кристалните решетки на твърди разтвори от разредени нитриди GaAsN, InGaAsN при кристализация от течна фаза. Посредством методите на Раманова и ИЧ спектроскопия е определена локалната микроструктура на получените съединения от разредени нитриди. Получаването на изорешетъчни ненапрегнати дебели слоеве InGaAsN с високо кристалографско качество върху подложки от GaAs е свързано с преференциално формиране на In-N връзки в кристалната решетка на тези съединения.

Bulgarian Chemical Communications, Volume 47, Special Issue B (pp. 76–79) 2015

UV selective photodetector based on nanosized TiO_2 layers

L. Bedikyan*, S. Zakhariev, M. Zakharieva

Central Laboratory of Applied Physics, Bulgarian Academy of Sciences, 61 Sankt Peterburg Blvd., 4000 Plovdiv, Bulgaria

Nanosized TiO_2 layers were obtained by conventional vacuum thermal evaporation of Ti and triode-cathode sputtering of Ti target in a vacuum system on silicon and quartz substrates, with high temperature post annealing to TiO_2 in the range of (450÷750)°C. Structures for UV sensors are formed by contact thermal evaporation of combing contact Al, Ni, In and In-Sn on TiO_2 layers of silicon substrates. The optical properties of TiO_2 were studied by measuring the transmittance spectra in the range of wavelengths (200÷900) nm.

Spectral characteristics of structures with Al and Ni contacts show a maximum spectral sensitivity in the range of (280÷330) nm. I-V characteristics are measured at 4÷30 V forward voltage in the dark and under illumination with blue LED (380 nm) and with an Hg lamp 50 W (365 nm). Under Hg lamp illumination, and (6÷10) V bias voltage, photocurrent increases of magnitude, which shows that the structure of Al and Ni contacts are suitable for UV sensors.

Key words: titanium dioxide, UV sensors, I-V characteristics, spectral characteristics

INTRODUCTION

The need of monitoring the UV radiation led to the development of the UV sensors based on different materials. TiO_2 is one of the most attractive metal oxides as a cheap, safe, simple and chemically stable material. Absorption of UV light by TiO_2 is widely applied when used as a photocatalyst, but the process of light absorption of TiO_2 and occurrence of photocurrent, hard work recent years, because the characteristics of TiO_2 photodiodes make them suitable for the detection of UV radiation.

Due to the band gap of TiO_2 (3.0 eV for rutile and 3.2 eV for anatase), it is generally sensitive to UV radiation and do not require UV filters unlike silicon UV photodiodes. Studies in the literature show that the TiO_2 can be used for UV and other types of sensors, due to a distinct characteristic absorption, high sensitivity and resolution, and possibility traditional silicon to be used as a substrate.

EXPERIMENTAL

TiO_2 was prepared by two methods: conventional vacuum thermal evaporation of Ti layer and sputtering of Ti target in a cathode-triode vacuum system in argon flow $(2 \div 6) \times 10^{-3}$ mbar with a preliminary ion scrubbing. The substrates are optical quartz, sital and silicon at temperatures up to 100°C. In both methods, TiO_2 is formed by high-temperature annealing of the titanium layer into a resistance furnace on air at temperatures $T_{ann} \approx 450, 600$ and 700°C for 1÷5 h. The layers have a thickness of 100÷300 nm, have a regular surface in both the method of preparation, such as the adhesion is improved with increasing annealing temperature. It is believed that at $T_{ann} \approx$ 450°C anatase phase is formed, at $T_{ann} > 450$°C both phases anatase/rutile are formed, and $T_{ann} > 650$°C formed rutile [1,2].

The optical properties of TiO_2 were analyzed using the spectra of transmittance. The spectral characteristics of the transition are measured with a spectrophotometer UV-VIS SPECTROMOM 195D within a range of wavelengths of 200÷900 nm. The spectra are dependent on the substrate temperature, the layer thickness and the temperature of annealing.

The width of the band gap energy for direct and indirect transitions was obtained by plotting the optical absorption $(\alpha h\nu)^2$ and $(\alpha h\nu)^{1/2}$ vs. photon energy $(h\nu)$ and extrapolating the linear portion of the curve to 0 [3]. Values obtained for the width of the band gap in the two used methods: thermal evaporation and cathode-triode sputtering correspond to TiO_2 anatase crystalline phase at annealing 450°C and predominant presence of rutile TiO_2 crystalline phase at temperatures from 600 to 750°C.

For the preparation of structures sensitive to UV radiation nanosized TiO_2 layers with thicknesses in the range of 90÷280 nm are formed on n-Si (100) wafers with a specific resistance (6÷9) Ω.cm. After that using a variety of metals such as Al, Ni, In and In-Sn on the layers are designed electrodes by thermal evaporation through a contact mask. The realized structures having a meander shape are mounted on

* To whom all correspondence should be sent:
lid_bed@yahoo.com

© 2015 Bulgarian Academy of Sciences, Union of Chemists in Bulgaria

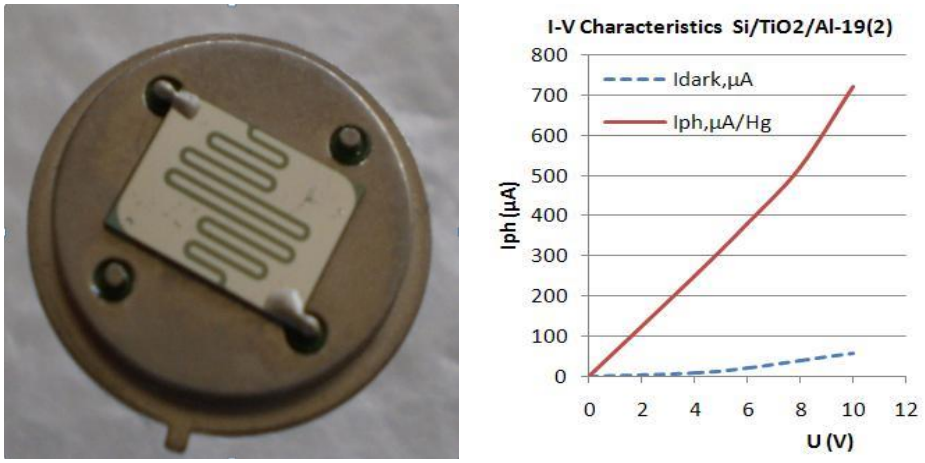


Fig. 1. Photograph (a) and I-V characteristic (b) of a structure n-Si/TiO_2/Al.

golden packages with conductive Ag paste. Fig. 1(a) presents a photograph of structure Si/TiO_2/Al.

RESULTS

I-V characteristics of the structures were measured in the range 4÷30 V in the dark, illuminated with blue LED (wavelength $\lambda = 380$ nm) and illuminated with an Hg lamp 50 W (with filter for radiation with $\lambda = 365$ nm). Best results when illuminated with both lengths λ, are obtained from the structures with Ni and Al contacts (n-Si/TiO_2/Ni and n-Si/TiO_2/Al).

Fig. 1(b) presents I-V characteristics of pattern 19(2) – structure Si/TiO_2/Al with thickness of TiO_2 – 90 nm and Al contacts. When the applied voltage 10 V, the dark current increased from 56 μA to photocurrent of 700 μA after illumination with Hg lamp, i.e. photocurrent increased one order of magnitude in comparison with the dark current.

The photocurrent depends on the thickness of TiO_2 layer. On the one side for thicker layers generation of carriers grows, but on the other it accelerates their recombination and photocurrent increase is slowing. Increasing of the bias voltage applied to the structure also slows the growth of photocurrent.

In Fig. 2 (a) and (b) are shown I-V characteristics of patterns 19 (3) and 51 with thicknesses 140 and 170 nm respectively and with Ni contacts, measured in the range of (4÷30) V. The best results for the photocurrent versus dark current was obtained in

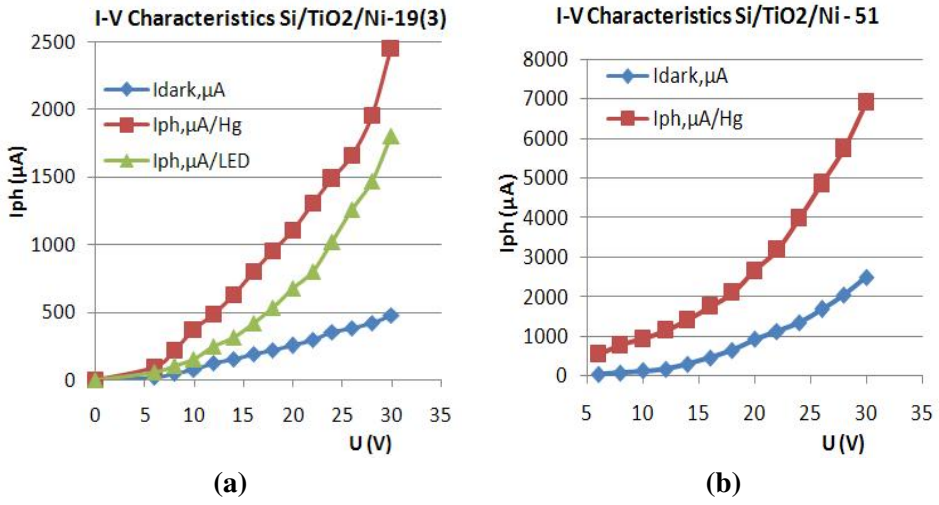
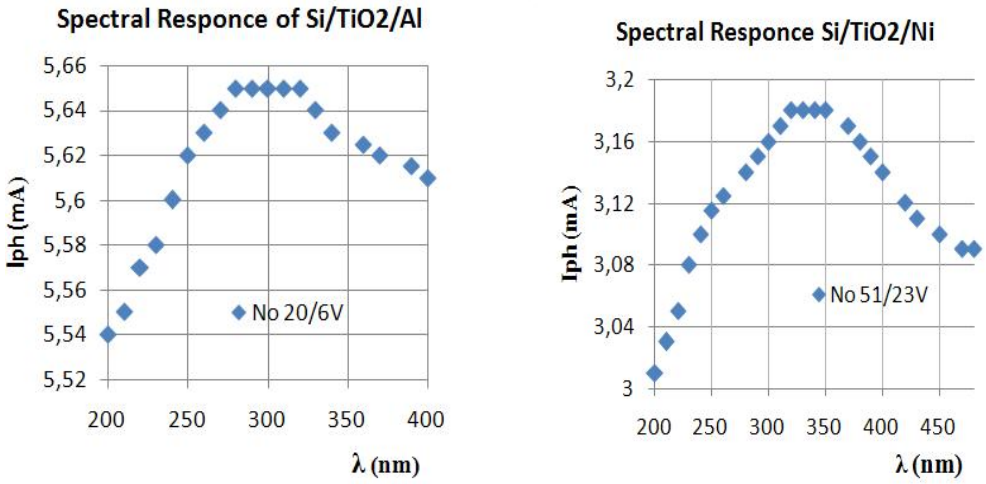


Fig. 2. I-V characteristics of structures n-Si/TiO_2/Ni - patterns 19 (3) (a) and 51 (b).



(a) **(b)**

Fig. 3. Spectral characteristics of structures with Al (a) and Ni (b) contacts.

layers with thicknesses 90 ÷170 nm and at applied bias voltage in the range of (6÷12) V.

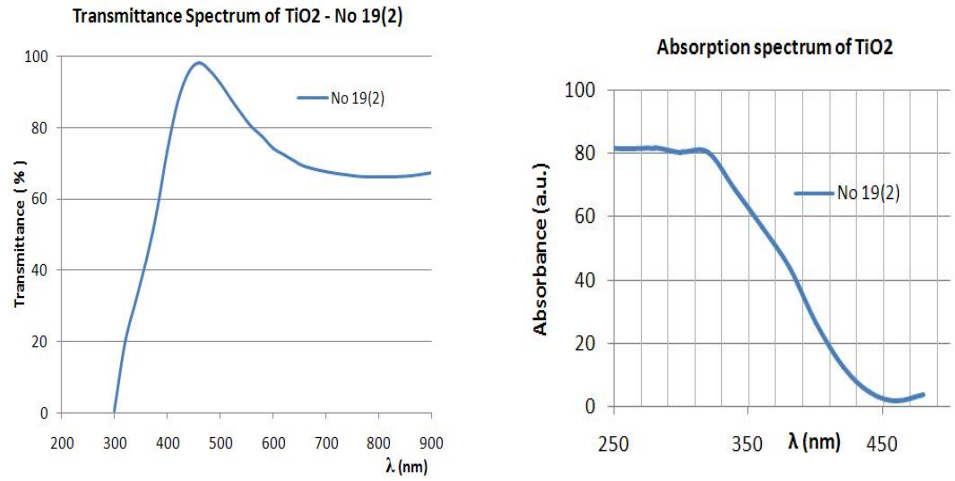
The spectral characteristics of the photocurrent of the structures with Al and Ni contacts are shown in Fig. 3. They show low dependence on the applied to the structure bias voltage and have photosensitivity in the range of 280÷330 nm, which is in good agreement with the results of the absorption spectra.

Fig. 4 presents the spectra of transmittance and absorption of a sample 19(2), which show a strong optical absorption in the range 250÷320 nm.

The width of the optical zone of direct and indirect transitions is obtained from a graphs of the optical absorption $(\alpha h\nu)^2$ and $(\alpha h\nu)^{1/2}$ vs. photon energy (hν) and linear extrapolation to 0. The width of the optical zone of direct transitions of TiO_2 is determined 3.4 eV at annealing temperature 450°C and 3.2 eV with increasing annealing temperature up to 600°C. The width of the optical zone of indirect transitions is 3.12 eV at annealing temperature 450°C and 3.02 eV with increasing annealing temperature up to 750°C.

CONCLUSIONS

In most published literature values for the width of the optical zone of TiO_2 – anatase and rutile, respectively, are in the range 3.0÷3.4 eV, i.e. within a range



(a) **(b)**

Fig. 4. Optical absorption in TiO_2 thin films.

of wavelengths of 370÷420 nm. Values obtained for the energy of the direct and indirect transitions correspond to TiO_2 anatase crystalline phase at annealing temperatures of 450°C and with increasing annealing temperature up to 750°C showed mostly presence of rutile crystal phase. Changes in the width of the optical zone with annealing temperature are related to changes in the dimensions of the crystallites, as well as varying the ratio between the crystalline phase of anatase and rutile [2].

I-V characteristics show good current differences between the dark current and photocurrent when illuminated by UV radiation. Half-width of the spectral characteristics showed good sensitivity range of 235÷420 nm. At applied bias voltage in the range of 6÷10 V photocurrent increased one order of magnitude in comparison with the dark current.

These results suggest that the structures and n-Si/TiO_2/Ni n-Si/TiO_2/Al are suitable for UV sensors.

REFERENCES

[1] Y. Fu Y. and W. Cao, *Chin. Sci. Bull.* **51**, 1657–1661 (2006).

[2] M. Sreemany, A. Bose and S. Sen, *Physica B* **405**, 85–93 (2010).

[3] L. Bedikyan, S. Zakhariev and M. Zakharieva, *J. Chem. Technol. Metall.* **48**, 555–558 (2013).

UV СЕНЗОРИ НА ОСНОВАТА НА TiO_2

Л. Бедикян, Ст. Захариев, М. Захариева

Централна лаборатория по приложна физика, Българска академия на науките, бул. "Санкт Петербург" №61, 4000 Пловдив, България

(Резюме)

Наноразмерни слоеве TiO_2 са получени чрез стандартно вакуумно термично изпарение на Ti и триодно-катодно разпрашване на Ti мишена във вакуумна система върху силициеви и кварцови подложки, с последващо високотемпературно окисление до TiO_2 при 450÷750°C. Структурите за UV сензори са формирани чрез контактно термично изпарение на гребеновидни контакти Al, Ni, In и In-Sn върху слоевете TiO_2/Si. Оптичните свойства на TiO_2 са изследвани чрез измерване спектрите на пропускане в интервал от дължини на вълната 200÷900 nm.

Спектралните характеристики на структурите с Al и Ni контакти показват максимум на спектрална чувствителност в интервал 280÷330 nm. Волт-амперните характеристики са измерени в интервал 4÷30 V на тъмно и при осветяване със син LED (380 nm) и Hg лампа 50 W (365 nm). При осветяване с Hg лампа и прилагане на 6÷10 V напрежение, фототокът нараства на порядък, което показва, че структурите с Al и Ni контакти са подходящи за UV сензори.

Bulgarian Chemical Communications, Volume 47, Special Issue B (pp. 80–83) 2015

Impurity absorption in uniaxial gyrotropic crystals of magnesium sulfite hexahydrate

A. Hristova[1]*, T. Dimov[2], I. Iliev[2]

[1] *Faculty of Engineering, 'N. Y. Vaptsarov Naval Academy, 73 Vasil Drumev str., 9026 Varna, Bulgaria*
[2] *Faculty of Science, Konstantin Preslavski University of Shumen, 115 Universitetska str., 9700 Shumen, Bulgaria*

There have been studied the features of absorption of uniaxial gyrotropic crystals Magnesium sulfite hexahydrate, doped with impure Co-ions ($MgSO_3.6H_2O$:Co). The experiment have been conducted using linear polarized light $\vec{E}\|\vec{c}$ and $\vec{E}\perp\vec{c}$ ($\vec{c}$ is the optical axis of the crystal) in the visible spectra range from 400 nm to 650 nm, where is the Co-ion's absorption band. Impurities cause the appearance of additional structures in the spectra of the crystal, which have been described and analyzed on qualitative level. The linear dichroism in the absorption of impurity ions inside the crystal lattice has been analyzed.

Key words: Magnesium sulfite hexahydrate ($MgSO_3.6H_2O$), absorption spectra, linear dichroism

INTRODUCTION

The crystals of Magnesium sulfite hexahydrate ($MgSO_3.6H_2O$) belong to the crystallographic class C_3 (without center of symmetry). The single cell of the crystal contains octahedron $Mg(H_2O)_6^{2+}$ and pyramidal ion SO_3^{2-}. Single crystals magnesium sulfite hexahydrate, pure and doped, are obtained for the first time in the world practice using doctor Kovachev's original method in the Laboratory for Crystal growth at the Faculty of Physics of Sofia University. The growth of monocrystals with relatively big size (40–50 mm) is performed using reaction in an aqueous solution in interaction of alkaline sulfites and soluble Magnesium salts. Samples of such great size (Fig. 1) allo one to explore in details the physics characteristics of the crystal. This exploration is being done at the Laboratory for optical properties of crystals in the Department of Experimental Physics (Faculty of Science of the University of Shumen).



Fig. 1. $MgSO_3.6H_2O$:Co single crystal.

Of particular interest in crystal optics are the cases of introducing impurity atoms. Impurities in the crystal cause changes in the electrical, magnetic and optical properties. The ions Co^{2+} are in the same isomorphous order with Mg^{2+} and replace them in the crystal lattice of magnesium sulfite hexahydrate ($MgSO_3.6H_2O$). Co-ion is located in octahedral surroundings of six water molecules [1]. Crystals Magnesium sulfite hexahydrate doped with cobalt ($MgSO_3.6H_2O$:Co) are extremely suitable for experimental proof of theoretical reasoning. The absorption spectrum of the examined crystal contains absorption band of Co -ion in the visible part of the spectrum (in the interval (450–550 nm).

The anisotropy of the crystal is due to the type of the particles in the crystal lattice, their mutual disposal and the nature of their chemical connection. The linear dichroism is a result of the anisotropy of the crystal and is determined by the difference of the absorption coefficients of the linear polarized light ($\vec{E}\perp\vec{c}$ and $\vec{E}\|\vec{c}$). The research of the dichroism spectrum allows us to find hidden electronic transitions and to determine their polarization.

The presented experiment in the current paper is sequel of the intial researches of the dichroism in $MgSO_3.6H_2O$:Co [2]. An attempt is made to explain the absorption of cobalt ions, embedded in a uniaxial gyrotropic crystal of magnesium sulfite hexahydrate ($MgSO_3.6H_2O$:Co). There is information that these crystals possess nonlinear optical properties [3], which gives the opportunity to apply them in the laser technologies.

* To whom all correspondence should be sent:
antonina05@abv.bg

© 2015 Bulgarian Academy of Sciences, Union of Chemists in Bulgaria

THEORETICAL CONSIDERATIONS

The incidence of linear polarized light in uniaxial, optically inactive crystal, excite and distribute two linear polarized orthogonal waves. In optically active and absorbing uniaxial crystal the waves are elliptical polarized and are not orthogonal. This orthogonal deviation is usually weak and could be ignored [4]. The coefficients of absorption of uniaxial crystal are determined using the equation of Bouget-Lambert:

$$\alpha_{\perp,\parallel} = \left(\frac{1}{d}\right) \ln\left(\frac{I_0}{I_{\perp,\parallel}}\right) \qquad (1)$$

where I_0 is the intensity of the falling and $I_{\perp,\parallel}$ are the intensities of the passed light trough sample with thickness d. $I_{\perp,\parallel}$ correspond to polarization of the falling light $\vec{E}\perp\vec{c}$ and $\vec{E}\parallel\vec{c}$ ($\vec{E}$ is the electric vector of the falling light).

The optical spectra give the opportunity to collect information about the thin spectral structure and impurity levels in the forbidden band of the crystal. The electronic band structure of the crystal is presented in [5].

EXPERIMENTAL SETUP AND MATERIALS

The sample of $MgSO_3.6H_2O$:Co is flatly parallel plate with thickness $d = 4.6$ mm. It is cut by the crystal in such manner that the light propagates of it in th dirrection $10\bar{1}0$ (Fig. 2). The crystals are suitable for taking down absorption spectra because the walls are parallel and optically smooth. The optical axis of the crystal lies on a plane which is perpendicular to the direction of propagation of light.

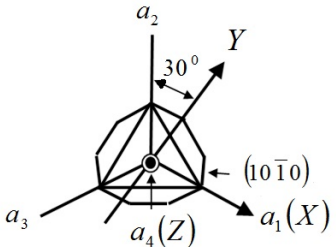


Fig. 2. Crystallographic (a_1, a_2, a_3, a_4) and crystallophysics (X, Y, Z) axes of $MgSO_3.6H_2O$:Co.

The crystal samples are oriented using a system of two polarizers = "polarizer P – crystal CR – analyzer A". The leaking directions, of polarizers P and A, are orthogonal. Monochromator SPM-2 and polarization prisms Glan-Taylor are used. The light beam is given by the monochromator SPM-2, it becomes parallel using a system of lenses L and passes through

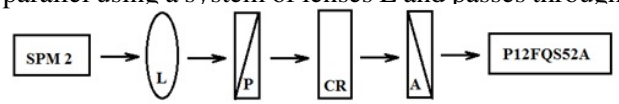


Fig. 3. Experimental scheme.

the polarizer P. Linearly light falls on the crystal sample. During the absorption measurement the analyzer A is removed and the intensity $I(\alpha)$ of the light is measured using a photomultiplier P12FQS52A with dark current 10^{-9}A (Fig. 3).

Absorption spectra (Fig. 4) of pure and doped Magnesium sulfite hexahydrate have been taken in the spectral interval 400–650 nm. In this interval are the absorption band of Co-ion and the forbidden zone of the pure $MgSO_3.6H_2O$.

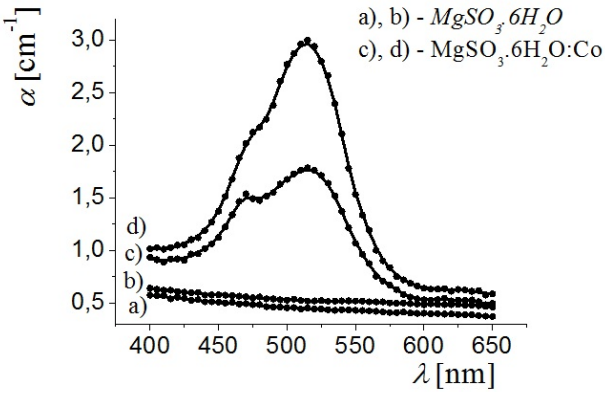


Fig. 4. Absorption spectra of pure and doped Magnesium sulfite hexadydrate Lines a) and c) – for $\vec{E}\parallel\vec{c}$; Lines b) and d) – for $\vec{E}\perp\vec{c}$.

EXPERIMENTAL RESULTS AND DISCUSSIONS

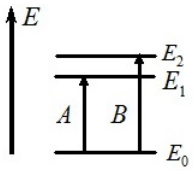
The analyze of the Fig. 4 spectra shows that the presence of Co-impurities in the crystal leads to appearance of absorption bands in the forbidden band of the pure $MgSO_3.6H_2O$. The two peaks in the absorption spectrum of doped with cobalt crystal $MgSO_3.6H_2O$:Co correspond to two energetic transitions A and B (Table 1) of the electrons in the d-zone of Co-ion.

Absorption band of Co-ion for both polarizations consists of two maxima, divided using a computer program (Fig. 5). The two derived Lorentzian curves that correspond to the two maxima, show that:

1. The values of the absorption coefficients $\alpha_{\max}$ are the same for both polarizations ($\vec{E}\parallel\vec{c}$ and $\vec{E}\perp\vec{c}$) in the transition B.

Table 1. Values of the absorption coefficients and schema of the energetic transitions in the *d*-zone of *Co*-ion.

	$\vec{E} \parallel \bar{c}$		$\vec{E} \perp \bar{c}$	
	Transition A	Transition B	Transition A	Transition B
E, [eV]	2.39	2.67	2.40	2.65
α_{max}, [cm^{-1}]	1.62	0.92	2.70	0.97



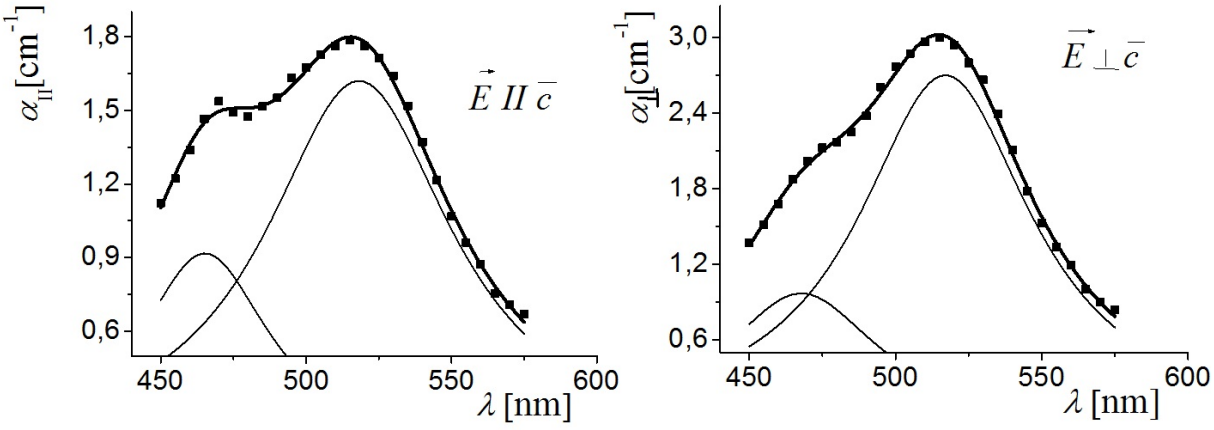


Fig. 5. Components decomposition of the absorption coefficients $\alpha_{\parallel}$ and $\alpha_{\perp}$ in the absorption band of Co-ion.

2. In the transition *A* the absorption coefficients α_{max} are different for the two polarizations (Table 1).

Fig. 6 shows the linear dichroism for the two absorption curves. It has high value in the spectral range, in relation to transition *A*. Moreover, it is not constant and depends on the length of the light wave λ. This allows us to assume that the moment of the transitions *A* and *B* are not parallel [6].

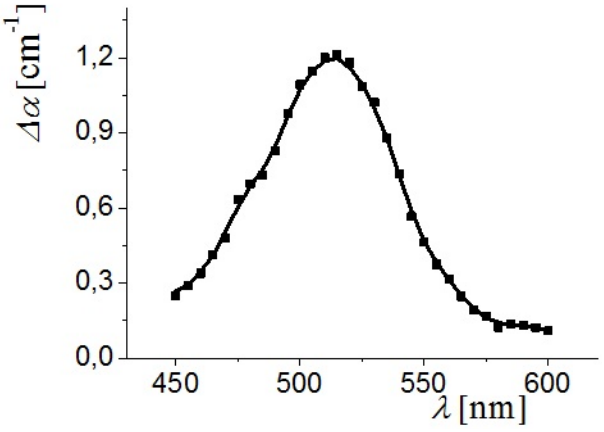


Fig. 6. Spectrum of the linear dichroism $\Delta\alpha = \alpha_{\parallel} - \alpha_{\perp}$ for $MgSO_3.6H_2O$:Co.

CONCLUSION

1. There have been measured the absorption spectra of pure and doped with cobalt Magnesium sulfite hexahydrate in the visible part of the spectrum from 400nm to 650nm with linear polarized light ($\vec{E} \| \bar{c}$ and $\vec{E} \perp \bar{c}$).
2. The computer's calculation show that the absorption band, connected with the doped Co-ion, could be considered with great authenticity as composed of two Lorentzian curves.
3. Due to the anisotropy of the crystal have been established and analyzed linear dichroism in the investigated region of the spectra.
4. The spectral dependency of the linear dichroism shows that the moments of electronic *d*-transitions are not parallel.

Acknowledgments: *The authors are very grateful to Tsanio Kovachev from the Faculty of Physics of Sofia University for the provided samples. Part of the present work has been supported by Grant 08-226/12.03.2014 from Konstantin Preslavsky University, Shumen.*

REFERENCES

[1] Z. Bunzarov, S. M. Saltiel, T. Kovachev, L. Ljutov and D. Russev, *Proc. of SPIE* **3052**, 197–200 (1996).

[2] Zh. Bunzarov, I. Iliev, T. Dimov, P. Petkova, Tz. Kovachev et al., "Circular dichroism in magnesium sulfite hexahydrate doped with cobalt" in *Proc. SPIE 7501, International Conference on Ultrafast and Nonlinear Optics 2009*, 75010X (November 11, 2009).

[3] L. Pavlov, I. Hadjichristov, S. Lazarov, Ts. Kovachev, Zh. Bunzarov, I. Buchvarov, I. Nikolov and M. Iliev, "Nonlinear X(2) and X(3) spectroscopy of Magnesium Sulfite Hexahydrate single crystal" in *Proc. of SPIE* **6604**, 1P1–1P4 (2007).

[4] A. Konstantinova, B. Grechushnikov, B. Bokut and E. Valiachko, *Optical Properties of the Crystals*, Nauka i Tekhnika, Minsk, 1995 (in Russian).

[5] A. P. Litvinchuk, Zh. Bunzarov and M. N. Iliev, *Electronic structure, optical properties, and lattice dynamics of* $MgSO_3.6H_2O$.

[6] Ch. Cantor and P. Schimmel, *Biophysical Chemistry*, Part II, Mir, Moskva, 1984, p. 28.

ПОГЛЪЩАНЕ И ОПТИЧНА АКТИВНОСТ В ЕДНООСНИ ЖИРОТРОПНИ КРИСТАЛИ ОТ МАГНЕЗИЕВ СУЛФИД ХЕКСАХИДРАТ

А. Христова[1], Т. Димов[2], И. Илиев[2]

[1] *Инженерен факултет, Висше военноморско училище "Н.Й. Вапцаров", ул. "Васил Друмев" №73, 9026 Варна, България*
[2] *Факултет по природни науки, Шуменски университет "Епископ Константин Преславски", ул. "Университетска" №115, 9700 Шумен, България*

(Резюме)

Изследвани са особеностите на поглъщане на едноосни жиротропни кристали магнезиев сулфид хексахидрат, дотиран с примесни Co-йони ($MgSO_3.6H_2O$:Co). Експериментът е извършен с линейно поляризирана светлина $\vec{E} \perp \vec{c}$ и $\vec{E} \parallel \vec{c}$ ($\vec{c}$ е оптичната ос на кристала) във видимия диапазон от 400 nm до 650 nm, където е абсорбционната ивица на Co-йон. Примесите предизвикват появата на допълнителни структури в спектъра на кристала, които са описани и анализирани на качествено ниво. Анализиран е линейният дихроизъм в поглъщането на примесните йони в кристалната решетка.

Bulgarian Chemical Communications, Volume 47, Special Issue B (pp. 84–94) 2015

On different models describing the equilibrium shape of erythrocyte

G. S. Valchev*, V. M. Vassilev, P. A. Djondjorov

Institute of Mechanics, Bulgarian Academy of Sciences, Acad. Georgy Bonchev Str., Bl. 4, 1113 Sofia, Bulgaria

Red blood cells (erythrocytes) fall to one of the most important families of cells in all vertebrate organisms. The study of the equilibrium shapes of this kind of cells is of particular importance for the understanding of their physical, chemical and mechanical properties. In the present work, several well-known and widely acknowledged models describing the equilibrium shapes of the red blood cells are analysed. For each of the regarded models we make a comparison between the shapes of the meridional contours predicted by it and the known experimental data. The obtained results can be used to choose a suitable model for the analytical study of the interactions between individual erythrocytes or between them and the walls of blood vessels, for the diagnosis of diseases associated with a change of the equilibrium shape of the cells or for the experimental study of the red blood cells by light scattering methods.

Key words: Red blood cells, Erythrocytes, Equilibrium shapes, Cassinian ovals

1. INTRODUCTION

The red blood cells (RBCs) or erythrocytes are the most common type of blood cell in all vertebrate organisms. They are responsible for the delivery of oxygen (O_2) from the respiration organs (lungs, gills, skin) to the body tissues and the return transport of carbon dioxide (CO_2) from the tissues via the blood flow through the circulatory system. This type of cells have specific biophysical properties for responding to a change in the local chemical and mechanical environment. Any deviation from these regular biophysical properties (regular shapes, for instance) impair the normal functions of RBCs in the human body and is a sensitive marker for various blood disorders and diseases, e.g., malaria and sickle cell anemia. For this reason, the development of relevant techniques for obtaining the biophysical characteristics of the RBCs have been of paramount significance in medical diagnostics [1].

Normal mature RBCs are shaped as biconcave oblate discs, which deform with pressure and physiological conditions in blood. This unique shape determines a large surface-area-to-volume ratio. The typical model geometry of a RBC is assumed to be axially symmetric, with the meridional cross-section characterised by the following morphological parameters [2]: the diameter – D, the dimple (minimal) thickness – $\tau_{\min}$, the maximum thickness – $\tau_{\max}$, and the diameter of a circle that determines the location of the maximum thickness – d.

Several well-known and widely acknowledged models describing the equilibrium (biconcave) shape of the RBCs are analysed in the present work. For each model we give the relationship between the aforementioned morphological parameters and those used in the particular model. Analytic expressions for the surface area, volume and sphericity index are also obtained. Starting with the lowest degree polynomial approximation suggested by Beck [3], and ending with the highest one proposed by Evans and Fung [4], we compare the meridional contours predicted by each of these models with a set of experimental data (for concrete values of the morphological parameters characterising those contours see Table 1).

Table 1. Values of the morphological parameters and albumin tonicities of RBC solutions, taken from Ref. [4] (Cell 1 and Cell 2) and Ref. [5] (Cell 3 and Cell 4). The red blood cells in cases "Cell 1" and "Cell 2" were obtained from a 30-year-old male, separated into four samples, centrifuged at 4000 rpm for 20 min, and the plasma and white cell layer were removed. The packed RBCs were then diluted by a factor of ten with Eagle-albumin solution, centrifuged again and the Eagle-albumin solution removed. In cases "Cell 3" and "Cell 4" the erythrocytes were obtained, by finger-prick, from seven apparently healthy subjects (male and female), and drawn into micro-haematocrit capillaries coated with sodium heparin. About 0.05 ml of the blood was added to 5 ml of an isotonic THAM–HCl–buffered Ringer solution (10 mM THAM, pH 7.4 ± 0.02) with (in case "Cell 4") and without (in case "Cell 3") albumin.

	D [μm]	d [μm]	$\tau_{\max}$ [μm]	$\tau_{\min}$ [μm]	albumin tonicity [mOsmol]
Cell 1	7.59	4.68	3.26	2.08	217
Cell 2	7.82	5.52	2.52	0.81	300
Cell 3	8.04	5.30	2.62	1.54	0
Cell 4	7.64	4.55	2.86	1.45	310

* To whom all correspondence should be sent:
gvalchev@imbm.bas.bg

© 2015 Bulgarian Academy of Sciences, Union of Chemists in Bulgaria

In our opinion, the results presented here would be helpful for one to choose a suitable model for the specific purposes of its usage, e.g., for analytical study of the interactions between individual erythrocytes or between them and the walls of blood vessels, for the diagnosis of diseases associated with a change of the equilibrium shape of the cells, and for the experimental study of the RBCs by light scattering methods.

The article is arranged as follows: in Section 2 we introduce the Beck model. Sections 3.1 and 3.2 are focused on models based on Cassinian ovals. In Sections 3.3 and 3.4 we comment a model proposed by Kuchel and Fackerell, later on modified by Yurkin. The last two models that we analyse are those of Fung and Tong in Section 4.1 and Evans and Fung in Section 4.2. The article ends with a discussion and concluding remarks – Section 5.

2. QUADRATIC POLYNOMIAL APPROXIMATION – BECK'S MODEL

The mathematical representation of the meridional cross-section of a RBC used by Beck [3] is that of the arcs of two circles, one being the cross-section of a torus at the periphery of the cell centred on the x-axis, and another one, which is centred on the z-axis (the axis of revolution), representing the dimple region. These arcs are constrained to be continuous with equal first derivatives at a specified value x_0. The equation of the resulting curve is obtained by writing separate expressions for the two arcs over their respective intervals

$$z=\begin{cases} C_{0B}+\dfrac{\tau_{\min}}{2}-\sqrt{C_{0B}^2-x^2}, & 0\le x\le x_0 \\ \sqrt{\dfrac{D}{4}(2\tau_{\max}-D)+(D-\tau_{\max})x-x^2}, & x_0<x<\dfrac{D}{2} \end{cases} \tag{1}$$

where

$$C_{0B}=\frac{D(D-2\tau_{\max})+\tau_{\min}^2}{4(\tau_{\max}-\tau_{\min})} \quad \text{and} \quad x_0=\frac{(D-\tau_{\max})C_{0B}}{2C_{0B}+\tau_{\max}}. \tag{2}$$

Once the approximated meridional cross-section of a RBC is given in an explicit analytic form, one can easily derive expressions for the surface area A, volume V and sphericity index Ψ of these cells. Using simple mathematical techniques (see p. 364 and p. 572 in [6]) one obtains

$$A=4\pi\int_0^{D/2} x\sqrt{1+\left(\frac{\mathrm{d}z}{\mathrm{d}x}\right)^2}\,\mathrm{d}x, \qquad V=4\pi\int_0^{D/2} x\,z\,\mathrm{d}x, \qquad \Psi=\frac{\pi^{1/3}(6V)^{2/3}}{A}. \tag{3}$$

Within this model, Beck obtained the following analytical expressions for the above mentioned quantities

$$A_B=4\pi\left\{C_{0B}\left(C_{0B}-\sqrt{C_{0B}^2-x_0^2}\right)+\frac{\tau_{\max}}{2}\left[C_{1B}+\frac{D-\tau_{\max}}{2}\left(\frac{\pi}{2}-\arcsin C_{2B}\right)\right]\right\}, \tag{4a}$$

where

$$C_{1B}=\sqrt{\frac{D}{4}(2\tau_{\max}-D)+(D-\tau_{\max})x_0-x_0^2} \quad \text{and}$$

$$C_{2B}=\frac{2x_0-D+\tau_{\max}}{\tau_{\max}};$$

$$V_B=\frac{4}{3}\pi\left\{\frac{3}{4}(2C_{0B}+\tau_{\min})x_0^2+\left[(C_{0B}^2-x_0^2)^{3/2}-C_{0B}^3+C_{1B}^3\right]\right.$$
$$\left.+\frac{3\tau_{\max}(D-\tau_{\max})}{8}\left[\frac{\tau_{\max}}{2}\left(\frac{\pi}{2}-\arcsin C_{2B}\right)-C_{1B}C_{2B}\right]\right\}; \tag{4b}$$

$$\Psi_B=\frac{\pi^{1/3}(6V_B)^{2/3}}{A_B}. \tag{4c}$$

A comparison between the meridional contours of RBCs predicted by Beck's model and the experimentally obtained data can be seen in Figures 1 and 2.

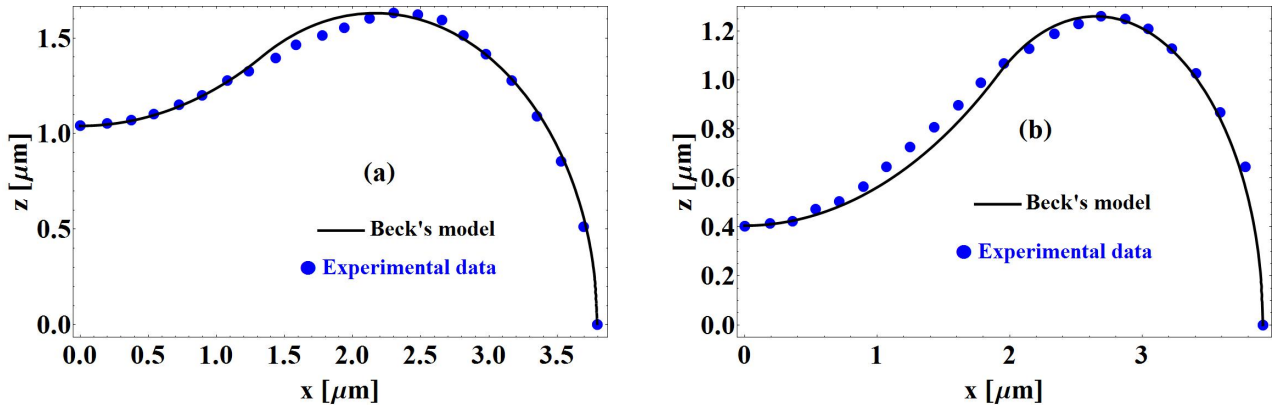


Fig. 1. Meridional contours of RBCs obtained via Beck's model (the black thick curves) in comparison to experimentally obtained ones [(Cell 1 in (**a**)] and [Cell 2 in (**b**)] (•) of normal red blood cells taken from [4] (see also [7]). Only one quadrant of the contour is shown. For the values of the model parameters one has: (**a**) $C_{0B} = 2.64$ μm and $x_0 = 1.34$ μm; (**b**) $C_{0B} = 3.27$ μm and $x_0 = 1.91$ μm.

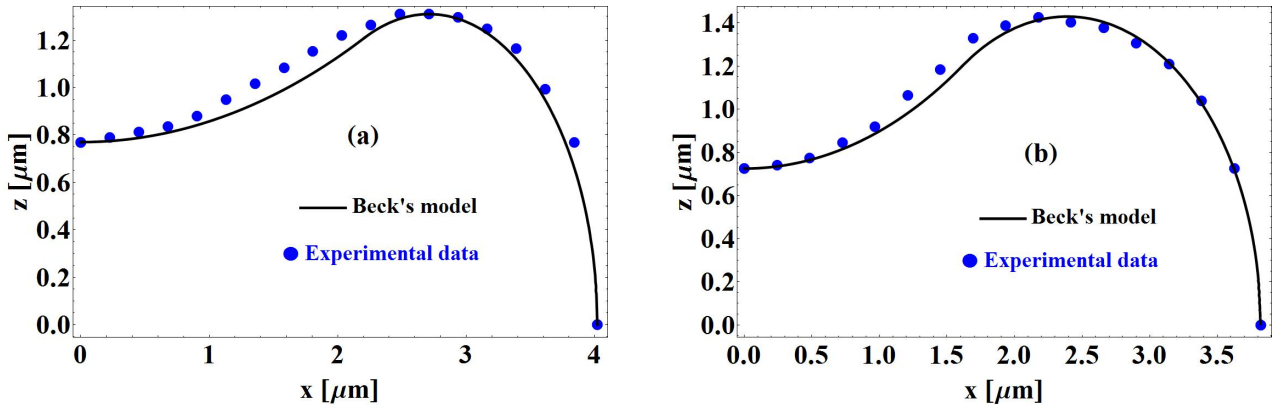


Fig. 2. Meridional contours of RBCs obtained via Beck's model (the black thick curves) in comparison to experimentally obtained ones [Cell 3 in (**a**)] and [Cell 4 in (**b**)] (•) of normal red blood cells taken from [5]. Only one quadrant of the contour is shown. For the values of the model parameters one has: (**a**) $C_{0B} = 5.76$ μm, $x_0 = 2.21$ μm; (**b**) $C_{0B} = 2.97$ μm, $x_0 = 1.61$ μm.

3. BIQUADRATIC POLYNOMIAL APPROXIMATIONS

3.1. Model based on single loop Cassinian ovals

Modelling the equilibrium biconcave shape of RBCs via Cassinian ovals is the simplest and probably the most widely used technique [8–21]. Within the framework of this description the meridional cross-section of the considered cells in the $(x,z)-$plane is given by the equation

$$\left(a^2+x^2+z^2\right)^2-4a^2x^2=c^4, \tag{5}$$

where the parameters a and c are such that for a point on that curve, the product of its distances from two fixed points (the foci) a distance $2a$ apart is a constant c^2. The shape of a curve given by Eq. (5) depends, up to similarity, on the ratio $\varepsilon = c/a$. When $\varepsilon > 1$ (or $c > a$), the curve is a single, connected loop enclosing both foci, while when $\varepsilon < 1$ (or $c < a$), the curve consists of two disconnected loops each of which containing a focus. In the limiting case $\varepsilon = 1$, the curve is the lemniscate of Bernoulli.

In order that the considered description of the equilibrium shape has physical meaning one must relate the two parameters a and c with the morphological ones. For this relationship one finds

$$\tau_{\min}=2\sqrt{c^2-a^2}, \qquad \tau_{\max}=\frac{c^2}{a}, \qquad D=2\sqrt{c^2+a^2} \tag{6}$$

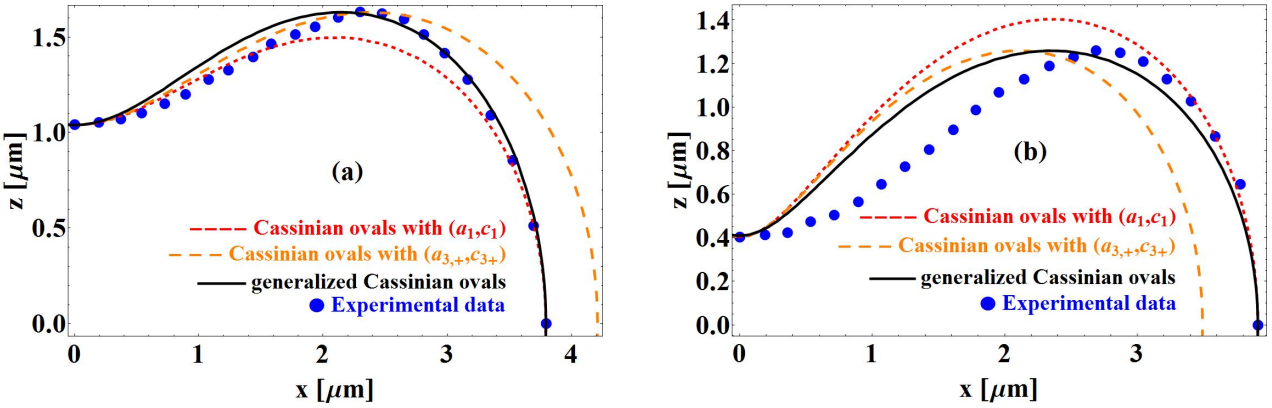


Fig. 3. Contours of RBCs modeled via Cassinian [(---------) and (– – – –)] and generalized Cassinian ovals (————) in comparison to an experimentally obtained contours [Cell 1 in (**a**)] and [Cell 2 in (**b**)] (●) of normal red blood cells taken from [4]. The red short-dashed curve (---------) corresponds to the set of parameters (a_1, c_1), while the orange long-dashed one (– – – –) to $(a_{3,+}, c_{3,+})$. In case (**a**) for the values of the parameters of the Cassinian ovals one has: $a_1 = 2.58\ \mu$m, $c_1 = 2.78\ \mu$m and $a_{3,+} = 2.89\ \mu$m, $c_{3,+} = 3.07\ \mu$m, while for those of the generalized Cassinian ovals the result is: $a_g = 2.60\ \mu$m, $b = 1.11$ and $c_g = 2.76\ \mu$m. In case (**b**) these values are as follows: $a_1 = 2.75\ \mu$m, $c_1 = 2.78\ \mu$m; $a_{3,+} = 2.45\ \mu$m, $c_{3,+} = 2.49\ \mu$m; $a_g = 2.75\ \mu$m, $b = 0.89$ and $c_g = 2.78\ \mu$m.

From Eqs. (6) we have

$$a_1 = \frac{\sqrt{D^2 - \tau_{\min}^2}}{2\sqrt{2}}, \quad c_1 = \frac{\sqrt{D^2 + \tau_{\min}^2}}{2\sqrt{2}}; \tag{7a}$$

$$a_2 = \frac{\sqrt{D^2 + \tau_{\max}^2} - \tau_{\max}}{2}, \qquad c_2 = \frac{\sqrt{\tau_{\max}\sqrt{D^2 + \tau_{\max}^2} - \tau_{\max}^2}}{\sqrt{2}}; \tag{7b}$$

$$a_{3,\pm} = \frac{1}{2}\left(\tau_{\max} \pm \sqrt{\tau_{\max}^2 - \tau_{\min}^2}\right), \qquad c_{3,\pm} = \frac{1}{\sqrt{2}}\sqrt{\tau_{\max}^2 \pm \tau_{\max}\sqrt{\tau_{\max}^2 - \tau_{\min}^2}}. \tag{7c}$$

Comparing each pair of parameters and taking into account the condition for closeness of the ovals ($c > a$), one concludes that only the curves characterized by (a_1, c_1) [see Eq. (7a)] and $(a_{3,+}, c_{3,+})$ [see Eq. (7c)] resemble the meridional cross-section of a RBC (see Figures 3 and 4).

Substituting Eq. (5) in Eq. (3) we find that within the model based on Cassinian ovals one has

$$A_C = 4\pi c^2 \mathscr{A}_C(\varepsilon), \tag{8a}$$

where

$$\mathscr{A}_C(\varepsilon) = \sqrt{\varepsilon^2 - 1}\left\{E\left[\frac{\pi}{2}, k(\varepsilon)\right] - E[\varphi(\varepsilon), k(\varepsilon)] + F[\varphi(\varepsilon), k(\varepsilon)] - F\left[\frac{\pi}{2}, k(\varepsilon)\right]\right\},$$

$$k(\varepsilon) = \sqrt{\frac{1+\varepsilon^2}{1-\varepsilon^2}}, \qquad \varphi(\varepsilon) = \arcsin\left(\sqrt{\frac{\varepsilon^2 - 1}{\varepsilon^2 + 1}}\right);$$

$$V_C = \frac{4}{3}\pi c^3 \mathscr{V}_C(\varepsilon), \tag{8b}$$

where

$$\mathscr{V}_C(\varepsilon) = \frac{1}{4\varepsilon^3}\left\{(2+\varepsilon^2)\sqrt{\varepsilon^2 - 1} + 3\varepsilon^4\left[\frac{\pi}{4} - \arctan\left(\frac{\varepsilon^2 - 2}{\varepsilon^2 + 2\sqrt{\varepsilon^2 - 1}}\right)\right]\right\};$$

$$\Psi_C(\varepsilon) = \frac{\mathscr{V}_C^{2/3}(\varepsilon)}{\mathscr{A}_C(\varepsilon)}. \tag{8c}$$

Note that the relationship between the morphological parameters and those of the Cassinian ovals is *not unique* [see Eqs. (7)] since the dimensionless parameter ε can be either $\varepsilon_1 \equiv c_1/a_1$ or $\varepsilon_{3,+} \equiv c_{3,+}/a_{3,+}$. In Eq. (8a) $F[\varphi(\varepsilon), k(\varepsilon)]$ and $E[\varphi(\varepsilon), k(\varepsilon)]$ denote the first, and respectively the second kind of incomplete elliptic integrals.

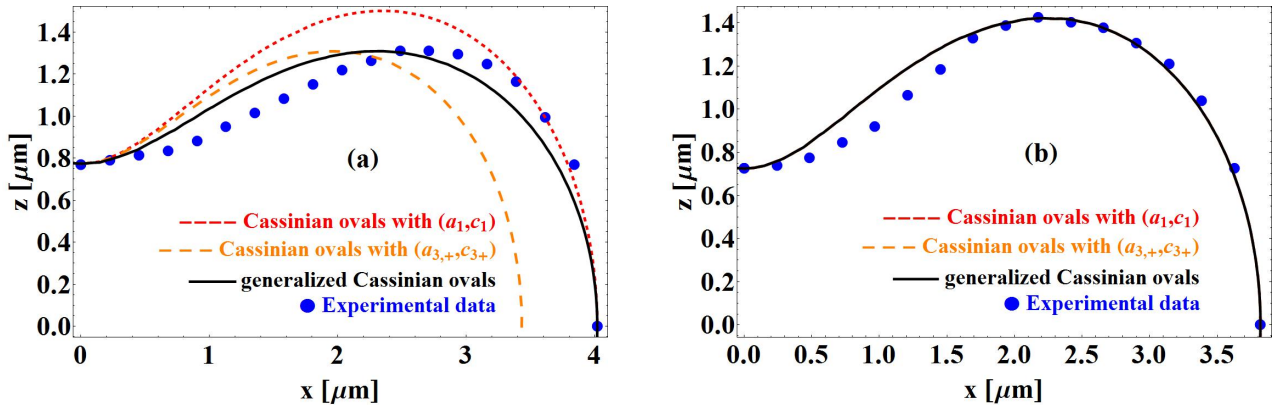


Fig. 4. Contours of RBCs modeled via Cassinian [(---------) and (– – – –)] and generalized Cassinian ovals (————) in comparison to experimentally obtained contours [Cell 3 in (**a**)] and [Cell 4 in (**b**)] (•) of normal red blood cells taken from [5]. The short-dashed curve (---------) corresponds to the set of parameters (a_1, c_1), while the orange long-dashed one (– – – –) to $(a_{3,+}, c_{3,+})$. For the values of the parameters of the Cassinian and generalized Cassinian ovals one finds that: (**a**) $a_1 = 2.79$ μm, $c_1 = 2.84$ μm; $a_{3,+} = 2.65$ μm, $c_{3,+} = 2.75$ μm; $a_g = 2.77$ μm, $b = 0.86$ and $c_g = 2.91$ μm and (**b**) $a_1 = a_{3,+} = a_g = 2.65$ μm, $c_1 = c_{3,+} = c_g = 2.75$ μm and $b = 1.00$.

3.2. Model based on single loop generalized Cassinian ovals

In order to avoid the lack of uniqueness in the relationship between the morphological parameters and those of the Cassinian ovals, one could introduce an additional degree of freedom (parameter) in Eq. (5) [22–25]. The equation which determins such a generalized Cassinian oval reads

$$\left(a_g^2 + x^2 + b^{-2}z^2\right)^2 - 4a_g^2x^2 = c_g^4, \tag{9}$$

where now one has

$$\begin{aligned} \tau_{\min} &= 2b\sqrt{c_g^2 - a_g^2}, \\ \tau_{\max} &= b\frac{c_g^2}{a_g}, \\ D &= 2\sqrt{c_g^2 + a_g^2}. \end{aligned} \tag{10}$$

Hence we find that

$$\begin{aligned} a_g &= \frac{\sqrt{b^2D^2 - \tau_{\max}^2} - \tau_{\max}}{2b}, \\ b &= \frac{\sqrt{4\tau_{\max}\sqrt{\tau_{\max}^2 - \tau_{\min}^2} + 4\tau_{\max}^2 - \tau_{\min}^2}}{D}, \\ c_g &= \frac{\sqrt{\tau_{\max}\sqrt{b^2D^2 + \tau_{\max}^2} - \tau_{\max}^2}}{\sqrt{2}b}. \end{aligned} \tag{11}$$

For the surface area, volume and sphericity index within this model one has

$$\begin{aligned} A_{gC} &= 4\pi b^2 c_g^2 \mathscr{S}_C(\varepsilon), \\ V_{gC} &= \frac{4}{3}\pi b c_g^3 \mathscr{V}_C(\varepsilon), \\ \Psi_{gC} &= b^{-4/3}\frac{\mathscr{V}_C^{2/3}(\varepsilon)}{\mathscr{A}_C(\varepsilon)}, \end{aligned} \tag{12}$$

where the dimensionless functions $\mathscr{S}_C(\varepsilon)$ and $\mathscr{V}_C(\varepsilon)$ are defined in Eqs. (8), and $\varepsilon \equiv c_g/a_g$.

3.3. Kuchel–Fackerell's model

Within the model suggested by Kuchel and Fackerell [26] the equation for the meridional cross-section of a RBC has the form

$$(x^2 + z^2)^2 + C_{0KF}x^2 + C_{1KF}z^2 + C_{2KF} = 0, \tag{13}$$

where the parameters of the model C_{iKF}, $i = 0, 1, 2$ are related to the morphological ones in the following way

$$\begin{aligned} C_{0KF} = &-\frac{D^2}{2} + \frac{\tau_{\max}^2}{2}\left(\frac{D^2}{\tau_{\min}^2} - 1\right) \\ &- \frac{\tau_{\max}^2}{2}\left(\frac{D^2}{\tau_{\min}^2} - 1\right)\sqrt{1 - \frac{\tau_{\min}^2}{\tau_{\max}^2}}; \end{aligned} \tag{14a}$$

$$\begin{aligned} C_{1KF} &= \frac{D^2}{\tau_{\min}^2}C_{0KF} + \frac{\tau_{\max}^2}{4}\left(\frac{D^4}{\tau_{\min}^4} - 1\right), \\ C_{2KF} &= -\frac{D^2}{4}C_{0KF} - \frac{D^4}{16}. \end{aligned} \tag{14b}$$

The corresponding surface area, volume and sphericity index within the model are

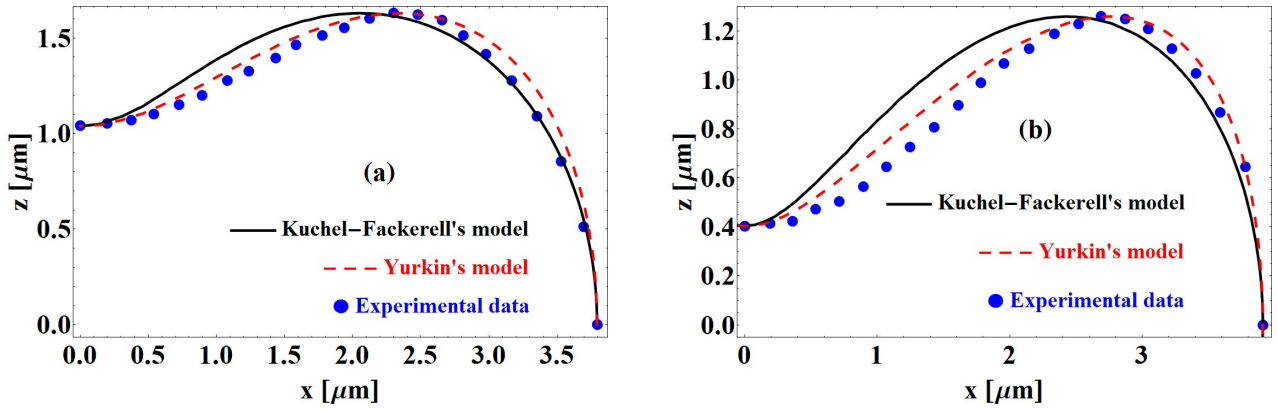


Fig. 5. Contours of RBCs modeled via Kuchel–Fackerell's model (————) and Yurkin's one (– – – –) in comparison to experimentally obtained contours [Cell 1 in (**a**)] and [Cell 2 in (**b**)] (•) of normal red blood cells taken from [4]. For the parameters of the considered models in case (**a**) one has: $C_{0KF} = -13.75\ \mu\text{m}^2$, $C_{1KF} = 7.56\ \mu\text{m}^2$, $C_{2KF} = 9.35\ \mu\text{m}^4$; $C_{0Y} = 0.42$, $C_{1Y} = -13.17\ \mu\text{m}^2$, $C_{2Y} = 15.29\ \mu\text{m}^2$, $C_{3Y} = -17.71\ \mu\text{m}^4$, while in case (**b**) their values are as follows: $C_{0KF} = -15.04\ \mu\text{m}^2$, $C_{1KF} = 22.97\ \mu\text{m}^2$, $C_{2KF} = -3.80\ \mu\text{m}^4$; $C_{0Y} = -0.12$, $C_{1Y} = -14.87\ \mu\text{m}^2$, $C_{2Y} = 39.01\ \mu\text{m}^2$, $C_{3Y} = -6.43\ \mu\text{m}^4$.

$$A_{KF} = \frac{\pi}{\sqrt{C_{1KF}-C_{0KF}}} \int_{\chi_l}^{\chi_u} \sqrt{\frac{(C_{1KF}+C_{0KF})\chi^2 - 2(C_{1KF}^2-4C_{2KF})\chi + (C_{1KF}-C_{0KF})(C_{1KF}^2-4C_{2KF})}{\chi^2 - 2(C_{1KF}-C_{0KF})\chi - 2C_{1KF}C_{0KF} + C_{1KF}^2 + 4C_{2KF}}}\, \mathrm{d}\chi, \quad (15a)$$

where

$$\chi_l = \sqrt{C_{1KF}^2 - 4C_{2KF}} \quad \text{and} \quad \chi_u = \sqrt{C_{1KF}^2 - 4C_{2KF} + 2(C_{1KF}-C_{0KF})\left(\sqrt{C_{0KF}^2 - 4C_{2KF}} - C_{0KF}\right)};$$

$$V_{KF} = \frac{\pi}{2(C_{1KF}-C_{0KF})^{3/2}} \int_{\chi_l}^{\chi_u} \chi \sqrt{-\chi^2 + 2(C_{1KF}-C_{0KF})\chi - (C_{1KF}^2 + 4C_{2KF} - 2C_{1KF}C_{0KF})}\, \mathrm{d}\chi; \quad (15b)$$

$$\Psi_{KF} = \frac{\pi^{1/3}(6V_{KF})^{2/3}}{A_{KF}}. \quad (15c)$$

3.4. Yurkin's model

Based on Eq. (13), Yurkin proposed the following four-parametric model (see p. 127 in [2]), describing the meridional cross-section of a RBC

$$x^4 + 2C_{0Y}x^2z^2 + z^4 + C_{1Y}x^2 + C_{2Y}z^2 + C_{3Y} = 0, \quad (16)$$

where the relationship between the parameters of the model C_{iY}, $i = 0,1,2,3$ and the morphological ones is

$$\begin{aligned} C_{1Y} &= -\frac{D^2}{4} - \frac{\tau_{\min}^2\tau_{\max}^2}{4D^2} + \frac{\tau_{\min}^2 d^2}{4D^2(\tau_{\max}^2 - \tau_{\min}^2)}, \\ C_{2Y} &= \frac{D^4 + 4D^2C_{1Y} - \tau_{\min}^4}{4\tau_{\min}^2}; \end{aligned} \quad (17a)$$

$$\begin{aligned} C_{3Y} &= -\frac{D^2}{16}(D^2 + 4C_{1Y}), \\ C_{0Y} &= -\frac{d^2 + 2C_{1Y}}{\tau_{\max}^2}. \end{aligned} \quad (17b)$$

The surface area, volume and sphericity index corresponding to Yurkin's model can be obtained by using Eq. (3), in which the function

$$z = \left\{ \left[(2C_{0Y}x^2 + C_{2Y})^2 - 4(x^4 + C_{1Y}x^2 + C_{3Y}) \right]^{\frac{1}{2}} - 2C_{0Y}x^2 - C_{2Y} \right\}^{\frac{1}{2}} \quad (18)$$

has to be substituted. The limits of integration are $[0; D/2] \equiv \left[0; 2^{-1/2}\sqrt{(C_{1Y}^2 - 4C_3Y)^{1/2} - C_{1Y}}\right]$

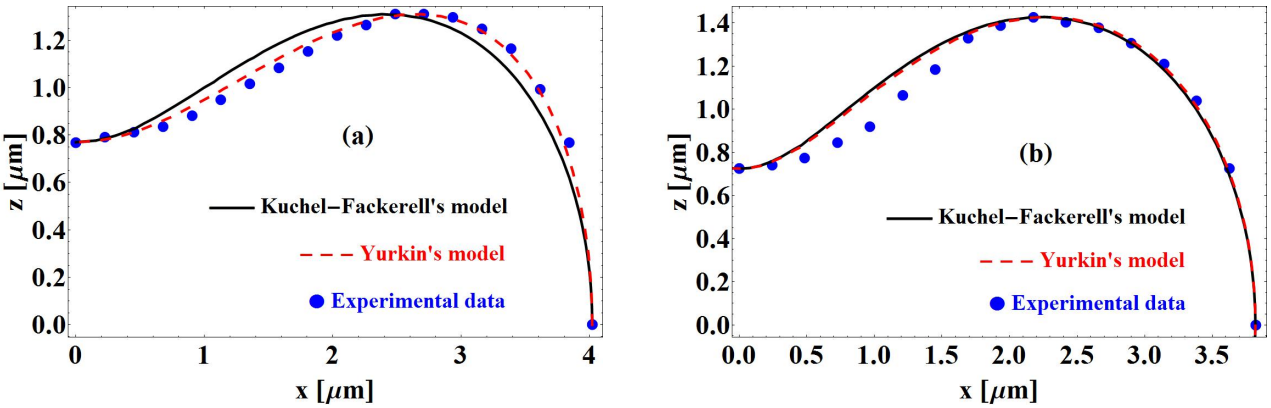


Fig. 6. Contours of RBCs modeled via Kuchel–Fackerell's model (————) and Yurkin's one (– – – –) in comparison to experimentally obtained contours [Cell 3 in (**a**)] and [Cell 4 in (**b**)] (•) of normal red blood cells taken from [5]. For the parameters of the considered models in case (**a**) one has: $C_{0KF} = -15.11\ \mu\text{m}^2$, $C_{1KF} = 28.04\ \mu\text{m}^2$, $C_{2KF} = -16.98\ \mu\text{m}^4$; $C_{0Y} = 0.17$, $C_{1Y} = -14.61\ \mu\text{m}^2$, $C_{2Y} = 41.60\ \mu\text{m}^2$, $C_{3Y} = -25.02\ \mu\text{m}^4$, while in case (**b**) their values are as follows: $C_{0KF} = -14.08\ \mu\text{m}^2$, $C_{1KF} = 15.06\ \mu\text{m}^2$, $C_{2KF} = -8.19\ \mu\text{m}^4$; $C_{0Y} = 0.9$, $C_{1Y} = -14.03\ \mu\text{m}^2$, $C_{2Y} = 15.06\ \mu\text{m}^2$, $C_{3Y} = -8.19\ \mu\text{m}^4$.

4. POLYNOMIAL APPROXIMATIONS WITH A DEGREE HIGHER THAN FOUR

4.1. Fung-Tong's model

The model proposed by Fung and Tong [27] is based on a three-parametric polynomial of the from

$$\left(\frac{2z}{D}\right)^2 = \left[1-\left(\frac{2x}{D}\right)^2\right] \times \left[C_{0FT} + C_{1FT}\left(\frac{2x}{D}\right)^2 + C_{2FT}\left(\frac{2x}{D}\right)^4\right], \quad (19)$$

For the relationship between the parameters C_{iFT}, $i = 0,1,2$ and those characterising the geometry of the cell one has

$$C_{0FT} = \frac{\tau_{\min}^2}{D^2},$$
$$C_{1FT} = \frac{D^2}{d^2}\left[\frac{\tau_{\max}(2D^2-3d^2)}{(D^2-d^2)^2} - 2C_{0FT}\right], \quad (20)$$
$$C_{2FT} = \frac{D^4}{d^4}\left[C_{0FT} - \frac{\tau_{\max}^2(D^2-2d^2)}{(D^2-d^2)^2}\right].$$

In integral form, for the surface area, volume and sphericity index within the framework of the model one finds

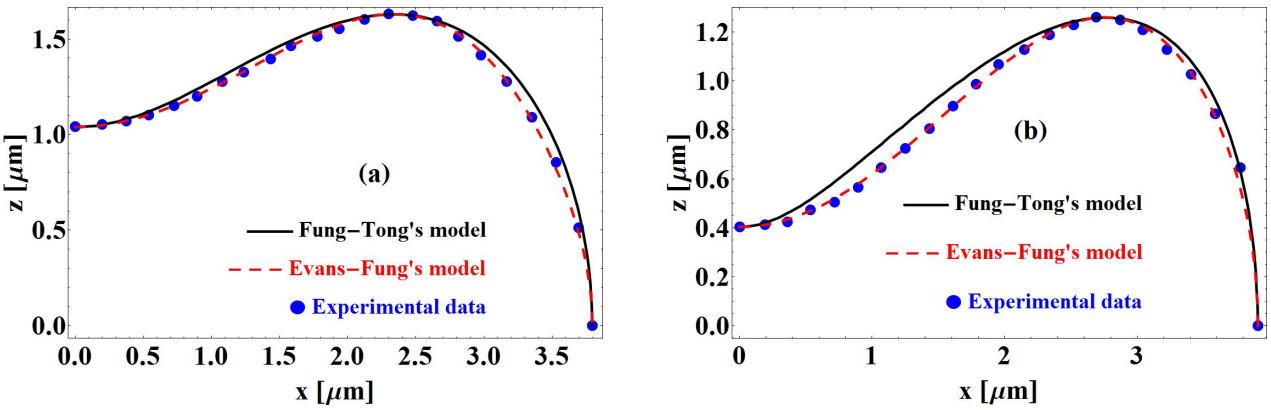


Fig. 7. Contours of RBCs modeled via Fung–Tong's model (————) and the Evans-Fungs's one (– – – –) in comparison to an experimentally obtained contours [Cell 1 in (**a**)] and [Cell 2 in (**b**)] (•) of normal red blood cells taken from [4]. For the parameters of the considered models in case (**a**) one has: $C_{0FT} = 0.075$, $C_{1FT} = 0.691$, $C_{2FT} = -0.277$; $C_{0EF} = 0.274$, $C_{1EF} = 0.988$, $C_{2EF} = -0.721$, while in case (**b**) their values are as follows: $C_{0FT} = 0.011$, $C_{1FT} = 0.375$, $C_{2FT} = 0.038$; $C_{0EF} = 0.104$, $C_{1EF} = 0.957$, $C_{2EF} = -0.505$.

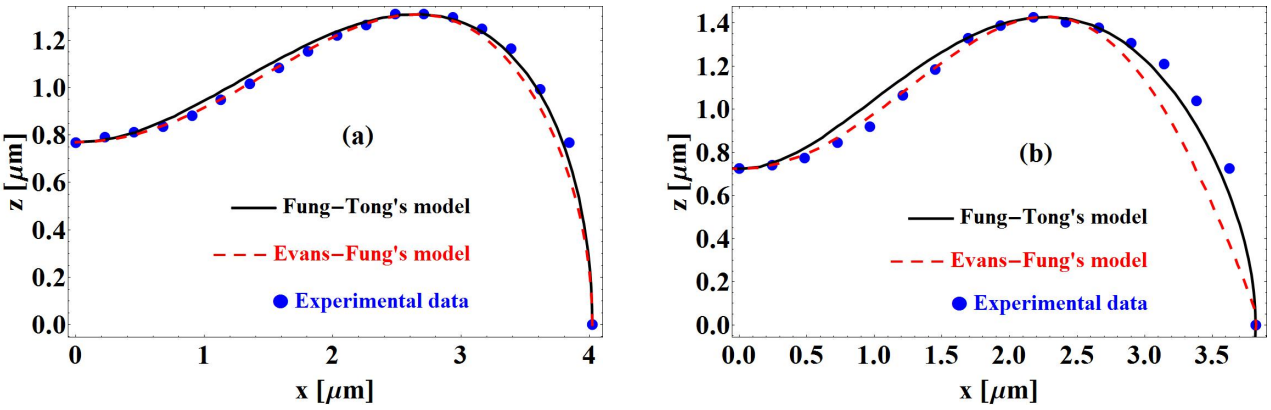


Fig. 8. Contours of RBCs modeled via Fung–Tong's model (————) and the Evans-Fungs's one (– – – –) in comparison to experimentally obtained contours [Cell 3 in (**a**)] and [Cell 4 in (**b**)] (•) of normal red blood cells taken from [5]. For the parameters of the considered models in case (**a**) one has: $C_{0FT} = 0.037$, $C_{1FT} = 0.363$, $C_{2FT} = -0.036$; $C_{0EF} = 0.192$, $C_{1EF} = 0.730$, $C_{2EF} = -0.399$, while in case (**b**) their values are as follows: $C_{0FT} = 0.036$, $C_{1FT} = 0.685$, $C_{2FT} = -0.491$; $C_{0EF} = 0.190$, $C_{1EF} = 1.197$, $C_{2EF} = -1.178$.

$$A_{FT} = \frac{\pi D^2}{2}\int_0^1 \sqrt{1+\frac{(1-\chi)[(C_{0FT}+C_{1FT}+C_{2FT})-2(C_{1FT}+2C_{2FT})\chi+3C_{2FT}\chi^2]^2}{\chi[(C_{0FT}+C_{1FT}+C_{2FT})-(C_{1FT}+2C_{2FT})\chi+C_{2FT}\chi^2]}}\,\mathrm{d}\chi; \tag{21a}$$

$$V_{FT} = \frac{\pi D^3}{4}\int_0^1 \sqrt{\chi[(C_{0FT}+C_{1FT}+C_{2FT})-(C_{1FT}+2C_{2FT})\chi+C_{2FT}\chi^2]}\,\mathrm{d}\chi; \tag{21b}$$

$$\Psi_{FT} = \frac{\pi^{1/3}(6V_{FT})^{2/3}}{A_{FT}}. \tag{21c}$$

In Ref. [24], the authors credited this model to Skalak [28], although it was first introduced by Fung and Tong (compare Eq. (24) from [27] with the one given in Figure 7 (a) in [28]).

4.2. Evans–Fung's model

In order to approximate the obtained experimental results for the thickness distribution of RBCs, Evans and Fung proposed the following three-parametric model [4]

$$\left(\frac{2z}{D}\right)^2 = \left[1-\left(\frac{2x}{D}\right)^2\right] \times \left[C_{0EF}+C_{1EF}\left(\frac{2x}{D}\right)^2+C_{2EF}\left(\frac{2x}{D}\right)^4\right]^2, \tag{22}$$

where one finds for the relationship between the model parameters and the morphological ones the following expressions

$$C_{0EF} = \frac{\tau_{\min}}{D},$$
$$C_{1EF} = \frac{D^2}{2d^2}\left[-4C_{0EF}+\frac{\tau_{\max}|5d^2-4D^2|}{(D^2-d^2)^{3/2}}\right], \tag{23}$$
$$C_{2EF} = \frac{D^4}{2d^4}\left[2C_{0EF}+\frac{\tau_{\max}(2D^2-3d^2)}{\mathrm{sgn}(5d^2-4D^2)(D^2-d^2)^{3/2}}\right].$$

The corresponding expressions for the surface area, volume and sphericity index are

$$A_{EF} = \frac{\pi D^2}{2}\int_0^1 \sqrt{1+\frac{(1-\chi)}{\chi}[(C_{0EF}+C_{1EF}+C_{2EF})-3(C_{1EF}+2C_{2EF})\chi+5C_{2EF}\chi^2]^2}\,\mathrm{d}\chi; \tag{24a}$$

$$V_{EF} = \frac{\pi D^3}{4}\int_0^1 \sqrt{\chi}[(C_{0EF}+C_{1EF}+C_{2EF})-(C_{1EF}+2C_{2EF})\chi+C_{2EF}\chi^2]\mathrm{d}\chi = \pi D^3\frac{(35C_{0EF}+14C_{1EF}+8C_{2EF})}{210}; \tag{24b}$$

$$\Psi_{EF} = \frac{\pi^{1/3}(6V_{EF})^{2/3}}{A_{EF}}. \tag{24c}$$

Here we note, that the reader can find a slight modification of this model in Ref. [29], where the authors introduced an additional factor (the aspect ratio $\eta \equiv \tau_{\max}/D$) in the right hand side of Eq. (22).

5. DISCUSSION AND CONCLUDING REMARKS

In the current article we have summarized the existing polynomial approximations of the meridional cross-section of a RBC, and compared each model to a set of experimental data. For every model we have given the relationship between the parameters that characterise it and the ones describing the geometry of the biconcave shape (cross-section), namely D, d, $\tau_{\max}$, and $\tau_{\min}$.

We started with the lowest degree polynomial approximation – Beck's model – representing second order polynomial [see Eq. (1)], where the obtained expressions for the relationship between the model parameters and the morphological ones [see Eq. (2)], as well as the expressions for the surface area and volume [see Eqs. (4a)] were derived by the author. The comparison with the experimental data is shown in Figures 1 and 2.

Following this model we have commented on four quartic polynomial models, first of which was the one based on Cassinian ovals [see Eq. (5) in Section 3.1]. Here we showed that the relationship between the parameters of the model and the morphological ones is not unique, which generates two distinct curves, resembling the RBC's meridional cross section [see Figures 3 and 4]. Here we derived explicit expressions for the surface area, volume and sphericity index, see Eqs. (8). An interesting observation about the model is that when $\varepsilon \to \infty$ (or equivalently $a \to 0$), $\mathscr{A}_C \to 1$, $\mathscr{V}_C \to 1$ and consequently $\Psi_C \to 1$. This justifies the obtained results, due to the fact that when $a \to 0$ the foci of the Cassinian ovals coincide with the zero of the coordinate frame and Eq. (5) describes the cross-section of a sphere with radius c, surface area $4\pi c^2$ and volume $(4/3)\pi c^3$. By definition the sphericity index of a spherical particle is unity.

After slightly modifying Eq. (5) by introducing an additional degree of freedom [see Eq. (9)], we obtained an unique relationship between the model and morphological parameters, as can be clearly seen from Figures 3 and 4, thus achieving a better approximation then that based on the standard Cassinian ovals equation. Within this model, expressions for A, V and Ψ were also obtained [see Eq. (12)].

The last two models of Section 3 are those of Kuchel-Fackerell [see Eq. (13)] and Yurkin [see Eq. (16)]. Unfortunately due to the complexity of these two models, the expressions for A, V and Ψ are only given in integral form. The given relations between the parameters were derived by the authors. Looking at Figures 5 and 6, one can conclude that the modification introduced by Yurkin is significant. Note that so far all model parameters were related to only three morphological ones – D, $\tau_{\max}$, and $\tau_{\min}$. The introduction of a fourth pa-

Table 2. Tabular comparison between the experimental values (first row) of the surface area (A [μm^2]), volume (V [μm^3]) and sphericity index (Ψ) of four different experimentally obtained mean red blood cell contours and different approximating models - Beck's model (B), models based on single loop Cassinian (CO) and generalized Cassinian (gCO) ovals, Kuchel-Fackerell's model (KF), Yurkin's model (Y), Fung-Tong's model (FT) and Evans-Fung's model (EF).

	Cell 1			Cell 2			Cell 3			Cell 4		
Model	A	V	Ψ	A	V	Ψ	A	V	Ψ	A	V	Ψ
Exp. data	135	116	0.852	135	94	0.741	134	99	0.771	129	95	0.776
B	134	117	0.863	134	91	0.730	139	105	0.774	132	103	0.805
CO*	129	110	0.861	135	107	0.807	134	122	0.832	129	105	0.834
CO†	158	131	0.790	108	77	0.810	105	78	0.841	129	105	0.834
gCO**	134	119	0.873	130	96	0.780	135	107	0.807	129	105	0.834
KF	133	118	0.875	131	96	0.774	137	108	0.801	129	105	0.834
Y	137	122	0.868	135	97	0.756	140	110	0.793	130	105	0.828
FT	136	120	0.865	135	97	0.756	140	110	0.793	127	102	0.831
EF	133	116	0.865	134	93	0.741	138	107	0.780	123	93	0.807

*The parameters of the model are (a_1, c_1) [see Eq. (7a)]
†The parameters of the model are $(a_{3,+}, c_{3,+})$ [see Eq. (7c)]
**The parameters of the model are (a_g, b, c_g) [see Eq. (11)]

rameter allowed Yurkin to include in his model additionally the parameter d (the diameter of a circle that determines the location of the maximum thickness) [see Eq. (17)], and by that to improve the approximating ability of the polynomial suggested by Kuchel and Fackerell.

Last but not least we have considered the models by Fung and Tong [see Section 4.1] and Evans and Fung [see Section 4.2]. The first, described by a three-parametric sixth degree polynomial [see Eq. (19)] while the second – by a three-parametric eight degree one [see Eq. (22)]. Here we managed to obtain the relationship between the model and morphological parameters [see Eqs. (20) and (23)], as well as integral expressions for the surface area, volume and sphericity index. The comparison with the experimental data is depicted on Figures 7 and 8. The comparison between the experimental and model calculated quantities A, V and Ψ is shown in Table 2.

REFERENCES

[1] L. Bi, and P. Yang, *J. Biomed. Opt.* **18**, 055001 (2013).

[2] M. Yurkin, *Discrete dipole simulations of light scattering by blood cells*, Ph.D. thesis, University of Amsterdam (2007).

[3] J. S. Beck, *J. Theor. Biol.* **75**, 587–501 (1978).

[4] E. Evans, and Y.-C. Fung, *Microvasc. Res.* **4**, 335–347 (1972).

[5] A. Jay, *Biophysical Journal* **15**, 205–222 (1975).

[6] J. Steward, *Calculus*, Cengage Learning, 2012, 7th edn.

[7] H. J. Deuling, and W. Helfrich, *Biophys J.* **16**, 861–868 (1976).

[8] H. Funaki, *Jpn. J. Physiol.* **5**, 81–92 (1955).

[9] P. Canham, *Journal of Theoretical Biology* **26**, 61–81 (1970).

[10] H. W. Vayo, *Can. J. Physiol. Pharmacol.* **61**, 646–649 (1983).

[11] H. W. Vayo, and M. K. Shibata, *Jap. J. Physiol.* **34**, 357–360 (1984).

[12] Y. Fan, and W. Wang-yi, *Appl. Math. Mech. (English Edition)* **8**, 17–30 (1987).

[13] L. D. Spears, *Theoretical constructs and the shape of the human erythrocyte*, Ph.D. thesis, Southern Illinois University at Carbondale (1993).

[14] V. Kralj-Iglic, S. Svetina, and B. Zeks, *Eur. Biophys. J.* **22**, 97–103 (1993).

[15] P. Mazeron, and S. Müller, *J. Opt.* **29**, 68–77 (1998).

[16] B. Angelov, and I. Mladenov, "On the Geometry of Red Blood Cell," in *Geometry, Integrability and Quantization*, edited by I. Mladenov, and G.Naber, Coral Press, 2000, vol. 1, pp. 27–46.

[17] I. M. Mladenov, *Comptes Rendus de l'Academie Bulgare des Sciences* **53**, 13–16 (2000).

[18] C. A. Long, "Mathematical models and enigmas in evolution of erythrocytes," in *Proceedings of the 2006 WSEAS International Conference on Mathematical Biology and Ecology, Miami, Florida, USA, January 18-20*, 2006, pp. 74–80.

[19] A. Di Biasio, and C. Cametti, *Bioelectrochemistry* **71**, 149–156 (2007).

[20] J. O. Ricardo, M. Muramatsu, F. Palacios, M. Gesualdi, O. Font, J. L. Valin, M. Escobedo, S. Herold, D. F. Palacios, G. F. Palacios, and A. Sánchez, *J. Phys. Conf. Ser.* **274**, 012066 (2011).

[21] K. A. Melzak, G. R. Lázaro, A. Hernández-Machado, I. Pagonabarraga, J. de Espadae, and J. L. Toca-Herrera, *Soft Matter* **8**, 7716–7726 (2012).

[22] J. Hellmers, E. Eremina, and T. Wriedt, *J. Opt. A: Pure Appl. Opt.* **8**, 1–9 (2006).

[23] E. Eremina, H. J, Y. Eremin, and T. Wriedt, *Journal of Quantitative Spectroscopy & Radiative Transfer* **102**, 3–10 (2006).

[24] T. Wriedt, J. Hellmers, E. Eremina, and R. Schuh, *Journal of Quantitative Spectroscopy and Radiative Transfer* **100**, 444–456 (2006).

[25] D. Dantchev, and G. Valchev, *Journal of Colloid and Interface Science* **372**, 148–163 (2012).

[26] P. W. Kuchel, and E. D. Fackerell, *Bull. Math. Biol.* **61**, 209–220 (1999).

[27] Y. B. Fung, and P. Tong, *Biophysical Journal* **8**, 175–198 (1968).

[28] R. Skalak, A. Tozeren, R. P. Zarda, and S. Chien, *Biophys J.* **3**, 245–264 (1973).

[29] M. A. Yurkin, K. A. Semyanov, P. A. Tarasov, A. V. Chernyshev, A. G. Hoekstra, and V. P. Maltsev, *Appl. Opt.* **44**, 5249–5256 (2005).

ВЪРХУ РАЗЛИЧНИТЕ МОДЕЛИ, ОПИСВАЩИ РАВНОВЕСНАТА ФОРМА НА ЕРИТРОЦИТ

Г. Вълчев, В. Василев, П. Джонджоров

Институт по механика, Българска академия на науките, ул. "Акад. Г. Бончев", блок 4, 1113 София, България

(Резюме)

Като един от най-важните типове кръвни клетки във всички гръбначни организми, изучаването на равновесната форма на еритроцитите е от особена важност за разбирането на техните физико-химични и механични свойства. Настоящата работа представлява обобщение на съществуващите до момента модели и методи, описващи равновесната форма на червените кръвни клетки. Започвайки с най-опростения модел – този базиран на овали на Касини и завършвайки с най-общия вид на уравнението за формата на ососиметрични флуидни мембрани, ние правим сравнение на всеки от моделите с набор от експериментални данни. Целта ни е да създадем класификация на моделите за специфичните цели на тяхното приложение, като например за аналитично изучаване на взаимодействията между отделните еритроцити или между тях и стените на кръвоносните съдове, за диагностика на заболявания, свързани с промяна на равновесната форма на клетките, както и за експериментално изучаване на червените кръвни телца чрез разсейване на светлина.

Bulgarian Chemical Communications, Volume 47, Special Issue B (pp. 95–102) 2015

Structure and properties of polypropylene containing organo-clay and carbon nanotubes as fillers

I. Petrova*, E. Ivanov, R. Kotsilkova

Open Laboratory for Experimental Mechanics of Micro and Nanomaterials, Institute of Mechanics, Bulgarian Academy of Sciences, Acad. G. Bontchev Str., Bl. 4, BG-1113 Sofia, Bulgaria

The present work is focus on polymer composites containing multiwall carbon nanotubes (MWCNT) and organically modified clay (OC) in different proportions as nanofiller in isotactic polypropylene (iPP). The composites were prepared by extrusion method in a twin-screw co-rotating extruder and were subjected to a number of studies as X-ray diffraction (XRD), Scanning electron microscopy (SEM), Transmission electron microscopy (TEM) and Thermogravimetric analysis (TGA). Establishing a connection between the structure and properties are expected to provide opportunities for controlling the processes of the resulting materials. An XRD result shows changes in the position of the diffraction peaks towards right side of the clay basal reflection peak, which can be explained by collapsing of the clay layers after compounding. XRD results are consistent with TEM images confirming that the layered silicate particles are dispersed in thin stacks consisting only of few layers. TEM and SEM structure analysis on the state of organo-clay and carbon nanotubes dispersed in PP matrix proves homogeneous, but non-uniform filler dispersion due to formation of regions with well dispersed fillers and on the other hand, the presence of regions with nanofiller aggregates. The thermal stability and thermal degradation of the matrix as well two- and three-component materials was analyzed in nitrogen atmosphere. It was found a significant improvement on thermal stability of PP with nanotubes loading in the investigated concentration range (0.5–5 wt.%). The conducted studies concerning those composites showed that the structural changes or changes in the properties was not the result of the synergistic effects or in other words fillers exhibit self-influence on the host matrix and its properties.

Key words: polypropylene, multiwall carbon nanotubes, organo-clay, XRD, TGA, SEM, TEM

INTRODUCTION

Although, the interest in polymer/layered silicate nanocomposites is still at high level in the last few years began to appear a new area on polymer nanocomposites which refers to nanocomposites with more than one filler. The most common reason for investigating hybrid composite blends containing two fillers is synergy effects which could occur when using two different types of nanofiller and the resulted properties of nanocomposites are substantially different or better than those of the matrix [1]. In our studies on polymer composites we have chosen to use polypropylene (PP) because it is the second most commercial polymer with wide use in many areas such as packaging, automotive industry, consumer goods, fibers and textiles [2]. Furthermore, PP offers good chemical and fatigue resistance and have stress cracking resistance, good hardness and ease of machining, together with good processability by injection molding and extrusion [3]. Great part of modern applications of plastics is associated with specific requirements in terms of performance, processing and good price make the introduction of fillers in polymer matrices [1]. Usually layered silicates offers good opportunities to overcome the disadvantages, but organo-clay (OC) truly affects the structure and properties of polypropylene [4]. Many results have been reported in the literature relating to the study of polymer reinforced with layered silicates [5] and is described the use of compatibiliser in nanocomposites to improve dispersion of the silicate layers in the volume of the surrounding polymer. Secondly point of view in this study refers to multiwall carbon nanotubes (MWCNTs) which are recently used to reinforce the polymer and to add novel physical properties to the composite, due to their remarkable electrical, mechanical, optical, thermal and chemical properties [6–9] this making them a perfect for many engineering applications.

Literature reveals limited information [10–12] on hybrid composites combining two types of nanofiller in a common matrix. This provokes our interest to find joint effect between the two additives (MWCNTs and OC), and to study the influence of fillers on the structure and subsequent properties.

MATERIALS AND METHODS

Isotactic polypropylene, PP6231 (Buplen 6231 Lukoil Neftochim Bourgas AD, having MFI 16–25 g/10 min at 230°C) is the matrix polymer. Organi-

* To whom all correspondence should be sent:
ivanka.petrova01@gmail.com

© 2015 Bulgarian Academy of Sciences, Union of Chemists in Bulgaria

Table 1. Two-component and three-component blends containing MWCNT and OC in isotactic polypropylene.

Short name	**Composites**	**PP**	**MA-g-PP** (wt.%)	**MWCNT** (wt.%)	**Clay** (wt.%)
PP	PP6231	100	—	—	—
PP0.5CNT	PP+0.5%MWCNT	99.5	—	0.5	—
PP1CNT	PP+1%MWCNT	99	—	1	—
PP3CNT	PP+3%MWCNT	97	—	3	—
PP5CNT	PP+5%MWCNT	95	—	5	—
PPMA	PP+12%MA-g-PP	88	12	—	—
PPMA3OC	PP+3%Clay	85	12	—	3
PPMA0.5CNT3OC	PP+0.5%MWCNT+3%Clay	84.5	12	0.5	3
PPMA1CNT3OC	PP+1%MWCNT+3%Clay	84	12	1	3
PPMA3CNT3OC	PP+3%MWCNT+3%Clay	82	12	3	3
PPMA5CNT3OC	PP+5%MWCNT+3%Clay	80	12	5	3

cally modified clay, Cloisite 30B (Southern Clay Products, Inc) and PLASTICYLTMPP2001 – commercial masterbach of 20 wt.% MWCNT in PP, with real density 872 G/L are used as fillers. For the preparation of nanocomposites 20 wt.% clay is dispersed by extrusion mixing in PP adding 12 wt.% MA-g-PP (Fusabond 613, Maleic anhydride content 0.5 wt.%, Mw = 95000; MFI = 120 g/10 min, Du Pont data), as a compatibiliser. Then, the appropriate amount of both masterbatches – 20 wt.% MWCNT/PP and 20 wt.% OC/PP are diluted with the polypropylene by melt mixing with a 25-mm twin-screw co-rotating extruder Collin Teach-line Compounder (L/D=24) and Collin Teach-line Strand Pelletizer. The temperature setting of the extruder from the hopper to the die was 180/200/200/190/180°C and the screw speed was 45 rpm. In order to improve the carbon nanotube dispersion, the compositions were extruded in three runs. Variety of compositions was prepared containing 3 wt.% OC and 0.5–3 wt.% MWCNT in PP, summarized in Table 1.

X-ray analysis

The X-ray characteristics of tested composites were obtained using Bruker D8 Advance diffractometer. Powder X-ray diffraction patterns were collected within the range from 5.3 to 80 deg 2θ with a constant step 0.02 deg 2θ. Measurements were performed using a nickel-filtered Cu Kα radiation and LynxEye detector with wavelength $\lambda = 1.5418$ nm at 40 kV and 30 mA. To obtain diffraction patterns at small angles it was used plug-in device attached to the diffractometer which provides 2–10 deg 2θ diffraction range. The results are superimposed on a common graphics and the typical clay peak is analyzed. The peak is indicative of the platelet separation or d-spacing in clay structure. Any changes in this peak (width or height) provide information about delamination of clay stacks in the matrix volume which in turn depends on the dispersion. The interlayer distance of clay in the hybrids was calculated using Bragg's law (Eq. (1)).

$$d_{001} = \frac{n\lambda}{2\sin\theta}, \tag{1}$$

where n is an integer, λ is the wavelength of incident wave, d is the spacing between the planes in the atomic lattice, and θ is the angle between the incident ray and the scattering planes.

From the results, it was possible to calculate the number of clay platelets per average stack [13, 14] with the interlayer distance d_{001} using Eq. (2)

$$N = 1 + t/d_{001}, \tag{2}$$

where t is given by the Scherrer Eq. (3)

$$t = 0.9\lambda/(B_{1/2}\cos\theta_b), \tag{3}$$

where λ is the wavelength, $B_{1/2} = \theta_1 - \theta_2$ (in radians) at half peak height $(I_{\max}/2)$, $\theta_b = (\theta_1 + \theta_2)/2$.

Thermogravimetric analysis

Thermogravimetric analysis (TGA) is a well-known method used to study polymer degradation mechanisms and kinetic to predict the thermal stability of the polymers. The effect of nano-fillers presence on thermal stability of the composites was observed by TGA Diamond Perkin-Elmer Instrument

(TG/DTA) at the following conditions 30°C to 800°C at 20°C/min under nitrogen atmosphere. Charts allow defining features as temperature corresponding to initial 10% of weight loss (T_{10}) and peak temperature (T_p).

Electron microscopy

Microstructure and morphology of the fresh-cut nanocomposite samples was studied by scanning electron microscopy (SEM), using an FEI Quanta 600 SEM equipped with a field emission gun. All samples were cut in liquid nitrogen and coated with chromium prior to examination. Transmission electron microscopy (TEM) was carried out with a Philips CM20 instrument with an accelerating voltage from 60 kV to 200 kV and is equipped with a 4 megapixel AMT camera, enabling digital recording of images.

RESULTS AND DISCUSSION

The XRD diffraction pattern of composite materials, neat PP and Cloisite 30B using in this study are shown in Fig. 1. The diffraction peaks of PP/CNT/OC composite and neat PP show a number of characteristic peaks in the range $2\theta = 14^\circ \div 22^\circ$ due to the semi-crystalline structure of polypropylene. The addition of carbon nanotubes and clay is not influenced significantly the characteristic peaks within this range of 2θ. However, a strong effect of the clay is found in the small angle region of $2\theta = 3^\circ \div 7^\circ$ due to the clay dispersion.

The basal reflection peak of Cloisite 30B, as well as the clay containing composites (PPMA3OC, PP1CNT3OC) and masterbatch of 20%Cloisite30B/PPgMA are shown on Fig. 2. The interlayer distances are calculated from the basal peak by Bragg's equation Eq. (1). Pure Cloisite 30B indicates a (d_{001}) peak around 2θ = 4.9° corresponding to an interlayer spacing of 1.8 nm. The 20%Cloisite30B/PPgMA masterbatch shows (d_{001}) peak between the values of Cloisite 30B and the PPMA3OC composite indicating that the dilution with pure PP led to a decrease in the d-spacing in comparison – 1.44 nm. It is seen from Fig. 2. that nanocomposite peaks is appear to the right side of the main peak of Cloisite 30 B, which indicates collapsing of the silicate layers after compounding with no evidence of exfoliation. Brief review of the literature [15–17] related to the use of Cloisite 30B as filler in different polymers shows that there are many reports of collapsing of the silicate layers after compounding in nanocomposite. At the same time, this behavior is not typical for other clays, as for example Cloisite 15A [13,16] or Cloisite 20B [18,19]. Results can be explained otherwise, the Cloisite 30B peak

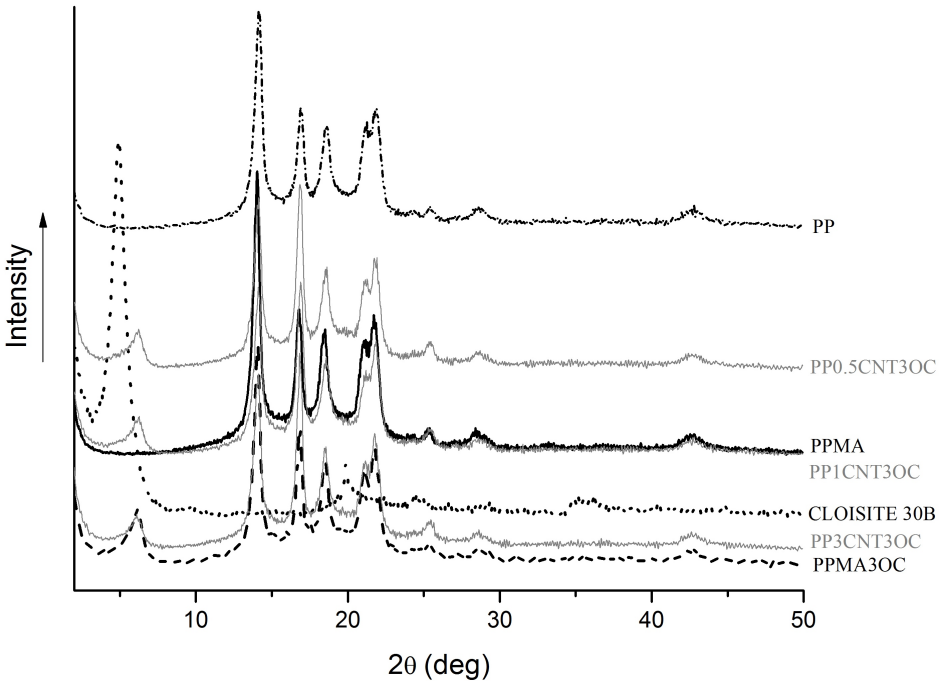


Fig. 1. X-ray diffraction patterns of Cloisite 30B, neat PP, PPMA, PPMA3OC and selected three-component systems.

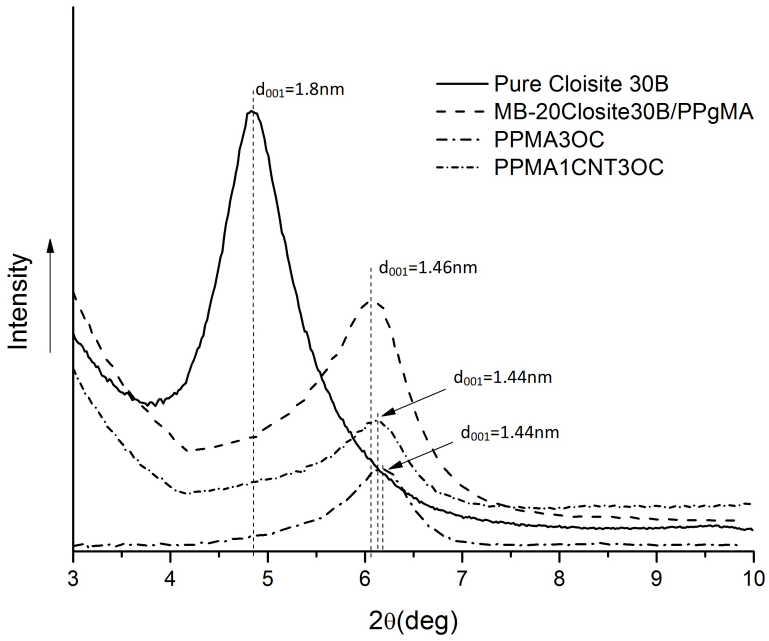


Fig. 2. X-ray diffraction patterns covering small angles region where 2θ values are between 2-10 deg.

in the composites is masked by the angular shoulder slope and appears at $2\theta = 6.1^{\circ}$, which assume the hypothesis that the layered silicate particles are dispersed in thin stacks consisting only of few layers, as shown in Fig. 3. These fine stacks are fastened each other at their end parts forming edge-to-edge structure and the distance between the plates (stack) at these points of contact decreases causing a reduction in peak height.

The XRD parameters calculated for the Cloisite 30B, as well as MB-20Closite30B/PPgMA and two composites (PPMA3OC, PPMA1CNT3OC) are summarized in Table 2 below. By using Eq. (2) and Eq. (3), the number of clay platelets per average stack was calculated. The interlayer distance of the clay does not increases in the nanocomposite or masterbatch, but XRD peak profiles shown that some reorganization occurs.

Table 2. XRD results obtained for Cloisite30B, MB-20Closite30B/PPgMA and two composite blends, where 2θ indicate main peak location, d_{001} is interlayer distance, and N is the number of clay platelets per average stack.

Sample name	2θ (deg)	d_{001} (deg)	N
Cloisite30 B	4.9	1.8	5.55
MB-20Closite30B/PPgMA	6.05	1.46	5.42
PPMA3OC	6.1	1.44	6.97
PPMA1CNT3OC	6.3	1.44	6.55

TEM analysis allows a qualitative understanding of the internal structure, spatial distribution of the various phases, and views of the defect structure through direct visualization Fig. 3. TEM morphology images show clay tiles divided into finer stacks, with confirming the result suggested by the XRD. Fig. 3(a) shows a TEM micrograph with focus on single tubes of ternary blend at a low CNTs concentration (0.5 wt.%). It is difficult to determine the distribution of the clay in the first micrograph, but Fig. 3(b) clear shows several individual flakes clay scattered in the volume, as well as a stack of parallel plates in the middle of the image. The last TEM image (Fig. 3(c)) at highest concentration of nanotubes – PP/3CNT/3OC composite shows nanotube aggregation section.

In Fig. 4(a, b), SEM images are shown in different magnifications in order to observe the details. The fractured surfaces of neat PP extruded three times are shown in magnification $\times$5000 (a) and $\times$30000 (b). SEM micrographs show that the fracture surface of neat PP is smooth with linear propagation lines. Fig. 4(c, d) shows the micrographs of PP1CNT3OC system at magnifications of $\times$5000 and $\times$50000, respectively. It is observed by PP1CNT3OC image at magnification $\times$50000 the presence of nanotubes and clay stacks leads to significantly different structure related to pure PP morphology. Fig. 4(e, f) micrograph of PP3CNT3OC nanocomposite is similar

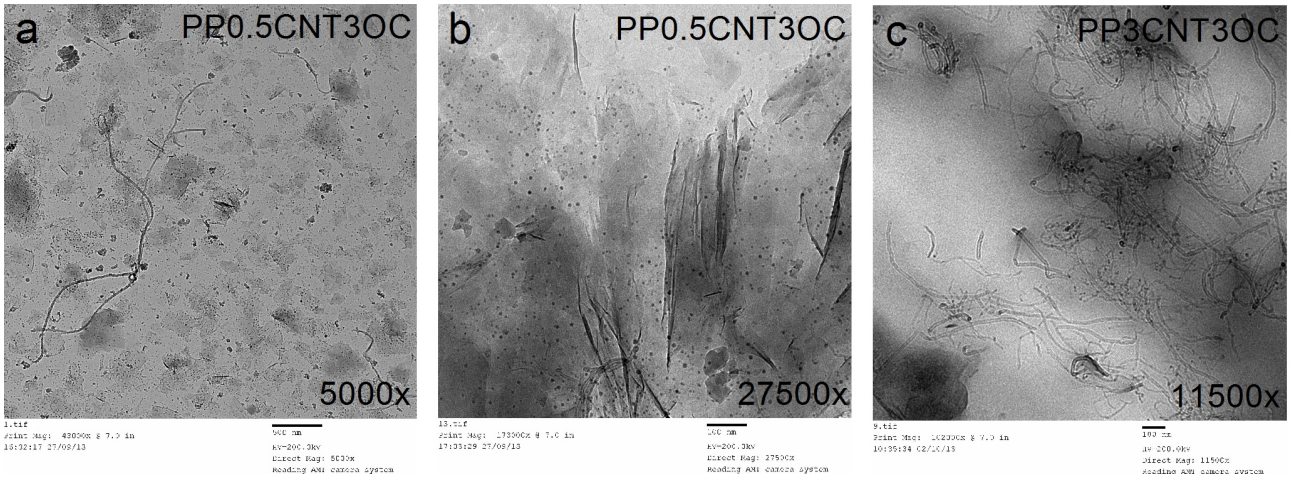


Fig. 3. TEM micrographs of PP0.5CNT3OC nanocomposites on (a) and (b); and PP3CNT3OC on (c).

to PP1CNT3OC, but surface fracture looks much rougher with small cracks indicating a more rigid structure. The surface in Fig. 4(d) reveals group of relatively closely located MWCNTs in this area and adjacent to this part of image is visible surrounding matrix structure. The structure image analysis on state of organo-clay and carbon nanotubes dispersed in PP matrix investigated by TEM and SEM proves homogeneous, but non-uniform filler dispersion due to formation of areas with presence of better nanotubes distributions, but also areas with poor dispersion.

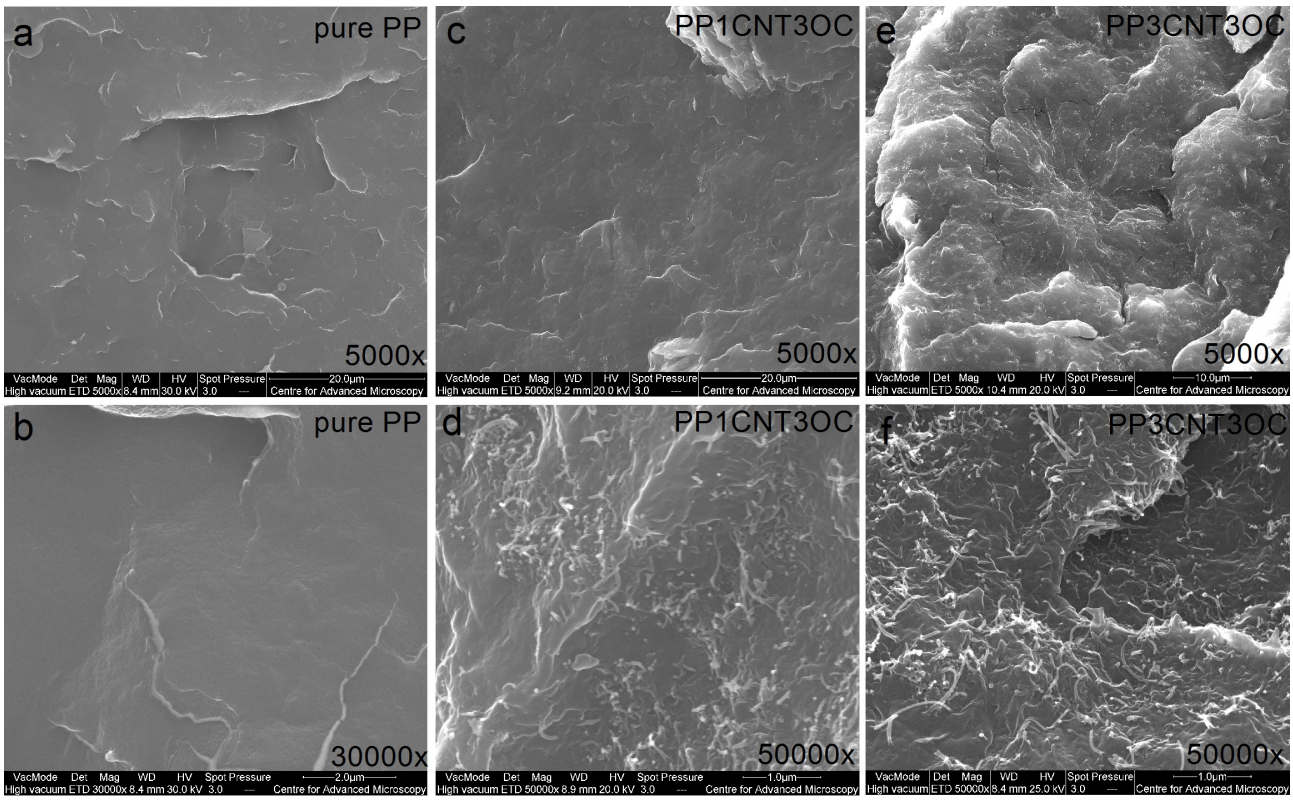


Fig. 4. SEM micrographs of pure PP (a, b); PP1CNT3OC on (c, d); and PP3CNT3OC nanocomposites on (e, f) at low and high magnification.

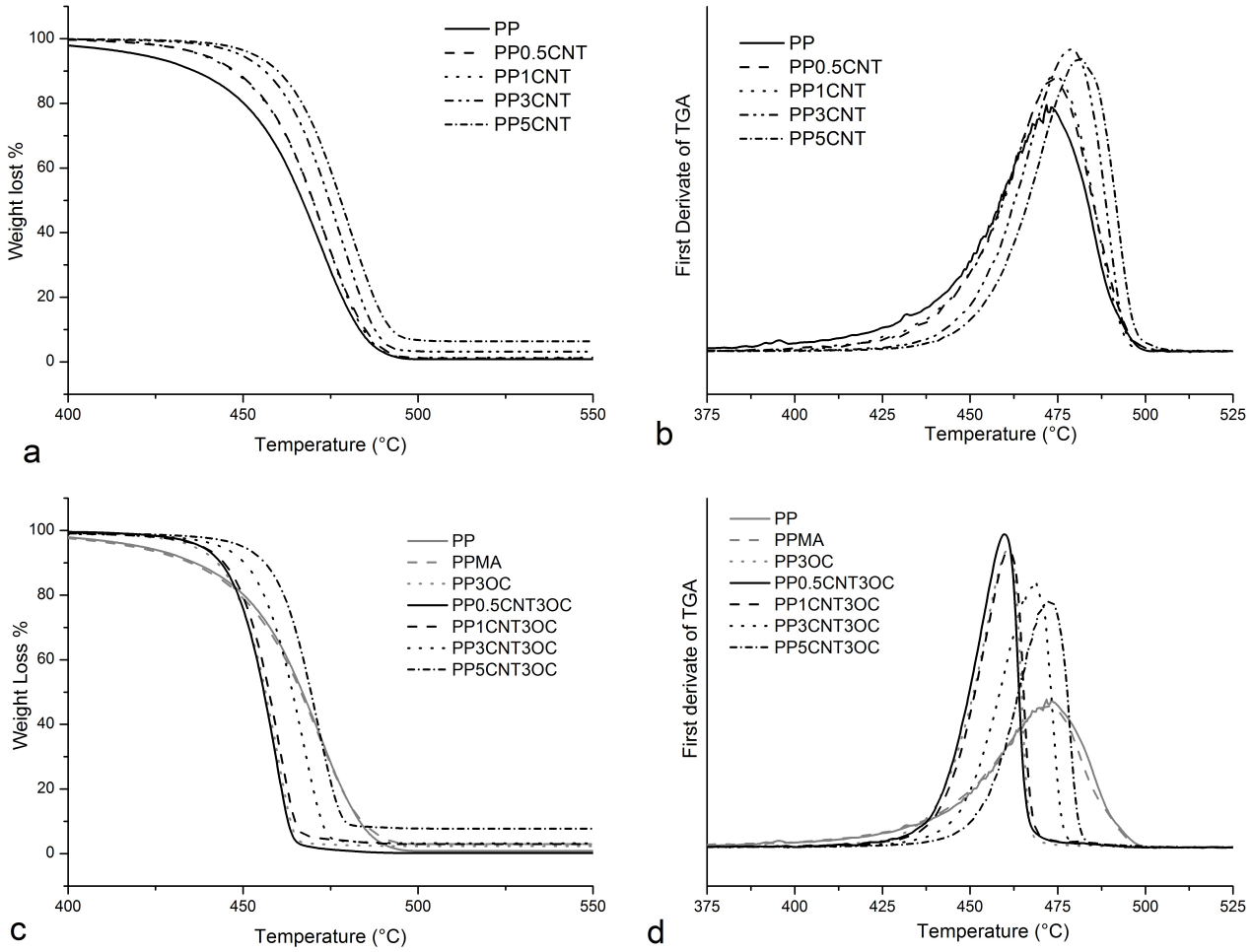


Fig. 5. TGA and DTG curves in nitrogen atmosphere for binary PP/CNT (a, b) and ternary PP/CNT/OC(c, d) systems

TGA and DTG curves for neat PP and PP/CNT nanocomposites at a heating rate of 20°C/min under nitrogen atmosphere are presented in Fig. 5(a, b). Temperature values at 10% weight loss ($T_{10\%}$) and peak temperature (T_P) for pure PP, PPMA, PPMA3OC, binary PP/CNT and ternary PP/CNT/OC composites are presented in Table 3. The addition of the nanotubes in the investigated concentration range (0.5–5 wt.%) improves the thermal stability of PP in nitrogen atmosphere. The addition of carbon nanotubes causes a weak displacement of the curves in the direction on the high temperatures from 2 to 7°C. Further increase on amount of nanotubes in two-phase compositions up to 5 wt.% shifts the curves 10°C toward higher temperature values. The thermal stability of the binary composites is improved by approximately 25°C and around 20°C of ternary composites. Regarding the three-phase composites there is a slight shift of the curves at low temperatures from 4 to 12°C by adding organoclay Fig. 5(c, d).

Table 3. Temperature values at 10% weight loss ($T_{10\%}$) and peak temperature (T_P) in nitrogen atmosphere determined from corresponding TGA and DTG diagrams

Sample name	$T_{10\%}$ (°C)	T_P (°C)
PP	436.19	471.88
PP0.5CNT	447.79	473.48
PP1CNT	447.15	474.21
PP3CNT	456.23	478.84
PP5CNT	460.01	481.45
PPMA	434.89	472.16
PPMA3OC	442.66	460.53
PPMA0.5CNT3OC	443.70	459.79
PPMA1CNT3OC	444.63	460.99
PPMA3CNT3OC	450.39	468.01
PPMA5CNT3OC	456.08	472.88

Thermal degradation of binary and ternary composites under nitrogen decreases with 7°C and 10°C, respectively.

CONCLUSIONS

In this work, the effect of the addition of two different types of nanofillers (MWCNT and OC) upon the structure and properties of PP was investigated through XDR, Electron microscopy and TGA. According to the XRD results the diffraction peaks of composites are shifted to right side of the main clay peak, which indicates collapsing of the silicate layers after compounding. These results are explained with the dispersion of clay in fine stacks, which form edge-to-edge structure and the distance between the edges at the points of contact decreases causing a reduction in peak height.

This is consistent with the analysis of the microscopic images. TEM and SEM observations proved relatively homogeneous, but non-uniform filler dispersion due to formation of areas with presence of better nanotubes distributions, but also areas with poor dispersion. Thermal stability increases with 30% at 10% mass loss, but this effect is mostly due to the addition of MWCNTs and there is no difference between the thermal stability in a two-phase and three-phase composites. Finally, it is important to note that despite the changes in the structure and properties of the composites studied, these changes dependent on either one (OC) or the other (MWCNT) filler, but a synergistic effect is not confirmed.

Acknowledgments *This research work was done within the COST Action MP1105, the Bilateral project BAS-CNR and the Joint Project DNTC/India 01/10. The support from the FP7-280987 NanoXCT project is acknowledged.*

REFERENCES

[1] E. Manias, *Nature Materials* **6**, 9–11 (2007).

[2] A. Ujhelyiová, M. Slobodová, J. Ryba, E. Borsig and P. Vencelová, *Open Journal of Organic Polymer Materials* **2**, 29–37 (2012).

[3] K. Chrissafis and D. Bikiaris, *Thermochim. Acta* **523** 1–24 (2011).

[4] C. Ding, D. Jia, H. He, B. Guo and H. Hong, *Polym. Test.* **24**, 94–100 (2005).

[5] S. Zhu, J. Chen, Y. Zuo, H. Li and Y. Cao, *Appl. Clay Sci.* **52**, 171–178 (2011).

[6] M. Musaddique, A. Rafique and J. Iqbal, *Journal of Encapsulation and Adsorption Science* **1**, 29–34 (2011).

[7] R. Kotsilkova, E. Ivanov, E. Krusteva, C. Silvestre, S. Cimmino and D. Durracio, "Evolution of Rheology, Structure and Properties around the Rheological Flocculation and Percolation Thresholds in Polymer Nanocomposites" in *Ecosustainable Polymer Nanomaterials for Food Packaging, Inovative Solutions, Characterization Needs, Savety and Environmental Issues*, edited by C. Silvestre and S. Cimmino, Taylor & Francis Group, London & NewYork, 2013, pp. 55–86.

[8] R. Kotsilkova, E. Ivanov, E. Krusteva, C. Silvestre, S. Cimmino and D. Duraccio, *J. Appl. Polym. Sci.* **115**, 3576–3585 (2010).

[9] I. Petrova, E. Ivanov, R. Kotsilkova, Y. Tsekov and V. Angelov, *J. Theor. Appl. Mech.* **43**, 67–76 (2013).

[10] H. Palza, B. Reznik, M. Wilhelm, O. Arias and A. Vargas, *Macromol. Mater. Eng* **297**, 474–480 (2012).

[11] H. Palza, C. Garzón and O. Arias, *eXPRESS Polym. Lett.* **6**, 639–646 (2012).

[12] V. Levchenko, Y. Mamunya, G. Boiteux, M. Lebovka, P. Alcouffe, G. Seytre and E. Lebedev, *Eur. Polymer. J.* **47**, 1351–1360 (2011).

[13] M. Morreale, N. Tz. Dintcheva, F. P. La Mantia, *eXPRESS Polym. Lett.* **7**, 703–715 (2013).

[14] M. Tokihisa, K. Yakemoto, T. Sakai, L. A. Utracki, M. Sepehr, J. Li and Y. Simard, *Polym. Eng. Sci.* **46**, 1040–1050 (2006).

[15] C. O. Rohlmann, M. F. Horst, L. M. Quinzani and M. D. Failla, *Eur. Polym. J.* **44**, 2749–2760 (2008).

[16] F. Perrin-Sarazin, M-T. Ton-That, M. N. Bureau and J. Denault, *Polymer* **46**, 11624-11634 (2005).

[17] G. G. Aloisi, F. Elisei, M. Noccetti, G. Camino, A. Frache, U. Costantino and L. Latterini, *Mater. Chem. Phys.* **123**, 372-377 (2010).

[18] L. B. d. Paiva, A. R. Morales and T. R. Guimarães, *Mater. Sci. Eng. A* **447**, 261–265 (2007).

[19] H. Palza, R. Vergara, M. Yazdani-Pedram and R. Quijada, *J. Appl. Polym. Sci.* **112**, 1278–1286 (2009).

СТРУКТУРА И СВОЙСТВА НА ПОЛИПРОПИЛЕН, СЪДЪРЖАЩ ОРГАНИЧНА ГЛИНА И ВЪГЛЕРОДНИ НАНОТРЪБИЧКИ КАТО ПЪЛНИТЕЛИ

Ив. Петрова, Е. Иванов, Р. Коцилкова

Лаборатория ОЛЕМ, Механика на флуидите, Институт по механика, Българска академия на науките, ул. "Акад. Г. Бончев" блок 4, 1113, София, България

(Резюме)

Нанонауката и технологията дават уникални възможности за създаване на революционно нови комбинации от материали със специфични свойства и със значителни предимства по отношение на качество и нови свойства пред класическите материали. По тази причина напоследък се отделя все повече внимание на напълнените инженерни полимери с наноразмерни пълнители.

В настоящата работа се разглеждат хибридни композити съдържащи многостенни въглеродни нанотръбички (MWCNT) и органично модифицирана глина (ОС) в различно съотношение като нанопълнители в изотактен полипропилен (iPP). Композитите са получени чрез екструзия в двушнеков екструдер и са подложени на редица изследвания за пълното им характеризиране и изучаване [1,3]. Установяването на връзка между структурата и свойствата се очаква да предостави възможности за управляване на процесите на получените материали [2]. Ефективен метод за получаване на информация за кристалографската структура и структурни промени на полимерите е рентгеноструктурен анализ (XRD). Органичната глина показва характерен пик, дължащ се на нейната регулярна структура, който е показателен за разслояването на силикатните стековете или така нареченото d-разстояние в композитната структура, което се изчислява по закона на Браг. Термичната стабилност и термичната деградация на матрицата и дву- и трикомпонентни състави в азотна и въздушна среда се анализира посредством термогравиметричен анализ (TGA). Значително подобряване на термичните свойства се появява при ниско съдържание на пълнител от 0.5 об.%, където TGA-кривите на iPP/MWCNT композитите са изместени към по-висока температура в сравнение с чистия полипропилен. Сканиращата електронна микроскопия (SEM) осигурява възможност за директна визуализация на степента на диспергиране на пълнителите в матрицата, формата и структурното разпределение на частиците, междуфазовата повърхност в композитите. Основната цел на тези експериментални изследвания е намирането на съвместен ефект на двата вида нанопълнители върху свойствата и структурата на получените композитните материали.

1. R. Kotsilkova, E. Ivanov, E. Krusteva, C. Silvestre, S. Cimmino, D. Duraccio. Ch. 3, *Evolution of Rheology, Structure and Properties around the Rheological Flocculation and Percolation Thresholds in Polymer Nanocomposites*, In: *Ecosustainable Polymer Nanomaterials for Food Packaging. Inovative Solutions, Characterization Needs, Safety and Environmental Issues* (Eds. C. Silvestre, S. Cimmino) Taylor & Francis Group (2013) 55–86.
2. R. Kotsilkova, E. Ivanov, E. Krusteva, C. Silvestre, S. Cimmino, D. Duraccio. Isotactic Polypropylene Composites Reinforced with Multiwall Carbon Nanotubes, Part 2: Thermal and Mechanical Properties Related to the Structure. *J. Appl. Polym. Sci.*, **115** (2010), 3576–3585.
3. I. Petrova, E. Ivanov, R. Kotsilkova, Y. Tsekov, V. Angelov. Applied Study on Mechanics of Nanocomposites with Carbon Nanofillers. *J. Theor. Appl. Mech.*, **43** (2013), 67–76.

Bulgarian Chemical Communications, Volume 47, Special Issue B (pp. 103–108) 2015

Charge depth in polylactic acid electret filled with fine filler

A. Guzhova, M. Galikhanov*

Department of Processing Technology of Polymers and Composite Materials,
Kazan National Research Technological University, 68 Karl Marx Str., 420015, Kazan, Russian Federation

Charge depth of corona electrets based on polylactic acid was studied. Model of homo- and heterocharge distribution in the polymer was offered according to the observed electret behavior. Three different levels are specified in bulk of the polymer. At the first level dipole polarization that occurs due to surface oxidation dominates. At the second level injected charge carriers prevail. at the third level there is no injected charge carriers. For polylactic acid film first level thickness is up to 10 μm, for the second one it is up to 20 μm

Key words: corona electrets, polylactic acid, charge depth

INTRODUCTION

Modern technology has created the plastic age. Most of package is made from plastics. However, wide spread of polymers resulted in significant increase of plastic wastes and environmental pollution since plastic decay time is more than a hundred years. Biodegradable plastics are advanced materials that allow to meet this challenge and reduce decay period many times. Thus, they help to deal with the problem of waste disposal [1].

Another advanced materials used in packaging industry are polymer electrets – dielectric materials that have a quasi-permanent electric charge or dipole polarization and generate internal and external electric fields [2].

Polylactic acid (PLA) – a plastic substitute made from fermented plant starch (usually corn) - is quickly becoming a popular alternative to traditional petroleum-based plastics that are the basic material for electret production [1]. Application of PLA for manufacturing electrets offers opportunity for different industries including packaging [3, 4].

However, PLA being polar polymer may not perform characteristics required for industrial use of electret materials [5, 6]. In order to improve electret properties of PLA it is necessary to understand mechanisms of charging and charge relaxation. Fine filler particles are known to increase electret properties of polymers [7–12].

Hence, the objective of the paper is to study charge carrier (homo- and heterocharge) depth in corona electrets based on polylactic acid and estimate fine filler effect on it.

* To whom all correspondence should be sent:
mgalikhanov@yandex.ru

Nowadays there are a few techniques to determine charge distribution in the bulk of a polymer such as sectioning and chipping method, thermal impulse method, method of charge neutralization by light and etc. [13–16]. Nevertheless, these techniques are either indirect or involve mechanical treatment of the samples requiring certain assumptions that affect significantly the results of experiments. Following technique [17] may be considered to be the most reasonable for measuring charge depth: double-layered films are manufactured from different polymers with varied top layer thickness. Then samples are polarized in the field of negative corona discharge. After measuring electret characteristic of the samples top layer is removed by the solvent, under layer (substrate) is dried and electret properties are measured again. There is no charge on a substrate if the removed top layer thickness exceeds injected charge carrier depth.

This technique requires selection of compatible polymer pairs. Basic requirements to substrate are resistance to applied solvent (or minimum swell value) and chemical nature similar to polymer studied.

MATERIALS AND METHODS

L-polylactic acid (PLA) was studied. Polyethylene Terephthalate (PET) was used as substrate; trichloromethane (chloroform) was used as a solvent. To begin, 5% solution of PLA or PLA+4%$BaTiO_3$ in trichloromethane was made. Then, top layer of the polymer studied of various thickness was solvent-casted to the PET under layer followed by solvent removal. Top layer thickness was measured by micrometer MK.

Samples were charged in the field of negative corona discharge after being heated at 90°C for

© 2015 Bulgarian Academy of Sciences, Union of Chemists in Bulgaria

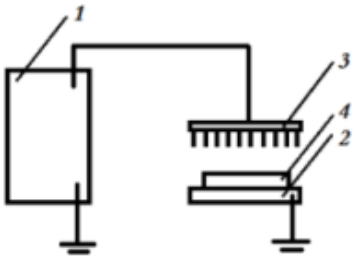


Fig. 1. Experimental set-up for corona treatment: 1 – corona electrode power supply; 2 – grounded electrode; 3 – corona electrode; 4 – sample.

10 min. Corona treatment unit is shown in Fig. 1. Corona electrode consists of 196 needles equally spaced on 49 cm^2 area. The gap between corona electrode and the sample was 20 mm, polarization time was 30 s, polarization voltage – 30 kV.

Samples were stored under room conditions in paper envelopes.

Surface potential V_s, electric field strength E and efficient surface charge density σ_{ef} were measured by IPEP-1 unit. Its working principle is based on periodic shielding of receiving electrode located at a certain distance from the electrets surface. Measurement error did not exceed 3%.

Top layer was removed from the samples with solvent (trichloromethane) under extract ventilation.

Thermal stability of electret state was investigated by thermally stimulated potential relaxation (TSPR) technique [18] that involves measuring surface potential of the samples being heated at the constant rate of 0,08 K/s right after polarization. Surface potential curves were normalized and given at relative unit V_s/V_{s0}, where V_{s0} is initial value of the sample surface potential.

RESULTS AND DISCUSSION

It was shown earlier in [5, 6] that polylactic acid performs poor electrets properties. Surface potential of PLA electrets decays in two-three days. Heating above 50°C results in complete electret charge relaxation. Studying thermal stability of PLA electret state showed that surface potential decay curve falls into three regions: region of the surface potential relative stability, region of sharp drop and complete surface potential relaxation region. (Fig. 2, curve 1).

One can see that at 307 K (34°C) PLA surface potential sharp drop region begins, while at 317 K (44°C) complete charge relaxation occurs (Fig. 2, curve 1). The fact that this temperature is close to PLA glass transition temperature allows to suggest that during polarization in corona discharge charge carriers entering the polymer polarize nearby dipoles and their orientation occurs in injected charge field [19]. At that, most of charge carriers are located at surface traps. Relaxation time of this dipole polarization is short, while temperature increase results in relatively free rotation of PLA macromolecule units. When PLA glass transition temperature is reached ordered dipole system breaks with the release of injected charge i.e. electret state relaxation occurs.

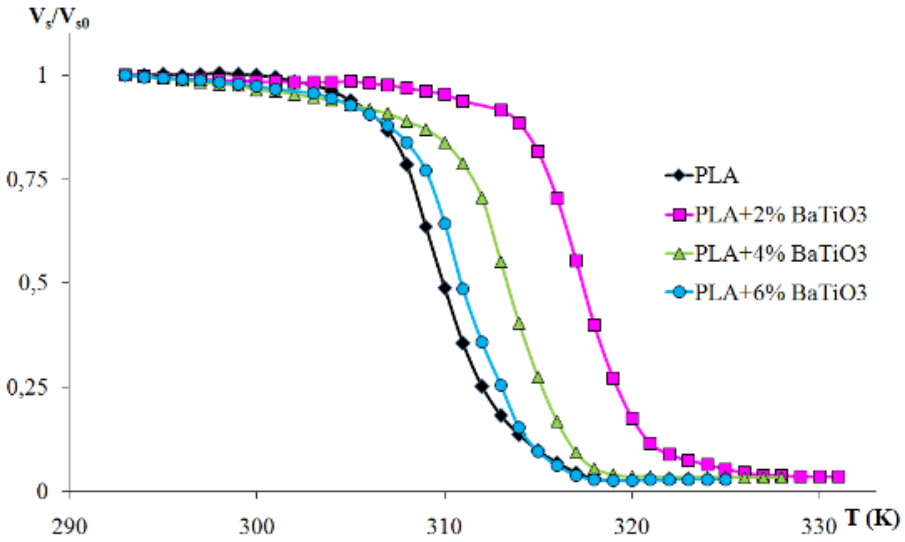


Fig. 2. Thermally stimulated potential relaxation curves of PLA compositions with barium titanate.

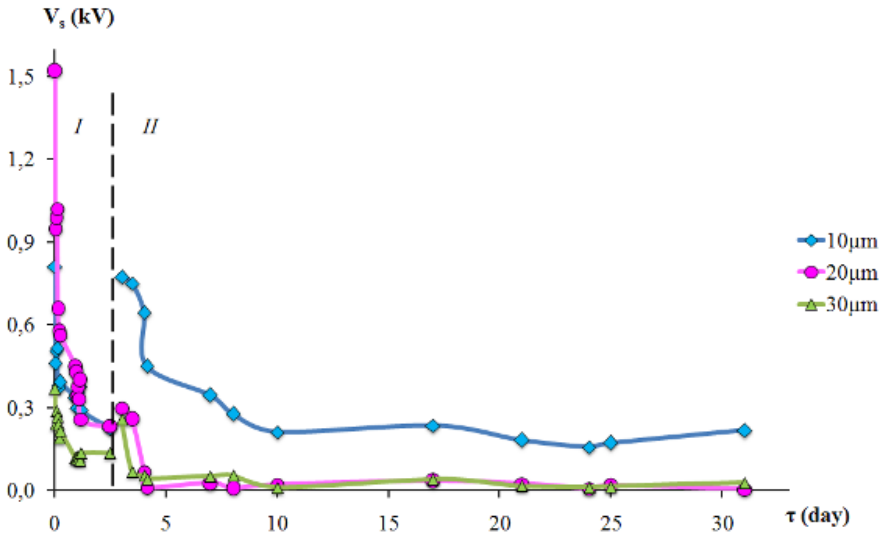


Fig. 3. Surface potential vs. storage time before (I) and after(II) PLA layer removal.

Figure 3 shows the results of charge depth study in the polymer. It is obvious that PLA layer removal affects significantly electrets properties of the samples. In one case substrate efficient surface charge density is higher (Fig. 3, curve 1), while in other cases it is lower (Fig. 3, curves 2 and 3) than for double-layered corona electrets.

The same behavior showed surface potential and electric field strength of the samples. Their values are given in Table 1.

Observed behavior can be explained by model of homo- and heterocharge distribution in polymer corona electrets described in [17] allowing for polylactic acid to be polar polymer. According to the model given in Fig. 4 three different levels are specified in bulk of the polymer. At the first level (Fig. 4, lvl.1) dipole polarization of polar groups dominates that occurs due to surface oxidation during corona treatment. At the second level injected charge carriers prevail (Fig. 4, lvl. 2). There are dipoles in the bulk of PLA as well. They can be oriented during corona discharge treatment, but this polarization is limited by hindered mobility of the polymer macromolecules at the given conditions. At the third level there are no injected charge carriers. (Fig. 4, lvl. 3).

At the second level injected charge carriers prevail. For polylactic acid film first level thickness is up to 10 μm, for the second one it is up to 20 μm. When PLA is filled with $BaTiO_3$ fine particles heterocharge influence increases resulting in less injected charge penetration depth.

Table 1. Electret properties of double-layered PLA-PET films vs. storage time.

Electret Properties	**PLA layer thickness,** (μm)	**before PLA layer removal** **0 day**	**1st day**	**3rd day**	**after PLA layer removal** **4th day**	**31st day**
V_s, kV	10	0.81	0.3	0.24	0.67	0.2
	20	1.52	0.34	0.20	0.67	0.01
	30	0.37	0.15	0.14	0.06	0.03
E, kV/m	10	48.4	21.9	14.3	40.2	13.1
	20	86.9	27.0	14.6	0.4	0.4
	30	21.9	7.3	8.5	3.5	1.4
σ_{ef}, μC/m^2	10	0.43	0.19	0.13	0.36	0.12
	20	0.58	0.24	0.13	0.00	0.00
	30	0.2	0.00	0.08	0.03	0.01

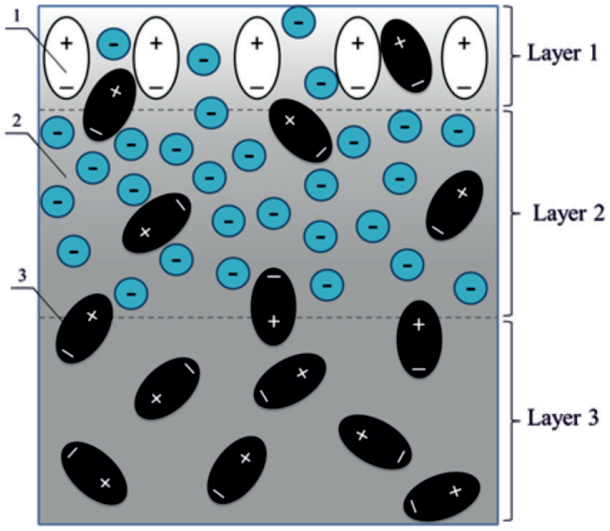


Fig. 4. Model of homo- and heterocharge distribution in PLA: 1 – dipoles formed due to surface oxidation; 2 – injected charge carriers; 3 – dipoles in the bulk of a polymer.

Electret performances of the samples increase after removal of the PLA layer where dipole polarization due to oxidation prevails since it contributes negatively to the electret total electric field value. In the case of PLA this layer thickness is about 10 μm (Fig. 3, curve 1).

When removed layer thickness is greater, injected charge carriers composing homocharge are removed as well resulting in almost complete charge decay shown in Fig. 3 (curves 2 and 3).

Therefore, it may be concluded that heterocharge depth in PLA that appears due to surface oxidation is 10μm, while homocharge depth is up to 20 μm.

It was mentioned above that fine filler is often used to enhance electret properties of the polymers [7–10]. Research conducted showed that filling PLA with barium titanate affect significantly stability and values of electret properties. It is seen (Fig. 2, curve 2) that 2% $BaTiO_3$ added to the polymer shifted the beginning of surface potential sharp decay region at 313K (39°C),while complete charge relaxation occurs at 326K (53°C).

PLA electret properties enhance when filled fith barium titanate can be explained by formation of new structural elements that can act as charge carrier traps (phase boundary, polymer loosened adsorption layer near filler surface). Increased number of injected charge traps contributes to the ability of dielectric to be polarized in corona discharge and enhances stability of the surface potential. Fillers affect mobility of different polymer kinetic units and relaxation time range. It occurs due to macromolecule adsorption on the solid surface to form adhesion polymer-filler bond resulting in macromolecule fixation and motion restriction at the surface adjacent segments. In other words, in filled PLA there is macromolecular layer with limited mobility near barium titanate surface. It hinders dipole polarization relaxation in PLA compositions and increases thermal stability of their electret properties (Fig. 2).

However, when barium titanate content in PLA is more than 2 wt.% gradual decrease of the surface potential stebility is observed (Fig. 2, curves 3-4), although composition surface potential is more stable compared to pure polymer. It is worth mentioning that the trends of electret performance dependence on filler content (with maximum at 2-4% dispersion component load) are common for polymer-filler systems [7–9, 20]. Reducing surface potential stability at greater filler content can be explained by two factors. Firstly, it is ferroelectric domain orientation that forms heterocharge. Secondly, it is content reduc-

Table 2. Electret properties of double-layered PLA+4%$BaTiO_3$-PET films vs. storage time.

Electret Properties	**PLA layer thickness,** (μm)	**before PLA layer removal** **0 day**	**1st day**	**3rd day**	**after PLA layer removal** **4th day**	**31st day**
V_s, kV	10	1.25	0.29	0.08	0.23	0.06
	20	1.70	0.56	0.17	0.34	-0.20
	30	1.14	0.52	0.11	0.66	0.14
E, kV/m	10	78.1	18.3	4.5	14.7	3.7
	20	101.8	35.1	10.8	21.3	-12.2
	30	71.2	33.7	6.7	41.5	9.1
σ_{ef}, μC/m^2	10	0.69	0.16	0.04	0.13	0.03
	20	0.67	0.31	0.10	0.25	-0.10
	30	0.63	0.29	0.06	0.37	0.08

tion of the component polarizable in corona discharge (polymer).

It should come as no surprise that structural modification affects charge depth in polylactic acid composite. At 4% $BaTiO_3$ content heterocharge contribution increases due to filler domain structure with high polarizability. It reduces charge penetration depth (Table 2).

Reduced homocharge penetration depth should result in decrease of polymer electret characteristics. However, injected charge carrier capture energy of composite structural elements is higher compared to pure polymer that was shown earlier in [20].

CONCLUSIONS

Therefore, polylactic acid performs insufficient electret characteristics. Heterocharge depth in PLA that appears due to surface oxidation is up to 10 μm, while homocharge (injected charge) penetration depth is up to 20 μm. Fine filler addition enhances surface potential stability of PLA composites. The most stable values of the surface potential were observed for PLA compositions with 2 wt.% $BaTiO_3$. Charge penetration depth in PLA composite is less owing to barium titanate domain structure with high polarizability.

REFERENCES

[1] V. A. Fomin and V. V. Guzeev, *Plastmassy* **2**, 42–46 (2001).

[2] *Plastics packaging Materials for food. Barrier function, mass transport, quality assurance, and legislation*, Ed. by Piringer O.G., Baner A.L. Wein-heim: Wiley-VCH, 2000.

[3] E. T .H. Vinka, K. R. Rabago, D. A. Glassner and P. R. Gruber, *Polymer Degradation and Stability* **80**, 403–419 (2003)

[4] J. Ren, *Biodegradable Poly(Lactic Acid): Synthesis, Modification, Processing and Applications*, Springer Berlin Heidelberg, 2010, pp. 208–239

[5] Y. A. Gorokhovatsky, N. Y. Meleshkina, V. V. Kochervinskiy and S. N. Chvalun, *Proceedings of the XII International conference "Physics of Dielectrics"*, Herzen State Pedagogical University of Russia, Saint Petersburg, 2011, pp. 172–175.

[6] W. Urbaniak-Domagala, *Journal of Electrostatics* **71**, 456–461 (2013).

[7] E. M. Godzhaev, A. M. Magerramov, S. S. Osmanova, M. A. Nuriev and E. A. Allakhyarov, *Surface Engineering and Applied Electrochemistry* **43**, 148–151 (2007).

[8] V. A. Goldade, A. G. Kravtsov, L. S. Pinchuk, V. S. Zotov, Y. A. Gorokhovatsky and D. E. Temnov, *Proc. of Int. Conf. on Advances in Processing, Testing and Application of Dielectric Materials*, Wroclaw, Poland, 2001, pp. 76–79.

[9] D. E. Temnov and E. E. Fomicheva, *Proc. of Int. Conf. Nanomaterials: Applications and Properties*, **2**, pp. 03NCNN48(1)–03NCNN48(2) (2013).

[10] A. Kilic, E. Shim, B. Y. Yeom and B. Pourdeyhimi, *J. Electrostatics* **71**, 41–47 (2013).

[11] N. Mohmeyer, N. Behrendtc, X. Zhangd, P. Smithe, V. Altstädt, G. M. Sessler and H.-W. Schmidt, *Polymer* **48**, 1612–1619 (2007)

[12] M. A. Ramazanov, S. A. Abasov, R. L. Mamedov and A. A. Rasulov, *Surface Engineering and Applied Electrochemistry* **47**, 481–483 (2011)

[13] M. E. Borisova and S.N. Koikov, *Russian Physics Journal* **1**, 74–89 (1979).

[14] G. Sessler, *Electrets*, Berlin: Springer, 1987, pp. 1–215.

[15] G. A. Lusheykin, *Methods of polymer electric properties study*, Moscow, Chimiya, pp. 109–114.

[16] A. I. Drachev, A. B. Gilman, A. A. Zhukov and A. A. Kuznetsov, *High Energy Chemistry* **38**, 344–347 (2004).

[17] M. F. Galikhanov,R. M. Garipov, A. A. Kozlov and R. Y. Deberdeev, *Materialovedenie* **11**, 13–17 (2010).

[18] Y. A. Gorokhovatsky and D. E. Temnov, *IZVESTIA: Herzen University Journal of Humanities and Sciences* **38**, 24–34 (2007).

[19] V. N. Kestelman, L. S. Pinchuk, V. A. Goldade, *Electrets in Engineering: Fundamentals and Applications* Boston-Dordrecht-London: Kluwer Acad. Publ., (2000) pp. 2–33.

[20] M. F. Galikhanov, R. Y. Deberdeev and V. A. Goldade, *Polymer Science. Ser. A* **47**, 134–138 (2005).

РАЗПРЕДЕЛЕНИЕ НА ЗАРЯДИТЕ В ЕЛЕКТРЕТИ ОТ ПМК С ФИН НАПЪЛНИТЕЛ

А. Гуджова, М. Галиханов

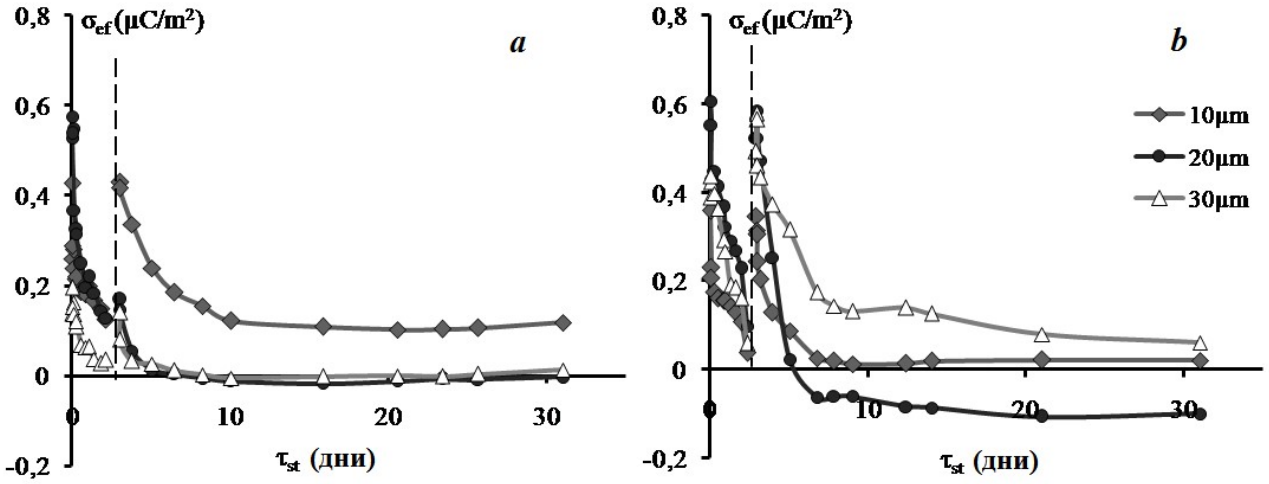
Казански национален изследователски технически университет,
ул. "Карл Маркс" №68, Казан, 420015, Федерация Русия

(Резюме)

Полимлечната киселина (ПМК) е полимерен заместител, направен от ферментирало заводско нишесте (обикновено царевица) и бързо се превръща в популярна алтернатива на традиционните полимери на петролна основа, които са основен материал за получаването на електрети. ПМК обаче няма подходящи характеристики, необходими за промишлената й употреба като електретен материал. За да се подобрят електретните й свойства, могат да се използват фини частици като напълнители на ПМК. При това е изключително важно да се изследват механизмите на зареждане и релаксация на зарядите. Затова, целта на доклада е да се изследва дълбочината на хомо- и хетерозарядите в короноелектретите на основата на полимлечна киселина и да се оцени влиянието на вкараните в нея фини напълнители.

Дълбочината на разпределение на зарядите се изследва чрез двуслойна техника, предложена от авторите. Горният слой на изследвания полимер (ПМК или ПМК+4%$BaTiO_3$ фини частици) с различна дебелина се получава като върху подходяща полимерна подложка (ПЕТ) се излива съответният разтвор. Образците се нагряват при 90°C за 10 мин. и след това се зареждат в отрицателен коронен разряд.

Повърхностният потенциал V_s, интензитетът на електричното поле E и ефективната повърхностна плътност на заряда σ_{ef} са измерени с времето преди и след премахването на горния слой с разтвор. Поведението на ефективната повърхностна плътност на заряда е показано на Фиг. 1. Подобни времеви зависимости имат V_s и E.



Фиг. 1. Времеви зависимости на ефективната повърхностна плътност на заряда за ПМК (a) и ПМК+4%$BaTiO_3$ (b) преди и след отстраняване на филмите.

Разработен е модел за разпределението на хомо- и хетерозаряди в полимер, чрез изследването на електретното му поведение. Три различни нива са определени в обема на полимера. Първото ниво се дължи на диполна поляризация, в резултат на повърхностно окисляване. На второто ниво преобладават инжектирани носители на заряд. На третото ниво няма инжектирани носители на заряд. За полимлечната киселина дебелината на първото ниво е до 10 μm, за второто – до 20 μm. Когато ПМК е напълнена с фини частици $BaTiO_3$ нараства влиянието на хетерозаряда в резултат на по-малката дълбочина на проникване на инжектирания заряд.

Bulgarian Chemical Communications, Volume 47, Special Issue B (pp. 109–114) 2015

Intensification of breaking of water-in-oil emulsions by membranes treated in the area of corona discharge or in the plasma flow

V. Dryakhalov[1]*, T. Shaikhiev[1], I. Shaikhiev[1], I. Zagidullina[1], B. Bonev[2], V. Nenov[2]

[1] *Kazan National Research Technological University, 68 Karl Marx Str., Kazan, 420015, Russian Federation*
[2] *Prof. d-r Assen Zlatarov University of Burgas, 1 Prof. Yakim Yakimov Str., Burgas, Bulgaria*

Influence of constant corona discharge high-frequency low-pressure plasma on the surface structure change, adhesion characteristics and internal structure of polyacrylonitrile membranes has been studied. It was demonstrated that the effect of plasma and corona discharge increases productivity and selectivity of breaking of model "I-20A" brand industrial oil based water-in-oil emulsion.

Key words: plasma, corona discharge, polyacrylonitrile membranes, effect, surface structure change, water-in-oil emulsion, intensification of breaking

INTRODUCTION

Pollutants of various qualitative and quantitative composition are generated because of industrial activities - from low hazard ones to superecotoxicants. Water pollution holds a special place in this problem, since water plays a crucial role in many processes in nature and in ensuring the normal human life and activities. Water pollution by anthropogenic components leads to degradation of the biosphere. Oil contaminated wastewater takes on enormous importance in this problem. Oftentimes those discharges constitute aggregative "water-in-oil" type slow-breaking emulsions.

Membrane breaking methods [1, 2], ultrafiltration in particular, have been currently used for cleaning oil-in-water emulsions. The main advantages of this method are high efficiency, absence of chemicals used, as well as a small area occupied by the equipment.

The disadvantage of using membranes is pollutant particles concentration polarization on the surface resulting in reduced productivity to a complete process shutdown. In order to prevent the abovementioned phenomena, treatment of polyacrylonitrile (PAN) membranes with cut off particle mass of 25 kDa has been performed, particularly in the low-pressure capacitive high-frequency plasma or the area of constant corona discharge, to intensify the breaking of water-in-oil emulsions [3–6].

* To whom all correspondence should be sent:
vladisloved@mail.ru

MATERIALS AND METHODS

Corona discharge exposure was carried out under the following conditions: treatment time (τ) – 0.5, 1.5 or 1 minute; electrode polarization voltage (U_{pol}) – 5, 10, 15 kV. Low-pressure plasma treatment was performed in the argon/nitrogen (70 : 30) and argon/air (70 : 30) gas environments with the following parameters variability: plasma exposure time (τ) – 1.5, 4, or 7 minutes; plasma torch anode voltage (U_a) – 1.5, 3.5, 5.5 or 7.5 kV. Constant plasma treatment parameters are as follows: plasma torch anode current rate (I_a) – 0.5 A, gas mixture flow rate (G) – 0.04 g/s, work chamber pressure (P) – 26.6 Pa.

Research on the internal and surface structure of the initial and modified filter elements used has been conducted in order to detect physical and chemical laws of corona and plasma effects on the membranes being studied.

Determination of the topography and microimages of the initial and modified membranes was performed with a scanning electron microscope "Multi-Mode V" company "VEECO". When scanning apply rectangular cantilevers "RTESP" with silicone probe. The resonant frequency of the cantilevers – 200–300 kHz, the tip curvature radius – 10–14 nm. Images with a resolution of 256×256 pixels per frame were produced at a scan rate of 1 Hz. In this case, the scanner "8279JV" used to scan the largest field. In order to eliminate errors caused by vibration of the microscope under the influence of external noise, anti-vibration system "SG0508" is used for smoothing fluctuations in the frequency of 0.5 Hz.

© 2015 Bulgarian Academy of Sciences, Union of Chemists in Bulgaria

RESULTS AND DISCUSSION

The analisys of the images shown in Fig. 1 has revealed the presence of the modified membrave surface changes (Fig. 1b-d) as against the baseline one (see Fig. 1a).

The histograms shown in Fig. 1 represent the distribution graph of projections on the membrane surface, wherein the projection height is located along the horizontal axis in nm, and the relative number of the latter with the height value data is located along the vertical axis.

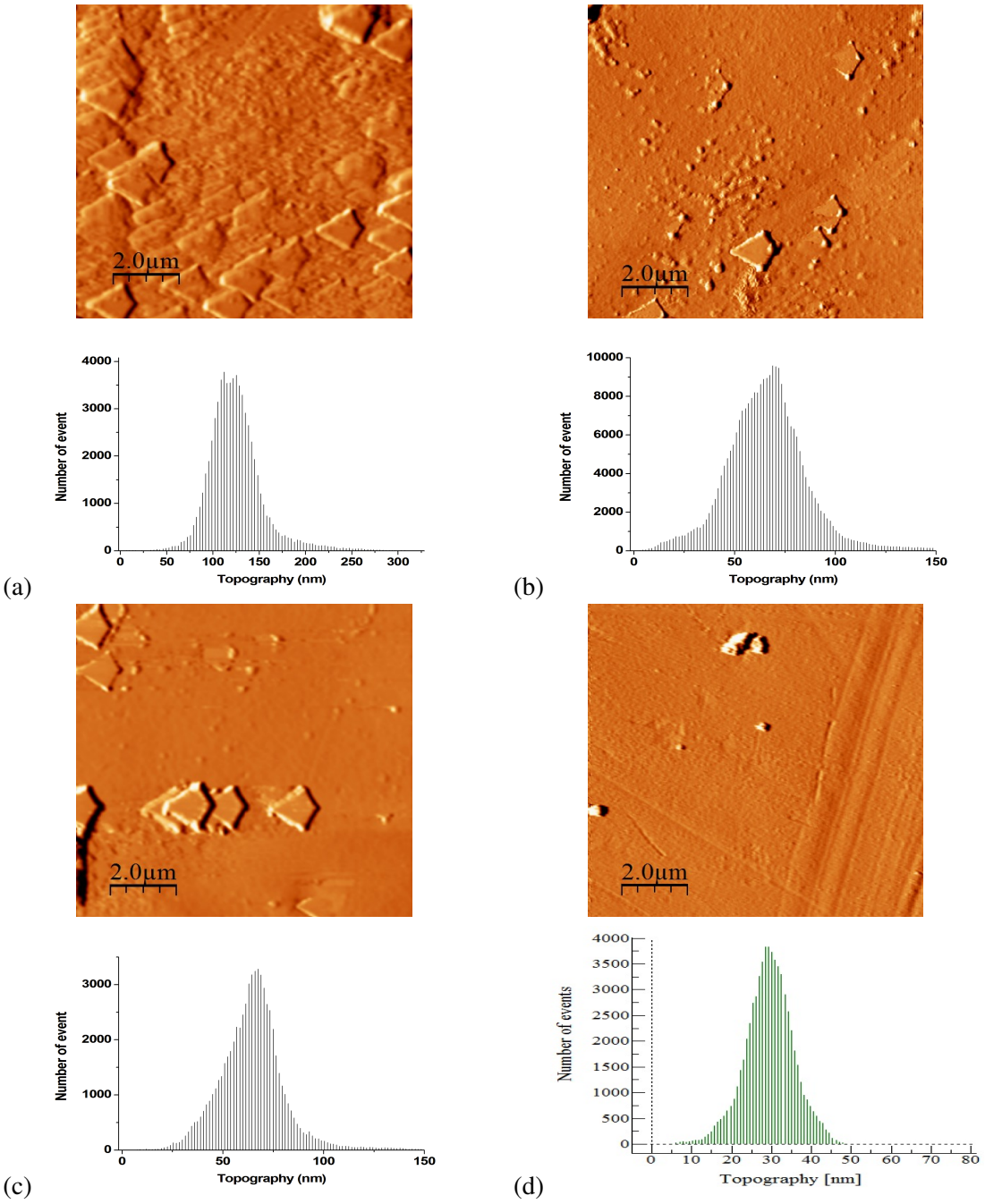


Fig. 1. Photographs of the surfaces and the corresponding histograms of projections on the surface of membranes: a) initial; b) treated in the argon/nitrogen environment at $U_a = 5.5$ kV, $\tau = 4$ min; c) treated in the argon/air environment at $U_a = 5.5$ kV, $\tau = 4$ min; d) treated in the area of corona discharge at $U_{pol} = 10$ kV, $\tau = 1$ min.

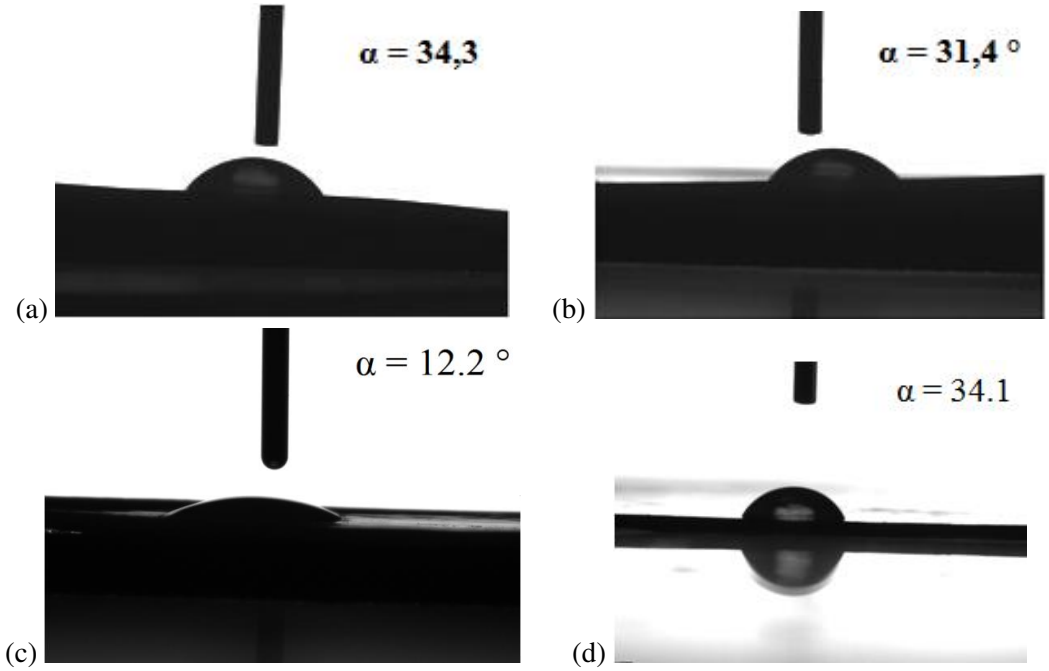


Fig. 2. Images of membrane surface contact angle through distilled water drop: a) unmodified; b) treated in the argon/nitrogen environment at $U_a = 5.5$ kV, $\tau = 4$ min; c) treated in the argon/air environment at $U_a = 5.5$ kV, $\tau = 4$ min; d) treated in the area of corona discharge at $U_{Pol} = 10$ kV, $\tau = 1$ min.

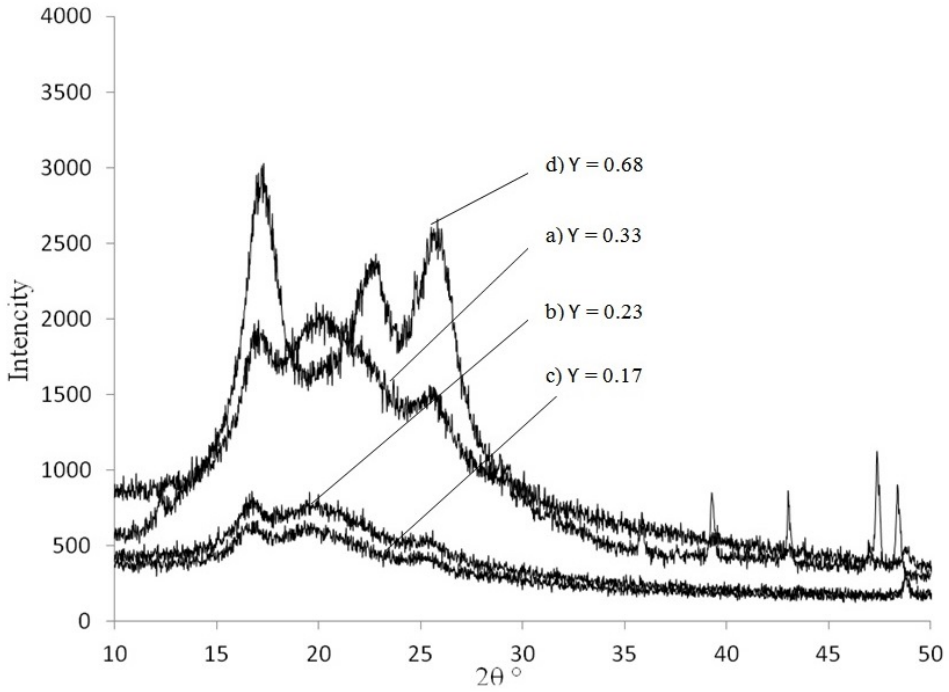


Fig. 3. X-ray diffraction patterns of PAN membranes: a) unmodified; b) treated in the argon/nitrogen environment at $U_a = 5.5$ kV, $\tau = 4$ min; c) treated in the argon/air environment at $U_a = 5.5$ kV, $\tau = 4$ min; d) treated in the area of corona discharge at $U_{Pol} = 10$ kV, $\tau = 1$ min.

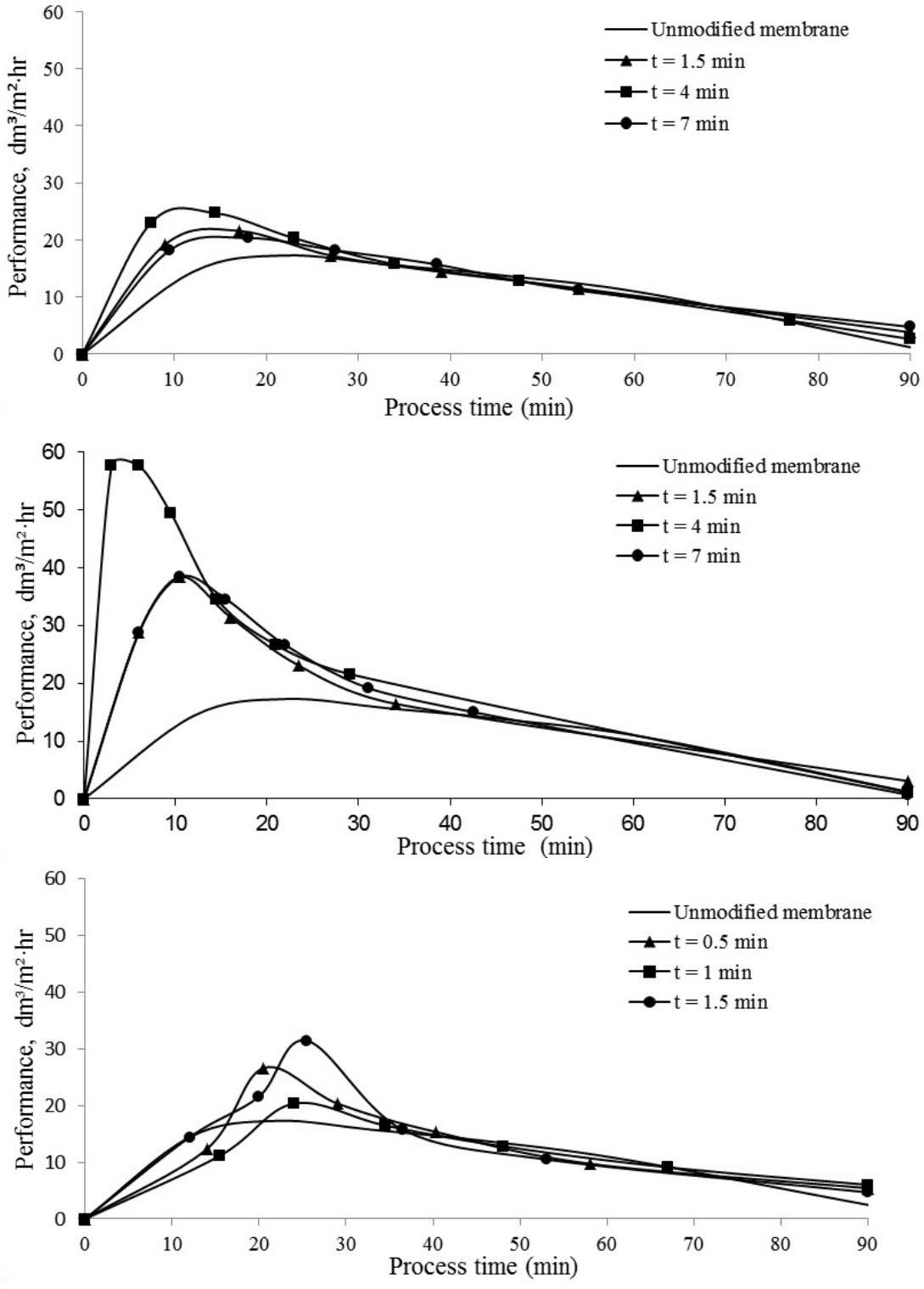


Fig. 4. Productivity of breaking of emulsion by PAN membranes with transmitted particle mass of 25 kDa treated in a plasma flow at $U_a = 5.5$ kV in a gaseous environment: a) argon and nitrogen; b) argon and air; c) treated in the area of corona discharge at $U_{Pol} = 10$ kV.

Capacitive high-frequency plasma effect leads to a decrease in bumps height on the surface of PAN filter elements. Most of the projections on the surface of the unmodified membrane have a size of 120–125 nm, while most of the projections on the surface of the membranes treated with plasma and corona discharge has a size of 65–70 and 30 nm, respectively.

The aforementioned event is a consequence of bombing of projecting membrane fragments with negatively charged ions formed during plasma treatment and filter element surface smoothing. Corona discharge causes the formation of ozone, which oxidizes the projecting fragments of the membrane polymer matrix.

It is known from literature references [7] that the most important result of the influence/effect of low-temperature plasma on polymeric materials in practical terms is the change of their adhesion characteristics. Under the influence of plasma, polymer surface may become both more hydrophilic and more hydrophobic; however, there is no such information available concerning the treatment in the area of corona discharge.

The Fig. 2 shows images of a distilled water drop on the surface of the initial and modified membranes, as well as the contact angle values.

Value of contact angle through distilled water drop for the initial membrane was $\alpha = 34.3^\circ$ (Fig. 2a). Effect of plasma produced in the argon/nitrogen environment reduces the parameter under consideration to $\alpha = 31.4^\circ$, and to a value of $\alpha = 12.2^\circ$ in the argon/air environment, i.e. polyacrylonitrile surface becomes more hydrophilic (Fig. 2b and Fig. 2c). Treatment of the membrane in the constant corona discharge does not contribute to significant change in the indicator; contact angle value decreases slightly to a value of $\alpha = 34.1^\circ$ (Fig. 2d).

It is known from literature references [8] about interdependence of wettability parameters and the degree of polymer crystallinity. Fig. 3 shows X-ray diffraction patterns of the initial and plasma-treated membrane with the corresponding crystallinity degree values.

The analysis of the data presented in Fig. 3 has identified dependences similar to those identified in the study of the contact angle: plasma treatment of PAN membranes in hydrophilic mode leads to reduction in the degree of crystallinity. It was determined that the minimum value of the parameter under consideration had been achieved by exposure to the plasma formed in a mixture of argon and air ($\Upsilon = 0.17$). At the same time, treatment in the area of corona discharge also increases the degree of crystallinity of the membrane. This fact suggests some degree of correlation between the wettability parameters and the degree of crystallinity, which makes it further possible to modify PAN membranes in order to achieve the desired properties.

Thus, a more hydrophilic membrane exhibits greater selectivity for water molecules promoting more intense passage of the latter through the membrane and rejection of non-polar hydrocarbon molecules that make up the oil. This fact helps to increase productivity (Fig. 4) and selectivity of breaking of filtrate emulsions obtained using filter elements treated in the plasma flow.

It is clear that plasma treatment of membranes in the flow of argon and air for 4 minutes increases the productivity during the initial period of filtration more than 3-fold compared to the initial membrane.

When using the membranes treated in the area of corona discharge, there is less effect of productivity in comparison with the filter elements exposed to the plasma (Fig. 4c). Nevertheless, corona treatment for 1.5 min at $U_{\text{Pol}} = 10$ kV improves productivity in the 25th minute of the process by more than 1.7 times compared to the initial sample of the membrane.

CONCLUSION

Thus, the research conducted has identified that the influence/effect of high-frequency low-pressure plasma and constant corona discharge contributes to changes in the internal and surface characteristics of PAN membranes thus allowing intensifying the process of breaking of water-in-oil emulsions.

REFERENCES

[1] K. R. Kull, M. L. Steen and E. R. Fisher, *J. Membrane Sci.* **2**, 203-215 (2005).

[2] N. Drouiche, M. W. Naceur, H. Boutoumi, N. Aitmessaoudene, R. Henniche and T. Ouslimane, *Desalination and water treatment* **4-6**, 713–716 (2013).

[3] E. Finot, S. Roualdes, M. Kirchner, V. Rouessac, R. Berjoin, J. Durand, J. P. Goudonnet and L. Cot, *Appl. Surf. Sci.* **3-4**, 326–338 (2002).

[4] P. Wanichapichart, R. Sungkum, W. Taweepreda and M. Nisoa, *Surf. Coat. Tech.* **17-18**, 2531–2535 (2009).

[5] E. G. Sessler, *Electrets*, Springer, Berlin, 1987.

[6] V. N. Kestelman, L. S. Pinchuk and V. A. Goldade, *Electrets in Engineering: Fundamentals and Applications*, Kluwer Acad. Publ., Boston-Dordrecht-London, 2000.

[7] A. Gilman, M. Piskarev, N. Shmarkova, M. Yablokov and A. Kuznetsov, *Mater. Sci. Forum* **636**, 1019–1023 (2010).

[8] G. L. Slonimsky, *Modern Physical Methods of Research of Polymer*, Chemistry Publication, Moscow, 1982.

ИНТЕНЗИФИКАЦИЯ НА РАЗРУШАВАНЕТО НА ЕМУЛСИИ ВОДА-В-МАСЛО ПОСРЕДСТВОМ МЕМБРАНИ, ТРЕТИРАНИ В КОРОНЕН РАЗРЯД ИЛИ В ПЛАЗМЕН ПОТОК

В. Дряхлов[1], Т. Шайхиев[1], И. Шайхиев[1], И. Загидулина[1], Б. Бонев[2], В. Ненов[2]

[1] *Казански национален изследователски технологичен университет, ул. "Карл Маркс" 68, Казан, 420015, Руска Федерация*

[2] *Университет "Проф. д-р Асен Златаров", ул. "Проф. Яким Якимов" 1, Бургас, България*

(Резюме)

Емулсиите вода-в-масло (ЕВМ) се образуват в целия свят в резултат на преработката на нефт и използването на петролни продукти в предприятията от химическата и нефтохимическата промишленост и са в размер на повече милиона тона годишно. ЕВМ образуват агресивна, стабилна, многокомпонентна структура, която съдържа повърхностно активни вещества (ПАВ) и различни емулгатори, като соли, асфалтен, смоли, разтворими в масло органични киселини и незначителни количества тиня и глина.

В последно време за разрушаване на ЕВМ се използва методът на ултрафилтрация. Сред основните предимства на този метод са: висока ефективност, липса на реактиви, малка площ за оборудване, енергийна ефективност и възможност за организиране на затворен воден цикъл. Недостатък на мембранния метод е замърсяването на повърхността на мембраната с дисперсната фаза на замърсителя. В резултат се наблюдава забавен процес на разделяне.

С оглед на споменатото по-горе, високо-енергетичното третиране на мембраните, главно чрез коронен разряд, или в поток на нискотемпературна високо-честотна плазма при ниско налягане, е перспективенв инженерни и екологични аспекти метод заинтензификация на ултрафилтрацията на ЕВМ.

В настоящата работа са представени експерименталните резултати при разрушаване на моделна ЕВМ чрез мембрана от полиакрилонитрил(PAN) с разделяне по молекулна маса (MWCO) 25 kDa. Така филтрираните частици бяха третирани в коронен разряд или в плазмен поток. Третирането в коронен разряд беше осъществено при следните условия: времетраене (τ): 0.5, 1, 1.5 min, напрежение на електрода (U): 5, 10, 15 kV; третирането в плазма беше извършено в газова среда (аргон и азот, аргон и въздух) за време (τ): 1.5, 4, 7 min и анодно напрежение (U): 1.5, 3.5, 5.5 и 7.5 kV.

За основни параметри при мембранното разделяне на емулсията се считат продуктивността и ефективността. Първият фактор е отношението на преминалия през мембраната поток от разделяната среда към произведението от продължителността на процеса и площта на филтриращия елемент, който в този случай е 1.73×10^{-3} m^2. Ефективността се определя от промяната на стойностите на химическа потребност от кислород (ХПК) преди и след процеса на разделяне на емулсията. Този процес е измерван чрез автотитратор "T70" на фирма "MettlerToledo".

Bulgarian Chemical Communications, Volume 47, Special Issue B (pp. 115–120) 2015

Study of polylactic acid corona electrets

A. Guzhova[1*], T. Yovcheva[2], A. Viraneva[2]

[1] *Department of Processing Technology of Polymers and Composite Materials, Kazan National Research Technological University, 68 Karl Marx Str., 420015, Kazan, Russian Federation*
[2] *Faculty of Physics, Paisii Hilendarski University of Plovdiv, 24 Tsar Asen Str., BG-4000 Plovdiv, Bulgaria*

Electret and surface properties of the PLA film treated in a negative or a positive corona discharge at two different temperatures were studied. Vibrating electrode method with compensation was used to measure the electret surface potential value. The changes in the surface free energy were investigated by means of contact angle measurements. The Bickerman's method was applied to determine the polar and dispersion components of the polymer surface free energy, FTIR-spectroscopy was used to analyze the polymer functional groups content. It was found that in all cases the corona treatment increases the polar component of surface free energy of polylactic acid. The effects of negative and positive corona polarities display some specific features which could be associated with different charged group introduced into the film during the corona treatment. The total final effect depends on the simultaneous action of the two competing factors – temperature and corona polarity. The most pronounced effect was observed for high temperature negative corona treatment.

Key words: electret, corona discharge, polylactic acid, surface free energy

INTRODUCTION

Electrets are dielectrics that possess excess or distributed charge and create constant electric field. They have found various applications in different industries. To manufacture electrets synthetic polymers are commonly used [1–3]. However, nowadays there is a demand in new advanced materials for their manufacturing since industrial polymers have long decomposition period resulted in increase of polymer wastes and environmental pollution [4, 5]. One of the solutions is application of biodegradable polymers e.g. polylactic acid (PLA) derived from renewable resources [6, 7].

One of the most popular techniques to produce electrets is polymer polarization in a corona discharge. Its advantages include high process rate and simple instrumentation. During unipolar corona discharge injection of charge carriers (electrons, ions) occurs into dielectric where these charge carriers are held by surface or volume traps.

Therefore, the objective of the paper was to produce film material based on PLA and study its electrets properties.

MATERIALS AND METHODS

The subject of research was L-polylactic acid (PLA) (Direct Corporation Lot # 902-57-1 with density 1.25 g/cm^3 and glass transition temperature 327 K (54°C)).

PLA films were solvent-casted using trichlormethane. The films thickness was about 5-10 μm measured by electronic micrometer Micromaster IP54, TESA SA, Switzerland.

The corona charging of the samples was carried out by the method of the negative and positive corona discharge shown in Figure 1. The distance between the grounded plate electrode and the grid was 10 mm, the distance from the grid to the corona electrode was 7 mm. The samples were divided in two groups.

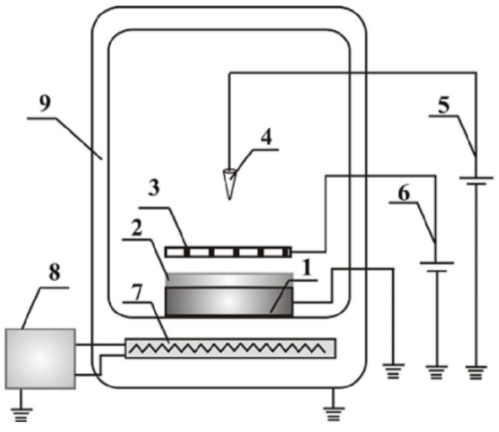


Fig. 1. Experimental set-up for corona treatment: 1 – grounded electrode; 2 – sample; 3 – grid; 4 – corona electrode (needle); 5 – corona electrode power supply; 6 – grid power supply; 7 – heating element; 8 – thermocontrol system; 9 – thermochamber

* To whom all correspondence should be sent:
alina_guzhova@mail.ru

© 2015 Bulgarian Academy of Sciences, Union of Chemists in Bulgaria

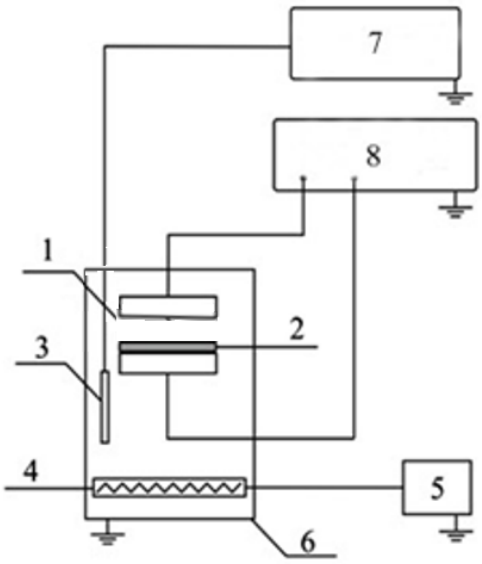


Fig. 2. Thermally stimulated surface potential relaxation measuring unit: 1 – upper vibrating electrode; 2 – sample; 3 – thermal couple; 4 – heating element; 5 – power suply with temperature control; 6 – thermochamber; 7 – digital multimeter; 8 – surface potential meter.

The samples of the first group were placed on the grounded plate electrode and were charged for 3 min at temperature 25ºC. Another group of samples was heated up to 90ºC, charged for 3 min at temperature 90ºC and then cooled to 25ºC in corona discharged for 30 minutes. Positive or negative 5 kV voltage was applied to the corona electrode. 1 kV voltage of the same polarity as that of the corona electrode was applied to the grid.

The surface potential values were measured using a vibrating electrode method with compensation. The estimated error was less than 5%. Thermally stimulated surface potential relaxation was measured by vibrating electrode method at constant heating rate of 1.65 degree/min. Figure 2 illustrates unit for measuring thermally stimulated surface potential relaxation.

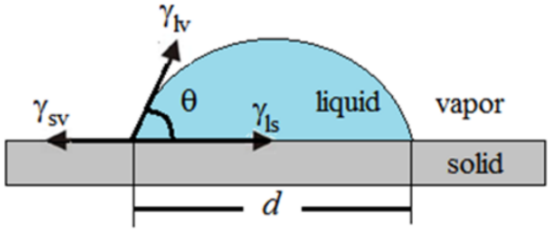


Fig. 3. Scheme of the surface energy: γ_{sv} at solid-vapor interface, γ_{ls} at liquid-solid interface, and γ_{lv} at liquid-vapor interface; θ is the contact angle; d is the drop diameter

Contact angle formation between a liquid drop and solid surface is presented in Fig. 3. The contact angle depends on the energies at the interfaces: solid-liquid (sl), solid-vapor (sv), and liquid-vapor (lv). The symbols γ with two indices describe the surface energy between the two phases in contact.

Following the theory of Owens and Wendt [8], and Kaelble and Uy [9], the surface free energy of a solid, γ_s, can be expressed as a sum of contributions from γ_s^d and "γ_s^p components. Both can be determined from the contact angle data of polar and non-polar liquids with known dispersion, γ_{lv}^d, and polar, γ_{lv}^p, parts of their interfacial energy:

$$\gamma_{lv}(1+\cos\theta) = 2\sqrt{\gamma_s^d \gamma_{lv}^d} + 2\sqrt{\gamma_s^p \gamma_{lv}^p} \qquad (1)$$

where $\gamma_{lv} = \gamma_{lv}^d + \gamma_{lv}^p$.

To measure the contact angle, θ, distilled water and diiodomethane drops with varying volume were inserted onto the solid PLA film surface, at room temperature, using a precise 10 μl micro syringe (Innovative Labor System GmbH, Germany) supplied with steel needle. The drop volume was from 2 μl to 6 μl. The drop diameters were measured with optical microscope (MBC-9, USSR) provided with a micrometer scale eyepiece (Fig. 4). For each drop volume, and each testing liquid, 5 measurements were performed at different places onto the sample surface. The same procedure was repeated with six different samples. The final value of the contact angle is the mean value of the six samples measurements. The estimated error was less than 5%.

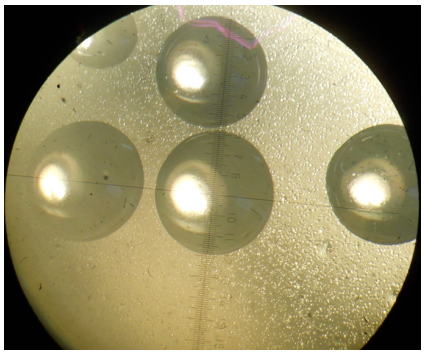


Fig. 4. Microscope drop image.

Bickerman's method [10, 11], in which the effect of gravity distortion is negligible and the drop may be considered as a segment of a sphere, was applied to derive the contact angle:

$$\frac{d^3}{V} = \frac{24\sin^3\theta}{\pi(2-3\cos\theta+\cos^3\theta)} \qquad (2)$$

where V is the drop volume, and d is the drop diameter.

RESULTS AND DISCUSSION

Charge behavior of PLA-based electrets produced at various polarization conditions is shown in Fig. 5.

Electrets properties depend on quantity of injected charges penetrating into the material during polarization in corona discharge and fixed to different energy traps. Initial sharp decay of the surface potential curve occurs due to escape of injected charge from small surface energy traps. Then charge stabilizes and surface potential changes slightly. Charge value in this case is determined by injected charge carriers captured by volume traps. Therefore, polylactic acid polar groups promote trapping of injected charge carriers by small surface energy traps resulting in rapid charge decay of corona electrets.

Differences in electret properties of negative- and positive-charged films are due to different nature of injected charge carriers that are formed during air ionization. According to [3], if positive corona occurs in air, the prevailing ions are of the type $(H_2O)_nH$ and n enhances with increasing relative humidity. In the case of low relative humidity values, the $(H_2O)_nNO^+$ and $(H_2O)_n(NO2)^+$ groups are dominant. If negative corona occurs in air, the most important ions are the CO_3^- ions, while at 50% relative humidity, 10% of all ions are of the type $(H_2O)_nCO_3^-$. In case of polar PLA films the most stable values of surface potential were observed for negatively charged electrets.

One can see (Fig. 5) that PLA electrets charged in negative corona discharge at 90°C performed the most stable surface potential values. At other polarization conditions, significant charge relaxation occurs in as little as 5 hours after polarization.

Higher surface potential values of the PLA corona electrets charged at 90°C compared to ones charged at room temperature were expected since initial heating is known [1,12] to enhance electrets stability. The reason for this is that charge carriers penetrate deeper into the bulk of a polymer due to greater chain mobility leading to increased electric conductivity.

More information on corona electret charge stability was obtained by the method of thermally stimulated surface potential relaxation. It includes measuring electrets surface potential during linear heating right after polarization. Figure 6 shows thermally stimulated surface potential relaxation curves for the samples positively and negatively charged at room temperature.

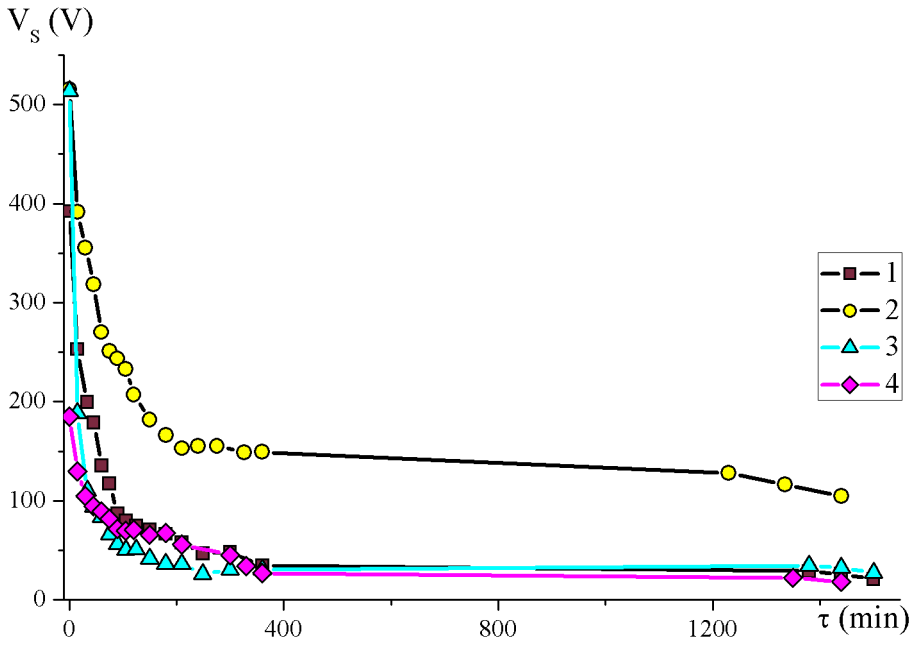


Fig. 5. Surface potential of PLA films vs. storage time: 1 – negatively charged at 25°C, 2 – negatively charged at 90°C, 3 – positively charged at 25°C, 4 – positively charged at 90°C.

Heating above 25°C was shown to cause sharp surface potential decay. Complete relaxation occurred at 50°C. Almost identical curves of surface charge decay in negative- and positive-charged PLA films indicate similar charge carrier trap nature. Complete charge relaxation temperature in PLA is close to its glass transition temperature (50–55°C). It means that dipoles in PLA macromolecules act as charge traps. Rise in temperature above this point enables polymer dipole group to move freely resulting in disappearance of dipole-group or dipole-segment polarization. It is reported in [13, 14] that electrets effect in corona electrets based on polar polymers is caused by both external (injected charge) and internal (dipole-group) polarizations. Therefore, above PLA glass transition temperature ordered dipole system breaks down and injected charge escapes i.e. electrets state relaxation occurs (Fig. 6). Thus, it is inefficient to produce electrets based on pure PLA. To enhance stability and values of electret performances different modifications may be used, e.g., fine filler addition [13, 15, 16].

Surface properties are ones of the most important application performances of any polymer film (including electret). Distilled water and diiodomethane contact angles on PLA films and calculated data on surface energy and its dispersion and polar components are given in Table 1.

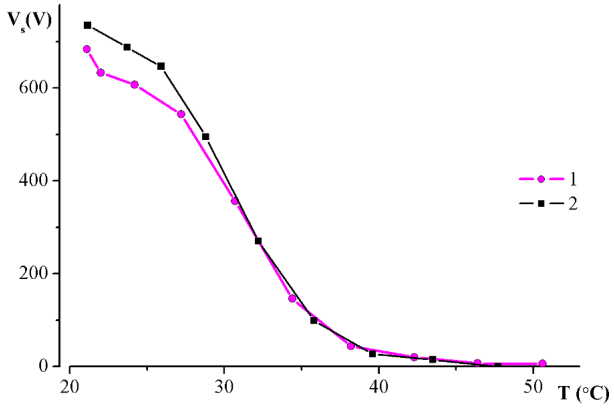


Fig. 6. Surface potential vs. Temperature for PLA electrets films negatively (1) and positively (2) charged when uniform heated at the rate of 1,65°?/min.

Polarization at room temperature increases polar and decreases dispersion component of the surface energy regardless of corona polarity (Fig. 3). It occurs due to formation of different oxygen containing groups on a polymer surface that contribute to surface energy polar component of the PLA films.

Temperature rise results in surface free energy increase of uncharged samples due to surface oxidation leading to increase in the amount of polar groups on the film surface. Meanwhile, surface free energy of electret samples reduces while the number of polar groups is grater compared to uncharged ones.

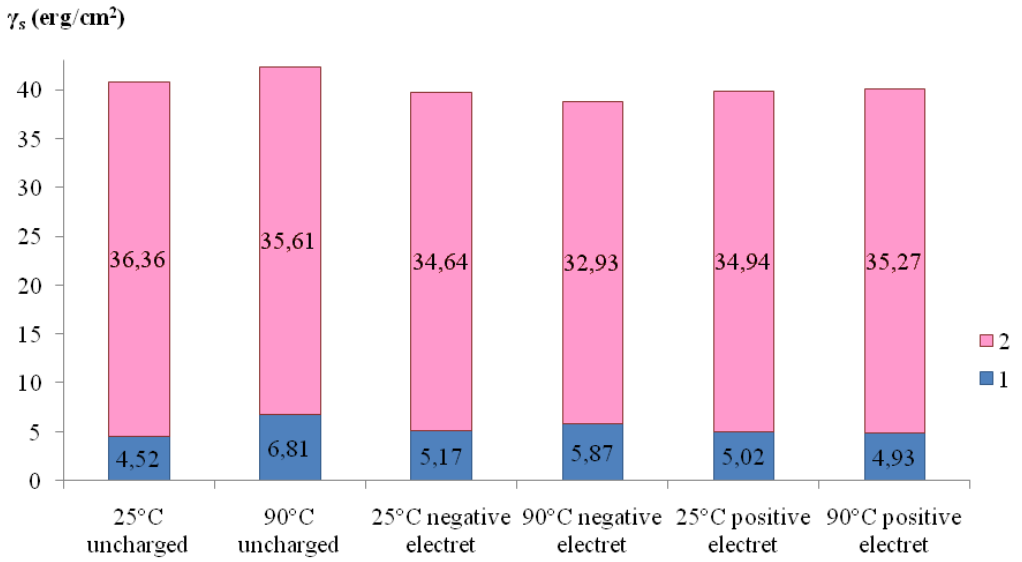


Fig. 7. Total surface energy of uncharged and electrets PLA films: 1 – polar component γ_s^p, erg/cm^2; 2 – dispersion component γ_s^d, erg/cm^2.

Table 1. PLA film surface properties

Film charge	T, °C	γ_s, erg/cm^2	γ_s^p, erg/cm^2	γ_s^d, erg/cm^2	Polarity	θ_{H_2O}	$\theta_{CH_2J_2}$
Uncharged	25	40.89	4.52	36.36	0.11	79,0° ± 0,6°	40,0° ± 0,6°
Uncharged	90	42.42	6.81	35.61	0.16	73,9° ± 0,3°	39,6° ± 1,3°
Negative	25	39.81	5.17	34.64	0.13	78,4° ± 0,6°	42,9° ± 0,8°
Negative	90	38.79	5.87	32.93	0.15	77,8° ± 1,0°	45,7° ± 0,6°
Positive	25	39.95	5.02	34.94	0.13	78,6° ± 0,7°	42,5° ± 0,4°
Positive	90	40.20	4.93	35.27	0.12	80,7° ± 0,7°	41,3° ± 1,3°

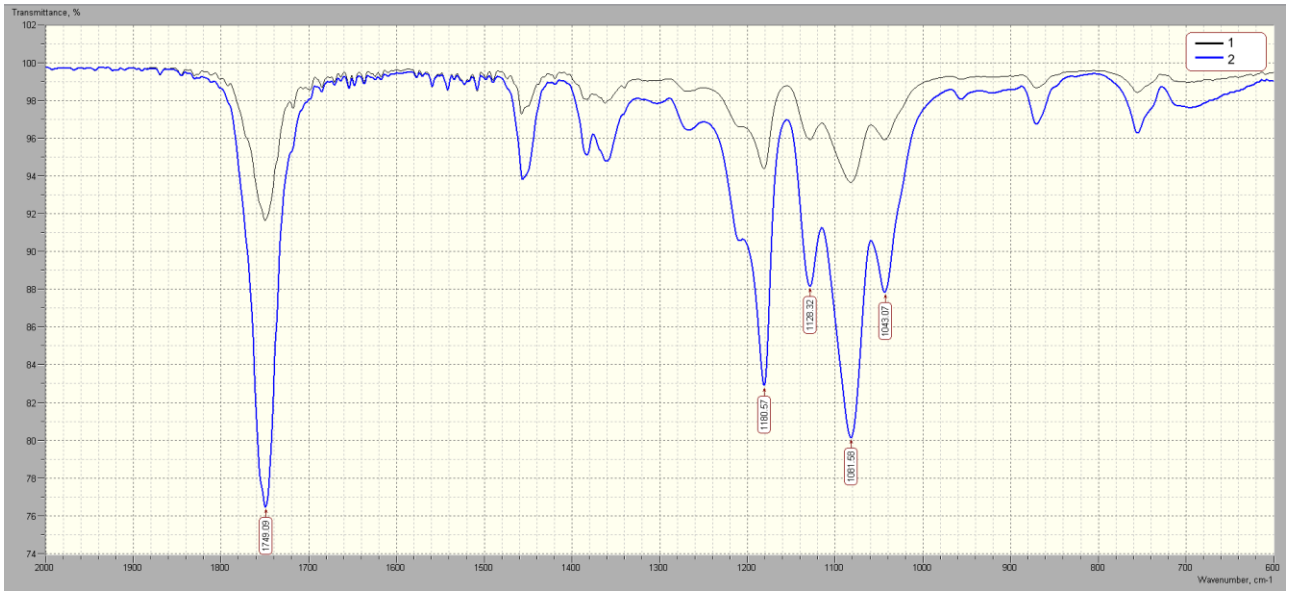


Fig. 8. Surface potential vs. Temperature for PLA electrets films negatively (1) and positively (2) charged when uniform heated at the rate of 1.65°C/min.

It is evidenced by transmittance peak intensity of the IR-spectra (Fig. 8) at 1749 cm $^{-1}$ corresponding to C=O stretch vibrations and at the range of 1200–1050 cm $^{-1}$ corresponding to C-C(O)-C stretching vibrations. It can be explained by the presence of the electrets surface charge that prevents drop spreading on the surface and thereby increasing contact angle.

CONCLUSIONS

Thus, optimal parameters to manufacture PLA electrets are negative corona discharge and initial heating at 90°C Injected charge carrier traps were shown to be dipole groups of PLA macromolecules oriented in corona discharge. When PLA electret sample is heated above glass transition temperature (about 50-55°C) complete charge relaxation occurs. Polarization at room temperature increases polar and decreases dispersion component of the surface free energy.

REFERENCES

[1] G. Sessler, *Electrets*, Berlin: Springer, 1987, pp. 1–215.

[2] V. N. Kestelman, L. S. Pinchuk and V. A. Goldade, *Electrets in Engineering: Fundamentals and Applications* Boston-Dordrecht-London: Kluwer Acad. Publ., 2000, pp. 13–33.

[3] T. Yovcheva, *Corona charging of synthetic polymer films*, New York: Nova Science Publishers Inc, 2010, pp. 5–8.

[4] *Marine Pollution and Human Health* edited by R. E. Hester and R. M. Harrison, Royal Society of Chemistry, 2011, pp. 84–85.

[5] R. C. Thompson, C. J. Moore, F. S. Vom Saal and S. H. Swan, *Phil. Trans. R. Soc. B 27*, **364**, 1526, pp. 2153–2166 (2009).

[6] Tsutomu Ohkita and Seung-Hwan Lee, *Journal of Applied Polymer Science*, **100**, 4, pp. 3009–3017, (2006).

[7] V. A. Fomin and V. V. Guzeev, *Plast.massy*, 2, pp. 42–46 (2001).

[8] D. K. Owens and R. C. Wendt, *J. Appl. Polym. Sci.*, 13, pp. 1741–1747 (1969).

[9] D. H. Kaelble and K. C. Uy, *J. Adhesion*, 2, pp. 50–60 (1970).

[10] S. Kitova, M. Minchev, and G. Danev, *J. Optoelectron. Adv. M.*, 7, pp. 249–252 (2005).

[11] R. E. Johnson and R. H. Dettre Jr., "Wettability and Contact Angles" in *Surface and Colloid Science*, ed. E Matijevic, **2**, New York: Wiley-Interscience, 1969 pp. 85–153.

[12] M. F. Galikhanov and L. A. Budarina, *Plast. Massy*, 1, pp. 40–42 (2002).

[13] M. F. Galikhanov, V. A. Goldade and R. Ya. Deberdeev, *Polymer Science, Ser. A*, **47**, 2, pp. 134–138 (2005).

[14] Y. A. Gorokhovatsky, D. A. Rychkov and N. A. Chepurnaya *Proceedings of the X International conference "Physics of Dielectrics"*, Herzen State Pedagogical University of Russia, Saint Petersburg, 2004 pp. 283—285.

[15] A. Viraneva, T. Yovcheva, I. Bodurov and M. Galikhanov, *Bulgarian Chemical Communications* , **45**, Special Issue B, pp. 73–76 (2013)

[16] A. A. Guzhova, D. E. Temnov, M. F. Galikhanov and Y. A. Gorokhovatsky, *Herald of Kazan Technological University* ,**16**, 3, pp. 73–75 (2013).

ИЗСЛЕДВАНЕ НА КОРОНОЕЛЕКТРЕТИ ОТ ПОЛИМЛЕЧНА КИСЕЛИНА

А. Гуджова[1], Т. Йовчева[2], А. Виранева[2]

[1] *Казански национален изследователски технически университет, ул. "Карл Маркс" 68, Казан, 420015, Руска Федерация*

[2] *Пловдивски университет "Паисий Хилендарски", ул. "Цар Асен" №24, Пловдив 4000, България*

(Резюме)

Получаването на електрети на основата на полимлечна киселина привлича научния интерес, т.к. заменя синтетичните полимери, произведени от невъзобновяеми въглеводороди и оставя биоразграждащи се отпадъци без екологични вреди.

Изследвана е полимлечна киселина (ПМК) (Direct Corporation Lot #: 902-57-1). Филми с дебелина 10 μm са получени чрез изливане на 5% разтвор на ПМК в трихлорметан. Образците са зареждани в положителна и отрицателна корона с помощта на триелектродна система. Разстоянието между заземения електрод и решетката е 10 mm, а разстоянието между решетката и корониращия електрод е 7 mm. Част от образците се поставят на плоския заземен електрод и се зареждат 1 мин. Друга група образци се нагряват до 90°C, включва се полето на коронния разряд за 5 мин. и след това образците се охлаждат линейно в електричното поле за 30 мин. Положително или отрицателно напрежение 5 kV се подава на корониращия електрод. Напрежение 1 kV със същата полярност като на корониращия електрод се подава на решетката. Повърхностният потенциал на електретите се измерва по метода на вибриращия електрод с компенсация. Термично стимулираната релаксация на повърхностния потенциал се измерва по същия метод на вибриращия електрод при постоянна скорост на нагряване 1.65°/min.

Най-стабилен повърхностен потенциал е установен за филми от ПМК, отрицателно заредени при 90°C. При другите условия на зареждане е наблюдавана значителна релаксация на заряда за по-малко от 5 часа след поляризацията.

Електретните свойства на отрицателно и положително заредените филми се дължат на различния характер на инжектираните йони, които се образуват по време на коронния разряд. Съгласно [1], при положителна корона във въздух преобладаващите йони са от типа $(H_2O)_nH^+$ и n се увеличава с увеличаване на относителната влажност. При ниска относителната влажност групите $(H_2O)_nNO^+$ и $(H_2O)_n(NO_2)^+$ са доминиращи. При отрицателна корона във въздух най-важните йони са CO_3^-, а при 50% относителна влажност, 10% от всички йони са $(H_2O)_nCO_3^-$.

Повече информация за стабилността на електретния заряд е получена чрез метода на термично стимулираната релаксация на повърхностния потенциал. Установено беше, че нагряването над 25°C причинява рязко спадане на повърхностния потенциал, като пълна релаксация настъпва при 50°C. Наблюдаваните идентични експериментални криви за отрицателно и положително заредените филми от ПМК показват наличие на подобни носители на заряд, захванати в различни енергетични уловки. Температурата на пълна релаксация на заряда в ПМК е близка до температурата на встъкляване (50–55)°C. Това означава, че диполите в ПМК макромолекулите действат като захванати в уловки заряди.

1. Yovcheva T. *Corona charging of synthetic polymer films*. – New York: Nova Science Publishers Inc, 2010.

Bulgarian Chemical Communications, Volume 47, Special Issue B (pp. 121–126) 2015

Electret stability of gamma irradiated PP and PET films

A. Viraneva[1]*, T. Yovcheva[1], K. Krezhov[2], S. Sotirov[1]

[1] *Faculty of Physics, Paisii Hilendarski University of Plovdiv, 24 Tsar Asen Str., BG-4000 Plovdiv, Bulgaria*
[2] *Institute of Nuclear Research and Nuclear Energy, Bulgarian Academy of Sciences, 72 Tsarigradsko Chaussee Blvd., BG-1784 Sofia, Bulgaria*

The influence of the gamma irradiation on electrets stability of the polymer films of polypropylene and poly(ethylene terephtalate) was studied by following the surface potential decay with time and with sample's storage temperature. The electret surface potential was measured by the method of the vibrating electrode with compensation. Polymer film samples were subjected to integral irradiation doses ($\langle E\gamma \rangle = 1.25$ MeV, ^{60}Co source) of 5 kGy and 25 kGy accumulated in air at a dose rate of 0.26 Mrad/h. After irradiation, the samples were charged in a corona discharge by means of a corona triode sistem for 1 minute under room conditions. Positive or negative 5 kV voltage was applied to the corona electrode and 1 kV voltage of the same polarity as that of the corona electrode was applied to the grid. Significant changes in the electret behaviour of the polimer films after gamma irradiation were established. The surface potential dacay depended on factors such as the corona polarity, the type of material and the irradiation dose. At 25 kGy the gamma-irradiation-induced enhancement of the electrets efficiency of the PP films achieved the highest value. The possible mechanisms of surface potential decay responsible for the observed irradiation dependent behaviour are discussed.

Key words: corona discharge, electrets, gamma irradiation, polypropylene, poly (ethylene terephthalate)

INTRODUCTION

Electrets are dielectric materials capable to retain electric charges over a long period of time and to create an external quasistatic electric field. The electret state is an important cross-scientific subject of dielectric physics, material science, sensor engineering, medical and bio-engineering [1–3]. Over the years, a considerable interest in the surface potential decay of corona-charged polymeric materials has been shown. Besides the electret's material and conditions of electret's manufacturing the surface potential decay depends on a number of factors under which the electrets have been stored or used, for example: temperature, humidity, pressure, gamma irradiation etc. [4–6]. The influence of these factors on the charge decay has been studied in order to obtain stable electrets for numerous applications. However, there are only a few publications about the influence of gamma irradiation on the charge decay of polymer electret films. In [7] the gamma irradiation effect (up to 100 kGy) on the electret behaviour of corona charged biobased polymer films of polylactic acid have been investigated. It has been shown by viscometric, DSC, and SEM studies that the degradation process is predominant. As compared to the non-irradiated samples the values of the surface potential of the irradiated samples, independently of the corona polarity and irradiation dose, were higher. In [8] the surface potential decay after dc corona charging of gamma irradiated low density polyethylene (LDPE) has been studied. The irradiation was carried out in air, nitrogen gas and vacuum to investigate the effect of the irradiation environment on the surface potential of LDPE. Significant changes occurred in the surface potential decay characteristics in dependence on irradiation dose. The dynamic behavior of the surface charge of gamma rays irradiated polybutylene naphthalate has been studied in [9] by applying a negative bias voltage between two aluminum plate electrodes. It was established that with the increase of the total dose of gamma irradiation, both the capacity of surface charge and the rate of charge decay decrease. The charge accumulation depends upon the density of localized surface states, which is varied by the radiation induced cross-linking and the degradation reactions of the molecule structure. The decay is caused by the recombination of surface charge with ions of the opposite sign in air. The gamma irradiation effect on the chain segment motion and charge detrapping in polyamide 610 has been investigated by means of thermally stimulated depolarization current in [10]. The gamma irradiation increases the stability of trapped charge in both amorphous phase and interphase, but does not affect the stability of trapped charge in crystalline phase. The effect of 1.25 MeV gamma radiation on the structural properties of pristine and gamma irradiated (0–2000 kGy) poly(ethylene terephthalate) polymer sam-

* To whom all correspondence should be sent:
asia83@abv.bg

© 2015 Bulgarian Academy of Sciences, Union of Chemists in Bulgaria

ples have been analyzed in [11] and certain increase in the crystallinity was observed. Polymeric materials as polypropylene (PP) and poly(ethylene terephthalate) (PET) are widely used for the formation of electrets, because of their important commercial significance, structure and appropriate mechanical and electrical properties [12, 13]. In the literature however, there are no data available for the influence of gamma irradiation on the charge decay of PP and PET electret films. Therefore, we undertook such a study on some polymers. The present paper reports on the influence of low dose gamma irradiation on the stability of electret characteristics of corona charged PP and PET films.

EXPERIMENTAL

Formation of gamma irradiated polymer films

Initially, the 20 μm PP and 40 μm PET films were cleaned in an ultrasonic bath with alcohol for 4 minutes, followed by rinsing with distilled water and drying on filter paper in air at ambient temperature. Samples of 30 mm diameter were cut from the clean films and subjected to gamma irradiation treatment. The irradiations were performed in air by a ^{60}Co source with total doses of 5 kGy and 25 kGy accumulated in a single step at a dose rate of 0.25 kGy/h. It was checked by thermometric control that the sample temperatures during the irradiation did not appreciably increase above room temperature. This was expected because of the low dose rate of the irradiation.

Corona charging and surface potential measurement of the samples

The charging of the samples in a corona discharge was carried out by a conventional corona triode system (Fig. 1), consisting of a corona electrode (needle), a grounded plate electrode and a grid placed between them. The distance between the corona electrode and the grid was 10 mm and the distance between the grid and the grounded plate electrode was 3 mm.

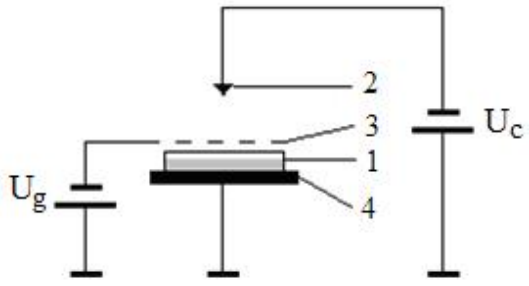


Fig. 1. Corona charging set-up: 1 – sample on a metal pad; 2 – corona electrode; 3 – grid; 4 – grounded plate electrode; U_g – grid voltage power supply; U_c – corona voltage power supply.

The samples of the non-irradiated (0 kGy) and gamma irradiated (5 kGy and 25 kGy) PP and PET films were charged at a room temperature for 1 minute. Positive or negative 5 kV voltage was applied to the corona electrode. Voltage of 1 kV of the same polarity as that of the corona electrode was applied to the grid. The electret's surface potential of the charged samples was measured by the vibrating electrode method with compensation and the estimated error was less than 5%.

RESULTS AND DISCUSSION

Influence of time storage on electrets surface potential decay

The dependences of normalized surface potential on the time of storage under room conditions for positively and negatively charged non-irradiated and gamma irradiated PP and PET films have been followed for 115 days. The surface potential was measured once a week except for the first 30 days because the charge was rapidly decaying. After this period (115 days) steady state values of the surface potential were established for all of the samples.

Time dependences of the normalized surface potential for PP electrets charged in a positive or in a negative corona are presented in Fig. 2 and Fig. 3, respectively. Similar dependences for PET electrets are presented in Fig. 4 and Fig. 5, respectively.

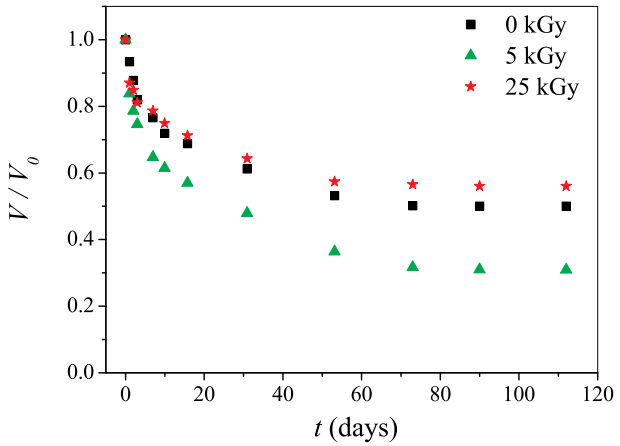


Fig. 2. Time dependences of the normalized surface potential for positively charged non-irradiated and gamma irradiated PP films.

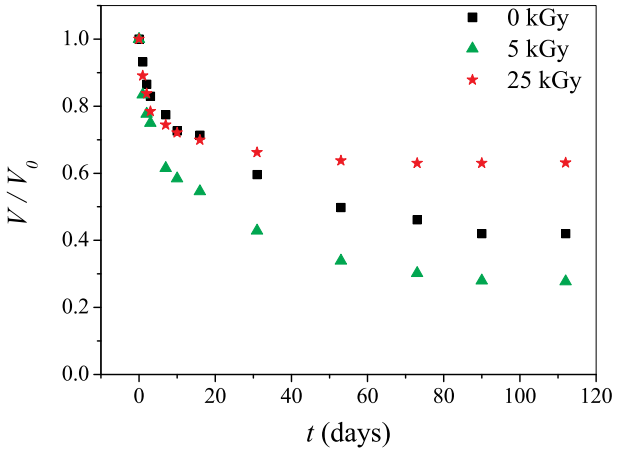


Fig. 3. Time dependences of the normalized surface potential for negatively charged non-irradiated and gamma irradiated PP films.

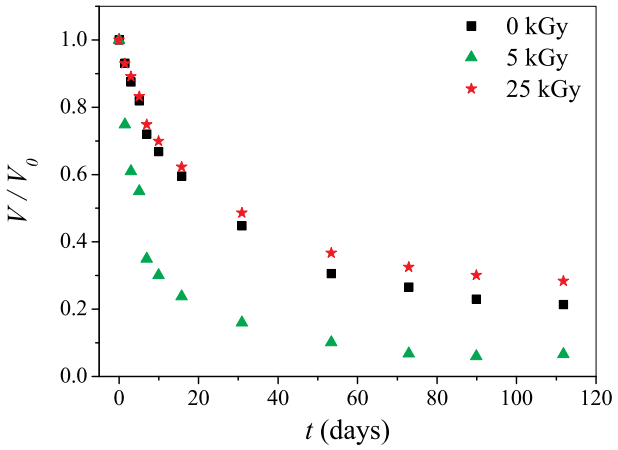


Fig. 4. Time dependences of the normalized surface potential for positively charged non-irradiated and gamma irradiated PET films.

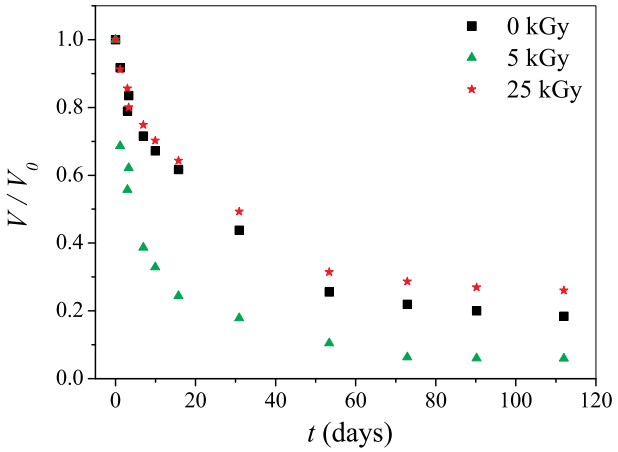


Fig. 5. Time dependences of the normalized surface potential for negatively charged non-irradiated and gamma irradiated PET films.

Each point in the figures is a mean value from 6 samples. The calculated standard deviation was better than 5% from the mean value with confidence level 95%.

The results, presented in Figs. 2-5 show the following peculiarities:

- For all investigated samples the normalized surface potential are initially decaying exponentially for the first 30 days and then are slowly decreasing and are practically stabilized to the 115th day.

The value of the surface potential of electrets depends on the amount of trapped charges in the different localized surface states of the samples. In the initial period of time after the charging in the corona, the surface potential rapidly decreases due to the release of the weakly captured charges from the shallow energy states. Then the surface potential stabilizes to a steady state value caused by the tightly captured charges in the deep energy traps.

- The final values of the normalized surface potential are higher for the PP electrets than those for the PET electrets irrespective of the corona polarity. We assume that this is due to the different structures of the polymers, which leads to the formation of different localized surface states that capture electrical charges.
- The surface potential values of the samples irradiated by dose of 25 kGy, independently of the corona polarity and the type of material were higher in comparison with the non-irradiated samples and the irradiated ones by dose of 5 kGy. The final values of the normalized surface potential for the PP electrets charged in a negative corona and irradiated by dose of 25 kGy are the highest.

Therefore, the gamma irradiation by a greater dose of 25 kGy leads to an increase of the electrets surface potential value and to obtain the stable electrets. When the semicrystalline polymers as PP and PET are exposed to irradiation, the crystalline lamellas may be broken into two or more portions, whereas the long molecular chains of amorphous regions may be broken at different places, leaving a free smaller chains which immediately comes to a stable position by collecting its whole length into regularly arranged lamella form, of course, of smaller size [14]. Probably the low dose of 5 kGy causes changes that have blocked the formation of charge trapping surface state but the increase of dose to 25 kGy leads to a density

increase of the localized surface states and the captured surface charge increase.

Influence of the temperature storage on electrets surface potential decay

The dependences of the normalized surface potential on the temperature for positively and negatively charged non-irradiated and gamma irradiated PP and PET films were investigated. The surface potential measurements were performed by means of the surface potential measurement set-up at elevated temperatured. The surface potential was measured every two minutes for two hours at a constant temperature increase rate – 1.2°C/min. Temperature dependences for the normalized surface potential for PP electrets charged in a positive or in negative corona are presented in Fig. 6 and Fig. 7, respectively. Similar dependences for PET electrets are presented in Fig. 8 and Fig. 9, respectively.

The results presented in Figures 6-9 show that for all investigated samples two relaxation processes are observed.

The first process corresponds to the decay of the normalized surface potential in the range of 22°C to 40°C for positively and negatively charged PP samples and in the range of 22°C to 55°C to positively

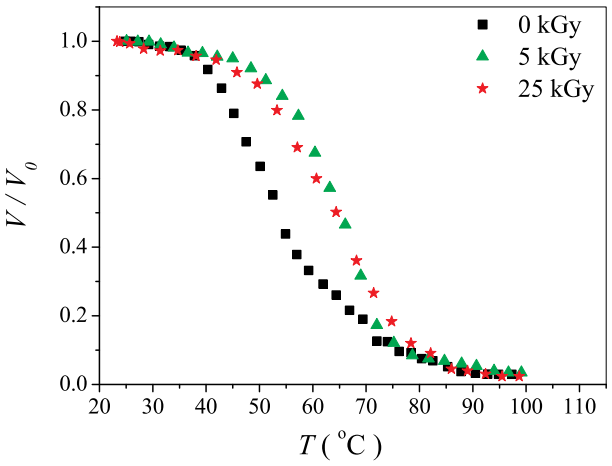


Fig. 6. Temperature surface potential decay curves for positively charged non-irradiated and gamma irradiated PP films.

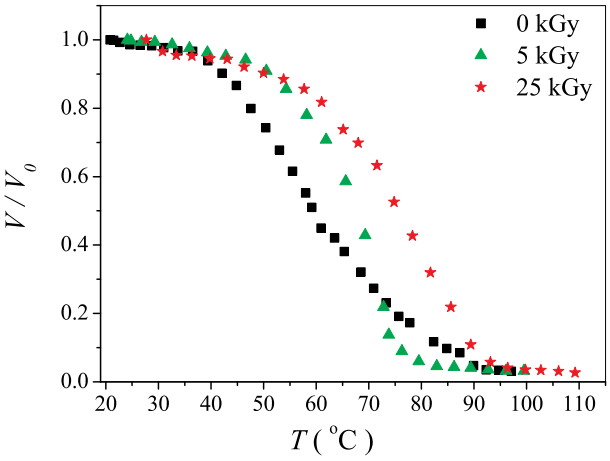


Fig. 7. Temperature surface potential decay curves for negatively charged non-irradiated and gamma irradiated PP films.

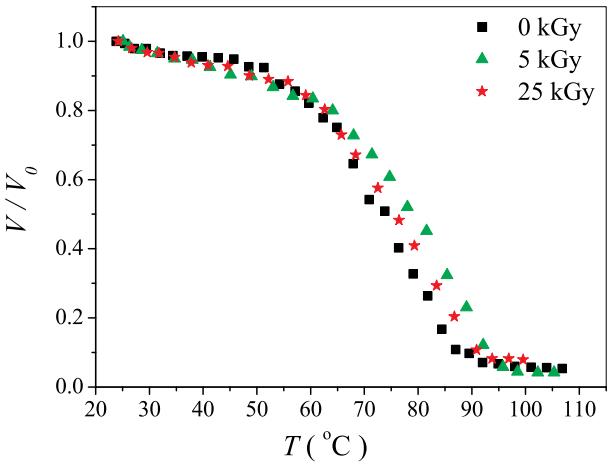


Fig. 8. Temperature surface potential decay curves for positively charged non-irradiated and gamma irradiated PET films.

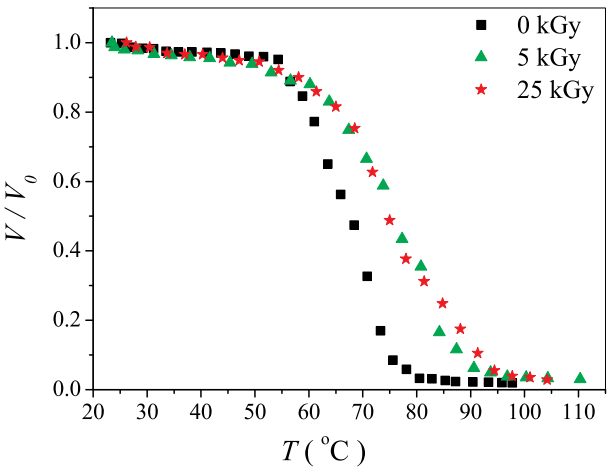


Fig. 9. Temperature surface potential decay curves for negatively charged non-irradiated and gamma irradiated PET films.

and negatively charged PET samples. These is the low energy process, i.e. it was observed at temperatures near room temperatur, and it is most likely due to the release of the weakly captured charges from the shallow energy states.

The second relaxation process depends on the type of material (PP or PET), the corona polarity (positive or negative) and the dose of irratiation (0 kGy, 5 kGy, 25 kGy). In Table 1 the temperature ranges for the second decay of the normalized surface potential are presented.

Table 1. Temperature ranges for the second decay of the normalized surface potential

Materials	Corona polarity	ΔT, °C 0 kGy	5 kGy	25 kGy
PP	positive	43–67	48–75	46–78
PP	negative	44–82	51–74	50–89
PET	positive	54–84	57–92	56–85
PET	negative	57–73	60–87	58–91

It can be seen from the data presented in Table 1 that the second process is observed at higher temperatures. According to our experimental data from DSC measurements with DSC 204 F1 Phoenix NETZSCH, Germany it has been established that there is a release of energy at these temperatures. Hence, we could assume that the charges are released from the deep energy traps and a sharp decrease of the surface potential is observed. The decrease of the normalized surface potential is observed. The decrease of the normalized surface potential is shifted to the higher temperatures for gamma irradiated samples compared to the non-irradiated samples, irrespective of the radiation dose. Consequently, the gamma irradiation of different polymer materials leads to creation of high energy traps. It has been established that the temperatures at which the decrease of the surface potential is shifted are higher for samples of PET, compared to those of PP, irrespectively of the corona polarity. Threfore, the generated charge trapping surface state in PET are more highly energetic than those in PP.

CONCLUSION

The observed significant changes in the electret behaviour of the polymer films induced by gamma irradiation are of complex origin. The surface potential decay depends on several factors. The corona polarity, polymer matrix type and gamma irradiation dose are factors that interplay. The PP electrets charged in a negative corona and irradiated by dose of 25 kGy achieved the highest surface potential. The possible surface potential decay mechanisms responsible for the above may be due to degradation, scissioning and crosslinking of the polymer chains with the increasing dose of gamma irradiation and formation of different charge trapping surface states.

Acknowledgements. *This paper was performed with the financial support of the projects: MU-15-FFIT-003, Department of Scientific Research at the Plovdiv University "Paisii Hilendarski" and BG161PO003-1.2.04-0012-C0001 "Enhancing the capacity of the Plovdiv University for applied research by equipping laboratories for biocompatible materials and molecular biosensors".*

REFERENCES

[1] G. M. Sessler, and R. Gerhard-Multhaupt, *Electrets* 3rd edition, Laplacian Press, Morgan Hill, California (1999).

[2] N. Kestelman, *Electrets in engineering: Fundamentals and applications*, Kluwer Academic Publishers, Massachusetts (2000).

[3] M. Goel, *Current science* **85(4)**, 443–453 (2005).

[4] X. Pei, and Z. Xing-Yuan, *Chin. Phys. B* **23(3)**, 1–53 (2014).

[5] C. Gang-Jin, X. Hui-Ming, and Z. Chun-feng, *Journal of Zhejiang University Science* **5(8)**, 923–927 (2004).

[6] A. Aragoneses, I. Tamayo, A. Lebrato, J. Canadas, J. Diego, D. Arencon, and J. Belana, *Journal of Electrostatics* **71(4)**, 611–617 (2013).

[7] T. Yovcheva, M. Marudova, A. Viraneva, E. Gencheva, N. Balabanov, and G. Mekishev, *Journal of Applied Polymer Science* **128(1)**, 139–144 (2013).

[8] G. Chen, *Journal of Electrostatics* **68**, 487–491 (2010).

[9] B. Du, Y. Gao, *Polymer Degradation and Stability* **94**, 139–141 (2009).

[10] P. Xu, and X. Zhang, *Radiation Physics and Chemistry* **80**, 842–847 (2011).

[11] S. Siddhartha, S. Aarya, K. Dev, S. Kumar Raghuvanshi, J. Krishna, and M. Wahab, *Radiation Physics and Chemistry* **81**, 458–462 (2012).

[12] A. Kilic, E. Shim, B. Yeol Yeom, and B. Pourdeyhimi, *Journal of Electrostatics* **71**, 41–47 (2013).

[13] L. Herous, M. Nemamcha, M. Remadnia, and L. Dascalescu, *Journal of Electrostatics* **67**, 198–202 (2009).

[14] A. Srivastava, and H. Virk, *Radiation Physics and Chemistry* **59(1)**, 31–37 (2000).

ЕЛЕКТРЕТНА СТАБИЛНОСТ НА γ-ОБЛЪЧЕНИ ПОЛИМЕРНИ ФИЛМИ ОТ ПОЛИПРОПИЛЕН И ПОЛИЕТИЛЕНТЕРЕФТАЛАТ

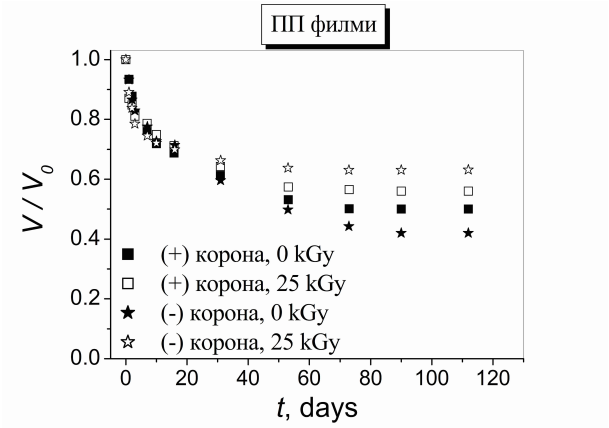
А. Виранева[1], Т. Йовчева[1], К. Крежов[2], С. Сотиров[1]

[1] *Физически факултет, Пловдивски университет "Паисий Хилендарски", ул. "Цар Асен" №24, Пловдив 4000, България*
[2] *Институт за ядрени изследвания и ядрена енергетика, Българска академия на науките, бул. "Цариградско шосе" №72, 1784 София, България*

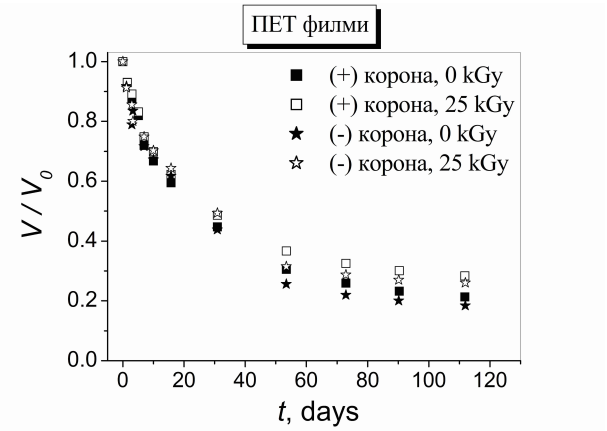
(Резюме)

В настоящата работа е изследвано влиянието на γ-облъчването върху електретната стабилност на полимерни филми от полипропилен (ПП) и полиетилентерефталат (ПЕТ). Първоначално ПП и ПЕТ филмите са облъчвани с кобалтов източник ^{60}Co с различни дози: 0 kGy, 5 kGy и 25 kGy. След това облъчените образци са зареждани в коронен разряд с помощта на триелектродна система в продължение на 1 минута при стайна температура. На корониращия електрод е подавано напрежение ±5 kV, а на решетката напрежение ±1 kV със същата полярност както на корониращия електрод. Повърхностният потенциал на получените електрети е измерван по метода на вибриращия електрод с компенсация.

За определяне на влиянието на γ-облъчването върху стабилността на електретните филми е изследвано спадането на повърхностния потенциал с времето и с температурата на съхранение на образците. Времевите зависимости на нормирания повърхностен потенциал са показани на Фиг. 1 и Фиг. 2.



Фиг. 1. Времеви зависимости на нормирания повърхностен потенциал за необлъчени и γ-облъчени ПП образци.



Фиг. 2. Времеви зависимости на нормирания повърхностен потенциал за необлъчени и γ-облъчени ПЕТ образци.

Получените резултати показаха значително изменение в електретното поведение на полимерните филми след облъчването им с различни дози γ-лъчи. Беше установено, че спадането на повърхностния потенциал зависи комплексно от няколко фактора: полярност на короната, вид на материала и доза на облъчване. В статията са дискутирани механизмите, отговорни за спадането на повърхностния потенциал. Експериментално беше доказано, че γ-облъчването с доза 25 kGy води до увеличаване на електретната ефективност на изследваните филми.

Bulgarian Chemical Communications, Volume 47, Special Issue B (pp. 127–134) 2015

Mechanical properties of composite films based on chitosan and poly(L-lactic acid)

M. Marudova[1]*, E. Delcheva[1], G. Zsivanovits[2]

[1] *Paisii Hilendarski University of Plovdiv, 24 Tsar Asen Str., 4000 Plovdiv, Bulgaria*
[2] *Food Research and Development Institute, Agricultural Academy, 154 Vassil Aprilov Blvd., 4003 Plovdiv, Bulgaria*

Mechanical properties of chitosan/poly(L-lactic acid) (Ch/PLLA) blend films have been studied in the present research. The films were prepared by dissolving different weight fractions of the polymers in a solvent, which is mixture of formic acid and acetone. The films were casted in Teflon petri dishes and dried at temperature 35°C till constant weight was achieved. Mechanical tests are provided at constant deformation rate 0.1 mm/s and room temperature. Based on the force-deformation curve the rupture point, rupture work and modulus of elasticity have been evaluated. The degree of elasticity was determined using a mechanical hysteresis test. Relaxation test has been also done in order to estimate the average relaxation time and the broadness of relaxation time distribution. Based on the mechanical properties just partial technological compatibility between the compounds could be assumed. For further understanding the structure of chitosan/PLLA films thermal and morphological characterization have been done. Based on the results from the Differential scanning calorimetry (DSC) and SEM analysis it was concluded that no miscibility on molecular level between chitosan and PLLA could be achieved in the proposed solvent.

Key words: chitosan, poly(L-lactic acid), mechanical properties, DSC, SEM, compatibility

INTRODUCTION

Nowadays, the use of natural polymers that are biodegradable and biocompatible has become increasingly important. This is due to their characteristics: natural abundance, low costs, and wide range of applications [1, 2]. These polymers are being widely used in the biomedical area, including wound dressing, drug delivery system, and tissue engineering scaffolds [3, 4].

Chitosan (poly-1, 4-D-glucosamine) is a renewable, natural, nontoxic, edible, and biodegradable polymer which is produced by alkaline deacetylation of chitin. It is one of the most abundant polymers that can be found in nature. Owing to its biodegradability and biocompatibility, chitosan is reported to be an active polymer with antimicrobial and antifungal activities [3, 5–8]. It has a potential as a packaging polymer and, more particularly, as an edible packaging or coating because of its ability to form a film without any use of additives [9]. Moreover, chitosan film has good oxygen and carbon dioxide permeability, which is lower than that of polyethylene film [10, 11], and good mechanical properties, which are comparable with those of many medium-strength commercial polymers [12]. Unfortunately, there are some limitations to the application of chitosan film for packaging, because of its high sensitivity to moisture. Perspective way to overcome this drawback is to associate chitosan with a moisture resistant polymer, while maintaining the overall biodegradability of the product.

An interesting candidate to blend with chitosan is polylactic acid (PLA). PLA belongs to the family of aliphatic polyester commonly made from lactic acid, which can produced from renewable resource such as starch via fermentation processes [12]. It is a thermoplastic, high-strength, high modulus polymer and is considered as biodegradable and compostable [13].

Several attempts have been done for blending chitosan and PLA [14, 19]. Unfortunately all of them were unsuccessful and it is difficult to achieve miscibility of these two polymers at micro level. The basic reason for this incompatibility is their very different polarities and high interfacial tension. Normally chitosan can only be dissolved in dilute aqueous acidic solutions and PLLA can be dissolved only in some organic solvents. Even the attempt to mix them in common solvent was unfortunate [20].

The aim of the present study is to investigate the abilities to prepare chitosan polylactic acid casted films using a new two component solvent and to characterize the mechanical properties of the films.

EXPERIMENTAL

Materials

Low molecular weight chitosan (Ch) with degree of deacetylation greater than 75% and viscosity of 20–300 cps (measured for 1% chitosan concentra-

* To whom all correspondence should be sent:
margo@uni-plovdiv.bg

© 2015 Bulgarian Academy of Sciences, Union of Chemists in Bulgaria

tion in 1% acetic acid water solution at 25°C) was purchased from SIGMA ALDRICH and used without further purification or characterization. Poly(L-lactic acid) (PLLA) was purchased from LACTEL ABSORBABLE POLYMERS, USA. It is with ester end groups and intrinsic viscosity 0.9–1.2 dL/g, measured at 25°C in $CHCl_3$. All other chemicals used are with analytical grade.

Sample preparation

Blends of chitosan with PLLA were formed in several steps. Firstly a common solvent, which is a mixture of equal volume parts of formic acid and acetone, and 0.5% relative to the total amount of the solution glycerol, was prepared. Then chitosan (2% by weight) and PLLA (2% by weight) were dissolved separately in the common solvent. Dissolution was performed with a magnetic stirrer at 80°C to provide fully transparent and clear solutions. The two solutions were then blended under vigorous stirring. The final homogeneous solution was poured into Teflon petri dishes and dried at atmospheric pressure and a temperature of 35°C until constant mass. Usually, the drying process was continued about 72 h. After drying the films were stored in a desiccator at room temperature and a relative humidity (RH) of 54%. Ten different series of samples were produced and designated as Ch/PLLA 10:0, Ch/PLLA 9:1, Ch/PLLA 8:2, Ch/PLLA 7:3, Ch/PLLA 6:4, Ch/PLLA 5:5, Ch/PLLA 4:6, Ch/PLLA 3:7, Ch/PLLA 1:9 and Ch/PLLA 0:10, where the numbers represent respectively the weight fraction of Ch and PLLA, in the blends.

The thickness of the dried films was measured by digital micrometer Micromaster IP54, Switzerland with resolution 1 μm. Each sample was measured at 10 different point and the average value of the thickness was used in data evaluation. It was in the range of 200 μm.

Sample analysis

Mechanical measurements: Tensile Machine LS2.5, Lloyd Instruments, United Kingdom equipped with Film Support Rig probe was used for investigation of rheological properties of the Ch/PLLA blend films. The following test were used:

1) Rupture test. The test was carried out at a deformation rate of 0.1 mm/s until a deformation of 10 mm was reached. The instrument was manually stopped immediately after the breaking of the film. The rupture test was used for determining the strength at the point of breakage of the film (rupture force), the rupture energy (the area under the force-deformation curve) and the modulus of elasticity.

2) Hysteresis test. The hysteresis testing was performed at a deformation rate of 0.1 mm/s until reaching a deformation 0.35 mm. The degree of elasticity was calculated using the dependence:

$$K = A_1/A_2\,, \tag{1}$$

where A_2 is the area under the unloading section and A_1 is the area under the loading section of the hysteresis.

3) Relaxation test. The test was conducted under pressure, firstly at constant deformation rate while the desired strength was achieved, after which the deformation was kept constant for 60 s. The average relaxation time and the β-parameter, characterizing the relaxation time distribution were calculate using fitting of the experimental data with the stretched exponent model:

$$F = F_\infty + F_1(-(t/\tau)^\beta), \tag{2}$$

where F_∞ is the force at equilibrium, F_1 is the difference between the initial force and the equilibrium force.

All the tests were carried out at room temperature and the results were taken as an average of ten tests.

Differential scanning calorimetry (DSC): The thermal properties of the films were investigated by the DSC 204 F1 Phoenix NETZSCH, Germany calibrated with an indium standard. Samples (10–20 mg) were cut from a film after conditioning and placed in sealed aluminum pans. For each sample, the following thermal cycle was applied: the sample was cooled from room temperature to 0°C at cooling rate 10 K/min, 1 min at 0°C, and then heated to 250°C at heating rate 10 K/min. The glass transition temperature (T_g), melting temperature (T_m) and melting enthalpy (ΔH_m) were calculated from these experiments.

Scanning electron microscopy (SEM): The morphology of the chitosan/PLLA blend films was investigated by scanning electron microscopy (SEM). The samples were coated with gold in a vacuum evaporator Jeol JFC-1200 fine coater, the thickness of the gold coating was 0.1 nm. The SEM micrographs were carried out on a scanning electron microscope Jeol JSM-5510, with the cathode voltage of 10 kV and magnification of 5000 and 10000. The cross-sections of the films were investigated.

RESULTS AND DISCUSSION

Formation of Ch/PLLA composite films

The basic challenge in a solvent-casting approach is a proper selection of a solvent in which a homogeneous mixture of the two components on micro level is achieved. Therefore the first task, which was performed in the present study was to choose a suitable combination of solvents that dissolve both chitosan and PLLA. Initial experiments were performed to dissolve separate the chitosan in aqueous solution of acetic acid and PLLA in chloroform and to mix the two solutions. It turned out that such a system is unstable and will separate due to the incompatibility of the two solvents. Therefore further experiments were carried out for system, in which both of the polymers are dissolved in common solvent obtained by mixing acetone and formic acid. It was found out that the PLLA could be dissolved in acetone at temperatures about 80°C that necessitated heating the solutions during mixing.

Another challenge in casting the film turned out to be the strong adhesion of the dried film on the surface of the glass petri dishes and the impossibility to be separated from the dish. Therefore composite films have to be casted in Teflon petri dishes, specially made for the purposes of this study. It was originally planned to prepare films with a weight rations between the chitosan and the PLLA (Ch/PLLA) as follows: 10:0, 9:1, 8:2, 7:3, 6:4, 5:5, 4:6, 3:7, 2:8, 1:9, and 0:10. It turned out that the addition of PLLA leads to worsen the film forming properties of chitosan, so that in a weight portion of the PLLA greater than 0.6 the formation of films was not observed. Probable cause for the observed effect is insufficiently good dissolving of PLLA in acetone and the difficult formation of a uniform continuous matrix of the polymer. Successful blend with the maximum content of PLLA is a film with composition chitosan/PLLA=4:6.

Mechanical results

Basic mechanical parameter characterizing the exploitation properties of Ch/PLLA films is their strength, which is characterized by the rupture force and rupture work – (Fig. 1). To take account into the film thickness the last two parameters are normalized to unit sample thickness and therefore they are measured in N/mm and J/mm respectively. Increasing the content of PLLA leads to non-linear decrease of rupture force and rupture work. This observation could

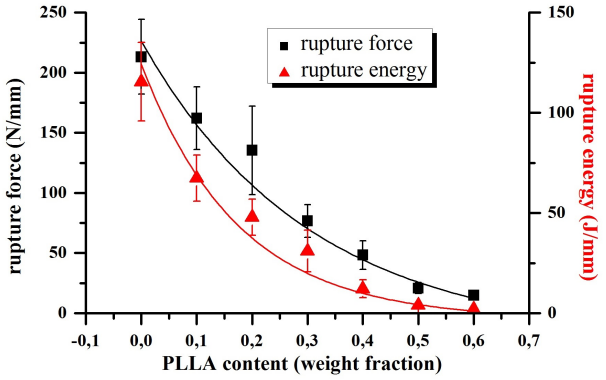


Fig. 1. Rupture force and rupture work for Ch/PLLA blends with different weight fractions of the components.

be interpreted as partial or complete incompatibility of the two materials and occurrence of phase segregation. The poorer solubility of PLLA in the common solvent causes the formation of agglomerates of the PLLA molecules, which is scattered in a continuous matrix of chitosan. When increasing the PLLA concentration, the continuous phase decreases, which results in drastic worsening of the mechanical properties.

The dependence of the modulus of elasticity of the composite films on the weight fraction of PLLA is presented in Fig. 2. The increased content of PLLA results in a decrease of modulus of elasticity and a drastic drop is observed in case of 0.3 weight fraction.

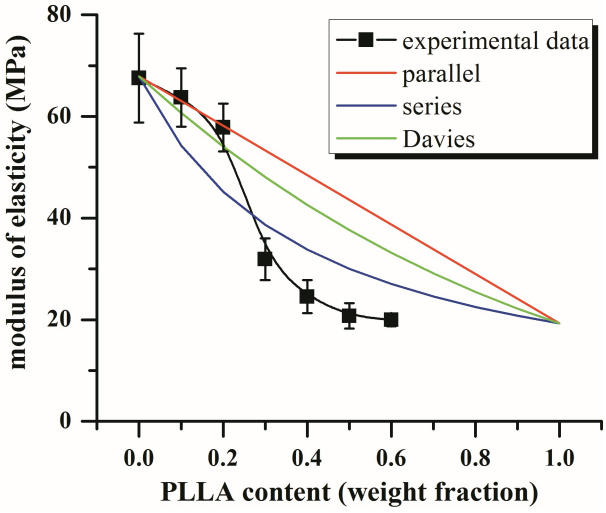


Fig. 2. Experimental modulus of elasticity for Ch/PLLA blends compared with the parallel, series, and Davies models.

No film from pure PLLA was able to be prepared in the common solvent used in this research. Therefore in order to evaluate its elastic properties, films from PLLA dissolved in chloroform were casted and their mechanical properties were examined. The modulus of elasticity designed for these films was 19.3 MPa. Comparing the mechanical characteristics of chitosan and PLLA films it can be seen that chitosan has a better performance than PLLA. As a consequence, all blends show a decrease in the elastic modulus.

It is well known that the mechanical properties of the composite films can be used to evaluate the compatibility of polymers by comparing the experimental results and estimates based on various models. The mechanical properties of the polymer blends depend on the inter-molecular forces, the conformation of the molecule (the rigidity of the main chain) and the symmetry of the molecule of the individual polymers used for the preparation of the mixtures. Furthermore, the modulus of elasticity of polymer blends is strongly dependent on the composition and morphology of the mixture and theoretically it is located between the upper limit set by the parallel theoretical model [18]

$$E = \phi_1 E_1 + \phi_2 E_2 \tag{3}$$

and a lower limit given by the series model

$$E = \frac{\phi_1}{E_1} + \frac{\phi_2}{E_2} \tag{4}$$

Moreover, for a co-continuous system, the modulus has to agree with the Davies model, whose the equation is given by

$$E = \phi_1 E_1^{1/5} + \phi_2 E_2^{1/5} \tag{5}$$

in which E_i and ϕ_i are the elastic modulus and the weight fraction of phase i, respectively.

In Fig. 2 the experimentally obtained moduli of the chitosan/PLLA films are compared with the theoretical corresponding to ideal homogeneous systems. The following conclusions could be drawn:

1. The addition of a small amount PLLA (up to 0.2 weight fractions) does not interfere the homogeneity of the composite films. In this case, the reduction in elastic modulus is described by the parallel model.
2. Increase the volume of the PLLA in the films above 0.2 leads to degraded mechanical properties that cannot be described with any of the theoretical models. The reduction of the modulus of elasticity is likely to be due to phase separation, which indicates that chitosan and PLLA are incompatible in the given volume ratios.

The degree elasticity of the Ch/PLLA films (Fig. 3) was determined by hysteresis test performed for force values that are in the linear section of the force-deformation curves. Relatively low degree of elasticity for pure chitosan films is an indication of a strong visco-elastic behavior. A possible reason for this observation could be the strong hydrophilicity of chitosan. As a result bound water in the films acts as a plasticizer which lowers the glass transition temperature and thus enhances the visco-elastic properties at room temperature. The increase of the PLLA weight fraction leads to a linear increase of the degree of elasticity. The addition of PLLA causes hydrophobic effect and reduction of water content; hence increase of films stiffness and strengthening of elastic properties. Except with increased hydrophobicity it can be explained by appearance of phase separation and structural changes of the films. Another possible reason is the presence of a crystalline structure in the PLLA, which reduces the molecules mobility and increase material rigidity.

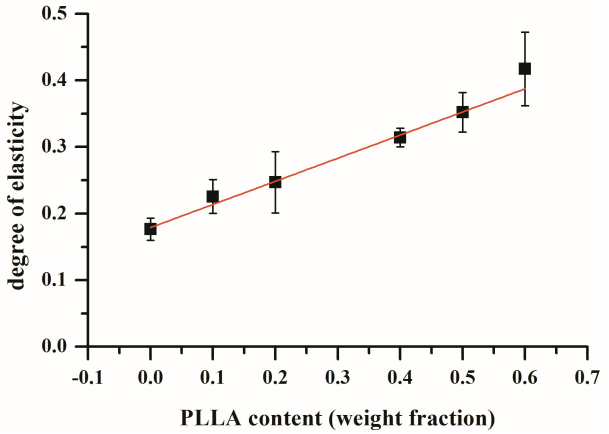


Fig. 3. Degree of elasticity for Ch/PLLA blends with different weight fractions of the components.

Some relaxation parameters of the Ch/PLLA films were determined by generalized Maxwell model in which the exponential function is modified by the stretched exponent [21, 22].

The stress relaxation is more rapid as the higher is the temperature and as the weaker are the macromolecular interactions, which depend on chemical structure of the polymer. In the case of two com-

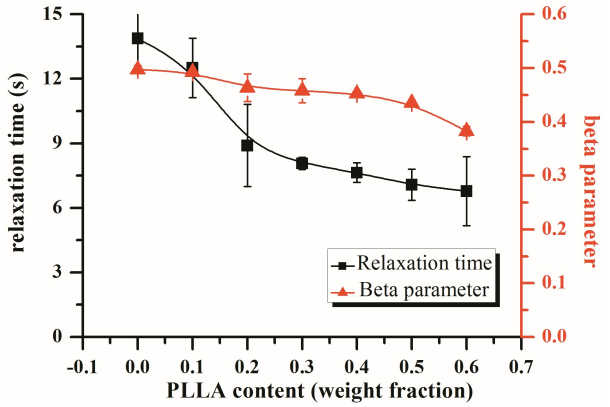


Fig. 4. Average relaxation time and β-parameter for Ch/PLLA blends with different weight fractions of the components.

ponent system the interactions between the components should be taken into account.

The dependence of the relaxation time of the content of the PLLA is presented in Fig. 4. It is noteworthy that the relaxation time decreases with increasing content of the PLLA. Reducing of the relaxation time shows that the films become more elastic and lose their viscous properties. This fact is fully consistent with the increase of the degree of elasticity that occurs with increased content of PLLA.

It is well known that spectrum of relaxation times is observed in the polymers, the width of which depends on the molecular weight distribution, the presence of cross-linkings, the presence of a crystalline phase, etc. The parameter, which describes the spectrum of relaxation times in the "stretched exponential" model, is the exponent β.

The dependence of the parameter β on the PLLA content in the composite film is shown in Fig. 4.

Increasing the weight concentration of PLLA leads to reduced values of the β-parameter. This fact should be analyzed as widening of the relaxation times distribution. Wider distribution could be connected to the existence of two types of molecules with different flexibility, molecular weight and tendency to crystallize. It is also possible to relate it with inhomogeneous phase-separated areas with different size and hardness.

Thermal properties

Thermal properties of the Ch/PLLA composite films are investigated by DSC. It is know from the literature that in addition to the mechanical properties of polymer blends their glass transition temperature T_g is an important criteria for the miscibility of the components. In case of fully miscibility, just one value of T_g which is between the T_g values of the pure polymers is observed. If the two components are just partially miscible the T_g value of each component phase should be affected by the other one, and it is usually composition dependent [23].

The values for T_g the Ch/PLLA films are presented in Table 1. It is extremely difficult to determine the glass transition temperature of chitosan because the associated heat capacity changes are very small to be measured. The reason is the stiffness of the macromolecules and the strong intramolecular hydrogen bonds on the backbone [14,24]. Therefore the chitosan T_g was not determined in this work and only the changes in the PLLA thermal behavior will be discussed. However, according to some authors the T_g of chitosan is about 194°C and in case of miscibility increasing in the T_g values of PLLA is expected.

Based on the experimental results the increase of the chitosan weight fraction in the composite films lead's to a decrease in the T_g values. Therefore an assumption could be done that there is no compatibility of the components on microlevel. The decreasing T_g could be explained by some additional action of chitosan – most probably the increased hydrophilicity of the composite films causes higher amount of bound water, which acts as a plasticizer.

Table 1. Thermal properties of Ch/PLLA composite films, investigated by DSC.

Ch/PLLA weight fraction	T_g (°C)	T_1 (°C)	ΔH_1 (J/g)	T_2 (°C)	ΔH_2 (J/g)	Crystallinity (%)
10:0	-	—	—	—	—	—
9:1	41.68	145.21	1.78	166.03	4.17	64
8:2	45.12	143.90	1.66	165.25	10.27	64
7:3	48.07	143.31	2.34	163.32	13.94	58
6:4	51.23	143.54	3.43	163.90	19.70	62
5:5	64.53	144.67	3.91	165.86	23.88	60
4:6	65.51	149.42	4.82	167.51	28.44	60

For all composites two endothermic peaks at about 145°C and 165°C are observed. They are related to the fusion process of the PLLA. The lower temperature of fusion could be due to some degradation processes of PLLA (which are engaged at the time of dissolving) or to different crystal form. The clarification of the observed melting behaviour will be an object of further investigations.

Crystallinity may influence strongly the properties of PLLA-based materials, including its glass transition dynamics and mechanical behavior [25, 26]. From the DSC results it is possible to calculate the crystallinity degree (X_c) of the PLLA fraction by applying the following equation:

$$X_c = \frac{\Delta H_m}{\Delta H_m^o \omega}, \qquad (6)$$

where ΔH_m^0 is the melting enthalpy of fully crystalline PLLA (93 J/g [27]) and ω is the weight fraction of PLLA in the blend.

These values are also included in Table 1. It can be seen that the degree of crystallinity of PLLA is not affected by the presence of chitosan and is relatively high. Thus, the PLLA phase in the blends prepared by the developed method was present predominantly in the crystal state. This observation could be associated with the increased elastic properties of composites with higher PLLA content.

Morphological analysis

To get a clear picture of the morphology of the composite films SEM analysis has been done. SEM micrographs for cross-sections of various films are shown in Fig. 5.

It is noting that the film of pure chitosan is possesses very homogeneous and dense structure. The observed fractures and micro-cracks are due to fracture of the specimen during sample preparation. Therefore it could be concluded that the selected two-component solvent (formic acid/acetone) completely dissolves the chitosan.

The addition of PLLA rises to a porous structure, in which no structured texture is observed. Pores are irregular in shape and their sizes are of the order of several microns. The size and the surface roughness of the domains forming the film differs depending PLLA content.

Increasing the amount of the added PLLA leads to an increase in the size of the domains. It is clear from the microphotographs, that the domains are built-up from both polymers. Domains at a low concentration of PLLA apparently seem homogeneous, and only in rare cases smaller spherical formations are observed on the surface of the domains. In this case, most probably the beginning of the phase separation is observed, assuming that the entities are precipitated on the surface PLLA drops. The increase of PLLA leads to a drastic change in the surface topography of the domains. Spherical formations with dimensions of the order of 0.5-1.0 microns grow on the surface, which later merged to form a rough unordered topography.

The observed by SEM morphology is evidence for the occurrence of phase separation (as was suggested on the basis of mechanical characteristics), which subsequently influence the macroscopic properties of the films. Most probably the broader spectrum of relaxation time, which is noted during the mechanical relaxation experiments, is a result of proved phase separation and immiscibility of PLLA and chitosan.

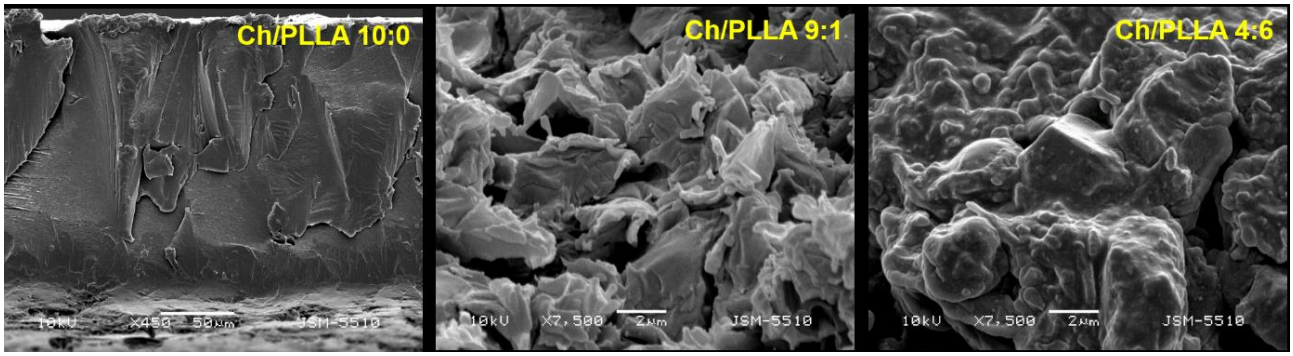


Fig. 5. SEM micrographs of pure chitosan, Ch/PLLA blend film, weight fraction 9:1 and Ch/PLLA blend film weight fraction 4:6.

CONCLUSIONS

A new two component solvent system to mix chitosan and PLLA for casted blends is presented. The proposed method resulted in macroscopically homogeneous blends, which possess technological miscibility at low PLLA content (less than 20%). Thermal and morphological analysis pointed to phase separation at the microscopic level between the two polymers, independently of the composition of the studied blends.

***Acknowledgments**: This paper was published with the financial support of the projects: SP13 FF003, Department of Scientific Research at the Plovdiv University "Paisii Hilendarski" and BG161PO003-1.2.04-0012-C0001 "Enhancing the capacity of the Plovdiv University for applied research by equipping laboratories for biocompatible materials and molecular biosensors".*

REFERENCES

[1] D. Li and Y. Xia, *Advanced Materials* **16**, 1151–1170 (2004).

[2] M. K. M. Haafiz, S. J. Eichhorn, A. Hassan and M. Jawaid, *Carbohydrate Polymers* **93**, 628–634 (2013).

[3] N. M. Julkapli, H. M. Akil and Z. Ahmad, *Composite Interfaces* **18**, 449–507 (2011).

[4] A. Domard, *Carbohydrate Polymers* **84**, 696–703 (2011).

[5] T. Tanabe, N. Okitsu, A. Tachibana and K. Yamauchi, *Biomaterials* **23**, 817–825 (2002).

[6] R. A. A. Muzzarelli, *Carbohydrate Polymers* **76**, 167–182 (2009).

[7] M. N. V. R. Kumar, R. A. A. Muzzarelli, C. Muzzarelli, H. Sashiwa and A. J. Domb, *Chemical Reviews* **104**, 6017–6084 (2004).

[8] Z. Zakaria, Z. Izzah, M. Jwaid and A. Hassan, *Bioresources* **7**, 5568–5580 (2012).

[9] C. Tual, E. Espuche, M. Escoubes and A. Domard, *J. Polym Sci. B: Polym. Phys.* **38**, 1521–1529 (2000).

[10] J. Hosokawa, M. Nishiyama, K. Yoshihara and T. Kubo, *Ind. Eng. Chem. Res.* **29**, 800–805 (1990).

[11] B. L. Butler, P. J. Vergano, R. F. Testin, J. M. Bunn and J. L. Wiles, *J. Food Sci.* **61**, 953–955 (1996).

[12] D. Garlotta, *J. Polym. Environ.* **9**, 63–84 (2001).

[13] A. Jarerat and Y. Tokiwa, *Macromol. Biosci.* **1**, 136–140 (2001).

[14] C. Chen, L. Dong and M. K. Cheung, *Eur. Polym. J.* **41**, 958–966 (2005).

[15] S. Fimbeau, S. Grelier, C. Alain and C. Veronique, *Carbohydrate Polymers* **65**, 185–193 (2006).

[16] R. Grande and A. J. F. Carvalho, *Biomacromolecules* **12**, 907–914 (2011).

[17] M. Prabaharan, M. A. Rodriguez-Perez, J. A. de Saja and J. F. Mano, *The Journal of Supercritical Fluids* **54**, 282–289 (2010).

[18] N. E. Suyatma, A. Copinet, L. Tighzert and V. Coma, *J. Polym. Environ.* **12**, 1–6 (2004).

[19] Y. Wan, H. Wu, A. Yu and A. D. Wen, *Biomacromolecules* **7**, 1362–1372 (2006).

[20] N. M. Alves, L. S. Fernandes, R. Levato and J. F. Mano, *Journal of Macromolecular Science, Part B* **50**, 1121–1129 (2011).

[21] H. Schiessel, R. Metzler, A. Blumen and T. F. Nonnenmacher, *Journal of Physics A: Mathematical and General* **28**, 6567–6584 (1995).

[22] R. Metzler and J. Klafter, *Journal of Non-Crystalline Solids* **305**, 81–87 (2002).

[23] X. Shuai, Y. He, N. Asakawa and Y. Inoue, *J. Appl. Polym. Sci.* **81**, 762–772 (2001).

[24] F. S. Kittur, K. V. H. Prashanth, K. U. Sankar and R. N. Tharanathan, *Carbohydr. Polym.* **49**, 185–193 (2002).

[25] J. F. Mano, J. L. Gómez Ribelles and N. M. Alves, *Polymer* **46**, 8258–8265 (2005).

[26] C. Saiz-Arroyo, Y. Wang, M. A. Rodriguez-Perez, N. M. Alves and J. F. Mano, *J. Appl. Polym. Sci.* **105**, 3860–3864 (2007).

[27] E. W. Fischer, H. J. Sterzel and G. Wegner, *Colloid Polym. Sci.* **251**, 980–990 (1973).

РЕОЛОГИЧНИ СВОЙСТВА НА КОМПОЗИТНИ ФИЛМИ НА ОСНОВАТА НА ХИТОЗАН И БИОРАЗГРАДИМИ ПОЛИЕСТЕРИ

М. Марудова[1], Е. Делчева[1], Г. Живанович[2]

[1] *Физически факултет, Пловдивски университет "Паисий Хилендарски", ул. "Цар Асен" №24, 4000 Пловдив, България*
[2] *Институт за изследване и развитие на храните – Пловдив, ССА, бул. "Васил Априлов" №154, 4003, Пловдив, България*

(Резюме)

В настоящата работа е изследвано реологичното поведение при едноосна деформация на композитни филми от хитозан/полимлечна киселина и хитозан/поли-ε-капролактон. Филмите са получени при различни масови части на двата полимера в разтворител, представляващ смес на мравчена киселина и ацетон в обемно отношение 1:1. Филмите са отляти в петрита от тефлон и изсушени до постоянна маса в сушилня при температура 35°C. Реологичните тестове са проведени при постоянна скорост на деформация 0.1 mm/s и стайна температура. От основната физико-механична крива за композитните филми са определени точката на разрушаване и модула на еластичност. От проведените тестове на механичен хистерезис са изчислени коефициента на еластичност и остатъчната деформация. Получените реологични параметри са пряко свързани с експлоатационните характеристики на филмите при приложението им за опаковъчен материал.

Bulgarian Chemical Communications, Volume 47, Special Issue B (pp. 135–139) 2015

Optical spectra of the complexes $[M(H_2O)_6]^{2+}$ and MSO_3–$(H_2O)_2$ (M = Ni^{2+})

P. Petkova[1]*, P. Vasilev[1], M. Mustafa[1], V. Nedkov[2], J. Tacheva[1], Y. Tzoukrovsky[3]

[1] *Faculty of Natural Sciences, Konstantin Preslavsky University of Shumen, 115 Universitetska Str., BG-9712 Shumen, Bulgaria*
[2] *Faculty of Chemistry and Pharmacy, St. Kliment Ohridski University of Sofia, 1 James Boucher Blvd., BG-1164 Sofia, Bulgaria*
[3] *Department of Radiophysics and Electronics, Faculty of Physics, St. Kliment Ohridski University of Sofia, 5 James Boucher Blvd., BG-1164 Sofia, Bulgaria*

In this work, the absorption spectra of complexes $[M(H_2O)_6]^{2+}$ and MSO_3–$(H_2O)_2$ (M = Ni^{2+}) are measured in spectral region 360–800 nm. The energies of electron transitions in Ni^{2+} are calculated in both cases. The Lorentz curves of nickel complexes $[Ni(H_2O)_6]^{2+}$ and $NiSO_3$–$(H_2O)_2$ are presented. The refractive index of aqueous solution of $MgSO_3.6H_2O$:Ni is calculated.

Key words: ions of transition metals, absorption spectra, electron transitions, Lorentz curves

INTRODUCTION

The crystals of magnesium sulphite hexahydrate ($MgSO_3.6H_2O$) are related to the point group C_3 (without symmetry center). They are anisotropic (uniaxial) and gyrotropic in accordance to the symmetry point group [1]. The pure crystals of $MgSO_3.6H_2O$ are colourless. An original method has been developed for single crystals of $MgSO_3.6H_2O$ growing. This method allows producing samples with linear sizes 40–50 mm [2]. The $MgSO_3.6H_2O$ crystals are still not enough investigated. The first investigation on the nonlinear optical properties of single crystals of $MgSO_3.6H_2O$ is reported in 1997. The appearance of the second harmonics is observed by illumination the crystal with Nd:YAG laser radiation [2]. The optical properties of $MgSO_3.6H_2O$ are investigated partially for separate spectral lines or in narrow spectral ranges in connection with its application of the crystals in the laser technique.

In this paper, we would like to discuss the Lorentz curves of the complexes $[Ni(H_2O)_6]^{2+}$ and $NiSO_3$–$(H_2O)_2$ which are the basic components of the crystal $MgSO_3.6H_2O$:Ni. We are investigated the unsaturated solutions where the distance between the complexes is large. Thus, the Ni^{2+} ions do not interact each other. The results of our experiment demonstrate that nickel impurity can find future application in the laser technique.

EXPERIMENTAL DETAILS AND RESULTS

The experimental set up for the measurement of the absorption coefficient in the visible region consisted of the following: a halogen lamp with a stabilized 3H-7 rectifier, a SPM-2 monochromator, a system of quartz lenses, a polarizer, a crystal sample holder, and a Hamamatsu S2281-01 detector. The thickness of the used cuvette is $d = 0.995$ cm.

The absorption coefficient of the investigated samples has been measured between 360 nm and 800 nm (Figs. 1a, 2a). The first derivative of the absorption coefficient at photon energy is calculated in the 360–800 nm spectral region. The $[d\alpha/d(h\nu)]$ determines only the number of electron transitions in Ni^{2+} ions and it does not give an exact information about the energy position of these transitions (Figs. 1b, 2b). This is the reason for the calculation of the second derivative of the absorption coefficient $[d^2\alpha/d(h\nu)^2]$ (Figs. 1c, 2c). The absorption coefficient is calculated using the formula: (1) $\alpha = (1/d)ln(I_0/I)$, where I_0 is the intensity of the incident light, I is the intensity of the passing light and d is the sample thickness. The calculated Lorentz curves for $[Ni(H_2O)_6]^{2+}$ and $NiSO_3$–$(H_2O)_2$ complexes in the spectral regions 360–460 nm and 550–800 nm are presented in Figs. 3a, b. They are compared with the experimental Lorentz curves in the same spectral regions (Figs. 4a, b).

* To whom all correspondence should be sent:
Petya232@abv.bg

© 2015 Bulgarian Academy of Sciences, Union of Chemists in Bulgaria

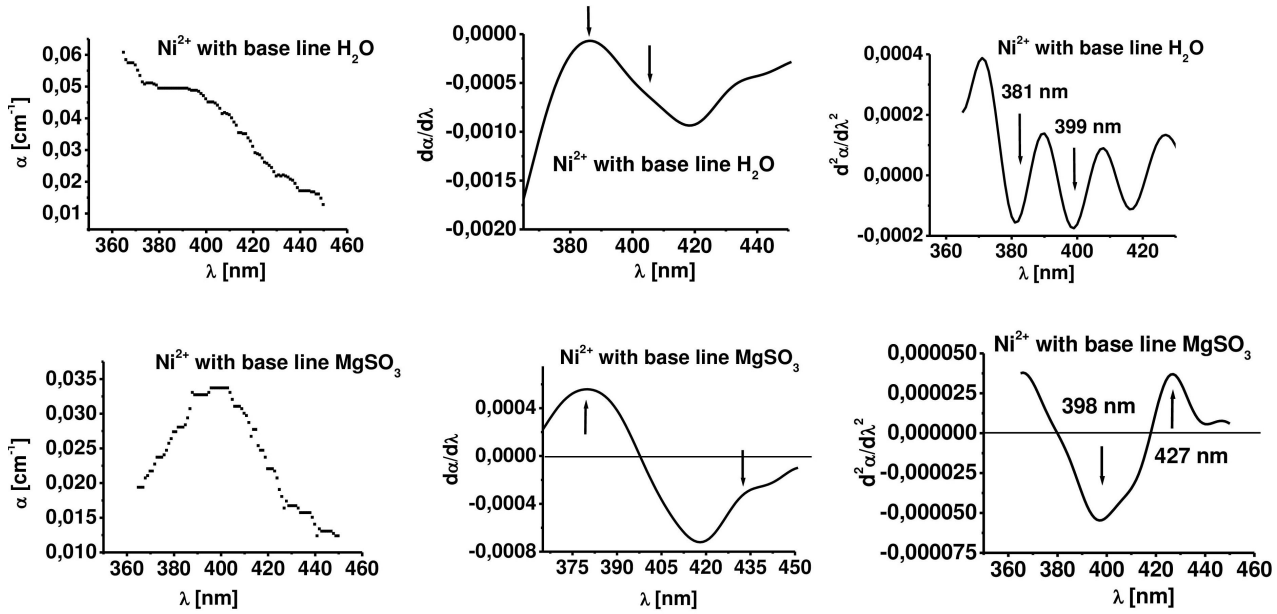


Fig. 1. a) Absorption spectrum of $[Ni(H_2O)_6]^{2+}$ and $NiSO_3$–$(H_2O)_2$ complexes in the spectral region 360–460 nm; b) Calculated first derivative of the absorption coefficient in the same spectral region; c) Calculated second derivative of the absorption coefficient.

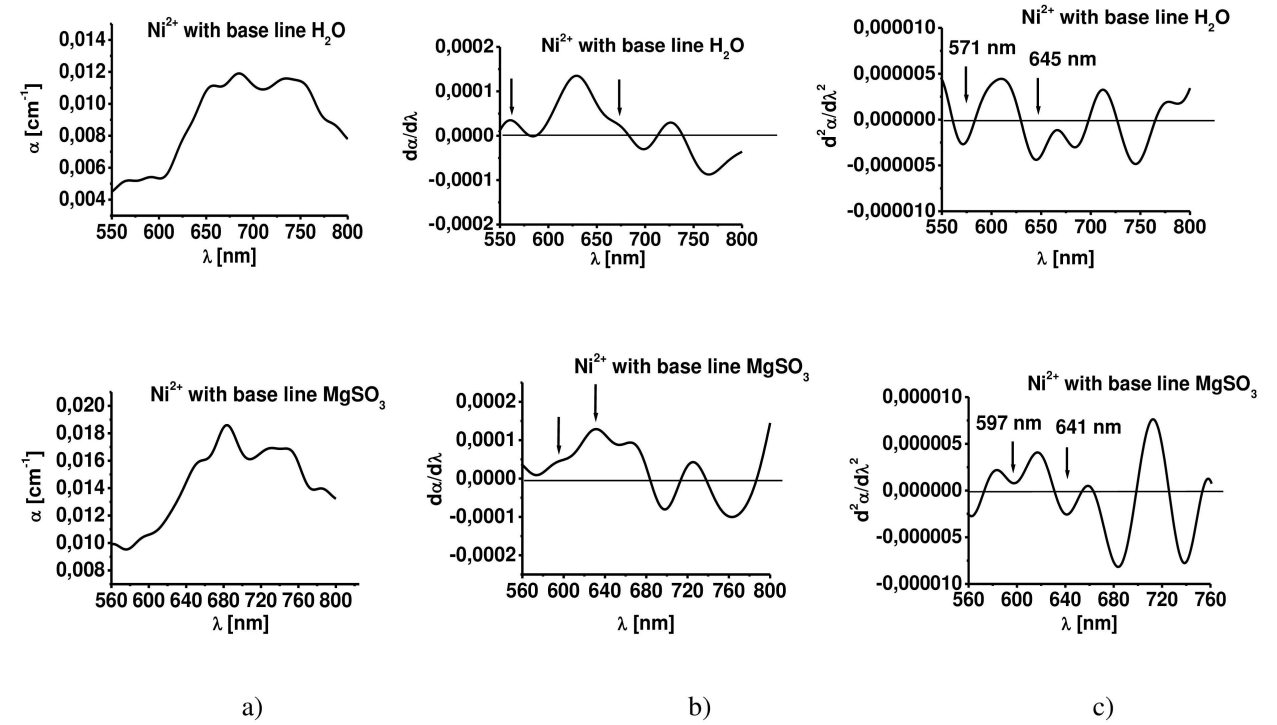
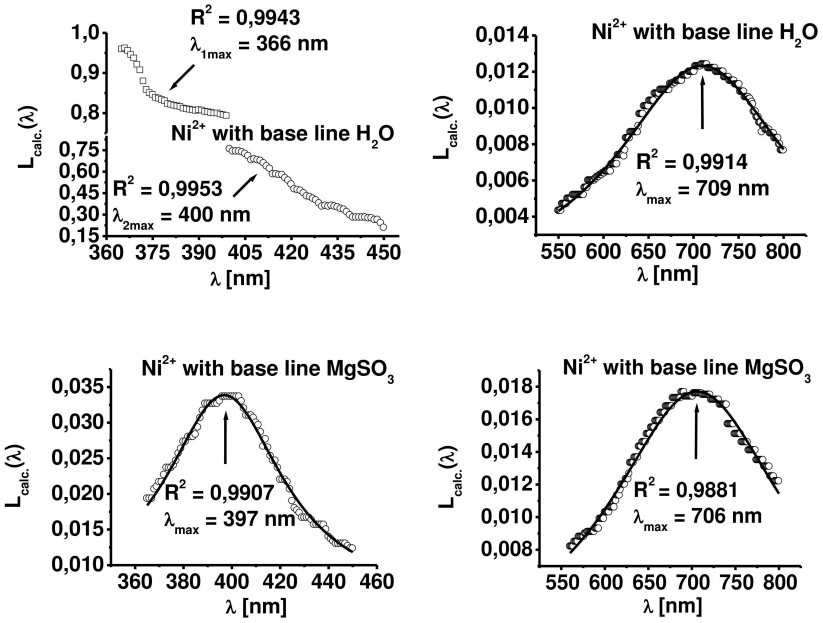
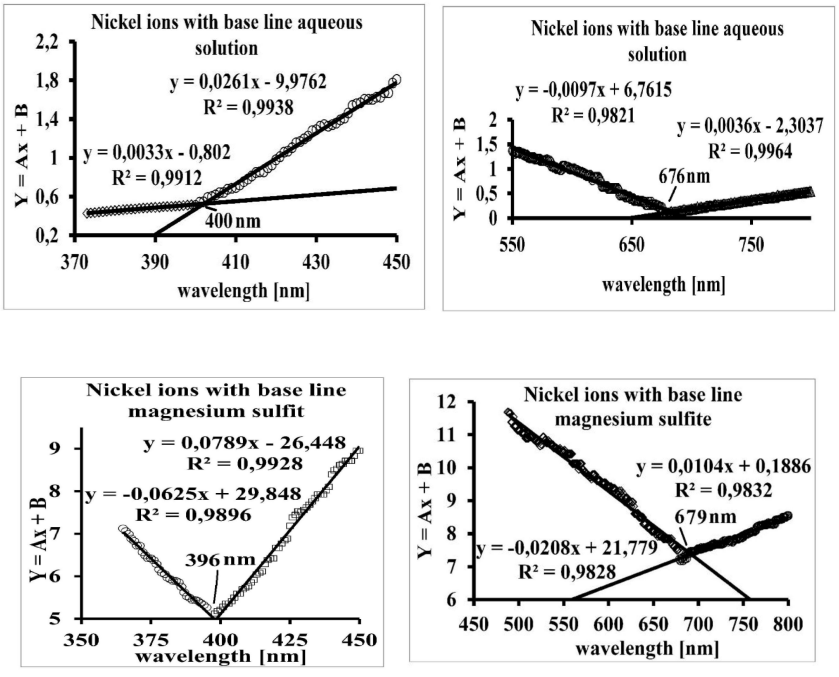


Fig. 2. a) Absorption spectrum of $[Ni(H_2O)_6]^{2+}$ and $NiSO_3$–$(H_2O)_2$ complexes in the spectral region 550–800 nm; b) Calculated first derivative of the absorption coefficient in the same spectral region; c) Calculated second derivative of the absorption coefficient.



a) b)

Fig. 3. The calculated Lorentz curves for $[Ni(H_2O)_6]^{2+}$ and $NiSO_3$–$(H_2O)_2$ complexes in the spectral regions: a) 360–460 nm; and b) 550–800 nm.



a) b)

Fig. 4. The linearized experimental Lorentz curves for $[Ni(H_2O)_6]^{2+}$ and $NiSO_3$–$(H_2O)_2$ complexes in the spectral regions: a) 360–460 nm; and b) 550–800 nm.

DISCUSSION

The theory [3] shows that:

The absorption spectrum of impurities in the crystals, glasses and thin films consist of phonon and non-phonon part in low electron-phonon connection. The phonon part of spectrum consists of quasi-Lorentz curves. In harmonic approximation, these curves have intensity and half-width which depend on the electron-phonon interaction and temperature. The phonon part of spectrum manifests as structureless band. The separate maxima can be observed on the background of this band.

The form of the curve of first-order derivative consists of two maxima (positive and negative (Fig. 1b) or two positive (Fig. 2b)) [4]. Therefore, the enveloping Lorentz curve of absorption nickel structures includes two Lorenz components.

The ground state of Ni^{2+} in the octahedral coordination is $^3A_{2g}(t_{2g})^6(e_g)^2$. The ion Ni^{2+} has two unpaired spins in this coordination. Thus, we can observe three absorption bands connected with the transitions $^3A_{2g} \rightarrow {}^3T_{2g}$, $^3A_{2g} \rightarrow {}^3T_{1g}(F)$ and $^3A_{2g} \rightarrow {}^3T_{1g}(P)$ [5–7]. In our case the electron transitions in Ni^{2+} are two as follow: $^3A_{2g}(F) \rightarrow {}^3T_{1g}(F)$ (Fig. 1c) and $^3A_{2g} \rightarrow {}^3T_{1g}(P)$ (Fig. 2c). Therefore, we can solve the system of the next equations $\nu_1 = 14793\ cm^{-1} = 15Dq + 1.47B$ and $\nu_2 = 25000\ cm^{-1} = 15Dq + 13.53B$ for the complex $[Ni(H_2O)_6]^{2+}$. The values of ν_1 and ν_2 present the cross point of two Lorentz curves which are included in the complex spectral structure of nickel (Figs. 4a, b). When the impurity spectral structures are very wide, we can present only the experimental Lorentz curves, because the difference between their cross point and λ_{max} of the calculated Lorentz curve is very large (Figs. 3b and 4b).

The crystal field parameter Dq is 903 cm^{-1} and Racah's parameter B is 846 cm^{-1} for the same complex. The other system of equations is: $\nu_1 = 14728\ cm^{-1} = 15Dq + 1.47B$ and $\nu_2 = 25253\ cm^{-1} = 15Dq + 13.53B$ for the complex $NiSO_3$–$(H_2O)_2$. The crystal field parameter and Racah's parameter for this complex are respectively $Dq = 896\ cm^{-1}$, $B = 873\ cm^{-1}$. The Racah's parameter C for the complexes $[M(H_2O)_6]^{2+}$ and MSO_3–$(H_2O)_2$ ($M = Ni^{2+}$) has values respectively 3985 cm^{-1} and 4112 cm^{-1}.

When the plane electromagnetic wave propagates in the absorbing isotropic medium, the absorption coefficient is presented as:

$$\alpha(\lambda) = \frac{Ne^2(\gamma/2)}{2cn\varepsilon_0 m(\lambda_0 - \lambda)^2 + (\gamma/2)^2}. \qquad (1)$$

The normalized curve of the absorption coefficient has the form:

$$L(\lambda) = \frac{\alpha(\lambda)}{\alpha_{max}} = \frac{(\gamma/2)^2}{(\lambda_0 - \lambda)^2 + (\gamma/2)^2}, \qquad (2)$$

where

$$\alpha_{max} = [Ne^2]/[2en\varepsilon_0 m(\gamma/2)]. \qquad (3)$$

We can calculate the refractive index n of the solution, when the equation (3) is transformed into

$$n = \frac{N_d q_d^2}{2c\alpha_{max}\varepsilon_0 m_d(\gamma/2)} = 1.3721, \qquad (4)$$

where $N_d = 1.02 \times 10^{31}\ m^{-3}$ (number of Ni^{2+} ions per unit volume), $q_d = 44.8 \times 10^{-19}$ C, $c = 3 \times 10^8$ m/s, $\alpha_{max} = 96.14\ m^{-1}$, $\varepsilon_0 = 8.85 \times 10^{-12}$ F/m, $m_d = 0.9941$ kg, $\gamma/2 = 294$.

If the curve is Lorentz curve, it should be checked as follows: The dependence $L(\lambda)$ is reduced to a linear and a linear correlation analysis is used.

Thus, the equation (2) is transformed into the equation

$$[(1/L(\lambda)) - 1]^{1/2} = [\lambda_0/(\gamma/2)] - [1/(\gamma/2)]\lambda. \qquad (5)$$

λ_0 is the own wavelength of vibration of oscillators per unit volume and γ is the damping ratio takes into account the loss of energy of the oscillators. If $Y = [(1/L(\lambda)) - 1]^{1/2}$, $B = [\lambda_0/(\gamma/2)]$, $A = -[1/(\gamma/2)]$ and $x = \lambda$, then $Y = Ax + B$.

If the coefficient of correlation is $R^2 = 0.98$, then the probability P is 0.95. Therefore, the relationship between Y and x is linear and the curve is Lorentz curve.

CONCLUSIONS

The different coordination of Ni^{2+} gives different energy positions of electron transitions in this ion. The methodology for the experimental Lorentz curves gives opportunity for determination of the refractive index of the solutions. The calculated Lorentz curves are used in well expressed sharp maxima and their λ_{max} coincides with the cross point of experimental Lorentz curves.

***Acknowledgments**: This paper was developed with the financial support of project 2015, Shumen University "Konstantin Preslavsky", Bulgaria.*

REFERENCES

[1] I. Kostov, "*Crystallography*", Sofia, Science and Art, 1963 (in Bulgarian).

[2] Zh. Bunzarov, S. Saltiel, Ts. Kovachev, L. Ljutov and D. Russev, *SPIE* **3052**, 197–200 (1998).

[3] A. F. Lubchenko, *Quantum transitions in impurity centers in solids*, Kiev, Naukova Dumka, 1978, pp. 264-268.

[4] V. S. Saakov, V. Z. Drapkin, A. I. Krivchenko, E. V. Rozengart, Y. V. Bogachev and M. N. Knyazev, "*Derivative Spectrophotometry and Electron Spin Resonance (ESR) Spectroscopy for Ecologigal and Biological Questions*", Springer, 2013, XVI, p. 357.

[5] L. E. Orgel, *J. Chem. Phys.* **23**, 1004 (1955).

[6] Y. Tanabe and S. Sugano, *J. Phys. Soc. Japan* **9**, 766 (1954).

[7] C. J. Ballhausen, Kgl. Danske Videnskab. Selskab, *Mat.-fys. Medd.* **29**, 8 (1955).

ОПТИЧНИ СПЕКТРИ НА MSO_3 И $[M(H_2O)_6]^{2+}$ ($M = Ni^{2+}$)

П. Петкова[1], П. Василев[1], М. Мустафа[1], В. Недков[2], Й. Тачева[1], Ю. Цукровски[3]

[1] *Факултет по Природни науки, ШУ "Епископ К. Преславски", ул. "Университетска" №115, 9712 Шумен*
[2] *Факултет по Химия и Фармация, СУ "Св. Климент Охридски", бул. "Джеймс Баучер" №1, 1164 София, България*
[3] *Физически факултет, СУ "Св. Климент Охридски", бул. "Джеймс Баучер" №5, 1164 София, България*

(Резюме)

В тази работа са измерени спектрите на поглъщане на комплексите $NiSO_3$ и $[Ni(H_2O)_6]^{2+}$ в спектралния диапазон (400–600) nm. Изчислени са енергиите на преходите на електроните в Ni^{2+} и в двата случая. Представени са и са дискутирани напречните сечения на поглъщане σ_a^1 и σ_a^2 на никела съответстващи на комплексите MSO_3 и $[M(H_2O)_6]^{2+}$ ($M = Ni^{2+}$). Определени са големините на спин-орбиталното взаимодействие и Зеемановото разцепване.

Bulgarian Chemical Communications, Volume 47, Special Issue B (pp. 140–146) 2015

Ellipsometry of micro-objects and structures

D. L. Lyutov*, G. G. Tsutsumanova, S. C. Russev

Department of Solid State Physics and Microelectronics, Faculty of Physics,
St. Kliment Ohridski University of Sofia, 5 James Bourchier Blvd., BG-1164 Sofia, Bulgaria

The conventional ellipsometry is very sensitive to changes of the surface in direction, normal to the surface of the specimen. The resolution in the plane of the surface is much lower – of the order of the width of the probe beam. For examination of micro-objects greater resolution is needed. In this work, construction and characterization of prototype of ellipsometric device with improved lateral resolution is presented. Its potential for local measurement of the ellipsometric angles is demonstrated and it is tested on different structures and micro-objects.

Key words: ellipsometry, micro-objects, lateral resolution

INTRODUCTION

In recent years, the interest in research on microstructures and micro-objects has increased considerably. The conventional ellipsometry has very high sensitivity in direction normal to the surface – it is sensitive to submonoatomic changes of the surface. However its lateral resolution is much lower – it is limited by the width of the probe beam. There are techniques that improve the lateral resolution like Brewster angle microscopy [1–3], focusing ellipsometry [4, 5] and imaging ellipsometry [6–10], but the aim of most of them is acquiring image rather than measuring the ellipsometric parameters ψ and Δ. Although quantitative measurements are possible with some of these techniques [10], their accuracy is lesser than that of the conventional ellipsometry. Our aim is to assemble ellipsometric devices with improved lateral resolution but to keep the accuracy of the measurement of the ellipsometric parameters ψ and Δ. Two prototypes of such ellipsometric devices are presented in this work. They are tested on different samples dielectric, metal and semiconductor. The tests on micro-objects require objective with appropriate magnification. Therefore other tests are made to examine how the magnification of the optical system affects the ellipsometric measurement. Comparison is made between measurements on micro-objects and large surface of the same material by the conventional ellipsometry.

* To whom all correspondence should be sent:
d_lyutov@phys.uni-sofia.bg

EXPERIMENTAL SECTION

Two experimental setups, based on null type ellipsometer arrangement are made in this work. The two setups are distinguished by the position of the magnifying optical system. The two possible arrangements are polarization state generator/sample/optical system (objective)/polarization state detector (PSG-S-OS-PSD) and polarization state generator/sample/polarization state detector/optical system (objective) (PSG-S-PSD-OS). Each of them has its own advantages and drawbacks.

The first arrangement (PSG-S-OS-PSD) has the advantage that the objective is close to the sample and the resolution is greater but the objective itself changes the polarization and gives deviation in the measurement. In the second arrangement (PSG-S-PSD-OS) the objective does not change the polariza-

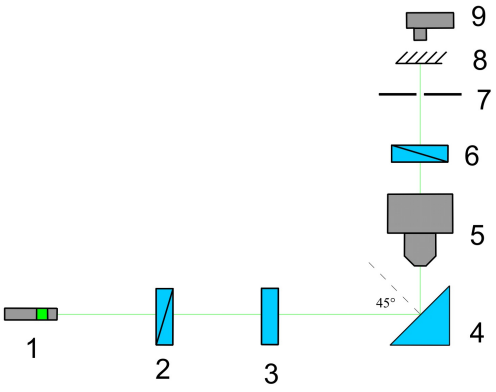


Fig. 1. Scheme of the first prototype arrangement (PSG-S-OS-PSD): 1 – laser; 2 – polarizer; 3 – compensator; 4 – sample on the micrometric table; 5 – objective; 6 – analyzer; 7 – aperture for selection of single object; 8 – screen; 9 – photo detector.

© 2015 Bulgarian Academy of Sciences, Union of Chemists in Bulgaria

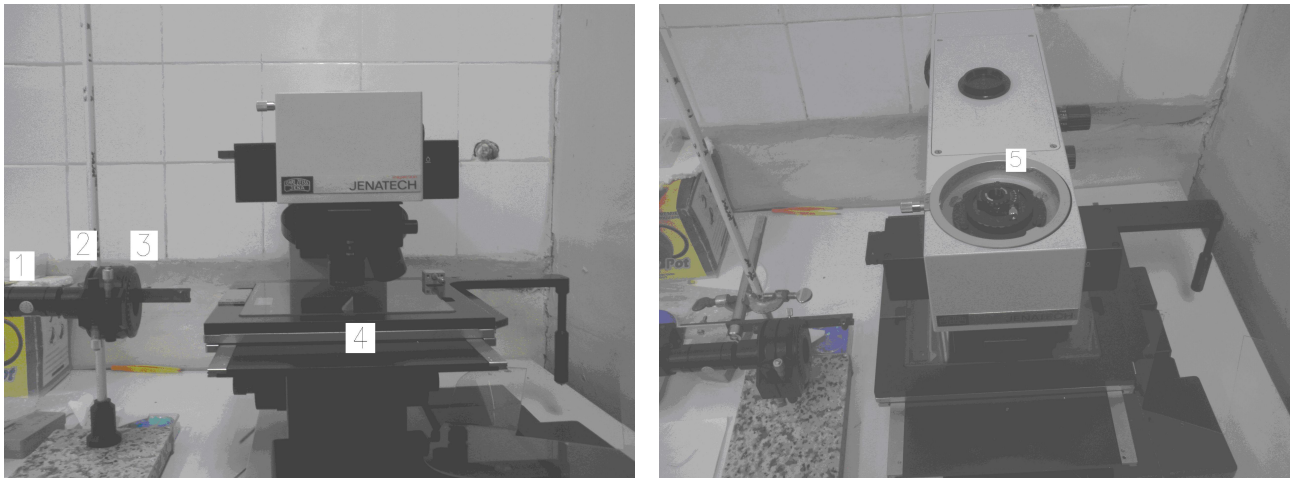


Fig. 2. Prototype (PSG-S-OS-PSD) viewed in front: 1 – laser; 2 – polarizer; 3 – compensator; 4 – sample and viewed from above: 5 – analyzer.

tion because it is after the polarization state detector and it does not change the conditions for the ellipsometric null.

The scheme of the PSG-S-OS-PSD prototype is shown in Fig. 1 and the construction – in Fig. 2. Microscope "Carl Zeiss", light source, polarizer, compensator, analyzer and screen are used for the assembling of the first experimental setup. The light source is laser with wavelength $\lambda = 532$ nm. The polarizer is type Glan-Thompson and the analyzer is made of dichroic polymer. The polarizer, compensator and analyzer can be rotated at arbitrary angle which allows four-zone measurement. The angle of incidence is fixed at 45°. The microscope's x-y table allows localization of the micro-objects. Photo detector can be used for more accurate measurement of the minimum of the intensity instead to be determined visually at the screen. The numerical aperture and the resolution are the same as these of the microscope because the working distance is the same as in normal mode. So the resolution is approximately 1 μm.

Conventional ellipsometer "Rudolf Research" and microscope "Carl Zeiss" are used for assembling the second experimental setup (PSG-S-PSD-OS) – Fig. 3.

Laser with wavelength $\lambda = 532$ nm, polarizer Glan-Thompson, compensator, micrometric table for the sample, analyzer Glan-Thompson, movable optical system (Fig. 3), microscope system and screen or

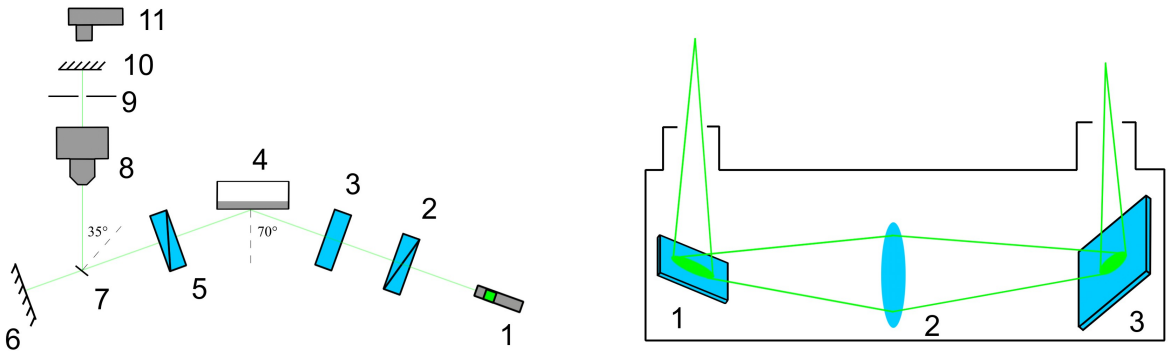


Fig. 3. *Left:* Scheme of the prototype with arrangement (PSG-S-PSD-OS): 1 – laser, 2 – polarizer, 3 – compensator, 4 – sample on micrometric table, 5 – analyzer, 6 – screen, 7 – movable optical system for relaying the image close to the objective of the microscope, 8 – optical system (objective), 9 – aperture for selection of single object, 10 – screen, 11 – photo detector. *Right:* Movable system in profile: 1,3 – mirrors, 2 – relay lens.

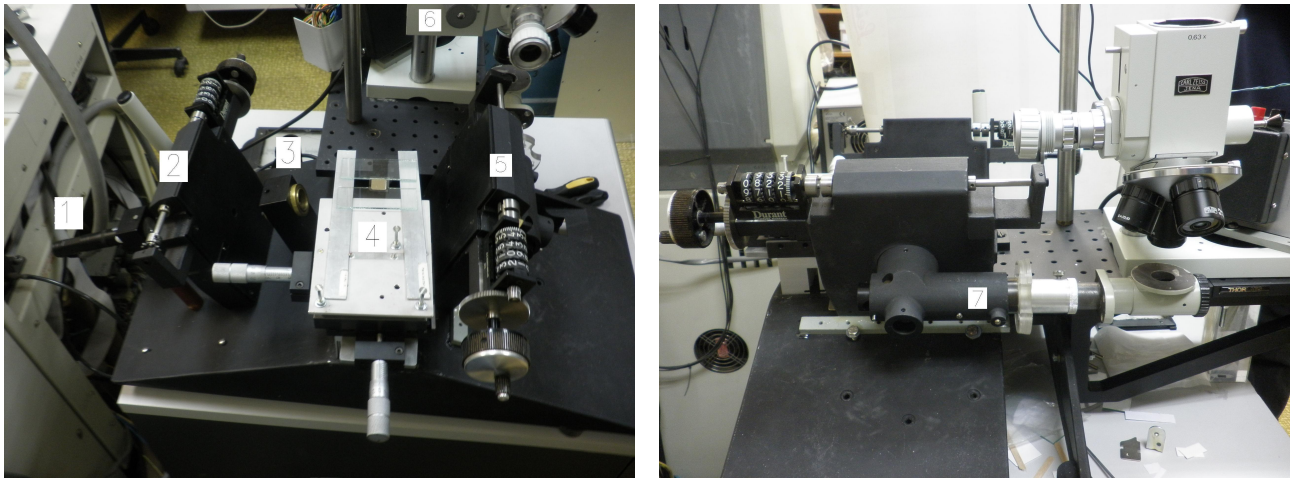


Fig. 4. Experimental setup with ellipsometer "Rudolf Research" and microscope "Carl Zeiss". *Left:* Top view. 1 – laser, 2 – polarizer, 3 – compensator, 4 – x-, y- micrometric table, 5 – analyzer, 6 – microscope. *Right:* Side view. 7 – optical system used to relay the image close to the microscope.

photo detector are used in the second configuration. In this experimental setup, the polarizer and analyzer can be rotated at an arbitrary angle, but the compensator is fixed and only two zone measurements are possible. A possible improvement is adding azimuth indicator which will allow four zone measurements. The angle of incidence is 70° and is fixed. Pictures of the second experimental setup are shown at Fig. 4.

This setup can be used for conventional ellipsometric measurements by pulling out the optical system 7 (Fig. 4, right) and the intensity of the whole beam spot is minimized at the screen 6 (Fig. 3, left). If the system 7 is placed the beam is guided through microscope and the image is focused at the screen 10 (Fig. 3, left).

In this arrangement (PSG-S-PSD-OS) the objective is at long distance from the sample so the numerical aperture of the used relay lens is determining for the resolution of the whole system. The result is that the resolution is lower than that of the microscope. The resolution is determining for the minimal size of the objects which can be observed. Therefore it is estimated for this experimental setup.

The criterion for resolution of optical system is

$$r = \frac{1.22\lambda}{2n\sin(\theta)}, \tag{1}$$

where n is the refractive index of the medium, λ is the wavelength and θ is the aperture angle. The refractive index of the air is $n \approx 1$, the wavelength of the laser is $\lambda = 532nm$, θ is determined from the distance from the sample to the lens $l = 200$ mm and diameter of the lens $d = 20$ mm.

$$\sin(\theta) \approx \tan(\theta) = \frac{d}{2l} = \frac{20}{2\times 200} = 0.05 \tag{2}$$

The resolution is

$$r = \frac{1.22\lambda}{2n\sin(\theta)} = \frac{0.61\lambda}{\sin(\theta)} = 0.61\times 532\times 10^{-9}/0.05 = 6.5\ \mu\text{m}. \tag{3}$$

RESULTS

To determine their potential capabilities, null measurements are made with both experimental setups. The ellipsometric angles are calculated from the azimuth angles of the optical elements [11]:

$$\rho = -\tan A\left[\frac{\tan C + \rho_C \tan(P-C)}{1-\rho_C \tan C\tan(P-C)}\right] \tag{4}$$

where ρ is the ellipsometric ratio

$$\rho = \tan\psi e^{i\Delta} \tag{5}$$

and ρ_C is the ratio of coefficients of transmission between slow and fast axis of the compensator

$$\rho_C = T_C e^{i\Delta} \tag{6}$$

P, C and A are the azimuth angles of polarizer, compensator and analyzer. The uncertainty is estimated from the width of the minimum of the intensity.

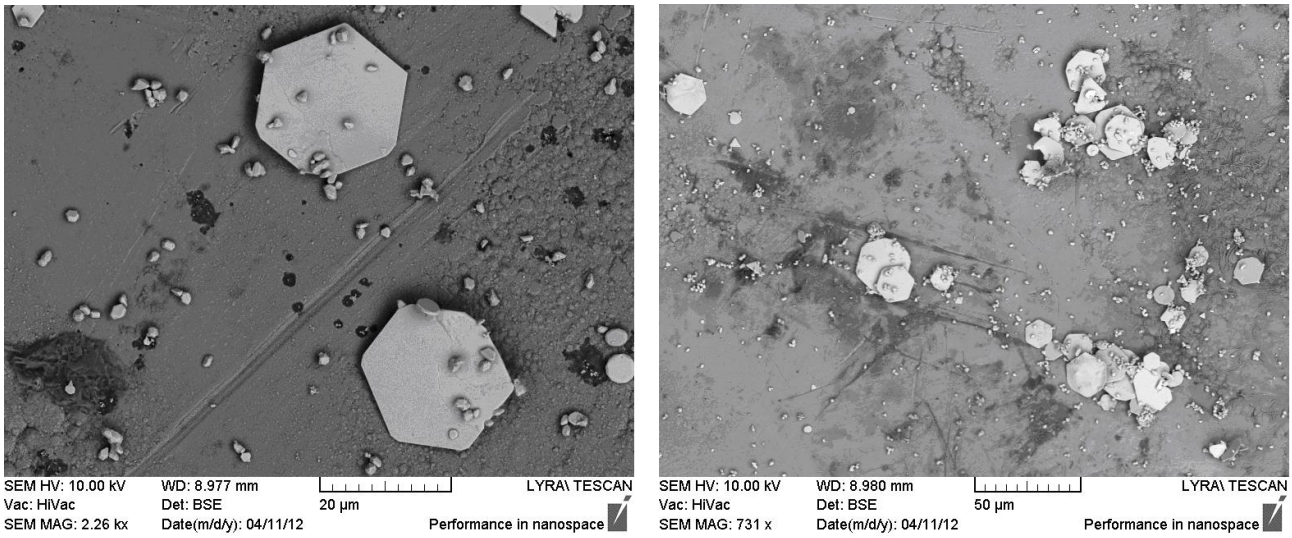


Fig. 5. Scanning electron microscope images of the Ag microparticles.

Measurements with prototype (PSG-S-OS-PSD)

Silver microparticles [12] with lateral dimensions in the range 10–20 μm are used as test objects – (Fig. 5). Four-zone measurements were performed using microscope objective with magnification $\times 10$.

The measured values of the ellipsometric angles ($\psi = 39.45^\circ \pm 1.44^\circ$ and $\Delta = 160^\circ \pm 2.00^\circ$) differ from the calculated values for bulk silver ($\psi = 44.84^\circ$ and $\Delta = 156.50^\circ$ for refractive index $N = 0.05 - 3.324i$ and wavelength $\lambda = 521.5$ nm [13]). This can be caused by the effect of the optical system (the objective) which changes the polarization. The main advantage of this configuration (PSG-S-OS-PSD) is that the intensity of the light reflected from micro-object is minimized so ellipsometric null is achieved. A good spatial resolution is attained – the size of the particle is 10 μm.

Measurements with prototype (PSG-S-PSD -OS)

Measurements on samples made of three different materials are performed: glass K8, chrome (200 nm electron beam evaporation Cr layer on glass) and silicon (thickness 0.35 mm, $\langle 111 \rangle$ orientation). Conventional ellipsometric measurements and measurements with magnification $\times 5$, $\times 10$ and $\times 50$ are made to examine if the objective affects the measurement for each sample.

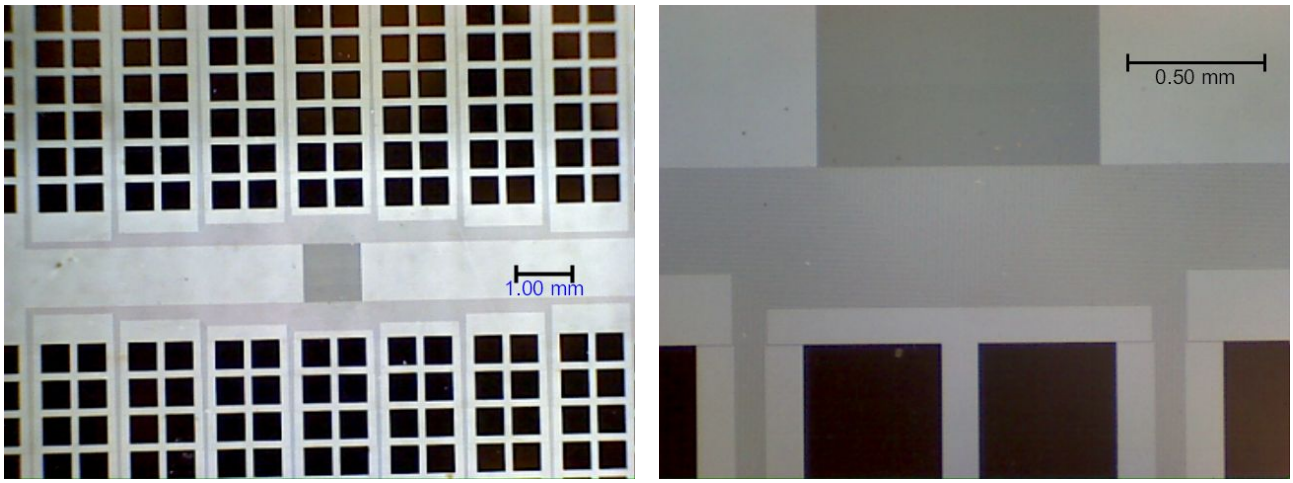


Fig. 6. Optical microscope image of the photolithographic mask No 1 at different mignifications. Squares are 500×500 μm.

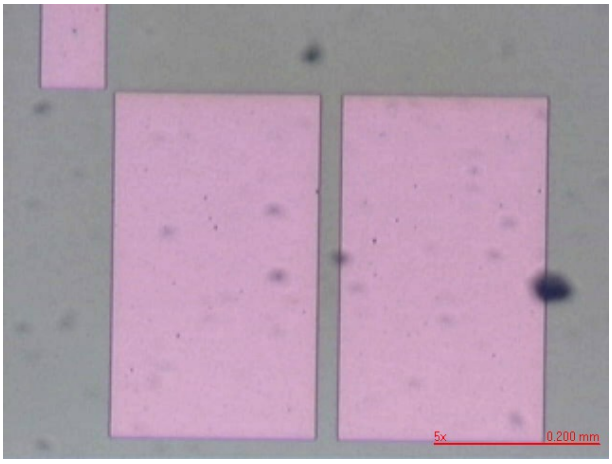


Fig. 7. Optical microscope image of the photolithographic mask No 2 with rectangle structures 200×400 μm and 50×100 μm.

ψ and Δ are measured on two photolithographic masks, labeled photolithographic mask No. 1 (Fig. 6) and photolithographic mask No. 2 (Fig. 7). ψ and Δ are measured on photolithographic mask No 1 by conventional method on large surface, with objectives with magnification $\times 5$, $\times 10$ and $\times 50$ and on 500×500 μm area with objective with magnification $\times 50$. Two regions of photolithographic mask No 2 (size 200×400 μm and 50×100 μm) are measured. An attempt is made to measure ψ and Δ on large area in photolithographic mask No2 but it is determined that the thickness of the layer is not the same on the whole surface. The results from these measurements are summarized in Table 1 and shown in Figs. 8 and 9.

Table 1. Ellipsometric angles measured on three different materials by conventional method and with objective with different magnification (configuration (PSG-S-PSD-OS))

Structure/magnification	ψ [°]	Δ [°]
K8 conventional	19.69 ± 0.21	0.89 ± 0.63
K8 $\times 5$	19.79 ± 0.22	0.77 ± 0.86
K8 $\times 10$	19.69 ± 0.33	0.88 ± 0.85
K8 $\times 50$	19.77 ± 0.55	0.89 ± 1.29
Cr conventional	26.99 ± 0.29	113.23 ± 0.86
Cr $\times 5$	27.03 ± 0.40	113.65 ± 0.78
Cr $\times 10$	27.12 ± 0.29	113.51 ± 0.78
Cr $\times 50$	27.13 ± 0.42	113.25 ± 1.13
Si conventional	12.74 ± 0.28	167.62 ± 0.76
Si $\times 5$	12.67 ± 0.25	168.05 ± 0.74
Si $\times 10$	12.69 ± 0.25	167.62 ± 0.96
Si $\times 50$	12.56 ± 0.38	167.79 ± 0.90

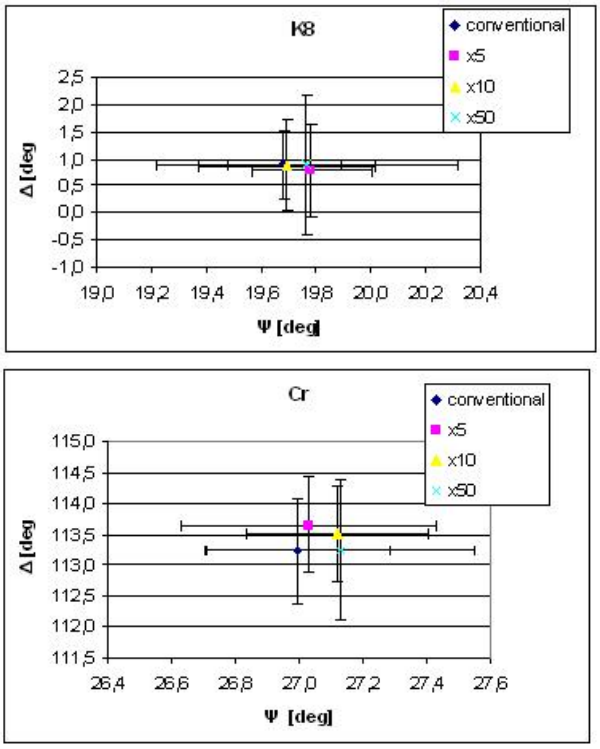


Fig. 8. Results attained for glass K8 and Cr with estimated uncertainty.

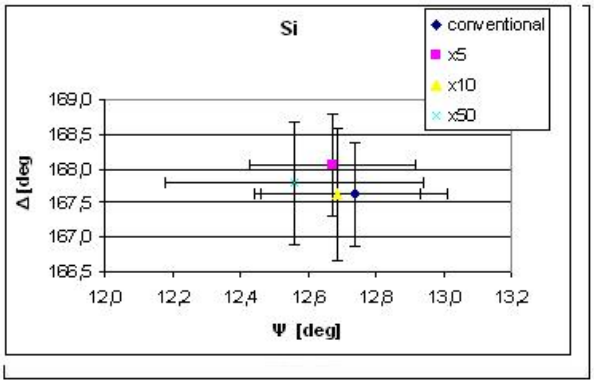


Fig. 9. Results attained for Si with estimated uncertainty.

The results from measurements on photolithographic mask No 1 (Table 2, Fig. 10, up) demonstrate that the variation of ψ and Δ are in the range of the valued uncertainty. The uncertainty increases when the magnification increases. The uncertainty of ψ and Δ measured on micro-object is greater than that of flat surface with the same magnification. This can be caused by scattering of light from the edges of the micro-object. The reached local measurement is of object with size 500×500 μm.

Table 2. 1 – results from conventional measurement; 2, 3 and 4 measurement on large area with objectives with magnification ×5, ×10 and ×50, 5 – measurement on micro-object with size 500×500 μm

Lithographic mask No 1		ψ [deg]	Δ [deg]
1	Cr conventional	31.22 ± 0.19	50.44 ± 0.68
2	Cr ×5	31.22 ± 0.24	50.57 ± 0.59
3	Cr ×10	31.24 ± 0.41	50.27 ± 0.73
4	Cr ×50	31.14 ± 0.27	50.75 ± 0.66
5	Cr ×50 on micro-object	31.33 ± 0.51	50.34 ± 1.20

The results from measurement on photolithographic mask No 2 are shown in Table 3 and Fig. 10, down. The ellipsometric angles for objects with size 200×400 μm and 50×100 μm are in the range of the estimated uncertainty.

Table 3. Ellipsometric angles for lithographic mask No 2

200×400 μm		50×100 μm	
ψ [deg]	Δ [deg]	ψ [deg]	Δ [deg]
14.09 ± 0.67	28.73 ± 1.54	14.25 ± 0.98	29.30 ± 1.88

Example of minimizing the intensity on different objects is shown in Fig. 11. Under different conditions ellipsometric null is achieved on the object or in the background.

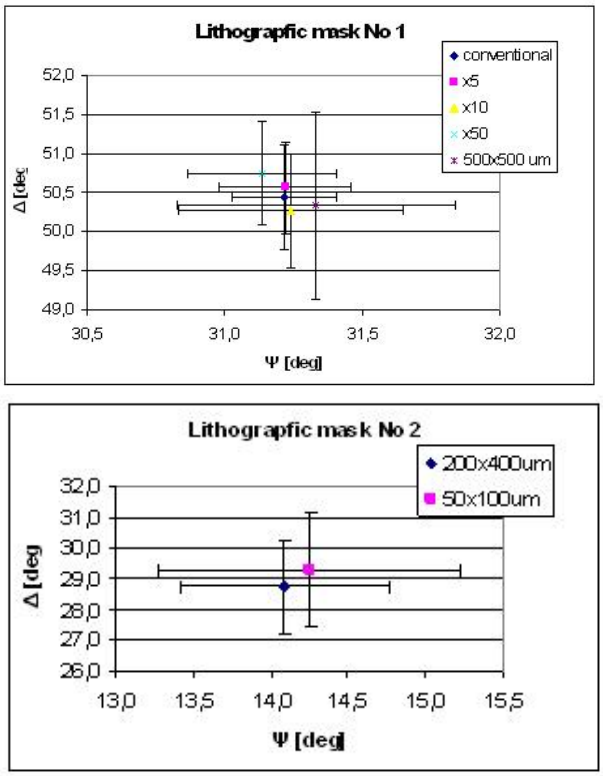


Fig. 10. Results for lithographic masks No. 1 and No. 2 with estimated uncertainty.

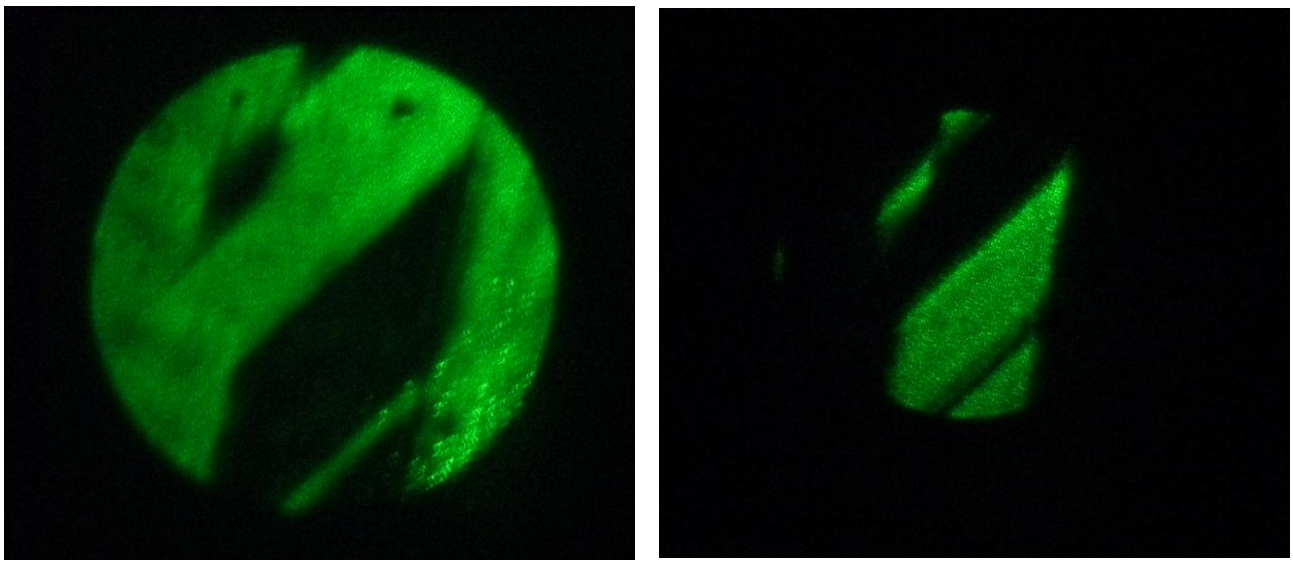


Fig. 11. Image of the photolithographic mask No 2, projected on the screen. **left**: the minimizing of the intensity is on metal surface. **right**: the minimizing of intensity is on the glass surface.

CONCLUSIONS

Two prototypes of ellipsometric devices for micro-ellipsometry were made. They were tested on micro-objects and compared by conventional measurements on large surfaces of the same material. It is demonstrated that ellipsometric measurement can be performed on micro-objects with accuracy close to that of the conventional measurement.

Several improvements can be made. One of them is adding azimuth indicator to the compensator which will allow four-zone measurements. This will remove the errors caused by imperfections of the optical elements. Another improvement is using photo detector which will increase the accuracy of detecting the ellipsometric null. The experimental setup can also be used for imaging ellipsometry.

REFERENCES

[1] M. A. Cohen Stuart, R. A. J. Wegh, J. M. Kroon, E. J. R. Sudhölter, *Langmuir* **12**, 2863-2865 (1996).

[2] Z. Kozarac, D. Moebius, M. T. Martin, *Water Res.* **34**, 1463–1472 (2000).

[3] I. Kubo, S. Adachi, H. Maeda, and A. Seki, *Thin Solid Films* **393**, 80-85 (2001).

[4] S.-H. Ye, Y. K. Kwak, S. H. Kim, H. M. Cho, Y. J. Cho, W. Chegal, D. G. Seiler, A. C. Diebold, R. McDonald, C. M. Garner, D. Herr, R. P. Khosla, E. M. Secula, "Development of a Focused-Beam Ellipsometer Based on a New Principle" in *AIP Conference Proceedings* **931**, 69–73 (2007).

[5] G. D. Feke, D. P. Snow, R. D. Grober, P. J. de Groot, L. Deck, *Appl. Opt.* **37**, 1796–1802 (1998).

[6] U. Wurstbauer, C. Röling, U. Wurstbauer, W. Wegscheider, M. Vaupel, P.H. Thiesen, D. Weiss, Dieter, *Appl. Phys. Lett.* **97**, 231901 (2010).

[7] A. J. Choi, T. H. Ghong, Y. D. Kim, J. H. Oh, J. Jang, *J. Appl. Phys.* **100**, 113529-113529-5 (2006).

[8] H. K. Pak, B. M. Law, *Rev. Sci. Instrum.* **66**, 4972-4976 (1995).

[9] K. R. Neumaier, G. Elender, E. Sackmann, R. Merkel, *EPL (Europhysics Letters)* **49** 14 (2000).

[10] L. Asinovski, D. Beaglehole, M. T. Clarkson, *Physica Status Solidi (a)* **205**, 764–771 (2008).

[11] R. M. A. Azzam, N. M. Bashara, *Ellipsometry and polarized light*, North-Holland personal library, North-Holland Pub. Co. (1977).

[12] D. L. Lyutov, K. V. Genkov, A. D. Zyapkov, G. G. Tsutsumanova, A. N. Tzonev, L. G. Lyutov, S. C. Russev, *Mater. Chem. Phys.* **143**, 642–646 (2014).

[13] P. B. Johnson, R. W. Christy, *Phys. Rev. B* **6**, 4370–4379 (1972).

ЕЛИПСОМЕТРИЯ НА МИКРООБЕКТИ И СТРУКТУРИ

Д. Лютов, Г. Цуцуманова, Ст. Русев

Физически факултет, Софийски университет "Св. Климент Охридски",
ул. "Джеймс Баучер" №5, 1164 София, България

(Резюме)

Елипсометрията е бърз, безразрушителен и безконтактен метод за изследване на оптични свойства на обемни материали, тънки слоеве и многослойни структури. Този метод намира приложение в много области като изследването на твърдотелни структури, образуването на слоеве върху твърда или течна повърхност, микроелектрониката, химията и биологията.

Едно от основните предимства на този метод е, че има висока точност и е много чувствителен към изменения на повърхността. Конвенционалната елипсометрия има тази чувствителност по направление нормално на повърхността на образеца. Разделителната ѝ способност по повърхността на образеца е малка – от порядъка на милиметри. За изследванията на микро обекти е необходима значително по-добра разделителна способност.

В тази работа е представена конструкцията и характеризирането на прототип на елипсометрична апаратура с подобрена странична разделителна способност с възможност за локално измерване на елипсометричните ъгли и тестването ѝ върху различни структури и микрообекти.

Bulgarian Chemical Communications, Volume 47, Special Issue B (pp. 147–154) 2015

Ellipsometric detection of optically and electron-beam induced changes in the optical properties of materials

S. A. Hadjiiski*, D. L. Lyutov, K. M. Kirilov, K. V. Genkov, G. G. Tsutsumanova, A. N. Tzonev, S. C. Russev

Department of Solid State Physics and Microelectronics, Faculty of Physics, St. Kliment Ohridski University of Sofia, 5 James Bourchier Blvd., BG-1164 Sofia, Bulgaria

The main purpose of this paper is to present the results of a preliminary study of the possibility to combine two experimental methods: ellipsometry and scanning electron microscopy (SEM). Ellipsometry is a well-developed non-destructive contactless method with great sensitivity to optical properties and/or geometry of the investigated specimens in the direction perpendicular to the interface. Its lateral resolution, however, is limited by the size of the probe beam and is lesser than what could be achieved with SEM. With regard to the latter, along with the already exploited interactions (collecting secondary and/or backscattered electrons, cathodoluminescence, EDX, etc.), electron beam irradiation leads to local temperature changes and carrier injection. Ellipsometric measurement of the subsequent refractive index alteration could be used for visualization of thermal properties with micron resolution. A series of simulations were performed to study the electron beam heating effect in SEM and to estimate the optimal conditions for its optical detection. Model experiments were also conducted to confirm the results, obtained by the simulations.

Key words: ellipsometry, SEM, refractive index changes, electron beam heating, thermo-optic coefficient, carrier injection

INTRODUCTION

Ellipsometry is a well-developed method for studying the optical properties of materials by measuring changes in the polarisation of a probe beam after interaction (usually reflection) with the specimen. It is a contactless and non-destructive technique that is commonly used not only in science laboratories but in industrial facilities as well. In the context of ellipsometry a forward and inverse problem are considered. The latter involves estimating the values of some of the material properties by interpreting the measured optical response of the specimen. This is often a complex problem that has to be solved numerically, but with the contemporary computational resources and technology it is possible to conduct accurate measurements in real-time. With longitudinal resolution of 1 Å and less [1], ellipsometry can be used for high-precision control over thickness of thin films and layers. However, the signal is averaged over the entire irradiated area, so the lateral resolution is limited by the probe beam diameter. Furthermore, only a single point of the specimen is observed. It is possible to obtain a raster image of a larger area by translating the interaction spot over the specimen (scanning ellipsometry) [2]. Alternatively, a full-field image can also be achieved with imaging ellipsometry [1] – basically the photodetector is replaced by a CCD camera, each pixel of which is then used as a separate detector.

Significantly greater lateral resolution is inherent for SEM – top values are in the range of 1-10 nm [3]. The specimen is scanned by beam of accelerated electrons that interact with it in various ways. Some of the interactions can be used to collect data about the material [3]: topology can be observed by collecting secondary (SE) and/or backscattered electrons (BSE); elemental composition can be determined roughly by collecting BSE and more precisely with energy-dispersive (EDX) or wavelength-dispersive x-ray spectroscopy (WDX). However, there are electron-matter interactions that are still unexploited as data sources, e.g. electron-beam induced heating of the specimen [4–6] and carrier injection. Both effects result in local refractive index changes, modulated at the scanning frequency. Such alterations can be detected optically, ellipsometrically in particular.

Our work involves investigating the possibility to employ a new data source in SEM – the ellipsometric measurement of local electron-beam induced changes in the refractive index of the specimen. Although, our present investigations are focused on thermal effect modulation, they can be easily extended to carrier injection effect as well. Despite the fact that similar studies are already present (e.g. thermo- [7, 8] and

* To whom all correspondence should be sent: shadjiiski@gmail.com

© 2015 Bulgarian Academy of Sciences, Union of Chemists in Bulgaria

photoreflectance [9, 10], scanning electron acoustic microscopy (SEAM) [11]), the combination of SEM and ellipsometry up to our best knowledge has never been considered. Therefore a series of simulations have been performed to study the possibility for signal generation and the optimal conditions for its optical detection. Furthermore, model experiments have been conducted to verify and confirm that it is indeed possible to achieve detectable signal.

THERMAL BALANCE SIMULATIONS

Theoretically speaking, the specimen temperature should be locally risen by the electron beam irradiation and the heating effect should vanish shortly after the beam moves to another location. Therefore the process of signal extraction from this effect is very similar to the thermoreflectance problem [7, 8]. However the already conducted experiments usually employ light beams that are collimated or focused by objective lens from regular optical microscope. In the case of SEM the diameter of the electron beam is significantly smaller, so it is possible that the heating effect would be negligible and therefore impossible to measure. Furthermore there is a possibility that the material under examination is too inert (with respect to the heating modulation), which would cause dephasing of the induced thermal signal and the modulated incident beam, and additionally trouble the interpretation of the measured results.

All of the mentioned potential problems are prerequisites for conducting a more in-depth study of the

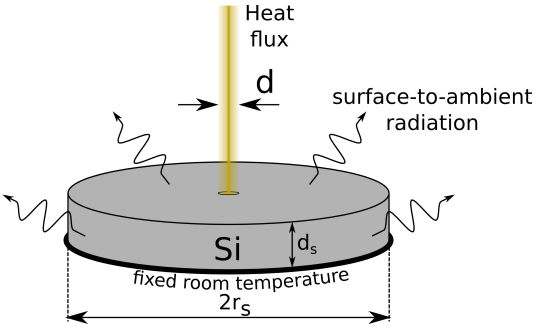


Fig. 1. Schematic representation of the set-up used for the simulations. A cylindrical Si-specimen with diameter $2r_s = 5$ mm and thickness $d_s = 1$ mm is heated by a beam (heat flux), with an integral energy of 90 mW, having Gaussian distribution of the energy. The beam diameter $d = 6\sigma$ may vary (1 μm $\leq d \leq$ 50 μm). The bottom side of the specimen has constant temperature (293 K), whereas the other surfaces may cool down via surface-to-ambient radiation mechanism

electron-beam heating effect on micron scale. For this purpose a series of thermal balance simulations has been performed by specialised software – COMSOL Multiphysics. The simulated experimental setup is shown in Fig. 1: a cylindrical silicon specimen with diameter $2r_s = 5$ mm and thickness $d_s = 1$ mm is considered.

By means of the simulations, the heat transfer equation, Eq. (1), is solved(k stands for the material's thermal conductivity, and Q_i are all the heat sources (positive value) and heat sinks (negative sign) in W/m^3 units).

$$\rho C_P \frac{\mathrm{d}T}{\mathrm{d}t} - \nabla \cdot (k \nabla T) = \sum Q_i \qquad (1)$$

To reach the desired solution some boundary conditions have been set. The bottom side of the cylindrical shaped sample has constant temperature of 293 K, which is also considered to be the initial temperature of the entire specimen. The rest of the surface is cooled by surface-to-ambient radiation, described by the following equation:

$$-\vec{n} \cdot (-k \nabla T) = \varepsilon \sigma_S \left(T_0^4 - T^4\right) \qquad (2)$$

The left-hand side of this equation represents the heat flux through the specimen surface. Since the only considered in our model way for the specimen to cool down is radiation, the right-hand side of Eq. (2) is simply the Stefan-Boltzmann law, applied for grey body. In the discussed equation $\vec{n}$ is normal vector to the specimen surface, k is the specimen's thermal conductivity, σ_S is the Stefan-Boltzmann constant and T_0 is the room temperature. The material's emissivity ε accounts for the deviation from the black-body radiation model.

Due to heating, the boundary condition for the top side is slightly more complicated.

$$-\vec{n} \cdot (-k \nabla T) = \varepsilon \sigma_S \left(T_0^4 - T^4\right) + P_0 G(r, \sigma)\, w(t) \qquad (3)$$

Here a Gaussian-distribution $G(r, \sigma)$ of the energy is considered, the beam diameter is estimated by the standard deviation ($D = 6\sigma$). P_0 is the integral power of the heat source and $w(t)$ is a modulation function that simulates chopping of the heating beam. The nature of the energy flux source is not defined, so any result from these simulations apply for both heat sources: electron and laser beams. This is an important notice, as some of our experiments model the SEM heating effect by introducing a focused laser beam.

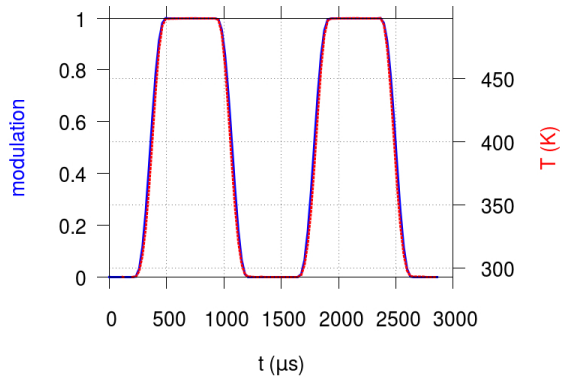


Fig. 2. Time dependences of the thermal (solid blue line) and the incident modulated signal (700 Hz, d= 5 mm, 90 mW.) (dashed red line). Modulation is a (smoothed) square-wave signal that is used to chop the flux of the heat source. T(k) is the temperature in the center of the heated area (measured on the specimen surface).

The simulations show that under typical conditions (beam diameter, integral heating power, modulation, etc.), the expected dephasing between the modulated incident and the induced thermal signals is negligible. Representative time dependences for incident 700 Hz modulated signal, with a beam diameter of 5 micrometers, and integral power of the heat source 90 mW, and that of the induced thermal signal are shown in Fig. 2. Simulations covered frequencies up to 1 kHz and no dephasing was observed even at the upper boundary. The results show the possibility of employing a thermoreflectance-like technique for material investigations.

The possible temperature amplitudes have also been simulated. A representative plot is shown in Fig. 3 where the incident beam modulation frequency of 700 Hz and 90 mW integral incident power were fixed and the beam diameter was varied. It is evident that with well focused beam it is possible to achieve relatively high temperature amplitudes. To ensure that such temperature changes are measurable a simple calculation was performed. For silicon the thermo-optic coefficient has order of magnitude $\mathrm{d}n/\mathrm{d}T \sim 10^{-4}$ K^{-1} [12]. By means of an appropriate simulation, the relative changes in the reflection, R, at normal incidence, caused by infinitesimal refractive index alteration, could be estimated to be $(\mathrm{d}R/\mathrm{d}n)/R \sim 10^{-1}$. Therefore the relative reflection change, caused by temperature variations (see Fig. 3), is of the order of $10^{-}5$ K^{-1}, estimated by the following equation:

$$\frac{1}{R}\frac{\mathrm{d}R}{\mathrm{d}T} = \left(\frac{1}{R}\frac{\mathrm{d}R}{\mathrm{d}n}\right)\frac{\mathrm{d}n}{\mathrm{d}T} \qquad (4)$$

Hence, if in the experimental set-up a lock-in amplifier with threshold $\left(\frac{\Delta R}{R}\right)_{\mathrm{th}} \sim 10^{-6}$ is employed, the discussed relative variation of the reflectance, caused by the discussed temperature variations (see Fig. 3) can be considered detectable.

As stated above, the signal detection is optical – a probe beam is used to measure the changes in the materials reflection coefficient. Thus another concern raises – the heating effect could be focused in such a

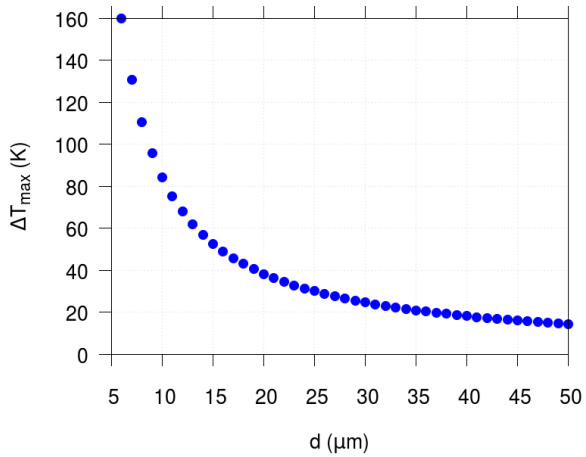


Fig. 3. Amplitude of the induced signal in the center of the heated area (see the red plot on Fig. 2), ΔT_{max}, as function of the beam diameter d. The simulations are done for constant modulation frequency of 700 Hz and integral power of 90 mW of the incident beam.

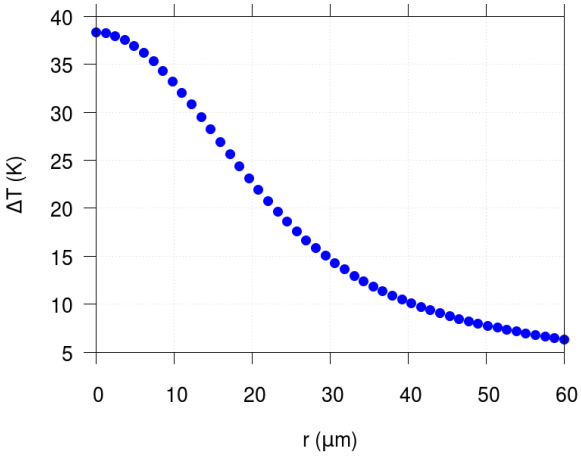


Fig. 4. Dependence of the induced thermal signal amplitude (see the red plot on Fig. 2), ΔT, on the radial distance from the beam (heat source) center. The incident beam has modulation frequency of 700 Hz, integral power 90 mW and 20 μm diameter.

tiny area, that it is much smaller than the field, illuminated by the probe beam. As already mentioned, the received signal is integrally averaged over the entire irradiated area, i.e. it is possible that the generated signal would be too weak for detection even with the used lock-in amplification methods. Therefore the radial distribution of the surface temperature of the specimen has also been examined. Fig. 4 shows the dependence of the induced thermal signal amplitude on the radial distance from the heating center (all data points are located on the specimen's top surface). Simulation results show that under these conditions the temperature amplitude is detectably high even at the distance of 60 μm. Our experience shows that with the use of standard optics a probe laser beam of about 200 microns in diameter can be achieved. Hence, the induced thermal signal, even localized around the incident beam, could be detected by means of optical methods.

OPTIMAL CONDITIONS FOR DETECTION OF THERMALLY-INDUCED ALTERATION OF THE REFRACTIVE INDEX

Even if one has achieved a measurable SEM beam heat effect, a lack of optimal experimental conditions could trouble the success of the experiments. Thus an important part of the current research is to define the optimal conditions for optical detection of the thermally-induced changes in the refractive index, i.e. to examine the sensitivity of the ellipsometric angles (ψ,Δ) with respect to the incident angle of the probe beam. The sensitivity of the reflection coefficients for both polarizations, R_p and R_s, having more general meaning, were also investigated, in order to find out whether optimal conditions exist, at which utilizing simple model experiments the general idea of the present work could be tested. Here, the theoretical optical response of a bulk material is simulated. For each of the four investigated parameters (ψ,Δ,R_p or R_s) several steps are performed. Let F be any of those 4 parameters, then the simulation steps were as follows:

- Tabulation of F for discreet set of incidence angles, in the interval from 0° to 90°, with a step of 0.1°, assuming a constant refractive index;
- Alteration of the refractive index by $\Delta n = 0.001$ and subsequent tabulation of F_{alt} in the same interval as F;
- as the thermo-optic coefficient $\mathrm{d}n/\mathrm{d}T$ is relatively stable under constant external conditions, the sensitivity S, with respect to the angle of incidence, ϕ, can be evaluated by a derivative of type:

$$S(\phi) = \left(\frac{\mathrm{d}F}{\mathrm{d}T}\right)_{\phi} \approx \frac{\mathrm{d}n}{\mathrm{d}T}\,\frac{F_{\mathrm{alt}}(\phi) - F(\phi)}{\Delta n} \qquad (5)$$

In the simulations, three different types of materials were involved: with real refractive index (glass); with complex refractive index (gold and silver); system with complex refractive index of the substrate and a dielectric thin layer with known thickness, grown onto the substrate (SiO_2 layer applied onto a silicon substrate). Representative graphics for the last group are shown in Fig. 5. Based on the detailed analysis of the obtained results, the optimal values of the incident angle depending on the particular investigated optical parameter were defined (see Table 1).

MODEL EXPERIMENTS

The satisfactory simulation results were a strong motive for going further and conducting some simple model experiments. Their main purpose was to confirm the possibility to achieve optically detectable changes in the refractive index of a material, induced by heat source(beam), mimicking the SEM electron beam interaction with the specimens.

Initial experiments were performed with a set-up, which scheme is given in Fig. 6, where the heating effect is achieved by applying square-wave electrical pulses to the specimen (a 20 nm gold layer).

Table 1. Optimal angle of incidence, ϕ_{opt}, and polarization for investigation of different ellipsometric angles (ψ,Δ) and reflection coefficients (R_p,R_s) for different materials

Material	With regard to ψ,Δ	With regard to R_p,R_s	
Glass	$\phi_{\mathrm{opt}} = 60^\circ$	$\phi_{\mathrm{opt}} = 0^\circ$	s-polarization
Silver	$65^\circ \le \phi_{\mathrm{opt}} \le 75^\circ$	$0^\circ \le \phi_{\mathrm{opt}} \le 75^\circ$	both
Gold	$65^\circ \le \phi_{\mathrm{opt}} \le 75^\circ$	$0^\circ \le \phi_{\mathrm{opt}} \le 75^\circ$	both
Si / SiO_2 (5 nm)	$\phi_{\mathrm{opt}} = 75^\circ$ (narrow interval)	$\phi_{\mathrm{opt}} = 0^\circ$	s-polarization
Si / SiO_2 (180 nm)	$55^\circ \le \phi_{\mathrm{opt}} \le 75^\circ$	$\phi_{\mathrm{opt}} = 70^\circ$	both

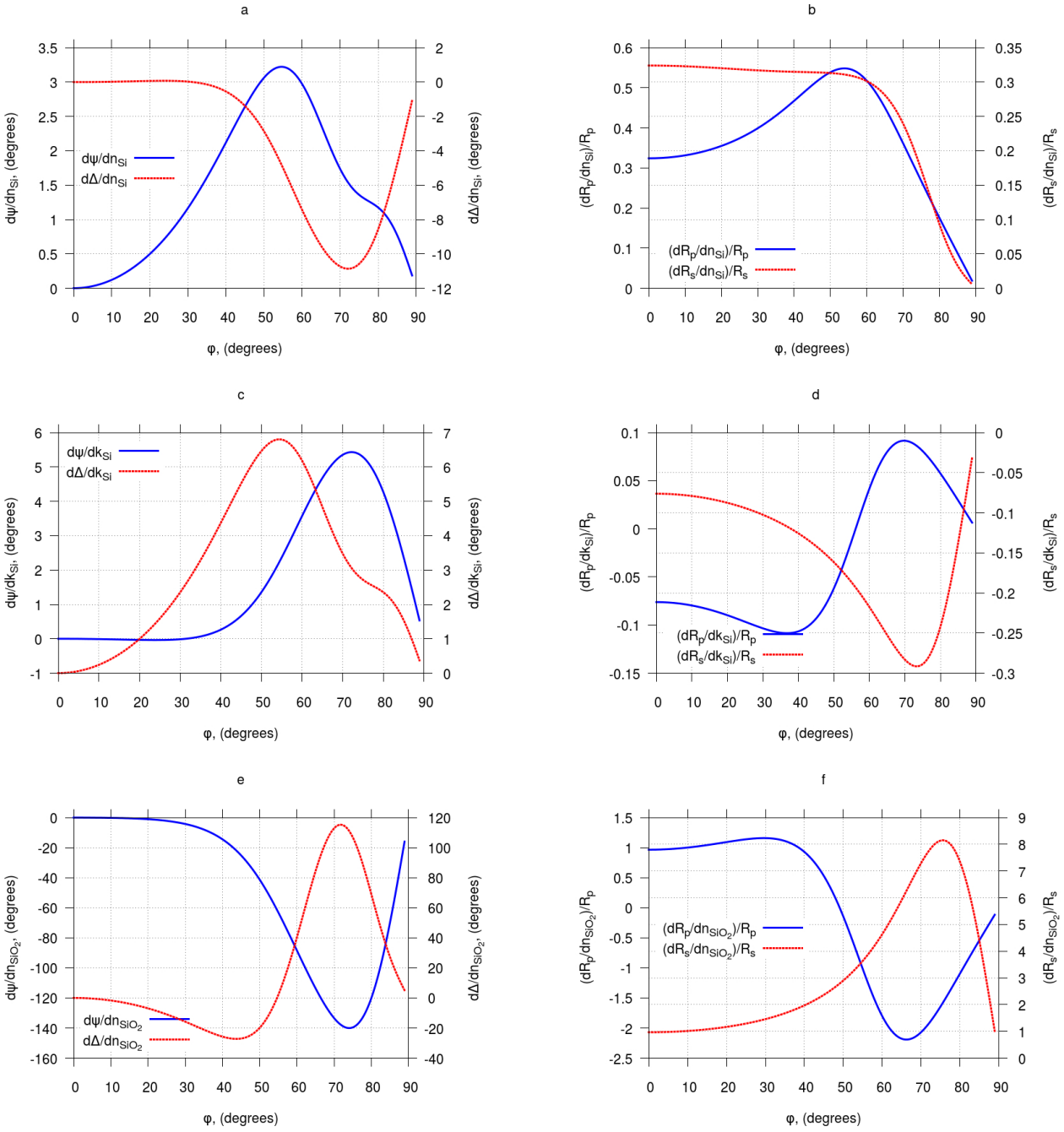


Fig. 5. Results (simulation) for a thin 180 nm SiO_2 layer, grown onto a Si substrate. Dependences on the angle of the beam incidence, ϕ, of the optical response of the system with respect to different ellipsometric and optical parameters: **a)** The optical response $d\psi/dn$ and $d\Delta/dn$ where ψ and Δ are the ellipsometric angles and dn is infinitesimal change in the real part of the refractive index of Si. The complex part, k, as well as the refractive index of SiO_2 are considered constant; **b)** the optical response with respect to the more general parameters, the reflection coefficients R_p and R_s (same conditions as a.); **c)** $d\psi/d\kappa$ and $d\Delta/d\kappa$, where the complex part of the Si refractive index is varied (constant real part and SiO_2 refractive index); **d)** Optical response with respect to R_p and R_s under the same conditions as c.; **e)** $d\psi/dn$ and $d\Delta/dn$, when the refractive index of SiO_2 is varied and that of the silicon remains constant; **f)** Optical response of the system with respect to R_p and R_s (same conditions as e.).

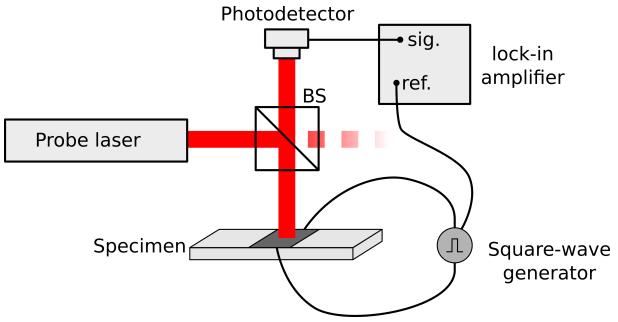


Fig. 6. Set-up for the electrically heating sample experiment. A 20 nm thick gold film(specimen) was heated by square-wave current pulses with chosen frequency and duty cycle (heating power is approximately 1.3 W). A 658 nm semiconductor laser provided the probe beam. A lock-in amplifier was used to analyze the signal. The photodetector used was Thorlabs PDA36A.

Refractive index changes were detected by continuous monitoring the intensity of a normally reflected probe beam. The pulse frequency and duty cycle could be controlled by the operator. Synchronizing pulses were also fed from the generator to the lock-in amplifier, which analyses the signal and measures its amplitude at low signal-to-noise ratio. Due to insufficient isolation from external noises, good reproducibility of the experiments was not achieved, but our observations made it evident that variation of the

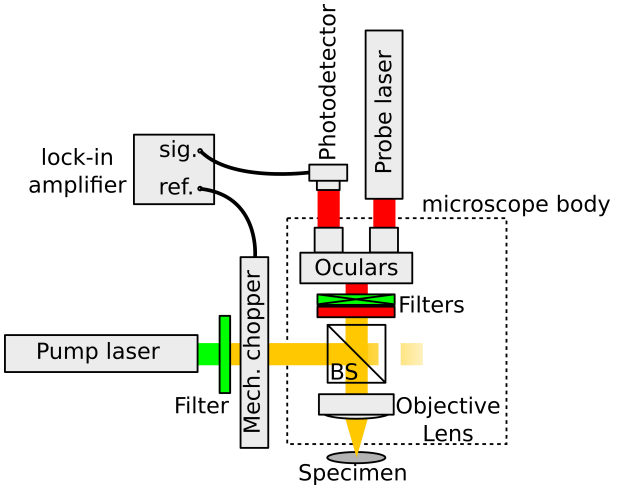


Fig. 7. Set-up for the laser heating experiment. A pump laser (532 nm) is focused on the specimen, providing the heating effect. Incident beam modulation (723 Hz, 50% duty cycle) is achieved by mechanical chopper. The probe laser (658 nm) passes through the oculars and the objective lens, then reflects normally. The photodetector used was Thorlabs PDA36A. Both laser beams are spectrally isolated.

pulse amplitude changed the indication of the lock-in amplifier, i.e. a desired sensitivity of the method existed. We believe that the generated thermal signal could be measured, provided that the external noises are eliminated.

Apart from the expected optical signal, also acoustic wave generation was detected. Surprisingly, the sound was loud enough to be heard by the operator in a silent laboratory, i.e. the acoustic signal seemed to be much more intense than the optical one. However, future use of this side effect is yet to be discussed, since the sound waves, which were generated in our experiment in air, have to be detected in appropriate manner, since the experiments in SEM chamber are carried out under vacuum. Similar results have been obtained before, and an entire experimental technique has been developed, known as SEAM [11].

A second series of experiment was also conducted. The experimental set-up (Fig. 7) was built to better resemble the real experimental conditions. As heat source, a laser beam (semiconductor laser with wavelength of 658 nm) was used, which modulation was achieved by mechanical chopper. For more stable and easily constructed assembly, a standard optical microscope was used. Its objective lenses focus both the probe and the pump laser beams on the specimen surface. To spectrally isolate the beams colour filters were used.

The probe laser beam passes through one of the oculars, and then normally reflected beam (from the specimen surface) reaches the photodetector, mounted into the other ocular. The signal is once again analyzed by a lock-in amplifier. A total of two materials were examined: silicon and indium phosphide plates. The obtained initial results are shown in Table 2. Despite the small amount of conducted experiments, a good data reproducibility under constant conditions was observed. However, there were

Table 2. Experimental values of relative reflection coefficient, $\Delta R/R$, with respect to the gain, B, of the photodetector, for two different samples, obtained by the set-up, shown in Fig. 7

.

Specimen	$(\Delta R/R) \times 10^6$	B, dB
Si	25	60
InP	10	50
InP	7	50
InP	20	60
InP	16	60

still external noise sources present, e.g. the vibrations of the mechanical chopper. An interesting observation was the non-linearity of the gathered signal – although the relative reflection coefficient changes were measured ($\Delta R/R$), different gain levels of the detector's pre-amplifier yielded different signal amplitudes (see Table 2). This result is still to be investigated, since the DC signal levels were well below the detector's saturation cap in all measurements.

CONCLUSIONS

In general, heating effect and/or carrier injection induced by accelerated electrons, result in material refractive index variation. The possibility to detect such alterations by means of optical methods and in particular with ellipsometry, was investigated. A series of simulations has been performed, and the results confirmed that detectable signal could be generated, when a heat effect appeared in a sample, heated by a beam (heat source). Another series of simulations helped one to find the optimal condition for signal detection. Based on these results, two simple set-ups were built up and model experiments were conducted. The experimental results confirm in general, the sensitivity of the reflection coefficient to the induced, by the heat, local optical properties changes. Thus it is noteworthy to continue the research with new, more realistic experiments, e.g. measuring the optical response under high vacuum and moving on to determine the ellipsometric angles instead of reflection coefficient.

REFERENCES

[1] H. Fujiwara, *Spectroscopic Ellipsometry: Principles and Applications*, Wiley (2007).

[2] R.M.A. Azzam, N.M. Bashara, *Ellipsometry and polarized light*, North-Holland personal library, North-Holland Pub. Co. (1977).

[3] R. Egerton, *Physical Principles of Electron Microscopy: An Introduction to TEM, SEM, and AEM*, Springer (2006).

[4] D. Bouscaud, R. Pesci, S. Berveiller, E. Patoor, *Ultramicroscopy* **115**, 115–119 (2012); http://dx.doi.org/10.1016/j.ultramic.2012.01.018

[5] M. Liu, L. Xu, X. Lin, *Scanning* **16**, 1–5 (1994); http://dx.doi.org/10.1002/sca.4950160102

[6] J. A. Morrison, S. P. Morgan, *Bell System Technical Journal* **45**, 661–687 (1966); http://dx.doi.org/10.1002/j.1538-7305.1966.tb01051.x

[7] D. G. Cahill, P. V. Braun, G. Chen, D. R. Clarke, S. Fan, K. E. Goodson, P. Keblinski, W. P. King, G. D. Mahan, A. Majumdar, H. J. Maris, S. R. Phillpot, E. Pop, L. Shi, *Appl. Phys. Rev.* **1**, 1–45 (2014); http://dx.doi.org/10.1063/1.4832615

[8] A. J. Schmidt, R. Cheaito, M. Chiesa, *Rev. Sci. Instrum.* **80**, 1–6 (2009); http://dx.doi.org/10.1063/1.3212673

[9] C. R. Brundle, C. A. Evans, S. Wilson, *Encyclopedia of Materials Characterization: Surfaces, Interfaces, Thin Films*, Characterization Series, Butterworth-Heinemann (1992).

[10] J. Misiewicz, P. Sitarek, G. Sek, *Opto-Electron. Rev.* **8**, 1–24 (2000).

[11] D. G. Davies, R. E. Green, M. Somekh, G. Busse, *Philos. Trans. R. Soc. London, Ser. A* **320**, 243–255 (1986).

[12] B. J. Frey, D. B. Leviton, T. J. Madison, *Proc. SPIE* **6273**, 62732J–62732J-10, (2006); http://dx.doi.org/10.1117/12.672850

ЕЛИПСОМЕТРИЧНА ДЕТЕКЦИЯ НА ОПТИЧНО И ЕЛЕКТРОННО-ЛЪЧЕВО ИНДУЦИРАНО ИЗМЕНЕНИЕ НА ОПТИЧНИТЕ СВОЙСТВА НА МАТЕРИАЛИ И СТРУКТУРИ

Ст. Хаджийски, Д. Лютов, К. Кирилов, К. Генков, Г. Цуцуманова, А. Цонев, Ст. Русев

Физически факултет, Софийски университет "Св. Климент Охридски",
ул. „Джеймс Баучер" №5, 1164 София, България

(Резюме)

Целта на тази работа е предварително изследване на възможността за съчетаване на предимствата на две различни експериментални техники – елипсометрия и сканираща електронна микроскопия (СЕМ). Елипсометрията е добре развит безконтактен и безразрушителен метод с много добра чувствителност по отношение на изменение на оптичните свойства и/или геометрията, перпендикулярно на интерфейса, но има ограничена разделителна способност в равнината. От друга страна СЕМ предлага много по-добра разделителна способност, като обикновено детектирания сигнал са вторични или обратно разсеяни електрони, фотони (катодолуминесценция) или рентгеново лъчение (EDX). В допълнение, взаимодействието на електронния лъч с повърхността на образеца води до локално изменение на температурата и до инжекция на токоносители. Това от своя страна изменя локално показателя на пречупване и може да бъде детектирано по принцип елипсометрично, давайки възможност за визуализация на термичните свойства с микронна разделителна способност.

Проведени са редица симулации за изучаване на електронно-лъчевото загряване в СЕМ и са изследвани оптималните условия за оптична детекция. Поставени са и моделни експерименти, потвърждаващи получените от симулациите данни.

Bulgarian Chemical Communications, Volume 47, Special Issue B (pp. 155–161) 2015

Electron-beam annealing of micro-sized objects and structures in SEM

K. V. Genkov*, G. G. Tsutsumanova, S. A. Hadjiiski, A. N. Tzonev, D. L. Lyutov, S. C. Russev

Department of Solid State Physics and Microelectronics, Faculty of Physics,
St. Kliment Ohridski University of Sofia, 5 James Bourchier Blvd., BG-1164 Sofia, Bulgaria

The heating effect of the focused electron beam in a Scanning Electron Microscope (SEM) opens up possibilities for annealing of micro-sized objects and structures. These possibilities are studied by investigating the heating effect under different conditions (beam power, spot size, etc) both by simulations and experiments. By reaching the melting point of the micro objects, it is shown that temperatures, sufficient for annealing, are achievable. Three setups are studied: heating via electron-beam, via tungsten heater and a combined setup.

Key words: SEM, electron beam heating, micro-scale annealing, zone melting

INTRODUCTION

The main purpose of this paper is to demonstrate that a scanning electron microscope (SEM) has the potential to be used as a tool for annealing of micro-sized objects.

SEM is a modern microscopy technique that uses a focused electron beam, scanning on the surface of the specimen. Various detectors analyze the electron-specimen interaction: back-scattered electrons (BSE), secondary electrons (SE), x-ray emission, cathodoluminescence (CL), emission of Auger electrons, etc [1–3]. Apart from all these effects, another consequence is heating of the specimen due to inelastic scattering [2, 4]. In fact, a major part of the energy of the primary electrons turns into heat. At higher beam currents, compared to the normal working conditions for imaging in SEM, the heating effect becomes more significant and could be sufficient for reaching a temperature of the specimen that is close to (and even beyond) its melting point. Further more, since the position of the beam can be precisely manipulated, it can be used for localized annealing of micro-sized objects and structures [5].

This method could be used for enhancing the crystalline structure of microcrystals, evaporating foreign particles, deposited on their surface, microwelding, etc. The production of near-perfect Ag/Au microcrystals is highly demanded in the field of plasmonics since any kind of defects act as scattering centers, leading to losses.

The applicability of SEM for thermal manipulation of micro-sized objects is demonstrated by simulations that evaluate the temperature of the specimen under different conditions and by preliminary experiments where silver microparticles were melted.

* To whom all correspondence should be sent:
kgenkov@uni-sofia.bg

SIMULATIONS

Preliminary data on the temperature across the volume of the electron-beam heated microparticle is obtained by computer simulations performed on COMSOL Multiphysics. The model consists of an Ag hexagonal microplate (same as the particles, used in the experiments) on top of a Si substrate.

For obtaining the thermal balance, the heat equation is solved [6]:

$$\frac{\partial T}{\partial t} = \frac{1}{\rho C_P}\nabla\cdot(k\nabla T) + \frac{q}{\rho C_P}, \qquad (1)$$

where k stands for the material's conductivity and q is the density of the heat power (Wm^{-3}, positive values stand for heat sources while negative – for heat sinks).

The electron-beam heating is modeled as a volumetric heat source, shaped as a rectangular prism with width w, length l and depth h. Reasonable lengths of these dimensions are $w = l = 0.5$ μm (the cross section depends on the field of view and therefore on the magnification) and $h = 200$–300 nm (equals the thickness of the microparticle).

The total power P_{beam} of the beam of accelerated electrons is

$$P_{\mathrm{beam}} = eU\frac{\mathrm{d}N_e}{\mathrm{d}t} = IU, \qquad (2)$$

where e is the electron charge, U – the accelerating voltage, $\frac{\mathrm{d}N_e}{\mathrm{d}t}$ is the flow of electrons and I – the beam current. A typical value for the accelerating voltage is $U = 30$ kV and the maximal beam current (measured by using a Faraday's cage specimen)

© 2015 Bulgarian Academy of Sciences, Union of Chemists in Bulgaria

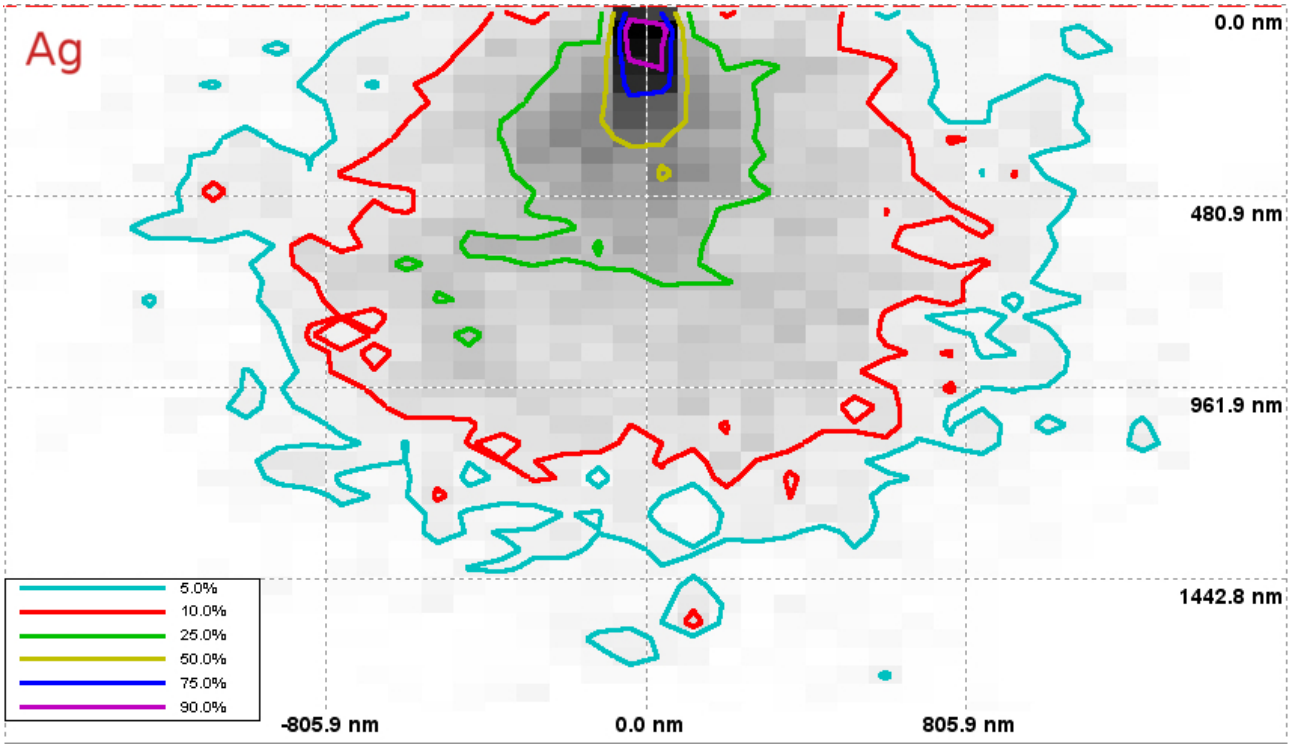


Fig. 1. Distribution of the dissipated energy in Ag. Each contour labeled as $X\%$ surrounds a region, in which $(100-X)\%$ of the energy was dissipated. For example, inside the red contour $(100-10)\% = 90\%$ were dissipated.

Table 1. Boundary conditions of the simulations

Boundary	Condition
Top face of Ag hexagonal prism Side faces of Ag hexagonal prism	Gray body radiation
Interface between Ag and Si substrate	Thermal contact
Bottom face of Si substrate	Fixed at room temperature
Side faces of Si substrate Top face of Si substrate (excluding Ag-Si interface)	Thermally insulated

is $I_{\max} = 18.4\ \mu$A (by specifications, $I_{\max} = 300\ \mu$A, see Table 2).

The heating power Q is less than the total power of the beam:

$$Q = cP_{\text{beam}}, \tag{3}$$

where $0 < c < 1$ is a coefficient that represents the portion of the energy of the primary beam that is transfered as heat in the area of interest and c depends on various parameters, for example the chemical composition of the specimen, its thickness, accelerating voltage, etc. A reasonable value $c = 0.5$ was obtained using the specialized software CASINO that performs Monte-Carlo simulations of the trajectories of the electrons in specimen [7] (Fig. 1).

Finally, assuming that the density of the heating power q is homogeneous across the heating region, it is described by the following equation:

$$q = \frac{cP_{\text{beam}}}{wlh} \tag{4}$$

In order to reach the desired solution, the boundary conditions, listed in Table 1 were set.

The simulations show that, provided the beam is powerful enough and focused on a small area, the heated region has a significantly higher temperature than room temperature. For instance, typical simulations results are shown on Fig. 2. Another important observation is that the temperature rapidly drops outside the heated region, which is crucial for the implementation of zone-melting recrystallization (ZMR) [8].

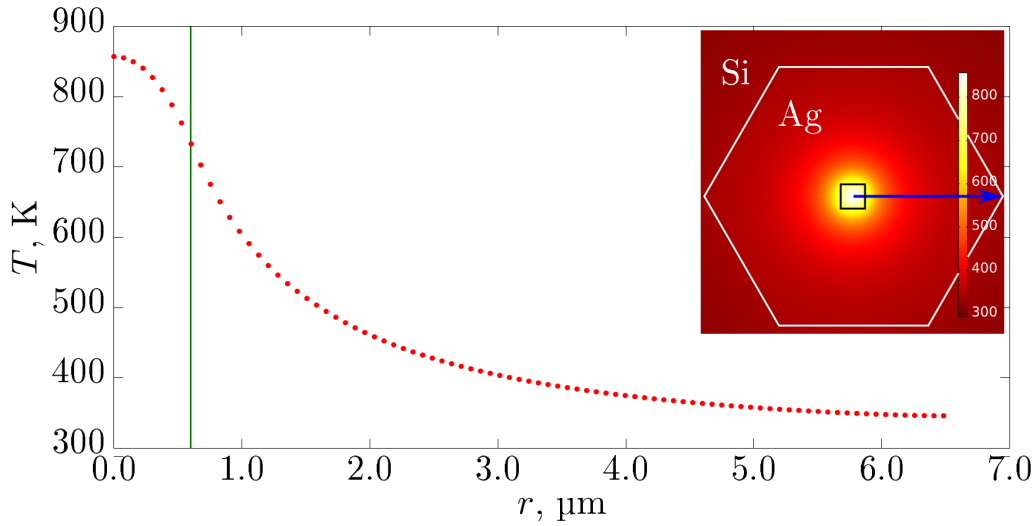


Fig. 2. Line profile of the temperature across the surface of the Ag microparticle (the parameters of the simulation are $l = w = 1.2$ µm, $h = 300$ nm, $P_{\text{beam}} = 0.54$ W). The green line indicates the boundary between the heated and non-heated region. Inset: Colour map of the temperature. The blue arrow corresponds to the x-axis of the figure.

EXPERIMENTAL SETUP AND RESULTS

The experiments were performed in SEM Hitachi S-570, modified to acquire digital images [9].

Table 2. Specifications of SEM Hitachi S-570

Accelerating voltage	3–30 kV
Electrons source	Tungsten filament
Max. beam current	300 µA
Magnification	20×–100000×
Objective aperture	4 holes with different sizes, additional setting with no aperture
Detectors	– Upper in-lens SE detector – Lower SE detector – Measurement of the current through the specimen is possible

Some of the characteristics of the microscope are listed in Table 2. All of the experiments involving high beam current were performed without an aperture. The beam current was controlled by changing the settings of the two condenser lenses. The current through the coils of each condenser lens can be regulated by corresponding knobs (with positions, labeled from 1 to 10, 1 corresponding to the lowest current, therefore longest focal length). By modifying of the focal length of each condenser lens, the image of the filament moves in respect to the condenser apertures, resulting a different amount of electrons passing through the condenser apertures. The electron beam current has been measured using Keithley 617 electrometer. Under normal working conditions for imaging (both condensers knobs set to position 6), the beam current measures up to $I_0 = 5.5$ nA at $U = 28$ kV. When both of the condensers are set to their largest focal distance (position 1), the beam current is maximal: $I_{\text{max}} = 18400$ nA $\approx 3300 I_0$. The beam current was measured at multiple combinations of condenser lens settings and accelerating voltages. Its highest beam power was

$$P_{\text{beam, max}} = 28 \text{ kV} \times 18 \text{ µA} = 0.5 \text{ W} \qquad (5)$$

When the microscope is working at a high beam current, the secondary electrons signal increases drastically. Degradation of the image quality was observed, due to saturation of the scintillator detector and/or photomultiplier. A special remotely-controlled screen (Fig. 3) was constructed to protect the secondary detector in the subsequent experiments.

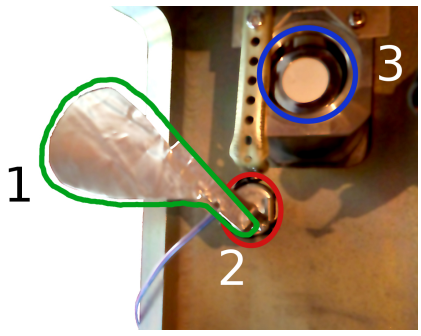


Fig. 3. Protective screen for the SE detector. 1 – aluminum screen, 2 – electric motor, 3 – SE detector.

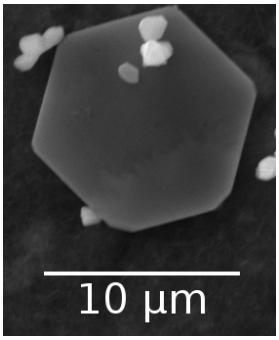


Fig. 4. Silver hexagonal microplate, used in the electron-beam heating experiments.

The micro objects used in the experiments are chemically synthesized silver hexagonal microplates [10]. Their diameter varies between 5–20 μm and their thickness: 200–300 nm. A typical example is shown on Fig. 4.

The goal of these preliminary experiments is to attempt melting of these microplates. If they can be successfully melted, then the beam is powerful enough and after series of further refinements of the experimental setup, the temperature could be set precisely enough for actual annealing.

Results – electron-beam heating

When only electron-beam heating was used, melting was observed at only one configuration of the microscope – the one, giving highest beam power: $U = 30$ kV, both condensers knobs set to 1 (maximal beam current), no objective aperture. One of the successful attempts is shown on Fig. 5. Despite the multiple attempts to melt the particles at lower beam powers, there was no success.

In conclusion, melting of the silver microplates is possible, but only at the beam power set to the maximum possible. In this case, fine tuning of the settings is a challenging task. Furthermore, the resolution of the microscope at these extreme settings is significantly worse, which is an additional complication.

Results – heating by a tungsten filament

These experiments are a preliminary step to the realization of combined heating. The Ag hexagonal microplates were placed on top of a tungsten filament, extracted from a 6 V light bulb (shown on Fig. 6) and then put into the specimen chamber of SEM. The voltage U_{filament}, applied to the filament was gradually increased until melting of the microplates was observed.

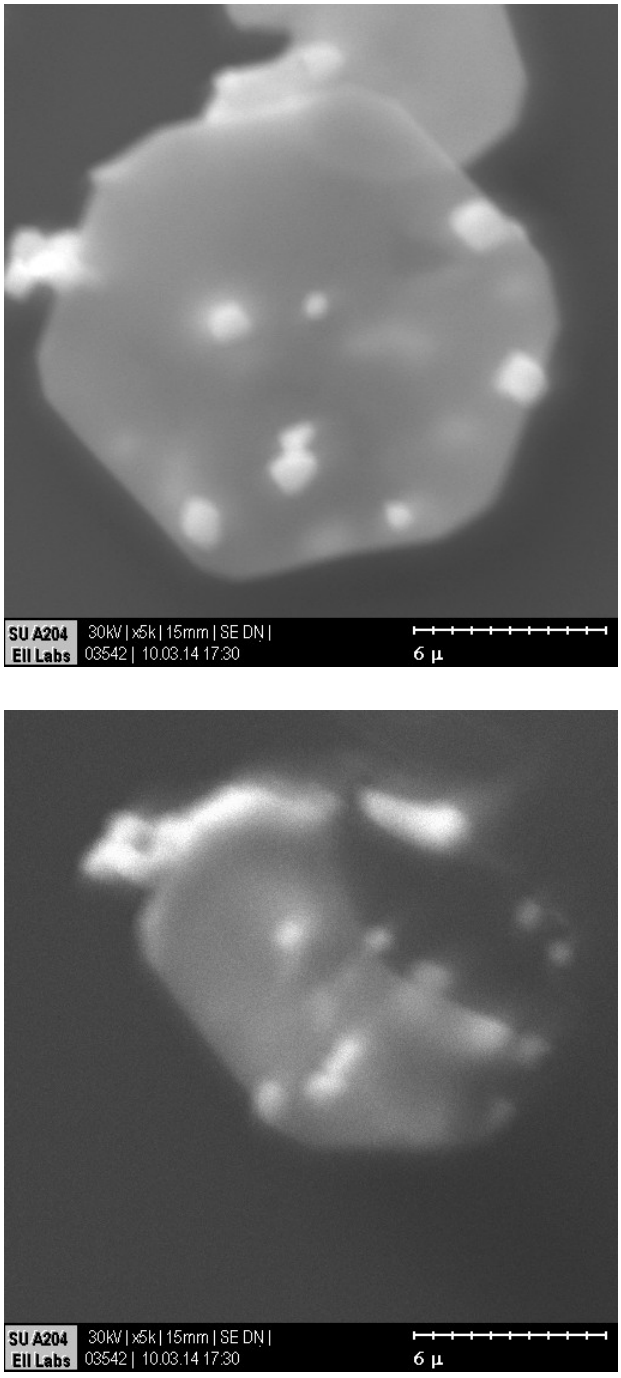


Fig. 5. A successful melting of silver microplates. $U = 30$ kV, both condensers set to 1 (maximal current).

It is worth to mention that the temperature of the filament varies across its length. Typically, it's hottest at the center and cooler at the ends since the copper wires act as a heat sink. A consequence of this is the fact that according to their location, the Ag microplates begin to melt at different filament voltages. More observations are listed in Table 3.

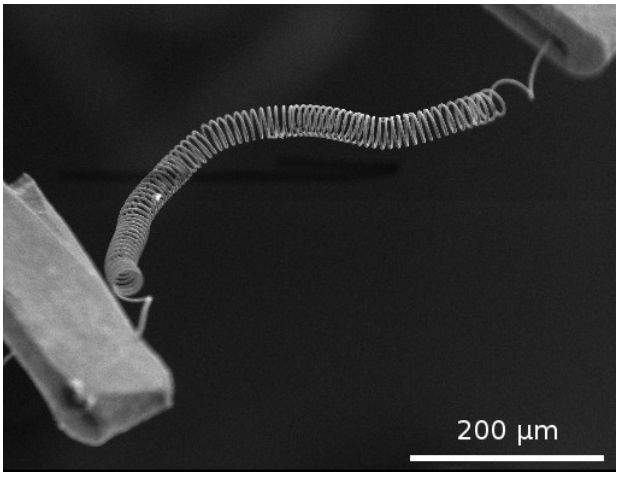


Fig. 6. Tungsten filament, used as a heater

Table 3. Results from the preliminary filament-only heating

Filament voltage	Observations
1.5 V	Particle *A* near the center of the filament start to melt slowly (Fig. 7, top). Particle *B* near the center, attached lightly to the filament shows weak signs of melting (Fig. 7, bottom).
2 V	Particle *B* starts rapid evaporation (Fig. 7, bottom-right).
4 V	Formation of Ag microspheres is observed (Fig. 7, left)
6 V	At the ends of the filament, there are still unaffected silver hexagonal microparticles (Fig. 7, right).

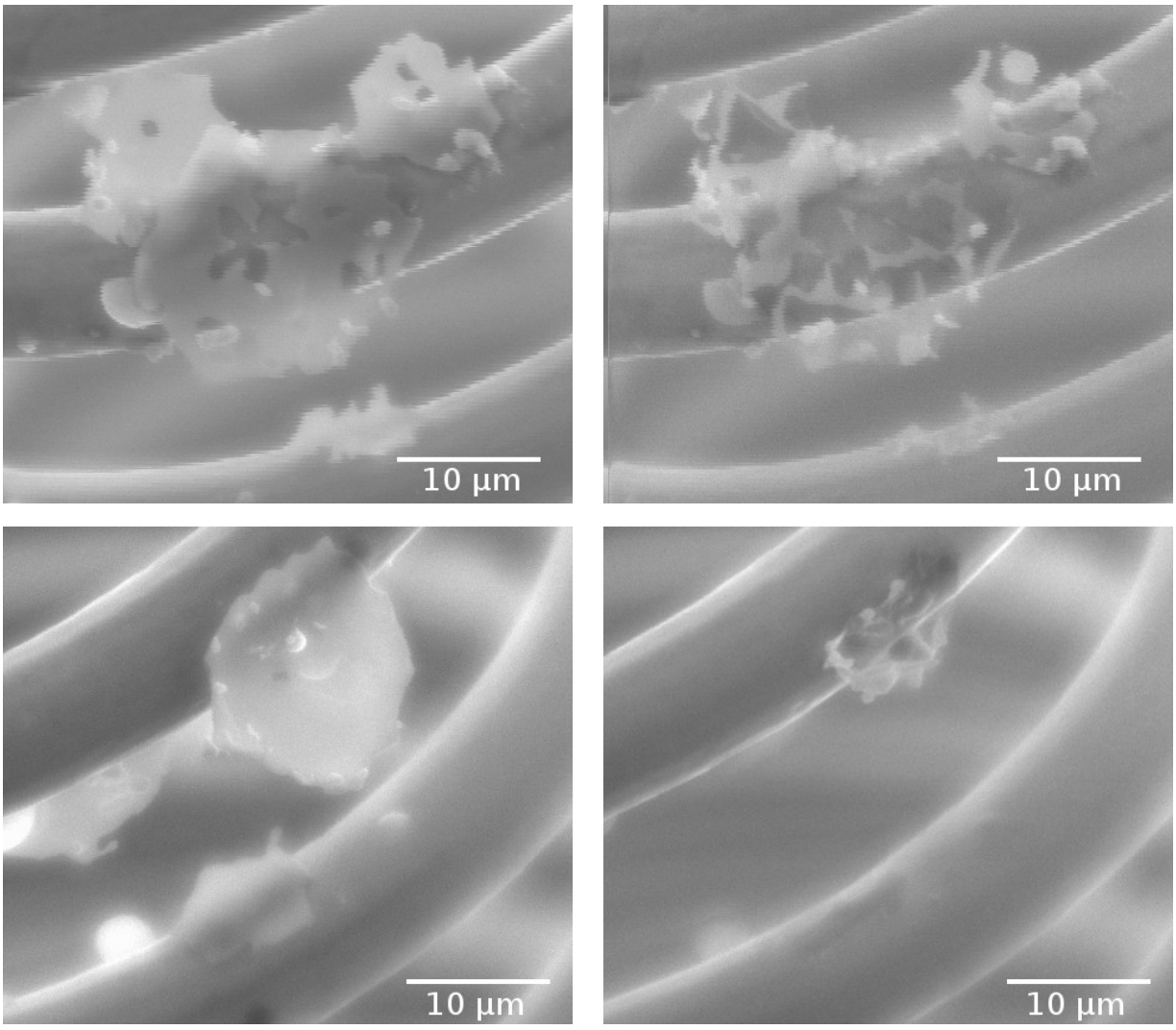


Fig. 7. Top: Particle *A* at two different moments of melting at $U_{\text{filament}} = 1.5$ V. Bottom: Particle *B* starts rapid melting at $U_{\text{filament}} = 2$ V.

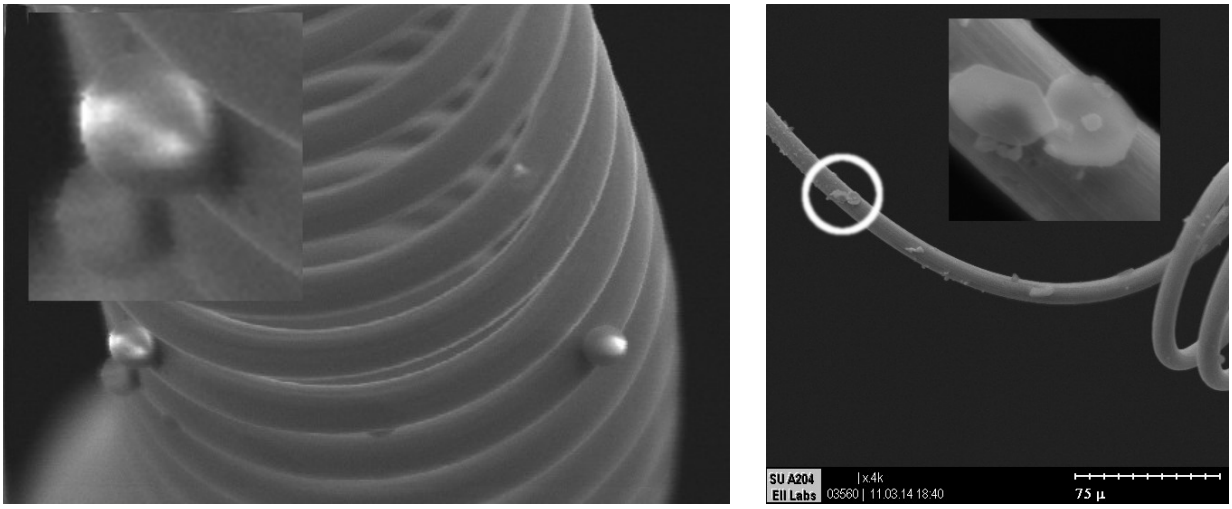


Fig. 8. Left: Silver microspheres at 4 V. Right: Even after heating at 6 V, the particles near the ends of the filament remain unaffected.

Results – combined heating

The combined heating method is proposed to overcome the flaws of the electron-beam only heating. Again, a tungsten filament is used as a heater. It preheats the silver microparticle and less beam power is needed to melt it.

The condenser knobs were both set to 3 (providing less than the maximum beam current, but still noticeably higher, compared to imaging regime). The voltage, applied to the heating filament was gradually increased until melting of the observed microplates started at $U_{\text{filament}} = 0.8$ V (see Fig. 9).

Compared to the previous experiments, the combined heating method needs much less beam power (6.6 mW vs 540 mW in the case of electron-beam heating) and lower filament voltage (0.8 V vs 1.5 V). This method allows finer control of the heating power, while keeping the SEM resolution good enough.

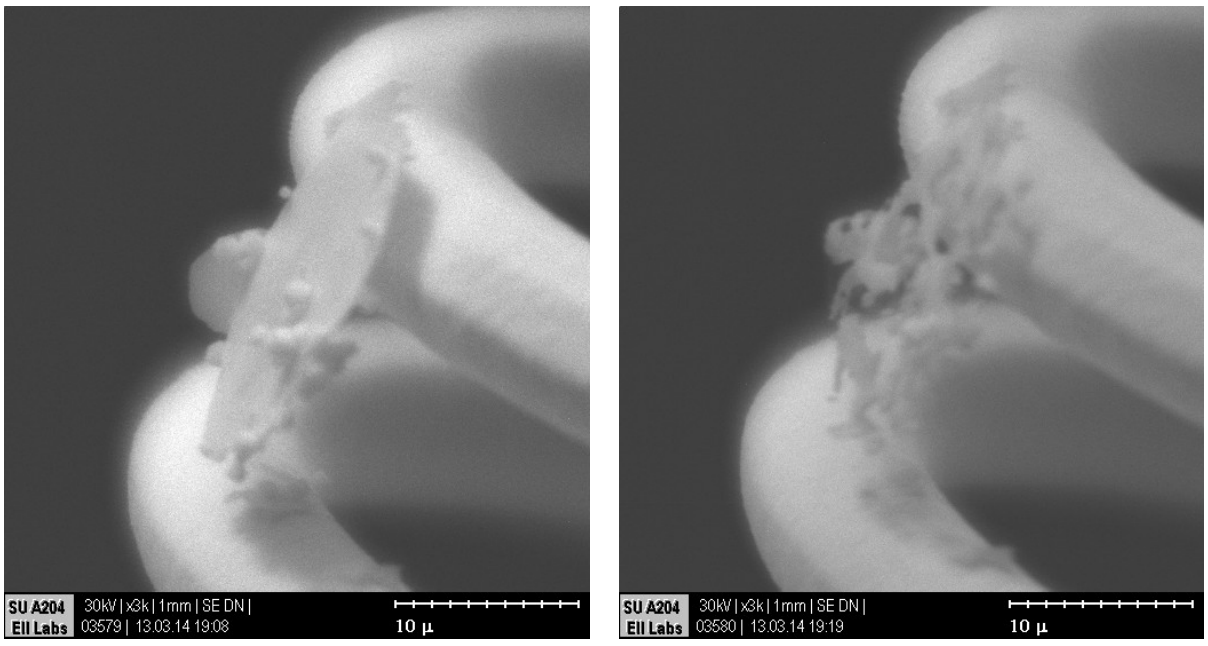


Fig. 9. A successful melting of silver microplates, using both electron-beam heating and filament heating.

CONCLUSIONS

It was shown (both by simulations and by experiments) that it is possible to melt silver microparticles by heating them with electron beam in SEM. Successful melting experiments were only performed when the beam power was set to maximum. To overcome this, a more appropriate setup for precise control of the heating process was proposed, combining electron-beam heating and tungsten filament heater. After further improvements of the setup, it has the potential to be used for zone-melting recrystallization of micro objects. As a side result, spherical Ag microparticles were obtained.

REFERENCES

[1] R. F. Egerton, *Physical Principles of Electron Microscopy*, Springer US, Boston, MA (2005); http://www.springerlink.com/index/10.1007/b136495

[2] P.J. Goodhew, J. Humphreys, R. Beanland, *Electron Microscopy and Analysis, Third Edition*, CRC Press (2000); http://www.crcpress.com/product/isbn/9780748409686

[3] Z. L. Wang, *Scanning Microscopy for Nanotechnology*, Springer New York, New York, NY (2006); http://www.springerlink.com/index/10.1007/978-0-387-39620-0

[4] S. Reed, *Electron microprobe analysis and scanning electron microscopy in geology*, Cambridge University Press (2005); http://bilder.buecher.de/zusatz/14/14770/14770790_vorw_1.pdf

[5] A. T. Fiory, "Methods in rapid thermal annealing" in *Proceedings of RTP 2000, Eighth International Conference on Advanced Thermal Processing of Semiconductors* (2000) pp. 15–25.

[6] F.P. Incropera, *Fundamentals of heat and mass transfer*, Sixth edition, John Wiley & Sons (2011).

[7] D. Drouin, A.R. Couture, D. Joly, X. Tastet, V. Aimez, R. Gauvin, *Scanning* **29**, 92–101 (2007).

[8] T. Kieliba, "Zone-Melting Recrystallization for Crystalline Silicon Thin-Film Solar Cells", Ph.D. Thesis (2006).

[9] S. Russev, G. Tsutsumanova, S. Angelov, K. Bachev, *J. Microsc.* **226**, 64-70 (2007).

[10] D. L. Lyutov, K. V. Genkov, A. D. Zyapkov, G. G. Tsutsumanova, A. N. Tzonev, L. G. Lyutov, S. C. Russev, *Mater. Chem. Phys.* **143**, 642–646 (2014).

ЕЛЕКТРОННО-ЛЪЧЕВО ОТГРЯВАНЕ НА МИКРООБЕКТИ И СТРУКТУРИ В SEM

К. Генков, Г. Цуцуманова, Ст. Хаджийски, А. Цонев, Д. Лютов, Ст. Русев

Физически факултет, Софийски университет "Св. Климент Охридски", ул. "Джеймс Баучер" №5, 1164 София, България

(Резюме)

Целта на тази работа е да провери възможностите за използване на фокусирания електронен сноп в сканиращ електронен микроскоп (SEM) за прецизно отгряване на обекти и структури с микронни размери. Освен наблюдаването на вторични електрони, обратно разсеяни електрони, рентгеново лъчение, при взаимодействието на ускорения електронен сноп със сканираната повърхност се наблюдава и отдаване на енергия по повърхността ѝ. Това позволява при големи токове на електронния сноп, SEM да бъде използван за отгряване на микрообекти и структури.

Възможни приложения на този метод са подобряването на кристалната структура чрез зонно отгряване, премахването на дефекти или нежелани микрообекти, микрозапояване, получаване на нови микрообекти (например със сферична форма) и други. Възможността за получаване на микрокристали с идеална кристална структура чрез зонно отгряване позволява подготвянето на подходящи златни и сребърни образци с приложение в плазмониката.

Bulgarian Chemical Communications, Volume 47, Special Issue B (pp. 162–167) 2015

Structural and electro-physical parameters of n-GaAs

Ts. Mihailova[1]*, S. Nedev[1], E. Toshkov[2], A. Stoyanov[2]

[1] *Paisii Hilendarski University of Plovdiv, 24 Tzar Asen Str., 4000 Plovdiv, Bulgaria*
[2] *Department of Mechanics, Technical University of Sofia, Branch Plovdiv, 25 Tsanko Diustabanov Str., 4000 Plovdiv, Bulgaria*

Samples of single crystal GaAs tellurium doped, obtained by Czochralski method from different kind of melts were tested. Preliminarily synthesized poly-crystals and, alternatively, remelts (undoped, indium doped or GaAs:Te residues) were used as input material in the experiments. A comparison was made between effect of doped impurity and thermal annealing upon carrier mobility and dislocation density. Crystals of diameters above 35 mm. pulled from synthesized material have dislocation density (1-4)$\times 10^4$ cm^{-2} and mobility from 2000 to 3400 cm^2/V.s. With the same experimental set-up, low dislocation density crystals with diameters up to 30 mm and concentration of doping tellurium above 2×10^{18} cm^{-3} were pulled. Structural and electro-physical parameters of crystals obtained from remelts vary in a wider diapason, as best results are observed with crystals pulled from GaAs:In residues. The thermal annealing does not considerably influence the dislocation density and electro-physical parameters, slightly increasing carrier mobility and mechanical strength at cutting. From analysis of experimental data and literature sources a model is proposed to use remelt material and doping with InAs and Te. Combined doping improves the electro-physical and structural parameters of obtained crystals including at low concentrations of the electrically active doping element.

Key words: gallium arsenide, structural defects, electron concentration

INTRODUCTION

Gallium arsenide is one of the most popular semiconductor materials for single- and multiple-junction solar elements [1-3]. It is possible the influence of substrate on active structures to be reduced through the use of buffer layers, porous structures and the capabilities of modern epitaxial techniques [3,4]. The perspectives of a broader application of $A^{III}B^{V}$ solar cells are intended to improve effectiveness of elements and lowering the substrates price [5]. Production of cheap substrates in case of silicon is achieved using pre-crystallization of residue material or multicrystal silicon [6,7].

GaAs:Te substrates are often used in the production of heterosructures based on A^3B^5 compounds. Tellurium as a doping impurity is a shallow donor with high limit solubility allowing controlled manipulation of the electro-physical parameters in a wide diapason. Also it effects on critical tensions to form dislocations and tends to reduce [8]. Gallium arsenide is a decomposing compound but it allows crystals to be grown with a significant stoichiometry deviation and, respectively from remelt material. Frigerri et al. obtain undoped high resistivity GaAs, Czochralski pulled, from Ga rich melt with As content over 0.475 [9]. Through thermodynamic calculations Morozov has shown that doping with Te, Sn and Si changes the GaAs homogeneity region and supersaturated native point defect behavior occurs during crystallization and post-crystallization cooling [10]. Te-doping shifts the GaAs homogenity region to the As-rich half of the phase triangle and it is possible to obtain As rich crystals from Ga rich melt. A problem with intensive Te-doping is the occurrence of microdefects, which change their sizes and concentrations at thermal annealing [11,12] and probably impact the structural and electro-physical parameters of the substrates. Annealing of n-type substrates with over stoichiometric As leads to suppression of the dominant recombination center and increases in hole diffusion lengths [13]. Thermal annealing is a final stage of the production of undoped semi-insulated GaAs from an As-rich melt which improves significantly the structural and electro-physical parameters of crystals in the presence of As precipitates. Decoration of dislocations with arsenic or gallium is identified through etching with AB and molted KOH [8,14,15].

A problem observed in some of the tested crystals is cracking and chipping of wafers at cutting. Therefore the impact of annealing on mechanical strength is an issue of practical interest.

EXPERIMENTS

Wafers with thickness between 1 and 1.5 mm, sliced at the top and end of mono-crystalline ingots

* To whom all correspondence should be sent:
tsmihail@uni-plovdiv.bg

© 2015 Bulgarian Academy of Sciences, Union of Chemists in Bulgaria

of LEC Czochralski GaAs:Te, were studied. All the crystals were pulled under a layer of B_2O_3 in an argon-filled chamber under pressure of 1.7 atm. and weight of the charged poly-crystal of 1 kg. The input material was divided in 4 groups. From each wafer, a small part was chipped and a sample of each was prepared for evaluation of the electro-physical parameters. The specific resistivity, Hall carrier concentration and mobility were measured.

Standard etching: all the wafers from the crystals are mechanically grinded and chemically polished with solution H_2SO_4:H_2O_2:H_2O in 3:1:1 ratio. The structural defects of all samples were developed in molted KOH in Ag crucible at temperature 470°C for 12–15 min. A resistivity furnace with thermoregulation accuracy $\pm$ 4°C was used. Dislocation density was calculated based on the method of averaging on 9 points of pits counted with metallographic microscope with 500 times magnification.

Annealing was carried out in vacuum sealed quartz ampoules, in which certain additional quantity of arsenic was loaded. Preliminary preparation of ampoules comprised of mechanical washing and acid treatment, washing with deionized water, vacuum heating at 1100°C for 4 hours and slow cooling down. The quantity of added arsenic was such as to ensure pressure of 1.5 atm. and was calculated considering the particular ampoule volume and process temperature.

RESULTS AND DISCUSSION

The results of measured carrier concentration at the top and end of the tested crystals from synthesized material (Melt I) are presented in Table 1.

The results of measured carrier concentration at the top and end of the tested crystals from remelt material are presented in Table 2. The type of the melt is indicated as follow: Melt II – from GaAs:Te residues from the beginning and the bottom part of crystals; Melt III - residues from high resistivity GaAs crystals

Table 1. Electron concentration from Hall measurements

Number of the crystal and type of the melt	Top cm^{-3}	End cm^{-3}
1 - Melt I	2.6×10^{17}	5.2×10^{17}
2 - Melt I	3×10^{17}	6.5×10^{17}
3 - Melt I	4.8×10^{17}	6.6×10^{17}
4 - Melt I	5.6×10^{17}	1.3×10^{18}
5 - Melt I	7×10^{17}	2.5×10^{18}
6 - Melt I	8.3×10^{17}	1.4×10^{18}

Table 2. Electron concentration from Hall measurements

Number of the crystal and type of the melt	Top cm^{-3}	End cm^{-3}
7 - Melt II	5×10^{17}	1×10^{18}
8 - Melt II	7.2×10^{17}	1.5×10^{18}
9 - Melt II	7.6×10^{17}	1.2×10^{18}
10 - Melt II	8.2×10^{17}	2.3×10^{18}
11 - Melt II	9.3×10^{17}	2×10^{18}
12 - Melt III	5.2×10^{17}	1×10^{18}
13 - Melt III	6×10^{17}	1×10^{18}
14 - Melt III	7.5×10^{17}	9×10^{17}
15 - Melt III	8.4×10^{17}	2.4×10^{18}
16 - Melt III	9×10^{17}	1.8×10^{18}
17 - Melt IV	7.2×10^{17}	1.5×10^{18}
18 - Melt IV	8.4×10^{17}	2×10^{18}

pulled in high pressure installation; Melt IV - residues from GaAs:In crystals pulled in high pressure installation.

The results from Tables 1 and 2 show that carrier concentration of the crystals pulled from preliminary synthesized material varies in wider diapason than crystals from remelt material. Best reproducibility is observed in indium doped GaAs material (Melt-IV) and residues from high resistivity undoped crystals (Melt-III).

Fig. 1 shows the dislocation densities developed in molted KOH:

The average dislocation density of the most crystals doped only with Te varies in the range 1-3×10^4 cm^{-2} and the results are similar, irrelevant of the type of melt. The higher density of dislocations at the end of crystals No. 9 and 13 is explained with the formation of impurities defects and clusters. The surface around dislocations is rough, which is asso-

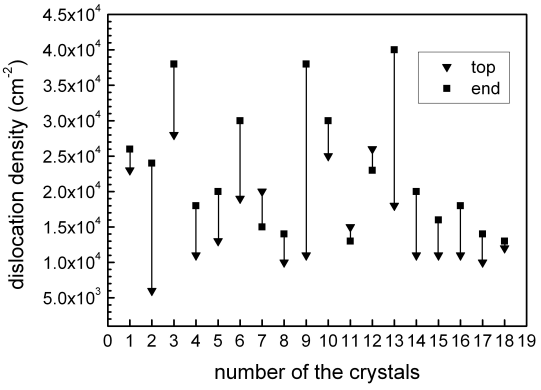


Fig. 1. Dislocation density revealed in molted KOH.

ciated with the presence of micro-defects. To illustrate capabilities of the pulling installation, two crystals with diameter 30 mm, Te concentration above 2×10^{18} cm^{-3} were pulled. The measured dislocation density is 1.9×10^{3} cm^{-2} and 4×10^{3} cm^{-2} respectively at the top and end. With impurity concentration above 3-5×10^{18} cm^{-3} dislocation density starts to decrease effectively [8], but the application of such substrates is limited. The samples with lowest dislocation density (No.17 and 18) were obtained from remelt material with In and doped with Te. Measured parameter values are comparable with the parameters which characterize crystals that are highly Te-doped, as well as with the results published by other authors for small diameter crystals pulled from synthesized material and doped with Te and In [16].

The results for carrier mobility are shown in Fig. 2.

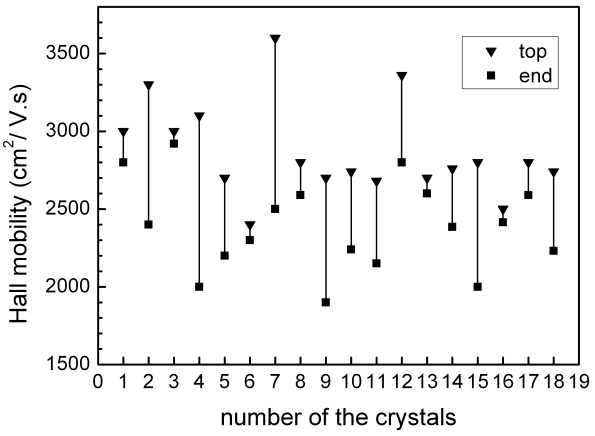


Fig. 2. Hall mobility from top and end of the crystals.

Electron mobility at the top and end of crystals is comparatively high, the values varying within (2×10^{3} – 3.4×10^{3}) cm^2/V.s for those pulled from synthesized material and (1.9×10^{3} – 3.6×10^{3}) cm^2/V.s for the rest. The presence of micro-roughness after etching in KOH, the lower concentration and high carrier mobility in crystals No. 2, 7, and 12 shows that most micro-defects are electrically neutral.

A problem in part of the crystals obtained from GaAs:Te residues is the observed cracking and chipping of wafers at mechanical slicing. Such crystals have comparatively high dislocation density, higher carrier and micro-defects concentration at the end and are obtained from a Ga-rich melt.

The stoichiometry of the same poly-crystals for the melt and mono-crystals used in the experiment was measured with a Philips SEM 515 scanning electron microscope operating in the energy-dispersive X-ray analysis mode (EDAX). The method precision error is about 1 at.%. In the preliminary synthesized poly-crystals, the ratio between components in atomic percentage is as follows: Ga (51.59) : As (48.41); in residues from undoped GaAs – Ga – (51.88 ÷ 52.63) : As (47.33 ÷ 48.22); in GaAs:In residues – Ga (51.14 ÷ 52.72) : As (47.27 ÷ 48.9), and In – (0.04); in GaAs:Te obtained from n-GaAs residues – Ga (52.43) : As (47.57).

According to other available sources, optimal annealing conditions depend on the stoichiometry of the material and the nature of micro-defects. Thermal processing of Ga-rich crystals leads to annealing of acceptors and/or generation of shallower from EL2 donors [13], but at higher temperature impurity clusters unify.

The effect from thermal annealing was studied at two temperature levels, namely: 700°C and 600°C. The experiments were carried out in vacuum sealed quartz ampoules: – 2 mono-crystals and 4 wafers obtained from different melts were loaded for the first experiment, and 1 crystal and 4 wafers for the second one. The obtained results at temperature 700°C are presented in Table 3.

The annealing at 600°C does not lead to changes in the indicated parameters, whereas some changes are observed at 700°C, which however are comparatively small. Only in crystal No. 9, a slight decreasing of carrier concentration and increasing of mobility at the end of the crystal was observed. This can be explained with non-uniform distribution of the impurities in the sample. Etching with molten KOH does not give information about the nature and magnitude of micro-defects, but it reveals clusters, twin lamellas and Ga inclusions. Such parts of the crystals which contain the aforementioned micro-defects are eliminated. It can be assumed that annealing in this temperature diapason does not impact significantly dislocation density and carrier concentration and mobility. All crystals annealed in the experiment improved their mechanical hardiness at slicing which led to a smaller number of broken wafers.

Impurity concentration in the melt is calculated with Eq. 1.

$$N = \frac{N_A m_{dop} \rho_{GaAs}}{M_{melt} A_{dop}}, \qquad (1)$$

where $N_A = 6.022\times10^{23}$ is Avogadro constant, $m_{dop.}$ – impurity mass, ρ – density of GaAs (5.317 g/cm^3), M_{melt} – mass of melt and A_{dop} – impurity atomic mass.

Table 3. Electro-physical and structural parameters on the crystals before and after thermal annealing, where: N [cm^{-3}] – Hall concentration; μ [cm^2/V.s] – Hall mobility and N_D [cm^{-2}] – dislocation density

Number of the crystal and type of the melt	Top			End		
	N	μ	N_D	N	μ	N_D
Before annealing						
3 - Melt I	4.8×10^{17}	3000	$2.8.\times10^{4}$	6.6×10^{17}	2920	3.8×10^{4}
9 - Melt II	7.10^{17}	2900	1.5×10^{4}	2.9×10^{18}	1900	2.8×10^{4}
15 - Melt III	8.4×10^{17}	2000	1.1×10^{4}	2.4×10^{18}	2000	1.6×10^{4}
19 - Melt IV	8.9×10^{17}	2333	1.1×10^{4}	2×10^{18}	2200	1×10^{4}
After annealing						
3 - Melt I	3.6×10^{17}	2960	1.8×10^{4}	6.7×10^{17}	2640	3.7×10^{4}
9 - Melt II	7×10^{17}	2990	1.8×10^{4}	1×10^{18}	2100	2×10^{4}
15 - Melt III	9×10^{17}	2070	1.3×10^{4}	3×10^{18}	2045	1.5×10^{4}
19 - Melt IV	8.4×10^{17}	2660	1.5×10^{4}	2×10^{18}	2580	1.8×10^{4}

The mass of the melt for all crystals was 1 kg and the mass of doping impurity Te is 0.7 g. Concentration of Te from Eq. 1 is equal to 1.75×10^{19} cm^{-3}.

Impurity distribution is calculated with Eq. 2:

$$C_S = C_0 k_{ef}(1-g)^{k_{ef}-1} \qquad (2)$$

Where C_s is expected impurity concentration, C_0 is impurity concentration in the melt, g crystallized part and k_{ef} is effective coefficient of distribution with values from 0.016 to 0.054 [17]. The mass of the crystallized part at reaching a diameter of 35 mm and angle of growing of 45° is 29.82 g, respectively $g = 0.0298$. The expected concentration at the top is 2.8×10^{17} cm^{-3} at $k_{ef} = 0.016$ and 9.7×10^{17} cm^{-3} at k_{ef} 0.054. The measured values of carrier concentration are in the range (2.3 - 9)$\times10^{17}$ cm^{-3}, and so for the next calculations we will use $k_{ef} = 0.054$.

The expected concentration when 0.6 and 0.7 parts of the melt is crystallized are respectively 2.2×10^{18} cm^{-3} and 2.9×10^{18} cm^{-3}. We assume that the melt from GaAs:Te residues has an average impurities concentration of 2×10^{18} cm^{-3} and upon adding the doping element it rises to 1.95×10^{19} cm^{-3}. The expected carrier concentrations at crystallization levels of the melt: 0.1; 0.6 and 0.7 parts of the melt are as follows: 1.1×10^{18} cm^{-3}, 2.5×10^{18} cm^{-3} and 3.4×10^{18} cm^{-3} and they are lower than the maximum impurity solubility. The values of measured concentration at the top and end are in the range from (5-9)$\times10^{17}$ cm^{-3} to (1-2.3)$\times10^{18}$ cm^{-3}.

The expected In concentration in the melt and in the crystals at $k_{ef} = 0.13$ can be calculated likewise. The residues are cut from crystals pulled at high pressure, melt weight is 4 kg and the weight of doping compound InAs - 117 g. In concentration in the melt is 4.9×10^{20} cm^{-3} and the expected concentration when 0.1, 0.4 and 0.7 parts of the melt are crystalized is respectively 6.9×10^{19} cm^{-3}, 9.9×10^{19} cm^{-3}, 1.8×10^{20} cm^{-3} at average concentration of the residues 1×10^{20} cm^{-3}. The expected concentration of In in the crystals is 1.4×10^{19} cm^{-3} at the top and 3.3×10^{19} cm^{-3} when 50% of the melt is crystallized.

The smallest gap between expected and measured concentration was obtained with crystals doped with Te and In. The deviation of expected concentration is greater at the top of all tested crystals. The explanation is probably that the top of a crystal is exposed to high temperature for a longer time, and so phenomena occur like complex formation, evaporation of some impurity, uncontrolled residual acceptors and melt stoichiometry deviation. The main residual impurities at Czochralski process are boron, carbon and silicon. We assume that the greater deviation in carrier concentration of crystals pulled from synthesized materials is explained with the amphoteric behavior of silicon and the different levels of evaporation of doping Te. The measured stoichiometry deviation of synthesized poly-crystals is comparably small and close to the method precision error. Surely some of the synthesized poly-crystals are with stoichiometric composition. Silicon is an amphoteric impurity and depending on the prevalent own vacancies it can behave as either a donor (Si_{Ga}) or an acceptor (Si_{As}) [8].

The quantity of silicon in the other types of crystals decreases during preliminary crystallization. The

concentration of other impurities depends on humidity and graphite heater quality. Boron is an isovalent impurity, it replaces gallium vacancies but tends to increase acceptor defects Ga_{As} and $B_{Ga}V_{As}$ [18]. Carbon is an acceptor and its concentration varies in wide diapason [19]. Te doping increases the concentration of neutral and acceptor complexes [8,9,20]. Additionally, the use of Ga-rich melts may lead to formation of gallium clusters with various magnitude and effects and may form tensions [21]. That explains the deterioration of mechanical parameters of most highly doped crystals.

Double doping with Te and In decreases the dislocation density and improves significantly reproducibility of electro-physical parameters. A stronger effect can be expected with increasing the In concentration up to 2×10^{20} cm^{-3} [16]. Usually the doping impurity is added in the form of InAs compound, which increases As content in the melt.

CONCLUSIONS

The possibilities to pull GaAs:Te from residues of crystals either doped or undoped with In or Te were shown. The results for dislocation density, carrier concentration and mobility are compared to the relevant parameters of crystals pulled form preliminary synthesized poly-crystal material. Double doping with Te and In decreases the dislocation density and improves reproducibility of the parameters.

Annealing at temperatures of 600°C and 700°C for 4 hours followed by slow cooling improves mechanical parameters of crystals without any influence on basic structural and electro-physical parameters.

***Acknowledgments**: The authors would like to thank to ICM Ltd. Plovdiv for kindly disposed samples for investigation.*

REFERENCES

[1] V. P. Khvostikov, A. S. Vlasov, S. V. Sorokina, N. S. Potapovich, N. Kh. Timoshina, M. Z. Shvarts and V. M. Andreev, *Semiconductors* **45**, 792–797 (2011).

[2] N. D. Lam, Y. Kim, K. Kim, K. Jung, H. K. Kang and J. Lee, *J. Crystal Growth* **370**, 244–248 (2013).

[3] T. H. Wu, Y. K. Su, R. W. Chuang, C. Y. Huang, H. J. Wu and Y. C. Lin, *J. Crystal Growth* **370**, 236–239 (2013).

[4] A. I. Belogorokhov, S. A. Gavrilov, I. A. Belogorokhov and A. A. Tikhomirov, *Semiconductors* **39**, 243–248 (2005).

[5] R. McConnell, *Semiconductors* **38**, 931–935 (2004).

[6] P. Bellanger, A. Sow, M. Grau, A. Augusto, J. M. Serra, A. Kaminski, S. Dubois and A. Straboni, *J. Crystal Growth* **359**, 92–98 (2012).

[7] L. Arnberg, M. Di Sabatino and E. J. Ovrelid, *J. Crystal Growth* **360**, 56–60 (2012).

[8] M. G. Milvidsky and V. B. Osvensky, *Structural defects in semiconductor monocrystals*, Moskva, Metallurgia (1984) (in Russian).

[9] C. Frigeri, J. L. Weyher and H. Ch. Alt, *Phys. Stat. Sol. (A)* **138**, 657–663 (1993).

[10] A. N. Morozov, *J. Crystal Growth* **106**, 258–272 (1990).

[11] P. V. Hutchinson and P. S. Dobson, *J. Mater. Science* **10**, 1636–1641 (1975).

[12] A. Djemel, J. Castaing, N. Burle-Durbec and B. Pichaud, *Revue Phys. Appl.* **24**, 779–793 (1983).

[13] D. Wong, T. E. Schlesinger and A. G. Milnes, *J. Appl. Phys.* **68**, 5588–5594 (1990).

[14] Y. Otoki, M. Watanabe, T. Inada and Sh. Kuma, *J. Crystal Growth* **103**, 85–90 (1990).

[15] J. L. Weyher and J. Van De Ven, *J. Crystal Growth* **78**, 191–217 (1986).

[16] I. V. Stepantsova, I. V. Mejenny, V. B. Osvensky, S. S. Shifrin, I. N. Bolsheva and I. A. Grigoriev, *Crystallography Reports* **33**, 938–943 (1988) (in Russian).

[17] S. S. Strelchenko and V. V. Lebedev, *Soedinenia A^3B^5*, Moskva, Metallurgia, (1984) (in Russian).

[18] K. R. Elliott, *J. Appl. Phys* **55**, 3856–3858 (1984).

[19] T. Kimuta, H. Emori, Ts. Fukuda and K. Ishida, *J. Crystal Growth* **76**, 517–520 (1986).

[20] B. Paquette, B. Ilahi, V. Aimez and R. Ares, *J. Crystal Growth* **383**, 30–35 (2013).

[21] S. N. Grinyaev and V. A. Caldyshev, *Semiconductors* **35**, 86–90 (2001).

СТРУКТУРНИ И ЕЛЕКТРОФИЗИЧНИ ПАРАМЕТРИ НА n-GaAs

Цв. Михайлова[1], Ст. Недев[1], Е. Тошков[2], А. Стоянов[2]

[1] *Физически факултет, Пловдивски университет "Паисий Хилендарски", ул. "Цар Асен" №24, 4000 Пловдив, България*
[2] *Технически университет София, филиал Пловдив, ул. "Цанко Дюстабанов" №25, 4000 Пловдив, България*

(Резюме)

Изследвани са образци от монокристален GaAs легиран с телур, получен по метода на Чохралски от различни видове стопилка. За изходен материал е използван предварително синтезиран поликристал или отработен материал (остатъци от нелегирани или легирани с индий кристали и остатъци от GaAs:Te). Направено е сравнение за влиянието на концентрацията на легиращия примес и температурното отгряване върху подвижността на токоносителите и плътността на дислокациите.

Получените от синтезиран материал кристали с диаметър над 35 mm са с плътност на дислокации (1-4)$\times 10^4$ cm^{-2} и подвижност от 2000 до 3600 cm^2/V.s. На същата установка са изтелени и нискодислокационни кристали с диаметър до 30 mm при концентрация на легиращия примес телур над 2×10^{18} cm^{-3}. Структурните и електрофизичните параметри на кристалите, получени от отработен материал, варират в по-широки граници, като най-добри са при използване на остатъци от GaAs:In. Температурното отгряване слабо влияе върху плътността на дислокациите и електрофизичните параметри, слабо увеличава подвижността на токоносителите и повишава механичната устойчивост на кристалите при рязане на пластини.

От анализа на експерименталните резултати и литературни данни е предложен модел за използване на отработен материал и легиране с InAs и Te. Съвместното легиране ще подобри електрофизичните и структурните параметри на получените кристали и при ниска концентрация на електрически активния примес.

Bulgarian Chemical Communications, Volume 47, Special Issue B (pp. 168–172) 2015

Low temperature photoluminescence studies of colloidal CdSe nanocrystals

E. Valcheva[1]*, G. Yordanov[2]

[1] *Faculty of Physics, Department of Solid State Physics and Microelectronics, St. Kliment Ohridski University of Sofia, 5 James Bourchier Blvd., 1164 Sofia, Bulgaria*
[2] *Faculty of Chemistry and Pharmacy, Department of General and Inorganic Chemistry, St. Kliment Ohridski University of Sofia, 1 James Bourchier Blvd., 1164 Sofia, Bulgaria*

We present the results from low temperature studies of the PL from colloidal CdSe nanocrystals prepared by the hot injection method in liquid paraffin. The synthesized nanocrystals were all within the quantum confinement range and showed the typical size-dependent UV-vis absorption, PL and Raman spectral characteristics. The photoluminescence spectra and their temperature dependences were measured from room temperature (295 K) down to temperatures as low as 15 K, demonstrating that the exciton PL transitions followed modified Varshni equation accounting for carrier localization. The smallest (2.6 nm in size) CdSe nanocrystals isolated in the beginning of the nanocrystal growth had a relatively symmetric size distribution and showed a single exciton emission band, while the samples isolated at later stages of the growth process showed exciton transitions from subpopulations of nanocrystals.

Key words: CdSe, Nanocrystals, Quantum dots, Photoluminescence, Low temperature

INTRODUCTION

The size-dependent photoluminescence (PL), broad excitation spectra and resistance to photobleaching makes colloidal quantum dots (QDs) quite attractive materials for applications in bioimaging and optoelectronics. For example, differently sized cadmium selenide (CdSe) nanocrystals emitting from blue to red can be used as fluorescent biolabels [1-3], components of light-emitting diodes [4], lasers [5], FRET sensors [6], etc. Therefore, achieving an effective control of the photoluminescence of QDs has been a major goal for scientists in the field of QDs synthesis and there are still unsolved issues of this problem.

The width of the absorption and emission bands in the QDs spectra is a result of homogeneous (thermal) and inhomogeneous broadening. The inhomogeneous broadening comes from the polydispersity of the nanocrystal size [7]. Therefore, the relative changes in the shape and the width of the PL bands during the growth of QDs can be used as an indication for changes in the nanocrystal size distribution [8]. Photoluminescence studies can be more informative when performed at low temperatures, when the thermal broadening of the emission bands is minimized and the effect of quantum confinement is observed in its most clear form. Most of the known low temperature photoluminescence studies of colloidal QDs include investigations of the exciton lifetimes and excitonic radiative decay [9], exciton fine structure [10], single dot spectroscopy [11].

In this work, we report studies on the photoluminescence properties of colloidal CdSe QDs as a function of the temperature, in the range from 15 to 295 K. The nanocrystals were prepared by the hot injection method in liquid paraffin. The synthesized nanocrystals were all within the quantum confinement range. The PL emission bands become narrower at low temperatures due to decrease of the thermal peak broadening, which facilitates the detection of nanocrystal subpopulations of different sizes in a heterogeneous sample.

EXPERIMENTAL SECTION

Nanocrystals of CdSe were synthesized in hot liquid paraffin according to a previously reported method [12]. Briefly, cadmium stearate precursor was prepared in liquid paraffin (15 ml) from cadmium oxide (50 mg; 0.39 mmol) and stearic acid (1.6 g) at 200°C. Tributylphosphine selenide precursor (1.0 ml) was injected to the reaction mixture at 250-260°C and nanocrystals of various sizes and optical properties were prepared by varying the reaction time.

The photoluminescence experiments were performed with a high resolution double monochromator (SPEX Model 1404, f=0.85 m) equipped with Hamamatsu R943 PMTs (GaAs photocathode) with thermoelectric cooler and in photon counting mode. The samples were placed in a closed cycle ARS helium cryostat working in temperature interval from 295 down to 10 K. Argon laser emitting at a wave-

* To whom all correspondence should be sent:
epv@phys.uni-sofia.bg

© 2015 Bulgarian Academy of Sciences, Union of Chemists in Bulgaria

length of 488 nm (2.54 eV) was used as an excitation source. For the photoluminescence experiments the nanocrystal powders were embedded into potassium bromide (KBr) tablets in order to be placed within the cryostat holder. For that purpose, dried nanocrystal powder (∼20 mg) was homogenized with anhydrous powdered KBr (2 g) and compressed into tablets of suitable sizes (∼2 cm in diameter; 5 mm thickness) by using a tablet press.

RESULTS AND DISCUSSION

Photoluminescence appears as one of the most sensitive methods for analysis of QDs, which allows one to obtain information and to discriminate between different recombination processes, related with various recombination centers in the nanocrystal lattice. In the case of QDs PL measurements could provide information about the energy levels and quantum confinement effects. The correct interpretation of the PL peaks could also provide information about the existence of excitons, the morphology of the heterointerface, the presence of defects and impurities, etc. As mentioned above, the energy of the PL peak, its shape and width could provide information about the average size and size distribution of the nanocrystals. Since the homogeneous (thermal) broadening of the PL bands could be minimized at lower temperatures, we performed PL measurements at low temperatures (down to 15 K) in order to investigate the temperature dependence of the PL peak energy and to evaluate the size homogeneity of the samples.

Fig. 1 represents PL-spectra of three CdSe nanocrystal samples of different size at 15 K. The spectra are normalized to the highest energy peak. The most intensive peak for the three different nanocrystal sizes was shifted toward higher energies than the band gap of the bulk CdSe (1.74 eV). The photoluminescence maximum shifts toward higher energies with decreasing of the nanocrystal size, which is a characteristic observation of quantum-size effects for nanocrystals of sizes that are smaller than the exciton Bohr radius (∼ 5.6 nm for CdSe).

As a result of the quantum confinement effect the energy of the lowest excited state, $E(R)$, according to a simplified version of the effective mass model of Bawendi [13], is given by the following expression (Eq. 1) that is valid for spherical nanocrystals of small radii R.

$$E(R) = E_g + \frac{h^2}{8mR^2} \qquad (1)$$

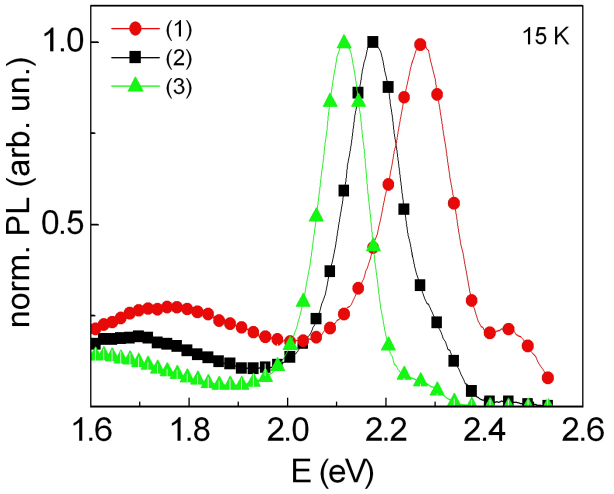


Fig. 1. Normalized PL-spectra of the three samples labeled (1), (2) and (3) at 15 K.

Here, E_g is the energy band gap for the bulk semiconductor, h is the Planck constant, m is the effective mass of the exciton. Accordingly, nanocrystal sizes between 2.6 and 3.6 nm are determined from the PL energy positions.

The temperature dependent PL spectra for two of the samples labeled (1) and (2) measured from 15 K to 295 K are given in Fig. 2 a and b, respectively. Most of the emission spectra show two shoulders at the high-energy side visible also in the room temperature spectra but more pronounced at low temperatures, and a low intensity shoulder at the low energy side. To take into account these features, the PL curves at each temperature were deconvoluted with a sum of Gaussians.

For sample (1) the best fit of the low temperature (15 K) spectrum was done with four Gaussians, while the spectrum of sample (2) was fitted with a combination of five Gaussians. The spectrum of sample (3) is best fitted with five Gaussians similar to (2). The peak at ∼2.5 eV does not depend on the temperature and is situated around the same position for all the three groups of samples. Its nature is currently unclear. The low energy peaks ∼1.8 eV are probably due to surface-state-mediated recombination [14].

The temperature dependences of the main peak and the shoulder (Fig. 2b) correspond to the expected behavior for exciton transitions. The existence of a subpopulation of smaller nanocrystals could be associated with the appearance of a “shoulder” on the shorter wavelength side of the main peak.

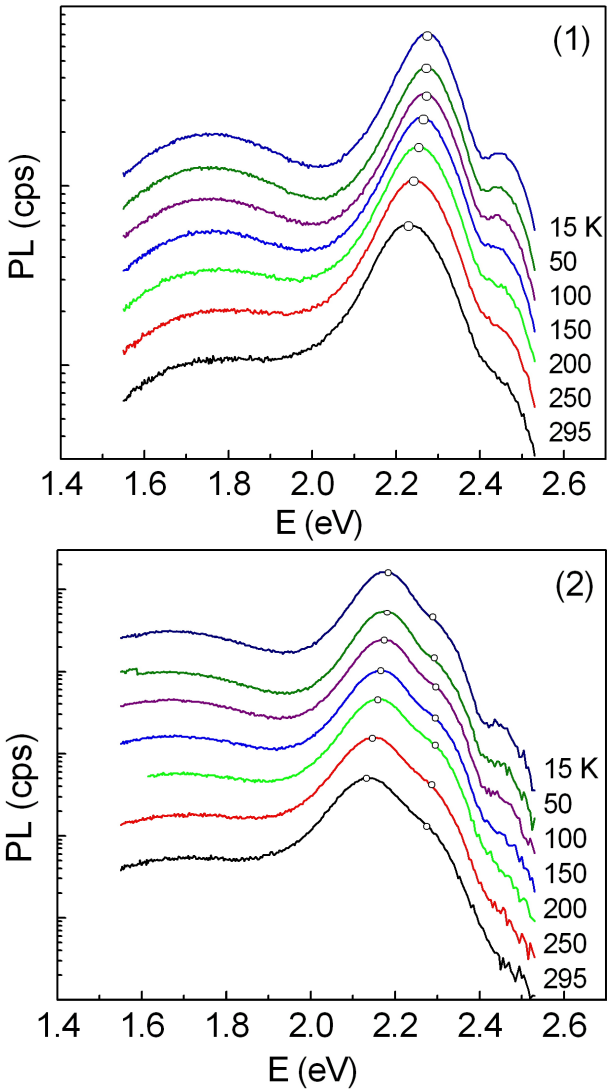


Fig. 2. (a) PL-spectra of sample (1) and (b) of sample (2) at various temperatures (from 15 to 295 K, log scale; offset for clarity).

The temperature dependence of the energy gap of bulk semiconductors is known as the Varshni relation [15] (Eq. 2).

$$E_g(T) = E_g(0) - \alpha \frac{T^2}{T+\beta} \qquad (2)$$

Here, $E_g(0)$ is the energy gap at 0 K, α is the temperature coefficient, and the value of β is close to the Debye temperature of the material. The experimental data for the three QDs were fitted to the Varshni relation. Eq. (2) fits very well the high temperature range 100-295 K (Fig. 3, fits for the three samples) consistent with the known temperature dependence of bulk semiconductor band gap. However, at temperatures lower than 100 K obviously the PL energies deviate from Varshni equation, plateau and even "S-shape" behavior is observed pointing out at involvement of different mechanism connected with relaxation dynamics of localized carriers and confinement. Indeed, better fits in the low temperature range were obtained if a modified equation (Eq. 3) was used:

$$E_g(T) = E_g(0) - \alpha \frac{T^2}{T+\beta} - \frac{\sigma^2}{kT} \qquad (3)$$

where the parameter σ represents a measure of the depth of localization potentials [16] and k is the Boltzmann's constant. Similar behavior is observed in quantum dots and in quantum well structures where it is explained in terms of localized exciton freeze-out at low temperatures, followed by the onset of thermalization of excitons with increasing temperature. The fitted parameters are consistent with the values given in the literature for bulk CdSe: $(2.8\text{-}4.1)\times10^{-4}$ eV/K for α and (181-315) K for β (Ref. [17]). The σ values reveal localization energy $\sim 2 \div 4$ meV from fitting the transition peaks.

Photoluminescence measurements appeared to be a sensitive approach for detection of heterogeneity in the size distribution of nanocrystals. It appears that in the beginning of the nanocrystal growth process there were nanocrystals of uniform size distribution and the size heterogeneity (the observation of a second subpopulation of smaller nanocrystals together with the basic component) appeared in the later stages of the

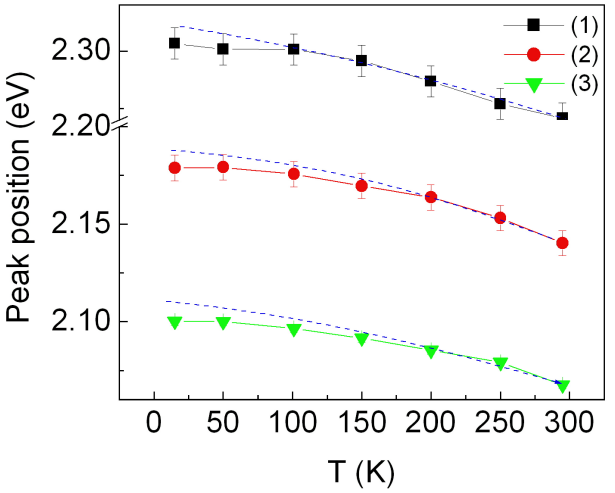


Fig. 3. Temperature dependences of the peak position (energy) of the main peaks of the three samples: sample (1) blacks quare; sample (2) red dot; sample (3) green triangle. Included are Varshni fits (dashed line) and modifiedVarshni fits (solid line).

nanocrystal growth. Our data are likely to be explained by the model of Ostwald ripening. This model of the growth kinetics of QDs in the conditions of the hot-injection synthesis has been described by Talapin et al. [18].

CONCLUSIONS

We reported in this paper results from low temperature photoluminescence studies on colloidal CdSe nanocrystals, prepared by the hot injection method in liquid paraffin. The average nanocrystal size of the nanocrystals was determined to be smaller than the exciton Bohr radius for CdSe. The temperature dependencies of the exciton PL transitions for temperatures higher than 100 K were found to follow the Varshni equation, while from 15 to 100 K the quantum confinement and localization of carriers shows modified Varshni dependance. The CdSe nanocrystals of smallest size (2.6 nm) show uniform size distribution and a single photoluminescence emission band. However, the CdSe samples obtained at later stages of growth, showed an asymmetrical size distribution and photoluminescence from a subpopulation of smaller nanocrystals found together with the larger ones.

REFERENCES

[1] W. Chan, D. Maxwell, X. Gao, R. Bailey, M. Han and S. Nie, *Curr. Opin. Biotechnol.* **13**, 40–46 (2002).

[2] F. Pinaud, X. Michalet, L. Bentolila, J. Tsay, S. Doosel, J. Li, G. Iyer and S. Weiss, *Biomaterials* **27**, 1679–1687 (2006).

[3] T. Jamieson, R. Bakhshi, D. Petrova, R. Pocock, M. Imani and A. Seifalian, *Biomaterials* **28**, 4717–4732 (2007).

[4] M. Schlamp, X. Peng and A. P. Alivisatos, *J. Appl. Phys.* **82**, 5837–5842 (1997).

[5] V. Klimov, A. Mikhailovsky, S. Xu, A. Malko, J. Hollingsworth, C. Leatherdale, H. Eisler and M. G. Bawendi, *Science* **290**, 314–317 (2000).

[6] I. L. Medintz and H. Mattoussi, *Phys. Chem. Chem. Phys.* **11**, 17–45 (2009).

[7] A. P. Alivisatos, A. Harris, N. Levinos, M. Steigerwald and L. Brus, *J. Chem. Phys.* **89**, 4001–4011 (1988).

[8] L. Qu and X. Peng, *J. Am. Chem. Soc.* **124**, 2049–2055 (2002).

[9] M. Califano, A. Franceschetti and A. Zunger, *Nano Lett.* **5**, 2360–2364 (2005).

[10] D. J. Norris, A. L. Efros, M. Rosen and M. G. Bawendi, *Physical Review B* **53**, 16347–16354 (1996).

[11] S. A. Empedocles, D. J. Norris and M. G. Bawendi, *Phys. Rev. Lett.* **77**, 3873–3876 (1996).

[12] G. Yordanov, H. Yoshimura and C. Dushkin, *Colloids Surf. A* **322**, 177–182 (2008).

[13] M. G. Bawendi, M. L. Steigerwald L. E. Brus, *Annu. Rev. Phys. Chem.* **41**, 477–496 (1990).

[14] *Nanocrystals: From Theory to Application*, edited by G. Schmid, Wiley-VCH, Weinheim, 2004 and references therein.

[15] J. H. Park, D. G. Choi, T. K. Lee, E. Oh, S. Lee and J. K. Furdyna, *Appl Phys Lett* **90**, 201916 (2007).

[16] *Numerical Data and Functional Relationship in Science and Technology*, edited by K. H. Hellwege, Landolt-Börnstein, New Series, Group III, Vol. 17, Pt. B (Springer-Verlag, Berlin, 1982).

[17] T. Schmidt, K. Lischka and W. Zulehner, *Phys. Rev. B* **45**, 8989–8994 (1992).

[18] D. Talapin, A. Rogach, M. Haase, H. Weller, *J. Phys. Chem. B* **105**, 12278–12285 (2001).

НИСКО-ТЕМПЕРАТУРНИ ФОТОЛУМИНЕСЦЕНТНИ ИЗСЛЕДВАНИЯ НА CdSe НАНОКРИСТАЛИ

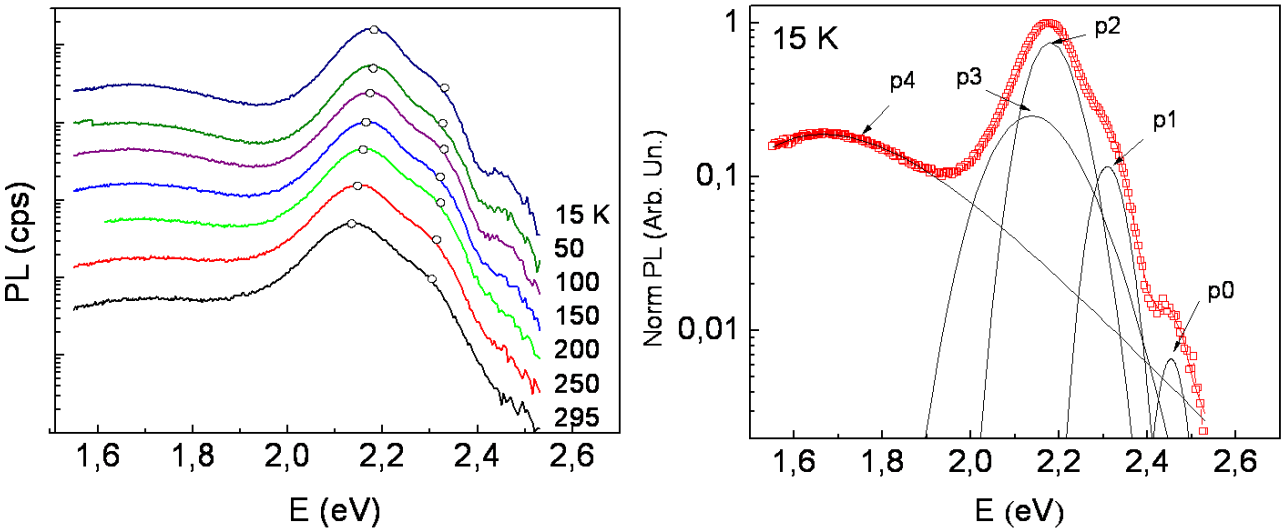
Е. Вълчева[1], Г. Йорданов[2]

[1] *Физически факултет, Катедра Физика на твърдото тяло и микроелектроника, СУ "Св. Климент Охридски", бул. "Джеймс Баучър" №5, 1164 София, България*
[2] *Факултет по химия и фармация, Катедра Обща и неорганична химия, СУ "Св. Климент Охридски", бул. "Джеймс Баучър" №1, 1164 София, България*

(Резюме)

Полупроводниковите нанокристали (монокристали с размер 2-10 nm в диаметър), известни и като квантови точки (КТ), са перспективни луминесцентни наноматериали, които абсорбират и излъчват видима светлина като резултат от квантовото ограничаване на екситоните [1]. Зависимостта на енергията на фотолуминесценция (ФЛ) от размера на частиците позволява проектиране на приложения в широк енергетичен диапазон. Това прави колоидните КТ атрактивни за използване в оптоелектрониката, медицината и др. Например, наночастици с различен размер от кадмиев селенид (CdSe) излъчват от синьо до червено и могат да се използват като флуоресцентни биомаркери, компоненти в излъчвателни диоди, лазери и др. Затова ефективният контрол на ФЛ от КТ е главна цел за изследователите при синтез на КТ, където има все още нерешени проблеми.

В този доклад представяме резултати от експерименти по ниско-температурна ФЛ на колоидни наночастици CdSe, получени чрез метода на гореща инжекция в течен парафин. Размерите на синтезираните частици са в диапазона на квантово ограничаване и показват типична зависимост от размера на частиците при абсорбция в UV-видимата област, ФЛ и Раманови спектри. ФЛ спектрите и тяхната температурна зависимост бяха измерени от стайна (295 K) до ниска температура от 15 K (Фиг.1), и показаха, че екситонните ФЛ преходи следват модифицирана Varshni-зависимост, показваща ефекта от локализиране на екситоните вследствие квантово-размерен ефект. Най-малките CdSe частици (с диаметър 2.6 nm), изолирани в началото на процеса на израстване, имат относително симетрично разпределение по размер и показват една линия на екситонна емисия, докато частиците, изолирани в по-късни етапи на процеса на израстване показват екситонна емисия от субпопулации от нанокристали.



Фиг. 1. (a) ФЛ-спектри от наночастициCdSe при температури (15 – 295) K; (b) ФЛ спектър (15K), фитиран с пет Гаусиана за определяне на наличието на субпопулации от нанокристали.

1. A.L. Rogach (ed.), *Semiconductor nanocrystal quantum dots: synthesis, assembly, spectroscopy and applications*, Springer-Verlag, Wien, 2008.

Bulgarian Chemical Communications, Volume 47, Special Issue B (pp. 173–176) 2015

Thin films of metal oxides for preparing of a position sensitive photodetector

V. Jelev*, P. Petkov, Iv. Markova, T. Petrov

University of Chemical Technology and Metallurgy, Sofia, Bulgaria

Highly transparent and conductive thin films of F-doped SnO_2 (FTO), and Sn-doped In_2O_3 (ITO) have been deposited on glass and silicon substrates, by spray pyrolysis technique. The deposition temperature 450°C and concentration of $InCl_3$ and $SnCl_4$ in the solutions 0.2 M/l. were used. The effects of the thickness on the film resistivity have been investigated. The physical characterization of the films was carried out by UV-VIS spectroscopy, scanning electron microscopy and AFM. The films are polycrystalline, present an optical transmission higher than 95% in the visible light, and resistivity in the range of $10^{-3} \div 10^{-4}\Omega$.cm. The optical and electrical properties of the films make them suitable for applying in a position sensitive structure "Si-SiO_2-metal oxide". Transient lateral photo effects (LPE) in the films deposited on n-type silicon substrate with native SiO_2 have been investigated. Under the nonuniform irradiation of a light beam a lateral photo voltage (LPV) shows high sensitivity to the light spot position in the oxide films plane. LPV as a function of the position of the light spot have been measured. The position characteristic of the structure is symmetric to the zero and linear in a large active area. The structure can be used to detect very small displacements due to its out put of lateral photo voltage changing linearly with light spot position.

Key words: transparent and conductive metal oxide films, SnO_2 and In_2O_3 thin films, spray pyrolysis method, large area position sensitive photodetectors

INTRODUCTION

Thin films of SnO_2 doped with F (FTO) an In_2O_3 doped with Sn (ITO) are being widely studied during recent years, due to their unique optical, electrical and mechanical properties [1–3]. Because of their high optical transparency in visible region low electrical resistivity and high reflectivity in infrared region of the spectrum [4, 5] these films are suitable for various applications: as transparent electrodes in various display devices [6], antireflection coatings for solar cells and heat mirrors [7], hetero-junction solar cells [8], photodiodes [9] and so on.

In the recent times various techniques have been developed for preparation of ITO and FTO thin films with high transmittance and high conductivity such as flash evaporation [10], electron beam evaporation [11], magnetron sputtering [12], chemical vapour deposition [13], sol-gel process [14], spray-pyrolysis [15, 16]. Chemical spray-pyrolysis has advantages among these methods because of the possibilities to obtain large area uniform coatings without high vacuum ambience [17].

The aim of this study was to obtain uniform large area thin FTO and ITO films on a mono-crystal silicon substrate by the method of spray-pyrolysis and to investigate the possibility to prepare of a two dimensional position sensitive photodetector with a Si-SiOx-ITO (FTO) structure.

* To whom all correspondence should be sent:
kazeus@abv.bg

EXPERIMENTAL DETAILS

The chemical reactions that provide thin film formation are:

$$2InCl_3 + 3H_2O \leftrightarrow In_2O_3 + 6HCl \quad (1)$$

$$SnCl_4 + 2H_2O \leftrightarrow SnO_2 + 4HCl \quad (2)$$

The doped In_2O_3 films were deposited by spraying an alcoholic O.25M solution of $InCl_3$ and $SnCl_4$ (as a source of tin dopant) onto the substrates heated at 420-480°C. The films of SnO_2 were obtained from alcoholic O.25M solution of $SnCl_4$ consisting HF as a F dopant at 380–460°C. Monocrystal n-Si (111) plates with resistivity 6–9 Ω.cm and Corning glass were used as substrates. The atomization of the solution was carried out with a sprayer using as Carrier gas argon. The film thickness was measured by the weight method and estimated by a color scale during the process. The measurements of the electrical resistivity were carried out at room temperature using the standard four-probe method. Silver pasted leads were used as a contact to the films. The morphology and microstructure of the films were examined with Scanning Electron Microscopy (SEM) and Atomic Force Microscopy (AFM). A spectrophotometer SIMADZU-UV 3600 (300-1800nm) was used to study the transmission spectra of the films deposited onto the glass substrates.

© 2015 Bulgarian Academy of Sciences, Union of Chemists in Bulgaria

RESULTS AND DISCUSSION

The electrical and optical properties of the films depend on the technological parameters: the substrate temperature, the spraying rate, the angle of spraying, the distance between the nozzle and the substrates, and the quantity of impurity in the spraying solution, which in turn influence on the microstructure, stoichiometry and physical parameters of the layers. The best results (lowest resistivity and highest transparency in the visible spectrum) were obtained at Ts = 450°C (for In_2O_3 films) and 430°C for SnO_2 films, the spraying angle 45°, spraying rate 0,08 $cm^3.s^{-1}$. Under this technological conditions the influence of film thickness on the electrical resistivity was examined. The sheet resistance (Rs) of the films decreases with increase in thickness/deposition time (Fig. 1).

The lowest Rs were reached in the range of the thickness 150–300 nm. As the thickness of the films was uniform, the resistivity ρ of the films can be calculated from the equation $\rho = Rs.d$, where d is the film's thickness. A low resistivity was measured for the 200-250 nm thick ITO films in the range of $3.10^{-4} - 7.10^{-4}$ Ω.cm and for 250–300 nm thick FTO films – $2.5.10^{-4} - 5.10^{-4}$ Ω.cm respectively.

The In_2O_3: Sn and SnO_2: F films deposited on a glass substrate were investigated concerning the optical transmission by spectro-photometrical method in UV, VIS spectral ranges (300–1800 nm). The transmission characteristics are presented in Fig. 2.

A high transparency (over 95%) can be seen in the VIS spectral ranges for the two kinds of the films.

The SEM and AFM were used to characterize the surface morphology. The SEM and AFM images of all samples displayed a homogeneous surface with small crystallite size (granular structure) (Fig. 3).

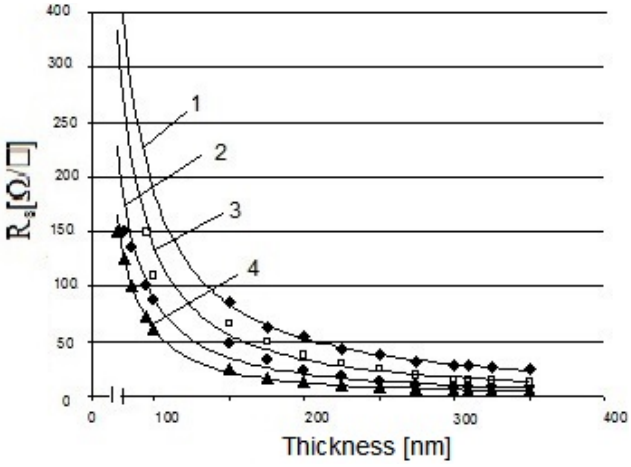


Fig. 1. The sheet electrical resistance (Rs) of the films as a function of the film's thickness: (1) pure In_2O_3 film; (2) doped In_2O_3; (3) pure SnO_2; (4) doped SnO_2.

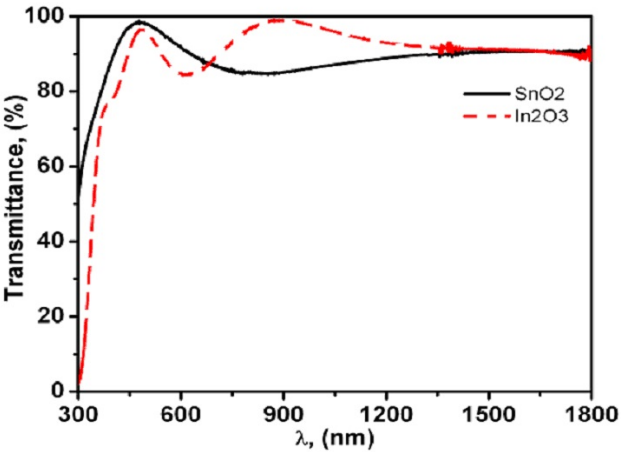


Fig. 2. Optical transmittance of doped SnO_2 and In_2O_3 films on a glass substrate with thickness 200 nm at 450°C.

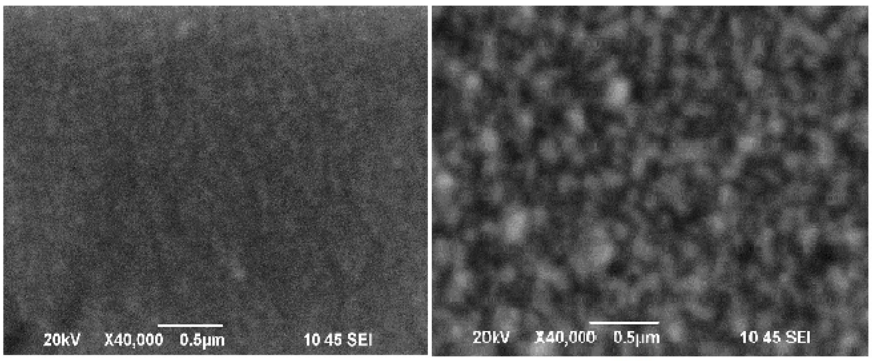


Fig. 3. SEM image of the surface of In_2O_3 (a) and SnO_2 (b) obtained at a magnification 40000.

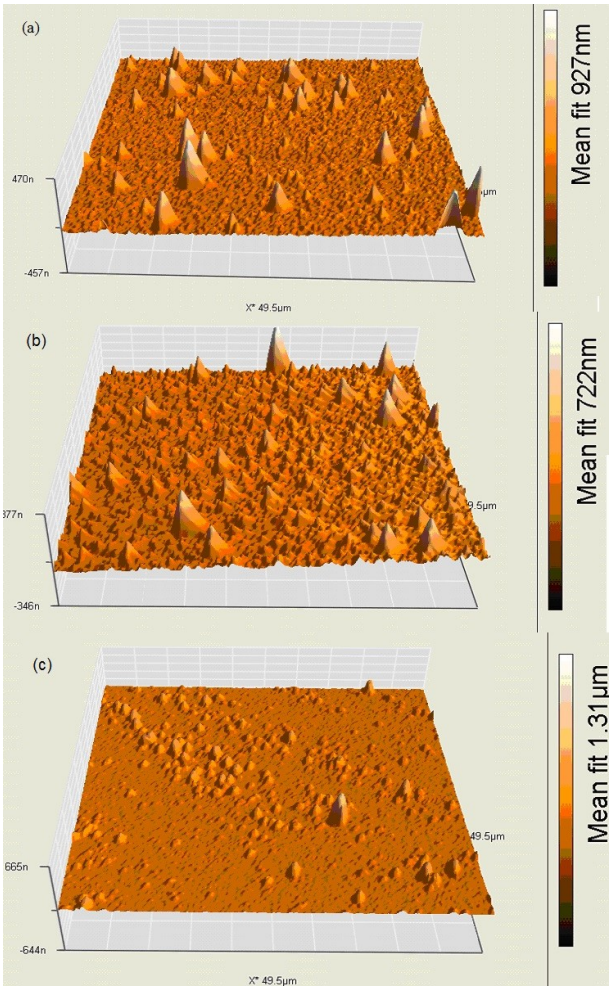


Fig. 4. 3D image of the topography of the layers of In_2O_3 with a thickness: 163 nm (a), 210nm (b) and 300nm (c).

The particles are close together without any pores separating them. The grain size and the roughness of the SnO_2 films are bigger than that of In_2O_3.

The AFM surface morphology of ITO films with different thickness is shown in Fig. 4 (a–c).

Whit increasing the thickness of the layers the grain size increase and the surface became more uniformity.

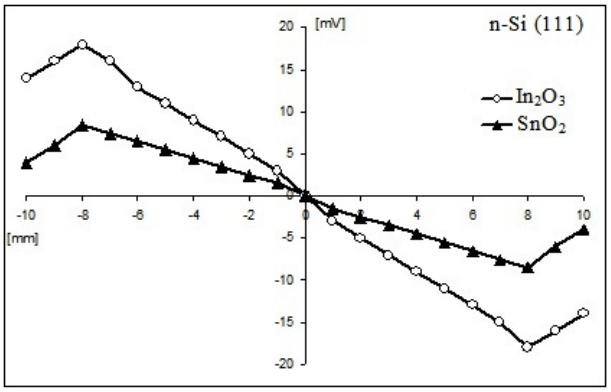


Fig. 6. Position characteristics of the two types of structures.

The films have a very smooth surface, which is beneficial for their application in optoelectronic devices with transparent conducting layers.

In this work we used the films deposited onto silicon substrate with a thin 2 nm native SiO_2, to prepare a structure Si-SiO_2-ITO or FTO, which works on the base of the lateral photovoltaic effect (LPE) (Fig. 5 a, b).

This structure detects very small displacements due to its output of lateral photovoltage changing linearly with light spot position, over the metal oxide plane, between two Ag contacts.

The contacts distance was 40 mm.

All samples were scanned with a light spot with diameter 0.5mm and the resulting photovoltage was measured using standard lock-in techniques.

The LPV measurements of the structure show good linear characteristics with LPV sensitivities (Fig. 6)

LPV is the largest when the incident radiation spot is closest to the electrodes and shows linear decrease as the spot is scanned away from the contacts, becoming zero at the midpoint of these two contacts.

LPV sensitivities are about 20 mV/mm for the structure with In_2O_3 film and 8 mV/mm with SnO_2 film. The results show that Si/ITO structures have bet-

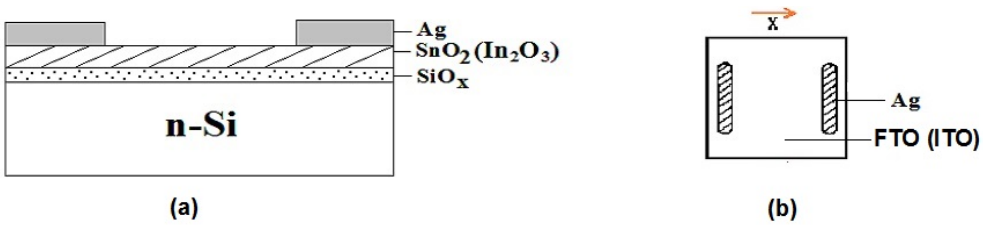


Fig. 5. Schematic view of a two dimensional position sensitive photodetector: (a) cross section, (b) over view.

ter LPV sensitivities than Si/FTO, which relates with the properties of the oxide materials.

CONCLUSION

The results demonstrate the availability of the as examined metal oxide thin films for optoelectronic device applications and especially for preparing position sensitive sensors.

REFERENCES

[1] M. A. Olopade, O. E. Awe, A. M. Awobode, N. Alu, *Afr. Rev. Phys.* **7:0018**, 177–181 (2012).

[2] M. Hassan Suhail, M. M. Abdulach and S. I. Abbas, *J. Chem. Biol. Phys. Sci. (JCBPSC)* **2**, 4, 1963–1973 (2012).

[3] R. Riveros, E. Romero, G. Gordilio, *Braz. J. Phys.* **36**, 3B, September (2006).

[4] M. H. Sohan, D. Kim, S. J. Kim, N. W. Paik, *J. Vac. Sci. Technol.* **A.21**, 1347 (2003).

[5] J. S. Cho, K. H. Yoon, S. K. Koh, *J. Appl. Phys.* **89**, 3223 (2001).

[6] J. E. Costellamo, Hand book of Display Technology Academic Prese, New York (1992)

[7] I. Chambouleyron, E. Saucedo, *Sol. Energ. Mater*. **1**, 299–311 (1979).

[8] D. E. Carlson, Proceeding of the 14th IEEE. Photovoltaic Specialists Conference, San Diego, California 1980, p. 291.

[9] N. Biyikli, T. Kartgoglu, O. Aytur, I. Kimukin, E. Ozbay, *Appl. Phys. Lett.* **79**, 2838 (2001).

[10] S. Kaleemulla, A. Sivasankar Reddy, S. Uthauna, P. Sreedhara Reddy, *Mater. Lett.* **61**, 4309–4313 (2007).

[11] A. Subrahmanyam, U. K. Bank, *J. Phys. Chem. Solids* **66**, 817–822 (2005)

[12] L. C. Chen, S. C. Lin, *Solid State Electron.* **50**, 1355 (2006).

[13] R. A. Sailer, A. Wanger, C. Schmit, N. Klaverkamp, D. L. Schulz, *Surf. Coat. Technol.* **203**, 835 (2008).

[14] M. A. Flores, R. Castanedo, G. Torres, J. Marquez, O. Zelaya, *Thin Solid Films* **570**, 681 (2008).

[15] A. V. Moholkar, C. M. Pawar, K. Y. Rajpure, V. Ganesan, C. H. Bhosale, *J. Alloys Compd*. **464**, 387 (2008).

[16] P. V. Nho, D. D. Thuan, P. H. Ngan, *J. Ovonic Research* **9**, 3, 73–79 (2013).

[17] S. S. Hanthi, C. Snbramanian, R. Ramasamy, *Mater. Sci. Eng.* **57**, 127–134 (1999).

ТЪНКИ СЛОЕВЕ ОТ МЕТАЛНИ ОКСИДИ ЗА ПОЛУЧАВАНЕ НА ПОЗИЦИОННО ЧУВСТВИТЕЛЕН ФОТОДЕТЕКТОР

В. Желев, Пл. Петков, Ив. Маркова, Т. Петров

Химикотехнологичен и металургичен университет, бул. "Св. Кл. Охридски" №8, София, България

(Резюме)

Получени са прозрачни проводящи слоеве легирани с флуор (F) SnO_2 (FTO) и легирани с калай (Sn) In_2O_3 (ITO) чрез пулверизиране на 0.2 M алкохоло-водни разтвори на In_2Cl_3 и $SnCl_4$ върху нагряти при 450°C подложки от стъкло и монокристален силиций. Изследвана е зависимостта на електричното съпротивление на слоевете от дебелината им.

Оптичните свойства са охарактеризирани с UV-VIS, микроструктурата и морфологията на повърхността - със сканираща електронна микроскопия (СЕМ) и AFM. Слоевете са поликристални, с високо оптично пропускане (над 95%) във видимата област и специфично съпротивление в диапазона $10^{-3} \div 10^{-4}$ Ω.cm. Отлагането на слоеве с високи прозрачност и проводимост върху окислени силициеви подложки, дава възможност да бъдат изготвени позиционно чувствителни структури от типа Si-SiO_2 – метален оксид, действащи на основата на латерален фотоефект.

Снети са позиционните характеристики на структурите. Те притежават висока линейност, стръмност и симетричност. Така създадените структури могат да бъдат използвани за прецизно измерване на линейни и ъглови отмествания.

Bulgarian Chemical Communications, Volume 47, Special Issue B (pp. 177–181) 2015

Predicting the erosion of the cathode material in PVD systems

N. Petkov*

Central Laboratory of Applied Physics, Bulgarian Academy of Sciences,
61 Sankt Petersburg Blvd., BG-4000 Plovdiv, Bulgaria

Predicting the erosion of the cathode material in cathodic arc evaporation of metal in a vacuum environment is an interesting task with a variety of applications. In this paper, a method for calculating of the evaporated cathode material as a function of the arc current by which it was evaporated is presented. The method is suitable for the processes of the cathodic arc evaporation of metals in a vacuum environment from massive cathodes by DC arc. In the model has introduced a correction factor that represents the differences in technical terms of the metal evaporation process in vacuum environment by electric arc. The correction factor is determined experimentally once-through for each different type of the cathode shape. The method is illustrated by an example of arc evaporation of massive titanium cylindrical shape cathode.

Key words: PVD, vacuum arc, cathode spot

INTRODUCTION

The ability to be able to determine the evaporated quantity of the cathode material depending on the magnitude of the electric arc current in the PVD systems is crucial and it is a first step in the modeling of coatings deposition process in such systems.

Cathode erosion has been theoretically studied by various researchers using models based on the balance of energy flux and charged particles between the spot and the near-cathode region.

The topic of arc discharges has been discovered at the beginning of the 19th century, serious efforts regarding their physical explanation and especially the modeling of electrode processes did not start until one century later [1]. One of the earliest investigations of this area are the works of Langmuir [2, 3], Tonks and Langmuir [4], Mackeown [5]. As Riemann reported in [6] the basic features of the plasma-sheath transition have been revealed in the works of Langmuir [3] – especially in the famous kinetic analysis of the low-pressure column due to Tonks and Langmuir [4]. Years later Dolan and Dyke [7] and Murphy [8] presented their works "Temperature and field emission of electrons from metal" and "Thermionic emission, field emission, and the transition region", following by Lee with his works over T-F theory of electron emission in high current arcs [9], energy distribution and cooling effect of electrons emitted from an arc cathode [10], and theory of the cathode mechanism in meal vapor arcs [11], which has been turned in a base for the later works over understanding and modeling the cathode arc processes.

The theory and conception of the cathode spot, as the cathode material erosion in vacuum is wide discussed in literature by Lee in 1951, 1960, 1961 [9–11], Ecker 1963 [12], Hantzsche in 1976 [13], Lyubimov in 1978 [14], Ivanov in 1985 [15], Nazarov in 1990 [16], Puchkarev in 1990 [17], Mitterauer in 1996 [18], Gayet in 1996 [19], Jüttner in 1997 [20], Anders in 1997 [21], Coulombe in 1997 [22–24], Anders in 2001 [25], Massaad in 2006 [26], Lefort in 2012 [27].

Kimblin [28] reported that the maximum ion current is in range of 7–10% of the arc current for electrodes with DC arc current level. He has made experiments with wide number of elements in arc current range of 50–1000 A. In [29], a year later, Kimblin reported that the maximum ion current from the cathode regions is approximately 8% of the arc current. This led to the conclusion that ion currents of approximately 8% of the arc current are emitted from the cathode regions associated with arc spots on the cathode materials in general.

Coulombe [23] reported that a net positive space charge sheath, or cathode sheath, of voltage drop is formed at the plasma-cathode boundary due to the presence, in different amounts, of three charge carriers [6]: 1) the ion generated by ionization of the atoms vaporized at the cathode spot surface, accelerated back toward the cathode; 2) the Boltzmann distributed plasma electrons retro-diffusing toward the cathode; and 3) the thermo-field electrons emitted by the cathode spot surface.

* To whom all correspondence should be sent:
petkovnik@gmail.com

© 2015 Bulgarian Academy of Sciences, Union of Chemists in Bulgaria

Boxman [1], Coulombe [22–24], Massaad [26] and Lefort [27] have suggested the models of the processes near to the cathode surface which are based on the knowledge the temperature of cathode spot and electrons, the material vapour pressure. Their models are quite good to understanding the processes around the electric arc and the cathode spot region, but in these cases making the mathematical modeling and simulation require additional information (the temperature of cathode spot and electrons, the material vapour pressure) to be predict the cathode erosion.

In this paper, a method for calculation of the evaporated cathode material, in PVD systems, as a function of the arc current is presented. Correction factor that represents the differences in technical terms of the metal evaporation process in vacuum environment by electric arc is introduced in the model. The method is illustrated by an example of arc evaporation of massive titanium cylindrical shape cathode.

SURFACE OF CATHODE

The main processes which occur at the cathode surface are emission of electrons and atoms. The emission process, when the temperature and the field are high, is strongly dependent on both variables, and has been named T-F emission by Dolan and Dyke [7, 9]. The electron emitted current density from the heated metal surface to the temperature T_s by the T-F emission is expressed with the Ridchardson-Dushman equation for the thermionic emission once corrected for the Schottky effect is [1, 24, 30]:

$$J_{TF} = \frac{4\pi e m_e k^2 T_s^2}{h^3} \exp\left(-\frac{e\phi_{eff}}{kT_s}\right) \tag{1}$$

$$\phi_{eff} = \phi - \sqrt{\frac{eE}{4\pi\varepsilon_0}} \tag{2}$$

where: m_e and e are the mass and charge of the electron, k and h are the Boltzmann and Planck constants, ϕ_{eff} and ϕ are the effective work function and the work function of the cathode material, ε_0 is the permittivity of vacuum, and E is the electric field near to the cathode surface.

The total current density J_T on the cathode surface is composed of three parts [1]:

$$J_T = J_i + J_e + J_{e,p} \tag{3}$$

where the electron current density J_e is given mainly by J_{TF}; $J_{e,p}$ is the electron current density from plasma to the cathode, and J_i is the ion current density. The influence of the $J_{e,p}$ can be neglected and for the current density is obtained:

$$J_T = J_i + J_e \tag{4}$$

The total current density, from other hand, can be calculated as a ratio between the arc current I_a and cathode spot area $S_{cs} = \pi r_{cs}^2$, where r_{cs} is the cathode spot radius [1, 26].

$$J_T = \frac{I_a}{S_{cs}} \tag{5}$$

The electric field at the cathode E is calculated by equation [5, 9, 11]:

$$E^2 = \frac{4}{\varepsilon_0} J_T \left[(1-s)\sqrt{\frac{M}{2e}} - s\sqrt{\frac{m_e}{2e}}\right]\sqrt{V_C} \tag{6}$$

where: M is the ion mass, V_C is the cathode fall, s is the fraction of current carried by electrons in the cathode spot region; $J_T(1-s)$ is equal to the ion current density and $J_T s$ is equal to the electron current density, so the equation Eq.(6) can be writes as:

$$E^2 = \frac{4}{\varepsilon_0}\left[J_i\sqrt{\frac{M}{2e}} - J_e\sqrt{\frac{m_e}{2e}}\right]\sqrt{V_C} \tag{7}$$

The power density of heat conduction in the cathode body is estimated as is presented in [26]:

$$S_T = \frac{K_T(T_s - T_0)\sqrt{\pi}}{r_{cs}} \tag{8}$$

where: T_s is the cathode spot temperature, $T_0 = 300K$ is the temperature far from the cathode spot (the ambient temperature), K_T is the thermal conductivity of the cathode material.

The Joule heating power density, in a massive cathode, is calculated following the method of Rich [31] reduced to the cathode spot area:

$$S_J = \frac{32 r_{cs}}{100\sigma_{el}} J_T^2 \tag{9}$$

where σ_{el} is the electrical conductivity of the cathode material.

The energy balance at the cathode surface is expressed as [1]:

$$\frac{J_i}{e}(eV_c + V_i - \phi_{eff}) - \frac{J_e\phi_{eff}}{e} + \frac{2kT_e J_{e,p}}{e} - \left(W_{ev} + \frac{2kT_s}{m_n}\right)\Gamma_T m_n - \sigma_{sb}T_s^4 + S_r + S_J - S_T = 0 \tag{10}$$

where V_i is the ionization potential, S_r is the radiation from the plasma, W_{ev} is the energy of evaporation (J/kg), and σ_{sb} is the Stefan-Boltzmann constant. In the Eq. (10): the first term expresses ion impact heating; the second term expresses electron emission cooling; the third term expresses heating from the back-flux of plasma electrons; the fourth term expresses evaporative cooling; the fifth term expresses radiative cooling from the cathode surface; the sixth term expresses the plasma radiation; the seventh - expresses the Joule heating; and the eighth term expresses the conductive cooling. The third and the sixth term have an insignificant influence in the equation, so they can be neglected. Therefore the balance expression can be writes as:

$$\frac{J_i}{e}(eV_c + V_i - \phi_{eff}) - \frac{J_e\phi_{eff}}{e} - \left(W_{ev} + \frac{2kT_s}{m_n}\right)\Gamma_T m_n - \sigma_{sb}T_s^4 + S_J - S_T = 0 \quad (11)$$

By Eq. (11) is calculated full flow of particles which have left the cathode, including the particles forming cathode sheath plasma, irreversibly left the cathode particles, as well as those which are returned to the cathode. We are only interested in the cathode erosion - those particles that irreversibly cathode-out particles. The technical and the practical realizations of the PVD systems have influence on the cathode material evaporation processes. So, to be accounted this influence in the calculation procedure is included a correction factor. The correction factor is determined experimentally once-through for each type cathodes (first generation, second generation, and etc.). When the correction factor has determined, the erosion of the cathode material (Ti, Al, Cr, and etc.) is calculated for the respective cathode type.

CALCULATIONS

The presented mathematical model for prediction the erosion of the cathode material in PVD systems has follows steps: chosen value of the arc current; determination the cathode spot radius; calculation the total current density; calculation the ion and electron current density; calculation the electric field value; calculation the effective work function of the cathode material; calculation the cathode spot temperature; calculation the Joule heating; calculation the conductive cooling; and calculation the evaporated quantity material.

To illustrate the calculation procedure, an example of metal evaporation of massive cylindrical shape titanium cathodes in vacuum environment is used, as the arc current is chosen to be 70 A. The cathode spot radius is determined according the value of the arc current by the extrapolation of the Fig. 12 from [17]. For the chosen arc current the cathode spot radius is $r_{cs} = 4.6125 \times 10^{-6}$ m.

The total current density is calculated by the Eq.(5) and it is $J_T = 1.047 \times 10^{12}$ Am^{-2}. The ion current density for titanium cathode is 8% from the total current density [28,29], so the ion current density, for in the example, is $J_i = 8.378 \times 10^{10}$ Am^{-2}. Therefore using the Eq.(4) for the electron current density is received $J_e = 9.635 \times 10^{11}$ Am^{-2}.

The electric field value of $E = 9.248 \times 10^9$ V/m is calculated by the Eq.(7). The Joule heating is calculated by Eq.(9): $S_J = 6.8 \times 10^{11}$ Wm^{-2}. The conductive cooling $S_T = 2.394 \times 10^{10}$ Wm^{-2} is calculated by Eq.(8). So the full flow of evaporated particles of the material (the total heavy particle flux [1]) $\Gamma_T = 2.986 \times 10^{30}$ atoms/(sm^2) is calculated by Eq.(11), which is 57.58×10^{-3} kg/h for the 70A arc current.

Several measurements have been made on the used massive cylindrical shaped titanium cathodes, according to which the data for erosion rate is 9033 Ah/kg, which means that with the arc current of 70A the erosion rate is 7.75×10^{-3} kg/h, or 13.46% from the calculated value Γ_T is the real evaporated quantity of material. Therefore, the correction factor for the massive cylindrical shape cathode is 0.1346.

Fig. 1 shows the evaporation rate of the massive cylindrical shaped titanium cathode as a function of the arc current.

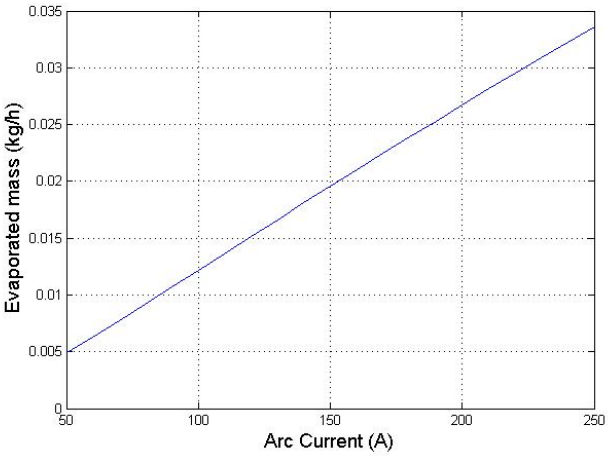


Fig. 1. The evaporation rate of the massive cylindrical shape titanium cathode as a function of the arc current.

CONCLUSIONS

Predicting the erosion of the cathode material in cathodic arc evaporation of metal in a vacuum environment is an interesting task with a variety of applications. The paper presents the model to predicting the erosion of the cathode material in PVD systems. The model gives the correlation between the arc current and the evaporated quantity of the cathode material in PVD processes. Additional preliminary information as the cathode spot temperature and/or the vapor pressure of the cathode material is not necessary.

Correction factor that represents the differences in technical terms of the metal evaporation process in vacuum environment by electric arc is introduced in the model. The correction factor is determined experimentally once-through for each generation cathodes. When the correction factor is determined, the erosion of different cathode material can be calculated.

The model has been developed on the basis of massive titanium cathodes and is applicable to all massive metal cathodes evaporated by an electric arc in vacuum environment by DC arc.

REFERENCES

[1] R. L. Boxman, D. M. Sanders, Ph. J. Martin and J. M. Lafferty, *Handbook of vacuum arc science and technology*, Noyes Publications, New Jersey, 1995.

[2] I. Langmuir, *Phys. Rev.* **22**, 585–613 (1925).

[3] I. Langmuir, *Phys. Rev.* **13**, 954–989 (1929).

[4] L. Tonks and I. Laugmuir, *Phys. Rev.* **34**, 876–922 (1929).

[5] S. S. Mackeown, *Phys. Rev.* **34**, 611–614 (1929).

[6] K-U. Riemann, *J. Phys. D: Appl. Phys.* **24**, 493–518 (1991).

[7] W. W. Dolan and W. P. Dyke, *Phys. Rev.* **95**, 327–332 (1954).

[8] E. L. Murphy and R. H. Good Jr., *Phys. Rev.* **102**, 1464–1473 (156).

[9] T. H. Lee, *J. Appl. Phys.* **30**, 166–171 (1959).

[10] T. H. Lee, *J. Appl. Phys.* **31**, 924–927 (1960).

[11] T. H. Lee and A. Greenwood, *J. Appl. Phys.* **32**, 916–923 (1961).

[12] G. Ecker and W. Kröll, *The Physics of Fluids* **6**, 62–69 (1963).

[13] E. Hantzsche, B. Jüttner, V. F. Pushkarov, W. Rohrbeck and H. Wolff, *J. Phys. D: Appl. Phys.* **9**, 1771–1781 (1976)

[14] G. A. Lyubimov and V. I. Rahovskij, *Adv. Phys. Sci.* **125**, 665–706 (1978).

[15] V. A. Ivanov, B. Juttner and H. Pursch, *IEEE Transactions on Plasma Science* **PS13**, 334-336 (1985).

[16] S. N. Nazarov, V. I. Rakhovsky and V. G. Zhurbenko, *IEEE Transactions on Plasma Science* **18**, 682–684 (1990).

[17] V. F. Puchkarov and A. M. Murzakayev, *J. Phys. D: Appl. Phys.* **23**, 26–35 (1990).

[18] J. Mitterauer, *Appl. Surf. Sci.* **94/95**, 161–170 (1996).

[19] R. Gayet, C. Harel, T. Josso and H. Jouin, *J. Phys. D: Appl. Phys.* **29**, 3063–3070 (1996).

[20] B. Jüer, *J. Phys. IV France* **7**, 31–45 (1997).

[21] A. Anders, *Phys. Rev. E* **55**, 969–981 (1997).

[22] S. Coulombe and J-L. Meunier, *Plasma Sources Sci. Technol.* **6**, 508-517 (1997).

[23] S. Coulombe and J-L. Meunier, *IEEE Transactions on Plasma Science* **25**, 913–918 (1997).

[24] S. Coulombe, "A Model od the Electric Arc Attachment on Non-refractory (Cold) Cathodes", Ph.D. Thesis, McGill University, 1997.

[25] A. Anders, *Appl. Phys. Lett.* Manuscript Code # L01-3420, LBNL-48989 (2001).

[26] M. Messad, A. W. Belarbi, A. Lefort and M. Abbaoui, *Acta Electrotech. Inform.* **6**, 1–8 (2006).

[27] A. Lefort and M. Abbaoui, *IOP Conf. Ser.: Mater. Sci. Eng.* **29**, art. num. 012006 (2012).

[28] C. W. Kimblin, *J. Appl. Phys.* **77**, 3074-3081 (1973).

[29] C. W. Kimblin, *J. Appl. Phys.* **45**, 5235–5244 (1974).

[30] J. Paulini, T. Kiein and G. Simon, *J. Phys. D: Appl. Phys.* **26**, 1310–1315 (1993).

[31] J. A. Rich, *J. Appl. Phys.* **32**, 1023–1031 (1961).

ПРЕДСКАЗВАНЕ НА ЕРОЗИЯТА НА МАТЕРИАЛА НА КАТОДА ПРИ PVD СИСТЕМИ

Н. Петков

Централна лаборатория по приложна физика, Българска академия на науките,
бул. "Санкт Петербург" №61, 4000 Пловдив, България

(Резюме)

Предсказването на ерозията на материала на катода при системите за катодно дъгово изпарение на метали във вакуумна среда е интересна задача с различни приложения. В този материал е представен метод за изчисление на изпареното количество вещество на материала на катода като функция от тока на електрическата дъга, чрез която той се изпарява. Методът е подходящ за процеси на катодно дъгово изпарение на метали във вакуумна среда на масивни катоди чрез постояннотокова дъга. Въведен е коригиращ коефициент, чрез който се отчитат различията в техническо отношение и при техническата реализация на самия процес на изпарение при различните PVD системи като геометрията на катода и магнитните му полета. Коригиращият коефициент се определя експериментално еднократно за всеки геометричен тип катоди. Методът е илюстриран чрез катодно дъгово изпарение на масивни цилиндрични катоди.

Възможността да може да се определя количеството изпарено вещество от катода в зависимост от големината на тока на дъгата, при системите за катодно дъгово изпарение на метали във вакуумна среда е решаващо, или е първа стъпка към моделирането на процесите на израстване на слоеве в този PVD системите.

ATOMIC AND NUCLEAR PHYSICS

АТОМНА И ЯДРЕНА ФИЗИКА

Bulgarian Chemical Communications, Volume 47, Special Issue B (pp. 185–191) 2015

Resistive plate chambers for the LS1 muon upgrade in CMS experiment at LHC

M. Shopova[1*], M. S. Kim[2], Y. Ban[3], J. Cai[3], Q. Li[3], S. Liu[3], S. Qian[3], D. Wang[3], Z. Xu[3], F. Zhang[3], Y. Choi[4], D. Kim[4], J. Goh[4], S. Choi[5], B. Hong[5], J. W. Kang[5], M. Kang[5], J. H. Kwon[5], K. S. Lee[5], S. K. Lee[5], S. K. Park[5], L. M. Pant[6], A. K. Mohanty[6], R. Chudasama[6], J. B. Singh[7], V. Bhatnagar[7], A. Mehta[7], R. Kumar[7], S. Cauwenbergh[8], S. Costantini[8], A. Cimmino[8], S. Crucy[8], A. Fagot[8], G. Garcia[8], A. Ocampo[8], D. Poyraz[8], S. Salva[8], F. Thyssen[8], M. Tytgat[8], N. Zaganidis[8], W. V. Doninck[9], L. Chaparro[9], A. Cabrera[10], J. P. Gomez[10], B. Gomez[10], J. C. Sanabria[10], C. Avila[10], A. Ahmad[11], S. Muhammad[11], M. Shoaib[11], H. Hoorani[11], I. Awan[11], I. Ali[11], W. Ahmed[11], M. I. Asghar[11], H. Shahzad[11], A. Sayed[12,13,**], A. Ibrahim[12,13,**], S. Aly[12,13,**], Y. Assran[12,13,**], A. Radi[12,13,**], T. Elkafrawy[12,13,**], A. Sharma[14], S. Colafranceschi[14], M. Abbrescia[15], C. Calabria[15], A. Colaleo[15], G. Iaselli[15], F. Loddo[15], M. Maggi[15], S. Nuzzo[15], G. Pugliese[15], R. Radogna[15], R. Venditti[15], P. Verwillingen[15], L. Benussi[16], S. Bianco[16], D. Piccolo[16], P. Paolucci[17], S. Buontempo[17], N. Cavallo[17], M. Merola[17], F. Fabozzi[17], O. M. Iorio[17], A. Braghieri[18], P. Montagna[18], C. Riccardi[18], P. Salvini[18], P. Vitulo[18], I. Vai[18], A. Magnani[18], A. Dimitrov[19], L. Litov[19], B. Pavlov[19], P. Petkov[19], A. Aleksandrov[1], V. Genchev[1], P. Iaydjiev[1], M. Rodozov[1], G. Sultanov[1], S. Stoykova[1], R. Hadjiiska[1], H. S. Ibargüen[20], M. I. P. Morales[20], S. C. Bernardino[20], I. Bagaturia[21], Z. Tsamalaidze[21], I. Crotty[22]

[1] *Institute for Nuclear Research and Nuclear Energy, Bulgarian Academy of Sciences, 72 Tzarigradsko Chaussee Blvd., 1784 Sofia, Bulgaria*
[2] *Kyungpook National University, Department of Physics, 80 Daehakro, Bukgu, Daego, 702-701, Republic of Korea*
[3] *Peking University, Department of Technical Physics, CN-100 871 Beijing, China*
[4] *Department of Physics, SungKyunKwan University, 2066, Seobu-ro, Jangahn-gu, Suwon, Gyeonggi-do, Republic of Korea*
[5] *Department of Physics and Korea Detector Laboratory, Korea University, Aman-dong 5-ga, Sungbuk-gu, Seoul, Republic of Korea*
[6] *BARC, Electronics Division (BARC), Trombay, Mumbai 400 085, India*
[7] *Panjab University, Department of Physics, Chandigarh Mandir 160 014, India*
[8] *Ghent University, Department of Physics and Astronomy, Proeftuinstraat 86, BE-9000 Ghent, Belgium*
[9] *VUB, Dienst Elementaire Deeltjes, Pleinlaan 2 BE-1050 Brussel, Belgium*
[10] *Universidad de Los Andes, Apartado Aéreo 4976, Carrera 1E, no. 18A 10, CO-Bogotá, Colombia*
[11] *Islamabad-NCP, Quaid-I-Azam University, Islamabad-44000 Pakistan*
[12] *Academy of Scientific Research and Technology of the Arab Republic of Egypt, 101 Sharia Kasr El-Ain, Cairo, Egypt*
[13] *Helwan University, Qsim Helwan, Cairo governatorate, Egypt*
[14] *CERN, CH-1211 Geneva 23, Switzerland*
[15] *Universita e INFN, Sezione di Bari, Via Orabona 4, IT-70126 Bari, Italy*
[16] *INFN, Laboratori Nazionali di Frascati, PO Box 13, Via Enrico Fermi 40, IT-00044 Frascati, Italy*
[17] *Universita e INFN, Sezione di Napoli, Complesso Univ. Monte S. Angelo, Via Cintia, IT-80126 Napoli, Italy*
[18] *Universita e INFN, Sezione di Pavia, Via Bassi 6, IT-Pavia, Italy*
[19] *University of Sofia, Faculty of Physics, 5, James Bourchier Boulevard, BG-1164 Sofia, Bulgaria*
[20] *Benemérita Universidad Autónoma de Puebla, Av. San Claudio y 18 sur, edif. 111 A Ciudad Universitaria, Col. San Manuel, Puebla, Pue. C.P. 72570, Mexico*
[21] *Tibilisi-IHEPI, Tbilisi State University University Street 9 GE-380 086 Tbilisi, Georgia*
[22] *University of Wisconsin, Department of Physics 1150 University Avenue Madison, WI 53706 USA*
[**] *Supported by the European FP7 EENP2 project*

In the view of the high luminosity run of LHC from 2015 onwards, during the last two years (2013/2014 – Long Shutdown LS1) one of the major upgrades of the CMS experiment is completing and improving the muon system performances by installing a fourth layer of RPC detectors in the forward region. The fourth trigger station (on two new endcap disks) consists of 144 double-gap RPC chambers, which are assembled and tested at three different production sites – CERN (Switzerland/France), Ghent (Belgium) and BARC (India). The complete chamber construction, quality control procedures and preliminary results are detailed here.

Key words: resistive-plate chambers; muon spectrometers

© 2015 Bulgarian Academy of Sciences, Union of Chemists in Bulgaria

INTRODUCTION

The Compact Muon Solenoid (CMS) experiment [1] has been collecting data successfully, since the start of the first Large Hadron Collider (LHC) physics run in 2009. Phase 1 of the LHC will continue until about 2022 and during that period, the instantaneous luminosity delivered to the experiments is foreseen to increase gradually up to more than twice its nominal value of 10^{34} cm^{-2}s^{-1}. There are two shutdown periods [2] scheduled to give the machine and the experiments the necessary time to anticipate these luminosity increases - Long Shutdown 1 (LS1) in 2013/2014 prepares the accelerator to run at its nominal luminosity and Long Shutdown 2 (LS2) in 2018/2019 should take it to 2.2 times this value. In particular the muon system during LS1 is upgraded with the installation of a new layer of Resistive Plate Chambers (RPC) [3] detectors on the endcap regions. Before this upgrade only three RPC layers were installed. Adding the fourth RPC station, called RE4, is going to increase the overall robustness of the CMS muon spectrometer while improving the trigger efficiency by adopting a three-out-of-four stations majority trigger logic, covering the region up to $|\eta| = 1.6$.

The RE4 project [4] is multi-national and is carried out by several institutions. The gas gaps for the RPC detectors are produced in Korea, while Pakistan, Italy and Finland are working on the front-end electronics, DAQ and power system. 200 cooling sets are produced and tested in India, while Bulgaria, Georgia, Mexico and Pakistan are responsible for detector assembly and testing. The chamber services (gas, cooling and cabling) are built in Italy, India and Pakistan, while China provides the readout strips and mechanical frame boxes. All countries provide participants in the chamber construction and testing.

The RE4 project consists of 72 super-modules, each of which is made by two RPC chambers, so the total is 144 double-gap RPCs. The new RE4 detectors are going to instrument two disks, called RE+ and RE-, located on the opposite endcaps of the detector. Each disk is made out of two rings - the inner one is called RE4/2, while the outer ring is called RE4/3. As shown in Fig. 1, there are 36 trapezoidal shaped detectors in each of the two rings, which are built in three different assembly sites: India (BARC), Belgium (Ghent University) and Switzerland/France (CERN). BARC and Ghent are in charge of 25% of the production each, respectively RE4/2 and RE4/3, while the remaining 50% of the production is carried out by CERN which work on both chamber types RE4/2 and RE4/3.

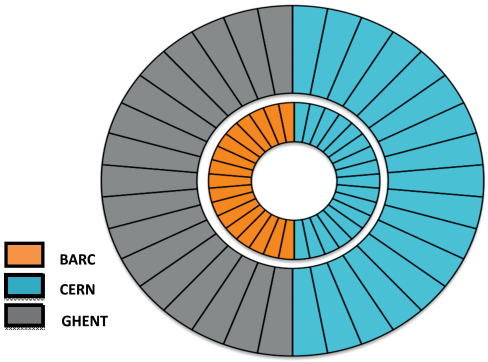


Fig. 1. Schematic layout of one of the two new endcap disks.

CHAMBER DESIGN, PRODUCTION AND QUALITY CONTROLS

The present RPC trigger logic requires hits in at least three layers and since in the system before the upgrade there are only three RPC detector stations in the endcaps, this causes the observed drop in the efficiency shown in Fig. 2. As the figure shows, adding the 4th layer in the endcaps, enabling a 3-out-of-4 trigger logic in those regions will bring the RPC endcap performance to a similar level as the barrel system (up to $|\eta| = 1.6$).

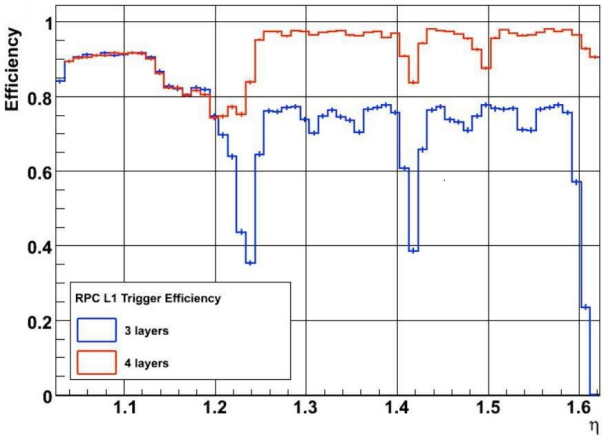
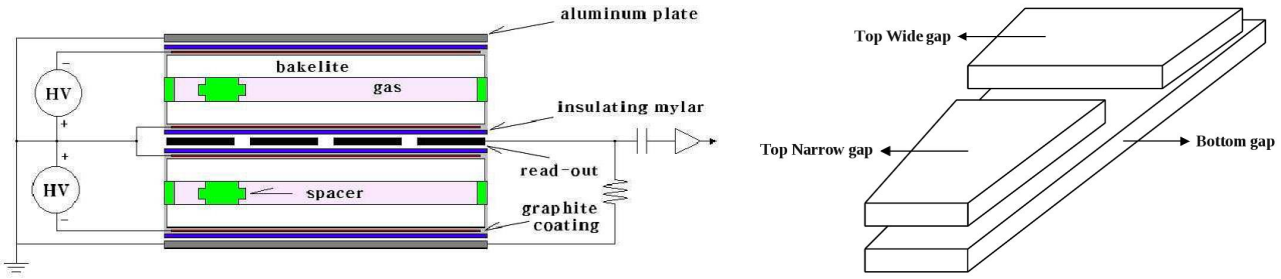


Fig. 2. Simulated RPC Level-1 trigger efficiency for the present system with three endcap layers compared to the system after the upgrade with four endcap layers.

* To whom all correspondence should be sent:
mariana.vutova@cern.ch



(a) (b)

Fig. 3. Schematic representation of the double-layer layout of the endcap chambers (a). Configuration of the gas gaps of the endcap chambers (b).

The RE4 project is inheriting the chamber design from the already existing RPC Endcap chambers, shown in Fig. 3. The detector relies on 2 mm trapezoidal shaped HPL gas gaps, that are organized in a double-layer configuration with a copper strip readout panel placed in between. The resistivity of the HPL sheets is of the order of 2 - 5 $\times$ 10^{10} Ωcm. A chamber is made of three kinds of different gap geometries - the bottom layer uses one large gas gap, while the top layer is segmented into two parts. This is done to simplify the signal cable routing.

The readout strips are segmented in three η-partitions with increasing strip pitch from 1.5 cm to 4 cm. Each partition has 32 strips, yielding a total of 96 strips per chamber. Coaxial cables are used to connect strips to Adapter Boards which are linked to 3 Front-End Boards (FEBs) per chamber. Every chamber has 1 Distribution Board (DB) for the electronics control. Link Boards (LBs) are the main components of the off-detector electronics. They receive signals in LVDS (Low-Voltage Differential Signaling) standard from the FEBs. The LBs perform the synchronization with the LHC clock and transmit the signals to Trigger Electronics in the control room. In each LB crate there is a Control Board (CB) that drives the crate, provides inter-crate communication and takes care of the connection to the readout and trigger systems.

The HPL sheets ($\approx$ 3500 m^2) are the first step in producing RPC gas gaps. The raw material comes from Italy, where the HPL panels are produced by the Puricelli firm (Milan), validated by INFN (Pavia), cut by RIVA firm (Milan) and finally the surface is cleaned by General-Tecnica (Frosinone). Then they are sent to Korea where the HPL panels are used for assembling RPC gaps. The Korean gap manufacturing site – KOrea DEtector Laboratory (KODEL) performs several measurements on the HPL panels in order to ensure the correct resistivity, color, roughness and thickness. Next step is graphite coating for the HPLs, which is protected with a polyethylene terephthalate (PET) film [5]. The assembled gaps are treated with linseed oil mixed with heptane. Once fabricated, the new RPC gaps go through series of tests to ensure the quality during the construction process. First are gas leak and spacer tests. Then gaps are subjected to high voltage (HV) scan to measure the dark current and to current monitoring at the expected operating voltage (9.7 kV) over one week. This first gaps validation is called Quality Control 1 (QC1). Once it is over, a box containing a number of gaps between 30 and 40 is dispatched from Korea to chamber assembly sites.

The chamber mechanics (honeycomb boxes, screen boxes, readout strip panels, etc.) are produced by two Chinese companies – Beijing Axicomb Technology Co., Ltd. and Beijing Gaonengkedi SGT Co., Ltd, while the detector electronics are produced in Pakistan. The new off-detector electronics are produced by the INFN (Italy), while the CMS Warsaw group (Poland) takes the responsibility to integrate the new electronics in the trigger system.

The final assembly of the RPC detectors is shared by three institutions – BARC (Mumbai, India), Ghent University (Ghent, Belgium) and CERN (Switzerland). Each of these assembly sites has built up special RPC labs with setups for detailed quality control of both RPC gas gaps and completed chambers.

In the second phase of the quality control (QC2) the RPC gaps performance is validated by repeating some of the tests performed in Korea. Once taken out of the boxes in the assembly sites, gaps are subjected to visual inspection, gas tightness, spacer test and electrical dark current measurement. While inspected visually, each gap is characterized with a de-

tailed checklist which ensures that there are no visual damages present and the gap is eligible to be used. The gas gap spacer and leak tests check that there are no detached gap spacers and the leak rate is within specifications (0.4 mbar/10 min). The last test in QC2 is the high voltage scan which main aim is measuring the dark current and its stability over a period of 3 days. There has been found an overall rejection factor of 10% at QC2.

When a site fully validates a set of three gaps, these are used to start the chamber construction. The quality control at this stage of detector production (QC3) goes through chamber visual inspection, gas tightness, electrical and dark current measurement, as well as cosmic muon commissioning by means of a dedicated cosmic ray stand (telescope). While under visual inspection, each chamber needs to pass through a detailed checklist in order to validate the manufacturing process of the chamber. After that comes the leak test, which measures the chamber gas leak. This is done in order to check whether, during chamber manufacturing, the gap gas inlets are correctly connected to chamber service panel. The electric test is done by powering and checking the front-end boards while the gaps are subjected to a high voltage scan in order to ensure that the RPC gaps operate without problems. The final procedure in the QC3 protocol is the chamber by chamber performed high voltage scan that aims at characterizing detector response while measuring main detector performance parameters such as efficiency, cluster size and noise. Each detector is subjected to three independent efficiency scans using three different configurations - double-gap, top single-gap and bottom single-gap. This is done because the RE4 chambers are based on double-gap RPCs. During each efficiency scan there are 7 runs taken at different effective HV, from 8.5 to 10 kV. In each run there are 10k events collected in approximately 2 hours. In order to maintain each RPC chamber gain constant against environmental changes, the scan is performed using the effective high voltage to correct the applied one on the chamber. The applied HV is corrected in response to the changes in environmental pressure according to Eq. (1) [6]:

$$HV_{\text{eff}} = HV \frac{p_0}{p} \frac{T}{T_0} \qquad (1)$$

where $p_0 = 990$ mbar.

The cosmic stand in each assembly site is equipped with two scintillator layers (top and bottom) that form the trigger. The front-end boards of the chambers are connected via flat cables to TDCs to tag and record all hits. Three reference chambers installed in the stand are used by the analysis routine to perform a tracking algorithm in order to reconstruct cosmic muon tracks.

After passing successfully the cosmic test, every chamber is powered on and monitored for about three weeks in order to check its stability over time. This is the next step (QC4) in quality control protocols for RPC detectors. If there are no problems with the dark current and it is stable, a pair of chambers, one RE4/2 and one RE4/3 type, is assembled into a Super Module. This assembly task is done in order to reduce the amount of time needed to install all RE4 detectors at CMS. Since RE4/2 and RE4/3 share the same cooling circuit and gas pipes, and are attached mechanically to the same structure, this allows for several commissioning protocols to be performed before the real detector installation at CMS. The first disk (RE4 positive) was installed in December 2013 while the installation of the second one (RE4 negative) finished in May 2014.

The full history of each chamber and every component is stored in an Oracle based Construction Database, which includes all measurements performed before, during and after the detector assembly. This enables CMS to follow the evolution of each chamber in time.

The RPC detector performance [7] starts with evaluating the gap performance during QC2 at assembly sites. First is the leak rate test, shown in Fig. 4(a), which is performed measuring the leak drop in time of each gap. The gaps are initially pressurized to 20 mbar over ambient pressure. Also at the end of this test, all gap spacers are checked in order to spot any detached one. Once the leak and the spacer tests are successfully ended, the gaps are subjected to a high voltage scan in order to measure the dark current response. During this test, the high voltage is ramped from 1 kV to 10 kV. There are two different steps of ramping - a step of 1 kV up to high voltage of 8 kV and a step of 100 V between 8 kV and 10 kV. Moreover, after the high voltage scan, all gaps are kept at 9.7 kV for 3 days for monitoring possible dark current drift in connection with pressure and temperature. Fig. 4(b) shows the dark current distribution for all gaps at the 10 kV.

After the gap performance evaluation is the turn of QC3, where the assembly sites have to fully commission each detector. The full evaluation of the

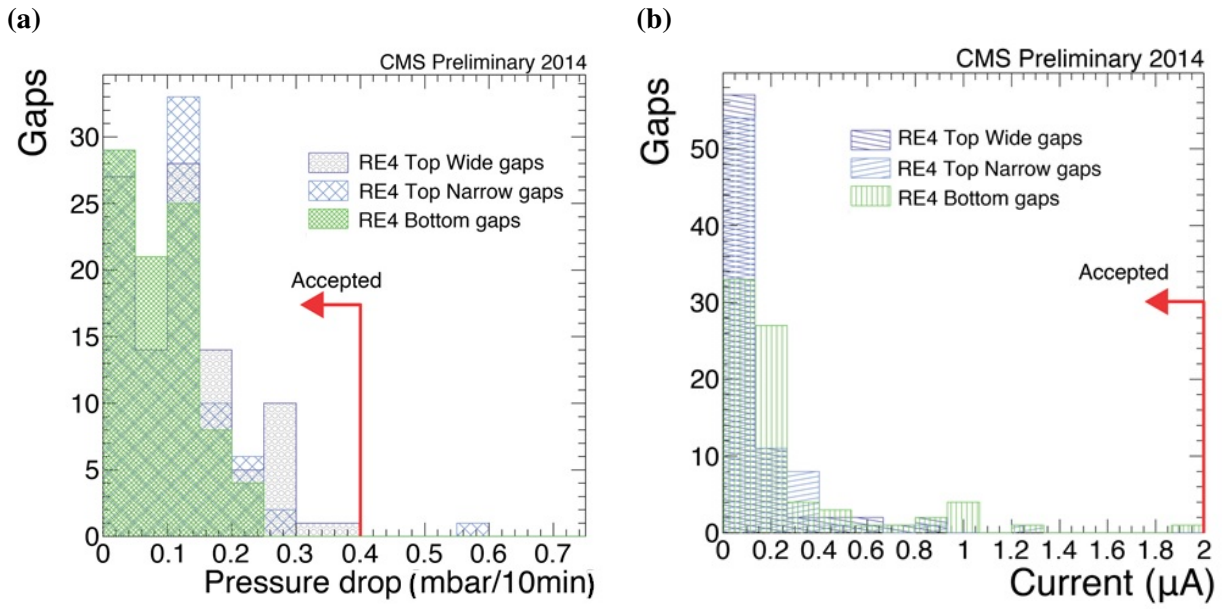


Fig. 4. Leak rate (a) and dark current (b) distributions of gaps adopted for the RE4 detector construction.

performance of RPC detectors under test and the full characterizing of each chamber is done using the tracking telescope. The average cluster size distribution, evaluated in three different η segments at the expected working point is shown in Fig. 5(a). The distribution of the expected working point is shown in Fig. 5(b).

The expected working point is defined by adding 150 V to the measured efficiency at 95%. The efficiency along the high voltage scan and the fitting of the data-points are described by Eq. (2) [8]:

$$\eta = \frac{\varepsilon_{\max}}{1+\exp^{-\lambda(HV_{\text{eff}}-HV_{50\%})}} \tag{2}$$

The high voltage at 50% efficiency (HV50%) is shown in Fig. 6. The overall average maximum

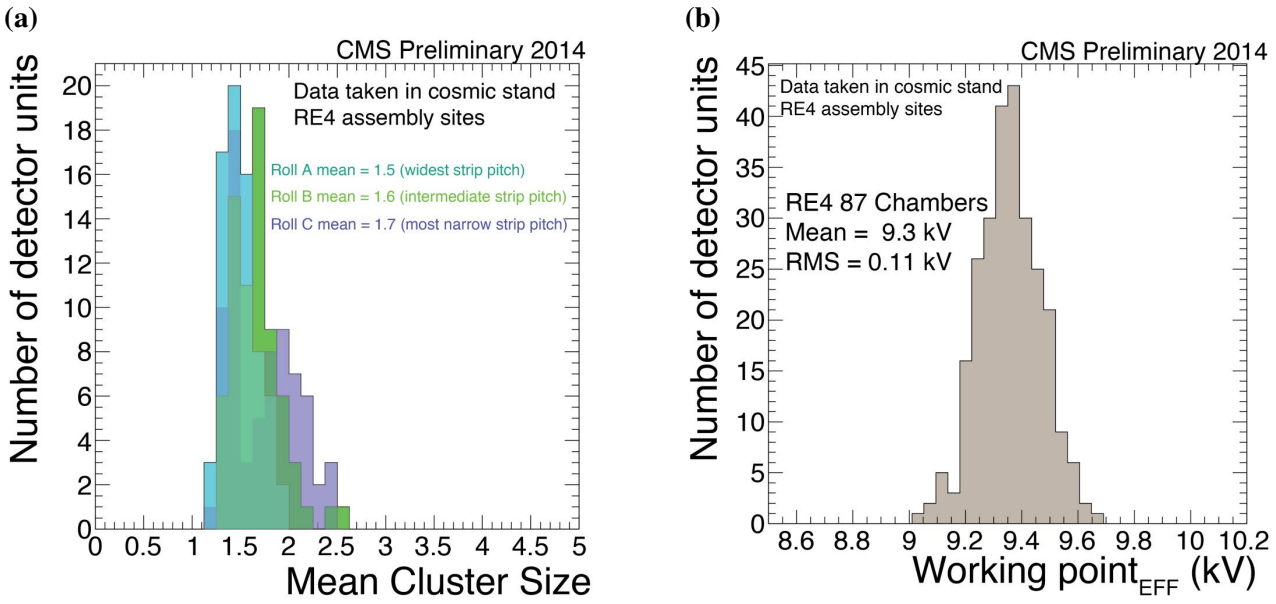


Fig. 5. Mean cluster size at the expected nominal HV working point of commissioned RE4 detectors.

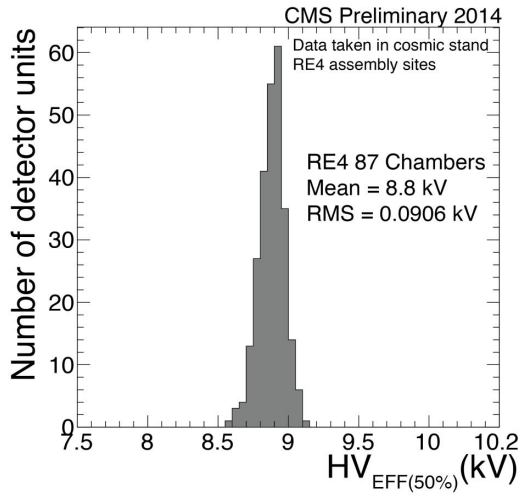


Fig. 6. High voltage distribution at 50% efficiency, as defined in Eq. (2).

efficiency in double gap mode ($\varepsilon_{\max}$) for the endcap chambers before the upgrade (only three layers) is shown in Fig. 7(a), while the one for the new RE4 layer of detectors is shown in Fig. 7(b).

CONCLUSIONS

During LS1 the RPC collaboration built and commissioned more than 144 RPC chambers. The RE4 project finished on schedule and in the budget, thanks to the good organization of every Institution and the professional work of all of the participants. At the present moment both disks have been instrumented and commissioned successfully. The new detector performance is in agreement with expectations and previous results.

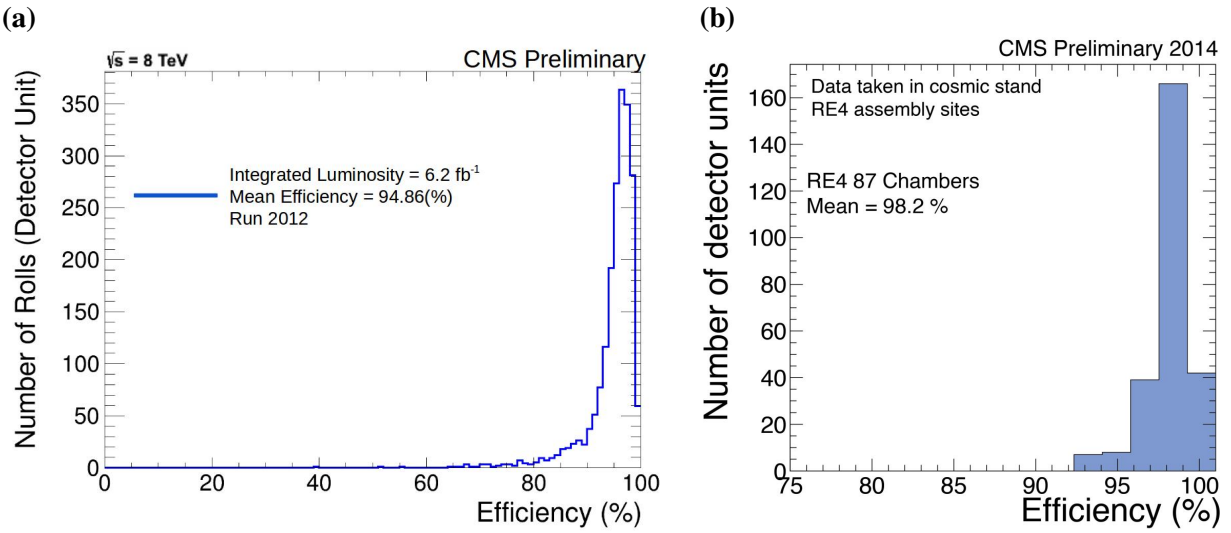


Fig. 7. The average maximum chamber efficiency of the endcap chambers before the upgrade (a) and the average maximum chamber efficiency of the RE4 chambers (b), extrapolated from the plateau curve, see Eq. (2).

REFERENCES

[1] CMS Collaboration, "*The CMS experiment at the CERN LHC*", JINST 3 (2008) S08004.

[2] CMS Collaboration, "*Technical Proposal for the Upgrade of the CMS Detector through 2020*", CERN-LHCC-2011-008, CMS-UG-TP-1, LHCC-P-004.

[3] R. Santorico and R. Cardarelli, *Nucl. Instrum. Meth* **187**, 377 (1981).

[4] M. Tytgat, "The Upgrade of the CMS RPC System during the First LHC Long Shutdown" in *Proceedings of RPC2012, XI Workshop on Resistive Plate Chambers and Related Detectors*, February, 5-10, 2012 INFN - Laboratori Nazionali di Frascati, Italy.

[5] S. Park, "Production of RPC Gaps for the CMS Upgrade" in *Proceedings of RPC2012, XI Workshop on Resistive Plate Chambers and Related Detectors*, February, 5-10, 2012 INFN - Laboratori Nazionali di Frascati, Italy.

[6] M. Abbressia et. al., *Nucl. Instrum. Meth. A* **359**, 603 (1995).

[7] S. Colafranceschi, "Resistive Plate Chambers for 2013-2014 muon upgrade in CMS at LHC", presented at RPC2014, XII Workshop on Resistive Plate Chambers and Related Detectors, February, 23-28, 2014, Beijing, China.

[8] M. Abbressia et. al., *Nucl. Instrum. Meth. A* **550**, 116 (2005).

ИЗРАБОТКА И ТЕСТВАНЕ НА КАМЕРИ СЪС СЪПРОТИВИТЕЛНА ПЛОСКОСТ ЗА ОБНОВЯВАНЕ НА МЮОННАТА СИСТЕМА НА ЕКСПЕРИМЕНТА CMS

М. Шопова (от името на CMS екипа)

Институт за ядрени изследвания и ядрена енергетика, Българска академия на науките, бул. "Цариградско шосе" №72, 1784 София, България

(Резюме)

При подготовка за периода на работа с по-висока светимост от 2015 г., през последните 2 години една от основните задачи за експериметна CMS на ускорителя LHC в CERN е довършване и обновяване на мюонната система чрез поставяне на четвърти слой (RE4) камери със съпротивителна плоскост (Resistive Plate Chambers - RPC) в предната част на детектора. Четвъртата мюонна станция (два нови диска за затварящите части) се състои от 144 RPC камери, които са произведени и тествани в три производствени лаборатории – CERN (Швейцария), GHENT (Белгия) и BARC (Индия). Целта на този доклад е запознаване с процесите на конструиране и качествен контрол при производство на камерите, както и представяне на предварителни резултати получени при работата им.

Bulgarian Chemical Communications, Volume 47, Special Issue B (pp. 192–199) 2015

Model calculations of positron interaction in materials for ITER

E. Popov[1]*, T. Troev[1], L. Petrov[1], K. Berovski[1], S. Peneva[1], B. Kolev[2]

[1] *Institute for Nuclear Research and Nuclear Energy, Bulgarian Academy of Sciences, 72 Tsarigradsko Chaussee Blvd., 1784 Sofia, Bulgaria*

[2] *St. Kliment Ohridski University of Sofia, Faculty of Physics, 5 James Bourchier Blvd., BG-1164 Sofia, Bulgaria*

There will be conducted model calculations based on the local density approximation model, Kohn and Sham method based on two-component density functional theory. This is studied the defective structure of α-Fe and W, through simulations of the positron lifetime and momentum distribution of electrons in the defects of different sizes, including nano-defects containing hydrogen and helium atoms, produced by irradiation 14 MeV neutrons - a product of the fusion.

Key words: TCDFT, LDA, PLT, CDB, positron states, method of Kohn and Sham, momentum distribution

INTRODUCTION

The experimental apparatus used to determine the positron lifetime is improved significantly and thus exploring angular correlation of the γ-quanta. There is established the influence of temperature on annihilation spectra. Confirmation of anisotropy in the angular distribution of the γ-quanta in many crystals allows studying the Fermi surface forms not only in pure metals, but and in different combinations of alloys. Modern computers and modern methods based on First Principle are opening up new possibilities for determining the microscopic picture, due to the decay processes in fusion materials. Research in this area is developed. Methods for calculating the positron lifetime in the material are able to predict with great accuracy the structural defects. This thesis presents calculating of positron lifetime in Fe and W (and momentum distribution of the electrons), based on the Two Component Density Functional Theory [TCDFT] in conjunction with local density approximation [LDA] used in calculation of the exchange correlation functional. This is a powerful method for studying the properties of thermonuclear materials in atomic order.

METHODOLOGY

Density functional theory, method of Kohn and Sham, local density approximation

Using density functional, we have consideration the dependence of the quantum system from one parameter in which are included the wave functions of all electrons [1]:

$$n(r) \rightarrow \varphi(r_1, r_2, \ldots r_k) \rightarrow V(r). \quad (1)$$

Electron density (the density of the probability distribution of the electrons in the quantum system) is set as a function of the radius vector of an arbitrary electron:

$$n(r) = k \int d^3 r_2 \int d^3 r_3 \ldots \ldots \int d^3 r_k \varphi^*(r, r_2, \ldots r_k) \varphi(r, r_2, \ldots r_k). \quad (2)$$

In view of the theorem of Hohenberg-Kohn [2] the total energy of the ground state of an electronic system of many electrons can be calculated as a functional of the electron density [3]:

$$E[n(r)] = T[n(r)] + U[n(r)] + \int V_{ext}(r) n(r) d^3 r. \quad (3)$$

According to Method of Kohn and Sham [4], for a system of interacting electrons in an external field $V_o(r)$, can be made a comparison with a system of non-interacting electrons with local potential $V_{s,o}(r)$ such that the ground state of the densities for the two systems - $n(r)$ and $n_s(r)$ will be derived from the following equations:

$$\Big(-\frac{\nabla^2}{2} + V_{s,o}(r) \Big) \varphi_i(r) = \varepsilon_i \varphi_i(r), \quad (4)$$

$$\Big(-\frac{\nabla^2}{2} + V_o(r) + \int \frac{n(r')}{r - r'} dr' + \frac{\delta E_{ex}}{\delta n(r)} \Big) \varphi_i(r) = \varepsilon_i \varphi_i(r). \quad (5)$$

where $v = \delta E_{ex} / \delta n(r)$ is the exchange-correlation potential for a one particle and the part $\int \frac{n(r')}{r - r'} dr'$ characterized Coulomb potential. There are undefined parts E_{xc} and E_c^{e-p}, approximations from which

* To whom all correspondence should be sent: evpetropov@abv.bg

© 2015 Bulgarian Academy of Sciences, Union of Chemists in Bulgaria

the results can be highly dependent. Using LDA [4,5] is an opportunity to overcome this problem for Functional of exchange correlation energy E_{xc} should be used approximation of Functional exchange correlation energy of a homogeneous electron gas e_{xc}^{hom} for an electron multiplied by density in of electrons in the integral relation:

$$E_{xc}^{LDA}[n] = \int drn(r)e_{xc}^{hom}n(r). \quad (6)$$

In the inhomogeneous system allows changing the constant density n_0 to local $n(r)$ displayed by quantum Monte Carlo simulations.

Two-component density functional theory, annihilation rate and contact density, effect of the electron-positron correlation on the annihilation rate of the positron

In order to interpreted participate in the system of two types of particles (electrons and positrons) density functional theory should be complete its two component extension. Functional of the total energy $E[n_-,n_+]$ electron-positron system in an external potential V_{ext} is the sum of functional of positrons and functional electrons in distinct and functionally of the Coulomb interaction of these two systems (MIKA-DOPPLER) [4,6]:

$$E[n_-,n_+] = F[n_-]+F[n_+] + \int drV_{ext}(r)[n_-(r)-n_+(r)] - \int dr\int dr'\,\frac{n_-(r)\,n_+(r')}{|r-r'|}+E_c^{e-p}[n_+,n_-] \quad (7)$$

with the following significance of the one-component density functional corresponding to a particular type of particle:

$$F[n] = T[n]+\frac{1}{2}\int dr\int dr'\frac{n_-(r)\,n_+(r')}{|r-r'|}+E_{xc}[n], \quad (8)$$

where T[n] is the functional of the kinetic energy of interacting electrons or positrons E_{xc} corresponds to part exchange correlation energy and $E_c^{e-p}[n_+,n_-]$ is a functional of the electron-positron correlation energy.

The main characteristic of positron annihilation, providing information about the structural features of the environment is the lifetime of positrons τ or annihilation rate λ ($\tau=\frac{1}{\lambda}$). The lifetime of the positron is a function of the positron densities in place of annihilation [7]:

$$\lambda = \frac{1}{\tau} = \pi r_0^2 c\int n_-(r)n_+(r)\gamma(r)d(r), \quad (9)$$

where $\gamma=\gamma[n-(r)]=1+\frac{\Delta n_-}{n_-}$ is a correlation function describing the increase in electron density due to the Coulomb attraction between the electron and the positron. This effect is called a enhancement [4] r_0 is the radius of the electron in its classical sense.In the LDA, annihilation rate is calculated in the form:

$$\lambda = \pi r_0 c\sum_i\int dr\ \gamma_i^{LDA}|\varphi_+(r)|^2|\varphi_i(r)|^2, \quad (10)$$

where φ_+ is the wave function of the positron and $\gamma_i(r)$ is the enhancement factor for the ith electronic state.There is can be made approximation of a physical meaning of two particles, electron-positron wave function:

$$\varphi_i^{e-p}(r) = \varphi_+(r)\varphi_i(r)\sqrt{\gamma_i(r)}, \quad (11)$$

where you can make a comparison of annihilation rate to each electron orbital:

$$\lambda_i = \pi r_0 c\int dr\ \gamma_i|\varphi_+(r)|^2|\varphi_i(r)|^2. \quad (12)$$

The correlating movement strongly depends on the initial condition i (without the presence of a positron). Should be the core and the localized d and f valence electrons to be a less affected by the positron than valence orbitals. The correlating the movement strongly depends on the initial condition of electron i (without the presence of a positron). The positron annihilation rate as a function of the momentum p of the annihilating pair - electron-positron, is determined by the following integral form:

$$\rho(p) = \pi r_0 c\sum_i|\int e^{ip.r}dr\ \varphi_+(r)\varphi_i(r)\sqrt{\gamma_i(r)}dr|^2. \quad (13)$$

With momentum distribution for density picture of the annihilation rate in LDA have the following recording:

$$\rho(p) = \pi r_0 c\sum_i\int e^{ip.r}dr\gamma_i^{LDA}|\varphi_+(r)|^2|\varphi_i(r)|^2. \quad (14)$$

Positron states

The correlating movement strongly depends on the initial condition i (without the presence of a positron). Should be the core and the localized d and f valence electrons to be a less affected by the

positron than valence orbitals. The correlating the movement strongly depends on the initial condition of electron i (without the presence of a positron). A approximation for examination of positron conditions in condensed matter is an estimate of the density of the positrons and that the electronic gas, in which takes place the annihilation. Addition to functional energy of the system is electron-positron correlation potential $E_c^{e-p}[n_+,n_-]$. The outer potential is in function depending on both – by the electronic and by the positron densities:

$$n_-(r) = \sum_{\xi_i \le \xi_f} |\varphi_i(r)|^2, \qquad n_+(r) = \sum_i^N |\varphi_i^+(r)|^2. \tag{15}$$

Using the self-consistent procedure of Kohn-Sham [2, 8] are obtained in the ground state electronic and positron densities, which requires calculation of one-particle Schrödinger equation for positron wave functions. For the positron is the same in the form:

$$-\frac{1}{2}\bigtriangledown^2 \psi_i^+(r) + V_{eff}(r)\psi_i^+ = \xi\,\psi_i^+(r), \tag{16}$$

effective potential is written as:

$$V_{eff}(r) = \phi(r) + \frac{\delta E_{xc}[n_+]}{\delta n_+(r)} + \frac{\delta E_{xc}^{e-p}[n_+,n_-]}{\delta n_+(r)}. \tag{17}$$

The last two parts are included in the so-called correlation potential - V_{corr}, and Coulomb potential has the following form:

$$\phi(r) = \int dr' \frac{-n_-(r') + n_+(r') + n_0(r')}{|r-r'|}, \tag{18}$$

where n_0 is the charge density of the outer potential involved in the complete functionality of the system [2].

RESULTS

Positron state is calculated taking into account the reduction in the exchange-correlation energy E_{ex}, which decrease with given coordinates depends only on the electron density at the corresponding point. The rate of annihilation (and the positrons lifetime - PLT, in a given environment) is calculated as the integral of the local annihilation rates.

PLT

Fig. 1 (a) and (b) shows the change of the lifetime of positrons in the tungsten in increasing vacancy cluster 1 to 30 vacancies filling successively with atoms of hydrogen and helium [10–12]. There is observed reduction in the value of the lifetime of a positron with an increase in the impurity atoms in the vacancy cluster. Increasing the concentration of impurity atoms in the vacancy clusters leads to saturation of the lifetime of the positron and the values at the same has approximate perfect lattice without defects. The conclusions from results of Figure 2 (a) and (b) for iron are similar to findings from the results for the positron lifetime in tungsten.

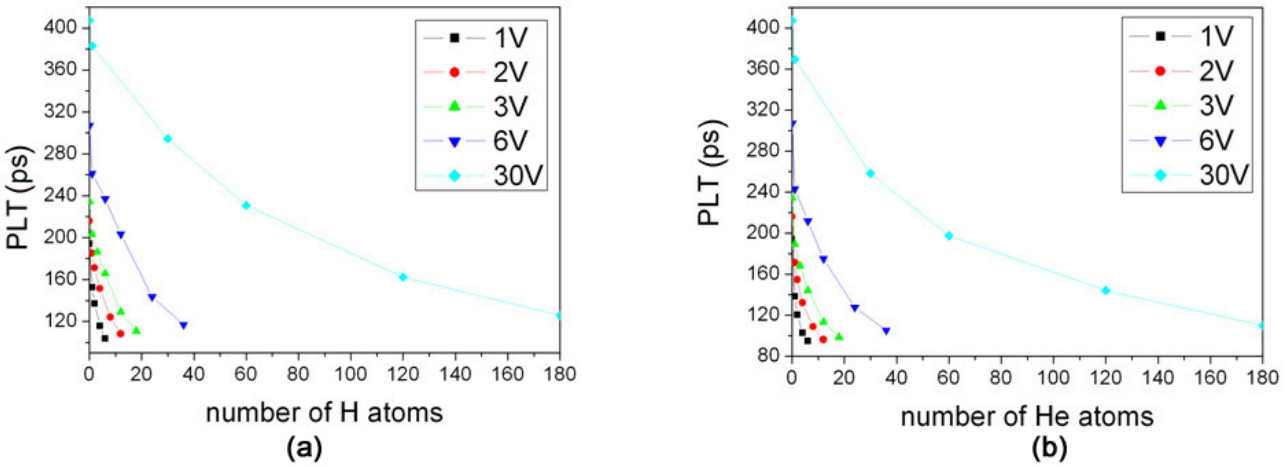


Fig. 1. (a) Comparison of the values of the lifetime of positrons in tungsten with an increase of the impurity hydrogen atoms in 1, 2, 3, 6 and 30 vacations [9]. (b) Comparison of the values of the lifetime of positrons in tungsten with an increase of the impurity helium atoms in 1, 2, 3, 6 and 30 vacations [9].

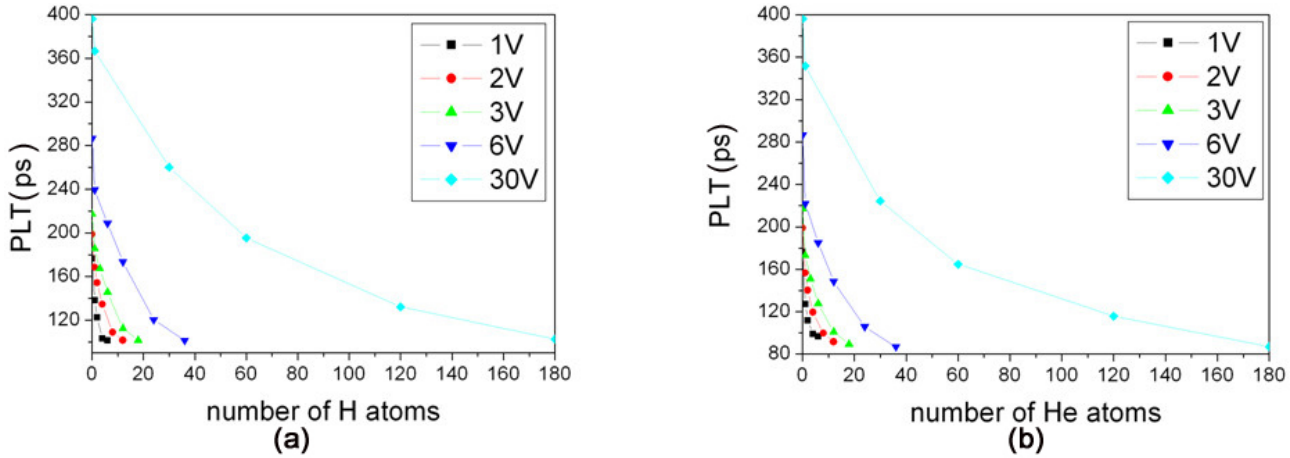


Fig. 2. (a) Comparison of the values of the lifetime of positrons in iron with an increase of the impurity hydrogen atoms in 1, 2, 3, 6 and 30 vacations [9]. (b) Comparison of the values of the lifetime of positrons in iron with an increase of the impurity helium atoms in 1, 2, 3, 6 and 30 vacations [9].

CDB

Coincidence Doppler Broadening (CDB) is interpretation of the momentum distribution for electrons witch is projected with the S (shape) and W (wing) parameters, where S parameter is corresponded of the annihilation with a valance electrons and W parameter corresponded of the annihilation with a core electrons.With an increasing number of vacancies in the cluster are visible expressed extreme values (maximum at S parameter and minimum at W parameter) at saturation with hydrogen atoms. It follows that at a given electron density, relative contributions of the valence electrons to the annihilation is maximum, and for a core electrons is minimum. Where the density is changed is observed increasing in the contribution of core electrons and the reduction from the valence electrons.

There are considered this parameters in case when the impurity atoms are helium Fig. 4 (a) and (b). Maxima for the S parameter and minima for the W parameter as in saturation with hydrogen were not observed. The explanation for this fact may be associated with the specificity of hydrogen and helium electronic structures.

In Figures 5 (a) and (b) are considered the parameters S and W as a function of the increasing number

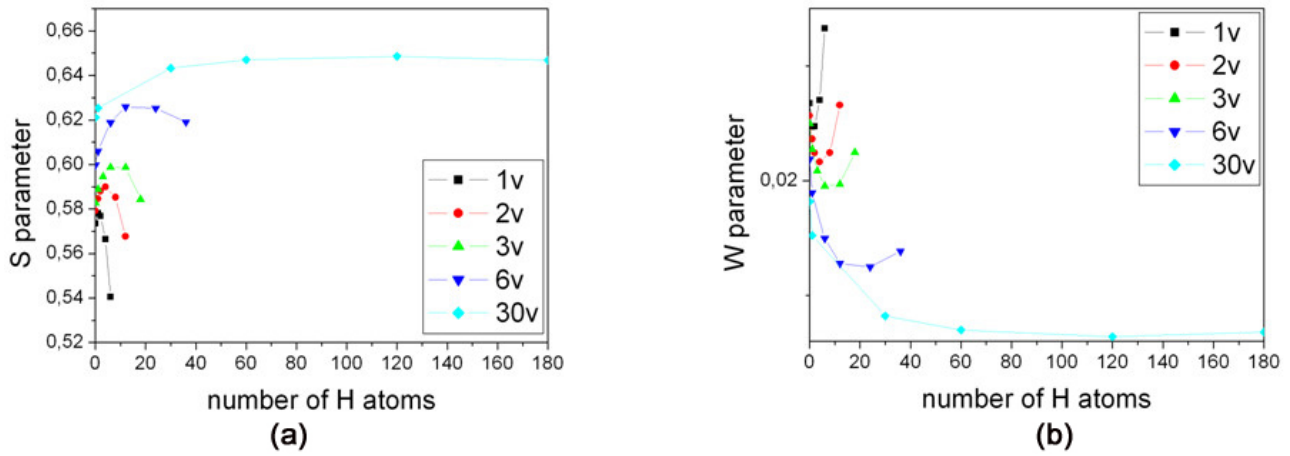


Fig. 3. (a) Comparison of the values of S parameters in the tungsten with increased number of addition hydrogen atoms in different vacancy clusters (1v, 2v, 3v, 6v, 30v). (b) Comparison of the values of W parameters in the tungsten with increased number of addition hydrogen atoms in different vacancy clusters (1v, 2v, 3v, 6v, 30v).

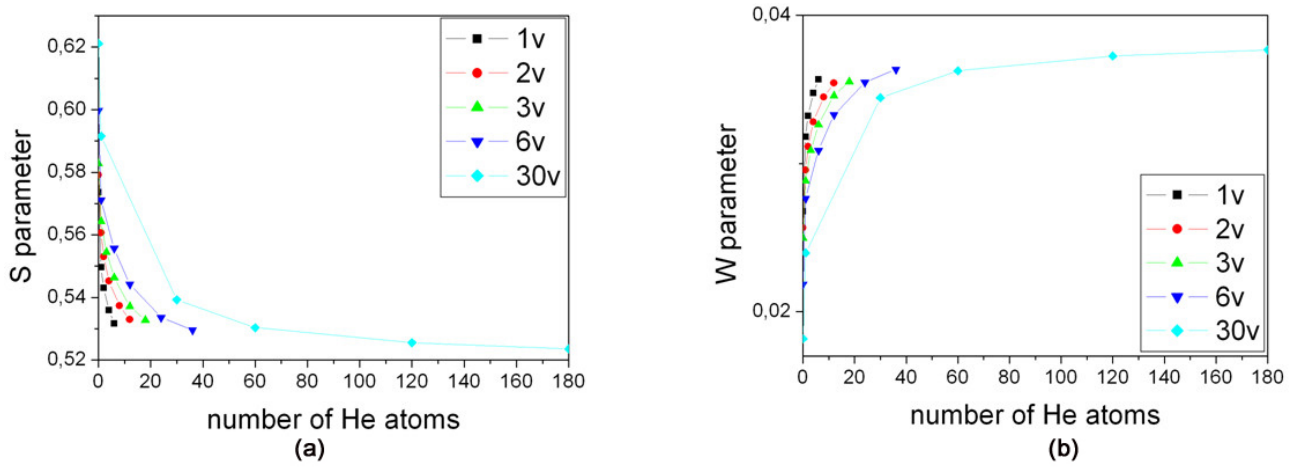


Fig. 4. (a) Comparison of the values of S parameters in the tungsten with increased number of addition helium atoms in different vacancy clusters (1v, 2v, 3v, 6v, 30v). (b) Comparison of the values of W parameters in the tungsten with increased number of addition helium atoms in different vacancy clusters (1v, 2v, 3v, 6v, 30v).

of hydrogen atoms, in clusters of vacations, containing 1, 2, 3, 6 and 30 vacations.

There is seen that the extremum in iron has more steepen compared with the extremum in tungsten. This effect is due to the electronic structure of the iron, tungsten and hydrogen, and the annihilation of the positron with electrons from various orbitals. Annihilation occurs mainly with electrons of s and d orbitals. Since iron has 2 more electrons from tungsten in its valence d orbital, it is reasonable to expect an increase in the probability of annihilation in this orbital Fig. 6 compared with the same in tungsten, and higher values for the S parameter. For the same reason, in case of defects, it is expected annihilation generally to be higher in the iron. Behavior and values of the annihilation of the hydrogen electrons are similar in both cases. In consideration figures Fig 6 (a) and (b) is presents the relative contribution to the annihilation, ie higher rate of annihilation in iron (in the presence of defects).

At Figure 7 (a) and (b) is shown the dependency of the S and W parameters with the increasing number of helium atoms. In a comparison between the

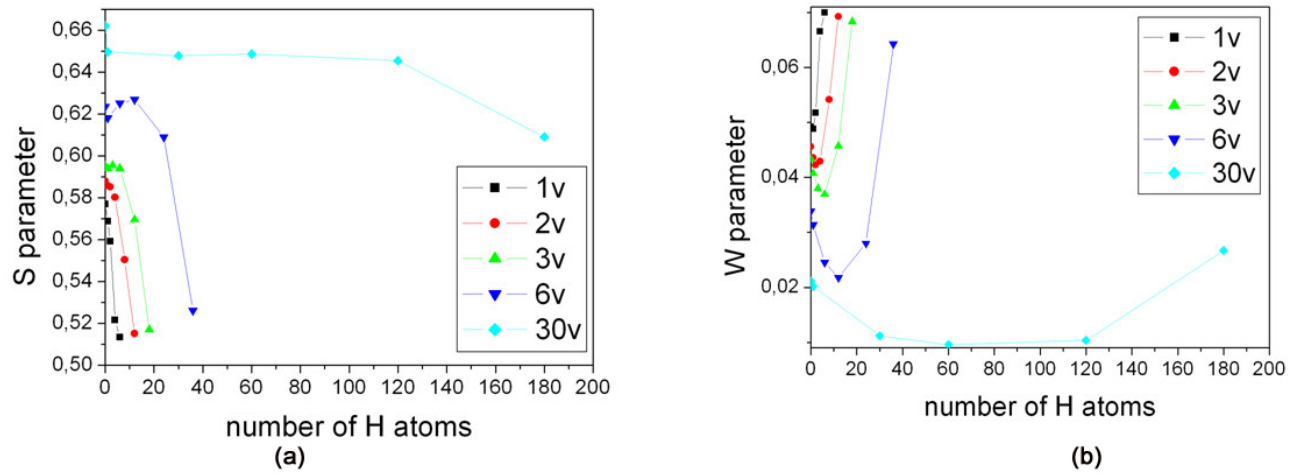


Fig. 5. (a) Comparison of the values of S parameters in the tungsten with increased number of addition hidrogen atoms in different vacancy clusters (1v, 2v, 3v, 6v, 30v). (b) Comparison of the values of W parameters in the tungsten with increased number of addition hidrogen atoms in different vacancy clusters (1v, 2v, 3v, 6v, 30v).

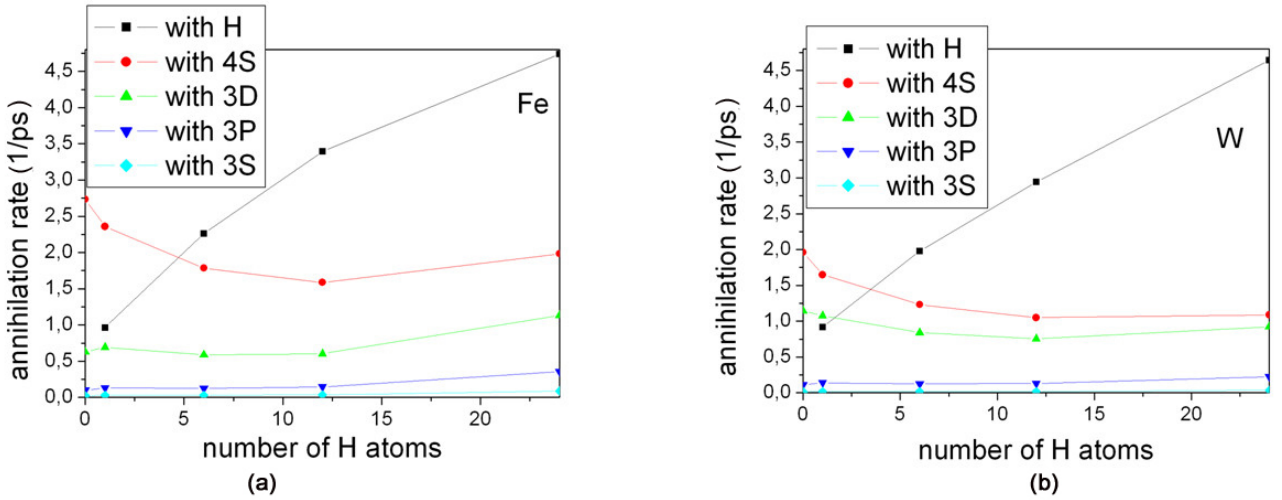


Fig. 6. (a) Speed annihilation in orbitals in vacancy cluster from 6 vacancies in iron with depending of the number of hydrogen atoms in the cluster. (b) Speed annihilation in orbitals in vacancy cluster from 6 vacancies in tungsten with depending of the number of hydrogen atoms in the cluster.

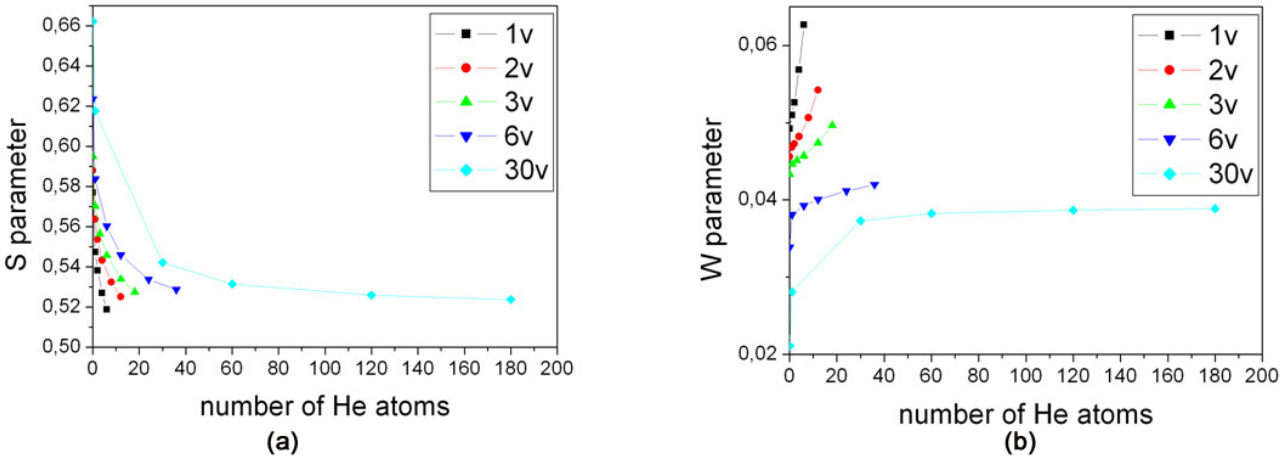


Fig. 7. (a) Comparison of the values of S parameters in the iron with increased number of addition helium atoms in different vacancy clusters (1v, 2v, 3v, 6v, 30v). (b) Comparison of the values of W parameters in the iron with increased number of addition helium atoms in different vacancy clusters (1v, 2v, 3v, 6v, 30v).

graphics of Fig. 3 and Figure 7 we can see a wider range of variation of the values for the different S and W parameters in iron than tungsten. The explanation of this fact, again is in the specificity of the electronic structure on the two elements.

CONCLUSIONS

Since iron has two electrons more from tungsten in its free d orbital, it is logical to expect increased annihilation in this orbital, and higher values for the S parameter. For the same reason, in case of defects, it is expected annihilation generally is higher in the iron. In some electron density the relative contribution of valence electrons to annihilation is maximum, while the same relative contribution from the core electrons is minimum. Where the density is changed the relative contribution of the core electrons is increased while from the valence is decreased.

By increasing the number of impurity atoms in the small vacancy clusters (1, 2 and 3 vacancies), the positron lifetime in iron and tungsten approach, which is a consequence of a changing in the condi-

tions in which is flow annihilation. The overlap of the wave functions of the positron with those of electrons from the material that study becomes less and the basic process is determined by the electrons from cover of the impurity atoms.

When clusters are small enough can be expected the interacting electrons on the boundary of the defect to have a relatively larger contribution to the annihilation. The functional of the density of the exchange-correlation energy is expected to have higher values in a small volume of the defects. The influence of the exchange-correlation energy over to the general functional after a certain size of defect is changed the trend on the S and W parameters in the saturation of the same defect with impurity hydrogen atoms.

Acknowledgements. *One of the authors (E.P.) is gratitude to State Enterprise for Radioactive Waste (SERAW) for financial support for his participation in this conference.*

REFERENCES

[1] P. Valminen, *Positron parameter calculations using the TB-LMTO-ASA software*, Special Assignement, Helsinki University of Technology, Espoo (2002).

[2] P. Hohenberg and W. Kohn, *Physical Review B* **864**, 136 (1998).

[3] I. Makkonen, M. Hakala and M. J. Puska, *Physical Review B* **73**, 035103, 112 (2006).

[4] W. Kohn and L. Sham, *Physical Review* **140**, A1133–A1138 (1965).

[5] R. Krause-Rehberg, H. S. Leipner, *Positron Annihilation in Semiconductors - Defect Studies*, Springer, Berlin (1999).

[6] T. Torsti, *MIKA: Multigrid-based program package for electronic structure calculations*, Laboratory of Physics, Helsinki University of Technology, Espoo, Finland (2003).

[7] R. M. Nieminen and M. J. Manninen, *Positrons in Solids*, edited by P. Hautojarvi, Springer, Berlin, 1979, p. 145.

[8] R. M. Nieminen and C. H. Hodges, *Physical Review B* **18**, 2568 (1978).

[9] E. Popov, *Innovative Approaches to physical investigations, International Workshop*, Bachinovo **145**, 130-133 (2010).

[10] T. Troev, E. Popov, P. Staykov, N. Nankov and T. Yoshiie, *Nucl. Inst. Meth. Phys. Res. B* **267**, 535–541 (2009).

[11] T. Troev, E. Popov, N. Nankov and T. Yoshiie, *J. Phys. Conf. Ser.* **207**, (2010).

[12] T. Troev, N. Nankov and T. Yoshiie, *Nucl. Inst. Meth. in Phys. Res. B* **269**, 566–571 (2011).

МОДЕЛНИ ПРЕСМЯТАНИЯ НА ПОЗИТРОННОТО ВЗАИМОДЕЙСТВИЕ В МАТЕРИАЛИ ЗА ИТЕР

Е. Попов[1], Т. Троев[1], Л. Петров[1], К. Беровски[1], С. Пенева[1], Б. Колев[2],

[1] *Институт за ядрени изследвания и ядрена енергетика, Българска академия на науките, бул. "Цариградско шосе" №72, 1784 София, България*

[2] *Физически факултет, Софийски университет "Св. Климент Охридски", бул."Дж. Баучер" №5, 1164 София, България*

(Резюме)

Пресметнати са позитронната и електронната вълнови функции във волфрам и желязо, чрез локалния функционал на плътността на базата на TCDFT. Установено е съществуването на корелация между времето на живот на позитроните, импулсното разпределение на електроните (S и W параметрите) и концентрацията на образуваните дефекти.

Тъй като желязото притежава 2 електрона повече от волфрама в своята свободна d орбитала, то е логично да очакваме увеличена анихилация в тази орбитала, спрямо същата при волфрам, както и по-високи стойности за S параметъра. По същата причина, при наличие на дефекти, се очаква анихилацията като цяло да е по-висока при желязото. При определена електронна плътност относителния принос на валентните електрони, към анихилацията, е максимален, докато същият от свързаните е в своя минимум. При промяна на тази плътност се отчита покачване на относителния принос на свързаните електрони и намаляването му от валентните. Измерванията в стойностите за S и W параметрите са по-големи при желязо отколкото при волфрам. Обяснението е в спецификата на електронната структура на двата елемента.

С увеличаване на броя примесни атоми в малките ваканционни клъстери (1, 2 и 3 ваканции), времето на живот на позитрона при желязо и волфрам се доближава, което е следствие от промяната на условията в които протича анихилацията. Препокриването на вълновите функции на позитрона с тези на електроните от съответния материал, който изследваме става все по-малко и основно процесът се определя от електроните от обвивката на примесните атоми.

Когато клъстерите са достатъчно малки може да се очаква взаимодействащите си електрони на границата на дефекта да имат относително по-голям принос към анихилацията. Функционалът на плътността на обменно-корелационната енергия се очаква да има по-високи стойности в по-малки обеми на дефектите. Влиянието на обменно-корелационната енергия върху общия функционал след определен обем на дефекта променя тенденцията на S и W параметрите в насищането на същия дефект с примесни водородни атоми.

Bulgarian Chemical Communications, Volume 47, Special Issue B (pp. 200–207) 2015

A feasibility study of hyperon measurements in Au-Au collisions at NICA/MPD

D. Suvarieva*, M. Ilieva, V. Kolesnikov, V. Vasendina, A. Zinchenko

Veksler and Baldin Laboratory of High Energy Physics, Joint Institute for Nuclear Research, 141980 Dubna, Moscow region, Russia

One of the main tasks of NICA/MPD physics program is a study of the strangeness production in nuclear collisions. In this paper the MPD detector performance for measurements of Λ, Ξ^- and Ω^- hyperons in central Au+Au collisions at NICA energies is presented. The investigation has been performed at the Laboratory of High Energy Physics, JINR.

Key words: hyperons, strangeness production, heavy-ion collisions, NICA/MPD

INTRODUCTION

The main goal of studying heavy-ion collisions is to explore the properties of nuclear matter under extreme density and temperature conditions. Production of strange particles is of particular interest because enhanced production of rare strange hadrons (Ξ^-, Ω^-) in A+A collisions (relative to the yields from elementary pp reactions) was predicted as a signal for the QGP formation [1].

At present, a complete theoretical description of the (multi)strangeness production mechanism at collision energies ($\sqrt{s}$) of several GeV, has not yet been achieved. In order to better understand the dynamics of hot and dense hadronic matter the MPD experiment at NICA [2] will provide new precise experimental data on the total yields, rapidity, transverse momentum, and azimuthal angle distributions of hyperons The production of baryons and antibaryons with different strangeness content produced in central heavy ion collisions will be compared with those produced in proton induced reactions where no QGP formation is expected.

The goal of this study is to evaluate the performance of the MPD detector for reconstruction of hyperons in Au+Au collisions.

* To whom all correspondence should be sent:
DilyanaSuvarieva@mail.bg

MPD at NICA

The Nuclotron-based Ion Collider fAcility (NICA) [3], shown in Fig. 1, is a new accelerator complex being constructed at JINR, Dubna, Russia. NICA's aim is to provide collisions of heavy ions over a wide range of atomic masses, from Au+Au collisions at $\sqrt{s} = 4$–11A GeV (for Au^{79+}) and an average luminosity of $L = 10^{27}$ cm^{-2}s^{-1} to proton-proton collisions with $\sqrt{s_{pp}} = 20$ GeV and $L = 10^{32}$ cm^{-2}s^{-1}.

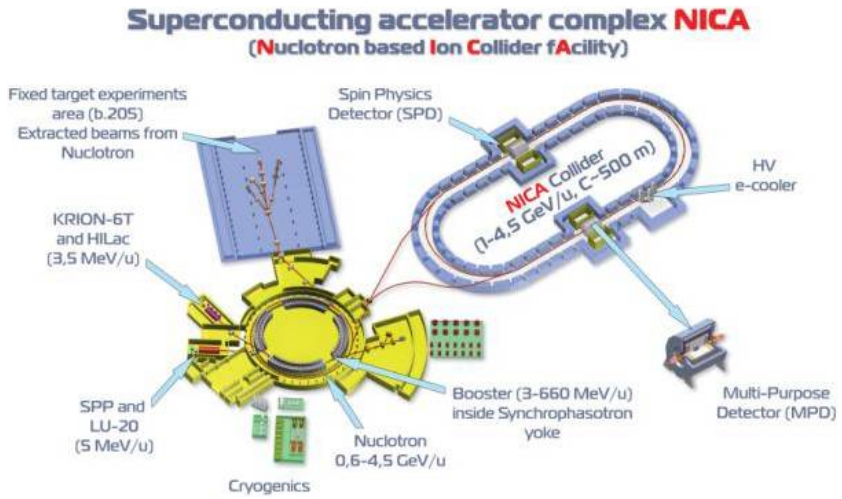


Fig. 1. NICA complex.

© 2015 Bulgarian Academy of Sciences, Union of Chemists in Bulgaria

Two interaction points are foreseen at NICA which provide a possibility for two detectors to operate simultaneously – MultiPurpose Detector (MPD) and Spin Physics Detector (SPD).

The main goal of the NICA/MPD program [4] is a comprehensive experimental investigation of the properties and dynamics of the hot and dense nuclear matter in a poorly explored region of the QCD phase diagram, with a main emphasis to such QCD subjects as properties of deconfinement phase transition, critical phenomena and chiral symmetry restoration.

The NICA/MPD experimental program includes simultaneous measurements of observables that are presumably sensitive to high nuclear density effects and phase transitions. In the first stage of the project are considered – multiplicity and spectral characteristics of the identified hadrons including strange particles, multi-strange baryons and antibaryons; event-by-event fluctuations in multiplicity, charges and transverse momentum; collective flows (directed, elliptic and higher ones) for observed hadrons. In the second stage the electromagnetic probes (photons and dileptons) will be measured. It is proposed that along with heavy ions NICA will provide proton and light ion beams including the possibility to use polarized beams. Study of heavy ion collisions at the collider will be complemented by spin physics research with polarized beams of protons and deuterons as well as collisions in a fixed-target mode at center of mass energy from 1 to 4 GeV.

The detector for exploring phase diagram of strongly interacting matter in a high track multiplicity environment has to cover a large phase space, be functional at high interaction rates and comprise high efficiency and excellent particle identification capabilities. The MPD detector [2, 5], shown in Fig. 2, matches all these requirements. It consists of central detector (CD) and two optional forward spectrometers (FS-A and FS-B). CD consists of a barrel part and two end caps. The barrel part is a set of various subdetectors. The main tracker is the time projection chamber (TPC) supplemented by the inner tracker (IT). IT and TPC have to provide precise tracking, momentum determination and vertex reconstruction. The time of flight (TOF) system must be able to identify charged hadrons and nuclear clusters in a broad pseudorapidity range. The electromagnetic calorimeter (ECAL) should identify electrons, photons and measure their energy with high precision. The zero degree calorimeter (ZDC) should provide event centrality and event plane determination, and also measurement of the energy deposited by spectators. There are also a straw-tube tracker (ECT) and a fast forward detector (FFD).

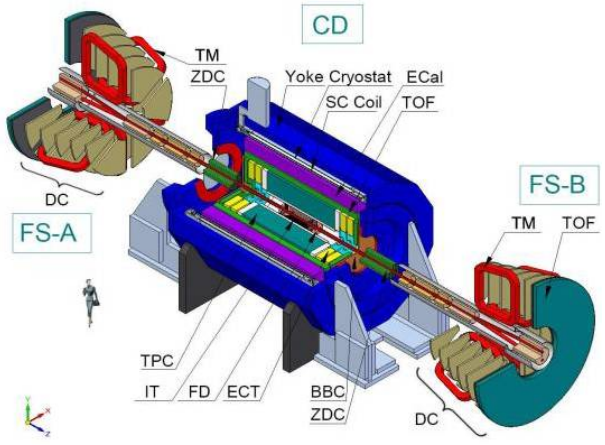


Fig. 2. MPD detector.

The magnet of MPD is a solenoid with a thin superconducting NbTi winding and a flux return iron yoke. The magnet should provide a homogeneous magnetic field of 0.5 T. The field inhomogeneity in the tracker area of the detector is about 0.1%.

The MPD time projection chamber (TPC) is the main tracking detector of the central barrel and has to provide charged particles momentum measurement with sufficient resolution (about 2% at $p_t =$ 300 MeV/c), particle identification and vertex determination, two track separation (with a resolution < 1 cm) and dE/dx measurement (dE/dx resolution better than 8%) for hadronic and leptonic observables at pseudorapidities $|\eta| < 2.0$ and $p_t > 100$ MeV/c. TPC readout system is based on Multi-Wire Proportional Chambers (MWPC) with cathode readout pads.

The identification of charged hadrons (PID) at intermediate momentum (0.1-3 GeV/c) is achieved by the time-of-flight (TOF) measurements which are complemented by the energy loss (dE/dx) information from the TPC and IT detector systems. TOF system should provide a large phase space coverage $|\eta| < 3.0$, high combined geometrical and detection efficiency (better than 80%), identification of pions and kaons with $0.1 < p_t < 2$ GeV/c and (anti)protons with $0.3 < p_t < 3$ GeV/c. The choice for the TOF system is Multigap Resistive Plate Counters (MRPC) which have good time resolution of $\sigma < 70$ ps. The barrel covers the pseudorapidity region $|\eta| < 1.5$ and the geometry efficiency in it is above 90%. The end cap system covers the pseudorapidity region $1.5 < |\eta| < 3.0$.

EVENT GENERATORS AND DATA SETS

The software framework for the MPD experiment (MpdRoot [6]) is based on FairRoot and provides a powerful tool for detector performance studies, development of algorithms for reconstruction and physics analysis of the data [2]. The event samples used for the present study were produced with the UrQMD [7] generator at $\sqrt{s} = 9$A GeV.

Produced by the event generators particles have been transported through the detector using the GEANT3 transport package (describing particle decays, secondary interactions, etc.). It should be noted here that the overall detector material budget is dominated by the contribution from the TPC inner and outer cages which are multilayer structures made of composite materials like kevlar and tedlar with high strength and long radiation length. As a result, the total amount of the material does not exceed 10% of the radiation length in the region of interest.

DETECTOR PERFORMANCE

Track reconstruction

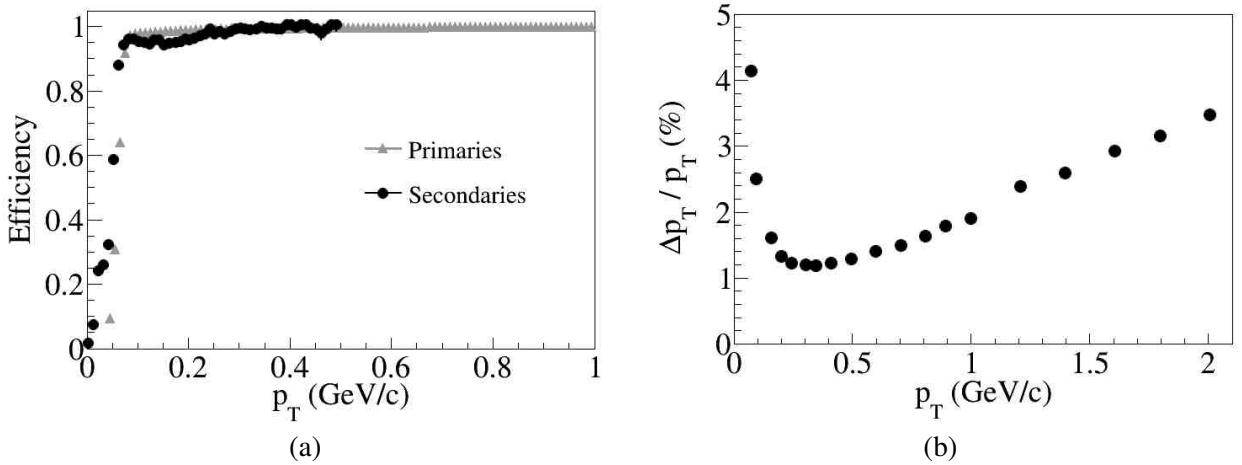
The track reconstruction method is based on the Kalman filtering technique (see, e.g. [8]) and the number of TPC points per track was required to be greater than 10 to ensure a good precision of momentum and dE/dx measurements. In addition, we have restricted our study to the mid-rapidity region with $|\eta| < 1.3$. The track finding efficiency in TPC for primary and secondary tracks is shown in Fig. 3 (a) as a function of the track transverse momentum. The secondary track sample there included particles produced within 50 cm of the primary vertex both in transverse and longitudinal directions and did not include electrons and positrons from the photon conversion, which are not relevant for the current study. The transverse momentum resolution as a function of p_T can be seen on Fig. 3 (b). The result has been obtained with the assumption on the TPC coordinate resolution of 0.5 and 1.0 mm in transverse and longitudinal directions, respectively. Fig. 4(a) shows the transverse and longitudinal position uncertainties of primary tracks at their point of the closest approach to the interaction point versus track momentum. These detector characteristics are important for secondary vertex reconstruction.

Both the primary and secondary vertex reconstruction methods utilized make use of the similar approach based on the Kalman filtering formalism [9]. The primary vertex reconstruction errors as functions of the track multiplicity in the event are shown in Fig. 4(b).

For all the reconstructed in the TPC tracks the specific energy loss dE/dx is calculated as a truncated mean of the charges of TPC hits assigned to the tracks. The truncation level of 70% was chosen, i.e. 30% of hits with the highest charges were excluded from the mean value.

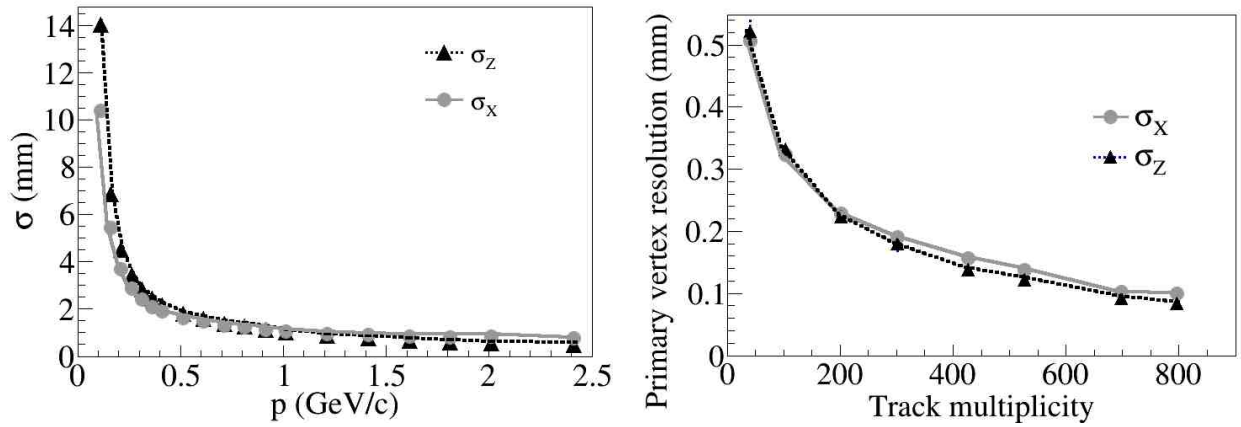
Next, the TPC reconstructed tracks are extrapolated to the TOF detector and matched to the TOF hits. For the matched candidates the mass square (M^2) is derived through the relation:

$$M^2 = (p/q)^2 \left(\frac{c^2 t^2}{l^2} - 1 \right)$$



(a) (b)

Fig. 3. (a) – track reconstruction efficiency as a function of track p_T for primary and secondary particles; (b) – relative transverse momentum resolution for primary tracks with $|\eta| < 1.3$ reconstructed in TPC.



(a) (b)

Fig. 4. (a) – transverse and longitudinal position errors in the point of the closest approach (PCA) to the interaction point for TPC reconstructed primary tracks with $|\eta| < 1.3$ versus particle momentum; (b) – transverse and longitudinal position errors of the reconstructed primary vertex as functions of track multiplicity.

where p is the track momentum, q is its charge, t is the time-of-flight from TOF, l is the path length from the collision vertex to the TOF hit, and c is the speed of light. p/q, so-called magnetic rigidity, is the value directly returned by the track reconstruction algorithm. For particles with the unit charge it is equal to the momentum and M^2 corresponds to the particle mass, whereas for multiple-charged particles the obtained value of M^2 is scaled by the factor of $1/q^2$ with respect to the true mass.

Particle identification

Particle identification (PID) in the MPD experiment will be achieved by combining specific energy loss (dE/dx) and time-of-flight measurements. The basic detector parameters, namely, dE/dx and TOF resolutions of $\sigma_{dE/dx} \approx 6\%$ and $\sigma_{TOF} \approx 100$ ps will provide a high degree of selectivity for hadrons at momenta below 2 GeV/c (see Fig. 5).

An identified hadron candidate is assumed to lie within the boundaries of the PID ellipse (3σ around the nominal position for a given particle specie). In addition, the probability for a given particle to belong to each of the species can be calculated knowing the widths of the corresponding distributions (along the dE/dx and M^2 axes) and the difference from the predicted position for the specie. It was found that by requiring this probability to be greater than 0.75 one can get distributions for the PID efficiency and contamination (of wrongly identified hadrons) shown in Fig. 6. The PID efficiency is defined as a ratio of correctly tagged to the total number of generated particles.

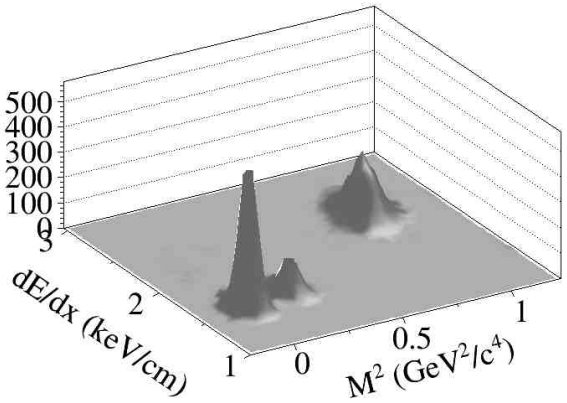


Fig. 5. A typical distribution of the specific energy loss dE/dx versus mass-squared for π^-, K^-, and protons (from left to right) at $p = 1$ GeV/c.

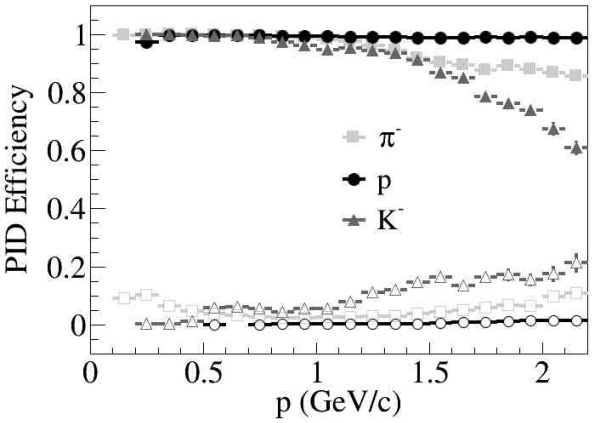


Fig. 6. PID efficiency (filled symbols) and contamination of wrongly identified particles (empty symbols) as a function of their total momentum.

The contamination is determined as the number of incorrectly tagged particles divided by the number of correctly tagged particles.

As can be seen from Fig. 6, the PID efficiency for protons is close to 1.0, while due to a partial overlap of the distributions for pions and kaons at high momenta, the efficiency of charged kaons drops down to ≈ 0.6 at $p = 2.5$ GeV/c.

ANALYSIS PROCEDURE

Multistrange hyperons were reconstructed using their decay modes into a charged particle and a Λ hyperon followed by Λ decay into a proton and a pion. The topologies of hyperon decays are shown in Fig. 7.

The event topology (decay of a relatively long-lived particle into two particles) defines the selection criteria: relatively large distance of the closest approach (*DCA*) to the primary vertex of decay products, small track-to-track separation in the decay vertex, relatively large decay length of the mother particle. Moreover, both the *DCA* and two-track separation cuts should be more efficient if applied in χ^2 - space, i.e if normalized to their respective errors.

The exact values of selection cuts were found by performing a multidimensional scan over the whole set of selection criteria with a requirement to maximize the invariant mass peak significance, defined as $S/\sqrt{S+B}$, where S and B are total numbers of signal (described the gaussian) and background (polynomial function) combinations inside $\pm 2\sigma$ interval around the peak position. While different physics analyses might prefer different selection quality criteria, the significance looks convenient to quantitatively evaluate effect of different factors on the reconstruction quality.

The corresponding scan procedure was realized as follows: during the particle combinations the parameters which have been chosen to serve as selection criteria (see above) were recorded along with the invariant mass value. Later, multiple loops over those variables were performed in some steps and their values were used as low or high thresholds, yielding the invariant mass peak significance for each set of selection cut values. Then, the maximum value was taken along with the corresponding set of selection parameters.

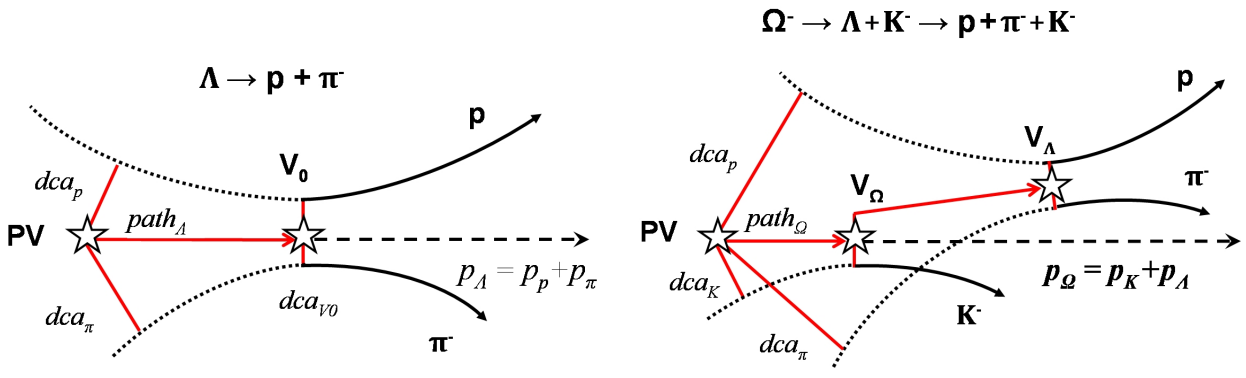
RESULTS AND DISCUSSION

Reconstruction of Λ hyperons

The results (Table 1 and Fig. 8) have been obtained for 10^4 central events, corresponding to about 30 seconds of data taking time.

Table 1. Factors affecting Λ reconstruction efficiency

Factor	Efficiency, %
Branching ratio: $\Lambda \to p + \pi^-$	63.4
p and π^- at $\lvert\eta\rvert < 1.3$	29.9
p and π^- at $\lvert\eta\rvert < 1.3$ and $p_T > 0.05$ GeV/c	28.3
p and π^- at $\lvert\eta\rvert < 1.3$ and $p_T > 0.1$ GeV/c	22.0
p and π^- at $\lvert\eta\rvert < 1.3$ and $p_T > 0.2$ GeV/c	8.6
Reconstructed p and π^- at $\lvert\eta\rvert < 1.3$	22.7
Maximum siginificance	8.6



(a) (b)

Fig. 7. (a) – event topology of two-particle decays of a neutral particle (e.g. $\Lambda \to p + \pi^-$); (b) – event topology of cascade-type decays (e.g. $\Omega^- \to \Lambda + K^- \to p + \pi^- + K^-$) (transverse view). Here dca_p, dca_π and dca_K are the distances of the closest approach of the decay tracks to the primary vertex PV, dca_{V0} is the distance between daughter tracks in the decay vertex V_0, $path$ is the decay length, $\mathbf{p_p}$, $\mathbf{p_\pi}$, $\mathbf{p_K}$, p_Λ and p_Ω are momenta of particles.

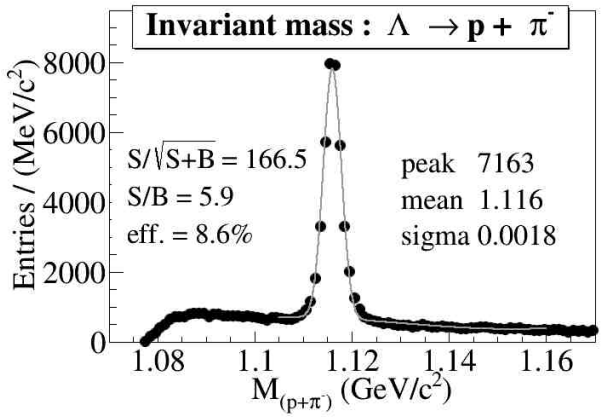


Fig. 8. Reconstructed invariant mass of proton and π^-.

Table 1 shows the effect of the detector acceptance (i.e. η-coverage and low-p_T cut for Λ decay products) on hyperon detection efficiency where the efficiency is defined with respect to the total number of hyperons. Lines 2-5 demonstrate the effect of the p_T-cut on the efficiency, where p_T is the true transverse momentum of the decay pion and proton. Line 6 shows the reconstruction efficiency, i.e. considering the reconstructed in the detector decay pions and protons without any explicit p_T-cut (and without PID efficiency). The last line includes all the relevant factors, i.e. reconstruction and PID efficiencies as well as selection efficiency. One can see that the detector provides efficient reconstruction of hyperons with p_T of decay tracks above 0.1 GeV/c in good agreement with Fig. 3. It is clear also that a higher p_T-threshold (e.g. 0.2 GeV/c) would significantly reduce the detector efficiency. The efficiency drop due to selection cuts comes from the necessity to suppress the combinatorial background in order to obtain a clean invariant mass peak.

Reconstruction of Ξ^- hyperons

The results (Table 2 and Fig. 9) have been obtained for $4 \cdot 10^4$ central events, corresponding to about 2 minutes of running time at the NICA collision rate of 6 kHz. Here, Λ-candidates in the invariant mass interval $\pm 3\sigma$ around the peak position were combined with negative pions to form Ξ^--candidates. In the selection procedure, additional acceptance cuts

Table 2. Factors affecting Ξ^- reconstruction efficiency

Factor	Efficiency %
Branching ratio: $\Xi^- \to \Lambda + \pi^-$ ($\Lambda \to p + \pi^-$)	63.6
p, π^- and π^- at $\|\eta\| < 1.3$	27.2
p, π^- and π^- at $\|\eta\| < 1.3$ and $p_T > 0.05$ GeV/c	24.6
p, π^- and π^- at $\|\eta\| < 1.3$ and $p_T > 0.1$ GeV/c	15.0
p, π^- and π^- at $\|\eta\| < 1.3$ and $p_T > 0.2$ GeV/c	2.9
Reconstructed p, π^- and π^- at $\|\eta\| < 1.3$	16.3
Maximum siginificance	2.5

Table 3. Factors affecting Ω^- reconstruction efficiency

Factor %	Efficiency
Branching ratio: $\Omega^- \to \Lambda + K^-$ ($\Lambda \to p + \pi^-$)	42.8
p, π^- and K^- at $\|\eta\| < 1.3$	18.4
p, π^- and K^- at $\|\eta\| < 1.3$ and $p_T > 0.05$ GeV/c	17.2
p, π^- and K^- at $\|\eta\| < 1.3$ and $p_T > 0.1$ GeV/c	12.2
p, π^- and K^- at $\|\eta\| < 1.3$ and $p_T > 0.2$ GeV/c	3.6
Reconstructed p, π^- and K^- at $\|\eta\| < 1.3$	10.0
Maximum siginificance	1.1

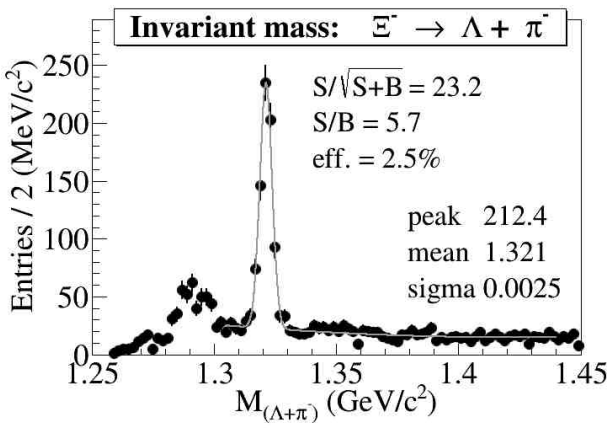


Fig. 9. Reconstructed invariant mass of Λ candidate and π^-.

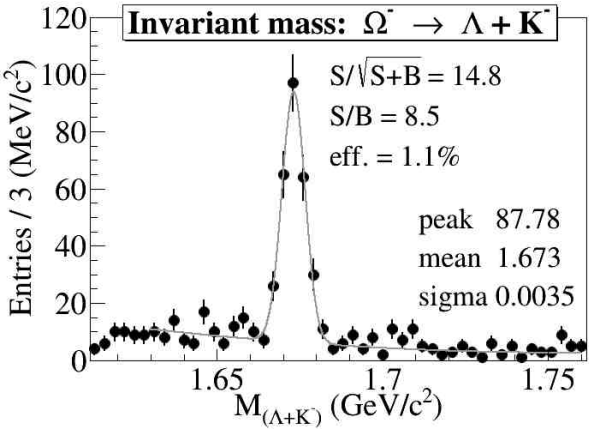


Fig. 10. Reconstructed invariant mass of Λ candidate and K^-.

were introduced to find the significance maximum for this cascade decay topology.

Reconstruction of Ω^- hyperons

The results (Tab. 3 and Fig. 10) have been obtained for $5 \cdot 10^5$ central events, corresponding to about 28 minutes of data taking time at NICA. Here the necessity of suppressing a larger combinatorial background and a requirement to have a sufficient significance of the signal results in stronger cuts and lower efficiencies. Also, as in the case of lighter hyperons we observed a large drop in the overall reconstruction efficiency when the low-p_t cut-off of decay products is increased from 0.1 to 0.2 GeV/c. Therefore, the MPD detector ability of reconstructing very low momentum particles (at least, down to $p_t = 0.1$ GeV/c) is of crucial importance for measurements of multistrange hyperons.

Table 4. Expected particle yields in central Au+Au collisions for 10 weeks of running time

Particle	Λ	Ξ^-	Ω^-
Expected yield	$5.8{\cdot}10^9$	$2.9{\cdot}10^7$	$1.4{\cdot}10^6$

SUMMARY

We have performed a simulation study of the MPD detector capabilities of reconstructing hyperons (Λ, Ξ^- and Ω^-) in central Au+Au collisions at $\sqrt{s}$ =9A GeV. The UrQMD event generator was used as the input for a study of the MPD detector set-up comprising the Time-Projecting Chamber (TPC) and barrel Time-Of-Flight system. Particle identification was achieved by combining the energy loss (from TPC) and time-of-flight (from TOF) measurements. A special procedure aimed at the maximization of the significance of the reconstructed invariant mass peak was applied for hyperons resulting in the observed signal-to-background ratio for $S/B \gtrsim 6$. The invariant mass resolution of $\approx$3 MeV/c^2 was achieved. Based on the results of this study and model predictions, we have estimated the expected yields of particle species under interest for 10 weeks of data taking (see Table 4).

REFERENCES

[1] J. Rafelski and B. Muller, *Phys. Rev. Lett.* **48**, 1066 (1982).

[2] K.U. Abraamyan et al., *Nucl. Instrum. Meth. A.* **628**, 99 (2011).

[3] http://nica.jinr.ru.

[4] *Searching for a QCD Mixed Phase at the Nuclotron Based Ion Collider Facility (NICA White Paper)*, https://indico.cern.ch/event/275003/contribution/1/material/paper/0.pdf.

[5] http://nica.jinr.ru/files/CDR_MPD/MPD_CDR_en.pdf.

[6] http://mpd.jinr.ru/.

[7] http://urqmd.org/.

[8] R. Fruehwirth, *Nucl. Instr. and Meth. A.* **262**, 444 (1987).

[9] R. Luchsinger and Ch. Grab, *Comp. Phys. Comm.* **76**, 263 (1993).

РЕКОНСТРУКЦИЯ НА ХИПЕРОНИ В МНОГОЦЕЛЕВИЯ ДЕТЕКТОР MPD (NICA)

Д. Сувариева, М. Илиева, В. Колесников, В. Васендина, Ал. Зинченко

Лаборатория по високи енергии, Обединен институт за ядрени изследвания,
ул. "Академик Балдин" № 4, 141980 Дубна, Московски регион, Русия

(Резюме)

Идентификация и реконструкция на странни частици е една от най-важните задачи на всеки експеримент с тежки йони, така е и за нашият проект NICA. Те биха могли да предоставят основна информация за горещата и плътна барионна материя. Представени са резултати от реконструкцията на ламбда Λ, кси Ξ^- и омега Ω^-) хиперони, които са получени на базата на Монте Карло симулации за сблъсъци на злато - злато, при енергии енергии – 9A GeV. За да се изследва създаването на ядрени фрагменти от такива сблъсъци се използва и генераторът UrQMD. Показано е, че стартовата версия на MPD и развитите методи, алгоритми и софтуер ще предоставят добра възможност за изследване на странни частици на ускорителния комплекс NICA (разрешение по маса 2-3 MeV/c^2).

Bulgarian Chemical Communications, Volume 47, Special Issue B (pp. 208–214) 2015

Feasibility study of $\phi(1020)$ production at NICA/MPD

L. S. Yordanova* for the MPD Collaboration

Veksler and Baldin Laboratory of High Energy Physics, Joint Institute for Nuclear Research, 141980 Dubna, Moscow region, Russia

The goal of this article is to give information about the new accelerator complex NICA at JINR, to provide overview of the MultiPurpose Detector (MPD) and its subdetectors and to present the current results of the MPD performance for ϕ-meson production. In our study we use the channel decay $\Phi \rightarrow K^+K^-$ to detect the formation of the ϕ-meson. UrQMD event generator is used and central events at $\sqrt{s} = 11$ GeV are analyzed. The obtained peak from the invariant mass distribution is fitted by a Breit-Wigner function. The calculated values of the parameters are consistent with the values given in literature. This study shows that the measurement of ϕ-mesons is feasible at NICA/MPD.

Key words: NICA/MPD, strange mesons, ϕ (1020) production

INTRODUCTION

The Nuclotron-based Ion Collider fAcility (NICA) is a new accelerator complex being constructed at JINR, Dubna, Russia (Fig. 1). The global scientific goal of the NICA/MPD project is to explore the phase diagram of strongly interacting matter in the region of highly compressed baryonic matter. The study of hot and dense baryonic matter provides relevant information on the in-medium properties of hadrons and nuclear matter equation of state; allows a search for deconfinement and/or chiral symmetry restoration, phase transition, mixed phase and critical end-point, possible strong P- and CP violation; gives information about the evolution of the Early Universe and the formation of neutron stars [1].

NICA's aim is to provide collisions of heavy ions over a wide range of atomic masses, from Au+Au collisions at $\sqrt{s_{NN}} = 11$ GeV (for Au^{79+}) and an average luminosity of $L = 10^{27}$ cm^{-2}s^{-1} to proton-proton collisions with $\sqrt{s_{pp}} = 20$ GeV and $L \sim 10^{32}$ cm^{-2}s^{-1}. Two interaction points are foreseen at NICA which provide a possibility for two detectors to operate simultaneously – MultiPurpose Detector (MPD) and Spin Physics Detector (SPD). This overview is focused on the MPD detector.

The MPD experimental program includes simultaneous measurements of observables that are presumably sensitive to high nuclear density effects and phase transitions.The goal to start energy scan as soon as the first beams are available and the present

* To whom all correspondence should be sent:
lyubka.s.yordanova@gmail.com

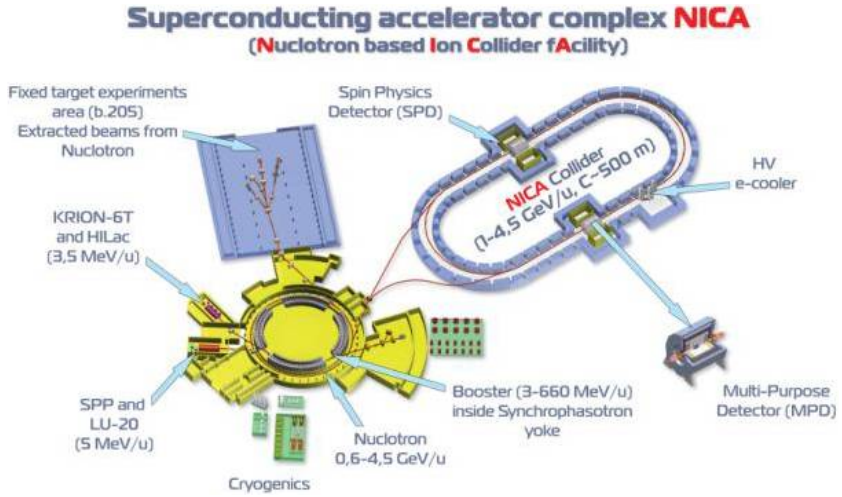


Fig. 1. NICA accelerator complex at JINR.

© 2015 Bulgarian Academy of Sciences, Union of Chemists in Bulgaria

constraints in resources and manpower lead to the MPD staging. In the first stage of the project (starting in 2017) are considered – multiplicity and spectral characteristics of the identified hadrons including strange particles, multi-strange baryons and antibaryons; event-by-event fluctuations in multiplicity, charges and transverse momentum; collective flows (directed, elliptic and higher ones) for observed hadrons. In the second stage (starting in 2020) the electromagnetic probes (photons and dileptons) will be measured. It is proposed that along with heavy ions NICA will provide proton and light ion beams including the possibility to use polarized beams [2].

The software of the MPD project is responsible for the design, evaluation and calibration of the detector; the storage, access, reconstruction and analysis of the data; and the support of a distributed computing infrastructure.The software framework for the MPD experiment (MpdRoot) is based on the object-orientated framework FairRoot (developed at GSI) and provides a powerful tool for detector performance studies, development of algorithms for reconstruction and physics analysis of the data [4]. Extended set of event generators for heavy ion collisions is used (UrQMD, LAQGSM, HSD).

OVERVIEW OF THE MPD DETECTOR

The detector for exploring phase diagram of strongly interacting matter in a high track multiplicity environment has to cover a large phase space, be functional at high interaction rates and comprise high efficiency and excellent particle identification capabilities. The MPD detector matches all these requirements (Fig. 2). It consists of central detector (CD) and two optional forward spectrometers (FS-A and FS-B).

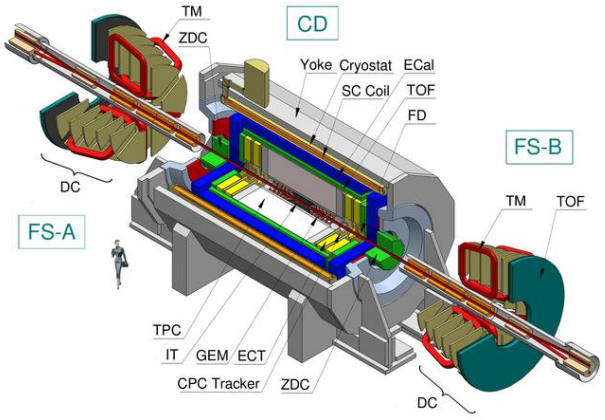


Fig. 2. General view of the MPD detector.

The central detector consists of a barrel part and two end caps. The barrel part is a set of various subdetectors. The main tracker is the time projection chamber (TPC) supplemented by the inner tracker (IT). IT and TPC have to provide precise tracking, momentum determination and vertex reconstruction. The high performance time of flight (TOF) system must be able to identify charged hadrons and nuclear clusters in a broad pseudorapidity range. The electromagnetic calorimeter (ECAL) should identify electrons, photons and measure their energy with high precision. The zero degree calorimeter (ZDC) should provide event centrality and event plane determination, and also measurement of the energy deposited by spectators. There are also a straw-tube tracker (ECT) and a fast forward detector (FFD).

The magnet of MPD is a solenoid with a thin superconducting NbTi winding and a flux return iron yoke. The magnet should provide a homogeneous magnetic field of 0.5 T. The field inhomogeneity in the tracker area of the detector is about 0.1%.

The MPD time projection chamber (TPC) is the main tracking detector of the central barrel and has to provide charged particles momentum measurement with sufficient resolution (about 2% at $p_t =$ 300 MeV/c), particle identification and vertex determination, two track separation (with a resolution ¡1 cm) and dE/dx measurement (dE/dx resolution better than 8%) for hadronic and leptonic observables at pseudorapidities $|\eta| < 2.0$ and $p_t > 100$ MeV/c. TPC readout system is based on Multi-Wire Proportional Chambers (MWPC) with cathode readout pads.

The inner tracker system (ITS) should enhance track reconstruction. ITS is able to restore tracks of particles with momentum less than 100 MeV/c and provides precise primary and secondary vertexes reconstruction with an accuracy of ~ 40 μm. ITS should also identify relatively rare events with production of hyperons. ITS is based on the Silicon Strip Detector (SSD) technology. It consists of a silicon barrel and discs which will register particles with large pseudorapidity $|\eta| < 2.5$.

The identification of charged hadrons (PID) at intermediate momentum (0.1–3 GeV/c) is achieved by the time-of-flight (TOF) measurements which are complemented by the energy loss (dE/dx) information from the TPC and IT detector systems. TOF system should provide a large phase space coverage $|\eta| < 3.0$, high combined geometrical and detection efficiency (better than 80%), identification of pions

and kaons with $0.1 < p_t < 2$ GeV/c and (anti)protons with $0.3 < p_t < 3$ GeV/c. The choice for the TOF system is Multigap Resistive Plate Counters (MRPC) which have good time resolution of $\delta < 70$ ps. The barrel covers the pseudorapidity region $|\eta| < 1.5$ and the geometry efficiency in it is above 90%. The end cap system covers the pseudorapidity region $1.5 < |\eta| < 3.0$.

The fast forward detector (FFD) should provide fast determination of a nucleus-nucleus interaction in the center of MPD, generation of a start pulse for TOF and production of L0-trigger signal. The proposed FFD design is a granulated Cherenkov detector which has a high efficiency for the high energy photons and for ultra-relativistic charged particles as well. Its acceptance in pseudorapidity is $2.0 \leqq |\eta| \leqq 4.0$. FFD has excellent time resolution of 38 ps.

The end cap tracker (ECT) has to provide charged particle identification and momentum measurement in the pseudorapidities $1 < |\eta| < 2.2$. ECT has high track reconstruction efficiency and momentum resolution about 10%. ECT consists of two end cap parts which are made with modules, containing layers of straw tubes.

The primary role of the electromagnetic calorimeter (ECAL) is to measure the spatial position and energy of electrons and photons. ECAL should have a high segmentation, should provide good space resolution, energy resolution about 3% and should allow a separation of overlapping showers. The Pb-scintillator ECAL of the "shashlyk" type will be used.

The zero degree calorimeter (ZDC) should provide a classification of events by centrality, event plane determination and measurement of the energy deposited by spectators. ZDC consists of modules of 60 lead-scintillator tile "sandwiches" with lead and scintillator plates. The light readout is provided by the wave-length shifting fibers (WLS-fibers) and the micropixel avalanche photodiodes (MAPDs).

More detailed description of the MPD detector can be found in the 'MPD Conceptual Design Report' [3].

MOTIVATION FOR STUDY OF THE Φ-MESON

The ϕ vector meson is the lightest bound state of hidden strangeness, consisting of a quark-antiquark pair. Although it is a meson, it is heavy in comparison with mesons consisting of u and d quarks, having a mass ($m_\phi = 1019.456 \pm 0.020$ MeV/c^2) comparable to the proton and Λ baryons. The ϕ-meson is expected to have a very small cross-section for interactions with non-strange hadrons. Its observables should remain largely undisturbed by the hadronic rescattering phase of the system's evolution. The ϕ-meson has a relatively long life-time of ~ 46 fm/c which means that it will mostly decay outside the fireball and its decay daughters won't have enough time to rescatter in the hadronic phase. Previous experimental measurements of the ϕ/K-ratio as a function of centrality showed the possibility of ϕ production via $K^+ + K^-$ coalescence in the hadronic stage. The observed ratios are flat as a function of centrality. These properties make the ϕ-meson an excellent probe of the hot and dense medium created in nucleus-nucleus collisions [5–7].

Measurements of the production of strange particles such as the ϕ-meson can provide important information on the properties of the medium and particle production mechanisms in ultra-relativistic Au-Au collisions. Measurements of the ϕ-meson pT spectra and their dependence in terms of shape and normalization on centrality may shed light on the constituents of the medium at the time of ϕ formation as well as the mechanism through which the ϕ-mesons are formed. Further insight into mechanisms of particle production for strange particles compared to non-strange particles can be gained through measurement of the particle ratios of multistrange hadrons. The medium produced at NICA/MPD can be also probed by measuring the elliptic flow of the ϕ-meson. Since multistrange hadrons and particles with hidden strangeness are assumed to freeze out early and undergo fewer interactions in the hadronic stage, their v2 signals should provide a clean signal from the early stage of the system's evolution. Measurements of the ϕ-meson v2 can give information on the collectivity and possible deconfinement of the system in the early stage and can serve to constrain different dynamical models of elliptic flow and particle production [8, 9].

The ϕ-meson with its mass comparable to Λ and p and low interaction cross-section can be exploited as a very good tool to probe the properties of the medium produced in nucleus-nucleus collisions at NICA/MPD. Φ-meson observables may help to distinguish further between different physical models of the dense medium and to enrich our knowledge of the system created in ultra-relativistic heavy-ion collisions.

DATA SET

In our study we use the channel decay $\Phi \to K^+K^-$ to detect the formation of the ϕ-meson. This channel is chosen because it has a high branching ratio (49.1%) and kaons are easy to detect. UrQMD event generator is used and gold-gold collisions are generated [10]. The number of the analyzed central events is 50 000 at $\sqrt{s} = 11$ GeV. The detector configuration used in the study includes the Time Projection Chamber (TPC) and the Time-Of-Flight system (TOF) for track reconstruction and particle identification in the pseudorapidity range $|\eta| < 1.5$.

RECONSTRUCTION OF Φ-MESONS

Signal distribution

The study of ϕ-meson production in central Au-Au collisions at $\sqrt{s} = 11$ GeV is performed using the UrQMD event generator. After the generation the events samples are transported through the MPD detector using the Geant 3 and Geant 4 transport packages.

In this analysis, ϕ-mesons are measured through the channel decay $\Phi \to K^+K^-$. The kaon daughter particles are identified through their ionisation energy loss (dE/dx) in the Time Projection Chamber (TPC) and also by using the information from the Time-Of-Flight system (TOF). A selection of kaon pairs by track quality cuts and particle identification (PID) is performed. The invariant mass of the kaon pairs is calculated by combination of all K^+ and K^- pairs of the same event. Consequently, we obtain data which contain the signal of ϕ-meson with the background. It is called same-event or signal distribution.

Background estimation

Since not all charged kaons in each event originate from ϕ-meson decays, the ϕ-meson signal extracted by this way is above a large combinatorial background of uncorrelated pairs. This combinatorial background should be removed from the signal distribution. There are two methods for removing background events in case of mass reconstruction: mixed-event technique and same-event technique [11,12]. In mixed-event technique to separate the signal from the background, pairs of K^+ and K^- are generated from different events. Such pairs create the background and pairs of K^+ and K^- from the same event give the signal. In same-event technique the background is generated from the pairs of K^+K^+ and K^-K^- of the same event, while K^+K^- pairs of the same event give the signal. In our analysis we use the mixed-event technique and the combinatorial background is estimated from the uncorrelated K^+K^- pairs. An invariant mass distribution is constructed using all positively charged kaon candidates from one event mixed with all negatively charged kaon candidates from n other events where n can be chosen relatively high in order to reduce effects from statistical fluctuations.

Extraction and scaling of the combinatorial background

The mixed-event background distribution is estimated by using a big number of events and it should be scaled before being subtracted from the signal distribution. The scaling can be performed by two different ways – scaling by the integral ratio and scaling iteratively [5]. In the scaling by the integral ration, the background distribution is scaled by the ratio of the integrals of the signal and the background distributions in a defined mass region. The mass region should not include the ϕ-meson mass peak. In the iterative scaling, the background distribution is scaled by the ratio of the integrals of the signal and the background distributions in a fixed mass region including the ϕ-meson mass peak. The background distribution is then subtracted from the signal distribution and the remaining signal is fitted with Breit-Wigner function plus a straight line. The signal integral is the integral in the mass range minus the integral of the Breit-Wigner function. Then the ratio is recalculated and the background is rescaled. After scaling the background distribution, the raw ϕ-meson yields are obtained by subtracting the scaled mixed-event background distribution from the signal distribution.

Breit-Wigner function

The obtained peak from the invariant mass distribution after the subtraction is then fitted by a Breit-Wigner function and the characteristics of the ϕ-meson such as its mass and its width are found. The Breit-Wigner distribution is a continuous probability distribution. It is most often used to model resonances (unstable particles)in high energy physics. The Breit-Wigner function has the following appearance:

$$BW_{(m_{inv})} = \frac{1}{2\pi} \frac{AW}{(m - m_\phi)^2 + (\frac{W}{2})^2}, \qquad (1)$$

In this function A is the area of the distribution and W is the width. The measured values of the ϕ-meson

mass and width are consistent, within the experimental resolution, with the particle data grop (PDG) values. The recent results of the ϕ-meson study are shown in the next section. This study shows that the measurement of ϕ-mesons is feasible and we can expect detection of them when NICA/MPD will be put in operation.

RESULTS

The recent results of the ϕ-meson study are shown in the following histograms (see Fig. 3, Fig. 4 and Fig. 5).

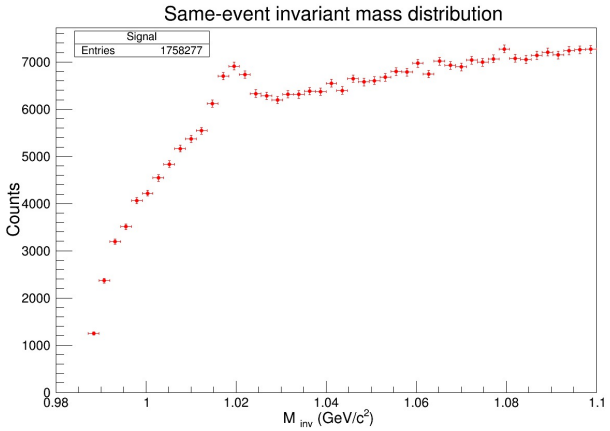


Fig. 3. Signal distribution.

In Fig. 3 an invariant mass signal distribution of the ϕ-meson is represented. The exact values of selection cuts for the kaons used for the reconstruction of the ϕ-mesons are found by performing a scan over the whole set of selection criteria with a requirement to maximize the invariant mass peak significance. The invariant mass peak significance is defined as $S/\sqrt{(S+B)}$ where S and B are total numbers of signal and background combinations inside $\pm 3\sigma$ interval around the peak position. For the current signal distribution it is – $S/\sqrt{(S+B)} = 18.11$. It is still seen that the peak of the signal is above a large combinatorial background, due to the uncorrelated kaon pairs.

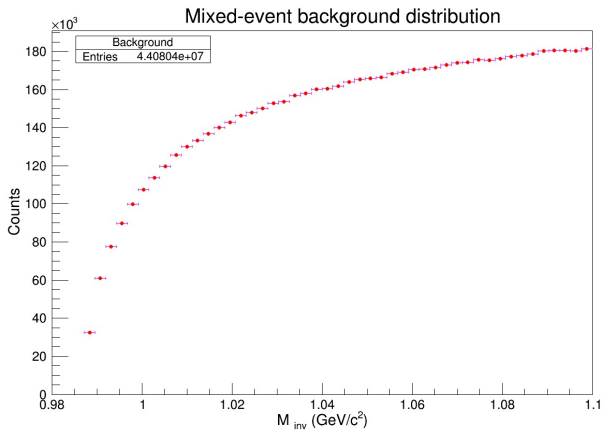


Fig. 4. Mixed-event background distribution.

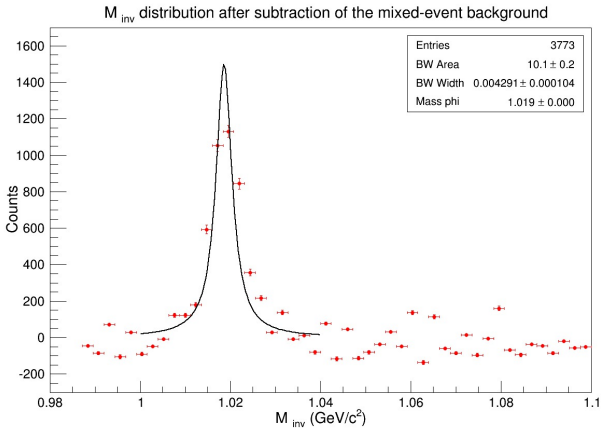


Fig. 5. Φ-meson invariant mass distribution after subtraction of the mixed-event background.

Fig. 4 shows a background estimation by using the mixed-event technique. The values of selection cuts correspond to those for the signal distribution. The background distribution has a smooth shape because of the relatively high number of events n chosen for calculating it.

The final results for the raw yields of the ϕ-meson are shown in Fig. 5. The values of the parameters obtained by the Breit-Wigner fit (Width $= 4.291 \pm 0.104$ MeV/c^2 and $M_{inv} = 1019.995 \pm 0.022$ MeV/c^2) are consistent with the values given in literature. All these preliminary results show that the measurement of ϕ-mesons is feasible at NICA/MPD. The next step of the ϕ-meson study is connected with detailed analyses of higher statistics and measurements of the elliptic flow. The properties of the ϕ-meson will be also studied in different types of collisions with different centrality.

SUMMARY

In conclusion, it should be said that the MPD detector has many advantages and meets all the ambitious physics requirements for exploring phase diagram of strongly interacting matter in a high track

multiplicity environment. The MPD detector's advantages comprise coverage of a large phase space, functionality at high interaction rates, high efficiency and excellent particle identification capabilities.

Measurements of the production of strange particles such as the ϕ-meson can provide important information on the properties of the medium and particle production mechanisms in ultra-relativistic collisions. The ϕ-meson with its mass comparable to Λ and p and low interaction cross-section can be used to probe the properties of the medium created at NICA/MPD. The study of the ϕ-meson, based on the current analyses, is feasible and gives quite good results. More detailed study of the ϕ-meson properties is included in the MPD physics programme. Therefore, NICA facilities provide unique capabilities for studying fundamental properties of the theory of strong interactions (QCD).

REFERENCES

[1] MPD Collaboration, *Booklet NICA* (2012), available at `http://nica.jinr.ru/files/NICA_booklet.pdf`.

[2] MPD Collaboration, *NICA White Paper* (2014), available at `http://theor.jinr.ru/twiki/pub/NICA/WebHome/WhitePaper_10.01.pdf`.

[3] MPD Collaboration, *The MultiPurpose Detector-MPD* (2011), available at `http://nica.jinr.ru/files/CDR_MPD/MPD_CDR_en.pdf`.

[4] M. Al-Turany, D. Bertini, F. Uhlig, R. Karabowicz, D. Kresan and T. Stockmanns, FairRoot Software V. 13.12, FairRoot Development Team (2014), see //fairroot.gsi.de.

[5] S. Blyth, *Using the ϕ-meson to Probe the Medium Created in Au-Au Collisions at RHIC*, Ph.D. thesis, University of Cape Town, Cape Town (2007).

[6] STAR Collaboration, *Phys.Rev.* C **79**, 064903 (2009).

[7] PHENIX Collaboration, *Phys. Rev.* C **72**, 014903 (2005).

[8] A. Shor, *Phys. Rev. Lett.* **54**, 1122-1125 (1985).

[9] J. Rafelski, *Nucl. Phys. A* **418**, 215C-235C (1984).

[10] UrQMD Collaboration, *The UrQMD User Guide* (2014), available at `http://urqmd.org/documentation/urqmd-user.pdf`.

[11] S. Pal, C.M. Ko, and Z. Lin, *Nucl.Phys.* A **707**, 525-539, (2002).

[12] STAR Collaboration, *J. Phys. G* **30**, S543-S548 (2004).

ИЗУЧАВАНЕ НА ДОБИВА НА ϕ (1020) В СБЛЪСЪЦИ НА ТЕЖКИ ЙОНИ НА NICA/MPD

Любка Йорданова (от името на MPD колектива)

Лаборатория по високи енергии, Обединен институт за ядрени изследвания,
ул. "Академик Балдин" № 4, 141980 Дубна, Московски регион, Русия

(Резюме)

Експериментът NICA/MPD предоставя уникални възможности за изследването на поведението на ядрената материя в екстремални условия при високи енергии и плътности на взаимодействащата система. Експериментът се отличава с предимства като висока светимост на сноповете частици – $L = 1 \cdot 10^{27}$ cm^{-2}s^{-1}, изключително ефективен детектор с прецизна идентификация на частиците и интересен енергиен диапазон за изследване 4–11 GeV. Досега няма достатъчно детайлна информация относно поведението и свойствата на ϕ мезоните при енергиините обхвати, които експериментът NICA/MPD покрива. Поради тази причина изучаването на добива на странни частици е не само актуално, но и необходимо в съвременната физика на високите енергии.

Изучаването на странните частици, каквито са ϕ мезоните, се счита за един от ключовете за разгадаване на механизмите на реакция в сблъсъците на тежки йони при високи енергии. Ясно изразеното увеличаване на добива на странни частици се свързва с прехода на адронната смес в съставните ѝ части (кварки и глуони) в началния етап на взаимодействието. ϕ мезоните се състоят от странен кварк и антикварк и именно чрез тях може да се определи кога системата преминава от нормална ядрена материя в кварк-глуонна плазма (деконфайнмънт). Изучаването на ϕ мезоните може да предостави информация за ранното състояние на взаимодействащата система ("fireball"), как тя се развива като функция на времето и яснота около механизмите на взаимодействие в нея. При изучаването на частиците при екстремални условия се очаква да се наблюдават изменения в техните свойства и поведение във взаимодействащата система. Добивът, ширината на резонанса и фазово-пространствените разпределения като функция на енергията на сблъсъка и централността са чувствителни към деконфайнмънт прехода.

В този анализ ϕ мезоните са реконструирани чрез използване на канала им на разпад на K^+ и K^-. Каналът е избран заради високата си вероятност на разпад и ефективното изследване на каоните. С изучаването на начина на работа на генераторите на сблъсъци на тежки йони при NICA енергии, изучаването на предвижданията на използвания модел за добива на частици и техните спектри, изследване на свойствата на реконструирани каони, с разработването на методи и алгоритми за получаване на инвариантна маса на елементарни частици, оптимизирането на алгоритмите за ϕ мезони и анализа на получените разпределения на инвариантната маса при реконструкция на ϕ мезони се показва, че изучаването на ϕ (1020) на NICA/MPD е възможно. Получените резултати до момента кореспондират с данните от литературата и показват ефективността на детектора.

Bulgarian Chemical Communications, Volume 47, Special Issue B (pp. 215–221) 2015

Fast detectors for the MPD/NICA time-of-flight system

V. Babkin, S. Bazylev, O. Batenkov, P. Dulov*, V. Golovatyuk, S. Lobastov, V. Petrov, M. Rumyantsev, A. Schipunov, A. Shutov, I. Slepnyov, V. Slepnyov, A. Veschikov, S. Volgin, V. Yurevich

Laboratory of High Energy Physics, Joint Institute for Nuclear Research
6 Joliot-Qurie Str., 141980 Dubna, Russia

The Multi-Purpose Detector (MPD) [1] is being developed to study properties of hot and dense baryonic matter in collisions of light and heavy ions on the collider NICA which is under construction at JINR, Dubna [2]. Identification of charged particles in the range 0.1–2 GeV/c is carried out with Time Projection Chamber (TPC) in solenoid magnetic field and time-of-flight (TOF) system. It has been decided to use MRPCs with strip and pad readouts as a basic element of the TOF detector. Beam tests results of full scale mRPC prototypes with readout electronics are described in this article. As a start detector for the time-of-flight system we used detector based on microchannel plate photomultipliers with the time resolution of ~ 37 ps.

Key words: MPD, MRPC, particle identification, ToF, FFD, fast electronics, transmition line

INTRODUCTION

The MultiPurpose Detector (MPD) is proposed for a study of hot and dense baryonic matter in collisions of heavy ions over the atomic mass range A = 1 – 197 at a centre-of-mass energy up to $\sqrt{s_{NN}} = 11$ GeV (for Au^{+78}) and luminosity $L = 10^{27} m^{-2} c^{-1}$. The MPD experiment is foreseen to be carried out at accelerator complex facility for heavy ions – the Nuclotron-based Ion Collider fAcility (NICA) which under construction now at JINR, Dubna.

The MPD consits of a barrel part and two endcaps located inside the magnetic field. The barrel part is a shell-like set of various detector systems surrounding the interaction point and aimed to reconstruct and identify both charged and neutral particles in the pseudorapidity region of $|\eta| < 1.2$. The endcaps are aimed for precise tracking and particle identification over pseudorapidity range $(1.2 < |\eta| < 2)$. The principal tracker is the time projection chamber (TPC) supplemented by the inner tracker (IT) surrounding the interaction region. Both subdetectors (IT and TPC) has to provide precise track finding, momentum determination, vertex reconstruction and pattern recognition. The TPC and IT together with time of flight system have to provide charged particles momentum measurement.

Due to the fact that in most recent experiments in high energy physics such as Alice(LHC) and STAR(RICH) time-of-flight systems are based on multi-gap resistive plate chambers (MRPC) [3] were successfully used in the TOF systems, we decided also to use MRPCs on the base of flat glass for the time-of-flight system of the MPD. This article presents the results of the tests of MRPCs on the deuteron beam of Nuclotron at JINR of different design and readout electrode geometry [4].

DESIGN OF MRPC PROTOTYPES

Two types of MRPCs were considered: with the pad signal readout and with the strip readout. Both options have their special traits in terms of assembling and operation. But at low multiplicity of events, it makes sense to use a strip electrode for readouts. It reduces the number of channels making the system more cost-effective. Therefore, strip MRPCs have been chosen for the barrel part of the MPD. At the end cup parts of the detector, there will be combined pad and strip readouts.

The pad prototype (Fig. 1) consists of two stacks having 5 gaps each. A 210 μm gas gap is formed by a ordinary fishing line of appropriate thickness. The readout electrodes are fiberglass boards of 140×120 mm^2 with etched rectangles of 16×35 cm^2. They make up in total two rows of 8 pads in each. In order to supply high voltage to glasses closest to the readout electrodes, they are coated with a graphite conductive layer with a surface resistance of 2 – 10 MOhm per 1 square. Signals from the pads are transferred via the twisted pair cable to the amplifier. The detector is situated in a leak-tight box in which a gas mixture (C2H2F4 – 90%/iC4H10 – 5%/SF6 – 5%) is injected.

* To whom all correspondence should be sent:
dulov.bg@abv.bg

© 2015 Bulgarian Academy of Sciences, Union of Chemists in Bulgaria

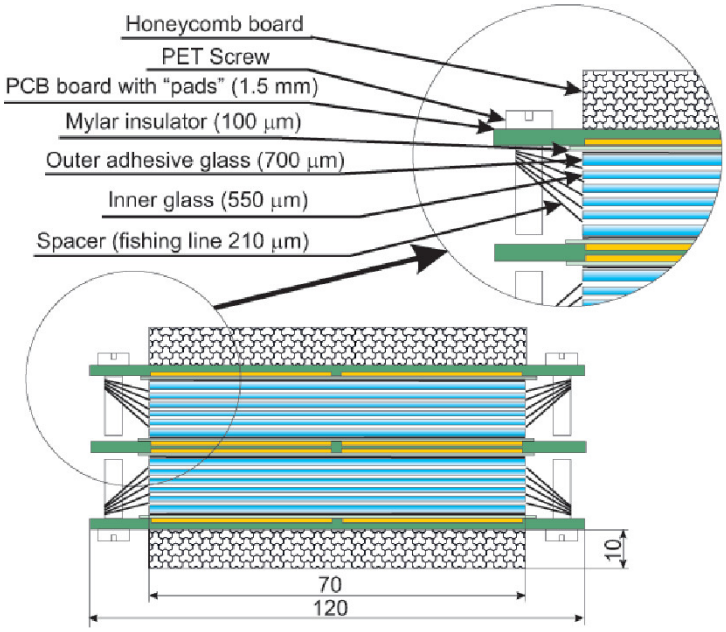


Fig. 1. Schematic view of a pad MRPC.

Full-scale strip MRPC prototypes were developed and produced for the barrel part of the time-of-flight system. The readout electrodes of these prototypes were designed as thin narrow strips. The sectional view of this prototype is shown in Fig. 2. The active region area of the MRPC was determined by the size of the glass and amounts 590×290 mm^2. The design almost completely duplicated the one of pad detectors. Three different strip MRPCs were assembled for the first test run. A single-stack MRPC prototype was assembled for the first test run at the Nuclotron beam having 5 gas gaps with the thickness of 250 μm and 24 strips with the size of 600×10 mm^2. For the second run the design of the strip detector was changed and two prototypes were assembled: a single-stack prototype having 6 gas gaps of 220 μm and 48 strips of 600×5 mm^2 and a double-stack MRPC with 12 gas gaps of 220 μm (6 per a stack) and the same strips that the single-stack prototype had. Such a design modification was fulfilled based on the first experiment's results.

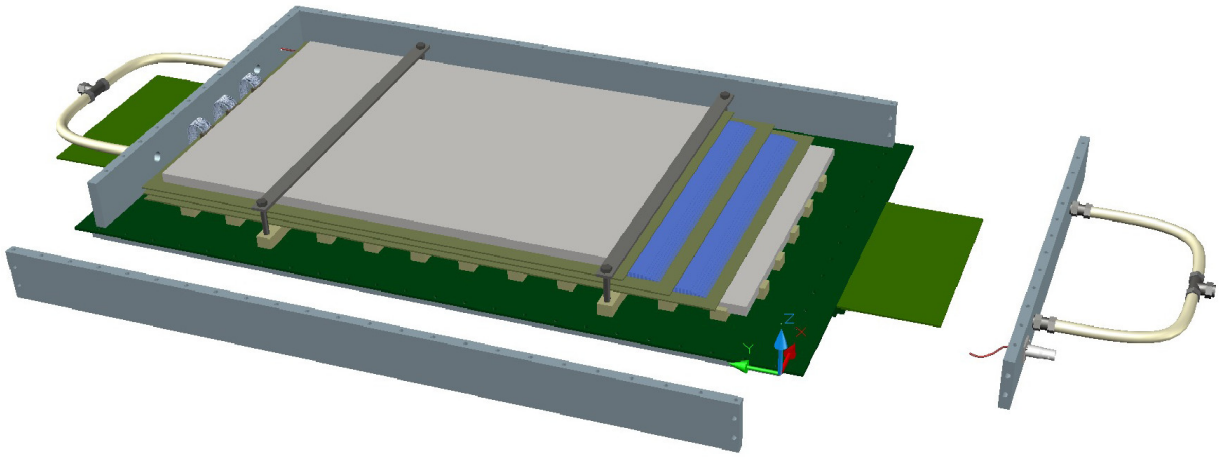


Fig. 2. Sectional view of the full-scale strip MRPC prototype.

FFD START DETECTOR

The signal from the Fast Forward Detector (FFD) will be used as a start signal for the time-of-flight system [5]. The Fast Forward Detector is a double-arm Cherenkov detector for high energy photons. Each arm of the detector consists of 12 modules laid in the shape of square around the beam pipe. The arms are placed 75 cm off the expected interaction point on both sides along the beam axis. The main functions of the detector are the following:

- generation of the fast high-precision start signal for time-of-flight measurements;
- reconstruction of the interaction point along the beam axis with the accuracy of ± 1.5 cm;
- production of signal for the L0-trigger system with selection of nuclei collisions occurring close to IP.

Each module of the FFD is a sequential assembly of the following elements: a 7–10-mm thick lead plate; a 15-mm thick quartz radiator; a micro-channel XP85012Q photomultiplier by Photonis; front-end electronics and a high voltage divider. High energy photons are converted into relativistic electrons in the lead plate. These electrons entering the quartz radiator emit Cherenkov light which is registered by the photomultiplier. The active area of the photocathode of the XP85012Q photomultiplier, which is sensitive to the visible and ultraviolet regions of wave lengths (170–670 nm), is 53×53 mm^2 and covers 81% of the front area of the photomultiplier. The photomultiplier has multi-anode structure of 8×8 anodes; its gain of the order of $\sim 10^5$–10^6 depends on the applied high voltage value, good linearity of the output signal with the leading edge of 0.6 ns and the transit time spred of $\sigma \sim 37$ ps [6].

Each module has 4 quartz radiators of 3×3 cm^2 which are light-isolated from each other. There are 4×4 anodes of the photomultiplier per each quartz radiator; signals from them are added together and transferred to the front-end electronics. The front-end electronics produce analog and digital LVDS signals and its width informs of the pulse height. Thus, each module has 4 independent channels.

READOUT ELECTRONICS

In order to increase the differential signal accepted up from the MRPC's pads and strips, a 24-channel amplifier on the base of a NINO chip was used [7], which was specially designed for the time-of-flight system of ALICE and now is the most common amplifier for time-of-flight MRPCs. This amplifier has a highly rapid output signal ($<$1 ns) and small jitter of the output signal ($<$ 10 ps), which is provided by the low noise level of the amplifier. Another characteristic feature of the NINO chip is the possibility to change input resistance in order to match it with the readout electrodes. A discriminator with the minimal triggering threshold of about 25 fC is imbedded into the NINO chip. The discrimination threshold was set at 75 fC for all the conducted experiments. The output signal from the discriminator is LVDS-standard differential signal. The leading edge of the pulse corresponds to the time of its passing through the threshold, and its width corresponds to the amplitude of the input pulse, which allows one to make time-amplitude correction with the use of only one TDC.

32-channel time-to-digital converters (TDC32VL) based on HPTDC chip were developed and produced for digitization of LVDS signals and data acquisition [8].

Experiments on the MRPC time resolution evaluation conducted in March of 2011 showed that integral nonlinearity occurs with TDC operating in the mode of 24.4 ps per bin as a result of cross talk to channels of the signals from clock speed generators in the HPTDC chip. This nonlinearity causes strong degradation of time distribution. The contribution of this nonlinearity and the method to eliminate it has already been shown in the HPTDC Manual [9] as well as in other publications [10, 11].

The method of uniform filling the time gap with random events (code density test) was used for calibration (consideration of nonlinearity) of VME TDC32VL module. Minor differential (Fig. 3 (a)) and strong integral (Fig. 3 (b) nonlinearity in terms of time were observed distracting the measured value for 8 bins ($\sim$ 200 ps) from the real time, which deteriorated significantly the time resolution of the electronics. Calibration matrices were developed for further data processing for each channel of the TDC allowing for elimination of the integral nonlinearity contribution. Native time resolution of a TDC32VL channel made up about 25 ps after applying the calibrations.

TESTING THE PROTOTYPES AT THE ACCELERATOR BEAM

Tests of the prototypes were carried out at the Nuclotron deuteron beam at LHEP JINR in December 2012 and March 2013. The deuteron beam with the

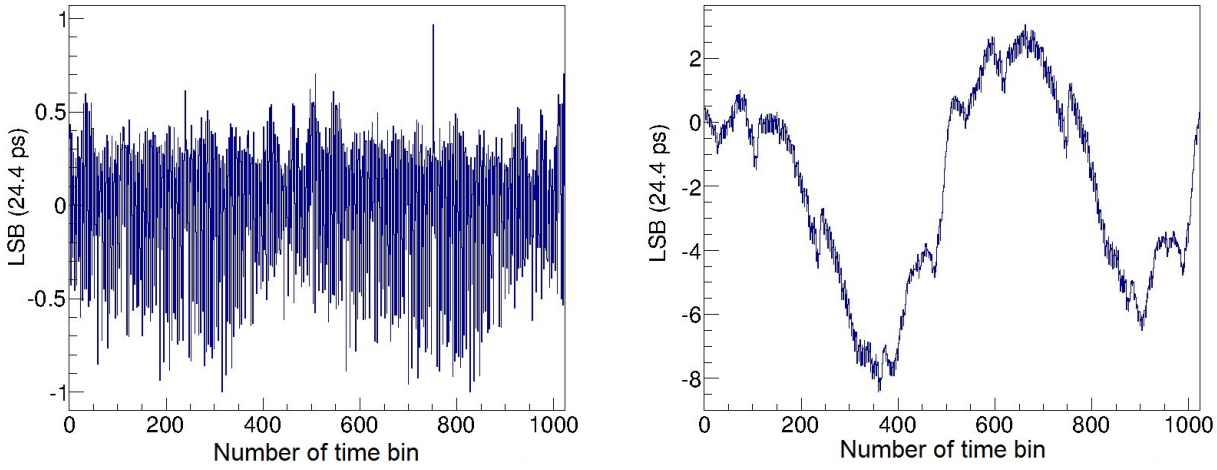


Fig. 3. Differential (a) and integral (b) nonlinearity of HPTDC.

energy of 1 GeV/n and spill duration of 2 s was injected into Building 205 and with the use of magnet optics was sent to the experimental setup (Fig. 4). A scintillation telescope made up of C1-C5 counters was used for trigger signal obtaining. At that, C5 counter corresponded in size to the FFD prototype's effective surface and was placed immediately before FFD-1. The following MRPC prototypes were tested: two identical double-stack pad prototypes (PRPC) and three full-sized strip prototypes (SRPC).

Two identical FFD prototypes were studied in the experiments. The detectors were placed one after another along the beam line with the minimal gap between them. The signal from one of the detectors was considered as "start", and the signal from another – as "stop".

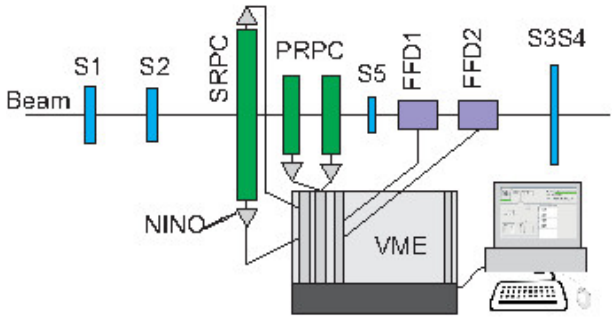
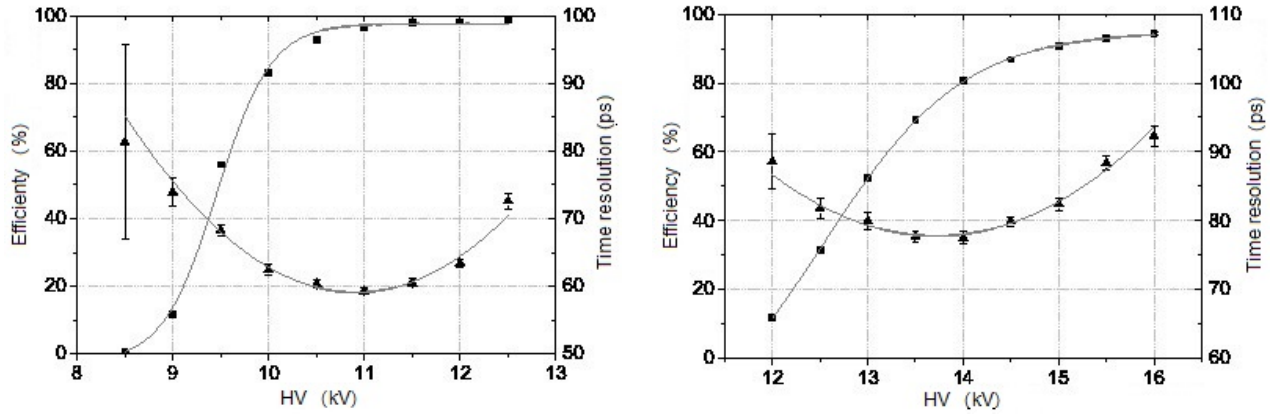


Fig. 4. Layout of the experimental setup. S1–S5 – a scintillation counters; FFD-1, FFD-2 – start detectors (FFD prototypes); PRPC – pad prototypes; SRPC – strip prototypes, VME – a crate with the readout electronics.

The detectors FFD1 and FFD2 was used as a start detector T0 in all the experiments and had the time resolution of 37 ps with TDC32VL, as it was measured early [5]. This value was used later on for calculation of the time resolution of MRPCs.

The dependencies of efficiency and time resolution on voltage for pad chambers and a single-stack chamber with a 10 mm-wide strip were measured in the experiment in December 2012. Time difference between the T0 detector and PRPC was measured without any corrections. Time distribution for PRPC is worse than 120 ps in this case. The LVDS pulse width corresponds to the height of the signal. Therefore the time-over-threshold method of correction was used. Approximation of the distribution of time depending on the width of the signal allows one to obtain the ratio for correction. When the time-over-threshold dependence was taken into consideration, time resolution improved significantly. The same procedure was done for the SRPC. The best time resolution came to 60 ps for PRPC and 80 ps for the SRPC in December 2012 experiment was achived.

Fig. 5 demonstrate the dependencies of the efficiency and time resolution of the first prototypes versus voltage. The detector operated in the optimal mode as the maximal resolution could be achieved at the efficiency of about 98%. In contrast to the pad MRPC, the efficiency of the first prototype of the strip MRPC made up 80% at the best time resolution and it didn't exceed 93% even at the voltage increased up to 16 kV. Such degradation of the time resolution at the low efficiency was associated with the contri-



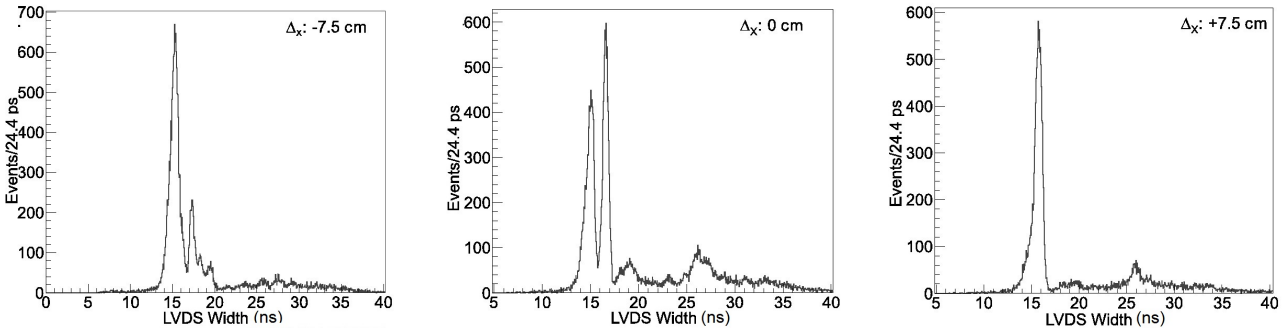
(a) (b)

Fig. 5. Time resolution and efficiency for PRPC (a) and SRPC (b) in first experiment.

bution of the signal reflection from the edge of the strip. The reflection was caused by bad matching of the strip (which impedance is about 75 Ohm, according to the calculations and measurements) with cable and amplifier. An 8-cm long ribbon twisted pair cable with the impedance of 110 Ohm was used. For this reason splitting was observed of the width spectrum of the output LVDS signal. As a consequence, the information on the actual pulse height was distorted. Such splitting may be caused by interference of the reflected signal with the trailing edge of the main pulse. It is supported by the fact that the position of the second width peak and its value depends on the coordinate of the particle passing the detector along the strip (Fig. 6).

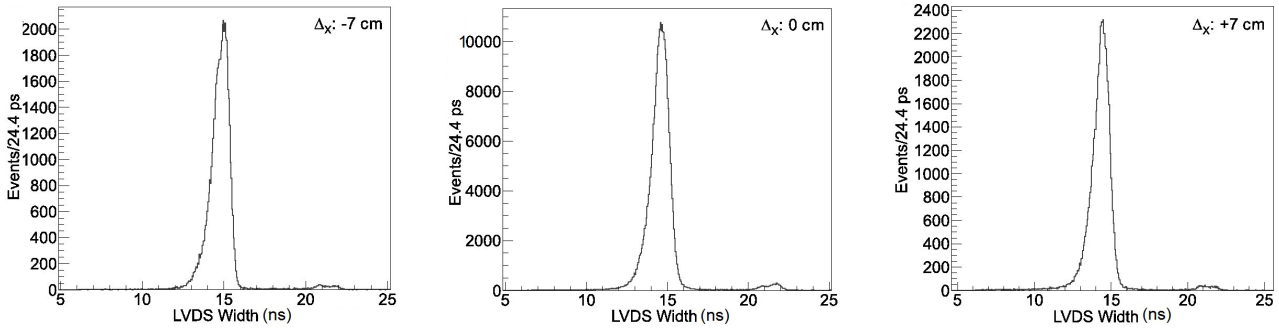
A similar problem arose during the work with the MRPC with a long strip [12]. In order to avoid splitting of the width spectrum, the strip is matched with the amplifier by adjusting the input impedance of the amplifier. According to the manual, the input impedance of the amplifier can be changed within the range of 20 – 100 Ohm. In our case, such a method hardly influenced the width spectrum and it was decided to change the design of the detector and the way of accepting the signal because the main reflection take place in the point of strip-cable.

Two new MRPC prototypes with strip readouts were assembled for the experiment at the Nuclotron beam in March 2013. The first prototype represented a single-stack six-gap chamber with the gap width of 220 μm and a 5-mm wide and 600-mm long readout strip. The active area of the detector remained of the same size of 290×590 mm^2, however the number of channels per one detector increased twice. As pulse generator tests demonstrated, this construction was well matched with the signal transmission line.



(a) (b) (c)

Fig. 6. Splitting of the width spectrum of the SRPC (10 mm) LVDS signal as a function of the coordinate. (a) shifted by 7.5 cm from the strip center; (b) in the center of the strip; (c) shifted by +7.5 cm from the center.



(a) (b) (c)

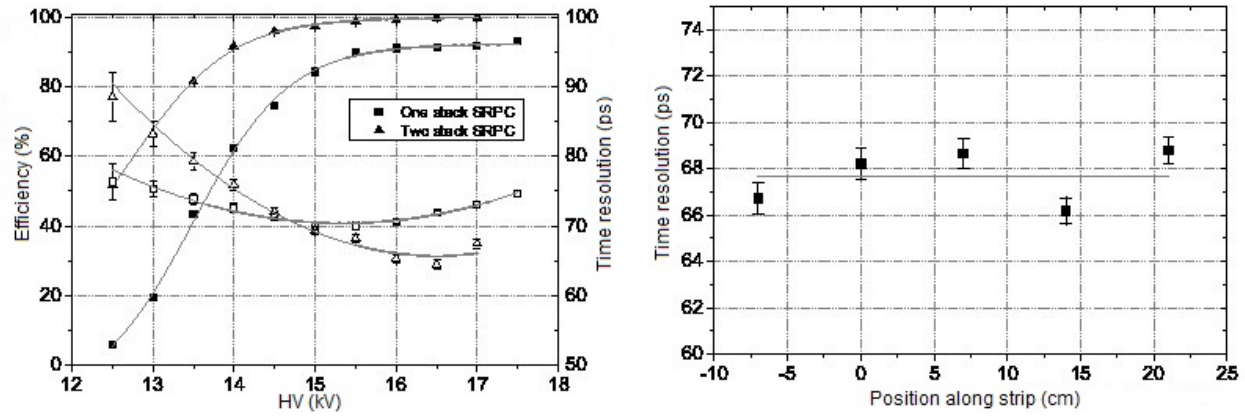
Fig. 7. Spectra of the single-stack MRPC (5 mm) prototype with the strip readout and a matched strip for particles passed through different points of the strip: (a) shifted by 7 cm from the strip center; (b) in the center strip; (c) shifted by +7 cm from the strip center.

It was discovered in the course of the experiment that the width spectrum splitting was almost absent with such a configuration (Fig. 7).

Calculations predicted the efficiency of the single-stack chamber will not exceed 90%. Therefore, a double-stack MRPC was assembled with the same stacks as the described single-stack one. The results on the efficiency and time resolution of the single- and double-stack strip MRPC prototypes obtained from March's run are shown in Fig. 8 (a).

As it was expected, the efficiency of the single-stack prototype made up 92%. In this case the best time resolution was in the limit of 70 ps. The efficiency of 99.9% and time resolution of about 65 ps were achieved for the double-stack version. An important feature of the two-ends strip readout is possibility to position quite precisely the particle passing along the strip. Using the time difference between arrivals of signals from the left and the right ends of the strip, it is possible to reconstruct the point of the particle transit. The position resolution in this case is about 5 mm.

It was suggested that due to non-symmetric location of strips in the double-stack SRPC, degradation of the pulse front edge might occur and, as a result, the time resolution might decrease. In order to prove this effect, the dependence was measured of the time resolution on the point of the particle transit through the strip (Fig. 8(b)). It is shown that the time resolution remains almost the same with the coordinate being changed. I.e. dispersion has little impact on the signal.



(a) (b)

Fig. 8. (a) test results for the MRPC prototype with a 5-mm wide strip. (b) time resolution of the double-stack SRPC as a function of the coordinate of a particle's flight.

CONCLUSIONS

The optimization of the full-sized MRPC prototype design was fulfilled for the time-of-flight system of the MPD. The two experiments at the Nuclotron beams allowed us to reveal imperfections of the detectors' design and to develop the MRPCs optimal for these conditions.

The results obtained for the double-stack MRPC with the strip readout and for the double-stack MRPC with the pad readout meet the requirements to the time-of-flight system of the MPD. Further investigations will be aimed at the optimization of the readout and front-end electronics. The matching will be performed for strips of various configurations, which will allow for reduction of the total number of the electronics channels.

REFERENCES

[1] Kh. U. Abraamyan, et al., *Nucl. Instrum. Methods Phys. Res., Sect. A* **628**, 99 (2011).

[2] A. N. Sissakian and A.S. Sorin, *J. Phys. G: Nucl. Part. Phys.* **36**, 064069 (2009).

[3] A. Akindinov, et al., *Nucl. Instrum. Methods Phys. Res., Sect. A* **456**, 16 (2000).

[4] V.A. Babkin, et al., *Bulletin of the Russian Academy of Sciences: Physics* **75**, 1277 (2011).

[5] V.I. Yurevich, et al., *Physics of Elementary Particles and Atomic Nuclei, Letters* **10**, 414 (2013).

[6] J. Va'vra, et al., Report SLAC-PUB-14279 (2010).

[7] F. Anghinolfi, et al., *Nucl. Instrum. Methods Phys. Res., Sect. A* **533**, 183 (2004).

[8] Internet site: http://afi.jinr.ru/TDC32VL

[9] J. Christiansen. *High performance time to digital converter (HPTDC)*, Digital Microelec. Group, CERN, *HPTDC manual version 2.2 for HPTDC version 1.3*.

[10] Daniel McDonald, *Calibration of the STAR Time-of-Flight Detector for Particle Identication*, MS degree thesis, Houston, Texas, December 2010.

[11] P. Antonioli, S. Meneghini, *9th Workshop on Electronics for LHC Experiments*, Amsterdam, The Netherlands, 29 Sep - 3 Oct 2003, 311.

[12] K. Doroud, et al., *Nucl. Instrum. Methods Phys. Res., Sect. A* **660**, 73 (2011).

ВРЕМЕ-ПРЕЛИТНА СИСТЕМА (TOF) НА ДЕТЕКТОРА MPD (NICA)

П. Дулов[1], В. Бабкин[1], М. Румянцев[1], В. Галватюк[1], В. Чолаков[2]

[1] *Лаборатория по високи енергии, Обединен институт за ядрени изследвания, ул. "Академик Балдин" № 4, 141980 Дубна, Московски регион, Русия*
[2] *Физически факултет, Пловдивски университет "Паисий Хилендарски", ул. "Цар Асен" №24, 4000 Пловдив, България*

(Резюме)

Концептуалният дизайн на многоцелевия детектор MPD (Multi-Porpose Detector) е създаден за изучаването на горещата и плътна барионна материя от сблъсъците на тежки йони с атомна маса в диапазона $A = 1$–197 с максимална енергия 11 GeV за Au79+.

MPD експеримента ще се извърши в Обединения институт за ядрени изследвания, Дубна в новостроящия се колайдер NICA (Nuclotron-based Ion Collider fAcility) при средна яркост $L = 10^{27}$ cm^{-2}s^{-1}.

Идентификацията на заредените адрони с междинни импулси (0,1-2) GeV се постига с измерване на времето за прелитане от TOF детектора. Основен елемент на TOF е mRPC (Multi-gap Resistive Plate Chambers) – многопроцепна

Bulgarian Chemical Communications, Volume 47, Special Issue B (pp. 222–226) 2015

Does chirality exist in nuclei? The case of ^{102}Rh

M. S. Yavahchova[1*], D. Tonev[1], N. Goutev[1], G. de Angelis[2], P. Petkov[1], R. K. Bhowmik[3], R. P. Singh[3], S. Muralithar[3], N. Madhavan[3], R. Kumar[3], M. Kumar Raju[4], J. Kaur[5], G. Mohanto[3], A. Singh[5], N. Kaur[5], R. Garg[6], A. Sukla[7], Ts. K. Marinov[1], S. Brant[8]

[1] *Institute for Nuclear Research and Nuclear Energy, Bulgarian Academy of Sciences, 72 Tzarigradsko Chaussee Blvd., 1784 Sofia, Bulgaria*
[2] *INFN, Laboratori Nazionali di Legnaro, Legnaro, Italy*
[3] *Inter-University Accelerator Center, New Delhi, India*
[4] *Nuclear Physics Department, Andhra University, Visakhapatnam, India*
[5] *Department of Physics, Punjab University, Chandigarh, India*
[6] *Department of Physics and Astrophysics, Delhi University, New Delhi, India*
[7] *Department of Physics, Banaras Hindu University, Varanasi, India*
[8] *Department of Physics, Faculty of Science, Zagreb University, Zagreb, Croatia*

Excited states in ^{102}Rh, populated in the fusion-evaporation reaction ^{94}Zr(^{11}B, 3n)^{102}Rh at a beam energy of 36 MeV, were studied using the INGA spectrometer at IUAC, New Delhi.A new chiral candidate sister band was found. Lifetimes of exited states in ^{102}Rh were measured for the first time by means of the Doppler-shift attenuation technique. A new band was found in the level-scheme of ^{102}Rh.

Key words: chirality, DSAM, INGA, transition strenghts, lifetimes

INTRODUCTION

Chirality is a phenomenon which is often found in nature. Examples for the existence of chirality are present in chemistry, biology, high energy physics etc. An interesting question arose last decade in nuclear physics, does chirality exists in this field? A spontaneous breaking of the chiral symmetry can take place for configurations where the angular momenta of the valence protons, valence neutrons, and the core are mutually perpendicular [1]. The projections of the angular momentum vector on the three principal axes can form either a left- or a right- handed system and therefore the system expresses chirality. Since the chiral symmetry is dichotomic, its spontaneous breaking by the axial angular momentum vector leads to a pair of degenerate $\Delta I = 1$ rotational bands, called chiral doublet bands. Pairs of bands, presumably due to the breaking of the chiral symmetry in triaxial nuclei, have been recently found in the mass regions $A \sim 130$ [2, 3], $A \sim 105$ [4–9], $A \sim 195$ [10] and $A \sim 80$ [11]. In many cases the energy degeneracy of the chiral candidate bands was almost observed but the transition probabilities are different. This is clearly seen in the case of ^{134}Pr [12–14]. According to the work [15] and [16], the nucleus of ^{102}Rh is candidate to express multiple chirality.The main goal of the present work was to check for the existence of chirality in the mass region A $\sim$ 100. In previous works [4–6], an island of chiral candidates has been proposed around ^{104}Rh. Next to the identification of the twin bands, some lifetimes have been reported for the yrast band of ^{104}Rh [6].

EXPERIMENT

Excited states in ^{102}Rh were populated using the reaction ^{94}Zr(^{11}B,3n)^{102}Rh at a beam energy of 36 MeV. The beam was delivered by the 15-UD Pelletron accelerator at the Inter University Accelerator Center (IUAC) in New Delhi. The target consisted of 0.9 mg/cm^2 ^{94}Zr, enriched to 96.5%, evaporated onto a 8 mg/cm^2 gold backing. The recoils were leaving the target with a mean velocity v of about 0.9% of the velocity of light, c. The de-exciting gamma-rays were registered by the Indian National Gamma Array (INGA), whose 15 Clover detectors are accommodated in a 4π geometry [17]. For the purposes of the Doppler-Shift Attenuation Method (DSAM) analysis the detectors of INGA which lie at approximately the same polar angle with respect to the beam axis were grouped in five rings. Doppler-broadened line shapes were observed for transitions depopulating higher spin levels. The rings where appreciable

* To whom all correspondence should be sent:
m.yavahchova@gmail.com

© 2015 Bulgarian Academy of Sciences, Union of Chemists in Bulgaria

Doppler-shifts are observed are these at angles of 32, 57, 123 and 148 degrees. Gain matching and efficiency calibration of the Ge detectors were performed using ^{152}Eu and ^{133}Ba radioactive sources before sorting the data in matrices and cubes.

DATA ANALYSIS AND RESULTS

The detectors of INGA were grouped into rings positioned with respect to the beam axis. This is needed for DSAM analysis. The rings with appreciable Doppler-shifts are these at angles of 32, 57, 123 and 148 degrees. For the investigation of the level scheme and electromagnetic properties of the transitions in ^{102}Rh we have performed four different types of data analyses. The ordering of the transitions in the level scheme was determined according to γ-ray relative intensities, γ-γ coincidence relationships, and γ-ray energy sums. The multipolarity and the character of the transitions were deduced from the investigation of linear polarization and angular correlations measurements. For this purpose the clover detectors from the ring at 90 degrees were used as a Compton polarimeter [18]. The lifetimes of excited states in ^{102}Rh were derived using the Doppler-shift attenuation methods. The analysis was carried out within the framework of the Differential decay method (DDCM) [19] according to the procedure outlined in [20] where details about the Monte-Carlo simulation of the slowing down process, determination of stopping powers and fitting of line shapes can be found.

In Fig. 1. is shown an example for the line shape analysis of the 669 keV transition and determination of the lifetime of the $I^{\pi} = 11^{-}$ level according to DDCM. Thus, we have succeeded to extend the known level scheme [21] by a new $\Delta I = 1$ band with a negative parity and to determine 8 new lifetimes. The reduced transition probabilities B($\sigma\lambda$) deduced from lifetime data are presented in [22]. The present results come to supercede the preliminary level-scheme published in [23]. To study the bands based on the $\pi g_{9/2} \otimes \nu h_{11/2}$ configuration, we have performed two

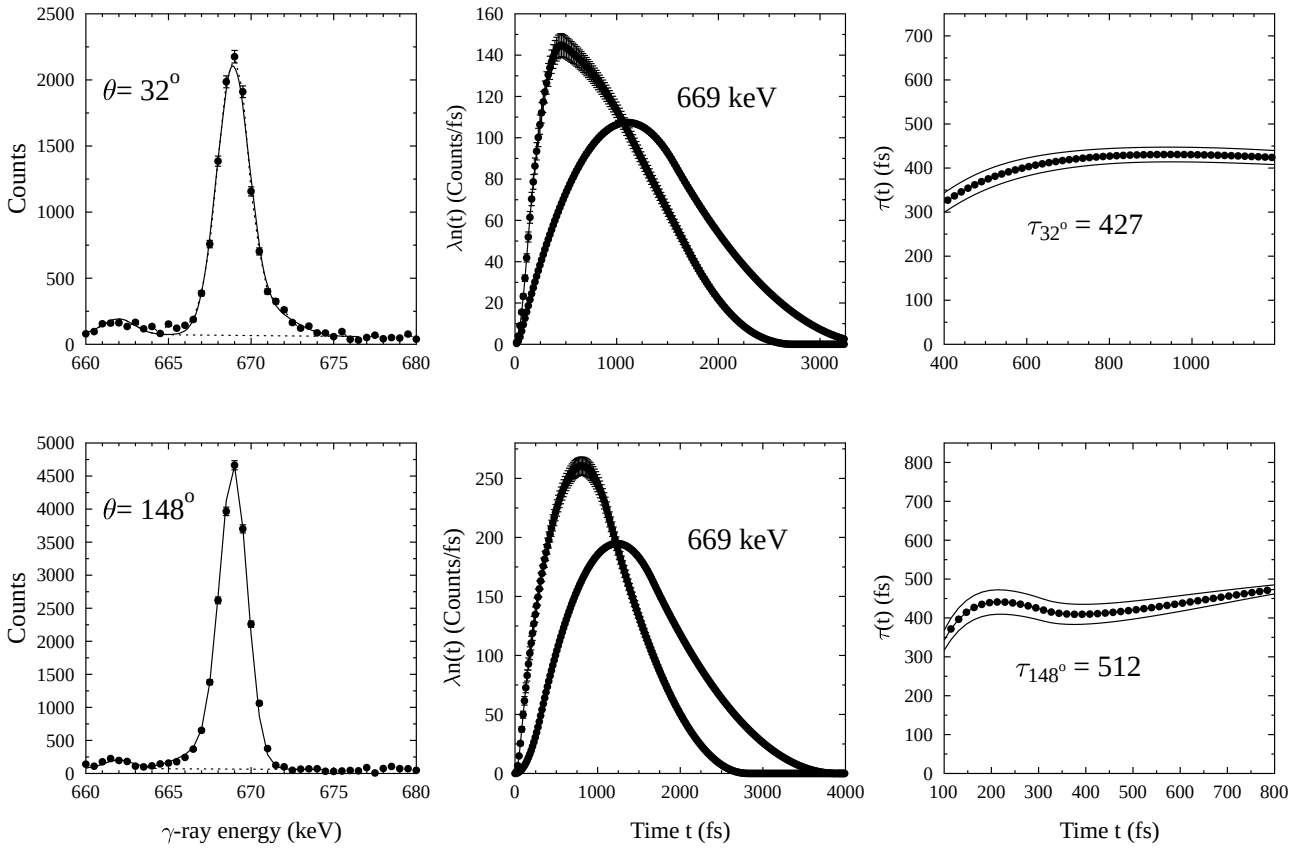


Fig. 1. Line shape analysis of the 669 keV transition in the first chiral-candidate band and determination of the lifetime of the I^{π}=11^{-} level according to DDCM.

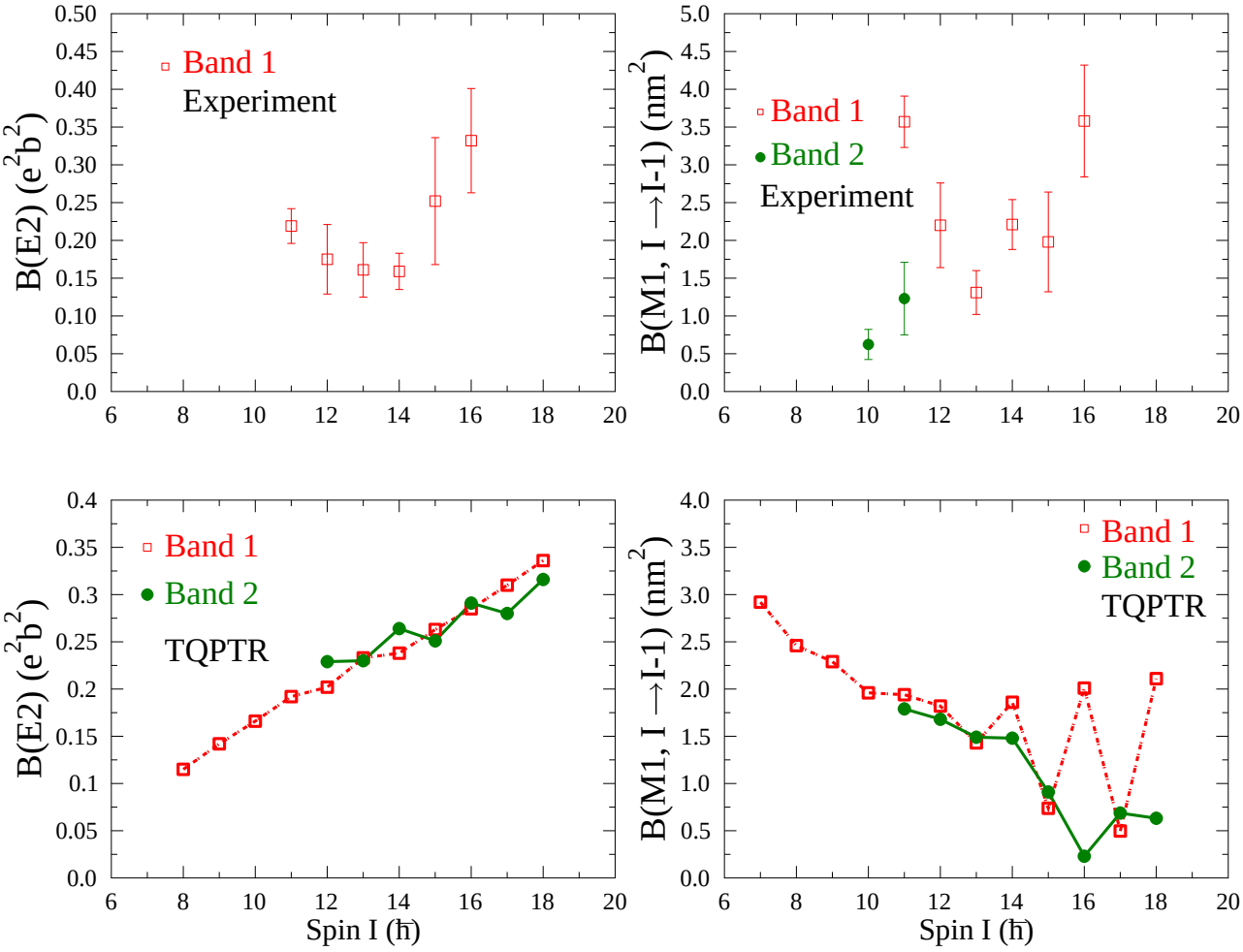


Fig. 2. Experimentally derived and theoretically calculated B(E2) and B(M1) transition strengths in ^{102}Rh. The experimental B(E2) and B(M1) values are presented in the upper panels. The results of TQPTR calculations are displayed in the second row.

quasiparticles + triaxial rotor (TQPTR) calculations in the framework of the model presented in Ref. [24]. The comparison between the experimental and calculated B(M1) transition strenghts leads to the conclusion that this model reproduce roughly the data in Band 1 and is consistent with the transition strenght in Band 2 (see Fig.2.). The TQPTR calculations reveal that the optimum value of the triaxiality parameter γ=20° differs from the value of 30° characterizing chirality.

CONCLUSIONS

In order to investigate the level-scheme and to determine lifetimes of the excited states in the chiral candidate nucleus of ^{102}Rh we have performed an experiment at the Inter University Accelerator Center in New Delhi using the INGA spectrometer. We have succeeded to extend the level-scheme with a new $\Delta I = 1$ band with a negative parity. Our lifetime measurements and the theoretical analysis do not support chirality in ^{102}Rh.

Aknowledgements. *This research has been supported by Bulgarian Science Fund under contrat DFNI-E 01/2 and by a NUPNET-NEDENSAA project funded by the Bulgarian Ministry of Education and Sciences.*

REFERENCES

[1] S. Frauendorf, Jie Meng, *Nucl. Phys.* **A 617**, 131 (1997).

[2] K. Starosta, T. Koike, C.J. Chiara, D.B. Fossan, D.R. LaFosse, A.A. Hecht, C.W. Beausang, M.A. Caprio, J.R. Cooper, R. Krücken *et al.*, *Phys. Rev. Lett.* **86**, 971 (2001).

[3] S. Mukhopadhyay, D. Almehed, U. Garg, S. Frauendorf, T. Li, P.V. Madhusudhana Rao, X. Wang, S.S. Ghugre, M.P. Carpenter, S. Gros *et al.*, *P*hys. Rev. Lett. **99**, 172501 (2007).

[4] J. Timǒar, C. Vaman, K. Starosta, D.B. Fossan, T. Koike, D. Sohler, I.Y. Lee, A.O. Macchiavelli, *Phys. Rev.* **C 73**, 011301 (2006).

[5] C. Vaman, D.B. Fossan, T. Koike, K. Starosta, *Phys. Rev. Lett.* **92**, 032501 (2004).

[6] T. Suzuki, G. Rainovski, T. Koike, T. Ahn, M.P. Carpenter, A. Costin, M. Danchev, A. Dewald, R.V.F. Janssens, P.Joshi *et al.*, *Phys. Rev.* **C 78**, 031302 (2008).

[7] P. Joshi, D.G. Jenkins, P.M. Raddon, A.J. Simons, R. Wadsworth, A.R. Wilkinson, D.B. Fossan, T. Koike, K. Starosta, C. Vaman *et al.*, *Phys.Lett.* **B 595**, 135 (2004).

[8] C. Y. He *et al.*, *Phys. Rev.* **C 86**, 047302 (2012).

[9] C. Y. He *et al.*, *Phys. Rev.* **C 89**, 014327 (2014).

[10] E.A. Lawrie, P.A. Vymers, J.J. Lawrie, Ch. Vieu, R.A. Bark, R. Lindsay, G.K. Mabala, S.M. Maliage, P.L. Masiteng, S.M. Mullins *et al.*, *Phys. Rev.* **C 78**, 021305 (2008).

[11] S.Y.Wang, B. Qi, L. Liu, S.Q. Zhang,H. Hua, X.Q. Li, Y.Y. Chen, L.H. Zhu, J. Meng, S.M. Wyngaardt *et al.*, *Phys. Lett.* **B 703**, 40 (2011).

[12] D. Tonev, G. de Angelis, P. Petkov, A. Dewald, S. Brant, S. Frauendorf, D. L. Balabanski, P. Pejovic, D. Bazzacco, P. Bednarczyk *et al.*, *Phys. Rev. Lett.* **96**, 052501 (2006).

[13] D. Tonev, G. de Angelis, S. Brant, S. Frauendorf, P. Petkov, A. Dewald, F. Dönau, D. L. Balabanski, Q. Zhong, P. Pejovic *et al.*, *Phys. Rev.* **C 76**, 044313 (2007).

[14] S. Brant, D. Tonev, G. De Angelis, A. Ventura, *Phys. Rev.* **C 78**, 034301 (2008).

[15] J. Meng, J. Peng, S. Q. Zhang, and S.-G. Zhou, *Phys. Rev.* **C 73**, 037303 (2006).

[16] J. Peng, H. Sagawa, S. Q. Zhang3, J. M. Yao, Y. Zhang, and J. Meng, *Phys. Rev.* **C 77**, 024309 (2008).

[17] S. Muralithar, K. Rani, R. Kumar, R.P. Singh, J.J. Das, J. Gehlot, K.S. Golda, A. Jhingan, N. Madhavan, S. Nath *et al.*, *Nucl. Instr. Meth.* **A 622**, 281 (2010).

[18] N. Goutev, M.S. Yavahchova, D. Tonev, G. de Angelis, P. Petkov, R.K. Bhowmik, R.P. Singh, S. Muralithar, N. Madhavan, R. Kumar *et al.*, *J. Phys. Conf. Ser.* **366**, 012021 (2012).

[19] G.Böhm, A. Dewald, P. Petkov, P. von Brentano, *Nucl. Instr. Meth.* **A 329**, 248 (1993).

[20] P.Petkov, J. Gableske, O. Vogel, A. Dewald, P. von Brentano, R. Krücken, R. Peusquens, N. Nicolay, A. Gizon, J. Gizon *et al.*, *Nucl. Phys.* **A 640**, 293 (1998).

[21] J. Gizon, A. Gizon, J. Timár, Gh. Căta-Danil, B.M. Nyakó, L. Zolnai, A.J. Boston, D.T. Joss, E.S. Paul, A.T. Semple *et al.*, *Nucl. Phys.* **A 658**, 97 (1999).

[22] D. Tonev *et al.*, *Phys. Rev. Lett.* **113**, 052501 (2014).

[23] S. C. Pancholi, *Exotic Nuclear Excitations, Springer, New York, 2011*.

[24] I.Ragnarsson and P.Semmes, *Hyp. Int.* **43**, 425 (1988).

СЪЩЕСТВУВА ЛИ ХИРАЛНА СИМЕТРИЯ В ЯДРОТО ^{102}Rh?

М. Явахчова[1], Д. Тонев[1], Н. Гутев[1], Дж. ди Анжелис[2], П. Петков[1], Р. К. Боумик[3], Р.П. Сингх[3], С.. Муралитар[3], Н. Мадхаван[3], Р. Кумар[3], М. Кумар Раджу[4], Дж. Каур[5], Г. Моханто[3], А. Сингх[5], Н. Каур[5], Р. Гарг[6], А. Сукла[7], Цв. К. Маринов[1], Ц. Брант[8]

[1] *Институт за ядрени изследвания и ядрена енергетика, Българска академия на науките, бул. „Цариградско шосе" №72, 1784 София, България*
[2] *INFN, Laboratori Nazionali di Legnaro, Legnaro, Italy*
[3] *Inter-University Accelerator Center, New Delhi, India*
[4] *Nuclear Physics Department, Andhra University, Visakhapatnam, India*
[5] *Department of Physics, Punjab University, Chandigarh, India*
[6] *Department of Physics and Astrophysics, Delhi University, New Delhi, India*
[7] *Department of Physics, Banaras Hindu University, Varanasi, India*
[8] *Department of Physics, Faculty of Science, Zagreb University, Zagreb, Croatia*

(Резюме)

Хиралността е често срещан феномен в природата. Примери за хиралност се срещат в химията, биологията и други. В ядрената физика въпросът за хиралността започва да се разглежда през последните 20 години. Тя е нещо ново за ротационните ядра и е един от най-изучаваните феномени в ядрената физика през последните години. Спонтанното нарушение на хиралната симетрия може да видим там, където ъгловите моменти на валентните протони и неутрони и ядката са перпендикулярни. Проекциите на вектора на ъгловия момент по осите на вътрешната система могат да оформят лява или дясна координатна система. От раздвоеността на хиралната система следва, че спонтанното и нарушаване от вектора на ъгловия момент води до двойка дегенерирани $\Delta I = 1$ ротационни ивици, наречени хирални ивици близнаци. Двойки ивици, вероятно дължащи се на нарушаването на хиралната симетрия в триосево ядро, са намерени в масовите области $A \sim 130$ [1,2], $A \sim 105$ [3-6], $A \sim 195$ [7] и $A \sim 80$ [8]. Въпреки това само в няколко случая (^{126}Cs, ^{128}Cs), свойствата на системата от хирални ивици, които произхождат от основната симетрия, са потвърдени включително преходите от хирални вибрации до статична хиралност в ^{135}Nd. В много от случаите, енергийната изроденост на ивиците, кандидати за хиралност, е била почти изучена, но вероятностите за преход са различни, като в случая на ^{134}Pr [12,13]. Съгласно работите на J. Meng [14,15] ядрото ^{102}Rh е един от кандидатите да покажат хирална структура. По тази причина и поради факта, че в масовата област $A \sim 100$ почти не са правени изследвания за съществуването на хирална симетрия поради, което решихме да го изследваме.

1. K. Starosta et al., *Phys. Rev. Lett.* **86** (2001) 971.
2. S. Mukhopadhyay et al., *Phys. Rev. Lett.* **99** (2007) 172501.
3. J. Timár et al., *Phys. Rev. C* **73** (2006) 011301.
4. C. Vaman et al., *Phys. Rev. Lett.* **92** (2004) 032501.
5. T. Suzuki et al., *Phys. Rev. C* **78** (2008) 031302.
6. P. Joshi et al., *Phys. Lett. B* **595** (2004) 135.
7. E. A. Lawrie et al., *Phys. Rev. C* **78** (2008) 021305.
8. S. Y. Wang et al., *Phys. Lett. B* **703** (2011) 40.
9. E. Grodner et al., *Phys. Lett. B* **703** (2011) 46.
10. E. Grodner et al., *Phys. Rev. Lett.* 97 (2006) 172501.
11. S. Mukhopadhyay et al., *Phys. Rev. Lett.* **99** (2007) 172501.
12. D. Tonev et al., *Phys. Rev. Lett.* **96** (2006) 052501.
13. D. Tonev et al., *Phys. Rev. Lett.* **76** (2007) 044313.
14. J. Meng et al., *Phys. Rev. C* **73** (2006) 037303.
15. J. Meng et al., *Phys. Rev. C* **77** (2008) 024309.

Bulgarian Chemical Communications, Volume 47, Special Issue B (pp. 227–231) 2015

Composite thin films of nanosized $CoFe_2O_4$ in polymer matrix

Ts. Lazarova[1], D. Kovacheva[1]*, T. Ruskov[2], S. Atanasova-Vladimirova[3], P. Krastev[2], N. Tanev[2]

[1] *Institute of General and Inorganic Chemistry, Bulgarian Academy of Sciences, Acad. G. Bonchev Str., Bl. 11, Sofia-1113, Bulgaria*
[1] *Institute for Nuclear Research and Nuclear Energy, Bulgarian Academy of Sciences, 72 Tzarigradsko Chaussee Blvd., 1784 Sofia, Bulgaria*
[3] *Institute of Physical Chemistry, Bulgarian Academy of Sciences, Acad. G. Bonchev Str., Bl. 11, Sofia-1113, Bulgaria*

Nanosized cobalt ferrite was prepared by a solution combustion method. Metal nitrates in a stoichiometric ratio and sucrose were used as starting reagents. The "as prepared" cobalt ferrite powder has a mean crystallite size up to 10 nm. By further thermal treatment at 600°C a nanosized material with average crystallite size of about 30–40 nm is obtained. The composite was prepared by adding cobalt ferrite to an aqueous solution of carboxymethylcellulose with a subsequent 5 minute sonication. Thin layers were deposited on a glass substrate by spin coating technique in a laboratory centrifuge at 6000 rpm. Drying was carried out at room temperature. Thin composite layers were characterized as to the crystal structure, crystallite size, magnetic phase, and oxidation state, by X-ray powder diffraction, transmission electron microscopy, scanning electron microscopy and Mössbauer spectroscopy.

Key words: polymer-$CoFe_2O_4$ composite, X-ray diffraction, electron microscopy, Mössbauer spectroscopy

INTRODUCTION

Spinel cobalt ferrite represents a type of magnetic material with a high magnetic stability, good magnetization properties, large magneto-optic rotation ability, and high coercitivity. Cobalt ferrites are usually prepared by a solid state reaction procedure: the reactants have to be grounded, mixed, and calcinated, and the reactions take place at high temperatures, lasting for a long period of time [1–3]. However, by this method, it is very difficult to obtain the pure spinel phase products; also the resultant particles are always obtained in a large size of the order of "μm". For many applications it is very important to develop different protection techniques to stabilize the magnetic nanoparticles against degradation. Various types of coating layers, both organic and inorganic were used for this purpose [4]. In the last several years many "soft chemistry" methods for preparing nanosized materials have been developed. One of them is the so-called solution combustion method, which is based on a combustion reaction of metal nitrates (oxidizers) and some organic reductors (such as glycine, urea, citric acid, etc.) acting as a fuel [5, 6]. The method provides simple operation procedures and short processing times, thus it is time and energy-saving. What is more important for the method is that the reactants are in highly homogeneous form during the whole reaction process. An additional advantage of the short time and low temperature of decomposition of the precursors and formation of the oxide materials is that the as obtained products are amorphous or have small crystallite size of the order of a few tens of "nm" and the particle size can be adjusted within a range by variation of the reaction parameters. For these reasons the method is very suitable for preparation of nanosized materials with controlled particle size. In the present work a composite material comprising cobalt ferrite nanoparticles (obtained by a solution combustion method) and carboxymethylcellulose (CMC) polymer (as a protector) is prepared. The composite material was deposited as a thin layer of a few "μm" thickness on a glass substrate. The composite layer was characterized as to the, crystal structure, crystallite size, magnetic phase, and oxidation state, by means of a X-ray powder diffraction, transmission electron microscopy, scanning electron microscopy, and Mössbauer spectroscopy.

EXPERIMENTAL

Magnetic nanoparticles of cobalt ferrite were synthesized by a solution combustion synthesis technique. The method is based on a combustion reaction of metal nitrates (oxidizers) and some organic redactors (glycine, urea, citric acid, etc.) acting as a fuel. As starting reagents $Co(NO_3)_2 \cdot 4\,H_2O$, $Fe(NO_3)_3 \cdot 9\,H_2O$ and sucrose ($C_{12}H_{22}O_{11}$) were used. The molar ratio between the nitrates and sucrose was calcu-

* To whom all correspondence should be sent:
didka@svr.igic.bas.bg

© 2015 Bulgarian Academy of Sciences, Union of Chemists in Bulgaria

lated according to the principles of combustion reaction on the basis of the total oxidising and reducing power of the metal nitrates (O) and the sucrose (F) ensuring that the oxidation power of nitrates is equal to the reducing power of sucrose i.e. F:O=1. The intense evolution of gaseous products of decomposition of initial reagents during the reaction causes the formation of a voluminous product consisting of loosely packed particles. The as-prepared materials consist of crystallites with mean size of about 3-5 nm. A heat treatment for 1h at 400°C is usually performed to ensure the burning of the residual organic components. The final thermal treatment for 1 hour at 600°C was applied to obtain cobalt ferrite nanoparticles with mean size in the range 30 nm. The composite CMC - $CoFe_2O_4$ was prepared by adding powder of cobalt ferrite to an aqueous solution of carboxymethylcellulose with a subsequent 5 minutes treatment with ultrasonic processor SONIX, USA (20 KHz, 750 W). Thin layers were deposited on a glass substrate by spin coating technique in a laboratory centrifuge at 6000 rpm. Drying was carried out at room temperature 10 min.

Powder X-ray diffraction patterns were collected within the range from 5.3 to 80° 2θ with a constant step 0.02° 2θ on Bruker D8 Advance diffractometer with Cu Kα radiation and LynxEye detector. Phase identification was performed with the Diffracplus EVA using ICDD-PDF2 Database. Mean crystallite size were determined with the Topas-4.2 software package using the fundamental parameters peak shape description including appropriate corrections for the instrumental broadening and difractometer geometry.

Transmission electron microscopy (TEM) investigations were performed by TEM JEOL 2100 with 200 kV accelerating voltage. The specimens were grinded and dispersed in ethanol by ultrasonic treatment for 6 min. The suspensions were dripped on standard holey carbon/Cu grids. SEM analyses were made in a JEOL-JSM-6390 scanning electron microscope.

^{57}Fe Mössbauer measurements were performed using a constant acceleration spectrometer. A source of ^{57}Co(Rh) with activity of 10 mCi was used. The Mössbauer absorber with a thickness of 40 mg.cm^{-2} Fe was made as follows. Small flakes of deposited thin film material were scraped from the glass substrate. They were mixed with powder of polyvinyl alcohol (glue material) and then pressed into a disk pellet. The $CoFe_2O_4$ spectrum was taken in transmission mode at room temperature (RT). The experimental Mössbauer spectrum was decomposed through the so-called "thin sample approximation" when the spectrum is represented as a sum of few simple spectra (sextets). The parameters of the fitted Mössbauer spectra corresponding to isomer shift (IS), quadrupole shift (QS), magnetic field at the site of the Fe nucleus (H) and relative spectral area are summarized in Table 1. The geometric effect is taken into account as well.

RESULTS AND DISCUSSION

Figure 1(a-c) shows the XRD patterns of the $CoFe_2O_4$ material-as prepared and thermally treated subsequently, at 400°C and C for 1 hour. All patterns were indexed within the cubic Fd-3m space group.

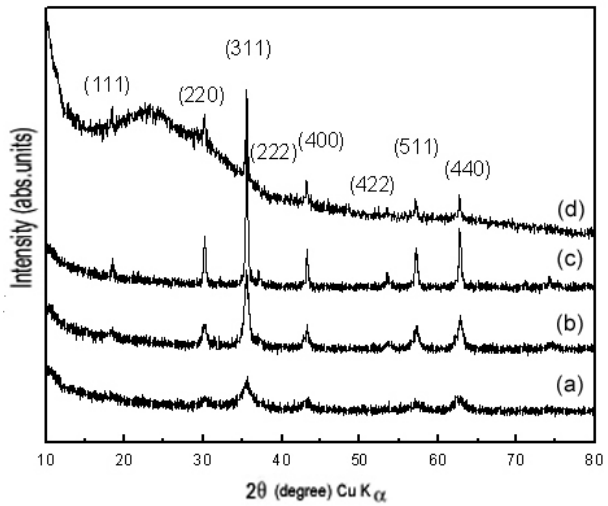


Fig. 1. XRD patterns of samples of $CoFe_2O_4$: (a) as prepared; (b) heated 1 hour at 400°C; (c) heated 1 hour at 600°C; (d) $CoFe_2O_4$ in CMC-film.

The unit cell parameter slightly increases with heating temperature due to the slight variation of the oxidation state of Co and Fe cations. The dependence of the mean crystallite size on the temperature is much more pronounced. It is seen that the mean crystallite size of the material increases with increasing the temperature of the thermal treatment. Fig. 1d represents the powder diffraction pattern of material heated at 600°C for 1h in carboxymethylcellulose matrix. The hump of amorphous CMC - matrix of the composite films is clearly seen as well as the peaks of the nanosized $CoFe_2O_4$ material. No reaction between the material and the matrix is observed.

In Fig. 2 a TEM photograph is shown of $CoFe_2O_4$ nanosized particles obtained by solution combustion

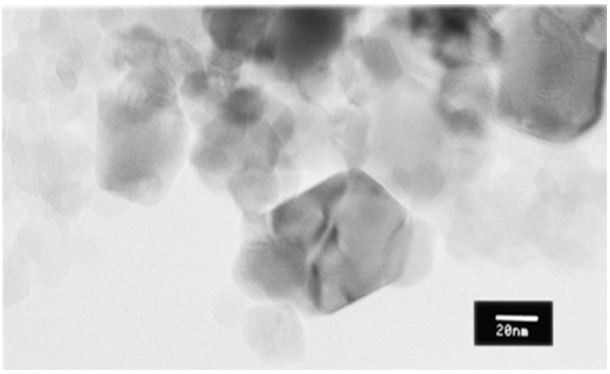


Fig. 2. A TEM photograph of $CoFe_2O_4$ nanosized particles obtained by a solution combustion method.

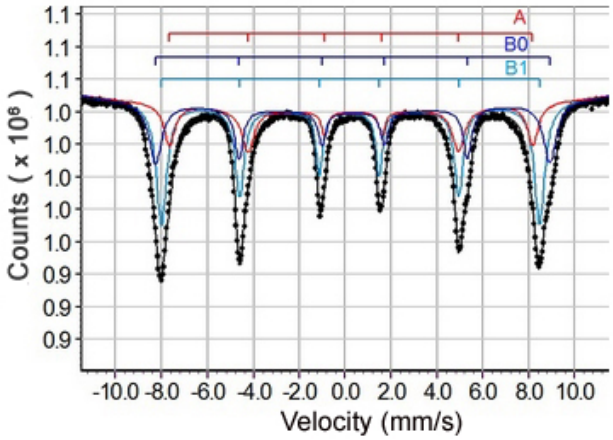


Fig. 4. Mössbauer spectrum of nanosized $CoFe_2O_4$ in polymer thin films.

method and heated 1h at 600°C. Individual well defined particles with hexagonal form and mean size about 30-40 nm can be observed.

Some smaller particles still have oval form. The distribution of the $CoFe_2O_4$ nanoparticles in CMC-matrix was studied by SEM imaging. Fig. 3 (a,b) shows the secondary electrons image (SEI) photographs of CMC-$CoFe_2O_4$ composite layer at different magnifications. The magnetic particle aggregates are uniformly distributed within the polymer CMC-layer. As can be seen, the $CoFe_2O_4$ nanoparticles tend to stick together and form relatively big aggregates from 500 nm to 3 μm in size.

In Fig. 4 the Mössbauer spectrum of $CoFe_2O_4$ at room temperature is shown. The experimental Mössbauer spectrum was decomposed as a sum of three sextets, which is an evidence of complete ferrimagnetic behavior of the sample. Indeed, within the experimental error, there is no any superparamagnetic components in the Mössbauer spectrum. The general formula of spinel ferrites is $MO \cdot Fe_2O_3$, where M is usually divalent transition metal ion.

The Spinel ferrite structure consists of a cubic close-packed oxygen arrangement, in which the cations occupy tetrahedral and octahedral sites within the unit cell. Occupation of tetrahedral sites with divalent metal ions yields a normal spinel structure typical for M^{2+}: Zn^{2+}, Cd^{2+}, Mn^{2+}, while occupation of octahedral sites with the divalent metal ions M^{2+}: Fe^{2+}, Co^{2+}, Ni^{2+}, Mn^{2+} results in an inverse spinel structure.

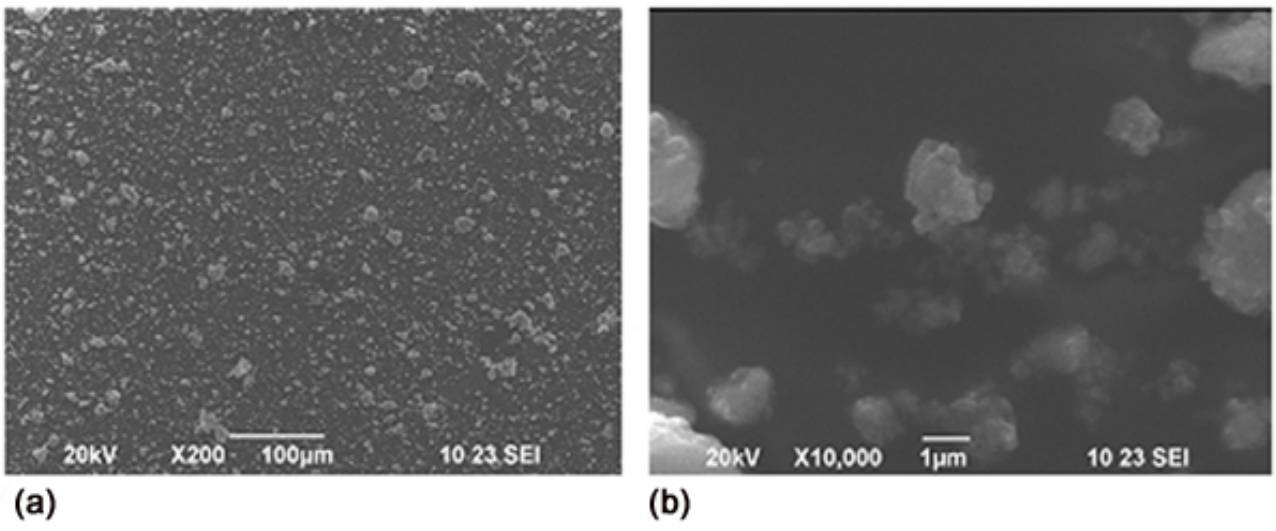


Fig. 3. SEI photographs of CMC-$CoFe_2O_4$ composite layers at different magnifications.

Table 1. The parameters of a Mössbauer spectrum of a nanocomposite $CoFe_2O_4$ layer.

Glassed $CoFe_2O_4$	T, K	Component	IS, mm/s	FWHM, mm/s	QS, mm/s	H, kOe	Specrt. area, %
	Room temperature (RT)	A	0.31	0.22	-0.0451	492.5	22.1
		B0	0.34	0.32	-0.0119	534.5	28.95
		B1	0.2	0.24	0.028	512.6	48.95

The cobalt ferrite, depending on the different ways of synthesising, could be completely inverse spinel or partially inverse spinel. In a partial inverse spinel system a fraction of the cobalt ions enters at the tetrahedral sites. In a complete inverse spinel system, concerning $CoFe_2O_4$ each Fe^{3+} ion in the octahedral B-site is surrounded by six Fe^{3+} ions in tetrahedral A-sites as the second nearest neighbors.

According to [7] the super-exchange interaction via oxygen anion between Fe^{3+} ions at A-B sites is strongest. The interaction at the A-A sites or at the B-B sites is much weaker. Entering of cobalt ions into tetrahedral sites will reduce A-B interaction and hence will reduce hyperfine magnetic field on Fe^{3+} ions in B-site. On the other hand each Fe^{3+} ion in a tetrahedral site is surrounded by twelve Fe^{3+} ions in a B-site. A replacement of Fe^{3+} ions by Co^{2+} ions in a B-site does not produce a large change in the total super-exchange interaction which would lead to negligible change of the hyperfine magnetic field on the Fe^{3+} in A-site. The presence of tree sextets for each Mössbauer spectrum in Fig. 4 shows unambiguously that we are dealing with a partial inverse spinel system. The sextet A with the smallest magnetic field should be assigned to the Fe^{3+} cations in a tetrahedral A-site. The sextet B0 with the largest magnetic field should be assigned to the Fe^{3+} ions in B-site at a sixfold Fe^{3+} surrounding from the A-site i.e. without any Co^{2+} in the A-site. The sextet B1 corresponds to Fe^{3+} in a B-site where one or more Fe^{3+} ions in a tetrahedral site were being replaced by Co^{2+}. From the measured relative spectral areas of the sextets A, B0, and B1, we can derive the formula for the cation distribution in the sample. In our case the formula reads $(Co_{0.56}Fe_{0.44})[Co_{0.44}Fe_{1.56}]O_4$.

CONCLUSIONS

Nanosized $CoFe_2O_4$ has been obtained by solution combustion method. The method allows producing oxide materials with a predefined particle size within the nanoscale range by simple control of heating temperature. A composite material comprising $CoFe_2O_4$ nanoparticles in amorphous CMC-film was prepared. Thin composite layers were characterized by X-ray powder diffraction, high resolution transmission electron microscopy, scanning electron microscopy and Mössbauer spectroscopy. The Mössbauer spectroscopy measurements of the nanosized $CoFe_2O_4$ reviled partially inverse spinel structure where the cation distribution (of the Co and Fe cations) is presented by the formula $(Co_{0.56}Fe_{0.44})[Co_{0.44}Fe_{1.56}]O_4$.

Acknowledgements. *The financial support of the Bulgarian National Science Foundation - contract DTK-02/77 is gratefully acknowledged.*

REFERENCES

[1] S. R. Ahmed, S. B. Ogale, G. C. Papaefthymiou, R. Ramesh, P. Kofinas, *Applied Physics Letters* **80**, 1616-1618 (2002).

[2] J. G. Lee, J. Y. Park, C. S. Kim, *Journal of Materials science* **33**, 3965-3968 (1998).

[3] P. Chandramohan, M. P. Srinivasan, S. Velmurugan, S. V. Narasimhan, *Journal of Solid State Chemistry* **184**, 89-96 (2011).

[4] D. Kovacheva, T. Ruskov, P. Krystev, S. Asenov, N. Tanev, I. Mönch, R. Koseva, U. Wolff, T. Gemming, M. Markova-Velichkova, D.Nihtianova, K.F. Arndt, *Bulgarian Chemical communications* **44**, 90-97 (2012).

[5] S.R.Jain, K.C.Adiga, V.R.Pai Verneker, *Combust. Flame* **40**, 71-79 (1981).

[6] M.M.A.Sekar, K.C.Patil, *J.Mater.Chem.* **2**, 739-743 (1992).

[7] G.A.Sawatzky, F. Van Der Woude and A.H. Morrish, *J.Appl.Phys* **39**, 1204 -1206 (1968).

КОМПОЗИТНИ ТЪНКИ СЛОЕВЕ ОТ НАНОРАЗМЕРЕН $CoFe_2O_4$ В ПОЛИМЕРНА МАТРИЦА

Цв. Лазарова[1], Д. Ковачева[1], Т. Русков[2], С. Атанасова-Владимирова[3], П. Кръстев[2], Н. Танев[2]

[1] *Институт по обща и неорганична химия, Българска академия на науките, ул. "Акад. Г. Бончев" блок 11, 1113 София, България*
[2] *Институт за ядрени изследвания и ядрена енергетика, Българска академия на науките, бул. "Цариградско шосе" №72, 1784 София, България*
[3] *Институт по физикохимия, Българска академия на науките, ул. "Акад. Г. Бончев" блок 11, 1113 София, България*

(Резюме)

Прахообразен материал от наноразмерен кобалтов ферит беше синтезиран по метода на горене от разтвор (комбустивен синтез). Като изходни реагенти са използвани съответни кобалтов нитрат и железен нитрат в стехиометрично съотношение, както и захароза. Така полученият кобалтов ферит има среден размер на кристалитите около 10 nm. Чрез допълнително термично третиране при 600°C е получен материал със среден размер на кристалитите 30–40 nm. Композитът бе получен чрез добавяне на кобалтов ферит към воден разтвор на карбоксиметил целулоза с последваща ултразвукова обработка. Нанасянето на тънките слоеве върху стъклена подложка е извършено по метода на спинеруването в лабораторна центрофуга при 6000 rpm Изсушаването е извършено при стайна температура. Тънките композитни слоеве бяха характеризирани с методите на праховата рентгенова дифракция, сканираща електронна микроскопия и Мьосбауерова спектроскопия.

Bulgarian Chemical Communications, Volume 47, Special Issue B (pp. 232–238) 2015

Hypernuclei reconstruction at NICA/MPD: a feasibility study

M. Ilieva*, V. Kolesnikov, D. Suvarieva, V. Vasendina, A. Zinchenko

Veksler and Baldin Laboratory of High Energy Physics, Joint Institute for Nuclear Research, 141980 Dubna, Moscow region, Russia

The study of production of light hypernuclei is essential for understanding the production mechanism of exotic objects such as multi-hypernuclei and can help us to understand strangeness degrees of freedom in hadronic system. This study shows the ability of the NICA/MPD complex to measure the lightest hypernucleus ${}^{3}_{\Lambda}$H.

Key words: hypernucleus, reconstruction, Monte Carlo, production, heavy-ion collisions, NICA/MPD

INTRODUCTION

NICA (Nuclotron-based Ion Collider fAcility) is a new facility at the Join Institute for Nuclear Research [1]. The global goat of NICA is to study the behavior of nuclear matter under extreme conditions. A transition is expected of hot and dense baryon matter into a state of deconfined quarks and gluons - so called quark gluon plasma (QGP). In such matter phase transition might be accompanied by a restoration of chiral symmetry due to melting of the quark condensate [2–4]. Recent results on hadron-production from the CERN SPS [5] and RHIC [6] indicate that the onset of the deconfinement is likely to be observed in central A+A collisions at energies $\sqrt{s} = 4$ GeV. Moreover, the analysis of the thermodynamic freeze-out parameters extracted from the data over a wide energy range performed in [7] reveals that the net-baryon density in central collisions of heavy ions has a maximum in the energy range from $\sqrt{s} =$ 5A to 9A GeV. So, the energy range of the NICA collider ($4 < \sqrt{s} < 11$A GeV) is ideal for an experimental exploration of fundamental QCD properties that are sensitive to the both phenomena: chiral symmetry and confinement [8]. Our experimental research plan is to perform a detailed energy scan with ion beams from protons to gold nuclei addressing the following objectives: (1) strangeness production, (2) in-medium properties of vector mesons, (3) event-by-event fluctuations, and (4) correlations. The measurements will be performed with the MultiPurpose Detector (MPD) [9, 10] capable of detecting both the hadronic (π, K, p, Λ, Ξ, Ω) and non-hadronic (e, γ) probes.

* To whom all correspondence should be sent:
maiailieva@mail.bg

Relativistic heavy-ion collisions where lots of strange particles (kaons and hyperons) are produced, offer a unique possibility to create exotic nuclear objects with strangeness - hypernuclei [11]. Recently, the first results on the production of (anti)hypertritium in relativistic Au+Au collisions at the RHIC and LHC were reported by the STAR and ALICE experiments [12, 13]. The mechanism and dynamics of hypernuclei formation is not well understood - several approaches are suggested to explain their production rates: coalescence of lambdas with nucleons at midrapidity [14], thermal models [15], or absorption of some of the produced hyperons by the residual spectator nuclei [16]. To distinguish between different models new experimental data on hyper-nuclei production taken in different initial conditions (i.e. collision energy and impact parameter) over large phase-space are needed.

The energy range of the NICA research program covers the region of the maximal baryon density where the production rates of nuclear clusters with strangeness are predicted to be enhanced considerably: as many as $3 \cdot 10^2$ of ${}^{3}_{\Lambda}$H and 10^{-5} of ${}^{5}_{\Lambda\Lambda}$He per unit of rapidity are expected in a central Au+Au collision at $\sqrt{s} = 5$A GeV [15]. With a typical event rate of 6 kHz for the design NICA luminosity of 10^{27} cm^{-2}c^{-1} a detailed study of the production mechanism of single hypernuclei as well as an observation of double hypernuclei at NICA look feasible.

DETECTOR GEOMETRY

The present analysis is based on the so-called start version of MPD, which includes the main tracker Time Projection Chamber (TPC) and barrel Time-Of-Flight system (TOF). The detectors cover the mid-rapidity region $|\eta| < 1.3$. The detailed description of the MPD geometry can be found in Refs. [9, 10].

© 2015 Bulgarian Academy of Sciences, Union of Chemists in Bulgaria

EVENT GENERATOR AND DATA SET

The event sample for the present study has ben produced with the DCM-QGSM (Dubna Cascade Model - Quark-Gluon String Model) generator [17–19]. The choice of this event generator was motivated by the fact that it can produce nuclear clusters via the coalescence mechanism and describe hypernuclei yield in NICA energy region. The DCM-QGSM generator is based on the Monte Carlo solution of a set of the Boltzmann- Uehling-Uhlenbeck relativistic kinetic equations with the collision terms, including cascade- cascade interactions. For particle energies below 1 GeV it considers only nucleons, pions and deltas. The model includes a proper description of pion and baryon dynamics for particle production and absorption processes. At energies higher than about 5 GeV, the Quark-Gluon String Model is used to describe elementary hadron collisions.

DCM-QGSM model predictions for cluster formation have been compared with experimental data [20, 21]. The model was used to predict cluster production over a wide range of beam energies [16].

For this study, the generator was used to produce a sample of central Au-Au collisions (0-3.8 fm) at $\sqrt{s}$ = 5A GeV. The number of events was $5{\cdot}10^5$ corresponding to about 30 minutes of NICA running time.

Particles produced by the event generators were transported through the detector using the GEANT3 transport package. The decay properties of hypernuclei (modes and branching ratios) have been introduced into GEANT from Ref. [22] (Tab. 1) and the lifetime has been taken to be the same as of Λ-hyperon.

Table 1. ${}^{3}_{\Lambda}$H decay modes and branching ratios. The studied ones are marked in bold

Decay channel	Branching ratio,%
π^- + ^{3}He	**24.7**
π^0 + ^{3}H	12.4
π^- + p + d	**36.7**
π^0 + n + d	18.4
π^- + p + p + n	1.5
π^0 + n + n + p	0.8
d + n	0.2
p + n + n	1.5

TRACK RECONSTRUCTION

The track reconstruction method is based on the Kalman filtering technique (see, e.g. [23]) and the number of TPC points per track was required to be greater than 10 to ensure a good precision of momentum and dE/dx measurements. The track finding efficiency in TPC for primary and secondary tracks is shown in Fig. 1 (a) as a function of the track transverse momentum. The secondary track sample there included particles produced within 50 cm of the primary vertex both in transverse and longitudinal directions and did not include electrons and positrons from the photon conversion. The transverse momentum resolution as a function of p_T can be seen in Fig. 1 (b). The result was obtained with the assumption on the TPC coordinate resolution of 0.5 and 1.0 mm in transverse and longitudinal directions, respectively.

Figure 2 (a) shows the transverse and longitudinal position uncertainties of primary tracks at their point of the closest approach to the interaction point versus track momentum. These detector characteris-

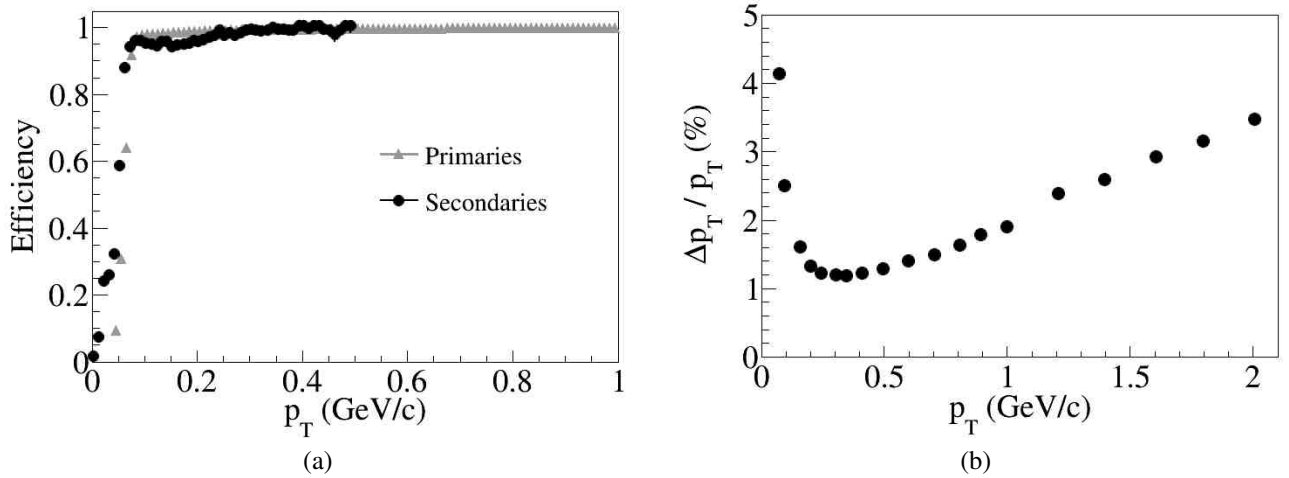
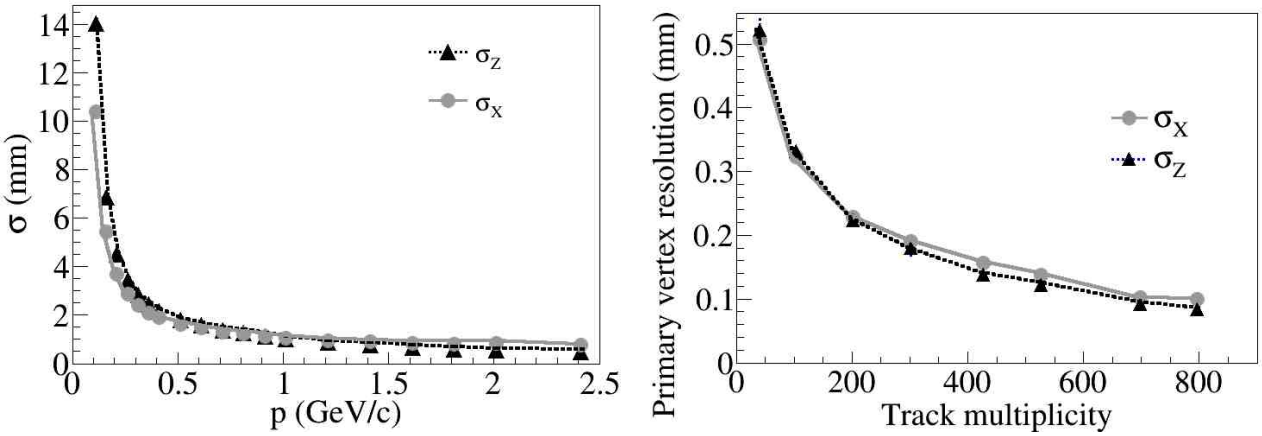


Fig. 1. (a) Track reconstruction efficiency as a function of track p_T for primary and secondary particles. (b) Relative transverse momentum resolution for primary tracks with $|\eta| < 1.3$ reconstructed in TPC.



(a) (b)

Fig. 2. (a) Transverse and longitudinal position errors in the point of the closest approach (PCA) to the interaction point for TPC reconstructed primary tracks with $|\eta|$ <1.3 versus particle momentum; (b) Transverse and longitudinal position errors of the reconstructed primary vertex as functions of the track multiplicity.

tics are important for secondary vertex reconstruction. Both the primary and secondary vertex reconstruction methods utilized make use of the similar approach based on the Kalman filtering formalism [24]. The primary vertex reconstruction errors as functions of the track multiplicity in the event are shown in Fig. 2 (b).

For all the reconstructed in the TPC tracks the specific energy loss dE/dx is calculated as a truncated mean of the charges of TPC hits assigned to the tracks. The truncation level of 70% was chosen, i.e. 30% of hits with the highest charges were excluded from the mean value. Next, the TPC reconstructed tracks are extrapolated to the TOF detector and matched to the TOF hits. For the matched candidates the mass square (M^2) is derived through the relation:

$$M^2 = (p/q)^2 \left(\frac{c^2 t^2}{l^2} - 1 \right)$$

where p is the track momentum, q is its charge, t is the time-of-flight from TOF, l is the path length from the collision vertex to the TOF hit, and c is the speed of light. p/q, so-called magnetic rigidity, is the value directly returned by the track reconstruction algorithm. For particles with the unit charge it is equal to the momentum and M^2 corresponds to the particle mass.For multiple-charged particles the obtained value M^2 is scaled by the factor of $1/q^2$ with respect to the true mass s can be seen, e.g., in Fig. 1 for ${}^{3}_{\Lambda}$He (factor of $1/4$ with respect to the expected squared mass of 9).

PARTICLE IDENTIFICATION

Particle identification (PID) in the MPD experiment will be achieved by energy loss (dE/dx) information from the TPC. As shown in Fig. 3 can discriminate kaons from pions up to momenta of 0.7 GeV/c and protons can be distinguished from π, K-mesons up to $p \approx 1.3$ GeV/c. Charged particles are selected if their dE/dx measurement lies within a 3σ interval around the predicted value which is taken from the Bethe-Bloch parameterization for the mean energy loss [25].

Particles within the pseudorapidity range $|\eta| <$ 1.1 can be identified using the combined time-of-flight information from the TOF detector and the dE/dx signal from TPC. Fig. 4 shows a typical

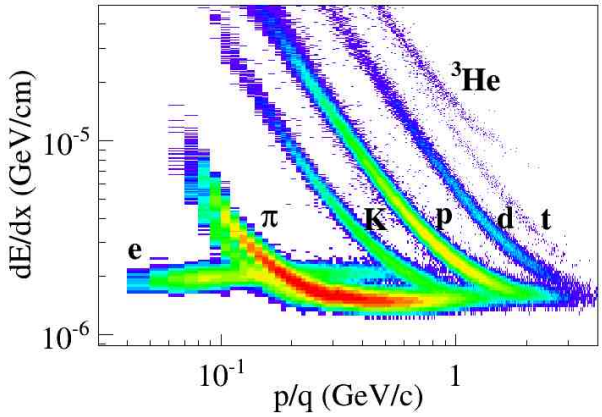
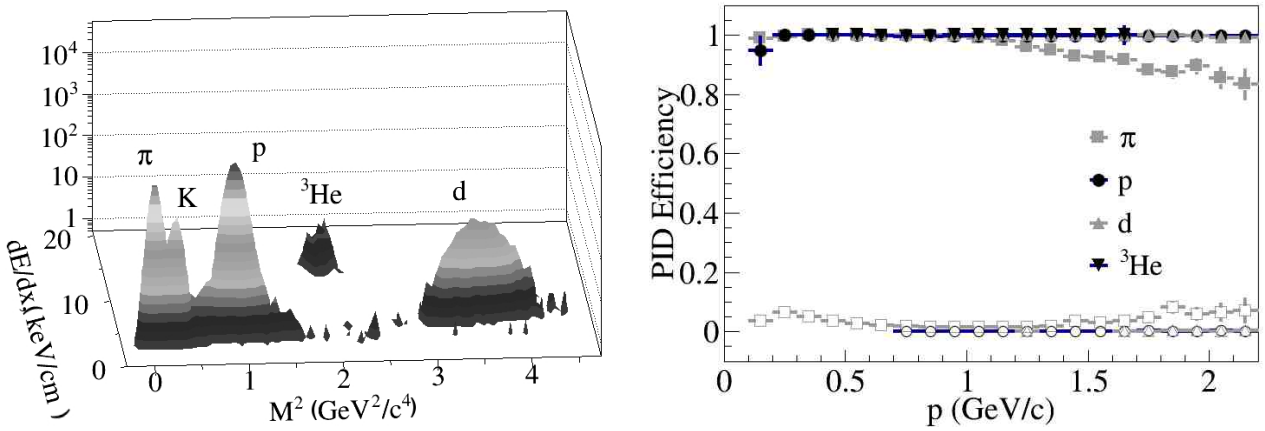


Fig. 3. Specific energy loss dE/dx versus magnetic rigidity p/q for π, K, p, d, t, ^3He.



(a) (b)

Fig. 4. (a) Specific energy loss dE/dx versus mass square M^2 for π, K, p, d, t,^3He at $p = 1.5$ GeV/c. (b) PID efficiency (filled symbols) and contamination of mis-identified particles (empty symbols) as functions of the total momentum.

dE/dx versus M^2 distribution for tracks with momentum $p = 1.5$ GeV/c.

Selected hadron and light nuclei candidates fall within the 3σ ellipses around the nominal position for a given particle type. In addition, the probability for a given particle to belong to each of the species can be calculated knowing the widths of the corresponding distributions (along the dE/dx and M^2 axes) and the difference from the predicted position for the specie. It was found that by requiring this probability to be greater than 0.75 one can get the efficiency and contamination distributions shown on the (b) panel of Fig. 4. The PID efficiency is defined as a ratio of correctly tagged to the total number of generated particles. The contamination is determined as the number of incorrectly tagged particles divided by the number of correctly tagged particles.

As seen from Fig. 4, the overall PID efficiency for p, d and ^{3}He is close to 100%, while due to a partial overlap of the distributions for pions and kaons the efficiency of π drops down to ≈ 0.8 at $p = 2.5$ GeV/c. The contamination of wrongly identified pions (basically from μ, e, and K) does not exceed 10%. For other species the observed contribution from the mis-identified particles is negligible.

ANALYSIS PROCEDURE

$^3_\Lambda$H hypernuclei were reconstructed using their decay modes into two (2-prong $^3_\Lambda$H) or three (3-prong $^3_\Lambda$H) charged tracks. The signal event topology (decay of a relatively long-lived particle into two or more tracks - Fig. 5) defines the selection criteria: relatively large distance of the closest approach (DCA) to the primary vertex of decay products, small track-to-track separation in the decay vertex, relatively large decay length of the mother particle. Both the DCA and two-track separation cuts should be more efficient if applied in χ^2 - space, i.e if normalized to their respective errors.

The exact values of selection cuts were found by performing a multidimensional scan over the whole set of selection criteria with a requirement to maximize the invariant mass peak significance, defined as $S/S+B$, where S and B are total numbers of signal (described the Gaussian) and background (polynomial function) combinations inside 2σ interval around the peak position.

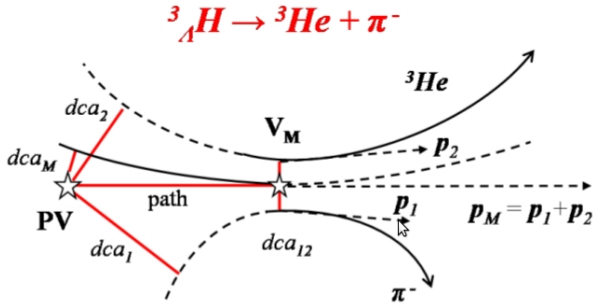


Fig. 5. Event topology of two-particle decays of a charged particle(e.g. $^3_\Lambda\mathrm{H} \rightarrow ^3 He + \pi^-$) (transverse view). Here dca_1 and dca_2 are the distances of the closest approach of the decay tracks to the primary vertex PV, dca_{12} is the distance between daughter tracks in the decay vertex V_M, dca_M is the distance of the closest approach of the mother particle to the primary vertex, path is the decay length, p_1 and p_2 are the momenta of daughter particles.

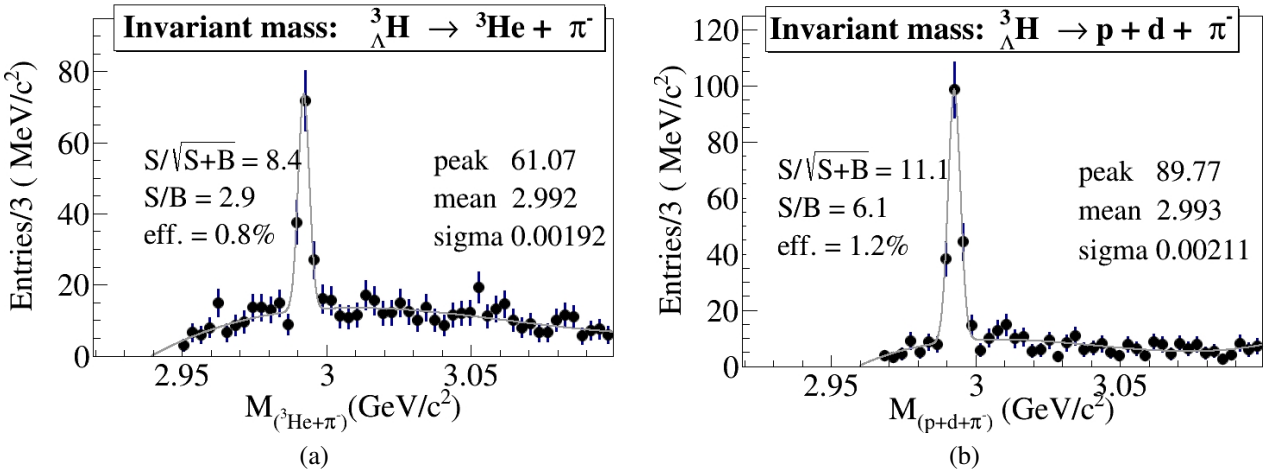


Fig. 6. (a) Reconstructed invariant mass of ^3He and π^-, (b) Reconstructed invariant mass of proton, deuteron and π^- ($DCM-QGSM$ generator at $\sqrt{s}$ = 5A GeV).

The corresponding scan procedure was realized as follows: during the particle combinations the parameters which have been chosen to serve as selection criteria (see above) were recorded along with the invariant mass value. Later, multiple loops over those variables were performed in some steps and their values were used as low or high thresholds, yielding the invariant mass peak significance for each set of selection cut values. Then, the maximum value was taken along with the corresponding set of selection parameters.

RESULTS

The results on $^3_\Lambda$H reconstruction are presented in Fig. 6 and Tab. 2. Figure 6 shows invariant mass distributions for 2-prong ($^3_\Lambda\mathrm{H} \rightarrow ^3 He + \pi^-$) and 3-prong ($^3_\Lambda\mathrm{H} \rightarrow p + d + \pi^-$) decay modes. As mentioned above, the results have been obtained for $5 \cdot 10^5$ central events, corresponding to about 30 minutes of NICA running time. One can see narrow peaks (σ of the Gaussian fit $\approx$2 MeV/c^2) with quite high significance and signal-to-background ratio.

Table 2 shows the effect of the detector acceptance (i.e. η-coverage and low-p_T cut for $^3_\Lambda$H decay products) on hypertriton detection efficiency, where the efficiency is defined with respect to the total number of hypernuclei. Lines 2-5 demonstrate the effect of the p_T-cut on the efficiency, where p_T is the true transverse momentum of decay products. Line 6 shows the reconstruction efficiency, i.e. considering the reconstructed in the detector decay particles without any explicit p_T-cut (and without PID efficiency). The last line includes all the relevant factors, i.e. reconstruction and PID efficiencies as well as selection efficiency. One can see that the detector provides rather efficient reconstruction of hypertritons with p_T of decay tracks above 0.1 GeV/c in good agreement with Fig. 1. It is also clear that a higher p_T-threshold (e.g. 0.2 GeV/c) would significantly reduce the detector efficiency. The efficiency drop due to selection cuts

Table 2. Factors affecting $^3_\Lambda$H reconstruction efficiency

Factor	Efficiency, %	
	2-prong decay	3-prong decay
Branching ratio	24.6	36.4
Decay products at $\|\eta\| < 1.3$	14.9	19.8
Decay products at $\|\eta\| < 1.3$ and $p_T > 0.05$ GeV/c	14.2	15.7
Decay products at $\|\eta\| < 1.3$ and $p_T > 0.1$ GeV/c	8.9	6.2
Decay products at $\|\eta\| < 1.3$ and $p_T > 0.2$ GeV/c	0.7	0.1
Reconstructed decay products at $\|\eta\| < 1.3$	7.9	8.3
Maximum siginificance	0.8	1.2

comes from the necessity to suppress the combinatorial background in order to obtain a clean invariant mass peak.

SUMMARY

We have performed a simulation study of the MPD detector capabilities to reconstruct hypertritons ${}^{3}_{\Lambda}$H in central Au+Au collisions at $\sqrt{s}$ =5A GeV. The DCM-QGSM event generator was used as the input for the study of the MPD detector set-up comprising the Time Projection Chamber and barrel Time-Of-Flight system. Particle identification was achieved by combining the energy loss (from TPC) and time-of-flight (from TOF) measurements. A special procedure aimed at the maximization of the significance of the reconstructed invariant mass was developed resulting in the observed signal-to-background ratio $S/B = 3-6$ for hypertritons. The invariant mass resolution of $\approx$2 MeV/c^2 has been achieved. Based on the results of this study and model predictions, we have estimated the expected yield of ${}^{3}_{\Lambda}$H for 10 weeks of data taking as $9 \cdot 10^5$ particles.

It is planned to develop a reconstruction algorithm for double-strange nuclei ${}^{4}_{\Lambda\Lambda}$H and ${}^{5}_{\Lambda\Lambda}$H.

REFERENCES

[1] A.N. Sissakian and A.S. Sorin, *J. Phys. G: Nucl. Part. Phys.* **36**, 064069 (2009).

[2] R. Rapp, G. Chanfray and J. Wambach, *Phys. Rev. Lett.* **76**, 368 (1996).

[3] R. Rapp and J. Wambach, *Adv. Nucl. Phys.* **25**, 1 (2000).

[4] T. Hatsuda and S. H. Lee, *Phys. Rev. C* **46**, 34 (1992).

[5] C. Alt et al., *Phys. Rev. C* **78**, 024903 (2008).

[6] L. Kumar (STAR Collaboration), *J. Phys. G: Nucl. Part. Phys.* **38**, 124145 (2011).

[7] J. Randrup and J. Cleymans, *Phys. Rev. C* **74**, 047901 (2006).

[8] http://nica.jinr.ru/files/NICA CDR.pdf, last access: 31.10.2014.

[9] K.U. Abraamyan et al., *Nucl. Instrum. Meth. A* **628**, 99 (2011).

[10] http://nica.jinr.ru/files/CDR MPD/MPD CDR en.pdf, last access: 31.10.2014.

[11] A.K. Kermann and M.S. Weiss, *Phys. Rev. C* **8**, 408 (1973).

[12] The STAR Collaboration, *Science* **328**, 58 (2010).

[13] B. Dönigus (ALICE Collaboration), *Nucl. Phys. A* **904-905**, 547 (2013).

[14] M. Wakai, H. Bando and M. Sano, *Phys. Rev. C* **38**, 748 (1998).

[15] A. Andronic et al., *Phys. Lett. B* **697**, 203 (2011).

[16] J. Steinheimer et al., *Phys. Lett. B* **714**, 85 (2012).

[17] V.D. Toneev and K.K. Gudima, *Nucl. Phys. A* **400**, 173 (1983).

[18] V.D. Toneev et al., *Nucl. Phys. A* **519**, 463 (1990).

[19] N.S. Amelin et al., *Sov. J. Nucl. Phys.* **52**, 272 (1990).

[20] T.A. Armstrong et al. (E864 Collaboration), *Phys. Rev. Lett.* **83**, 5431 (1999).

[21] T.A. Armstrong et al. (E864 Collaboration), *Phys. Rev. C* **61**, 064908 (2000).

[22] H. Kamada et al., *Phys. Rev. C* **57**, 1595 (1998).

[23] R. Fruehwirth, *Nucl. Instr. and Meth. A* **262**, 444 (1987).

[24] R. Luchsinger and Ch. Grab, *Comp. Phys. Comm.* **76**, 263 (1993).

[25] J. Beringer et al. (Particle Data Group), *Phys. Rev. D* **86**, 010001 (2012).

ИЗУЧАВАНЕ И РЕКОНСТРУКЦИЯ НА ХИПЕРЯДРА КЪМ ПРОЕКТА NICA/MPD

М. Илиева, В. Колесников, Д. Сувариева, В. Васендина, Ал. Зинченко

Обединен институт за ядрени изследвания,
ул. "Жолио Кюри" №6, Дубна, Московская область, 141980, Русия

(Резюме)

Хиперядрата се получават при хиперон-нуклонни взаимодействия. Това са ядра съдържащи поне един допълнителен хиперон към нуклоните. Ние изучавахме разпада на най-лекото хиперядро: хипертритон на ^{3}He+π^{-}.

Изследване получаването на леки хиперядра е от съществено значение за разбирането на механизма на производството на екзотични обекти, като мултихиперядра. Също така ще ни помогне да разберем странните степени на свобода в адронни системи.

Възможността да произвеждаме хиперядра ще ни позволи да изследваме всички населени региони в триизмерната ядрена карта.

Bulgarian Chemical Communications, Volume 47, Special Issue B (pp. 239–246) 2015

Feasibility of flow studies at NICA/MPD

N. S. Geraksiev[1,2]* for the MPD collaboration

[1] *Paisii Hilendarski University of Plovdiv, 24 Tsar Asen Str., BG-4000 Plovdiv, Bulgaria*
[2] *Veksler and Baldin Laboratory of High Energy Physics, Joint Institute for Nuclear Research, 141980 Dubna, Moscow region, Russia*

In the light of recent developments in heavy ion physic, anisotropic flow measurements play a key role in a better understanding of the hot and dense barionic matter. In the presented article a short introduction to the proposed NICA/MPD project is given, as well as a brief description of the event plane method used to estimate the elliptic flow of reconstructed and identified hadrons (p, π, K, Λ).

Key words: HEP, NICA, MPD, UrQMD, event plane, elliptic flow, hadron, hyperon

INTRODUCTION

Nuclotron-based Ion Collider fAcility (NICA)

Investigation of the hot and dense baryonic matter is currently an exciting field in modern high energy physics. Besides being crucial to a better understanding of the early stages of the Universe and the formation of neutron stars, it is useful for the comprehension of in-medium properties of hadrons and nuclear matter equation of state, and may prove to be a means of search for manifestations of deconfinement and/or chiral symmetry restoration.

The Nuclotron upgrade, which is a substantial part of the JINR scientific program, is dedicated to the investigation of hot and dense baryonic matter. The Nuclotron-based Ion Collider fAcility (NICA) will create Au+Au collisions over a wide range of atomic masses, at a centre-of-mass energy of $\sqrt{s_{NN}} =$ 11A GeV (for Au^{79+}) and an average luminosity of $L = 10^{27}\text{cm}^{-2}\text{s}^{-1}$, proton-proton collisions with $\sqrt{s_{pp}} = 26$A GeV and $L = 10^{30}\text{cm}^{-2}\text{s}^{-1}$.

Along with the heavy ion programme, the NICA facility will provide proton and light ion beams, and the possibility to obtain and utilize unique polarized beams. This holds a great potential for studies of the nuclear quark-gluon structure in processes with large momentum transfer, as well as in measurements with target/projectile polarization, and research on experimental verification of quark counting rules, clarification of the abnormal behavior known as color nuclear transparency, as well as comprehension of large spin effects in production of mesons and hyperons.

The accelerator will also allow collisions of mass-

* To whom all correspondence should be sent:
nikolay.geraksiev@gmail.com

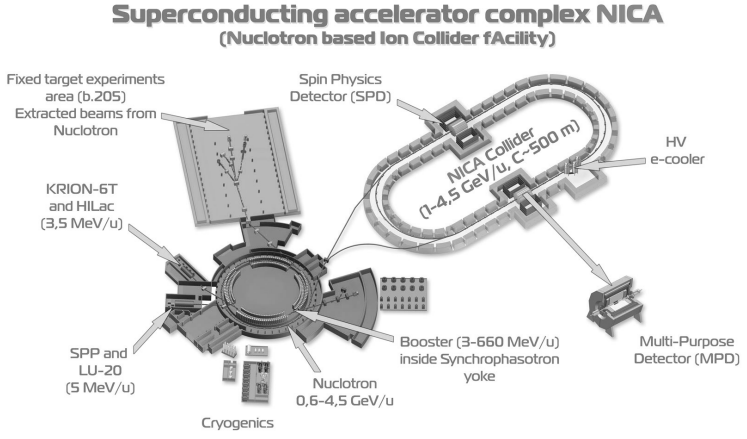


Fig. 1. The NICA accelerator complex at JINR

© 2015 Bulgarian Academy of Sciences, Union of Chemists in Bulgaria

asymmetric beams including *pA* collisions. In and of itself an interesting field, it is also quite important as a reference point for comparison with heavy ion data. Furthermore, as a long-term goal, the accelerator facility may provide electron-ion collisions for measurements of nucleon and nuclei electro-magnetic form factors to large momenta, *e.g.* investigation of spatial distributions of charge and magnetization in nuclei and the nucleon including the determination of the valence quark generalized parton distribution, revealing the correlation between spatial and momentum distributions.

It should be noted that while the NICA project is aimed at fundamental scientific research, other applications of the particle beams such as biomedical research and radiation technology have been planned [1, 2].

MultiPurpose Detector (MPD)

The NICA collider is going to have two interaction points, allowing for two detectors to operate simultaneously. The MultiPurpose Detector (MPD) is one of these detectors. In the first stage of the NICA/MPD project are considered analyses on multiplicity and spectral characteristics of identified hadrons including strange particles, multi-strange baryons and antibaryons, characterizing entropy production and system temperature at freeze-out. Moreover, event-by-event fluctuations in multiplicity, charges, transverse momenta and K/π ratios are to be studied as a generic property of critical phenomena, along with collective flow effects, HBT correlation, and femtoscopy. In the second stage measurements of the electromagnetic probes (photons and dileptons) will be carried out. The MPD detector will be operated at a rate of about 7×10^3 interactions per second, with multiplicities of up to ~ 1500 charged particles per central gold-gold collision at maximal energy of $\sqrt{s_{NN}} = 11$A GeV [1–3].

The design of the detector requires a very low material budget as the average transverse momentum of the particles produced in a collision at NICA energies is below 500 MeV/c.

The barrel part, consisting of a tracker and particle identification system is shown in Fig. 2. The time projection chamber (TPC) is the principal tracker yielding precise track finding, momentum determination, vertex reconstruction and pattern recognition up to $|\eta| < 2$. The energy loss (dE/dx) measurements

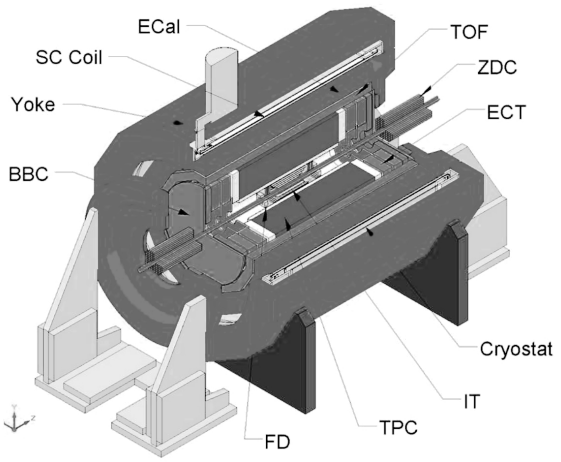


Fig. 2. Central part of the MultiPurpose Detector.

in the TPC gas will provide an additional capability for particle identification in the low momentum region [4].

The high performance time-of-flight (TOF) system must be able to identify charged hadrons and nuclear clusters in the broad rapidity range and up to total momentum of 2 GeV/c. The TOF detector covers $|\eta| < 3$ and its performance should allow the separation of kaons from protons up to a total momentum of 3 GeV/c [5].

Fast timing and triggering is performed by arrays of quartz counters (FD). The forward going energy for centrality selection and event plane reconstruction will be measured by to sets of hadron calorimeters (ZDC), covering the pseudorapidity region $2.5 < |\eta| < 4$ [6].

The main aim of the electromagnetic calorimeter (EMC) is identification of electrons and photons, and high precision measurements of their energy. The high granularity, excellent energy resolution and good timing performances of the EMC will enhance the overall efficiency and particle identification capabilities of the MPD detector [3, 7].

ANISOTROPIC FLOW

Measurements of collective flow phenomena are crucial tools for the study of properties in the dense matter created in relativistic heavy ion collisions (such as the equation of state - EOS, formation conditions, *etc.*). The physics dynamics at the early stages of non-central heavy ion collisions is assessed by the azimuthal anisotropy of particle production with respect to the reaction plane [8].

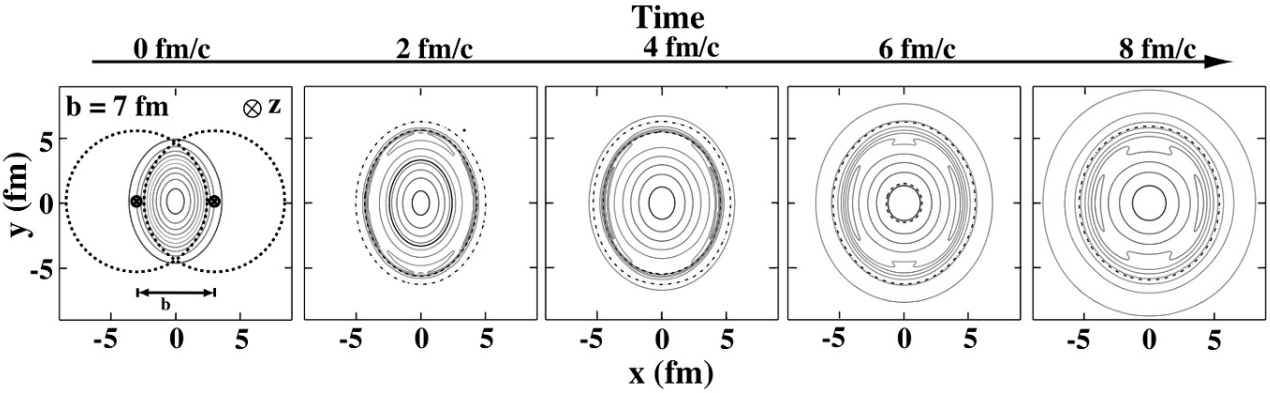


Fig. 3. Evolution of the transverse energy density profle in coordinate space for non-central heavy ion collisions.

The reaction plane is defined by the impact parameter and the beam direction z. The Fourier expansion of the invariant triple differential distributions proves to be a convenient way of characterizing the various patterns of anisotropic flow

$$E\frac{\mathrm{d}^3N}{\mathrm{d}^3\mathbf{p}} = \frac{\mathrm{d}N}{p_T\mathrm{d}p_T\mathrm{d}\phi\mathrm{d}y} \quad (1)$$
$$= \frac{1}{2\pi}\frac{\mathrm{d}N}{p_T\mathrm{d}p_T\mathrm{d}y}\Big(1+2\sum_{n=1}^{\infty}v_n\cos(n(\phi-\Psi_{RP}))\Big),$$

where E is the energy of the particle, $\mathbf{p}$ the momentum, p_T the transverse momentum, ϕ the azimuthal angle, y the rapidity, and Ψ_{RP} the reaction plane angle. The sine terms in such an expansion vanish because of the reflection symmetry with respect to the reaction plane. The Fourier coefficients are p_T and y dependent and are given by

$$v_n(p_T,y) = \langle\cos(n(\phi-\Psi_{RP})\rangle, \quad (2)$$

where the angular brackets denote an average over the particles summed over all events in the (p_T, y) bin under study. Fig. 3 depicts the evolution of the almond shaped interaction volume. Plots from left to right show how the system evolves from an almond shaped transverse overlap region into an almost symmetric system and contours indicate the energy density profile. During this expansion, governed by the velocity of sound, the created hot and dense system cools down [8].

The coefficient v_1 is also known as directed flow and it presents a means of measuring the total amount of transverse flow. It is most pronounced in the cases of semi-central interactions around target and projectile rapidities where the spectators are deflected away from the beam axis due to a bounce-off from the compressed and heated matter in the overlap region.

The elliptic flow is paid special attention as this collective motion is formed mainly at an early stage of the collision. According to the typical hydrodynamic scenario, the $v_2(p_T)$ values at relatively low transverse momenta (p_T ¡ 2 GeV/c) are determined mainly by the internal pressure gradients of the expanding fireball during the initial high density phase of the reaction. The elliptic flow of hadrons at low transverse momenta can be related to the degree of thermalization, viscosity, and EoS of the produced matter. However, the elliptic flow of the high momentum particles is related to the jet fragmentation and energy loss of the primordially produced hard antiquark-quark pair traveling through the hot QCD medium. At moderate p_T the experimental data indicate a gradual increase of v_2 with p_T. A deeper insight into the bulk properties of the produced matter is obtained by an accurate v_2 mesurement.

Two main reasons justify the increased demand for an accurate study of (anti)hyperon production. Firstly, a signature for deconfinement might be manifested by strangeness enhancement in heavy-ion collisions relative to proton induced reaction [9–11]. Secondly, due to the small hadronic cross-sections of multi-strange hyperons, additional rescaterring effects in the dense hadronic matter for strange hadrons are not as significant as compared to other hadrons. Therefore, measurements of phase-space distributions of strange hyperons reveal key characteristics of the fireball at the early stages of the system evolution. Moreover, it has recently been observed by the STAR experiment that the characteristic azimuthal anisotropy pattern (*e.g.* the elliptic flow coefficient v_2

as a function of transverse momemtum p_T) for anti-baryons is different from the one for baryons in mid-central Au+Au collisions at energies $\sqrt{s_{NN}} < 11$A GeV [12]. There is interplay between particle production and subsequent absorption in the medium meaning that anti-baryons are strongly affected by the co-moving baryon density in the course of the reaction. Different values of the collision energy and beam atomic mass number at NICA will provide a valuable insight into the reaction dynamics on (anti)hyperon production.

ANALYSIS AND RESULTS

The analysis procedure was carried out using the MPDroot software (based on FairRoot) and the flow analysis package used by the STAR and ALICE experiments. Events were generated with the UrQMD 3.3 model, commonly used in heavy ion research [13,14]. A total of 3.10^5 gold-gold (Au^{79+}) collisions with impact parameter in the range of 0–9 fm and energy $\sqrt{s_{NN}} = 11$A GeV were analyzed. The produced particles were transported through the TPC and TOF detectors using the GEANT3 transport package [15]. Tracks were reconstructed with the Kalman filtering technique [16]. In order to achieve a good precision of momentum and energy loss measurements, a track selection criteria of minimum 10 TPC points was required. The full range of TPC pseudorapidity was used ($|\eta| < 2$). The reconstructed TPC tracks were extrapolated to the TOF detector and matched to TOF hits.

Table 1. Particle identification efficiency and contamination

Particle	$\mathbf{p},\bar{\mathbf{p}}$	$\pi^{\pm}$	$\mathbf{K}^{\pm}$
$\mathbf{P_{trust} > 0}$			
Efficiency, %	90.84	91.48	66.01
Contamination, %	22.92	7.25	43.76
$\mathbf{P_{trust} > 0.6}$			
Efficiency, %	82.41	83.62	47.41
Contamination, %	19.48	5.82	26.70

Several particle identification methods are available for the MPD experiment. For this particular study the Bayesian approach based on energy loss dE/dx from TPC and TOF M^2 information was used (see [17]) to differentiate between track candidates' probabilities to be of certain particle species. For the elliptic flow study identification of charged hadrons (p, π, K) was done in terms of highest probability *e.g.* if the track has the highest probability value to be that of a proton than say pion, we regard the track as to be that of a proton. A selection criteria threshold was introduced so that only tracks above a certain probability P_{trust} may be tagged. Particle identification quality was estimated (see Fig. 4 and Table 1) by efficiency and contamination as functions of transverse momentum

$$E^i = \frac{N^i_{corr}}{N^i_{ana}},\ C^i = \frac{N^i_{incorr}}{N^i_{Ncorr} + N^i_{incorr}} \qquad (3)$$

where E^i and C^i are the efficiency and contamination of a particle species i, N^i_{corr} is the number of correctly

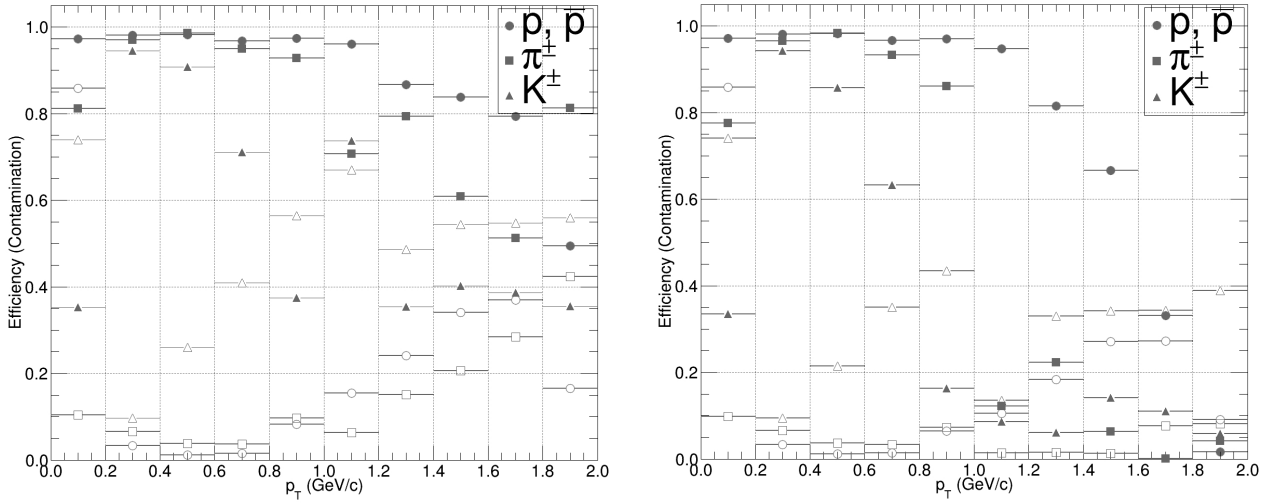


Fig. 4. Particle identification efficiency and contamination as a function of transverse momentum for probability thresholds of (a) $P_{trust} > 0$ and (b) – $P_{trust} > 0.6$

where E^i and C^i are the efficiency and contamination of a particle species i, N^i_{corr} is the number of correctly identified particles, N^i_{ana} - the number of generated particles with more than 10 points in TPC and N^i_{incorr} is the number of incorrectly identified particles.

It should be noted that particle identification plays a key role in elliptic flow determination and while the purpose of this study was not particle identification itself, the optimization of the identification criteria is to be carried out in subsequent studies.

Event plane angle

A well established method of analysing the anisotropic flow is given in [18, 19]. The event plane angle was reconstructed by all identified charged tracks ($P_{trust} \geq 0$) using two sub-events in negative and positive rapidity. The tracks in these sub-selections build sub-Q vectors from which two sub-event plane angles are then determined:

$$Q_{n,x} = \sum w_i \cos(n\phi_i) \tag{4}$$

$$Q_{n,y} = \sum w_i \sin(n\phi_i) \tag{5}$$

$$\Psi_n = \frac{1}{n} \arctan\left(\frac{Q_{n,y}}{Q_{n,x}}\right) \tag{6}$$

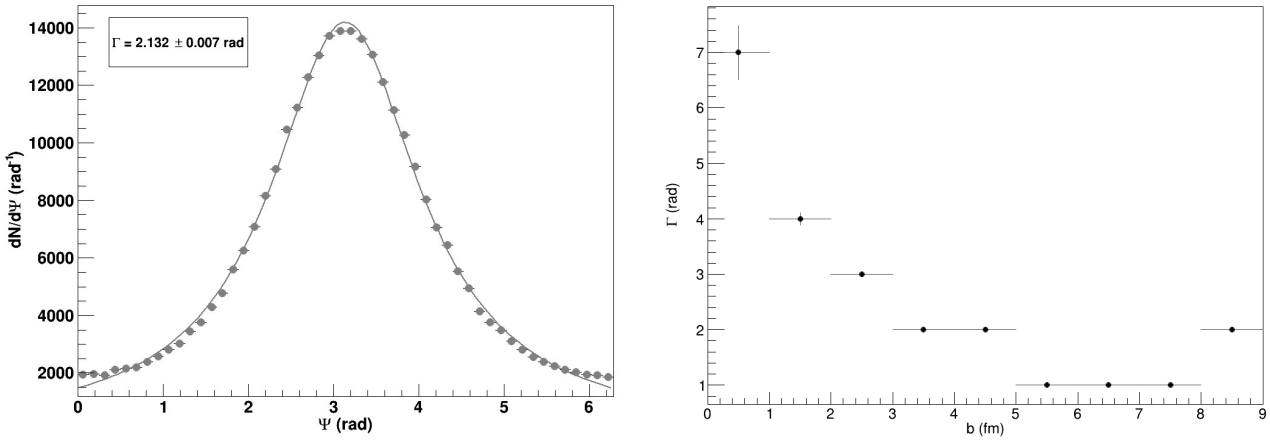
where the sum is carried on every selected track i in the sub-event, $Q_{n,x}$ and $Q_{n,y}$ are the components of the two-dimensional Q-vector, w_i are weight corrections, n denotes the order of Fourier harmonic expansion, ϕ is the track azimuth angle and Ψ is the reconstructed event plane angle.

Event plane determination is sensitive to a non-uniform acceptance in azimuth angle, so weights are used in ϕ, additionally p_T weights are used to improve the event plane resolution. Other methods to correct for acceptance issues include recentering of the event or event mixing (both not used in this study). It should be noted that the UrQMD model has an event plane angle equal to a constant of zero. For convenience the event plane angle is shifted to positive values *e.g.* $\Psi_1 \in [-\pi;+\pi] \rightarrow \Psi_1 \in [0;2\pi]$ for the first harmonic ($\Psi_2 \in [-\pi/2;+\pi/2] \rightarrow \Psi_2 \in [0;+\pi]$ for the second harmonic), which transforms the UrQMD event plane angle of 0 rad into π rad.

The results were fit with a Breit-Wiegner function as a means of assessing event plane angle estimation versus centrality (impact parameter in this case), as shown in Fig. 5. The event plane resolution over all events is determined by:

$$R_n = \sqrt{2\langle\cos(\Psi_{n,A} - \Psi_{n,B})\rangle} \tag{7}$$

where R_n is the resolution for the n-th harmonic and $\Psi_{A,B}$ are the sub-event plane angles. For this data set the resolution was calculated to be $R_2 = 0.4805 \pm 0.0023$. Alternatively, the approach of event-by-event resolution may be used for future studies [20]. One may argue that using the event plane resolution from two sub-events as a function of centrality may provide a more obvious illustration of EP determination quality than the provided Breit-Wigner fits, but that will be an objective for subsequent studies at higher statistics and a wider range of centrality selections. Furthermore, the Zero Degree Calorimeter may provide a complementary role in the event plane determination [6] which is also to be addressed in the future.



(a) (b)

Fig. 5. (a) – reconstructed event plane angle Ψ_1, (b) – width of Breit-Wiegner fit Γ versus the impact parameter b

Elliptic flow of identified hadrons

Following the determination of the event plane angle and the corresponding resolution, particles are correlated to the event plane to reveal the observed differential distributions $v_2^{obs}(p_T)$ and $v_2^{obs}(y)$, however they need to be corrected by the event plane resolution to obtain the final results given by $v_2 = v_2^{obs}/R_2$. The integrated elliptic flow coefficient was determined to be $v_2 = 0.0266 \pm 0.0002$ which is in line with measurements made for the elliptic flow versus energy excitation function in several experiments (*e.g.* [21–23]). It should be noted that the integrated elliptic flow coefficient versus centrality and/or beam energy will also be goals for future studies.

In Fig. 6 are shown differential distributions of $v_2(p_T)$ for probability trust thresholds. Misidentification of particles in the higher p_T region is more pronounced, so after applying the $P_{trust} > 0.6$, a more "pure" sample was derived at the cost of statistics, leading to a requirement of a larger data set and further investigation.

Elliptic flow of Λ-hyperons

Reconstruction of $\Lambda(\bar{\Lambda})$-hyperons was performed using the decay mode $\Lambda \to p + \pi^-$. The secondary vertex reconstruction utilizes a similar approach to the Kalman filtering formalism described in [24]. For the Λ-hyperon reconstruction the trust probability threshold was not used and tracks were tagged by means of highest probability.

The applied topological cuts are: distance of the closest approach (DCA) of the daughter particles to the primary vertex, small distance of separation in the decay vertex between the tracks, and relatively large decay length of the mother particle. Both the DCA and the two-track separation cuts should have increased efficiency if applied in χ^2-space, *i.e.* when normalized to their respective errors.

The exact values of selection cuts were found by multidimensional scan over the whole set of selection criteria with a requirement to maximize the invariant mass peak significance. It is defined as $S/\sqrt{S+B}$, where S and B are total numbers of signal (described by

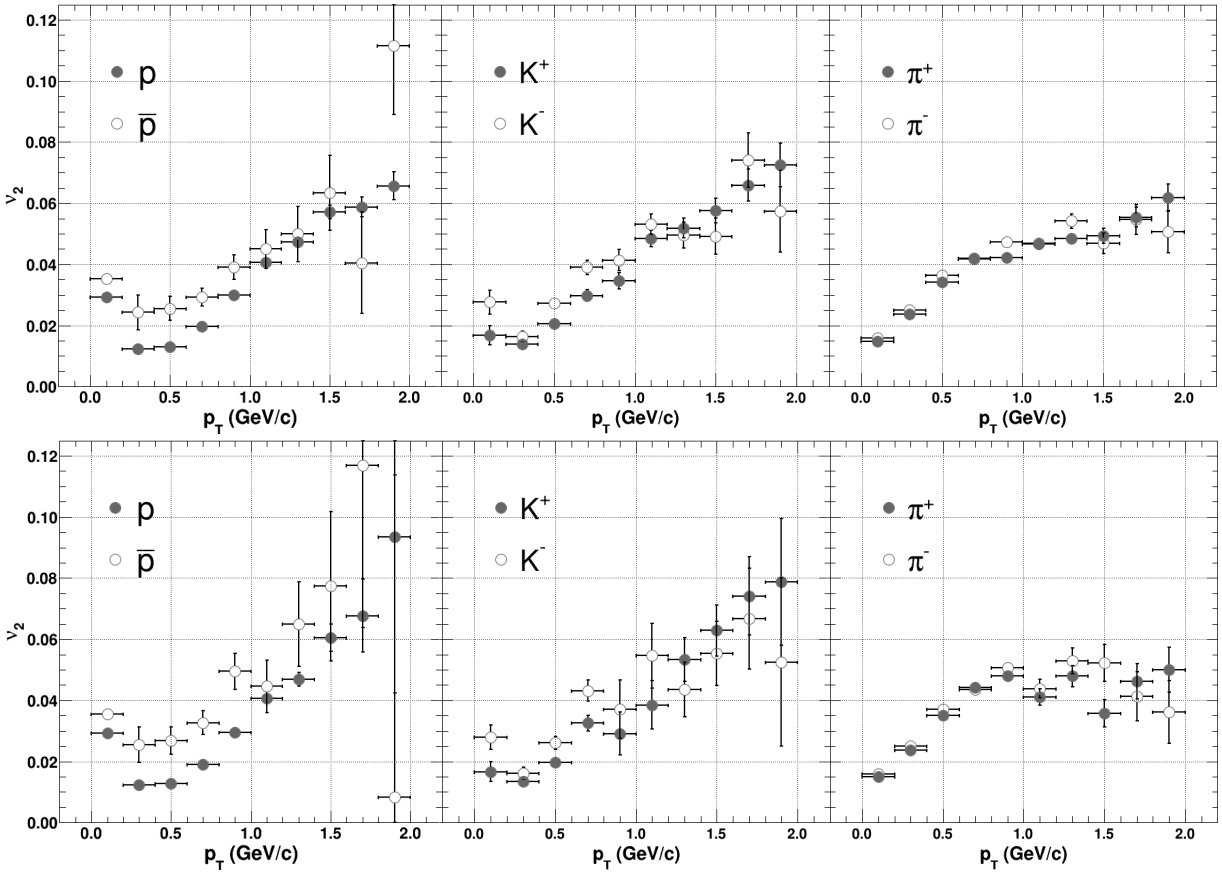
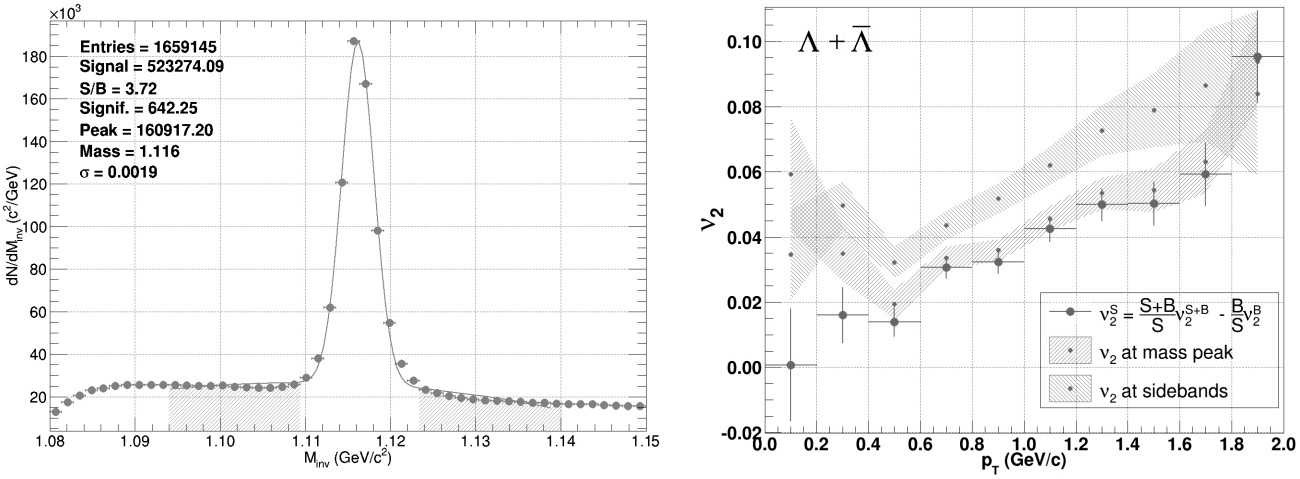


Fig. 6. Differential elliptic flow values in bins of transverse momentum, (a) – $P_{trust} > 0$, (b) – $P_{trust} > 0.6$.



(a) (b)

Fig. 7. (a) – Invariant mass distribution in bins of 1.4 MeV/c^2 each, (b) – $\Lambda,\overline{\Lambda}$-hyperon elliptic flow

the gaussian) and background (polynomial function) combinations inside $\pm 2\sigma$ interval around the peak position.

The selection cuts used for this study were optimized for $\sqrt{s_{NN}} = 9$A GeV and it should be noted that better signal to background ratio may be achieved for the $\sqrt{s_{NN}} = 11$A GeV data set used in this study. Moreover, for the flow analysis procedure the signal and background are evaluated in bins of p_T and optimal results can be obtained with further signal to background ratio maximization carried out in these bins.

The Λ elliptic flow is evaluated in the invariant mass peak region and in the sidebands region, and the background contribution is removed from the signal by

$$v_2^S = \frac{S+B}{S} v_2^{S+B} - \frac{B}{S} v_2^B \qquad (8)$$

where v_2^S is the Λ-hyperon flow "pure" signal, v_2^{S+B} is the flow signal as measured in the mass peak region and v_2^B is the flow signal contribution by the background, measured in the hatched area (see Fig. 7 (a). This approach of background subtraction is very straight forward and simple to implement, however, different methods of background subtraction may be added for comparison in further studies. In Fig. 7 (b) with markers is shown the $v_2(p_T)$ differential flow calculated by (8) and the right and left hatched areas represent the measured flow in the mass peak and sideband regions respectively.

CONCLUSIONS

A short description of the proposed NICA/MPD project was given. Several points have been made on the prospects of hadron flow studies and the important role hyperons may provide for the better understanding of the initial fireball conditions. Future improvements of the presented results of reconstructed and identified hadrons (p,π,K, Λ) elliptic flow as well as an outlook on subsequent studies in this area of research have been noted.

REFERENCES

[1] NICA Conceptual Design Report, 2008, http://nica.jinr.ru/files/NICA_CDR.pdf.

[2] NICA White Paper, 2011, http://nica.jinr.ru/files/WhitePaper.pdf.

[3] MPD Conceptual Design Report, 2011, http://nica.jinr.ru/files/MPD_CDR_en.pdf.

[4] MPD TPC Technical Design Report, 2013, http://nica.jinr.ru/files/MPD/TPC\%20TDR-v1_2_1.pdf.

[5] V.Babkin, V.Golovatyuk, Yu.Fedotov, S.Lobastov, S.Volgin, N.Vladimirova, 2009, http://nica.jinr.ru/files/TOF-MPD.pdf.

[6] M. B. Golubeva, F. F. Guber, A. P. Ivashkin, A. Yu. Isupov, A. B. Kurepin, A. G. Litvinenko, E. I. Litvinenko, I. I. Migulina, V. F. Peresedov, *Physics of Atomic Nuclei*, **76**, 1-15 (2013).

[7] V. Kolesnikov and A. Zinchenko for the MPD Collaboration, preprint arXiv:1312.1091v1 [nucl-ex] (2013).

[8] R. Snellings, preprint arXiv:1102.3010v2 [nucl-ex] (2011).

[9] J. Rafelski and B. Muller, *Phys. Rev. Lett.* **48**, 1066 (1982).

[10] F. Antinori et al. (WA97 Collaboration), *Eur. Phys. J. C* **11**, 79 (1999).

[11] F. Antinori et al. (NA57 Collaboration), *J. Phys. G* **32**, 427 (2006).

[12] L. Adamczyk et al. (STAR Collaboration), *Phys. Rev. C* **88**, 014902 (2013).

[13] S. A. Bass, M. Belkacem, M. Bleicher, M. Brandstetter, L. Bravina, C. Ernst, L. Gerland, M. Hofmann, S. Hofmann, J. Konopka, G. Mao, L. Neise, S. Soff, C. Spieles, H. Weber, L. A. Winckelmann, H. Stocker, W. Greiner, Ch. Hartnack, J. Aichelin and N. Amelin, *Prog. Part. Nucl. Phys.* **41**, 225-370 (1998).

[14] M. Bleicher, E. Zabrodin, C. Spieles, S.A. Bass, C. Ernst, S. Soff, L. Bravina, M. Belkacem, H. Weber, H. Stocker, W. Greiner, *J. Phys. G: Nucl. Part. Phys.* **25**, 1859-1896 (1999).

[15] R. Brun, F. Bruyant, M. Maire, A.C. McPherson, P. Zanarini, *CERN-DD-EE-84-1* (1987).

[16] R. Fruehwirth, *Nucl. Instr. and Meth.* **262**, 444 (1987).

[17] S.P. Merts, S.V. Razin, O.V. Rogachevsky,*Matem. Mod.* **12**, 102 (2012).

[18] S. Voloshin and Y. Zhang, preprint arXiv:hep-ph/9407282v1 (1994), *Z. Phys. C* **70**, 665 (1996).

[19] A. M. Poskanzer and S. Voloshin, preprint arXiv:9805001v2 [nucl-ex] (1998), *Phys. Rev. C* no.CS6346 (1998).

[20] H. Masui and A. Schmah, preprint arXiv:1212.3650v1 [nucl-ex] (2012).

[21] C. Pinkenburg *et al.*, *Phys. Rev. Lett.* **83**, 1295 (1999).

[22] P. Braun-Munzinger, J. Stachel *Nucl. Phys.* **638**, 3c (1998).

[23] H. Appelshäuser *et al.*, *Nucl. Phys.* **698**, 253c (2002).

[24] R. Luchsinger and Ch. Grab, *Comp. Phys. Comm.* **76**, 263 (1993).

РАЗРАБОТКА НА МЕТОДИ ЗА АНАЛИЗ НА АНИЗОТРОПИЧЕН ПОТОК НА ЧАСТИЦИ КЪМ ЕКСПЕРИМЕНТА MPD/NICA

Н. Гераксиев (от името на MPD колектива)

ВБЛФВЕ, Обединен институт за ядрени изследвания, Дубна, Русия

(Резюме)

Измерването на азимуталните анизотропии в разпределението на напречния импулс на частиците може да разкрие информация за ранните етапи в релативистките сблъсъци на тежки йони. Степента на трансфер от пространствена към импулсна анизотропия зависи от плътността на средата по време на еволюцията на системата след сблъсъка и от сеченията на взаимодействащите частици.

Основна част от работата представя подбор на събитията по централност и методите за реконструкция на плоскостта на сблъсък чрез трекове от времепроекционната камера (TPC) или енергията отложена в калориметъра при нулев градус (ZDC) при експеримента MPD@NICA.

От съществена важност е изследването на странни бариони, поради малкото им сечение на взаимодействие, а като такива специално внимание е отделено на ламбда хипероните.

Представени са резултати от реконструирани събития, генерирани от модела UrQMD 3.3, чрез софтуера на експеримента MPDroot. Получените данни са сравнени с актуални експерименти.

Bulgarian Chemical Communications, Volume 47, Special Issue B (pp. 247–250) 2015

Monte Carlo study of the electromagnetic calorimeter optimization for MPD/NICA

B. Marinova*, N. Javadov, I. Tyapkin

Veksler and Baldin Laboratory of High Energy Physics, Joint Institute for Nuclear Research, 6 Joliot-Curie Str., 141980 Dubna, Moscow region, Russia

Different constructions of the electromagnetic calorimeter were simulated with a Monte Carlo generator. The influence of lead-scintillator sampling on the energy resolution in the conditions of fixed total length was tested. Energy resolution of the calorimeter built from rectangular modules has been compared with that of the one built from trapezoidal modules.

Key words: MC, ECAL, NICA, MPD, MpdRoot, GEANT4, energy resolution

INTRODUCTION

Electromagnetic probes, such as real and virtual photons (i.e. dileptons), provide key information on temperature, system size at the early stage of collision, and temperature evolution of the system from its formation to thermal freeze-out.

Input conditions to choose the design of electromagnetic calorimeter for MPD are the following:

- The expected high multiplicity environment implies the high segmentation of the calorimeter.
- Use of dense active medium, with a small Molière radius.
- The particle occupancy should not exceed 5% to determine the photon reconstruction efficiency with high accuracy.
- The photon detector must be able to operate in magnetic field of up to 0.5 T.
- Enough compactness to be integrated into the MPD set-up.

As a baseline option is selected heterogeneous calorimeter type "Shashlyk" which meets the above requirements. The calorimeter will consist of active medium (scintillator) and absorber (lead) and the light will be collected with the help of wavelength shifting (WLS) fibers. Such calorimeters are used in PHENIX, LHCB, KOPIO and others.

Detailed information can be found in [1].

ELECTROMAGNETIC CALORIMETER

The calorimeter will have cylindrical structure and positioned in MPD at a radius of $R = 1.78$ m. The barrel part of ECAL covers the pseudorapidity interval $-2.5 < \eta < 2.5$.

The basic building block of the calorimeter will be a module (120×120 mm^2) consisting of 9 optically isolated towers which are read out individually. Each Pb-scintillator tower consists of lead and scintillator plates. The cells of each tower are optically combined by 9 longitudinally penetrating wavelength shifting fibers.

The longitudinal dimension of the calorimeter module is limited by the design of MPD. The allocated space is 400 mm for the active media and 150 mm for the light detection module.

Table 1. Main parameters of Type 1 and Type 2

Parameters	**Type 1**	**Type 2**
Transverse size, mm^2	120×120	120×120
Number of layers	220	198
Lead absorber thickness, mm	0.3	0.5
Polystyrene scintillator thickness, mm	1.5	1.5
Molière radius, mm	26	39
Radiation length, X_0	11.8	17.7
Effective radiation length, mm	32.4	22

Different samplings were studied, but here only two of them are presented. They differ in the thickness of the absorbing plates and their parameters are given in Table 1.

Energy resolution

As shown [1] in many physical studies it is necessary to have good energy resolution of the electromagnetic calorimeter - at the level of 5-7% for electrons with energy of 1 GeV.

To obtain a permission within existing resources (the available space in the detector and and the allocated finances), all parameters of the calorimeter should be carefully optimized. Energy resolution of a Shashlyk module depends on a variety of factors [2]:

* To whom all correspondence should be sent:
boiana_marinova@abv.bg

© 2015 Bulgarian Academy of Sciences, Union of Chemists in Bulgaria

1. Sampling, i.e. thicknesses of lead and scintillator plates.
2. Longitudinal leakage, i.e. fluctuation of energy leakage due to the finite length of module.
3. Transverse leakage, i.e. fluctuation of energy leakage due to the limited number of modules used to reconstruct an electromagnetic shower.
4. Effects of the presence of holes, fibers, and steel strips.
5. Light attenuation in the fiber.
6. Photostatistics.

In our case, the longitudinal dimension is determined by the structure of MPD. Longitudinal leakage (2) can be optimized only by varying the sampling (1), as will be shown below. The effects of factors 4-6 on the calorimeter resolution are determined by the technology. They will not be studied in this paper.

The energy resolution can be parameterized as:

$$\frac{\sigma_E}{E} = \frac{a}{\sqrt{E}} \oplus \frac{b}{E} \oplus c$$

where sign $\oplus$ denotes quadratic addition, E is a beam energy in GeV, a is the stochastic term, b is determined by the readout noise, and the constant term c is due to the detector and readout inhomogeneity and the calibration error. Since the photon detector will measure relatively low-energy photons ($E < 2$ GeV), we can ignore electronic noise [4].

Detector simulation

The main task was to find a construction of the calorimeter, which has the best energy resolution in the given conditions. The simulation environment is MpdRoot, built on FairRoot. The FairRoot framework is an object oriented simulation, reconstruction and data analysis framework based on ROOT. By using the Virtual Monte Carlo concept it is possible to perform the simulations using either Geant3 or Geant4 without changing the user code or the geometry description [3].

To investigate the characteristics of ECAL, Geant4 was used. Photons with different energies were generated by the BoxGenerator. Detector response was observed in two cases - when the particles hit the calorimeter module in the center and when they are randomly distributed over a few modules.

Geometry with rectangular modules (V1)

In this case the barrel structure of the detector is assembled from modules having rectangular shape. The construction may look as follows - three modules are grouped together in one segment ($360 \times 120 \times 400$ mm^3) and forty-nine such segments form a row. Thirty-one rows are disposed at an azimuthal angle 11.6 degrees. This geometry is shown in Fig. 1.

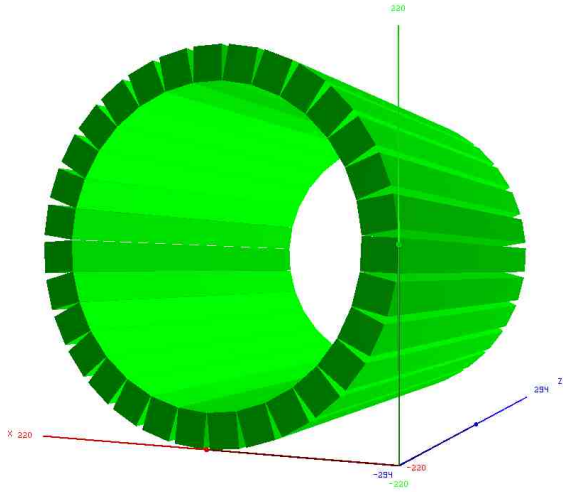


Fig. 1. Barrel part of the calorimeter in MPD built from rectangular units (Geometry V1).

The first step was to select such a thickness of the absorbing plate as to reach the best possible energy resolution. Characteristics of the two types of construction V1 were observed and the results are shown in Fig. 2. The graph shows that construction Type 1 has better resolution than Type 2 in energies less than 1 GeV, but in higher energies, electromagnetic showers begin to leak through the module. The energy interval we are interested in is less than 1 GeV, therefore it is better to use construction with 0.3-milimeter lead plates.

It is obvious that filling the cylinder with rectangular modules will leave spaces between them (Fig. 1).

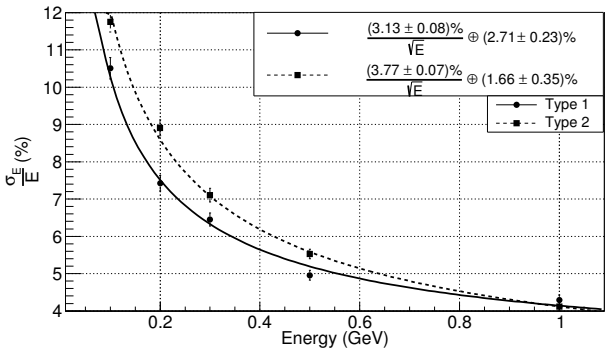


Fig. 2. Energy resolutions for both types of geometry V1 when beam photon energy hits the center of a module.

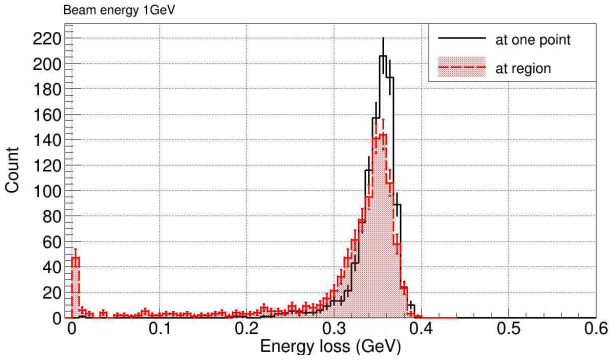


Fig. 3. Distribution of energy loss when the photon beam hits the center of a module and when it is randomly distributed in a region of few modules.

Fig. 3 shows the distribution of energy loss when the beam energy is 1 GeV and the photons hit the center of a module and when they are distributed over a region - $\phi(45^\circ, 135^\circ)$, $\theta(90^\circ, 90^\circ)$, covering few modules. The shift of energy loss to smaller values down to zero is the result of a dead zone in the calorimeter construction.

The constant term increases twice when the beam photons are generated in a region. This is shown in Fig. 4 and it is the result of the existence of empty spaces between the modules. For the improvement of the constant term and the energy resolution, a decision was taken to use a construction of trapezoidal modules.

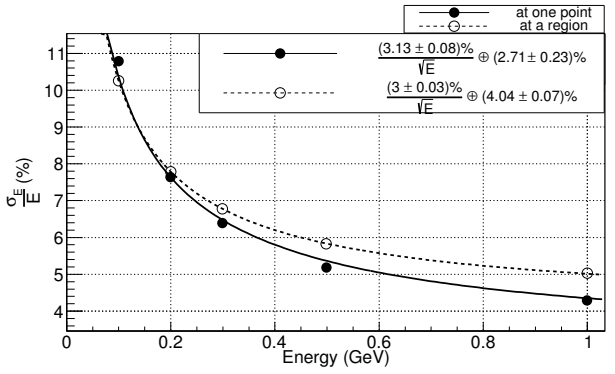


Fig. 4. Energy resolutions by type 1 when the photon beam hits the center of a module and when it is randomly distributed in a region of few modules.

Geometry with trapezoidal modules (V2)

The basic module (120×120 mm^2) is cut off on two sides at an angle 1.565 degrees in the ϕ plane. Each module is rotated by 3.13 degrees at azimuthal angle and is closely fit to the preceding one. The thickness of the lead plates is 0.3 mm. In this way a structure having no dead zones is formed (Fig. 5).

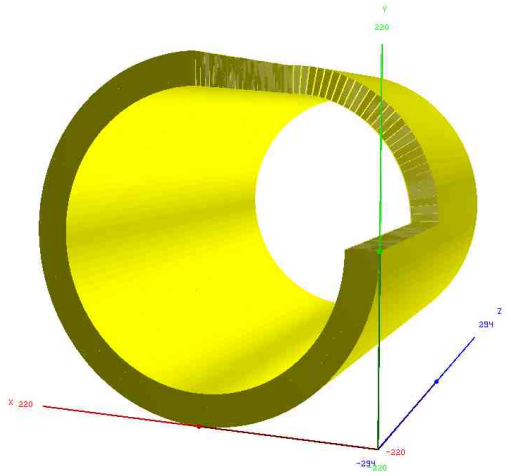


Fig. 5. Barrel part of the calorimeter in MPD built from trapezoidal units (Geometry V2).

Filling the space between modules keeps the constant term stable, which can be seen in Fig. 6.

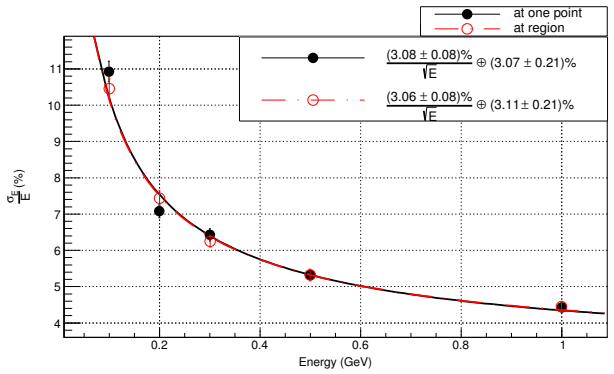


Fig. 6. Energy resolutions (Geometry V2) when the photon beam hits the center of the module and when it is randomly distributed in a region – $\phi(45^\circ, 135^\circ)$, $\theta(90^\circ, 90^\circ)$.

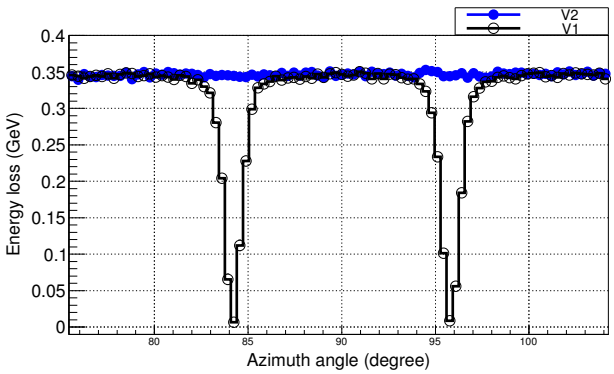


Fig. 7. Distribution of energy loss versus azimuthal angle (beam energy 1 GeV).

Figure 7 shows the distribution of energy loss versus azimuthal angle of the two constructions of ECAL with beam energy 1 GeV.

SUMMARY

It is shown a method for reducing the influence of dead zones between modules on the energy resolution of ECAL. The energy resolutions of calorimeters constructed from modules, having different cross-sections, were compared.

The test results lead to the decision to use a construction of trapezoidal modules, composed of lead plates 0.3 mm and 1.5 mm scintillator plates. In this case the detector shows the best performance, in relation to the imposed requirements.

REFERENCES

[1] The MultiPurpose Detector-MPD, *Conceptual Design Report*, Version 1.4, 2012.

[2] G. S. Atoian, V. V. Issakov et al., *Nucl. Instrum. Meth.*, **A531**, 467-480, 2004.

[3] M. Al-Turany et al., The FairRoot framework, *Journal of Physics: Conference Series* , **396**, 022001, 2012.

[4] A. V. Aref'ev, I. M. Belyaev et al., *Instruments and Experimental Techniques*, **51** (4), 511-522, 2008.

МОДЕЛИРАНЕ НА ЕЛЕКТРОМАГНИТНИЯ КАЛОРИМЕТЪР КЪМ NICA/MPD

Б. Маринова, Н. Джавадов, И. Тяпкин

Лаборатория по физика на високите енергии, ОИЯИ,
ул. "Жолио-Кюри" №6, 141980 Дубна, Московска област, Русия

(Резюме)

Основното предназначение на електромагнитния калориметър е да измерва координатите и енергиите на електроните и фотоните, родени при сблъсъци на тежки йони. Калориметърът ще служи и за идентификация на частици. Първа стъпка в реконструкцията на събитията ще бъде търсене на π^0-мезони и изваждането на фотони, свързани с π^0-мезони, от пълния поток фотони. Останалите фотони ще се считат кандидати за директни фотони. За да се достигне необходимата чувствителност в реконструкцията на π^0 при висок шум, енергията на фотоните трябва да се измерва с висока точност. Необходимо е разрешение по енергии около 3%.

За ECAL в MPD е избран хетерогенен калориметър тип „сандвич", изграден от пластини олово и сцинтилатор [1]. Основният модул е със страни 4×4 cm. Отделеното пространство в MPD за ECAL е 50 cm, което ограничава модула по дължина – не повече от 40 cm.

Главната задача бе да се моделира геометрия, която да покрива изискванията от 3% енергетично разрешение. Създадени бяха три основни модела геометрии и за всеки един от тях бяха разгледани различни вариации на запълващите сегменти (различни дебелини на оловните пластини и дължина на основния модул). Първоначално симулациите се извършваха с помощта на софтуер GEANT3, а след това с GEANT4. След проведените симулации се стигна до решение да се избере една от геометриите – с най-добро разрешение по енергии и оптимално запълване на пространството (дебелина на оловните пластини 0.3 mm и дължина на основния модул 40 cm).

Изготвени бяха два прототипа на основния модул с различни оптични влакна. Проведоха се два експеримента на електронен сноп в DESY (Германия). Извършиха се тестове на двата модула, енергийно и честотно сканиране, проверена бе електрониката, усилвателите и кабелите, изследваха се два типа фотодетектора – Zecotek и Hamamatsu. Достигна се енергетично разрешение 3.5% при 1 GeV и разрешение по време 100 ps на 1 GeV.

1. The MultiPurpose Detector – MPD. Concept Disign Report. JINR, Version 1.4.

THEORETICAL AND MATHEMATICAL PHYSICS

ТЕОРЕТИЧНА И МАТЕМАТИЧЕСКА ФИЗИКА

Bulgarian Chemical Communications, Volume 47, Special Issue B (pp. 253–261) 2015

Holographic mesons in Pilch-Warner geometry

V. Filev[1], R. C. Rashkov[2,3], T. Vetsov[3*]

[1] *School of Theoretical Physics, Dublin Institute for Advanced Studies, 10 Burlington Rd., 4 Dublin, Ireland*
[2] *Institute for Theoretical Physics, Vienna University of Technology, Wiedner Hauptstr. 8-10, 1040 Vienna, Austria*
[3] *Faculty of Physics, St. Kliment Ohridski University of Sofia, 5 James Bourchier Blvd., BG-1164 Sofia, Bulgaria*

In this paper we study the D7 probe brane scalar fluctuations in global Pilch-Warner background geometry. We chose to work with simple constant solutions that solve the classical embedding equations. This allows one to fix the position of the brane in space and considerably simplify the analysis of its fluctuations. The corresponding meson spectra, obtained by the fluctuations along the transverse directions, admit equidistant structure for the higher modes and a ground state given by the conformal dimension of the operator dual to the fluctuations.

Key words: AdS/CFT correspondence, gauge/gravity correspondence, holographic mesons

INTRODUCTION

The AdS/CFT correspondence is a magnificent duality relating 10 dimensional IIB string theory in the weak coupling regime to a 4 dimensional $SU(N)$ gauge field theory with strong coupling constant, and vice-versa. In this case the gauge field theory lives on the boundary of the spacetime where the strings move. This correspondence gives us the opportunity to study non-perturbative phenomena in Yang-Mills theory with tools available in the classical superstring theory and supergravity.

On the gauge theory side of the original Maldacena setup [1] there is a theory with huge amount of symmetry ($\mathcal{N}=4$ supersymmetric Yang-Mills theory), and on the string side of the correspondence we have a stack of N $D3$-branes, so that both endpoints of the strings are attached to the same stack of $D3$-branes, therefore the corresponding states transforms in the adjoint representation of the gauge group. Adding flavours in the setup is achieved by introducing a separate stack of N_f $D7$ probe branes [2]. Here, the $SU(N_f)$ is a global flavor symmetry. If we consider the case of $N_f \ll N_c$, where N_c is the number of the $D3$-branes, and further take N_c large, then we have a strongly coupled dual gauge theory, and a stack of $D3$-branes, which is the source of the background geometry, but in the limit of large N_c it can effectively be replaced by $AdS_5 \times S^5$. In this setup we can study the N_f $D7$-branes in the probe limit. The strings stretched between the two stacks of branes have finite length and thus finite energy, so that the quark mass is given by the separation distance and the string tension: $m_q = L/2\pi\alpha'$.

Although variety of meson spectra were found [3,4] (for a review see [5]), there is still too much supersymmetry we have to deal with in order to achieve string theory description of QCD and the Standard model. To produce more realistic QCD like string theories, deformations of the initial $AdS_5 \times S^5$ geometry [6,7], or introducing external magnetic or electric fields [8–11], have to be considered. Such configurations will break the supersymmetry and theories with less supersymmetry will emerge. In this context Pilch-Warner geometry [12,13] is a fine example of such deformed geometry. It is a solution of five-dimensional $\mathcal{N}=8$ gauged supergravity lifted to ten dimensions, which, in its infrared critical point, preserves 1/4 of the original supersymmetry.

GENERAL SETUP

Pilch-Warner geometry

Pilch-Warner geometry is a solution of five-dimensional $\mathcal{N}=8$ gauged supergravity lifted to ten dimensions. This geometry interpolates between the maximally supersymmetric $AdS_5 \times S^5$ in the ultraviolet critical point and warped AdS_5 times squashed five-sphere in the infrared point (IR). In this study we will restrict ourself to the IR critical point. An interesting feature on the gravity side is that it preserves 1/8 supersymmetry everywhere while at IR fixed point it is enhanced to 1/4. On the SYM side the IR fixed point corresponds to large N limit of the superconformal $\mathcal{N}=1$ theory of Leigh-Strassler [15]. The ten-dimensional Pilch-Warner metric is given by

* To whom all correspondence should be sent:
c.vecov@gmail.com

© 2015 Bulgarian Academy of Sciences, Union of Chemists in Bulgaria

$$ds^2 = ds^2_{1,4} + ds^2_5\,, \tag{1}$$

where we have the warped AdS_5 metric

$$ds^2_{1,4} = \Omega^2(e^{2A}\,ds^2(\mathbb{M}^4) + dr^2)\,, \tag{2a}$$

and the squashed five-sphere metric

$$\begin{aligned} ds^2_5 =& L_0^2\frac{X^{1/2}\mathrm{sech}\chi}{\overline{\rho}^3}\Big[d\theta^2 + \frac{\overline{\rho}^6\cos^2\theta}{X}(\sigma_1^2+\sigma_2^2) \\ &+ \frac{\overline{\rho}^{12}\sin^2 2\theta}{4X^2}\Big(\sigma_3 + \frac{2-\overline{\rho}^6}{2\overline{\rho}^6}d\phi\Big)^2 + \frac{\overline{\rho}^6\cosh^2\chi}{16X^2} \\ &\times(3-\cos 2\theta)^2\Big(d\phi - \frac{4\cos^2\theta}{3-\cos 2\theta}\sigma_3\Big)^2\Big]. \end{aligned} \tag{2b}$$

This is an example of warped geometry where the warp factor Ω is given by: $\Omega^2 = X^{1/2}\cosh\chi/\overline{\rho}$, and the function $X(r,\theta) = \cos^2\theta + \overline{\rho}^6\sin^2\theta$. Our left-invariant one-forms satisfy $d\sigma_i = \varepsilon_{ijk}\sigma_j\wedge\sigma_k$, so that $d\widetilde{\Omega}_3^2 = \sigma_i\sigma_i$ is the metric on the unit 3-sphere. In global coordinates they take the following form:

$$\begin{aligned} \sigma_1 &= \frac{1}{2}(\sin\beta\,d\alpha - \cos\beta\sin\alpha\,d\gamma), \\ \sigma_2 &= -\frac{1}{2}(\cos\beta\,d\alpha + \sin\beta\sin\alpha\,d\gamma), \\ \sigma_3 &= \frac{1}{2}(d\beta + \cos\alpha\,d\gamma)\,. \end{aligned} \tag{3}$$

At the IR point $r\to-\infty$, $\chi = \mathrm{arccosh}\left(\frac{2}{\sqrt{3}}\right)$, $\overline{\rho} = 2^{1/6}$, and $A(r) = r/L$. The AdS radius L is given in terms of the AdS radius L_0 of the UV spacetime by $L = (3/2^{5/3})L_0$. One finds that at the IR point the metric takes the form

$$ds^2_{1,4} = \Omega^2(e^{\frac{2r}{L}}\,ds^2(\mathbb{M}^4) + dr^2)\,, \tag{4a}$$

and the squashed five-sphere metric

$$\begin{aligned} ds^2_5 = \frac{2}{3}L^2\Omega^2\Big[&d\theta^2 + \frac{4\cos^2\theta}{3-\cos 2\theta}(\sigma_1^2+\sigma_2^2) \\ &+\frac{4\sin^2 2\theta}{(3-\cos 2\theta)^2}\sigma_3^2 + \frac{2}{3}\Big(d\phi - \frac{4\cos^2\theta}{3-\cos 2\theta}\sigma_3\Big)^2\Big]. \end{aligned} \tag{4b}$$

As shown in [14] there is a natural global $U(1)_\beta$ action $\beta\to\beta+const$ which rotates σ_1 into σ_2 and leaves σ_3 invariant. We adopt the set up where the S^3 Euler angle $\beta\to\beta+2\phi$ is shifted to give a solution with a global $U(1)_R = U(1)_\phi$ symmetry. Performing this coordinate transformation on the solution (4a) and (4b) we arrive at the final result for the Pilch-Warner metric in global coordinates

$$ds^2_{1,4}(IR) = L^2\Omega^2(-\cosh^2\rho\,d\tau^2 + d\rho^2 + \sinh^2\rho\,d\Omega_3^2), \tag{5a}$$

$$\begin{aligned} ds^2_5(IR) = \frac{2}{3}L^2\Omega^2\Big[&d\theta^2 + \frac{4\cos^2\theta}{3-\cos 2\theta}(\sigma_1^2+\sigma_2^2) \\ &+\frac{4\sin^2 2\theta}{(3-\cos 2\theta)^2}(\sigma_3+d\phi)^2 + \frac{2}{3}\Big(\frac{1-3\cos 2\theta}{\cos 2\theta-3}\Big)^2 \\ &\times\Big(d\phi - \frac{4\cos^2\theta}{1-3\cos 2\theta}\sigma_3\Big)^2\Big], \end{aligned} \tag{5b}$$

where $d\Omega_3^2 = d\phi_1^2 + \sin^2\phi_1(d\phi_2^2 + \sin^2\phi_2 d\phi_3^2)$ is the metric on the 3-sphere, and

$$\Omega^2 = \frac{2^{1/3}}{\sqrt{3}}\sqrt{3-\cos(2\theta)} \tag{6}$$

is the warp factor at the IR point.

R-R and NS-NS potentials

The Pilch-Warner background includes non-trivial Ramond-Ramond (R-R) and Neveu-Schwarz (NS-NS) form fields entering the $D7$ probe brane action. The full action is given by two terms – a Dirac-Born-Infeld (DBI) term and a Wess-Zumino (WZ) term [16, 17]

$$\begin{aligned} S_{D_7} &= S_{DBI} + S_{WZ} \\ &= -T_7\int d^8\xi e^{-\Phi}\sqrt{-\det(P[G]+\mathscr{F})} \\ &\quad - T_7\int\Big(P[C_8] - P[C_6]\wedge\mathscr{F} + \tfrac{1}{2}P[C_4]\wedge\mathscr{F}\wedge\mathscr{F} + \cdots\Big), \end{aligned} \tag{7}$$

where $\mathscr{F} = P[B_2] + 2\pi\alpha' F$, T_7 is the $D7$-brane tension, Φ is the dilaton, F is the worldvolume gauge field, B_2 is the Kalb-Ramond 2-form, and P denotes the pullback of the bulk spacetime tensor to the worldvolume of the brane:

$$P[G]_{ab} = G_{AB}\frac{\partial X^A}{\partial\xi^a}\frac{\partial X^B}{\partial\xi^b}\,. \tag{8}$$

The indices $a,b = 0,\ldots,7$ span the world volume of the $D7$-brane, while $A,B = 0,\ldots,9$ span the whole spacetime. We will consider $D7$-brane embeddings in static gauge where θ and ϕ directions are transverse to the brane

$$\begin{aligned} \xi^a &= (\tau,\rho,\phi_1,\phi_2,\phi_3,\alpha,\beta,\gamma), \\ a &= 0,\ldots,7, \quad \phi = \phi(\rho), \quad \theta = \theta(\rho)\,. \end{aligned} \tag{9}$$

In static gauge the pullback is given by

$$P[G]_{ab} = g_{ab} + G_{mn}\frac{\partial X^m}{\partial \xi^a}\frac{\partial X^n}{\partial \xi^b}\,, \tag{10}$$

where g_{ab} is the induced metric on $D7$, and G_{mn} $(m,n=\theta,\phi)$ are the metric components in front of the transverse coordinates governing the $D7$-brane fluctuations. D–branes carry an R-R charge which due to charge conservation turns them into stable objects. In the IIB string theory the R-R potentials are C_0, C_2, C_4, C_6, C_8 and corresponding field strengths, which satisfy certain Bianchi identities and equations of motion [16]

$$\Phi = C_0 = 0, \quad F_1 = dC_0 = 0\,, \tag{11a}$$
$$C_2 = \Re e(A_2), \quad B_2 = \Im m(A_2)\,, \tag{11b}$$
$$H_3 = dB_2, \quad F_3 = dC_2 - C_0\wedge H_3 = dC_2\,, \tag{11c}$$
$$\mathrm{d}F_3 = \mathrm{d}H_3 = 0, \quad \mathrm{d}F_5 = H_3\wedge F_3\,, \tag{11d}$$
$$\mathrm{d}(\star F_3) = -H_3\wedge F_5,\ \mathrm{d}(\star H_3) = F_3\wedge F_5,\ F_5 = \star F_5, \tag{11e}$$
$$dC_4 + d\widetilde{C}_4 = F_5 + C_2\wedge H_3\,, \tag{11f}$$
$$F_7 = \star F_3 = dC_6 - C_4\wedge H_3\,, \tag{11g}$$
$$F_9 = \star F_1 = 0 = dC_8 - C_6\wedge H_3 = C_6\wedge H_3,\ \chi = C_8 = 0\,. \tag{11h}$$

Here the field strengths are defined in terms of the corresponding potentials as

$$H_3 \equiv \mathrm{d}B_2, \quad F_\mathrm{p} \equiv \mathrm{d}C_{\mathrm{p}-1} - C_{\mathrm{p}-3}\wedge H_3. \tag{12}$$

In this setup the axion/dilaton system of scalars (11a) and (11h) is trivial along the flow. We also have an ansatz for the self-dual five form

$$F_5 = -\frac{2^{5/3}}{3}L^4\cosh\rho \times \sinh^3\rho(1+\star)\mathrm{d}\tau\wedge\mathrm{d}\rho\wedge\varepsilon(S^3_\phi), \tag{13}$$

where $\varepsilon(S^3_\phi) = \sin^2\phi_1\,\sin\phi_2\,\mathrm{d}\phi_1\wedge\mathrm{d}\phi_2\wedge\mathrm{d}\phi_3$ is the volume element of the unit 3-sphere S^3_ϕ, and $\star$ is the Hodge star operator. The ansatz for the 2-form potential A_2 at the IR point is also known

$$A_2(IR) = C_2 + iB_2 - \frac{i}{2}e^{-2i\phi}L_0^2\cos\theta\Big(\mathrm{d}\theta - \frac{2i\sin 2\theta}{3-\cos 2\theta}(\sigma_3+\mathrm{d}\phi)\Big)\wedge(\sigma_1+i\sigma_2)\,. \tag{14}$$

Two additional constraints are necessary for (11a) to be consistent, namely

$$F_3\wedge\star H_3 = 0, \qquad F_3\wedge\star F_3 = H_3\wedge\star H_3\,. \tag{15}$$

Equipped with this setup we are ready to begin our study of the classical D7-brane embeddings and its scalar fluctuations in global Pilch-Warner geometry.

D7-BRANE EMBEDDINGS

In order to proceed with the classical D7 embeddings we will set the worldvolume gauge field $F = 0$. There are three relevant cases of classical D7-brane embeddings we will consider here. The first two correspond to fixed values of θ, and the third one corresponds to fixed value of ϕ. The firs case we are going to consider is $\theta = 0$, $\phi = \phi(\rho)$. The classical profile of the $D7$-brane is governed by the following non-linear equation:

$$\phi''(\rho) + (3\coth\rho + \tanh\rho) \times\Big(\phi'(\rho) + \frac{4}{9}(\phi'(\rho))^3\Big) = 0\,. \tag{16}$$

The simplest solution to this equation is the constant solution $\phi(\rho) = const$. In the second case we take the ansatz $\theta = \pi/2$, $\phi = \phi(\rho)$. The classical equation of motion is similar to the previous one

$$\phi''(\rho) + (3\coth\rho + \tanh\rho) \Big(\phi'(\rho) + \frac{8}{9}(\phi'(\rho))^3\Big) = 0\,, \tag{17}$$

solved again by any constant $\phi(\rho) = const$. Note that if we set $u(\rho) = \phi'(\rho)$ for both cases we get first order Bernoulli type equations. The third case we are going to consider is the ansatz $\phi = 0, \theta = \theta(\rho)$. The classical equation of motion takes complicated form

$$\theta''(\rho) + a(\rho)\theta'(\rho) + b(\rho)(\theta'(\rho))^2 + c(\rho)(\theta'(\rho))^3 + d(\rho)\varsigma(\rho) + e(\rho) = 0\,, \tag{18}$$

where the corresponding coefficients are

$$a(\rho) = 3\coth\rho + \tanh\rho,$$
$$b(\rho) = \frac{1}{9(z_2-3)^2}\Big[2\tan(\theta(\rho)) \times\big(-\varsigma(\rho)\sqrt{6-2z_2}(z_3-13z_1) - 90z_2 + 9z_4 + 117\big)\Big],$$
$$c(\rho) = \frac{28}{9}(\tanh\rho + \coth\rho + \mathrm{csch}2\rho),$$
$$d(\rho) = -\frac{2\sqrt{2}\,\sin(\theta(\rho))\sqrt{3-z_2}(z_2-7)}{7(z_2-3)^2},$$

$$e(\rho) = \frac{18}{7}\frac{\sin(2\,\theta(\rho)) - 3\tan(\theta(\rho))}{(z_2-3)},$$
$$\varsigma(\rho) = \sqrt{14(\theta'(\rho))^2+9},$$
$$z_n = \cos(n\,\theta(\rho)), \quad n = 1,2,3,4\,.$$

This equation has simple solutions, which satisfy the trigonometric equation $\sin\theta = 0$, i.e. $\theta(\rho) = k\,\pi$, $k \in \mathbb{N}_0$.

SCALAR FLUCTUATIONS OF THE $D7$-BRANE AND THE MESON SPECTRA

Fluctuations along ϕ, $\theta = 0$

Now we proceed with the study of the scalar fluctuations of the $D7$ probe brane along ϕ and θ, around the classical solution $\phi_{cl} = 0$. We consider the following ansatz for the fluctuations:

$$\theta = 0 + 2\,\pi\,\alpha'\,\Theta, \qquad \phi = 0 + 2\,\pi\,\alpha'\,\Phi\,, \tag{19}$$

where $\delta\phi = 2\,\pi\,\alpha'\,\Phi$, and $\delta\theta = 2\,\pi\,\alpha'\,\Theta$. The full Lagrangian is the sum of the DBI and WZ Lagrangians

$$\mathscr{L} = \mathscr{L}_{DBI} + \mathscr{L}_{WZ}\,. \tag{20}$$

Let us investigate only the Φ fluctuations. There are no contributions from $\mathscr{L}_{WZ}$, but it gives non-zero contributions for Θ, as we will see in the next section. The DBI Lagrangian, up to quadratic order in the fluctuations, is given by

$$\mathscr{L}_{DBI} = -\mu_7\sqrt{-g}\Big(1 + \frac{1}{2}g^{ab}G_{\theta\theta}\partial_a\Theta\partial_b\Theta + \frac{1}{2}g^{ab}G_{\phi\phi}\partial_a\Phi\partial_b\Phi\Big), \tag{21}$$

where $g = \det(g_{ab})$ is the determinant of the induced metric. The equation of motion for the fluctuation field Φ is given by the Laplace-Beltrami equation

$$\nabla_a\nabla^a\Phi = \frac{1}{\sqrt{-g}}\,\partial_a\left(\sqrt{-g}\,g^{ab}\,\partial_b\,\Phi\right) = 0\,. \tag{22}$$

Expanding equation (22) one finds

$$-\partial_\tau^2\Phi + \cosh^2\rho\Big(\partial_\rho^2\Phi + (3\coth\rho + \tanh\rho)\partial_\rho\Phi + \frac{1}{\sinh^2\rho}\Delta_{\phi_i}\Phi + 3\widetilde{\Delta}_{\alpha_i}\Phi\Big) = 0, \tag{23}$$

where $\phi_i = (\phi_1, \phi_2, \phi_3)$, $\alpha_i = (\alpha, \beta, \gamma)$, and

$$\Delta_{\phi_i}\Phi = \frac{1}{\sin^2\phi_1}\partial_{\phi_1}(\sin^2\phi_1\partial_{\phi_1}\Phi) + \frac{1}{\sin^2\phi_1\sin\phi_2}\partial_{\phi_2}(\sin\phi_2\partial_{\phi_2}\Phi) + \frac{1}{\sin^2\phi_1\sin^2\phi_2}\partial_{\phi_3}^2\Phi, \tag{24a}$$

$$\widetilde{\Delta}_{\alpha_i}\Phi = \frac{1}{\sin\alpha}\partial_\alpha(\sin\alpha\partial_\alpha\Phi) + \frac{1}{\sin^2\alpha}\Big(\frac{(\cos(2\alpha)+7)}{8}\partial_\beta^2\Phi + \partial_\gamma^2\Phi - 2\cos\alpha\partial_\beta\partial_\gamma\Phi\Big). \tag{24b}$$

Separation of variables leads to the following spectral equations:

$$\ddot{T}(\tau) + \omega^2\,T(\tau) = 0\,, \tag{25a}$$
$$\widetilde{\Delta}_{\alpha_i}Z(\alpha_i) = -\nu\,Z(\alpha_i)\,, \tag{25b}$$
$$\Delta_{\phi_i}Y^l(\phi_i) = -l\,(l+2)\,Y^l(\phi_i)\,, \tag{25c}$$
$$R''(\rho) + (3\coth\rho + \tanh\rho)R'(\rho) + \Big(\frac{\omega^2}{\cosh^2\rho} - \frac{l(l+2)}{\sinh^2\rho} - 3\nu\Big)R(\rho) = 0\,, \tag{25d}$$

where $Y^l(\phi_i)$ are the hyperspherical harmonics, $l \in \mathbb{N}_0$. In order to determine the conformal dimension and the spectrum, we will make the following change of variable $r = \sinh\rho$ in the radial equation. After some simple manipulations we find

$$R''(r) + \frac{3+5r^2}{r(r^2+1)}R'(r) + \Big(\frac{\omega^2}{(r^2+1)^2} - \frac{l(l+2)}{r^2(r^2+1)} - \frac{3\nu}{r^2+1}\Big)R(r) = 0. \tag{26}$$

There are two independent solutions $R(r) = R_+(r) + R_-(r)$ given in terms of Gaussian hypergeometric functions

$$R_+(r) = c_1 r^{-2-l}(r^2+1)^{-\frac{\omega}{2}}\,{}_2F_1(a,b;c;z), \tag{27a}$$
$$R_-(r) = c_2 r^l(r^2+1)^{-\frac{\omega}{2}} \times {}_2F_1(a-c+1, b-c+1; 2-c; z), \tag{27b}$$

where the arguments of the hypergeometric function are as follows:

$$a = (-l-\omega-\sqrt{3\nu+4})/2,$$
$$b = \frac{1}{2}(-l-\omega+\sqrt{3\nu+4})/2,$$
$$c = -l, \qquad z = -r^2 .$$

The second solution $R_-(r)$ is regular at the origin $r=0$, and at the boundary $r\to\infty$, which makes it our choice for normalizable solution, so that we always have finite fluctuations. The hypergeometric function is a polynomial of degree n if one of the first two arguments is equal to a negative integer $-n, n>0$. Thus, imposing normalizability for the solution $R_-(r)$ means to chose one of the first two arguments of the hypergeometric function have negative integer values, e.g. $b-c+1=-n, n>0$. This gives us the quantization condition from which one calculates the scalar meson spectrum

$$\omega = \sqrt{4+3\nu}+2+l+2n, \tag{28}$$
$$\omega>0, \qquad l,n\in\mathbb{N}_0, \qquad -\frac{4}{3}\le\nu\le 0.$$

By the standard AdS/CFT dictionary one can calculate the conformal dimension of the operators corresponding to Φ from the analysis of the radial equation (26) at the boundary $r\to\infty$. For large r we have the following asymptotic equation:

$$R''(r)+\frac{5}{r}R'(r)-\frac{3\nu}{r^2}R(r)=0, \tag{29}$$

which is solved by

$$R(r) = c_1 r^{-\sqrt{3\nu+4}-2}+c_2 r^{\sqrt{3\nu+4}-2}. \tag{30}$$

This solution contains normalizable and non-normalizable parts that behaves as $r^{k_1}=r^{\Delta-4+p}$, and $r^{k_2}=r^{-\Delta+p}$, for some constant p. Taking the difference of the powers one finds the conformal dimension

$$\Delta = \frac{k_1-k_2}{2}+2 = 2+\sqrt{3\nu+4}, \tag{31}$$

where $k_1=-2+\sqrt{3\nu+4}$, $k_2=-2-\sqrt{3\nu+4}$. Equation (31) allows us to express the spectrum in terms of the conformal dimension

$$\omega = \Delta+l+2n. \tag{32}$$

From (32) we see that the energy of the ground state is given by the conformal dimension of the operator dual to the fluctuations. For higher modes the spectrum is equidistant. This is consistent with similar results for the fluctuations in different background geometries [3, 7]. To calculate the spectrum of conformal dimensions we need to quantise the parameter ν from equation (25b). Separation of variables of the kind $Z=A(\alpha)e^{im_1\beta}e^{im_2\gamma}$ leads to the following quantized values of ν:

$$\nu = (m+m_2)^2+m+m_2-\frac{m_1^2}{4}, \tag{33}$$
$$m,m_1\in\mathbb{N}_0, \quad \frac{m_1}{3}<m_2\le m_1, \quad -\frac{4}{3}\le\nu\le 0.$$

Fluctuations along ϕ, $\theta=\pi/2$

This case needs more careful treatment, because at $\theta=\pi/2$ the radius of the 3-sphere spanned by (α,β,γ) shrinks to zero. This means that a direct substitution of $\theta=\pi/2$ into the equation of motion could cause problems. As it turns out the dependence on θ can be factor out. The equation of motion is once again the Laplace-Beltrami equation $\nabla_a\nabla^a\Phi=0$, which written explicitly gives

$$A(\theta)(I_0(\Phi)+\cos^2\theta I_2(\Phi)+\cos^4\theta I_4(\Phi))=0, \tag{34}$$

Here $A(\pi/2)=0$, so that setting $\theta=\pi/2$ causes the entire equation to become trivial, which is not a case of interest. The relevant equations for the fluctuation Φ comes from setting the coefficients I_0, I_2 and I_4 equal to zero, which leads to the following set of equations:

$$\Delta^{(a)}_{\alpha_i}\Phi=0, \tag{35a}$$
$$-\partial_\tau^2\Phi+\partial_\rho^2\Phi\cosh^2\rho+\partial_\rho\Phi(2\cosh(2\rho)+1)\coth\rho+\coth^2\rho\,\Delta_{\phi_i}\Phi-5\cosh^2\rho\,\Delta^{(b)}_{\alpha_i}\Phi=0, \tag{35b}$$
$$-\partial_\tau^2\Phi+\partial_\rho^2\Phi\cosh^2\rho+\partial_\rho\Phi(2\cosh(2\rho)+1)\coth\rho+\coth^2\rho\,\Delta_{\phi_i}\Phi-3\cosh^2\rho\,\Delta^{(c)}_{\alpha_i}\Phi=0, \tag{35c}$$

where we have the following differential operators:

$$\Delta_{\phi_i}\Phi = \frac{1}{\sin^2\phi_1}\,\partial_{\phi_1}\left(\sin^2\phi_1\,\partial_{\phi_1}\Phi\right) + \frac{1}{\sin^2\phi_1\sin\phi_2}\,\partial_{\phi_2}\left(\sin\phi_2\,\partial_{\phi_2}\Phi\right) + \frac{1}{\sin^2\phi_1\sin^2\phi_2}\,\partial^2_{\phi_3}\Phi\,, \tag{36a}$$

$$\Delta^{(a)}_{\alpha_i}\Phi = \frac{1}{\sin\alpha}\,\partial_\alpha\left(\sin\alpha\,\partial_\alpha\Phi\right) + \frac{1}{\sin^2\alpha}\left(\partial^2_\beta\Phi + \partial^2_\gamma\Phi - 2\,\partial^2_{\beta\gamma}\Phi\cos\alpha\right), \tag{36b}$$

$$\Delta^{(b)}_{\alpha_i}\Phi = \frac{1}{\sin\alpha}\left(\partial_\alpha\left(\sin\alpha\,\partial_\alpha\Phi\right) - \frac{1}{10\sin\alpha}\left(\partial^2_\beta\Phi\left(\cos(2\alpha)-11\right) - 10\,\partial^2_\gamma\Phi + 20\,\partial^2_{\beta\gamma}\Phi\cos\alpha\right)\right), \tag{36c}$$

$$\Delta^{(c)}_{\alpha_i}\Phi = \frac{1}{\sin\alpha}\left(\partial_\alpha\left(\sin\alpha\,\partial_\alpha\Phi\right) - \frac{1}{4\sin\alpha}\left(\partial^2_\beta\Phi\left(\cos(2\alpha)-5\right) - 4\,\partial^2_\gamma\Phi + 8\,\partial^2_{\beta\gamma}\Phi\cos\alpha\right)\right). \tag{36d}$$

After separation of variables one finds

$$\ddot{T}(\tau) + \omega^2\,T(\tau) = 0\,, \quad \Delta_{\phi_i}Y^l(\phi_1,\phi_2,\phi_3) = -l\,(l+2)\,Y^l(\phi_1,\phi_2,\phi_3)\,, \tag{37a}$$

$$\Delta^{(a)}_{\alpha_i}Z(\alpha,\beta,\gamma) = 0, \quad \Delta^{(b)}_{\alpha_i}Z = \lambda\,Z, \quad \Delta^{(c)}_{\alpha_i}Z = \mu\,Z\,, \tag{37b}$$

$$R''_{(b)}(\rho) + (3\coth\rho + \tanh\rho)\,R'_{(b)}(\rho) + \left(\frac{\omega^2}{\cosh^2\rho} - \frac{l\,(l+2)}{\sinh^2\rho} - 5\,\lambda\right)R_{(b)}(\rho) = 0\,, \tag{37c}$$

$$R''_{(c)}(\rho) + (3\coth\rho + \tanh\rho)\,R'_{(c)}(\rho) + \left(\frac{\omega^2}{\cosh^2\rho} - \frac{l\,(l+2)}{\sinh^2\rho} - 3\,\mu\right)R_{(c)}(\rho) = 0\,. \tag{37d}$$

If one subtracts (35b) and (35c) a relation between the eigenvalues μ and λ is found, namely $5\,\lambda = 3\,\mu$, which makes equations (37c) and (37d) equivalent to each other. Therefore one needs to study only one of them. The radial equation (37d) has the same form and solutions as equation (26), but the only difference here being the different values for μ. The spectrum also has the same form as (32)

$$\omega = \Delta + l + 2n\,, \tag{38}$$

where the conformal dimension is $\Delta = \sqrt{4+3\,\mu}+2$. In order to study the eigenvalue μ, we need to make sure that equations $\Delta^{(c)}_{\alpha_i}Z = \mu\,Z$ and $\Delta^{(a)}_{\alpha_i}Z(\alpha,\beta,\gamma) = 0$ are simultaneously satisfied. For that purpose we express $\partial^2_{\beta\gamma}Z\cos\alpha$ from (35a)

$$\partial^2_{\beta\gamma}Z\cos\alpha = \frac{1}{2}\frac{\sin^2\alpha}{\sin\alpha}\partial_\alpha(\sin\alpha\partial_\alpha Z) + \frac{1}{2}\partial^2_\beta\Phi + \frac{1}{2}\partial^2_\gamma\Phi,$$

and substitute this back into $\Delta^{(c)}_{\alpha_i}Z = \mu\,Z$ to find:

$$\partial^2_\beta Z(\alpha,\beta,\gamma) = 2\,\mu\,Z(\alpha,\beta,\gamma)\,. \tag{39}$$

Separation of variables $Z = A(\alpha)\,B(\beta)\,G(\gamma)$ gives an equation for $B(\beta)$

$$B''(\beta) - 2\,\mu\,B(\beta) = 0\,. \tag{40}$$

This equation has a simple solution of the form

$$B(\beta) = B_1\,e^{\sqrt{2\,\mu}\,\beta} + B_2\,e^{-\sqrt{2\,\mu}\,\beta}\,. \tag{41}$$

Therefore, if we want to study $\Delta^{(c)}_{\alpha_i}Z = \mu Z$, so that equation $\Delta^{(a)}_{\alpha_i}Z(\alpha,\beta,\gamma) = 0$ to be also satisfied, we must have the following separation of variables $Z = A(\alpha)\,e^{\sqrt{2\,\mu}\,\beta}\,e^{in_\gamma\gamma}$ in $\Delta^{(c)}_{\alpha_i}Z = \mu\,Z$, which gives an equation for $A(\alpha)$

$$A''(\alpha) + \cot\alpha A'(\alpha) - \frac{4\mu\sin^2\alpha + 2\mu(\cos(2\alpha)-5) + 4n_\gamma^2 + 8in_\gamma\sqrt{2\mu}\cos\alpha}{4\sin^2\alpha}A(\alpha) = 0, \tag{42}$$

The solution is a combination of hypergeometric functions. Requiring finite fluctuations everywhere one finds the general form of the eigenvalue μ:

$$\mu = -k^2/2\,, \tag{43}$$

where $k \in \mathbb{N}_0$. Therefore we conclude that $\mu \leq 0$. But

real and positive energy requires $\mu \geq -4/3$. which leads to only two possible values for μ, namely 0 and -1/2.

Although $\theta = 0$ and $\theta = \pi/2$ cases look similar due to their spectra, they are physically different cases. The $\theta = \pi/2$ is the massive direction from the point of view of the brane probe. Also in this case we have an enhancement of the supersymmetry from $\mathcal{N} = 1$ to $\mathcal{N} = 2$.

Fluctuations along θ, $\phi = 0$

Next we consider fluctuations of $D7$ along the θ transverse direction. In this case there are contributions from both the DBI and WZ parts of the action. Considering only quadratic lagrangian for the fluctuations one finds the equation of motion

$$-\partial_\tau^2\Theta+\cosh^2\rho\Big(\partial_\rho^2+(3\coth\rho+4\tanh\rho)\partial_\rho + \frac{\Delta_{\phi_i}}{\sinh^2\rho}+3\vec{?}\Delta_{\alpha_i}-6\Big)\Theta=0\,, \quad (44)$$

where $\Delta_{\phi_i}\Theta$ and $\widetilde{\Delta}_{\alpha_i}\Theta$ are the same as in (24a) and (24b). Separation of variables leads to the same equations as (25a), (25b) and (25c), but slightly different radial equation

$$R''(\rho)+(3\coth\rho+4\tanh\rho)R'(\rho) + \Big(\frac{\omega^2}{\cosh^2\rho}-\frac{l(l+2)}{\sinh^2\rho}-3\nu-6\Big)R(\rho)=0\,. \quad (45)$$

Making the change $r=\sinh\rho$ we get the following equation:

$$R''(r)+\frac{(8r^2+3)}{r^3+r}R'(r) + \Big(\frac{\omega^2}{(r^2+1)^2}-\frac{l(l+2)}{r^2(r^2+1)}-\frac{3\nu-6}{r^2+1}\Big)R(r)=0\,. \quad (46)$$

One can show that a solution regular at the origin $r=0$, and at the boundary $r\to\infty$, is given by

$$R(r)=c\,r^l\left(r^2+1\right)^{-\frac{1}{4}\sqrt{4\omega^2+9}-\frac{3}{4}}{}_2F_1\left(\frac{l}{2}+\frac{\Delta}{2}-\frac{1}{4}\sqrt{4\omega^2+9},\frac{l}{2}-\frac{\Delta}{2}-\frac{1}{4}\sqrt{4\omega^2+9}+2;l+2;-r^2\right)\,. \quad (47)$$

Quantizing one of the first two arguments of the hypergeometric function gives us the meson spectrum

$$\omega^2=(l+2n+\Delta)^2-\frac{9}{4}\,, \quad (48)$$

where $\Delta=\left(4+\sqrt{25+12\nu}\right)/2$ is the conformal dimension, $l,n\in\mathbb{N}_0$, $-2\geq\nu\geq-10/3$. Once again the spectrum is equidistant in its higher modes, but the ground state is not equal to the conformal dimension of the operators dual to the fluctuations. The additional shift in the ground state $(n,l=0)$ could be resolved by studying the symmetries of the theory and considering some supersymmetric D-brane embeddings. Other origins of the shift are also not excluded.

CONCLUSION

Quantum chromodynamics is the most successful theory describing the strong nuclear force so far. At low energy QCD is strongly coupled, which means that the force between the quarks grows immensely and they tend to form particles called hadrons – a phenomenon known as confinement. In this low energy regime of the theory the usual perturbative techniques are not applicable, which forces us to look for alternative non-perturbative methods. Such alternative techniques arise in String theory in the context of the AdS/CFT correspondence, where the physics of the supersymmetric Yang-Mills systems can be understood by that of the D-brane dynamics and vice versa. The original form of the conjecture focuses on the $\mathcal{N}=4$ super Yang-Mills theory, which is a gauge theory with a huge amount of symmetry. On the other hand generically QCD is neither supersymmetric, nor conformal. One way to make the correspondence more applicable to realistic gauge theories, such as QCD, is to reduce the amount of the supersymmetry. This goal can be achieved in several different ways, one of which is deforming the original $AdS_5\times S^5$ geometry. This was the approach we adopted here by looking at the dynamics of the flavor D7-brane embedded in a deformed background called Pilch-warner geometry.

In this study we obtained the classical embedding equations for the D7 probe brane in global Pilch-Warner background geometry for three relevant cases.

Although highly non-linear the embedding equations have simple constant solutions, which allowed us to fix the probe brane position in space and considerably simplify the study of its fluctuations. In the case when the number of the flavour branes is much smaller than the number of the color branes, the analysis of the scalar fluctuations of the D7 probe brane lead us to analytical results for the meson spectra. All obtained spectra are equidistant in the higher modes, but not all of them have ground states equal to the conformal dimension of the operators dual to the fluctuations.

The fluctuations of the D5-brane as well as the fluctuations of the world volume gauge field can also be studied. Some more complicated cases include turning on external electric or magnetic fields, which further break the supersymmetry. The asymptotic behaviour of the brane embedding equations can be used to extract information about the dual gauge theory, namely the quark condensate, which mixes the left and right degrees of the fundamental matter and leads to a breaking of their chiral symmetry.

REFERENCES

[1] J. M. Maldacena, "The large N limit of superconformal field theories and supergravity", *Adv.Theor.Math.Phys.* **2** (1998) 231, [arXiv:hep-th/9711200].

[2] A. Karch and E. Katz, "Adding flavor to AdS/CFT", *J. High Energy Phys.* **06** (2002) 043, [arXiv:hep-th/0205236].

[3] Johanna Erdmenger, Veselin Filev, "Mesons from global Anti-de Sitter space", JHEP **1101**, 119 (2011), [arXiv:1012.0496v2 [hep-th]].

[4] M. Kruczenski, D. Mateos, R. C. Myers, and D. J. Winters, "Meson spectroscopy in AdS/CFT with flavour", JHEP **07**, 049 (2003), [hep-th/0304032].

[5] J. Erdmenger, N. Evans, I. Kirsch, E. Threlfall, "Mesons in Gauge/Gravity Duals - A Review", *Eur. Phys. J.* **A35** (2008) 81-133, [arXiv:0711.4467 [hep-th]].

[6] Tameem Albash, Clifford V. Johnson, "Dynamics of Fundamental Matter in $\mathcal{N} = 2$ Yang-Mills Theory", JHEP **1104**, 012 (2011), [arXiv:1102.0554v2 [hep-th]].

[7] Dimo Arnaudov, Veselin Filev, Radoslav Rashkov, "Flavours in global Klebanov-Witten background", JHEP **03**, 023 (2014), DIAS-STP-13-14, [arXiv:1312.7224 [hep-th]].

[8] V. Filev, "Aspects of the holograpjic study of flavor dynamics", [arXiv:0809.4701v2 [hep-th]].

[9] Tameem Albash, Veselin Filev, Clifford V. Johnson, Arnab Kundu, "Quarks in an External Electric Field in Finite Temperature Large N Gauge Theory", *J. High Energy Phys.* **06** (2002) 043, [arXiv:0709.1554v3].

[10] Veselin G. Filev, Radoslav C. Rashkov, "Magnetic Catalysis of Chiral Symmetry Breaking. A Holographic Prospective", *Adv.High Energy Phys.* **2010** (2010) 473206, [arXiv:1010.0444 [hep-th]].

[11] Veselin G. Filev, Clifford V. Johnson, Jonathan P. Shock, "Universal Holographic Chiral Dynamics in an External Magnetic Field", JHEP **0908**, 013 (2009), [arXiv:0903.5345 [hep-th]].

[12] K. Pilch and N. Warner, *Phys.Lett.* **B487** (2000) 22-29, [arXiv:hep-th/0002192].

[13] K. Pilch and N. Warner, *Adv.Theor.Math.Phys.* **4** (2002) 627-677, [arXiv:hep-th/0006066].

[14] Dominic Brecher, Clifford V. Johnson and Kenneth J. Lovis, Robert C. Myers, "Penrose limits, deformed pp-waves and the string duals of $\mathcal{N} = 1$ large-N gauge theory", JHEP **10**, 008 (2002), [arXiv:hep-th/0206045].

[15] R. Leigh and M. Strassler, *Nucl.Phys.* **B447** (1995) 95-136, [arXiv:hep-th/9503121].

[16] S. Prem Kumar, David Mateos, Angel Paredesc and Maurizio Piaia, "Towards holographic walking from $\mathcal{N} = 4$ super Yang-Mills", JHEP **1105**, 008 (2011), arXiv:1012.4678 [hep-th]].

[17] J. Polchinski, "Dirichlet-Branes and Ramond-Ramond Charges", *Phys. Rev. Lett.* **75** (1995) 4724, arXiv:hep-th/9510017.

ХОЛОГРАФСКИ МЕЗОНИ В ГЕОМЕТРИЯ НА ПИЛЧ-УОРНЪР

В. Филев[1], Р. Рашков[2,3], Цв. Вецов[3]

[1] *Факултет по теоретична физика, Дъблински институт за напреднали изследвания, ул. „Бърлингтън“ №10, 4 Дъблин, Ирландия*
[2] *Институт по теоретична физика, Виенски технически университет, ул. “Wiedner Hauptstr” №8-10, 1040 Виена, Австрия*
[3] *Физически факултет, Софийски университет “Св. Климент Охридски”, бул. “Дж. Баучер” №5, 1164 София, България*

(Резюме)

AdS/CFT съответствието е удивителна дуалност, свързваща десет-мерна IIB суперструнна теория с малка константа на връзката с четири-мерна суперсиметрична калибровъчна $SU(N)$ теория с голяма константа на връзката, и обратно. В случая калибровъчната теория живее на границата на пространството, в което се движат струните. Това съответствие ни дава възможност да изучаваме непертурбативни проблеми в калибровъчни теории на Янг-Милс чрез методи на класическата Суперструнна теория или Супергравитация.

В оригиналната версия на съответствието от струнна гледна точка имаме стек от N_c на брой паралелни D_3-брани, които генерират ефективната $AdS_5 \times S^5$ геометрия на пространството, а от другата страна имаме $N = 4$ суперсиметрична калибровъчна теория на Янг-Милс. При тази конфигурация краищата на струните се закрепят върху брани от един и същ стек, което прави състоянията да се трансформират в присъединеното представяне на калибровъчната група, а това означава, че липсва фундаментална материя като кварки. Ако към конфигурацията от D_3-брани добавим N_f на брой D_7 пробни брани ($N_f \ll N_c$) ще получим състояния трансформиращи се по фундаменталното представяне на калибровъчната група и следователно ще получим фундаментална материя.

Въвеждането на допълнително външно магнитно или електрично поле деформира първоначалната $AdS_5 \times S^5$ геометрия, което води до нарушаване на суперсиметрията и постигане на теории с по-малко суперсиметрия. Също така се нарушава и киралната симетрия, което води до образуването на кварков кондензат и конфайнмънт, така че струнното описание да се доближава все повече до описание на Квантовата хромодинамика.

В настоящият труд сме изследвали спектъра на скаларните флуктуации на D_7 пробна брана в геометрия на Пилч-Уорнър в глобални координати. Тази геометрия представлява деформирано по определен начин $AdS_5 \times S^5$ пространство, което е решение на 5-мерна $N = 8$ супергравитация вдигната до 10-мерие, като запазва 1/4 от първоначалната суперсиметрия в инфрачервената критична точка, и 1/8 навсякъде другаде.

Bulgarian Chemical Communications, Volume 47, Special Issue B (pp. 262–268) 2015

Manoff's generalized deviation equation and its possible applications in celestial mechanics and relativistic astrometry

B. G. Dimitrov*

Institute for Nuclear Research and Nuclear Energy, Bulgarian Academy of Sciences, 72 Tzarigradsko Chaussee Blvd., 1784 Sofia, Bulgaria

This report proposes a relationship between celestial mechanics and gravitational theory on the base of the s.c. "generalized deviation equation" (GDE), proposed for the first time by Prof. S. Manoff. Using the Hill-Brown system of equations in the framework of the restricted three-body problem Earth-Moon-Sun, it has been proved that it is possible to find the metric tensor components of the gravitational field for the case of stationary, diagonal metric and in the vicinity of the libration points in the space between the Earth and the Moon. Possible applications of the GDE in relativistic astrometry are briefly discussed based on the property of the GDE to account for the relative acceleration and for non-infinitesimal trajectory deviations, caused by the curvature of the space-time geometry.

Key words: celestial mechanics (including n-body problems), astrometry and reference systems, general relativity and gravitation (fundamental problems and general formalism), modified theories of gravity

THE MATHEMATICAL LIMITATIONS OF THE GEODESIC AND GEODESIC DEVIATION EQUATIONS IN GENERAL RELATIVITY

Contemporary celestial mechanics and (Einsteinian) gravitational theory both treat one and the same physical object – the gravitational field around celestial bodies. However, the theoretical grounds of these two theories are different – celestial mechanics is based on the Newton's equation $m\ddot{r} = F_{ext.}$, while the central notion of Einstein's theory is based on the metric tensor $g_{\mu\nu}$ of the gravitational field and the notion of metric $ds^2 = g_{\mu\nu}dx^\mu dx^\nu$.

The implementation of the variational principle in Einstein's gravity with respect to a length functional allows one to derive the geodesic equation

$$\frac{Du^\mu}{Dt} = \frac{dx^\mu}{dt} + \Gamma^\mu_{\lambda\rho} u^\lambda u^\rho = 0\,. \qquad (1)$$

It is important to mention that the variational formalism (see [1]) is performed for proper variations (i.e. with fixed endpoints). Then γ will be stationary for the length functional and for the energy functional if γ is parametrized proportionally to arclength (meaning $\| \dot{\gamma}(t,0) \| = const.$).

Now if X is a vector field along the geodesic line $\gamma : [a,b] \to M$ and Y is a vector field along the same geodesic line, but with fixed endpoints, i.e. $Y(a) = Y(b) = 0$, then the vector field X is called a *Jacobi field* if it satisfies the equation

$$\nabla_{\frac{\partial}{\partial t}} \nabla_{\frac{\partial}{\partial t}} X + R(\dot{\gamma}, X)\dot{\gamma} = 0. \qquad (2)$$

The Jacobi equation (2) is a modified, but more general version of a geodesic deviation equation. Remarkably, in [2] the equation (2) was shown to follow from the standard definition for the *curvature operator* $R(X,Y)$

$$(\nabla_X \nabla_Y - \nabla_Y \nabla_X - \nabla_{[X,Y]})Z = R(X,Y)Z \qquad (3)$$

without the application of any variational principle and under the following more general assumptions:

1. the trajectories of the vector field X are affinely parametrized autoparallels, i. e. $\nabla_X X = 0$. These autoparallel lines have no fixed endpoints. The physical meaning of the autoparallels is that along these lines a test particle would not experience any relative acceleration.

2. the vector fields X and Y commute, i.e. $\pounds_X Y = [X,Y] = 0$.

3. torsion is assumed to vanish $T(X,Y) = 0$, which with account of the formulae

$$\pounds_X Y = \nabla_X Y - \nabla_Y X - T(X,Y) \qquad (4)$$

and the preceeding assumption, gives the equality $\nabla_X Y = \nabla_Y X$. The autoparallel line $\nabla_X X = 0$ is a more general notion compared to the geodesic line, since the autoparallel line is not necessarily a geodesic line. The main motivation for searching new types of deviation equations is the increasing accuracy (of the order of 1 μas - 1 microarcsecond and even less) for the future astrometric measurements for space missions.

* To whom all correspondence should be sent: dimitrov.bogdan.bogdan@gmail.com

© 2015 Bulgarian Academy of Sciences, Union of Chemists in Bulgaria

This Jacobi equation in the paper [2] is called *"the equation of deviation of autoparallels", since it describes geodesics, close to the reference geodesic and with velocities, close to the velocity of the reference geodesic.*

The linearization procedure and the closeness to the reference geodesic is fully consistent with the assumptions for zero relative acceleration $\nabla_X X = 0$ and zero Lie-derivative $\pounds_X Y = [X,Y] = 0$.

More interesting, however, is the case of non-zero Lie-derivative $\pounds_X Y \neq 0$. In such a case, in [3] it has been shown that the "infinitesimality" concept breaks down due to the "moving neighbourhoods" along the curve. In any case, for nonzero relative acceleration and Lie-derivative the deviation equation is not known.

THE MAIN OBJECTIVES OF THIS PAPER

The purposes of this paper is to discuss briefly and provide the motivation for possible applications of the "generalized deviation equation" (GDE) in relativistic astrometry and celestial mechanics. This equation has been proposed for the first time in 1999 by Prof. Sawa Manoff in the review paper [6]. Based on the unusual properties of this equation, related to non-infinitesimal deviations, a concrete application is considered, related to the libration points in the restricted three-body problem Earth-Moon-Sun. The application is based on using the unique solution of the linearized version of the Hill-Brown system of equations (see the known monograph [7]) for the description of the deviation of a single trajectory, which is given by the GDE for the case of coinciding trajectories. Thus, from the Hill-Brown system and the GDE, the metric field components can be found.

RELATIVISTIC ASTROMETRY AND SOME ASTROPHYSICAL MOTIVATION FOR SEARCHING NEW DEVIATION EQUATIONS IN GRAVITY THEORY

Relativistic astrometry investigates light propagation and light deflection from large celestial bodies, taking into account the action of the gravitational field. After perturbing the (flat Minkowski) gravitational background as $g_{\mu\nu} = \eta_{\mu\nu} + h_{\mu\nu}$, the light trajectory deviates slightly [8] and is described by the null geodesic equation in a weak gravitational field.

Such an approach is applied in the theoretical modelling of the relativistic *VLBI* experiment on September the 8, 2002 [9]. On 8 September, 2002 Jupiter passed within $3''.7$ ($\sim$ 14 Jovian radii) of the bright, distant radio quasar $J0842+1835$. The Jovian experiment enabled the measurement of the speed of gravity $c_g = (1.06 \pm 0.2)c$ and the additional retardation of the light signal due to the dragging of the light ray, caused by the time-dependent gravitational field, generated by the translational motion of Jupiter. The dependence on the translational speed v appears after the retarded velocity solution of the Einstein's equations is substituted into the solution of the light geodesic equation [10], where the first term is related with the unperturbed light ray trajectory - the straight line $x^i(t) = x^i_0 + k^i(t - t_0)$. However, the light geodesic equation by itself does not possess the property to account for light deflection by moving sources. Such a possibility exists for the Manoff's generalized deviation equation (GDE), since it can give the deviating trajectory with respect to two other vector fields (tangent to two non-infinitesimally deviating trajectories), as it will be shown in the next section. Evidently, the combination of the Manoff's GDE with the solution of the Einstein's equations would give higher order $\frac{v}{c}$ deflection terms. This is important, since the formalism should not be limited to first-order$\frac{v}{c}$ terms, as in [10]. The reason is that in future astrometric missions like *GAIA* and *SIM* (Space Interferometry Mission), the relativistic deflection terms of order $\frac{v^2}{c^2}$ may reach 1 μas and can be in principle detected [11].

The hypothesis about "isolateness" is not fulfilled, since the participation of the Solar system in the process of the global (Hubble) cosmological expansion [13] results in the fact that the Friedmann-Lemaitre-Robertson-Walker (FLRW) metric defines the properties of space-time not only on the scale of galaxy clusters, but also within the Solar system [14]. The local Hubble expansion [15] is equivalent to a deviation from inertial motion (if understood in the Newtonian sense), given with the Jacobi type of a equation $\frac{d^2x^k}{d\tau^2} + R^k_{0l0}x^k = 0$. This Newtonian type of an equation, as previously explained, is obtained for the case of a zero relative acceleration.

For the case of a non-zero relative acceleration, the usual geodesic equation will be inapplicable, since its mathematical derivation requires fixed endpoints of the geodesic line. From the simple formulae $l = g(u,u)$ for the length of the vector field u after covariant differentiation it can be seen that the change of length is related to the non-zero relative acceleration a. On the other hand, a perturbed theory on a curved FLRW background field would lead to the

s.c. "anisotropic scale factor" [4], since $g_{\mu\nu}g^{\alpha\nu} = (g^{(0)}_{\mu\nu} + h_{\mu\nu})(g^{(0)\alpha\nu} - h^{\alpha\nu}) = \delta^{\alpha}_{\mu} - h_{\mu\nu}h^{\alpha\nu} = l^{\alpha}_{\mu}$. This would lead to a non-zero relative acceleration. So again, the Generalized Deviation Equation would account for deviations of the trajectories of motion.

An example about non-infinitesimall trajectory deviations is given in the monograph of Seeber [5] on satellite geodesy, where several reasons are pointed out for the perturbation of the orbit of a *GPS*-satellite: due to the Earth's obliquity and the nonhomogeneous distribution of matter (inside the Earth and on its surface), the satellite can have an acceleration of $5 \times 10^{-5}\ m/s^2$, causing a deviation of 2 *km* from the orbit in the course of 2 hours. Other celestial bodies such as the Sun, the Moon cause an additional (tidal) acceleration of $5 \times 10^{-6} m/s^2$, leading a deviation of the orbit from 5 to 150 meters again for 2 hours. The last acceleration is 10% of the first one, so it is problematic whether deviating satellite trajectories can be considered as perturbations and infinitesimal deviations.

THE NEW UNUSUAL FEATURES OF THE GENERALIZED DEVIATION EQUATION AND ITS MATHEMATICAL DERIVATION

This section has the purpose to present briefly the mathematical derivation of the GDE and to point out some unusual features of this equation. A central initial moment in Manoff's derivation of the GDE in the paper [6] is the formulae for the Riemann operator

$$[R(\xi,u)] = \nabla_{\xi}\nabla_{u} - \nabla_{u}\nabla_{\xi} - \nabla_{\pounds_{\xi}u}, \qquad (5)$$

which can act on a given vector or tensor field. Then the commutator $[\nabla_w, R(\xi,u)]$ ($w,\xi,u \in T(M)$ - the tangent space to the manifold) can be obtained in the following form

$$[\nabla_w, R(\xi,u)] = [\nabla_w, \pounds\Gamma(\xi,u)] + [\nabla_w, [\nabla_{\xi}, \nabla_u]] - [\nabla_w, [\pounds_{\xi}, \nabla_u]]. \quad (6)$$

It is important to note that neither of the three vector fields w,ξ,u is assumed to be a geodesic line. A new operator has appeared in the above theoretical scheme - *the deviation operator* $\pounds\Gamma(\xi,u)$:

$$[\pounds\Gamma(\xi,u)]v = [R(\xi,u)]v + [\nabla_u\nabla_v - \nabla_{\nabla_u v}]\xi - T(\xi,\nabla_u v) + \nabla_u[T(\xi,v)], \quad (7)$$

where $T(\xi,v)$ is the torsion operator, which will be neglected further. After calculating the commutator

$$[\nabla_w, \pounds\Gamma(\xi,u)] \equiv [\nabla_w, [\pounds_{\xi}, \nabla_u]] - R(w, \pounds_{\xi}u),$$

the expression for the deviation operator $[\pounds\Gamma(\xi,u)]v$ can be rewritten as

$$\nabla_u\nabla_v\xi = ([R(u,\xi)]v) + \nabla_{\xi}\nabla_u v - \nabla_u\pounds_{\xi}v - \nabla_{\pounds_{\xi}u}v - \nabla_u[T(\xi,v)]. \quad (8)$$

This is the generalized deviation equation (GDE), proposed in 1999 by Prof. S. Manoff in [6]. This equation possess the following properties, quite different from the known equation:

1. The equation gives the deviation (vector field) ξ with respect to two other vector fields u and v. Neither of the trajectories, to which these vector fields are tangent, is assumed to be a geodesic line. This is one of the key arguments for the application of the GDE in celestial mechanics.

2. Equation (8) is written in terms of covariant derivatives, which are defined for non-infinitesimal transports of a given vector field along a contour. This equation gives also the non-infinitesimal deviation of the vector field ξ from the two other fields u and v. But this means also that each one of these fields can also be considered to be a deviation field. In other words, the GDE can be written also for the case of the cyclic transformations $\xi \to u \to v \to \xi$ and also $\xi \to v \to u \to \xi$. Thus, a configuration of three trajectories in a gravitational field can be considered to be a stable one, described by a system of three GDEs.

3. The physical reason for the non-infinitesimal deviations is the action of the relative acceleration. This can be seen from an earlierly proposed (again by S. Manoff in the paper [16]) version of the GDE

$$\frac{D^2\xi^i}{ds^2} = R^i_{klj}u^k u^l \xi^j + \xi^i_{;j}F^j + u^k u^l \pounds_{\xi}\Gamma^i_{kl} = u^k u^l \xi^n R^i_{nlk} + u^k\left[\left(\xi^i_{;l}u^l\right)_{;k}\right], \quad (9)$$

where the Lie-derivative $\pounds_{\xi}\Gamma^i_{kl} = \xi^i_{;k;l} - R^i_{klj}\xi^j$ and $a = F = \frac{Du}{d\tau} = u^{\alpha}\nabla_{\alpha}u$ is the relative acceleration. This equation differs from the proposed by J. L. Synge equation of geodesic deviation $\frac{D^2\xi^i}{ds^2} = u^k u^l \xi^n R^i_{nlk}$ only by the last term $u^k\left[\left(\xi^i_{;l}u^l\right)_{;k}\right]$, related to the second covariant derivative $\nabla_u\nabla_u\xi = (\xi^i{}_{;l}\cdot u^l)_{;m}\cdot u^m \cdot e_i$ of the vector field ξ along the vector field u. In fact, the *orthogonal to a non-isotropic vector field u ($g(u,u) = e \neq 0$) projection of this second covariant*

derivative, taken along the same non-isotropic vector field u, represents the relative acceleration ${}_{rel}a = \overline{g}(p_u(\nabla_u\nabla_u\xi))$.

The earlier version of the GDE (9) is derived under the restrictive assumptions $F^i u_i = 0$, $u_i u^i = e$, $e^2 = 1$, the first of which means that the relative acceleration is assumed to be perpendicular to the velocity and the second one is related to the normalization of the velocity vector field. The perpendicularity of the velocity vector and the relative acceleration is characteristic for shear- and expansion- free flows [3]. However, the more general equation (8) is valid for flows with shear and expansion.

The relative acceleration turns out to be of crucial importance for the GDE. Previously, a number of different geodesic deviation equations have been obtained by Synge and Schild, by Mashhoon, by Maugin. In Manoff's earlier paper [16] it was proved that by specifying the choice for the Lie-operator, all these different equations can be derived from equation (9). Most importantly, a solution has been found for the deviation vector describing non-infinitesimally deviating trajectories.

EARLIER ATTEMPTS FOR APPLICATION OF THE GEODESIC DEVIATION EQUATION IN CELESTIAL MECHANICS

An attempt to investigate the perturations of a geodesic trajectory in the gravitational field of a Schwarzschild Black Hole has been undertaken by R. Kerner in [18]. From the Jacobi equation $\nabla_Z^2([X,Y]) = R(Z,[X,Y])Z$ after assuming a zero relative acceleration $\nabla_Z Z = 0$ and also that X and Y are *two linearly independent Jacobi fields*, satisfying $[X,Z] = [Y,Z] = 0$, an (inhomogeneous) extension of the first-order geodesic deviation equation has been obtained. From the found solution (see also [19]), after developing into power series in the eccentricity e, the Kepler's law from celestial mechanics has been obtained:

$$r(t) = \frac{a(1-e^2)}{1+e\cos(\omega_0 t)} \simeq a(1-e\cos\omega_0 t)\,, \qquad (10)$$

where $\omega_0 = \frac{l}{a^2}$ and a is the greater half-axis. So the problem appears: what celestial mechanics trajectories can be found when the relative acceleration is not zero?

For the case in this paper, the trajectory will be found from the condition $\nabla_u\nabla_u u = 0$ for the non-geodesic deviation of a single trajectory, which however does not mean that the relative acceleration $\nabla_u u$ is zero. Also, no expansion in small eccentricity will be used.

APPLICATION OF MANOFF'S GENERALIZED DEVIATION EQUATION IN THE RESTRICTED THREE-BODY PROBLEM EARTH–MOON–SUN IN CELESTIAL MECHANICS

In this section the s.c. "inverse problem" for celestial mechanics will be solved - finding the metric field components if certain celestial mechanics trajectories are known for some specific case. In the present case, the trajectories will be taken from the known Hill-Brown system of equations, describing the motion of a material (not extended) body in the gravitational field of the three-body system Earth-Moon-Sun [20]

$$\frac{d^2x}{dt^2} - 2\frac{d\lambda'}{dt}\frac{dy}{dt} - \frac{d^2\lambda'}{dt^2}y = \frac{dU}{dx}\,, \qquad (11)$$

$$\frac{d^2y}{dt^2} + 2\frac{d\lambda'}{dt}\frac{dx}{dt} + \frac{d^2\lambda'}{dt^2}x = \frac{dU}{dy}\,, \qquad (12)$$

$$\frac{d^2z}{dt^2} = \frac{dU}{dz}\,, \qquad (13)$$

where U is the *potential function*

$$U = \frac{\mu}{\sqrt{x^2+y^2+z^2}} + \frac{n'a'^3}{\sqrt{(r'-x)^2+y^2+z^2}} - \frac{n'^2a'^3}{r'^2}\,. \qquad (14)$$

In the above formulaes, n' is the *mean angular velocity* of the Sun about the Earth, μ is the *sum of the Earth's and the Moon's masses.* In the original paper by Hill [20], another simplification is assumed - the solar eccentricity is neglected, which means that the mean angular velocity of the Sun is considered to be constant, i.e.

$$\frac{d\lambda'}{dt} = n'\,, \quad \frac{d^2\lambda'}{dt^2} = 0, \quad r' = a'\,. \qquad (15)$$

In the monograph [7] this system was analyzed in the aproximation of small deviation (X,Y) from the points (x_0,y_0), i.e. $x = x_0 + X$, $y = y_0 + Y$, where the points (x_0,y_0) are chosen to be non-moving in a reference system, rotating with the mean angular velocity n'.These are *the points of libration*, at which the potential energy has a minimum, i.e. $\frac{dU}{dx} = \frac{dU}{dy} = 0$.

Around the libration points, the Hill's system of equations in a linearized approximation can be presented in the form

$$\dot{X} = AX, \tag{16}$$

where X and A are the corresponding vector and 4×4 matrix respectively:

$$X^T := \left(X, A, \dot{X}, \dot{Y}\right), \tag{17}$$

$$A := \begin{pmatrix} 0 & 0 & 1 & 0 \\ 0 & 0 & 0 & 1 \\ U_{xx} & U_{xy} & 0 & 2 \\ U_{xy} & U_{yy} & 2 & 0 \end{pmatrix}. \tag{18}$$

Since the libration points (x_0, y_0) represent equilibrium (stationary) values, which can be determined uniquely and the solutions (19) for X and Y are also unique (and dependent on time) [7], it can be assumed that the three vector fields u, v and ξ in the generalized deviation equation (8) will coincide and can be determined in the following way

$$\xi = u = v = \left(u_0, \frac{\partial X}{\partial t}, \frac{\partial Y}{\partial t}, \frac{\partial Z}{\partial t}\right), \tag{19}$$

where u_0 will be the $t-$coordinate value of the vector field u, not specified by the Hill's system of equations - further it will be quite natural to put $u_0 = 0$.

Further if $u = v = \xi$ is put in the *generalized deviation equation* (8), then all the terms with the exception of the first on the left - hand side will be equal to zero and so one will be left only with the first term

$$\nabla_u \nabla_u u = 0, \tag{20}$$

which is the analogue of the first term $\frac{d^2x}{ds^2}$ in the usual geodesic deviation equation.

SOLUTIONS OF THE MANOFF'S GENERALIZED DEVIATION EQUATION FOR THE LINEARIZED CASE (NEAR THE LIBRATION POINTS) OF THE HILL-BROWN SYSTEM

We shall proceed with the representation of the equation $\nabla_u \nabla_u u = 0$ for the case of three coinciding solutions $u = v = \xi$ of the *linearized Hill's system of equations in the vicinity of the libration points in the form of a nonlinear system of equations with respect to the (background) metric tensor components.* It shall be assumed that these components are only diagonal.

Since the Hill-Brown system is formulated for the three-dimensional case (three components of the vector field u) and the system of deviation equations is formulated for the four-dimensional case, we shall make the additional assumption that the zero-velocity component u_0 is zero. Further, assuming again that the Greek letters α, β, γ, $\delta = 0,1,2,3$ are the four-dimensional indices and the Latin ones i, j, k, l - the three-dimensional ones, the following equation can be obtained for the $\alpha = 0$ component and for the stationary case $\dot{X} = \dot{Y}_l = 0$:

$$u_l u_{m,l} e^{-Y_l} X_{,m} + \frac{1}{2} u_l e^{-Y_m}\left[u_{[m} X_{,l]} Y_{l,m} - u_m X_{,m} Y_{m,l}\right] - \frac{1}{2}(u_l)^2 e^{-Y_l} X_{,l} Y_{l,l} = 0, \tag{21}$$

where the following variables have been introduced:

$$\begin{aligned} X &:= \ln g_{00}, \\ Y_l &:= \ln g_{ll}, \\ Z_l &:= \frac{g_{00}}{g_{ll}} = \exp\left(X - Y_l\right). \end{aligned} \tag{22}$$

For the second (again stationary) case, when $\alpha = p$ ($p = 1,2,3$), one can obtain the following expression

$$\frac{d}{dt} S_p(u,Y) + \frac{1}{4}(u_p)^2 X_{,p} Y_p = 0, \tag{23}$$

where for the different $p = 1,2,3$ the functions $S_p(u,Y)$ are defined in the following way

$$S_p(u,Y) := (u_{p,1}u_1 + u_{p,2}u_2 + u_{p,3}) - \frac{1}{2}\Big(u_1^2 Y_{1,p} + u_2^2 Y_{2,p} + u_3^2 Y_{3,p} + u_{p-1}u_p Y_{p,p-1} + u_{p+1}u_p Y_{p,p+1}\Big). \tag{24}$$

These equations, obtained from the generalized deviation equation $\nabla_u \nabla_u u = 0$ (14) for the case $\xi = u = v$, represent complicated *nonlinear differential equations* with respect to all the variables $X := \ln g_{00}$ and $Y_l := \ln g_{ll}$ ($l,m = 1,2,3$). The first equation (21) for the $\alpha = 0$ component can be rewritten in the following form

$$K_1(u_1,u_2,u_3,Y_1,Y_2,Y_3)X_{,1} + K_2(u_1,u_2,u_3,Y_1,Y_2,Y_3)X_{,2} + K_3(u_1,u_2,u_3,Y_1,Y_2,Y_3)X_{,3} = 0, \tag{25}$$

where $K_1(..)$, $K_2(...)$ and $K_3(.....)$ are functions, depending on u_l and $Y_{l,k}$, which shall not be written here.

Our further aim will be to show that from the system (23) of differential equations in partial derivatives it will be possible to determine Y_l $\alpha = l = 1,2,3$ and after that, if substituted into (25), the solutions with respect to X can be found. As a result, the whole system of equations for all the variables X, Y_l will turn out to be integrable.

Since the variables X and Y_p do not depend on time, one can differentiate eq. (23) once more with respect to time (the time dependence in this equation is preserved in the u_p-terms and their derivatives) and from both the equations one can obtain an equation, no longer depending on the variable X

$$\frac{\dot{S}_p}{\ddot{S}_p} = -\frac{1}{2}\frac{u_p}{\dot{u}_p} \Rightarrow \left[\ln \dot{S}_p\right]^{\cdot} = -\left[\ln u_p\right]^{\cdot}. \qquad (26)$$

From here the solution for S_p is easily found after two consequitive integrations.This means that using the *assumed* property of *stationarity* of the metric tensor components, the above nonlinear system of equations (25) with respect to the variables X, Y_p has been reduced to a system of equations (26) in partial derivatives with respect to the variables Y_p.

Concerning the equation (25) for the $X = \ln g_{00}$ component, it is shown in [21] (see also Cartan's well-known monograph [22]) that *a necessary and sufficient condition* for the function $X(x,y,z)$ to be a *first integral,* i.e. to satisfy (25) is the fulfillment of the following system of differential equations

$$\frac{dx}{K_1(Y_p(x,y,z)} = \frac{dy}{K_2(Y_p(x,y,z)} = \frac{dz}{K_3(Y_p(x,y,z)}. \qquad (27)$$

Then for all the variables (x,y,z), satisfying the above equations, the function $X(Y_p(x,y,z))$ will be a first integral of equation (25), i.e. will be a constant.

CONCLUSIONS

In this paper a qualitatively new problem has been considered- finding the metric tensor components if a celestial mechanics trajectory is known. Only the deviation from a single trajectory was considered, since then the GDE acquires the most simple form $\nabla_u \nabla_u u = 0$. Even in such a simple form, the equations for the (diagonal) metric tensor components turn out to be complicated nonlinear equations. However, for the case near the vicinity of the libration points, the system of equations turns out to be integrable - first the g_{ii} components can be found from a system of differential equations, and subsequently the g_{00} component. It will be more interesting to consider the case for deviation from two vector fields - for the case of the Jovian 2002 experiment these can be the translational vector of motion and the angular motion vector. This will enable finding the light deflection from rotating bodies, which would require more precise astrometric measurements.

REFERENCES

[1] Jurgen Jost, *Riemannian Geometry and Geometric Analysis*, 4th ed., Springer-Verlag, Berlin - Heidelberg, 2008.

[2] A. Trautman, Gen. Rel. Grav. **41,** 1195-1203 (2009).

[3] S. Manoff and B. G. Dimitrov, Class. Quant. Grav. **19,** 4377 - 4397 (2002) ; gr-qc/0207060.

[4] B.G. Dimitrov, *Intern. J. Geom.Meth.Mod. Phys.* **5**, 677-698 (2008).

[5] G. Seeber, *Satellite Geodesy*, Walter de Gruyter, Berlin, New York, 2003.

[6] S. Manoff, Part. Nucl. **30,** 517 - 549 (1999) [Rus. Edition: Fiz. Elem. Chast. Atomn. Yadra **30,** 1211 - 1269 (1999)]; gr-qc/0006024.

[7] C. D. Murray and S. F. Dermott, *Solar System Dynamics*, Cambridge University Press, Cambridge, 1999.

[8] S. M. Kopeikin and G. Schafer, Phys. Rev. **D60,** 124002-1 - 124002-44 (1999).

[9] S. M. Kopeikin, *Phys. Lett.* **A312**, 147-151 (2003).

[10] S. M. Kopeikin, *Class. Quant. Grav.* **21**, 3251-3286 (2004).

[11] E. B. Fomalont and S. M. Kopeikin, *Astroph. J.* **598**, 704-711 (2003).

[12] S. M. Kopeikin and E. B. Fomalont, *Found. Phys.* **36**, 1244-1285 (2006).

[13] S. M. Kopeikin, arXiv: 1012.0954v1 [astro-ph].

[14] S. M. Kopeikin, Einstein's Equivalence Principle in Cosmology, 52 p., arXiv: 1311.4912 [gr-qc].

[15] M. Carrera, D. Giulini, *Rev.Mod. Phys.* **82**,169-208 (2010).

[16] S. Manoff, Gen. Rel. Gravit. **11,** 189-204 (1979).

[17] J. Weber, *General Relativity and Gravitational Waves*, Interscience Publishers, New York, 1961 [Republication by Dover Publications Inc., Mineola, New York, 2004].

[18] R. Kerner, J. W. van Holten and R. Colistete Jr., Class. Quant. Grav. **18,** 4725-4742 (2001).

[19] R. Kerner and S. Vitale, *in Proceed. of Science, 5th International School on Field Theory and Gravitation*, April 20-24, 2009, Cuiaba city, Brazil.

[20] G.W. Hill, *Researches in the Lunar Theory* I,II,III, Amer. Journ. of Mathem. **1,** 5-26, 129-147, 245-261 (1878).

[21] A. P. Markeev, *Theoretical Mechanics*, Regul. and Chaotic Dynamics Publish. House, 2nd corrected edition, 1999 (in Russian).

[22] E. Cartan, *Integral Invariants*, Editorial URSS Publ. House, 1998 (in Russian).

ОБОБЩЕНО УРАВНЕНИЕ НА ДЕВИАЦИЯТА НА С. МАНОВ И ВЪЗМОЖНИТЕ МУ ПРИЛОЖЕНИЯ В НЕБЕСНАТА МЕХАНИКА И РЕЛАТИВИСТКАТА АСТРОМЕТРИЯ

Б. Димитров

Институт за ядрени изследвания и ядрена енергетика, Българска академия на науките, бул. "Цариградско шосе" №72, 1784 София, България

(Резюме)

Съвременната релативистка небесна механика (РНМ) води своето начало от работите на де-Ситтер от 1918 г., в които чрез методите на ОТО се извеждат формули за изменението на перихелия на Меркурий, Венера, Марс и Земята. Независимо от това и последващото развитие на РНМ (например монографиите на В.А. Брумберг), обратната задача за намиране на метрическия тензор на гравитационното поле при зададени параметри на небесно-механическите траектории и досега остава нерешена.

В доклада се обосновава и прилага нов подход за решаването на такава (обратна) задача чрез използуването на т. н. "обобщено уравнение на девиация" (ОУД), предложено за първи път от проф. С. Манов (ИЯИЯЕ, БАН) през 1999 г. За разлика от известното уравнение за геодезична девиация в ОТО, което задава инфинитезимални отклонения от една геодезична линия, ОУД задава произволно (неинфинитезимално) отклонение от две произволно зададени (негеодезични) векторни полета (траектории) при зададени компоненти на метрическия тензор, което прави възможно приложението му в небесната механика

Предлаганият нов подход се основава на решаването на обратната задача, която условно би могла да се раздели на два етапа: 1. задаване на небесно-механичните траектории (векторни полета) посредством решенията на известната система уравнения на Хилл-Браун в рамките на т. н. "ограничена задача за движение на три тела Земя-Луна-Слънце" 2. заместване на тези решения в ОУД и решаването на съответните (в общия случай – нелинейни) диференциални уравнения относно компонентите на метрическия тензор при предположение за диагонална и стационарна метрика. Показано е, че за случая на либрационните точки върху траекториите на движение, където потенциалната енергия има екстремум, намирането на компонентите на метрическия тензор е възможно, тъй като получените уравнения могат да се интегрират.

Дискутират се накратко и възможните приложения на ОУД в релативистката астрометрия, предвид на свойството на ОУД да отчита относителното ускорение, породено от кривината на пространствено-временната геометрия при отклонението на светлинен лъч например в силно гравитационно поле. Стандартните уравнения на геодезичните и на геодезична девиация от ОТО не притежават това свойство, тъй като математическият им извод предполага закрепени краища на геодезичната линия, което се нарушава при наличие на относително ускорение.

Bulgarian Chemical Communications, Volume 47, Special Issue B (pp. 269–274) 2015

Non-universal critical properties of the ferromagnetic mean spherical model with long-range interaction

E. S. Pisanova*, S. I. Ivanov

Department of Theoretical Physics, University of Plovdiv, 24 Tzar Assen Str., 4000 Plovdiv, Bulgaria

The bulk critical behavior of the mean spherical model with long-range interaction (decaying at large distances r as $r^{-d-\sigma}$, where d is the space dimensionality and $0 < \sigma \leq 2$) is studied at the upper critical dimension by using the properties of the Lambert W-function. Exact expressions for the spherical field, the free energy density and the specific heat per spin are presented. The exact results are compared with the asymptotic ones on the basis of the calculated absolute and relative errors. Asymptotic analytical expressions for the absolute errors are also provided. It is shown that the obtained results are valid in a broader neighborhood of the critical point.

Key words: bulk critical behavior, upper critical dimension, long-range interaction, the Lambert W-function

INTRODUCTION

The spherical model of a ferromagnet of Berlin and Kac [1] is one of the few statistical mechanical models which have been exactly solved in any space dimensionality d and exhibit a non-trivial critical behavior for $d_l < d < d_u$, where d_l and d_u are the lower and the upper critical dimensions, respectively. It has been defined on the regular d-dimensional lattice. With each lattice site one associates a continuous real variable (spin). The spins of this model are subject to a global constraint with spherical symmetry, while those of the Ising model are subject to local ones. When the global constraint of Berlin and Kac [1] is satisfied in the sense of an ensemble average, the model is known as the mean spherical model. As it could be expected, the spherical model and the mean spherical model have the same thermodynamic properties (see [2]). The equivalence between the infinite translational invariant standard spherical model and the Heisenberg model with n spin components, in the case $n \to \infty$, has been discussed in [2–4].

The investigation of systems with long-range interaction was initiated on the ferromagnetic spherical model [5]. The spherical model has been extensively used for analytic exploration of the scaling properties of confined systems, in one or more directions (see e.g. [2, 6–11] and references therein). The Casimir effect which remains the central theme of both theoretical and experimental investigations, has been theoretically studied on the spherical model in several papers [12–16].

Different quantum versions of the spherical model (or the large n-limit of $O(n)$ symmetric models), some of which are models of Bose gas, are also available [17–27].

Recently it has been shown [28–30] that the Lambert W-function can be applied for an exact computation of non-universal critical properties with leading logarithmic behavior at the upper critical dimension of the system. The basic mathematical properties of the Lambert W-function, some of its applications as well as interesting historical remarks have been presented in [31].

In this paper, using the properties of the Lambert W-function we study the bulk critical behavior of the ferromagnetic mean spherical model with long-range interaction (decreasing at long distances r as $r^{-d-\sigma}$, $0 < \sigma \leq 2$) at the upper critical dimension, $d = 2\sigma$. At zero field in the neighborhood of the critical point, exact analytical results for the spherical field, the free energy density and the specific heat per spin are obtained and compared with the known asymptotic ones [2] on the basis of the calculated absolute and relative errors. Special attention is paid to the cases when the upper critical dimension coincides with the real physical dimensions (chains, thin layers, i.e. films and three-dimensional systems). It is shown that the obtained results hold true in a broader neighborhood of the critical point. Besides, the expansion of the critical region is estimated.

* To whom all correspondence should be sent:
katia_pisanova@abv.bg

© 2015 Bulgarian Academy of Sciences, Union of Chemists in Bulgaria

THE MODEL

The Hamiltonian of the mean spherical model on a d-dimensional lattice is

$$H = -\frac{1}{2}\sum_{ij} J_{ij} s_i s_j + \frac{\mu}{2}\sum_i s_i^2 - h\sum_i s_i, \qquad (1)$$

where the spin at the i-th site, $s_i \equiv s_i(\mathbf{r})$, is a continuous real variable, J_{ij} is the interaction matrix between spins at sites i and j, and h is an ordering external magnetic field. The spherical field μ provides the spherical constraint

$$\sum_i \langle s_i^2 \rangle = N, \qquad (2)$$

where N is the total number of spins on the lattice and $\langle \cdots \rangle$ denotes the standard thermodynamic average computed with the Hamiltonian (1).

For long-range interaction potential

$$J(r) \sim r^{-(d+\sigma)}, \quad \sigma > 0 \quad \text{and} \quad r \to \infty, \qquad (3)$$

the long-wavelength (small $k \equiv |\mathbf{k}|$) leading asymptotic of its Fourier transform is $U(k) \sim k^{\sigma}$. The case $\sigma \geq 2$ corresponds to short-range interaction, i.e. in this case the universality class does not depend on σ. For $0 < \sigma < 2$, we have long-range interaction and the critical behavior depends on σ. The critical behavior of systems with long-range interaction in restricted geometry was discussed in [32].

At zero field, the thermodynamic limit form of the mean spherical constraint (2) is

$$\frac{dU_{d,\sigma}(\phi)}{d\phi} = K, \qquad (4)$$

where $K = \beta J$, $\beta = 1/(k_B T)$ (with the Boltzmann's constant $k_B = 1$), $\phi = \mu/J$ is the scaled spherical field and the function U is defined by

$$U_{d,\sigma}(\phi) = (2\pi)^{-d} \int_{-\pi}^{\pi} dk_1 \cdots \int_{-\pi}^{\pi} dk_d \ln(\phi + |\mathbf{k}|^{\sigma}). \qquad (5)$$

The left hand side of (4) is a strictly decreasing function of $\phi \geq 0$ attaining its maximum at $\phi = 0$ if $d > \sigma$. The considered model undergoes a phase transition at the critical point K_c, determined by

$$K_c = \frac{dU_{d,\sigma}}{d\phi}(0), \quad d > \sigma. \qquad (6)$$

The bulk free energy density of the model has the following form [2]:

$$\beta f(K) = \frac{1}{2}(U_{d,\sigma}(\overline{\phi}) - K\overline{\phi}) + \frac{1}{2}\ln K - K, \qquad (7)$$

where $\overline{\phi}$ is the solution of (4).

Equations (7) and (4) provide the basis for studying the bulk critical behavior of the model. By differentiating twice the free energy density (7) with respect to the temperature, one obtains the zero-field specific heat per spin

$$c(K) := -K^2 \frac{\partial^2}{\partial K^2}(\beta f(K)) = \frac{1}{2} + \frac{1}{2}K^2 \frac{\partial \overline{\phi}}{\partial K}. \qquad (8)$$

Since ϕ decreases when K increases, see (4), and $\phi = 0$ for $K > K_c$, then the zero-field specific heat per spin keeps its maximum value $c(K) = 1/2$ for all $K \geq K_c$ and the Dulong-Petit low of classical thermodynamics holds for all $T \leq T_c$ [2].

SOME EXACT RESULTS AND THE ASYMPTOTIC ONES

The function U, defined by (5), can be represented in the form

$$U_{d,\sigma}(\phi) = \frac{S_d}{(2\pi)^d} \int_0^{x_D} x^{d-1} \ln(\phi + x^{\sigma}) dx, \qquad (9)$$

where $x_D = 2\pi(d/S_d)^{1/d}$ is the radius of the spherically Brillouin zone, $S_d = 2\pi^{d/2}/\Gamma(d/2)$ is the surface of the d-dimensional unit sphere and Γ is the Euler gamma function.

At the upper critical dimension $d = 2\sigma$ in the neighborhood of the critical point ($K_c/K - 1 \to 0^+$), i.e. when $\phi \ll 1$, the asymptotic behavior of the function (9) is

$$U_{2\sigma,\sigma}(\phi) \approx \left(\ln x_D^{\sigma} - \frac{1}{2}\right) + 2\left(\frac{\phi}{x_D^{\sigma}}\right) + \left(\frac{\phi}{x_D^{\sigma}}\right)^2 \ln\left(\frac{\phi}{x_D^{\sigma}}\right) - \frac{1}{2}\left(\frac{\phi}{x_D^{\sigma}}\right)^2, \qquad (10)$$

and for the mean spherical constraint (4), one obtains

$$\left(\frac{\phi}{x_D^{\sigma}}\right) \ln\left(\frac{\phi}{x_D^{\sigma}}\right) \approx -\left(\frac{K_c}{K} - 1\right). \qquad (11)$$

The critical value, determined by (6), is $K_c = 2/x_D^{\sigma}$. By the substitution $\ln(\phi/x_D^{\sigma}) = t$, the equation (11) takes the form of the defining equation for the Lambert W-function [31]

$$W(x)e^{W(x)} = x$$

which always has an infinite number of solutions, most of them complex, and so $W(x)$ is a multivalued function. When x is a real variable, then for $-1/e \le x < 0$ there are two branches with real values of $W(x)$: the branch $W_0(x)$ satisfying $-1 \le W_0(x)$ and the branch $W_{-1}(x) \le -1$, as $\lim_{x\to 0^-} W_{-1}(x) = -\infty$.

Thus, in therms of the Lambert W-function, the exact solution of (11) is

$$\overline{\phi} = x_D^{\sigma} \exp[W_{-1}(-t)], \tag{12}$$

where the variable $t = K_c/K - 1$ is a measure of the deviation from the critical point K_c. The choice of the real branch $W_{-1}(x)$ of the Lambert W-function among the solutions of (11) corresponds to the fact that at $t = 0\,(K = K_c)$ the scaled spherical field ϕ vanishes.

For the free energy density near the critical point, from (7), (10) and (12) omitting the terms of order $O(\overline{\phi}^2 \ln \overline{\phi})$, we obtain

$$\beta f(t) \approx \beta_c f(0) + \beta \delta f(t), \tag{13}$$

where the free energy density at $t = 0\,(K = K_c)$ is

$$\beta_c f(0) = \frac{1}{2}\left(\ln x_D^{\sigma} - \frac{1}{2}\right) + \frac{1}{2}\ln K_c - K_c \tag{14}$$

with correction

$$\delta(\beta f(t)) = \frac{1}{2} K_c t\, \overline{\phi} = t \exp[W_{-1}(-t)]. \tag{15}$$

For the specific heat per spin near the critical point from (8) and (12), using the derivative of the Lambert W-function, we get the following exact result

$$c(t) = \frac{1}{2} + \frac{1}{1 + W_{-1}(-t)}. \tag{16}$$

The last result shows that the specific heat capacity remains finite at $t = 0\,(K = K_c)$ but at this point its graph has a cusp. The obtained expression (16) allows us to find a critical region $(0, t_0]$ in which the zero-field specific heat per spin decreases to zero and at the endpoint, we have $c(t_0) = 0$. From this and (16), we obtain

$$W_{-1}(-t_0) = -3.$$

Thus, for the endpoint of the critical region, we get $t_0 = 3\,e^{-3}$.

Using the absolutely convergent series [31]

$$W_{-1}(-t) = L_1 - L_2 + \frac{L_2}{L_1} + \frac{L_2(-2 + L_2)}{2L_1^2} + \frac{L_2(6 - 9L_2 + 2L_2^2)}{6L_1^3} + \frac{L_2(-12 + 36L_2 - 22L_2^2 + 3L_2^3)}{12L_1^4} + O\left(\left(\frac{L_2}{L_1}\right)^5\right), \tag{17}$$

where $L_1 = \ln t$ and $L_2 = \ln(-\ln t)$, we get the asymptotic expressions for the scaled spherical field $\overline{\phi}$, the correction to the free energy density at $t = 0\,(K = K_c)$ and the specific heat per spin. Retaining the leading two terms of (17) from (12), (15) and (16), we obtain as follows

$$\overline{\phi}_{appr.} \approx -x_D^{\sigma} \frac{t}{\ln t}, \tag{18}$$

$$\delta(\beta f(t))_{appr.} \approx -\frac{t^2}{\ln t}, \tag{19}$$

and

$$c_{appr.}(t) \approx \frac{1}{2} + \frac{1}{\ln t}. \tag{20}$$

In the theory of phase transitions these asymptotic expressions show a typical behavior at the upper critical dimension. The logarithmic solution (18) is well known (see e.g. [2, p. 88]. It was obtained, neglecting the linear ϕ-term in (11). From (20), for the endpoint of the interval $(0, t_{0appr.}]$, we obtain $t_{0appr.} = e^{-2}$. The specific heats (16) and (20), are graphically presented in Fig. 1.

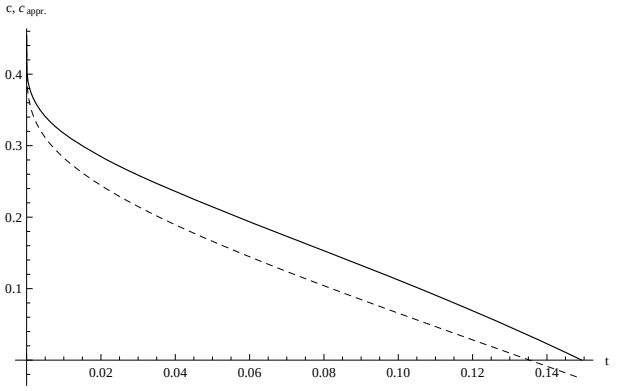


Fig. 1. The dependences of the specific heats c and $c_{appr.}$ on the deviation from the critical point t. The dashed line corresponds to $c_{appr.}$.

COMPARISON BETWEEN THE EXACT RESULTS AND THE ASYMPTOTIC ONES

From (17), retaining the leading L_1/L_2-term, we get the following asymptotic expressions for the absolute errors:

$$\Delta\overline{\phi} = |\overline{\phi} - \overline{\phi}_{appr.}| \approx x_D^{\sigma} \frac{t}{\ln^2 t}, \tag{21}$$

$$\Delta(\beta f) = \beta |f - f_{appr.}| \approx \frac{t^2}{\ln^2 t} \tag{22}$$

and

$$\Delta c = |c - c_{appr.}| \approx \frac{1}{2|\ln t|^3}. \tag{23}$$

On the other hand, we get the following estimate for the expansion of the critical region

$$\Delta t = t_0 - t_{0appr.} = (3-e)/e^3. \tag{24}$$

For more detailed analysis, some numerical data for the absolute errors and relative errors are given in Table 1 and Table 2, respectively. Special attention is paid to systems with real physical dimensions (chains, thin layers, i.e. films and three-dimensional systems).

CONCLUSIONS

In a broader neighborhood of the critical point, the critical behavior of the mean spherical model with long-range interaction (decaying at large distances r as $r^{-d-\sigma}$, where d is the space dimensionality and $0 < \sigma \leq 2$) is studied.

Exact expressions for the scaled spherical field (12), the correction to the free energy density (15) and the specific heat per spin (16), in terms of the Lambert W-function are obtained. These results are compared with the known asymptotic ones on the basis of the calculated absolute and relative errors. Besides, using the series expansion of the Lambert W-function, asymptotic analytical expressions for the absolute errors are presented (see (21), (22) and (23)).

The obtained expressions (16) and (20) for the specific heat capacity per spin allow us to estimate the expansion of the critical region (24). This expansion easily can be seen in Fig. 1.

Let us note that the absolute error $\Delta\overline{\phi}$ and the relative error $|\Delta(\beta f)/(\beta f)|$ depend on both the deviation from the critical point t and the upper critical dimension $d = 2\sigma$ of the system, while the absolute errors $\Delta(\beta f)$ and Δc and the relative errors $|\Delta\overline{\phi}/\overline{\phi}|$ and $|\Delta c/c|$ depend only on t (see Table 1 and Table 2).

Finally, this treatment by using the Lambert W-function is applicable in a broader neighborhood of the critical point. Moreover, it can be applied to a wide class of models with leading logarithmic behavior at the upper critical dimensions.

Table 1. Numerical data for the absolute errors

	$\Delta\overline{\phi}$			$\Delta(\beta f)$	Δc
t	$d=1(\sigma=1/2)$	$d=2(\sigma=1)$	$d=3(\sigma=3/2)$		
1×10^{-5}	2.881×10^{-7}	5.762×10^{-7}	1.250×10^{-6}	1.625×10^{-12}	0.010
1×10^{-4}	4.052×10^{-6}	8.104×10^{-6}	1.759×10^{-5}	2.286×10^{-10}	0.014
1×10^{-3}	6.219×10^{-5}	1.243×10^{-4}	2.700×10^{-4}	3.509×10^{-8}	0.021
1×10^{-2}	1.110×10^{-3}	2.221×10^{-3}	4.821×10^{-3}	6.265×10^{-6}	0.034
1×10^{-1}	0.027	0.054	0.119	1.547×10^{-3}	0.046

Table 2. Numerical data for the relative errors

	$\lvert\Delta(\beta f)/(\beta f)\rvert$[%]			$\lvert\Delta\overline{\phi}/\overline{\phi}\rvert$[%]	$\lvert\Delta c/c\rvert$[%]
t	$d=1(\sigma=1/2)$	$d=2(\sigma=1)$	$d=3(\sigma=3/2)$		
1×10^{-5}	1.575×10^{-10}	3.476×10^{-10}	9.952×10^{-10}	23.023	2.568
1×10^{-4}	2.215×10^{-8}	4.889×10^{-8}	1.399×10^{-7}	26.674	3.649
1×10^{-3}	3.401×10^{-6}	7.504×10^{-6}	2.148×10^{-5}	31.996	5.727
1×10^{-2}	6.072×10^{-4}	1.339×10^{-3}	3.836×10^{-3}	40.554	10.849
1×10^{-1}	0.150	0.332	0.963	55.353	41.321

REFERENCES

[1] T. H. Berlin, and M. Kac, *Phys. Rev.* **86**, 821 (1952).

[2] J. G. Brankov, D. M. Danchev and N. S. Tonchev, in *Series in Modern Condensed Matter Physics* (World Scientific, Singapore, 2000), p. 1.

[3] H. E. Stanley, *Phys. Rev.* **176**, 718 (1968).

[4] A. M. Khorunzhy, B. A Khoruzhenko, P. L. A. and M. V. Shcherbina, in *Phase Transitions and Critical Phenomena*, edited by C. Domb and L. Lebowitz (Academic Press, New York, 1992), p. 73.

[5] G. S. Joyce, *Phys. Rev.* **146**, 349 (1966).

[6] M. N. Barber, and M. E. Fisher, *Annals of Phys.* **77**, 1 (1973).

[7] S. Singh, and R. K. Pathria, *Phys. Rev. B* **32**, 4618 (1985).

[8] V. Privman, in *Finite Size Scaling and Numerical Simulations of Statistical Systems*, edited by V. Privman (World Scientific, Singapore, 1990), p. 1.

[9] X. S. Chen, and V. Dohm, *Phys. Rev. E* **67**, 056127 (2003).

[10] D. M. Dantchev, and J. G. Brankov, *J. Phys. A: Math. Gen.* **36**, 8915 (2003).

[11] H. Chamati, *J. Phys. A.: Math. Theor.* **41**, 375002 (2008).

[12] D. M. Dantchev, *Phys. Rev. E* **53**, 2104 (1996).

[13] D. M. Dantchev, *Phys. Rev. E* **58**, 1455 (1998).

[14] H. Chamati, and D. M. Dantchev, *Phys. Rev. E* **70**, 066106 (2004).

[15] D. M. Dantchev, H. W. Diehl, and D. Grüneberg, *Phys. Rev. E* **73**, 016131 (2006).

[16] D. M. Dantchev, and D. Grüneberg, *Phys. Rev. E* **79**, 041103 (2009).

[17] A. Verbeure, and V. Zagrebnov, *J. Stat. Phys.* **69**, 329 (1992).

[18] Y. Tu, and P.B. Weichman, *Phys. Rev. Lett.* **73**, 6 (1994).

[19] T. W. Nieuwenhuizen, *Phys. Rev. Lett.* **74**, 4289 (1995).

[20] T. Vojta, *Phys. Rev. B* **53**, 710 (1996).

[21] B. Momont, A. Verbeure, and V. Zagrebnov, *J. Stat. Phys.* **89**, 633 (1997).

[22] T. W. Nieuwenhuizen, and F. Ritort, *Physica A* **250**, 8 (1998).

[23] H. Chamati, D. M. Dantchev, E. S. Pisanova, and N. S. Tonchev, *Preprint No IC/97/82* Trieste, cond-mat/9707280 (1997).

[24] H. Chamati, E. S. Pisanova, and N. S. Tonchev, *Phys. Rev. B* **57**, 5798 (1998).

[25] H. Chamati, D. M. Dantchev, and N. S. Tonchev, *Eur. Phys. J. B* **14**, 307 (2000).

[26] M. Napiorkowski, and J. Piasecki, *Phys. Rev. E* **84**, 061105 (2011).

[27] M. Napiorkowski, P. Jakubczyk, and K. Nowak, *J. Stat. Mech.* P06015 (2013).

[28] E. S. Pisanova, N. S. Tonchev, and Hr. T. Kisov, *AIP Conf. Proc.* **1203**, 255 (2009).

[29] E. S. Pisanova, and N. S. Tonchev, *J. Phys.: Conf. Ser.* **253**, 012020 (2010).

[30] E. S. Pisanova, and S. I. Ivanov, *Bulg. J. Phys.* **40**, 159 (2013).

[31] R. M. Corlles, G. H. Gonnet, D. E. Hare, D. J. Jeffrey, and D. E. Knuth, *Advances in Comput. Math.* **5**, 329 (1996).

[32] H. Chamati, and N. S. Tonchev, *Mod. Phys. Lett. B* **17 (23)**, 1187 (2003).

НЕУНИВЕРСАЛНИ КРИТИЧНИ СВОЙСТВА НА СРЕДНОСФЕРИЧНИЯ МОДЕЛ НА ФЕРОМАГНЕТИК С ДАЛЕКОДЕЙСТВИЕ

Е. Писанова, С. Иванов

Физически факултет, Пловдивски университет "Паисий Хилендарски",
ул. "Цар Асен" №24, 4000 Пловдив, България

(Резюме)

Разгледан е класически средносферичен модел с далекодействие [1] в горната критична размерност. На основата на свойствата на функцията на Ламберт [2] са получени точни резултати за сферичното поле, плътността на свободната енергия и специфичната топлина (отнесена към един спин) в една по-широка околност на критичната точка. За случаите, когато горната критична размерност на системата съвпада с реалните физични размерности (верижка, тънък слой и тримерна система) получените точни резултати са сравнени с асимптотичните такива на база пресметнатите абсолютни и относителни грешки.

Разглеждането е приложимо към широк клас модели за точно пресмятане на неуниверсални критични свойства с асимптотично логаритмично поведение в горната критична размерност.

1. J. G. Brankov, D. M. Danchev and N. S. Tonchev, *Theory of Critical Phenomena in Finite-Size Systems: Scaling and Quantum Effects*, Series in *Modern Condensed Matter Physics,* vol. **9**, World Scientific, Singapore, 2000.
2. R. M. Corlles, G. H. Gonnet, D. E. Hare, D. I. Jeffrey and D. E. Knuth, *Advances in Comput. Math*. **5** (1996) 329-359.

Bulgarian Chemical Communications, Volume 47, Special Issue B (pp. 275–281) 2015

Fundamental quantum limit in Mach-Zehnder interferometer

A. Angelow*, E. Stoyanova

Institute of Solid State Physics, Bulgarian Academy of Sciences,
72 Tzarigradsko Chaussee Blvd., 1784 Sofia, Bulgaria

In this article we discuss the concept of standard quantum (shot-noise) limit and fundamental quantum limit (completely quantum mechanical) in Mach-Zehnder Interferometer. With the method of linear invariants the three independent quantum fluctuations are determined in Schrödinger Minimum Uncertainty States. On the base of more general Uncertainty Relation (Schrodinger-1930), we accurately define the notion of fundamental quantum limit. The analytical consideration involves the general term Covariance (compare to Variance) of two quantum variables. Explicit new formula for the fundamental quantum limit is obtained.

Key words: quantum mechanics, uncertainty relations, Heisenberg limit, Schrödinger limit, interferometry

INTRODUCTION

The light interferometry is a one of the primary methods to prove experimentally basic laws in physics. For example a lot of discussions in the scientific literature was done, dedicated to improve gravitational radiation using Quantum Mechanical interferometry [1,2]. Much work has been done on reduction of the quantum noise by using input light prepared in non-classical states [3–9]. Because of the particle nature of the light, there exists some fundamental limitations of its sensitivity, which are the subject of present article: standard Quantum Limit(semiclassical) and the Fundamental Quantum Limit, the latter known as Heisenberg Limit [10–12]. Introducing the more accurate Uncertainty Relation than that of Heisenberg, we will precise the formulation of Quantum Limit. Classical and semiclassical treatments of these measurements is less precise as quantum one. Quantum interferometry is the best tool for phase estimation due to its sensitivity. The goal of quantum interferometry is to estimate phases beyond the standard quantum limit. It was discovered that squeezed vacuum, injected into the normally unused port of an interferometer, provides sensitivity below the shot-noise limit [1]. It is possible to reach even better sensitivity if a nonlinear interaction between photons in the Mach-Zehnder interferometer takes place (for example – parametric down-conversion, [1]).

In this article we consider shortly the method of linear integrals of motion (in second section). In the third section we interpret the two notions *Standard Quantum Limit* and *Fundamental Quantum Limit*. We examine the resemblances and distinctions between them and we derive a new formula for the Fundamental Quantum Limit using the general uncertainty relation.

* To whom all correspondence should be sent:
a.angelow@issp.bas.bg

METHOD OF LINEAR INTEGRALS OF MOTION

One of the most revolutionary consequences that quantum mechanics bequeathed as a fundamental principle in physics is the refusal of strong determinism. That is why the uncertainty relation (called uncertainty principle in the beginning of quantum mechanics) plays fundamental role. The uncertainty relation for the two canonical variables was introduced for the first time by Heisenberg (1925), and generalized to any two observables by Schrödinger [13, 14]:

$$(\Delta A)^2(\Delta B)^2 \geq Cov^2(A,B) + |\frac{1}{2}\langle [A,B]\rangle|^2, \quad (1)$$

where the covariance for non-commuting operators A and B is defined as

$$Cov(A,B) \equiv \frac{1}{2}\langle AB + BA\rangle - \langle A\rangle\langle B\rangle, \quad (2)$$

and the variance is defined as $(\Delta A)^2 = Cov(A,A)$.

Neglecting the first term on the right side, we receive the Heisenberg Uncertainty Relation:

$$(\Delta A)^2(\Delta B)^2 \geq |\frac{1}{2}\langle [A,B]\rangle|^2. \quad (3)$$

We will remind the method of linear integral of motions presented in [15–17] Let us consider a classical system with s degree of freedom and let $u = u(q_1,...q_s,\ p_1,...p_s,t)$ be a dynamical variable of this system. Expressed in terms of Poisson brackets $\{,\}$, the full derivative of u with respect to t is

$$\frac{du}{dt} = \frac{\partial u}{\partial t} + \{u, H_{class}\}. \quad (4)$$

© 2015 Bulgarian Academy of Sciences, Union of Chemists in Bulgaria

By definition u^{inv} will be an integral of motion (invariant) iff $du^{inv}/dt = 0$, i.e.

$$\frac{\partial u^{inv}}{\partial t} + \{u^{inv}, H_{class}\} = 0. \tag{5}$$

As far as there is a principle of correspondence between classical and quantum mechanics, the analogy requires the existence of $2s$ Hermitean operators - integrals of motion for any quantum system, and the relevant equations of the quantum invariants are [16]

$$\frac{\partial \widehat{I}_{\nu}^{inv}}{\partial t} + \frac{1}{i\hbar}[\widehat{I}_{\nu}^{inv}, \widehat{H}] = 0, \quad \nu = 1, ..., 2s. \tag{6}$$

Note that these equations for the invariants (6) are different from the Heisenberg equations of motion:

$$\frac{d\widehat{A}}{dt} - \frac{1}{i\hbar}[\widehat{A}, \widehat{H}] = 0. \tag{7}$$

The same difference in the sign exists in classical mechanics between (5) and the Hamilton equations written in terms of Poisson brackets [18]:

$$\frac{du}{dt} - \{u, H_{class}\} = 0, \quad u = q_k, p_k. \tag{8}$$

The independent solutions of (6) for any quantum system are also $2s$: $\widehat{I}_{\nu}^{inv}(t) = \widehat{U}(t) I_{\nu}^{inv}(0) \widehat{U}^{\dagger}(t)$, where $U(t)$ is the unitary evolution operator. This difference arise in our days with new impact, due to mismatching some times of the equations for invariants with those for motion (see for example wikipedia).Method of Linear Integrals of Motion was developed for quadratic Hamiltonians $\widehat{H}$ in [15] and full-time evolution for all three independent quantum fluctuations $Cov(q,p), (\Delta q)^2$ and $(\Delta p)^2$ were obtain in [16, 17]. Linear invariants, obeying (6), are expressed through solution of equation for non-stationary harmonic oscillator $\ddot{\varepsilon}(t) + \Omega(t)\varepsilon(t)^2 = 0$. Remarkable advantage of this method is, that the solution ψ of Schrödinger equation $\widehat{H}\psi = i\hbar\frac{\partial \psi}{\partial t}$ are found in explicit form, and also minimize the Schrödinger Uncertainty Relation (1). Becouse of that reason the obtained states are often call Schrödinger Minimum Uncertainty States (SMUS) [19]. This class of SMUS includes MUS introduced by C. Caves [20], Lectures 7.5 – 10, p. 3, Coherent and p. 8, Squeezed states, respectively. SMUS includes the sub-class of Covariance States, with non-vanishing covariance $Cov(A,B) \neq 0$ (2).

STANDARD QUANTUM LIMIT AND FUNDAMENTAL QUANTUM LIMIT

The topic of Fundamental Quantum Limit (Heisenberg Limit) and its generalization was discused also in [21], where it is stated that other limit exists (Schrödinger Limit), but the exact formulation is given here as follows.

In this article we don't argue whether Heisenberg Limit can be beaten or not. We discuss only the two limits: Heisenberg and Schrödinger, taking into account the Covariance.

As a particular experimental setup and to provide our consideration we will consider Mach-Zehnder Interferometer, see Fig. 1. In that case Heisenberg uncertainty principle links phase ($A = \widehat{cos(\phi)}$), [22]) of a state to its photon number ($B = \widehat{n}$),(similarly to [23], p. 322):

$$\Delta\phi\Delta n \geq 1/2, \tag{9}$$

and for low level bound of the product we receive $\Delta\phi\Delta n = 1/2$.

To escape misunderstanding between the two limits (Standard and Fundamental) we will consider Max-Zehnder Interferometer fed by power laser prepared in Coherent States. Due to particle nature of photons, they obey classical Poisson distribution (see for example [24] or [25], chapter 8.4):

$$P[N = n] = \frac{e^{-\lambda}\lambda^n}{n!} \qquad \lambda > 0. \tag{10}$$

(In this paragraph N is the photon number, classical random variable, and $n = 0, 1, 2, ...,$. From the

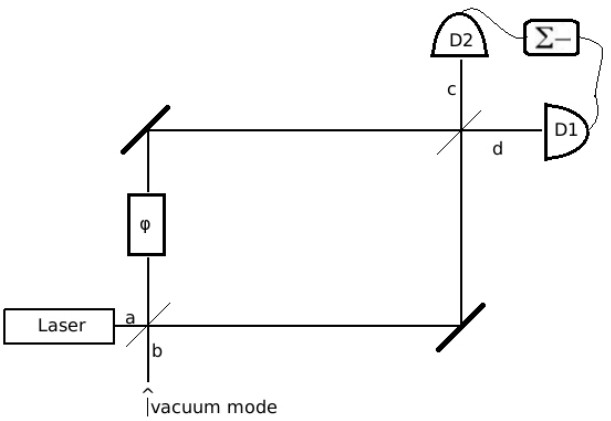


Fig. 1. Schematic representation of the Mach-Zehnder interferometer. The input modes are a coherent and a squeezed-vacuum field, respectively.

central limit theorem in the theory of Probability and Statistics follows $E[N] = \lambda = D[N]$, so in our notation

$N = \lambda = (\Delta N)^2$.

$$(\Delta N) = \sqrt{N}. \tag{11}$$

Minimizing Heisenberg Uncertainty Relation (3) with (11) we get the so called semiclassical Standard Quantum Limit for the phase in Mach-Zehnder interferometer:

$$(\Delta\phi)_{SQL} = \frac{1}{\sqrt{N}}. \tag{12}$$

It is worth to mention that the same dependence can be obtained [9] $(\Delta(N)) = \sqrt{N}$ if we consider N separate single-photon beams, producing the so called "shot noise" and N being the number of photons used. In this case, $cos^2(\phi/2)$ is the probability of the photon exiting at output **c**, and $sin^2(\phi/2)$ is the probability of the photon exiting at output **d** [9] . The Standard Quantum Limit is not fundamental and is only semi-classical: quantum in respect to Heisenberg Uncertainty Relation and classical in respect to state preparation and detection strategy. Standard Quantum Limit for position and momentum observables is discussed in [23, 26, 27]

Let us consider completely Quantum case. The discovery of squeezed states gives a new challenge to quantum interferometry, with the possibility to reach better sensitivity. Injecting non-classical states (such as squeezed states or N00N-states [1, 28]) in unused port **b** will improve the phase sensitivity of Mach-Zehnder interferometer. Quantum Mechanics does not set any restriction on the fluctuation Δn of the photon number operator $\widehat{n}$ - the only upper bound is

$$\Delta n \leq N \quad (N = \langle\widehat{n}\rangle). \tag{13}$$

This limit of photon number uncertainty together with minimized Heisenberg Uncertainty Relation (3) gives the phase limit:

$$(\Delta\phi)_{HL} = \frac{1}{2N}, \tag{14}$$

known in the literature as Heisenberg Limit. Here we use $N = N_{in}/2$, which is the total number of photons in the arm of the interferometer that experiences the phase shift. For Mach-Zehnder Interferometer

$$(\Delta\phi)_{HL} = \frac{1}{N}.$$

And now let us consider the Fundamental Quantum Limit based on General Uncertainty Relation (1). In terms of photon number and phase operators the Schrödinger Uncertainty Relation is

$$(\Delta\phi)^2(\Delta n)^2 \geq \frac{1}{4} + Cov^2(\phi, n). \tag{15}$$

In similar way as above we define the thorough bound for phase sensitivity. The upper bound for the variance of photon number operator is

$$\Delta n \leq N \quad (\text{again} \quad N = \langle\widehat{n}\rangle). \tag{16}$$

Taking the root mean square and multiplying (16) by $(\Delta\phi)$ we receive

$$(\Delta\phi)N \geq (\Delta\phi)(\Delta n) \geq \frac{1}{2}\sqrt{1 + 4Cov^2(\phi, n)}. \tag{17}$$

The lower bound of these inequalities (17) gives the rigorous quantum limit (we call it Shrödinger Quantum Limit):

$$(\Delta\phi)_{SL} = \frac{1}{2N}\sqrt{1 + 4Cov^2(\phi, n)}. \tag{18}$$

Similarly to work [21] we present the "uncertainty ellipse" as a cross-section of quasi probability distribution (Wigner function) with horisontal plane. To consider in details the interference pattern in Mach-Zehnder interferometer, it is necessary to take into account the electro-optic coefficients and the orientation of the cristal in arm g, leading to presence of Squeezed and Covariant states, which is not subject of this article. For the moment, we will illustrate Squeezed and Covariant states for the two quadratures components, showing the Wigner quasi probability function in presence of non-vanishing covariance. As an example for Covariant states we choose

$$\Psi = \frac{e^{-\frac{1}{2}x^2} e^{\frac{1}{4}ix^2 + 4}}{\pi^{1/4} e^4},$$

which leads to $Cov(q, p) = \hbar/2$. The Wigner quasi probability function is presented in Fig. 2. The uper plane at $1/e$ from the top presents Heisenberg Limits for q and p respectively. The cross-section is "uncertainty ellipse" with semi-axes equal to Heisenberg Limits for q and p respectively. The actual "uncertainty ellipse" (and more precise vision on this topic) is shown on lower plane with semi-axes equal to Shrödinger Limits for q and p respectively, where the non-vanishing covariance plays essential role. The distance between Heisenberg Limit and Schrödinger

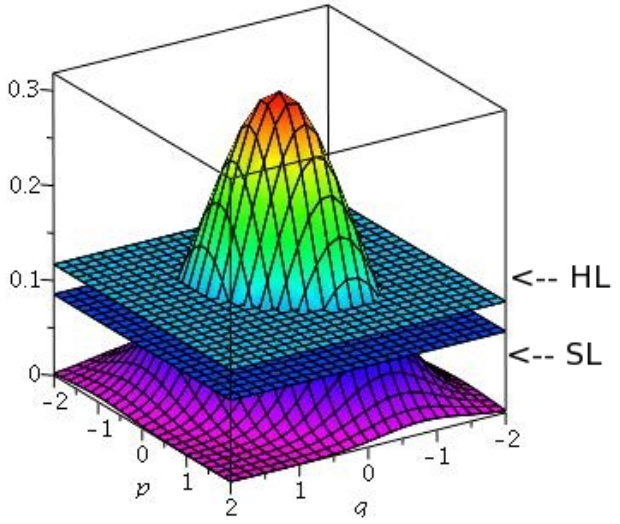


Fig. 2. Quantum fluctuations in Heisenberg limit and Schrödinger limit.

Limit depends on the third independent quantum fluctuation – the covariance.

Going back to Mach-Zehnder interferometer with the same argument ($N = N_{in}/2$) on both ports **c** and **d** we have

$$(\Delta\phi) = \frac{1}{N}\sqrt{1+4Cov^2(\phi,n)}. \qquad (19)$$

An argument in favour of general formula (18) (and in particular for Mach-Zehnder interferometer formula (19)) is that in case of power laser beams [30–32] we have strong nonlinearity leading always to covariance term.

Moreover, considering the dark fringes of the interference picture, where the photon number is very small, the states are still mixture of coherent and squeezed state $|\alpha\rangle_a|\zeta\rangle_a$ (even when the time-interval is very large in the case of single-photon registration, and looks like there is no correlation, but it exists).

We would like to emphasize that the precise phase estimation should include covariance, taken from operators, for particular $\widehat{\phi}$. This is still difficult question, because of ambiguously defining phase operator $(\widehat{\phi}, \widehat{exp(i\phi)}, \widehat{cos(i\phi)}, \widehat{sin(i\phi)})$ – which one we should take? [22]. There are a lot of discussions [22, 33, 34] and the problem of defining phase operator still exists. We choose one of the cases described in [22].

CONCLUSIONS

In this article we discuss the concept of standard quantum (shot-noise) limit, the Heisenberg Limit and rigorous Schrödinger Limit (the last two – completely quantum-mechanically). With the method of linear invariants the three independent quantum fluctuations are determined in Schrödinger Minimum Uncertainty States (SMUS). On the base of more general Uncertainty Relation (Schrödinger-1930), we accurately define the notion of fundamental quantum limit. The newly obtained Schrödinger Limit formula is applied for Mach-Zehnder Interferometer also, fed with coherent light mixed with squeezed vacuum, including the sensitivity of dark fringes in the interferometer. The analytical consideration involves the general term Covariance (compare to Variance) of two quantum variables. This term should be always taken into account, since it increases the fundamental quantum limit, especially in experiments, with strong nonlinearity. Neglecting it, would lead to serious errors in experimental results. Explicit new formulas for arbitrary two non-commuting observables (not only $\widehat{\phi}, \widehat{n}$) for the Schrödinger limit are received in similar way, but this will be a topic of next work.

Acknowledgements. *Authors thank professor D. Trifonov from Institute for Nuclear Research and Nuclear Energy for valuable comments on the manuscript.*

We thank also, professor E. Garmire (former director of Center for Laser Studies at USC, where the curiosity on QO of one of us (AA) started) for valuable discussions and interesting stories about interferometers at the time she visited our laboratory.

Special thanks to businessman Bob Russell for his advise in electronics work preparing the experiment with Sagnac Interferometer. The theoretical results received here could be taken into account for future research activities in the field of Interferometry.

APPENDIX

Derivation of Schrödinger uncertainty relation

The proof follows Schrödinger derivation, where the substitution in Schwarz inequality is split in two steps, as we will see later. Let ψ denotes the wavefunction of our quantum system, and $\mathscr{H}$ is the corresponding Hilbert space with scalar product $\langle\psi|\varphi\rangle$ and norm $|\psi| = \sqrt{\langle\psi|\psi\rangle}$, where $\psi, \varphi \in \mathscr{H}$. For any two vectors $\psi, \varphi \in \mathscr{H}$ the Schwarz inequality holds

$$|\psi|^2|\varphi|^2 \geq |\langle\psi|\varphi\rangle|^2. \qquad (20)$$

We accept the following notation: $\langle C\rangle \equiv \langle\psi|\widehat{C}|\psi\rangle \equiv \langle\psi|(\widehat{C}\psi)\rangle$, where C is self-adjoin operator, associated with certain physical variable. Let us

substitute $\psi, \varphi \in \mathscr{H}$ into inequality (20) with

$$\psi \to \widehat{C}^{\dagger}\psi^{*}, \quad \varphi \to \widehat{D}\psi. \tag{21}$$

The product of two Hermitean operators is in general non-Hermitean, but it could be split into Hermitean part (symmetrical product) and skew-Hermitean part (half of its commutator $[C,D]$):

$$CD = \frac{CD+DC}{2} + \frac{CD-DC}{2}. \tag{22}$$

This splitting corresponds in many aspects to the splitting of a complex number z into real and imaginary parts - $z = Re(z) + iIm(z) = (z+z^{*})/2 + (z-z^{*})/2$.

Using inequality.(20), we obtain

$$\langle D^2\rangle\langle C^2\rangle \geq |\langle CD\rangle|^2. \tag{23}$$

If we decompose the right hand side according to (22) and applying $|z|^2 = |Re|^2 + |Im|^2$, where $z = \langle CD\rangle$ and $z^{*} = \langle D^{\dagger}C^{\dagger}\rangle = \langle DC\rangle$ we get

$$\langle C^2\rangle\langle D^2\rangle \geq \Big(\frac{\langle CD+DC\rangle}{2}\Big)^2 + \Big|\frac{\langle CD-DC\rangle}{2}\Big|^2. \tag{24}$$

In order to arrive at the general case instead of the operators A and B we use $C = A - \langle A\rangle\widehat{I}$ and $D = B - \langle B\rangle\widehat{I}$. Than, for the first term on the right we have

$$\Big(\frac{\langle CD+DC\rangle}{2}\Big)^2 = \Big(\frac{\langle (A-\langle A\rangle)(B-\langle B\rangle) + (B-\langle B\rangle)(A-\langle A\rangle)\rangle}{2}\Big)^2$$
$$= \Big(\frac{\langle AB - A\langle B\rangle - \langle A\rangle B + \langle A\rangle\langle B\rangle + BA - B\langle A\rangle - \langle B\rangle A + \langle B\rangle\langle A\rangle\rangle}{2}\Big)^2 = \Big(\frac{\langle AB+BA\rangle}{2} - \langle A\rangle\langle B\rangle\Big)^2 = Cov^2(A,B).$$

And for the second term on the left

$$\Big|\frac{\langle CD-DC\rangle}{2}\Big|^2 = \Big|\frac{\langle (A-\langle A\rangle)(B-\langle B\rangle) - (B-\langle B\rangle)(A-\langle A\rangle)\rangle}{2}\Big|^2 = \Big|\frac{\langle AB-BA\rangle}{2}\Big|^2 = \Big|\frac{1}{2}\langle [A,B]\rangle\Big|^2.$$

Finally, we end up Schrödinger derivation with

$$(\Delta A)^2(\Delta B)^2 \geq Cov^2(A,B) + \Big|\frac{1}{2}\langle [A,B]\rangle\Big|^2. \tag{25}$$

If we move the covariance on the left side of the inequality, and use the definition of covariance matrix [24]

$$\Sigma_{\mathbf{A},\mathbf{B}} = \begin{pmatrix} Var(A,A) & Cov(A,B) \\ Cov(A,B) & Var(B,B) \end{pmatrix},$$

we receive for SUR in very compact, canonical form

$$det(\Sigma_{\mathbf{A},\mathbf{B}}) \geq \Big|\frac{1}{2}\langle [A,B]\rangle\Big|^2, \tag{26}$$

showing some group symmetry in a phase space!

REFERENCES

[1] C. M. Caves, Quantum-mechanical noise in fan interferometer *Phys. Rev. D* **23**, 1693–1708 (1981).

[2] L. Pezze and A. Smerzi, Mach-Zehnder Interferometry at the Heisenberg Limit with coherent and squeezed-vacuum light, *PhysRevLett.*, **100** ,073601–0736044(2008).

[3] R. Loudon.Phys. *Rev. Lett.***47** , 815 (1981).

[4] M. O. Scully and M. S. Zubairy, *Quantum Optics*, Cambridge University Press, Cambridge.

[5] L. A. Wu, H. J. Kimble, J. L. Hall and H. Wu. *Phys. Rev. Lett.*, **57**, 2520 (1986).

[6] G. Breitenbach, S. Schiller and J. Mlynek. *Nature*, **387**, 471 (1997).

[7] M. Xiao, L. Wu, and H. J. Kimble,*Phys. Rev. Lett.*,**59**, 278 (1987); P. Grangier, R. E. Slusher, B. Yurke, and A. LaPorta, *Phys. Rev. Lett.*, **57**, 687 (1986).

[8] V. Giovannetti,S. Lioyd and L. Maccone, "Quantum-enhanced positioning and clock synchronization", *Nature*, **412**, 417–419 (2001)

[9] V. Giovannetti,S. Lioyd and L. Maccone, "Quantum-Enhanced Measurements: Beating the Standart Quantum Limit",*Science*, **306**, 1330–1335 (2004).

[10] Z. Y. Ou, "Fundamental quantum limit in precision phase measurement", *PhysRev A*, **55**, 2598–2609 (1997).

[11] M. Hall, D. Berry, M. Zwierz, and H. Wiseman, "Universality of the Heisenberg limit for estimates of random phase shifts", *Phys.Rev. A*, **85**, 041802-1–041802-4 (2012).

[12] M. Holland and K. Burnett, "Interferometric Detection of Optical Phase Shifts at the Heisenberg Limit" *Phys.Rev.Lett*, textbf71, 1355–1358 (1993).

[13] E. Schrödinger, "Zum Heisenbergschen Unschfeprinzip " *Sitzungsber. Preuss. Akad. Wiss., Phys. Math. Kl.* **19**, 296–323 (1930).

[14] A. Angelow and M. Batoni, "Translation with annotation of the original paper of Erwin Schrödinger (1930) in English", *Bulg. J. Phys.* **26(5/6)**, 193–203 (1999). (free copy: http://arxiv.org/abs/quant-ph/9903100).

[15] I. A. Malkin, V. I. Manko, D. A. Trifonov, *Phys.Rev. D*, **2**, 1371–1385 (1970);
I. A. Malkin, V. I. Manko, D. A. Trifonov, *J.Math. Phys.*, **14**,576 (1973);
I. A. Malkin, V. I. Manko, D. A. Trifonov, *Nuovo Cimento A*, **4**, 773 (1971).

[16] D. A. Trifonov, "Coherent States of Quantum Systems", *Bulgarian J. Phys.*, **2**, 303–311 (1975),
D. A. Trifonov," Coherent States and Evolution of Uncertainty Products", *Preprint ICTP IC/75/2* (1975).

[17] A. Angelow, "Light propagation in nonlinear waveguide and classical two-dimensional oscillator", *Physica A*, **256** 485–498, (1998).

[18] I. Zlatev, A. Nikolov, *Theoretical Mechanics*, Vol. 1, N.I., Sofia, 1981.

[19] D. Trifonov, *Completeness and geometry of Schrödinger minimum uncertainty states* J. Math. Phys. 34, 100 (1993).

[20] C. M. Caves, "Lectures on Quantum Optics",Lecture 0-4, p. 3, Spring, (1989).

[21] A. Angelow, "Covariance, squeezed and coherent states: Proposal for experimental realization of covariance states", American Instite of Physics, Conference Proceedings BPU6, **899**, pp. 293–294 (2007).

[22] R. Loudon, *The quantum theory of light*, Oxford University Press, p. 144, 2000.

[23] C. W. Gardiner and P. Zoller, *Quantum noise*, Springer, New York, 2004.

[24] L. Cankov, *Probability and Statistics in Physics (Lecture Notes)*, Sofia University Press, 2011. (Note: Since, we consider in this article quantum-mechanical non-commuting random variables the elements of covariance matrix, p. 30, eq. 4-5 should be taken as $c_{ij} = Cov(\overset{\boldsymbol{\mu}}{?}x_i, \overset{\boldsymbol{\mu}}{?}x_j) = E[\frac{\overset{\boldsymbol{\mu}}{?}x_i \overset{\boldsymbol{\mu}}{?}x_j + \overset{\boldsymbol{\mu}}{?}x_j \overset{\boldsymbol{\mu}}{?}x_i}{2}] - E[\overset{\boldsymbol{\mu}}{?}x_i]E[\overset{\boldsymbol{\mu}}{?}x_j]$, in our case: $0 < i, j \leq 2$ and $\overset{\boldsymbol{\mu}}{?}x_1 = A$ and $\overset{\boldsymbol{\mu}}{?}x_2 = B$.)

[25] H. Tucker, *An introduction to probability and mathematical statistics*, New York, Academic Press, 1962.

[26] V. Braginskii, "Classical and quantum restrictions on the detection of weak disturbances of a macroscopic oscillator", *Sov.Phys.JETP*, **26**, 831–834 (1968).

[27] V. Braginskii and F. Khalili, *Measurement*,Cambridge university press, Cambridge, 1992 .

[28] K. Seshadreesan,P. M. Anisimov, H. Lee and J. P. Dowling,"Parity detection achieves the Heisenberg limit in interferometry with coherent mixed with squeezed vacuum light", *NewJ.Phys*, **13**, 083026 (2011).

[29] R. Loudon and P. Knight,"Squeezed light", *J. Modern Optics*, **34**, 709–759 (1987).

[30] M. Lang, C. Caves, Optimal Quantum-Enhanced Interferometry Using a Laser Power Source *PhysRevLett*,**111**,173601 (2013).

[31] M. Zwierz,C. Perez-Delgado and P. Kok, "General Optimality of the Heisenberg Limit for Quantum Metrology" *Phys.Rev.Lett.*, **105**, 180402 (2010).

[32] L. Pezze, "Sub-Heisenberg phase uncertainties", *Phys.Rev A*,**88**, 060101(R) (2013).

[33] M. Nieto,"Quantum phase and quantum phase operators", http://arXiv:hep-ph/9304036v1.

[34] J. Sarfatt, *Nuovo Cimento*, **27**, 1119 (1963).

ФУНДАМЕНТАЛНО КВАНТОВО ОГРАНИЧЕНИЕ В МАХ-ЦЕНДЕР ИНТЕРФЕРОМЕТЪР

А. Ангелов, Е. Стоянова

Институт по физика на твърдото тяло, Българска академия на науките,
бул. "Цариградско шосе" №72, 1784 София, България

(Резюме)

Статичния шум (на английски: *Shot noise*) съществува понеже феномени като светлината и електрическият ток се състоят от движение на отделни квантови обекти. Светлина идваща от отдалечени звезди например, пристига на малки порции, наречени фотони. Подобни са процесите, когато изследваме тъмните зони на интерференчната картина. При такива малки стойности интензитета вече не е непрекъсната функция. Тогава се регистрират само единични фотони, неравномерно пристигащи по време. Тези явления дават ограничения при реалните физични измервания на много слаби сигнали. В тази връзка е въведено физичното понятие *стандартно квантово ограничение* (на английски - Heisenber limit, shot-noise limit), основаващо се на Хайзенберговото съотношение на неопределеност [1].

В настоящата статия разглеждаме статичния шум в интерферометър на Макс-Цендър (и по-специално в областта на тъмните ивици на интерференчната картина). През 1930 година Шрьодингер обобщава и уточнява Хайзенберговото съотношение на неопределеност [2]. Превод на оригиналната работа на Шрьодингер от немски на английски е направен в [3], където в анотацията към превода са показани нови свойства на съотношението на неопределеност, каквито Хайзенберговото не притежава. Прилагайки по-общото съотношение на неопределеност, ние преразглеждаме това централно понятие *стандартно квантово ограничение*. Аналитичното разглеждане включва понятието ковариация на две квантови променливи. Получена е нова (поточна) формула за стандартния квантов лимит.

Настоящата публикация е едно продължение на [4], където се дискутира необходимостта от уточняване на *стандартното квантово ограничение,* но точната формула е изведена тук.

1. W. Heisenberg, Über den anschaulichen Inhalt der quantentheoretishen Kinematik und Mechanik, *ZS für Physik* **43** (1927) 172-198.
2. E. Schrödinger, "Zum Heisenbergschen Unschfeprinzip", *Sitzungsber. Preuss. Akad. Wiss., Phys. Math. Kl.* **19** (1930) 296–323.
3. A. Angelow and M. Batoni, "Translation with annotation of the original paper of Erwin Schrödinger (1930) in English," *Bulg. J. Phys.* **26** (5/6) (1999) 193–203 (free copy: http://arxiv.org/abs/quant-ph/9903100).
4. A. Angelow, "Covariance, squeezed and coherent states: Proposal for experimental realization of covariance states", *American Institute of Physics, Conference Proceedings BPU6* **899** (2007) 293–294.

Bulgarian Chemical Communications, Volume 47, Special Issue B (pp. 282–286) 2015

Scattering of solitons from point defects in two coupled Ablowitz-Ladik chains

R. S. Kamburova*, M. T. Primatarowa

Institute of Solid State Physics, Bulgarian Academy of Sciences,
72 Tzarigradsko Chaussee Blvd., 1784 Sofia, Bulgaria

The interaction of solitons with point defects in a system of coupled Ablowitz-Ladik (AL) chains is studied numerically. The system is a discrete analog of coupled nonlinear Schrödinger equations. The interchain coupling which couples opposite sites of the AL chains includes linear and nonlinear interactions. The soliton dynamics depends on the soliton parameters (width, velocity), interchain coupling constant and defect strength. It is obtained that solitons which are exited in one of the two chains can be perfectly switched and at the same time transmitted, trapped or reflected by the attractive impurities. The point defects do not influence the period of energy transfer and it is close to the period for the homogeneous case.

Key words: solitons, Ablowitz-Ladik equation, soliton-impurity interaction

INTRODUCTION

The study of nonlinear waves is receiving much attention due to the potential application within different branches of physics from nonlinear optics to Bose-Einstein condensate. The interplay between discrete diffraction and nonlinearity leads to the formation of discrete solitons. They promise an efficient way to control switching of optical signals in a system of coupled waveguides. So waveguide-based devices have received considerable attention in literature and this field has been extensively explored theoretically and experimentally [1,2]. A discrete coupler involving two waveguides which exchange power as a result of weak overlap of their evanescent fields is the basic realization of a waveguide switch. The rate of power swapped back and forth between waveguides depends on the strength of the coupling, the degree of similarity of the waveguides and the initial pulse energy [3-7]. Waveguide arrays are particularly interesting because of their possible applications in signal processing [8-12]. All considerations regard discrete soliton switching mainly in homogenous waveguides with constant or smoothly varying coupling between them. However in practical applications the properties of inhomogeneous waveguides are more interesting and rather inevitable for switching [13-17].

Widely investigated are the standard discrete nonlinear Schrödinger (NLS) equation, as well as the completely integrable discrete Ablowitz-Ladik (AL) equation [18-20]. Although the two equations have the same linear properties and yield the same NLS equation in the continuum limit, their nonlinear properties are different. This leads to differences in the dynamics of narrow solitons (bright or dark) for the two models. Soliton solutions in two coupled discrete nonlinear chains were found and their stability was investigated in [21-24].

In the present paper we study the interaction of propagating solitons with impurities in two Ablowitz-Ladik chains with a complicated coupling that includes linear and nonlinear interactions between the chains.

THE MODEL

We shall consider two parallel chains of particles described by the following system of coupled Ablowitz-Ladik equations:

$$\begin{aligned} i\frac{\partial \alpha_n}{\partial t} =& M(\alpha_{n+1}+\alpha_{n-1})(1+\gamma|\alpha_n|^2) \\ &+ 2d\beta_n(1+\gamma|\alpha_n|^2)+\varepsilon\delta_{n,n_0}\alpha_n \\ i\frac{\partial \beta_n}{\partial t} =& M(\beta_{n+1}+\beta_{n-1})(1+\gamma|\beta_n|^2) \\ &+ 2d\alpha_n(1+\gamma|\beta_n|^2)+\varepsilon\delta_{n,n_0}\beta_n \end{aligned} \tag{1}$$

$\alpha_n(t)$ $[\beta_n(t)]$ is the amplitude of an excitation at site n of the first (second) chain, interacting with an impurity of the strength ε localized at the point n_0. M is the coupling interaction between neighboring particles in one and the same chain. The two chains are coupled to each other through the real parameter d which governs the interchain coupling between opposite sites (nondispersive) and includes linear and nonlinear terms. The parameter γ determines the type of the soliton solution (bright for $\gamma > 0$ and dark for $\gamma < 0$) of the AL equation. In what follows we con-

* To whom all correspondence should be sent:
krad@issp.bas.bg

© 2015 Bulgarian Academy of Sciences, Union of Chemists in Bulgaria

sider only bright solitons and set $\gamma = 1$ due to the scaling property of the AL system.

First we shall consider the homogeneous case ($\varepsilon = 0$). We briefly outline the influence of the coupling between opposite sites on the soliton properties [24]. Equation (1) can be derived from the Hamiltonian

$$H = \sum_n \Big[M(\alpha_n \alpha_{n-1}^* + \alpha_n^* \alpha_{n-1} + \beta_n \beta_{n-1}^* + \beta_n^* \beta_{n-1}) + 2d(\alpha_n \beta_n^* + \alpha_n^* \beta_n) \Big] \quad (2)$$

using the deformed Poisson brackets [19,20]

$$\begin{aligned} \{\alpha_n, \alpha_m^*\} &= i(1+|\alpha_n|^2)\delta_{n,m}\,, \\ \{\alpha_n, \alpha_m\} &= \{\alpha_n^*, \alpha_m^*\} = 0\,, \\ \{\beta_n, \beta_m^*\} &= i(1+|\beta_n|^2)\delta_{n,m}\,, \\ \{\beta_n, \beta_m\} &= \{\beta_n^*, \beta_m^*\} = 0 \end{aligned} \quad (3)$$

and the equations of motion

$$\frac{\partial \alpha_n}{\partial t} = \{H, \alpha_n\}\,, \quad \frac{\partial \beta_n}{\partial t} = \{H, \beta_n\}\,. \quad (4)$$

The system (1) is nonintegrable but has two integrals of motion, the Hamiltonian H and the total number of particles

$$N = \sum_n [\ln(1+|\alpha_n|^2) + \ln(1+|\beta_n|^2)]\,. \quad (5)$$

For $d = 0$ and the symmetric reduction $\alpha_n(t) \equiv \beta_n(t)$ the system (1) turns in an AL equation with the well known bright soliton solution:

$$\alpha_n(t) = \beta_n(t) = \sinh\frac{1}{L}\,\mathrm{sech}\frac{n - vt}{L}\, e^{i(kn - \omega t)} \quad (6)$$

$$v = -2ML\sinh\frac{1}{L}\sin k, \qquad \omega = 2M\cosh\frac{1}{L}\cos k$$

The parameters k (wavenumber) and L (width) determine the velocity v and frequency ω of the soliton. In this case the conserved quantities have the form

$$H = 8M\sinh\frac{1}{L}\cos k, \quad N = 4/L \quad (7)$$

and it holds $\omega = \partial H/\partial N$.

In the continuum limit $\alpha_n(t) \to \alpha(x,t)$, $\beta_n(t) \to \beta(x,t)$ which holds for wide solitons ($L \gg 1$) and for $\alpha(x,t) \equiv \beta(x,t)$ the system (1) reduces to the standard NLS equation of the form

$$i\frac{\partial \alpha}{\partial t} = 2(M+d)\alpha + M\frac{\partial^2 \alpha}{\partial x^2} + 2(M+d)|\alpha|^2\alpha \quad (8)$$

with the bright soliton solution

$$\alpha(x,t) = \varphi_0\,\mathrm{sech}\frac{x - vt}{L} e^{i(kx - \omega t)} \quad (9)$$

$$\varphi_0 = \frac{1}{L}\sqrt{\frac{M}{M+d}}, \qquad v = -2Mk,$$

$$\omega = 2(M+d) - Mk^2 + \frac{M}{L^2}\,.$$

An attempt to include the discreteness effects which become important for narrow solitons ($L \sim 1$) will lead to a correction of the velocity of the form $\Delta v \sim \varphi_0^2$.

Fig. 1 shows the propagation of two narrow solitons with equal amplitudes [$\alpha_n(t) \equiv \beta_n(t)$] excited simultaneously in the two chains for different coupling constants. As can be expected the coupling between opposite sites in the two chains d which besides the linear term has also a nonlinear term changes significantly the soliton's amplitude through the factor $\sqrt{M/(M+d)}$ as well as the velocity with the amount Δv. For positive values of d the amplitude φ_0 and the velocity become larger [figures 1(a)] while for negative values of d they become smaller [figure 1(a′)].

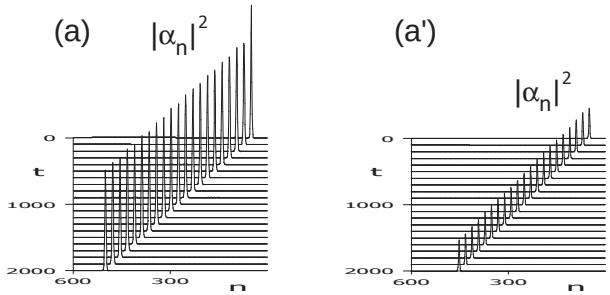


Fig. 1. Propagation of equal narrow ($L = 2$) solitons in the two chains with $M = -1$, $k = 0.1$ and (a): $d = 0.628$; (a′): $d = -0.628$. The time is in units of $1/|M|$.

SCATTERING OF BRIGHT SOLITONS FROM POINT DEFECTS

The inhomogeneous static case $\varepsilon \neq 0$, $k = v = 0$ is investigated in detail in [25]. Now we shall study the propagation of an AL soliton which at the initial time is launched in one of the chains

$$\alpha_n(0) = \sinh\frac{1}{L}\,\mathrm{sech}\frac{|n - n_s|}{L}\, e^{ikn}\,, \quad \beta_n(0) = 0 \quad (10)$$

solving numerically the system (1). The simulations are carried out for 250 sites of each chain and periodic boundary conditions. n_s is the place where the soliton is launched initially and is far enough from the defect.

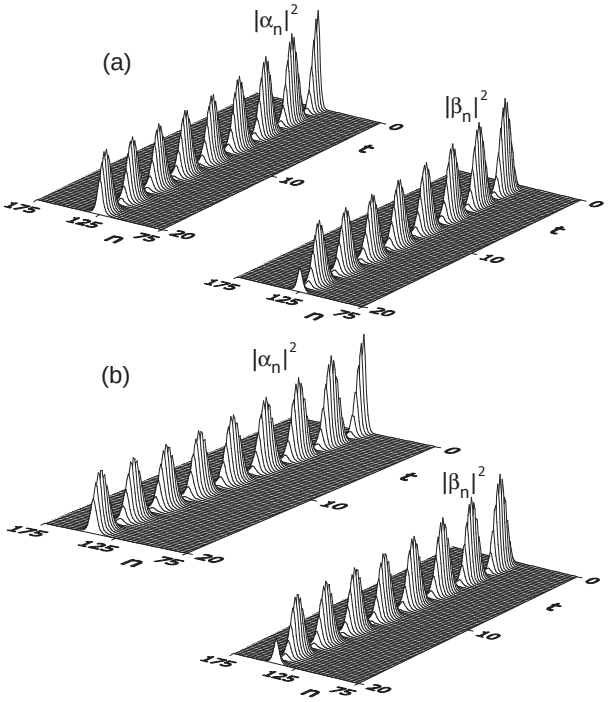


Fig. 2. Perfect switching of a narrow soliton ($L = 2$) in the homogenous case with $d = 0.628$ for (a): $k = 0$ and (b): $k = 0.4$. The time is in units of $1/|M|$.

The width of the solitons is $L = 2$, which underline the discreteness of the system. For wide solitons we can use the continuum approximation and (1) turns in a system of coupled NLS equations. We have chosen $M = -1$ which determines that impurities with $\varepsilon > 0$ are repulsive while impurities with $\varepsilon < 0$ are attractive.

In the homogeneous linear case ($\varepsilon = 0$, $\gamma = 0$) the excitation will transfer from one chain to the other and back with a period

$$t_0 = \pi/2|d|\,, \tag{11}$$

where $2d$ is the linear coupling. For our complicated homogeneous model ($\varepsilon = 0$, $\gamma = 1$), which is not linear we observe that an energy exchange between the two chains take place with nearly the same period t_0 and the energy exchange rate depends on the strength of the coupling. For small values of the coupling constant the soliton is only partially transferred. When the coupling increases the transferred rate grows. This behavior is due to the nonlinear coupling terms. We obtained that a soliton can transfer (perfect soliton switching) when the simple condition

$$4|d|L^2 \gg 1 \tag{12}$$

is fulfilled. Fig. 2 shows perfect soliton switching for the homogenous chains ($\varepsilon = 0$) and different soliton velocities. The process does not depend on the sign of the coupling d. The period from the numerical simulations for the static case [$k = v = 0$, figure 2(a)] as well as for the propagating soliton [$k = 0.4$, $v = 0.81$, figure 2(a)] is approximately 2.5 and is in a good agreement with the value calculated from (11).

For large values of the coupling constant between opposite sites of the chains d the soliton switching is preserve.

In the case of perfect soliton switching ($|d| = 0.628$) the scattering pattern depends strongly on the initial soliton velocity and the strength of the defect. For repulsive defects ($\varepsilon > 0$) the soliton can by only transmitted or reflected. The evolution is more complex in the case of attractive defects ($\varepsilon < 0$). Fig. 3 shows the dynamics of a soliton with a given small velocity ($v = 0.146$) when it interacts with an attractive impurity. Depending on the strength of the impurity

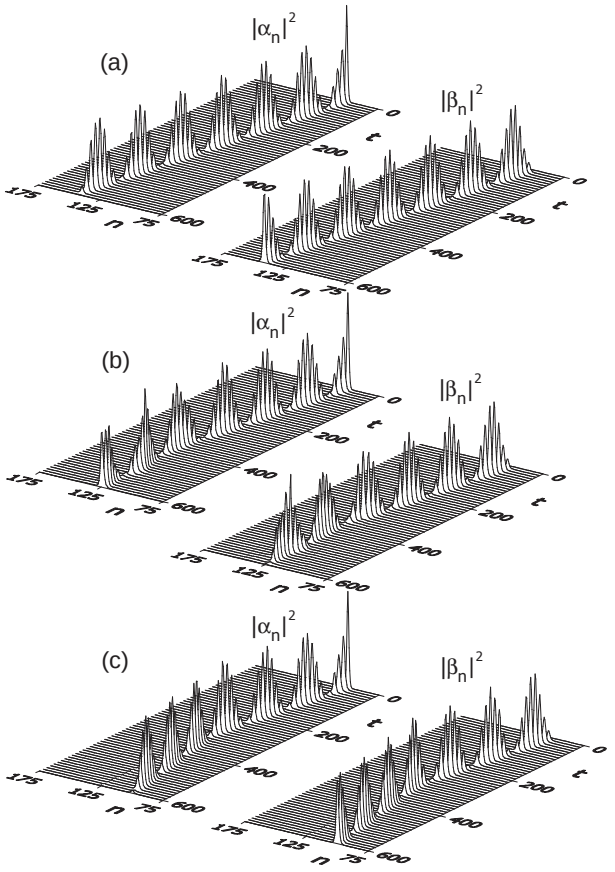


Fig. 3. Scattering of a soliton launched initially in one of the chains at $n_s = 100$ with $k = 0.07$ from an attractive defect placed at $n_0 = 125$ for (a): $\varepsilon = -0.01$; (b): $\varepsilon = -0.1$; (c): $\varepsilon = -1$.

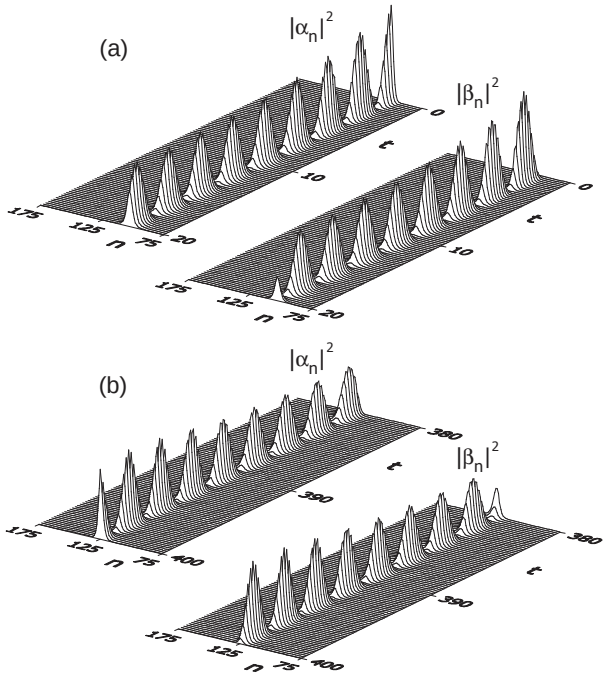


Fig. 4. Evolution of the trapped soliton shown in figure 3(b) for the initial time interval (a) and the time interval after the soliton interaction with the impurity (b).

the soliton can be transmitted [Fig. 3(a), $\varepsilon = -0.01$], trapped [Fig. 3(b), $\varepsilon = -0.1$] or reflected [Figu. 3(c), $\varepsilon = -1$]. We have obtained that in all three cases the soliton transfers from one chain to the other and back periodically. The period of the energy transfer is the same as for homogeneous chains and has a value close to 2.5. Fig. 4 demonstrates in detail the period of the soliton transfer for the parameters when the soliton is trapped. The soliton period before the interaction with the defect [figure 4(a)] and after the interaction with the defect [figure 4(b)] remains the same.

CONCLUSION

We have studied the interaction of discrete bright solitons with impurities in a system of two coupled Ablowitz-Ladik chains. Perfect soliton switching can be obtained for large enough values of the coupling constant. We have investigated the interaction of propagating solitons with point defects. The numerical simulations have shown that solitons which are excited in one of the two inhomogeneous chains with a given velocity can be perfectly switched and at the same time transmitted, trapped or reflected by the attractive impurities depending on the impurity strength.

Acknowledgments. *This work is partially supported by the EU FP7 funded project INERA (Grant agreement no: 316309).*

REFERENCES

[1] I. L. Garanovich, S. Longhi, A. A. Sukhorukov, and Y. S. Kivshar, *Phys. Rep*. **518**, 1-79 (2012).

[2] J. D. Joannopoulos, S. G. Johnson, J. N. Winn, and R. D. Meade, "*Photonic Crystals: Molding the Flow of Light*" (Prinston University Press, 2008).

[3] S. M. Jensen, *IEEE J. Quantum Electron*. **18**, 580-3 (1982).

[4] S. Trillo, S. Wabnitz, and G. Stegeman, *IEEE J. Quantum Electron*. **25**, 1907-16 (1989).

[5] C. Paré and M. Florjańczyk, *Phys. Rev. A* **41**, 6287-95 (1990).

[6] Y. S. Kivshar, *Optics Lett*. **18**, 7-9 (1993).

[7] P. L. Chu, G. D. Peng, and B. A. Malomed, *Optics Lett.* **18**, 328-30 (1993).

[8] A. B. Aceves, C. De Angelis, T. Peschel, R. Muschall, F. Lederer, S. Trillo, and S. Wabnitz, *Phys. Rev. E* **53**, 1172-89 (1996).

[9] D. N. Christodoulides and E. D. Eugenieva, *Phys. Rev. Lett*. **87**, 233901(4) (2001).

[10] U. Peschel, R. Morandotti, J. M. Arnold, J. S. Aitchison, H. S. Eisenberg, Y. Silberberg, T. Pertsch, and F. Lederer, *J. Opt. Soc. Am. A* **19**, 2637-44 (2002).

[11] R. A. Vicencio, M. I. Molina, and Y. S. Kivshar, *Optics Lett*. **28**, 1942-4 (2003).

[12] M. I. Molina, R. A. Vicencio, and Y. S. Kivshar, *Optics Lett*. **31**, 1693-5 (2006).

[13] W. Królikowski and Y. S. Kivshar, *J. Opt. Soc. Am. B* **13**, 876-87 (1996).

[14] S. Longhi, *Phys. Rev. E* **74**, 026602(9) (2006).

[15] L. Morales-Molina and R. A. Vicencio, *Optics Lett*. **31**, 966-8 (2006).

[16] R. H. Goodman and M. I. Weinstein, *Physica D* **237**, 2731-60 (2008).

[17] J. Belmonte-Beitia, V. M. Pérez-García, and P. J. Torres, *Nonlin. Science* **19**, 437-51 (2009).

[18] M. J. Ablowitz and J. F. Ladik, *J. Math. Phys*. **17**, 1011-8 (1976).

[19] R. Scharf and A. R. Bishop, *Phys. Rev. A* **43**, 6535-44 (1991).

[20] D. Cai, A. R. Bishop, and N. Grønbech-Jensen, *Phys. Rev. E* **53**, 4131-6 (1996).

[21] A. Bülow, D. Hennig, and H. Gabriel, *Phys. Rev. E* **59**, 2380-92 (1999).

[22] B. A. Malomed and J. Yang, *Phys. Lett. A* **302**, 163-70 (2002).

[23] R. S. Kamburova and M. T. Primatarowa, *AIP Conf. Proc.* **1203**, 261-6 (2010).

[24] M. T. Primatarowa and R. S. Kamburova, *J. Phys.: Conf. Series* **398**, 012041(6) (2012).

[25] R. S. Kamburova and M. T. Primatarowa, *J. Phys.: Conf. Series* **558**, 012022 (2014).

РАЗСЕЙВАНЕ НА СОЛИТОНИ ОТ ТОЧКОВИ ДЕФЕКТИ В СИСТЕМА ОТ ДВЕ СВЪРЗАНИ ВЕРИЖКИ НА АБЛОВИЦ–ЛАДИК

Р. Камбурова, М. Приматарова

Институт по физика на твърдото тяло, Българска академия на науките,
бул. "Цариградско шосе" №72, 1784 София, България

(Резюме)

Изследвана е еволюцията на дискретни солитони в система от две свързани чрез параметъра d нехомогенни ($\varepsilon \neq 0$) верижки на Абловиц-Ладик. Тази система представлява дискретен аналог на системата от две свързани нелинейни уравнения на Шрьодингер. В хомогенния случай ($\varepsilon = 0$) тя е неинтегрируема, но има два интеграла на движение.

$$i\frac{\partial \alpha_n}{\partial t} = M(\alpha_{n+1} + \alpha_{n-1})(1 + \gamma|\alpha_n|^2) + 2d\beta_n(1 + \gamma|\alpha_n|^2) + \varepsilon\delta_{n,n_0}\alpha_n$$
$$i\frac{\partial \beta_n}{\partial t} = M(\beta_{n+1} + \beta_{n-1})(1 + \gamma|\beta_n|^2) + 2d\alpha_n(1 + \gamma|\beta_n|^2) + \varepsilon\delta_{n,n_0}\beta_n\,.$$

Разгледано е разпространението на светъл солитон ($\gamma > 0$), който първоначално е формиран само в едната от хомогенните верижките. Определени са периодът на прехвърляне на възбуждението и условието за пълно солитонно превключване. За линейния случай прехвърлянето е с период $t_0 = \pi/|d|$. Числените изследвания показват, че този период е почти същият за изследвания модел, който не е линеен и пълно прехвърляне на енергията на солитона от едната верижка в другата и обратно има при условие $4|d|L^2 \gg 1$, където L е ширината на солитона.

Процесът на превключване се запазва при големи стойности на d. Той не зависи от знака на свързващия коефициент и скоростта на солитона остава непроменена.

Солитонната динамика в нехомогенната система зависи от параметрите на солитона (ширина и скорост), свързващата константа и стойността на дефекта. Линейните точкови дефекти не влияят върху периода на енергиен обмен и той е близък по стойност на този за хомогенния случай. Числените изследвания показват, че когато в едната верижка е формиран солитон с определена скорост той запазва периодичната си динамика на преминаване от едната верижка в другата и обратно, като в същото време в зависимост от стойността на дефекта на привличане може да премине, да се захване или отрази от него.

Bulgarian Chemical Communications, Volume 47, Special Issue B (pp. 287–295) 2015

Application of finite-difference method for numerical investigation of eigenmodes of anisotropic optical waveguides with an arbitrary tensor

I. K. Ivanov*

Department of Theoretical Physics, University of Plovdiv, 24 Tzar Assen Str., 4000 Plovdiv, Bulgaria

In this paper 3D finite-difference methods is developed for analyzing anisotropic optical waveguides. An eigenvalue matrix equation is derived through considering simultaneously four transverse field components. The numerical results show that the proposed scheme is highly efficient and yields complex effective indices while requiring match less computer memory and calculation time than the commonly used methods. Algorithm is used to study modes on a electrooptic polymer waveguide and a liquid-crystal optical waveguide with arbitrary director orientation, clearly demonstrated in the numerical examples.

Key words: 3D finite-difference optical waveguides, complex effective indices, fullvector modesolver

INTRODUCTION

In fiber and integrated optics, a fundamental problem is to compute the eigenmodes of optical waveguides. Several techniques are commonly used to compute the electromagnetic modes of waveguides, including finite element methods, mode-matching techniques, method of lines, and finite difference methods. Many methods completely neglect the anisotropy of the constituent materials. Of those that do account for material anisotropy, most require that the permittivity tensor be diagonal when expressed in the coordinate system of the waveguide. In this paper, we present an finite-difference (FD) method for solving full-vector modes of optical waveguides with arbitrary permittivity tensor, i.e. with general three-dimensional (3-D) anisotropy. Only fewer FD works deal with structures including anisotropic materials [1-5] and they at most considered anisotropy in the transverse plane, i.e. in the waveguide cross-section. In [5] was developed a more rigorous vector FD mode solver, based on the traditional approach for anisotropic waveguides, but again assuming non-diagonal anisotropy only in the transverse plane (in permittivity tensor all $\varepsilon_{xz}, \varepsilon_{yz}, \varepsilon_{zx}, \varepsilon_{zy} = 0$). Now, we derive a matrix standard eigenvalue problem from the FD method, which is easier to solve for the all modes. For absorbing boundary condition is used method of perfectly matched layers (PMLs) for anisotropic media [6] at the outer boundaries of the computational domain. In so doing, leaky waveguide modes having complex propagation constants can also be analyzed.

* To whom all correspondence should be sent:
ik_ivanov@yahoo.com

For optimize numerical realization we proposed scheme with only one complex array similar complex potential of Riemann-Silberstein [7], instead four field components (two for transverse electric field components E_x, E_y and two for transverse magnetic field components H_x and H_y - total four arrays).

The eigenmodes and eigenvalues of the waveguide were calculated using an iterative shift-inverse power method with Rayleigh criteria.

FORMULATION

For analysis of a waveguide is used computational domain (Fig. 1), where the waveguide cross-section in the transverse $x-y$ plane is truncated and surrounded by PML regions of thickness d. The incorporation of PML regions allows the analysis of leaky modes.

We consider anisotropic material, which permittivity tensor $[\varepsilon]$ is formulated as:

$$[\varepsilon] = \varepsilon_0 \begin{Bmatrix} \varepsilon_{xx} & \varepsilon_{xy} & \varepsilon_{xz} \\ \varepsilon_{yx} & \varepsilon_{yy} & \varepsilon_{yz} \\ \varepsilon_{zx} & \varepsilon_{zy} & \varepsilon_{zz} \end{Bmatrix}, \qquad (1)$$

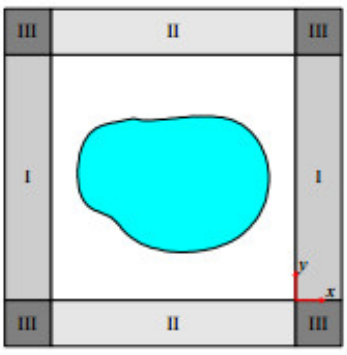


Fig. 1. The cross-section of arbitrary waveguide with the PML, placed at the edges of the computing domain.

© 2015 Bulgarian Academy of Sciences, Union of Chemists in Bulgaria

where ε_0 is the permittivity of free space, and $\varepsilon_{i,j}$ may be a complex value.

For permeability tensor $[\mu]$ is assumed diagonal structure:

$$[\mu] = \mu_0 \begin{Bmatrix} \mu_{xx} & 0 & 0 \\ 0 & \mu_{yy} & 0 \\ 0 & 0 & \mu_{zz} \end{Bmatrix}, \tag{2}$$

where μ_0 is the permeability of free space, and $\mu_{i,j}$ probably are equal to 1 for non-magnetic waveguide structures.

Assuming a z dependence of $e^{-i\beta z}$ for all fields and a time dependence of $e^{i\omega t}$, with β being the modal propagation constant Maxwell's equations can be written as:

$$\nabla \cdot ([\varepsilon]\vec{E}) = 0 \tag{3}$$
$$\nabla \times \vec{E} = -i\omega([\mu]\vec{H}) \tag{4}$$
$$\nabla \cdot ([\mu]\vec{H}) = 0 \tag{5}$$
$$\nabla \times \vec{H} = i\omega([\varepsilon]\vec{E}) \tag{6}$$

In the matrix form assuming $\dfrac{\partial}{\partial z} = -i\beta$ curl equations can be written as:

$$\begin{Bmatrix} 0 & i\beta & \dfrac{\partial}{\partial y} \\ -i\beta & 0 & -\dfrac{\partial}{\partial x} \\ -\dfrac{\partial}{\partial y} & \dfrac{\partial}{\partial x} & 0 \end{Bmatrix} \begin{Bmatrix} E_x \\ E_y \\ E_z \end{Bmatrix} = = -\omega\mu_0 \begin{Bmatrix} \mu_{xx} & 0 & 0 \\ 0 & \mu_{yy} & 0 \\ 0 & 0 & \mu_{zz} \end{Bmatrix} \begin{Bmatrix} H_x \\ H_y \\ H_z \end{Bmatrix} \tag{7}$$

$$\begin{Bmatrix} 0 & i\beta & \dfrac{\partial}{\partial y} \\ -i\beta & 0 & -\dfrac{\partial}{\partial x} \\ -\dfrac{\partial}{\partial y} & \dfrac{\partial}{\partial x} & 0 \end{Bmatrix} \begin{Bmatrix} H_x \\ H_y \\ H_z \end{Bmatrix} = = \omega\varepsilon_0 \begin{Bmatrix} \varepsilon_{xx} & \varepsilon_{xy} & \varepsilon_{xz} \\ \varepsilon_{yx} & \varepsilon_{yy} & \varepsilon_{yz} \\ \varepsilon_{zx} & \varepsilon_{zy} & \varepsilon_{zz} \end{Bmatrix} \begin{Bmatrix} E_x \\ E_y \\ E_z \end{Bmatrix} \tag{8}$$

For eigenmode form equations we need to eliminate E_z and H_z form (7) and (8).

Expression for H_z can be obtained from equation (5) or from third of equations (7).

$$H_z = \frac{1}{i\beta\mu_{zz}} \left(\mu_{xx} \frac{\partial H_x}{\partial x} + \mu_{yy} \frac{\partial H_y}{\partial y} \right) \quad \text{or}$$
$$H_z = -\frac{1}{i\omega\mu_0\mu_{zz}} \left(-\frac{\partial E_x}{\partial y} + \frac{\partial E_y}{\partial x} \right). \tag{9}$$

For E_z in general case we have from third of equation (8)

$$E_z = -\frac{\varepsilon_{zx}}{\varepsilon_{zz}E_x} - \frac{\varepsilon_{zy}}{\varepsilon_{zz}E_y} + \frac{1}{i\omega\varepsilon_0\varepsilon_{zz}} \left(-\frac{\partial H_x}{\partial y} + \frac{\partial H_y}{\partial x} \right). \tag{10}$$

By substituting the E_z and H_z expressions into (7) and (8) can be derived eigenvalue matrix equation for the four transverse field components.

Our new original proposal is to replace these four field components with only one complex filed component $\vec{F}$ and its conjugate $\vec{F}^*$

$$\vec{F} = \frac{1}{2}\vec{E} + i\frac{1}{2}\vec{H}. \tag{11}$$

Evidently we have

$$\vec{E} = \vec{F} + \vec{F}^*, \qquad i\vec{H} = \vec{F} - \vec{F}^* \tag{12}$$
$$\nabla \times \vec{F} = \frac{1}{2}\nabla \times \vec{E} + i\frac{1}{2}\nabla \times \vec{H} \tag{13}$$
$$\nabla \cdot \vec{F} = \frac{1}{2}\nabla \cdot \vec{E} + i\frac{1}{2}\nabla \cdot \vec{H} \tag{14}$$

Therefore, the equations (7) and (8) are reduced to an equation:

$$\begin{Bmatrix} 0 & i\beta & \dfrac{\partial}{\partial y} \\ -i\beta & 0 & -\dfrac{\partial}{\partial x} \\ -\dfrac{\partial}{\partial y} & \dfrac{\partial}{\partial x} & 0 \end{Bmatrix} \begin{Bmatrix} F_x \\ F_y \\ F_z \end{Bmatrix} = = \frac{1}{2}[T_1] \begin{Bmatrix} F_x \\ F_y \\ F_z \end{Bmatrix} + \frac{1}{2}[T_2] \begin{Bmatrix} F_x^* \\ F_y^* \\ F_z^* \end{Bmatrix}, \tag{15}$$

where $F_z = \frac{1}{2}E_z + i\frac{1}{2}H_z$ already known from expressions (9) and (10),

$$[T_1] = \omega\mu_0[\mu] + \omega\varepsilon_0[\varepsilon]$$
$$[T_2] = -\omega\mu_0[\mu] + \omega\varepsilon_0[\varepsilon]. \tag{16}$$

For the boundary conditions of considered anisotropic waveguide in the PML (perfected

matched layer) regions, the permittivity and permeability tensors are taken to be

$$[\varepsilon_{PML}] = \mu_0 \begin{Bmatrix} \frac{s_y s_z}{s_x}\varepsilon_{xx} & s_z\varepsilon_{xy} & s_y\varepsilon_{xz} \\ s_z\varepsilon_{yx} & \frac{s_x s_z}{s_y}\varepsilon_{yy} & s_z\varepsilon_{yz} \\ s_y\varepsilon_{zx} & s_x\varepsilon_{zy} & \frac{s_x s_y}{s_z}\varepsilon_{zz} \end{Bmatrix} \quad (17)$$

$$[\mu_{PML}] = \mu_0 \begin{Bmatrix} \frac{s_y s_z}{s_x}\mu_{xx} & 0 & 0 \\ 0 & \frac{s_x s_z}{s_y}\mu_{yy} & 0 \\ 0 & 0 & \frac{s_x s_y}{s_z}\mu_{zz} \end{Bmatrix}, \quad (18)$$

where s_x, s_y and s_z are the complex PML parameters defined as

$$s_x = 1 - i\alpha_x, \quad s_y = 1 - i\alpha_y, \quad s_z = 1 - i\alpha_z \quad (19)$$

witch appropriate values controlling the field attenuation in PML regions. As in [6] we may determine parameter s as follows

$$s = 1 - i\alpha = 1 - i\frac{\sigma_e}{\omega\varepsilon_0 n^2} = 1 - i\frac{\sigma_m}{\omega\mu_0}, \quad (20)$$

where σ_e and σ_m are the electric and magnetic conductivities of the PML, respectively, and n is the refractive index of the adjacent computing domain. This relation means that the wave impedance of a PML medium exactly equals to that of the adjacent medium in the computing window regardless of the angle of propagation. Assume that the electric conductivity of the PML medium has an m-power profile as

$$\sigma_e(\rho) = \sigma_{\max}\left(\frac{\rho}{d}\right)^m, \quad (21)$$

where ρ is the distance from the beginning of the PML and d is thickness. At the interface of the PML and the computing window, the theoretical reflection coefficient for the normal incident wave is

$$R = \exp\left[-2\frac{\sigma_{\max}}{\varepsilon_0 cn}\int_0^d (\rho/d)^m d\rho\right], \quad (22)$$

and the maximum conductivity $\sigma_{\max}$ can then be determined as

$$\sigma_{\max} = \frac{m+1}{2}\frac{\varepsilon_0 cn}{d}\ln\left(\frac{1}{R}\right), \quad (23)$$

where c is the speed of light in free space. For the case of $m = 2$

$$s = 1 - i\frac{3\lambda}{4\pi nd}\left(\frac{\rho}{d}\right)^2 \ln\left(\frac{1}{R}\right). \quad (24)$$

In our considerations we choose

$$\alpha_j = \alpha_{j,\max}\left(\frac{\rho}{d}\right)^2 \quad (25)$$

for $j = x$ and $j = y$, and $\alpha_z = 0$, where ρ represents the distance in the j-direction from the beginning of the PML region and $\alpha_{j,\max}$ is determined by the assumed reflectivity value from the PML layer.

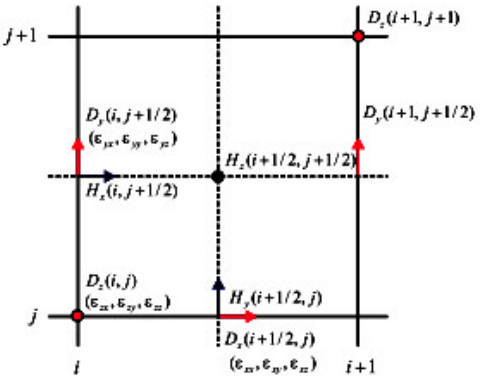
When the waveguide media can be represented with diagonal permittivity tensor it is more convenient to use modified differential operator in PML regions:

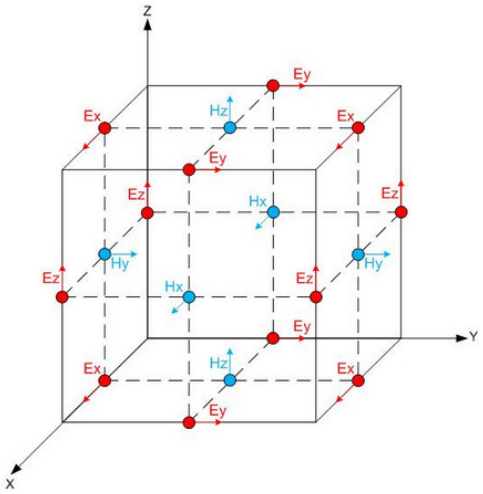
$$\nabla = \left(\frac{1}{s_x}\frac{\partial}{\partial x}, \frac{1}{s_y}\frac{\partial}{\partial y}, \frac{1}{s_z}\frac{\partial}{\partial z}\right) \quad (26)$$

without changes of permittivity and permeability tensors.

NUMERICAL SCHEME REALISATION

For numerical discretisation of equations (15) is used (FD) finite difference method based Yee's mesh algorithm by applying the central difference scheme for the differential operators. In brackets i and j is not indexes of arrays, they presented Yee's cells coordinates.





Applying the Yee's mesh and the central difference scheme expressions for curl operators

$$\nabla \times (\vec{F} + \vec{F}^*) = \nabla \times \vec{E} = -i\omega\mu_0[\mu]\vec{H} = \omega\mu_0[\mu](\vec{F} - \vec{F}^*) \tag{27}$$

$$\nabla \times (\vec{F} - \vec{F}^*) = \frac{1}{i}\nabla \times \vec{H} = \omega\varepsilon_0[\varepsilon]\vec{E} = \omega\varepsilon_0[\varepsilon](\vec{F} + \vec{F}^*) \tag{28}$$

become

$$0 \cdot E_{x,(i,j+1/2)} + i\beta E_{y,(i,j+1/2)} + \frac{E_{z,(i,j+1)} - E_{z,(i,j)}}{y_{(j+1)} - y_{(j)}} = -i\omega\mu_0\mu_{xx}H_{x,(i,j+1/2)} \tag{29}$$

$$-i\beta E_{x,(i+1/2,j)} + 0 \cdot E_{y,(i+1/2,j)} + \frac{E_{z,(i+1,j)} - E_{z,(i,j)}}{x_{(i+1)} - x_{(i)}} = -i\omega\mu_0\mu_{yy}H_{y,(i+1/2,j)} \tag{30}$$

$$\frac{E_{y,(i+1,j+1/2)} - E_{y,(i,j+1/2)}}{x_{(i+1)} - x_{(i)}} - \frac{E_{x,(i+1/2,j+1)} - E_{x,(i+1/2,j)}}{y_{(j+1)} - y_{(j)}} + 0 \cdot E_{z,(i+1/2,j+1/2)} = -i\omega\mu_0\mu_{zz}H_{z,(i+1/2,j+1/2)} \tag{31}$$

$$\begin{aligned} 0 \cdot H_{x,(i+1/2,j)} + i\beta H_{y,(i+1/2,j)} + \frac{H_{z,(i+1/2,j+1/2)} - H_{z,(i+1/2,j-1/2)}}{y_{(j+1/2)} - y_{(j-1/2)}} &= i\omega\varepsilon_0\varepsilon_{xx}E_{x,(i+1/2,j)} \\ &+ i\omega\varepsilon_0\varepsilon_{xy}E_{y,(i+1/2,j)} + i\omega\varepsilon_0\varepsilon_{xz}E_{z,(i+1/2,j)} \end{aligned} \tag{32}$$

$$\begin{aligned} -i\beta H_{x,(i,j+1/2)} + 0 \cdot H_{y,(i,j+1/2)} + \frac{H_{z,(i+1/2,j+1/2)} - H_{z,(i-1/2,j+1/2)}}{x_{(i+1/2)} - x_{(i-1/2)}} &= i\omega\varepsilon_0\varepsilon_{yx}E_{x,(i,j+1/2)} \\ &+ i\omega\varepsilon_0\varepsilon_{yy}E_{y,(i,j+1/2)} + i\omega\varepsilon_0\varepsilon_{yz}E_{z,(i,j+1/2)} \end{aligned} \tag{33}$$

$$\begin{aligned} -\frac{H_{x,(i,j+1/2)} + H_{x,(i,j-1/2)}}{y_{(j+1/2)} - y_{(j-1/2)}} + \frac{H_{y,(i+1/2,j)} - H_{y,(i-1/2,j)}}{x_{(i+1/2)} - x_{(i-1/2)}} + 0 \cdot H_{z,(i,j)} &= i\omega\varepsilon_0\varepsilon_{zx}E_{x,(i,j)} \\ &+ i\omega\varepsilon_0\varepsilon_{zy}E_{y,(i,j)} + i\omega\varepsilon_0\varepsilon_{zz}E_{z,(i,j)} \end{aligned} \tag{34}$$

In our case $F_x = E_x + F_x^*$, $F_y = E_y + F_y^*$, $F_z = E_z + F_z^*$, $F_x^* = F_x - iH_x$, ... etc.
Assuming field vectors functions represents one column array according Yee's cells.
For example if $\Delta x = x_{i+1} - x_i$ where $i = 0, 1, 2, \ldots, n$ and $\Delta y = y_{j+1} - y_j$ where $j = 0, 1, 2, \ldots, m$

$$E = (E_{x_0,y_0}, E_{x_0+\Delta x,y_0}, \ldots, E_{x_0+n\Delta x,y_0}, E_{x_0,y_0+\Delta y}, E_{x_0+\Delta x,y_0+\Delta y}, \ldots, E_{x_0+n\Delta x,y_0+\Delta y}, \ldots, E_{x_0+n\Delta x,y_0+m\Delta y})^{tr} \tag{35}$$

$$H = (H_{x_0,y_0}, H_{x_0,y_0+\Delta y}, \ldots, H_{x_0,y_0+m\Delta y}, H_{x_0+\Delta x,y_0}, H_{x_0+\Delta x,y_0+\Delta y}, \ldots, H_{x_0+n\Delta x,y_0+\Delta y}, \ldots, H_{x_0+n\Delta x,y_0+m\Delta y})^{tr}, \tag{36}$$

where E can be any of E_x, E_y or E_z and H can be H_x, H_y or H_z.

Then we can define derivates of functions using matrices according [8]

$$\frac{\partial}{\partial x}E = \mathbf{U_x}\mathbf{E} = \frac{1}{\Delta x}\begin{bmatrix} -1 & 1 & & & \\ & -1 & 1 & & \\ & & \ddots & & \\ & & & -1 & 1 \\ & & & & -1 \end{bmatrix}\begin{bmatrix} E_1 \\ E_2 \\ \vdots \\ E_{n\times(m-1)} \\ E_{n\times m} \end{bmatrix}, \tag{37}$$

$$\frac{\partial}{\partial y}E = \mathbf{U_y}\mathbf{E} = \frac{1}{\Delta y}\begin{bmatrix} -1 & \text{“n”}\ldots & 1 & & \\ & -1 & & \ddots & \\ & & \ddots & & 1 \\ & & & -1 & \\ & & & & -1 \end{bmatrix}\begin{bmatrix} E_1 \\ E_2 \\ \vdots \\ E_{(n-1)\times m} \\ E_{n\times m} \end{bmatrix}, \tag{38}$$

$$\frac{\partial}{\partial x}H = \mathbf{V_x}\mathbf{H} = \frac{1}{\Delta x}\begin{bmatrix} 1 & & & & \\ & -1 & 1 & & \\ & & \ddots & & \\ & & -1 & 1 & \\ & & & -1 & 1 \end{bmatrix}\begin{bmatrix} H_1 \\ H_2 \\ \vdots \\ H_{(n-1)\times m} \\ H_{n\times m} \end{bmatrix}, \tag{39}$$

$$\frac{\partial}{\partial y}H = \mathbf{V_y}\mathbf{H} = \frac{1}{\Delta y}\begin{bmatrix} 1 & & & & \\ & 1 & & & \\ -1 & & \ddots & & \\ & & & 1 & \\ & & -1 & & 1 \end{bmatrix}\begin{bmatrix} H_1 \\ H_2 \\ \vdots \\ H_{n\times(m-1)} \\ H_{n\times m} \end{bmatrix}. \tag{40}$$

Final eigenvalue matrix equation for the four transverse field components can be derived as in the fooling form:

$$\begin{bmatrix} A_{11} & A_{12} & A_{13} & A_{14} \\ A_{21} & A_{22} & A_{23} & A_{24} \\ A_{31} & A_{32} & A_{33} & A_{34} \\ A_{41} & A_{42} & A_{43} & A_{44} \end{bmatrix}\begin{bmatrix} E_x \\ H_x \\ E_y \\ H_y \end{bmatrix} = \beta\begin{bmatrix} E_x \\ H_x \\ E_y \\ H_y \end{bmatrix} \tag{41}$$

After some obvious algebraic simplification (41) can be written as:

$$\begin{bmatrix} B_{33} & B_{34} \\ B_{43} & B_{44} \end{bmatrix}\begin{bmatrix} F_x \\ F_y \end{bmatrix} = \beta\begin{bmatrix} F_x \\ F_y \end{bmatrix}, \tag{42}$$
$$2F_x = E_x + iH_x, \qquad 2F_y = E_y + iH_y$$

and once solved this matrix equation, then can find four transverse field components by formulas (12). Or we can solve equation (41) and directly find field components. Note, if choose (42) matrix equations are twice less, which reduces memory and optimize iterative work of eigen solver.

Below are listed coefficients of matrix A. They are similar to [8], distinguished by their ranking

$$\begin{cases} A_{11} = -i\dfrac{\varepsilon_{zx}}{\varepsilon_{zz}}\mathbf{U_x}, \\ A_{12} = -\dfrac{1}{\omega\varepsilon_0\varepsilon_{zz}}\mathbf{U_x}\mathbf{V_y}, \\ A_{13} = -i\dfrac{\varepsilon_{zy}}{\varepsilon_{zz}}\mathbf{U_x}, \\ A_{14} = \dfrac{1}{\omega\varepsilon_0\varepsilon_{zz}}\mathbf{U_x}\mathbf{V_x} + \omega\mu_0\mu_{yy}\mathbf{I}, \end{cases} \tag{43}$$

$$\begin{cases} A_{21} = -\omega\varepsilon_0\varepsilon_{yx}\mathbf{I} + \dfrac{1}{\omega\mu_0\mu_{zz}}\mathbf{V_x}\mathbf{U_y} + \dfrac{\omega\varepsilon_{yz}\varepsilon_{zx}}{\varepsilon_{zz}}\mathbf{I}, \\ A_{22} = -i\dfrac{\varepsilon_{yz}}{\varepsilon_{zz}}\mathbf{V_y}, \end{cases} \tag{44}$$

$$\begin{cases} A_{23} = -\omega\varepsilon_0\varepsilon_{yy}\mathbf{I} - \dfrac{1}{\omega\mu_0\mu_{zz}}\mathbf{V_x}\mathbf{U_x} + \dfrac{\omega\varepsilon_{yz}\varepsilon_{zy}}{\varepsilon_{zz}}\mathbf{I}, \\ A_{24} = i\dfrac{\varepsilon_{yz}}{\varepsilon_{zz}}\mathbf{V_x}, \end{cases} \tag{45}$$

$$\begin{cases} A_{31} = -i\dfrac{\varepsilon_{zx}}{\varepsilon_{zz}}\mathbf{U_y}, \\ A_{32} = -\dfrac{1}{\omega\varepsilon_0\varepsilon_{zz}}\mathbf{U_y}\mathbf{V_y} - \omega\mu_0\mu_{xx}\mathbf{I}, \\ A_{33} = -i\dfrac{\varepsilon_{zy}}{\varepsilon_{zz}}\mathbf{U_y}, \\ A_{34} = \dfrac{1}{\omega\varepsilon_0\varepsilon_{zz}}\mathbf{U_y}\mathbf{V_x}, \end{cases} \tag{46}$$

$$\begin{cases} A_{41} = \omega\varepsilon_0\varepsilon_{xx}\mathbf{I} + \dfrac{1}{\omega\mu_0\mu_{zz}}\mathbf{V_y}\mathbf{U_y} - \dfrac{\omega\varepsilon_{xz}\varepsilon_{zx}}{\varepsilon_{zz}}\mathbf{I}, \\ A_{42} = i\dfrac{\varepsilon_{xz}}{\varepsilon_{zz}}\mathbf{V_y}, \end{cases} \tag{47}$$

$$\begin{cases} A_{43} = \omega\varepsilon_0\varepsilon_{xy}\mathbf{I} - \dfrac{1}{\omega\mu_0\mu_{zz}}\mathbf{V_y}\mathbf{U_x} - \dfrac{\omega\varepsilon_{xz}\varepsilon_{zy}}{\varepsilon_{zz}}\mathbf{I}, \\ A_{44} = -i\dfrac{\varepsilon_{xz}}{\varepsilon_{zz}}\mathbf{V_x}. \end{cases} \tag{48}$$

NUMERICAL EXAMPES AND RESULTS

To demonstrate the accuracy and applications of the proposed 3D method, we present two numerical examples, one with electrooptic polymer waveguide that is poled at an oblique angle relative to the direction [9 - 10], and the other involving LCs with arbitrary director orientation [11].

In first example the cladding layers are assumed to be nonpolar (and hence immune to the poling field) with an isotropic refractive index of $n_1 = n_3 = 1.60$. The middle layer is modeled as an electrooptic polymer with a refractive index of $n_2 = 1.65$ prior to poling. This waveguide structure provides an interesting challenge for mode calculations because both the orientation and strength of the birefringence are nonuniform throughout the waveguide core. Moreover,

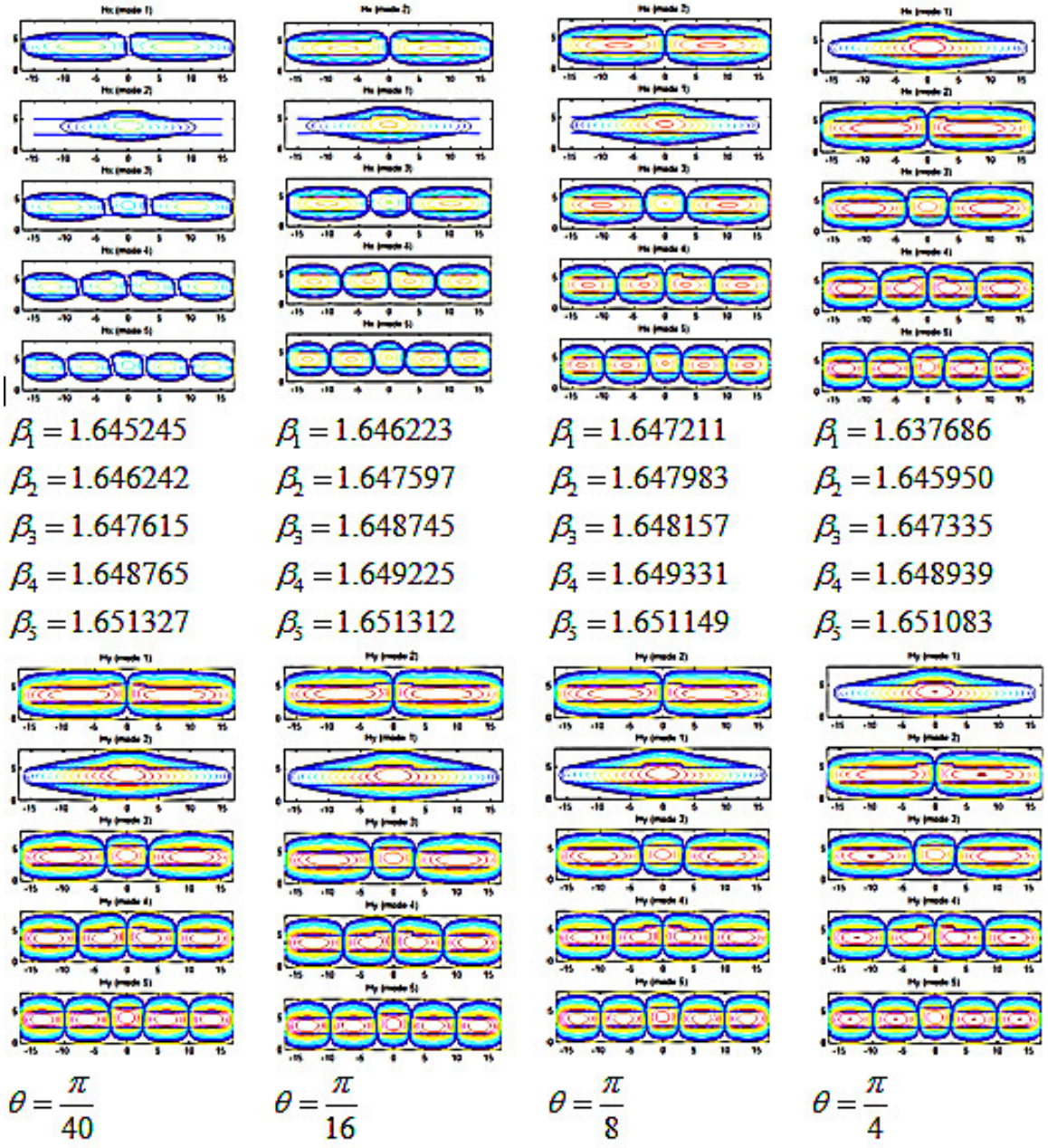


Fig. 2. H_x and H_y modes of electrooptic polymer waveguide.

the induced anisotropy, although small, plays an essential role in guaranteeing transverse mode confinement. The net birefringence is assumed to be split between the ordinary and extraordinary indices in the following way:

$$n_{2e} = n_2 + (2/3)\Delta n, \quad n_{2o} = n_2 - (1/3)\Delta n \qquad (49)$$

with Δn given by eq (18) in [5]. The local permittivity tensor in the middle layer is then described by

$$\begin{bmatrix} n_{2e}^2\cos^2\theta + n_{2o}^2\sin^2\theta & (n_{2e}^2 - n_{2o}^2)\sin\theta\cos\theta & 0 \\ (n_{2e}^2 - n_{2o}^2)\sin\theta\cos\theta & n_{2e}^2\cos^2\theta + n_{2o}^2\sin^2\theta & 0 \\ 0 & 0 & n_{2o}^2 \end{bmatrix}, \qquad (50)$$

where θ is an angle of axis of anisotropy.

Our results for first 5 modes (H_x, H_y) and for 4 different values of θ are shown in Fig. 2.

In [5] is shown only fundamental mode.

In second example we study an LC (liquid crystal) optical waveguide. The substrate being glass with the refractive index $n_1 = 1.45$ and the core region being filled with nematic LCs (5CB). The elements of the relative permittivity tensor of the nematic LCs are given as:

$$\varepsilon_{xx}/\varepsilon_0 = n_o^2 + (n_e^2 - n_o^2)\sin^2\theta\cos^2\phi \quad (51)$$
$$\varepsilon_{xy}/\varepsilon_0 = \varepsilon_{yx} = (n_e^2 - n_o^2)\sin^2\theta\sin\phi\cos\phi \quad (52)$$
$$\varepsilon_{xz}/\varepsilon_0 = \varepsilon_{zx} = (n_e^2 - n_o^2)\sin\theta\cos\theta\cos\phi \quad (53)$$
$$\varepsilon_{yy}/\varepsilon_0 = n_o^2 + (n_e^2 - n_o^2)\sin^2\theta\cos^2\phi \quad (54)$$
$$\varepsilon_{yz}/\varepsilon_0 = \varepsilon_{zy} = (n_e^2 - n_o^2)\sin\theta\cos\theta\sin\phi \quad (55)$$
$$\varepsilon_{zz}/\varepsilon_0 = n_o^2 + (n_e^2 - n_o^2)\cos^2\theta. \quad (56)$$

We have made many calculations at different rotation angles (θ, ϕ) defining the director of LC, where θ is the angle between the crystal c-axis and the z-axis, and ϕ is the angle between the projection of the crystal c-axis on the $x-y$ plane and the x-axis, as shown at Fig. 3.

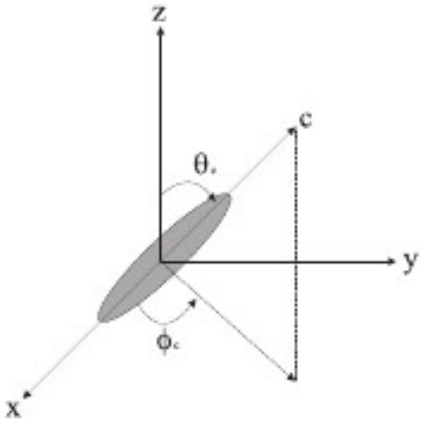


Fig. 3. Schematic definition of rotation angles for the LC molecular or director.

We use that where $n_o = 1.5292$ and $n_e = 1.7072$ are, respectively, the ordinary and extraordinary refractive indices of the nematic LCs.

To illustrate 3D features of our method we present all four field modes for selected values $\theta = 60°$, $\phi = 0$ and $\theta = 60°$, $\phi = 60°$. Results are shown at Fig. 4 and Fig. 5.

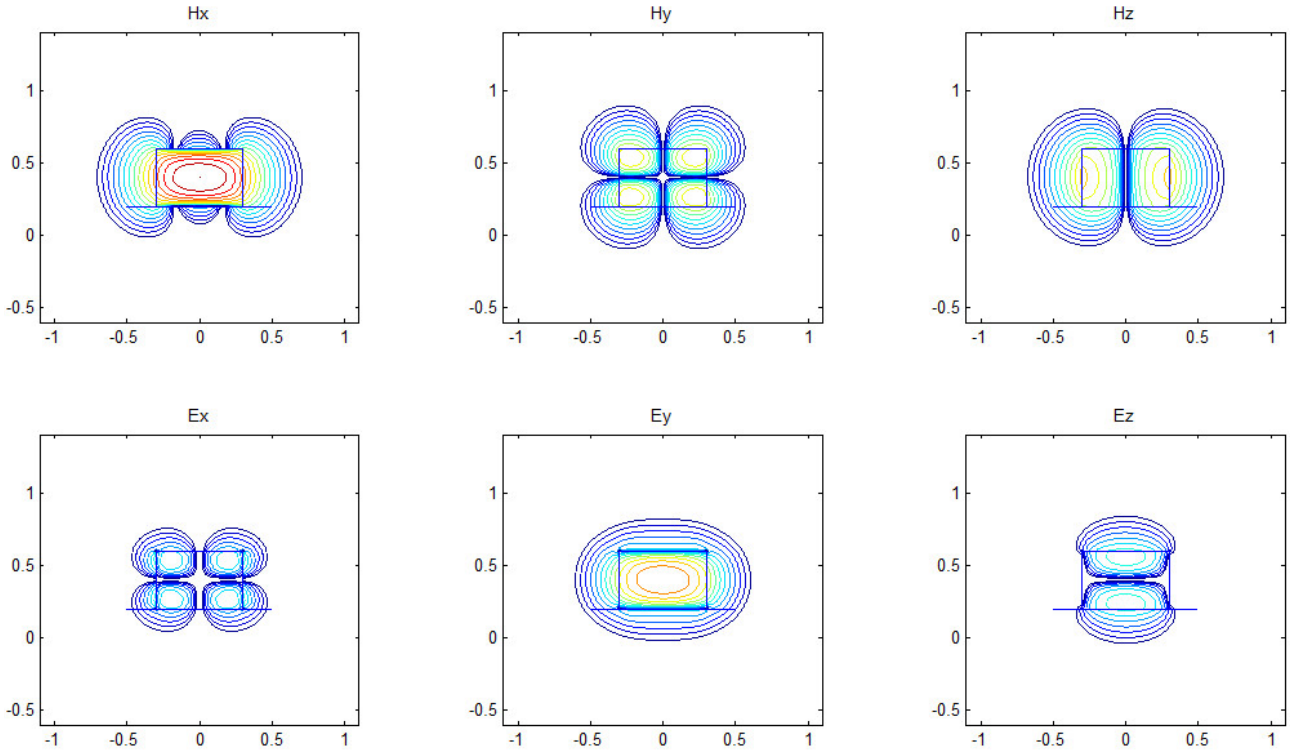


Fig. 4. All mode–field profiles for the first mode of the LC waveguide with $\theta = 60°$, $\phi = 0$.

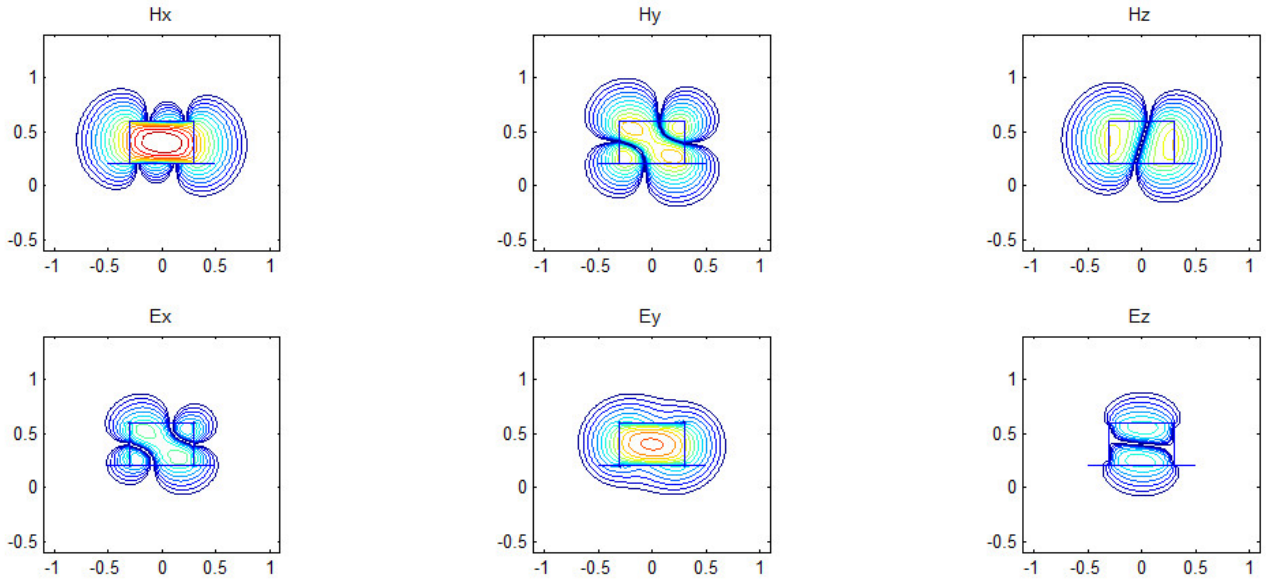


Fig. 5. All mode–field profiles for the first mode of the LC waveguide with $\theta = 60^\circ$, $\phi = 60^\circ$.

CONCLUSIONS

We have presented a new FD method based eigenvalue algorithm for computing guided modes of anisotropic optical waveguides with arbitrary permittivity tensor. Instead of using the standard eigenvalue matrix equation involving four transverse field components, we involve only two (complex vector of Riemann- Silberstein and its conjugated) witch halves the required computer memory. Algorithm has been used to solve guided modes on a liquid-crystal optical waveguide with arbitrary molecular director orientation. This established mode solver provides an efficient tool for studying and designing as ordinary waveguides and waveguides with complicated materials such as liquid crystals.

REFERENCES

[1] L. Thylen, and D. Yevick, *Appl. Opt.* **21**, 2751–2754 (1982).

[2] C. L. Xu, W. P. Huang, J. Chrostowski, and S. K. Chaudhuri, *J. Lightwave Technol.* **12**, 1926–1931 (1994).

[3] C. L. D. S. Sobrinho, and A. J. Giarola, *IEE Proc.* **H140**, 224–230 (1993).

[4] P. Lüsse, K. Ramm, and H.G. Unger, *Electron. Lett.* **32**, 38–39 (1996).

[5] A. B. Fallahkhair, K. S. Li, and T. E. Murphy, *J. Lightwave Technol.* **26**, 1423–1431 (2008).

[6] C. P. Yu, and H. C. Chang, *Opt. Express* **12**, 6165V–6177 (2004).

[7] L. Silberstein, *Annalen der Physik* **327**, 579–586 (1907).

[8] M. Chen, S. Hsu, and H. Chang, *Opt. Express* **17**, 6177 (2009).

[9] J. Yang, Q. Zhou, X. Jiang, M. Wang, Y. Wang, and R. T. Chen, *J. Lightw. Technol.* **22**, 1930-1934 (2004).

[10] M.-C. Oh, S.-S. Lee, and S.-Y. Shi, *J. Quantum Electron.* **31**, 1698-1704 (1995).

[11] P. Yeh, and C. Gu, in *Optics of Liquid Crystal Displays*, (John Wiley and Sons, New York, 1999).

ПРИЛОЖЕНИЕ НА МЕТОДА НА КРАЙНИТЕ РАЗЛИКИ ЗА НАМИРАНЕ НА СОБСТВЕНИТЕ СТОЙНОСТИ И ВЕКТОРИ НА МНОГОСЛОЙНИ АНИЗОТРОПНИ ОПТИЧНИ ВЪЛНОВОДИ

Ив. Иванов

Физически факултет, Пловдивски университет "Паисий Хилендарски",
ул. "Цар Асен" №24, 4000 Пловдив, България

(Резюме)

В работата се предлага числов модел на основата на 3D метода на крайните разлики за изследване на анизотропни оптични вълноводи с произволна конфигурация на тензора на диелектрична проницаемост. Прилагането му води до получаване на удобно матрично уравнение, от което се определят спектъра и собствените му функции, които представят четирите напречни полеви компоненти, подредени плъно едно под друго в едноразмерен масив. Намирането на възможните комплексни собствени стойности и вектори се извършва посредством shifted inverse power method, чието отместване се определя динамично посредством коефициента на Релей. Той е особено ефективен при разредени лентъчни матрици и притежава почти кубична сходимост. Алгоритмът е приложен за изчисление на модите на: 1) вълновод с електрооптичен полимерен слой; и 2) вълновод с течнокристален слой с произволна ориентация на направляващия вектор. Числовите резултати се съгласуват много добре с получени чрез други числови алгоритми.

PHYSICS OF EARTH, ATMOSPHERE AND SPACE. OCEANOLOGY

ФИЗИКА НА ЗЕМЯТА, АТМОСФЕРАТА И КОСМОСА. ОКЕАНОЛОГИЯ

Bulgarian Chemical Communications, Volume 47, Special Issue B (pp. 299–308) 2015

Seismicity and nowadays movements along some active faults in SW Bulgaria

N. Dobrev[1]*, E. Botev[2], V. Protopopova[2], I. Georgiev[2], D. Dimitrov[2]

[1] *Geological Institute, Bulgarian Academy of Sciences, Acad. G. Bonchev Str., Bl. 26, 1113-Sofia, Bulgaria*
[2] *National Institute of Geophysics, Geodesy and Geography, Bulgarian Academy of Sciences, Acad. G. Bonchev Str., Bl. 3, 1113-Sofia, Bulgaria*

Some results from the seismic, geodetic and extension-metric monitoring of the seismoactive Krupnik source zone in SW Bulgaria during the last 33 years are presented. Special attention is paid to the seismological analysis and fault plain modeling of the stronger earthquakes as a seismic activity investigation. Some extension-metric data and geodetic analysis using present-day GPS data are used in order to constrain the nowadays geodynamics of this region.

Key words: seismicity, earthquake, fault, Krupnik

The South Western part of the Bulgarian territory is the most seismoactive region in Bulgaria and Krupnik seismic zone is the most active part in it. Krupnik seismogenic area is well known by its high seismicity: since I century BC at least 10 events with magnitude M $\geq$ 6 have been occurred on its territory and the adjacent lands. The strongest known event is the earthquake of April 4, 1904 with a magnitude Ms 7.8 [1]; it occurred in the Krupnik source zone, which is nearby the present-day contact area between Southwestern Bulgaria and FYR of Macedonia. Since that time the seismic activity is relatively moderate and scarce along this region. A very complex fault structure characterizes this part of Bulgaria [2]. Several main fault structures build this region. The Krupnik and Struma faults are the most significant of them (Fig. 1).

The geology of the research area is rather complex and is associated with the here situated Pirin, Rila and Vlahina mountains, and first of all with the local structure of the Struma lineament. In fact the Struma lineament is an S-SE oriented asymmetric graben which present view is formed by the Post Alpine activation. Several important faults cross this zone – the subject of our paper is connected with the most significant of them- Krupnik fault lineament (N-NE oriented), which is assumed to be the most active fault structure in Bulgaria. During the Neotectonic stage, the realized vertical movement along this fault is estimated as 3400 m [3]. Some seismotectonics problems of this zone have been discussed in some previous papers of the authors [4–6] and others. In this paper an attempt to elucidate more detailed the lasts seismic manifestations of the fault structures and to identify the geometry and the movements along the main active faults and their relations to the earthquakes is made. To approach to this main goal first of all we analyze the epicentral, magnitude and depth distribution of the earthquakes and their fault plane

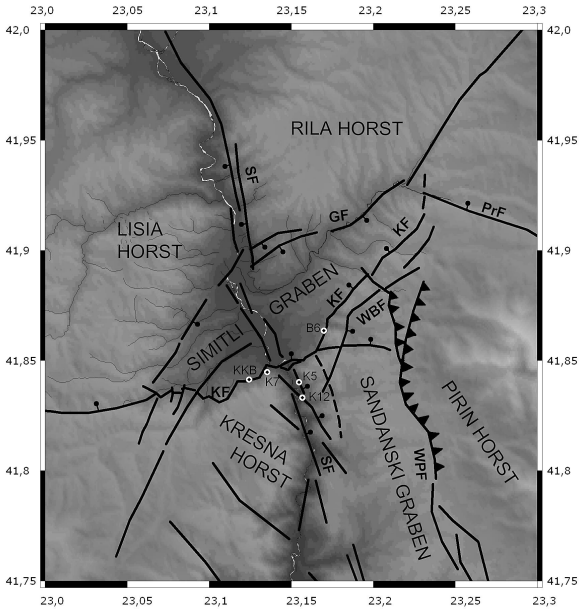


Fig. 1. Simplified sketch of the Simitli graben and adjacent area [4]. The map shows the main tectonic structures, faults and observation points. The main faults are as follows: KF, Krupnik Fault; GF, Gradevo Fault; SF, Struma Fault Zone; WPF, West Pirin Fault (mostly reverse); PrF, Predela Fault; WBF, West Brezhani Fault. The extension monitoring points localities are shown, KKB is the Seismic Station Krupnik.

* To whom all correspondence should be sent:
ndd@geology.bas.bg

© 2015 Bulgarian Academy of Sciences, Union of Chemists in Bulgaria

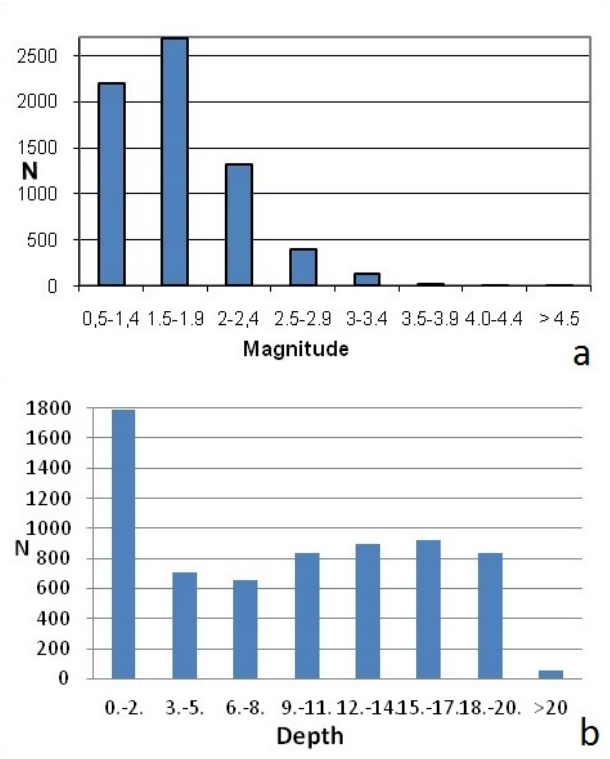


Fig. 3. Magnitude (a) and depth (b) distribution of the seismic events.

mechanisms in the region with coordinates φ = 41.7 – 42.1 N; λ = 22.7 – 23.4 E for the period of working of National seismological network NOTSSI (1981–2013), as well as the surface geodetic and extensionmetric manifestations of some satellites of Krupnik fault lineament.

Because of the small number of instrumentally recorded strong earthquakes, the investigation of the well recorded relatively weak seismicity in the last 33 years is required to overcome the existing laps. Conditions for detailed investigations of the weak seismicity around the Krupnik source zone are created after 1980 with the starting of NOTSSI operation. In such a way for the period 1981-2013 in this area more than 6800 earthquakes are recorded in a magnitude interval M = 0.5 – 4.8 (Fig. 2). The magnitude-frequency distribution for the entire data set in Fig. 2a shows that the number of localized events increases with the magnitude decreasing: for M = 4.5–4.9 is 1 event, for M = 4.0–4.4 are 4 events, for M = 3.5–3.9 are 26 events, for M = 3.0–3.4 are 134 events, for M = 2.5–2.9 – 400, for M = 2.0–2.4 – 1326 and so on. The abrupt diminishing of the number of earthquakes in the first two intervals ($M < 1.5$) in Fig. 2a determines also the registration power of the seismic stations network. Taking the latter into account, it can be supposed that the magnitude sample for levels with $M > 1.5$ is comparatively closer to the reality for this part of the Bulgarian territory.

The picture of the depth distribution in Fig. 2b shows that the majority of events occur down to 20 km depth. It is possible the established predominating depth (from 0 to 5 km) to be also due to the presence of unidentified industrial explosions. In the same time the number of events in the interval 11-20 km is comparative with this one. The magnitude distribution of the events in depth (Fig. 3) permits to note some differentiation of depth "floors" with the increase of magnitude – some tendency of formation of some maximums can be traced out for the depth intervals of 10 and 20 km.

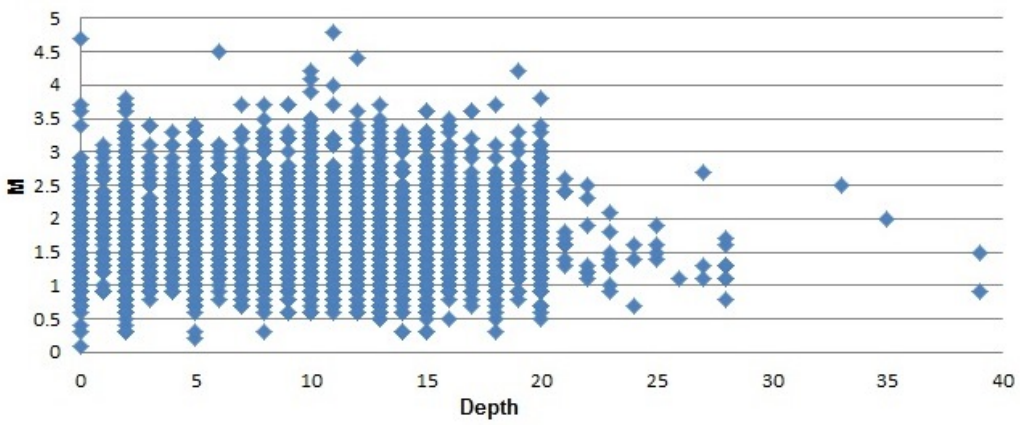


Fig. 3. Magnitude-depth distribution of the seismic events.

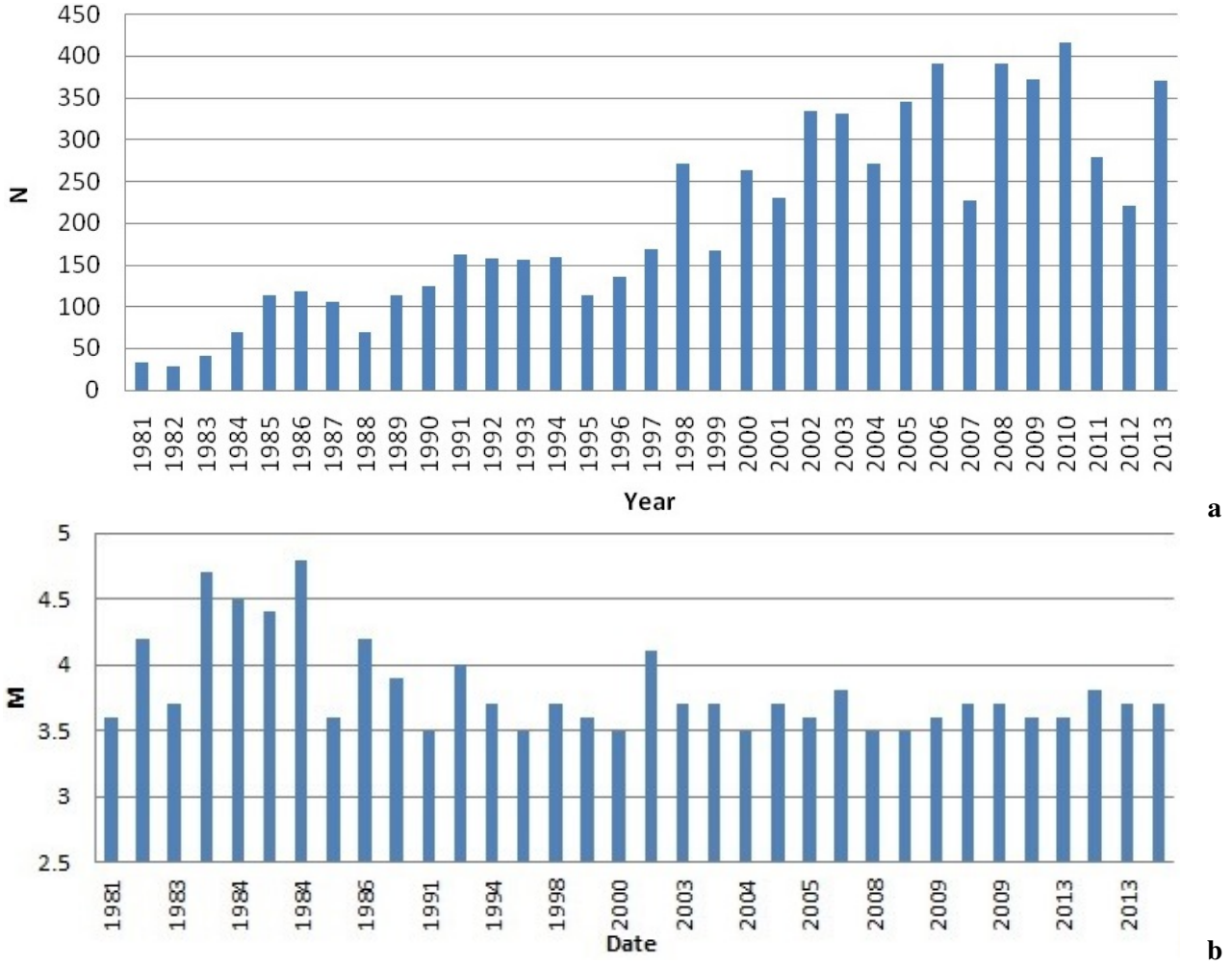


Fig. 4. Time (a) and Magnitude-time (b) distribution of the seismic events.

Fig. 4a illustrates the distribution of seismicity in time according to the number of events per years. The biggest earthquake's amount is displayed in 2010, when about 400 earthquakes occurred – mainly because of local Krupnik fault's earthquake activity. The lowest earthquake quantity is in 1981 and 1982, when about 40 events occurred. Fig. 4b shows the energy release in time through the earthquake magnitude-time distribution. It suggests that in the beginning of 1984, when enough small number of events occurred, is the maximum of energy release. Some other strongest events occurred in 1982 and in 2001. The released high energy amount in the first half of the whole period of study compensates the large number of low magnitude events during the second half of the time period. The low number of small earthquakes in the beginning of the investigated period could be associated with some low registration peculiarities of the network during the beginning of its operation.

The epicenter distribution for the data described above is shown in Fig. 5. The magnitude of the earthquakes is differentiated in five groups – as it is mentioned in Legend of the figure below. From this figure it is clear, that there is no significant number of earthquakes with magnitude $M > 2$. in the NW and SE parts of the region of interest. The present seismological data demonstrate some grouping of earthquake epicenters. The biggest earthquake density is observed in the NE part of the investigated region, as well as in the SW part (with smaller number of events). It is remarkable that there is no some background of the everywhere space distribution. So, two relatively outlined zones of grouping of the epicenters can be marked, but the zone of concentration of seismic events in east-west direction in the NE part

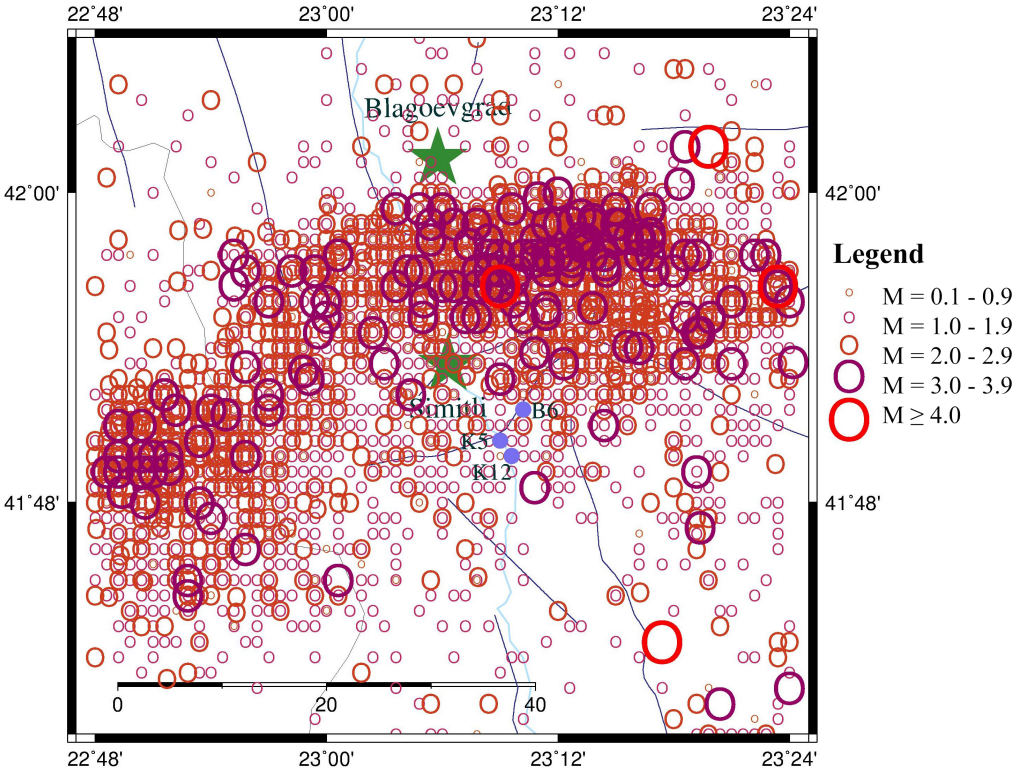


Fig. 5. Epicenter distribution of the seismic events (The Generic Mapping Tools - http://gmt.soest.hawaii.edu/home, the tectonic map is compiled after [7] and [8]).

is more active. This zone can be related with the manifestation of the namely Krupnik fault and its NE branch - West Brezhani fault, as well as with Gradevo fault (Fig. 1). In fact the most significant part of the epicenters is concentrated to the NorthWest from the Krupnik faults lineament with an ENE – WSW direction of the maximum density. The strongest earthquakes for the period of investigation (with magnitude M = 4.4 and M = 4.8) has occurred in one of the same place here during the beginning of 1984. The distribution of the epicenters northern of the Simitli graben can be explained only with the bigger depth of these shocks. The strongest earthquakes are about 10 and 20 km depth and this fact allows us to associate them with the depth activity of the steeple Krupnik-Brezhani fault lineament.

To the SW corner of the territory of interest it can be seen the grouping of epicenters northward from the continuation of the Krupnik fault rupture. More of these earthquakes are located with big depth, which confirm the NW dipping of the fault plane. Having in mind this big hypocentral depth (averaged about 10 km) a hidden penetration of this fault lineament (Pehchevo lineament) to the N-NW direction could be assigned. In such a way this identification may be considered as a manifestation of a particular seismotectonic structure without surface expression, but with an association to well known active fault in around (Krupnik fault). From the picture of Fig. 5 it is clear, that in general, the obtained territorial distribution of the earthquakes shows some agreement with the depth structure of the all shown morphotectonic dislocations, confirming the decisive role of the Krupnik fault system, associated with the surface ruptures from 1904. Only one group of epicenters located to the SE from the maximum concentration could be associated with the influence of the western border of Predela fault - with discordance direction to the Kroupnik system. In this paper the present activity of this eastern faults (with strongest earthquakes with magnitude M = 4.2 and M = 4.0) is out of our interest.

As in the most tectonic region in Bulgaria, the earthquakes in Krupnik source zone are confined to the upper part of the crust, suggested that the depth seismic activity is connected with the depth distribution of morphotectonic dislocations. The orientation of the dislocations and the tectonic stresses in depth in the present work are investigated additionally [9, 10]

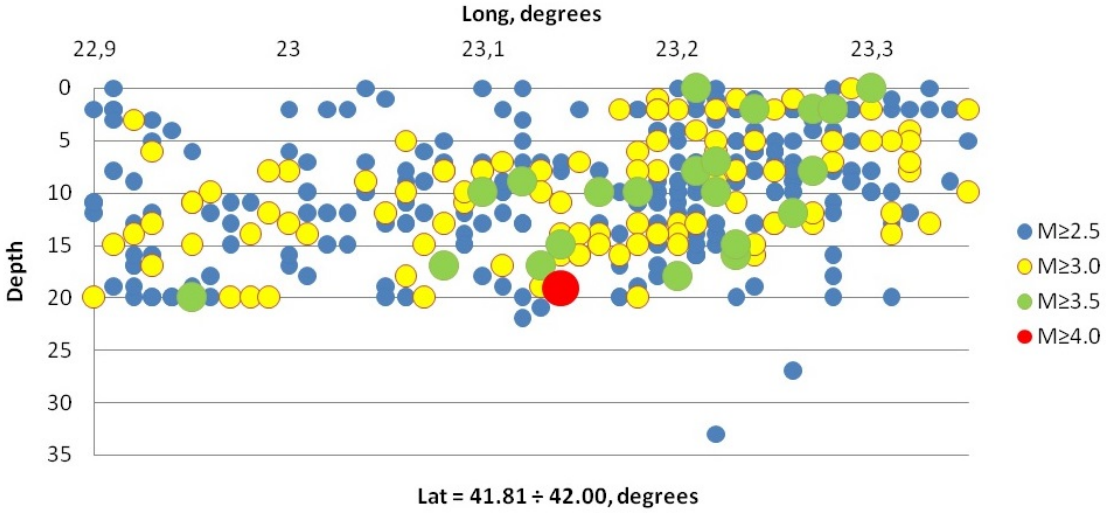


Fig. 6. Depth distribution along a longitudinal profile for the events in NE part.

by means of analysis of the morphotectonic and depth manifestations of the main active faults during the last years. Because of some inaccuracies in the bulletin coordinates for the period 1981–1984, the more precise profile depth distributions were especially made for the events with magnitude M $>$ 2.5 (Fig. 6 and Fig. 7). Concerning the depth parameters of the investigated earthquakes with M $>$ 2.5, approximately uppersrustal distribution is marked. In fact almost all earthquakes (in depth interval between 0 km and 20 km) are located in the upper crust (or so called "granite" layer) of the region, where the crust thickness varies down to 40 or 45 km depths. In general, it could be confirmed, that the depth distribution of the epicenters of the weak earthquakes at the present, as well as the depth distribution of the stronger earthquakes since the beginning of the century, are located mainly to the depth of 20 km, suggesting the relatively small thickness of the seismogenic layer in the investigated region.

From a geotectonic point of view, the projection of the depth distribution of the seismic events on vertical cross sections is of significant interest – to clarify the seismic structures in depth. To get an idea about the

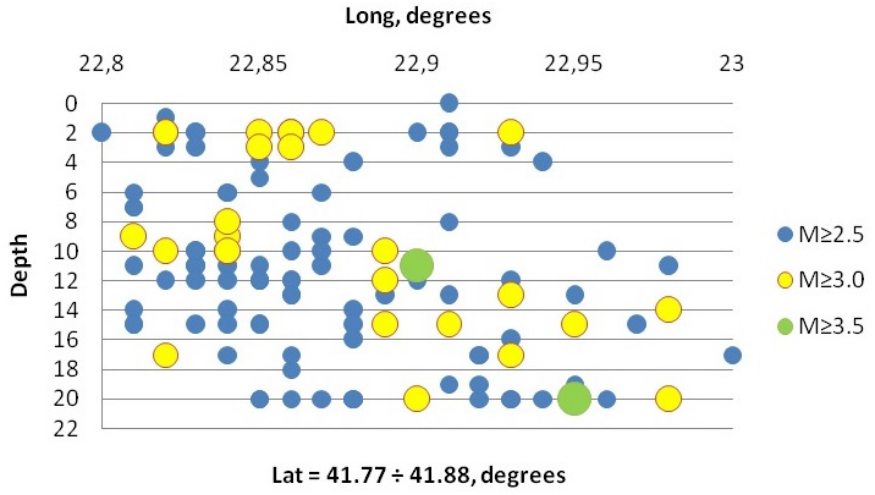


Fig. 7. Depth distribution along a longitudinal profile for the events in SW part.

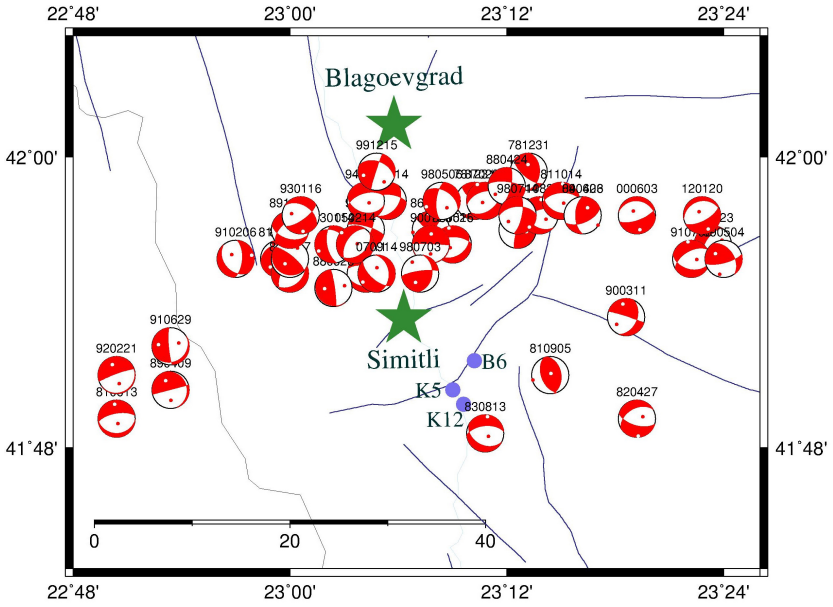


Fig. 8. Fault plane solutions of the stronger events (1981-2013).

distribution of these structures in depth, two vertical cross sections are presented in Fig. 6 and Fig. 7. To present the data more adequately the region of interest is divided into two parts: NE part, including the all area associated with the Krupnik and Gradevo faults (from $\lambda = 22.90$ to $\lambda = 23.35$ and from $\varphi = 41.81$ to $\varphi = 42.00$), and SW one, including almost all earthquakes associated with the depth manifestation of the western part of the Krupnik fault system – Pehchevo lineament (from $\lambda = 22.80$ to $\lambda = 23.00$ and from $\varphi = 41.77$ to $\varphi = 41.88$). The depth distribution of the events is presented by two transversally vertical cross sections with longitudinal directions for each separated parts.

In Fig. 6 it can be seen the depth distribution of the all events from the NE part projected along a longitudinal profile (E-W direction). The vertical cross section reveals stronger seismicity in the deeper layers, which can be generally related to the depths between 6 and 20 km. The level of seismicity in the upper layers is significant lower – there is no one event with magnitude in the interval M = 3.5–3.9 or more. In general it can be seen that the strongest earthquakes are released beneath the central part of the profile. It is interesting to mark some dipping of the seismicity from East to West towards to the central part. To the West from the central part a very slight dipping of the seismogenic layer goes on. The dipping of seismicity in the western part of the profile could be associated with the deep structural influence of older Struma lineament which crosses here transversally the profile.

The depth distribution of the data for SW part of the all region under investigation is presented in Fig. 7. Almost all these earthquakes could be generally related to the hidden manifestation of the E-NE oriented satellite of the western part of Krupnik fault system. The seismicity here is rather weak, but involves the whole surficial 20 km depths. The level of seismicity beneath of 10 km depth is higher - all events with magnitude M > 3.0 are concentrated here. The strong shocks gravitate predominantly towards the eastern end of the profile, but not so abrupt increasing of the depth of the earthquakes towards eastern part is observed. In fact, all differentiated by magnitude groups of earthquakes go deeper to the east situated Struma lineament. This is consistent with the hypothesis of the hidden deep influence of the older Struma fault satellites.

The fault plane solutions of the stronger events (magnitude M > 3.5) are presented on Fig. 8. More than 80% of the focal plane solutions are with normal dip-slip component and the predominant orientation of the nodal planes is 70° to 90°. This prevailing plane direction coincidence with the orientation of the Krupnik fault sistem. The most relevant evidence for this zone is the almost horizontal orientation of the T-axes in the NNW – SSE direction. There is no clear predominant trend of the P-axes, but mainly for the

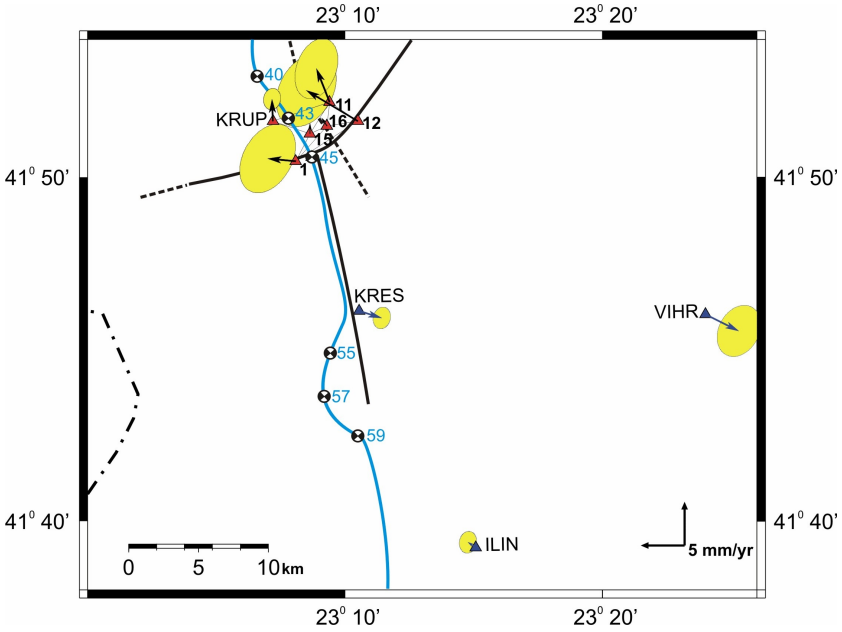


Fig. 9. Extension regime in the Krupnik region by geodetic data.

cases of subhorizontal axes, the ENE – WSW direction dominates. In many of these cases a strike-slip mechanism of faulting (with relevant normal dip component) could be recognized. The plunge angle of the P-axes is larger in comparison with that of T-axes. In general, the calculated focal mechanisms of the earthquakes show that the earthquakes are caused by the tectonic activation of predominantly normal faults, situated around the Krupnik source zone. As well as the Krupnik zone is the zone with the biggest regional significance in SW Bulgaria, special multidisciplinary investigations have been performed namely here by National Institute of Geophysics, Geodesy and Geography (NIGGG) and Geological Institute (GI) of Bulgarian Academy of Sciences (BAS). Special attention is paid to the complex analysis in order to constrain the geodynamics of this region using present-day GPS and extension-metric data.

The local geodetic network in the Krupnik region is designed for monitoring the horizontal crustal block motion [11]. The original configuration consists of 16 points with and the first GPS measurements are performed during the period 1984-1992, but horizontal motions are not revealed. Higher precise GPS measurements started in 1995 by means of many times measuring of the classical points and correlations with other measurements until now. For monitoring of horizontal motions after careful estimation of the tectonic settings and access to the points' state, six of them – two on the southern side and four from the northern side of the Krupnik fault are chosen for GPS observations One idea about the geodetic network and the distribution of geodetic points of measurements in this part of SW Bulgaria could be assumed by the picture in Fig. 9. Geodetic data constrained the recent crustal motions along the Krupnik fault and confirmed its tectonic activity. They also show that the region is undergoing the extension and are in agreement with the seismological and geological information. The field of seismotectonic deformations is generally characterized by predominance of NW-SE horizontal extension. From NE to SW the direction of extension changed gradually to WNW-ESE.

To detect the real rates of fault movements along the fault in the region of interest one extension-metric monitoring at many points in and around the Krupnik region have been organized by GI of BAS [4–6, 12] and others. The obtained results confirmed the decisive role of the Krupnik fault - the main extension movements have been observed for the points K5, K12 and B6 (Fig. 8) which are located very closed to the Krupnik-Brezhani fault surface line. The most expressive results have been obtained along the Krupnik fault for the monitoring site B6. In Fig. 10 some unpublished results for this point during the period

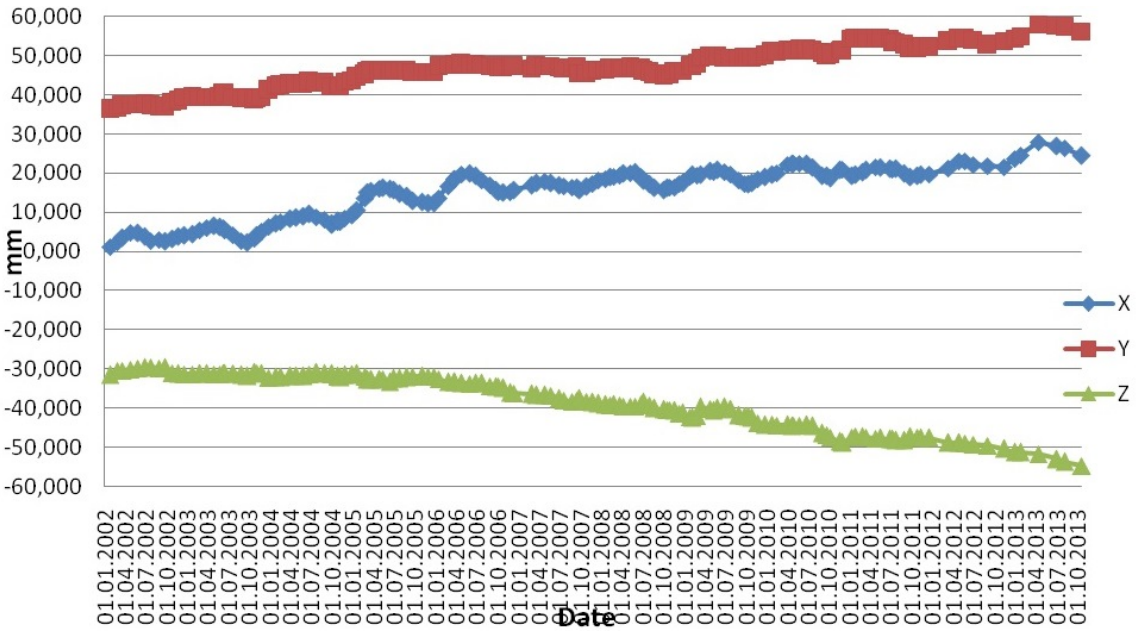


Fig. 10. Displacements found at point B6.

Jan. 2002 – Dec. 2013 are presented. Concerning horizontal movements, varying periods of compression and extension at fault are established. The deformation accumulated so far is impressive. The total displacement till now – after 11 years of monitoring, shows about 30 mm of sinistral displacement, and about 27 mm of thrusting. The permanent trend of extension of about 2 mm/a, left-lateral slip of about 2.7 mm/a and a reverse slip of about 2.5 mm/a is preserved like one reliable tendency for many years. In comparison with seismological data (Fig. 11) some very general correlations are obvious - the horizontal displacements change their directions as if following the picks and gap in the seismic activity.

As a conclusion it could be emphasized that the realized weak seismicity in the region of interest dur-

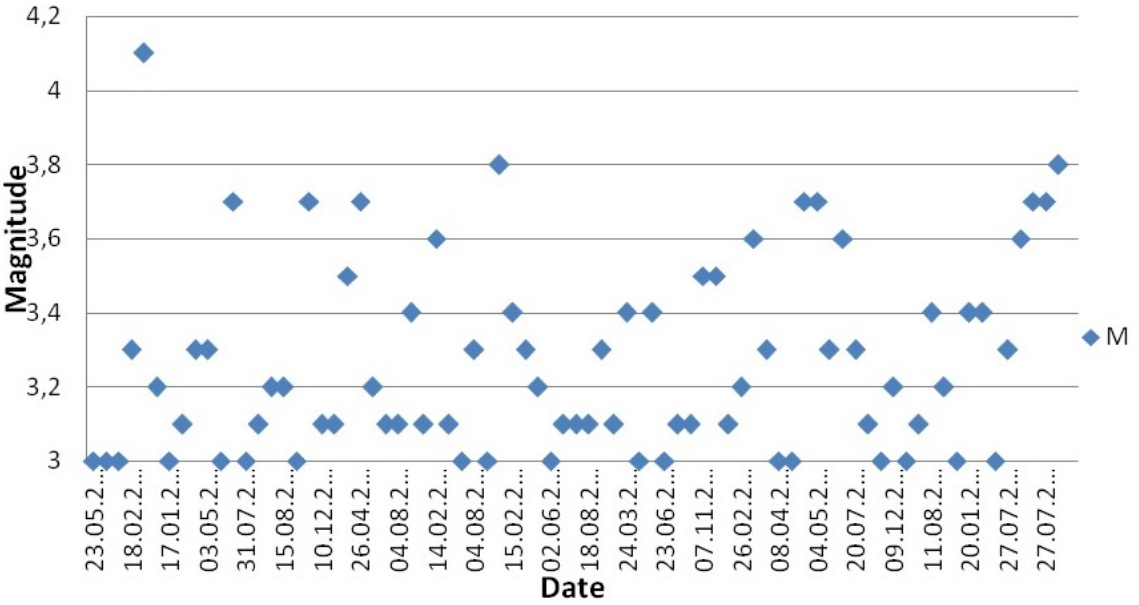


Fig. 11. Magnitude-time distribution of the strongest events during the extension monitoring time.

ing the last 33 years confirms the decisive role of the Krupnik fault lineament, associated with the E-NE oriented surface ruptures caused by the very strong 1904 earthquakes. Distribution of the epicenters shows obvious activity in NE direction. The depth distribution of earthquakes probably marks a prevailing activity of the northern boards of Simitli graben and some depth influence of Struma lineament. The main result of fault plane solutions modeling is that the seismological results confirmed the geological hypothesis of the extensional regime of the Krupnik region in SW Bulgaria. Orientation of the extension is S-SE, perpendicularly to the Krupnik fault. According to geodetic data at the same time the all territory of SW Bulgaria is moving towards S-SE with velocity of about 2–3 mm/yr relative to stable Europe. The good correlation between the geodetic and seismological investigation is a reliable evidence for the identity of the deformation of the crust and the seismic activity of this seismogenic area, where the regional tectonic stress are released periodically by activation of normal faulting. The extension-metrics monitoring shows also very quiet contemporary extensional deformations associated with the Krupnik fault. All this leads to the conclusion that the crust around the Krupnik source zone is relatively homogeneous in strength, according to regional point of view. On the base of the complex analysis of the contemporary seismicity, fault plane solutions, geodetic and geological modeling, it could be conclude that the present seismotectonic activity in the Krupnik region is associated very well with the main geodynamic processes in the central part of Balkan region.

REFERENCES

[1] N. Shebalin, V. Karnik and D. Hadzievski, *Catalogue of earthquakes, UNDP/UNESCO survey seismicity of the Balkan region*, Printing Office of the University Cyril and Methodius, Skopje, 1974.

[2] I. Zagorchev, *Geological Magazine* **129**, 197–222 (1992).

[3] B. Vrablyanski and G. Milev, *Acta Montana Ist AS CR, Series A* **4**, 111–132 (1993).

[4] N. Dobrev, *Acta geodynamica et geomaterialia* **8**, 377–388 (2011).

[5] E. Avramova-Tacheva, B. Vrablyanski and B. Košták, *Review of the Bulgarian Geological Society* **XLV**, 276–288 (1984) (in Bulgarian).

[6] N. Dobrev and B. Kostak, *Engineering Geology* **57**, 179–192 (2000).

[7] E. Barrier, N. Chamot-Rooke and G. Giordano, *Geodynamic map of the Mediterranean*, Sheet 1 - Tectonics and Kinematics, CGMW, France, 2004.

[8] I. Georgiev, D. Dimitrov, T. Belijashki, L. Pashova, S. Shanov and G. Nikolov, *Geodetic constraints on kinematics of southwestern Bulgaria from GPS and leveling data*, Geological Society, London, Special Publications, 2007, 291, pp. 143-157.

[9] E. Botev, D. Dimitrov and I. Georgiev, *Geologica Balcanica* **31**, 92–93 (2001).

[10] E. Botev, I. Georgiev and D. Dimitrov, *Journal of Geodesy* **17**, 53–69 (2006).

[11] D. Dimitrov, I. Georgiev and E. Botev, "New results from Geodetic monitoring of the Kroupnik-Kresna seismotectonic area (SW Bulgaria)" in *Book of abstracts of the 3rd National Geophysical conference*, Sofia, 2000, p. 26.

[12] S. Shanov and N. Dobrev, *Comptes rendus de l'Academie bulgare des Sciences* **6**, 95–98 (1997).

СЕИЗМИЧНОСТ И СЪВРЕМЕННИ ДВИЖЕНИЯ ПО АКТИВНИ РАЗЛОМИ В ЮГОЗАПАДНА БЪЛГАРИЯ

Н. Добрев[1], Е. Ботев[2], В. Протопопова[2], Ив. Георгиев[2], Д. Димитров[2]

[1] *Геологически институт, Българска академия на науките, ул. "Акад. Г. Бончев" блок 26, 1113 София, България*
[2] *Национален институт по геофизика, геодезия и география, Българска академия на науките, ул. "Акад. Г. Бончев" блок 3, 1113 София, България*

(Резюме)

В настоящия доклад се предлага детайлна информация за параметрите на сеизмичността през последните 30 години в Югозападна България – района южно от Благоевград. Чрез интерпретация на механизмите на земетресенията се анализира поведението на активните разломи и статуса на тектонските напрежения в района като част от Струмската, Пределската и Крупнишката разломна система (известна с едно от най-силните корови земетресения на територията на Европа за последните 200 години). Представени са и резултатите от дългогодишните екстензометрични измервания на скоростите на тектонските движения около трите разломни системи. Проведен е комплексен сеизмотектонски анализ на представените резултати и са установени известни корелационни зависимости между отделните геодинамични параметри на изявените разломни системи в изследваната част на Югозападна България.

Bulgarian Chemical Communications, Volume 47, Special Issue B (pp. 309–313) 2015

Biased magnitude estimates – impact on the magnitude-frequency distribution assessment

D. Solakov*

National Institute of Geophysics, Geodesy and Geography, Bulgarian Academy of Sciences, Acad. G. Bonchev Str., Bl. 3, 1113-Sofia, Bulgaria

"Apparent" distributions of random variables are usually considered in seismology. This is due to the fact that, instead of the actual values of the monitored parameter, the evaluated values are used. The coordinates and magnitude of earthquakes are typical examples. Errors in these estimates can lead to significant shifts in the earthquake relevant parameters distribution (magnitude-frequency distribution, spatial distribution etc). In the present work it is shown that due to the limited capabilities of seismic equipment (seismic networks) and the presence of microseismic noise the magnitude estimates are biased. It is numerically illustrated that the bias is significant for relatively small earthquakes (depending on network density and the noise level at the seismic stations) leading to Gutenberg-Richter $b-value$ biased estimates. A procedure for corrected magnitude estimate considering the noise level at the seismic stations is proposed. The use of corrected magnitudes result in negligible bias of $b-value$ estimates.

Key words: magnitude, Gutenber-Richter b value, statistical methods

INTRODUCTION

Uncertainties are an inherent part of seismic studies. Their evaluation as well as the assessment of their impact on following studies is essential both in theoretical and in practical terms. The recording system also has a significant impact on the assessment of the seismicity. This is substantially important for the assessment of the earthquake magnitude-frequency distributions. The concept of "apparent" magnitude was proposed for the first time in Tinti, Mulargia [1]. As a result of errors in the magnitude determination we have not a sample from the true distribution but a sample from "apparent" (observed) distribution, which is a convolution of two distributions - the real one and determination error distribution. In [1] is considered the case of a double side truncated exponential magnitude-frequency distribution and Gaussian distributed estimation error $-N(0,\sigma^2)$. Thus the "apparent" density function is convolution of the two densities (exponential and normal one):

$$g(M) = \int_{-\infty}^{\infty} f(M-\tau)h(\tau)d\tau$$

where M is the earthquake magnitude and

$$f(M) = \begin{cases} 0, & M < M_0 \\ \beta e^{-\beta M}/(1-e^{-\beta M_1}), & M_0 \le M \le M_1 \\ 0, & M_1 < M \end{cases}$$

is the density of the double side truncated exponential distribution with lower and upper earthquake magnitude bounds M_0 and M_1 respectively and

$$h(\tau) = \frac{1}{\sigma\sqrt{2\pi}} e^{-\frac{\tau^2}{2\sigma^2}}$$

is a normal distribution of the estimation error. In case of a sufficiently large difference $M_1 - M_0$ in a wide magnitude interval we will have:

$$g(M) = e^{\frac{\beta^2\sigma^2}{2}} f(M),$$

where $\beta = b\ln 10$ (b – slope of the recurrence graph), i.e. the "apparent" number of earthquakes will be $\exp(\beta^2\sigma^2/2)$ times larger than the real one. In this study it is shown that in real terms the estimate of the magnitude is biased, particularly for small earthquakes and the influence of this bias on the b value estimates is considered.

THEORETICAL JUSTIFICATION

Present-day broadband seismometers measure ground motion velocity over a wide frequency range. The following relation is valid in this range: $A/T = V/2\pi$, where A is the ground displacement amplitude, T is the corresponding period and V is the ground motion velocity. In general, to "recognize" the earthquake on seismograms it is necessary:

$$\log(V_{max})_j - \log(V_n) > 0, \qquad (1)$$

where $V_{\max}$ is the maximum velocity for wave type $j = P,S$ etc. and V_n is the level of microseismic noise

* To whom all correspondence should be sent: dimos@geophys.bas.bg

© 2015 Bulgarian Academy of Sciences, Union of Chemists in Bulgaria

at the corresponding station. Let us consider the magnitude equation:

$$M_j = \log(\frac{V_{\max}}{2\pi})_j + \delta_j(\Delta) + S_j \pm \varepsilon, \qquad (2)$$

where $\delta_j(\Delta)$ is the calibration function for each wave type j at a distance Δ, S_j – station correction for the corresponding wave type j, ε – random variable, reflecting the uncertainty of the maximum ground motion velocity for the relevant magnitude and distance (a normal distribution with a mean 0 and variance σ^2 for all magnitudes and distances is assumed in this study), due to the complex nature of the physical phenomenon earthquake. For a convenience, it is assumed that the calibration function takes in the constant $-\log(2\pi)$. From equation (1) follows that an earthquake with a magnitude M_j at a distance Δ will generate a maximum ground motion velocity:

$$\log(V_{\max})_j = M_j - \delta_j(\Delta) - S_j \pm \varepsilon, \qquad (3)$$

To recognize the earthquake ground motion on the seismogram the following condition is to be satisfied:

$$\log(V_n) < M_j - \delta_j(\Delta) - S_j \pm \varepsilon. \qquad (4)$$

From (3) follows that the logarithm of the maximum ground motion velocity $\log(V_{\max})_j$, generated by an earthquake M_j at a distance Δ is a random variable that is generally considered as normally distributed (assuming distribution $N(0,\sigma^2)$ of ε) with mean $M_j - \delta_j(\Delta) - S_j$ and variance σ^2. Considering inequality (4), the distribution of the logarithm of the recorded maximum ground motion velocity $\log(V_{\max})_j > \log(V_n)$ will be left side truncated normal distribution. The distribution is similar when a trigger mode is used. In this case, the lower limit is not the noise level but the value of the specified trigger. In practice, for strong earthquakes at short distances, the distribution will be right side truncated, due to the limited capabilities of the seismic equipment. From the foregoing,it follows that for small earthquakes the mean of the logarithm of the reported maximum ground motion velocity will be shifted from the real one – $M_j - \delta_j(\Delta) - S_j$. The bias depends both εdistribution and the difference $M_j - \delta_j(\Delta) - S_j - \log(V_n)$. In Table 1 are given the normal distributions with variance 0.25 and different mean values, as well as the mean of the corresponding left truncated normal distributions with boundary 0 (i.e. $\log(V_n) = 0$).

The table shows that there will be significant differences between the mean of the actual (normal) and the reported (truncated normal) for small mean values of the normal distribution. These results indicate that, theoretically, the magnitude estimate will be biased to higher values. Generally, for magnitudes which generate mean maximum ground motion velocity $10^{3\sigma}$ times greater than the noise level the estimates will be not biased. If this condition is satisfied for all stations used in magnitude determination, the estimates will be practically not biased. If for one or more stations this condition is not satisfied, the estimate will be biased. In general, these considerations are valid for any magnitude, regardless of the used ground motion parameter. This is result of the uncertainties related to the complex nature of earthquakes and seismic wave propagation paths, which form ε error and its variance. It is worth to be noted that in practice are used maximum amplitudes exceeding several times the noise level.

NUMERICAL MODELING

Numerical experiments were carried out to assess the influence of the seismic network, station conditions (geotechnical properties and microseismic noise level), error ε and its variance on the magnitude determination and hence the evaluation of the magnitude-frequency distribution. The following assumptions are accepted in the numerical modeling:

- considered area Q – rectangle with sides X and Y km;
- observation network of N stations uniformly distributed in the area Q. To avoid the case of close stations additionally is accepted the condition that the distance between two stations must be greater than $(X * X/\pi/N)^{0.5}$;
- uniform distribution of the earthquakes in the area Q;

Table 1. Mean values of the normal distribution with $\sigma = 0.25$ and the corresponding left truncated distribution (at value 0)

Mean value of the normal distribution	-1	-0.5	0	0.5	1	1.5
Average value of the truncated distribution (limit 0)	0.187	0.263	0.399	0.644	1.028	1.502
Difference between the average values(normal - truncated normal)	-1.187	-0.763	-0.399	-0.144	-0.028	-0.002

— the magnitude determination is based on the maximum ground motion velocity $V_{\max}$ for P wave (a calibration function $\delta(\Delta)$ that is presented in [2]) is used;
— uniform distribution of station corrections in the interval $[-0.5, 0.5]$;
— double truncated exponential distribution with parameter β in the range $[m, M_{\max}]$ for magnitude, where m is sufficiently small ($m \approx M_0$) – minimal magnitude which could be documented by the network);
— uniform distribution of the logarithm of V_n $[10^{-2.5}\mu m/s, 10^{-0.5}\mu m/s]$. These values are approximately in the range of observed seismic noise at bulgarian stations;
— earthquake with a magnitude M at a distance Δ generates mean maximum ground motion velocity $10^{M_j - \delta_j(\Delta) - S_j \pm \varepsilon}$, where S-station correction, $\varepsilon\ N(0, \sigma^2)$;
— an earthquake is considered reliably documented if at least at k $(0 < k \leq N)$ stations is recorded the maximum ground motion velocity of P wave SNR times greater than the noise level. The magnitude is determined as a mean of the estimates for all the stations satisfying this requirement.

The following algorithm (concerning the above presented assumptions) is applied:

1. N random seismic stations that are uniformly distributed in the area Q are generated;
2. Random station corrections S_i and seismic noise level V_{ni} (with distributions as described above), where $i = 1, 2, \ldots N$ are generated for each of the seismic stations;
3. An earthquake is generated randomly distributed in the area Q;
4. A magnitude M is generated – random variable with double side truncated exponential distribution in the range $[m, 7]$ with parameter $\beta (\beta = \ln(10) * b)$ is generate;
5. For each station j=1,2,...,N is generated maximum ground motion velocity $V^j_{\max} = M - \delta_j(\Delta) - S_j \pm \varepsilon$, where $\varepsilon\ N(0, \sigma^2)$. If inequality $V^{j_{\max}} > SNR * V_{nj}$ is fulfilled for a station, it is assumed that this station has recorded the earthquake;
6. If the earthquake is eligible for documentation (i.e. the number of stations registered the earthquake is greater than or equal to k), the mean magnitude $\overline{M}$ is calculated from the estimated magnitudes of all stations which have registered the event.

   A corrected magnitude is estimated taking into account the offset $\overline{M}$ of resulting from the truncated distribution of ε (i.e. distribution of the measured maximum ground motion velocity) by the following procedure: For each station which have recorded the earthquake the "corrected" magnitude is calculated:

$$M_{\text{corr}} = \log(V) + \delta(\Delta) + S - E(\varepsilon \mid \overline{M}, \log SNR * V_n)),$$

   where Δ – epicentral distance of the station, $E(\varepsilon \mid \overline{M}, \log SNR * V_n))$ – mathematical mean of ε for the distance Δ, assuming $\overline{M}$ that a magnitude is the real one. M_{corr} accounts the fact that the distribution of the measured maximum ground motion velocity for $\overline{M}$ is truncated with a lower boundary $SNR * V_n$. An averaged corrected magnitude $\overline{M_{corr}}$ is calculated using the corrected magnitudes M_{corr} for each station.
   The procedure is repeated iteratively until the modulus of the difference between two successive iterations is greater than δ.
7. If the earthquake is documented it is included in a catalog as magnitude $\overline{M}$ and $\overline{M_{\text{corr}}}$ and the magnitude values are rounded to 0.01;
8. Steps from 3 to 7 are repeated, while in the catalog 1000 earthquakes with magnitude more than or equal to 4.0 are recorded;
9. For the generated catalogue, the slope b of the magnitude – frequency distribution is estimated for different minimum magnitudes – from m to M_1, where M_1 is the maximum magnitude, for which $N(M \geq M_1) > 25)$. Estimates are obtained by using maximum likelihood method [3];
10. 1000 catalogues are generated (steps from 3 to 9) and the resulting estimates of b for different minimum magnitudes are averaged.

The described algorithm is applied for different values of X, Y, N, k, m, b and σ. In Fig. 1 are given the obtained results for a rectangle area Q with sides 600 and 200 km, $N = 50, k = 4, m = 1.5, b = 1.0, \sigma = 0.5, SNR = 6$ and $\delta = 0.01$. In the adopted terms, the minimum magnitude $M_{\min}$, above which all earthquakes are recorded is about 1.7. The figure shows that for a large magnitude interval the b-value estimates are biased and for some minimal magnitudes is more than 20% larger than the real one. The same behavior (uncorrected magnitudes) as it is suggested

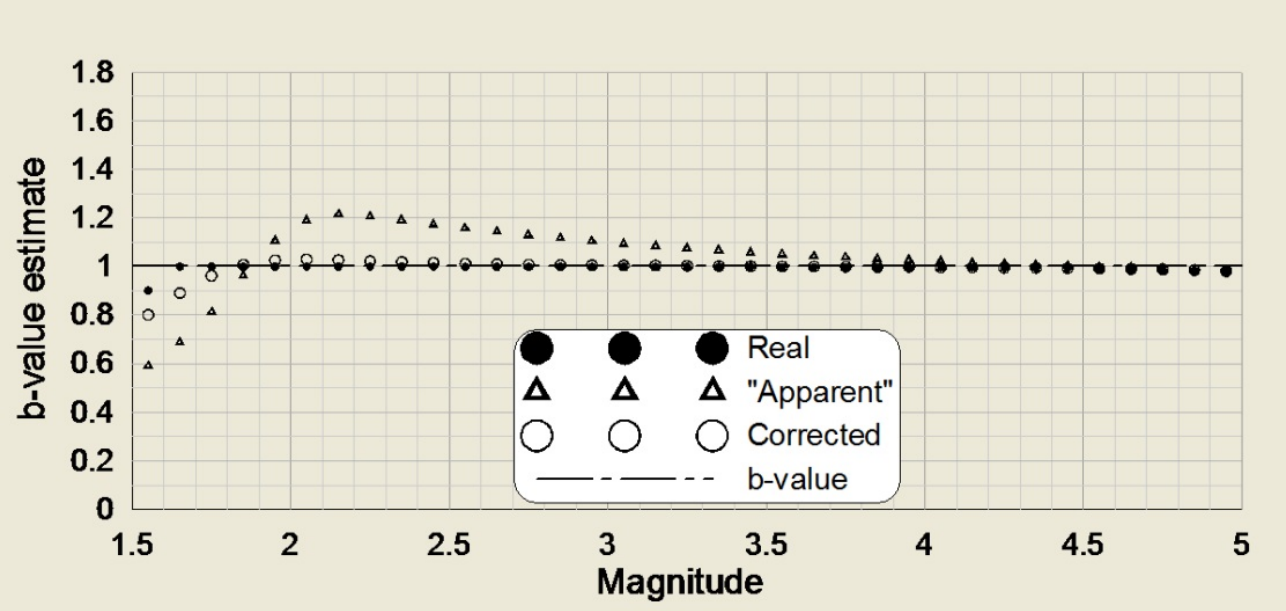


Fig. 1. Calculated b-value versus $M_{\min}$.

by Figure 1 was observed for earthquakes in California between 1984 and 1999 as presented in [4]. The effect is explained [4] by a larger determination error of the small earthquake magnitudes. Corrected magnitudes lead to practically non biased estimates of b. This tendency is not dependant of Q, N, k, m, b and SNR. The bias decreases with decreasing of σ but $\sigma = 0.5$ seems to be a realistic value for scatter of the V_{max} modeling (standard deviations of the PGV attenuation relationships are close to 0.5 (for example [5]).

FINDINGS AND CONCLUSIONS

It has been shown that, the estimation of the earthquake magnitude is biased to higher values due to the level of seismic noise. This offset is considerable for relatively small earthquakes (depending on the density of the network and the level of the noise at the seismic stations) and this leads to a bias of the b estimates (slope of the magnitude frequency distribution). The proposed procedure for the magnitude correction based on the noise level leads on practically not biased assessments. Biases appear in estimates, with assumed normal distribution of the uncertainties that is in reality truncated normal, such as: ground motion attenuation models; models for various parameters of earthquakes in dependence of the magnitude (for example rupture length, fault displacement, size of the rupture etc). In all these cases, for low magnitudes (or for large distances in attenuation models) predominantly observed extreme values are considered. This results in a shift of the parameter estimates.

REFERENCES

[1] S. Tinti and F. Mulargia, *Bull. Seis. Soc. Am.* **75**, 1681-1697 (1985).

[2] E. Samardjieva, "Magnitude classification for near earthquakes based on short-period seismometers and some applications", *PhD thesis*, Geophysical Institute, Sofia (1986).

[3] R. Page, *Bull. Seismol. Soc. Am.* **58**, 1131-1168 (1968).

[4] K. Felzer, *U. S. Geological Survey, 525 S. Wilson, Pasadena, CA 91106 United States AGU Fall Meeting Abstracts* (2006).

[5] K. Campbell and Y. Bozorgnia, *Earthquake Spectra* **24**, 139-171 (2008).

ОТМЕСТВАНЕ НА МАГНИТУДНИТЕ ОЦЕНКИ – ВЛИЯНИЕ ВЪРХУ ОЦЕНКАТА НА МАГНИТУДНО-ЧЕСТОТНОТО РАЗПРЕДЕЛЕНИЕ

Д. Солаков

Национален институт по геофизика, геодезия и география, Българска академия на науките, ул. "Акад. Г. Бончев" блок 3, 1113 София, България

(Резюме)

За сеизмичните райони земетресенията са неделима част от средата, която ни заобикаля и не съществува друго явление, което да е така "безценно" от научна гледна точка и така катастрофално от социално икономическа и психологична гледна точка като силното земетресение.

Съвременната сеизмология се основава на интерпретацията на огромно количество наблюдателни данни. Развитието й е немислимо без необходимата теоретична база и прилагането на надеждни статистически и изчислителни методи и процедури. Математическите и статистическите подходи играят съществена роля в сеизмологията. Използването на статистическите подходи в сеизмологията трябва да бъде мостът между физически базираните модели (без статистика) и статистически базираните модели (без физика).

В сеизмологията винаги се работи с "привидни" ("видими") разпределения на случайни величини. Това се дължи на факта, че вместо с истинските стойности на наблюдаваните величина, се работи с оценки на тези стойности. Типични примери за това са магнитудът и координатите на земетресенията. Грешките в оценките на тези параметри могат да доведат до значими отмествания в разпределенията на земетресенията по съответните параметри (магнитудно-честотна зависимост, пространствено разпределение).

В настоящата работа е доказано, че в следствие ограничените регистриращи възможности на сеизмичната апаратура (съответно сеизмичните мрежи) и наличието на микросеизмичен шум, оценката на магнитуда на земетресенията е отместена. Числено е показано, че това отместване е значимо за относително по-слаби земетресения (в зависимост от плътността на мрежата и нивото на шума в сеизмичните станции) и води до отместване на оценките за наклона *b*на магнитудно-честотната зависимост. Предложена е процедура за оценка на магнитуда, отчитаща нивото на шума в сеизмичните станции, при която се получават оценки с практически пренебрежимо отместване на оценките на параметъра *b* на магнитудно-честотната зависимост.

Bulgarian Chemical Communications, Volume 47, Special Issue B (pp. 314–322) 2015

RETAS model software to identify the best fit model version of aftershock temporal decay

D. Gospodinov*

Paisii Hilendarski University of Plovdiv, 24 Tsar Asen Str., BG-4000 Plovdiv, Bulgaria

The options and the applicability of a FORTRAN 95 software program to model aftershock rate decay in time have been demonstrated in this paper. The program was designed to perform computations of the maximum likelihood estimates of the restricted epidemic type aftershock sequence (RETAS) model parameters. This is a trigger model, which provides a stochastic description of aftershocks temporal evolution in a sequence. The advantage of RETAS is that it offers a number of model versions, including the Modified Omori formula (M)F) and the epidemic type aftershock sequence (ETAS) models as limit cases. In that way RETAS offers a wider variety of model versions to fit best the temporal distribution of aftershocks in a sequence. The author has provided examples on simulated data to demonstrate the use of the software to different types of aftershock sequences and the interpretation of the results obtained.

Key words: RETAS model, stochastic modelling, aftershock decay, ETAS model, FORTRAN software

INTRODUCTION

The intensive study of earthquake clustering, especially aftershocks, is motivated by several key objectives. First, aftershocks shed light on the physical processes occurring in the fault zone [1-3]. Strong earthquakes change the stress in the surrounding crust, leading to the occurrence of new earthquakes and aftershocks [4-5]. Exploring aftershock sequences of mainshocks presents another way to examine faults geometry and non-linear features of seismicity [6-7].

Second, random process modeling of aftershocks sequences allows identifying and interpreting of the actual process deviations from the model prior strong aftershocks or new earthquakes [8-10]. Stochastic short-term models that describe the phenomenon of earthquake clustering are achieving increasing success in the seismological community [11-14]. These models delineate seismicity as a random point-process, for which a continuous space-time density distribution of the earthquake occurrence can be defined. Except for its scientific importance, stochastic modeling of aftershocks sequence evolution could be important for operational activity after a strong earthquake. After such an event, the possibility of the occurrence of either significant aftershocks or an even stronger mainshock is a continuing hazard that hinders the resumption of critical services and reoccupation of partially damaged structures. A stochastic parametric model allows determination of probabilities for aftershocks and larger mainshocks during intervals following the mainshock [15-16, 8]. Because these probabilities are estimated through a particular model, the closeness between the formulation of the model and the reality is the essentially important factor influencing the output. The closer the model is to the real data, the more reliable the output is. That is why it is important to consider many models fitted to the same set of data and to apply some model selection procedures to choose the best model among them.

The Modified Omori formula (MOF) and the epidemic type aftershock sequence (ETAS) model are among the ones of greatest successes in empirical studies [17-18]. They, however, consider only two limit cases, the MOF model with only one parent event and the ETAS model in which every event shares in the generation of the subsequent ones. Gospodinov and Rotondi [12] proposed the restricted epidemic type aftershock sequence (RETAS), a kind of trigger model, which is based on the assumption that only aftershocks with magnitudes larger than or equal to a threshold M_{th} can induce secondary seismicity. By varying M_{th} between the cut-off M_0 and the maximum magnitude M_{max} one considers a number of RETAS versions, including MOF and ETAS as limit cases. In that way RETAS offers a wider variety of model versions from which to choose the one that fits best the data.

Following a quasi-Newton method, Gospodinov & Rotondi [12] have developed a program in

* To whom all correspondence should be sent:
drago@uni-plovdiv.bg

© 2015 Bulgarian Academy of Sciences, Union of Chemists in Bulgaria

FORTRAN 95, which exploits subroutines of the IMSL library to obtain the maximum likelihood estimates (MLEs) of the RETAS model parameters. The purpose of this paper is to demonstrate the options of this software and its applicability for modelling aftershocks temporal distribution (the RETAS model software and simulated data are available at http://geo.physics.uni-plovdiv.bg/download.htm).

RETAS MODEL FORMULATION

Each stochastic model is developed on the basis of some basic physical assumptions. For the Modified Omori Formula (MOF) it is supposed that the total relaxation process is controlled by the stress field changes caused by a main shock. The aftershocks are conditionally independent and follow a nonstationary Poisson process. By the MOF model the decaying frequency of aftershocks per unit time is described to follow a negative power law [17]

$$n(t) = \frac{K}{(t+c)^p} \tag{1}$$

where t is the time elapsed from the occurrence of the main shock, K is a parameter related to the magnitude of the main shock and to the magnitude cut-off, p is a coefficient of attenuation and c is a constant.

The frequency $n(t)$ in Eq. (1) corresponds to the intensity function of a point process, i.e.

$$n(t) \approx \lambda(t) \tag{2}$$

where $\lambda(t)$ is the conditional intensity function

$$Pr\{\text{an event occurs in } (t, t+dt)\} = \\ = \lambda(t|H_t)dt + o(dt) \tag{3}$$

Formula (3) reveals the probability of an event to occur in the time interval $(t,\ t+dt)$. Here H_t is the history of the process which for the MOF is only given by the time and the magnitude of the main shock.

The ETAS model [18] assumes that every aftershock in a certain zone can trigger further shocks and the contribution of any previous earthquake to the occurrence rate of the subsequent events is decomposable into separate terms representing the time and magnitude distribution as:

$$\lambda_j(t,m) = h(t-t_j|m_j) = k(m_j)g(t-t_j) \tag{4}$$

The temporal decay rate follows the MOF $g(t) \propto (t+c)^{-p}$ and the functional form of $k(m_j)$ is chosen to be exponential on the basis of the linear correlation between the logarithm of the aftershock area and the main shock's magnitude, studied extensively by Utsu and Seki [19]. Hence, the expected resultant rate of aftershocks is given by Ogata [18]:

$$\lambda(t/H_t) = \mu + \sum_{t_j<t} \frac{K_0 e^{\alpha(m_j - M_o)}}{(t-t_j+c)^p} \tag{5}$$

where μ (shocks/day) is the rate of background activity, the history H_t consists of the times t_j (days) and magnitudes m_j of all the events which occurred before t and the summation is taken over every $j-th$ aftershock with a magnitude stronger than the cut-off $m_j \geq M_0$ i.e. over all events in the sample. The main shock in this case is indicated by $j=1$. In probabilistic terminology, the first term on the right-hand side of (5) stands for the "independent" seismicity and in the second the "induced" seismicity is represented by a superposition of the modified Omori functions shifted in time. In formula (5) the coefficient α measures the magnitude efficiency of a shock in generating its aftershock activity and K_0 is a multiplier, common to all aftershocks, which has an impact on the total aftershock productivity. The MOF and the ETAS model are two limit cases, the former with only one parent-event and the latter with all events sharing in the generation of the subsequent ones. Gospodinov and Rotondi [12] offer the Restricted Epidemic Type Aftershock Sequence (RETAS) model, which is based on the assumption that not all events in a sample but only aftershocks with magnitudes larger than or equal to a threshold M_{th} can induce secondary seismicity. Then the conditional intensity function for the model is formulated as:

$$\lambda(t/H_t) = \mu + \sum_{\substack{t_j<t \\ m_j \geq M_{th}}} \frac{K_0 e^{\alpha(m_j - M_o)}}{(t-t_j+c)^p} \tag{6}$$

An advantage of the RETAS model is that this gap is not fixed and by varying M_{th} all RETAS versions between the MOF and the ETAS model can be examined on the basis of the Akaike criterion [20], given by

$$AIC = -2 \max \log L(\theta) + 2k \tag{7}$$

where k is the number of parameters of the model and $\log\ L$ is the logarithm of the likelihood function, given by

$$\log\ L(\theta) = \sum_{i=1}^{N} \log\ \lambda_\theta(t_i|H_{t_i}) - \int_S^T \lambda_\theta(t|H_t)dt \tag{8}$$

The smallest value of the Akaike criterion recognizes the best fit model. Gospodinov and Rotondi [12] have developed a program in Fortran 95 which exploits subroutines of the IMSL library to maximize the likelihood of the RETAS model following a quasi-Newton method and we apply the same software in this study.

One can see how well or poorly the estimated model is fitted to an earthquake sequence by comparing the cumulative number of earthquakes with the predicted rate offered by the estimated models. If a series of events $\{t_0, t_1, \ldots, t_N\}$ is simulated based on a statistical model $\lambda(t)$, which is the predicted occurrence rate of events per unit time, then by integrating:

$$\Lambda(S,t) = \int_S^t \lambda(u)\, du \qquad (9)$$

we obtain the expected cumulative number of events over the time interval (S,t). To estimate quantitatively the significance of deviations of observed to model cumulative numbers we can first focus on formula (1), which presents the MOF model. The basic assumption behind this model, as revealed above, is that the events in an aftershock sequence follow a nonstationary Poisson process. Then the process, offered by formula (6), being a superposition of such models ($\mu = 0$), is a nonstationary Poisson process itself. For such processes the common mean and variance are both given by formula (9) for $S = 0$ [21]. Thus, we may use this formula to calculate the standard deviation of the expected cumulative number and use it as error bounds for quantitative estimation of the possible departure between real data and model.

Relation (9) also produces a transformation of time from t to $\tau = \Lambda(t)$ [9] so that the occurrence times t_j are transformed 1:1 into τ_j and the earthquakes follow the standard stationary Poisson process on the new axis if the intensity function is the true one for the data.

INPUT DATA FILES

Two types of input data files are used in the RETAS model analysis. One should contain the real catalog data in two columns; left column values are events' magnitudes and the right column values are the time periods [days] after the first earthquake occurrence (see example of part of *retas297.txt* file in Table 1).

The second input file contains parameter values, necessary for the program implementation (see the contents of *dataretas297.txt* file in Table 2). This file's name should be input interactively after running the program. The parameters in the file are as follows:

Table 1. Example of a catalog data file (part of *retas297.txt* file). Left column – magnitudes, right column – the time periods [days] after the first earthquake occurrence.

7.2	0
5.1	0.004166664
4	0.008333331
3.8	0.010416664
3.8	0.013194442
3.8	0.013888887
3.7	0.017361109
...	.....

1st row – name of the catalog data file, which will be analyzed by the program (*retas63.txt* in our example)

2nd row – lower magnitude cut-off of the data sample. For computational reasons, if this value is 3.7 (as in the example), it should be written down as 3.695. In fact this magnitude is usually the magnitude of completeness of your broader data sample and its value should be estimated before analyzing the data through the RETAS software.

3rd row – number of runs for each triggering value M_{th}. Usually the program converges quickly.

4th row – number of runs, after which there is an onscreen printing of the maximum likelihood function value, the corresponding threshold magnitude, and the triggering magnitude, which yields lowest AIC for the moment. If the value in this row is 1, the program will print the mentioned parameters for each run. If the value is equal to the one in the 3rd row (as in the example in Table 2) then onscreen printing will be only once for all runs of a corresponding triggering magnitude.

Table 2. Parameter values, necessary for the program implementation (contents of *dataretas297.txt* file; see details in text)

retas297.txt
3.695
10
10
1.d-6 20.d0
1.d-6 5.d0
1.d-7 6.d0
6.d-1 3.d0

The next four rows – from 5th to 8th, contain the value ranges (lower and upper cut-offs), which the initial model parameter values are taken from. For each run the program takes an initial set of random parameter values (within these ranges) for K, α, c, p (formula 6; μ in the formula is accepted to be 0 and not estimated) and after that evaluates the maximum likelihood estimates (MLE) of these parameters for the corresponding M_{th}.

The package contains three input data sets for different types of aftershock sequences: one, for which the best fit model is RETAS with $M_{th} = 4.4$ (retas297.txt and dataretas297.txt); a second one, for which the best fit model is ETAS with $M_{th} = M_0 = 3.8$ (etas215.txt and dataetas215.txt); the third data set is best fitted by the MOF model with $M_{th} = M_{main} = 6.6$ (mof215.txt and datamof215.txt).

RETAS ANALYSIS SOFTWARE

The executable program file is *retasanalysis.exe*. It evaluates the maximum likelihood parameters estimates (MLE) for the RETAS model, which best fits the examined data set (minimum AIC). The program was developed in Fortran 95 which exploits subroutines of the IMSL library to maximize the likelihood of the RETAS model following a quasi-Newton method. As usual, the program runs after double clicking over its icon. After starting, a window opens (see Fig. 1a) and the user is invited to input a file name (the one which contains parameter values, necessary for the program implementation; *dataretas215.txt* in our example). File extension should also be included (Fig. 1b) and then 'ENTER' should be pressed.

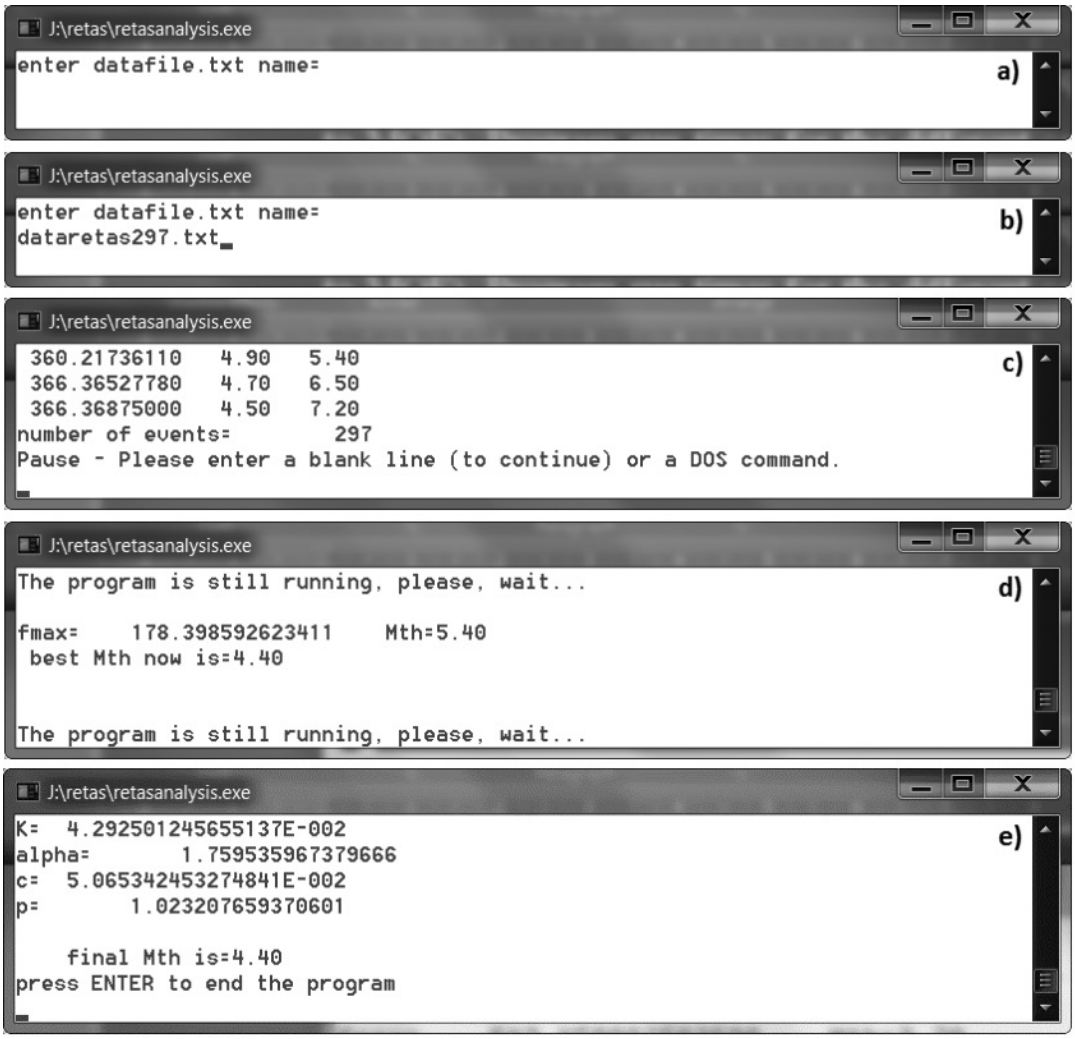


Fig. 1. Subsequent windows of the RETAS software implementation.

The program reads the catalog data file (*retas297.txt*) and the other parameters, and the catalog data is printed oncreen - time periods after the first shock in days (left), magnitudes (center) and again magnitudes in an increasing order (right). The last row presents the number of events (Fig. 1c). The purpose of this operation is that the user verifies he is analyzing the right data set. After pressing 'ENTER', code execution continues and the program issues an announcement 'The program is still running. Please, wait ...'. Different times for program completion are needed depending on the number of events. This is so because the program verifies all RETAS model versions for different M_{th}. It starts form the lower magnitude cut-off ($M_{th} = M_0$ - RETAS degenerates into ETAS; see Fig. 1d) and then M_{th} is increased step by step to the case when it is equal to main shock magnitude (RETAS turns to MOF).

Program run times for the different catalog data files are presented in Table 6. At the end the program prints on the screen the parameter MLEs (K, α, c, p) for the identified best fit model version (Fig. 1e).

OUTPUT FILES

The RETAS software generates three output files in the same directory as follows:

output.txt – The file includes the catalog data file name (*retas297.txt*), the lower magnitude cut-off (usually magnitude of completeness), number of events, ranges for initial model parameter values, parameter MLEs, number of estimated parameters, the M_{th} value for which the best fit model was recognized and the corresponding value of the Akaike criterion (see Table 3).

aichist.txt (Table 4) - The file keeps the AIC values and model parameter estimates (K, α, c, p) for the different values of the threshold magnitude M_{th}. The two left columns (M_{th}, AIC) allow to plot the Akakike criterion versus the triggering magnitude M_{th} and thus to recognize the prevailing clustering pattern for the studied sequence. The graphic interpretation not only reveals the best fit model (its parameter estimates are also printed in *output.txt*), but provides the possibility to analyze secondary minima of the curve, too.

When using the AIC criterion to select between competing models, individual AIC values are not suitable as they are less interpretable and contain arbitrary constants. It is more reasonable to rescale *AIC* or AIC_i to the differences

$$dAIC_i = AIC_i - AIC_{\min} \qquad (10)$$

Table 3. Contents of the *output.txt* file

Data set : retas297.txt
Magnitude cut-off : [3.69, ...]

Number of data = 297

parameter	inf	sup
k	.0000010	20.0000000
alpha	.0000010	5.0000000
c	.0000001	6.0000000
p	.6000000	3.0000000

parameter	estimate
k	.042925012457
alpha	1.759535967380
c	.050653424533
p	1.023207659371

Number of parameters = 4 final Mth = 4.40

AIC = -376.067754063429200

Table 4. Example of the AIC values and model parameter estimates (formula (6)) for the different values of the threshold magnitude M_{th}. This information is included in *aichist.txt*

M_{th}	AIC	K	α	c	p
3.7	-368.254	0.0144	2.068	0.049	1.036
3.8	-368.225	0.015	2.058	0.049	1.03
—	—	—	—	—	—
6.5	-350.308	0.009	2.277	0.057	0.964
7.2	-312.726	10.945	0.284	0.057	0.926

$dAIC_i^{\min}$ where $AIC_{\min}$ is the minimum of the different AIC_i values for a dataset. After this transformation the best model has $dAIC_i = 0$, while the rest of the models have positive values.

The $dAIC_i$ allow meaningful interpretation without the unknown scaling constants and sample size issues that enter into AIC values. These differences are easy to interpret and allow comparison and ranking of candidate models [22]. The larger the $dAIC_i$, the less probable the model i is as being the best approximating model in the candidate set. It is generally important to know which model is the second best, as well as some measure of its standing with respect to the best model. There are some simple rules of thumb, which are useful in measuring the relative strength of models in the set: Models having $dAIC_i \leq 2$ have substantial support for being alternatives of the best fit

Table 5. Example of real and expected cumulative number of events in time according to the best fit model. Standard deviation stands for the error bounds. This information is included in *outcum.txt*

Time [days]	M	Cum.N	Cum.Nm	Cum.Nm + st.d.	Cum.Nm - st.d.
0	7.2	1	1	1	1
0.00416666	5.1	2	2.73239	4.3853844	1.0793958
0.00833333	4	3	4.378021	6.4703936	2.2856492
0.01041666	3.8	4	5.156669	7.427499	2.8858389
—	—	—	—	—	—

model, those in which $4 \leq dAIC_i \leq 7$ have considerably less support, and models having $dAIC_i > 10$ have essentially no support [22].

outcum.txt (Table 5) - By substituting the ML estimates of the best fit model parameters in relation (6) we may calculate the expected cumulative number of events, using the standard deviation (formula 9) as error bounds. These are presented in the above mentioned output file. The columns in the file represent:

Time [days] — Time periods after the occurrence of the first event in the sequence in days
M — Events magnitudes
Cum.N — Real cumulative number of earthquakes in time
Cum.Nm — Expected cumulative number of earthquakes for the best fit model, calculated by formula (6).
Cum.Nm + st.d. — upper error bound (after calculating the variance by formula (6))
Cum.Nm - st.d. - lower error bound (after calculating the variance by formula (6))

The results of *outcum.txt* can be plotted to enable analysis of earthquakes temporal distribution in the sequence.

CHARTS AND RESULTS INTERPRETATION

The RETAS software only provides the results from the RETAS analysis in the output files, revealed above. If one wants to plot the results, any adequate software can be applied. Below we present the results from the RETAS model analysis for the three input data sets:

retas297.txt - the file contains a sequence of $N = 297$ aftershocks, starting with a main shock of magnitude $M_{main} = 7.2$

The model, for which the minimum AIC ($dAIC_i = 0$) value was obtained, turned out to be RETAS with $M_{th} = 4.4$ (see Table 3 and Fig. 2a). A highly competitive model is also RETAS with $M_{th} = 4.5$ ($dAIC_i = 0.599$, much less than 2). That points to a clustering type, where predominantly aftershocks with magnitudes equal to or bigger than 4.4 cause secondary activity. If the data is for a defined seismic region, these results could be correlated to its geotectonic features like faults etc. Some small deviations between actual and expected numbers are observed from the 50th to the 200th day (Fig. 2b), but they are not significant as the real values stay within the error bounds for the entire period.

etas215.txt - this is a sequence of $N = 215$ aftershocks, the first being the strongest of magnitude $M = 6.6$. The $dAIC_i$ values on Fig. 3a identify the best fit model for the data to be ETAS ($M_{th} = M_0 = 3.8$).

The ETAS model is clearly identified as the RETAS version, which best describes the temporal evolution of this sequence, as the $dAIC$ value to the second best fit model (RETAS; $M_{th} = 3.9$) is more than 5. The $dAIC$ curve on Fig. 3a has a secondary minimum for $M_{th} = 4.9$.

This result reveals that if we analyze only stronger aftershocks ($M_0 = 4.4$), the clustering type would be different. Gospodinov and Rotondi [12] obtained similar results for the Umbria-Marche region in Italy).

Table 6. MLEs of the RETAS model parameters (Formula (6)) for the different data sets. Right most column provides information about the time needed for the program implementation on a PC (Intel®Core™i3 CPU, 4.00GB, 32-bit OS)

Data sets	K	α	c	p	Time needed for the program implementation [min]
retas297.txt	0.042	1.759	0.05	1.023	~ 15
etas215.txt	0.058	1.562	0.042	1.22	~ 10
mof215.txt	0.007	2.495	0.002	0.871	~ 15

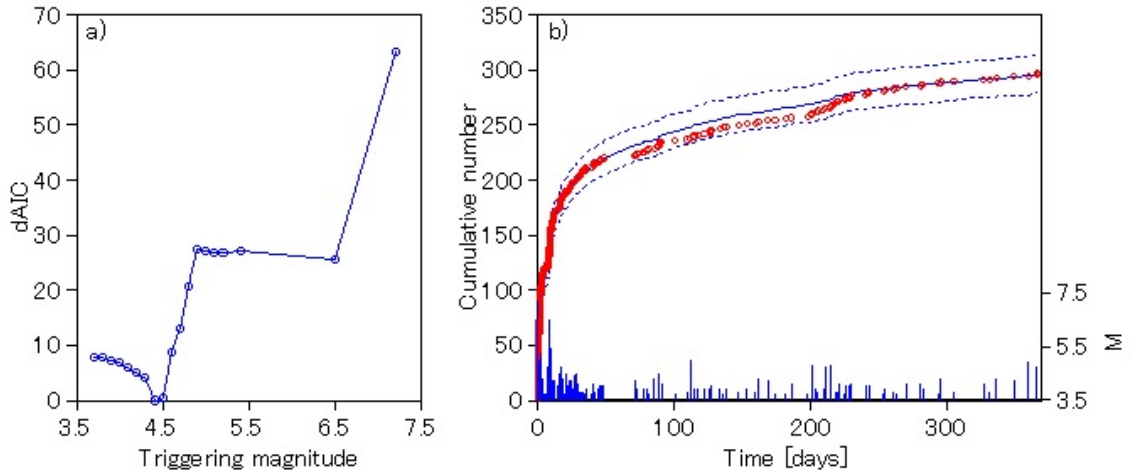


Fig. 2. a) Values of $dAIC_i$ versus the triggering magnitude M_{th} from the analysis of the data in *retas297.txt*. The model for which $dAIC_i = 0$ is the one, best fitting the data ($M_{th} = 4.4$); b) Cumulative real (circles) and expected (continuous line) numbers in time (days). The expected values were calculated by relation (6) for the best fit model. Standard deviation stands for the error bounds (dashed curves) and the vertical lines are magnitudes.

Aftershocks with magnitudes above this cutoff seem to be more clustered temporally to events of magnitudes $M = 4.9$ or stronger, while weaker shocks are more scattered in time. All this comes to support that the RETAS model analysis (*dAIC* curve) throws light not only on the best fit model, but also about more details of aftershock clustering features in a sequence. The results on Fig. 3b point out that there is a relative deviation of actual numbers, compared to model, for the time span between the 7th and the 17th day, which probably is due to the occurrence of several aftershocks of magnitude $M = 5$ or higher, which have rate productivity higher than the one predicted by the model.

mof215.txt - this data set is composed of $N = 215$ earthquakes. The strongest of them is the first one of magnitude $M = 6.6$. The $dAIC_i$ values on Fig. 4a identify the best fit model for the data to be MOF ($M_{th} = M_{main} = 6.6$). The MOF model does not have a competing alternative as *dAIC* to the second best fit model (RETAS; $M_{th} = 5.4$) is more than 5. No significant divergence between real and model cumulative numbers is observed on Fig. 4b (actual values stay within the error bound for the total time period).

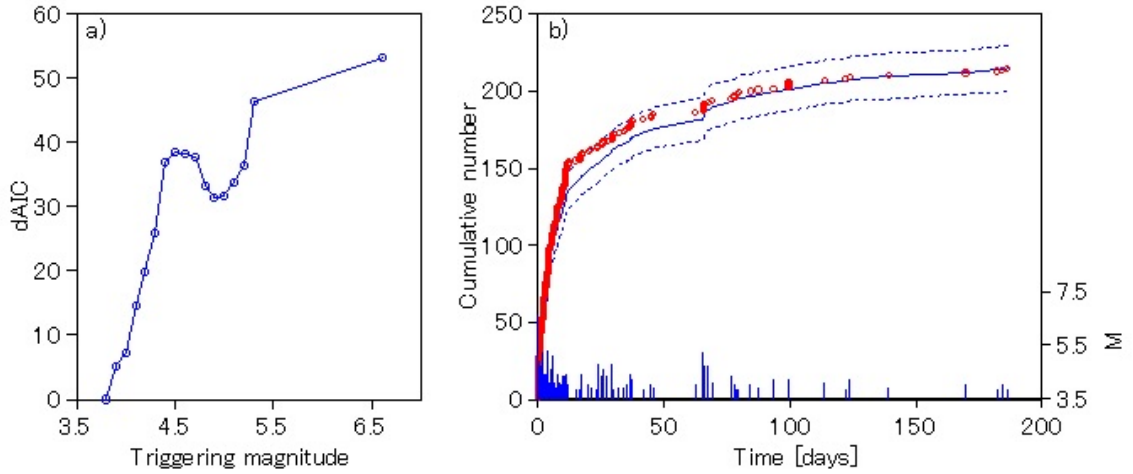


Fig. 3. The results from the RETAS software analysis for *etas215.txt* (best fit model is ETAS for $M_{th} = M_0 = 3.8$). Notation as in Fig. 2

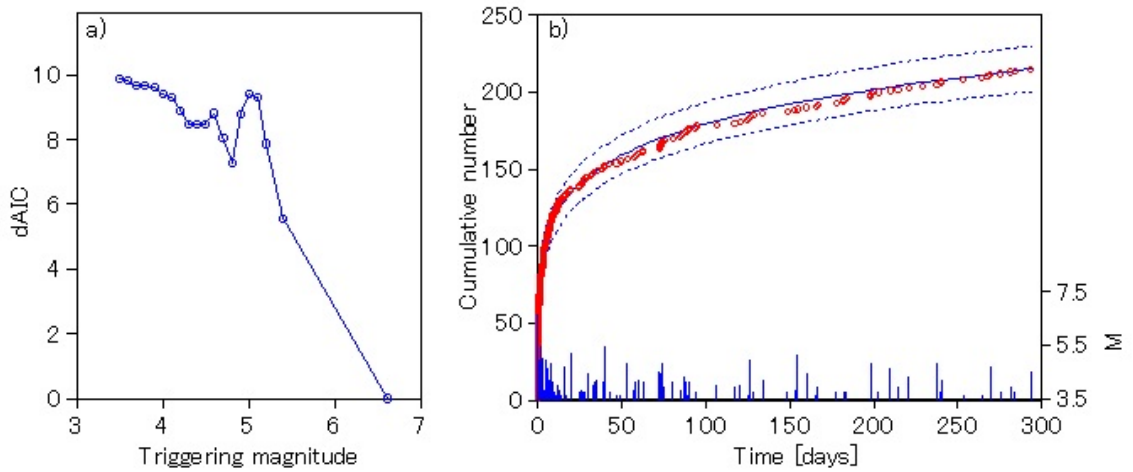


Fig. 4. The results from the RETAS software analysis for *mof215.txt* (best fit model is MOF for $M_{th} = M_{main} = 6.6$). Notation as in Fig. 2

CONCLUSIONS

In fact, by RETAS we denote a number of stochastic model versions, defined by formula (6). The MOF and the ETAS model are two limit cases of these versions, the former with only one parent-event and the latter with all events sharing in the generation of the subsequent ones. In that case the advantage of using RETAS is that we estimate the MLEs for the ETAS and MOF models as limit cases (we lose nothing), but we also verify all intermediate cases (for the different M_{th} values), for which only aftershocks of magnitudes equal to or bigger than M_{th} can induce secondary aftershocks. We identify the model, best fitting our data, as the one with the minimum AIC value. In the present paper the author applied the RETAS software on three data sets, presenting completely different types of aftershock sequences. The software correctly identified the corresponding best fit model versions, providing the necessary files to plot the expected and real cumulative numbers in time. Except that RETAS gives us a wide range of model versions to depict the temporal evolution of a series of aftershocks, it also provides broader possibility to relate the results from the stochastic analysis to other information about a seismic region, as for example, the possible length distribution of faults, which have triggered secondary aftershocks.

Acknowledgments. *The author thanks Renata Rotondi and Elisa Varini from IMATI-CNR, Milan for the support received, and the very useful discussions on the paper.*

REFERENCES

[1] E. Hauksson, The Frank Evison Volume II, *Pageoph Topical Volumes 2010*, pp. 125–143, (2010).

[2] A. Meltzner and D. Wald, *Bull. Seismol. Soc. Am.* **93**, 2160–2186 (2003).

[3] V. Karakostas, E. Papadimitriou, G. Karakaisis, C. Papazachos, E. Scordilis, G. Vargemezis and E. Aidona, *Geophys. Res. Lett.* **30**, 12-1–12-4 (2003).

[4] C. Hu, Y. Cai, M. Liu and Z. Wang, *Tectonophysics* **588**, 179–188 (2013).

[5] S. Lasocki, V. Karakostas and E. Papadimitriou, *J. Geophys. Res.* **114**, 1–19 (2009).

[6] B. Ranguelov, *Geodynamics and Tectonophysics* **1**, 225–230 (2010).

[7] D. Gospodinov, A. Marinov and E. Marekova, *Acta Geophys* **60**, 794–808 (2012).

[8] E. Papadimitriou, D. Gospodinov, V. Karakostas and A. Astiopoulos, *J. Seismol.* **17**, 735–752 (2013).

[9] Y. Ogata, *J. Geophys. Res.* **97**, 19845–19871 (1992).

[10] R. Bansal and Y. Ogata, *J. Geophys. Res.: Solid Earth* **118**, 616–629 (2013).

[11] A. Helmstetter, Y. Y. Kagan and D. D. Jackson, *Bull. Seismol. Soc. Am.* **96**, 90–106 (2006).

[12] D. Gospodinov and R. Rotondi, *Pure Appl. Geophys.* **163**, 1597–1615 (2006).

[13] D. Gospodinov, E. Papadimitriou, V. Karakostas and B. Ranguelov, *Phys. Earth Planet. Inter.* **165**, 158–175 (2007).

[14] R. Console, D. Rhoades, M. Murru, F. Evison, E. Papadimitriou and V. Karakostas, *J. GeoPhys. Res.* **111**, 1–13 (2006).

[15] W. Marzocchi and A-M. Lombardi, *Geophys. Res. Lett.* **36**, L21302 (2009).

[16] P. Reasenberg and L. Jones, *Science* **265**, 1251–1252 (1994).

[17] T. Utsu, *Geophys. Mag.* **30**, 521–605 (1961).

[18] Y. Ogata, *J. Am. Stat. Assoc.* **83**, 9–27 (1988).

[19] T. Utsu and A. Seki, *Zisin 2nd Ser.* **7**, 233–240 (1955).

[20] H. Akaike, *IEEE Trans. Automat. Control.* **AC–19**, 716–723 (1974).

[21] H. Taylor and S. Karlin, *An introduction to stochastic modeling*, Academic Press, Inc., 1984, p. 399.

[22] K. Burnham and D. Anderson, *Model Selection and Multimodel Inference: A Practical Information-Theoretic Approach*, 2nd edition, New York: Springer-Verlag, 2002.

СОФТУЕРНА ПРОГРАМА ЗА ИДЕНТИФИЦИРАНЕ НА НАЙ-ДОБРАТА ВЕРСИЯ НА RETAS МОДЕЛА ЗА ПРЕДСТАВЯНЕ ЗАТИХВАНЕТО НА АФТЕРШОКОВАТА АКТИВНОСТ ВЪВ ВРЕМЕТО

Др. Господинов

Физически факултет, Пловдивски университет "Паисий Хилендарски", ул. "Цар Асен" №24, 4000 Пловдив, България

(Резюме)

В тази статия са демонстрирани възможностите и приложимостта на софтуерна програма, написана на FORTRAN 95, за моделиране спада на афтершоковата активност във времето. Програмата е предназначена за извършване изчисления на параметрите на ограничен епидемичен тип модел на афтершокова активност (RETAS) за описание времевото разпределение на афтершоците. Това е тригериращ модел, който осигурява статистическо описание на времевата еволюция на вторичните трусове в серията. Предимство на RETAS е, че моделът предлага редица версии, като едновременно включва най-използваните модели - модифицираната формула на Омори (MOF) и епидемичния тип модел на афтершокова активност (ETAS) като гранични случаи. По този начин RETAS предлага по-голямо разнообразие на модели за подбиране на най-добрия от тях с цел описание времевото разпределение на вторични трусове в една сеизмична последователност. Авторът е предоставил примери на симулирани данни, за да демонстрират използването на софтуера за различни типове афтершокови серии, като е посочил и начините за интерпретация на получените резултати.

Bulgarian Chemical Communications, Volume 47, Special Issue B (pp. 323–330) 2015

Crustal and upper mantle structure in the southen part of the Moesian platform obtained by data from seismic stations MPE, PVL and SZH

G. D. Georgieva*

Department of Meteorology and Geophysics, Faculty of Physics, St. Kliment Ohridski University of Sofia, 5 James Bourchier Blvd, 1164 Sofia, Bulgaria

Receiver function technique is used to study the crustal and upper mantle structure beneath Bulgaria. It is applied to the data from National Digital Seismological Network. The results for three seismic stations, situated in the southern part of Moesian platform, are reported. These stations, Malopestene (MPE), Pavlikeni (PVL) and Strazhitsa (SZH), are equipped with broad-band seismometers and RefTech 130 digitizers. The crustal structure beneath the seismic stations is very complex and the Moho discontinuity can't be tracked in all azimuths around the stations. The shallow Earth's crust discontinuities are obtained close to the three seismic stations. The most complex crustal structure is observed beneath the seismic station MPE.

The main discontinuities in the upper mantle are well observed beneath the territory of Bulgaria. These are asthenosphere-mantle discontinuity, which has a depth between 190–220 km, and discontinuities at 410 and 660 km. In North of Bulgaria these two discontinuities have different depths than in iasp91 velocity model.

Key words: seismology, Earth's structure, Earth's crust, receiver function

INTRODUCTION

Moesian platform is characterized by a very thick sediment layer. Its thickness is estimated to 8-10 km from different geophysical investigations and increases towards Fore Balkan zone to 18-20 km [1, 2]. The Moho depth varies in range 30-33 km and increases in the edge zones of the platform [2].

Mantle structure beneath Bulgaria is not well observed. Several studies of the crustal structure [3, 4] show results up to 250 km, which includes the upper mantle. Yegorova [5] use gravimetry techniques to estimate the density beneath Balkans. They found lifting of 410 discontinuity in the central part of the Balkans and Sredna gora mountain.

DATA AND METHOD

Receiver function technique, which has developed in recent decades, offers good opportunities for the study of the crustal and upper mantle structure. It does not require an array of seismic stations and may be applied also in areas where the number of stations is limited. The frequency of the seismic waves used in the technique allows to obtain information on the structure to a relatively great depth.

The receiver function is called the radial component of the seismogram, deconvolved with the vertical component. Few percent of the energy of the incident P wave in some teleseismic events are converted into the S wave (Ps), if we have a relatively sharp discontinuity in the crust or upper mantle. This converted seismic phase arrives at the station in the coda of the P wave. The Ps onset, amplitude and polarity depended on the distribution of the S waves velocities beneath the seismic station. Therefore, if Ps onset is estimated and an initial velocity model is used, one can determine the depth of the discontinuity that generated the converted phase.

Rotation of the seismogram is needed before the deconvolution to separate the energy of P and Ps phases. The new coordinate system is so called LQT coordinate system, where L axis is in the direction of incoming P wave. Q and T axes are perpendicular to L. In this case L, Q and T components contain mainly the energy of P, SV and SH waves respectively. In case of isotropic media and horizontal layers (with slope up to 10° [6]) no energy should be observed on T component. Below the perpendicular components, Q and T, will be analyzed.

It is difficult to determine the converted Ps phase on a single receiver function. So the receiver functions are stacked together and easy to determine the coherent phase, converted from the Mohorovicic discontinuity.

The depth of the Mohorovicic discontinuity is estimated in two ways - by the method of [7] and from the velocity model, computed by seismic inversion. The stacked receiver functions were divided in azimuthal intervals so that in each interval they have a similar shape.

* To whom all correspondence should be sent:
ggeorgieva@phys.uni-sofia.bg

© 2015 Bulgarian Academy of Sciences, Union of Chemists in Bulgaria

Zhu and Kanamori [7] use a stacking method in depth-velocity ratio space. For each receiver function they compute the depth of Moho and V_P/V_S ratio. Where most of the phases are grouped coherent is the area where with 95 % probability the real Moho depth and V_P/V_S ratio can be estimated.

The piercing points, where the seismic rays cross a discontinuity, for mantle discontinuities at 410 and 660 km are mapped and three groups of profiles through the area are traced. Migration is done along each profile, analogously to migration in seismic investigations, to obtain the depth section.

Earthquakes with epicentral distances 30°–95° are used in the study to satisfy the mentioned above condition for the energy distribution of the P wave. It is required that earthquakes have a magnitude is in the range of 5–7 and records have high signal/noise ratio. Results for stations, located in Northern Bulgaria – Malopeshtene (MPE), Pavlikeni (PVL) and Strazhitsa (SZH), are presented in this study. Earthquakes used in the study are recorded between December 2005 and July 2010, they have magnitudes in range from 5,7 to 7,5, and epicentral distance as in the condition. The selected seismic events are about 200 for each station and provide good azimuthal coverage.

RESULTS

The structure of the Earth's crust

Seismic station MPE is located in the southwest corner of the Moesian platform. About 180 events are

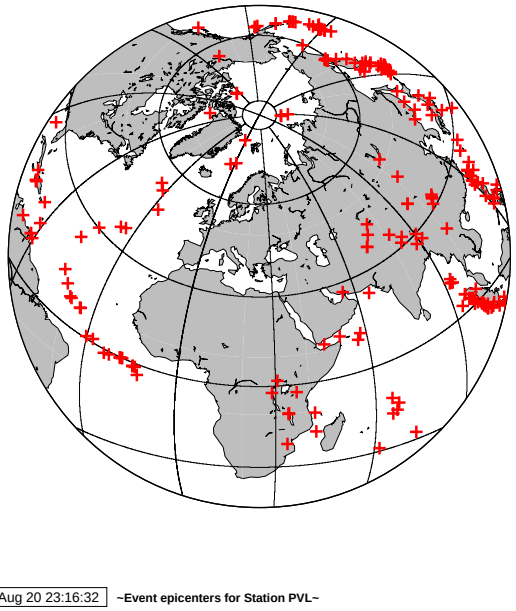


Fig. 3. Map of the earthquakes epicenters recorded at PVL station and used in the study.

used to calculate receiver functions for this station. PVL station is located in the middle of the Moesian platform while SZH station is located in the eastern part of the Moesian platform. Receiver functions for 217 seismic events are calculated for both stations. Good azimuthal coverage with data is achieved for all seismic stations (Fig. 1).

Stacked receiver functions (Q components) for station MPE are presented in (Fig. 2A), and the

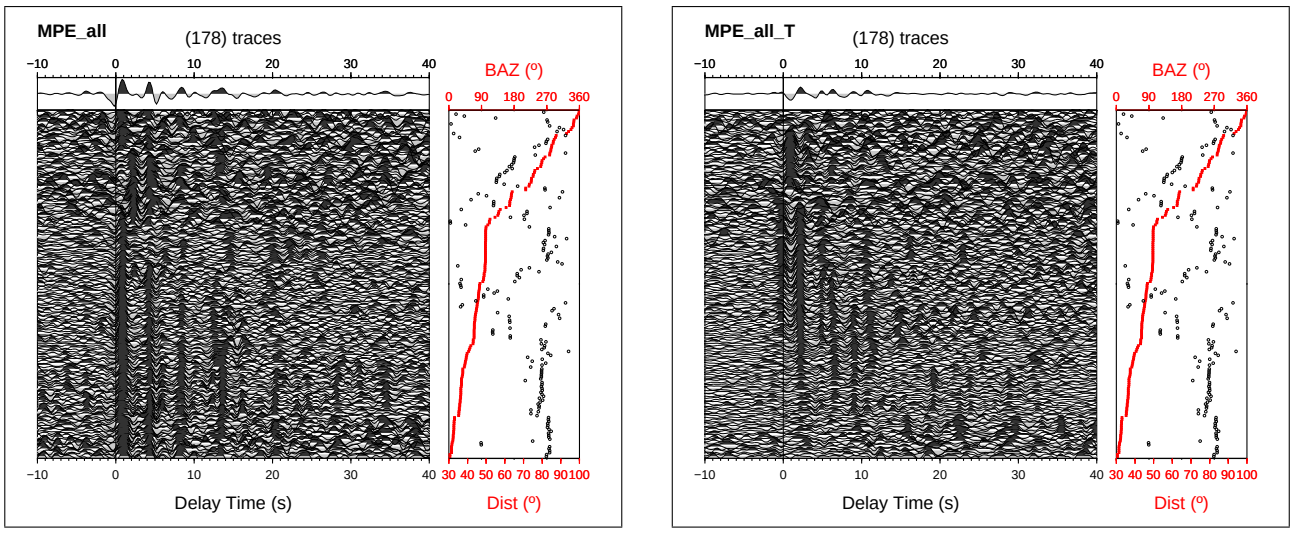


Fig. 2. Staked and sorted from 0° to 360° azimuth receiver functions (A) and stacked and sorted from 0° to 360° azimuth T components (B) for seismic station MPE. First trace above the plot represents the sum of receiver functions. Red squares represents the back azimuth for each trace (earthquake) and black dots represents the epicentral distance.

stacked T components -– in (Fig. 2B). Mohorovicic discontinuity, which is presented by the Ps phase with 4.2 s onset, is tracked clear across the whole azimuth range around the station. Some converted phases, coming from discontinuities in the crust, occurred in several azimuth intervals. For example, in the range 180°–270° a phase is observed at onset time 2.5 s on T component. Any phases should not be observed on the T component under ideal conditions – horizontal borders with a slope no more than 10° [6] and homogeneous medium. In case of station MPE, for same azimuth intervals, when Ps phase is not observed on the radial component, distinct positive and negative amplitudes are presented on the T component. Such a plot of stacked receiver functions can be observed when an anisotropic layer is presented in the crust. The results for the receiver functions and the T components of station MPE show that the existence of anisotropic layer or tilted discontinuity with a slope of more than 10° can be expected beneath this station. This means that more techniques should be applied to investigate the crustal structure beneath this seismic station.

Stacked receiver functions for station PVL are presented in (Fig. 3). As phase, converted by the Mohorovicic discontinuity, is identified positive peak with 4,5 s onset. This phase is not clearly visible in all azimuth ranges. Analogically to the results obtained by Eckhard and Rabbel [8] and similarly to the results from MPE, it can be assumed that beneath the station PVL an anisotropic layer in the Earth's crust is presented.

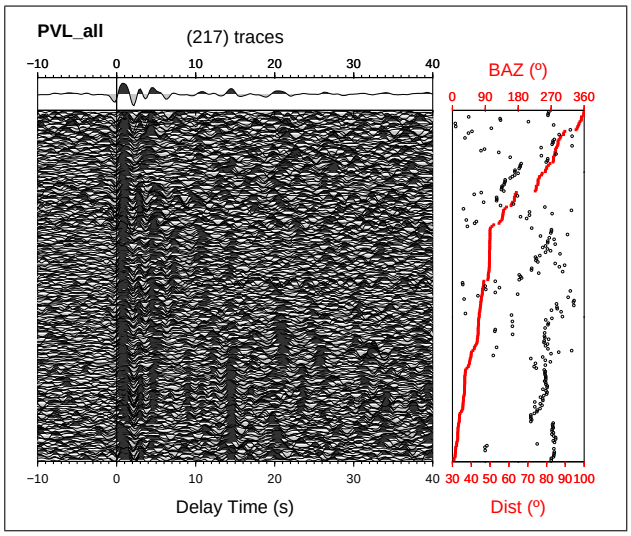


Fig. 3. Stacked and sorted from 0° to 360° azimuth receiver functions for station PVL.

Two converted phases are presented in the summed receiver function for seismic station SZH (Fig. 4) The phase with 4.8 s onset time is identified as converted from Mohorovicic discontinuity. This phase has earlier onset and smaller amplitude in some azimuth ranges, like 210°–350°. Such a phase is not observed in the range 120°–180°. The reason for this would be the existence of a fault structure close to the station in the same azimuth range.

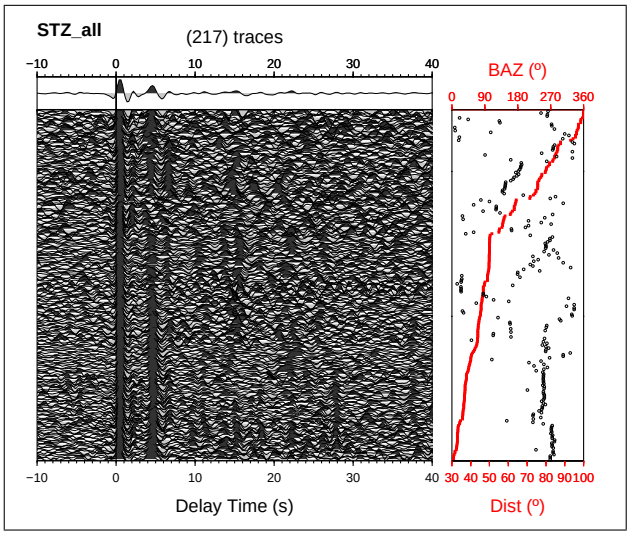


Fig. 4. Stacked and sorted from 0° to 360° azimuth receiver functions for station SZH.

On the stacked receiver functions for all three stations a phase with about 1 s onset is observed. It is presented in the whole azimuthal interval around the stations PVL and SZH while for the station MPE there is azimuthal interval where this phase is not observed. Instead a later phase is presented with onset time about 2 s.

Using the method of Zhu and Kanamori [7] for MPE station is obtained the depth of Moho in the range 29–31 km and the range for the V_P/V_S ratio is from 1.81 to 1.92 with 95% probability (Fig. 5A).

The computed velocity models show that the seismic inversion is very unstable (Fig. 6A). The inversion is done only in two azimuthal intervals 0°–90° and 100°–110°. The Mohorovicic discontinuity can not be defined clear in the obtained velocity model. The only layer, that is shaping close to the Earth's surface, is the sediment layer and has a depth of about 7 km with S wave velocity 2.5 km/s.

The data show the presence of anisotropic structures in depth. The results by the method of [7] show

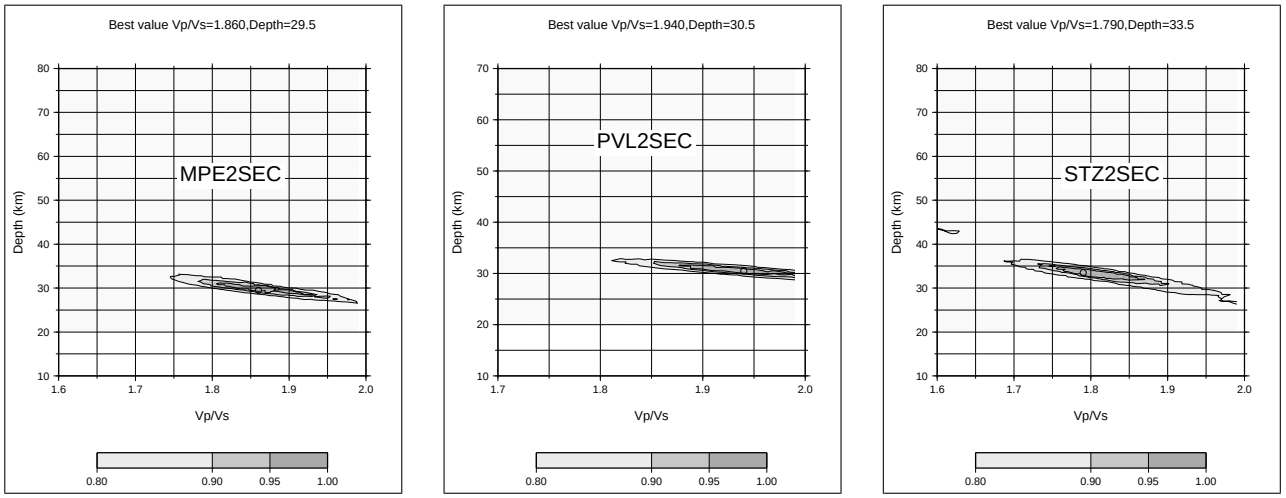


Fig. 5. Areas of solution for depth of Mohorovicic discontinuity and V_P/V_S ratio for seismic stations (A) MPE, (B) PVL and (C) SZH.

very high values of the velocities ratio and the seismic inversion is unstable. Thus the results for station MPE should be regarded as preliminary. It is necessary to carry out further research and to apply other geophysical methods.

Depth of Mohorovicic discontinuity beneath the station PVL was obtained with 95% probability in the interval 31–33 km (Fig. 5B) by method of Zhu and Kanamori. Seismic velocities ratio varies greatly in different azimuth intervals. It ranges from 1.74 to 1.81 for the range 260°–300°, where no anisotropic layers is assumed. Elsewhere around the station values of V_P/V_S is very high, between 1.84 and 1.93, yielding a two areas of solution. Such values are usually not observed in the Earth's crust, and therefore the method of Zhu and Kanamori doesn't give reliable results in these azimuth intervals.

Inversion for station PVL was made in four azimuth ranges: 300°–40°; 40°–68°; 70°–230°; and 260°–300°. Initial parameters for the inversion are: slowness in the range 6.0–6.4 $s/^\circ$, angle of incidence 20°–24°, and initial velocity structure is obtained by averaging the model computed by [3] for the cell 25° E/43° N.

Inversion of receiver function is extremely unstable in the azimuthal range 300°–40° and small changes in the initial parameters lead to large differences in the final velocity models. Synthetic seismograms, computed for velocity models obtained by inversion, have a relatively small overlap with real seismograms. Although, three layers can be identified, with small changes of their depth and significant jump in S waves velocity. Near the Earth's surface a layer is obtained with thickness of about 1 km and a very low seismic waves velocities ($V_S = 1.5$ km/s). The thickness of the sedimentary layer, where the V_S is around 3.2 km/s, is about 9 km. Depth of the Mohorovicic discontinuity is obtained about 32 km for the most of the initial parameters.

The overlap between synthetic and recorded waveforms is not good also in the azimuthal range 40°–68° and there is a visible gap in amplitudes. Inversion is relatively stable in this range. The very low velocity layer ($V_S = 1.5$ km/s) close to the surface has a thickness of about 2 km, while the sedimentary layer reaches a depth of 5 km ($V_S = 3.0$ km/s). The Mohorovicic discontinuity in this azimuth interval is obtained 34 km, where the S waves velocity has jump from 3.7 km/s to 4.3 km/s.

Inversion in the azimuth range 70°–230° shows also existence of sediment layer with $V_S = 3.1$ km/s. It extends to a depth of 5 km, and the depth of Mohorovicic discontinuity is computed 32 km. A low velocity layer ($V_S = 3.5$ km/s) is shaped at a depth of 17–23 km.

Ameliorated inversion results are obtained in the azimuth range 260°–300°. The depth of Mohorovicic discontinuity is obtained about 32 km where the S waves velocity changes from 3.8 km/s to 4.1 km/s. Several layers are individuated into the earth's crust. A sedimentary layer with thickness of 2 km and V_S about 2.5 km/s exists near the earth's surface. Sediment layer continues to a depth of 7 km ($V_S =$ 3.3 km/s). In this azimuthal range also a low velocity

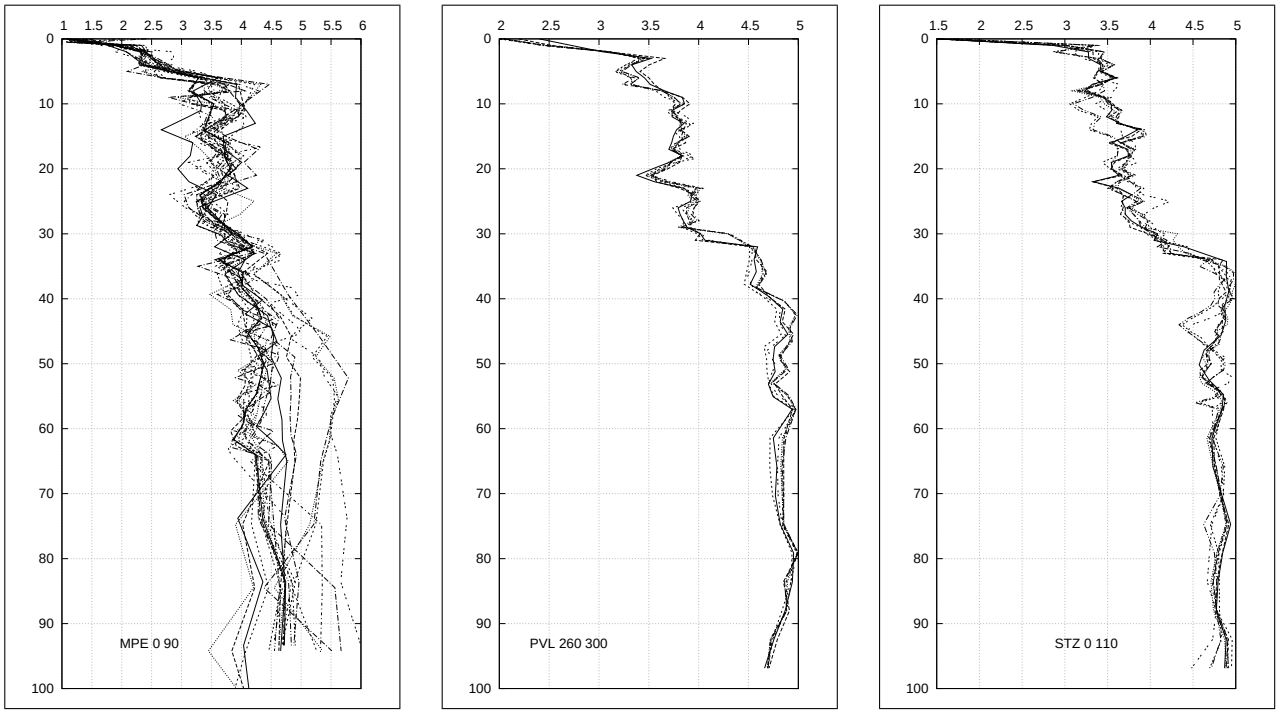


Fig. 6. Velocity models, computed from seismic inversion for some of azimuth intervals for seismic stations (A) MPE, (B) PVL and (C) SZH.

($V_S = 3.5$ km/s) layer at a depth of 19–22 km (Fig. 6B) is observed.

Thickness of the crust beneath the station PVL is 32–33 km. Different ways of estimation give similar results. The most reliable are the results for the thickness and structure of the crust in the azimuth range 260°–300°. For other areas more detailed studies should be made.

Thickness of the crust beneath the station SZH, estimated by the method of Zhu and Kanamori [7] with probability 95% is in range 32–34 km, and the ratio of the seismic waves velocities is in the range from 1.79 to 1.87 (Fig. 5C).

The data for inversion are divided in three azimuth intervals: 0°–110°, 120°–180° and 210°–350°. Crustal thickness for the three intervals is estimated 34 km (Fig. 6C). A sedimentary layer with a thickness of about 1 km and very low seismic waves velocity ($V_S = 2$ km/s) is identified. In the azimuth interval 0°–110° S waves velocity increases to 3.3 km/s down to a depth of 7 km, where jumps to 3.5 km/s and again continues to increases smoothly up to a depth of 34 km where jump to the value of V_S=4,9 km/s. A layer with thickness of 14 km and S wave velocity of 4 km/s is detected in the azimuthal range 120°–180°. In the last azimuth interval 210°–350° S wave velocity changes with a jump from 1.5 km/s to 3.4 km/s at depth of 2 km. The velocity amends with a jump from 5.8 km/s to 6.3 km/s at a depth of 8 km. Another abrupt change of the seismic waves velocity (from $V_S = 3.8$ km/s to $V_S = 4.4$ km/s) occurs at a depth of 29 km.

Results for the three stations located in northern Bulgaria can be summarized as follows. Typical of their receiver functions is the existence of a distinct phase with 1 s onset time. This phase indicates the presence of well distinguishable sedimentary layer beneath the three seismic stations. Beneath the MPE station there is a break for this phase on the plot of stacked receiver functions. Such a break is observed also for the phase, converted from Moho. Such kind of gaps are observed beneath other two stations SZH and PVL. Beneath station PVL the converted by Moho phase has a smaller amplitude of the phase in the crust. Break beneath the station SZH could be explained by the fault passing near the seismic station. Overall, beneath the three stations, the complex plots of stacked receiver functions, show a strong azimuthal dependence, an indication of the presence of the anisotropic layers. This is confirmed by the

phases observed on the plot with stacked T components.

Results for the depth of Mohorovicic discontinuity obtained by the method of Zhu and Kanamori with 95% probability are in the range 29–31 km for station MPE, 31–33 km beneath the station PVL and 32-34 km beneath the station SZH. Intervals for the ratio of seismic waves velocities are: 1.81 to 1.92 at station MPE, at station PVL is 1.74–1.81 and 1.79 to 1.87 at station SZH.

Inversion of receiver function waveforms is performed in different azimuth intervals around the seismic stations. Inversion for station MPE is extremely unstable and further studies should be performed, including different techniques and other geophysical methods, to obtain a velocity model for that station. Inversion for station PVL is stable only in the range 260°–300°, where the obtained thickness of the crust is about 32 km. Inversion for station SZH is performed in three azimuth intervals and the obtained crustal thickness in all intervals is 34 km.

Structure of the mantle transition zone

Stacked receiver functions is not a good option for representing the results from the research in the mantle. Instead a map with piercing points of the seismic rays should be made and profiles should be traced across the area of interest. In (Fig. 7) the map with piercing points for 410 discontinuity and traced profiles are presented. The results for profiles C2 and C3 are analyzed in this study.

Profiles of the C series are chosen parallel to the geographical parallels with direction from west to east. Their western end is located on the territory of Serbia (C2 and C3) and eastern end is located in the Black Sea. Profiles have a length of about 600 km and are 1° apart each other.

Main discontinuities in the upper mantle are identified relatively well in this series of profiles. Deviations from the initial velocity model are observed along profiles of C2 and C3. From the middle of the profile C2 to east the 410 discontinuity is estimated of 420 km. The depth of 660 discontinuity is shallower and it is estimated as 650 km in some parts of the profile (Figure 8). In the greater part of the profile C3 410 discontinuity has also a depth of 420 km.

Lithosphere – mantle discontinuity is estimated at 190 km along the profiles from C series. In certain parts of the profiles the depth is greater and reaches up to 220 km. Phases from depths of about 300 and 500 km are also observed. Along profile C2 are observed phases at a depth of 300 and 340 km, and along profile C3 – at depth of 300 km. Identifications for the presence of discontinuity at a depth 500–510 km are obtained along profiles C2 and C3. A phase of depth 600 km can be observed on profile C3, which

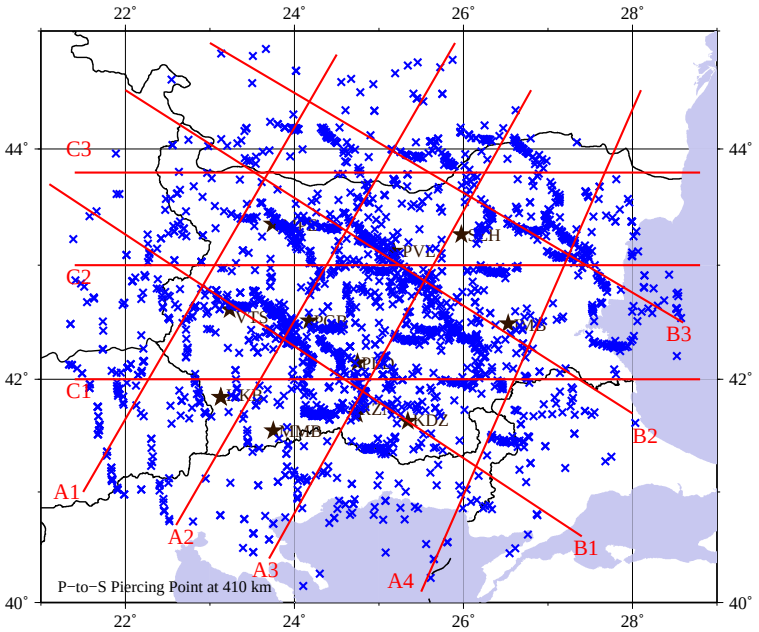


Fig. 7. Map of piercing points for 410 discontinuity and traced profiles. Only profiles C2 and C3, located in the southern part of Moesian platform, are considered in this study.

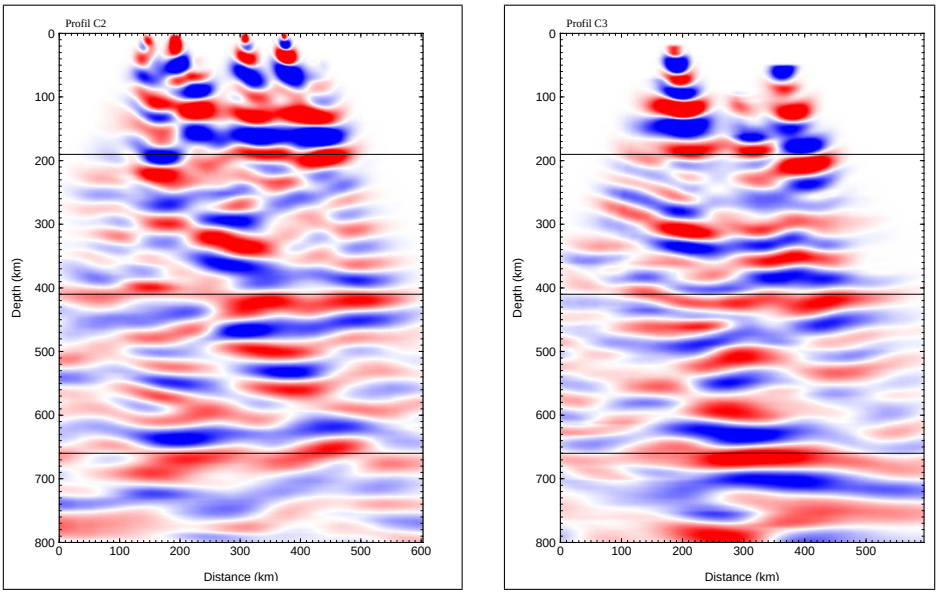


Fig. 8. Depth sections along profiles C2 and C3, obtained after migration. Horizontal lines show discontinuities 410 and 660, and also Lithosphere-mantle discontinuity.

origin is not identified yet. The appearance of these phases may be due to deep structure in the Vrancea region [9, 10].

The results along the profiles from C series can be summarized as follows. Depth of 410 km discontinuity is greater in northern Bulgaria. This is an indication of the presence of a hot mantle in this region [11]. The depth of 660 is shallower, which is as expected in the regions with hot mantle [11].

CONCLUSIONS

The results obtained by the receiver function method for the area of seismic stations in North Bulgaria MPE, PVL and SZH, show complex structure of the crust. The Mohorovicic discontinuity is not shaped throughout the azimuth range around the seismic stations. The reason for this could be the presence of a fault structure, as beneath the station SZH. On the plots with the stacked receiver functions although converted by Moho phase, another distinct phase in the Earth's crust is observed. One explanation for its existence is that it is generated at the bottom of the sediments. Performed seismic inversion, however, showed unstable results in some of the azimuth intervals (station MPE). This means that probably the structure of the earth's crust beneath the seismic station is more complex: most probably existence of anisotropic structures. The main discontinuities in the mantle transition zone, namely the 410 and 660 are obtained after migration of the data, but the obtained depth is different than in iasp91 velocity model.

REFERENCES

[1] T. Dobrev, V. Ivanova, R. Radkov, *Complex geophysical investigations (in Bulgarian)*, (Technique, 1989).

[2] H. Dachev, *Structure of the Earth's crust in Bulgaria (in Bulgarian)*, (Sofia, 1988).

[3] R. Raykova, S. Nikolova *Stud. Geophys. Geod.* **51**, 164–180 (2007).

[4] E. Spasov, E. Botev, *Bul. Geoph. J.* **13/4**, (1987).

[5] T. Yegorova, V. Kozlenko, V. Starostenko, E. Shen, E. Botev, *Geophys. J. Int.* **132**, 283–294 (1998).

[6] C. Langston, *Bull. Seism. Soc. Am.* **67**, 1029–1050 (1977).

[7] L. Zhu, H. Kanamori, *J. of Geoph. Res.* **105/B2**, 2969–2980 (2000).

[8] C. Eckhard, W. Rabbel, *Geophys. J. Int.* **187**, 439–479 (2011).

[9] O. Heidbach, P. Ledermann, D. Kurfess, G. Peters, T. Buchmann, L. Matenco, M. Negut, B. Sperner, B. Müller, A. Nuckelt, G. Schmitt *Int. Symp. On Strong Vrancea Earthquakes and risk Mitigation, Romania*, (2007)

[10] M. Martin, J. Ritter, CALIXTO working group, *Geophys. J. Int.* **162**, 448-460 (2005)

[11] G. Helfrich, *Rev. Of Geoph.* **38/1**,141-158 (2000).

СТРУКТУРА НА ЗЕМНАТА КОРА И ГОРНАТА МАНТИЯ В ЮЖНАТА ЧАСТ НА МИЗИЙСКАТА ПЛАТФОРМА ПО ДАННИ ОТ СС MPE, PVL И SZH

Г. Георгиева

Физически факултет, Софийски университет "Св. Климент Охридски", бул. "Джеймс Баучер" №5, София, България

(Резюме)

В изследването е използван метода на функциите на приемане. Той е приложен към данни от станциите на Националната Цифрова Сеизмична Мрежа (НЦСМ). Обработени са данните от 11 сеизмични станции, екипирани с широколентови сеизмометри. В този доклад ще бъдат представени получените резултати за три станции разположени в южната част на Мизийската платформа – Малопещене (MPE), Павликени (PVL) и Стражица (SZH).

Мизийската платформа се характеризира с наличието на много дебел седиментен слой. От различни геофизични измервания неговата дебелина е определена на до 8-10 km. Резултатите, получени по метода на функциите на приемане показват наличието на слой с ниски скорости на сеизмичните вълни и голяма дебелина под повърхността на Земята. Дебелината на границата на Мохоровичич варира между 29 km и 34 km, като нейната дебелина се увеличава от станция MPE към станция SZH. Като цяло времевите разрези, получени за отделните станции за строежа на земната кора, имат изключително сложен характер. Границата на Мохоровичич не се проследява в целия азимутен диапазон и при трите станции.

При изследването на строежа на мантията са избрани три групи от профили, които пресичат територията на България в различни посоки. Идентифицирани са фази, които идват от основните граници, ограждащи зоната на преход в мантията. Северна България е установено слабо отклонение в дълбочината на тези граници спрямо isap91 модела. Установено е наличието на фази, които идват от граници в зоната на преход мантията.

Bulgarian Chemical Communications, Volume 47, Special Issue B (pp. 331–342) 2015

Land surface state anomalies and related severe meteorological phenomena

J. S. Stoyanova[1]*, I. A. Zamfirov[2],

[1] *National Institute of Meteorology and Hydrology (NIMH), Bulgarian Academy of Sciences, 66 Tsarigradsko chaussee Blvd., 1784 Sofia, Bulgaria*
[2] *National Institute of Meteorology and Hydrology (NIMH), Bulgarian Academy of Sciences, 60 Hadzi Dimiter str., 5800 Pleven, Bulgaria*

A conceptual approach (developed at NIMH-BAS) for quantitative description of land-atmosphere interactions and some regional applications at climate-weather extremes related with "dry"-"wet" anomalies in land surface state for territory of Bulgaria is presented. Based on specially designed experimental numerical schemes, combined with information from meteorological models, geostationary satellites Meteosat Second Generation and ground observations, knowledge about the environmental conditions for development of meteorological phenomena related to natural hazards (agrometeorological drought and yield reduction, forest fires and regions with increase risk, convective storms and soil overmoistening effects, climate forcing due to biomass burning) are extracted. The obtained results might serve as a methodological basis for further studies, operational applications, climatic assessments and forecasts as related to multifunctional risk from severe meteorological phenomena.

Key words: Land/atmosphere interactions, natural hazards, fire-carbon emissions, climate-wheather

INTRODUCTION

The importance of land-atmosphere interactions and all processes they involve for the climate system is increasingly being recognized. Similar to the oceans, land areas provide the lower boundary for the atmosphere, with which they exchange energy, water and chemical compounds such as CO2. While the role of land for climate variability has often been neglected in the past, recent studies have highlighted how land atmosphere interactions can be critical in modulating variations in climate on a range of temporal (seasonal to centennial) and spatial (local to global) scales. Land-atmosphere interactions tend to be particularly important in transitional zones between dry and wet climates. For present climate, this applies also to the Mediterranean region [1]. Moreover, these "hot spots" of land-atmosphere coupling are also inherently modified with shifts in climate regimes, for instance due to climate change. They can thus be displaced on longer time scales. One of the problems that are still underestimated is the assessment of the role of land-atmosphere interactions and Land Surface Processes /LSPs/ related to climate dynamics/extremes on a regional scale. The current study is focused on evaluation the land-atmosphere coupling for the region of eastern Mediterranean resulting in different levels in soil moisture and related evapotranspiration and the possible impacts of soil moisture on climate (weather) extremes on a local/regional scale.

Drought as a normal, recurrent feature of climate is one of the major environmental disasters in Mediterranean that has taken great influence to socio-economic development in the region. It does not belong to the group of climate extremes based on simple climate statistics, as anomalies in daily temperature or heavy rainfall amount that occur every year. Drought is a more complex event-driven extreme, which do not necessarily occur every year at a given location. In the current study drought on the vegetated land surface is referred as a "dry" biogeophysical cycling anomaly with a complex nature. Its assessment calls for a comprehensive and integrated approach, accounting for specific regional and local reveals with possibilities for drought extent and impacts to be monitored routinely by numerous indicators. In contrast, "wet" land surface anomalies might be produced by synoptic or mesoscale weather systems that in some cases may lead to soil overmoistening and produce floods over the land ("meteorological floods") or in case of deep convection in comparatively "dry" preconvective environment are often related to showers with hail.

The primary purpose of the work is to highlight typical climate-weather extremes where the land surface state is of relevance to the occurrence of natural hazards like: drought, agricultural yield reduction, disturbed environmental sustainability (via forest fires); convective storms and related severe

* To whom all correspondence should be sent:
julia.stoyanova@meteo.bg

© 2015 Bulgarian Academy of Sciences, Union of Chemists in Bulgaria

weather. Accordingly, the main specific research objectives are focused to: 1) Present a methodological approach to extract knowledge from the combined use of ground observations, modelling of soil-vegetation-atmosphere interface and satellite imageries for near real-time detection and monitoring of weather-climate induced terrestrial natural hazards; 2) To test this approach as a research tool and in some operational applications for the region of Bulgaria; 3) To illustrate the results and current available knowledge by specific constrained case studies.

The complex approach of land surface analyses and its application for severe meteorological phenomena is developed by the first author. The second author has contribution in synoptic analyses of convective processes and the interpretation of related satellite products of atmosphere convective environment.

METHODOLOGY

In our preceding work [2] the developed conceptual framework for Land Surface Analyses (LSA) at the National Institute of Meteorology and Hydrology (NIMH) during the last 10 years and more was introduced. The adopted LSA concept in research and operational work is based on quantification of local-regional scale biogeophysical cycling (for territory of Bulgaria) at two different land cover types. A lot of biogeophysical indexes have been developed on the bases of SVAT modelling outputs or are inferred from satellite information and they both are introduced in operational mode (or applied as research tools). In this study, the approach adopted includes the combined use of the already developed local scale biogeophysical indexes on the bases of "SVAT.bg", meteorological indexes bases of space-time resolution of meteorological Meteosat Second Generation (MSG) geostationary satellites, as well as the application of new blended parameters between satellite products and ground observations from meteorological network. In terms with this, climate-weather extremes in land surface state related to disturbances in energy and water cycles, as well as some disturbances in terrestrial carbon cycling are studied on the bases of the following operationally inferred and applied quantitative characteristics:

- Index of site-scale Soil Moisture Availability (SMA) to different root zone depths, scaled by a 6-level threshold scheme and visualised by colour coded maps (SMAI), developed on the basis of "SVAT.bg" model outputs [3];
- Specialized meteorological SMAI Index with indicated effective rainfall or flood producing rainfall quantities. This Index is visualised by colour-coded maps and updated daily for wheat field land cover (LC) and run each 12 hour per day at grass LC;
- Land surface state (and vegetation water stress) characteristics on the basis of MSG SEVIRI data: Radiative skin temperature according to the LSASAF Land Surface Temperature (LST) product (http://landsaf.meteo.pt) and the temperature difference between LSA SAF LST and air temperature at 2 m height measured at synoptic stations (Tair). The temperature difference is constructed between the 5x5 pixels mean MSG LST values for the pixels containing corresponding synoptic station and corresponding Tair measured at this site. The CLC200 vegetation types classification is used;
- MSG satellite products for assessing air humidity: RGB DUST product and MPEF Total Perceptible Water (TPW) product;
- Colour enhanced IR images of MSG are used to depict the convective cloud systems;
- Carbon-equivalent emissions from vegetation fires according to the LSA SAF SAF Fire Radiative Power (FRP) product (derived every 15 min at the native SEVIRI pixel resolution). Biomass burning effects related to forest fuel moistening (depending on climate, fuel type and availability) of 2011 are assessed applying the Plant Functional Types (PFTs) concept according to a regional bioclimatic classification scheme [4].

WEATHER-CLIMATE EXTREMES IN LAND SURFACE STATE. CASE STUDIES AS EXAMPLES

Soil moisture availability to vegetation land cover is an important variable for evaluating vegetation transpiration, a key factor in models of ecosystem and carbon cycle processes, energy and water budgets of crop canopies, as well as a basic parameter in mesoscale atmospheric circulation models and forecasting systems. SMA being the main determinant of plant systems development, at the same time might serve as information source for "warnings" for environmental constrains.

The main limitation of its use is the lack of ground observations of key variables such as soil moisture or evapotranspiration. Approaches that allow obtaining

indirect estimates of relevant land surface parameters such as soil moisture or evapotranspiration are very promising and could significantly advanced research in this field. In our work, different types of numerical schemes for studying LSPs and their extremes are applied and discussed below towards: their physical meaning and applicapability in detection and monitoring of extreme meteorological phenomena on land as well as requirements and capabilities of improving satellite applications for eastern Mediterranean in parallel to regional modelling in the scope of the current LSA SAF data usages.

Land-atmosphere coupling

Soil moisture, terrestrial vegetation, and atmospheric flows are parts of a complex interacting system, characterized by the presence of many feedback mechanisms between the various components. For example, soil moisture anomalies, associated with the lack of precipitation, have been suggested to play a crucial role in the variability of the large-scale water balance [5] and in determining the strength of summer heat waves at continental midlatitudes [6]. Precipitation has a clear impact on soil moisture: large rain events tend to wet the soil. To what extent, though, do land surface moisture and temperature states affect, in turn, the evolution of weather and the generation of precipitation? Such questions lie at the heart of much recent climatological research that addresses questions of land-climate interaction [5]. One of hypotheses in climate models is that the atmosphere responds strongly to anomalies in surface fluxes, which in turn respond to anomalies in land surface state, where term "land surface" refers to the combination of the vegetation canopy, the soil-atmosphere interface, and the top meters of the soil.

Soil-vegetation-atmosphere feedbacks are particularly important in water-limited ecosystems, where water is the main factor controlling vegetation growth. Through evapotranspiration, vegetation determines the flux of moisture from the soil to the atmosphere, i.e. the surface moisture flux. This can have significant effect on the hydrologic cycle, especially in regions where local precipitation recycling plays a relevant role such as continental Europe during summer. Despite the apparent association between soil moisture feedbacks and precipitation variability [7,8] the mechanisms that maintain or amplify drought are still not well understood.

Drought on the land surface

Drought is a part of the natural climate variability and therefore can be observed in all climate regimes. It is one of the most important natural disasters in Mediterranean, considered by many to be the most complex but least understood of all natural hazards, making it difficult to predict and monitor. One of the major problems in a drought investigation is its definition, which often depends on the user and on the geographical region in question (e.g. between tropical and arid climates) and this variety makes a single global definition for drought nearly impossible [9]. There are three universally recognized physically based forms of drought: meteorological, hydrological and agricultural. Meteorological drought is measured by a shortage of precipitation, hydrological drought is measured through a deficiency in the water supply relating to reservoir storage and streamflow, and agricultural drought is measured by a shortage in water available for plant growth or sufficient soil moisture to replace evapotranspirative loss.

Agricultural drought as a result of biogeophysical cycling. Although all types of droughts originate from a precipitation deficiency, it is insufficient to monitor solely this parameter to assess severity and resultant impacts. Dryness or absence of rain is not enough to constitute a drought. Physiological and physical signals of terrestrial vegetation water stress are important to be considered and this calls for an interdisciplinary approach in studying drought in the context of geophysical processes. In the Climate Prediction Center's (CPC) percentile scheme, drought is defined as the number of consecutive days where a measured quantity (soil moisture or precipitation) is below a threshold [10] and classified by severity.

In accordance with all these knowledge, in our work drought on the land (i.e. agricultural drought) is characterized by two types of indexes. First, an original physically based SMA threshold scheme (comprising "dry"-, "wet"-anomalies and "optimal" conditions) with capabilities to reflect specific climate-soil environment for Bulgaria has been developed [3]. It is scaling soil moisture available to specific vegetation type accounting for the soil water capacity defined by maximum moisture content of capillaries in equilibrium with the force of gravity that is the field moisture capacity and the minimal of soil moisture that plant requires not to wilt are distinguished. Defining "dry"-"wet" conditions on land surface in this manner

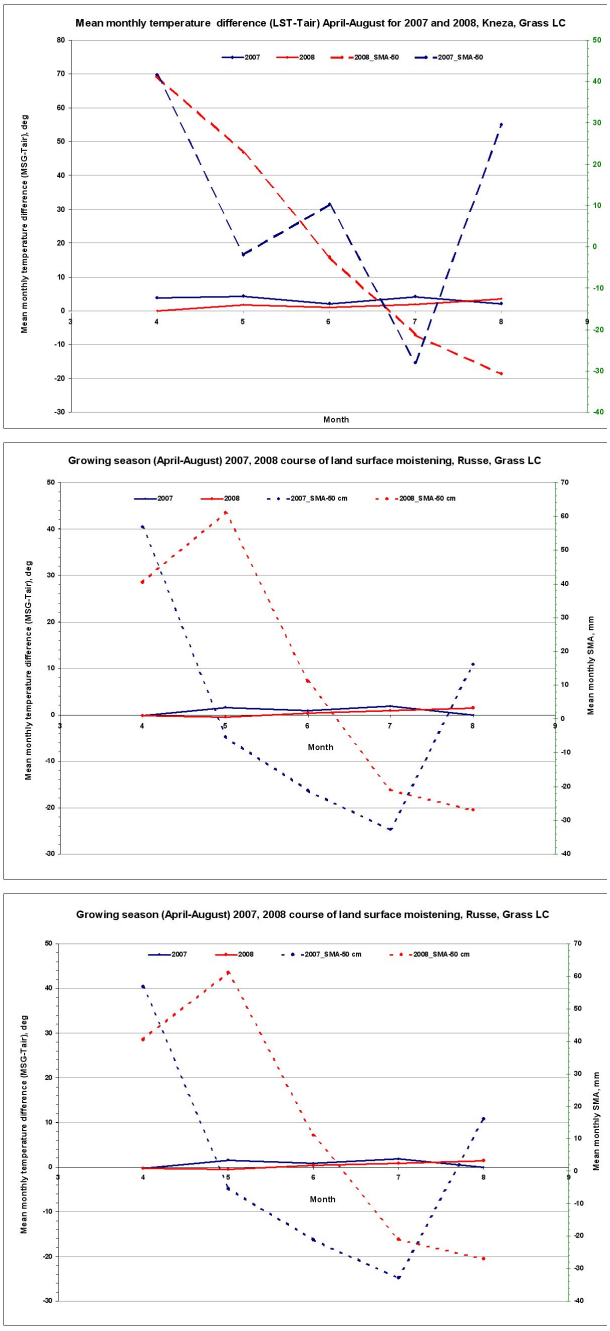


Fig. 1. Land surface moistening conditions (grass LC) derived by mean monthly values of: SMAI (dashed) and temperature difference between MSG LST and Tair (solid) for the (April-August) period of the 2007 (red) and 2008 (blue) for: (upper) central-north (Kneza), (middle) north-eastern (Russe), (lower) southern (Plovdiv) parts of Bulgaria.

eliminates biases between models, observations and climate, and provides a physical, consistent method of drought-overmoistening persistence and strength quantification at different climates and soils. It is also possible drought characteristic of interest: drought severity, magnitude, frequency, persistence or spatial extent to be derived. Second, the surface soil moisture dynamics is characterized in terms of the radiative skin temperature, as derived by the LSA SAF LST product on the basis of MSG information. LST is one of the key parameters in the physics of land surface processes on regional and global scales as it is involved in the processes of energy and water exchange with the atmosphere and its space variability is modulated by surface properties (like vegetation density and soil moisture).

As approximation of land surface moistening conditions, the temperature difference between LSA SAF LST (digital values at MSG pixel resolution) and Tair at synoptic stations measurements has been introduced. The reliability of this approach has been initially studied for selected periods of heat waves and "dry-optimal" land cover states for 2007 and 2012 [11]. 1200 UTC values of the temperature difference were used and compared with site-scale SMA assessment based on operational run of a 1D site-scale Soil-Vegetation-Atmosphere-Transfer "SVAT.bg" model to assess drought and pre-fire conditions. The mean monthly values of both indexes characterizing soil moistening for the (April-August) growing season periods of 2007 and 2008 (at grass LC) are depicted in Fig. 1. The trends in SMAI and the (LST-Tair) difference for three different climate-soil type environment are examined and compared for consistency. Although some specificity for each region, a similar trend of moistening conditions during the growing season for north-west (Kneza), north-eastern (Russe) and southern (Plovdiv) parts of Bulgaria are derived: more dry conditions for 2007, steadily depleted soil moisture according to SMAI in parallel to an increase of the temperature difference especially in cases of strong heat waves (like July of 2007). After precipitations (if any) this is reflected by a specific increase of SMAI as well as corresponding decrease in (LST-Tair) temperature difference.

Economic effects: agricultural drought and yield reduction. In general, drought in crop vegetation is defined as a stage when the soil moisture is not sufficient to meet the evapotranspiration demands of the plants. It is also well known that there will be drought for crops even though there is no meteorological drought by the definition. Thus, drought for crops is related not only with quantum of rainfall but also related to its distribution. The agricultural drought has several specificities like soil type, crop, crop variety, crop du-

ration, time of occurrence (crop stage), quantity of deficiency, duration of deficiency, etc. Thus agricultural drought analyses often is restricted to a specific crop and specific location and also for a specific soil. For example, a given amount of rainfall may result in water stress conditions in light soils but not in heavy soils. Similarly, a given amount of rainfall may result in drought conditions in upland (wheat) but not in lowland (wheat).

Therefore, it is necessary to understand the concept of drought and assess the impact based on the specifities that exist in that area. For assessing drought it should be considered that growth, development and productivity of agroecosystems are strongly dependent on their functional coupling with the environment via biogeophysical and biogeochemical functional relations and feed back mechanisms. Knowledge about mass- and energy- exchange with the environment is possible after the energetic aspects of agroecosystem functioning are considered. Energetic modelling of exchange processes are here performed on the bases of thermodynamic description of agroecosystems functioning as open thermodynamic systems.

A conceptual thermodynamic approach for quantitative description of the energy flow conversions in living organisms, motivated and referred to as "surface-boundary approach" (SBA) in biothermodynamics [12] is here applied. From SBA viewpoint the analytical description of intensity-efficiency of energy conversions at a molecular level are quantified by applying linear irreversible thermodynamic of steady-state to the boundary surface between canopy leaves-environment. For quantification of specific ecosystem-site capacity to utilize the solar energy into biochemical energy and related growth response, the quantification of accompanying energetic looses (not involved in biochemical energy) is proposed. From a thermodynamic point of view these are characterized by the entropy production (or function of dissipation, Φ) in the main photosynthetic apparatus (i.e. function of dissipation, Φ) [12]. Φ quantified as a sum of the entropy produced during the heat- and the water- exchange between leaves and environment (the first and the second terms respectively of Eq. (1):

$$\Phi = T\frac{\triangle S}{\triangle t} = \Phi_H + \Phi_E = \frac{H \triangle T}{T \triangle t} + LE\frac{\triangle q}{\triangle t} \qquad (1)$$

where $\triangle S/\triangle t$ – the entropy production rate; E – evapotranspiration rate; H – leaf-air heat exchange rate; T – mean leaf-air absolute temperature; $\triangle T$– leaf-air temperature difference; $\triangle q = (q_s - q)$– the difference between specific air humidity at the transpiring leaf level and the surrounding air, respectively; q_s– specific humidity of saturated water vapour at the leaf surface at corresponding leaf temperature; L– latent heat of vaporization of water.

The entropy production in canopy leaves ($\Phi = T \triangle S/\triangle t$) is introduced as a complex biophysical state parameter and can reflect the environmental (climate-weather) resources and vegetation capacity to accumulate solar energy in biochemical energy (responsible for growth and yield production). This is a complex indicator of hydrothermal environmental conditions and the state of main photosynthetic apparatus (leaves) during the growing season. This biophysical state parameter is a function of meteorological parameters and soil hydro-physical properties, and thus can reflect the environmental (climate-weather) resources and vegetation capacity to accumulate solar energy in biochemical energy (responsible for growth and yield production).

Applying this approach, the relationship between winter wheat yield and climate-weather has been investigated for selected climate/soil conditions of north Bulgaria (referring the region of Russe from NIMH agrometeorological network) and of south Bulgaria (referring the region of Plovdiv). Drought occurrence during critical phenological phases affecting yield production is quantified by the entropy production for these periods. Φ is calculated for six growing seasons (2007-2012) according to Eq. (1) (using parameters derived from "SVAT.bg" model outputs) and compared with corresponding wheat yield production.

It is found a strong relation between accumulated energetic looses quantified by entropy production in canopy leaves and winter wheat yield, left plot of Fig. 2(left). for north-south- regions in Bulgaria. It is found that drought increases the entropy production after Eq. (1) and decreases the efficiency of metabolic processes and related yield production for both stations. For example, mean temperature difference in "dry May" of 2007 for region Russe is significantly higher than this in 2011 (6.93 vs. 3.45°C respectively) that corresponds to the lower yield observed (261/600 kg/dk correspondingly).

In addition, the temperature difference (LSA SAF LST-Tair) is applied as an approximation of the Φ values. In order to illustrate its applicability as a climatic

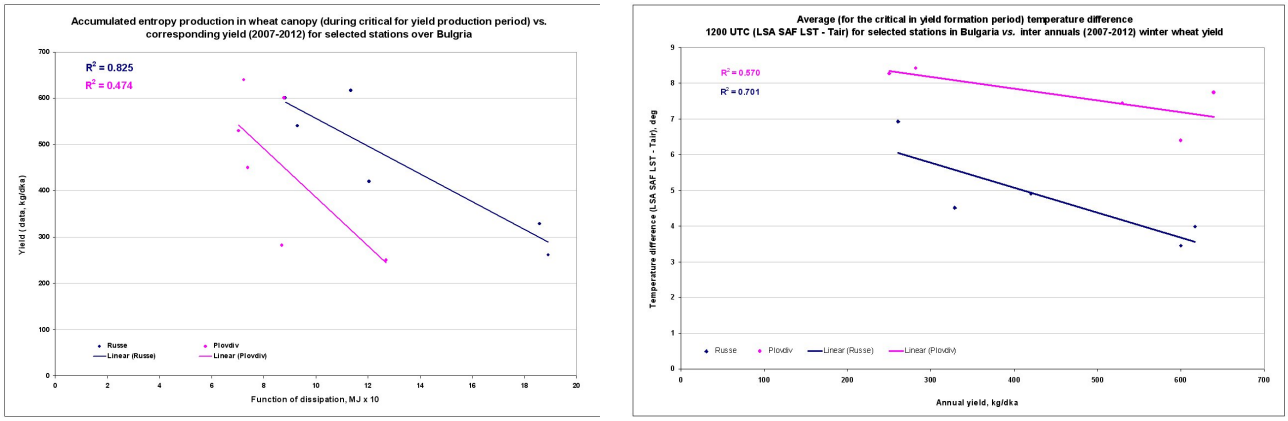


Fig. 2. Left: Comparison between dissipated energy and annual wheat yields (2007-2012) for Russe (blue) and Plovdiv (magenta). Right: Correspondence between mean inter-annual (MSG LST-Tair) difference and annual wheat (2007-2012) yields for Russe (blue) and Plovdiv (magenta).

index for characterizing bioenergetic resources, its relation to yield production is presented in right plot of Fig. 2(right).

These results show that drought effect might be assessed by a single complex index introduced by the entropy production, adequately reflecting the bioenergetic growth capacity of soil-agroecosystem system at specific climate-weather-soil-stage of crop development. Also (LST-Tair) might be a roughly approximation of climatic resources.

Environmental and security effects: Regional spatial distribution of vegetation fires as determined from geostationary satellite observations. Although humans are often the primary cause for fire occurrence, fuel types, moisture, and distribution vertically and horizontally, are very important for fire ignition and spread. Fuel moisture couples fire to climate as the fuel loads accumulate according to forest structure and composition at the specific climate conditions. Accounting this, the relation of climate, fire regimes and biomass burning effects across a range of environmental conditions and vegetation types on a regional scale is examined. To derive the forest fire regimes and link fire activity to specific fuel moistening/load (depending on climate, fuel type and availability), the Plant Functional Types (PFTs) concept is applied. Forest Functional Types FFTs definition according to a Bulgarian static equilibrium scheme for regional bioclimate classification [4] is explored in a comparative analyses with LSA SAF FRP product behaviour. The study is performed for 2011 having a "moderate" fire activity and referred to the region of SE-S Bulgaria. Three FFTs are distinguished and compared: FFT1 (Xeromesophytes, broadleaved in the Lower Forest Belt); FFT2 (Xerophytes, open deciduous, shrubs in Lower Forest Belt); FFT3 (Native coniferous, evergreen vegetation from Mid Forest Belt). The differences (and trends) in fuel moistening /and fire activity of each FFT during vegetation are evaluated on the basis of daily 0600 UTC LSA SAF LST digital values inferred at MSG pixel resolution for the growing season May-September of 2011 (left plot of Fig. 3), and by the total Carbon-equivalent emitted from biomass burning (right plot of Fig. 3). As can be seen, deciduous forests and shrubs FFT1 and FFT2 have higher skin temperature than these of coniferous from the Mid Forest Belt, FFT3. FFT2 composed predominantly by native dry oak stands and shrubs, are the most dry and fire prone areas confirmed also by the total number of MSG registered thermal anomalies (182 fire pixel detected) and highest Carbon-eq. released (right plot of Fig. 3). FFT3, composed predominantly by native coniferous stands at lower evaporative demands implying more wet environment are characterized by lower fire activity (30 fire pixel detected) that corresponds to lower climatic forcing (see right plot of Fig. 3). FFT1, composed predominantly by xero-mesophytes native deciduous oak stands, are the less fire prone area although the high evaporative demands (similar to FFT2) because of more precipitations, and thus providing the lowest climatic forcing (right plot of Fig. 3). The results indicate that the used LSA SAF parameters in the context of applied concept can be further exploited for characterizing climate-forest fire relations.

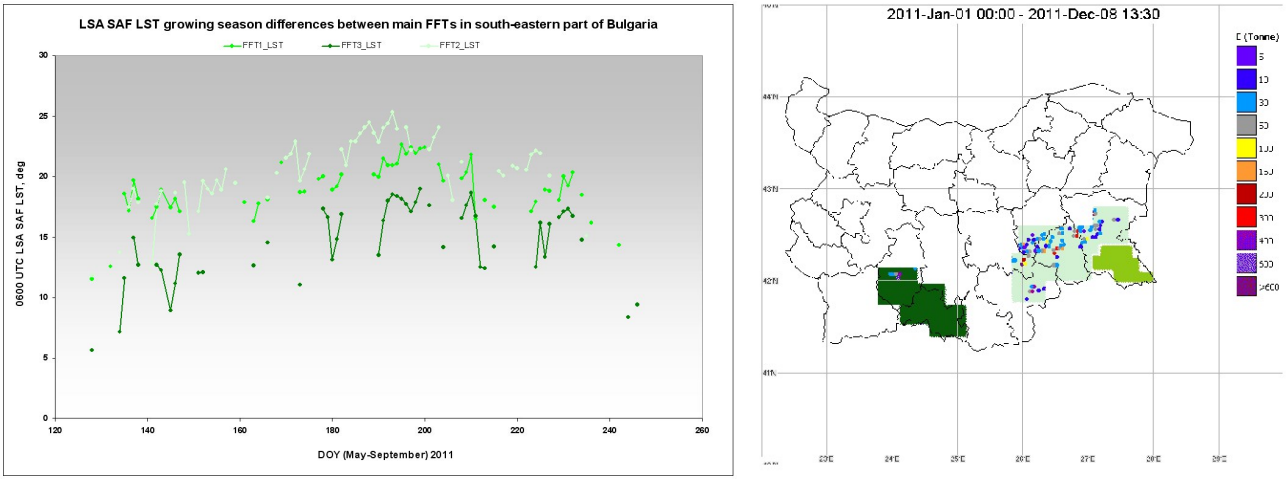


Fig. 3. Climate-fire relations at different native Forest Functional Types /FFTs/ in SE-S Bulgaria, May-September 2011. Left plot: The course of skin temperature 0600 UTC LSA SAF LST in stations representative for each FFT; Right plot: Carbon-eq. emitted by biomass burning MSG detections calculated on the bases of LSA SAF FRP product. FFT1 – bright green, FFT2 – light green, FFT3 – dark green.

Soil overmoistening and risk of flood

From operational perspective, besides the forecast of space-time structure of the rainfall, the initial soil water content is an important parameter within flash-flood predictions. Information about SM content from operational numerical weather prediction (NWP) models could be used for weather forecasting. However, in most operational atmospheric models the simulated prognostic variable "soil moisture" does not have an unambiguous meaning [13]. It is a strongly model-specific quantity with a dynamic range defined by the specific model formulation and the soil parameters such as porosity, hydraulic conductivity, wilting point, and layer depth, which are not known at the NWP model spatial and temporal scales.

Based on our knowledge about SMA after modelling of land-atmosphere interactions and accounting for local climate/soil for Bulgaria, a specialized index intended as a diagnostic tool for operational forecasting purposes of extreme weather events has been developed [3]. It is generated via visualized colour-coded maps indicating SMA in the region of each synoptic station (covering the main administrative regions of Bulgaria) in combination with a numerical part, which indicates the required flood-producing rainfall quantities (specific for each region and environmental conditions). In case of overmoistening conditions, the numerical part denotes the rainfall excess above the soil saturation moisture content. SMAI is generated for two land cover types: for wheatland cover it is updated daily and for grassland cover it is run twice per day. Actually the numerical part indicates the effective rainfall of any given region and time, which is considered as 100 per cent effective while computing the water balance at the specific water holding capacity of different soils. The utility of this approach in combination with NWP rainfall predictions was tested for diagnosis and prediction for two case studies of severe weather produced by deep convection and a rapid cyclogenesis developed at initial "dry"/"wet" soil moisture anomalies, respectively. In this study, this concept is further approved introducing an additional index for diagnosing pre-convective environment (paragraph 3.4.). Two other cases of flood-producing convective developments associated with different types of large-scale circulation patterns are considered below to illustrate the utility of the approach.

In the first case, deep convection developed over Bulgaria on 30 May 2014 in an environment of upper-level dynamic forcing through vorticity advection from north-east in strong blocking regime. The right plot of Fig. 4 (d) shows a satellite image in IR channel of MSG with cloud tops colder than -30°C colour enhanced. The process developed in the leading diffluent part of the upper level vorticity feature producing deep convective clouds with cloud top temperature less than -50°C (yellow). Thunderstorms with

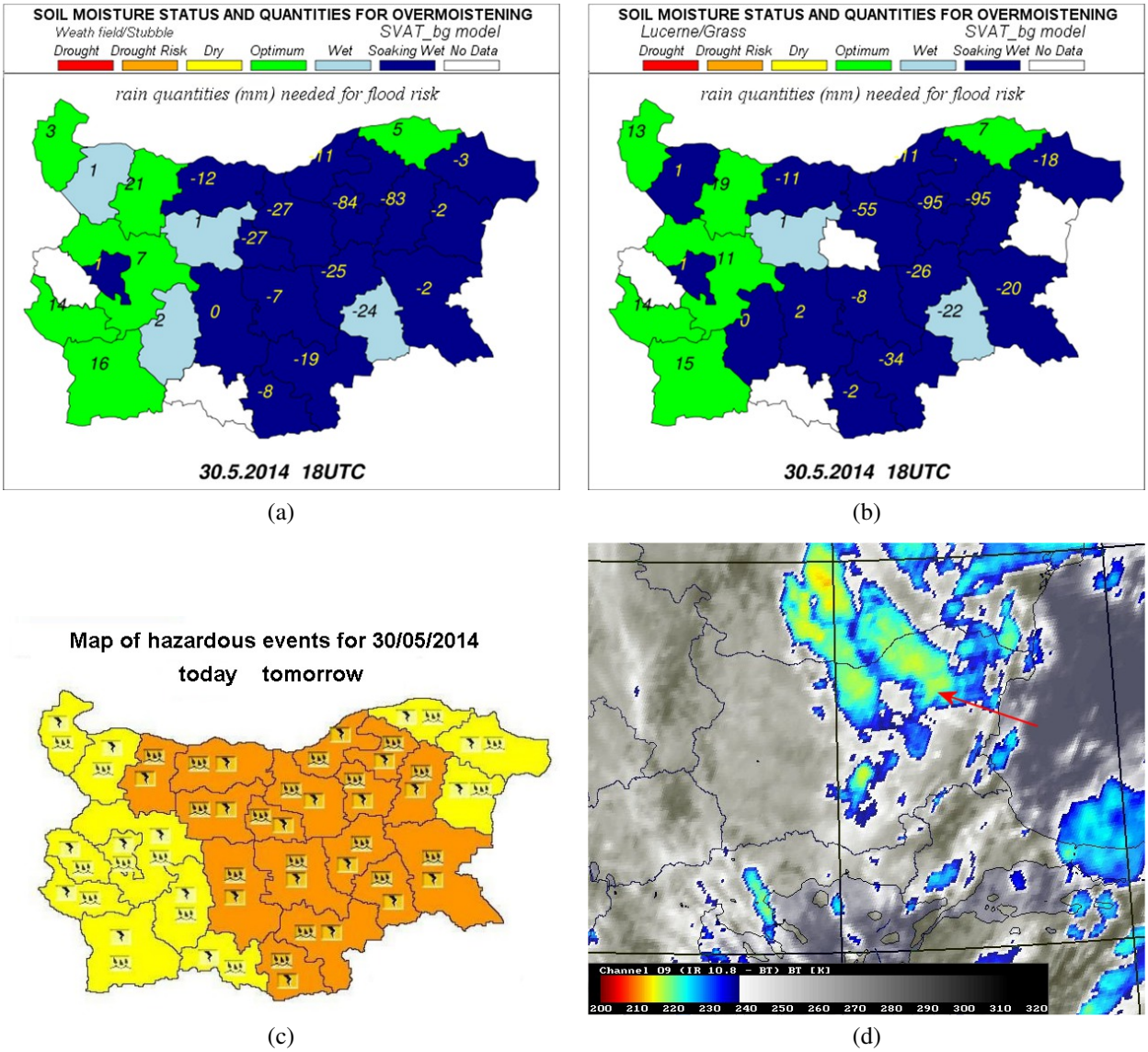
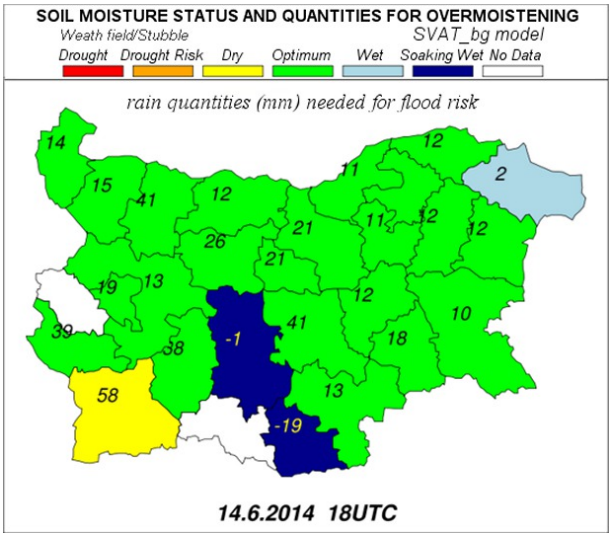


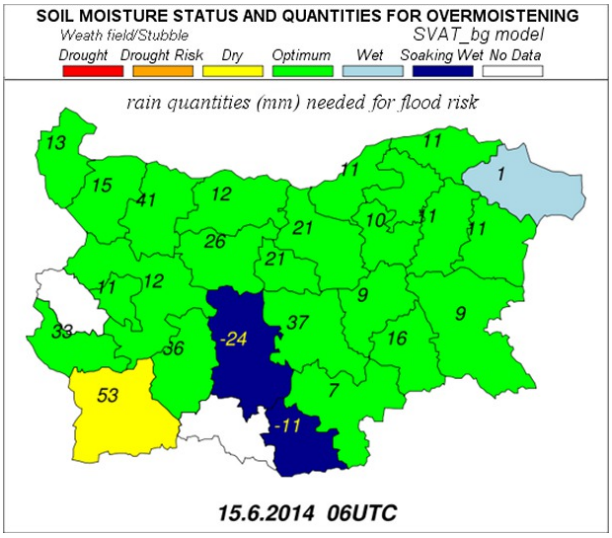
Fig. 4. Analyses of 30 May 2014 case: (a) Soil moistening at grass land cover according to SMAI, (b) Soil moistening at wheat field according to SMAI, (c) Weather severity warning according to Meteo Alarm forecast, (d) Colour enhanced IR image of MSG at 1330 UTC (cloud top temperature below -30°C coloured, $\leq$ -50°C yellow, $\leq$ -60°C red.

showers (40-60 l/m^2 precipitation) and hail were predicted for 11 administrative units of Bulgaria as well as for the other 17 regional units with expected rain up to 36 l/m^2). The corresponding operational Meteo Alarm product for Bulgaria with warnings for danger (orange) and potentially danger weather (yellow) is shown on Fig. 4(c).

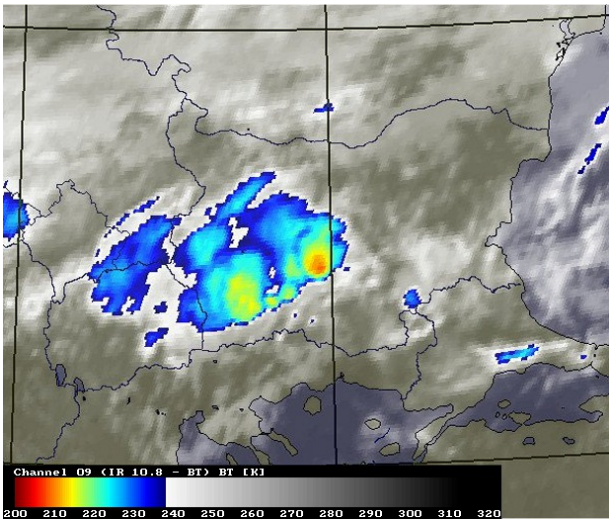
The analyses of soil moistening reveals an "optimal" soil moistening (green colour) over the most part of the country. More precise analyses for the Shumen region (north-eastern part of Bulgaria) a green colour with 0 mm effective rainfall below overmoistening conditions is observed on 28 May 2014 (here not illustrated). After two consecutive days with precipitations (17.8 mm on 29 May and 96.0 mm on 30 May 2014) soil moisture capacity is full and large negative flood-producing quantities are indicated (for grass land in Fig. 4(a) and wheat field in Fig. 4(b). Based on the NWP guidance and the SVAT model analysis of SMAI, the operational forecast issued at NIMH of Bulgaria indicate probability for heavy rain and floods on 30 May 2014 `http://radar.bg/bg/2014-05-30/article`.



(a)



(b)



(c)

Fig. 5. Analyses of night tine 14-15 June 2014 case: (a) 14 June 2014, 1800 UTC soil moistening at grass land cover according to SMAI, (b) 15 June 2014, 0600 UTC soil moistening at grass land cover according to SMAI, (c) Colour enhanced IR image of MSG, 14 June 2014 2115 UTC (cloud top temperature below -30°C coloured, $\leq$ -50°C yellow, $\leq$ -60°C red.

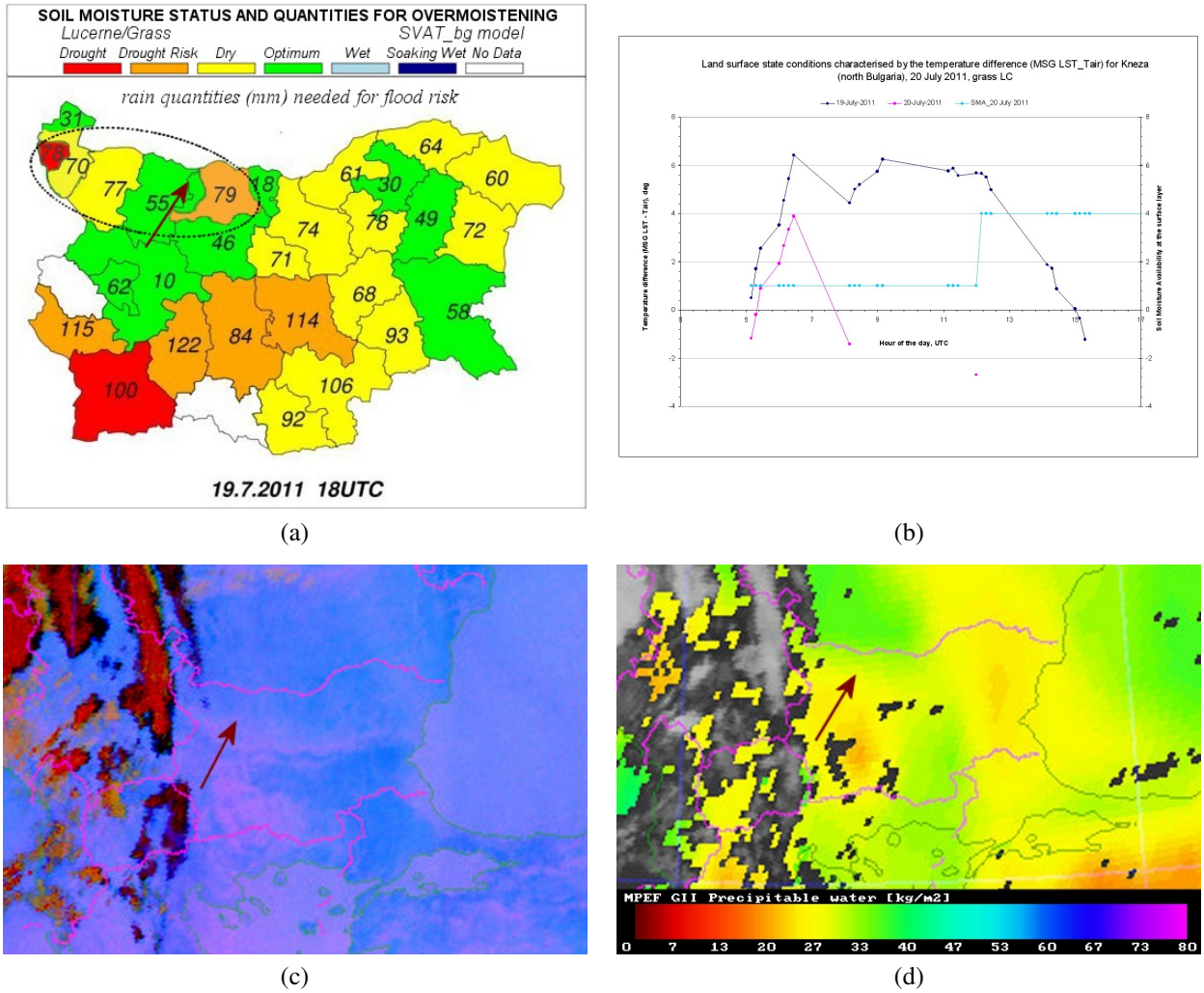
The second case-study is on a local convective development during the night time of 14-15 June 2014 that caused showers in town Plovdiv (south Bulgaria). This process is developed in a deformation zone of the upper-level flow. The colour enhanced IR image (Fig. 5 c) shows the existence of an overshooting top of the convective cloud system (red, less than – 60°C) that is indicative for severe weather.

Soil moistening analyses on 14 June 2014 at 0600 UTS shows "optimal" soil moistening (green colour with 4 mm effective rainfall below overmoistening conditions, here not illustrated). On 14 June at 18 UTC 6 mm precipitations are measured and this caused a slight overmoistening conditions according to SMAI map (Fig. 5(a), the left plot). After 24 mm additional rain quantities at 0600 UTC of 15 June are accounted, the midnight shower produced local overmoistening in Plovdiv and flooding (Fig. 5(b), the middle plot). However it was difficult to forecast such a local event `http://flip.bg/cluster/e7a4a0132ef30d318a64eea4d61c94dfskip=140`.

Convective storms: land surface effects

Soil moisture influences a number of processes in land-atmosphere interactions, some of which concern the initiation of convection, the influence on the surface temperature and the availability of moisture in the planetary boundary layer [14].

The convective storm on 20 July 2011, analysed in our preceding work [3] is here further studied using additional characteristics of land surface state and air moistening on the basis of MSG information. SMAI analysis shows that the pre-convection process developed at extremely dry low-level conditions. Soil moisture has been reduced to the wilting point (drought risk, orange/red colour) over the great part of northwestern Bulgaria (within the dashed ellipse zone) a day before the convection storm – the left plot of Fig. 6(a) also see [3] Fig. 4a. As an index of land surface pre-convective environment we introduce for application the radiative temperature on the land



(a) (b)

(c) (d)

Fig. 6. Surface moistening evolution in the area of convective storm development on 20 July 2011 derived by SVAT.bg output: (a) Colour-coded SMAI at grass land cover a day before, (b) daily course of temperature difference between MSG LST and air temperature during the storm (magenta) and a day before (dark blue) along with the SMA level (light blue). MSG satellite products showing air humidity: (c) RGB DUST at 0715 UTC (moist surface air in bluish, dry surface air in reddish) and (d) Total perceptible water at 0715 UTC. The area of convective storm development is indicated by arrows in (a), (c), (d).

surface (as an indicator of energy and water exchange on the land surface) derived through the LSA SAF LST product over Bulgaria. The difference between LST (digital values at MSG pixel resolution) and the air temperature measured at 2 m height from synoptic stations is applied as a diagnostic characterize of the near-surface state. Daily course of the temperature difference (LST-Tair) of cloud free pixels, approximating near-land surface moistening a day before the storm (Fig. 6(b), dark blue) is higher than this during the storm (magenta line). During the storm development (on the afternoon of 20 July 2011) the lowest cloud-free temperature difference of -2.68°C is detected at 1200 UTC, while for the same time slot a day before the temperature difference accounts to 5.69°C. During this "dry" case of convective storm showers (more than 40 mm for 30 min) were reported but in these dry soil conditions (seen in Fig. 6 (a)), floods were not able to occur. The severity of this case was due to damaging wind (maximum wind speed 24 m/s with gusts up to 42 m/s) and large hail (about 5 cm in diameter). 41 mm rain quantities measured at 1800 UTC on 20 July are reflected by the immediate increased SMA (Fig. 6(b), light blue).

As seen by the advanced satellite products the pre-storm environment are characterised by compar-

atively dry low-level air (more reddish in Dust RGB product on Fig. 6(c)) as well as comparatively lower values of TPW (yellow indication) on Fig. 6(d).

CONCLUSIONS

The investigation of land-atmosphere interactions is a growing interdisciplinary research field offering significant promises for climate research. This paper concentrates on some biophysical, hydrological and biogeochemical aspects of land surface processes on a regional/local scale for the environmental conditions of Bulgaria. Climate-weather extremes and severe meteorological phenomena are studied in relation to associated land surface state anomalies, their regional reveals and regimes. For that purpose, numerous numerical schemes integrating information from LS modelling, MSG observation, standard meteorological observations are introduced and applied.

— A SVAT model driven by standard meteorological observations was used to simulate the spatial variability and temporal evolution of soil moisture for the specific climate/soil environment over the country and used as a source for development meteorological products for assessing land surface states (including "dry", "wet" anomalies) in the operational environment of NIMH. Tuning these site-scale state variables with spatial-temporal MSG information for land and atmosphere moistening conditions, relation between soil moisture and features of deep convection development are analysed. The quality of these simulations are evaluated by real convective storms development;

— The proposed approach for quantification of biogeophysical cycling and its coupling with the biogeochemiocal cycle on a local and regional scale is of importance not only as a fundamental knowledge but has an operational and practical meaning for multifold biosphere and environmental applications: e.g. description and even prediction of economic looses due to agricultural drought effects on yield reduction; development of a regional bioclimatic classification for Bulgaria; assessing regimes of forest fires; defining the most fire-prone forest areas; quantification of possible climate change effects via biomass carbon-equivalent emissions. For each one of these climate-weather driven problems relevant research scheme has been developed and the results are illustrated by cases studies in the paper.

Results are encouraging as a basis for improving knowledge in further studies and operational applications on the bases of the proposed LSA concept in early detection, monitoring and climate services of the numerous climate-weather related meteorological processes and phenomena.

REFERENCES

[1] S. I. Seneviratne, D. Luthi, M. Litschi and C. Schär, *Nature* **443**, 205–209 (2006).

[2] J. S. Stoyanova, "Conceptual framework for land surface analyses over Bulgaria" in *Proceedings of the Second National Congress on Physical Sciences* (Sofia, Bulgaria, 25-29 September, 2013). DVD, ISBN 978-954-580-333-8, 2013.

[3] J. S. Stoyanova and C. G. Georgiev, *Atmospheric Research* **123**, 384–399 (2013).

[4] J. S. Stoyanova, "Bioclimatic concept for assessment of atmosphere and forest land cover coupling at a regional scale" in *Proceedings of 29th Int. Conf. Alpine Meteorol* (Chambéry, France, 4-8 June, 2007), Meteo-France, 2007, pp. 773-776.

[5] J. Shukla and Y. Mintz, *Science* **215**, 1498–1501 (1982).

[6] E. M. Fischer, S. I. Seneviratne, D. Luthi, and C. Schar, *Geophys. Res. Lett.* **34**, **L06707**, doi:10.1029/2006GL029068, (2007).

[7] S. D. Schubert, M. J. Suarez, P. J. Pegion, R. D. Koster and J. T. Bacmeister, *Journal of Climate* **17**, 485–503 (2004).

[8] G. T. Narisma, J. A. Foley, R. Licker and N. Ramankutty, *Geophysical Research Letters* **34** (2007).

[9] J. A. Dracup, K. Seong Lee and E. G. Paulson Jr., *Water Resources Research* **16**, 297–302 (1980).

[10] NDMC, `http://drought.unl.edu/whatis/concept.htmoperational` (2008).

[11] J. S. Stoyanova, C. G. Georgiev and, C. Barroso, "MSG land surface temperature product as a biogeophysical diagnostic parameter of terrestrial water status" in *Proceedings EUMETSAT Meteorological Satellite Conference* (Sopot, Poland, 7-10 September, 2012). ISSN 1011–3932, 2012.

[12] R. I. Florov, Study on applying irreversible thermodynamics in plant physiology and ecology, DrSci Thesis, Moskva, ANSSR (1978).

[13] R. D. Koster, Z. Guo, R. Yang, P. A. Dirmeyer, K. Mitchell, M. J. Puma, *Journal of Climate* **22**, 4322–4335 (2009).

[14] C. Hohenegger, P. Brockhaus, C.S. Bretherton, C. Schär, *Journal of Climate* **22**, 5003–5020 (2009).

АНОМАЛИИ В СЪСТОЯНИЕТО НА ЗЕМНАТА ПОВЪРХНОСТ И СВЪРЗАНИ С ТОВА ОПАСНИ МЕТЕОРОЛОГИЧНИ ЯВЛЕНИЯ

Ю. Стоянова[1], И. Замфиров[2]

[1] *Национален институт по метеорология и хидрология, Българска академия на науките, бул. "Цариградско шосе" №66, 1784 София, България*
Национален институт по метеорология и хидрология, Българска академия на науките, ул. "Хаджи Димитър" №60, 5800 Плевен, България

(Резюме)

Докладът представя съвременния опит на Националния Институт по Метеорология и Хидрология (НИМХ-БАН) при анализ на физичното състояние на земната повърхност (като част от климатичната система) формирано на основата на функционалната връзка между енергетичния и водния цикъл. Разглеждат се локални оценки на достъпните за конкретен тип растителна повърхност количества енергия и вода за територията на България и техния принос за формиране на "сухи" и "влажни" аномалии свързани с възникване на опасни метеорологични явления.

Първостепенна задача на работа е разглеждането на типични режими на време-климат, при които състоянието на системата почва-растителност е от значение за формирането на опасни метеорологични явления като: преовлажнение и риск от порои; селскостопанска суша; дефицит в почвеното овлажнение и риск от растителни пожари. За диагноза на състоянието на земната повърхност и негови аномалии се прилага интегрален подход за количествено описание на биогеофизичния цикъл като се отчитат специфичните почвени и климатични условия за страната. Подходът включва съвместно използване на локални метеорологични оценки на оснавата на разработен метеорологичен числен SVAT модел (за описание на енерго- и водо-обмен в системата почва-растителност-атмосфера), информация от метеорологичните геостационарни спътници (MSG) и наземи наблюдения от националната метеорологична мрежа. На тази основа са разработени биогеофизични индекси (индекс за оценка достъпно количество почвена влага; количествена оценка на ефективни валежи; индекс за пожароопасен риск и др.) както и спътникови продукти (за детекция на термични аномалии; радиационна температура на земната повърхност и др.). Продуктите са въведени за оперативно използване в прогностичната среда на НИМХ с цел издаване на предупреждения.

Значението на методологията за регионални оценки на риска от опасни явления свързани с екстремуми на време и климат се илюстрира чрез изследване на примерни реални синоптични ситуации отнасящи се за: засушаването през зимния период на 2014 г. и свързаната с това повишена пожароопасност; дъждовния период през април-май 2014 г. и свързано с това почвено преовлажнение и порои; топлинни вълни и дефицит на почвено овлажнение определящи агрометеорологичната суша през 2007 г.

Bulgarian Chemical Communications, Volume 47, Special Issue B (pp. 343–348) 2015

Harmonic analysis of tide gauge data 2013-2014 in Bulgaria

A. I. Ivanov*

National Institute of Geophysics, Geodesy and Geography, Bulgarian Academy of Sciences, Acad. Georgi Bonchev str., Bl. 3, 1113 Sofia, Bulgaria

In last few years a subject of many scientific researches is the variation mean sea level, which is sure indicator occurring climate change. At Bulgarian Black Sea coast is situated tide gauges in harbor area of cities Varna and Burgas. The measurements were started at 1928. The measured data may present as sum of mean sea level, tidal influence and storm surges. Computed trend from tide gauge data clearly indicates increase of MSL (1.4 mm/y. for Varna and 2.00 mm/y for Burgas).

The subject of research is analyzing of short term tidal components. The analysis determines order of influence of short term tides at mean monthly values of MSL. For purpose of research one year of radar gauges data is used.

New radar gauges are installed in 2013. For processing of data it was used method of harmonic analysis, based on theory that the data of research could be represented as sum of harmonic functions with a amplitudes and phases.

Key words: sea level, harmonic analysis, tidal constituents

INTRODUCTION

Main cause of variation of sea level is tidal and non-tidal influence. Non-tidal variation is caused by changing in atmospheric pressure, temperature, and influence of wind.

The variation of gravity field of Earth is caused by gravity forces of Moon and Sun is the main force for occurring tides. Tides are result of periodical influences acting at previously known frequencies and amplitudes.

These influences are known as tidal constituents. The period of observations from 365.25 days is enough for analyzing diurnal and semi-diurnal tidal constituents. It is required period of observations of several years to examine influence long period tidal constituents.

The radar gauges provide systematic base of observations independent of human support. This high quality data ensure opportunity to analyze importance of short-term variations and its contributions for calculating MSL.

Least-squares based harmonic analysis was used for solve tidal constituents. This method is based on theory that observed data series can be presented by sum of components whit previously known frequencies stable in time.

The purpose of research is to analyze tidal constituents and their influence to mean sea level variation. The least squares technique has many advantages over other methods: no restrictions of equally spaced continues data with no gaps, does not have to stick strictly to synodic periods for tidal constituents, easily compute variance between the data time series and the predicted time series.

USED DATA

Tide gauges at Bulgarian Black sea coast is situated in cities Burgas and Varna. The measurements started in 1928. At this site tide gauges is mechanical type - stilling well gauges "A.Ott" (Kempten).

It is necessary the maintenance of the system to be observed regularly by operator, who takes control measurements. In past decade new tide gauge systems had been improved which could operate independently. These are acoustic, pressure and radar gages [1].

The radar gauges emits microwave impulses by antenna of system, reflected signal is received back again by antenna. Time from emission to reception of signals is proportional to level of measured sea surface. The main advantages of radar gauges to other systems are easy maintenance, and independency of emitted signal from temperature and pressure change.

In 2013 new radar gauges VegaPuls s60 were installed above high water level in draw well of tide gauges in Varna (lat./long. – 43.1926^{o}/27.9114^{o}) and Burgas (lat./long. – 42.4887^{o}/27.4795^{o}). Observations of sea surface are registered in every 15 seconds at these sites.

For the purpose of this research hourly data for period 01.05.2013-01.05.2014 for station Varna and 27.05.2013-27.05.2014 for station Burgas was analyzed.

* To whom all correspondence should be sent:
anton_iv66@abv.bg

© 2015 Bulgarian Academy of Sciences, Union of Chemists in Bulgaria

For station Varna 8072 from 8760 hourly values, for station Burgas registered data is 7260 from 8760 hourly values.

SEPARATION OF TIDAL CONSTITUENTS

The frequencies of tidal constituent is related to astronomical parameters of celestial bodies which have major influence at gravity field of Earth- the Sun and the Moon. Important periods are: mean solar day (24.00 hours), mean lunar day (24.84 hours), period of tropical month 27days, tropical year-365.25days, period of lunar perigee 8.847 years, period of lunar node 18.61 years.

Tidal constituents are divided into groups according their frequencies to: astronomical half daily, astronomical daily and long period. Most important of them are written in Table 1.

Table 1. Important tidal constituents

Tides	**Period** (days)	**Frequency** (^{o}/hours)	**Origin**
Astronomical half daily			
K_2	0.499	30.0821^o	Sun/Moon
R_2	0.499	30.0411^o	Sun
S_2	0.500	30.0000^o	Sun
T_2	0.501	29.9589^o	Sun
L_2	0.508	29.5378^o	Moon
M_2	0.518	28.9841^o	Moon
N_2	0.527	28.4397^o	Moon
Astronomical daily			
K_1	0.997	15.0411^o	Sun / Moon
P_1	1.000	14.9589^o	Sun
M_1	1.035	14.4967^o	Moon
O_1	1.076	13.9430^o	Moon
Q_1	1.120	13.3987^o	Moon
Long period			
M_F	13.66	0.0027^o	Moon
M_M	27.55	0.0055^o	Moon
S_{SA}	182.70	0.0363^o	Sun
S_A	364.96	0.0732^o	Sun

The harmonic analysis presents observed data as sum of harmonic functions sine and cosines at previously known frequencies with amplitude and phase. The selection of tidal constituents included in the model, was based to length of time series and quality of data.

According to [3] for period of one year of observations its necessary to use 60 to 100 tidal constituents, for 19 years of observations, analysis would include 300 constituents. The frequencies of some tidal constituents are very close.

The separation of tidal constituent was made according to synodic period. The minimum period of time required to separate two nearby tidal constituents is synodic period. It is defined as interval between two consecutive conjunctions of phase of two constituents. For the analysis is important to separate not only two tidal constituent, but correctly separate many pairs of constituents with different synodic period. We should use the longest synodic period.

According to [4] separation of two tidal constituent we need for diurnal: O1 from M1 (27.55 days), P1 from M1 (32.5 days); P1 from K1 (182.6 days); K1 from S1 and K1 from P1 (365.25 days); for semidiurnal K2 from S2 (182.6 days), T2 from S2 (365.25 days).

The period of observations from 365 days sufficient for performing least squares harmonic analysis and to separate key constituents. It is necessary to use data from several years of observations to solve Sa and semiannual -Ssa constituent.

To define the influence of nodal tide should be analyzed data of 19 years observations. Data was corrected for nodal tide. For harmonic analysis with error estimates has been used MatLab program T_Tide.m [2].

Used function of harmonic analysis is

$$x(t) = b_0 + b_1 t + \sum_{k=1\ldots M} A_k \cos(\sigma_k t) + B_k \sin(\sigma_k t) \quad (1)$$

Here $x(t)$ is hourly sea level for time moment t, b_0 is mean sea level at epoch of measurement b_1 is annual mean sea level trend, σ_k – frequency of tidal constituent, A_k, B_k – components of tidal constituents amplitude. M – number of tide constituents used in model

$$H_t = \sqrt{A_k^2 + B_k^2} \quad (2)$$

$$g_t = \arctan\frac{B_k}{A_k} \quad (3)$$

(2) is amplitude of tidal constituent, (3) is phase of tidal constituent.

The significant constituents have been separated with respect to Signal to Noise Ratio (SNR). Tidal constituents with SNR greater than 2 are significant. SNR is set as a proportional of signal power to noise power. According to [2] SNR greater than 2 is significant and should been used for calculating predicted value.

RESULTS

The analysis determinates that significant tidal constituents are some diurnal O1, P1, K1, PHI1, THE1, semi diurnal N2, M2, S2, K2, third diurnal MK3, M3 and quarter diurnal – SK4. Major influence has constituents K1 and M2 with amplitudes of 1.8 cm and 1.9 cm.

The significant tidal constituents solved from harmonic analysis from tide gauge Varna are presented in Table 2.

Table 2. Significant parameters solved from harmonic analysis for station Varna – frequencies of tidal constituents, amplitudes, phases, estimated errors and SNR values

Tide Varna	freq	Amp (cm)	amp_err (cm)	Phase (^{o})	Phase_err	SNR
O1	0.0387307	0.81	0.3	52.15	23.25	8.1
P1	0.0415526	0.97	0.3	67.46	16.69	12
K1	0.0417807	1.84	0.3	63.37	9.7	42
PHI1	0.0420089	0.59	0.3	333.87	27.91	4.3
THE1	0.0430905	0.41	0.3	351.76	42.88	2.1
N2	0.0789992	0.4	0.1	5.41	20.43	7.4
M2	0.0805114	1.9	0.1	9.69	4.27	170
MKS2	0.0807396	0.7	0.1	314.72	14.57	23
S2	0.0833333	1.02	0.1	10.65	8.23	49
K2	0.0835615	0.53	0.1	335.58	19.65	13
M3	0.1207671	0.05	0.01	330.03	30.12	3.3
MK3	0.1222921	0.05	0.01	117.1	38.94	2.5
SK4	0.1668948	0.04	0.01	252.26	45.55	2.5
3MK7	0.2833149	0.03	0.01	239.98	39.77	2.1

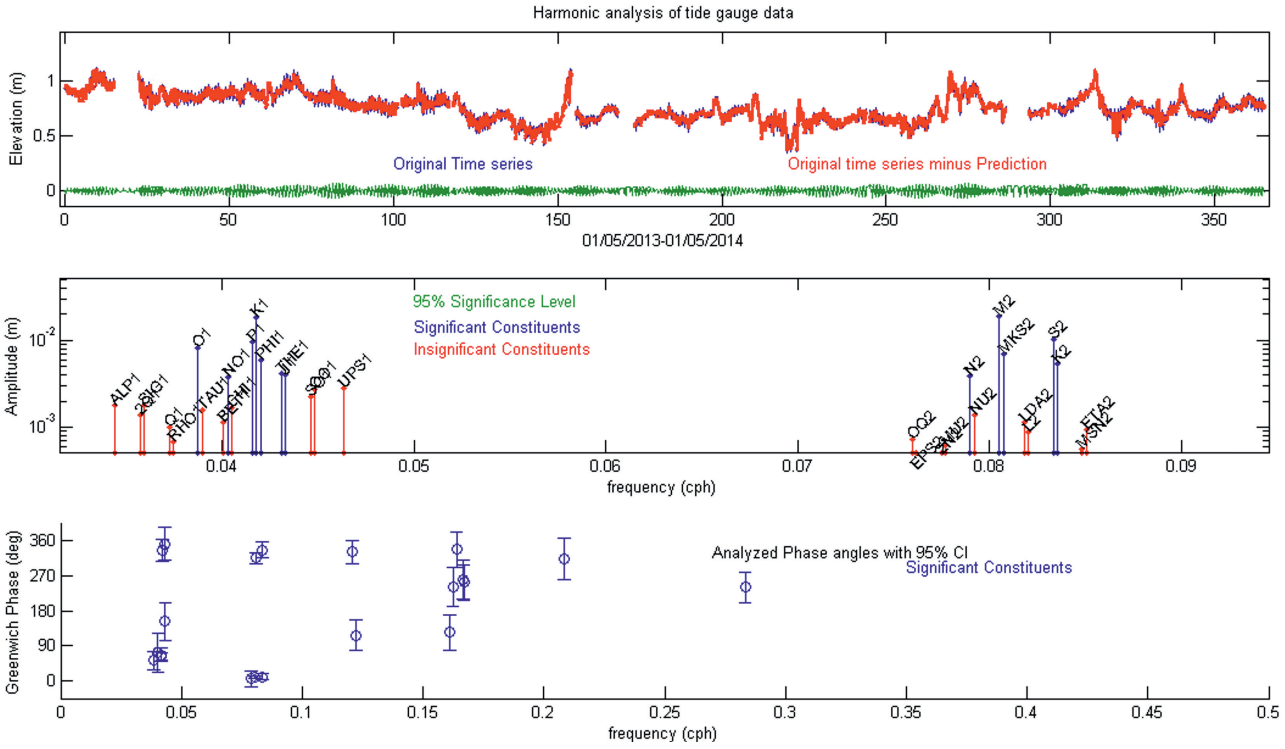


Fig. 1. Station Varna: (a) – whit blue line is shown observed data, green line – prediction according to significant constituents, red line – residual series - prediction; (b) – amplitudes of significant constituents(SNR>2) – blue line; red line – insignificant amplitudes (c) – phases whit error of significant tidal constituents to Greenwich meridian.

Table 3. Significant parameters solved from harmonic analysis for station Burgas – frequencies of tidal constituents, amplitudes, phases, estimated errors and SNR values

Tide Burgas	freq	amp (cm)	amp_err (cm)	Phase (^{o})	Phase_err (^{o})	SNR
ALP1	0.034397	0.24	0.2	184.8	48.24	2.1
Q1	0.037219	0.25	0.2	67.64	45.83	2.2
O1	0.038731	0.82	0.2	65.47	13.73	24
BET1	0.04004	0.33	0.2	166.19	35.34	3.8
NO1	0.040269	0.3	0.2	123.16	36.7	3.1
P1	0.041553	0.72	0.2	89.63	13.35	18
K1	0.041781	1.56	0.2	77.17	6.82	85
PHI1	0.042009	0.56	0.2	17.24	17.65	11
OO1	0.044831	0.25	0.2	53.32	73.78	2.1
N2	0.078999	0.4	0.1	20.24	16.35	11
M2	0.080511	2.13	0.1	27.76	3.07	330
MKS2	0.08074	0.75	0.1	8.75	10.97	41
S2	0.083333	1.08	0.1	29.87	6.24	85
K2	0.083562	0.69	0.1	11.34	12.3	34
M3	0.120767	0.06	0.01	0.76	23.44	5.5
SO3	0.122064	0.06	0.01	115.75	28.75	5.4
MK4	0.164073	0.05	0.01	318.16	33.11	4.4
2SK5	0.208447	0.08	0.01	19.52	24.49	6.6

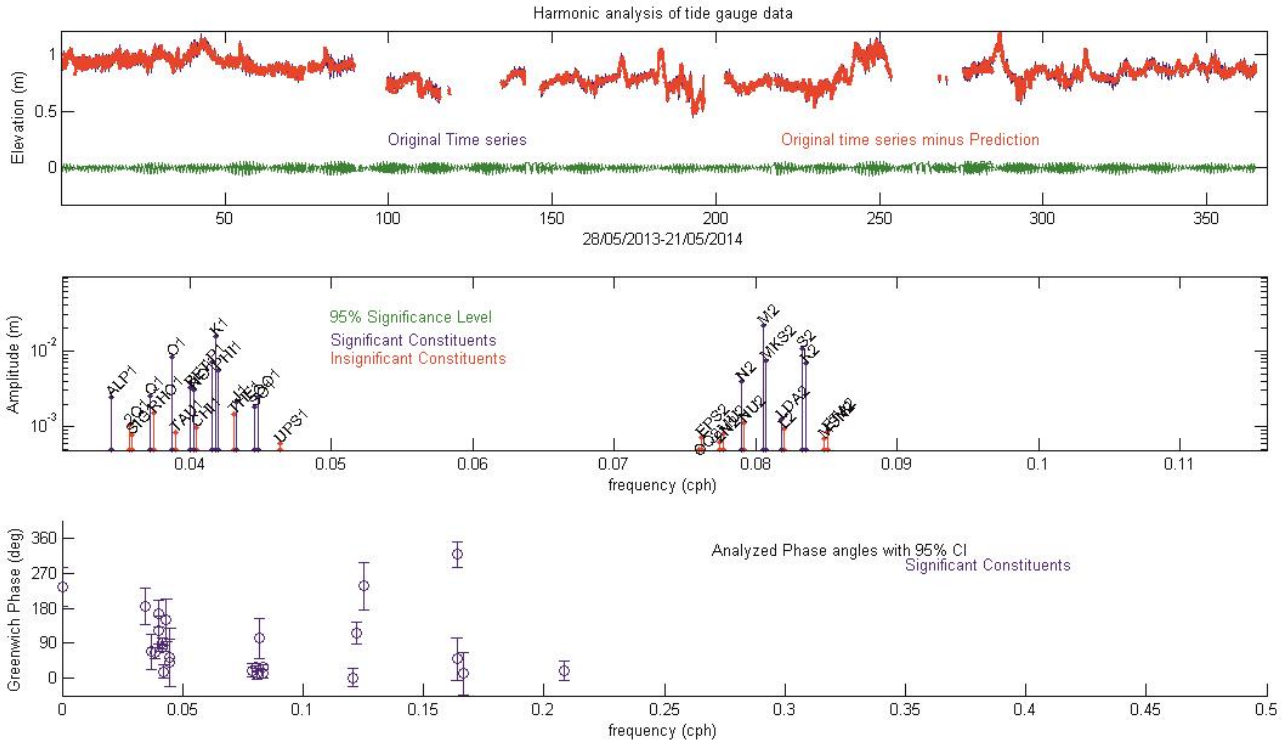


Fig. 2. Station Burgas: a – with blue line is shown observed data, green line – prediction according to significant constituents, red line – residual series – prediction; b – amplitudes of significant constituents(SNR>2) – blue line; red line – insignificant amplitudes; c – phases whit error of significant tidal constituents to Greenwich meridian.

Table 4. Calculated amplitudes for tidal constituents: a) from this research b) from [5]

	VARNA Amplitudes (cm)			BURGAS Amplitudes (cm)	
Tidal constituent	**a)**	**b)**	**Tidal constituent**	**a)**	**b)**
O1	0.81	0.7	O1	0.82	0.9
P1	0.97	0.6	P1	0.72	0.8
K1	1.84	1.8	K1	1.56	2.3
PHI1	0.59	—	PHI1	0.56	—
THE1	0.41	—	OO1	0.25	—
N2	0.4	0.4	N2	0.4	0.4
M2	1.9	2.2	M2	2.13	2.4
MKS2	0.7	—	MKS2	0.75	—
S2	1.02	1.2	S2	1.08	1.4
K2	0.53	0.3	K2	0.69	0.4
M3	0.05	—	M3	0.06	—
MK3	0.05	—	SO3	0.06	—
SK4	0.04	—	MK4	0.05	—
3MK7	0.03	—	2SK5	0.08	—

Calculated significant tidal constituents for station Burgas are presented in Table 3. From data we can establish diurnal Q1, O1, P1,K1, PHI1 semidiurnal N2, M2, S2, K2, MKS2 third diurnal – M3, SO3, quarter diurnal – MK4 tidal constituents.

CONCLUSION

The harmonic analysis determinates significant short term tidal constituents at tide gauge station Varna and Burgas. In Table 4 were compared the amplitudes calculated from analysis and amplitudes determinate in [5], they are in a good agreement. Because of longer period of investigation in this research more constituents were estimated. To fill data gaps we should use overall impact of short and long term tidal constituents.

The long period tidal constituent wasn't calculated because of the insufficient data period. The analysis of several years of observations will improve calculated results, and allow opportunity to compare annual changes in tides, and mean sea level.

REFERENCES

[1] *Manual on Sea-level Measurements and Interpretation*, Volume IV: An update to 2006. Paris, Intergovernmental Oceanographic Commission of UNESCO. p. 78.

[2] R. Pawlowicz, B. Beardsley and S. Lentz, *Computers and Geosciences* **28**, 929–937 (2002).

[3] D. Pugh, *Tides, surges and mean sea level*, John Wiley and son, 1987.

[4] P. Schuerman, *Manual of harmonic analysis and prediction of tides*, Washington, United states government printing office (1958), p. 338.

[5] B. Rogev, *Fluctuations in the levels at Burgas and Varna*, Proceedings of CLG, BAS, Book II, S. 163–224p, 1959.

ХАРМОНИЧЕН АНАЛИЗ НА МАРЕОГРАФНИ ДАННИ 2013–2014 г.

А. Иванов

Департамент Геодезия към Националния институт по геофизика, геодезия и география, Българска академия на науките, ул. "Акад. Г. Бончев" № 3, София 1113, България

(Резюме)

През последните години обект на много научни изследвания е глобалното изменение на морското ниво, което е сигурен индикатор за настъпващите климатични промени.

На българското черноморско крайбрежие са разположени мареографни станции в пристанищата на градовете Варна и Бургас. Регистрациите започват от 1928 г. Регистрираните данни могат да се разглеждат като сума от средната стойност на морското ниво, приливни влияния и щормови влияния.

Получените от обработка на мареографни измервания резултати показват положителен тренд на изменението на средното морско ниво на Черно море (1.4 mm/y за Варна, 2.00 mm/y за Бургас), който е съпоставим със средните стойности в глобален мащаб.

Обект на изследванията са късопериодичните приливни компоненти. Проведеният анализ установява степента на влиянието им върху изчислените средно месечни стойности на морското ниво.

Използвани са данни от аналоговите мареографни апарати, както и от новите радарни мареографи, инсталирани през 2013 г. За целта се използва период на наблюдения от една година от радарните мареографи.

За обработването на данните е използван метода на хармоничния анализ, основаващ се на тезата, че регистрираните стойности на морското ниво могат да се представят като определен брой хармонични функции, амплитуда и фазова честота

Bulgarian Chemical Communications, Volume 47, Special Issue B (pp. 349–354) 2015

Calculation of oxygen concentration in the Black Sea using data from Argo automatic profiling floats

N. Nikolov*, A. L. Pandelova

Technical University of Sofia, 8 Kliment Ohridski Blvd., Sofia, Bulgaria

In the last years in connection with climate change on Earth more relevant and discussed is the question of the characteristics of the World Ocean. Measurements there are labor-intensive and expensive, so there is no comprehensive information, especially in the deep layers. Therefore a number of programs to monitor of ocean are recently funded. The purpose of the Argo program is to investigate the sea water to a depth of 2000 m using automatic profiling floats equipped with sensors for temperature, salinity, depth and others. The data is distributed freely on the Internet. Examination of the oxygen content is very important for studying marine ecosystems, especially in the Black Sea, which is one of the largest oxygen-free pool in planet.

The purpose of this study is to calculate the concentration of dissolved oxygen in seawater by using data from Argo float for pressure, temperature, salinity and attenuation of blue light. The oxygen content is very difficult to determine in a laboratory or in conditions of sea expedition, so the more common way is to calculate it from the above-mentioned parameters.

The raw data from Argo float 6900804 for 25 profiles in 2011 are downloaded and interpolated on standard horizons. By an algorithm, provided by the manufacturer of the optical sensor Aandera Optode 3830, the concentration of dissolved oxygen (micromoles) in the programming environment MATLAB is calculated.

Key words: oxygen concentration, Argo floats, Aandera Optode, Black Sea

INTRODUCTION

In the last years in connection with climate change on Earth more relevant and discussed is the question of the characteristics of the World Ocean. Measurements there are labor-intensive and expensive, so there is no comprehensive information, especially in the deep layers. The satellite observations are one of the best for data collection, but the disadvantage is that they do not provide information about the deeper layers of the ocean. Therefore a number of programs to monitor ocean are recently funded. Cheap and efficient method to collect profiles continuous information over the whole water column is Argo program. It aims is to study the ocean to 2000 m depth using automatic profiling floats which are equipped with sensors for temperature, salinity, depth, dissolved oxygen, etc.. Examination of oxygen content is very important in the study of marine ecosystems, particularly in the Black Sea, which is one of the largest oxygen-free pools on the planet.

The Argo floats were introduced in 2000 and in November 2007 a 100 percent of initially scheduled network is full. Now days Argo network has 3560 floats, but in order to maintain this level should be produced and placed in service in 800 probes per year [1].

Argo data for the Black Sea are needed because the data collection so far is related to the organization of costly expeditions in different territorial waters. The aim is to establish a new national maritime infrastructure for observations in the Black Sea, which is based on autonomous profiling floats. The main priority of Bulargo program is monitoring the status of the Black Sea from the surface to deep stagnant layers. The Black Sea region is extremely important because of their specific sensitivity to climatic and anthropogenic influences, therefore is so important monitoring in depth of the sea basin. There are a large number of coastal meteorological and oceanographic observations, but the observations at sea are still insufficient. This deficiency can be compensated by the observations from floating buoys, which will measure the concentration of dissolved oxygen, physical processes and optical characteristics of seawater.

STRUCTURE OF AUTOMATIC MEASURING FLOATS ARGO

The measuring float is designed to collect high quality profiles of temperature and salinity from the upper 2000 m of the ice-free part of the global ocean and the currents from intermediate depths. They operate from battery power and spend most of their time of life, floating on the depths in which they are stable. With the aid of the hydraulic device buoyancy equal to the surrounding environment is achieved. This al-

* To whom all correspondence should be sent:
niki.nikolow87@gmail.co

© 2015 Bulgarian Academy of Sciences, Union of Chemists in Bulgaria

lows the passage of a float on isobaric surface. Isobaric surface can be changed, which leads to floating or sinking of the float. The most commonly used profiling floats are three types. They work in a similar way, differing in the characteristics of their design. The floats pumped fluid in the outer bladder, and come to the surface for about 6 hours at a given interval, which is programmed in advance. During this time the floats measure salinity, temperature and other characteristics, if they are equipped with appropriate sensors. Through satellite communication the position of the probe is determined after its ascent to the surface and the data transmission is performed. Then the bladder was emptied, the float returns to its normal buoyancy and sinking into the parking depth, where it navigate until the cycle is repeated. The floats are designed to make about 150 such cycles, after that their batteries are exhausted. The construction of the Argo float includes four main parts (Fig. 1)

- Hydraulics: it controls the buoyancy of the probe by an external inflatable rubber bladder so that the probe can emerge and dive
- Microprocessors: to control the functions and interval of data collection;
- System for data transfer: control the link with the satellite;
- Power system: 7.2 V and 14.4 V, lithium or alkaline batteries

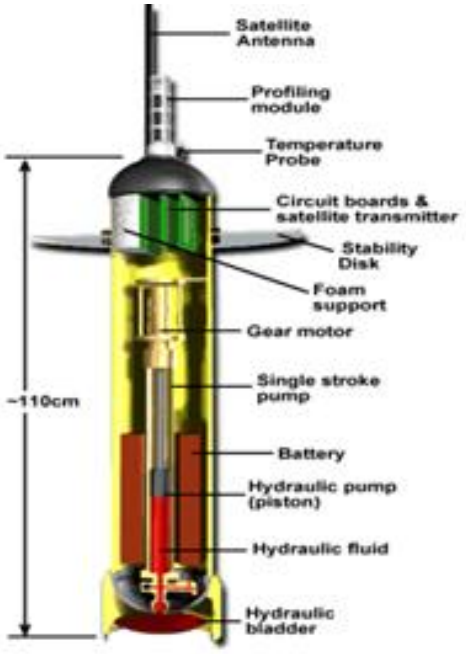


Fig. 1. Construction of Argo float.

The lifetime of the float is about 3 years, but the data quality is not always good. Often there are missing data, there are also errors arising from unrealistic measured values for pressure, temperature and salinity [2].

MODE OF OPERATION OF OXYGEN SENSOR AANDERA OPTODE 3830

The principle of operation of the optical sensor for oxygen determination is based on the phenomenon of dynamic fluorescent quenching and the ability of certain molecules, such as oxygen, to appear as a fluorescent quenchers [3, 4].

Optical part of the oxygen electrode includes the following elements: sensing foil, indicator layer, support layer, optical window, blue LED, red LED and photodiode (see Fig. 2). The sensing foil is exposed into the water. The indicator layer is a platinum porphyrine complex. There are a two LED diodes and a photo diode placed on the inner part of the optical window. The blue light (505 nm) from the blue LED is used for excitation of the sensing folio. The sensing foil will return the red light thanks to its fluorescent properties. In the presence of oxygen the fluorescent will be quenched. Therefore, the concentration of dissolved oxygen depends on the change in the intensity of the reflected light.

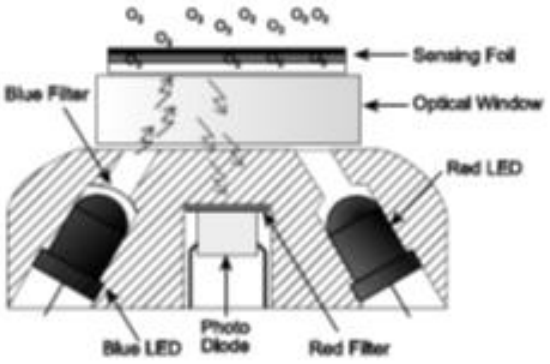


Fig. 2. Optical part of the oxygen sensor, source [5]

EXPERIMENTAL PART

To calculate of the oxygen concentration an algorithm represented by the manufacturer of the sensor Aanderaa Optode 3830 is used. The phase difference (DPhase) is calculated as a polynomial of third degree of the difference between the measured phase with excitation with blue light and excitation with red

light [5]. The oxygen concentration is calculated in micromols (microM):

$$[O_2] = C_0 + C_1 P + C_2 P^2 + C_3 P^3 + C_4 P^4 \quad (1)$$

where P is calibrated phase of measurement (DPhase), $C_0, \ldots, C_4$ are dependent temperature coefficients which is calculated using the formula:

$$C_X = C_{x0} + C_{x1} t + C_{x2} t^2 + C_{x3} t^3 \quad (2)$$

$C_{x0}, \ldots, C_{x3}$ – constants, provided by the manufacturer of the sensor, t – ambient temperature. Uncalibrated phase (UPhase) is the difference between the phase obtained with blue light (BPhase) and phase obtained with red light (RPhase):

$$\text{UPhase} = \text{BPhase} - \text{RPhase} \quad (3)$$

Typically RPhase is not used and it is taken equal to zero (RPhase = 0). Here you have to calculate also DPhase, necessary for calculating the oxygen in the form:

$$C_x = A_0 + A_1 \text{UPhase} + A_2 \text{UPhase}^2 + A_3 \text{UPhase}^3 \quad (4)$$

$A_0, \ldots, A_3$ – constants, provided by the manufacturer of the sensor.

For the calculation of the oxygen concentration in the Black Sea data obtained from autonomous profiling float APEX 6900804 are used. This float is used to monitor sea currents, to measure profiles of temperature, salinity, depth, and dissolved oxygen. For the purposes of the study the data for 25 profiles from 2011 for temperature, depth and Bphasedoxy are downloaded in its original from [6] and interpolated of standard horizons.

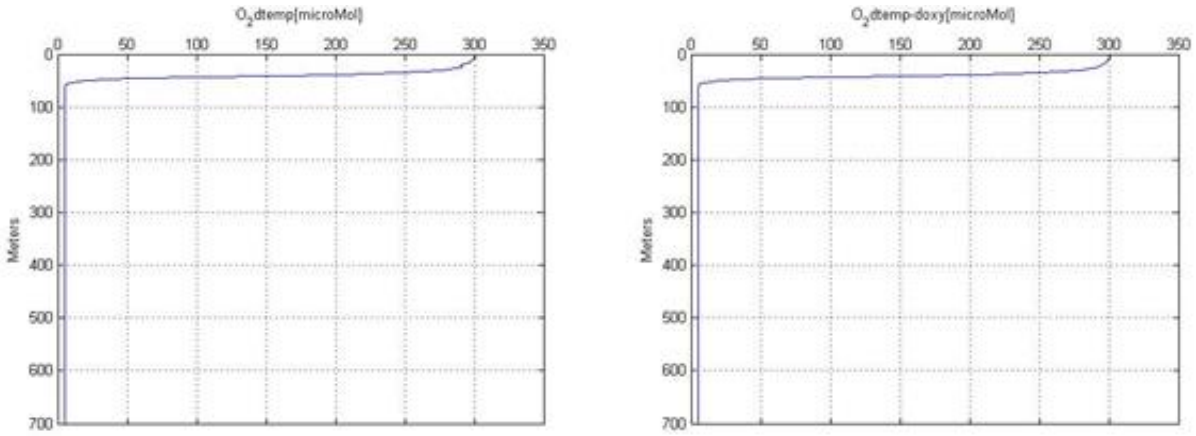


Fig. 3. Oxygen profiles for 20.04.2011; a) with temperature data from T-sensor of the float; b) with temperature data from thermistor in DO-sensor of the float.

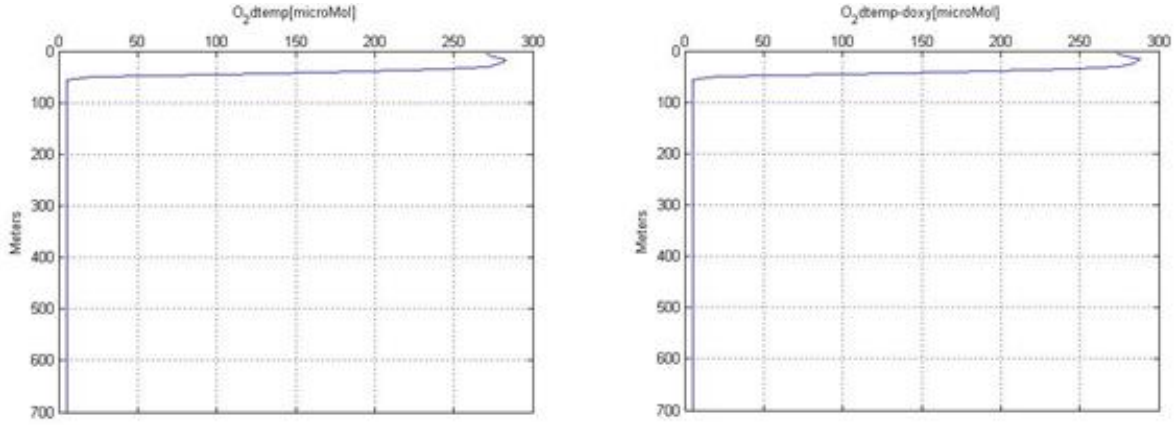


Fig. 4. Oxygen profiles for 23.05.2011; a) with temperature data from T-sensor of the float and b) with temperature data from thermistor in DO-sensor of the float.

By suggestions from the manufacturer of oxygen sensor Aandera Optode 3830 algorithm the concentration of dissolved oxygen is calculated in the programming environment MATLAB. As turned out that APEX 6900804 has two temperature sensors - T-sensor for profiling temperature and built-in thermistor in the oxygen sensor, oxygen concentration is calculated twice. First, using the temperature data from T - sensor of APEX float and the data for BPhasedoxy from the oxygen sensor (O2dtemp), in the second calculation of the oxygen temperature data obtained from the thermistor in the oxygen sensor (O2dtempdoxy) is used. In Fig. 3, Fig. 4, Fig. 5, and Fig. 6, the resulting profiles for oxygen content are shows. Data for four randomly selected profiles are shown: 20.04.2011, 23.05.2011, 07.07.2011, 11.08.2011. The obtained values for the oxygen in both temperature sensors are almost identical, but there is a slight difference. This difference is more pronounced in the profiles of 07.07.2011 and 11.08.2011.

A comparison between the values obtained for the concentration of dissolved oxygen at two temperatures is made. In graphical form are shown the results obtained for the difference in the concentration of dissolved oxygen in the temperature of the T-sensor and a thermistor (delta DO = O2dtemp-O2dtempdoxy) depending from the depth (see Fig. 7). It was found that a large difference in concentration of dissolved oxygen was observed in the profiles for 07.07.2011 and 11.08.2011.

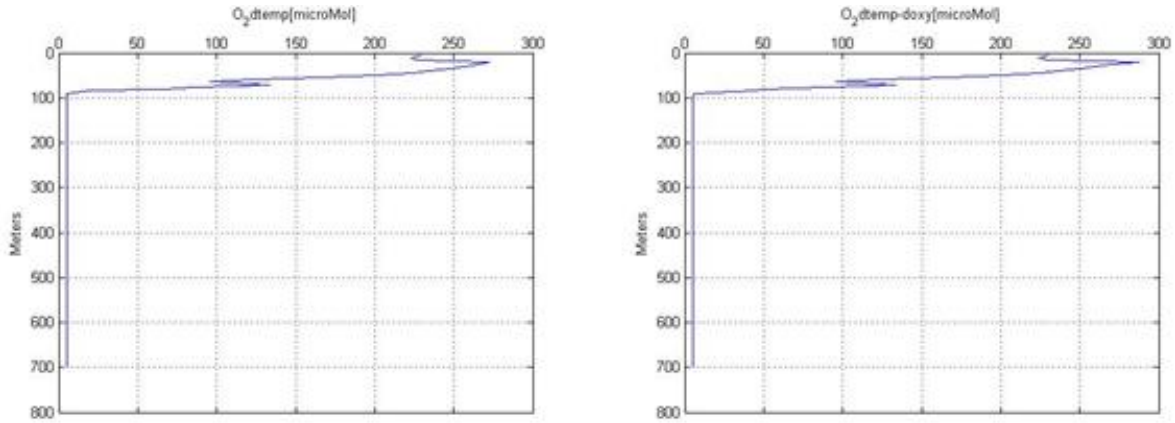


Fig. 5. Oxygen profiles for 07.07.2011; a) with temperature data from T-sensor of the float and b) with temperature data from thermistor in DO-sensor of the float.

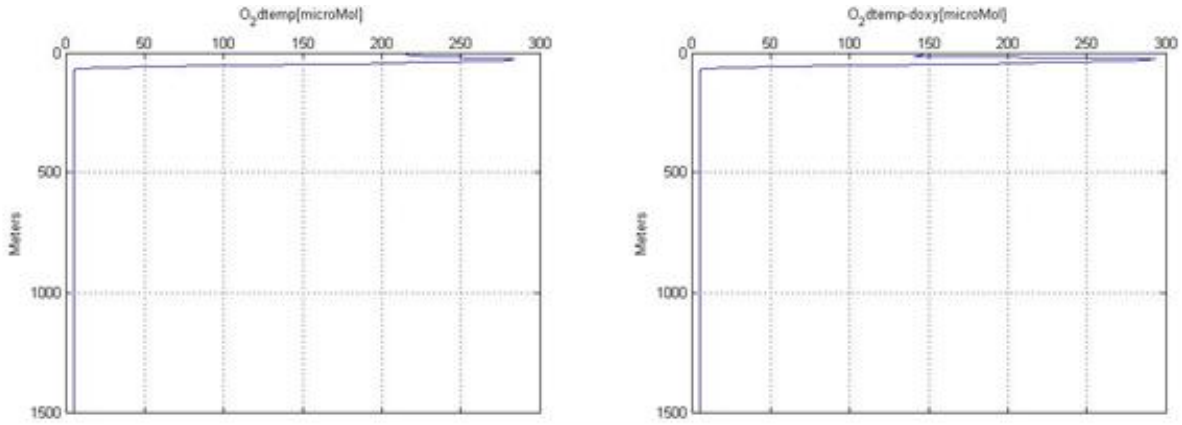


Fig. 6. Oxygen profiles for 11.08.2011; a) with temperature data from T-sensor of the float and b) with temperature data from thermistor in DO-sensor of the float.

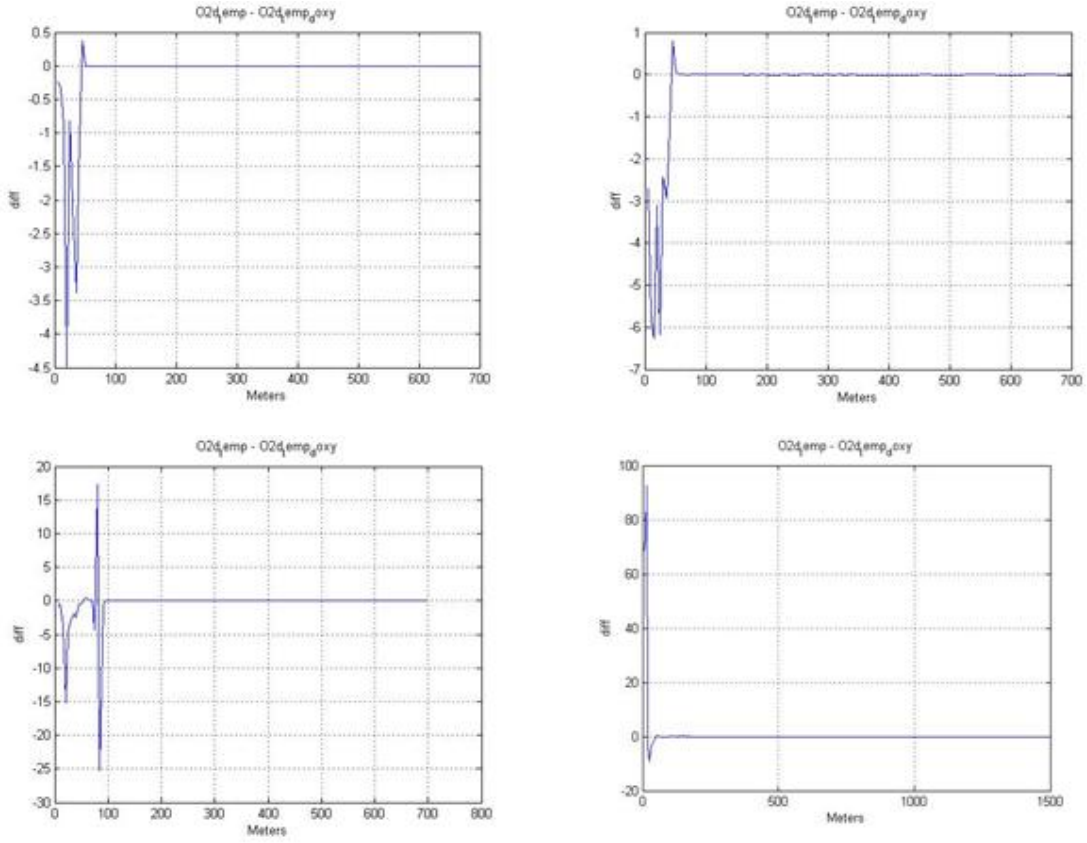


Fig. 7. Difference in concentration of DO at both temperatures for different dates a) 20.04.2011 b) 23.05.2011 c) 07.07.2011 d) 11.08.2011.

CONCLUSIONS

For the first time in the programming environment MATLAB algorithm to calculate the concentration of dissolved oxygen in seawater was developed. The data for pressure, temperature, salinity and decay of blue light from Argo APEX float 6900804 Black Sea are used. As it turned out that the float has a temperature data from two temperature sensor dissolved oxygen concentration is calculated twice. The difference in oxygen content using temperature data from T-sensor of float and built-in thermistor in DO-sensor of float is shown. It was found that the concentration of dissolved oxygen depends on the temperature and depth. The different seasons also affect of the oxygen content. After the hundredth meter there is no difference in the reading of the two temperature sensors and there is no difference in the oxygen concentration.

Acknowledgements.*The authors express their gratitude to the scientific Research Sector at Technical University-Sofia for the financial support under contract N 141PD0016-08.*

REFERENCES

[1] D. Roemmich, W. B. Owens, *Oceanography*, **13(2)**, 45-50 (2000)

[2] E. Peneva, E. Stanev, At. Palzov, G. Rachev, V. Slabakova, M. Milanova, A. Gencheva, Proceedings from the 10th international conference on marine sciences and technologies: Black Sea, Varna Bulgaria, 2010, pp. 1314-0957 (2010)

[3] A. Tengberg, J. Hovdenes, D. Barranger, O. Brocandel, R. Diaz, J. Sarkkula, *Sea tehnol.* **44**, 10-15 (2003)

[4] A. Tengberg, J. Hovdenes, O. Brocandel, R. Diaz, D. Hebert, *Limnol. Oceanogr. Methods*, **4**, 7-17 (2006)

[5] Oxygen optode Guide `http://serf.clarkson.edu/Support/InstrumentSupport/TD218_Oxygen_Optode_3830_3930_Aug03.pdf`

[6] `http://www.ifremer.fr/co-argoFloats/`

ИЗЧИСЛЯВАНЕ НА КОНЦЕНТРАЦИЯТА НА КИСЛОРОД В ЧЕРНО МОРЕ ПО ДАННИ ОТ АРГО АВТОМАТИЧНИ ПРОФИЛИРАЩИ СОНДИ

Н. Николов, А. Панделова

Технически университет София, бул. "Климент Охридски", 8, София, България

(Резюме)

В последните години във връзка с климатичните промени на Земята все по-актуален и обсъждан е въпросът за характеристиките на Световния океан. Измерванията там са трудоемки и скъпоструващи, поради което липсва изчерпателна информация, особено в дълбоките слоеве. Ето защо напоследък се финансират редица програми за мониторинг на океана. Програмата Арго цели изследване на соленоводните маси в океана до 2000 м дълбочина посредством автоматични профилиращи сонди, които имат сензори за температура, соленост, разтворен кислород и др. Данни се разпространяват свободно в интернет. Изследването на съдържанието на кислород е изключително важно при изучаване на морската екосистема, особено в Черно море, което е един от най-големите безкислородни басейни на планетата.

Настоящето изследване цели да разработи и автоматизира алгоритъм за изчисление на концентрацията на разтворен кислород в морската вода, използвайки данните за налягане, температура, соленост и затихване на синята светлина на една Арго сонда в Черно море. Съдържанието на кислород е много трудно да се определи в лаборатория или при условия на морска експедиция, затова по-разпространения начин е да се изчисли от посочените по-горе параметри.

Данните от Арго сонда 6900804 за 25 профила през 2012 година са изтеглени в суров вид и са интерполирани на стандартни хоризонти. Чрез алгоритъм, предоставен от производителя на оптичния сензор Aandera Optode 3830 се изчислява концентрацията на разтворен кислород (микромол) в програмната среда MATLAB. При този алгоритъм се използва температурата на околната среда, но сондата има два температурни сензора. Сравнени са концентрациите на кислород, получени чрез двете температури и е направен извод за грешките в зависимост от дълбочината, които могат да се очакват.

Bulgarian Chemical Communications, Volume 47, Special Issue B (pp. 355–363) 2015

Hyperspectral remote sensing applications for early stress detection of young plants

D. Krezhova[1]*, S. Maneva[2], I. Moskova[3], K. Krezhov[4]

[1] *Space Research and Technology Institute, Bulgarian Academy of Sciences, Acad G. Bonchev Str., Bl. 1, 1113 Sofia, Bulgaria*
[2] *Institute of Soil Science, Agrotechnology and Plant Protection, Bulgarian Academy of Agriculture, 3B Panayot Volov Str., 2230 Kostinbrod, Bulgaria*
[3] *Institute of Plant Physiology and Genetics, Bulgarian Academy of Sciences, Acad. G. Bonchev Street, Bl. 21, 1113 Sofia, Bulgaria*
[4] *Institute for Nuclear Research and Nuclear Energy, Bulgarian Academy of Sciences, 72 Tsarigradsko Chaussee Blvd., 1784 Sofia, Bulgaria*

Remote sensing technologies have advanced significantly at last decades and have improved the capability to gather information about Earth's resources and environment. They have many applications in Earth observation, such as mapping and updating land-use and cover, deforestation, vegetation and water dynamics and quality, etc. In this study, the physical principles and some applications of two hyperspectral remote sensing techniques, reflectance and fluorescence, are briefly discussed with a view to achieve an early diagnosis of stress in young deciduous trees (Paulownia tomentosa) in response to adverse environmental conditions (abiotic stresses). Leaf reflectance and fluorescence data were collected in the visible and near infrared spectral ranges (350–1000 nm) using a portable fiber-optics spectrometer. Statistical analyses and spectral normalization procedures were used to account the changes in the spectral features of the trees in response of adverse conditions. Spectral analyses were performed at ten narrow bands in green, red, red edge and near-infrared spectral ranges. Fluorescence spectra were investigated at five characteristic wavelengths in a spectral region 600–850 nm. Spectral data analyses were compared with the results from the accompanying biochemical tests for the assessment of damage to the trees.

Key words: Hyperspectral remote sensing, reflectance, fluorescence, Earth observation, abiotic and biotic stresses

INTRODUCTION

Earth observation from space and ground through various remote sensing technologies and instruments has provided vantage means of monitoring land surface dynamics, natural resources management, and the overall state of the environment itself [1-4]. Remote sensing is basically a multi-disciplinary science including various disciplines such as optics, spectroscopy, photography, electronics and telecommunication, etc. Remote sensing is broadly defined as a technique of obtaining information about properties of an object without coming into physical contact with that object. A more specific definition of remote sensing relates to studying the environment from a distance [5]. Remote sensing involves the use of ground-, aircraft-, or satellite based sensors to gather information by measuring the electromagnetic radiation (EMR) that is reflected, transmitted and absorbed by the objects in various spectral regions, from gamma-rays to radio waves. After interaction of the EMR with the surface of terrestrial materials a number of changes are acquired in its magnitude, direction, wavelength, polarization and phase [6,7]. These changes are detected by the remote sensors and enable to obtain useful information about the objects.

Different types of sensors including aerial photographs, airborne multi-spectral scanners, satellite imagery, low and high spatial and spectral resolution and ground based spectrometers and fluorometers collect electromagnetic information. In last decades, the used sensors and techniques have improved significantly the capability to gather information about Earth's resources and environment [8]. Future sensors will continue the progress toward more comprehensive and more accurate measurements. Further improvements in the spatial, spectral, radiometric, and temporal characteristics of the measurements are expected.

One of the recent applications of hyperspectral remote sensing is monitoring and preservation of plant ecosystems. The distribution of vegetation, its properties and state, is of major importance for a wide range of applications, such as environmental management, natural hazards monitoring, agriculture and forestry, climate change studies, numerical weather forecast models [9–11]. The spectral features of the plants

* To whom all correspondence should be sent:
dkrezhova@stil.bas.bg

© 2015 Bulgarian Academy of Sciences, Union of Chemists in Bulgaria

may be investigated by measuring reflected (spectral reflectance) and emitted radiation (chlorophyll fluorescence) directly from the plant surface and identifying unique spectral features that change in response to changes in environment [12]. Understanding the physical and biological responses of plants to environmental stresses, governing leaf reflectance, transmission, and absorption at the leaf level represents the first step to identifying unique spectral responses for extension to the canopy and regional scales [13]. Recent research has demonstrated the advances and merit of hyperspectral data in a range of applications including quantifying agricultural crops, modeling forest canopy biochemical properties, detecting crop stress and disease, mapping leaf chlorophyll content as it influences crop production, etc. [14–16].

With the progress of the hyperspectral remote sensing technology, more detailed data are potentially available. Therefore, extracting of meaningful relationships from the vast quantity of data is necessary. Currently, a variety of techniques have been implemented including a number of different vegetation indices, band absorption analysis, spectral mixture analysis, "red edge" position, statistical analysis, wavelet transform and neural networks [17–19]. Common problems in the area of hyperspectral analyses concerning data relevancy include optimal selections of wavelength, number of bands, and spatial and spectral resolution. Hyperspectral narrow-band spectral data are fast emerging as practical solutions in modeling and mapping vegetation. The goal is to develop some special algorithms and models for hyperspectral data processing, information extraction, classification and identification. In the field of vegetation study some successful progresses are already achieved by using derivative spectral analysis model for background noise elimination, radiative transfer models, "red edge" determination or biochemical parameter detection [20–22]. The need for significant improvements in quantifying, modeling, and mapping plant chemical, physical, and water properties is more critical than ever before to reduce uncertainties in our understanding of the Earth and to better sustain it.

In this study, the physical principles of two hyperspectral remote sensing techniques, reflectance and fluorescence, are briefly considered and their applicability with a view to achieve an early diagnosis of stress in young deciduous trees (Paulownia tomentosa) caused by adverse environmental conditions (enhanced content of hydrogen peroxide, treatment with herbicide 2,4-D and their combination) is discussed. The remote sensing findings were validated through accompanying biochemical tests broadly implemented in plant science practice.

REMOTE SENSING TECHNIQUES

Spectral reflectance

When electromagnetic radiation reaches an object three different interactions may occur. From the incident light on a surface, there may be a fraction which is transmitted, another which is absorbed, and a third fraction that is reflected. This portion of reflected radiation is the reason why we can actually see the objects. Moreover, the colour of the object results from the combination of wavelengths of the reflected portion of light from the object [23]. The proportions of reflected, absorbed, and transmitted fractions of the EMR vary for different terrestrial objects (rocks, minerals, soil, vegetation, water, etc.), depending on their material type and condition [24]. Thus, the objects can be differentiated in the remotely sensed images by the reflected EMR at varying wavelengths in ultraviolet (UV), visible (VIS, 400–700 nm), near infrared (NIR, 700–1200 nm), and short wave infrared (SWIR, 1200–2500 nm) spectral ranges, known as spectral signature. The property that is used to quantify the spectral signatures is called spectral reflectance $R(\lambda)$, a function of wavelength (λ), defined by the ratio:

$$R(\lambda) = [E_R(\lambda)/E_I(\lambda)] \times 100$$

where: $E_R(\lambda)$ – energy of wavelength λ reflected from the object, $E_I(\lambda)$ – energy of wavelength λ incident upon the object. $R(\lambda)$ is expressed as a percentage.

The plot between $R(\lambda)$ and λ, called spectral reflectance curve (SRC), of three different classes of natural objects (conifers, water and soil) are shown in Fig. 1 [25]. Soil, water and vegetation have clearly different patterns of reflectance and absorption over different wavelengths.

Green vegetation species all have unique spectral features which evolve with the plant life cycle. Spectral reflectance is influenced by leaf surface features, internal architecture and biochemical composition (pigments, water, nitrogen, etc.) [26,27]. The configuration of the spectral reflectance curves is important in the determination of the wavelength regions in which remote sensing data is acquired as the SRC give insight into the spectral characteristics

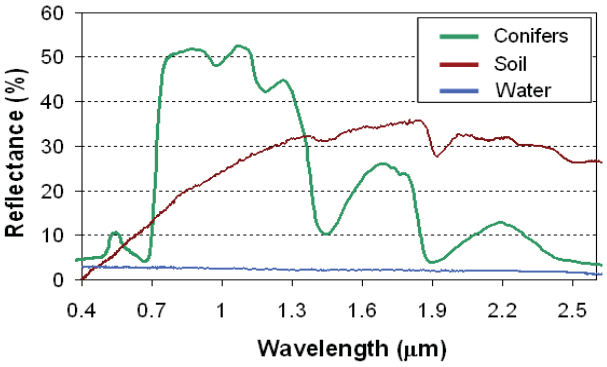


Fig. 1. Spectral reflectance curves of three different natural objects.

of an object [22]. Spectral reflectance of green vegetation has several characteristic features. The values of $R(\lambda)$ in the VIS portion of the EMR (0.4–0.68 μm) are low (Fig. 1) and are dictated by the pigments in plant leaves, mainly by strongly chlorophyll (Chl) absorption for photosynthesis. The other feature is the dramatic increase in the reflectance for healthy vegetation in the spectral region 0.68–0.72 μm (red edge position). In the NIR range (0.72–0.85 μm) the values of the reflectance are highest and the magnitude depends on leaf development and cell structure. Because this structure is highly variable between plant species, reflectance measurements in this range often permit us to discriminate between species, even if they look the same in VIS wavelengths [22]. In the SWIR range (0.95–2.5 μm) strong absorption bands around 1.45, 1.95 and 2.50 μm appear and the reflectance is mainly determined by the leaf tissue and water content.

If a plant is subject to some form of stress that interrupts its normal growth and productivity, it may decrease or cease chlorophyll production. The result is less chlorophyll absorption in the blue and red spectral bands (centered at about 0.45 μm and 0.65 μm, respectively) [28]. Often the red reflectance increases to the point that we see the plant turn yellow. Shifts in the red edge position can be a sensitive indicator of plant stress by degree of reduced absorption owing to falling levels of chlorophyll and a decrease in the NIR reflectance due to changes in plant cell structure [29].

Chlorophyll fluorescence

Chlorophyll fluorescence (ChlF) allows studying the different functional levels of photosynthesis indirectly (e.g. process at pigment level, primary light reaction, electron transport reaction, slow regulatory process) and can be used to study components of the photosynthetic apparatus and their reactions to changes in the environment [30,31]. Together with other spectroscopic and biochemical methods, recording of ChlF helps elucidate many important mechanisms of photosynthesis and nowadays ChlF is widely used as a nondestructive diagnostic tool in photosynthesis research [32]. Chl is the primary pigment of the plants that absorbs light energy from the sun for photosynthesis. Excess energy can be dissipated as heat or re-emitted as light at longer wavelength, i.e. chlorophyll fluorescence, Fig. 2. The increase in efficiency of one of these three processes (absorption, fluorescence and thermal emission) will result in a decrease in yield of the other two. As such, the relative intensities of ChlF are strongly related to the efficiency of photochemistry and heat dissipation [33] and may provide additional data to detect plant stress in an early stage [29]. Generally, fluorescence yield is highest when photochemistry and heat dissipation are lowest.

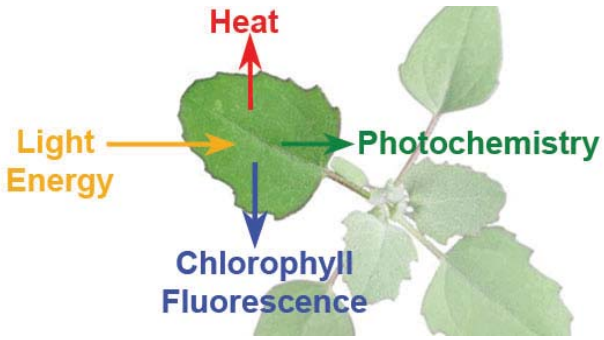


Fig. 2. Plant chlorophyll fluorescence technology.

Although the total amount of ChlF is very small (only 2 or 3% of total light absorbed), measurement is quite easy. The spectrum of fluorescence is different to that of absorbed light with the peek of fluorescence emission being at longer wavelength than that of absorption. At room temperature, Chl is emitting fluorescence in the red and NIR spectral ranges between 650–800 nm, in two broad bands with peaks at $\lambda_{max\,1}$ (684–695 nm) and $\lambda_{max\,2}$ (730–740 nm) [34].

It is well known that plant photosynthesis is a sensitive indicator of environmental perturbations such as excessive ozone, pollutants, cold or heat stress, salinity, deficiency of light and nutrients or water. Currently, vegetation stress is poorly described in numerical models. Changes in Chl function take place before changes in Chl content, before any physical

signs of tissue or chlorophyll deterioration are manifested in the plant, and therefore alterations in the fluorescence signal occur before any visible signs are apparent [35,36]. Under conditions of stress, some plant mechanisms for disposing of excess energy do not work efficiently, thus causing changes in the competing reactions of photochemistry, heat loss and fluorescence.

PLANT MATERIAL

Leaf reflectance and chlorophyll fluorescence techniques were applied for investigation of the responses of paulownia trees to stress factors – applying the herbicide 2,4-D (2,4-Dichlorophenoxy acid) and H_2O_2 (hydrogen peroxide) and their combination. Paulownia is ideal tree species for afforestation and improvement and restoration of contaminated and poor soils. Paulownia grows in contaminated with heavy metals and harmful substances soils where other trees would not survive. Consuming these substances, it released them from the soil. Our investigations were conducted with three months old paulownia seedlings (fully developed 5th leaf) grown as soil cultures in a growth chamber under controlled conditions (12 h light/12 h dark photoperiod, photon flux density 90 μmol m^{-2} sec^{-1}, humidity 60–70%, and temperature 25 ± 1^oC). The trees were divided into four groups. The first group included healthy, untreated (control) trees. The trees from the second group were sprayed with 2.0 mM H_2O_2. After 24 h the third group trees were sprayed with 1 mM 2,4-D. The forth group trees were treated with both H_2O_2 and 2,4-D. Spectral measurements were conducted after three days on leaf samples without visual symptoms.

DATA ACQUISITION AND ANALYSESS

Spectral measurements

Hyperspectral reflectance data were collected in the VIS and NIR spectral ranges by using a portable fibre-optics spectrometer USB2000 (Ocean Optics) [37]. In the range investigated (450–850 nm) the main part of the reflected from leaves radiation is concentrated. Data were analyzed at 1170 spectral bands with a step of 0.3 nm and a spectral resolution of 1.5 nm. The spectral reflectance characteristics (SRC) were obtained as a ratio of the intensity of leaf reflected light to the light reflected from a diffuse reflectance standard for each wavelength in VIS and NIR ranges. As a light source a halogen lamp providing homogeneous illumination of measured leaf surfaces was used.

The spectral measurements of the chlorophyll fluorescence were carried out under laboratory conditions using the same portable fibre-optics spectrometer (USB2000). Data were investigated in the VIS and NIR spectral ranges (600–900 nm) at 910 spectral bands with a step of 0.3 nm where the main part of the emitted from the plants fluorescence radiation is concentrated. As a source of actinic light, a LED diode with light output maximum at 470 nm was used. The tested leaves were dark adapted before the measurements for ten minutes.

Data processing

The Student's t-test was applied for determination of the statistical significance of differences between the means of sets of the values of the reflectance spectra of healthy (control) and subjected to adverse environmental conditions paulownia trees. Hierarchical cluster analysis (tree graph) was performed on reflectance data to examine and visualize how the groups of data are merged. The clustering method uses the dissimilarities or distances between objects when forming the clusters.

The spectral reflectance analyses were performed in four most informative for investigated plants spectral ranges: green (520–580 nm, maximal reflection of green vegetation), red (640–680 nm, maximal chlorophyll absorption), red edge (680–720 nm, maximal slope of the reflectance spectra) and the NIR (720–770 nm). The statistical significance of the differences between SR of control and treated trees was examined in ten wavelengths ($\lambda_1 = 475.22$ nm, $\lambda_2 = 489.37$ nm, $\lambda_3 = 524.29$ nm, $\lambda_4 = 539.65$ nm, $\lambda_5 = 552.82$ nm, $\lambda_6 = 667.33$ nm, $\lambda_7 = 703.56$ nm, $\lambda_8 = 719.31$ nm, $\lambda_9 = 724.31$ nm, and $\lambda_{10} = 758.39$ nm) chosen to be disposed uniformly over these ranges. The fluorescence spectra were analyzed in five characteristic spectral bands, chosen at specific wavelengths: the middle of the forefront edge, first maximum, the middle between first and second maximum), second maximum, and the middle of the rear slope.

RESULTS AND DISCUSSION

The averaged SRC (over 24 measured leaves) of control and treated with H_2O_2 and 2,4-D and their combination trees are shown in Fig. 3. It is seen that

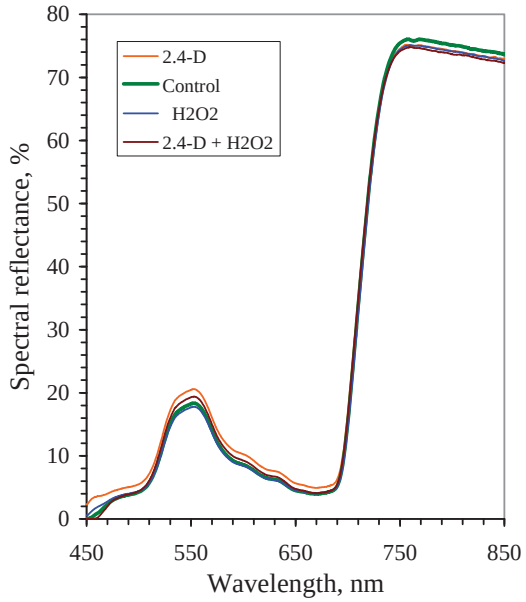


Fig. 3. Averaged spectral reflectance characteristics of paulownia trees treated with H_2O_2 and 2,4-D and their combination.

the values of the SRC of the group treated with 2,4-D differed most significant against the control. SRC of the group treated with H_2O_2 is closed to the control. In the case of combined treatment SRC values approached to the control.

The Student's t-test was applied for determination of the statistically significance of differences between the means of sets of the values of the SRC of control and treated paulownia trees. The results are set in Table 1. In the case of treatment with H_2O_2 the differences are not statistically significant ($p > 0.05$) against the control SRC at eight of the ten investigated wavelengths which indicates that these curves

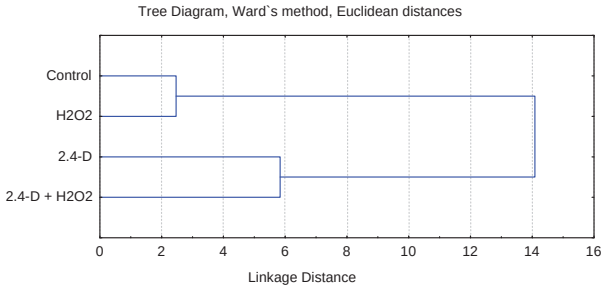


Fig. 4. A hierarchical tree diagram of data sets of paulownia trees under adverse environmental conditions.

are very closly lying each to other. For the treatment with herbicide 2,4-D the number of not statistically significant differences (ns) decreased to three in the wavelengths in NIR spectral range which means that this SRC differs signifficantly from the control SRC. For combined treatment not statistically significant difference was assessed at six wavelengths – SRC is more close to the control than in the case of herbicide treatment only.

Hydrogen peroxide in used concentration has a protective effect and almost no effect or beneficial effect on the treated plants. Therefore, differences of SRC were not statistically significant against the control. The herbicide 2,4-D applied in field concentration does not act quickly. Initially it stimulates growth. Plants grow rapidly and lose their power as the membranes are damaged. This is manifested in the increase of the values of SRC in VIS range and statistically significant differences. In combined treatment, H_2O_2 inhibits the action of the herbicide and changes against the control SRC decreased.

Hierarchical cluster analysis (tree graph) was applied to the SRC of four group of trees in the

Table 1. p-Values of the Student's t-criterion for pairs of the control and treated paulownia leaves

Pairs compared	Control	P<	2,4-D	P<	H_2O_2	P<	2,4-D + H_2O_2
λ_1/λ_{1c}	2.98	***	4.35	*	3.42	ns	2.79
λ_2/λ_{2c}	3.73	***	4.96	*	4.09	ns	3.76
λ_3/λ_{3c}	12.12	***	14.06	ns	12.03	***	12.93
λ_4/λ_{4c}	17.16	***	19.31	ns	17.03	***	18.12
λ_5/λ_{5c}	18.15	***	20.30	ns	17.98	***	19.14
λ_6/λ_{6c}	3.92	***	4.92	ns	4.16	ns	4.01
λ_7/λ_{7c}	21.20	**	22.85	ns	20.63	**	23.57
λ_8/λ_{8c}	50.06	ns	51.05	ns	50.01	ns	50.85
λ_9/λ_{9c}	57.77	ns	58.41	ns	57.93	ns	58.14
$\lambda_{10}/\lambda_{10c}$	75.20	ns	74.72	ns	75.86	ns	74.16

ns – no significance between obtained differences (p > 0.05); * – p < 0.05; ** – p < 0.01; *** – p < 0.001

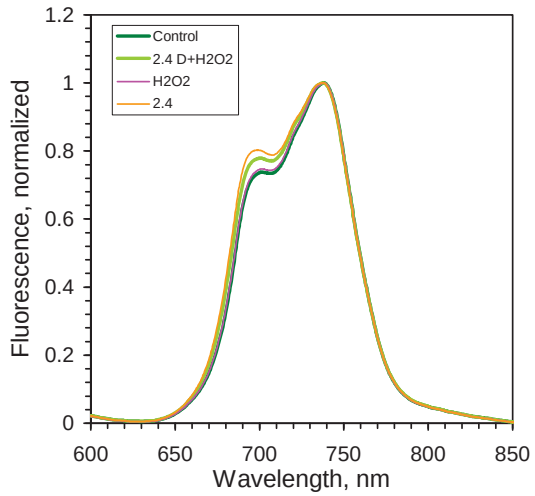


Fig. 5. Averaged fluorescence spectra of paulownia leaves treated with H_2O_2, 2,4-D and their combination.

spectral range 520–580 nm, Fig. 4. Two completely separate clusters were received. The first one includes the spectral data of control and H_2O_2 groups and the second – data of the rest two treatments.

The averaged fluorescence spectra of control and treated paulownia leaves are shown in Fig. 5. Most significant are differences between SRC of control and treated with herbicide 2,4-D. For combined treatments differences decreased because of regenerating action of hydrogen peroxide.

The Student's t-test was applied to fluorescence data in above mentioned five characteristic wavelengths. The significant differences were obtained in first three wavelengths, most significant ($p < 0.001$) in the case of H_2O_2 treatment.

The remote sensing findings were validated through complementary biochemical tests commonly applied in plant science practice in studies of abiotic and biotic plant stresses.

The biochemical parameters – stress markers such as phenols, proline, and thiol groups (-SH) were determined using a spectrophotometer Multiskan Spectrum (Thermo Electron Corporation). Phenols and proline are important protective components of the plant cells and they accumulate when cells are in stress conditions. Treatment with 2,4-D causes increased levels of free proline and reduced levels of free thiol groups and total phenols. When pre-treated with H_2O_2 plants the proline content is not increased, corresponding level of thiol groups and total phenols is higher, in comparison with plants treated with 2,4-D. On the basis of these investigations it could be concluded that the preliminary application of H_2O_2 reduces oxidative damage.

Table 2. Results from biochemical analysis – stress markers.

Investigated groups	Proline mkmol/gFW	Phenols nmol/gFW	-SH nmol/gFW
control	0.381	66.811	0.512
H_2O_2	0.330	34.085	0.406
2,4-D	0.426	36.524	0.306
H_2O_2+2,4-D	0.366	53.253	0.455

CONCLUSIONS

In this research hyperspectral reflectance and fluorescence data from leaves of paulownia trees were tested upon their sensitivity to two abiotic stresses. Hydrogen peroxide and herbicide 2,4-D were applied in low concentrations. Measurements were conducted on the fourth day after the treatment on leaf samples without visual symptoms. It was demonstrated that the spectral behavior of stressed and unstressed leaves was clearly different. The examination of differences of mean reflectance values of stressed and healthy leaves indicated that some regions in the spectrum were more sensitive than others. Furthermore those regions were situated around places in the spectrum where from the biophysical point of view we expected them to occur.

The strong correlation which was found between the results from the two remote sensing techniques and the biochemical analyses of plant stress markers indicates the importance of remote sensing hyperspectral data for conducting, early and without damage, rapid assessments of plant health condition. These data have great potential for assessing changes in various biophysical and biochemical properties of plants and ecosystems in response to the changes in the environment. This study exemplifies the benefits of integrating remote sensing and ecology and conducting of interdisciplinary investigations of vegetation.

REFERENCES

[1] W. Zhang and S. Sriharan, Using hyperspectral remote sensing for land cover classification, SPIE Conference Proceeding 5655, *Multispectral and Hyperspectral Remote Sensing Instruments and Applications II*, 2005, pp. 261-270, doi:10.1117/12.578104.

[2] J. R. Jensen, *Remote sensing of the environment: an Earth resource perspective* (2nd ed.), New Jersey: Prentice Hall, 2006, 608 pages, ISBN 0-13-188950-8.

[3] C. Yang, J. H. Everitt, D. Murden, Evaluating high resolution SPOT 5 satellite imagery for crop identification, *Comput. Electron. Agricult.* **75**, 347–354 (2011).

[4] M. A. Schull et al., Canopy spectral invariants, Part 2: Application to classification of forest types from hyperspectral data, *J. Quant. Spectrosc. Radiat Transf.* **112**(4), 736–750 (2011).

[5] J. B. Campbell, *Introduction to remote sensing* (3rd ed.). New York: The Guilford Press, 2002, 621 pages, ISBN: 1-57230-640-8.

[6] L. Grant, C. S. T. Daughtry, V. C. Vanderbilt, Polarized and specular reflectance variation with leaf surface features, *Physiol. Plant* **88**(1), 1–9 (1993).

[7] V. C. Vanderbilt, L. Grant, S. L. Ustin, Polarization of light by vegetation. *Photon-Vegetation Interactions: Applications in Plant Physiology and Optical Remote Sensing*, eds R. B.Myneni, J. Ross, Berlin, Springer, 1991, pp 191–228.

[8] S. L.Ustin, D. A. Roberts, J. A. Gamon, G. P. Asner, R. O. Green, Using imaging spectroscopy to study ecosystem processes and properties, *Bioscience* **54**(6), 523–534 (2004).

[9] P. J. Pinter, J. L. Hatfield, J. S. Schepers, E. M. Barnes, M. S. Moran, C. S. T. Daughtry, D. R. Upchurch, Remote Sensing for Crop Management, *Photogramm. Eng. Remote Sens*. **69**, 647–664 (200).

[10] S. Aggarwal, Principles of remote sensing, Satellite Remote Sensing and GIS Applications in Agricultural Meteorology, Proceeding of Training Workshop, Dehra Dun, India, WMO/TD-No. 1182, 2003, pp. 23–38.

[11] K. Usha and S. Bhupinder, Potential applications of remote sensing in horticulture—A review, *Sci. Horticul.* **153**, 71–83 (2013).

[12] D. D. Krezhova, Hyperspectral remote sensing of reflected and emitted radiation as a means for preservation of terrestrial ecosystems, RAD Proceedings of 1st International Conference on Radiation and Dosimetry in Various Fields of Research, Niš, Serbia, 2012, pp. 71–74.

[13] J. R. Jensen, *Digital Image Processing: a Remote Sensing Perspective* (3rd ed.), New Jersey: Prentice Hall, 2004, ISBN-10: 0131453610.

[14] P. M. Mehl, Y. R. Chen, M. S. Kim, D. E. Chan, Development of hyperspectral imaging technique for the detection of apple surface defects and contaminations, *J. Food Eng.* **61**, 67–81 (2004).

[15] P. Butz, C. Hoffmann, B. Tauscher, Recent developments in non-invasive techniques for fresh fruit and vegetable internal quality analysis, *J. Food Sci.* **70**, 131–141 (2005).

[16] D. A. Sims, J. A. Gamon, Relationships between leaf pigment content and spectral reflectance across a wide range of species, leaf structures and developmental stages, *Remote Sens. Environ*. **81**, 337–354 (2002).

[17] S. T. Prasad, B. S. Ronald, E. D. Pauw, Hyperspectral vegetation indices and their relationships with agricultural crop characteristics, *Remote Sens. Environ.*, **71**, 158–182, (2000).

[18] V. K. Shettigara, D. O'Mara, T. Bubner and S. G. Kempinger, Hyperspectral Band Selection Using Entropy and Target to Clutter Ratio Measures, Proceedings of the 10th Australasian Remote Sensing and Photogrammetric Conference, Adelaide, 2000, pp. 1008–1018.

[19] K. L. Smith, M. D. Steven, J. J. Colls, Use of hyperspectral derivative ratios in the red-edge region to identify plant stress responses to gas leaks, *Remote Sens. Environ.* **92**, 207–217 (2004).

[20] B. Zhang, X. Wang, J. Liu, Hyperspectral image processing and analysis system (HIPAS) and its applications, *Photogram. Eng. Remote Sens*., **66**(5), 605–609 (2000).

[21] D. D. Krezhova, N. M. Petrov, S. N. Maneva, Hyperspectral remote sensing applications for monitoring and stress detection in cultural plants: viral infections in tobacco plants, in Remote Sensing for Agriculture, Ecosystems, and Hydrology XIV, edited by C. M. Neale, A. Maltese, K. Richter, SPIE Proceedings 8531 Bellingham, WA, 2012, pp. 85311H-1 - 85311H-9. ISSN: 0277-786X, ISBN: 9780819492715,

[22] T. Lillesand, R. Kiefer, J. Chipman, *Remote Sensing and Image Interpretation*. 5th ed., New York: John Wiley and Sons, (2004).

[23] S. Aggarwal, Spectral Signature of Earth Objects. Lecture Delivered in Edusat based Training Programming. Indian Institute of Remote Sensing, Dehradun.

[24] Optical Remote Sensing, CRISP, 2008, `http://www.crisp.nus.edu.sg/~research/tutorial/optical.htm`

[25] `http://www.ucalgary.ca/GEOG/Virtual/Remote%20Sensing/reflectance.gif`

[26] R. B. Smith, Introduction to remote sensing of the environment, 2001 `www.microimages.com`

[27] E. Underwood, S. Ustin, D. Dipietro, Mapping Non-Native Plants using Hyperspectral Imagery, *Remote Sens. Environ*. **86**, 150–161 (2003).

[28] D. Krezhova, "Spectral remote sensing of the responses of soybean plants to environmental stresses," Chapter 11, in: *Soybean – Genetics and Novel Techniques for Yield Enhancement*, Edited by D. Krezhova, InTech Publisher, 2011, pp. 215–256.

[29] B. Li, O. W. Liew, A. K. Anand, "Early detection of calcium deficiency in plants using red edge position". In *Proceedings of SPIE 5996, Optical Sensors and Sensing Systems for Natural Resources and Food Safety and Quality*; Chen, Y.R.; Meyer, G. E.; Tu, S.I., Ed., 2005, pp. 609–617.

[30] G. H. Krause and E. Weis, Chlorophyll fluorescence and photosynthesis: The basics, *Annu. Rev. Plant Physiol. Plant Mol. Biol.*, **42**, 313–349 (1991).

[31] U. Schreiber, Chlorophyll a Fluorescence: A Signature of Photosynthesis, G. C. Papageorgiou, and Govindjee (Eds.), Springer, Dordrecht, 2004, 279.

[32] K. Maxwell and G. Johnson, Chlorophyll fluorescence - a practical guide, *J. Exper. Botany*, **51**(345), 659–668 (2000).

[33] Govindjee Chlorophyll a fluorescence: a bit of basics and history, in: G.C.Papageorgiou, Govindjee (Eds.), Chlorophyll a Fluorescence: A Signature of Photosynthesis, *Advances in Photosynthesis and Respiration*, The Netherlands: Springer, Dordrecht, **19**, pp. 1–41 (2004).

[34] A. Blum, Plant breeding for water-limiting environments. New York: Springer Science Publishing, 2011.

[35] P. J. Zarco-Tejada, J. R. Miller, G. H. Mohammed, T. L. Noland, Chlorophyll Fluorescence Effects on Vegetation Apparent Reflectance: I. Leaf-Level Measurements and Model Simulation, Rem. Sens. Environ. **74**(3), 582-595 (2000).

[36] H. K. Lichtenthaler and F. Babani, Chlorophyll a Fluorescence: A signature of Photosynthesis, G.C. Papageorgiou, and Govindjee (Eds.), Springer, Dordrecht, 2004, 713.

[37] `http://oceanoptics.com/product/`

ПРИЛОЖЕНИЕ НА ХИПЕРСПЕКТРАЛНИТЕ ДИСТАНЦИОННИ ИЗСЛЕДВАНИЯ ЗА РАННО ОТКРИВАНЕ НА СТРЕС В МЛАДИ РАСТЕНИЯ

Д. Крежова[1], Св. Манева[2], И. Москова[3], К. Крежов[4]

[1] *Институт за космически изследвания и технологии, Българска академия на науките, ул. "Акад. Г. Бончев" блок 1, 1113 София, България*
[2] *Институт по почвознание, аграрни технологии и растителна защита, Селскостопанска академия, ул. "Панайот Волов" №13, 2230 Костинброд, България*
[3] *Институт по физиология на растенията и генетика, Българска академия на науките, ул. "Акад. Г. Бончев" блок 22, 1113 София, България*
[4] *Институт за ядрени изследвания и ядрена енергетика, Българска академия на науките, бул. "Цариградско шосе" №72, 1784 София, България*

(Резюме)

През последното десетилетие хиперспектралните данни от дистанционни изследвания на земната повърхност доказаха, че са много ефективни за идентифициране на растежни аномалии в културни растения вследствие на влиянието на естествени неблагоприятни фактори на околната среда, вирусни инфекции и др. Промените във физиологичното състояние на растенията, симптоми на стрес, се отразяват върху техните спектрални отговори и могат да се установяват чрез спектрални измервания във видимата и близката инфрачервена области на електромагнитния спектър. Целта на това изследване е да се постигне ранна диагностика на стрес в млади растителни видове чрез прилагане на два метода за дистанционни изследвания (отразена радиация и флуоресценция на хлорофила) и да се вземат навременни управленчески решения за предотвратяване или ограничаване на последствията. Отразената от изследваните растения радиация е регистрирана с портативен спектрометър с гъвкав световод в спектралния диапазон 450-850 nm със спектрална разделителна способност 1.5 nm. Данните за флуоресценция на хлорофила са получени със същия спектрометър в спектралния диапазон 600-900 nm, като е използван източник за възбуждане в синята област на спектъра. Статистически анализи, първа производна и спектрални нормиращи процедури са използвани за отчитане на разликите в спектралните свойства на растенията. В някои от случаите е установено, че позицията на червения ръб на спектрите на отразената радиация на увредените растения е отместена към по-късите дължини на вълната, което е надежден показател за наличие на стрес в растенията. Тези резултати са съпоставени с резултатите от проведени съпътстващи биохимични и серологични анализи за оценка на увреждания на растенията.

Bulgarian Chemical Communications, Volume 47, Special Issue B (pp. 364–367) 2015

Extinction and massive stellar population in Andromeda galaxy

P. L. Nedialkov*

Department of Astronomy, Faculty of Physics, St. Kliment Ohridski University of Sofia, 5 James Bourchier Blvd., BG-1164 Sofia, Bulgaria

We probed to derive a new information on the massive star population and the extinction in the disc of Andormeda galaxy from a ground based *UBV* stellar photometry. Classical dereddening procedure was applied to evaluate both the extinction of starlight caused by the dust and the intrinsic properties (luminosity, color) of stars themselves. Thus, we were able draw conclusions about the spatial distribution of the dust, and – with the use of isocrones – to estimate the age of each successfully dereddened star. The last parameter allowed us to perform a search for sites of coherent star fomation on different time and size scales. We paid a special attention to the spiral arm S4 where we confirm that evidences exist in support to the density wave theory. Some hidden star formation may be detectable with the available catalog data along the lanes of highest concentration of dust and gas.

Key words: spiral galaxies, interstellar medium in external galaxies, stellar content and populations, spiral arms, stellar characteristics and properties

INTRODUCTION

Due to its large angular extend on the sky the spiral galaxy Andormeda (hereafter M31) is not an easy target for complete surveys and photometry of individual stars. Even nowadays when HST is equipped with the wide field WFPC3 and ACS detectors only 1/3 of disc will be covered by a survey like PHAT [2]. When it comes to ground based telescopes, *UBV* photometry is crucial for deriving the intertwined extinction and physical characteristics of massive stars. In this paper we used the *UBVRI* catalog of [1], containing about two hundred thousands of stars with that appropriate photometry.

DATA REDUCTION

We started with the construction of the classical two-color diagram in terms of $(U-B)$ vs. $(B-V)$ colors. Dereddening was performed by the means of constant slope κ of the reddening vector, equal to 0.72 and total-to-selective- extinction ratio $A_U/E_{B-V} = 4.85$ [3]. These commonly accepted parameters are typical for the diffuse component of the ISM of Milky way rather than for the dense clouds in which some newborn stars could be found. Adopting of the above values is only a first step approximation allowing us to acquire physically meaningful extinction, luminosity, true color and age to some of stars. On the other hand, the usage of these values simply means that we expect the extinction by the diffuse ISM to predominate the extinction by the dense ISM which is reasonable for a highly inclined system as M31 disk. All stars with normal Q-index earlier than B6V (AOIa) were slide backward to the zero reddening line for the main sequence stars and their true color and absolute magnitude were calculated.

Later on we put them of color magnitude-diagram to figure out whether they belong to the main sequence or they are blue supergiants candidates. The Hertzsprung-Russell diagram (see Fig. 1) was constructed using the synthetic *UBV* photometry from the Database of Geneva stellar evolution tracks and isochrones [4] based on the grids of 5 to 120 $M_\odot$ tracks of Geneva's stellar evolution models for solar initial composition and standard mass loss of $M_{dot} = 10^{-6} M_\odot/yr$ and corresponding 46 isochrones with ages in the range of 10^3 yr to 10^8 yr in time steps of $\Delta \log t = 0.05$ dex. We have excluded of further consideration both stars with negative extinction on two color diagram or bluer than the left end of the main sequence (zero age curve). Since the fraction of ground-based sources that turned out to be multiple sources in HST is qute high [2] we also put a conservative limit for the absolute magnitude $M_U > -10$ mag. The right end of the main sequence was defined as a curve that connects the turn off points of all the tracks within the studied mass range. The stars falling between these two curves and between the tracks of the most massive and the lowest mass star are actually the main sequence candidates which will be hereafter called dwarfs for simplicity. Finally we have $\sim 34\,000$ dwarf candidates and $\sim 45\,000$ blue supergiants candidates in total area of 8 170 $\square'$ of the M31 disc.

* To whom all correspondence should be sent:
japet@phys.uni-sofia.bg

© 2015 Bulgarian Academy of Sciences, Union of Chemists in Bulgaria

Since [1] did not provide additional photometry useful for estimation of the foreground contamination we selected several fields with a total area of 522 $\square'$ in the outskirts of M31 disc well beyond the standard isophote at $\mu_B = 25^m/\square''$ and as far as possible – away from the major axis. Thus we compare a photometry of the same quality and origin but the contamination estimates should be taken as upper limits because some star formation could be presented even at these remote places. Taking into account the area correction the corresponding percentage of the expected foreground contamination is 2.5% for the dwarfs sample and 9.7 % for the blue supegians candidates sample.

Following error propagation technique we calculated the error of the derived physical quantities for each successfully dereddened star. In the case of extinction, luminosity and true color its application is straightforward. The acquried age is the mean of ages of all isochrones weighted by the inverse square of the ratio of two distances measured on HRD. The first one is the distance star-isochrone, and the second is 1σ radius of the ellipse of errors towards each isochrone. The error of the age is just the weighted standard deviation from the weighed mean.

RESULTS AND DISCUSSION

A preliminary analysis of the intial mass function (IMF) which is based on counts of stars between the evolutionary tracks like those on Fig. 1 showed that one could relay on sample of M31 massive dwarfs which is completed down to 20 $M_\odot$. Moreover, the obtained slope of the IMF $\Gamma = -1.5 \pm 0.1$ is close to the empirical Salpeter slope [5] and to the theoretical slope [6]. Practically, it coincides with the result of [7] where some high resolution HST data was also involved.

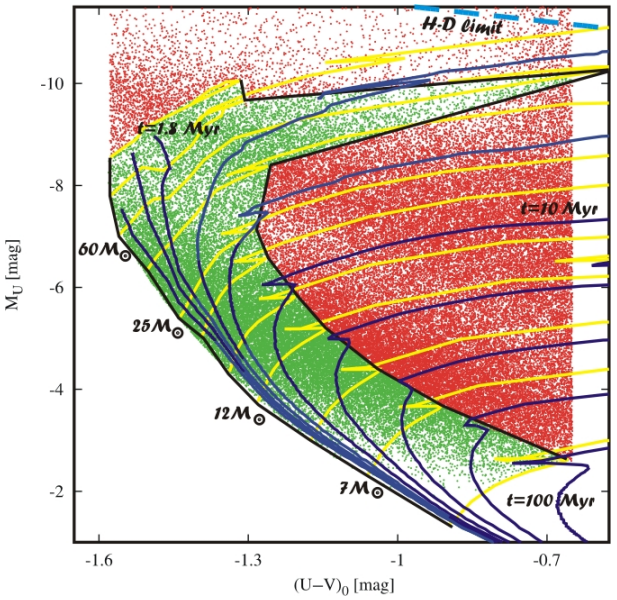


Fig. 1. Hertzsprung-Russell diagram for the massive stellar population in M31 galaxy. Stellar tracks of different initial masses (yellow solid lines) and isochrones (violet solid lines) of different ages are indicated on the plot. Stars between the two black solid lines and the stellar tracks of the most massive star and less massive star are Main sequence stars, which spent the bulk of their life burning hydrogen in their cores. The empirical edge where stars become unstable or Humphrey-Davidson limit is plotted (blue dashed line) on the right upper corner.

We consider the azymuthally averaged distribution of the mean extinction. It is expected in a magnitude limited sample as ours the Malquist bias to be

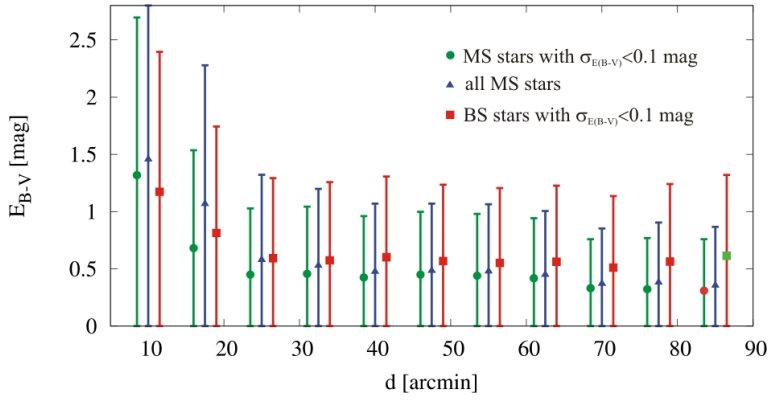


Fig. 2. Radial distribution of the mean extinction versus galactocentric distance as derived for all main sequence stars (blue triangles) and stars with individual extinctional error $\sigma_{E(B-V)} < 0.1$ mag, plotted with red circles (main sequence) and squares (blue supergians). The error bars represent the standard deviation of the mean.

presented. When a highly inclined disc and a large vertical optical thickness are combined the maximum extinction, including the mean, will depend on the absolute magnitude of the dereddened star. Surprisingly, that is not the case with the studied distribution which have been found almost independent from the imposed different absolute magnitude limits. As seen on Fig 2, there exists a constancy of of the mean extinction $E_{B-V} \backsimeq 0.5^m$ with the galactocentric distance which may indicate optically thick case, indeed. The standard deviation of the mean extinction is of the same order as the extinction itself which reflects the large variance rather than big errors of the derived quantity. Some information about the optical thickness of the disk may be locked in the distribution of E_{B-V} at a certain galactocentric distance or spiral arm fragment which demands Monte-Carlo simulations, analogous to those perfomed in [8].

In Fig. 3 we show the spatial distribution in the view plane of the NE part of M31 disc. The dereddened dwarfs were divided into three subsamples of different age: oldest stars: $\log t > 7.0$, intermediate age stars: $6.0 < \log t < 7.0$ and youngest stars: $\log t > 6.0$ (blue circles). By taking only stars with individual logarithmic age error $\sigma_{\log t} < 0.3$ in the first two samples we aimed at distinguishing them confidently. The idea here is to compare the clustering of the samples. We confirm the finding of [9] that the younger stars are being systematically more strongly clustered than the older, which are more dispersed. Most clearly it can be seen in the large complexes OB102 and OB54 [10], though there are 'clusters' like OB7 less populated by young stars. The faint stars in OB7 are real older stars rather than heavily obscured young stars which is proved here by the means of proper dereddening. The resolution of our data for certain goes down to size scales of few 10 pc, characteristic of unbound stellar aggregates and OB associations.

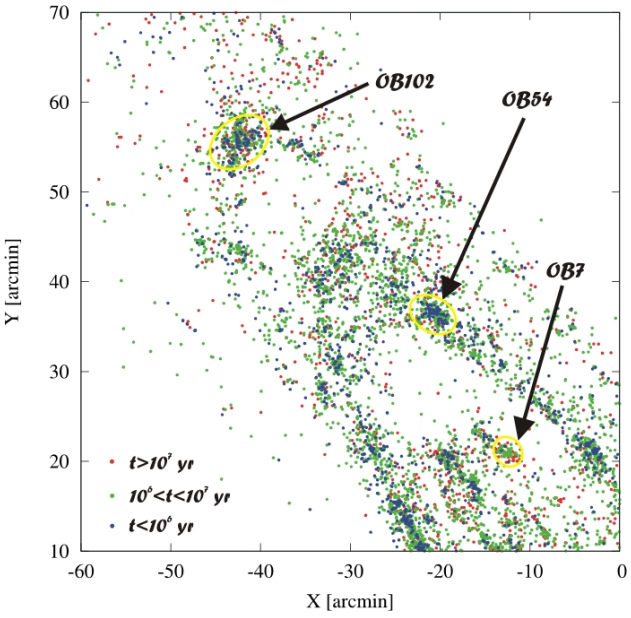


Fig. 3. Spatial distribution in the view plane of the NE part of M31 disc of three subsamples of main sequence stars wiith different age: oldest stars: $\log t > 7.0$ (red circles), intermediate age stars: $6.0 < \log t < 7.0$ (green circles) and youngest stars: $\log t > 6.0$ (blue circles). In order to distinguish between to first two samples only stars with individual logarithmic age error $\sigma_{\log t} < 0.3$ were considered. Note the blurring of the stars with the age hinting that the young groups do dissipate with time. The location of of 3 prominent van den Bergh's associations outlined by solid yellow line are shown as well.

Finally, on Fig. 4 we superimposed the stars younger than 10^6 yr over all dereddened dwarfs to check for signs of density wave. It was done on the rectified plane the M31 which corresponds to a face on orientation of the disc. The only fragment of spiral arm where the youngest stars are located along its

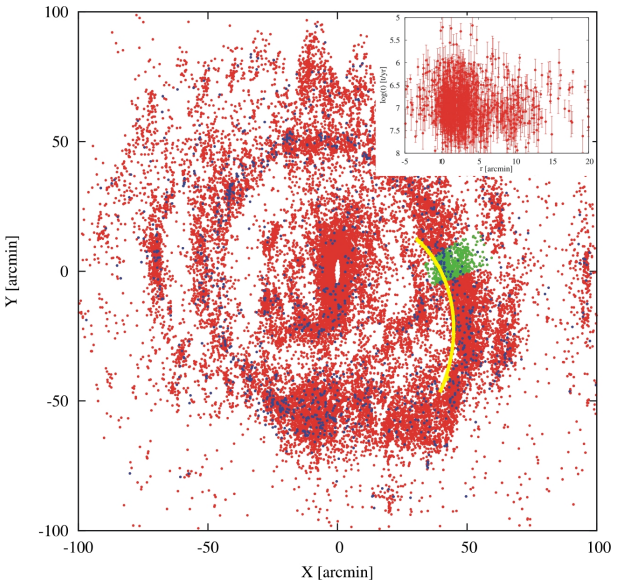


Fig. 4. Spatial distribution in the rectified plane the M31 disk of all main sequence stars with individual logarithmic age error $\sigma_{\log t} < 0.5$ (green circles for the fragment of spiral arm S4 in the area of association OB78 and red circles elsewhere) with a subsample containing only stars younger than $\log t = 6.0$ (blue circles) superimposed. The maxima of gas and dust emission were used to approximate the S4 fragment with a logarithmic spiral (yellow solid line). The age gradient across the spiral arm fragment is shown on the

inset in the upper right corner.
inner edge is S4. At the region of association OB78 the age gradient across the spiral arm fragment is most prominent.

CONCLUSIONS

By the means of a standard dereddening procedure we derive extinction estimates along $\sim 80\,000$ sight-lines towards M31 galaxy and obtained meaningful physical characteristics (luminosity, color, age) of the same number of stars. Their masses varies form 5 to 120 $M_{\odot}$ with a completeness limit of $\sim 20 M_{\odot}$.

The azymuthally averaged mean extinction is nearly constant with the galactocetric distance indicating thick disk in the optical: $A_V \backsimeq 1.5^m$. We assign this to the high inclination of the M31 disc, but more sophisticated approach is needed to derive its true vertical thickness. Highly variable extinction from star to star even within the boundaries of one and the same stellar group is the main cause for the high dispersion of the mean extinction.

The younger the stars are, the stronger they are clustered pointing that the groups with mean size-scales like those of the OB associations ($\sim$80 pc) are gravitationally unbound and will be dissolved into disc background after a certain time.

Spiral arm S4 is still the only place where some new evidences can be raised in support to the density wave theory. They come from the age gradient of stars across the arm which is most prominent in the region of association OB78.

REFERENCES

[1] P. Massey, K. Olsen, P. Hodge, S. Strong, G. Jacoby, W. Schlingman and R. Smith *The Astronomical Journal* **131**, 2478–2496 (2006).

[2] L. Bianchi, Y. Kang, P. Hodge, J. Dalcanton and B. Williams *Advances in Space Research* **53**, 928–938 (2013).

[3] J. Cardelli, G. Clayton and J. Mathis *The Astrophysical Journal* **345**, 245–256 (1989).

[4] T. Lejeune and D. Schaerer *Astronomy & Astrophysics* **366**, 538–546 (2001).

[5] P. Kroupa *Science* **295**, 85–88 (2002).

[6] D. Weisz, M Fouesneau, D. Hogg; H.-W. Rix, A. Dolphin, J. Dalcanton, D. Foreman-Mackey, D. Lang, L. Johnson, L. Beerman, E. Bell, K. Gordon, D. Gouliermis, J. Kalirai, E. Skillman and B. Williams *The Astrophysical Journal* **762**, 123–144 (2013).

[7] T. Veltchev, P. Nedialkov and G. Borisov *Astronomy & Astrophysics* **426**, 495–501 (2004).

[8] P. Nedialkov and V. Ivanov *Astronomical & Astrophysical Transactions* **17**, 367–391 (1999).

[9] D. Gouliermis, L. Beerman, L. Bianchi, J. Dalcanton, A. Dolphin, M. Fouesneau, K. Gordon, P. Guhathakurta, J. Kalirai, D. Lang, A. Seth, E. Skillman, D. Weisz and B. Williams *(astro-ph.GA* **1407.0829**, 1–10 (2014).

[10] S. van den Bergh *The Astrophysical Journal Supplement* **9**, 65–80 (1964).

ЕКСТИНКЦИЯ И МАСИВНО ЗВЕЗДНО НАСЕЛЕНИЕ В ГАЛАКТИКАТА АНДРОМЕДА

П. Недялков

Катедра Астрономия, Софийски университет "Св. Климент Охридски", бул. "Дж. Баучер" №5, 1164 София, България

(Резюме)

Изследвахме потенциала на фотометрията от звездния каталог на галактиката M31 (Massey et al. 2006) да служи като източник на нова информация относно звездобразуването и екстинкцията в нейния диск. За целта разработихме процедура за освобождаване от почервеняване, причинено от праховата компонента на междузвездната среда. Тя позволява да бъдат направени изводи както за количеството и пространственото разпределение на праха, така и за физическите параметри (светимост, температура, възраст) на населението от масивни звезди. Потърсени са области на кохерентно звездообразуване на различни времеви скали и размери. Намерени са както доказателства в подкрепа на теорията на спиралната вълна на плътността за ръкава S4, така и свидетелства за скрито звездобразуване, близо до областите с най-висока концентрация на газ и прах.

Bulgarian Chemical Communications, Volume 47, Special Issue B (pp. 368–379) 2015

Heating of the solar corona by Alfvén waves – self-induced opacity

T. M. Mishonov*, N. I. Zahariev, R. V. Topchiyska, B. V. Lazov, S. B. Mladenov

Department of Theoretical Physics, Faculty of Physics, St. Kliment Ohridski University of Sofia, 5 James Bourchier Blvd., BG-1164 Sofia, Bulgaria

Static distributions of temperature and wind velocity at the transition region are calculated within the framework of magnetohydrodynamics (MHD) of completely ionized hydrogen plasma. The numerical solution of the derived equations gives the width of the transition layer between the chromosphere and the corona as a self-induced opacity of high-frequency Alfvén waves (AW). The domain wall is direct consequence of the self-consistent MHD treatment of AW propagation. The low-frequency MHD waves coming from the Sun are strongly reflected by the narrow transition layer, while the high-frequency waves are absorbed – that is why we predict considerable spectral density of the AW in the photosphere. The numerical method allows consideration of incoming AW with arbitrary spectral density. The idea that Alfvén waves might heat the solar corona belongs to Alfvén, we simply solved the corresponding MHD equations. The comparison of the solution to the experiment is crucial for revealing the heating mechanism.

Key words: Alfvén waves, Magnetohydrodynamics, Plasma, Numerical Methods, Solar corona

ALFVÉN MODEL FOR CORONA HEATING

The discovery of the lines of the multiply ionized iron in the solar corona spectrum [1] posed an important problem for the fundamental physics - what is the mechanism of the heating of the solar corona and why the temperature of the corona is 100 times larger than the temperature of the photosphere.

The first idea by Alfvén [2] was that Alfvén waves (AW) [3] are the mechanism for heating the corona. AW are generated by the turbulence in the convection zone and propagate along the magnetic field lines. Absorption is proportional to ω^2 and the heating comes from high-frequency AW. Alfvén's idea for the viscous heating of plasma by absorption of AW was analyzed in the theoretical work by Heyvaerts [4]. In support of this idea is the work by Chitta [5] (Figures 8, 9 therein). The authors came to the conclusion that the spectral density satisfies a power law with an exponent of 1.59. This gives a strong hint that this scaling can be extrapolated in the nearest spectral range for times less than 1 s and frequencies in the 1 Hz range. We should also mention two recent papers [6, 7] investigating the possibility of heating the Solar corona by AW. Furthermore, Tomczyk [8] states that there exist very few direct measurements of the strength and orientation of coronal magnetic fields, meaning that the mechanisms responsible for heating the corona, driving the solar wind, and initiating coronal mass ejections remain poorly understood. However, recently discovered spatially and temporally ubiquitous waves in the solar corona [9] gave strong support for Alfvén's idea. A clear presence of outward and inward propagating waves in the corona was noted. $k-\omega$ diagnostics revealed coronal wave power spectrum with an exponent of $\approx -\frac{3}{2}$ (cf. Fig. 2 of [8]). The low frequency AW, on the other hand, reach the Earth orbit and thanks to the magnetometers on the various satellites we "hear" the bass of the great symphony of solar turbulence.

The purpose of the present work is to examine whether the initial Alfvén idea is correct and to solve the MHD equations which give the dependence of the temperature on the height $T(x)$ and the related velocity of the solar wind $U(x)$ supposing static density of the incoming AW. Due to the high density of the transition layer MHD is an adequate tool to analyze the beginning of the process. Without a doubt the kinetic approach is indispensable for the treatment of low density solar corona but this problem is beyond the purpose of the present work. When the plasma gets hotter and more dilute the MHD treatment is not sufficient and a detailed kinetic theory is required.

Our starting point are the MHD equations for the velocity field $\mathbf{v}$ and magnetic field $\mathbf{B}$

$$\partial_t \rho + \mathrm{div}\mathbf{j} = 0, \qquad \mathbf{j} = \rho\mathbf{v}, \tag{1}$$

$$\partial_t \left(\frac{1}{2}\rho\mathbf{v}^2 + \varepsilon + \frac{\mathbf{B}^2}{2\mu_0} \right) + \mathrm{div}\,\mathbf{q} = 0, \tag{2}$$

$$\partial_t(\rho\mathbf{v}) + \nabla\cdot\Pi = 0, \tag{3}$$

* To whom all correspondence should be sent:
tmishonov@phys.uni-sofia.bg

© 2015 Bulgarian Academy of Sciences, Union of Chemists in Bulgaria

where

$$\mathbf{q} = \rho\Big(\frac{1}{2}\mathbf{v}^2 + h\Big)\mathbf{v} + \mathbf{v}\cdot\Pi^{(\mathrm{visc})} - \varkappa\nabla T + \mathbf{S} \quad (4)$$

is the energy density flux, ρ is the mass density, ε is the internal energy density, $\varkappa$ is the thermal conductivity, h is the enthalpy per unit mass;

$$\mathbf{S} = \frac{1}{\mu_0}\left[\mathbf{B}\times(\mathbf{v}\times\mathbf{B}) - \nu_{\mathrm{m}}\mathbf{B}\times(\nabla\times\mathbf{B})\right], \quad (5)$$

is the Poynting vector and $\nu_{\mathrm{m}} \equiv c^2\varepsilon_0\rho_\Omega$ is the magnetic diffusion determined by Ohmic resistance ρ_Ω and vacuum susceptibility ε_0; vacuum permeability is μ_0. For hot enough plasma ρ_Ω is negligible and we ignore it hereafter. The total momentum flux

$$\Pi = \rho\mathbf{v}\mathbf{v} + P\mathbb{1} + \Pi^{(\mathrm{visc})} + \Pi^{(\mathrm{Maxw})} \quad (6)$$

is a sum of the inviscid part $\rho\mathbf{v}\mathbf{v} + P$ of the fluid, with pressure P,

$$\Pi^{(\mathrm{visc})}_{ik} = -\eta\left(\partial_i v_k + \partial_k v_i - \frac{2}{3}\delta_{ik}\nabla\cdot\mathbf{v}\right) - \zeta\,\delta_{ik}\nabla\cdot\mathbf{v}, \quad (7)$$

the viscous part of the stress tensor, with viscosity η and second viscosity ζ, and lastly, the Maxwell stress tensor

$$-\Pi^{(\mathrm{Maxw})}_{ik} = \frac{1}{\mu_0}\left(B_iB_k - \frac{1}{2}\mathbf{B}^2\delta_{ik}\right), \quad (8)$$

with δ_{ik} the Kronecker delta. We model coronal plasma with completely ionized hydrogen plasma

$$\varkappa = 0.9\frac{T^{5/2}}{e^4 m_e^{1/2}\Lambda}, \quad \eta = 0.4\frac{m_p^{1/2}T^{5/2}}{e^4\Lambda}, \quad \zeta \approx 0, \quad (9)$$

$$\Lambda = \ln\Big(\frac{r_{\mathrm{D}}T}{e^2}\Big), \quad \frac{1}{r_{\mathrm{D}}^2} = \frac{4\pi e^2 n_{\mathrm{tot}}}{T}, \quad e^2 \equiv \frac{q_e^2}{4\pi\varepsilon_0},$$

where q_e is the electron charge, m_e is the mass of electron, m_p is the proton mass, T is the temperature and $n_{\mathrm{tot}} = n_e + n_p$ is the total density of electrons and protons; $\rho = m_p n_p$. We suppose that $\mu_0 = 4\pi$ and $\varepsilon_0 = 1/4\pi$, but in the practical system all formulae are the same; as well as in Heaviside-Lorentz units where $\mu_0 = 1$ and $\varepsilon_0 = 1$. As we mentioned above

$$\nu_{\mathrm{m}} = \frac{c^2}{4\pi}\frac{e^2 m_e^{1/2}\Lambda}{0.6\,T^{3/2}} \ll \nu_{\mathrm{k}} \equiv \frac{\eta}{\rho} = \frac{0.4\,T^{5/2}}{e^4 m_p^{1/2} n_p \Lambda}; \quad (10)$$

i.e. the hot hydrogen plasma is sticky, dilute, and "superconducting" $\nu_{\mathrm{m}} \approx 0$. Let us mention also the relations $\varkappa\rho_\Omega = 1.5\,T/q_e^2$ and $\eta/\varkappa \approx \frac{4}{9}\sqrt{m_e m_p}$,

$$\rho_\Omega = \frac{1}{4\pi\varepsilon_0}\frac{e^2 m_e^{1/2}\Lambda}{0.6\,T^{3/2}}. \quad (11)$$

For weakly ionized plasma the magnetic viscosity definitely dominates $\nu_{\mathrm{m}} > \nu_{\mathrm{k}}$. As the plasma gets hotter absorbing AW the ohmic resistance becomes negligible. For illustrative purposes we shall completely ignore it $\nu_{\mathrm{m}} = 0, \rho_\Omega = 0$ in order to emphasize the importance of the viscosity at high final temperatures.

MHD EQUATIONS AND ENERGY FLUXES

The time derivative $\partial_t\mathbf{B}$ which implicitly participates in the energy conservation Eq. (2) at zero Ohmic resistivity obeys the equation

$$\mathrm{d}_t\mathbf{B} = \mathbf{B}\cdot\nabla\mathbf{v} - \mathbf{B}\,\mathrm{div}\,\mathbf{v}, \quad \mathrm{d}_t \equiv \partial_t + \mathbf{v}\cdot\nabla. \quad (12)$$

Analogously the momentum equation Eq. (3) can be rewritten by the substantial derivative

$$\rho\,\mathrm{d}_t v_i = -\partial_i P + \partial_k\left\{\eta\left(\partial_k v_i + \partial_i v_k - \frac{2}{3}\delta_{ik}\partial_j v_j\right)\right\} + \partial_i\left(\zeta\,\partial_j v_j\right) - \frac{1}{\mu_0}\left(\mathbf{B}\times\mathrm{rot}\,\mathbf{B}\right)_i. \quad (13)$$

In our model we consider AW propagating along magnetic field lines $\mathbf{B}_0$. We focus our attention on the narrow transition layer, where the static magnetic field is almost homogeneous and the waves are within acceptable accuracy one dimensional. For the velocity and magnetic fields we assume

$$\begin{aligned}\mathbf{v}(t,x) &= U(x)\widehat{\mathrm{x}} + u(t,x)\widehat{\mathrm{z}},\\ \mathbf{B}(t,x) &= B_0\widehat{\mathrm{x}} + b(t,x)\widehat{\mathrm{z}},\end{aligned} \quad (14)$$

with homogeneous magnetic field $B_0\widehat{\mathrm{x}}$ perpendicular to the surface of the Sun. The transverse wave amplitudes of the velocity $u(t,x)$ and magnetic field $b(t,x)$ we represent with the Fourier integrals

$$u(t,x) = \int_{-\infty}^{\infty}\widetilde{u}(\omega,x)\mathrm{e}^{-\mathrm{i}\omega t}\frac{\mathrm{d}\omega}{2\pi}, \quad (15)$$

$$b(t,x) = \int_{-\infty}^{\infty}\widetilde{b}(\omega,x)\mathrm{e}^{-\mathrm{i}\omega t}\frac{\mathrm{d}\omega}{2\pi}. \quad (16)$$

For illustrative purposes it is convenient to consider monochromatic AW with $u(t,x) = \widehat{u}(x)\mathrm{e}^{-\mathrm{i}\omega t}$ and $b(t,x) = \widehat{b}(x)\mathrm{e}^{-\mathrm{i}\omega t}$.

Wave equations

For linearized waves the general MHD equations (13) and (12) give the following system for $\widehat{u}(x)$ and $\widehat{\overline{b}}(x) \equiv \widehat{b}(x)/B_0$

$$(-\mathrm{i}\omega + U\mathrm{d}_x)\,\widehat{u} = V_\mathrm{A}^2 \mathrm{d}_x \widehat{\overline{b}} + \frac{1}{\rho}\mathrm{d}_x\left(\eta \mathrm{d}_x \widehat{u}\right), \quad (17)$$

$$-\mathrm{i}\omega\widehat{\overline{b}} = \mathrm{d}_x\widehat{u} - \mathrm{d}_x(U\widehat{\overline{b}}), \quad (18)$$

where

$$V_\mathrm{A}(x) = B_0/\sqrt{\mu_0\rho(x)} \quad (19)$$

is the Alfvén velocity. In our numerical analysis we solve the first order linear system of equations

$$-\mathrm{i}\mathrm{d}_x\ \Psi = \frac{\mathrm{i}}{\nu_\mathrm{k} U}\,\mathsf{M}\Psi = \mathsf{K}\Psi, \quad (20)$$

$$\Psi \equiv \begin{pmatrix} \widehat{u} \\ \widehat{\overline{b}} \\ \widehat{w} \end{pmatrix}, \quad \mathsf{K} = \frac{\mathrm{i}}{\nu_\mathrm{k} U}\mathsf{M},$$

$$\Psi^\dagger = \left(\widehat{u}^*, \widehat{\overline{b}}^*, \widehat{w}^*\right),$$

where $\widehat{w} \equiv \mathrm{d}_x\widehat{u}$, and

$$\mathsf{M} \equiv \begin{pmatrix} 0 & 0 & -\nu_\mathrm{k} U \\ 0 & \nu_\mathrm{k}(-\mathrm{i}\omega + \mathrm{d}_x U) & -\nu_\mathrm{k} \\ \mathrm{i}\omega & -V_\mathrm{A}^2(-\mathrm{i}\omega + \mathrm{d}_x U) & \left(V_\mathrm{A}^2 - U^2\right) + \frac{U}{\rho}\mathrm{d}_x\eta \end{pmatrix}.$$

For homogeneous medium with constant η, ρ, V_A, and U, in short for constant wave-vector matrix K, the exponential substitution $\Psi \propto \exp(\mathrm{i}kx)$ in Eq. (20) or equivalently Eq. (17) and Eq. (18) gives the secular equation

$$\mathrm{i}\,\nu_\mathrm{k} U \det(\mathsf{K} - k\mathbb{1}) = \omega_\mathrm{D}\left(\omega_\mathrm{D} + \mathrm{i}\nu_\mathrm{k}k^2\right) - V_\mathrm{A}^2 k^2 = 0, \quad (21)$$

where $\omega_\mathrm{D} \equiv \omega - kU$ is the Doppler shifted frequency. This secular equation gives the well-known dispersion

$$\omega_\mathrm{D}\left(\omega_\mathrm{D} + \mathrm{i}\nu_\mathrm{k}k^2\right) = V_\mathrm{A}^2 k^2$$

of the AW. This equation is quadratic with respect to ω and cubic with respect to k.

Wind variables

We solve the wave equation Eq. (20) from "Sun's surface" $x = 0$ to some distance large enough $x = l$, where the short wavelength AW are almost absorbed. This distance is much bigger than the *width of the transition layer* λ, but much smaller than solar radius. The considered one-dimensional $0 < x < l$ time-independent problem has three integrals corresponding to the three conservation laws related to mass, energy and momentum. The mass conservation law Eq. (1) gives the constant flow

$$j = \rho(x)U(x) = \rho_0 U_0 = \rho_l U_l = \mathrm{const}, \quad (22)$$

where $\rho_0 = \rho(0)$, $\rho_l = \rho(l)$, $U_0 = U(0)$, and $U_l = U(l)$. The energy conservation law reduces to a constant flux along the x-axis

$$q = q_\mathrm{wind}^\mathrm{ideal}(x) + \widetilde{q}(x) = \rho U\left(\frac{1}{2}U^2 + h\right) + \widetilde{q} = \mathrm{const}. \quad (23)$$

Here the first term describes the energy of the ideal wind, i.e. a wind from an ideal (inviscid) fluid. The second term $\widetilde{q}(x)$ includes all other energy fluxes; in our notations tilde will denote sum of the non-ideal (dissipative) terms of the wind and wave terms. In detail the non-ideal part of the energy flux $\widetilde{q}(x)$ consists of: the wave kinetic energy $\propto |\widehat{u}|^2$, viscosity (wind $\propto \frac{4}{3}\eta + \zeta$ and wave $\propto \eta$ components), heat conductivity $\propto \varkappa$, and Poynting vector $\propto \widehat{b}^*$,

$$\widetilde{q}(x) \equiv \frac{j}{4}|\widehat{u}|^2 - \xi U \mathrm{d}_x U - \frac{1}{4}\eta\,\mathrm{d}_x|\widehat{u}|^2 - \varkappa \mathrm{d}_x T + \frac{1}{2\mu_0}\left(U\left|\widehat{b}\right|^2 - B_0\,\mathrm{Re}(\widehat{b}^*\widehat{u})\right), \quad (24)$$

where $\xi \equiv \frac{4}{3}\eta + \zeta$. Here time averaged energy flux is represented by the amplitudes of the monochromatic oscillations, this is a standard procedure for alternating current processes. In our case we have, for example, $\langle\widehat{u}^2\rangle_t = \left\langle(\mathrm{Re}\,\widehat{u})^2\right\rangle_t = \langle\frac{1}{4}(\widehat{u} + \widehat{u}^*)^2\rangle_t = \frac{1}{2}|\widehat{u}|^2$. The other terms from Eq. (4) are averaged in a similar way in the equation above.

The momentum conservation law Eq. (6) gives constant flux $\Pi = \Pi_{xx}$

$$\Pi = \Pi_\mathrm{wind}^\mathrm{ideal}(x) + \widetilde{\Pi}(x) = \rho U U + P + \widetilde{\Pi}, \quad (25)$$

the sum of the ideal wind fluid and the other terms

$$\widetilde{\Pi}(x) \equiv \frac{1}{4\mu_0}\left|\widehat{b}\right|^2 - \xi\,\mathrm{d}_x U, \quad (26)$$

which take into account the wave part of the Maxwell stress tensor $\propto b^2$ and viscosity of the wind $\propto \xi$.

We have to solve the hydrodynamic problem for calculation of wind velocity and temperature at known energy and momentum fluxes. The problem

is formally reduced to analogous one for a jet engine, cf. Ref. [10]. We approximate the corona as completely ionized hydrogen plasma, i.e. electrically neutral mixture of electrons and protons. The experimental data tells us that proton temperature T_p is higher than electron one T_e. This is an important hint that heating goes through the viscosity determined mainly by protons. However for illustration purpose and simplicity we assume proton and electron temperatures to be equal $T_e = T_p = T$. For such an ideal (in thermodynamic sense) gas the local sound velocity is

$$c_s^2(x) = \frac{c_P}{c_V}\frac{P}{\rho} = \gamma\frac{T}{\langle m\rangle}, \quad \gamma = \frac{c_P}{c_V} = \frac{5}{3}, \tag{27}$$
$$\langle m\rangle = \frac{n_p m_p + n_e m_e}{n_p + n_e} \approx \frac{1}{2}m_p, \quad n_e = n_p = \frac{1}{2}n_{\rm tot},$$
$$P = n_{\rm tot}T = \frac{\rho T}{\langle m\rangle} = \frac{j}{U}\frac{T}{\langle m\rangle}, \quad h = c_P\frac{T}{\langle m\rangle} = \frac{\varepsilon + P}{\rho},$$

where, as we mentioned earlier, h is the enthalpy per unit mass and ε is the density of internal energy.

In order to alleviate the final formulae we introduce two dimensionless variables χ and τ which represent the non-ideal part of the energy and momentum flux respectively

$$\chi(x) \equiv \left.\frac{\widetilde{q}(x)}{\rho_0 U_0^3}\right|_x^0, \quad \tau(x) \equiv \left.\frac{\widetilde{\Pi}(x)}{\rho_0 U_0^2}\right|_x^0, \tag{28}$$

and analogously for the wind velocity and temperature

$$\begin{aligned} \overline{U}(x) &\equiv \frac{U(x)}{U_0}, \\ \Theta(x) &\equiv \frac{T(x)}{\langle m\rangle U_0^2}, \\ \Theta_0 &= \Theta(0), \end{aligned} \tag{29}$$

where $U_0 = U(0)$. The energy and momentum constant fluxes Eq. (23) and Eq. (25) in the new notation take the form

$$\frac{q - \widetilde{q}(0)}{\rho_0 U_0^3} = \frac{1}{2}\overline{U}^2 + c_P\Theta - \chi = \frac{1}{2} + c_P\Theta_0, \tag{30}$$
$$\frac{\Pi - \widetilde{\Pi}(0)}{\rho_0 U_0^2} = \overline{U} + \Theta/\overline{U} - \tau = 1 + \Theta_0. \tag{31}$$

From the second equation we express the dimensionless temperature Θ and substitute in the first one. Solving the quadratic equation for the wind velocity U we derive

$$\begin{aligned} U &= U_0\overline{U}, \\ \overline{U}(x) &= \frac{1}{\gamma+1}\left(\gamma + s^2 + \tau(x) - \sqrt{\mathscr{D}(x)}\right), \end{aligned} \tag{32}$$

where for the discriminant we have

$$\begin{aligned} \mathscr{D} &= (s^2-1)^2 - 2(\gamma^2-1)(\chi+1) \\ &\quad + \gamma\tau\left[\gamma\tau + 2\left(\gamma + s^2\right)\right], \\ s^2 &\equiv \frac{c_s^2(0)}{U_0^2} = \gamma\Theta_0, \\ c_s^2(x) &= \left(\frac{\partial P}{\partial\rho}\right)_S = \frac{\gamma T(x)}{\langle m\rangle}. \end{aligned} \tag{33}$$

Here γ is the constant ratio of the heat capacities, and $s \equiv c_s(0)/U_0$ is the ratio of the sound and wind velocity at $x = 0$. We suppose that initial wind velocity is very small $U(0) \ll c_s(0)$. The velocity distribution Eq. (32) can be substituted in Eq. (31) and we derive the dimensionless equation for the temperature distribution

$$T(x) = \langle m\rangle U_0^2\Theta(x), \tag{34}$$
$$\Theta(x) = \overline{U}(x)\left(1 + \Theta_0 + \gamma\tau(x) - \overline{U}(x)\right), \ \Theta_0 = \frac{s^2}{\gamma}.$$

The solutions for velocity $\overline{U}(x)$ Eq. (32) and temperature $\overline{T}(x)$ Eq. (34) distributions are important ingredients in our analysis and derivation of the self-consistent picture of the solar wind. We use a one dimensional approximation and in addition the constant flux of mass, energy and momentum gives 3 integrals of motion. This enables us to solve the nonlinear part of the problem analytically. That is why we do not solve the differential equations for the density $\rho(x) = \rho(0)U(0)/U(x)$, temperature $T(x)$ and wind velocity $U(x)$, and use analytical expressions containing the energy and momentum fluxes. Thus the numerical problem is reduced to a system of three linear differential equations.

Boundary conditions for the waves

At known background wind variables $U(x)$ and $T(x)$ we can solve the wave equation Eq. (20) for run-away AW at $x = l$. As we will see later the run-away boundary condition Eq. (49) corresponds to right propagating AW at the right boundary of the interval. The wave equation Eq. (20) is extremely stiff

at small viscosity, and numerical solution is possible to be obtained only downstream from $x=0$ to $x=l$. We have to find the linear combination of left and right propagating waves at $x=0$, which gives the run-away condition at $x=l$.

The solution of wave equation according to Eq. (23) determines the energy flux related to the propagation of AW

$$\widetilde{q}_{\rm wave}\left(\Psi(x)\right) \equiv \Psi^{\dagger} g \Psi = \frac{j}{4}\left|\widehat{u}\right|^2 - \frac{1}{2}\eta\,{\rm Re}\left(\widehat{u}^{*}\widehat{w}\right) + \frac{B_0^2}{2\mu_0}\left(U\left|\widehat{\widetilde{b}}\right|^2 - {\rm Re}\left(\widehat{\widetilde{b}}^{*}\,\widehat{u}\right)\right), \quad (35)$$

where

$$g(x) \equiv \begin{pmatrix} \frac{1}{4}j & -\frac{B_0^2}{4\mu_0} & -\frac{1}{4}\eta \\ -\frac{B_0^2}{4\mu_0} & \frac{UB_0^2}{2\mu_0} & 0 \\ -\frac{1}{4}\eta & 0 & 0 \end{pmatrix}. \quad (36)$$

Here j-term represents kinetic energy of the wave, η-term comes from the viscous part of the wave energy flux, and B_0-terms describe the Poynting vector of the wave.

In order to take into account the boundary condition at $x=l$ we calculate the eigenvectors of the matrix K, which according to Eq. (20) determine the wave propagation in a homogeneous fluid with amplitude $\propto \exp({\rm i}kx)$. Then the eigenvalues of K give the complex wave-vectors

$$k = k' + {\rm i}k'' = {\rm eigenvalue}(\mathsf{K}), \quad (37)$$

i.e.

$$\det\left(\mathsf{K} - k\mathbb{1}\right) = 0. \quad (38)$$

The three eigenvectors L, D and R are ordered by spatial decrements of their eigenvalues

$$k''_{\rm L} < 0 < k''_{\rm R} < k''_{\rm D}, \quad (39)$$

and are normalized by the conditions

$$-{\rm L}^{\dagger} g\,{\rm L} = {\rm R}^{\dagger} g\,{\rm R} = {\rm D}^{\dagger} g\,{\rm D} = 1, \quad (40)$$

where the sign corresponds to the direction of wave propagation. Notation L corresponds to left propagating wave, R to right propagating wave, and D for an overdamped at small viscosity mode.

For technical purposes we introduce the matrix notations

$${\rm L} = \begin{pmatrix} {\rm L}_u(x) \\ {\rm L}_b(x) \\ {\rm L}_w(x) \end{pmatrix},\ {\rm R} = \begin{pmatrix} {\rm R}_u(x) \\ {\rm R}_b(x) \\ {\rm R}_w(x) \end{pmatrix},\ {\rm D} = \begin{pmatrix} {\rm D}_u(x) \\ {\rm D}_b(x) \\ {\rm D}_w(x) \end{pmatrix}. \quad (41)$$

For low enough frequencies $\omega \to 0$ and wind velocities the modes describe: 1) right-propagating AW with $k'_{\rm R} \approx \omega/V_{\rm A}$ and small $k''_{\rm R} \approx \nu_{\rm k}\omega^2/2V_{\rm A}^3 \ll k'_{\rm R}$, 2) left propagating wave $k_{\rm L} = -k_{\rm R}$, and a diffusion overdamped mode $k''_{\rm D} \approx V_{\rm A}^2/\nu_{\rm k}U \gg k'_{\rm D}$ which describes the drag of a static perturbation by the slow wind $U \ll V_{\rm A}$ in a fluid with small viscosity. In this low frequency and long wavelength limit the stiffness ratio of the eigenvalues is very large

$$r_{\rm DR} = \frac{|k_{\rm D}|}{|k_{\rm R}|} \approx \frac{k''_{\rm D}}{k'_{\rm R}} \approx \frac{V_{\rm A}^3}{\nu_{\rm k}U\omega} \gg 1. \quad (42)$$

The strong inequality is applicable to the chromosphere where the viscosity of the cold plasma is very low. As we emphasized the wave equations Eq. (20) form a very stiff system and indispensably has to be solved downstream from the chromosphere $x=0$ to the corona $x=l$ using algorithms for stiff systems. Let

$$\psi_{\rm L}(x) = \begin{pmatrix} u_{\rm L}(x) \\ b_{\rm L}(x) \\ w_{\rm L}(x) \end{pmatrix}, \quad \psi_{\rm R}(x) = \begin{pmatrix} u_{\rm R}(x) \\ b_{\rm R}(x) \\ w_{\rm R}(x) \end{pmatrix} \quad (43)$$

are the solutions of the wave equation Eq. (20) with boundary conditions

$$\psi_{\rm L}(0) = {\rm L}(0), \quad \psi_{\rm R}(0) = {\rm R}(0). \quad (44)$$

We look for a solution as a linear combination

$$\psi(x) = \psi_{\rm R}(x) + r\,\psi_{\rm L}(x), \quad (45)$$

in other words we suppose that from the low viscosity chromosphere plasma do not come overdamped diffusion modes. The strong decay rate make them negligible at $x=0$. Physically this means that AW (R-modes) are coming from the Sun and some of them are reflected from the transition layer (L-modes)

$$\psi(0) = {\rm R}(0) + r\,{\rm L}(0). \quad (46)$$

Analogously for the configuration of open corona we have to take into account the run-away boundary condition for which we suppose zero amplitude for the wave coming from infinity

$$\psi(l) = \widetilde{t}\,{\rm R} + \widetilde{c}\,{\rm D}(l). \quad (47)$$

Written by components

$$\begin{pmatrix} u_{\rm R}(l) \\ b_{\rm R}(l) \\ w_{\rm R}(l) \end{pmatrix} + r \begin{pmatrix} u_{\rm L}(l) \\ b_{\rm L}(l) \\ w_{\rm L}(l) \end{pmatrix} = \widetilde{t} \begin{pmatrix} {\rm R}_u(l) \\ {\rm R}_b(l) \\ {\rm R}_w(l) \end{pmatrix} + \widetilde{c} \begin{pmatrix} {\rm D}_u(l) \\ {\rm D}_b(l) \\ {\rm D}_w(l) \end{pmatrix}. \quad (48)$$

This boundary condition gives a linear system of equation for the reflection coefficient r, transmission coefficient $\widetilde{t}$ and the mode-conversion coefficient $\widetilde{c}$.

For $l \to \infty$ when $\exp[-k''_{\rm D}(l)l] \ll 1 \exp[-k''_{\rm R}(l)l]$ the amplitude of D-mode is negligible and the run-away boundary condition reads

$$\psi(l) = \psi_{\rm R}(l) + r\psi_{\rm L}(l) \approx \widetilde{t}{\rm R}(l), \quad (49)$$

or by components

$$\begin{pmatrix} u_{\rm R}(l) \\ b_{\rm R}(l) \end{pmatrix} + r \begin{pmatrix} u_{\rm L}(l) \\ b_{\rm L}(l) \end{pmatrix} = \widetilde{t} \begin{pmatrix} {\rm R}_u(l) \\ {\rm R}_b(l) \end{pmatrix}. \quad (50)$$

These systems give the amplitudes of the reflected wave r and transmitted wave $\widetilde{t}$ in the solution Eq. (45). For this solution we have the energy fluxes

$$\mathscr{T} \equiv \psi^\dagger(l)\, g(l)\, \psi(l) = |\widetilde{t}|^2 + |\widetilde{c}|^2 + (\widetilde{t}\widetilde{c}^* {\rm D}^\dagger(l) g(l) {\rm R}(l) + {\rm c.c.}), \quad (51)$$

$$1 - \mathscr{R} \equiv \psi^\dagger(0)\, g(0)\, \psi(0) = 1 - |r|^2 + \left(r^* {\rm L}^\dagger(0)\, g(0)\, {\rm R}(0) + {\rm c.c.}\right). \quad (52)$$

Then we introduce the absorption coefficient

$$\mathscr{A} \equiv -\psi^\dagger(x)\, g(x)\, \psi(x)\Big|_0^l = 1 - \mathscr{R} - \mathscr{T}. \quad (53)$$

The described solution is normalized by unit energy flux of the R-wave. If we wish to fix energy flux of the right propagating wave to be $q_{\rm wave}(0)$ we have to make the renormalization

$$\Psi(x) = A_{\rm wave}\, \psi(x). \quad (54)$$

In this section we have described Absorbing Boundary Conditions (ABC) well known from radar calculations, but realization for AW is more complicated and require eigenvector analysis. Now using $\Psi(x)$ we can calculate the wave part of the energy flux Eq. (35) and the wave part of the momentum flux

$$\widetilde{\Pi}_{\rm wave}(x) \equiv \frac{1}{4\mu_0} \left|\widehat{b}(x)\right|^2. \quad (55)$$

This section is written in dimensional variables, but all equations can be easily converted in dimensionless variables as is done in the next sub-sub-section.

Dimensionless wave variables, convenient for numerical calculations

Using mechanical units for length l, velocity U_0 and density ρ_0 we can convert all equations in dimensionless form. The formulae remain almost the same and we wish to mention only the differences. Introducing dimensionless density

$$\overline{\rho}(x) = \rho(x)/\rho_0 = 1/\overline{U}(\bar{x}) \quad (56)$$

and wave energy flux

$$\mathscr{Q}_{\rm wave}(0) = \frac{q_{\rm wave}(0)}{\rho_0 U_0^3} = (1 - \mathscr{R})\, |A_{\rm wave}|^2, \quad (57)$$

we have dimensionless matrices

$$\overline{\mathsf{M}} = \begin{pmatrix} 0 & 0 & -\overline{v}\overline{U} \\ 0 & \overline{v}(-{\rm i}\overline{\omega} + \overline{W}) & -\overline{v} \\ {\rm i}\overline{\omega}\overline{U} & -\overline{V}_{\rm A}^2(-{\rm i}\overline{\omega} + \overline{W}) & \left(\overline{V}_{\rm A}^2 - \overline{U}^2\right) + \overline{U}^2 {\rm d}_{\bar{x}}\overline{\eta} \end{pmatrix},$$

and

$$\overline{g} \equiv \frac{1}{4} \begin{pmatrix} 1 & -a^2 & -\overline{\eta}(\bar{x}) \\ -a^2 & 2a^2\overline{U}(\bar{x}) & 0 \\ -\overline{\eta}(\bar{x}) & 0 & 0 \end{pmatrix}, \quad (58)$$

$$\overline{V}_{\rm A}^2(\bar{x}) = a^2\overline{U}(\bar{x}), \quad \overline{V}_{\rm A}^2(0) = a^2\overline{U}(0) = a^2. \quad (59)$$

For the dimensionless energy flux we have (Fig. 1b)

$$\mathscr{Q}_{\rm wave}(\bar{x}) = \frac{1}{4}\left|\widehat{\overline{u}}\right|^2 + \frac{a^2}{2}\left(\overline{U}\left|\widehat{\overline{b}}\right|^2 - {\rm Re}(\widehat{\overline{b}}^*\, \widehat{\overline{u}})\right) - \frac{1}{2}\overline{\eta}\, {\rm Re}\left(\widehat{\overline{u}}^*\, \widehat{\overline{w}}\right) = \overline{\Psi}^\dagger \overline{g}\, \overline{\Psi}, \quad (60)$$

where (Fig. 1a)

$$\widehat{\overline{u}} = \frac{\widehat{u}}{U_0}, \quad \widehat{\overline{w}} = \frac{l{\rm d}_x\widehat{u}}{U_0}, \quad \overline{\omega} = \frac{l\omega}{U_0}. \quad (61)$$

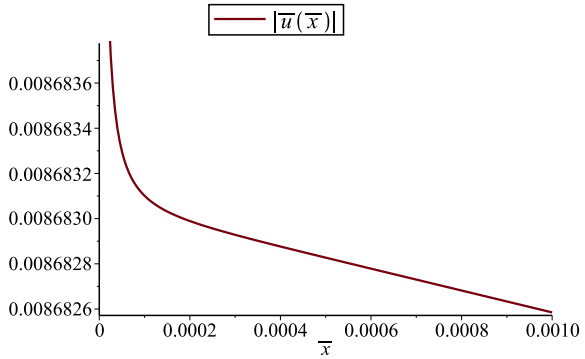
Then for the dimensional wave energy flux we have

$$q_{\rm wave}(x) = \rho_0 U_0^3\, \mathscr{Q}_{\rm wave}(\bar{x}), \quad (62)$$

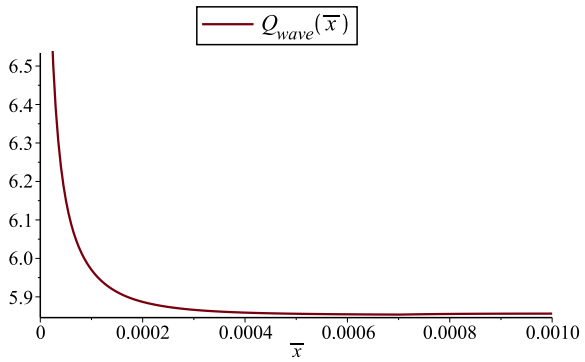
and analogously for the momentum flux of the wave (Fig. 1c)

$$\Pi_{\rm wave}(x) = \rho_0 U_0^2\, \mathscr{P}_{\rm wave}(\bar{x}), \quad \mathscr{P}_{\rm wave} = \frac{1}{4}\left|\widehat{\overline{b}}\right|^2. \quad (63)$$

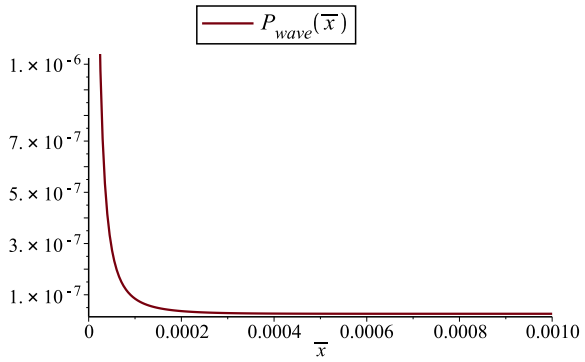
in the next section we will consider all parts of the energy and momentum fluxes.



(a)



(b)



(c)

Fig. 1. AW profiles of velocity (a), energy flux (b) and momentum flux (c).

Total wave fluxes

The total energy and momentum fluxes are integrals over all frequencies. From Eq. (60) we have

$$\mathscr{Q}_{\mathrm{wave},\overline{\omega}}(\overline{x}) = \Psi^{\dagger}_{\overline{\omega}}\overline{g}\Psi_{\overline{\omega}} = \mathscr{W}_{\overline{\omega}}\psi^{\dagger}_{\overline{\omega}}(\overline{x})\overline{g}(\overline{x})\psi_{\overline{\omega}}(\overline{x}), \quad (64)$$

where $\mathscr{W}_{\overline{\omega}}$ is the spectral density of the waves. We can construct the total energy flux of the waves as

$$\mathscr{Q}^{\mathrm{total}}_{\mathrm{wave}}(\overline{x}) = \int_{\overline{\omega}=0}^{\infty} \mathscr{W}_{\overline{\omega}}\psi^{\dagger}_{\overline{\omega}}(\overline{x})\overline{g}(\overline{x})\psi_{\overline{\omega}}(\overline{x})\frac{\mathrm{d}\overline{\omega}}{2\pi} = \sum_{\overline{\omega}>0} \mathscr{W}_{\overline{\omega}}\psi^{\dagger}_{\overline{\omega}}(\overline{x})\overline{g}(\overline{x})\psi_{\overline{\omega}}(\overline{x}), \quad (65)$$

$$\mathscr{Q}^{\mathrm{total}}_{\mathrm{wave}}(0) \equiv \mathscr{Q}_0 = \sum_{\overline{\omega}>0} \mathscr{W}_{\overline{\omega}}\psi^{\dagger}_{\overline{\omega}}(0)\overline{g}(0)\psi_{\overline{\omega}}(0). \quad (66)$$

Observational data gives a power law dependence of the spectral density of AW in the solar corona. One can suppose that the spectral density of the waves coming from the chromosphere has the same power law dependence, *i.e.* $\mathscr{W}_{\overline{\omega}} = C/\overline{\omega}^{\alpha}$. α is between 1.5 and 2: $\frac{3}{2}$ [8], 1.59 [5], 2 [11]. C is the unknown parameter of the theory, which we vary for fixed α in order to reproduce the temperature increase in the transition layer. Note that here we have used the dimensionless frequency. If we want to use the dimensional one, then the parameter C also has to become dimensional. If we know the initial total energy flux of the waves, we can calculate the spectral density as

$$\mathscr{W}_{\overline{\omega}} = \mathscr{Q}_0 / \sum_{\overline{\omega}>0} \psi^{\dagger}_{\overline{\omega}}(0)\,\overline{g}(0)\,\psi_{\overline{\omega}}(0). \quad (67)$$

Analogously to Eq. (65), the total momentum flux is calculated from Eq. (63) as

$$\mathscr{P}^{\mathrm{total}}_{\mathrm{wave}}(\overline{x}) = \sum_{\overline{\omega}>0} \mathscr{W}_{\overline{\omega}}\,\mathscr{P}_{\mathrm{wave},\overline{\omega}}(\overline{x}) = \int_{\overline{\omega}=0}^{\infty} \mathscr{W}_{\overline{\omega}}\,\mathscr{P}_{\mathrm{wave},\overline{\omega}}(\overline{x})\frac{\mathrm{d}\overline{\omega}}{2\pi}. \quad (68)$$

In order to simulate plasma heating by AW with power law spectral density, in the work by Topchiyska [12] an illustration is given with 8 AW with different frequencies. Wave propagation can be easily seen for moderate of $T(l)/T_0 = 3$. In order to concentrate our attention on a realistic temperature increase $T(l)/T_0 = 100$ in the present work we take into account only one wave with frequency 300 Hz. No doubt waves in the Hz range do not exist in the solar corona because they are absorbed during the heating, but we wish to emphasize the importance of Hz range waves in the solar photosphere, which are not observable at the moment.

Mass, energy and momentum fluxes

In the one-dimensional model which we analyze the conservation laws Eq. (1), Eq. (2) and Eq. (3) are converted in three integrals of our dynamic system describing the mass $j = \rho_0 U_0 \overline{j}$, energy $q = \rho_0 U_0^3 \mathscr{Q}$, and momentum $\Pi = \rho_0 U_0^2 \mathscr{P}$ fluxes

$$\overline{j} = \overline{U}\overline{\rho} = 1, \tag{69}$$

$$\mathscr{Q} = \frac{1}{2}\overline{U}^2 + c_{_P}\Theta_0\overline{T} - \overline{\varkappa}\Theta_0 d_{\bar{x}}\overline{T} - \left(\frac{4}{3}\overline{\eta} + \overline{\zeta}\right)\overline{U}\, d_{\bar{x}}\overline{U} + \sum_{\overline{\omega}>0} \mathscr{W}_{\overline{\omega}} \left(\frac{1}{4}\left|\widehat{\overline{u}}_{\overline{\omega}}\right|^2 + \frac{a^2}{2}\left(\overline{U}\left|\widehat{\overline{b}}_{\overline{\omega}}\right|^2 - \mathrm{Re}\left(\widehat{\overline{b}}^*_{\overline{\omega}}\widehat{\overline{u}}_{\overline{\omega}}\right)\right)\right) - \sum_{\overline{\omega}>0} \mathscr{W}_{\overline{\omega}}\frac{1}{2}\overline{\eta}\,\mathrm{Re}\left(\widehat{\overline{u}}^*_{\overline{\omega}}\widehat{\overline{w}}_{\overline{\omega}}\right) = \mathrm{const}, \tag{70}$$

$$\mathscr{P} = \overline{U} + \frac{\Theta_0\overline{T}}{\overline{U}} - \left(\frac{4}{3}\overline{\eta} + \overline{\zeta}\right) d_{\bar{x}}\overline{U} + \sum_{\overline{\omega}>0} \mathscr{W}_{\overline{\omega}}\frac{1}{4}\left|\widehat{\overline{b}}_{\overline{\omega}}\right|^2 = \mathrm{const}. \tag{71}$$

Here we can recognize the energy flux of an ideal inviscid gas

$$\mathscr{Q}^{\mathrm{ideal}}_{\mathrm{wind}} = \frac{1}{2}\overline{U}^2 + c_{_P}\Theta_0\overline{T}, \qquad \Theta = \Theta_0\overline{T}, \tag{72}$$

dissipative energy flux of the wind related to heat conductivity and viscosity

$$\mathscr{Q}^{\mathrm{diss}}_{\mathrm{wind}} = -\overline{\varkappa}\Theta_0 d_{\bar{x}}\overline{T} - \left(\frac{4}{3}\overline{\eta} + \overline{\zeta}\right)\overline{U}\, d_{\bar{x}}\overline{U}, \tag{73}$$

the non-absorptive part of the wave energy flux

$$\mathscr{Q}^{\mathrm{ideal}}_{\mathrm{wave}} = \sum_{\overline{\omega}>0} \mathscr{W}_{\overline{\omega}}\left\{\frac{1}{4}\left|\widehat{\overline{u}}_{\overline{\omega}}\right|^2 + \frac{a^2}{2}\left[\overline{U}\left|\widehat{\overline{b}}_{\overline{\omega}}\right|^2 - \mathrm{Re}\left(\widehat{\overline{b}}^*_{\overline{\omega}}\widehat{\overline{u}}_{\overline{\omega}}\right)\right]\right\}, \tag{74}$$

and the absorptive part of the wave energy flux

$$\mathscr{Q}^{\mathrm{diss}}_{\mathrm{wave}} = -\sum_{\overline{\omega}>0} \mathscr{W}_{\overline{\omega}}\frac{1}{2}\overline{\eta}\,\mathrm{Re}\left(\widehat{\overline{u}}^*_{\overline{\omega}}\widehat{\overline{w}}_{\overline{\omega}}\right) \tag{75}$$

proportional to the viscosity. Analogously for the momentum flux we have:

$$\mathscr{P}^{\mathrm{ideal}}_{\mathrm{wind}} = \overline{U} + \frac{\Theta_0\overline{T}}{\overline{U}}, \tag{76}$$

$$\mathscr{P}^{\mathrm{diss}}_{\mathrm{wind}} = -\left(\frac{4}{3}\overline{\eta} + \overline{\zeta}\right) d_{\bar{x}}\overline{U}, \tag{77}$$

$$\mathscr{P}^{\mathrm{ideal}}_{\mathrm{wave}} = \sum_{\overline{\omega}>0} \mathscr{W}_{\overline{\omega}}\frac{1}{4}\left|\widehat{\overline{b}}_{\overline{\omega}}\right|^2, \tag{78}$$

$$\mathscr{P}^{\mathrm{diss}}_{\mathrm{wave}} = 0 \tag{79}$$

for the transversal AW. As a rule the dissipative fluxes are against the non-dissipative ones. One can introduce non-ideal wind energy flux

$$\widetilde{\mathscr{Q}} \equiv \mathscr{Q}^{\mathrm{nonideal}}_{\mathrm{wind}} = \mathscr{Q}^{\mathrm{diss}}_{\mathrm{wind}} + \mathscr{Q}^{\mathrm{total}}_{\mathrm{wave}} = \mathscr{Q} - \mathscr{Q}^{\mathrm{ideal}}_{\mathrm{wind}} = -\overline{\varkappa} d_{\bar{x}}\overline{T} - \left(\frac{4}{3}\overline{\eta} + \overline{\zeta}\right)\overline{U} d_{\bar{x}}\overline{U} - \sum_{\overline{\omega}>0} \mathscr{W}_{\overline{\omega}}\left(\frac{1}{2}\overline{\eta}\mathrm{Re}\left(\widehat{\overline{u}}^*_{\overline{\omega}}\widehat{\overline{w}}_{\overline{\omega}}\right)\right) + \sum_{\overline{\omega}>0} \mathscr{W}_{\overline{\omega}}\left[\frac{1}{4}\left|\widehat{\overline{u}}_{\overline{\omega}}\right|^2 + \frac{a^2}{2}\left(\overline{U}\left|\widehat{\overline{b}}_{\overline{\omega}}\right|^2 - \mathrm{Re}\left(\widehat{\overline{b}}^*_{\overline{\omega}}\widehat{\overline{u}}_{\overline{\omega}}\right)\right)\right], \tag{80}$$

$$\mathscr{Q}^{\mathrm{total}}_{\mathrm{wave}} = \mathscr{Q}^{\mathrm{ideal}}_{\mathrm{wave}} + \mathscr{Q}^{\mathrm{diss}}_{\mathrm{wave}}. \tag{81}$$

The non-ideal wind momentum flux is

$$\widetilde{\mathscr{P}} \equiv \mathscr{P}^{\mathrm{nonideal}}_{\mathrm{wind}} = \mathscr{P}^{\mathrm{diss}}_{\mathrm{wind}} + \mathscr{P}^{\mathrm{total}}_{\mathrm{wave}} = \mathscr{P} - \mathscr{P}^{\mathrm{ideal}}_{\mathrm{wind}} = -\left(\frac{4}{3}\overline{\eta} + \overline{\zeta}\right) d_{\bar{x}}\overline{U} + \sum_{\overline{\omega}>0} \mathscr{W}_{\overline{\omega}}\frac{1}{4}\left|\widehat{\overline{b}}_{\overline{\omega}}\right|^2, \tag{82}$$

$$\mathscr{P}^{\mathrm{total}}_{\mathrm{wave}} = \mathscr{P}^{\mathrm{ideal}}_{\mathrm{wave}} + \mathscr{P}^{\mathrm{diss}}_{\mathrm{wave}}. \tag{83}$$

Then according to Eq. (28) we have

$$\chi(\bar{x}) \equiv \widetilde{\mathscr{Q}}\Big|_{\bar{x}}^{0} = \mathscr{Q}_{\text{wind}}^{\text{ideal}}\Big|_{0}^{\bar{x}}, \tag{84}$$

$$\tau(\bar{x}) \equiv \widetilde{\mathscr{P}}\Big|_{\bar{x}}^{0} = \mathscr{P}_{\text{wind}}^{\text{ideal}}\Big|_{0}^{\bar{x}}. \tag{85}$$

This analysis finally reveals the usefulness of dimensionless variables. The dimensional momentum flux τ and energy flux χ participate in the important analytical expressions for the wind variables Eq. (32) and Eq. (34).

Self-consistent procedure and results

First we fix the boundary condition, the temperature T_0 and proton density $n_p(0)$ for $x = 0$. For these parameters we calculate density ρ_0, Debye radius length $r_{\text{D}}(0)$, Coulomb logarithm Λ_0, viscosity η_0, heat conductivity $\varkappa_0$, Ohmic resistivity $\rho_{\Omega 0}$, and sound speed $c_{\text{s}}(0)$. Initial velocity of the wind is better to be parameterized by the dimensionless parameter $s \gg 1$, i.e. $U_0 = c_{\text{s}}(0)/s$. Analogously plasma beta parameter β_0 determines the Alfvén speed at $V_{\text{A}}(0) = \sqrt{\frac{\gamma}{2\beta}} c_{\text{s}}(0)$. Let us also fix the maximal frequency for which we will consider plasma waves ω and calculate the absorption rate of the energy density of Alfvén waves $2k''(0)$. One can choose the interval of the solution of MHD equations to be much larger than the AW mean free path $1/2k''(0)$, for example

$$l = \frac{10}{2k''(0)} = \frac{10V_{\text{A}}^3(0)}{\nu_{\text{k}}(0)\omega^2}. \tag{86}$$

Having units for length l, velocity U_0 and density ρ_0 we can calculate dimensionless variables at $\bar{x} = 0$: $\overline{\varkappa}_0$, $\overline{\eta}_0$, and Θ_0.

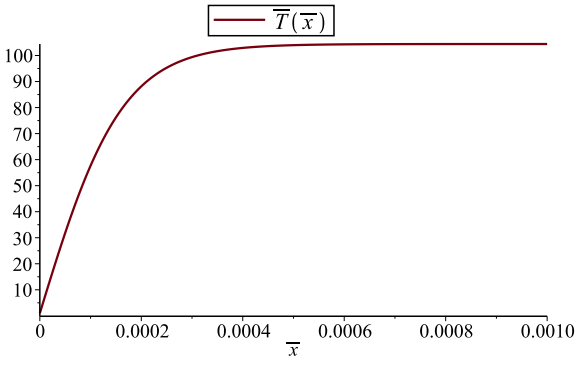


Fig. 2. Dimensionless temperature vs dimensionless distance. A hundred times increase of the plasma temperature by absorption of AW.

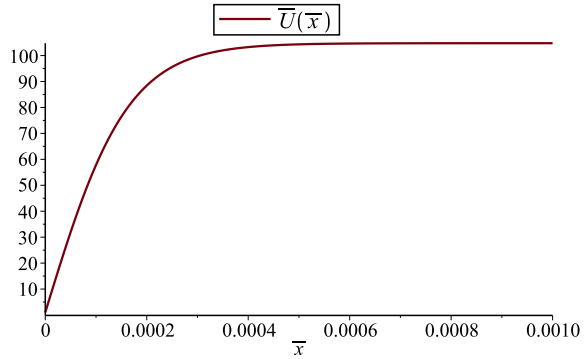


Fig. 3. Dimensionless wind velocity vs dimensionless distance. A hundred times increase of the plasma velocity by absorption of AW.

The input parameters of the program are T_0, $n_{\text{tot}}(0)$, β_0, ω, and s which parameterizes $j = \langle m \rangle n_{\text{tot}}(0) U_0$. We have obtained our results by setting $T_0 = 6000$ K, $n_{\text{tot}}(0) = 5 \times 10^{14}$ m^{-3}, $\beta_0 = 1$, $\omega/2\pi = 300$ s^{-1}, $s = 137$. We calculate l, a, $\overline{\eta}_0 = \overline{\nu}_0$, $\overline{\kappa}_0$ and choose some A_{wave} which finally determines increasing of the temperature $\overline{T}(1) = T(l)/T(0)$.

In our self-consistent calculation we use the nonlinear fit $\overline{T}(\bar{x}) = 1 + \left(\sum_{n=0}^{3} a_n \bar{x}^n\right) \tanh(b_1 \bar{x})$ for the numerically calculated profile of the temperature $\overline{T}(\bar{x})$ (Fig. 2) as well as for the velocity $\overline{U}(\bar{x})$ (Fig. 3). In order to accelerate the convergence for the initial approximation we use $a_0 = 20$, $a_1 = a_2 = a_3 = 0$, $b_1 = 10$. Let us explain in detail the successive approximations.

1. At fixed wind profiles $\overline{T}(\bar{x})$ and $\overline{U}(\bar{x})$ we calculate $\Lambda = \Lambda_0 + \frac{3}{2}\ln\overline{T} + \frac{1}{2}\ln\overline{U}$, $\overline{\eta}$, $\overline{\varkappa}$, $\mathrm{d}_{\bar{x}}\overline{\eta}$, and dimensionless matrices $\overline{\mathsf{M}}$ and $\overline{g}$. Then we have to solve the wave equation and to renormalize the solution with some fixed dimensionless energy flux for the R-mode $\mathscr{Q}_{\text{wave}}(0)$.

2. Using so obtained wave variables Ψ we have to solve equations (30) and (31) to find $\overline{U}(\bar{x})$ and $\overline{\Theta}(\bar{x})$, and respectively $\overline{T}(\bar{x})$ from Eq. (29). The variables $\overline{\eta}$, $\overline{\varkappa}$, $\mathrm{d}_{\bar{x}}\overline{\eta}$, and $\mathrm{d}_{\bar{x}}\overline{\varkappa}$, which participate in the coefficients have to be calculated simultaneously.

3. Having solved the equations for the wind variables and formerly the equations for the wave variables we can calculate the total energy and momentum flux. If the maximal relative difference between two successive temperature profiles is larger than some predetermined value we go to step 1 and repeat the procedure.

The width of the transition layer λ, and the increasing of the temperature $\overline{T}(1)$ are functions of

the wave energy flux coming from the chromosphere $q_{\rm wave}(0)$.

$$\frac{l}{\lambda} = \max_x \left| \mathrm{d}_x \ln \overline{T} \right| \simeq \frac{1}{l\, b_1}. \qquad (87)$$

The wave amplitude $A_{\rm wave}$ is determined in a way that ensures the desired temperature increase $\overline{T}(1;A_{\rm wave}) = \overline{T}(l)/\overline{T}(0)$ in the end (Fig. 2) of the space interval. In our numerical illustration we used one wave which corresponds to δ-like spectral density of AW. In general, at fixed temperature increase and chosen spectral density of the AW the MHD theory has no more free parameters. All that is left is to compare the calculations with other models and observational data for heating of the solar corona and launching of the solar wind.

CONCLUSION

Discussions

In spite that iron was suspicious from the very beginning the problem of Coronium was a 70 year standing mystery until unambiguous identification as Fe^{13+} by Grotrian and Edlen in 1939. The same 70 year time quantum was repeated. In 1947 Alfvén [2] advocated the idea that absorbtion of AW is the mechanism of heating of solar corona. Unfortunately the idea by Swedish iconoclast [13] was never realized in original form: what can be calculated, what is measured, what is explained and what is predicted. That is why there is a calamity of ideas still on the arena, for a contemporary review see the SOHO proceedings ([14]). The wide variety of effects in the physics of the corona is not directly related with hydrodynamic mechanism of its creation from the chromosphere as gerontology has few common points with tocology. From qualitative point of view the narrow width of the transition layer $\lambda = \min |\mathrm{d}x/\mathrm{d}\ln T(x)|$ is the main property which should be compared against the predictions of other scenarios. For example, in order for the nanoflare hypothesis to be vindicated [15] such reconnections are needed to explain the narrow width of the transition layer at the same boundary conditions of wind velocity and temperature. Moreover electric fields of the reconnections heats mainly the electron component of the plasma. How then proton temperature in the corona is higher? Launching of Hinode gave a lot of hints for the existence of AW in the corona [16], see also [17]. However most of the research was in the UV region where high frequency AW are already absorbed. All observations are for low frequency (mHz range) AW for which hot corona is transparent. The best that can be done is to extract the low frequency behavior of the spectral density of AW and to extrapolate to higher frequencies responsible for heating. The observed AW are irrelevant for the heating. In order to identify AW responsible for the heating it is necessary to investigate high frequency (1 Hz range) AW in the cold chromosphere using optical not UV spectral lines. We are unaware whether such type of experiments have been planned. One of the purposes of the present work is to focus the attention of experimentalists on the 1 Hz range AW in the chromosphere, which we predict on the basis of our MHD analysis. For such purposes we suggest Doppler tomography [18] of Hα; Ca lines are another possibility. Doppler tomography was successfully used for investigation of rotating objects, such as accretion disks [19] and solar tornados [20]. Here we wish to mention the Doppler tomography by Coronal Multi-channel Polarimeter build by Tomczyk [8]. For investigation of AW by Doppler tomography we suggest development of frequency dependent Doppler tomography operating as a lock-in voltmeter. The data from every space pixel should be multiplied by $\sin\omega t$ and integrated over many wave periods. Finally one can observe time averaged distribution of the AW amplitude. Systematic investigation of such frequency dependent Doppler tomograms will reveal that the Swedish iconoclast [13, 21] is again right that AW heat the solar corona, after another 70 years of dramatic launching of vast variety of ideas.

Plasma heating by AW – a historical perspective

What have we learned from the one-dimensional static MHD problem? We have demonstrated that qualitatively predicted self-induced opacity of plasma is an intrinsic property. Absorption of AW causes viscous heating of ions and that is why the proton temperature is higher than the electron one. In this way we have revealed an effective method for ion heating which can be applied to many plasma problems. Actually plasma heating by MHD waves is used in the MIT alcator [22]. We suggest however that the toroidal geometry can be replaced by Budker probkotron geometry, in which the energy of the AW will be focused in a narrow jet with a hundred times increased temperature. A de Laval nozzle will be realized by strong magnetic fields. We do believe that that this will be an effective method for navigation in the Solar System (cf. [23]). Electric power from a nu-

clear reactor will create a fast electron-proton jet and this will dramatically decrease the initial mass of the rocket. For large-scale Earth-based installations such a jet of high-temperature deuterium will inject a fresh idea in nuclear fusion physics.

Acknowledgement. *Authors are thankful to Yana Maneva [24–27] and Martin Stoev for the collaboration in the early stages of the present research [28] when the idea of self-induced opacity was advocated and consideration of many problems related to physics of solar corona. Fruitful comments and discussions with Tsvetan Sariisky are highly appreciated. Authors are also thankful to Eckart Marsch for the hospitality during the conference "From the Heliosphere into the Sun – Sailing Against the Wind" (http://www.mps.mpg.de/meetings/hcor/) and to Ivan Zhelyaskov, Zlatan Dimitrov, Ramesh Chandra, Steven R. Cranmer, Leon Ofman, Jaime Araneda, Plamen Angelov, Yurii Dumin, and Yana Maneva for the interest and comments. This work was partially supported by Indo-Bulgarian scientific grant No CSTC/India 01/7. This work was completed during the 5th Black Sea School and Workshop on Space Plasma Physics, Kiten, 2014.*

REFERENCES

[1] P. Swings, Astrophys. J. **98**, 116–128 (1943); B. Edlén, Arkiv f. Matem. Astr. och Fys. **28**, B No. 1 (1941); B. Edlén, Zs. f. Ap. **22**, 30 (1942)

[2] H. Alfvén, MNRAS **107**, 211–219 (1947)

[3] H. Alfvén, Nature **150**, 405–406 (1942)

[4] J. Heyvaerts and E.R. Priest, A&A, 117, 220 (1983)

[5] L. P. Chitta, A. A. Ballegooijen, L. Rouppe van der Voort, E.E. DeLuca, and R. Kariyappa, Asprophys. J; http://arxiv.org/abs/1204.4362

[6] P. Antolin and K. Shibata, ApJ **712**, 494–510 (2010)

[7] M. Hahn and D. W. Savin, ApJ **776**, 78 (2013)

[8] S. Tomczyk and S.W. McIntosh, Asprophys. J; http://arxiv.org/abs/0903.2002

[9] S. Tomczyk, S.W. McIntosh, S.L. Keil, P.G. Judge, T. Schad, D.H. Seeley, and J. Edmondson, Science, 317, 1192 (2007)

[10] R.P. Feynman, R.B. Leighton, and M. Sands, *The Feynman Lectures on Physics. Exercises* (Addison-Wesley, London, 1965), Problems 40.4-5

[11] L.F. Burlaga and W.H. Mish, J. Gephys. Res., 92, 1261 (1987); E. Marsch, in Physics and Chemistry in Space – Space and Solar Physics, Vol. 21, Series Editors: M.C.E. Huber et al., Physics of the Inner Heliosphere, Vol. 2, Editors: R. Schwenn and E. Marsch, Springer-Verlag Berlin (1991); Fig. 10.4

[12] R.V. Topchiyska, N.I. Zahariev, T.M. Mishonov, Bulg. J. Phys. 40 (2013) 56–77

[13] A. J. Dessler, Science **170**, 604 - 606 (1970); http://www.sciencemag.org/content/170/3958/604

[14] *Proceedings of the SOHO 15 Workshop – Coronal Heating* 6-9 September 2004, St. Andrews, Scotland (ESA SP-575, December 2004) Editors: R.W. Walsh, J. Ireland, D. Danesy, and B. Fleck

[15] Ch. Day, Phys. Today **62**, May 18–21 (2009)

[16] B. De Pontieu, *et al.,* Science **318**, 1574–1577 (2007); T.J. Okamoto *et al.,* Science **318**, 1577-1580 (2007); R. Erdélyi and V. Fedun, Science **318**, 1572-1574 (2007); Y. Katsukawa *et al.*, Science **318**, 1594-1597 (2007)

[17] D. Jess *et al.,* Science **323**, 1582–1585 (2009)

[18] T. Marsh, Europhysicsnews **36** No. 4, 133-138 (2005)

[19] T. R. Marsh and K. Horn, MNRAS **235**, 269–286 (1988)

[20] http://www.mps.mpg.de/en/forschung/sonne/

[21] *"Students using astrophysical textbooks remain essentially ignorant of even the existence of plasma concepts, despite the fact that some of them have been known for half a century. The conclusion is that astrophysics is too important to be left in the hands of astrophysicists who have gotten their main knowledge from these textbooks. Earthbound and space telescope data must be treated by scientists who are familiar with laboratory and magnetospheric physics and circuit theory, and of course with modern plasma theory."* Hannes Alfvén quoted by Anthony L. Peratt, 'Dean of the Plasma Dissidents', Washington Times, supplement: The World and I (May 1988), 197. http://todayinsci.com/A/Alfven_Hannes/AlfvenHannes-Quotations.htm

[22] J. A. Snipes *et al.,* Phys. Plasmas **12**, 056102 (2005); http://dx.doi.org/10.1063/1.1865012

[23] E. Y. Choueiri, Scientific American, **300**, 58-65 (2009); doi:10.1038/scientificamerican0209-58

[24] J. A. Araneda, Y. Maneva, and E. Marsch, Phys. Rev. Lett., **102**, 175001 (2009)

[25] Y. G. Maneva, J. A. Araneda, and E. Marsch, ed. by I. Zhelyazkov, AIP Conference Proceedings, vol. **1121**, pp. 122–126 (2009)

[26] Y. G. Maneva, J. A. Araneda, and E. Marsch, Twelfth International Solar Wind Conference, eds. M. Maksimovic, K. Issautier, N. Meyer-Vernet, M. Moncu-

quet and F. Pantellini, AIP Conference Proceedings, vol. **1216**, pp. 227–230, (2010)

[27] Y. G. Maneva, Ph.D. Thesis, (Göttingen, uni-edition, 2010), ISBN 978-3-942171-39-7

[28] T. M. Mishonov, M. V. Stoev, and Y. G. Maneva, Eur. Phys. J. D **44**, 533–536 (2007)

НАГРЯВАНЕ НА СЛЪНЧЕВАТА КОРОНА ЧРЕЗ АЛФВЕНОВИ ВЪЛНИ – САМОИНДУЦИРАНА НЕПРОЗРАЧНОСТ

Т. Мишонов, Н. Захариев, Р. Топчийска, Б. Лазов, Ст. Младенов

Катедра по теоретична физика, Физически факултет, Софийски университет "Св. Климент Охридски", бул. "Дж. Баучер" №5, 1164 София, България

(Резюме)

За първи път Ханес Алфвен предлага идеята, че нагряването на слънчевата корона се осъществява благодарение на Алфвенови вълни (АВ) [1,2]. Тези вълни се генерират от турбуленцията в зоната на конвекция и се разпространяват по магнитните силови линии.

Цели. Пресметнато е статично разпределение на температурата и скоростта на вятъра в преходната зона, използвайки магнитохидродинамика (МХД) на напълно йонизирана водородна плазма.

Методи. Числено решение на изведените уравнения позволява да се определи дебелината на преходния слой между хромосферата и короната, в който се поражда явлението самоиндуцирана непрозрачност на високочестотни АВ. Обособяването на граница на зоната е директно следствие от самосъгласуваното МХД разглеждане на разпространението на АВ.

Резултати. Нискочестотните МХД вълни, идващи от Слънцето, се отразяват силно от тесния преходен слой, а високочестотните вълни се поглъщат. Това ни позволява да предскажем значителна спектрална плътност на АВ във фотосферата. Числено разглеждане позволява отчитането на падащи АВ с произволна спектрална плътност.

Заключение. Идеята, че АВ могат да нагреят слънчевата корона, принадлежи на Ханес Алфвен. Нашата работа се състои в решаването на съответните МХД уравнения. Сравняването на решението с експериментални данни е от съществено значение за разкриването на механизма на нагряване на короната.

1. H. Alfvén, *Nature* **150** (1942), 405-406.

2. H. Alfvén, *MNRAS* **107** (1947), 211-219.

Bulgarian Chemical Communications, Volume 47, Special Issue B (pp. 380–389) 2015

Temporal variations of the fractal properties of seismicity

E. Marekova*

Faculty of Physics, Paisii Hilendarski University of Plovdiv, 24 Tsar Asen Str., BG-4000 Plovdiv, Bulgaria

For many natural phenomena and objects a state of chaos and independence from the scale at which they are studied is typical. Examples of such phenomena are earthquakes, the study of which shows that many of their properties are independent from their scale. In the study of earthquakes the property of scale independence has first been established for their distribution in magnitude (*Gutenberg-Richter* law), as well as for the decline in the aftershocks intensity in time (*Omori* equation). Newer studies show that other properties of the earthquakes are also characterized by independence from the scale of realization. Both the aftershock occurrence and the regional seismic process, for example, exhibit fractal properties. This paper evaluates the temporal variation of the fractal coefficients of the earthquake distribution by area for a number of seismic regions. In the analysis of the spatial structure the so-called two-point correlation integral has been used. Analogical estimations of the **b**-value of the *Gutenberg-Richter* law of repeatability have been made. A negative correlation between the fractal coefficients of the earthquake series and their corresponding **b**-values has been found. The temporal variation of the fractal coefficients of the earthquake distribution by area has been similarly analyzed for several aftershock series. A positive correlation between the fractal coefficients of the aftershock series and their corresponding **b**-values has been established.

Key words: seismicity, fractal dimension, b-value, temporal variations

INTRODUCTION

Fractal structures are observed for a wide range of fractures – from microfractures (10^{-6} m) to megafaults (10^5 m) [1–4]. In such systems the numbers of fractures that are larger than a specified size are related by power law to the size. The physical laws governing the fractal structures are scale-invariant in nature.

The fractal structures may be either homogeneous or multiscaling characteristics. It is considered nowadays that many physical quantities disobey the conventional scaling laws.

Seismic activity in a given region has a fractal structure in relation to time, space and in magnitude [5]. The occurrence of earthquakes is causally linked to destructions, having a fractal structure. Fractal dimensions give a quantitative measure of the spatial clustering of epicenters/hypocenters, as well as of seismicity of the region. Therefore this approach can also be used for evaluation of the probabilistic seismic hazard [6].

Some authors have used this method in different seismically active regions in order to study the fractal nature of the earthquake occurrence, the fault structures, and the resultant seismic hazard, e.g., Kanto Japan [7], Mexican subduction zone [8], North Anatolian block [9], Himalayan region [10], Koyana-Warna region [11], Hokkaido, Japan [12], East Java-Indonesia [13], Northwest Himalayan region [14].

Aki [15] shows theoretically that the fractal dimension (**D**) holds a simple relation with the **b**-value of the Gutenberg-Richter law (i.e. **D**=2**b**). The **b**-value characterizes the fractal dimension in the domain of energy of the earthquakes [15, 16], whereas **D** provides a measure of the fractal dimension of the earthquake distribution in space. One could therefore expect a correlation between **D** and b values, but the character of the correlation can change [5, 17–19].

For an aftershock sequence, Ponomarev et al. [20] have shown that the **b**-values tend to increase with time, while the fractal dimension values tend to decrease. They have proposed that the temporal change in **D**- and **b**-values characterizes the specific evolution of the aftershock sequences. For the 2001 Bhuj earthquake sequence, the **b**-values and the spatial correlation dimensions suggest a negative correlation for the first 2 months, while they show a positive correlation for the remaining months of 2001 [21].

In this work, the correlation integral method [22, 23] is used to determine the correlation dimension and its variations with time. The temporal variation studies are carried out to see its variation by considering consecutive windows with overlapping. Similar kinds of studies have been realized by other workers and similar results have been reported [24].

* To whom all correspondence should be sent:
eligeo@uni-plovdiv.bg

© 2015 Bulgarian Academy of Sciences, Union of Chemists in Bulgaria

RESEARCH METHODOLOGY

The application of the methods of the fractal sets [25] has become widespread in geophysics. This reflects the fact that fractal analysis is one of the methods developed for studying self-similar phenomena and processes, and self-similarity plays an important role in geophysics [26, 27].

One example of a self-similar structure is the seismic regime, i.e., the set of earthquakes considered as points in space and time and associated with an additional parameter of energy. A classical example, confirming the self-similarity of the seismic regime is the Gutenberg-Richter law of repeatability, having fundamental significance in seismology. For the average number of earthquakes on a given area N (M) with magnitudes bigger than M, attributed to a single time interval, it is given by the expression:

$$\lg N(M) = a - bM, \tag{1}$$

where a and b are parameters of the law of recurrence.

Estimation of the value of the parameter b is made by the method of maximum likelihood [28]:

$$b = \frac{\lg e}{\overline{M} - M_C} \tag{2}$$

Where $\overline{M}$ is the average value of the magnitudes and M_C is the minimum value of completeness of the earthquake catalog.

The present study uses the fractal correlation dimension $\mathbf{D_2}$ of the earthquake epicentral distribution. The so-called *correlation integral* $C(\Delta)$ is used as statistical estimation of the fractal dimension in the realization of the N vector $\{x_1, \ldots, x_N\}$:

$$C(\Delta) = \frac{2}{N(N-1)} \sum_{i,j} H(\Delta - |\mathbf{x}_i - \mathbf{x}_j|) \tag{3}$$

where $H(z)$ is the Heaviside step function, equal to 1 at $z \geq 0$ and equal to 0 at $z < 0$, and the summation is carried out in all different pairs (x_i, x_j) [22, 23]. If the set of points is scale-invariant, then $C(\Delta)$ is represented by a power law: $C(\Delta) \propto \Delta^{\mathbf{D_2}}$, where $\mathbf{D_2}$ is defined as *correlation fractal dimension*.

$$\mathbf{D_2} = \lim_{r \to 0} \frac{\lg C(r)}{\lg r} \tag{4}$$

where N is the total number of points (earthquakes), $r = |\mathbf{x}_i - \mathbf{x}_j|$ is the distance between the vectors $\mathbf{x}_i$ and $\mathbf{x}_j$, which define the location of the points. The distance between two events in km is calculated by the formula:

$$r = 111 \arccos \Big[\cos\theta_1 \cos\theta_2 + \sin\theta_1 \sin\theta_2 \cos(\phi_1 - \phi_2) \Big] \tag{5}$$

where (θ_1, ϕ_1) and (θ_2, ϕ_2) are the latitude and longitude of each two earthquakes from the series.

Defined this way, the parameter gives a measure of the level of fractal clusterization of the points. The lower values define tighter clusters [3]. If the points are randomly distributed in a two-dimensional space, then $\mathbf{D_2}$ is 2. Reduction of its value to less than 2 means that the distribution of points tends to clustering to a greater extent than if it is completely random.

These two parameters - **b** and $\mathbf{D_2}$ - are independent measures of the scale-invariant properties of the earthquake distribution in magnitude, and, respectively, of the earthquake spatial clustering.

DATA AND OBTAINED RESULTS

Seismic Regions

For studying the temporal properties of seismicity the following data have been used: from the regions Riverside and Parkfield in California; from California North Coast; and from Central Asia. Each catalogue contains several thousands of earthquakes for the period 1900-2006.

The catalogues have first been filtered in order to remove the aftershock (secondary) events. This has been carried out by means of the program Zmap [29], in which the *Reasenberg* [30] method of declusterization has been embedded. In order to provide homogeneity of the declusterized catalogue, a check for data completeness has also been performed to define the minimum magnitude $\mathbf{M_C}$ of the catalogue data, over which all events in the considered spatial and temporal range, covered by the catalogue, have been registered.

This study defines the **b**-value from the *Gutenberg-Richter* law (1) and the fractal correlation dimension $\mathbf{D_2}$ – (3) and (4) – of the earthquake epicentral distribution. The graph of the cumulative number of distances between the pairs of epicenters in a double-logarithmic scale is used. The fractal coefficient is obtained from the slope of the straight-line portion of the dependency, built by the method of least squares.

Only the coordinates of the earthquake epicenters have been considered in the present study, although the analysis of the hypocenters in the real three-dimensional space would be more natural from a physical point of view. This is justified by the fact that in the existing catalogues the depth of the earthquakes is defined with lowest precision.

A major task is to trace the variation of the parameters **b** and $\mathbf{D_2}$ over time. In order to calculate the values of these parameters, a program in FORTRAN has been developed. A "sliding window" with a fixed number of events, for which **b** and $\mathbf{D_2}$ are obtained, has been used. The parameters are related to the period of time, covered by the corresponding window. Then this "window" is shifted at a certain pace, overlapping part of the data from the previous calculation, and the procedure is repeated again. The choice of windows with a certain number of events is a better option than fixing the duration of a time interval for making the same calculations.

After that diagrams are drawn to trace the development of both parameters over time and the availability of a correlation between them.

Table 1 presents the number of earthquakes for each studied region, remaining after the removal of the aftershock events, as well as the magnitude of completeness $\mathbf{M_C}$. The parameters of the "sliding windows", as well as the number of the overlapping earthquakes are also given in the table. The last column shows the obtained correlation between the parameters **b** and $\mathbf{D_2}$.

Parkfield region, California, is situated in a relatively straight-line section of the fault San Andreas in Central California. In this region the movement on the fault occurs as a right-lateral slip during earthquakes and also as an aseismic slip ("creep"). The catalogue contains 607 earthquakes with magnitude between 3.0 and 5.8 for the period (1932-2006). The catalogue data about the considered region are within the geographic window: $(35.5 \div 36.5^{\circ}N)$ and $(119.8 \div 121^{\circ}W)$. The depth interval of the hypocenters deployment is up to 30 km [31].

The results from the calculations related to this region are shown in Fig. 1. As it can be seen, both studied parameters develop in time, and the biggest dynamics is observed for the period (1983-1987), which is associated with the occurrence of two strong earthquakes in the region.

The earthquake catalogue related to the northern part of the coastal region of California contains 2057 events with magnitude of $M \geq 3.0$ for the period (1971-2001). The earthquakes are located in the geographic window $(36.5 \div 39.0^{\circ}N)$, $(120.5 \div 123.0^{\circ}W)$. [32]. The results from the analysis are shown in Fig. 1. Both studied parameters show development over time and the most variation is observed for the period (1984-1990), during which a number of strong earthquakes happened and in 1989 an earthquake with magnitude $M = 7.9$ occurred in this region.

The region of Central Asia is characterized by a high level of intercontinental seismicity, justified by intensive geodynamic interaction between a number of big lithospheric plates - the European, Asian, Indian, and Chinese. The catalogue contains 5218 earthquakes with magnitude between 3.3 and 7.7 for the period (1962-1993) [33]. The events are located in the following geographical window: $(35.0 \div 45^{\circ}N)$, $(65 \div 82^{\circ}E)$. A depth interval of up to 100 km has been chosen in order to analyze only the crustal seismicity. For this region the biggest variations are characteristic for the period (1971-1975).

South California is one of the most seismic regions in the world. Riverside region's geology is complex, mainly as a result of the interaction between the fault tectonics of San Andreas fault and the compression movements of the Peninsular Ranges chain. The full catalogue of the Riverside region contains 9263 earthquakes with magnitudes from 3.0 to 7.7 and depth up to 60 km, for the period (1932-2006) [34]. The data are placed in the geographical

Table 1. Data about the researched regions

Seismic zone/region	**Number of earthquakes**	**Magnitude of completeness $\mathbf{M_C}$**	**Number of events in "sliding window"**	**Number of overlapping events**	**Correlation equation**
Parkfield, California	527	3.3	100	90	$\mathbf{b} = 1.72 - 0.68\mathbf{D_2}, R = -0.79$
North Bay, California	2057	3.0	200	180	$\mathbf{b} = 1.72 - 0.68\mathbf{D_2}, R = -0.68$
Central Asia	3170	3.3	300	200	$\mathbf{b} = 1.23 - 0.32\mathbf{D_2}, R = -0.54$
Riverside, California	5131	3.0	200	180	$\mathbf{b} = 1.16 - 0.09\mathbf{D_2}, R = -0.14$

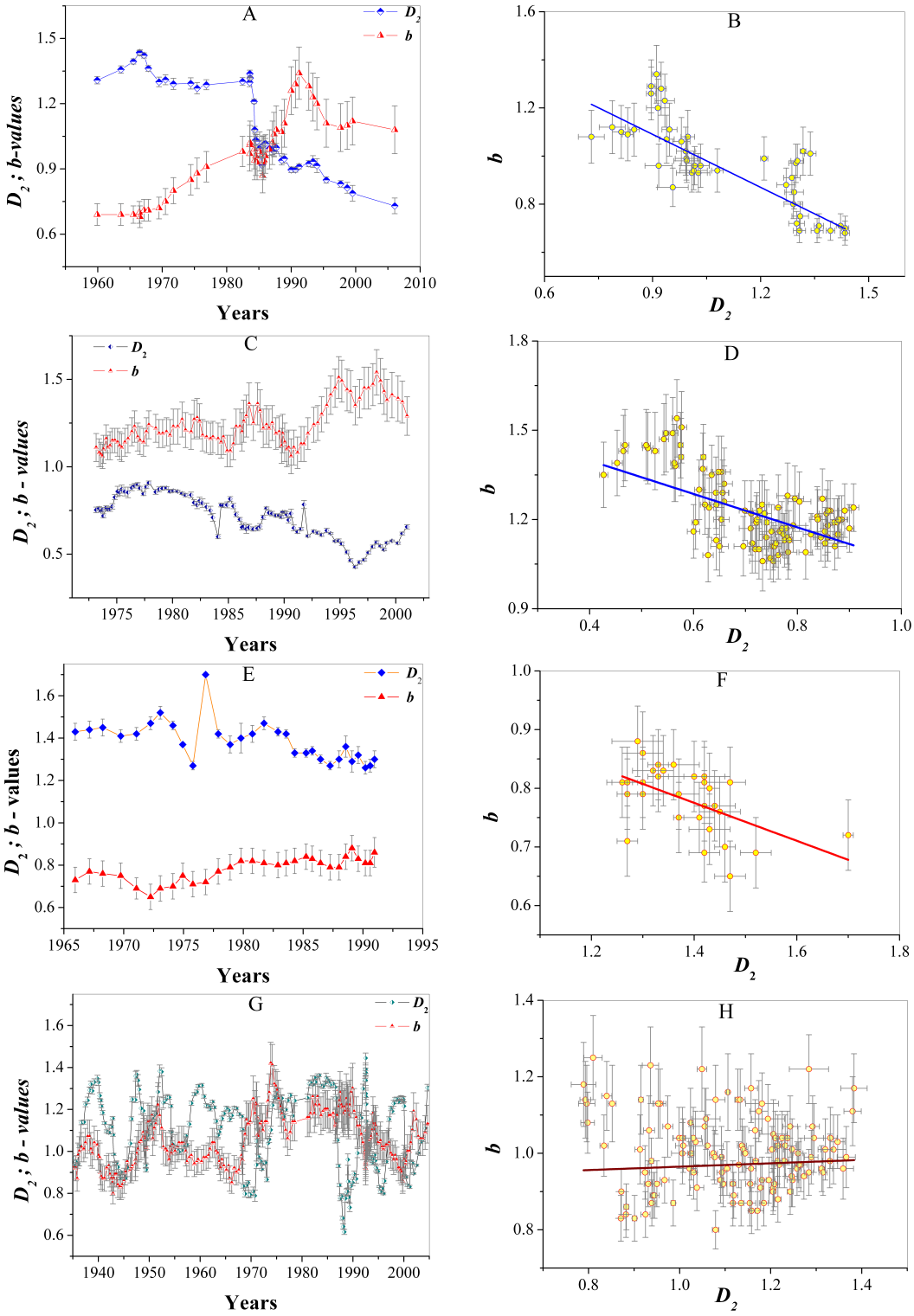


Fig. 1. Temporal variations of the parameter **b** and the fractal coefficient $\mathbf{D_2}$ for the studied seismic regions: A – Parkfield; C – North Bay, California; E – Central Asia; G – Riverside (The temporal coordinate corresponds to the date of the last earthquake, falling into the corresponding window of calculations.). Correlation between the parameter **b** and the fractal coefficient $\mathbf{D_2}$: B – Parkfield; D – North Bay, California; F – Central Asia; H – Riverside. For each value of the shown parameters the standard deviations are also depicted.

window $(32.5 \div 35.5^{\circ}N)$, $(114 \div 119^{\circ}W)$. As it can be seen from Fig. 1, the variations in both studied parameters - **b** and $\mathbf{D_2}$ - are very dynamic. For the period (1932-2006) thirteen (13) earthquakes occurred there with magnitude $M \geq 6.0$ and 50 - with magnitude $5.0 \leq M < 6.0$, not taking into account the aftershocks, observed after some of the strongest quakes. Strong activation was observed for the periods (1945-1952), (1968-1971), (1986-1992).

All studied seismic regions are characterized by a negative correlation between **b** and $\mathbf{D_2}$, whose parameters are given in Table 1.

Aftershock series

As a second stage of this research, the following aftershock series were considered: Sumatra 2004 and Sumatra 2007, Indian ocean; Kashmir 2005, Asia; Parkfield 2004, California; Kobe 1995, Japan; Loma Prieta 1989, California.

On 26.12.2004 a destructive earthquake with magnitude $M_W 9.0$ occurred on the island of Sumatra in the Indian Ocean. The catalogue of the aftershock series contains 6386 events with magnitude $M \geq 3.2$ for the period (2004-2008). For the second aftershock series of the earthquake with magnitude $M_W 8.5$ on the island of Sumatra on 12.09.2007, data about 607 events with $M \geq 3.2$ have been obtained for the period (2007-2008) [35].

The initial catalogue of earthquakes in the region of Kashmir, Northeren Pakistan, contains 710 quakes with magnitude $M \geq 2.9$ for the period (2005-2008). The main quake from 08.10.2005 was with $M_W 7.6$ [35].

Another studied aftershock series is related to an earthquake near Parkfield, California, which occurred on 28.09.2004. The series contains 10299 events with magnitude $M \geq 0.0$ for the period (2004-2008) [32].

On 17.01.1995 a destructive earthquake occurred in Kobe, Japan, with magnitude $M 7.2$. The Earthquake Information Center (EIC), Earthquake Research Institute, University of Tokyo is compiling observed data [36]. The catalogue contains 3464 events with magnitude $M \geq 2.0$ for the period (January-December 1995). After a preliminary analysis only the quakes at depth of up to 20km were included into the series.

For the earthquake sequence near Loma Prieta, California, which happened on 18.10.1989, 11132 events with magnitude $M \geq 0.1$ were registered in the period (1989-1991). The magnitude of the main shock was defined as $M_W 6.9$ [37].

All aftershock series have been analyzed for completeness. The numbers of earthquakes for each studied series, as well as the magnitude of completeness M_C, are given in Table 2. This table also shows the parameters of the "sliding windows" and the overlapping. The obtained correlation between **b** and $\mathbf{D_2}$ appears in the last column.

It is typical of this research that the correlation between the parameters **b** and $\mathbf{D_2}$ is positive; the only exception is the series of Sumatra 2004, for which the correlation is negative – Fig. 2. The correlation equations are shown in Table 2 together with the corresponding coefficient of correlation.

DISCUSSION AND CONCLUSIONS

The correlation fractal dimension $\mathbf{D_2}$, defined by the formulae (3) and (4), finds wide application in seismology, especially in description of the earthquakes spatial distribution. The fractal dimension is a measure of the spatial clustering of the set of seismic events, considered as points in a two- or three-dimensional space, i.e., it can be applied both for the epicentral distribution and for the distribution of the hypocenters of the earthquakes.

Table 2. Data about the considered aftershock series

Earthquake	**Number of earthquakes in series**	**Magnitude of completeness $\mathbf{M_C}$**	**Number of events in "sliding window"**	**Number of overlapping events**	**Correlation equation**
Sumatra 2004	3561	4.5	500	250	$\mathbf{b} = 1.69 - 0.51\mathbf{D_2}, R = -0.69$
Sumatra 2007	290	4.7	50	20	$\mathbf{b} = 0.57 + 0.13\mathbf{D_2}, R = 0.42$
Kashmir 2005	594	3.5	50	40	$\mathbf{b} = 0.41 + 0.32\mathbf{D_2}, R = 0.52$
Parkfield 2004	141	2.6	10	5	$\mathbf{b} = 0.58 + 0.67\mathbf{D_2}, R = 0.34$
Kobe 1995	3134	2.0	300	100	$\mathbf{b} = 0.70 + 0.32\mathbf{D_2}, R = 0.36$
Loma Prieta 1989	1052	2.0	100	50	$\mathbf{b} = 0.54 + 0.25\mathbf{D_2}, R = 0.42$

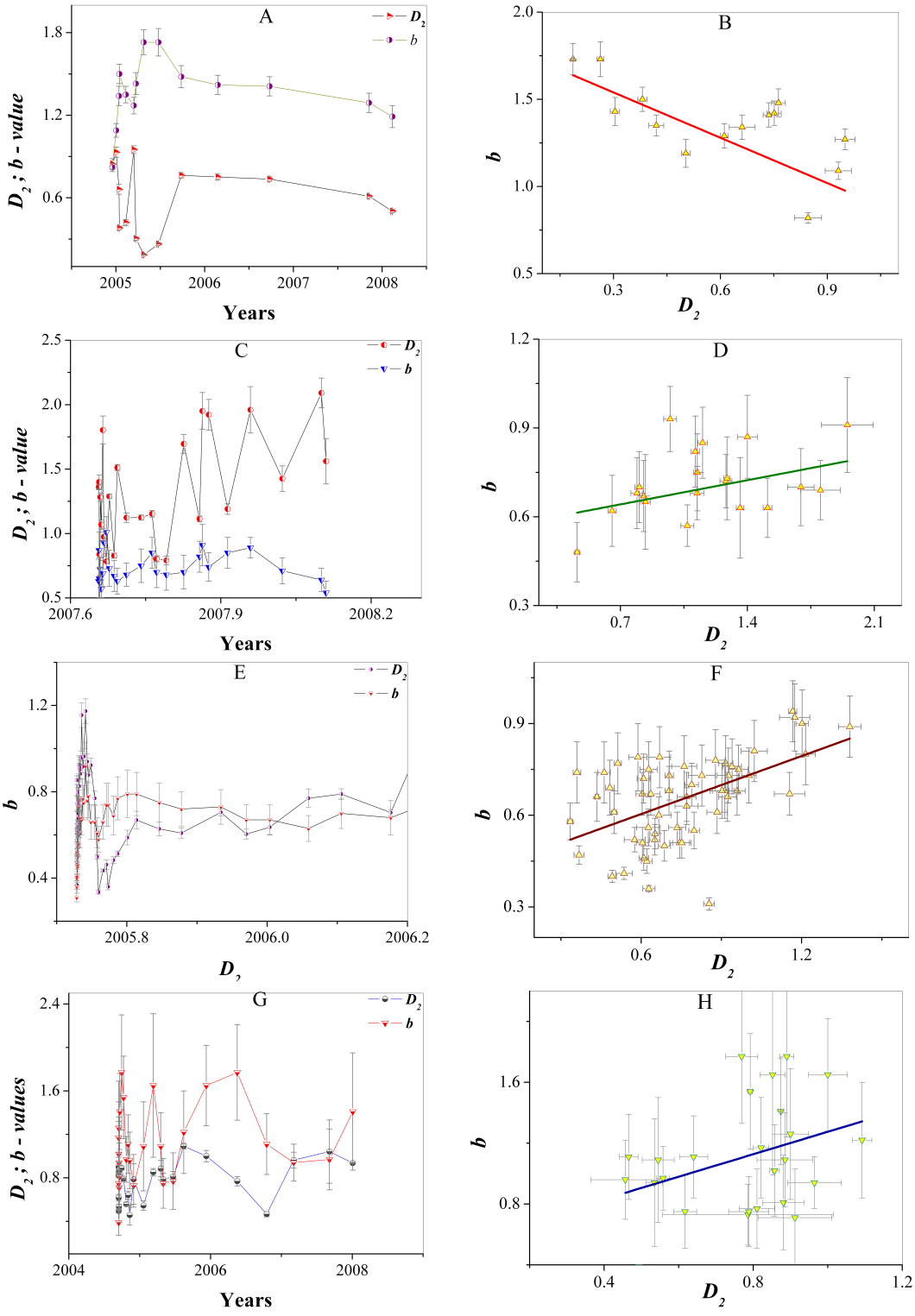


Fig. 2. Variations of the parameter **b** and the fractal coefficient $\mathbf{D_2}$, defined for the aftershock series: A – Sumatra 2004; C – Sumatra 2007; E – Kashmir 2005; G – Parkfield 2004; I – Kobe 1995; K – Loma Prieta 1989 (The temporal coordinate corresponds to the data of the last earthquake, falling into the respective window of calculations). Correlation between the parameter **b** and the fractal coefficient $\mathbf{D_2}$: B – Sumatra 2004; D – Sumatra 2007; F – Kashmir 2005; H – Parkfield 2004; J – Kobe 1995; L – Loma Prieta 1989. For each value of the shown parameters the standard deviations are also depicted.

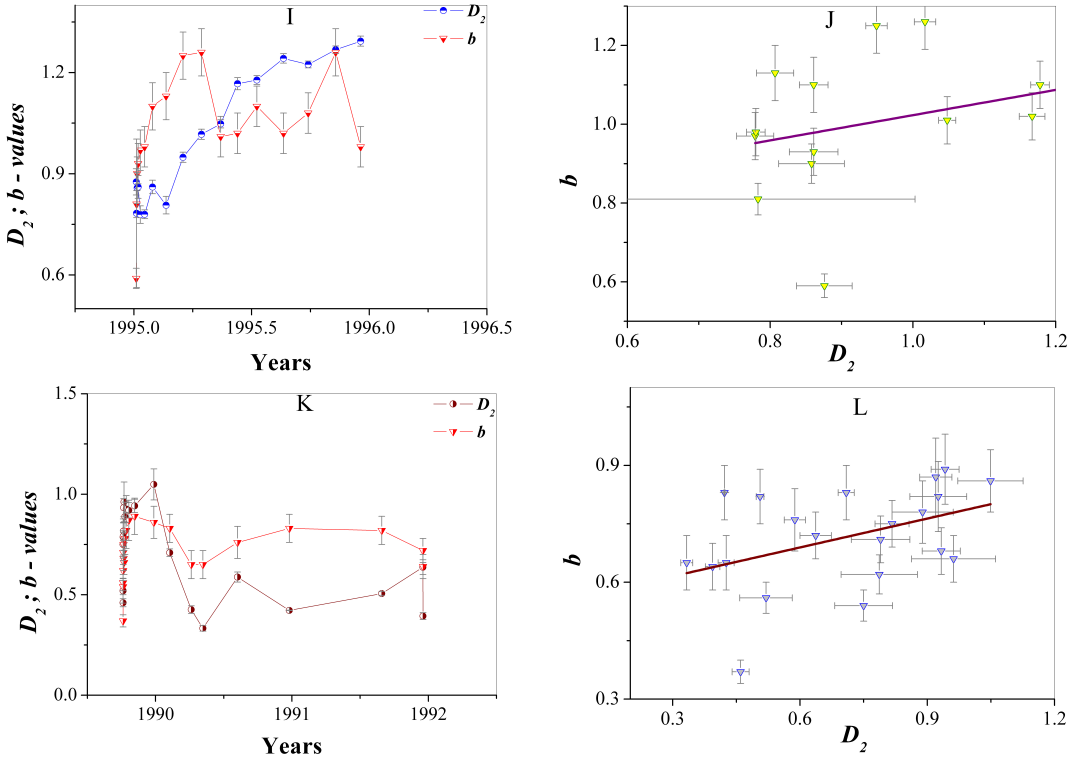


Fig. 2. (continued)

Many authors carry out research of the temporal evolution of seismicity, characterized by the two parameters: the **b**- value from the law of repeatability and the corresponding correlation fractal dimension $\mathbf{D_2}$ of their epicentral distribution. Such results are obtained for the region of Tohoku, Japan [5, 38]; for parts of California [39, 40]; for North-East Brazil [39]; Italy [41]; the region of the North Anatlolian fault in Turkey [9]; for region Koyna Dam, India [42], Central Alborz, Iran [43]. For all these cases a negative correlation between the two studied parameters has been obtained.

The results presented here correspond to the published results. It means that the described type of correlation between the **b**-value and the fractal coefficient $\mathbf{D_2}$ is also valid for the seismic regions studied in this paper. It is noteworthy that the correlation equation between **b** and $\mathbf{D_2}$ for the two studied regions - Parkfield and the Northern coast of California - is the same.

The study of the temporal variations of the **b**-value and the fractal dimension $\mathbf{D_2}$ is carried out mainly with the aim of looking for prognostic phenomena before strong earthquakes. Although the seismologists are far from finding a stable prognostic picture, considerable reduction of the **b**-value and increase in the value of the fractal dimension $\mathbf{D_2}$ before a strong earthquake have been described in many publications. It means reduction of the dominance of the weak earthquakes and at the same time a tendency for formation of tight clusters of earthquakes in the fault region.

When studying aftershock series another type of equation is obtained for the correlation between the parameters **b** and $\mathbf{D_2}$ - a positive one. The only exception is the series of earthquakes on the island of Sumatra from 2004. There are various hypotheses, explaining this positive correlation. Such a behavior could be due to the change in the properties of the rocks, caused by the main quake of the series. Fluids migrate into the destroyed region after that, and this leads to increase of the stress in the pores of the rock massifs. As a result groups of weaker earthquakes, clustered in space, appear. Observations of rock samples in laboratory experiments show that the variations in the **b**-value can be related to the stress in the environment. When the stress goes up, the **b**-value decreases.

The possible reasons for the negative correlation were discussed by Henderson [17], who compared

the observations of a local seismic sequence with an acoustic emission during a rock sample destruction. He found similarity in the distribution of the events magnitudes. This leads to considering a model of seismicity, characterized by a law of increase of the fractures, derived from Fracture Mechanics, which includes possibilities for both types of correlation - positive and negative. The model describes a process as a transition from a period of earlier scattered seismic events with small magnitude to a period of greater magnitudes (lower value of **b**) and greater clustering after that (accompanied by a higher value of the fractal coefficient $\mathbf{D_2}$).

The correlation between the **b**-value from the Gutenberg-Richter law and the fractal dimension $\mathbf{D_2}$ has been widely discussed over the past years. After Aki [15] proposed a simple relationship between the two parameters of the type $\mathbf{D_2} = 2\mathbf{b}$, both positive and negative correlations were described in different publications about the variations between these two scale coefficients. In some cases they can even change from one type into the other.

The variations in the **b**-value depend mainly on the degree of stress or the level of heterogeneity of the fault environment, while the variations of the fractal dimension depend mostly on complexity or the level of heterogeneity of the fault systems. Change in the **b**-value from $\mathbf{b} < 1$ to $\mathbf{b} > 1$ is observed immediately before and after a strong earthquake.

The negative correlation means that there is considerable occurrence probability for an earthquake with a greater magnitude, indicating release of stress over faults with greater fault planes.

A positive correlation means that the probability for a strong earthquake reduces in response to the increasing fragmentation of the fault region. This indicates further that the release of stress occurs on faults with narrower surface stretch.

Such variations in the correlations between **b** and $\mathbf{D_2}$ can be explained in terms of increasing stress on the main branch of the self-similar fault system before rupture and subsequent release of stress on and around the main fault and on secondary branches of the fracture system after the main quake.

Fractal properties of seismicity can be measured by fractal dimensions that are introduced as a statistical tool to quantify the dimensional distribution of seismicity, its randomness or clustering.

The fractal dimension may be used as a quantitative measure of the degree of heterogeneity of seismic activity in fault systems of a region, and it is controlled by the heterogeneity of the stress field and the existing and preexisting geological, mechanical, or structural heterogeneity. A change in the fractal dimension corresponds to the dynamic development of the states of the system.

One of the most important seismological parameters used to describe an set of earthquakes is the **b**-value in the Gutenberg-Richter frequency-magnitude equation. It characterizes the distribution of earthquakes over the observed range of magnitudes. It is a basic parameter in seismology for its association with geotectonic features of an seismic area. The b-value is influenced by the degree of heterogeneity and fracture density in the area. The **b**-value is influenced by the degree of heterogeneity and fracture density in the area. The state of stress, rather than the heterogeneity of the material constituting the rocks, plays the most important role in the **b**-value variation.

Therefore it is important to understand the frequency-magnitude relation and fractal dimension of seismicity in assessing the earthquake hazard of a tectonically active region.

Acknowledgments. *I would like to thank my colleague Associate Professor Alexander Marinov for development of programs, needed for the present research.*

REFERENCES

[1] C. A. Aviles, C. H. Scholz, and J. Boatwright, *J. Geophys. Res.* **92**, 331–344 (1987).

[2] S.R. Brown, and C.H. Scholz, *J. Geophys. Res.* **90**, 12575–12582 (1985).

[3] T. Hirata, T. Satoh, and K. Ito, *Geophys. J. R. Astron. Soc.* **90**, 360–374 (1987).

[4] P.G. Okubo, and K. Aki, *J. Geophys. Res.* **92**, 345–355 (1987).

[5] T. Hirata, *J. Geophys. Res.* **94**, 7507–7514 (1989a).

[6] D.L. Turcotte, *Tectonophysics* **167**, 171–177 (1989).

[7] T. Hirata, and M. Imoto, *Geophys. J. Int.* **107**, 155–170 (1991).

[8] F. Brown-Angulo, A. H. Ramirez-Guzman, E. Yepezl, A. Rudolg-Navarrol, and C. G. Pavial-Miller, *Geofisica International* **37**, 29–33 (1998).

[9] A.O. Öncel, O. Alptekin, and I. Main, *Nonlin. Process. Geophys.* **2**, 3/4, 147–157 (1995).

[10] S.S. Teotia, K.N. Khattri, and P.K. Roy, *Current Science* **73**(4), 359–365 (1997).

[11] L.A. Sunmonu, and V.P. Dimri, *Pure and Applied Geophysics* **157**, 1393–1405 (2000).

[12] K. Murase, *Earth Planets Space* **56**, 3, 401–405 (2004).

[13] S. Maryanto, and I. Mulyana, *Intl J. of Mathematical, Physical and Engineering Sciences* **3**(2), 113–117 (2009).

[14] P.N.S. Roy, and S.K. Mondal, *J. Indian Geophysical Union* **13**(2), 63–68 (2009).

[15] K. Aki, A probabilistic synthesis of precursory phenomena, in *Earthquake Prediction: An International Review*, edited by Simpson, D.W. & Richards. G., AGU, Washington, DC, 1981, pp. 566–574.

[16] D.L.Turcotte, *Fractals and Chaos in Geology and Geophysics*, Cambridge Univ. Press, 1992, p. 221.

[17] J. Henderson, I.G. Main, R.G. Pearce, and M. Takeya, *Geophys. J. Int.* **116**, 217–226 (1992).

[18] I.G. Main, *Geophys. J. Int.* **111**, 531–541 (1992).

[19] I.G. Main, *Reviews of Geophysics* **34**, 433–462 (1996).

[20] A.V. Ponomarev, A.D. Zavyalov, V.B. Smirnov, and A. Lockner, *Tectonophysics* **277**, 5, 7–81 (1997).

[21] P. Mandal, and B.K. Rastogi, *Pure and Applied Geophysics* **162**, 53–72 (2005).

[22] P. Grassberger, and I. Procaccia, *Phys. Res. Lett.* **50**, 346–350 (1983a).

[23] P. Grassberger, and I. Procaccia, *Physica D* **9**, 189 (1983b).

[24] L. Telesca, V. Cuomo, V. Lapenna, and M. Macchiato, *Tectonophysics* **330**, 93–102 (2001).

[25] B. Mandelbrot, *The fractal geometry of nature*, Freeman and Co., San Francisco, 1982, p. 460.

[26] M. B. Geilikman, T. V. Golubeva, and V. F. Pisarenko, *Earth Planet. Sci. Lett.* **99**, 127–132 (1990).

[27] D. Gospodinov, A. Marinov, and E. Marekova, *Acta Geophys.* **60**, 794–808 (2012).

[28] K. Aki, *Earthquake Res. Inst., Tokyo Univ.* **43**, 237–239 (1965).

[29] S. Wiemer, *Seism. Res. Let.* **72**(2), 373–382 (2001); http://seismo.ethz.ch/staff/stefan/IntrotoZMAP6_online.htm

[30] P. Reasenberg, *J. Geophys. Res.* **90**, 5479–5495 (1985).

[31] http://earthquake.usgs.gov/research/parkfield/livedata.php - USGS

[32] S. Wiemer - CD with software package Zmap (private communication).

[33] http://seismos-u.ifz.ru/centrasia.htm ; http://earthquake.usgs.gov/data/russia_seismicity/

[34] http://www.data.scec.org/eq-catalogs/date_mag_loc.php

[35] http://www.ncedc.org/anss/catalog_search.html

[36] ftp://ftp.eri.u-tokyo.ac.jp/pub/data/junec/hypo

[37] http://www.ncedc.org/ncedc/catalog-search.html

[38] T. Hirata, *Pure Appl. Geophys.* **131**, 157–170 (1989b).

[39] J. Henderson, "Fracture-Mechanics and the Evolution of Seismicity in an Intra-Plate Setting", PhD Thesis, 1992, University of Edinburgh.

[40] D. J. Barton et al., *Geophys. J. Int.* **138**, 563–570 (1999).

[41] V. De Rubeis et al., *Geophys. Res. Lett.* **20**(18), 1911–1914 (1993).

[42] A. Kumar et al., *Earthq. Sci.* **26**(2), 99–105 (2013).

[43] M. Agh-Atabai, and M. S. Mirabedini, *Acta Geophysica* **62**(3), 486–504 (2014).

ВРЕМЕВИ ВАРИАЦИИ НА ФРАКТАЛНИТЕ СВОЙСТВА НА СЕИЗМИЧНОСТТА

Е. Марекова

Физически факултет, Пловдивски университет "Паисий Хилендарски",
ул. "Цар Асен" №24, 4000 Пловдив, България

(Резюме)

За много природни явления и обекти е характерна хаотичност и независимост от мащаба, в който те се изучават. Пример за подобни явления са земетресенията, изучаването на които показва, че много техни свойства не зависят от мащаба им. При изучаването на земетресенията свойството на мащабна независимост най-напред е било установено за разпределението им по сила (закон за повторяемост на *Gutenberg-Richter*) и за спада на интензивността на афтершоците във времето. По-нови изследвания показват, че и други свойства на земетресенията се характеризират с независимост от мащаба на реализация. Така например фрактални свойства проявяват както афтершоковата реализация, така и регионалният сеизмичен процес.

В настоящата работа се прави оценка на изменението във времето на фракталните коефициенти на площното разпределение на земетресения от няколко сеизмични региона. При анализа на пространствената структура, се използва така наречения двуточков корелационен интеграл. Направени са и аналогични оценки на *b*-стойността от закона на *Gutenberg-Richter*. Между фракталните коефициенти за земетръсните серии и съответните им *b*-стойности е установена отрицателна корелационна връзка.

Аналогичен анализ е направен и на изменението във времето на фракталните коефициенти на площното разпределение на земетресения от няколко афтершокови серии. Между фракталните коефициенти за афтершоковите серии и съответните им *b*-стойности е установена положителна корелационна връзка.

Bulgarian Chemical Communications, Volume 47, Special Issue B (pp. 390–396) 2015

System of Earthquakes Alert (SEA) in the Romania-Bulgaria cross border region

L. Dimitrova*, D. Solakov, S. Simeonova, I. Aleksandrova

National Institute of Geophysics, Geodesy and Geography, Bulgarian Academy of Sciences, Acad. G. Bonchev Str., Bl.3, BG-1113 Sofia, Bulgaria

Among the many kinds of natural and man-made disasters, earthquakes dominate with regard to their social and economical impact on the urban environment. The prevention of the natural disasters and the performing management of reactions to crisis are common problems for many countries. The main objective of this study is to present the integrated warning system that was designed and put in operation in the Romania-Bulgaria cross-border area in the framework of DACEA (Danube Cross-border System for Earthquake Alert) project. The main goals of the implemented system are: monitoring of the seismogenic areas relevant for the cross-border area, in order to detect moderate to strong earthquakes and sending the seismic warning signals within seconds to the local public authorities in the cross-border area.

Key words: seismicity, intermediate-depth, earthquakes, seismic sources, warning systems, Romania-Bulgaria cross border region

INTRODUCTION

The cross-border region encompassing northern Bulgaria and southern Romania is a territory prone to effects of strong earthquakes. Romania and Bulgaria, situated in the Balkan Region as a part of the Alpine-Himalayan seismic belt are characterized by high seismicity, and are exposed to a high seismic risk. Over the centuries, the two countries experienced strong earthquakes. The considered cross-border region is significantly affected by earthquakes occurred in both territories on the one-hand, Vrancea seismic source (in Romania), with intermediate-depth events and on the other hand, crustal seismicity recorded in the northern part of Bulgaria (in seismic sources: Shabla, Dulovo, Gorna Orjahovitza).

The spatial pattern of seismicity in the cross border region and adjacent areas is shown in Fig. 1.

The Vrancea seismogenic zone in Romania is a very peculiar seismic source, often described as unique in the world, and it represents a major concern for most of the northern part of Bulgaria as well. Situated at distances larger than 200 km from the Vrancea zone, several cities in the northern Bulgaria suffered many damages due to high energy Vrancea intermediate-depth earthquakes; the March 4, 1977 event (M_w7.2) caused partial or total damages to 8470 buildings, and 125 casualties on the territory of Bulgaria (as illustrated in Fig. 2).

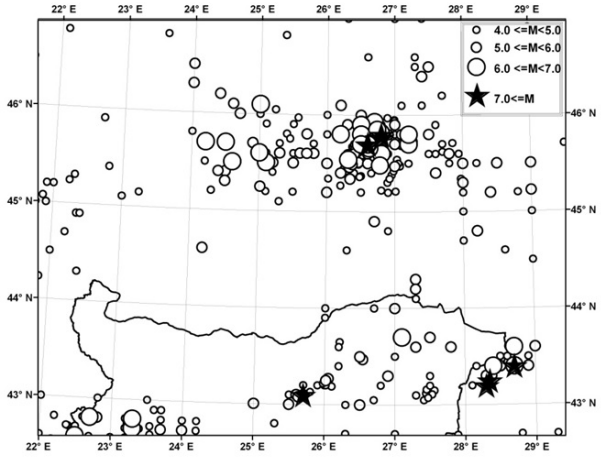


Fig. 1. Spatial distribution of seismicity (historical and instrumental $M_w \geq 4.0$) in Romania-Bulgaria cross-border region.

DACEA PROJECT

The project DACEA is implemented in the framework of the Romania–Bulgaria Cross Border Cooperation Programme (2007-2013), co-financed by the European Union through the European Regional Development Fund, the Bulgarian and Romanian Governments and the 5 project partners. DACEA project general objective is to develop a cross-border system for Earthquake alerts in order to prevent the natural disasters caused by those events in the cross-border area, taking into account the nuclear power plants and other high risk facilities located along the Danube on the territories of Romania and Bulgaria. The most important factor for a rapid action after a destructive earthquake is the real-time communication with the seismic sensors in the closer epicenter area and with

* To whom all correspondence should be sent:
ldimitrova@geophys.bas.bg

© 2015 Bulgarian Academy of Sciences, Union of Chemists in Bulgaria

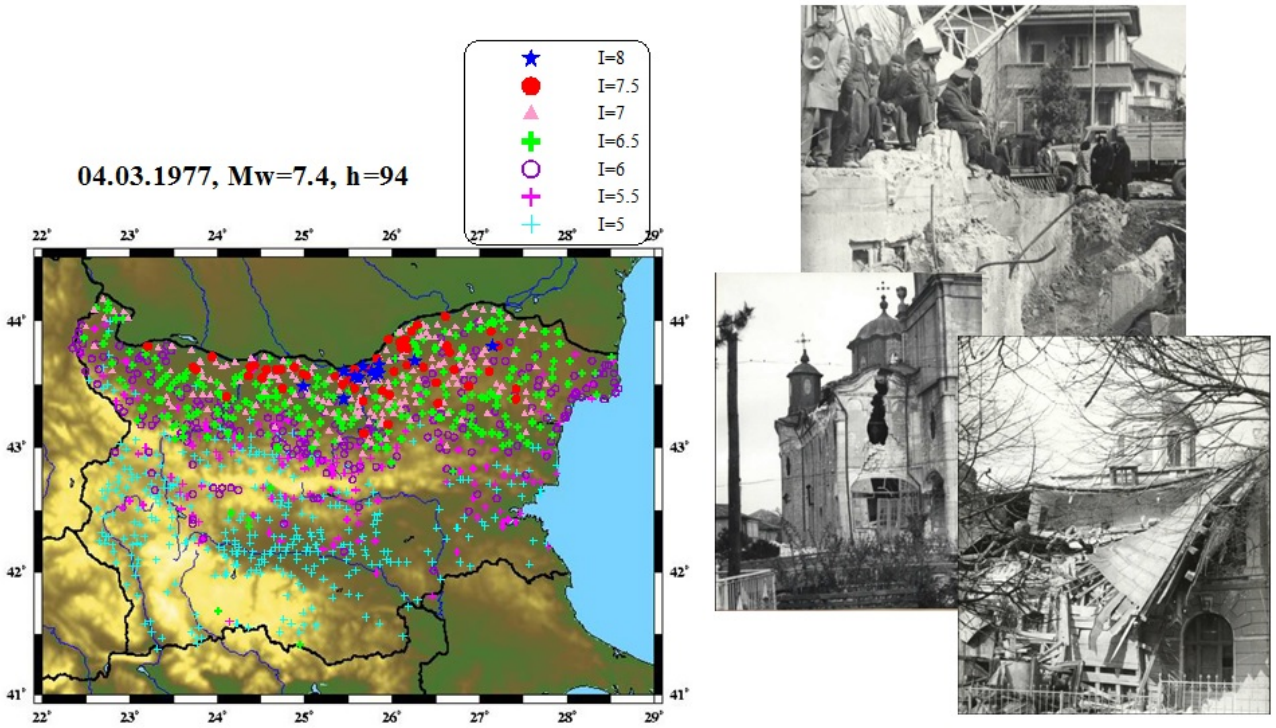


Fig. 2. The 1977 Vrancea earthquake effects on the territory of Bulgaria (modified from [1]).

dense station networks towards and within vulnerable cities and industrial plants. This will provide fast and reliable information for the near real-time hypocenter determination and the automated construction of Shake maps of the ground motions. A fast overview of an anticipated damage pattern will then be possible using this information. The project Danube Cross-border System for Earthquake Alert (DACEA) contributes significantly to these challenges.

As a principal strategic view, the first part of the project was focused on updating and integrating the current databases available at the two countries related to geological, seismological and tectonic information and on integration of computation procedures and techniques. A database for integration of the detailed information that was compiled for the Romania-Bulgaria Cross-border region is designed and implemented. Model of the compiled Data Base (DB) as a *UML* diagram is presented in Fig. 3.

The second part of the project activities was connected with the seismic hazard assessment for Romania-Bulgaria cross-border region on the basis of integrated basic geo-datasets. The hazard estimates are to be considered as a crucial phase of the risk management cycle associated with hazards (mitigation and preparedness, early warning, response, and recovery). The *MSK*64 intensity is used as output parameter for the hazard maps. A particular advantage of using intensities is that the very irregular pattern of the attenuation field of the Vrancea intermediate depth earthquakes (for example, as it is illustrated in [2]) can be estimated from detailed macroseismic observations that are available (in both countries) for the study region. The seismic hazard analysis was performed by carrying out the following steps: analysis of the seismic, geophysical and geological features; compilation of the seismic source model; hazard assessment for the target region; and producing of the hazard maps. The hazard results (presented in [3]) are obtained by applying two alternative approaches - probabilistic and deterministic. The probabilistic hazard map in intensity scale for return period of 475 (probability of exceedance of 10% in 50 years) is presented in Fig. 4.

The seismic hazard for a return period of 475 years (Fig. 4) displays nearly the same intensity level as previous hazard estimates (for example, presented in [2], [4], [5]) that were obtained using different approaches to simulate the observed attenuation field

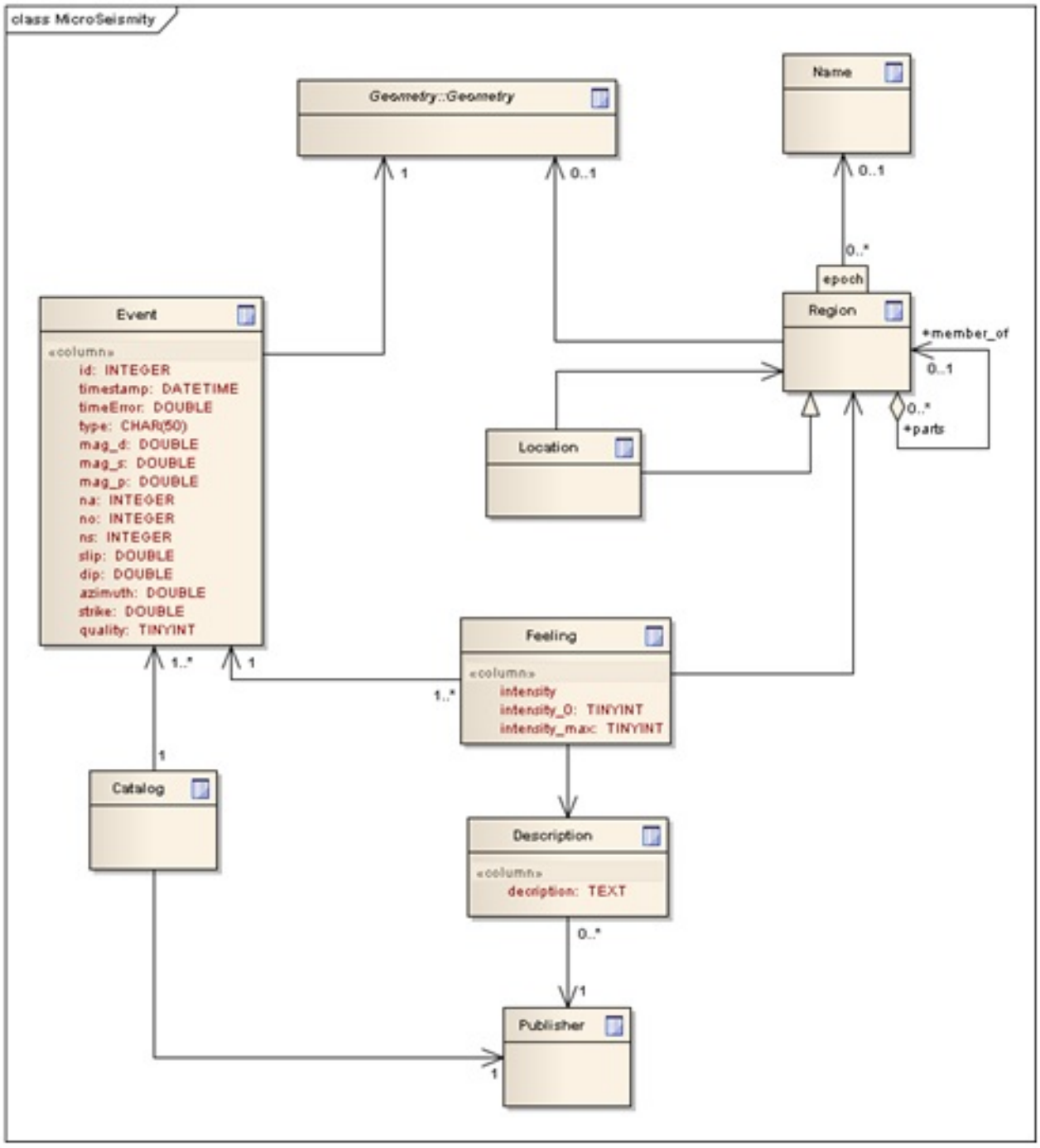


Fig. 3. Data Base model.

(for both shallow and subcrustal events), and source models mainly based on the spatial distribution of the seismicity. At the third step of the DACEA project - the most appropriate station sites were selected and studied - low level of noise was the most important requirement (Fig. 5). The method of McNamara and Bulland [6] was applied to evaluate ambient seismic noise at the potential sites. This method has been used for evaluation of the seismic noise and estimation of the performance of the broadband seismic stations belonging to Bulgarian national seismic network [7]. The advantage of the method is that there is no need

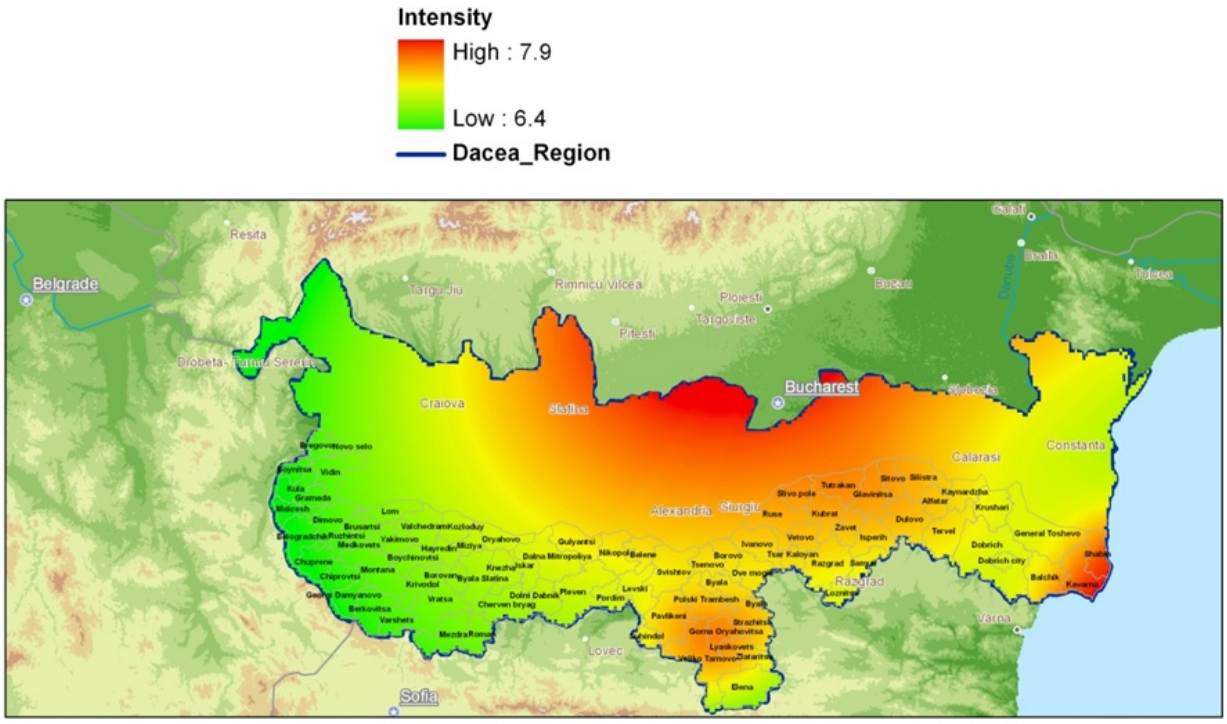


Fig. 4. Seismic hazard map for the cross-boarder region for 475 years return period (modified from [3]).

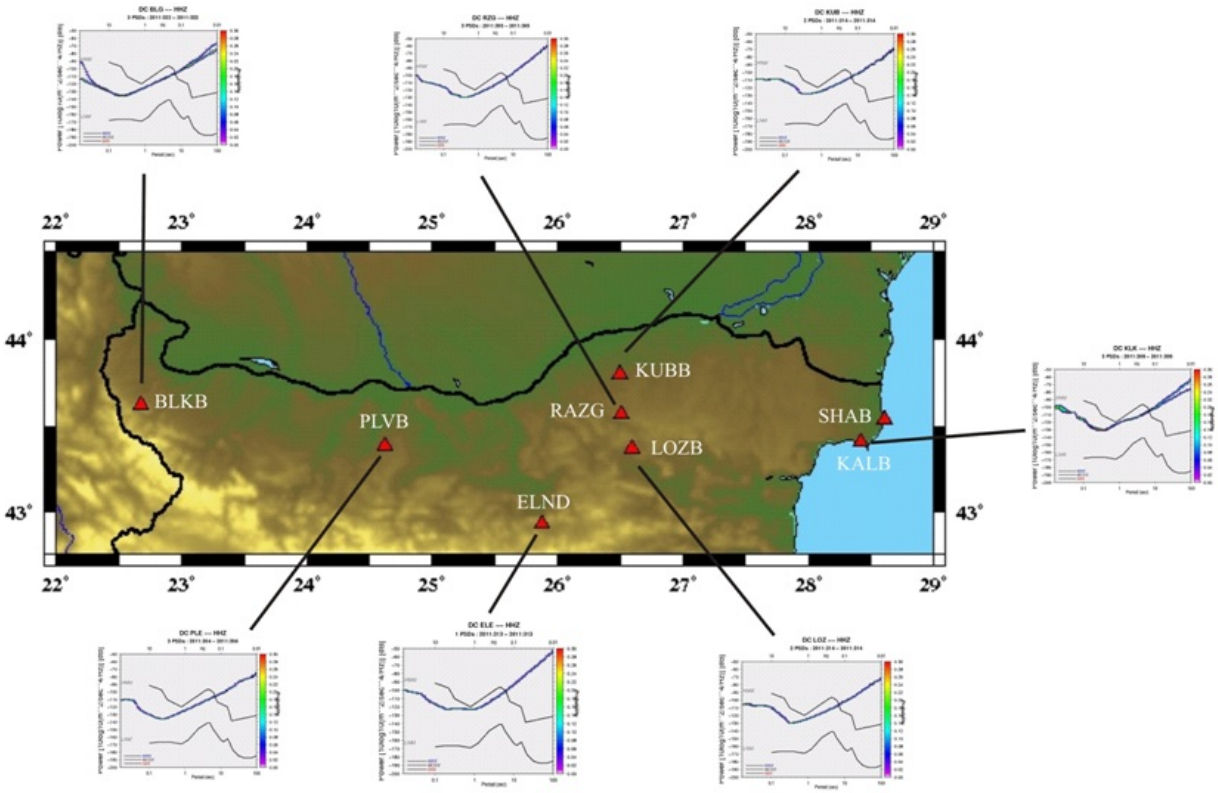


Fig. 5. Ambient seismic noise at the selected sites.

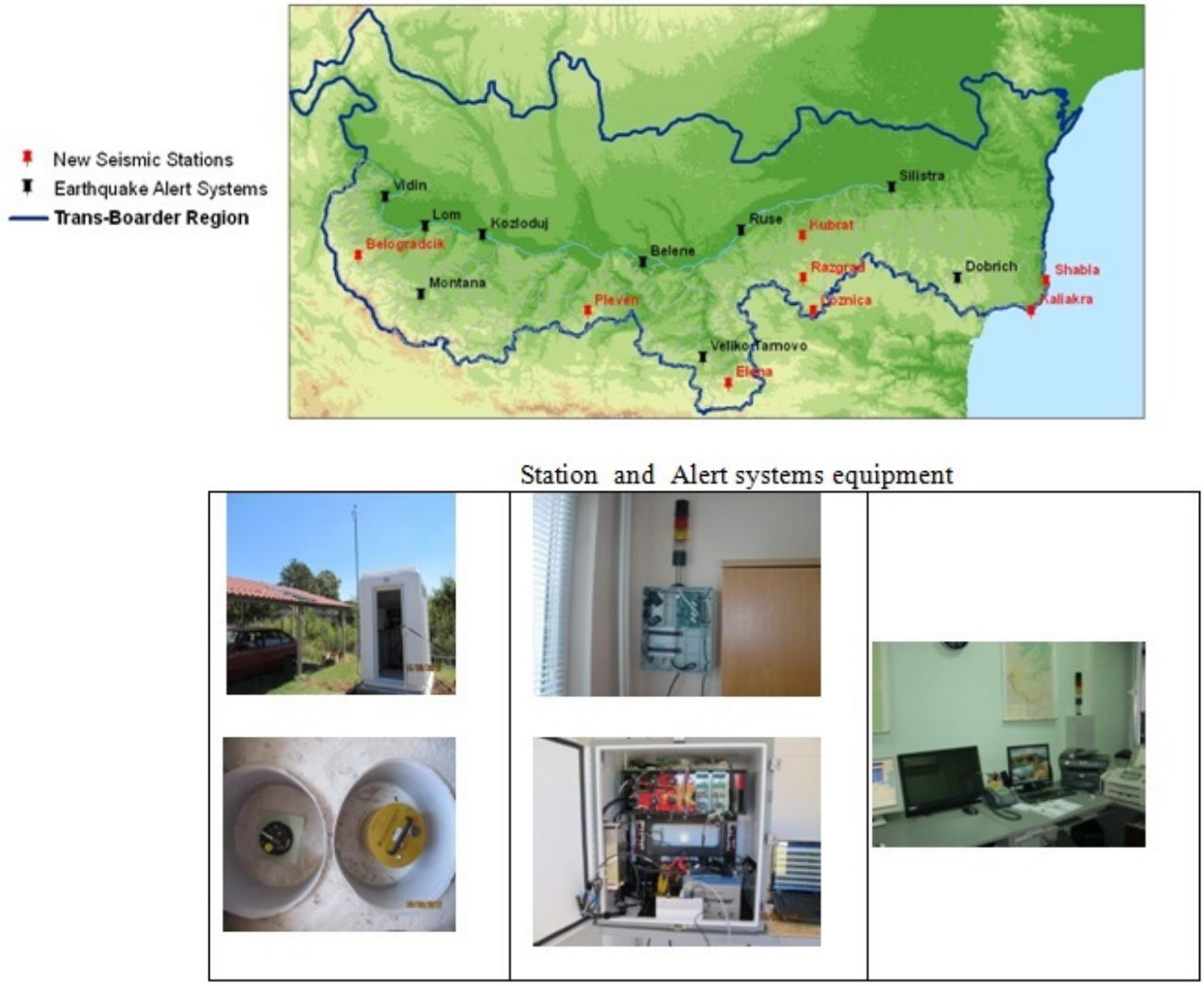


Fig. 6. Configuration and equipment of SEA on the territory of Bulgaria.

to filter data from earthquakes, gaps, spikes, calibrations pulses etc. Such kind of signals has low-level of occurrence while ambient noise reveals itself as a signal with high probability occurrence. The total power spectral density (PSD) is given by the following expression:

$$P_k = \frac{2\Delta t}{N} \mid Y_k \mid^2, \qquad (1)$$

where Y_k is the square of the amplitude spectrum with a normalization factor of $2\Delta t/N$, Δt is the sample interval, N is the number of samples in a time series segment and $k = 1, 2, ..., N-1$. The seismic noise is measured in respect to the ground acceleration. The PSD of the noise is also displayed against the ground acceleration. The equation of the PSD in unit of dB is

$$PSD = 10\log_{10}(m^2/sec^4)/Hz[dB] \qquad (2)$$

SYSTEM OF EARTHQUAKES ALERT (SEA)

The installed System of Earthquakes Alert (SEA) involves 8 seismic stations and 8 earthquake alert systems on the territory of Northern Bulgaria. Configuration and equipment of the stations and earthquake alert systems is presented in Fig. 6.

The installation and maintenance, as well as the data-processing are performed in close cooperation with the leading partner – National Institute for Earth Physics (NIEP), Bucharest, Romania. The aim of the installed system is to provide an early warning alert and a rapid damage assessment to the emer-

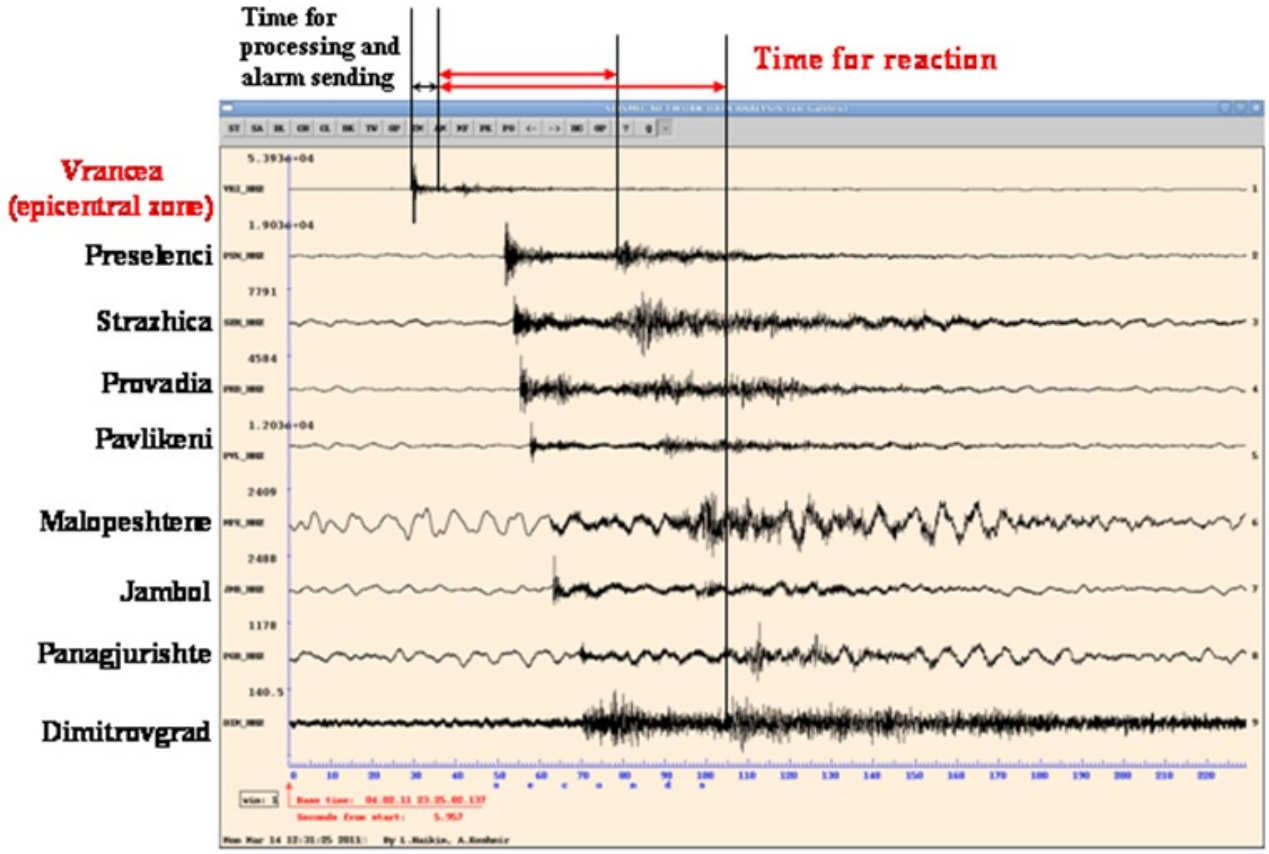


Fig. 7. Response time for several sites on the territory of Bulgaria after Vrancea earthquake.

gency management agencies immediately after a major seismic event. The system performs *P*-waves arrival detection and, once an event has been detected, it first provides location and magnitude estimations. The earthquake location is obtained through real-time probabilistic approach based on an equal differential time formulation that uses information from both triggered and not-yet-triggered stations. The earthquake magnitude is estimated exploiting its empirical correlation with the peak displacement measured on the first 2-4s of *P*-waves. All estimates are provided as probability density functions, with an uncertainty that typically decreases with time, and can be sent as alarm messages that can reach the vulnerable structures before the arrival of destructive *S*-waves. Fig. 7 shows the response time (for several sites on the territory of Bulgaria) after Vrancea earthquake.

Finally, SEA centers were established both in Sofia (in National Institute of Geophysics, Geodesy and Geography) and Bucharest (in National Institute of Research and Development for Earth Physics, NIEP). Real time data transfer (via internet) from stations to SEA centers is implemented. Both centers are equipped with servers for data analyses and storage. Specialized software for elaboration of scenarios of seismic hazard is designed and implemented. The software is designed on the base of the compiled data base of historical and contemporary seismicity in the cross-border region. The output shake maps and scenarios are to be used by the emergency intervention units, local public authorities and for general public awareness.

REFERENCES

[1] D. Solakov, (Ed.), *Project report: "'Microseismic zoning of Bulgaria according to EC*8*", Sofia, Geophysical Inst., BAS*, p. 205, (2007).

[2] G. Leydecker, H. Busche, K. P. Bonjer, T. Schmitt, D. Kaiser, S. Simeonova, D. Solakov, and L. Ardeleanu, *Nat.Hazards Earth Syst. Sci.*, 8, 1431-1439, (2008).

[3] D. Solakov, S. Simeonova, L. Ardeleanu, I. Alexandrova, P. Trifonova, C. Cioflan, *Com. Rend. de L'Acad. Bulg. des Sci.*, accepted, (2014).

[4] L. Ardeleanu, G. Leydecker, H. Busche, T. Schmitt, and D. Kaiser, *Nat. Hazards Earth Syst. Sci.*, 5, 679-684, (2005).

[5] S. Simeonova, D. Solakov, G. Leydecker, H. Busche, T. Schmitt and D. Kaiser, *Nat. Hazards Earth Syst. Sci.*, 6, 881–887, (2006).

[6] E. McNamara and P. Buland, *BSSA*, 94, 1517-1527, (2004).

[7] L. Dimitrova, S. Nikolova, *Bulgarian Geophysical Journal, Vol. 37*, pp. 48-61, (2011)

СИСТЕМА ЗА РАННО ОПОВЕСТЯВАНЕ НА ЗЕМЕТРЕСЕНИЯ В ТРАНС-ГРАНИЧНИЯ РАЙОН РУМЪНИЯ–БЪЛГАРИЯ

Л. Димитрова, Д. Солаков, С. Симеонова, И. Александрова

Национален институт по геофизика, геодезия и география, Българска академия на науките, ул. "Акад. Г. Бончев" бл.3, 1113 София, България

(Резюме)

В сеизмично активните райони на планетата, включително и в България, земетресенията и последствията от тях са най-катастрофалните природни бедствия. Обяснението е в спецификата на явлението земетресение – краткотрайно и силно въздействие с изключително не хуманни последствия върху значителни по площ територии. Последствията са изключително тежки особено, когато в засегнатите райони са съсредоточени големи човешки и материални ресурси. Превантивните мерки по отношение на природните бедствия и управлението на дейностите по време на кризи са глобален проблем. Проектът "Дунавска транс гранична система за ранно оповестяване на земетресения" (Danube Cross-border System for Earthquake Alert (DACEA)), реализиран в рамките на Програмата за транс гранично сътрудничество между Румъния и България (2010-2013), предоставя възможност за намаляване на последствията от силни земетресения.

Териториите на Румъния и България, като част от Алпо-Хималайския сеизмичен пояс, се характеризират с висока сеизмичност. Двете държави са изложени на висок сеизмичен риск. Транс-граничният регион, включващ южна Румъния и северна България, е подложен на въздействието от сеизмични източници, разположени на Румънска територия, каквото е огнище Вранча, така и на тези намиращи се на територията на България – Дулово, Шабла, Горна Оряховица. В изпълнение на проекта в транс-граничния район е изградена съвместна мрежа от еднотипни сеизмични станции с реално времева връзка с центровете за обработка на сеизмологичната информация. Реално времевата комуникация е важен фактор, който в голяма степен влияе върху бързината на реакция след силни земетресения. Осигурява се бърза и надеждна информация за местоположението и силата на земетресенията, автоматично съставяне на карти на сътресяемост и оценка на възможните разрушения и човешки загуби. Тази информация може да се използват от звената на ГД ПБЗН и местните администрации, за предприемане на необходимите мерки за защита на населението и намаляване на последствията от земетресението.

Изградени са два сеизмични центъра – в София (в Национален институт по геофизика, геодезия и география към БАН) и в Букурещ (в Националния институт по физика на Земята). Двата центъра са оборудвани със сървъри за анализ и съхранение на данните. Разработен и инсталиран е специализиран софтуер за изготвяне на карти на сътресяемост. Софтуерът е разработен на базата на богата база данни от исторически и съвременни земетресения, реализирани в транс-граничните територии.

Bulgarian Chemical Communications, Volume 47, Special Issue B (pp. 397–404) 2015

The 2012 M_w5.6 earthquake in Sofia seismic zone and some characteristics of the aftershock sequence

S. Simeonova*, D. Solakov, I. Aleksandrova, P. Raykova, V. Protopopova

National Institute of Geophysics, Geodesy and Geography, Bulgarian Academy of Sciences, Acad. G .Bonchev Str., Bl.3, BG-1113 Sofia, Bulgaria

The seismic sequence of May 2012 was studied using digital data from Bulgarian Seismological Network and macroseismic information available in Sofia municipality. The results favor the idea that the occurrence of the seismic sequence took place at the Pernik-Belchin fault extending in NW-SE direction. In the sequence the temporal distribution of aftershocks is dominated by the classic power law decay in time. More over, the results indicate that seismic energy is released very slowly and is mostly related to normal faulting with small strike-slip component. In the study is shown that for southwestern Bulgaria the seismicity characteristics, focal mechanisms and stress analysis confirm the hypothesis that neotectonics of this region is similar to that of northern Greece with predominant N-S extension.

Key words: seismicity, earthquake spectrum, aftershock activity, fault plane solution, South-Western Bulgaria

INTRODUCTION

The territory of Bulgaria represents a typical example of high seismic risk area in the eastern part of the Balkan Peninsula. The neotectonic movements on the Balkan Peninsula are controlled by extensional collapse of the Late Alpine orogen,and were influenced by extension behind the Aegean arc and by the complicated vertical and horizontal movements in the Pannonian region.

The Sofia seismic zone is located in southwestern Bulgaria - the area with pronounce tectonic activity and proved crustal movement. The capital of Bulgaria - Sofia is situated in the center of the Sofia area that is the most populated (the population is of more than 1.5 mil. inhabitants), industrial and cultural region of Bulgaria that faces considerable earthquake risk. The strongest known event in the region is the 1858 earthquake with intensity I_0=9-10 *MSK*, caused heavy destruction in the city of Sofia and the appearance of thermal spring. An earthquake of moment magnitude 5.6 hit Sofia seismic zone, on May 22nd, 2012. The earthquake occurred in the vicinity of Pernik city, at about 25 km south west of the city of Sofia. The quake was followed by intensive aftershock activity. It is worth mentioning that the seismic sequence of May 2012 occurred in an area characterized by a long quiescence (of 95 years) for moderate events. Moreover, a reduced number of small earthquakes have also been registered in the recent past.

* To whom all correspondence should be sent:
stelas@geophys.bas.bg

In the present study we first compiled relevant macroseismic information and estimate macroseismic effects caused by the 2012 M_w5.6 earthquake in the city of Sofia. Than analyze wave forms and find spectral characteristics of the main shock and some of the strongest aftershocks. Additionally, spatial and temporal distribution of aftershocks is studied. Finally, individual focal mechanisms of the main shock and the largest aftershocks are determined. In the study new results of the present state of stress in southwestern Bulgaria from 20 earthquake focal mechanisms are presented.

SEISMICITY IN SOFIA SEISMIC ZONE

The contemporary tectonic activity of the Sofia seismic zone is predominantly associated with the marginal faults of Sofia graben. The boundaries of the graben are represented by fault systems with expressive neotectonic activity. The available historical documents prove the occurrence of destructive earthquakes during the 15th-18th centuries in the Sofia zone. In 19th century the city of Sofia has experienced two strong earthquakes: the 1818 earthquake with epicentral intensity I_0=8-9 *MSK* and the 1858 quake with I_0= 9-10 *MSK*. The 1858 earthquake caused heavy destruction in the town of Sofia and the appearance of thermal springs in the western part of the town [1]. During the 20th century the strongest event occurred in the vicinity of the city of Sofia is the 1917 earthquake with $M_S = 5.3$ (I_0=7-8 *MSK*64). The earthquake caused a lot of damages in the city and changed the capacity of the thermal mineral springs

© 2015 Bulgarian Academy of Sciences, Union of Chemists in Bulgaria



Fig. 1. Damages caused by the 2012 M_w5.6 earthquake.

in Sofia and surroundings. The earthquake was felt in an area of 50000 km^2 and followed by aftershocks, which lasted more than a year [2] and [3]. Almost a century later (95 years after the 1917 earthquake) an earthquake of M_w5.6 hit Sofia seismic zone, on May 22nd, 2012. No casualties and severe injuries have been reported. Moderate to heavy damages (Fig. 1) were observed in the cities of Pernik and Sofia and their surroundings.

The earthquake is largely felt on the territory of Bulgaria and neighboring countries: northern Greece, FYROM, eastern Serbia and southern Romania (presented in Fig. 2).

Predominantly moderate (grade2,according to [4]) to substantial (grade3, according to [4]) damages were observed in the city of Sofia and surroundings. Distribution of macroseismic effects (generated by the 2012 M_w5.6 earthquake) along the city of Sofia is estimated on the base of documents and reliable information available in Sofia municipality. The

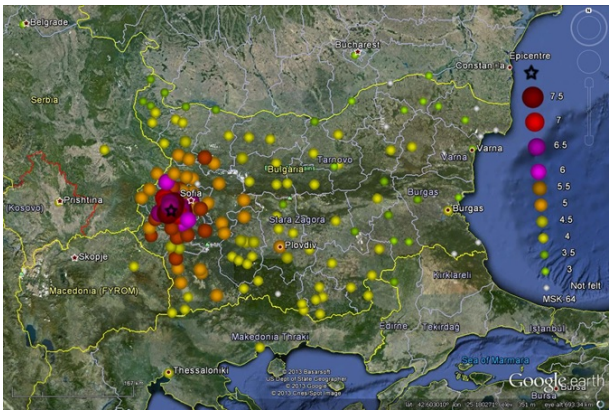


Fig. 2. Intensity field of the 2012 M_w5.6 earthquake.

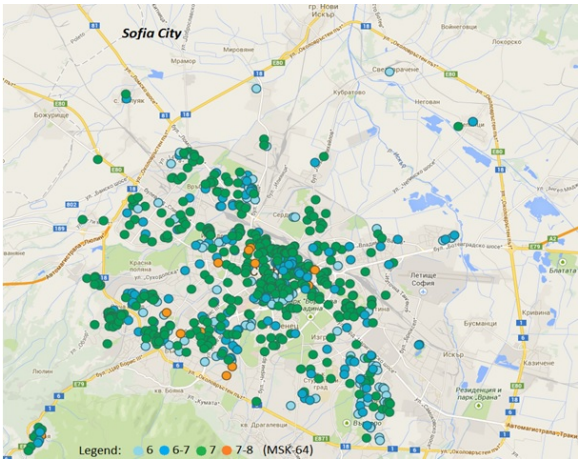


Fig. 3. Observed macroseismic effects (in *MSK* intensity scale) for the city of Sofia caused by the 2012 M_w5.6 earthquake.

intensity map illustrating the distribution of macroseismic intensity (*MSK*) along the city of Sofia is presented in Fig. 3. The figure shows that the intensity values range between 6th and more than 7th *MSK*. The highest intensity values (above 7 *MSK*) are related to old not well maintained buildings that were not reinforced (marked by orange spots in Fig. 3). Predominant level of damage to buildings in Sofia is 7th *MSK* concentrated in the central part of the city. Field with impacts of seventh degree grows mainly west of the city center from northwest to south-southeast (described in details in [5]).

SPECTRA ANALYSIS

P wave displacement spectra for the 2012 Pernik earthquake (M_w5.6; T_0=00:00:32 UTC) and two of the strongest early aftershocks (the first - M_w4.7, T_0=01:30:50 UTC; the second m_b4.2, T_0=02:13:28 UTC) are presented in Fig. 4. The spectra are estimated using records at station *MPE* - at epicentral distance of about 100 km. Both aftershocks occured in the first 3hs after the 2012 earthquake.

The figure shows low frequency content and not expressed spectrum plateau and corner frequency for the main shock while for the two aftershocks comparatively well outline a flat long period displacement spectrum (plateau between 0.7–3.0 Hz) is observed. The specific *P* wave displacement spectral of the 2012 M_w5.6 earthquake could be assumed as indicative for a very low rupture velocity [6]. The low rupture velocity means slow-faulting, which brings to slow release of accumulated seismic energy.

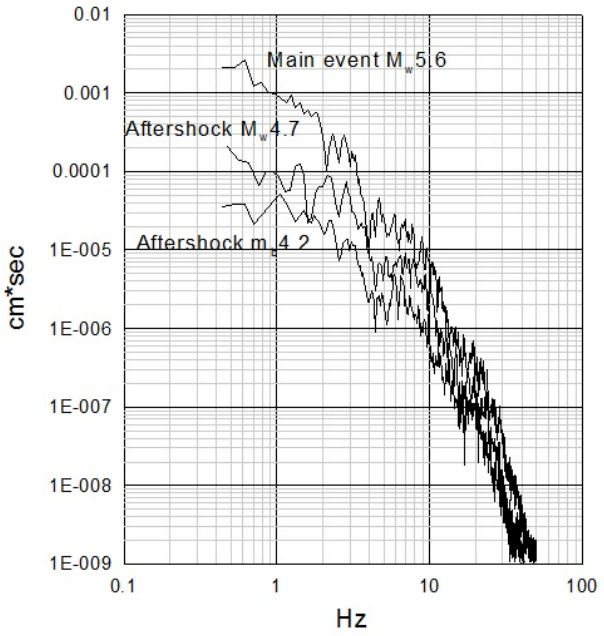


Fig. 4. Displacement spectra of *P* wave for main event and two of the strongest aftershocks.

SPACE-TIME DISTRIBUTION OF AFTERSHOCKS

Examination of the space-time distribution of earthquakes is of fundamental importance for understanding the physics of the earthquake generation process. One challenge in applying statistical methods to study the earthquake occurrence is to distinguish objectively the nonrandom from the random. The spatial and temporal clustering of aftershocks is the dominant non-random element of seismicity.

Spatial distribution of aftershocks

The spatial pattern of aftershock activity of earthquakes varies from event to event. Although the mechanism of aftershock occurrence has not been fully understood yet the spatial distribution of aftershocks seems to provide clues to the mechanical properties of the source region. It is assumed that aftershock area expansion pattern reflects the spatial variation of fault zone properties. On the assumption that the degree of spatial non randomness in the aftershock distribution is associated with the degree of non uniformity of stress in the area, an increased degree of clustering can then be related to an increased non uniformity in stress.

The aftershock patterns for different elapsed time after the 2012 Pernik earthquake are presented in Fig. 5.

Figures show the following characteristics in spatial pattern of aftershock activity:

- The aftershocks (presented in Fig. 5(a)) coincides with Pernik-Belchin fault (identified by Karagjuleva et al. [7] elongated in NW-SE direction;
- The first 3 hrs aftershocks occurred in the NW-SE oriented Pernik-Belchin fault (Fig. 5(a))

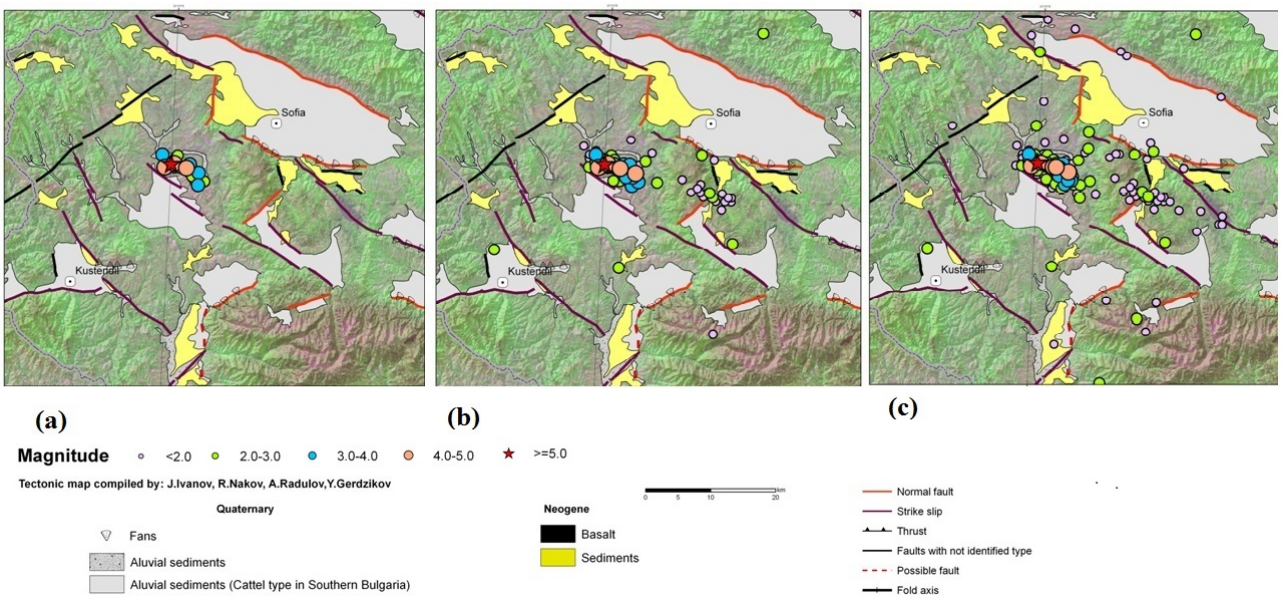


Fig. 5. Spatial pattern of aftershocks: (a)occurred 3 hrs after the 2012 M_w5.6 Pernik earthquake; (b)occurred 14 days after the 2012 M_w5.6 Pernik earthquake; (c)occurred 663 days after the 2012 M_w5.6 Pernik earthquake

and later (for elapsed time 14 days, Fig. 5(b)) aftershock activity migrates towards the fault with NE-SW orientation;
- A high degree of clustering of the strong aftershocks ($M \geq 3.0$) in a comparatively small and slightly elongated NW-SE area;
- A well expressed tendency of aftershock area expansion in time;
- Aftershock area expansion with decreasing of the threshold magnitude.

Temporal distribution of aftershocks

Aftershocks occur after the main shock and their frequency decays through time with approximately the reciprocal of time elapsed since the main earthquake. The occurrence rate of aftershock sequence in time is empirically well described by the modified Omori formula proposed by Utsu in 1961 [8]

$$n(t) = K(t+c)^{-p},$$

where t is the elapsed time since the occurrence of the main shock, and K, p, c are constant parameters. The power-low decay represented by the modified Omori relation is an example of temporal self-similarity of the earthquake source process. Aftershock decay rate (parameter p) contains information about the mechanisms of stress relaxation and frictional strength heterogeneity.

On the assumption that aftershocks are distributed as a non stationary Poisson process, Ogata [9] proposed to use the maximum likelihood method for estimating the parameters K, c and p in modified Omori formula. Using the modified Omori formula the intensity function of the Poisson process $\lambda(t)$ is defined by the relation:

$$\lambda(t,\theta) = K(t+c)^{-p}.$$

An integration of the intensity function $\lambda(t)$ gives a transformation from the time scale t to a frequency-linearized time scale τ [9]. On this time axis the occurrence of aftershocks becomes the standard stationary Poisson process if the choice of the intensity function (the parameters K, p, and c) is correct. The time scale τ is used for testing the goodness of fit between the aftershock occurrence and the selected model. A linear dependence between the observed cumulative numbers of aftershocks (N) and τ should be observed if an appropriate model has been selected.

The 2012 Pernik earthquake aftershock sequence is analyzed from 0 to $T = 663$ days by fitting it to the modified Omori formula. The maximum likelihood estimates (MLM,s) of the Omori formula parameters are as follows: $K = 15.04$, $c = 0.022$ and $p = 0.89$.

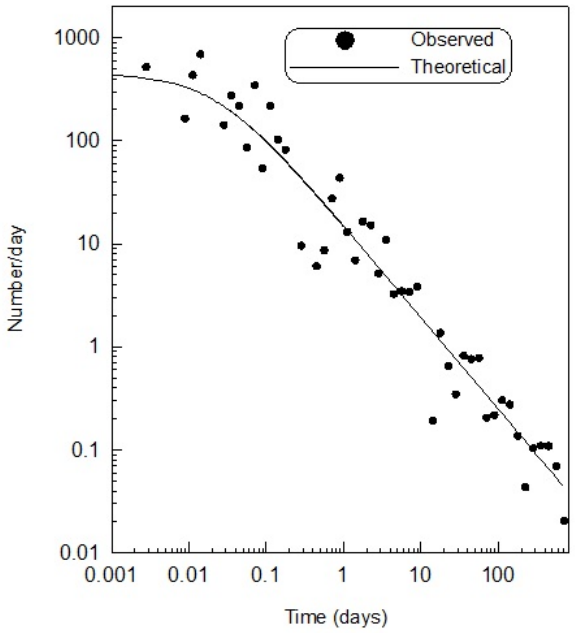


Fig. 6. The frequency-time distribution of 2012 Pernik earthquake aftershocks.

The frequency-time distribution of aftershocks is presented in Fig. 6. Figure 7 illustrate a plot

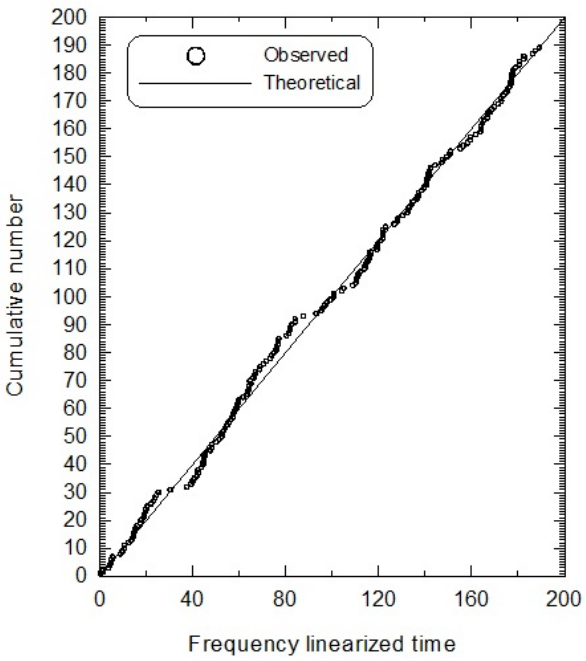


Fig. 7. Plot of cumulative number of events versus frequency linearized time τ.

of cumulative number of events versus the frequency-linearized time τ. In both figures the observed distribution is compared with the distribution (called "theoretical"), which is expected from the selected model (in the case, the model is the modifed Omori formula).

A comparison between empirical with theoretical distribution (Fig. 6 and Fig. 7) shows that as a first approximation the temporal distribution of events in aftershock sequence of the 2012 M_w5.6 Pernik earthquake is well described by the modified Omori formula.

Figure 7 shows that a nearly linear trend of aftershock decay continues up to 663 days; thus the modified Omori formula fits largely the observations up to 663 days after the main shock. The figure also suggests the existence of some discrepancies between observed and expected distributions (S-shaped deviations from the linear trend) – evident periods of decaying and activation of the process. Consequently models that take into account the effect of secondary aftershock activity were constructed. Two models for secondary sequences are test: 1) the first model with one secondary aftershock sequence after 0.5 days and 2) a combination of one main and two secondary sequences – after 0.5 and 53 days. The same p value for the main and secondary aftershock sequences is assumed for both models.

To select which model fits the observations better, the Akaike Information Criterion (AIC) [11] is used. AIC criterion is defined by following equation:

$$\mathrm{AIC} = (-2)\max(ln-\mathrm{likelihood}) + 2(\mathrm{Number\ of\ the\ used\ parameters}) \quad (1)$$

Results are presented in Table 1.

The maximum likelihood estimate of the parameters in the modified Omori formula, and the selection of a statistical model based on AIC, show that the aftershock sequence of the 2012 Pernik earthquake

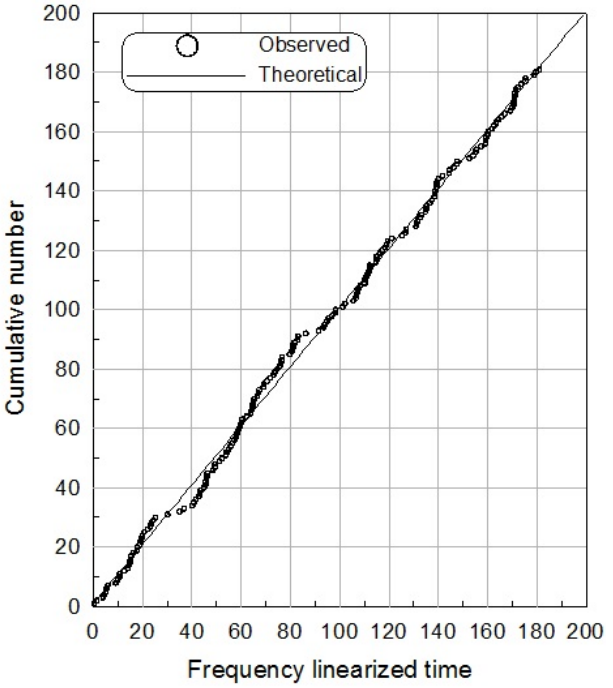


Fig. 8. Plot of the cumulative number of events versus the frequency-linearized time τ (one ordinary and two secondary aftershock sequences with $p = p_1 = p_2$).

is best modeled by one ordinary and two secondary sequences (presented in Fig. 8), although there remain S-shaped deviation from the linear trend – about 80 day after the main shock.

The temporal pattern of earthquake distribution in aftershock sequence of the 2012 M_w5.6 Pernik quake that is characterized with slow decay in time $p < 1.0$ (p value of the main and secondary sequences is 0.91) is similar to the temporal distribution of aftershocks in Northern Bulgaria [12]. The results give reason to be assumed that aftershocks are generated in slowly relaxing environment with low heterogeneity. (The same results are reported in [13] where the aftershock sequence is analyzed for 365 days elapsed time after the 2012 Pernik earthquake.)

Table 1. *MLE*'s of the Omori formula parameters and corresponding *AIC*

Model	K	p	c	K_1	p_1	c_1	K_2	p_2	c_2	*AIC*
An ordinary aftershock sequence	15.22	0.91	0.026	–	–	–	–	–	–	97.56
One ordinary and one secondary aftershock sequences, p=p_1	15.15	0.93	0.028	0.44	0.93	0	–	–	–	76.64
One ordinary and two secondary aftershock sequences, p=p_1=p_2	14.09	0.91	0.028	0.40	0.91	0	0.44	0.91	0	74.96

FOCAL MECHANISMS

Earthquake focal mechanisms provide one of the best observational materials for analyzing the current state of stress in the crust. The fault-plane orientations and slip directions of earthquakes can provide important information about fault structure at depth and the stress field in which the earthquakes occur.

Fault plane solutions for the 2012 M_w5.6 Pernik earthquake and 19 aftershocks with $M \geq 3$ are presented in Fig. 9.The focal mechanisms were calculated according to the definitions in Aki and Richards [14] using the polarities of the P wave, azimuth and incidence angle by applying the software FOCMEC [15] (details are presented in [16]).

As it is seen in the figure, the average strike of one of the nodal planes is 311 NW-SE for all estimated focal mechanisms. The predominant nodal plane can be accepted as the activated fault in the considered area. The fault is extending in NW-SE direction dipping (as average) at 50°. The identified seismogenic structure coincides with the well known Pernik-Belchin fault [7]. The faulting is right-literal if the chosen nodal plane of focal mechanisms is the main one. It means that the foot-wall block is on the right side of line Pernik-Belchin fault the so called Golo Burdo and hanging-wall block is on the left side – Pernik graben.

The main shock and all aftershocks, except those mark by numbers 7 and 16 (see Fig. 9), indicate normal right-lateral fault movement with small strike-slip component, faulting along a hidden fault plane, caused by extensional regional tectonic stresses. The aftershock number 7 indicates thrust faulting with small strike-slip component and the quake number 16 is clear strike-slip motion.

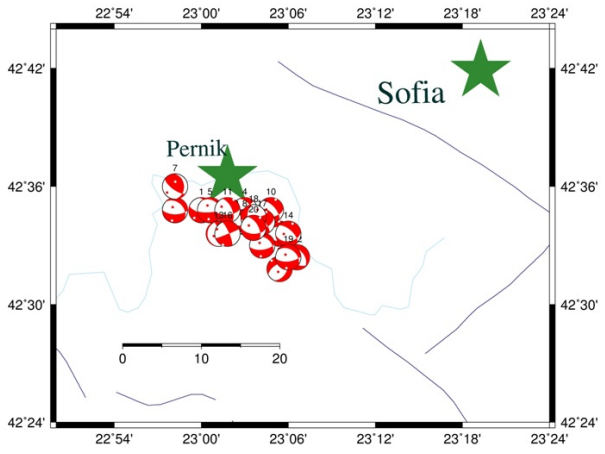


Fig. 9. Fault plane solutions of the 2012 M_w5.6 Pernik earthquake and aftershocks.

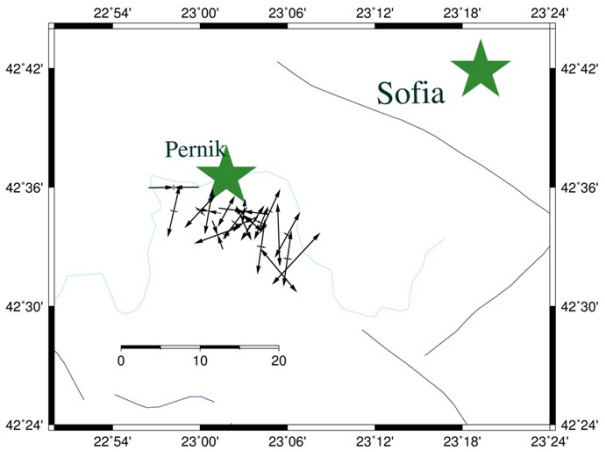


Fig. 10. Individual P and T axes of the 2012 M_w5.6 Pernik earthquake and aftershocks.

Figure 10 displays the horizontal projections of the individual P (pressure) and T (tension) axes of the twenty earthquakes. The axes of compression (P-axes) are orientated predominantly in NW-SE direction and are significantly smaller than the axis of decompression (T-axes) in NE-SW direction. The plunge of P-axes is varying in the range 10°−84°, about 51 in average, and the plunge of T-axes is in predominant sub horizontal orientation (0°-60°), about 15 in average.

The main results from the focal mechanism determination and stress analysis show the prevailing of a normal or extensional stress regime in the considered region (southwestern Bulgaria). Generally, the tension axes are with sub horizontal orientation and large values especially in NE-SW direction.

The observed sub horizontal extensional stresses with predominant NE-SW trend of the T-axes is consistent with the general trend of the regional extensional field of tension axes for southern Bulgaria and surroundings. This stress field corresponds to that found in southern Bulgaria (presented by among others in [17]) and confirms the hypothesis that the neotectonic movements in Balkan Peninsula are the consequence of the long lasting extensional movements in the inner parts of the Aegean region and Central Balkan region.

Acknowledgments. *We are very grateful to anonymous reviewer for his constructive comment and important suggestions, which help to improve the manuscript. We would like to thank employees of*

the Sofia municipality for providing access to all available documentations and reliable information for macroseismic effects caused by 2012 earthquake (M_w5.6). *The work is supported by PROJECT* $BG051PO001-3.3.06-0063$. *The project is funded by the Operational Programme "Human Resources Development", co-financed by the European Social Fund of the European Union.*

REFERENCES

[1] S. Watzof, *Earthdquakes in Bulgaria during XIX century, Central Meteor. St., Imprimerie de L'Etat, Sofia*, p. 93 (1902).

[2] K. Kirov, *Ann. Main Dep. Geol. and Mining Res.* **5**, 407 (1952).

[3] I. Petkov and L. Christoskov, *Annali Sofia Univ.* **58**, 163-179 (1965).

[4] G. Grünthal, *edit., EMS 98, ESC, 15, Luxembourg*, p. 99 (1998).

[5] I. Aleksandrova, *Bulgarian Geophysical Journal, BAS*, accepted (2013).

[6] J. F. Evernden and J. M. Thomson, *Earthquake hazards in the Los Angeles region- An Earth - Science Perspective, Edt. J.I.Ziony. U.S.G.S. Prof. Paper, 1360, U.S. Gov. Print. Office, Wash.*, 151-201 (1985).

[7] Ju. Karagjuleva, E. Bonchev, V. Kostadinov, *Tectonic map of Bulgaria. Sofia, Geological Inst. BAS*, (1973).

[8] T. Utsu, *Aftershocks and earthquake statistics (I), J. Fac. Sc., Hokaido Univ., Ser. VII (Geophys.)* **3**, 129-195 (1969).

[9] Y. Ogata, *J. Phys. Earth*, 115-124 (1983).

[10] Y. Ogata, K. Shimazaki, *BSSA* **74**, 1757-1765 (1984).

[11] H. Akaike, *A new look at the statistical model indentification, IEEE Trans. Autom. Control AC-19*, 716-723 (1974).

[12] S. Simeonova and D. Solakov, *Annali di Geofisica* **42**, 821-832 (1999).

[13] P. Raykova, *Bulgarian Geophysical Journal, BAS*, accepted, (2013).

[14] K. Aki and P. G. Richards, *Quantative seismology: Theory and Methods. New York*, p. 801, (1980).

[15] P. J. A. Snoke, *FOCMEC, Virginia Tech, Blacksburg, VA, USA*, Manual (2009).

[16] V. Protopopova, *Bulgarian Geophysical Journal, BAS*, accepted (2013).

[17] T. van Eck, T. Stoyanov, *Tectonophysics* **262**, 77-100 (1996).

ЗЕМЕТРЕСЕНИЕТО (M_W**5.6) ОТ 2012 ГОДИНА, РЕАЛИЗИРАНО В СОФИЙСКА СЕИЗМИЧНА ЗОНА И ПОСЛЕДВАЛАТА ГО АФТЪРШОКОВА АКТИВНОСТ**

С. Симеонова, Д. Солаков, И. Александрова, П. Райкова, В. Протопопова

Национален институт по геофизика, геодезия и география, Българска академия на науките, ул. "Акад. Г. Бончев" бл.3, 1113 София, България

(Резюме)

Софийска сеизмична зона, разположена в централна западна България, е област с висока плътност на населението, индустриален и културен център на България и силна сеизмична уязвимост.

Наличните исторически документи свидетелстват за разрушителни земетресения в зоната през 15-ти и 18-ти век. През 19-ти век в близост до град София, разположен в централната част на сеизмичната зона, са реализирани две силни земетресения: през 1818 г. с интензивност $I_0 = 8–9$ МШК и през 1858 г. с $I_0 = 9–10$ МШК. Земетресението от 1858 г. е нанесло сериозни щети в град София и е довело до появата на термални извори в западната му част. В началото на 20-ти век, през 1905 г., в околностите на град Трън, разположен в западната маргинална част на зоната, е реализирано силно сеизмично събитие с $M_S = 6.5$, последвано (през 1917 г.) от умерено силното земетресение (M_s =5.3 и $I_0 = 7.8$ МШК), локализирано в близост до град София. Земетресението е усетено в област с площ около 50000 km^2 и е последвано от афтършокова серия продължила повече от година. Почти век по-късно (95 години) на 22 май 2012 г., земетресение с магнитуд $M_w = 5.6$ ($I_0 = 8$ МШК) се реализира в околностите на град Перник, на около 25 км югозападно от град София. Земетресението е усетено в голяма част от територията на България (до приморските градове Бургас и Варна) в западна Македония, северна Гърция и Турция. Няма жертви и сериозно ранени. Установените щети в градовете София, Перник и Радомир (най-близко разположените градове) са предимно леки до умерени и в единични случи умерено силни. Събитието е последвано от интензивна сеизмична активност.

В настоящата работа са оценени въздействията от земетресението, реализирано на 22 май 2012 г., върху територията на България и околностите ѝ. Специално внимание е отделено на установените щети в град София. Анализирани са спектралните характеристики на главния удар и на най-силните афтършокови събития (M>4.0). Изследвано е пространствено-времевото разпределение на афтършоковите събития. На базата на решенията на механизмите е установено, че преобладаващият вид разломно движение в зоната е с нормален разседен фокален механизъм (в 19 случая от 20 решения на механизмите). Най-общо осите на максимална компресия (P-осите) на локалните напрежения са в направление СЗ-ЮИ.

Bulgarian Chemical Communications, Volume 47, Special Issue B (pp. 405–411) 2015

Tornado climatology for Bulgaria (2001-2010)

L. Bocheva*, I. Gospodinov

National Institute of Meteorology and Hydrology, Bulgarian Academy of Sciences,
66 Tsarigradsko Chaussee Blvd., BG-1784 Sofia, Bulgaria

The present work is an attempt to summarize and analyze all documented cases of tornado or waterspouts in Bulgaria between 2001 and 2010. A list of all known tornadoes and waterspouts within the 10-year period has been given. It includes the time and the location of occurrence, the strength and the type of the terrain beneath. Most of the tornadoes in Bulgaria have been classified as F0-F1 of the Fujita scale. The given climatology of the occurrence of tornadoes and waterspouts consists of analysis of its spatial and temporal distribution. By space, tornadoes in Bulgaria tend to occur in the southwestern, southcentral and northestern parts of the country. The frequency of occurrence of tornadoes in Bulgaria appears to be about 0.32 per unit area of 10^4 km^2 per year. The highest probability has been found to be in the administrative regions of Sofia-city and Razgrad. By time, tornadoes tend to occur in the warm half of the year, most often in July, and in the afternoon. The large-scale atmospheric patterns and the thermodynamic parameters and instability indices of the environment associated with the occurrence of tornadoes and water spurts in Bulgaria have also been given.

Key words: tornado, waterspout, Bulgaria

INTRODUCTION

Tornadoes occur relatively rarely in Bulgaria compared to other parts of the world. They have scarcely been documented in Bulgaria prior to 1995 mainly in popular editions [1, 2]. These publications are based on media reports of eyewitnesses' accounts or other reports of experts who had investigated in situ the damage left by tornadoes. Tornadoes are naturally associated with convective storms and therefore they occur in the context of large scale atmospheric conditions favoring deep convection. Statistically tornadoes in Bulgaria occur mainly over mountainous terrain or over large water surfaces (lakes, water dams, and sea). Tornadoes in Bulgaria may often remain unreported when they occur in remote and weakly populated mountainous regions of the country or if they leave no significant damage behind. The number of reports of tornadoes in Bulgarian in the last 10-15 years however has significantly increased thanks to the revolutionary development of the information technology. There exist even amateur websites where one can find up-to-date summary of suspect tornado cases in the country given either by description of the damage or by photos of the object. While some of them were indeed tornadoes others were rather downbursts or funnel clouds not touching the ground.

More elaborated analyses of individual tornado cases in Bulgaria for example can be found in [3–5]. In [4] the weather patterns associated with the occurrence of tornadoes in Bulgaria are presented. However he relied on unverified scarce data of tornado occurrences gathered from media.

This study mainly summarizes general features of the tornado and waterspouts statistics such as the geographical, yearly, monthly and diurnal distributions. Characteristics concerning tornado intensity are also presented. The main synoptic patterns and the thermodynamic parameters and instability indices related to tornado occurrence are also given.

METHODOLOGY

The present work is based on a collection of data of 36 tornados and waterspouts in Bulgaria between 2001 and 2010. Data originated from eyewitness reports, site investigations, media news, reports of the local administration of damage in crops and infrastructure. Press and TV are often the richest source of images of the tornadoes and waterspouts themselves or the damage they have caused. Data from site investigations of damage, scientific publications, the meteorological data base of National Institute of Meteorology and Hydrology (NIMH) and the archives of the Bulgarian Hail Suppression Agency (BAHS) are also included. All cases have been verified by means of analysis of the weather patterns based on the NCEP/NCAR Reanalysis [6] and maps from NOAA/ESRL Physical Sciences Devision, Boulder Colorado (http://www.esrl.noaa.gov/psd/). The analysis of the vertical structure of the atmosphere at the location and the time of occurrence based on the

* To whom all correspondence should be sent:
lilia.bocheva@meteo.bg

© 2015 Bulgarian Academy of Sciences, Union of Chemists in Bulgaria

sounding data from the archives of NIMH. The method applied for the later is the one of [3]. Some of the cases were also verified by using radar images and data from the automated radar system of NIMH (X and S-band AMS-MRL5) based in Gelemenovo and the 3 radar systems of BAHS (S-band AMS-MRL5) which have been upgraded to Doppler capability since 2008 and have been equipped with IRIS (Interactive Radar Information System) for imaging. The tornado cases have also been classified by strength according the Fujita scale [7].

The sounding data from the national (Sofia) or the closest foreign aerological stations (Thessaloniki, Belgrade, Bucharest) have been used to calculate some thermodynamic parameters and indices of instability at the vicinity of occurrence of the tornadoes. Surface data (pressure, temperature, humidity parameters, wind speed and direction) from the closest weather station have been fitted to the lower part of the vertical profile. All computations have been made by the upgraded in 2013 non-adiabatic empirical model presented in [8]. Alternatively other data from http://www.esrl.noaa.gov/psd/ (NOAA/ESRL Physical Sciences Division, Boulder Colorado) have been used for some of the cases. Based on all these the instability has been summarized statistically by using data analysis software system StatSoft.

SPATIAL AND TEMPORAL DISTRIBUTION OF TORNADOES IN BULGARIA BETWEEN 2001 AND 2010

The above mentioned 36 tornado cases have occurred in 32 days. Sioutas [9] defined the frequency P of tornado occurrence as the number of events per area unit of 10^4 km^2 per year. The average number per year in Bulgaria is 3.6 (σ=1.8) which therefore makes up a frequency of P=0.32/10^4 km^{2}year^{-1}. Holzer [10] has published a similar frequency for Austria (P=0.3/10^4 km^{2}year^{-1}) while the one for Greece appears to be 4 times bigger (P=1.1/10^4 km^{2}year^{-1} - [9]).

Figure 1 illustrates P per administrative regions. As can be seen only 17 out of 28 administrative regions have registered tornadoes for the 10-year period. The Sofia-city region has the highest frequency of 2.2/10^4 km^{2}year^{-1} followed by Razgrad (1.1/10^4 km^{2}year^{-1}). The regions of Veliko Turnovo and Smolyan (0.9/10^4 km^{2}year^{-1}), Plovdiv and Varna (0.8/10^4 km^{2}year^{-1}), Targovishte and Kyustendil (0.7/10^4 km^{2}year^{-1}), and Vratsa (0.6/10^4km^2) exhibit frequencies grater than the national average. Only

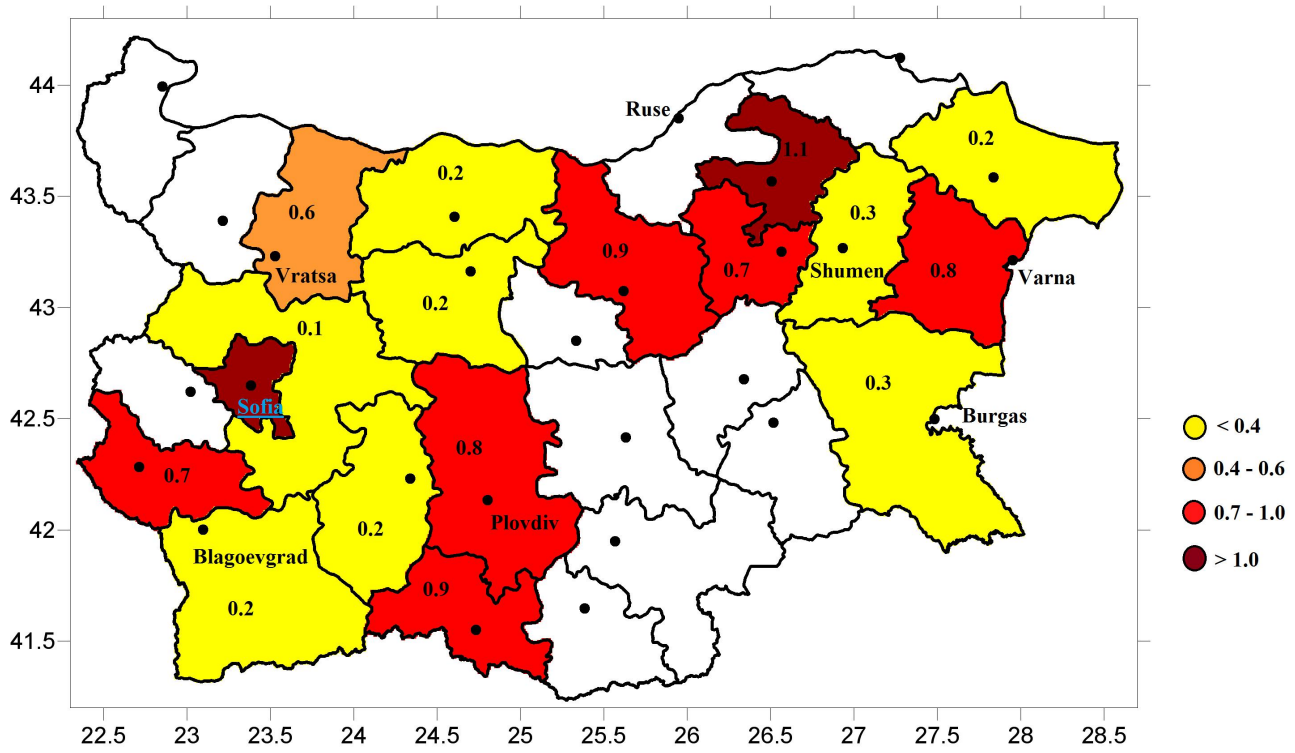


Fig. 1. Mean annual frequency of tornado occurrence in Bulgaria per administrative provinces (2001-2010).

Table 1. Tornadoes and waterspouts in Bulgaria (2001-2010): mw – mountainwooded; m – mountain; hw – hilly wooded; h – hilly; f – flat; WS (Ws) – waterspout; T – tornado

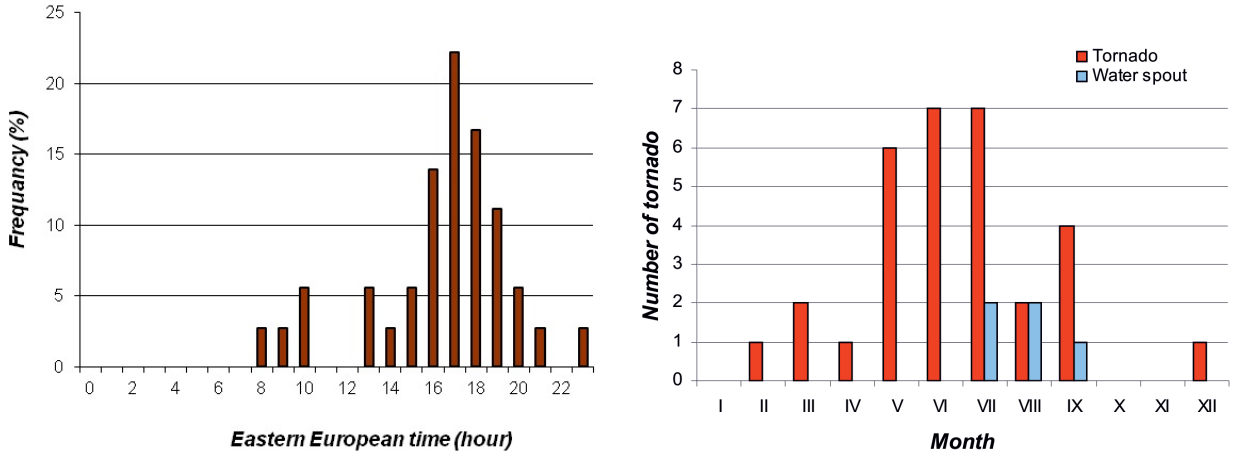
Tornado location	Date	Type	Time	F-scale	Land-scape
Zheleznitsa	22 May 2001	T	PM	F1-F2	mw
Dobroslavtsi	29 Aug 2001	T	PM	F1	f
Radanovo	11 Sept 2001	T	AM	F0	h
P. Trambesh	25 Sept 2001	T	PM	F0	h
Voivoda	10 June 2002	T	PM	F1	h
Palamartsa	23 June 2002	T	PM	F1	h
Trud	19 July 2002	T	AM	F2	f
Kavarna	20 July 2002	Ws	PM	?	WS
Karantsi	12 Aug 2002	T	PM	F1	h
Slavyanovo	23 May 2003	T	PM	F2	f
Bolyartsi	24 March 2004	T	PM	F1	f
Gramade	27 Sept 2004	T	PM	F1	m
Fatovo	15 Feb 2005	T	PM	F1	m
Alexandrovo	29 May 2005	T	PM	F2	hw
Perushtitsa	01 July 2005	T	PM	F1	m
Rezovo	05 Sept 2005	Ws	PM	?	WS
Bobeshino	02 June 2006	T	AM	F1	mw
Kaloyanovo	14 June 2006	T	PM	F0	f
Provadiya	28 July 2006	T	PM	F0	h
Varna	28 Aug 2006	Ws	PM	?	WS
M. Yonkovo	21 March 2007	T	PM	F1	h
Yoglav	21 May 2007	T	PM	F1-F2	h
Kalekovets	21 May 2007	T	PM	F1-F2	f
Krivina	21 May 2007	T	PM	F1-F2	f
Pavlikeni	12 July 2007	T	PM	F1	hw
dam Dospad	06 Aug 2007	Ws	PM	?	WS
Dospad	01 Sept 2007	T	PM	F0	mw
Kancelovo	22 April 2008	T	PM	F2	hw
Kyustendil	08 July 2008	T	PM	F0	f
Vulchedrum	02 June 2009	T	PM	F2	f
Tarnava	02 June 2009	T	PM	F2	f
Tsar Kaloyan	16 June 2010	T	PM	F1	hw
Vakarel	01 July 2010	T	AM	F0	f
Sozopol	26 July 2010	Ws	AM	?	WS
Slunchevo	26 July 2010	T	AM	F0	h
Bansko	02 Dec 2010	T	AM	F0	m

water spurts have been reported in the regions of Dobrich and Burgas which border the Black sea.

All documented tornado cases in Bulgaria from 2001 to 2010 have been classified by strength according to the Fujita scale and by the type of the topography and the land use of the terrain upon which they occurred (see Table 1). For these classifications the approach presented in [11] is used. There are 12 cases upon mountainous or hilly terrain covered by shrub or grass; 8 cases upon wooded mountainous or hilly terrain; 11 cases over flat terrain (plain); and 5 waterspouts. More than half (above 55%) of all cases in Bulgaria therefore have occurred over mountainous or hilly terrain which contrasts with other parts of Europe where tornadoes most often form and develop upon flat terrain or near water bodies [9,12,13]. All mountainous tornadoes were in the southwestern part of the country and mainly in the mountain of Rhodopes except 2 cases: one on the northern slopes of the mountain of Pirin and another one on the northern slope of the mountain of Vitosha right to south of Sofia. The outcome of mountainous tornadoes often remains unnoticed if they have been relatively weak or if they have occurred in relatively remote and hardly accessible parts of the mountains.

The classification by strength given in Table 1 excludes the 5 waterspouts. The reason is that they left no damage and this inhibits the attempts to classify them according to the Fujita scale. Most of the tornadoes (68%) from Table 1 match or even do not reach the F1 level of the Fujita scale which means that they were weak. This result corresponds well to similar statistics for Germany (55%, [14]) and Austria (62%, [10]) but is significantly less than in Finland (86%, [15]). There is an overall tendency of increase of the documented weak tornadoes in various databases in both Europe and the USA [14, 16]. The same has been identified for Bulgaria as well [5]. About 13% of all cases in Table 1 have been attributed with an intermediate class F1-F2 because the damage data corresponds to the higher class F2 but the wind data suggest only class F1. There have been no documented casess of a class higher than F2 in Bulgaria.

The diurnal ditribution of tornadoes and waterspouts in Bulgaria within the studied period is presented on Fig. 2a. Naturally most of the cases (about 80%) occured within the afternoon hours between 14:00 and 18:00 local time (East European Time (EET) which in summer is 3 hour ahead of the Universal Coordianted Time (UTC) and in winter – 2 h). This corresponds to the diurnal maximum of the thunder storm activity in Bulgaria [17] and also to similar statistics for other European countries [15, 18]. All documented cases occurred in daytime between 07:00 and 20:00 EET. This fact of course can be linked to the nature of the convective clouds which develop mostly in the afternoon hours. Another contributing factor could be the fact that people tend to report tornadoes during day when they are more active.



(a) (b)

Fig. 2. Diurnal (a) and monthly (b) distribution of all studied and proven tornadoes in Bulgaria (2001-2010).

On the other hand about half of all waterspouts over the Black sea take place in the morning hours (09:00–12:00 EET). This can be explained by the different surface conditions over water compared to those over land.

Figure 2b shows the monthly distribution of tornado cases from the list. Almost all cases (93%) occurred within the warm half of the year between April and September. The months of June and July exhibit the highest frequency. This corresponds to the statistics for other countries in Central and Eastern Europe. July appears to be the month with a maximum number of tornadoes in Germany [14], Austria [10], and Greece [9]. In Southern Europe however the maxima tend to occur later in August (Italy [13]) or in September (Spain [12]). Waterspouts in Bulgaria seem to occur between July and September as revealed by Fig. 2b. This matches the time of year when the sea water is the warmest. It also corresponds well to similar statistics for other neighbor countries (Croatia [19] and Northern Greece [9]).

In the list of documented tornadoes in the 10-year period there are 4 "winter" cases which occurred within the cold half of year: 3 of which in Southern Bulgaria and 1 - in Northeastern Bulgaria. They were associated with strong thunderstorms which developed along rapid and intense cold fronts introducing cold and moist air masses in Bulgaria after a prolonged period of unseasonably warm and dry weather. The newly detected "winter" tornadoes in the recent years can be due to the overall global warming trend or it can be the result of the revolutionary development of the information technologies.

METEOROLOGICAL CONDITIONS FAVORING DEVELOPMENT OF TORNADOES IN BULGARIA

Synoptic scale conditions

More detailed analisys and classification of synoptic-scale patterns conditioning tornadoes in Bulgaria have been given in our prvious works [5,20]. Based on these we can say that it seems that most tornadoes (90%) developed in the context of a cold front system with predominantly meridional extent from southwest to northeast which was associated with a strong air flow in the middle and upper troposphere [4, 5, 20]. The cold-front system should have crossed the country. Such cold fronts are most often associated with a deep upper-level trough to the west of Bulgaria over the Central Mediterranean. When associated with tornadoes though, they appear to be rather stationary for a certain period of time or progress slowly through the country. Additional factors play a favorable role for the development of tornadoes such as the time of day within which the cold front goes through the country and the characteristics of the terrain. The convection is facilitated if the front crosses the country during day time and if the front orientation is transversal to orographic obstacles like mountain chains [20].

Thermodynamic conditions

Similarly to [9, 21] we present short analysis of the thermodynamic conditions within which the tornadoes in Bulgaria developed. Only those 31 cases observed over land have been taken into account. There are many difficulties when attempting to study

the thermodynamics at the vicinity of occurrence of tornadoes. First of all, there are only a few sounding profiles available in the region. The NIMH operates only one aerological site and conducts only one sounding per day at 12:00 UTC which is in the afternoon. This inhibits the attempts to see the instability factors prior to events occurring before noon for example. Secondly, the tornadoes are a very short-lived phenomenon associated with strong convective storms. Quite very often the instability factors, if measured by popular indices like CAPE (Convective Available Potential Energy) for example, disappear when the storm passes. Depending on the location of the storm and the tornado associated with the storm the sounding data may or may not exhibit appropriate values of CAPE. These reasons led to the choice of 4 specific indices of instability based on sounding profiles of temperature, humidity, and wind in the lower and middle troposphere and they are:

- **K I**ndex [22]

$$KI = (T_{850} - T_{500}) + T_{d850} - (T_{700} - T_{d700}) \quad (1)$$

- **T**otal **T**otals Index [23]

$$TTi = (T_{850} - T_{500}) + (T_{d850} - T_{d500}) \quad (2)$$

where T_{850}, T_{700}, and T_{500} denote temperature at levels 850, 700, and 500 hPa and T_{d850} and T_{d700} denote dew point at levels 850 and 700 hPa.

- **L**ifted **I**ndex [24]

$$LI = (T_L - T_{500}) \quad (3)$$

where T_L is the temperature of an adiabatically (dry or wet depending on the level of saturation) ascending air parcel from level 850 hPa to level 500 hPa; T_{500} is the air temperature at level 500 hPa.

- **S**evere **WEA**ther **T**hreat index (SWEAT) [23]

$$SWEAT = 12T_{d850} + 20(TT - 49) + 2V_{850} + V_{500}g + 125(\sin(dd_{500} - dd_{850}) + 0.2) \quad (4)$$

where TT is the Total Totals index, V_{850} and V_{500} denote the wind velocity at levels 850 hPa and 500 hPa respectively, and $dd_{500} - dd_{850}$ is the difference between the directions of wind in degrees at the two levels.

High values of these 4 indices indicate increased instability. According to other authors [25] $KI > 25$ and $TT > 49$ indicate conditions favorable for the development of strong thunderstorms with hail and/or tornadoes. Table 2 summarizes some statistics of the 4 indices for the studied tornado cases. As it can be seen the means of KI, TTi, and LI (column 1) are above the threshold values. The TTi also corresponds to what has been found by David [26] for tornado cases in the USA. The means of LI and TTi are grater than those obtained for Northeastern India and Bangladesh [27]. The mean $SWEAT$ is greater than the one for Greece [9] but lower than 400 which was found to be a threshold value for summer tornado storms in the USA [26]. Nevertheless the mean $SWEAT$ corresponds to the one for the month of May in USA (253, [26]). The month of May is one of the months with the highest occurrence of tornadoes in the USA. The means of KI, TTi, and LI for Bulgaria correspond well to those for Greece and for the same 10-year period ($KI = 29.2$, $TTi = 48$, $LI = -1.6$ [9]).

Table 2. Instability indices of the environment of Bulgarian tornadoes

Index	***Mean***	***MIN***	***MAX***	***SDV***
KI, °C	30.6	13.9	43.7	7.8
TTi, °C	51.7	42.5	61.0	4.3
LI, °C	-5.4	-13.7	2.5	3.3
$SWEAT$	240.7	107.8	399.9	89.1

Table 3. Thermodinamic and wind parameters of the environment of Bulgarian tornadoes

Parameter	***Mean***	***MIN***	***MAX***	***SDV***
ΔT_{500}, °C	7.8	2.8	10.7	2.2
DT_m, °C	10.0	6.0	16.6	2.8
S_{DT754},°C	21.1	10.5	31.2	5.7
$w_{\max}$, m/s	17.1	12.0	24.5	3.5
Δv, m/s	13.0	-3.0	45.0	12.3
H_0, m	4454	2278	5899	917
$LfcEL$, m	11637	8484	13254	1305

The parameters in Table 3 are:

ΔT_{500} – temperature difference between the temperature profile and the adiabatic profile at level 500 hPa;

DT_m – the maximum temperature difference between the temperature profile and the adiabatic profile;

S_{DT754} – the sum of the temperature differences at levels 700 hPa, 500 hPa, and 400 hPa;

$w_{\max}$ – the maximum value of updraft velocity;

Δv – wind shear 300-700 hPa (for wind speed only);

H_0 – altitude of 0 °C;

$LfcEL$ – lifted convective equilibrium level.

They all show up near or above threshold values for strong thunderstorms in the warm half of the year in Bulgaria found by other authors [28, 29]. The values of ΔT_{500} and DT_m indicate conditions favorable for deep thermal convection. This correlates with the high value of $w_{\max}$. The values of Δv suggest that for 85% of all cases the maximum vertical velocity of the ascent is in the upper part of the convective cloud. The values of $LfcEL$ match those of [28] identified as being informative for the development of hail producing summer convective storms. The mean value of $LfcEL$ is even grater than the one of [29].

CONCLUSION

The analysed cases will enrich the database of NIMH of severe storm events and can be used for further improvement of techniques and practices for severe weather warnings as well as for studying the climate variability of such severe weather phenomena. Tornadoes in Bulgaria mainly occur in the north-central, north-eastern and south-central regions of Bulgaria over mountainous terrain but also over plains. There is a tendency of increase of the documented number of tornado events in Bulgaria during the last 10 years. From one side the mechanism of this trend from physical point of view remains to be studied but, from the other side, it may also be due to the fact that information (including amateur photos and videos) about such rare and short-lived meteorological phenomena have become available more frequently in the recent years. The intensity analysis indicated that the majority of the tornadoes in Bulgaria can be classified as F0-F1 of the Fujita scale which is equivalent to "weak" tornadoes. The analysis of the selected thermodynamic indices and wind parameters showed values comparable to those found in the literature. However, the high dispersion suggests that tornadoes can form and develop in significantly varying thermodynamic environments.

These results, although modest, will contribute to the enrichment of the tornado climatology of the Balkans and Europe. Further climatological research is needed for quantitative and qualitative improvement of the tornado and waterspout database.

Acknowledgments. *We are grateful to the experts from the BAHS of the Ministry of Agriculture and Food for the provision of radar images and data of damage left by some of tornadoes.*

REFERENCES

[1] B. Vekilska, *The atmosphere in motion, Small-scale vortices*, Publ. Narodna prosveta, Sofia, 1983 (in Bulgarian).

[2] M. Sirakova, D. Sirakov and K. Donchev, *Meteorology for everyone, Tornado*, edited by M Krumova, Publ. Science and art, Sofia, 1989 (in Bulgarian).

[3] P. Simeonov and Ch. C. Georgiev, *Atmos. Res.* **67–68**, 629–643 (2003).

[4] L. Latinov, *Wheather conditions for snow storms, frost, duststorms and tornado in Bulgaria, Tornado*, edited by B. Hristov, Publ. LITO Balkan AD, Sofia, 2006 (in Bulgarian).

[5] P. Simeonov, L. Bocheva and I. Gospodinov, *Atmos. Res.* **123**, 61–70 (2013).

[6] E. Kalnay, M. Kanamitsu, R. Kistler, W. Collins, D. Deaven, L. Gandin, M. Iredell, S. Saha, G. White, J. Woollen, Y. Zhu, A. Leetmaa, B. Reynolds, M. Chelliah, W. Ebisuzaki, W. Higgins, J. Janowiak, K. C. Mo, C. Ropelewski, J. Wang, R. Jenne and D. Joseph, *BAMS* **77**, 437–471 (1996).

[7] T. T. Fujita, *J. Atmos. Sci.* **38**, 1511–1534 (1981).

[8] P. Simeonov, *J. Appl. Meteorol.* **35**, 1574–1581 (1996).

[9] M. Sioutas, *Atmos. Res.* **100**, 344–356 (2011).

[10] A. M. Holzer, *Atmos. Res.* **56**, 203–212 (2000).

[11] J. Dessense and J. T. Snow, *Weath. and Forecasting* **4**, 110–132 (1989).

[12] M. Gaya, *Atmos. Res.* **100**, 334–343 (2011).

[13] D. Giaiotti, M. Giovannoni, A. Pucillo and F. Stel, *Atmos. Res.* **85**, 534–541 (2007).

[14] P. Bissolli, J. Grieser, N. Dotzek and M. Welsch, *Glob. And Plan. Change* **57**, 124–138 (2007).

[15] J. Rauhala, H. E. Brooks and D. Schultz, *Mon. Weath. Rev.* **140**, 1446–1456 (2012).

[16] N. Dotzek, *Workshop: Tornadoes and Hail* Bermuda, November, 2000.

[17] L. Bocheva, P. Simeonov and T. Marinova, *BJMH* **18**, 38–46 (2013).

[18] S. Szilard, *Atmos. Res.* **83**, 263–271 (2007).

[19] T. Renko, J. Kuzmic and N. Strelec Mahovic, Ext. abs. of 7th ECSS, 3-7 June 2013, Helsinki, Finland (http://www.essl.org).

[20] P. Simeonov, I. Gospodinov, L. Bocheva and R. Petrov, *BJMH* **11**, 78–85 (2011).

[21] H. Brooks, J. W. Lee and J. P. Craven, *Atmos. Res.* **67–68**, 73–94 (2003).

[22] J. J. George, *Weather Forecasting for Aeronautics*, Academic press, New York, 1960.

[23] R. C. Miller, *Notes on the analysis and severe-storm forecasting procedures of the Air Force Global Weather Central*, Air Weather Service Tech. Rept. 200 (Rev.), Air Weather Service, Scott Air Force Base, IL, 1972, pp 190.

[24] J. G. Galway, *BAMS* **37**, 528–529 (1956).

[25] M. Siedlecki, *Theor. Appl. Climatol.* **98**, 85–94 (2009).

[26] Cl. David, *Mont. Weath. Rev.* **104**, 546–551 (1976).

[27] R. Bhattacharya, A. Bhattacharya and R. Das, *International Journal of Electronics and Communication technology* **4**, 92–94 (2013).

[28] P. Boev and A. Marinov, *Hidrologiya I Meteorologiya XXXIII* **4**, 10–17 (1984) (in Bulgarian).

[29] P. Simeonov, P. Boev, R. Petrov, D. Sirakov and V. Andreev, *Problems of Hail Suppression in Bulgaria, Climate hail phenomena in the Upper Thracian valley*, edited by S. Panchev, University Publ. "Climent Ohridski", Sofia, 1990 (in Bulgarian).

КЛИМАТИЧНО ИЗСЛЕДВАНЕ НА ТОРНАДО (СМЕРЧ) В БЪЛГАРИЯ

Л. Бочева, Ил. Господинов

Национален институт по метеорология и хидрология, Българска академия на науките, бул. "Цариградско шосе" №66, 1784 София, България

(Резюме)

Макар и рядко, при обстановки, свързани с развитието на мощни конвективни бури, у нас се образуват торнада – най-често над пресечени планински терени или над морската акватория. Торнадото е дребномащабно и кратко по време опасно явление, което е трудно за прогнозиране без наличие на специализирана техника. Често смерчът се бърка с т.нар. "падащ" или шквалист вятър. За отличаването и определяне силата му по скалата на Фуджита (Fudjita) например, е важно да се знаят освен физически и пространствено-времени характеристики и данни за характера и размера на щетите.

През последните 10-15 години, благодарение на бурното развитие на електрониката, телекомуникациите, Интернет и др., съобщенията за торнада в медиите значително се увеличиха. Настоящето изследване се базира на данни за 36 случая на торнада и водни смерчове, регистристрирани в България през периода 2001-2010 г. Те са взети както от метеорологичните архиви и научни публикации, така и от медии, разкази на очевидци, данни от архивите на Национална служба „Гражданска защита", полеви обследвания и справки за щети от местната администрация. За потвърждение и доказване на случаите са използвани синоптична информация от метеорологичната база данни на Националния институт по метеорология и хидрология (НИМХ), радарна информация, данни от аерологичните сондажи в София, Солун, Белград и Букурещ, спътникови данни от EUMETSAT и синоптични карти от реанализите на NCEP/NCAR.

За 10-годишния период на изследване е получена средна годишна честота на торнадата в България от 0.32 на единица площ от 10^4 km^2. Изчислена е и средната годишна честота на явлението за всяка област в страната. Най-голяма е регистрираната годишна честота в областите София – град ($2.2/10^4$ km^2) и Разград ($1.1/10^4$ km^2). Изследвано е и денонощното разпределение на торнадата и водните смерчове в България. Около 80% от всички случаи на сушата са регистрирани в следобедните часове, главно между 14:00 и 18:00 часа местно време, докато над 50% от водните смерчове се развиват преди или около пладне. В близо 70% от случаите в България става дума за слаби торнада от категории F0-F1 според международната скала на Фуджита. Месечното разпределение на торнадата и водните смерчове показва, че те възникват главно през топлото полугодие – 89% от тях са регистрирани в периода април-септември. Все пак има регистрирани и 4 случая на торнадо през студеното полугодие, което може да е следствие както от наблюдаваното повишение на зимните температури (ефекта на т.нар. глобално затопляне), така и от бурното развитие на електрониката и комуникациите, причина за по-често документиране на торнада през последните години. И четирите случая на „зимно" торнадо са свързани с развитието на нетипични за сезона синоптични обстановки.

Изследвани са синоптични обстановки и е направена обобщена класификация на типичните синоптични структури, свързани с развитието на смерчове в страната. Изчислени са и редица термодинамични характеристики на атмосферата, както и набор от индекси на неустойчивост за всички случаи на торнадо над сушата. Пресметнати са и някои статистически характеристики на получените индекси на неустойчивост. Получените резултати са сравними с тези, пресметнати за територията на Гърция, Унгария и други страни от Средна и Южна Европа.

Bulgarian Chemical Communications, Volume 47, Special Issue B (pp. 412–419) 2015

Use of the numerical simulations with weather forecast model WRF as a proxy to atmospheric soundings

R. I. Penchev[1]*, E. L. Peneva[2]

[1] *Bulgarian Air Trafic Services Authority, 1, Brussels Blvrd., Sofia, Bulgaria*
[2] *Department of Meteorology and Geophysics, Faculty of Physics, St. Kliment Ohridski University of Sofia, 5 James Bourchier Blvd., BG-1164 Sofia, Bulgaria*

The present study aims to check the ability of numerical weather forecast models to represent the vertical structure in the atmosphere and thus to serve as an approximation of the in-situ atmosphere sounding. The advantage of using such proxy is the better resolution in both time and space and therefore the lack of measurement would be no longer a problem. The numerical model, used here is the model system Weather Research and Forecasting WRF. The model domain covers the whole territory of Bulgaria and by means of double nesting approach resolves the area with spatial resolution of 1.8 km. Several numerical experiments are performed to configure and tune the model parameters in order to obtain adequate model results. The data from atmosphere sounding in Sofia meteorological station are compared with the data coming from the Doppler channel of meteorological radar Gematronik c360, located in Sofia airport. The simulated vertical profiles of the temperature, humidity and wind are validated using available measurements from atmosphere sounding. Conclusions about the usability of numerical simulations as a proxy of atmosphere sounding are derived. A real application of this method, a case when the model gave useful information, is demonstrated.

Key words: numerical weather forecast, vertical atmosphere sounding, radar meteorology

INTRODUCTION

The need of information about the vertical distribution of the meteorological elements (temperature, humidity, wind speed and direction, dewpoint temperature) in the troposphere is getting more and more important and expressed. Several problems related to the weather forecast, like for example severe convections and storm events alarm, aviation safety, hail protection, require such type of information. Unfortunately the measurements from atmosphere sounding are very expensive and therefore limited in space and time. In Bulgaria sounding is performed once per day in 12 UTC in the meteorological station in Sofia. In general this is not representative for the whole Bulgarian territory having in mind the diurnal cycle, complex relief and different climatic characteristics in Bulgaria. The other remote sensing approach to obtain data are the meteorological radars, which give rich information about the distribution of hydrometeors in the air. The radar data from the Doppler channel could be used to calculate the wind vertical profile, but the ability is limited.

The lack of information about the vertical profile of the main meteorological elements with fine resolution could be partially compensated by the data from numerical weather forecast model. This method is shown further. An example of a real case with an airplane accident in the region of town Tran on 7.05.2014 is described, where the numerical simulation has given a useful information and has helped the investigation of the accident.

NUMERICAL MODEL CONFIGURATION

In this study the Advanced Research WRF (ARW) versionof the model system WRF 3.4.1, implemented in the National Center for Atmospheric Research (NCAR) and the National Centers for Environmental Prediction (NCEP) in United States is used [1]. The initial and boundary conditions for the air temperature, wind speed humidity, pressure and total cloud cover come from the operational global forecast system (GFS) distributed by NCEP with a spatial resolution of 0.5 deg. The model configuration uses the non-hydrostatic approximation. The model domain is resolved by a grid in Lambert Conformal Projection with three nests correspondingly with spatial resolution of 15:5:1.8 km (Fig. 1).

domain covers Bulgaria and adjacent regions, and the third domain with finest resolution is selected in a way to cover the mountain chains in the weather part of the country, and the center is located in Sofia, where the atmosphere sounding is performed every day. The third domain topography is shown in Fig. 2 and one could well identify the Balkan, Vitosha and

* To whom all correspondence should be sent:
rosen_penchev@digicom.bg

© 2015 Bulgarian Academy of Sciences, Union of Chemists in Bulgaria

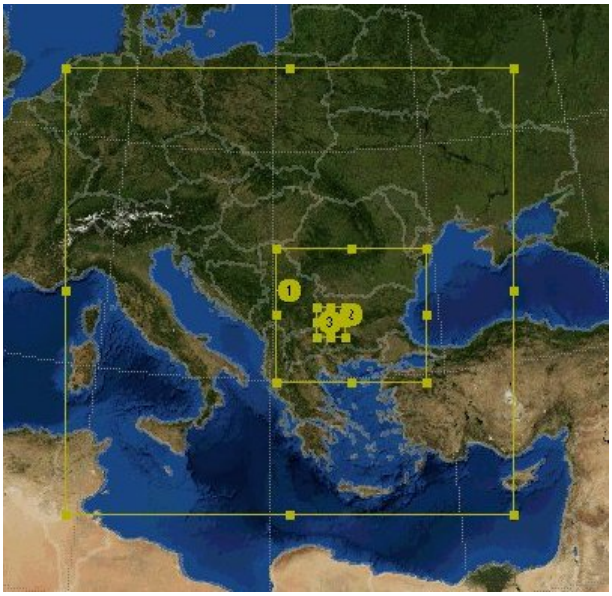


Fig. 1. Three nested model domains.

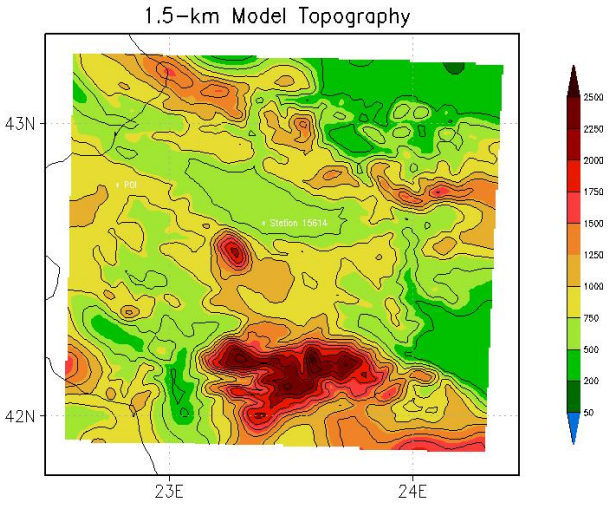


Fig. 2. Third domain topography 1.8 km resolution.

Rila mountains. The vertical coordinate system is sigma – terrain following with 65 levels. Several numerical experiments are performed to configure and tune the model parameters in order to obtain adequate model results. The most important parameters are related to the parameterization of the subgrid physics processes [2].

The following parameterization schemes are used in the model:

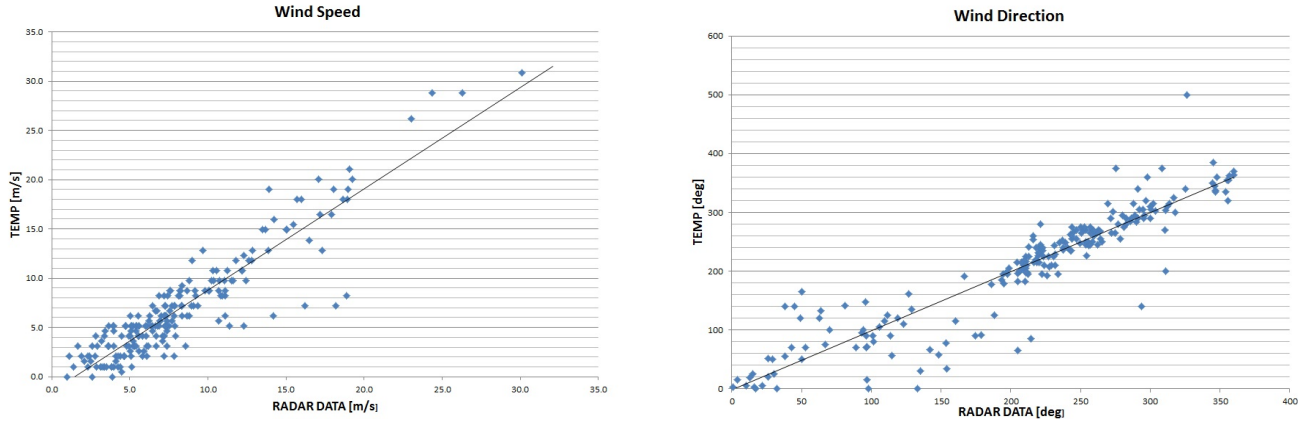
- For microphysical processe in the clouds: WRF Double-Moment 6 class scheme ([9])
- Longwave radiation processes: RRTM (Rapid Radiative Transfer Model) ([7])
- Shortwave radiation processes: Dudhia scheme ([8])
- Air-surface exchange processes: Noah Land Surface Model
- Planetary boundary layer parameterization: Yonsei University scheme
- Convective processes parameterization: Kain-Fritsch scheme ([6]). Note that this scheme is used only in first and second domains, in the third domain with resolution 1.8 km, the convection is not parameterizied.

The model simulation starts at 12:00UTC on 06 May 2014 and the integration is for 24 hours. The interesting period for the airplane accident investigation is around 06:00UTC on 07 May, thus the model spinup time is sufficient.

AVAILABLE DATA TO VALIDATE THE MODEL RESULTS

The simulated vertical profiles of the main meteorological elements could be compared with the data from atmosphere sounding. Such a comparison is performed for example by [3]. This study demonstrates very good positive correlation coefficient between model and sounding data ($r = 0.91$ for the temperature and $r = 0.7$–0.8 for humidity). The authors however show that for the wind the correlation is not so good especially in the low atmopheric layers. We are especially interested in the wind that is why in this chapter we concentrate on that element.

Another approach to validate the model results is the comparison with the wind field calculated from the radar data. A Doppler meteorological radar Gematronic C360 operates on Sofia airport, which is very near to the place of meteorological ballon sounde launching. The radar identifies the hydrometeors in th air and the special algorithm VVP (Volume Velocity Processing) calculates the wind on different vertical levels using the hydrometeors displacement. The output is a product which gives the horizontal wind speed and direction in the vertical column above the radar location. In fact this velocity is representative average for a circle with radi of 25 km. This means that one could expect the vertical wind profile to be smoothed. Another limitation is that the result is usable only in the presence of sufficient quantity of hydrometeors, which are used as indirect passive tracers. So in the clear sky days, the method would not work good. Nevertheless, the temporal resolution is very good (about 5 min) and gives the opportunity to follow fine processes evoluton and the data could give



a) b)

Fig. 3. Comparison of the wind vertical profiles from radar and sounding: a) speed b) direction.

very useful information when validating the model results. Our first objective is to compare the wind measurements from the atmosphere sounding and the radar aiming to quantify the usability of radar data. The period for which we have data is 1-20 May 2014.

The atmosphere sounding data are taken from University of Wyoming data base: http://weather.uwyo.edu/upperair/sounding.html for station 15614, coordinates 42.65N and 23.38E, elevation of 595m. The meteorological radar MRL is located on 530 m elevation and the data are made kindly available to us by the Bulgarian Air Traffic Services Authority. The radar data product gives the wind speed and direction on levels with 200 m step, reaching 10 km height. However, the information is nor regular, some levels are missing in the reports, as the data quality depends on the hydrometeors concentration and the algorithm sensitivity. In order to compare with the sounding data at midday, only the radar data in 12:01 UTC are taken. As the vertical levels differ in both sources of data, linear interpolation of sounding data to radar vertical levels is performed.

The results from the above described comparison are summarized in Fig. 3 a and b, and the main statistics are calculated in Table 1 for the wind speed and Table 2 for the wind direction. The good correlation between sounding and radar is evident ($r = 0.9$). The Root Mean Square Error (RMSE) for the wind speed is calculated following [4]. Very interesting is to check the correlation and RMSE in the different vertical heights, it is seen that better correlation is observed in the free atmosphere. The difference in the wind velocity is about 2 m/s. However, some of the differences are systematic errors, coming from

Table 1. Statistics about the comparison of wind speed in radar and atmosphere sounding

	600m	800m	1400m	1600m	All levels
RMSE	2.1	2.2	2.5	2.4	2.5
Correlation	0.67	0.82	0.79	0.75	0.91

Table 2. Statistics about the comparison of wind direction in radar and atmosphere sounding

	600m	800m	1400m	1600m	All levels
Correlation	0.69	0.87	0.88	0.89	0.88

the specific device functioning. A problem is also the limited sample (only 19 days). For example one of the days the radar observations show twice higher wind speed than the sounding.

The comparison in this chapter was done in order to assure that the data for the wind speed and direction calculated from the meteorological radars could be used for numerical model verification. As the midday sounding is not representative for each moment of the day the radar data could be used as a substitution when verifying the model simulated vertical wind profiles. However, this evaluation should be further extended to all seasons and more sample data, thus the conclusions made should be consider as an initial estimate.

NUMERICAL SIMULATION OF THE VERTICAL DISTRIBUTION OF THE METEOROLOGICAL ELEMENTS ON 07.05.2014

The period of the model integration in this study is chosen on purpose. On 07.05.2014 about 0600 UTC an agricultural airplane had to land emergently

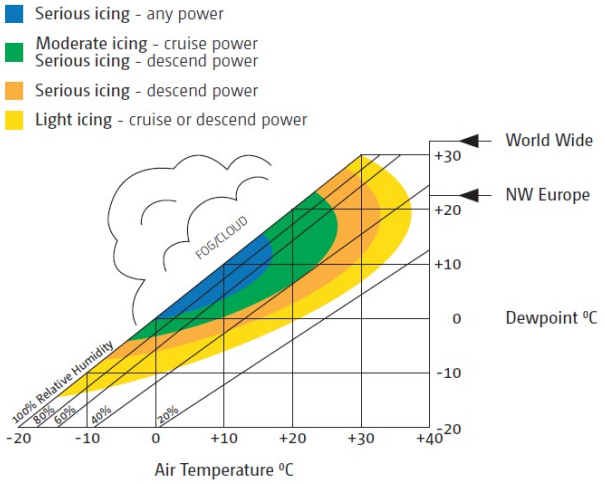


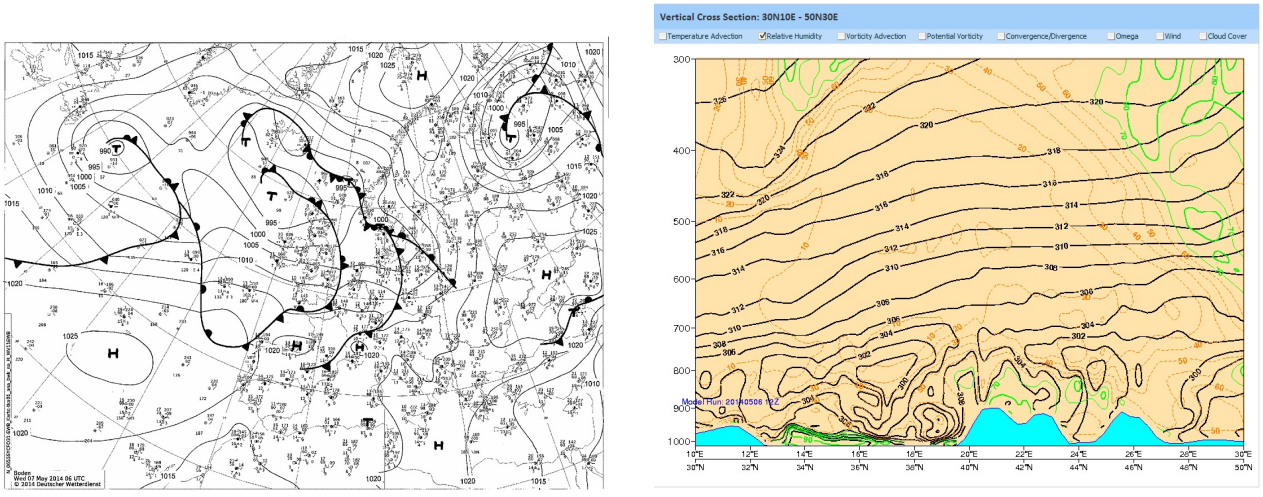
Fig. 4. Icing conditions.

because of the damage in the airplane engine. The landing was near the town Tran and the accident occurred in the location 42,65N and 23,38E, on 1000 m height above the ground. The pilot reported that the reason to cause the accident is a sudden and fast engine carburetor icing. The investigation of the case needed reliable meteorological information about the vertical profiles of temperature for this location. The place and time of the accident are very far from the nearest available atmosphere sounding and no radar data exist for the place. According to the Aeronautical Information Circular AIC: P 077/2009 [5] an engine icing initiates when the air temperature is above 0°C and the relative humidity exceeds 60% Fig. (4).

The important for the investigation was to know whether there were favorable condition for engine icing. As radar and sounding data are not useful in this case, only the surface synoptic measurements of the near high locations could be of help. These are the meteorological stations in Dragoman, Sofia, Kiustendil and Cherni vryh. In this case the numerical model approach proved to be very helpful.

The synoptic observations for the date of the accident are shown in Fig. 5a and Fig. 5b gives the vertical cross-section from the prognostic analysis of the European Center for Medium range weather forecast (source http://eumetrain.org/). The two analysis show that Bulgaria was in the periphery of a large anticyclone centered over Russia. This situation is favorable for formation of temperature inversion in the planetary boundary layer and the air mass was humid. The estimate of the weather conditions is only qualitative and more precise quantitative estimate is not possible based only on this data. That is why we used the described in Chapter 2 configuration of WRF model. The numerical experiment provided 3D fields of temperature, humidity and wind for the moment of the accident with a spatial resolution of 1.8km. The simulated vertical profiles for the temperature and relative humidity in the location of the accident in 0600 UTC are given in Fig. 6.

From the plots in Fig. 6 one can see that on level 820hPa, which correspond approximately to 900 m the values for the temperature is 3.5°C and the relative humidity of 63%. These are favorable conditions for icing and it could occur according to [5].



a) b)

Fig. 5. a) Synoptic maps of Europe for 7.05.2014 from wetterzentrale.de and b) ECMWF prognostic analyses cross-section from eumetrain.org.

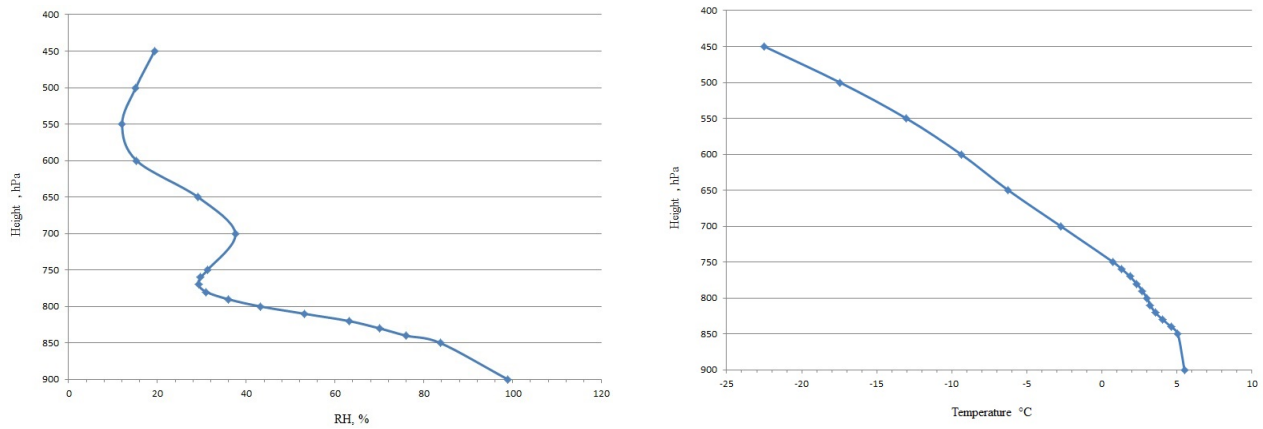


Fig. 6. Simulated vertical profiles for the temperature and relative humidity in the location of the accident.

MODEL RESULTS VERIFICATION

The model results confirm the pilot report plausible. But the question is whether the model results are reliable. Unfortunately this day the meteorological radar in Sofia airport did not produce a good wind profile that is why we can use only the available atmosphere sounding in Sofia at 12 UTC to validate the model results.

The taken model data refer to 1200Z on 7.05.2014. The comparison with the sounding data is shown in Fig. 7 in the form of aerological diagrams: the sounding temperature, relative humidity and wind profile on the left plot, and the corresponding model profiles - on the right. One can note the good agreement between the two sources of data. The layer of temperature inversion between 500 and 350 hPa is represented well by the model, the tropopause height at about 250 hPa coincides as well. The agreement between model and sounding wind profiles is excellent especially in the free atmosphere. The vertical variations of dewpoint temperature match also well, larger differences could be seen in low troposphere and the reason for that is the parameterized boundary layer processes and the discreet resolution in vertical.

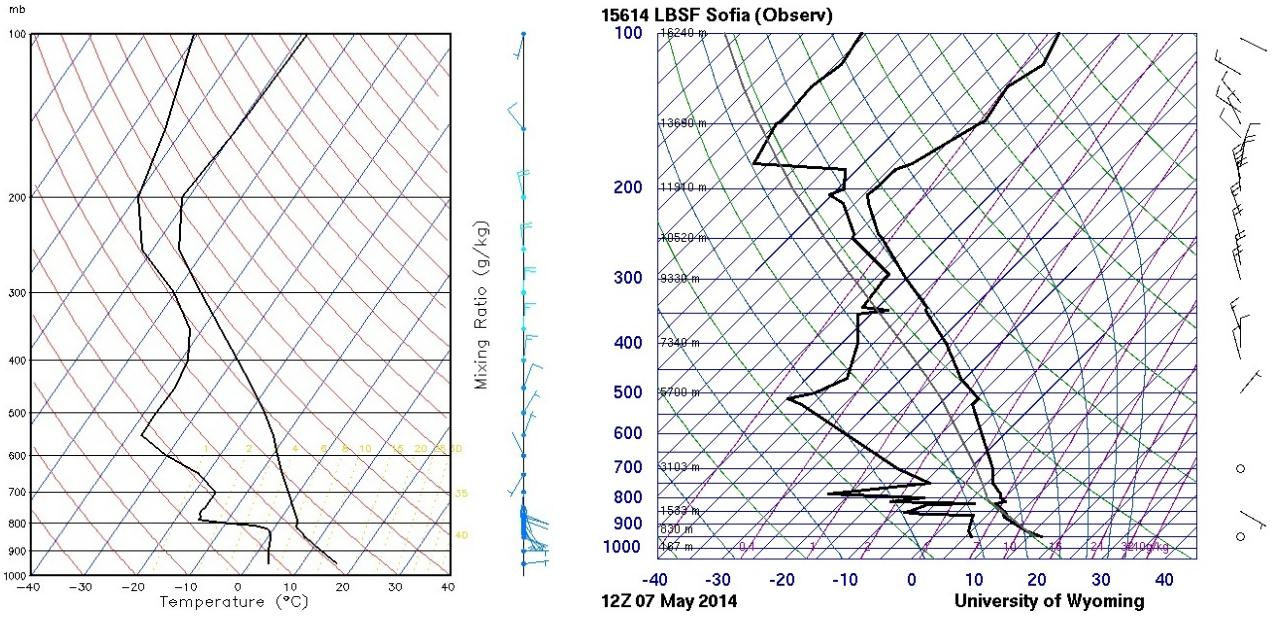


Fig. 7. Simulated vertical profiles for the temperature and relative humidity in the location of the accident.

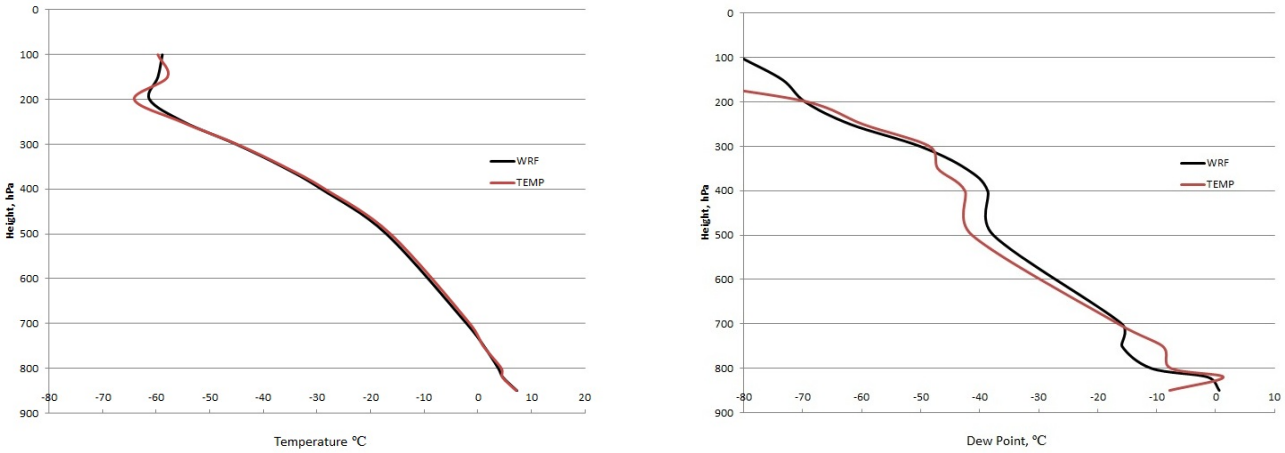


Fig. 8. Comparison between vertical profiles from sounding and WRF model for air (left) and dewpoint (right) temperature.

In order to better demonstrate the agreement between sounding data and model results we show in Fig. 8 the superimposed curves of the measured and simulated air temperature (the left plot) and dewpoint temperature (the right plot). The agreement is almost complete for the temperature in the lower and middle troposphere. The correlation coefficioent between the curves in the left plot is 0.99, and the RMSE about 1 deg C. Regarding the dewpoint temperature the differences are mainly in the layers between 800-700 hPa and 500-400 hPa and is related most probably to cloud formation. Nevertheless the correlation coeficient is 0.9, indicating good agreement.

The place of the airplane accident is situated about 50 km from Sofia. Thus, in principle, the meteorological radar at Sofia airport covers this area and the radar data are rather representative. As stated in Chapter 3, these data are also useful for model results validation. Unfortunately, the radar data for 7.05.2014 are not good quality so we had to take other dates for comparison of model and radar wind.

For this purpose, several other experiment for the period of the airplane accidents were run. Seven dates with valid radar wind profiles for 6h are chosen and the described in Chapter 2 model configuration was integrated for a 12 hours period starting at 0h on the corresponding date. The Fig. 9 shows the results from comparison between simulated and radar wind profiles, the speed is on the left plot and the direction - on the right. The data agree well, the correlation coefficient is calculated to 0.85 both for wind speed and direction which indicates very good positive correlation.

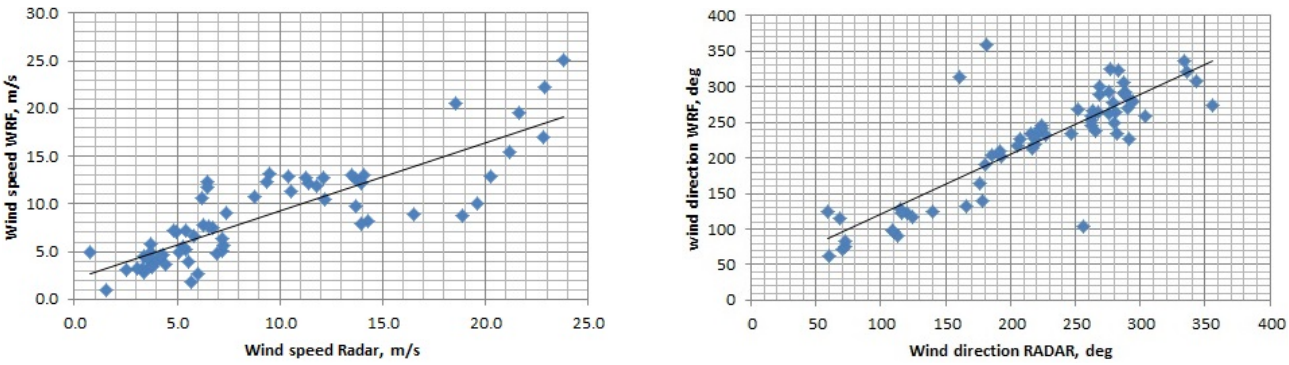


Fig. 9. Comparison between atmosphere sounding and meteorological radar data for wind speed (left) and direction (right).

CONCLUSIONS

Numerical simulations could present very useful source of data in cases when the information about vertical profiles of the meteorological element is needed. The advantage of these numerical data is the fine resolution both in time and space. In this study we have compared data from available atmosphere sounding and meteorological radar with the model simulated vertical profiles of temperature humidity and wind. The model used is in the study is the ARW version of the weather forecast model system WRF.

As a first step we have compared the measured sounding wind data and the calculated from the meteorological radar images wind speed and direction. The results present good positive correlation between two sources of data and demonstrated that the radar data can be used for model validation. The sounding data are more precise and reliable data source but the main advantage of the radar data is the very fine temporal resolution and the good sensitivity.

This study was motivated by the investigation of an airplane accident in the area of town Tran on 7.05.2014, which was caused most probably by engine carburetor icing. The necessary information about the vertical profiles of air temperature, humidity and wind for the place of the accident could be obtained only by numerical model, as the atmosphere sounding data are not available in this moment of time and location. The comparison between the model simulations and the aerological diagram further in the day of the accident demonstrated that the simulated model profiles agree well with the atmosphere sounding thus indicating that the model results could be used successfully as a proxy of the measured vertical profiles. The differences between model and measurements are mainly in the planetary boundary layer due to the model limitation to parameterize the subgrid physics processes. The model results for 6h on 7.05.2014 confirm the pilot report for airplane engine icing as plausible thus giving very useful information.

To conclude, the results presented in this study should be considered as preliminary because they refer only to May 2014. More detailed investigation on the relationship between data coming from atmosphere sounding or meteorological radar and obtained with numerical model should be performed for several seasons and years in order to confirm the good correlation and the usability of the model simulations. This is a motivation for the authors for future studies.

Acknowledgements.*The authors thank Gergana Kozinarova from Directorate Generale "Civil Aviation Administration" of the Ministry of transport, information technology and communication for providing the general information for airplane accident on 7.05.2014.*

REFERENCES

[1] NCEP, User's Guide for the ARW WRF Modeling System Version 3.5, (2014)

[2] R. Penchev and E. Peneva, Numerical simulation of extreme convective events during 2012 in Bulgaria using the weather forecast model WRF, *Proceedings of the 2nd National Congress in Physical Sciences, 25-29 September 2013, Sofia, Bulgaria* (in Bulgarian) (2013)

[3] H. Kirova and E. Batchvarova, Verification of mesometeorological model using aerological data from the Sofia experiment 2003, *Proceedings of the 2nd National Congress in Physical Sciences, 25-29 September 2013, Sofia, Bulgaria* (in Bulgarian) (2013)

[4] K. Soich and B. Rappenglueck. *J. Appl. Meteor. Climatol.* **52**, 1237-1252 (2013)

[5] Aeronautical Information Circular AIC: P 077/2009: Induction system icing on piston engines as fitted to aeroplanes, helicopters and airships (2009)

[6] J. S. Kain. *Appl. Meteor.* **43**, 170-181. (2004)

[7] E. J. Mlawer, S. J. Taubman, P. D. Brown, M. J. Iacono and S. A. Clough, *J. Geophys. Res.* **102(D14)** 16663-16682, (1997)

[8] J. Dudhia. *J. Atmos. Sci.* **46** 3077-3107 (1989)

[9] K.-S. Lim and S.-Y. Hong.*Mon. Wea. Rev.*, **138**, 1587-1612.(2010)

ЧИСЛЕНА АПРОКСИМАЦИЯ НА ПРОФИЛИ ОТ АЕРОЛОГИЧНИ СОНДАЖИ С ПОМОЩТА НА ЧИСЛЕНИЯ МОДЕЛ ЗА ПРОГНОЗА НА ВРЕМЕТО WRF

Р. Пенчев[1], Е. Пенева[2]

[1] *Държавно предприятие ръководство на въздушното движение, бул. "Брюксел" №1, София, България*
[2] *Физически факултет, Софийски университет "Св. Климент Охридски", бул. "Дж. Баучер" №5, 1164 София, България*

(Резюме)

Нуждата от информация за вертикалното разпределение на метеорологичните елементи (температура, влажност, скорост и посока на вятъра, точка на оросяване) в тропосферата е несъмнена и все по-изразена. Редица задачи, свързани с прогноза на времето, като например предупреждения за опасни конвективни явления, метеорологичното осигуряване на авиацията, борбата с градушките, изискват такъв тип информация. За съжаление данните от измервания посредством аерологични сондажи са скъпи и поради това твърде ограничени, както по пространство, така и по време. За България например, измерванията са веднъж дневно в 12UTC в метеорологична станция София. Това е недостатъчно, като се имат предвид климатичните характеристики, денонощната изменчивост и разнородния релеф на страната.

Настоящето изследване цели да провери, доколко резултатите от числени симулации могат да се използват като заместител (апроксимация) на аерологичния сондаж в дадена точка и момент от времето. Предимството е, че така се решава проблемът с недостатъчните данни от измервания. Численият модел, който се използва е на базата на моделната система Weather Research and Forecasting WRF [1]. Моделната конфигурация покрива територията на България с двойна нестинг-процедура, като достигнатата разрешаващата способност по пространство за част от страната е 1,8 км. Извършени са серия от числени експерименти за конфигуриране и настройка на моделните параметри с цел постигане на адекватни числени резултати [2]. Числено симулираните вертикални профили на температура, влажност и вятър са сравнени с наличните данни от аерологичния сондаж в София. Направени са изводи за достоверността на тази апроксимация. Показан е реален случай, в който така описаната процедура е дала полезна информация и реално приложение.

1. NCEP, *User's Guide for the ARW WRF Modeling System Version 3.5*, 2014
2. Р. Пенчев, Е. Пенева, *Числено симулиране на екстремни конвективни явления през 2012 г. на територията на България с числения модел за прогноза на времето WRF*, Сборник от 2-ри национален конгрес по физически науки, 2013.

INTERDISCIPLINARY PHYSICS

ИНТЕРДИСЦИПЛИНАРНА ФИЗИКА

Bulgarian Chemical Communications, Volume 47, Special Issue B (pp. 423–432) 2015

Integrated multiscale modeling approach for hierarchical biological nanocomposites applied to lobster cuticle

S. Nikolov[1*], H. Fabritius[2], M. Friák[2], D. Raabe[2]

[1] *Institute of Mechanics, Bulgarian Academy of Sciences, Acad. G. Bontchev Str. Bl. 4, 1113 Sofia, Bulgaria*
[2] *Max-Planck-Institut für Eisenforschung GmbH, Max-Planck-Str. 1, 40237 Düsseldorf, Germany*

Biological structural materials (e.g., bone, arthropod cuticles, shells) are organic-inorganic nanocomposites with hierarchically organized microstructure. A powerful tool to obtain the structure/property relations in such materials is multiscale modeling encompassing all length scales. Here we present an integral multiscale modeling approach for computing and prediction of the elastic properties of mineralized biomaterials. We combine *ab initio* calculations using Density Functional Theory (DFT) at the atomistic scale, step-by-step homogenization modeling at the mesoscale, and full-field spectral method based on Fast Fourier Transforms (FFT) for the macroscopic scale. An essential part of the concept is the experimental input to the model concerning the material structure and composition. We apply our multiscale concept to the cuticle of lobster. The cuticle consists of chitin nanofibrils, proteins, and mineral nanoparticles, and contains numerous pore canals across its thickness. The elastic properties at each hierarchical level are estimated and compared to experimental data for dry cuticle. At the mesoscale, the properties of cuticle proteins are identified and the bulk mineralized tissue is investigated. We find that the Young's modulus of the bulk tissue along the chitin fibrils is $\sim 60\%$ larger compared the modulus in direction perpendicular to the fibrils. At the macroscale, the highest stress concentrations in the cuticle in uniaxial in-plane loadings appear in planes where: (i) the major axes of the ellipsoidal pores (as well as the chitin fibrils) are oriented at about $\pm 45^\circ$ w.r.t. the loading direction, (ii) the separation regions between the pores are thinnest, and (iii) the shear stresses in the separation regions are close to their maximal values. We suggest that these are the necessary conditions for damage initiation in the lobster cuticle.

Key words: structural modeling, mechanical properties of tissues, biomaterials, organic-inorganic nanostructures, computational techniques; simulations

INTRODUCTION

Structural biomaterials (e.g., the bones of vertebrates, the exoskeletons of arthropods, mollusk shells) are known to possess excellent mechanical properties, e.g., in terms of stiffness-to-density ratio and fracture toughness, despite the modest characteristics of their constituents [1]. From the viewpoint of materials science, these materials are organic-inorganic nanocomposites formed via self-assembly of structural biopolymers like collagen (vertebrates) or chitin (arthropoda), various proteins, and nanoscopic mineral particles. As a rule, the basic components are hierarchically organized over multiple levels from the molecular to the macroscopic scales [2].

In order to understand the design principles and the performance of structural biomaterials, it is necessary to study the relationship between their structure, composition and the resulting physical properties. A powerful approach allowing to obtain and analyze structure/property relations is multiscale modeling encompassing all length scales [3]. To set up a proper multiscale model, a detailed structural description based on experimental findings is necessary. Specifically at the nanoscale, however, experimental studies of biomaterials are rather challenging and many properties of basic constituents are still unknown. To overcome these difficulties, *ab initio* quantum mechanical calculations can be used to determine experimentally inaccessible materials characteristics.

Because of the complexity of biomaterials, as well as the very limited size of studied systems inherent to the *ab initio* method, a complementary combination of *ab initio* calculations with higher-scale hierarchical modeling based on continuum micromechanics of heterogeneous materials represents an optimum strategy [3, 4]. A reliable hierarchical modeling over all length scales can identify the most important parameters relevant to certain structure/property relations and the tolerance of the overall material behavior against structural variations [4]. Moreover, such modeling can be very useful for the design and the optimization of new biomimetic hierarchical materials [5].

Here we present a hierarchical modeling approach for computing and prediction of the elastic properties of mineralized biomaterials at all length scales. In our concept, we combine *ab initio* calculations

* To whom all correspondence should be sent:
sv.nikolov@imbm.bas.bg

© 2015 Bulgarian Academy of Sciences, Union of Chemists in Bulgaria

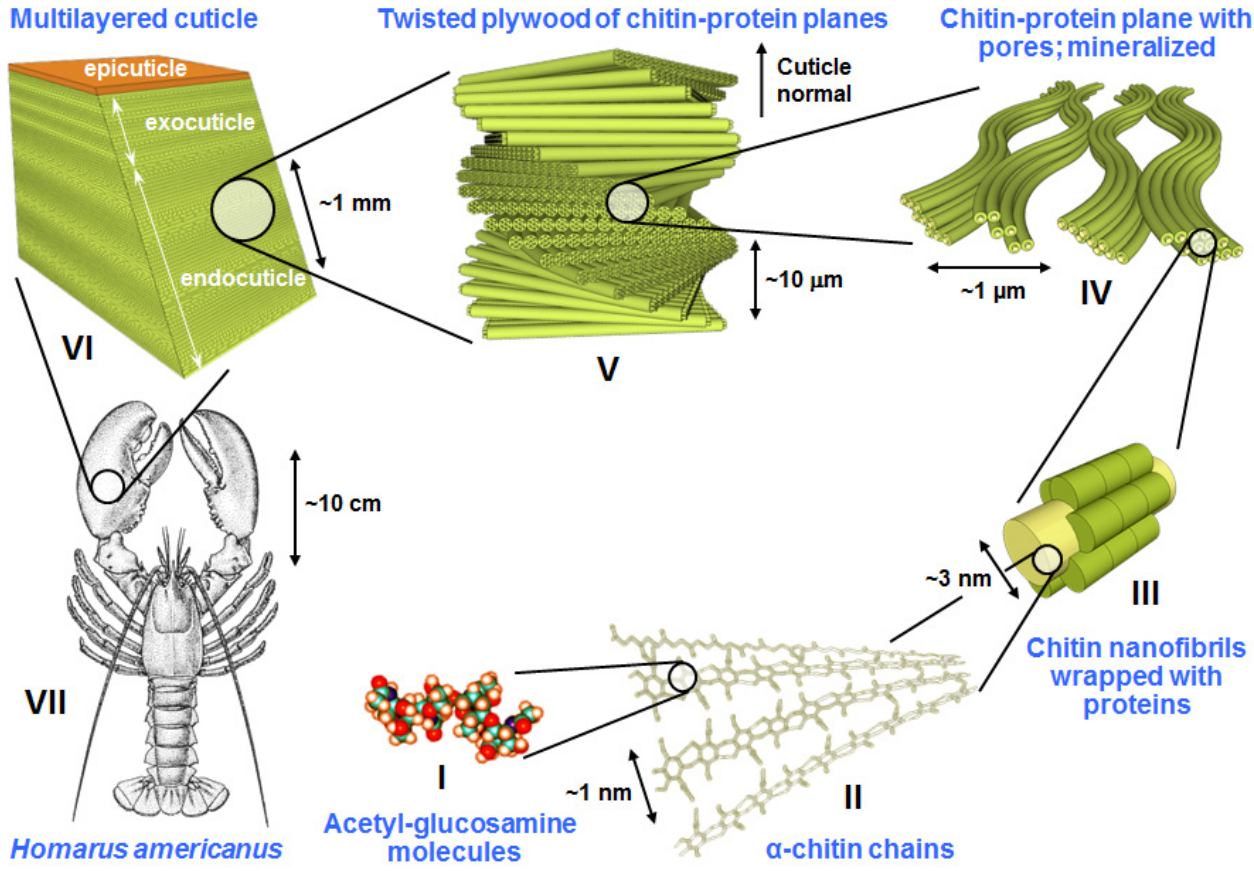


Fig. 1. Structural hierarchy of the cuticle of *Homarus americanus*. Mineral nanoparticles (levels IV, V, VI) and twisted ribbon-like pore canals (levels V, VI) are not visible.

using Density Functional Theory (DFT) at the nanoscale, step-by-step homogenization modeling at the mesoscale, and full-field spectral method based on Fast Fourier Transforms (FFT) for the macroscopic scale. The cuticle of a large marine crustacean, the lobster *Homarus americanus*, is chosen as a model material[1]. The necessary model input from experiments concerning the structure, the composition and the properties of the cuticle is obtained via different experimental techniques such as Scanning Electron Microscopy (SEM), Raman spectroscopy, X-ray diffraction, thermo-gravimetric analysis, nanoindentation, micro-tensile and micro-compression experiments [7–9].

The hierarchical structure of the mineralized lobster cuticle [4, 7, 8] is schematically shown in Fig. 1.

In Fig. 1, the lowest (nanoscale) hierarchical level is represented by N-acetyl-D-glucosamine molecules (I) which polymerize to form polysaccharide chains of chitin (II). At the next hierarchy level (III), 19 chitin chains arrange in anti-parallel pattern to form crystalline α-chitin nanofibrils [10] with diameter of $\sim 3\,\mathrm{nm}$ and length of $\sim 300\,\mathrm{nm}$. Each nanofibril is individually wrapped with proteins. Next, the chitin-protein fibrils cluster and associate with inorganic nanoparticles (mostly of amorphous calcium carbonate (ACC) [9]) and matrix proteins (see Fig. 2, III(b)) to form mineralized chitin-protein planes (IV). The wavy arrangement of the fibrils forms voids and gives the mineralized chitin-protein plane a honeycomb-like appearance. The individual planes (IV) are stacked over each other and gradually rotate around the normal direction of the cuticle, which results in a twisted plywood (Bouligand) structure (V) pierced by pore canals in the form of twisted ribbons with elliptical cross section. The stacking height (the distance

[1]The mineralized crustacean cuticle is the oldest (already present in the the Early Cambrian period ~ 515 Myr ago [6]) and one of the most successful natural materials for structural and armor applications produced by evolution.

in which a 180° rotation of superimposed planes is accomplished) of the twisted plywood in the endocuticle is $\sim 30\,\mu$m [8]. At the macroscale (VI), the cuticle consists of three layers: endocuticle, exocuticle, and a thin waxy epicuticle. The mechanically relevant exo- and endocuticle have the same basic microstructure but the mineral content in the exocuticle is higher and the pore canals are smaller. The stacking height in the exocuticle is $\sim 10\,\mu$m [8].

The main improvement of the present concept over our recently proposed model for crustacean cuticle [4] is in the modeling at the macroscopic scale. In [4], the twisted plywood geometry was approximated by honeycomb with thick walls and modeled via homogenization techniques. Here, the exact cuticle geometry taken from SEM micrographs (Fig. 2, V(exp.), V) is introduced in the model. The plywood mechanical behavior is computed via full-field FFT-based spectral method [11–13], which allows us to obtain and analyze the local stress and strain fields for different loadings. In contrast to our previous work dealing with wet cuticle, here we assess the properties of a dry cuticle. To refine our modeling and achieve better identification of the properties at the mesoscale, we use data from nanoindentation experiments [7] which can be properly performed only on dry cuticle.

Throughout the paper, notation is as follows: tensors without explicitly written indices are in boldface, the tensor product contracted over two indices is denoted by (:), tensor product is indicated by ($\otimes$), the inverse of a matrix (fourth-order tensors are in matrix representation because of symmetries) is denoted by $(\bullet)^{-1}$.

INTEGRATED MULTISCALE MODELING APPROACH

The multiscale hierarchical modeling of the cuticle is depicted in Fig. 2.

The main goal is to obtain the elastic constants of the cuticle (a fundamental characteristic of any het-

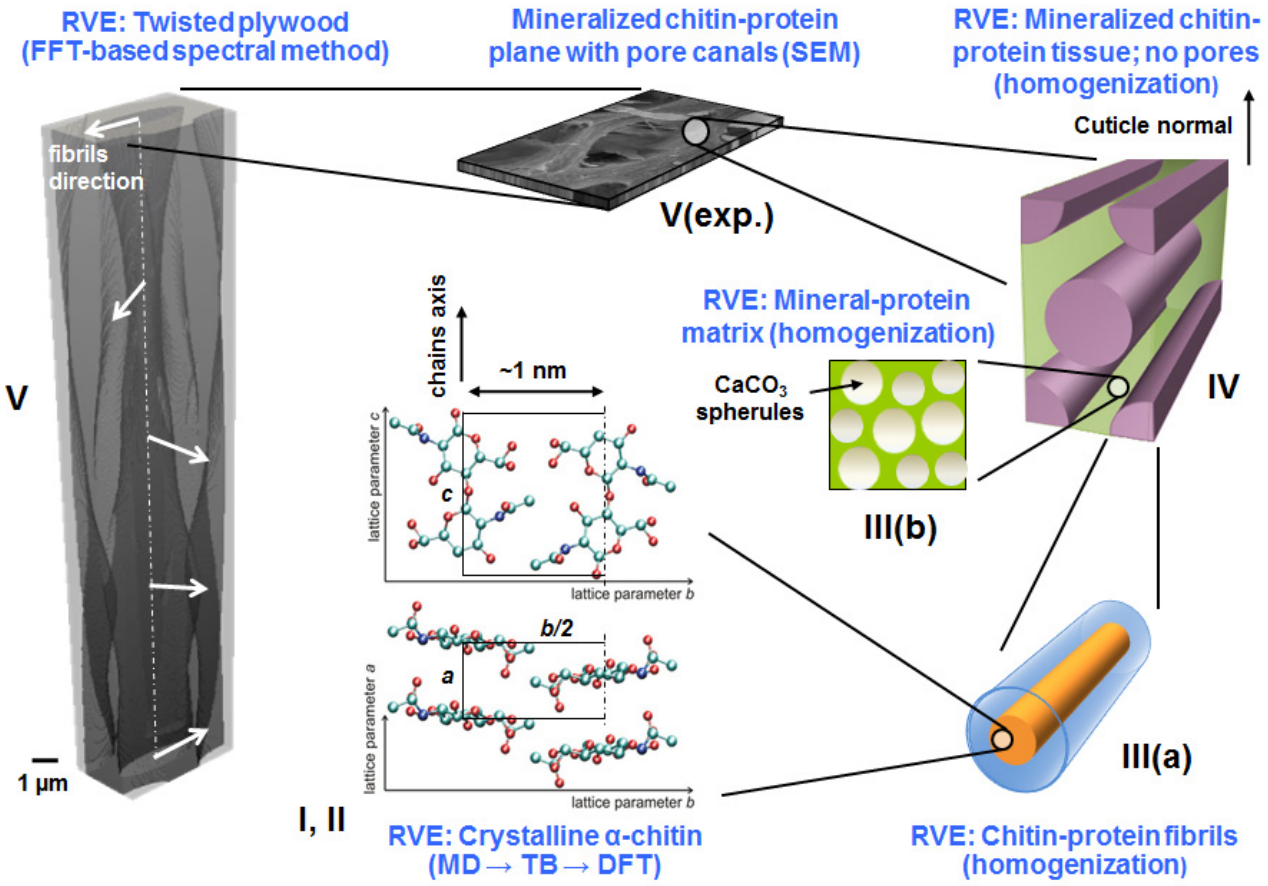


Fig. 2. Multiscale hierarchical modeling of the cuticle and methods used at different length scales.

erogeneous body) at each hierarchy level and corresponding length scale as a function of the underlying structure, composition, and the properties of the individual components. The information is passed from lower to upper hierarchy level of the model in a 'handshaking' manner. For example, the elastic constants of chitin obtained from *ab initio* calculations (Fig. 2, I,II) are directly introduced in a continuum-scale model to find the stiffness tensor of the chitin-protein fibrils (Fig. 2, III(a)). It is noted that the input from precise experimental measurements is an essential part in our integrated approach. For example, the Representative Volume Element (RVE) for the FFT-based calculations is constructed such that it matches as closely as possible the ensemble of the corresponding SEM micrographs (Fig. 2, V(exp.), V).

Ab initio modeling of α-chitin at the nanoscale

Because of the extremely small length scale and the difficulty to obtain a pure α-chitin sample, it is nearly impossible to experimentally measure the 3D elastic constants of the crystalline α-chitin nanofibrils (see Fig. 1, III). We used *ab initio* calculations to find the ground state atomic geometry and the stiffness tensor of the α-chitin crystal (for more details, see [4] and the references therein). Obtaining the atomic configuration of chitin is a rather challenging task because the exact positions of the hydrogen atoms and the number of hydrogen bonds are not directly accessible by experimental X-rays analysis. Moreover, the side groups ($-$OH, $-CH_2OH$, and $-NHCOCH_3$) of the chitin chains exhibit high structural flexibility. To tackle these difficulties we use a hierarchical approach using Valence Force Field Molecular Dynamics (VFFMD), Tight Binding (TB) and Density functional Theory (DFT) calculations.

As a first step, VFFMD simulations with probabilistic conformational search are performed. Starting from a rather arbitrary atomic geometry that conserves the chemical formula of α-chitin, an extended room temperature molecular-dynamics run sampled the multi-dimensional Born-Oppenheimer surface. Based on the criteria of minimum potential energy and maximum hydrogen bonds, about 10^2 out of 10^5 simulated structures emerged as likely. In a second step, the properties of the thus chosen configurations have been refined and re-checked employing self-consistent Density Functional Tight Binding (DFTB) calculations. About 10 low-energy structures emerged from the DFTB calculations and have been used as input to the subsequent DFT parameter-free calculations based on quantum mechanics.

The final result for the ground-state structure of crystalline α-chitin is shown in Fig. 2, I,II [4]. It has an orthorhombic unit cell with unit vectors a, b, and c[2]. The resulting lattice constants agree within 5% with the experimentally measured ones [14]. The corresponding stiffness tensor, $\mathbf{C}_{CH}$, was determined from the response of the chitin crystal on uniaxial stresses applied along the unit cell vectors a, b and c [4].

Homogenization modeling for hierarchy levels at the mesoscale

A classical problem in solid mechanics is the determination of the effective fourth-order stiffness tensor, $\mathbf{C}_e$, of a heterogeneous material consisting of inclusions embedded in a matrix. In elasticity, the goal of homogenization is to find $\mathbf{C}_e$ as a function of the microstructure so that a generalized Hooke's law holds:

$$\langle \boldsymbol{\sigma}(\mathbf{x}) \rangle = \mathbf{C}_e : \langle \boldsymbol{\varepsilon}(\mathbf{x}) \rangle \qquad (1)$$

where $\boldsymbol{\sigma}(\mathbf{x})$ and $\boldsymbol{\varepsilon}(\mathbf{x})$ are the second-order local stress and strain tensors, respectively; angular brackets denote ensemble average.

To solve the problem, one defines a Representative Volume Element (RVE), which is generally much smaller than the studied body but large enough to contain the same statistical information about the microstructure as the body itself. To compute $\mathbf{C}_e$, various mean-field homogenization models were developed (see, e.g., [15]). They assume that the stress and strain fields in the matrix and in the inclusions are adequately represented by their volume-averaged values. These models are limited to ellipsoidal inclusions and use as microstructural information the properties and the volume fractions of the phases, shape (but not dimensions) and orientations of the inclusions.

A different homogenization method has been developed by Torquato [16]. It consists in exact perturbation series expansion for the effective stiffness tensor, $\mathbf{C}_e$, of macroscopically anisotropic composite with two isotropic phases. This method is valid for arbitrary volume fractions and contrast between the phase properties. It also accounts for the specific arrangement of the inclusions (of arbitrary shape) via 3-

[2] The c (chain) direction of the α-chitin crystal coincides with the axis of the chitin nanofibrils (Fig. 1, III; Fig. 2, III(a)).

point statistical correlation parameters. The Torquato 3-point estimates are restricted to composites with two isotropic phases and have been specialized for 2D and 3D macroscopically isotropic composites [17].

Firstly, we derive the effective properties of the chitin-protein fibrils employing the Mori-Tanaka homogenization scheme [18, 19]. The RVE of a single chitin-protein fibril is shown in Fig. 2, III(a). Its homogenized stiffness tensor, $\mathbf{C}_F$, depends on the α-chitin stiffness tensor, $\mathbf{C}_{CH}$ (obtained through *ab initio* calculations), and the stiffness tensor of the surrounding protein matrix, $\mathbf{C}_{FP}$. The Mori-Tanaka estimate for $\mathbf{C}_F$ reads:

$$\mathbf{C}_F = \mathbf{C}_{FP} + \phi_{CH}[(\mathbf{C}_{CH} - \mathbf{C}_{FP}):\mathbf{A}_{CH}][(1-\phi_{CH})\mathbf{I} + \phi_{CH}\mathbf{A}_{CH}]^{-1} \quad (2)$$

where

$$\mathbf{A}_{CH} = [\mathbf{I} + \mathbf{S}_{CH}:(\mathbf{C}_{FP})^{-1}:(\mathbf{C}_{CH} - \mathbf{C}_{FP})]^{-1} \quad (3)$$

is the strain concentration factor for a chitin ellipsoidal inclusion in an infinite protein matrix; $\mathbf{I}$ is the fourth-order identity tensor; $\mathbf{S}_{CH}$ is the fourth-order Eshelby's tensor depending only on the shape of the inclusions and the elastic constants of the matrix (see, e.g., [15]); ϕ_{CH} is the volume fraction of the chitin nanofibril.

Next, from experimental evidence, the mineral-protein matrix is modeled as an isotropic composite of packed $CaCO_3$ spheres embedded in a protein matrix (Fig. 2, III(b)). Because of the very high volume fraction of the mineral spheres (the mineral content is $\sim 70\,\%$ of the weight of a wet cuticle) and the strong contrast between the mineral and protein properties, we use the Torquato 3-point estimates for the bulk and shear moduli. Let phases 1 and 2 with volume fractions ϕ_1 and $\phi_2 = 1 - \phi_1$ denote the protein matrix and the mineral particles, respectively. With K_1, K_2 being the bulk, and G_1, G_2 the shear moduli of the matrix and the inclusions, respectively, the effective bulk, K_M, and shear, G_M, moduli of the mineral-protein matrix read [17]:

$$K_M = K_1 \left(\frac{1 + \frac{4G_1}{3K_1}\kappa\phi_2 - \frac{10G_1}{3(K_1+2G_1)}\kappa\mu\phi_1\zeta_2}{1 - \kappa\phi_2 - \frac{10G_1}{3(K_1+2G_1)}\kappa\mu\phi_1\zeta_2} \right) \quad (4)$$

$$G_M = G_1 \left(\frac{1 + \frac{9K_1+8G_1}{6(K_1+2G_1)}\mu\phi_2 - \frac{2\kappa\mu G_1}{3(K_1+2G_1)}\phi_1\zeta_2 - \frac{\mu^2}{6}\left\{ \left[\frac{3K_1+G_1}{K_1+2G_1}\right]^2 \phi_1\eta_2 + 5G_1\left[\frac{2K_1+3G_1}{(K_1+2G_1)^2}\right]\phi_1\zeta_2 \right\}}{1 - \mu\phi_2 - \frac{2\kappa\mu G_1}{3(K_1+2G_1)}\phi_1\zeta_2 - \frac{\mu^2}{6}\left\{ \left[\frac{3K_1+G_1}{K_1+2G_1}\right]^2 \phi_1\eta_2 + 5G_1\left[\frac{2K_1+3G_1}{(K_1+2G_1)^2}\right]\phi_1\zeta_2 \right\}} \right) \quad (5)$$

where

$$\kappa = \frac{K_2 - K_1}{K_2 + \frac{4G_1}{3}} \quad (6)$$

$$\mu = \frac{G_2 - G_1}{G_2 + G_1\left[\frac{9K_1+8G_1}{6(K_1+2G_1)}\right]} \quad (7)$$

The 3-point parameters ζ_2 and η_2 are given by three-fold integrals depending on the volume fraction of the spheres, ϕ_2, and 2-point and 3-point probability functions. They have been numerically calculated for different spherical assemblies (e.g., random, fcc, bcc, poly- and monodisperse, overlapping and impenetrable) as a function of ϕ_2 [15].

The isotropic stiffness tensor of the mineralized matrix, $\mathbf{C}_M$, is trivially constructed from the moduli K_M and G_M:

$$\mathbf{C}_M = 2G_M\mathbf{I} + \left(K_M - \frac{2}{3}G_M\right)\mathbf{1}\otimes\mathbf{1} \quad (8)$$

where $\mathbf{1}$ is the second-order identity tensor.

Finally, the bulk tissue of a mineralized chitin-protein plane (without pore canals) is modeled as an unidirectional transversely isotropic fiber composite with hexagonal arrangement of the fibers (Fig. 2, IV). The effective stiffness tensor of the ply, $\mathbf{C}_P$, depends on $\mathbf{C}_F$ (Eq. (2)) and $\mathbf{C}_M$ (Eq. (8)). We use the Mori-

Tanaka model to find $\mathbf{C}_P$:

$$\mathbf{C}_P = \mathbf{C}_M + \phi_F[(\mathbf{C}_F - \mathbf{C}_M):\mathbf{A}_F][(1-\phi_F)\mathbf{I} + \phi_F\mathbf{A}_F]^{-1} \quad (9)$$

where

$$\mathbf{A}_F = [\mathbf{I} + \mathbf{S}_F:(\mathbf{C}_M)^{-1}:(\mathbf{C}_F - \mathbf{C}_M)]^{-1} \quad (10)$$

is the strain concentration factor for a chitin-protein fibril in a mineral-protein matrix; $\mathbf{S}_F$ is the corresponding Eshelby's tensor; ϕ_F is the volume fraction of the chitin-protein fibrils.

FFT-based spectral method for the macroscopic scale

For computing the elastic response of the cuticle at the macroscale (see Fig. 2, V), we use a spectral method based on Fast Fourier Transforms (FFT) [11–13] instead of the standard Finite Element Method (FEM). Compared to FEM, the FFT-based method is computationally more efficient and better adapted for periodic materials. Unlike the FEM, it does not require mesh generation prior to finding the solution of a particular boundary value problem.

The FFT-based method is conceived for periodic unit cells, which are discretized by means of a regular 3D grid $\{x\}$ of voxels. In turn, this partition of Cartesian space determines a corresponding grid of the same size in Fourier space $\{k\}$. The iterative algorithm described below is taken from [11] and is based on the use of a homogeneous reference medium of stiffness $\mathbf{C}^0$ that allows to rewrite the local constitutive equations, $\sigma(\mathbf{x}) = \mathbf{C}(\mathbf{x}):\varepsilon(\mathbf{x})$, as:

$$\sigma(\mathbf{x}) = \mathbf{C}^0:\varepsilon(\mathbf{x}) + \tau(\mathbf{x}) \quad (11)$$

where $\sigma(\mathbf{x})$, $\varepsilon(\mathbf{x})$, and $\tau(\mathbf{x})$ are the local stress, strain and polarization tensors, respectively. The polarization field

$$\tau(\mathbf{x}) = \left(\mathbf{C}(\mathbf{x}) - \mathbf{C}^0\right):\varepsilon(\mathbf{x}) \quad (12)$$

is a function of the periodic heterogeneity in terms of the elastic properties, and a current guess of the total strain field.

Enforcing equilibrium, $\sigma_{ij,j}(\mathbf{x}) = 0$, and using the definition $\varepsilon_{kl}(\mathbf{x}) = (u_{k,l}(\mathbf{x}) - u_{l,k}(\mathbf{x}))/2$ where $u_k(\mathbf{x})$ is the displacement field, from Eq. (11) the following system of differential equations is obtained:

$$C^0_{ijkl}u_{k,lj}(\mathbf{x}) + \tau_{ij,j}(\mathbf{x}) = 0 \quad (13)$$

The Green's function method is used to solve the system Eq. (13). It consists in writing the following auxiliary problem:

$$C^0_{ijkl}G_{km,lj}(\mathbf{x} - \mathbf{x}') + \delta_{im}\delta(\mathbf{x} - \mathbf{x}') = 0 \quad (14)$$

where $G_{km}(\mathbf{x})$ is the Green's function associated with the dispacement field, δ_{im} is the Kronecker's delta tensor, $\delta(\mathbf{x})$ is the Dirac delta function and $\mathbf{x}'$ is a constant. Once $G_{km}(\mathbf{x})$ has been determined, the solution of Eq. (13) can be obtained for any function $\tau_{ij}(\mathbf{x})$ from:

$$u_k(\mathbf{x}) = \int_{R^3} G_{ki,j}(\mathbf{x} - \mathbf{x}')\tau_{ij}(\mathbf{x}')d\mathbf{x}' \quad (15)$$

Expressing this convolution integral in Fourier space yields:

$$\widehat{u}_{i,j}(\mathbf{k}) = \widehat{\Gamma}_{ijkl}(\mathbf{k})\widehat{\tau}_{kl}(\mathbf{k}) \quad \text{for} \quad \mathbf{k} \neq 0, \quad \text{and} \quad \widehat{u}_{i,j}(\mathbf{0}) = E_{ij} \quad (16)$$

where $(\widehat{f})$ denotes the Fourier transform of (f), $\Gamma_{ijkl} = G_{ik,jl}$, and E_{ij} is the macroscopic strain applied to the unit cell. The operators in Eqs. (14) and (15) are calculated in Fourier space. Anti-transforming and symmetrizing Eq. (16) yields a new guess for the total strain field, $\varepsilon(\mathbf{x})$, which in turn is used in Eq. (12) to obtain a new guess for $\tau(\mathbf{x})$. The iterative loop is repeated until the input strain field coincides with the output field within a certain tolerance.

RESULTS AND DISCUSSION

The naturally wet cuticle exhibits nonlinear viscoelastic-viscoplastic behavior [8]. Here we consider dry cuticle. After drying, the cuticle becomes linear elastic material and has higher stiffness compared to the wet state but cannot sustain plastic deformations [8]. However, it is better suited for analysis of the substructures Fig. 2, III(a), III(b), IV using nanoindentation data which are reliable only for dry cuticle. Moreover, our modeling is strictly valid for composites with linear elastic components which makes the dry cuticle a good choice for validation purposes.

In Voigt notation, the stiffness tensor of α-chitin obtained from *ab initio* calculations reads [4]:

$$\mathbf{C}_{CH} = \begin{bmatrix} 28 & 2 & 0.1 & 0 & 0 & 0 \\ 2 & 24 & 1.1 & 0 & 0 & 0 \\ 0.1 & 1.1 & 119 & 0 & 0 & 0 \\ 0 & 0 & 0 & 8 & 0 & 0 \\ 0 & 0 & 0 & 0 & 2 & 0 \\ 0 & 0 & 0 & 0 & 0 & 5 \end{bmatrix} \text{GPa} \quad (17)$$

It is defined in a local Cartesian coordinate frame; the vectors of the orthorhombic unit cell a, b, c are along the axes 1, 2, 3, respectively. From Eq. (17) it is seen that α-chitin is strongly anisotropic. The crystal modulus along the chitin chains (c-axis) is determinated by strong covalent bonds. Along the directions a and b, a network of weak hydrogen bonds ensures the cohesion of the chitin chains. Consequently, the elastic constant $(C_{CH})_{33}$ along the c-direction is almost five times larger compared to $(C_{CH})_{11}$ and $(C_{CH})_{22}$ associated with deformations along the a and b directions.

As virtually all cuticle proteins have unknown atomic structure and mechanical properties, they are assumed to be isotropic media and are identified via combined approach using (continuum-scale) modeling and experimental data. The protein properties in the chitin-protein fibrils (Fig. 2, III(a)) are assumed to be the same as in a dry chitin-protein abdominal membrane of lobster reported in [7]. Using microtensile experimental data from [7] and Mori-Tanaka modeling for the membrane, we obtain the Young's modulus of the fibril protein as $E_{FP} = 56\,\text{MPa}$; the experimentally measured Poisson's ratio is $\nu_{FP} = 0.28$ [7]. The stiffness tensor $\mathbf{C}_{FP}$ is then trivially constructed from E_{FP} and ν_{FP}. The ratio length/diameter of the chitin nanofibrils needed to compute the Eshelby's tensor in Eq. (2) is 100, as observed. The volume fraction of chitin in the fibrils is $\phi_{CH} = 0.31$, obtained from measurements of the diameters of the fibrils (5.4 nm [9]) and the chitin nanorods (3 nm). The stiffness, $\mathbf{C}_F$, of the composite fibril is obtained with Eqs. (2) and (3).

In the mineral-protein matrix (Fig. 2, III(b)), the Young's modulus and the Poisson's ratio of the protein are identified as $E_1 = 570\,\text{MPa}$ and $\nu_1 = 0.28$, respectively; those of the ACC spherules are $E_2 = 37\,\text{GPa}$ and $\nu_2 = 0.35$ [20], respectively. The corresponding shear and bulk moduli are: $G_1 = 0.223\,\text{GPa}$, $G_2 = 13.7\,\text{GPa}$, $K_1 = 0.432\,\text{GPa}$, $K_2 = 41.1\,\text{GPa}$. The volume fraction of the ACC spherules, ϕ_2, is obtained using thermo-gravimetric analysis. After converting the weight- to volume fractions and taking into account that the mineral is excluded from the fibrils, we obtain $\phi_2 \approx 0.9$. We choose a microstructure that can accommodate such a high volume fraction of spherical particles, namely that of overlapping spheres. The corresponding 3-point correlation parameters are $\zeta_2 = 0.56$ and $\eta_2 = 0.66$ [15]. The stiffness tensor of the mineralized matrix, $\mathbf{C}_M$, is calculated with Eqs. (4-8).

The bulk tissue of the mineralized chitin-protein planes (Fig. 2, IV) is modeled as a regular hexagonal array of fibrils with (anisotropic) stiffness $\mathbf{C}_F$ embedded in a matrix with (isotropic) stiffness $\mathbf{C}_M$. The fibrils are assumed infinitely long. Their volume fraction, $\phi_F = 0.22$, is obtained from the average fibril diameter (5.4 nm), and the center-to-center distance (11 nm) measured from SEM micrographs. The stiffness tensor $\mathbf{C}_P$ is obtained with Eqs. (9) and (10).

We assume that all dry proteins in the cuticle have Poisson's ratio of $\nu = 0.28$ (as measured in lobster membrane [7]). This leaves the Young's modulus, E_1, of the matrix protein as a 'free' parameter estimated via combined modeling-experimental approach. We identify the above mentioned value of E_1 to be 570 MPa using the nanoindentation data in Fig. 3 obtained from dry endocuticle of lobster claw [7].

In Fig. 3 the Young's modulus obtained from nanoindentation is plotted against the angle between the indented sample surface and the chitin-protein fibrils axis. The experimental data are given by their mean value and the averaged minimum and maximum values of the Young's modulus. The original data points are shown in the insert. It is seen that the Young's modulus along the chitin fibrils is $\sim 60\,\%$ larger compared the modulus in direction perpendicular to the fibrils and the model reproduces the experimental data quite well. Therefore, the presence of chitin fibrils considerably reinforces the mineralized planes along the fibril direction. Because of the twisted plywood structure, at the macroscopic scale the cuticle has in-plane isotropic stiffness enhanced by the presence of the chitin fibrils.

A single mineralized chitin-protein plane without pore canals with fibrils oriented along the Y axis in Fig. 4 has the following stiffness tensor:

$$\mathbf{C}_P = \begin{bmatrix} 9.6 & 3.1 & 3.1 & 0 & 0 & 0 \\ 3.1 & 14.4 & 3.1 & 0 & 0 & 0 \\ 3.1 & 3.1 & 9.6 & 0 & 0 & 0 \\ 0 & 0 & 0 & 3.8 & 0 & 0 \\ 0 & 0 & 0 & 0 & 3.2 & 0 \\ 0 & 0 & 0 & 0 & 0 & 3.8 \end{bmatrix} \text{GPa} \qquad (18)$$

At the macroscale, we construct the periodic RVE geometry of the endocuticle using information from SEM micrographs (Fig. 4, a). The unit cell is for regular hexagonal array of pore canals.

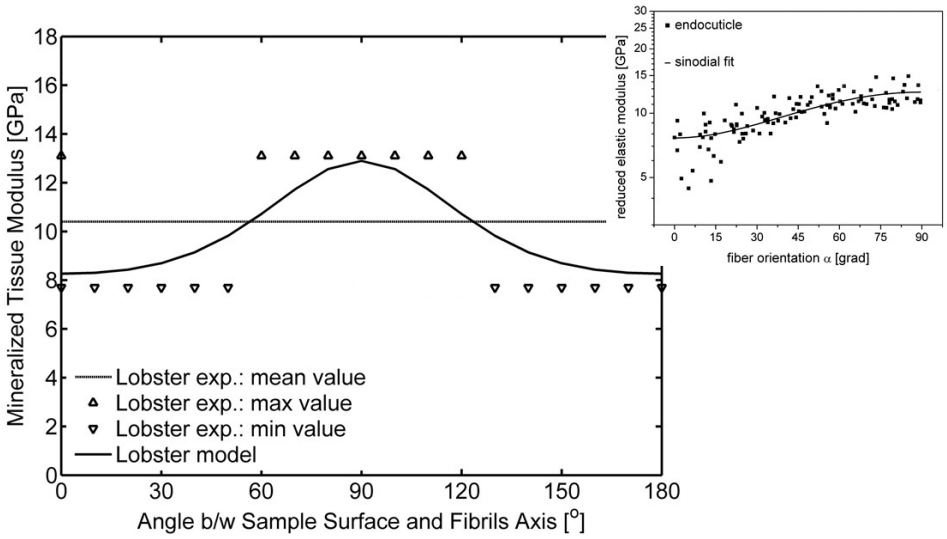


Fig. 3. Mesoscale Young's modulus of lobster endocuticle as a function of the angle between the sample surface (subjected to nanoindentation) and the fibrils axis. Symbols and horizontal line: nanoindentation data, solid line: model predictions. Insert is taken from [7], the original data are plotted for fibril angles from 0° to 90°; solid line in the insert is a fit not related to our model.

For the model set-up and subsequent FFT-based simulations we use the integrated simulation tool DAMASK [12, 13]. The RVE contains $64 \times 110 \times 700 \sim 4.9$ Mio voxels. The twisted plywood is discretized in 100 chitin-protein planes. The pore canals in the RVE are with ellipsoidal cross section (with the ellipse major axis oriented along the fibril direction) and rotate along the Z axis together with the fibrils in the planes (see Fig. 2, V). The rotation angle from bottom to top plate of the RVE is 180°. The area fraction of the pore canals is 36 %; the major/minor axes ratio of the pores ellipsoidal cross-section is 3.5. To avoid convergence problems, the pore canals are filled with perfectly compressible substance with negligible stiffness.

Experimentally, the dry endocuticle from lobster claws subjected to in-plane tension exhibits linear elastic behavior with in-plane Young's modulus ranging from 5.8 to 7 GPa [8]. The cuticle abruptly breaks at deformation of ~ 0.7 % [8]. To analyze the stress-

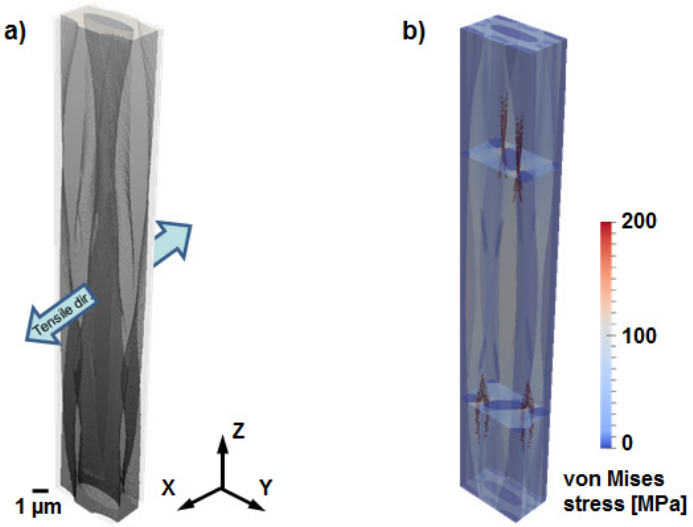


Fig. 4. a) RVE of lobster endocuticle used for FFT-based calculations; b) Stress field map for tensile experiment.

strain state of the cuticle just before failure, we apply tensile strain of 0.7 % to the RVE along the X axis in Fig. 4. The resulting 3D stress field is represented by von Mises stress field map in Fig. 4, b.

We examine the regions where stress concentrations occur because they are the most likely sites for damage initiation before failure. In the stress field map, the highlighted voxels represent stress concentration regions having von Mises stress greater than 154 MPa (the sample stress at failure ranges from 40.1 to 48.8 MPa [8]). It is seen that the stress concentration regions do not span across the whole cuticle thickness (this would strongly decrease its resistance to fracture) but are localized in certain layers with particular orientations of the ellipsoidal pores with respect to the loading direction. This is due to the specific twisted plywood architecture and the ellipsoidal pore shape.

In the pair of highlighted critical planes with highest stress concentrations, one observes that: (i) the major axes of the ellipsoidal pores (as well as the chitin-protein fibrils) are oriented at about $\pm 45^\circ$ w.r.t. the loading direction, (ii) the separation regions between the pores are thinnest, and (iii) the shear stresses in the thinnest separation regions are close to their maximum values (theoretically found at $\pm 45^\circ$ w.r.t. the loading direction). We suggest that these are the necessary conditions for damage initiation in the lobster cuticle.

CONCLUSIONS

We developed an integrated multiscale approach for modeling the elastic properties of biological organic-inorganic nanocomposites that combines three different modeling methods: ab-initio calculations at the nanoscale, homogenization at the mesoscale and FFT-based calculations at the macroscale. The concept is applied to the cuticle of lobster.

At the mesoscale, the properties of cuticle proteins are identified and the bulk mineralized tissue is investigated. The model confirms the experimental nanoindentation data that the Young's modulus of the bulk tissue along the chitin fibrils is $\sim 60\,\%$ larger compared the modulus in direction perpendicular to the fibrils.

At the macroscale, it is found that the highest stress concentrations in the cuticle in uniaxial in-plane loadings are in planes where: (i) the major axes of the ellipsoidal pores (as well as the chitin-protein fibrils) are oriented at about $\pm 45^\circ$ w.r.t. the loading direction, (ii) the separation regions between the pores are thinnest, and (iii) the shear stresses in the thinnest separation regions are close to their maximum values. We suggest that these are the necessary conditions for damage initiation in the lobster cuticle.

The presented approach is general and can be specialized for other organic-inorganic composites like bone, shells, etc. It can also be useful for design and optimization of new biomimetic nanocomposites.

Acknowledgements. *The authors gratefully acknowledge the financial support through the DFG priority program SPP 1420 funded by the Deutsche Forschungsgemeinschaft (German Research Foundation). S.N. is grateful to Dr. D. Ma and Dr. M. Diehl for the help in setting up the FFT 3D model in DAMASK, and to Dr. C. Sachs for providing his thesis.*

REFERENCES

[1] M. F. Ashby, and U. G. K. Wegst, *Phil. Mag.* **84**, 2167–2181 (2004).

[2] P. Fratzl, and R. Weinkamer, *Prog. Mater. Sci.* **52**, 1263–1334 (2007).

[3] M. J. Buehler, S. Keten, and T. Ackbarow, *Prog. Mater. Sci.* **53**, 1101–1241 (2008).

[4] S. Nikolov, H. Fabritius, M. Petrov, M. Friák, L. Lymperakis, C. Sachs, D. Raabe, and J. Neugebauer, *J. Mech. Behav. Biomed. Mater.* **4**, 129–145 (2011).

[5] H. D. Espinosa, J. E. Rim, F. Barthelat, and M. J. Buehler, *Prog. Mater. Sci.* **54**, 1059–1100 (2009).

[6] T. H. P. Harvey, and N. G. Butterfield, *Nature* **452**, 868–871 (2008).

[7] C. Sachs, *Microstructure and mechanical properties of the exoskeleton of the lobster Homarus americanus as an example of a biological composite material*, PhD Thesis, RWTH Aachen, (2008).

[8] H. Fabritius, C. Sachs, P. Romano, and D. Raabe, *Adv. Mater.* **21**, 391–400 (2009).

[9] A. Al-Sawalmih, C. Li, S. Siegel, P. Fratzl, and O. Paris, *Adv. Mater.* **21**, 4011–4015 (2009).

[10] E. Atkins, "Conformations in polysaccharides and complex carbohydrates" in *Proc. Int. Symp. Biomol. Struct. Interactions, Supp. J. Biosci.* **8**, Printed in India, 1985, pp. 375–387.

[11] B. S. Anglin, R. A. Lebensohn, and A. D. Rollett, *Comput. Mater. Sci.* **87**, 209–217 (2014).

[12] F. Roters, P. Eisenlohr, C. Kords, D. D. Tjahjanto, M. Diehl, and D. Raabe, "DAMASK: the Düsseldorf Advanced MAterial Simulation Kit for studying crystal plasticity using an FE based or a spectral numerical solver" in *IUTAM Symposium on Linking Scales in Computations: From Microstructure to Macro-scale Properties* (Pensacola, FL, USA, 17–19 May, 2011), *Procedia IUTAM* **3**, 2012, pp. 3–10.

[13] http://damask.mpie.de/

[14] R. Minke, and J. Backwell, *J. Mol. Biol.* **120**, 167–181 (1978).

[15] S. Torquato, *Random Heterogeneous Materials: Microstructure and Macroscopic Properties*, Springer, New York, 2002.

[16] S. Torquato, *J. Mech. Phys. Solids* **45**, 1421–1448 (1997).

[17] S. Torquato, *J. Mech. Phys. Solids* **46**, 1411–1440 (1998).

[18] T. Mori, and K. Tanaka, *Acta Metall.* **21**, 571–574 (1973).

[19] Y. Benveniste, *Mech. Mater.* **6**, 147–157 (1987).

[20] M. Faatz, W. Cheng, and G. Wegner, *Langmuir* **21**, 6666–6668 (2005).

КОНСТРУКТИВНИ ПРИНЦИПИ И МЕХАНИЧНИ СВОЙСТВА НА БИОЛОГИЧНИ НАНОКОМПОЗИТИ С ЙЕРАРХИЧНА СТРУКТУРА: МНОГОМАЩАБНО МОДЕЛИРАНЕ НА ЧЕРУПКАТА НА ОМАРА Homarus americanus

Св. Николов[1], Х. Фабрициус[2], М. Фриак[2], Д. Раабе[2]

[1] *Институт по механика, Българска академия на науките, ул. "Акад. Г. Бончев" блок 4, 1113 София, България*
[2] *Max-Planck-Institut für Eisenforschung, Max-Planck-Str. 1, 40237 Düsseldorf, Германия*

(Резюме)

От гледна точка на материалознанието, естествените материали чиято основна функция е запазването на устойчиви на механични натоварвания структура и форма (напр. кости, външни скелети) представляват нанокомпозити с йерархична структура, състоящи се от органични и неорганични съставки. Въпреки че съставните компоненти на тези материали имат доста скромни механични свойства, нанокомпозитната тъкан притежава изключителна здравина отнесена към единица плътност. Разбирането на основните конструктивни принципи на естествените органични/неорганични нанокомпозити е от фундаментално и практично значение което би довело до създаването на ново поколение нанокомпозити с изключителни механични свойства.

В тази работа ние комбинираме атомистично моделиране основано на квантовата механика с хомогенизационни методи за моделиране на хетерогенни материали за да получим макроскопичните еластични свойства на черупката на Американския червен омар. Този материал (както и външните скелети на 90% от живите същества на Земята) се състои от хитин, протеини, наноскопични частици от калциев карбонат и вода. Нашият подход е последователно моделиране на механичните свойства от нано- към макро ниво и демонстрира как механичните свойства на черупката се променят и оптимизират с всяко следващо възходящо ниво на йерархичната структура. Предсказаните стойности за модула на еластичност и коефициента на Поасон на черупката са сравнени с данните получени от експерименти. Показано е как от силно анизотропен материал с неподходящи механични свойства на нано-ниво, черупката се превръща в почти изотропен нанокомпозит с отлично отношение здравина/плътност благодарение на "интелигентната" йерархична структура.

1. S. Nikolov, M. Petrov, L. Lymperakis, M. Friák, C. Sachs, H.-O. Fabritius, D. Raabe, and J. Neugebauer, Advanced Materials 22 (2010) 519-526.

Bulgarian Chemical Communications, Volume 47, Special Issue B (pp. 433–441) 2015

Influence of crosslinking on micromechanical characteristics of liquid silicone rubber. Numerical simulations of microindentation process

G. Zamfirova[1*], S. Cherneva[2], V. Gaydarov[1], T. Vladkova[3]

[1] *Todor Kableshkov University of Transport, 158 Geo Milev Str., BG-1576 Sofia, Bulgaria*
[2] *Institute of Mechanics, Bulgarian Academy of Sciences, Acad. G. Bonchev Str., Bl. 4, BG-1113 Sofia, Bulgaria*
[3] *University of Chemical Technology and Metallurgy, 8 Kliment Ohridski Blvd., BG-1756 Sofia, Bulgaria*

Mechanical properties of three samples from liquid silicone rubber were investigated by means of microindentation experiments and finite-element simulations. The experimental and numerical load-displacement curves were compared and showed good coincidence. One of the aims of present work was seeking of correlation between some standard classical mechanical characteristics and parameters obtained by micro- and nanoindentation. The influence of the crosslinking on mechanical properties was investigated as well. Moreover parameters describing plastic behavior of investigated materials (such as yield strength, distribution of equivalent Von Mises stress in investigated materials during the process of microindentation, distribution of the equivalent plastic strain after unloading), which aren't possible to be obtained only by means of microindentaion experiments, were determined by means of numerical simulations.

Key words: liquid silicone rubber, microindentation, mechanical properties, numerical simulations, finite-element method

INTRODUCTION

Investigations of mechanical properties of polymer materials are very important, because they give information about the technological and exploitation characteristics of the materials and their applicability for different purposes. From classical mechanical investigations (for example tensile test) at constant deformation rate or creep test at constant load, or whatever static or dynamic mechanical experiment, we could not obtain direct information about the supramolecular structure because the standard mechanical approaches evaluate the material as a whole, including all types of its defects. Unfortunately, the complexity of the molecular and supramolecular structure of the polymers as well as the structural imperfections, macro-, micro- and nanodefects, the relations between standard mechanical properties and structure are difficult to be determined and interpreted. The increasing information and experience in the field of micromechanical methods give opportunity to consider the micro- and nano-mechanical investigations as adequate tools for elucidating some structural peculiarities of polymeric materials.

The aim of present work is to look for correlation between some standard classical mechanical characteristics and parameters obtained by micro- and nanoindentation. This could be considered as a link between structural peculiarities of the sample and its macromechanical behaviour.

* To whom all correspondence should be sent:
gzamfirova@mail.bg

EXPERIMENTAL

Materials

Three silicone rubber samples with different crosslinking were investigated. They are commercial product of KCC Corporation, Korea from the group Liquid Silicone Rubber (LSR) consisting mainly of silicone polymer and fumed silica. Liquid silicone rubber is cured automatically in liquid injection molding machines.

The components are supplied at a regular ratio. This mixed compound is measured by volume using some mechanical tools in the injection unit. Finally heat curing is done very quickly in a hot mold. After the fixed cure time, de-molding is completed and the cured articles are taken from the mold. In addition, the cure system includes curing by platunum catalyst so therefore, it is physiologically inert.

Mechanical properties of investigated silicon rubber materials, provided by producer are shown in the Table 1.

It is obviously from Table 1 that from sample 1 to sample 3 Shore hardness increases and elongation

Table 1. Mechanical properties of the three types of silicone rubber provided by the manufacturer

Sample	Hardness (Shore A)	Tensile strength (MPa)	Elongation (%)	Tear strength (N/mm)
1. SL7240	39	8	750	36
2. SL7250	49	10	600	27
3. SL7270	67	9	400	40

© 2015 Bulgarian Academy of Sciences, Union of Chemists in Bulgaria

decreases. There is inverse proportion between Shore hardness and elongation which is usually attributed to increasing the cross-linking. So the increasing the sample number means the increasing of the degree of cross-linking. Tensile strength is the maximum stress that a material can withstand while being stretched or pulled before failing or breaking.

Tear strength is a specific characteristic which is widely used when study mechanical behavior of rubber or textile materials. It is defined as a maximum stress obtained from stress-strain experiment divided to sample thickness. There is some similarity between the tear strength and yield strength what concerns to initiation of plastic deformation but loading test and sample geometry are different.

Tensile strength and tear strength are not influenced linearly by degree of crosslinking.

Methods

This investigation was carried out predominantly by method known as a depth-sensing indentation (DSI) or instrumented indentation testing (IIT). The method consists of recording by a testing device at a constant loading speed the magnitude of the force as a function of penetration depth for each point on the loading (or unloading). Large amount of mechanical parameters are determined using indentation curves, obtained by above mentioned method:

— Dynamic hardness (DH)

$$HD = \frac{aF}{h^2}, \tag{1}$$

where (F) is the value of the instant load at loading and unloading testing regime, $(a = 3.8584)$ is a constant which depends on the shape of the indenter and (h) is an indentation depth. This characteristic reveals how the material responds to plastic, elastic and viscoelastic deformation during the test.

— Martens hardness (HMs) is determined from the slope (m) of the increasing load-displacement curve in the 50% ÷ 90% Fmax interval and characterizes the material resistance of penetration:

$$HMs = \frac{1}{26.43m^2}. \tag{2}$$

This characteristic has similar physical sense as dynamic hardness, but characterizes material properties at maximum indentation depth and constant load.

— Indentation hardness (H_{it}) is determined using Oliver-Pharr approximation method and measure resistance to permanent deformation.

$$H_{it} = \frac{F_{\max}}{24.50h_c^2}, \tag{3}$$

where (h_c) is the depth of contact of the indenter with the test sample.

— Indentation Elastic Modulus (E_{it}) is calculated from unloading part of the load-displacement curve:

$$\frac{1}{E_r} = \frac{1-\nu_s^2}{E_{it}} + \frac{1-\nu_i^2}{E_i}, \tag{4}$$

where (E_r) is the experimentally converted elastic modulus, based on indentation contact, (ν_s) is the Poisson's ratio of specimen, whereas (E_i) and (ν_i) are the Young's modulus and Poisson's ratio for indenter, respectively.

— Indentation creep (C_{it}) which is a relative change in the indentation depth at constant test force is calculated as:

$$C_{it} = \frac{h_2 - h_2}{h_1}, \tag{5}$$

where (h_1) and (h_2) are indentation depths at the beginning and at the end of the creep measurement.

— Elastic part of indentation work (η_{it}) is determined from the areas under loaded and unloaded part of the load- unload test $(W = \int Pdh)$:

$$\eta_{it} = \frac{W_{el}}{W_{el} - W_{pl}}. \tag{6}$$

Vickers hardness, HV*, is obtained as a function of computed indentation hardness. Its direct measurement from the diagonal of the residual imprint was impossible because of the absence of residual imprint.

For more comprehensive characterization of the samples, we apply hybrid experimental-numerical approach to the indentation experiment, which combines microindentation experiments with numerical simulations by means of finite-element method (FEM). The combination of the indentation experiment and its numerical simulation has a number of advantages, because enables determination of some valuable mechanical properties (yield strength, distribution of equivalent Von Mises stress, distribution of the equivalent plastic and elastic strain in the zone under indenter and etc.).

The experimental conditions, which we used for conducting microindentation tests, are following:

— First mode is loading- unloading;

- Indenter is Vickers diamond pyramid with angle of 136°;

- Loading rate of 0.0250 mN/s;
- Maximum load – 0.8 mN;
- Minimum load – 0.020 mN;
- Holding time after unloading 0 s;
- Poisson's ratio 0.47;
- Indenter Poisson's ratio of 0.07;
- Indenter Modulus of 1140 GPa

Measurements have been carried out at room temperature. At least 30 indentations for each sample have been made and average value and the mean square error have been calculated, which could be considered as an indicator of the microstructural heterogeneity of the samples.

Also a measuring by the mode loading-holding at maximum load-unloading with holding time 60 s for determining the indentation creep has been made. All other experimental conditions are the same.

The equilibrium swelling and effective crosslink density were determined by Dogadkin-Tarrasova's method using toluene as a swelling agent [1].

Numerical simulations of microindentation process

Boundary value problem. The boundary value problem is defined under the following assumptions:

- The indentation process is quasistatic;
- The deformable axisymmetric specimen is composed by an isotropic linear elastic-plastic with linear hardening material;
- Normally indenter's material is very hard (usually this is a material with elastic modulus $\approx 10^3$ GPa). For that reason it is accepted, that the indenter can be modelled as a rigid body;
- The friction forces in the contact area are neglected;
- No stress-strain prehistory is taken into account.

The equation of motion of the deformable body is:

$$\sigma_{ij,j} = 0, \tag{7}$$

where σ_{ij} is the Cauchy stress tensor. Because of the axial symmetry the boundary condition on G_1 is (see Fig. 1):

$$u_{y|G_1} = 0. \tag{8}$$

The deformable body is imposed on a rigid base and this gives the following boundary condition on the surface G_5:

$$u_{x_{|G_5}} = 0. \tag{9}$$

The indenter I penetrates from the side of contact surface G_2 with a prescribed velocity v_I. The depth

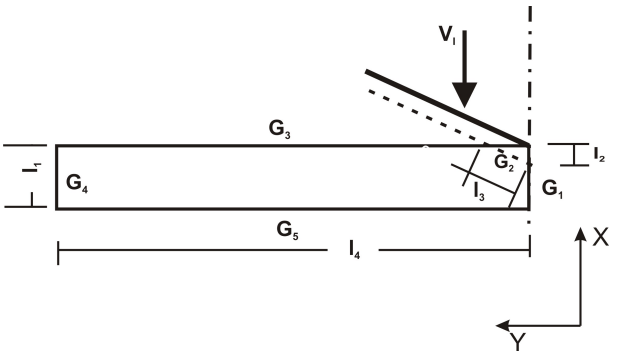


Fig. 1. Scheme of the boundary value problem.

of the contact zone l_2 during the deformation process changes. On the contact zone the velocity is given as:

$$v_{|G_2} = v_I, \tag{10}$$

Material model. The material model used in present work is elastic-plastic with linear hardening. The model involves the following material parameters: Young's modulus, Poisson's ratio, yield strength, strength coefficient.

The strain tensor ε_{ij} is used to describe the deformation in a material point belonging to the investigated material:

$$\varepsilon_{ij} = \frac{1}{2}\left(u_{i,j} + u_{j,i}\right), \tag{11}$$

where $\{u_1, u_2, u_3\}$ is the displacement vector of the material point at position $\{x_1, x_2, x_3\}$ in the reference configuration. The material model applied to investigated materials is described below.

The total strain tensor ε_{ij} is a sum of the elastic strain tensor ε^e_{ij} and the plastic strain tensor ε^p_{ij}:

$$\varepsilon_{ij} = \varepsilon^e_{ij} + \varepsilon^p_{ij}. \tag{12}$$

The elastic strain tensor is related to the stress tensor through Hooke's law:

$$\varepsilon^e_{ij} = \frac{1+\nu}{E}\delta_{ij} + \frac{1-2\nu}{3E}\sigma_{kl}\delta_{kl}\delta_{ij}, \tag{13}$$

where E is the Young's modulus and ν is the Poisson's ratio of the particular material.

Following the von Mises yield criterion, yielding occurs in a point when the next validates:

$$F\left(\sigma_{ij}, \overline{\varepsilon}^p\right) \equiv \frac{3}{2}s_{ij}s_{ij} - \sigma_p^2\left(\overline{\varepsilon}^p\right) = 0, \tag{14}$$

where s_{ij} is deviator of the stresses and $\overline{\varepsilon}^p$ is the equivalent plastic strain. The flow stress σ_p of the material depends on the accumulated plastic strain

and the value of the initial yield stress $\sigma_p^{0.2}$. If the initial yield stress is exceeded, the material starts to show plastic yielding. It is assumed that the material is isotropic with linear hardening behavior. In this case the evolution of σ_p during plastic deformation is given by:

$$\sigma_p(\overline{\varepsilon}^p) = \sigma_p^{0.2} + K\overline{\varepsilon}^p, \tag{15}$$

where K is the strength coefficient.

The accumulated equivalent plastic strain is given by:

$$\overline{\varepsilon}^p = \int_0^t \sqrt{\frac{2}{3}\dot{\varepsilon}_{ij}^p \dot{\varepsilon}_{ij}^p}\, dt \tag{16}$$

According to the associated plastic flow rule, the plastic strain rate is given by

$$\dot{\varepsilon}_{ij}^p = \dot{\lambda}\frac{\partial F}{\partial \sigma_{ij}}, \tag{17}$$

where $\dot{\lambda}$ is the plastic multiplier.

Indentation test procedure modelling. The process of indenter penetration and separation from the specimen is simulated as a contact problem. It is evident from the experiment that the deformation caused by the indenter is located in a small area around the indenter. For that reason a boundary value problem is defined in a cylindrical domain around the indenter's tip with sufficiently large radius compared to the size of the indenter. The radius is chosen in such way that the deformation due to the penetration vanishes at the lateral and the bottom of the considered cylindrical domain.

The friction forces on the contact surface are neglected. The experiment that has to be simulated numerically is a microindentation, where the indenter is a tetrahedral Vickers pyramid with tip angle 136°. Because of geometrical symmetry, the considered domain can be reduced and only one fourth of the whole domain is used for solving the boundary value problem. Often the problem is simplified by substituting the geometry of the Vickers pyramid with the circular cone with an angle of 70.3° between the axis and the generatrix. Such approach has been applied for example in [2–4]. In this case the problem can be considered as an axisymmetric one. The geometry of the 2D model is shown in Fig. 1.

Numerical simulations. The above described process of microindentation is modelled numerically. The finite- element model has been developed using the finite-element code MSC.MARC [5]. The boundary value problem is based on the model described in Sections 2.3.1, 2.3.2 and 2.3.3. The geometry of the domain is given on Fig. 1: l_1=0.5 mm, l_4=2 mm.

The relation between l_3 and l_4 is $\frac{l_3}{l_4} = \frac{1}{20}$. In this way the influence of boundary conditions on the numerical solution is avoided [6].

As initial values for the material properties of investigated materials, we used data taken from the certificates of these materials, available at the Web page of the producer (values are shown in Table 1) and literature [7]. They are given in second column of Table 3. For the modelling process of microindentation, 3 series of finite element simulations with 3600 fournodes isoparametric finite elements with full integration have been performed (Fig. 2). The experimental and calculated load-displacement curves were then compared. In this way we performed a trial-error procedure in order to obtain the material parameter set that gives the best fit to the experimental data. They are shown on third column of Table 3.

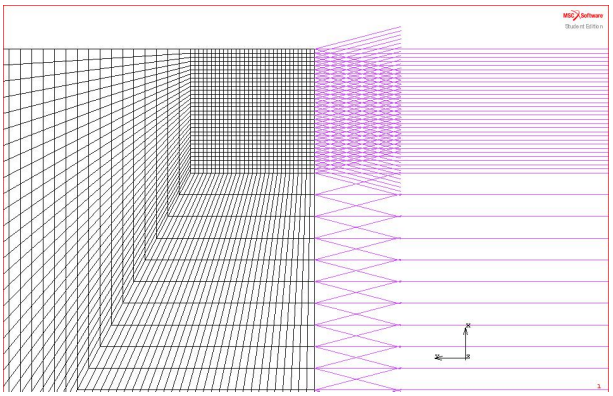


Fig. 2. Enlargement part from FE mesh for the 2D model around the indenter.

RESULTS AND DISCUSSIONS

Fig. 3 shows experimental indentation curves for three silicon rubber samples with different degrees of crosslinking. The loading and unloading parts of indentation curves are close to each other, which is typical for materials with high elasticity. Indentation curve for sample 2 is the most inclined, i.e. it posses the smallest hardness. This can be seen directly from the diagram in the Fig.4, which illustrate the values of dynamic hardness (DH), Martens hardness (MHs), indentation hardness (H_{it}) and Vickers hardness (HV*).

It is obviously from Figs. 3 and 4 that all microhardness characteristics are not directly dependent on

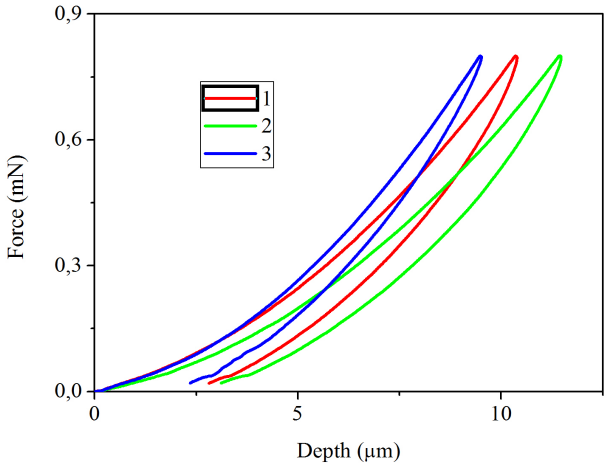


Fig. 3. Experimental indentation curves for three silicon rubber samples with different degrees of crosslinking.

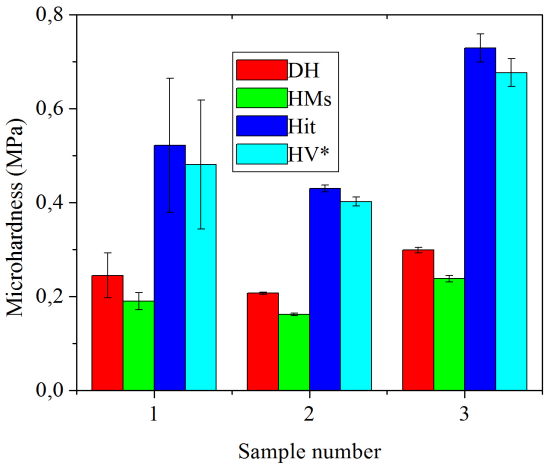


Fig. 4. All hardness characteristics for the three samples.

degree of crosslinking. The same is valid for indentation modulus and elastic part of the indentation work.

No relation has been found between the microindentation parameters and tensile strength, which could be expected because microindentation parameters characterize the local mechanical properties while the tensile strength is statistically measured parameter. It depends not only on material properties but also on existing of macro-defects in loaded zone, which become stress concentrators and increase until the break of the material.

The dependence of hardness characteristics from tear strength is shown on Fig. 5a. It is observed almost linear dependence. Moreover both characteristics which are related to resistance against plastic deformation (H_{it} and HV*) are more sensitive to tear strength. Dynamic and Martens hardnesses which characterize the resistance against total deformation, including elastic and plastic deformation components are less sensitive to tear strength. Also indentation modulus linearly depends on the tear strength (Fig. 5b).

As we mentioned in the experimental part it is physically unreasonable to look for some relation between microindentation parameters and parameters like yield strength and tensile strength, because they basically depend on macro defects. But when measure the indentation characteristic there is one indirect indicator for existence of macro-defects- it is the results scattering, i.e. the big error in measurements. Percentage errors vs. tensile strength are plotted in

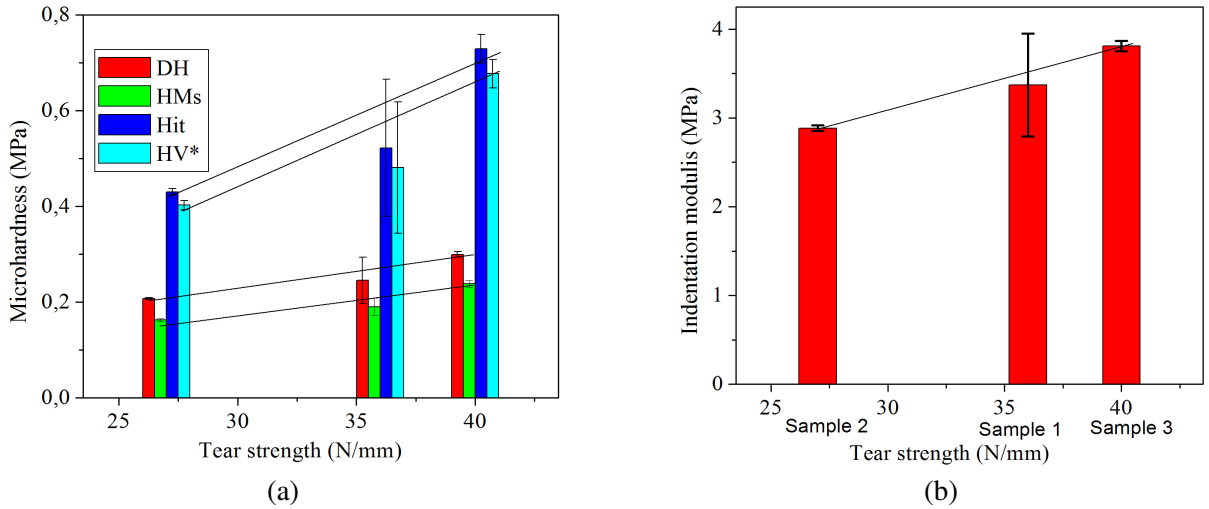


Fig. 5. All experimentally obtained microhardness characteristics (a) and indentation moduli (b) for the three investigated samples as a function of tear strength.

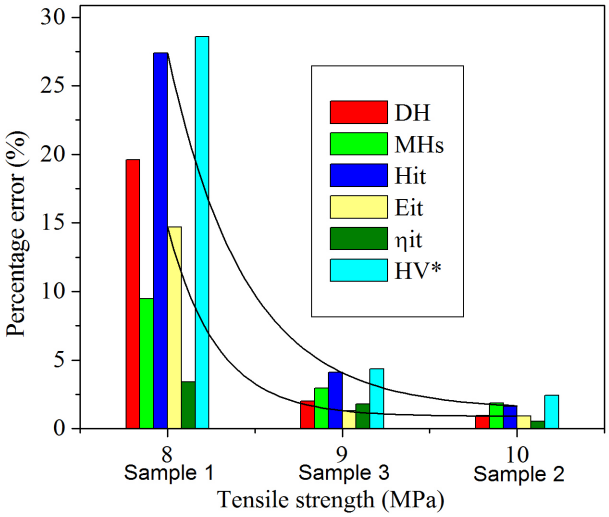


Fig. 6. Relation between percentage error for all microindentation characteristics and tensile strength.

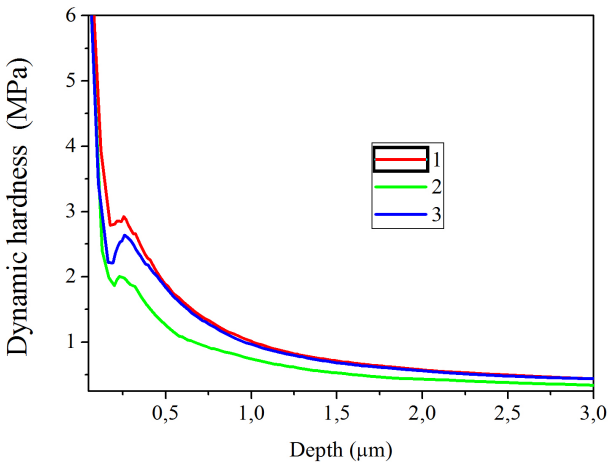


Fig. 7. Microindentation profiles.

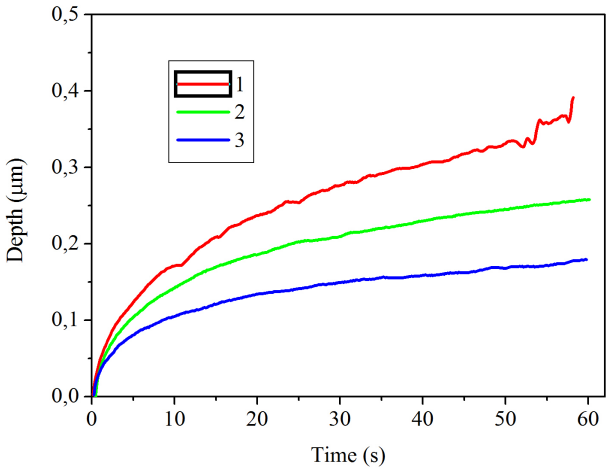


Fig. 8. Creep curves.

Fig. 6. Sample 1 is the most inhomogeneous one and it has small tensile strength. Sample 2 is very homogeneous and has the highest tensile strength. The dependence has exponential decreasing character.

Fig. 7 shows microhardness profiles i.e. how the dynamic hardness changes in the depth of the specimen. It should be emphasized that the hardness values do not indicate the resultant hardness of the material exactly at this depth but incorporate the properties of all surface layers up to that depth. Moreover at very small depths (in this case less than about 4 μm) the hardness increases sharply, which by now has no precise and unambiguous physical explanation. It's called "scale factor" or "size factor". In this zone some structural heterogeneity could be seen near to the surface, but it is difficult to make some comment in this not well studied area.

The results for equilibrium swelling and effective crosslink density, which were determined by means of Dogadkin-Tarrasova's method are shown in Table 2. It is observed almost linear dependence between effective crosslink density and Shore hardness of investigated samples from liquid silicone rubber.

Table 2. Values for equilibrium swelling and effective crosslink density, determined by Dogadkin-Tarrasova's method

Sample	Equilibrium swelling Q	Effective crosslink density n.10^{-19}/cm^3
1. SL7240	3.6	0.66
2. SL7250	3.1	0.91
3. SL7270	2.8	1.36

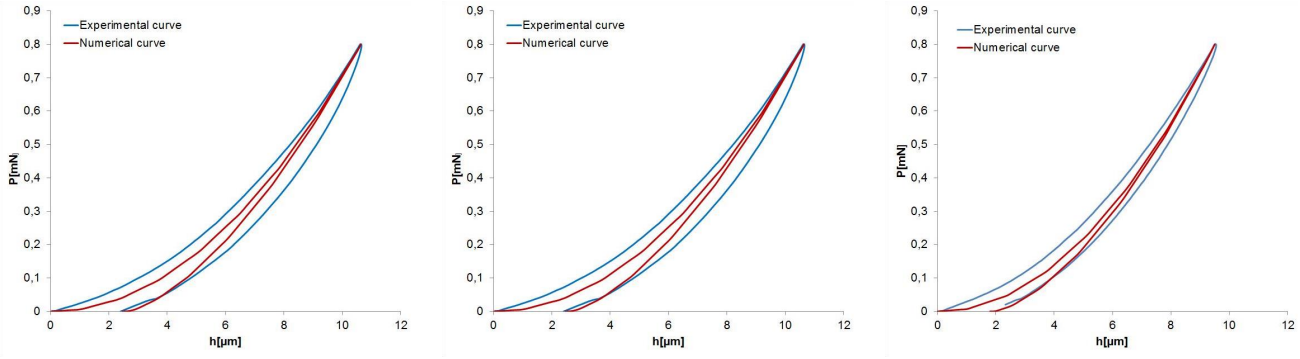
Fig. 8 shows the creep curves i.e. increasing of the depth with time in constant load. The creep is more pronounced for sample 1 which has less crosslinking and decreases with increasing of crosslinking. This is logical because denser lattice means bigger resistance to time-dependent deformation. The creep curve for specimen 1 is not smooth, confirming its low homogeneity.

Comparison between experimental and numerical load-displacements curves is shown in Fig. 9 and in the Table 3.

The distribution of equivalent Von Mises stress in investigated materials during the modelled process of microindentation, as well as the distribution of the equivalent plastic strain after unloading are shown in Figs. 10-12. These figures show sink-in of material

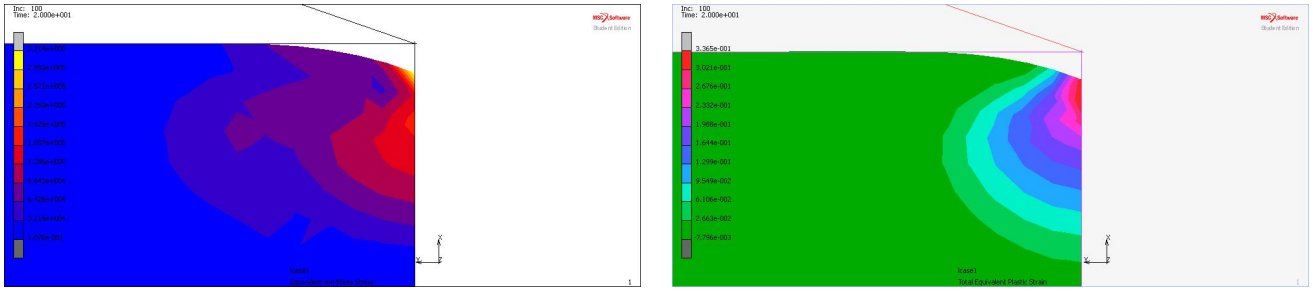
Table 3. Initial values for numerical simulations (taken from literature and manufacturer certificates) and material parameter set, which gives the best fit with experimental results

Material	Initial values				Best fit			
	σ_p (MPa)	K (-)	E_{it} (MPa)	ν (-)	σ_p (MPa)	K (-)	E_{it} (MPa)	ν (-)
1	3.73	2.41	3.37	0.47	0.426	2.41	2.77	0.47
2	3.73	2.41	2.89	0.47	0.400	2.41	2.35	0.47
3	3.73	2.41	3.81	0.47	0.600	2.41	3.45	0.47



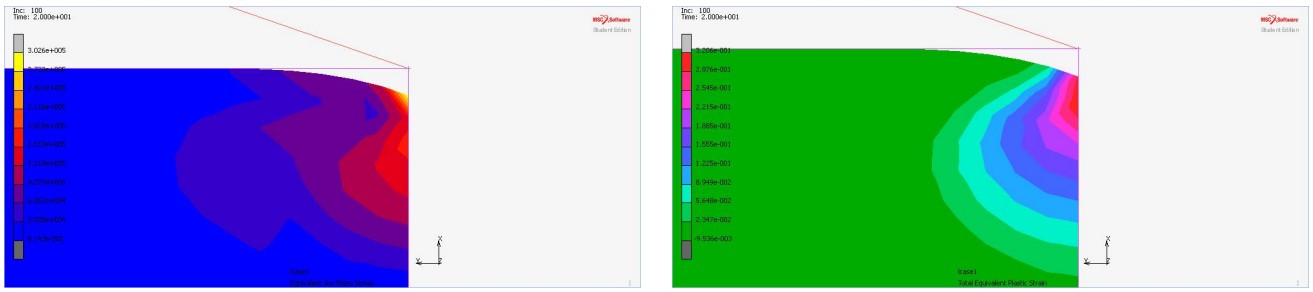
(a) (b) (c)

Fig. 9. Comparison between experimental and numerical load-displacement curves for material 1 (a), 2 (b) and 3 (c).



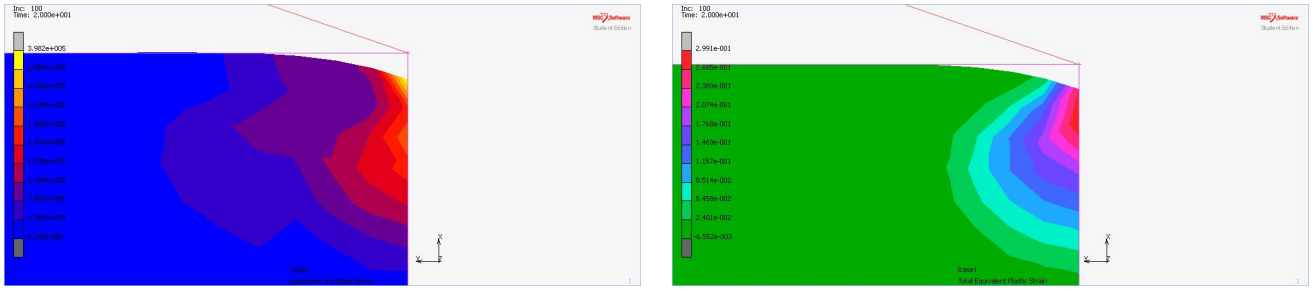
(a) (b)

Fig. 10. Distribution of equivalent Von Mises stress (a) and the equivalent plastic strain (b) in material 1.



(a) (b)

Fig. 11. Distribution of equivalent Von Mises stress (a) and the equivalent plastic strain (b) in material 2.



(a) (b)

Fig. 12. Distribution of equivalent Von Mises stress (a) and the equivalent plastic strain (b) in material 3.

around indenter imprint, which could be taken into account only by means of numerical simulations and could be one of the reasons for explaining the difference between experimental and numerical values of elastic modulus.

CONCLUSIONS

In present work we have investigated the influence of crosslinking on mechanical properties of three liquid silicon rubber samples. We established:

- Increasing in the degree of crosslinking confirm that elasticity has no direct influence on the microhardness characteristics because they are fully (H_{it}, HV*) or partially (DH, HMs) dependent from the plastic deformation (irreversible slippage of the macromolecules);
- Only creep curves are influenced by the crosslinking. The creep is more pronounced for the sample which has less crosslinking and decreases with increasing of crosslinking;
- There is a linear dependence between all microhardness characteristics and indentation modulus on one hand and tear strength and yield strength on the other hand. So this good correlation between these micro- and macro- characteristics indicates that both are affected in the same way by the structural features of the rubber, but crosslinking is not a main decisive factor;
- The scattering of the results in microindentation experiment, respectively magnitude of the experimental error can be regarded as an indirect indicator of the magnitude of tensile strength.

Three series of numerical simulations were realized by means of the finite-element method and the results were compared with experimental results from microindentation measurements. In this way, a trial-error procedure was performed in order to obtain the material parameter set that gives the best fit to the experimental data. The constitutive model used in the finite-element model of microindentation process is based on the Von Mises yield criterion in combination with a linear hardening law. Moreover figures 10-12 show sink-in of material around indenter imprint, which could be taken into account only by means of numerical simulations. Numerical simulations by means of finite-element method, which we realized, gave us additional information about mechanical properties of investigated materials, which is impossible to obtain by means of microindentation experiment only. Moreover this hybrid experimental-numerical approach save money and time for preparing of test samples and realizing conventional experiments in order to obtain plastic behavior of investigated materials.

Acknowledgments. *This paper was financially supported by Todor Kableshkov University of Transport (Project No 1620/22.04.2014).*

REFERENCES

[1] B. A. Dogadkin, Z. N. Tarasova and A. S. Linkin, *J. Vsesojusnovo Chimicheskova Obstestva Imeni Mendeleeva (USSR)* **13**, 87 (1968).

[2] J. C. Hay, A. Bolshakov and G. M. Pharr, *J. Mater. Res.* **14**, 2296–2305 (1999).

[3] G. M. Pharr and A. Bolshakov, *J. Mater. Res.* **17**, 2660–2671 (2002).

[4] A. Bolshakov and G.M. Pharr, "Inaccuracies in Sneddon's solution for elastic indentation by a rigid cone and their implications for nanoindentation data analysis" in *Proceedings of the Conference "Spring Meeting of the Materials Research Society"* CONF-960401-16, Materials Research Society, San Francisco, USA, May 1996.

[5] MSC. Software Corporation, USA, MSC.MARC User's Guide, 2013.

[6] S. Cherneva and R. Iankov, "Investigation on the influence of the boundary conditions by simulation with finite element method of microindentation process" in *Proceedings of the Thirty Sixth Spring Conference of the Union of Bulgarian Mathematicians*, St. Konstantin & Elena Resort, Varna, Bulgaria, 2007, pp. 197–202.

[7] Materials and Coatings for Medical Devices: Cardiovascular (book), ASM Materials for Medical Devices Database Committee, ASM International, USA, November 2009, pp. 297-303.

ВЛИЯНИЕ НА СТЕПЕНТА НА ОМРЕЖВАНЕ ВЪРХУ МИКРОМЕХАНИЧНИТЕ ХАРАКТЕРИСТИКИ. СИМУЛАЦИЯ НА МИКРОИНДЕНТАЦИОННИЯ ПРОЦЕС

Г. Замфирова[1], С. Чернева[2], В. Гайдаров[1], Т. Владкова[3]

[1] *ВТУ "Тодор Каблешков", ул. "Гео Милев" №158, 1574 София, България*
[2] *Институт по механика, Българска академия на науките, ул. "Акад. Г. Бончев" блок 4, 1113 София, България*
[3] *Химикотехнологичен и металургичен университет, бул. "Св. Кл. Охридски" №8, 1756 София, България*

(Резюме)

Изследвани са образци от силиконов каучук с различна степен на омрежване чрез метода на контролирано проникване на индентора (Depth Sensing Indentation (DSI)). От експериментално получените индентационни криви са определени редица микроиндентационни характеристики:

— микротвърдост по Викерс (HV*);
— индентационна твърдост (Hit);
— Мартенсова твърдост (HMs);
— динамична твърдост (HMV);
— модул на еластичност (E);
— отношение между еластичната и пластична компонента на деформацията;
— криви на пълзене;
— промяна на динамичната твърдост в дълбочина на образеца и др.

Установено е, че степента на омрежване няма директно влияние върху микротвърдостните величини и модула, защото те са свързани изцяло (Hit, HV*) или частично (HMV, HMs) с пластичните деформации. Но възвратимата деформация, която е сума от мигновенната Хуковска деформация и времезависимата вискоеластична деформация се влияят от гъстотата на мрежата. Затова степента на омрежване оказва почти линейно увеличение на работата, необходима за еластична деформация, и намаляване на дълбочината на проникване при режим на пълзене.

Направена е симулация по метода на крайните елементи, чрез която са определени:

— разпределение на еквивалентните напрежения на фон Мизес;
— разпределение на пластичните деформации за сложното напрегнато състояние под индентора в натоварено състояние;
— границата на пластично течение и нейната зависимост от степента на омрежване.

Така този хибрид на експериментално-числен подход спестява голямо количество материал за изготвяне на опитни образци, средства и време за подготовката на пробите за тестване и реализиране на допълнителни експерименти.

Благодарности: Изследването е финансово подкрепено от ВТУ "Тодор Каблешков" (Проект №1509/25.05.2013).

Bulgarian Chemical Communications, Volume 47, Special Issue B (pp. 442–449) 2015

Experimental-theoretical approach to the identification of effective sound attenuation panels from recycled materials

Y. Ivanova, V. Vassilev, P. Djondjorov*, S. Djoumaliisky

Institute of Mechanics, Bulgarian Academy of Sciences,
Acad. Georgy Bonchev Str., Bl 4, 1113 Sofia, Bulgaria

One of the most important problems of our modern urbanized society is associated with unwanted and potentially dangerous noises. The necessity for establishment of pleasant and healthy living and working environment implies development of effective methods and materials to reduce noise. Prototypes of noise reducing multilayer panels made from recycled materials, consisting of an outer layer of melded recycled rubber with adhesive and an inner layer of frittered mineral wool of various densities and thickness of the layers are presented in this work. The acoustic characteristics of different materials and multilayer panels are studied. Experimental data for the noise reduction coefficient in the frequency range from 65 to 4000 Hz have been obtained using the two rooms method. A theoretical model for determination of the effective noise reduction of the panels based on the experimental data is developed. The results obtained can be applied in developing noise absorbing barriers to achieve control of the environmental noise.

Key words: sound attenuation panels, recycled materials

INTRODUCTION

One of the serious problems of our modern urbanized society is associated with unwanted and potentially harmful noise. The requirement for a pleasant and healthy living and working environment inspires development of effective ways and materials to minimize the noise pollution.

Many studies have been focused on development and analysis of sound absorbing devices made of a variety of porous materials such as foams, fibrous and granular materials, etc., because of their high sound absorption capacity [1]. Open-celled polyurethane foams are widely used as sound absorbing materials because of good sound damping, low thermal conductivity and low density. The performance of polyurethane foams has been improved by the incorporation of micro-sized fillers [2, 3]. The addition of nano-silica leads to the significant increase of sound absorption ratio due to the multilevel microstructures of the materials and properties of polymer microparticles.

Seddeq investigated the influence of various factors like fiber type, fiber size, material thickness, density, airflow resistance and porosity on sound absorption behavior of different fibrous materials [4].

Granular materials based on crumb rubber of scrap tires have been extensively applied for absorption of sound and reduction of noise due to their attractive characteristics including porosity, relatively simple processing and commercial availability. A number of studies deal with the investigation of the relation between the acoustic behavior of these materials and the processing parameters such as granulometry, binder type and concentration, compaction ratio and final thickness [5–8].

Recently, lots of interest arises to multilayered panels, which can be an alternative to the sound absorbing materials. A number of multilayered panel prototypes have been developed using various combinations of absorbing materials: rubber-fibers-rubber [9], rubber-fabric-rubber-cork [10] and chipboard-crumb rubber-chipboard [11].

The aim of the present study is to prepare sandwich-like sound absorbing panels based on recycled rubber as outer layers and shredded mineral wool as an inner layer, to investigate their sound transmission properties depending on the material characteristic, layer arrangement and thickness, and to compare the experimental measurements to the theoretical results. For this reason, an experimental setup and a theoretical model are developed to identify the effective properties of the panels under consideration. The results can be applied in the design of sound transmission barriers to achieve control of the environmental noise.

EXPERIMENT

When a sound wave reaches a solid body it splits into a reflected, an adsorbed and a transmitted waves.

* To whom all correspondence should be sent:
padjon@imbm.bas.bg

© 2015 Bulgarian Academy of Sciences, Union of Chemists in Bulgaria

The fraction of the incident sound energy which is transmitted throughout the body is called the transmission coefficient or sound transmission loss R and can be expressed through the ratio of the sound pressures of the incident and the transmitted waves.

In this section, the sound transmission loss of single plates made of rubber waste or mineral wool as well as three kind of panels is studied experimentally.

Materials

Crumb rubber from retreaded car tires with density of about 1050 kg/m^3 are used in this study. The rubber particles are highly irregular in shape – crumbs (tapes) with dimensions of about $15 \times 2 \times 2$ mm.

Commercial diphenylmethane diisocyanate Desmodur® E22 (product of Bayer MaterialScience, Germany) is used as binder for consolidation of the recycled rubber particles.

Mineral wool slabs with density of about 150 kg/m^3 and thicknesses of 30 mm (product of Knauf Insulation GmbH, Austria) are widely used for production of heat and isolation products. The technological wastes of such kind of production are broken up into smaller particles and used for preparation of panels. The diameter of the mineral wool fibers is about 6–10 μm.

Sample preparation

The plates for the outer layer are prepared by compression moulding of crumb rubber. The composition ratio between the binder and rubber particles is 10:90 and the amount of spray water required for polymerization of the binder is 0.05%. The reaction between water and binder creates foam in the interstices between the rubber particles. The mixture is hot compression molded at pressure of 8 MPa and temperature of 100°C during 10 min by means of a hydraulic press (Metallic 63, Russia). The pressed plates are $480 \times 480 \times 30$ mm of dimensions and overall density in the range from 680 to 810 kg/m^3. These values of overall density mean that the plate macrostructure contains a large percentage of air voids.

The inner layer consists of fragmented mineral wool slabs and represents a set of continuous filaments that trap air between them.

For easy reference later, the following notation is used: $R1$, $R2$ and $R3$ are rubber plates of density 680, 710 and 810 kg/m^3, respectively; $MW1$ and $MW2$ refer to aggregations of mineral wool particles of density 50 and 100 kg/m^3, respectively, whereas MW refers to a mineral wool plate of density 150 kg/m^3.

Panel configuration

The multilayered sound absorbing panels developed in this study are sandwich-like type with outer layers from recycled rubber plates and an inner layer from mineral wool (Fig. 1). The arrangement of the multilayered panels and the characteristics of separate materials are given in Fig. 2.

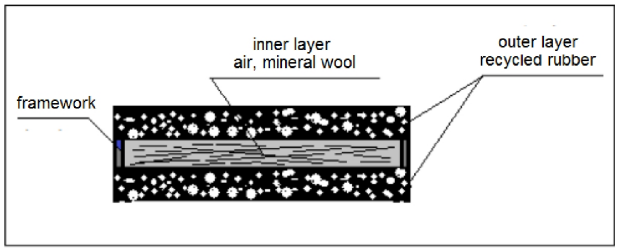


Fig. 1. Schema of multilayered sound absorbing panel.

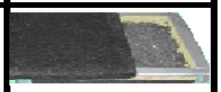
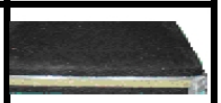
	Outer layer	Inner layer	Outer layer	Code	
1	Rubber plate ρ=710 кg/m^3	Air	Rubber plate ρ=710 кg/m^3	R2-A-R2	
2	Rubber plate ρ=710 кg/m^3	Mineral wool MW1 ρ=50 кg/m^3	Rubber plate ρ=710 кg/m^3	R2-MW1-R2	
3	Rubber plate ρ=710 кg/m^3	Mineral wool MW2 ρ=150 кg/m^3	Rubber plate ρ=710 кg/m^3	R2-MW2-R2	

Fig. 2. Arrangement of the multilayer panels and characteristics of the invloved materials.

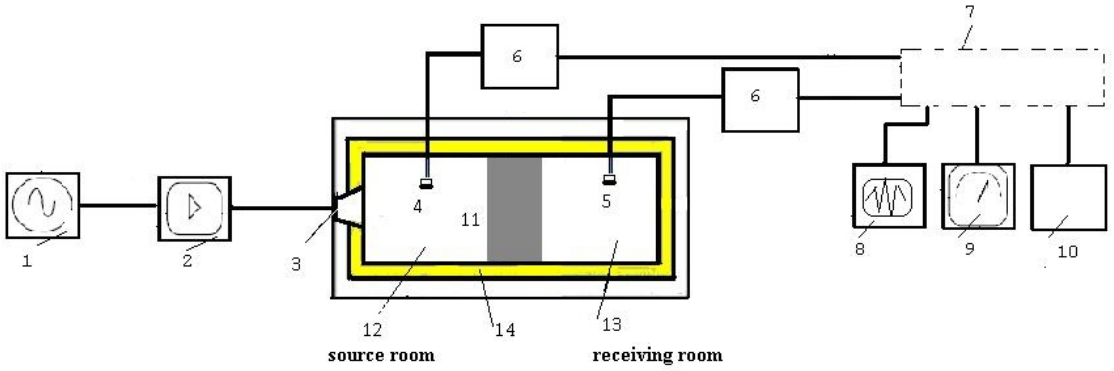


Fig. 3. Experimental setup: 1 – sound generator, 2 – amplifier, 3 – loudspeaker, 4 – reference measuring microphone, 5 – receiving microphone, 6 – microphone amplifiers, 7 – filters, 8 – digital scope, 9 – sound pressure measuring device, 10 – voltmeter, 11 – test specimen, 12 – source room, 13 – receiving room, 14 – sound absorbing walls.

Experimental setup

The experimental setup is shown in Figure 3. The experimental transmission loss measurements are carried out according to the procedures for field measurements of airborne sound insulation between two rooms [12, 13]. One of them (source room) contains the loudspeaker that creates a uniform sound field. The reference microphone measures the pressure of incident sound wave. Another microphone, placed in the receiving room, measures the pressure of the sound wave passed through the test specimen. The volume of the rooms is selected depending on the tested materials as well as the range of the frequencies under consideration. The cameras have thick walls, insulated with sound absorbing material. Thus, the generated sound field can be considered as homogeneous and isotropic and the transmission of the sound outside the test specimen is satisfactory reduced.

The sound transmission loss is determined in the frequency range from 65 to 4000 Hz by

$$R = L_{P_1} - L_{P_2} + 10\lg\frac{S}{A_2}$$

where L_{P_1} and L_{P_1} are the average sound pressure levels in the source and receiving rooms, respectively, S is the area of the test partition and A_2 is the absorption area of the receiving room. Each result is the averaged value from 5 measurements.

Experimental observations

The results from sound transmission loss measurements for the single plates $R1$, $R2$, $R3$ and MW are

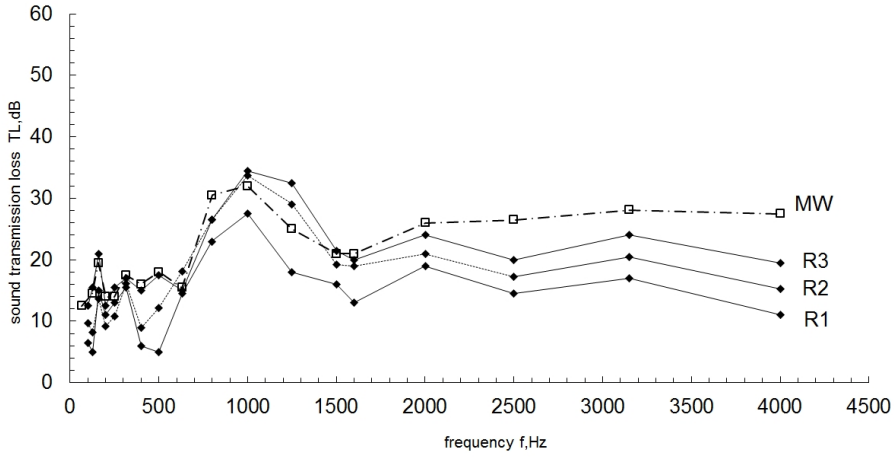


Fig. 4. Sound transmission loss as a function of frequency for single layer panels.

shown in Fig. 4. Three zones can be distinguished observing this graphic. A kind of chaotic behaviour is observed in the frequency range 65–500 Hz where the average value of R is found to be 15 ± 1 dB for the mineral wool specimen and 12 ± 2 dB – for the three rubber plates. A peak at approximately 1000 Hz is observed in the frequency range between 600 and 1500 Hz, and constant behaviour of the mineral wool specimen and small fluctuations for the rubber specimens are manifested in the second half of the frequency region under consideration. In general, the sound transmission loss increases with the density of rubber plates but it is apparent, that the density slightly changes this parameter.

The three-layer panels shown in Fig. 2 exhibit much higher noise reduction capability in the frequency range under consideration as can be observed in Fig. 5. This graphics comprises two regions – a monotone one below 1400 Hz and an almost constant one for the other frequencies, except for the $R2-MW1-R2$ panel exhibiting some variance. The use of the air gap between rubber plates rises the transmission loss from 20 dB (initial average value for a single plate) to above 40 dB.

The application of mineral wool as inner layer improves acoustic insulation in comparison with the case of air gap, especially for frequencies above 2500 Hz. The density of the inner layer also influences the results. The average values of the sound reduction by panels with inner layer from mineral wool type $MW1$ and $MW2$ are 45 dB and 48 dB, respectively.

NUMERICAL SIMULATION OF SOUND WAVE PROPAGATION WITHIN PLATES AND PANELS

Equations of motion

In this section the rubber and the mineral wool components of the panel are considered as homogeneous bodies. It is supposed that the incident wave front is a plane parallel to the panel external surface. Thus, the displacement field $\mathbf{u}$ within the panel is

$$\mathbf{u} = \mathbf{u}(x,t), \qquad \mathbf{u} = (u,v,w), \tag{1}$$

where x is the coordinate orthogonal to the largest panel side, t is the time, u is the displacement component parallel to x, while v and w are the displacements orthogonal to x.

Since the acoustic motions of the rubber or mineral wool particles are small, a linear strain-displacement hypothesis is considered, namely [14]

$$\begin{aligned} \varepsilon_{11} &= \frac{\partial u}{\partial x}, \qquad \varepsilon_{22} = \varepsilon_{33} = 0, \\ \varepsilon_{12} &= -\frac{\partial v}{\partial x}, \qquad \varepsilon_{13} = \frac{\partial w}{\partial x}, \qquad \varepsilon_{23} = 0, \end{aligned} \tag{2}$$

where ε_{ij} are the components of the strain tensor.

The propagation of acoustic waves within the panels studied here is supposed to be described by a linear elastic material model. The respective constitutive relations for each layer of the panel are [14]

$$\begin{aligned} \sigma_{11} &= (\lambda + 2\mu)\varepsilon_{11}, \qquad \sigma_{22} = \sigma_{33} = \lambda\varepsilon_{11}, \\ \sigma_{12} &= 2\mu\varepsilon_{12}, \qquad \sigma_{13} = 2\mu\varepsilon_{13}, \qquad \sigma_{33} = 0, \end{aligned} \tag{3}$$

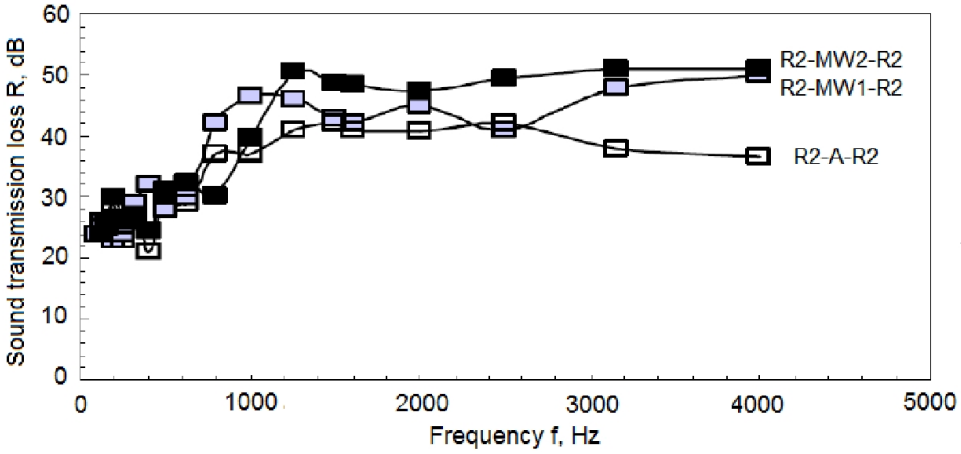


Fig. 5. Sound transmission loss as a function of frequency for absorbing 3 layers panels.

where σ_{ij} are the components of the stress tensor, and (λ,μ) are the Lame coefficients of the material of the particular layer.

The decay of the acoustic waves within the panels under consideration is supposed to be proportional to the velocity of the material particles with coefficients that have to be determined such that the ratio of the energies (amplitudes) of the incident and transmitted waves be the same as the experimentally observed one. Thus, the equations of motion read [14]

$$\begin{aligned}\frac{\partial\sigma_{11}}{\partial x}+\kappa_j\frac{\partial u}{\partial t}&=\rho_j\frac{\partial^2 u}{\partial t^2},\\ \frac{\partial\sigma_{12}}{\partial x}+\kappa_j\frac{\partial v}{\partial t}&=\rho_j\frac{\partial^2 v}{\partial t^2},\\ \frac{\partial\sigma_{13}}{\partial x}+\kappa_j\frac{\partial w}{\partial t}&=\rho_j\frac{\partial^2 w}{\partial t^2},\end{aligned}\tag{4}$$

where (κ_j,ρ_j) are the damping coefficient and the density of the material of the layer j.

Substituting the expressions (2) and (3) in the equations of motion (4), one obtains three independent wave equations of form

$$\begin{aligned}(\lambda_j+2\mu_j)\frac{\partial^2 u}{\partial x^2}+\kappa_j\frac{\partial u}{\partial t}&=\rho_j\frac{\partial^2 u}{\partial t^2}\\ \mu_j\frac{\partial^2 v}{\partial x^2}+\kappa_j\frac{\partial v}{\partial t}&=\rho_j\frac{\partial^2 v}{\partial t^2}\\ \mu_j\frac{\partial^2 w}{\partial x^2}+\kappa_j\frac{\partial w}{\partial t}&=\rho_j\frac{\partial^2 w}{\partial t^2},\end{aligned}\tag{5}$$

where $j=1,2,3$ identify the material properties of the panel layers.

Initial, boundary and compatibility conditions

Let the panel be of width L and the other two dimensions be much larger than the width meaning that without loss of generality it may be considered infinite in these directions. It is supposed that initially the panel is at rest and let $t=0$ be the time, when a flat incident wave reaches its left surface. Then, the initial conditions are

$$\begin{aligned}u(0,0)=\widehat{u},\qquad u(x,0)=0\quad\text{for}\quad x>0,\\ v(x,0)=w(x,0)=0,\\ \frac{\partial u}{\partial t}(x,0)=\frac{\partial v}{\partial t}(x,0)=\frac{\partial w}{\partial t}(x,0)=0,\end{aligned}\tag{6}$$

for the left layer, where $\widehat{u}>0$ is the magnitude of the incident wave, and

$$\begin{aligned}u(x,0)=v(x,0)=w(x,0)=0,\\ \frac{\partial u}{\partial t}(x,0)=\frac{\partial v}{\partial t}(x,0)=\frac{\partial w}{\partial t}(x,0)=0,\end{aligned}\tag{7}$$

for the other panel layers.

In order to model the experimental setting, it is supposed that the panel surfaces are free of supports and tractions. Then, the boundary conditions read

$$\begin{aligned}\frac{\partial u}{\partial x}(0,t)=\frac{\partial v}{\partial x}(0,t)=\frac{\partial w}{\partial x}(0,t)=0,\\ \frac{\partial u}{\partial x}(L,t)=\frac{\partial v}{\partial x}(L,t)=\frac{\partial w}{\partial x}(L,t)=0,\end{aligned}\tag{8}$$

where L is the thickness of either the single plate, or the panel under consideration.

Let us recall that our main interest in this study is determination of the noise transmittal properties of the panels developed here. Thus, it suffices to consider only one passing of the sound wave through the panel width and to compare the amplitudes of the incident and transmitted waves. Therefore, the computations are limited to the time interval necessary for the wave to traverse the panel width.

In the multi-layered panels considered here, the adjacent layers are not firmly fixed. Then, only the normal displacement and stresses across the common boundary between adjacent layers should be continuous, implying the compatibility conditions of form

$$\begin{aligned}u_k(x_0,t)=u_{k+1}(x_0,t),\\ \frac{\partial u_k}{\partial x}(x_0,t)=\frac{\partial u_{k+1}}{\partial x}(x_0,t),\end{aligned}\tag{9}$$

where x_0 denotes the boundary between layers k and $k+1$, and it is worth noting that the second relation involves the left derivative of u_k and the right derivative of u_{k+1}.

Numerical results

Let T and c such that $T=L/c$, $c=\sqrt{\dfrac{\lambda+2\mu}{\rho}}$ be the time necessary for the wave to traverse the body thickness and the sound velocity in the body material. The routine NDSOLVE of MATHEMATICA®is used to solve numerically the foregoing initial-boundary value problem. The right-hand side of the initial condition that suffers a jump at $x=0$ is approximated by the function $\exp(-10x^2)$. Here, this numerical scheme is applied to single rubber and mineral wool plates as well as to the panels, studied experimentally in

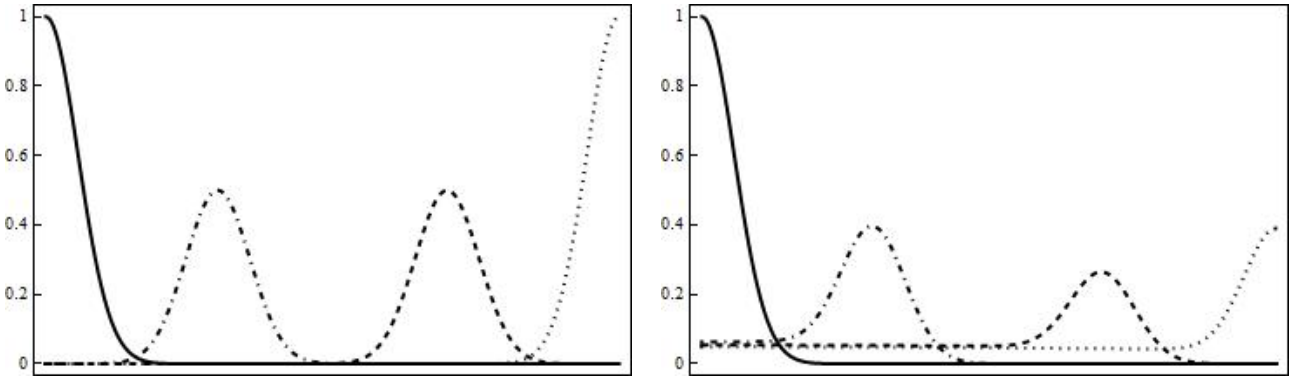


Fig. 6. Wave profiles corresponding to $t = 0$ (solid), $t = 0.3T$ (dot-dashed), $t = 0.7T$ (dashed) and $t = T$ (dotted): a) $\kappa = 0$; b) $\frac{\kappa L}{\rho c} = 0.029$.

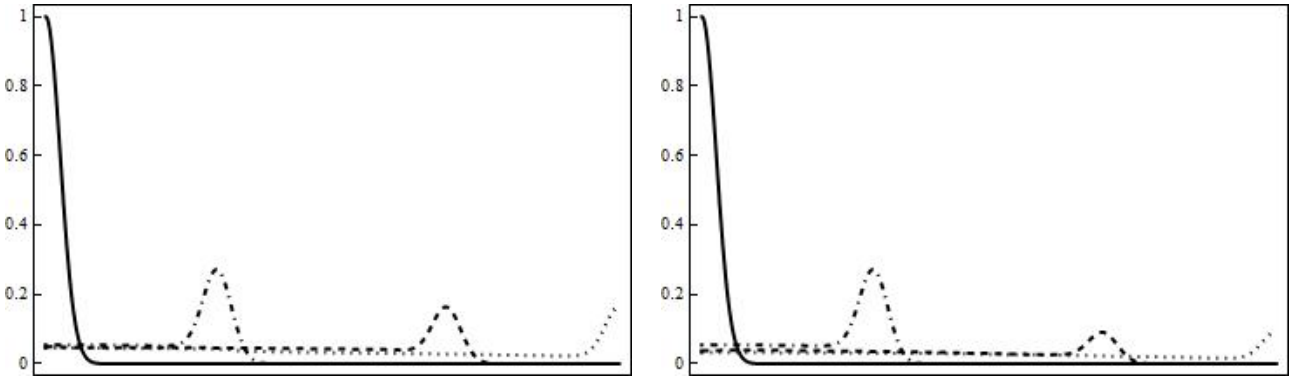


Fig. 7. Wave profiles corresponding to $t = 0$ (solid), $t = 0.3T$ (dot-dashed), $t = 0.7T$ (dashed) and $t = T$ (dotted): a) Inner layer – MW1; b) Inner layer – MW2.

Section 2. The purpose is to identify the damping coefficients κ of each material and the effective transmission loss of the panels.

First, plates by the three recycled rubber waste materials $R1$, $R2$ and $R3$ are studied. Typical picture of the propagation of a wave of initial magnitude $\widehat{u} = 1$ through the thickness of the $R2$ plate are shown in Figure 6. The case a) is presented only for verification of the numerical scheme and it displays the wave propagation if the damping is $\kappa = 0$, that is the classic solution of the undamped wave equation. The case b) corresponds to the wave profiles for damping coefficient $\kappa/(\rho c^2) = 0.029$, identified by matching the numerical results to the average value of the transmission loss results obtained experimentally and presented in Fig. 4.

Next, the panels with inner layers of $MW1$ and $MW2$ that are of better insulating properties obtained experimentally are studied numerically. The results from the numerical simulation are shown in Fig. 7. The dimensionless numerical solutions satisfy boundary and initial conditions exactly and the differential equation within a precision of 10^{-3}.

The amplitude reduction of the three-layer panels is apparent, comparing Fig. 7 to Fig. 6b. The amplitude of the incident wave at both figures is 1, whereas the amplitudes of the transmitted waves are 0.390 (Fig. 6b), 0.165 (Fig. 7a) and 0.091 (Fig. 7b).

CONCLUSIONS

The present study concerns a particular aspect on the way to manage two important problems of this century – the need to recycle the waste products and to reduce the noise pollution. Here, the waste of the isolation production using mineral wool cuts and rubber from retreading car tires are used to develop a

special kind of sound barriers suitable for application along highway roads. The rubber and mineral wool wastes are cut in small pieces. Plates of large volume fraction of air are produced and used as containers of the mineral wool cuttings as is shown in Fig. 1.

The experimental results show that the crumb rubber panels exhibit good noise reduction capability. Even greater sound reduction can be achieved by the arrangement of multilayer panels made from such recycled materials. An appropriate choice of the material, thickness and density will improve the insulating quality and sound transmission loss of the suggested barriers. The results presented here show that using the panels developed within this study one can achieve more than ten times reduction of the amplitude of the sound wave as can be observed in Fig. 7b.

Acknowledgment. *This research is supported by the Operational Programme "Development of the Competitiveness of the Bulgarian Economy 2007 – 2013" through Project BG161PO003-1.1.06-0066-C0001/07.12.2012, entitled "New thermo and sound insulation products and technology for their fabrication".*

REFERENCES

[1] J.P. Arenas, M.J. Crocker, Recent trends in porous sound-absorbing materials, Sound & Vibration, 2010, July, 12-17.

[2] H. Zhou, B. Li, G. Huang, Sound absorption characteristics of polymer microparticles, J. Appl. Polym. Sci., 2006, 101, 2675-2679.

[3] J. Lee, G.H. Kim, C.S. Ha, Sound absorption properties of polyurethane/nano-silica nanocomposite foams, J. Appl. Polym. Sci., 2012, 123, 2384-2390.

[4] H. S. Seddeq, Factors influencing acoustic performance of sound absorptive materials, Australian J. of Basic and Appl. Sci., 2009, 3(4), 4610-4617.

[5] J. Pfretzschner, R. M. Rodriguez, Acoustic properties of rubber crumbs, Polym. Testing, 1999, 18, 81-92.

[6] M.J. Swift, P. Bris, K.V. Horoshenkov, Acoustic absorption in recycled rubber granulates, Appl. Acoustic, 1999, 57, 203-212.

[7] K.V. Horoshenkov, M.J. Swift, The effect of consolidation on the acoustic properties of loose rubber granulates, Appl. Acoustic, 2001, 62, 665-690.

[8] F. Asdrubali, F.ď Alessandro, S. Schiavoni, Sound absorbing properties of materials made of rubber crumbs, Acoustic 08 Paris, June29-July4, 2008, Proceedings, 36-40.

[9] E. Julia, J. Segura, A. Nadal, J.M. Gadea, J.M. Crespo, Annals of Oradea University, 2013, 1, 147-150.

[10] A. Borlea, T. Rusu, O. Vasile, Materiale Plastice, 2012, 49 (4), 275-278.

[11] A. Venslovas, R.L. Idzelis, 8th Int. Conf., Environmental Engineering, May 19-20, 2011, Vilnius, Lithuania, Proceedings, 446-450.

[12] ISO 140-4, Acoustics – Measurement of sound insulation in buildings and of building elements: Field measurements of airborne sound insulation between rooms, 1998

[13] F. Fahy, *Foundation of Engineering Acoustics*, Elsevier Academic Press, San Diego, 2005.

[14] Gurtin, M.E., The Linear Theory of Elasticity. Encyclopedia of Physics, vol. VIa/2 Mechanics of Solids II, Ed. C. Truesdell, Springer-Verlag Berlin-Heidelberg-New York 1972.

ЕКСПЕРИМЕНТАЛНО-ТЕОРЕТИЧЕН ПОДХОД ЗА ИДЕНТИФИКАЦИЯ НА ЕФЕКТИВНОТО ШУМОЗАГЛУШАВАНЕ НА ПАНЕЛИ ОТ РЕЦИКЛИРАНИ МАТЕРИАЛИ

Й. Иванова, В. Василев, П. Джонджоров, Стр. Джумалийски

Институт по механика, Българска академия на науките, ул. "Акад. Г. Бончев" блок 4, 1113 София, България

(Резюме)

Един от сериозните проблеми на съвременното ни урбанизирано общество е свързан с нежелани и потенциално опасни шумове. Изискванията за по-приятна и здравословна жизнена и работна среда налагат необходимостта от разработване на ефективни начини и материали за намаляване на шума.

В настоящата работа се предлагат прототипи на многослойни звукопоглъщащи панели от рециклирани материали, които се състоят от външен слой пресована рециклирана гума с адхезив и вътрешен слой раздробена минерална вата или нетъкан текстил (полиестерна вата) с различна плътност и дебелина на слоевете.

Изследвани са акустичните характеристики на отделните материали и многослойните панели. Получени са данни за коефициента на звукоизолация по метода на "двете камери" в честотния интервал от 100 до 4000 Hz.

Разработен е теоретичен модел за идентифициране на ефективните свойства на панелите при поглъщане на преминаваща през тях звукова вълна, който е потвърден от експерименталните изследвания. Получените резултати са приложими при конструиране на звукопоглъщащи бариери за постигане на контрол на шума в околната среда.

Bulgarian Chemical Communications, Volume 47, Special Issue B (pp. 450–457) 2015

Investigation on the influence of the process parameters power and velocity to laser cutting of lamellae

L. Lazov[1*], H. Deneva[2]

[1] *Faculty of Engineering Rēzeknes Augstkola, Atbrivošanas aleja 115, Rezekne, Latvia*
[2] *Technical University of Gabrovo, 4 Hadji Dimitar Str., 5300 Gabrovo, Bulgaria*

The continuous development of mechanical engineering, automotive, electronics, etc. entail to the need for developing of new systems to electrical drives and mostly of the base module electromotor in them. Simultaneously with the design of the new drawing it is necessary in short terms to produce a test series for a rapid trial-run. These requirements give rise and the need of searching on a new technology in the production of lamellae for stator and rotor packages of the electric motors.

The paper examines the investigations related with the new laser technology for cutting through melting with disk laser TruDisk2001 of sheet material by electrical steel. The influence of laser power and cutting velocity are discussed to obtaining qualitative cuts. On the basic of a number of experimental studies are defined and taken out recommended working intervals for cutting of sheet material with 0.35 mm and 0.50 mm thickness.

Key words: laser cutting, disk laser, lamellae for rotor and stator packages

INTRODUCTION

Forecasts for the electric cars production shown that over the next 10 to 15 years it will dominate over that of diesel and petrol driven cars [1]. Therefore toward the modern design, development and testing of new mechanism for these types of electric cars appear new challenges. These entail and the demand for new production technology of lamellae for stator and rotor packages of the electric motors. In the existing until now punching technology for each new model motor it is necessary to make a special tool for production of a new design lamella. In principle, the production of the punching tool will entail great expense and long time for its elaboration which are justified only in large-batches production [2]. To small series and prototypes is necessary to search and develop a new technology for cutting. Such innovative technological solution for cutting of lamellae from Si-plate for the stator and rotor packages can be supplied by the laser technology on a contour cutting.

For the introducing of concrete technology for cutting of lamellae in production of motors is necessary to do some extensive specific studies [3, 4]. This is indispensable especially now after the appearance of a number of new, highly efficient lasers from a new generation - disk and fiber lasers [5, 6] providing high accuracy and production in the cutting process.

* To whom all correspondence should be sent:
llazov@abv.bg

PRESENTATION

In the recent years for the preparation of lamellae are mainly used multi-position punches, see Fig. 1. For example, presses with four- and six- position punch are used for asynchronous motors [7].

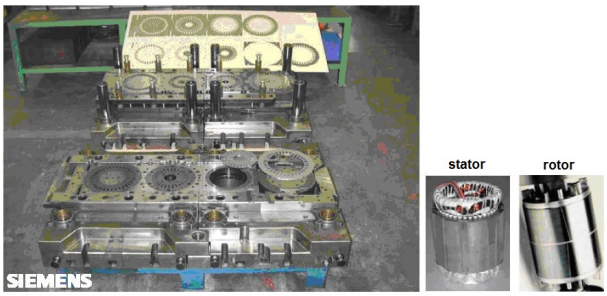


Fig. 1. A four-position punch for rotor and stator lamellae.

Despite its high performance the punching method has several disadvantages:

- ✓ A high cost of the punch (punches of solid metal-ceramic alloys are 2 to 3 times more expensive and with 2 times longer period of technological manufacture than those with high-alloy instrumental steels;
- ✓ A passage through several subsequent positions to give the final product (the lamella);
- ✓ Receiving defects: a strong distortion of a cutting detail, rounding of the cutting edges, breaking the edge of the cuts and burrs (especially large when the punch is wearied – see Fig. 2);

© 2015 Bulgarian Academy of Sciences, Union of Chemists in Bulgaria

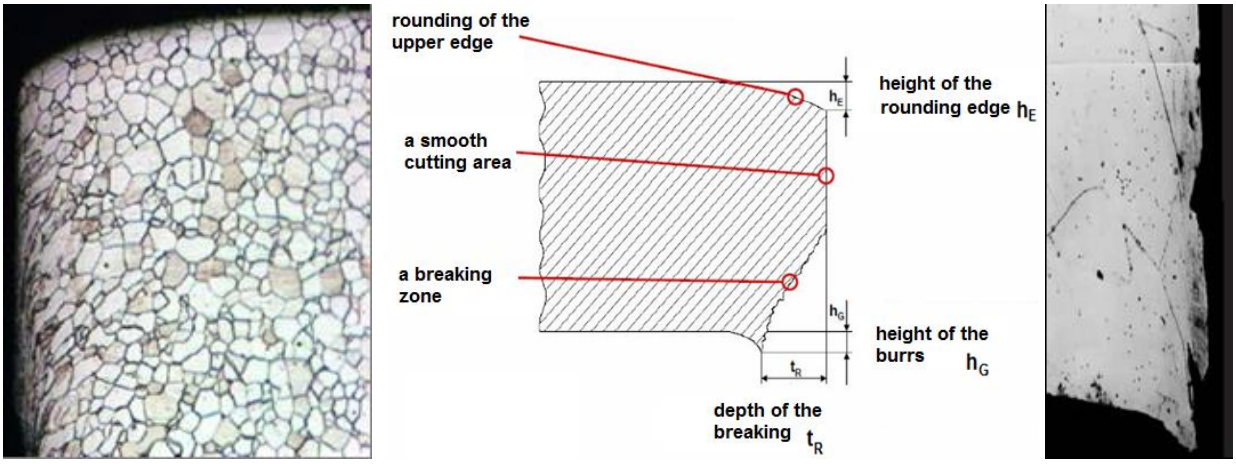


Fig. 2. Possible defects after punching of the lamellae [8].

- ✓ Distortion of varnish layers in the impact area that increases the losses from the eddy currents;
- ✓ Structural changes in the area of mechanical impact after the punching process of the material – see Fig. 2;
- ✓ Pollution of an environment area from the use of a cooling lubricant liquid to increase the wear resistance of the punch;
- ✓ One of the noisily production when used an automatic presses from 600 to 1 200 hits/min.

The appearance of the laser technology in the recent years is related with a number of advantages [9–11] that make it much more needed and affirmative in the industrial production for cutting of sheet material:

- — A contactless cutting process – there is no wear of the tool;
- — Processing of details with a complex configuration;
- — A rapid implementation of new design solutions to shorten time for testing the new model and to produce some prototypes;
- — Low production costs and high performance (it not required manufacturing of another punching tool for each new design idea);
- — A good quality (there are no burrs, with a small HAZ, etc.).

The correct selection of the technological parameters for production of lamellae is connected with the knowledge of the criteria for evaluating quality of the cuts (Fig. 3) [12, 13].

From the large set of factors that affect an influence on the complex process of laser beam interaction with the substrate of the material, it could be separated two major factors which have significant importance as well as the very operation of the process and processing quality. These are the power density in the irradiated area and the reaction time [14, 15].

For a given diameter d of working spot the power density q_s of laser beam is related with the output laser power P

$$q_s = \frac{4P}{\pi d^2} \tag{1}$$

In turn, cutting speed v as one of the most important technological parameter of laser cutting process through melt [16, 17] is connected with reaction time t of the laser beam in the irradiated area

$$t = d/v \tag{2}$$

Only in a certain combination between these two technological parameters: laser power and cutting speed (respectively laser power density and reaction time) can be maintained an optimum operation mode of the laser cutting process by melting for given material. The requirement is in the irradiated area to maintain the operating temperature in the range between that of the melting point T_m and evaporation T_v for the sheet material of electrical steel

$$T_m \leq T \leq T_v \tag{3}$$

Experimental investigations

Laser sources with different technological parameters are produced globally, but some of them are suitable for realizing of cutting process by melting of thin sheet material of electrical steel. That is why the process quality and its economic efficiency are directly

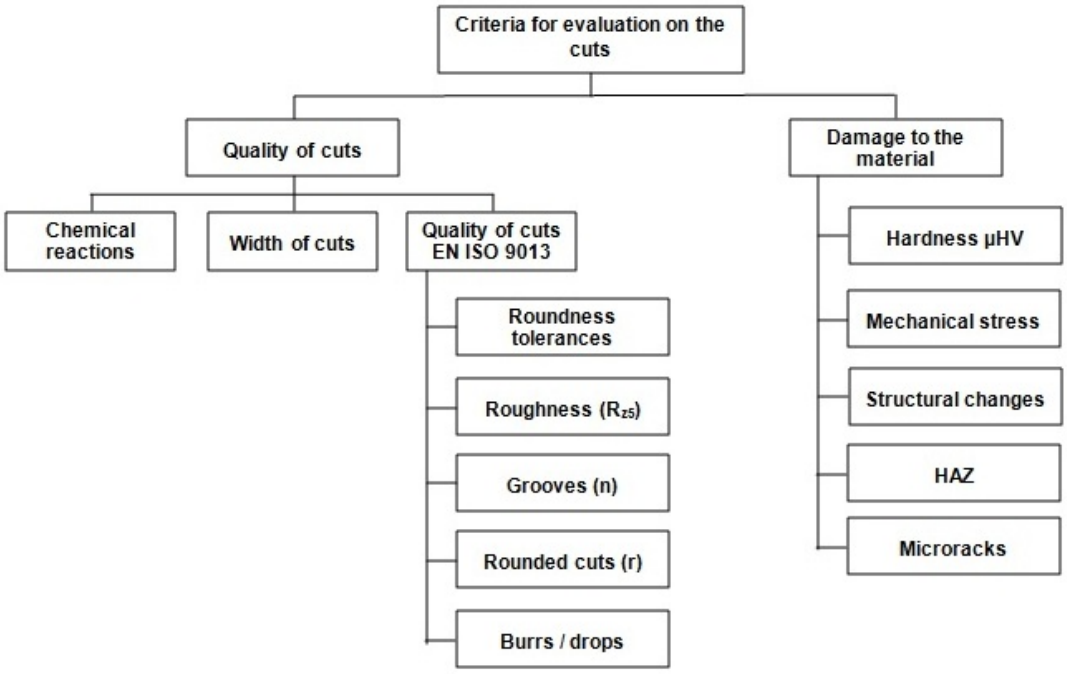


Fig. 3. An overview of a schema that include the cutting quality criteria [18].

related with the choice of a suitable laser cutting system.

The experimental investigations were made on industrial laser technological system TruLaser 1030 [19] with dimensions of working range $3000 \times 1500 \times 75$ mm, consumption power 35 kW, maximum cutting speed 80 m/min, focal length of the optical system 200 mm, maximum pressure of the working gas (nitrogen) 20 bar. Technological parameters of the laser sources: wavelength 1.03 μm, maximum frequency of following pulses 20 kHz, maximum laser power 2 kW, minimum diameter of working spot 0.200 mm, beam quality BPP = 4 mm.mrad.

The choice of disk laser TruDisk 2001 (wavelength 1030 nm) to perform the experiments conducted in our research on the laser cutting of lamellae by electrical steel with 0.35 mm and 0.50 mm thickness, is determined through the following considirations:

- High efficiency – 30%;
- A possibility for a transport the laser beam through fiber to the cutting area;
- High-speed cutting;
- Low maintenance and running costs;
- A stable quality of the laser beam parameters during the running;
- High productivity.

The investigations are grouped in several experimental series and accordingly is changing laser power P and $v = \text{const}$ or vice versa the velocity is a variable in a given operating range, but $P = \text{const}$.

For each group of experiments was monitored for a width of input b_{input} and the width of output b_{output} of the cuts – parameters connected with the treatment quality. Dependencies that investigated are:

— $b_{\text{input}} = b_{\text{input}}(P)$ and $b_{\text{input}} = b_{\text{input}}(v)$;

— $b_{\text{output}} = b_{\text{output}}(P)$ and $b_{\text{output}} = b_{\text{output}}(v)$,

as the observations and measurements were made using a microscope Neophot with a magnification to 2000.

Experimental results

Investigating the influence to the change of laser power P under constant cutting velocity v. In that study the technological parameter laser power P varies in the range $P \in [400 \div 2000]$ W with step $\Delta P = 200$ W. During a realization of the technological cutting process remain constants a diameter of a gas nozzle (1.7 mm) and the pressure of nitrogen gas (14 bar).

The experiments are conducted in four groups as in each one of them the cutting velocity is supported constant: 4 m/min, 8 m/min, 14 m/min, 20 m/min.

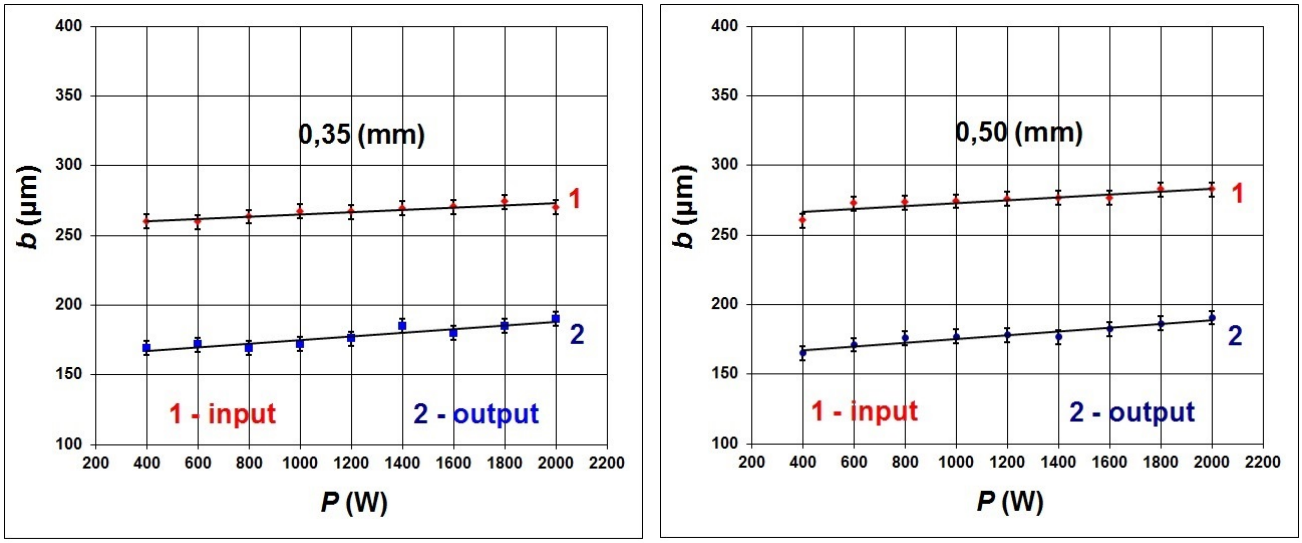


Fig. 4. Graphics of the experimental dependences $b_{\text{input}} = b_{\text{input}}(P)$ and $b_{\text{output}} = b_{\text{output}}(P)$ to the cutting process with velocity $v = 8$ m/min.

The results of changes on the cutting width in the input b_{input} and the output b_{output} as a function by variation of laser power P are graphical presented on Fig. 4.

Analogous graphical dependences have been seen in the experiments for which v is supported constant respectively 4 m/min, 14 m/min, 20 m/min.

Fig. 5 shows graphical relationships of $b_{\text{input}} = b_{\text{input}}(P)$ for cutting of samples with both thickness of steels to cutting velocity $v = 20$ m/min and focus position $\Delta f = -2.00$ mm.

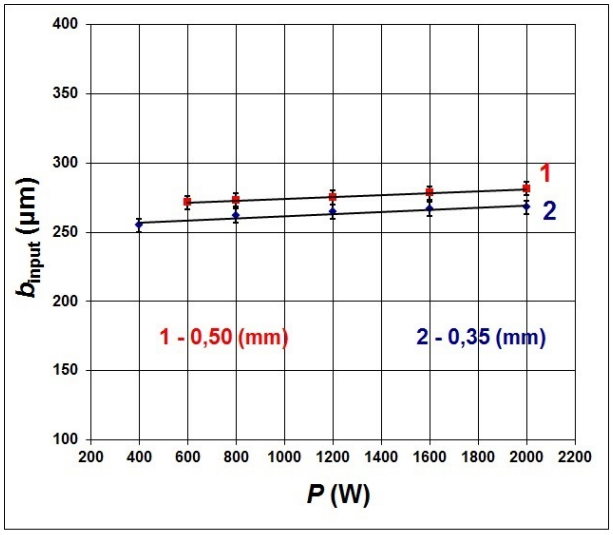


Fig. 5. Graphics of the experimental relationship $b_{\text{input}} = b_{\text{input}}(P)$.

By the analysis of the obtained experimental investigations can be made the following conclusions:

- ✓ The rapidity of which is being varied the cutting width as well as to the input Δb_{input} and the output Δb_{output} in a function of the studied power P have slight values, respectively on the input $\Delta b_{\text{input}}/\Delta P = 0.0081$ μm/W; on the output $\Delta b_{\text{output}}/\Delta P = 0.0061$ μm/W. The amendment of cutting width Δb_{input} and Δb_{output} in studied range of laser power P for both thickness steels is on the order of ± 5 μm.
- ✓ The change of the power of laser radiation in the studied range $P \in [400 \div 2000]$ W does not lead to significant variance in the cutting width b both the input and the output, i.e. the geometry of the cuts.

Investigating the variation of the cutting velocity v under constant laser power P. During the experiments the cutting velocity v varies in the interval $v \in [20 \div 60]$ m/min by step $\Delta v = 10$ m/min. All the rest technological parameters that have already been given up stand constant, as for each one series of experiments the laser power P is respectively: 500 W, 1000 W, 2000 W.

The results of experiments when studying the relationships $b_{\text{input}} = b_{\text{input}}(v)$ and $b_{\text{output}} = b_{\text{output}}(v)$ are given in graphical aspect. In Fig. 6 are shown the graphics of this study with the experiments of constant power of laser radiation $P = 2000$ W for cutting of lamellae with thickness 0.35 mm and 0.50 mm from the electrical steel.

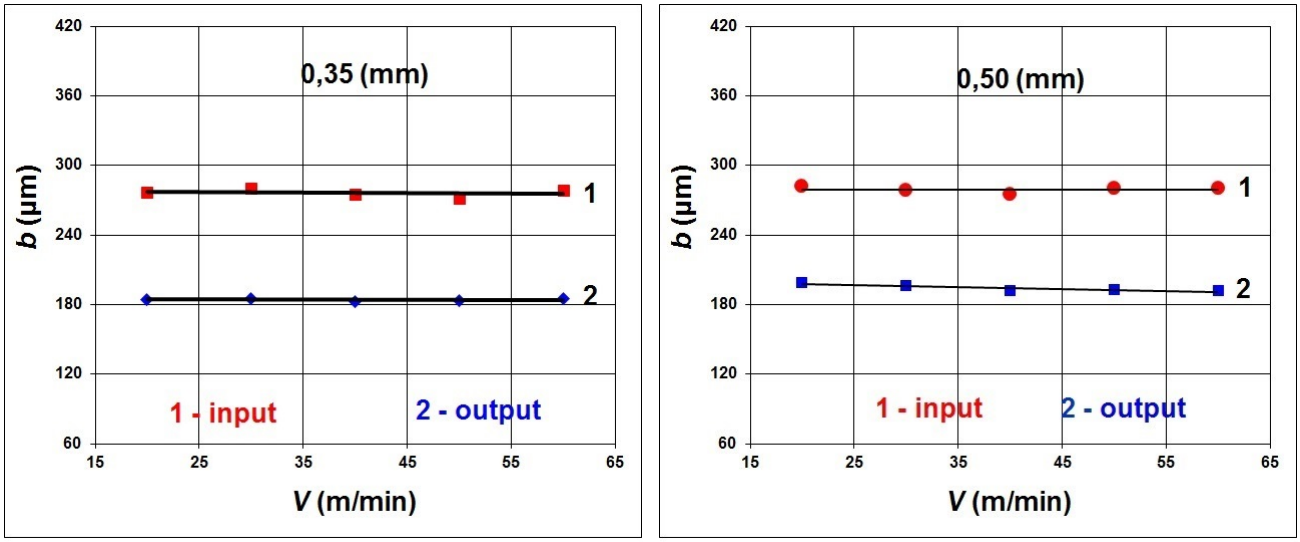


Fig. 6. Graphics of the relationships $b_{\text{input}} = b_{\text{input}}(v)$ and $b_{\text{output}} = b_{\text{output}}(v)$ to cutting of samples by electrical steel.

Analogous results of the dependencies $b_{\text{input}} = b_{\text{input}}(v)$ and $b_{\text{output}} = b_{\text{output}}(v)$ are obtained in the other two series of experimental studies: $P = 500$ W and $P = 1000$ W.

For the assessment the thickness of sheet material on the results of cutting process, some experiments were carried out on the samples with thickness 350 μm and 500 μm to the same process parameters. The results of the investigation are shown on Fig. 7.

By the analysis of the obtained results can be made the following conclusions:

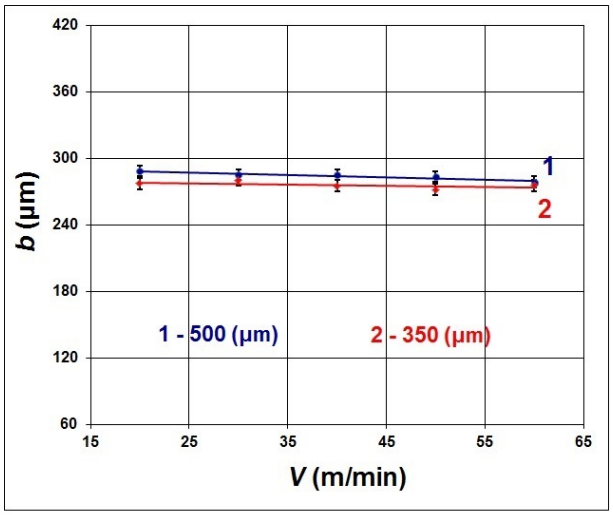


Fig. 7. Experimental dependence $b_{\text{input}} = b_{\text{input}}(v)$ throughout the same focus position $\Delta f = -2.00$ mm.

- ✓ The change of the cutting velocity v in the range $(20 \div 60)$ m/min with the step 10 m/min leads to no variation in the cutting width b as well as on both input and output. Average values of the cutting width b in the studied interval of speeds are as follows:
  - For 0.35 mm thickness – $b_{\text{input}} = (262 \pm 5)$ μm; $b_{\text{output}} = (173 \pm 5)$ μm;
  - For thickness of 0.50 mm – $b_{\text{input}} = (273 \pm 5)$ μm; $b_{\text{output}} = (186 \pm 5)$ μm.
- ✓ There is no significant change in the rapidity with which varies the cutting width Δb to the cutting velocity Δv for the both thickness of sheet steel (0.35 mm and 0.50 mm).

Microscopic analyzes. Using optical observations on the irradiated areas we evaluate the quality of cuts in the studied series experiments. There are defined limit values for the power P and cutting velocity v.

For example bending of the cutting edge and drops of molten material is ascertained on the output of the cuts obtained by cutting of samples with power of laser radiation $P = 1000$ W and velocities greater than 50 m/min, see photos on Fig. 8.

Accordingly, the visual observations showed good cuts in the interval of the laser power $P = 1000$–1400 W and cutting velocities 20 m/min – 40 m/min (Fig. 9).

Concerning the quality has been analyze and the heat affected zone with supporting of photos and optical observations, based on standard methods.

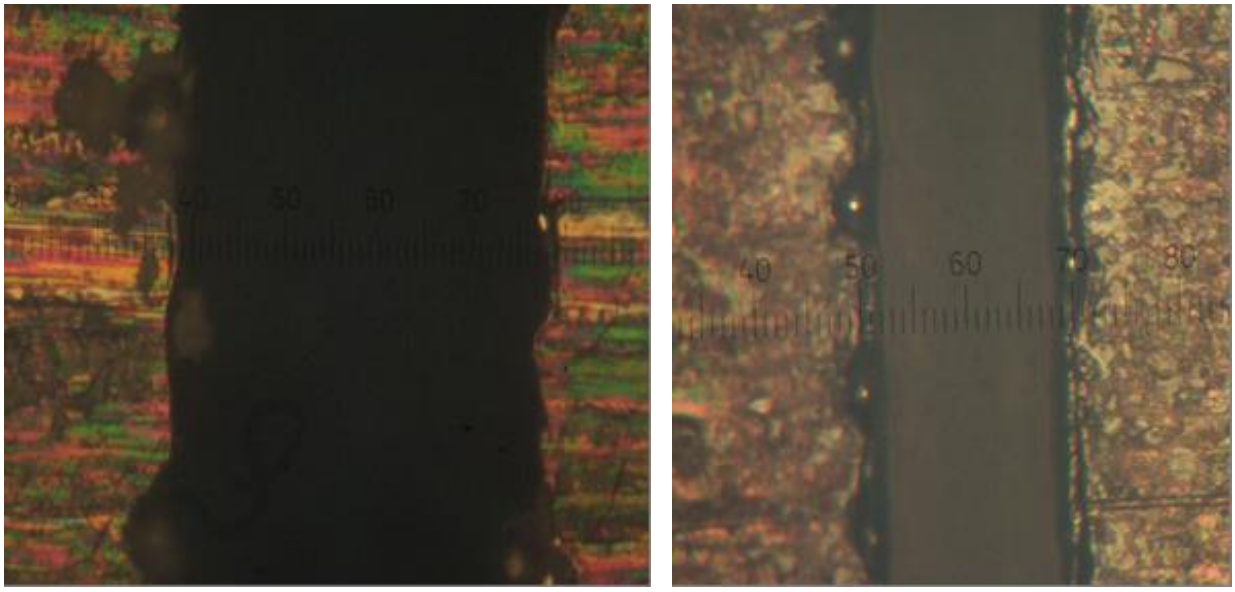


Fig. 8. Cutting parts in $P = 1000$ W of samples with thickness: a) 0.35 mm and $v = 60$ m/min; b) 0.50 mm and $v = 50$ m/min.

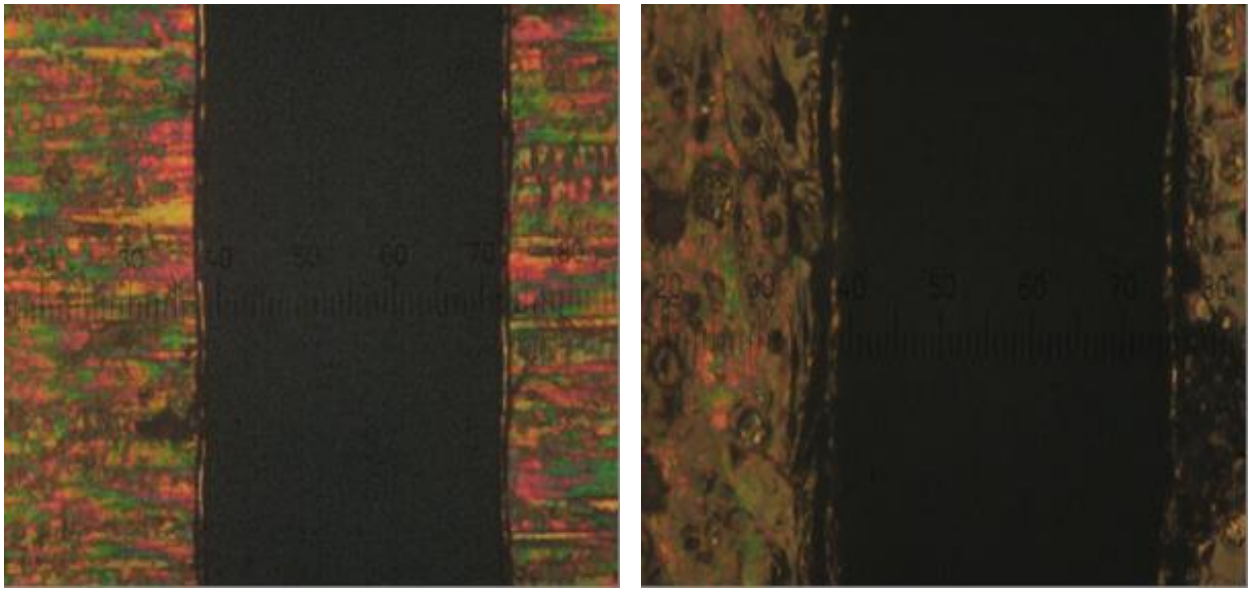


Fig. 9. Cutting parts of samples with thickness: a) 0.35 mm; b) 0.50 mm with $v = 20$ m/min in $P = 1200$ W.

In Fig. 9 are represented photos by that are being watched good cuts with laser power $P = 1200$ W and cutting velocity $v = 20$ m/min.

Summary. On based on to the received results by the experimental investigations of the influence of technological parameters: laser power P and cutting velocity v on the cutting quality determine their working intervals in which are realized laser cutting process by melting of lamellae with laser technological system TruLaser 1030 and disk laser TruDisk 2001 in good quality.

In terms of microscopic analysis and considerations of energy efficiency as advisable modes are defined the following intervals:

- For the power of laser radiation 1000 W – 1400 W;
- For the cutting velocity $v = (20 \div 40)$ m/min.

CONCLUSION

According to preliminary studies made by us we have reached a conclude that along with the considered two basic technological parameters (power P and velocity v) which exert influence upon the introducing of specific technology for laser cutting of lamellae through melting in the production of electric motors, it is necessary to make and other additional studies. By essential is to investigate the influence on the technological process from the gas pressure, the focus position toward the working surface, as well as the complexity to the contour of the lamella. These studies will be a subject of our next publications.

Acknowledgments. *This paper was published with the financial support of project "Technological equipment with parallel kinematics" under contract No 1208/2014 to fund "Scientific Research", Technical University – Gabrovo.*

REFERENCES

[1] U. Zimmermann and S. Wagner, *Alternative Antriebe Öko 2.0*, Auto Bild MARKT Barometer.GmbH, 2006.

[2] http://www.troymash.com/troymash.html

[3] http://balkanskoecho.com

[4] http://troyan-motor.dir.bg/index.html

[5] http://optics.org/indepth/3/7/2

[6] http://www.photonics.com/Article.aspx?AID=47616

[7] P. Petrov, *Razrabotvane na Technologia i Ekipirovka za Schtancovane na Rotorni i Statorni Plastini*, diplom No 1817, VMEI, Gabrovo, 1979.

[8] http://www.din.de/cmd?level=tpl-home&contextid=din&languageid=en

[9] A. Kratky, D. Schuöcker and G. Liedl, *Proc. of SPIE* textbf7131, 713111X-1–713111X-12 (2009).

[10] R. Poprawe, *Tailored Light 2. Laser Aplication Technology, B.*, Springer-Verlag, 2011, ISBN 978-3-642-01236-5.

[11] V. Apollonov, *American Journal of Modern Physics* **1**, 1–6 (2012).

[12] A. C. Goeke and C. Emmelmann, *Physics Procedia* **5**, 253–258 (2010).

[13] D. Schuöcker, *Appl. Phys.* **40**, 9–14 (1986).

[14] D. Schuöcker, *Handbook of the EuroLaser Academy*, Chapman & Hall, London, 1998.

[15] M. Grepl, M. Radáč and J. Petru, *Acta Politechnica* **52**, 62–67 (2012).

[16] S. Dinev, *Lazerite v modernite technologii*, ALFA, Sofia, 1993 (in Bulgarian).

[17] V. Kovalenko, *Lazerna obrabotka na materialite*, Technika, Sofia, 1988 (in Bulgarian).

[18] J. Hoffmann, *Laser in der industriellen Fertigung*, Schweißtechnische Lehr- und Versuchsanstalt Mecklenburg-Vorpommern.GmbH, 2010.

[19] http://www.trumpf-laser.com/en/products/solid-state-lasers/disk-lasers/trudisk.html

ИЗСЛЕДВАНЕ НА ВЛИЯНИЕТО НА ТЕХНОЛОГИЧНИТЕ ПАРАМЕТРИ МОЩНОСТ И СКОРОСТ ПРИ ЛАЗЕРНО РЯЗАНЕ НА ЛАМЕЛИ

Л. Лазов[1], Хр. Денева[2]

[1] *Faculty of Engineering Rēzeknes Augstskola Atbrīvošanas aleja 115,Rezekne, Latvia*
[2] *Технически университет Габрово, ул. "Х. Димитър" №4, 5300 Габрово, България*

(Резюме)

Непрекъснатото развитие на машиностроенето, автомобилостроенето, електротехниката и др. пораждат необходимостта от развитие на нови системи за електрозадвижвания. Основен модул в тях се явяват съвременните електромотори. Това, от своя страна, налага проектиране и тестване в кратки срокове на нови конструкции електромотори. Тези изисквания пораждат и потребността от търсене на нова технология при производство на ламели за статорните и роторни пакети на електродвигателите.

Докладът разглежда изследвания свързани с една нова иновативна технология за лазерно рязане чрез топене с шайбов лазер TruDisk 2001 на листов материал от електротехническа стомана. Дискутира се влиянието на мощността P на лазерното лъчение и скоростта v на рязане за получаване на качествени срезове. На базата на редица експериментални изследвания са определени и изведени препоръчителни работни интервали за рязане на листов материал с дебелини 0,35 mm и 0,50 mm.

Bulgarian Chemical Communications, Volume 47, Special Issue B (pp. 458–463) 2015

Dosimetry acceptance test of linear accelerator Varian Clinac iX

Ya. Gluhcheva[1,2*], T. L. Dimitrova[1], R. Dukova[2], N. Zheleva[2], I. Koleva[2], E. Encheva[2]

[1] *Faculty of Physics, Paisii Hilendarski University of Plovdiv, 24 Tsar Asen Str., BG-4000 Plovdiv, Bulgaria*
[2] *Radiotherapy Department, St. Marina University Hospital, 1 Hr. Smirnenski Blvd., BG-9000 Varna, Bulgaria*

Performance of acceptance test after the installation of a linear accelerator (linac) is obligatory. The aim is to prove that the machine meets the specification requirements. In this work are presented some dosimetry acceptance test results of linac Varian Clinac iX, recently installed at the University Hospital St. Marina, Varna. They include depth of ionization as well field flatness and symmetry for the following electron beam energies: 6 MeV, 9 MeV, 12 MeV, 16 MeV and 20 MeV. The measurements are performed using a MP3-M water scanning system and two ionization chambers Semiflex 0.125 cm^3, (PTW -Freiburg, equipment). The measured values were found to be in the tolerance interval given by Varian which proved that the tested linac corresponds to the technical specification of the vendor.

Key words: linac, acceptance test, electron beam, depth of ionization, flatness, symmetry

INTRODUCTION

The electron beams are not in common clinical use in Bulgarian radiotherapy practice because of lack of experience due to limited number of linear accelerators. The Orthovoltage treatment machines are available at most of the Radiotherapy departments and they are used in cases suitable for electron treatment. Two linear accelerators Varian Clinac iX were recently installed at the University Hospital St. Marina - Varna. Both machines have two X energies - 6 and 18 MV and five electron energies - 6, 9, 12, 16, 20 MeV. Treatment planning is computerised and the electron beam application will be introduced soon.

When an installation of a linear accelerator is completed several tests are required. This procedure is the acceptance test aiming to check if the machine meets the specification requirements, functions properly and can be safely used in clinical practice. The acceptance test is done together with the vendor. Tasks that need to be performed during acceptance test include: safety checks, mechanical checks and dosimetry measurements. All measurements initially are performed at the vendor factory with strict limits. The acceptance test precedes the commissioning of the linac, which is obligatory before the clinical start. The commissioning includes: measuring output factors, acquiring beam quality data, performing absolute dosimetry calibration of the linac, etc.

* To whom all correspondence should be sent:
yana_gl@abv.bg

THEORY

Electron beams have been in clinical use since 1950s. Historically they were firstly generated by betatrons followed by microtrons and linacs. Electron beams are considered nearly monoenergetic. The electron interacts with matter by multiple scattering - inelastic and elastic collisions with the atomic electrons and nuclei. Because of specific depth dose distribution with maximum dose deposition close to the surface electron beams are used for treatment of superficial lesions. The underlying normal tissue could be maximally protected because the rapid doses fall-off with the depth. Multimodality linacs provide two or three photon energies and several electron energies in the range from 4 MeV to 22 MeV. Electron dosimetry measurements for linac during the acceptance test do typically involve depth of ionization and field flatness, and symmetry. As far as this is relative dosimetry, none correction factors are needed. During the commissioning – the absolute dosimetry measurements - dose values should be corrected for temperature and pressure, polarity effect, etc [1].

Electron depth of ionization is defined from the central axis depth dose curve. The typical curve starts with surface dose higher then surface dose of photon beams. Beyond the surface the dose builds up to a maximum at a particular depth – electron beam depth dose maximum $z_{\max}$. After $z_{\max}$ dose drops off rapidly and levels to a bremsstrahlung tail. Due to this dose distribution electron beams have clinical advantages over the orthovoltage machines in irradiating superficially located lesions. When entering the matter the electrons exhibit fall-off after only a few centimetres [2].

© 2015 Bulgarian Academy of Sciences, Union of Chemists in Bulgaria

Percentage depth dose (PDD) is defined as the dose at certain point D_x of the central axis over the maximum dose D_{max} on the central axis multiplied by 100:

$$\mathrm{PDD} = \frac{D_x}{D_{max}}.100,\ \% \qquad (1)$$

PDD depends on the beam quality [3] that is defined mainly by energy, radiation field size and shape, source to surface distance (SSD), collimation of the beam, etc. Normally PDD is measured at the nominal treatment distance. In Varian protocol PDD of electron beams is defined with the use of a water phantom at SSD equal to 100 cm. The radiation field is 15 x 15 cm with applicator. The tolerance values are given for depth of ionization at 90%, 80%, 50% and 30% of the maximum beam intensity.

Electron field flatness and symmetry are given at z_{max} according to the International Electro-technical Commission (IEC). The profile requirement for the flatness is that the distance between 90% dose level and the geometrical beam edge does not exceed 1 cm along the major axes and 2 cm along the diagonals. Also, the maximum value of the absorbed dose in the 90% isodose region should not exceed 1.05 times the absorbed dose on the beam axis at the same depth [4].

A typical profile curve of the electron beam is shown in Fig. 1.

According to the Varian protocol, flatness and symmetry are calculated from profile curve measured at plane in a water phantom at certain depth. This depth is different from z_{max} (IEC) and specific for different electron energies. It is calculated as follows:

$$\mathrm{Depth} = \frac{85\%\ \text{beam intensity}}{2},\ \mathrm{cm} \qquad (2)$$

The scanning depths for different electron energies of linac Varian Clinac iX are given in Table 1.

Table 1. Electron energies scanning depths.

Energy, MeV	Depth, cm
6	1.0
9	1.4
12	2.0
16	2.7
20	3.3

Flatness specification is the maximum variation of the integrated dose between the minimum and the maximum points within the central 80% field width of the radial (inplane) and transversal (crossplane) major axes at SSD 100 cm:

$$\mathrm{Flatness} = \frac{D_{max} - D_{min}}{2}.100,\ \% \qquad (3)$$

Symmetry specification is the maximum variation of the integrated dose between any two corresponding points equidistant from the beam centreline within the central 80% field width of the radial (inplane) and transversal (crossplane) major axes at SSD 100 cm.

$$\mathrm{Symmetry} = \frac{D_{(x)} - D_{(-x)}}{2}.100,\ \% \qquad (4)$$

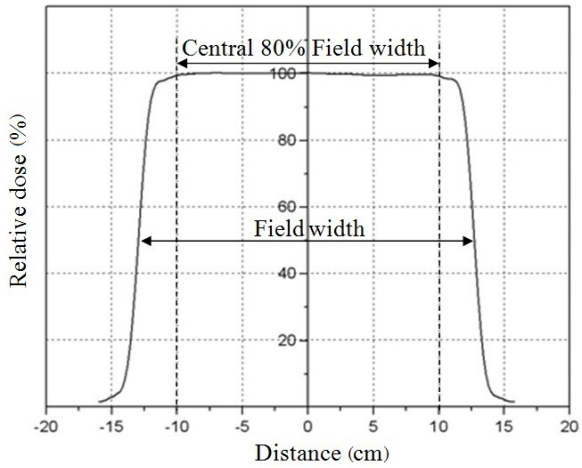


Fig. 1. Typical profile curve of megavoltage energy electron beam of linac.

MATERIALS AND METHODS

Dosimetry measurements for Varian Clinac iX linear accelerator are performed for the following electron energies: 6 MeV, 9 MeV, 12 MeV, 16 MeV and 20 MeV. Linac is equipped with five electron applicators defining radiation fields of 6×6 cm, 10×10 cm, 15×15 cm, 20×20 cm and 25×25 cm. The role of the applicator is to limit the radiation field, but more important to collimate the beam. The applicators are attached to the gantry head and provide homogeneity of the dose at irradiated area.

All measurements are performed with MP3-M Water Scanning System (PTW - Freiburg). This system includes water phantom made of Polymethyl methacrylate (PMMA). The water tank has outer dimensions of $636 \times 634 \times 522.5$ mm and inner dimensions of $596 \times 594 \times 502.5$ mm. The walls are 2 cm

thick and the water capacity is 171 l. For all performed measurements the tank is filled with distilled water. Water phantom is connected to TBA control unit which provides remote positioning of the basic detector. Before each measurement the positions of the detector are defined, i.e. the detector is providing data at certain points inside the phantom while moving from point to point by the software and TBA system. A stand is attached to the water tank to place a referent detector which usually is set at the edge of radiation field in air. Its data are applied as correction coefficient of the data taken from the basic detector. Detectors are connected to TANDEM dual-channel electrometer. Mephysto 3.0 software is used. All dosimetry equipment is manufactured by PTW – Freiburg.

Two Semiflex 0.125 cm^3 ionization chambers are used as detectors (PTW – Freiburg). Nominal voltage of both detectors is + 400 V. One of them is used as basic and the other one - as referent. For measuring PDD the basic chamber is positioned along the central beam axis from 15 cm depth up to the water phantom surface with several mm intervals. When studying the electron field flatness and symmetry, the basic chamber moves in horizontal planes at different depth level according to the measured electron energy – Table 1. The movement is both inplane (radial) and crossplane (transversal) in lines longer than the dimensions of the radiation field. The beam data are taken through several mm by the moving detector. For all presented measurements a referent detector is placed in the air at the edge of the radiation field.

RESULTS AND DISCUSSION

All results are calculated using the Varian protocol. Linac gantry and collimator are at position zero degrees during all measurements.

Electron depth of ionization

For PDD measurements 15×15 cm electron applicator is mounted on the linac head. SSD is 100 cm and this specifies radiation field 15×15 cm on the water phantom surface. The depth at 90%, 80%, 50% and 30% of the maximum dose intensity is defined in cm.

The tolerance intervals and measured values are presented in Table 2.

The protocol with measurement results from Mephysto 3.0 is given in Fig. 2.

The PDD curves of all electron energies are presented. As it is visible maximum dose for highest energy (20 MeV) is achieved in 1.59 cm (R100) [5]. Bremsstrahlung tail per energy levels as follows: 6 MeV – 3 cm, 9 MeV – 4.5 cm, 12 MeV – 6.2 cm, 16 MeV – 8.1 cm and 20 MeV – 10.2 cm.

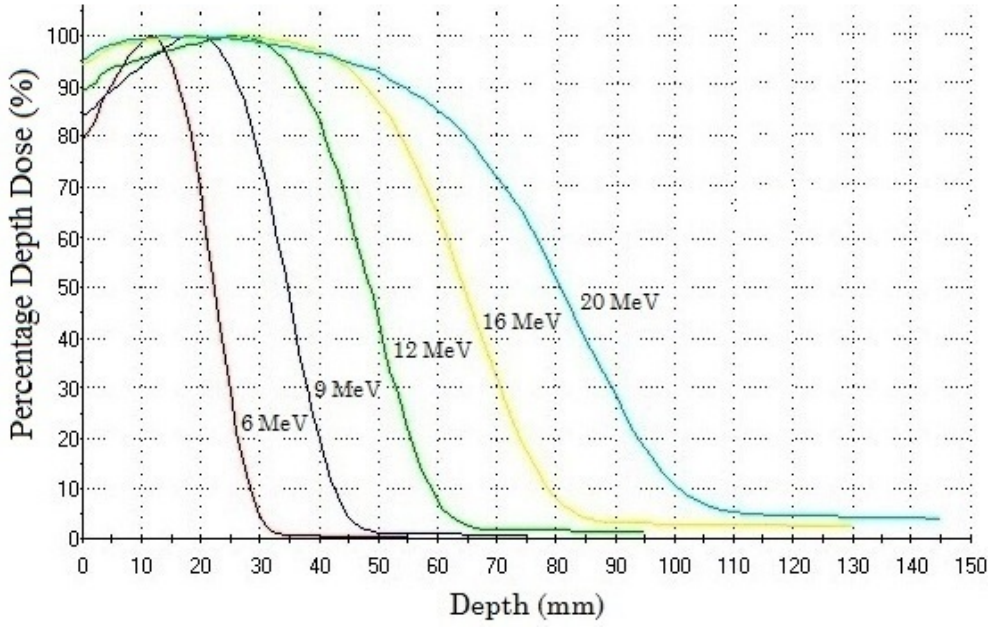


Fig. 2. PDD curves for all electron energies.

Table 2. PDD for all electron energies

Energy MeV	**Interval**	**Depth of respective percentage depth dose**, cm 90%	80%	50%	30%
6	Specification	1.71 ± 0.10	1.90 ± 0.07	2.30 ± 0.10	≤ 2.60
	Measured	1.63	1.83	2.23	2.49
9	Specification	2.68 ± 0.10	2.95 ± 0.07	3.50 ± 0.10	≤ 3.90
	Measured	2.64	2.90	3.47	3.78
12	Specification	3.77 ± 0.10	4.15 ± 0.07	4.89 ± 0.10	≤ 5.40
	Measured	3.71	4.08	4.86	5.29
16	Specification	4.87 ± 0.10	5.45 ± 0.07	6.49 ± 0.10	≤ 7.30
	Measured	4.80	5.38	6.44	7.10
20	Specification	5.52 ± 0.10	6.55 ± 0.07	8.13 ± 0.10	≤ 9.30
	Measured	5.43	6.49	8.08	8.94

Field flatness and symmetry

For electron field flatness and symmetry both inplane and crossplane profiles are taken. The setup is the same as for PDD but radiation fields are 10×10 cm and 25×25 cm on the water phantom surface (respectively 10×10 cm and 25×25 cm applicators are mounted to the gantry). Profiles of the different electron energies are taken in planes located at certain depth defined in Table 1. Table 3 presents the specification intervals and calculated values of inplane line.

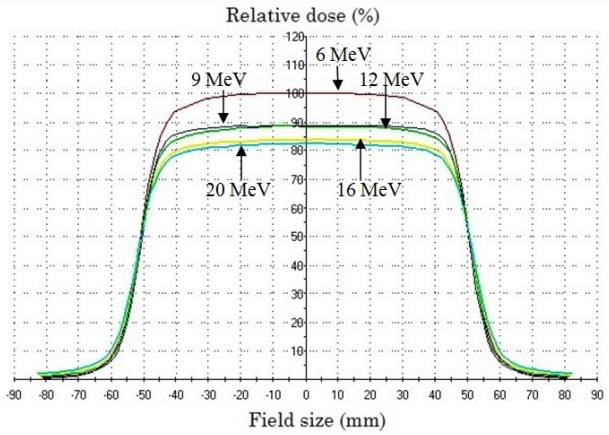


Fig. 3. Inplane profile curves for all energies – radiation field 10×10 cm. (Mephysto 3.0).

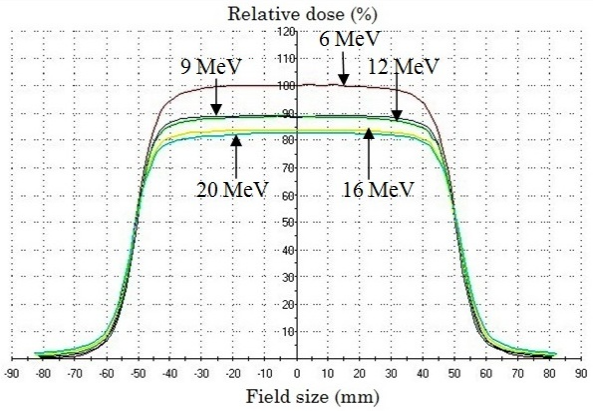


Fig. 4. Crossplane profile curves for all energies – radiation field 10×10 cm. (Mephysto 3.0).

Table 3. Electron field flatness and symmetry – Inplane

Energy, MeV	**Field**, cm	**Flatness**, % Specification	Actual	**Symmetry**, % Specification	Actual
6	25×25	$\pm$ 4.5	$\pm$ 1.13	2%	0.32
9	25×25	$\pm$ 4.5	$\pm$ 1.04	2%	0.44
12	25×25	$\pm$ 4.5	$\pm$ 0.77	2%	0.38
16	25×25	$\pm$ 4.5	$\pm$ 0.65	2%	0.46
20	25×25	$\pm$ 4.5	$\pm$ 1.50	2%	0.64
6	10×10	$\pm$ 5.0	$\pm$ 3.66	2%	0.62
9	10×10	$\pm$ 4.5	$\pm$ 2.04	2%	0.70
12	10×10	$\pm$ 4.5	$\pm$ 3.17	2%	1.05
16	10×10	$\pm$ 4.5	$\pm$ 3.12	2%	0.89
20	10×10	$\pm$ 4.5	$\pm$ 3.44	2%	0.75

Table 4. Electron field flatness and symmetry – Crossplane

Energy, MeV	**Field**, cm	**Flatness**, % Specification	Actual	**Symmetry**, % Specification	Actual
6	25 × 25	± 4.5	± 1.10	2%	0.62
9	25 × 25	± 4.5	± 0.96	2%	0.89
12	25 × 25	± 4.5	± 0.48	2%	0.65
16	25 × 25	± 4.5	± 1.25	2%	0.75
20	25 × 25	± 4.5	± 1.27	2%	0.98
6	10 × 10	± 5.0	± 3.61	2%	0.66
9	10 × 10	± 4.5	± 2.21	2%	0.78
12	10 × 10	± 4.5	± 2.87	2%	0.64
16	10 × 10	± 4.5	± 2.57	2%	0.71
20	10 × 10	± 4.5	± 2.84	2%	0.77

Fig. 3 presents a protocol from Mephysto 3.0. Inplane profiles for different electron energies per field 10 × 10 cm are shown.

Table 4 presents crossplane line specification intervals and calculated values.

Fig. 4 shows a protocol from Mephysto 3.0. Crossplane profiles for different electron energies and field 10 × 10 cm are given.

Results for the observed fields (10 × 10 cm and 25 × 25 cm) both inplane and crossplane are in the tolerance intervals. Calculated flatness and symmetry are quite lower than the specification. This means that the dose all over the radiation field is highly homogeneous with no dependence of radiation field size.

CONCLUSIONS

The presented measurements for percentage depth dose and field flatness and symmetry are in tolerance intervals given by Varian. This proves that the studied linac meets the specification and can be used in clinical practice with all available electron energies. After the complete acceptance test is finished, machine commissioning including the absolute dosimetry calibration should be performed. After acquisition of all beam quality data they need to be transferred to the treatment planning system. Then commissioning of the treatment planning system itself and a number of verification tests with the linac before clinical start are required.

Acknowledgments. *This paper is written after installation of two linear accelerators Varian Clinac iX at University Hospital St. Marina, Varna. The purchase and delivery of the machines and the construction of the Oncology and Radiotherapy centre at UH St. Marina, Varna is within projects, an integral part of the medium-term framework investment program, implementing the Framework Agreement BG161PO001-1.1.08-0001-1 scheme for providing grants BG161 PO001/1.1-08/2010 "Support for reconstruction, renovation and equipping of state medical and health facilities in urban areas", which are implemented with the financial support of Operative Program "Regional Development" 2007-2013, co-financed by the European Union through the European Fund regional development. The contracts were signed by the Ministry of Health and Ministry of Regional Development and public works.*

We would like to express our sincere gratitude to the people involved in this project. We would like also to thank University Hospital St. Marina for opportunity to present the current results and to introduce the electron treatment in Bulgaria.

REFERENCES

[1] AAPM Protocol: Task Group 21: A protocol for the determination of absorbed dose from high-energy photon and electron beams, Task Group 21, *Med. Phys.* **10**, 741–771 (1983).

[2] Absorbed Dose Determination in External Beam Radiotherapy: An Initial Code of Practice for Dosimetry based on Standards of Absorbed Dose to Water, IAEA - TRS-398 (2000).

[3] Eun-Hoe Goo, Jae-Seung Lee, Moon-Jib Kim, Kyung-Rae Dong, Dae-Cheol Kweon and Woon-Kwan Chung, *J. Korean Phys. Soc.* **57**, 506–513 (2010).

[4] E. B. Podgorsak, Technical editor, Radiation Oncology Physics: A Handbook for Teachers and Students, IAEA, (2005).

[5] E. G. A. Aird, J. E. Burns, S. Duane, T. J. Jordan, A. Kacperek, S. C. Klevenhagen, R. M. Harrison, S. C. Lillicrap, A. L. McKenzie, W. G. Pitchford, J. E. Shaw, C. W. Smith, *British Journal of Radiology* Supplement 25 (1996).

ДОЗИМЕТРИЧНИ ПРЕДВАРИТЕЛНИ ПРИЕМНИ ИЗПИТВАНИЯ НА ЛИНЕЕН УСКОРИТЕЛ Clinac iX, Varian

Я. Глухчева[1,2], Т. Димитрова[1], Р. Дукова[2], Н. Желева[2], И. Колева[2], Е. Енчева[2]

[1] *Физически факултет, Пловдивски университет "Паисий Хилендарски", ул. Цар Асен 24, 4000 Пловдив, България*
[2] *Клиника по нуклеарна медицина, УМБАЛ "Св. Марина", ул. "Хр. Смирненски" № 1, Варна, България*

(Резюме)

При приемане на линеен ускорител за медицински цели се провеждат цялостни тестове с оглед правилното сработване на всички системи и тяхната калибровка. Важна част от това са и дозиметричните приемателни тестове, включващи процентното разпределение на дозата в дълбочина по протежение на централната ос на лъчевия сноп и изследване на изравнеността и симетрията за различни лъчеви полета. Представените данни са за линеен ускорител Varian Clinac iX с енергии съответно: а) фотони – 6 MV, 18 MV; б) електрони – 6 MeV, 9 MeV, 12 MeV, 16 MeV, 20 MeV. Измерванията са направени във воден фантом MP3-M посредством йонизационни камери Semiflex 0,125 cm^3 и софтуерна система Mephysto 3.0 (производител PTW). Получените резултати са сравнени със заложените толерансни стойности от фирмата производител на линейния ускорител. За референтен документ служи също и Suplemant 25. Едва след като апаратът е калибриран, за да влезе в толеранс, могат да започнат пусковите изпитвания на линейния ускорител, включващи снемането на корекционни фактори и абсолютни дозиметрични измервания.

Bulgarian Chemical Communications, Volume 47, Special Issue B (pp. 464–468) 2015

Excitation-emission matrices for detection of colorectal tumors – initial investigations

Ts. Genova[1*], E. Borisova[1], L. Angelova[1], Al. Zhelyazkova[1], M. Keremedchiev[2], N. Penkov[2], B. Vladimirov[2], L. Avramov[1]

[1] *Institute of Electronics, Bulgarian Academy of Sciences, 72 Tsarigradsko Chaussee Blvd. 1784 Sofia, Bulgaria*
[2] *Queen Giovanna University Hospital (ISUL), 8 Bialo More Str., 1527 Sofia, Bulgaria*

Detection and evaluation of cancerous changes in gastrointestinal tract (GIT) are performed with standart endoscopy. Its limitations are significant challenge and initiate development of novel diagnostic modalities. Therefore many spectral and optical techniques are applied recently into the clinical practice for obtaining qualitatively and quantitatively new data from gastrointestinal neoplasia with different level of clinical applicability and diagnostic success. Investigations for new diagnostic techniques by applying spectral and optical methods in clinical practice show very promising direction for an improvement of the tumour detection. One of the most promising technologies in this area is the fluorescence spectroscopy. The technique is very topical with its practical application in intra-operative, image-guided resection of tumors, because it permits minimal surgical intervention and friendly therapeutic conditions. In our investigation we evaluate the fluorescence of in vitro samples of lesions and healthy tissue of lower gastrointestinal tract. Autofluorescence of biological tissues is based on endogenous fluorophores response to an excitation in 280 - 440 nm spectral range and is observed in spectral range 320-550nm. On the basis of the spectral data analysis we try to estimate the options for application of autofluorescence spectroscopy techniques in clinical practice for in vivo diagnostic of lower GIT tumors. Autofluorescence detection could make the entire diagnostics procedure more personal, patient friendly and effective and will help for further understanding of tumors nature and to improve patients' lives. These investigations are part of the concept to proof the feasibility of such a system for a real clinical application. Therefore, we plan to gain more significant data base for the main spectral characteristics of lower GI neoplasia. We foresee as well to develop appropriate algorithms for benign/malignant tissue differentiation, based on the spectral features, obtained for normal mucosa and colorectal pathologies. Initial results obtained are promising that the specific differences are observed between normal mucosa and tumor, as well as for dysplasia-tumor pairs.

Key words: autofluorescence spectroscopy, colorectal cancer, excitation-emission matrices

INTRODUCTION

Colorectal cancer is the third most commonly diagnosed cancer and a major cause of cancer-related deaths worldwide [1]. At its early stage colorectal cancer usually do not reveal significant structural changes, this characteristic makes its detection and evaluation with standard endoscopy rather difficult and strongly related to physician's experience. Autofluorescence spectroscopy is one of the optical techniques applied for improving diagnostic sensitivity of standard endoscopy [2,3]. Light-induced fluorescence imaging and spectroscopy are one of the most sensitive optical approaches for detection of neoplasia of gastrointestinal mucosa, especially fluorescence spectroscopy, because of its rapid and highly sensitive response to early biochemical and morphological changes in the tissues [3]. Autofluorescence signal of biological tissues depends on endogenous fluorophores presence and concentration. Metabolic and of the tissues reflect in concentration and appearance of endogenous fluorophores [2]. Therefore cancerous tissues and tumors exhibit different fluorescence in comparison with the healthy tissues. Endogenous fluorophores which have a major contribution in fluorescence signal from GIT mucosa depend on the applied excitation wavelength, but at general they are amino acids, lipids, enzymes and coenzymes and some structural proteins. Optimal excitation wavelengths and maxima of the fluorescence emissions of the primary endogenous fluorophores are presented in Table 1.

Fluorescence signal obtained from the biological tissue depends not only from the endogenous fluorophores but also from the native pigments – chromophores in the tissues. The chromophore, which mostly affects fluorescence spectra of GIT mucosa in the visible range, by absorbing in 400–700 nm, is hemoglobin [4]. For the needs of clinical diagnostic of GIT there are just a few existing endoscopic systems that combines white light and fluorescent mode. Some of them are digestive tract videoscopes, for example one such produced by Olympus Inc., is used

* To whom all correspondence should be sent:
ts.genova@gmail.com

© 2015 Bulgarian Academy of Sciences, Union of Chemists in Bulgaria

Table 1. Maximum of excitation and fluorescence emission of the main endogenous fluorophores in GIT mucosa. NADH – nicotinamide adenine dinucleotide; FAD – flavin adenine dinucleotide

Endogenous fluorophores	Maximum of excitation, nm	Maximum of emission, nm
Amino acids		
Tryptophan	280	350
Tyrosine	275	300
Porphyrines	400-450	630, 690
Enzymes and coenzymes		
NADH	450	535
FAD	290, 351	440, 460
Structural proteins		
Collagen	325, 360	400, 405
Elastin	290, 325	340, 400

to observe blood vessels in mucous membranes under infrared light in the regions 790–820 nm and 905–970 nm. Another endoscopic system - Xillix-LIFE-GI, jointly developed by Xillix and Olympus, is applied for autofluorescence detection of stomach neoplasia. In this system blue-light excitation is used in the range of 400–450 nm, with additional simultaneously excitation with red-near-infrared light in the newer version of the system. Fluorescence signal is evaluated by two CCD cameras with maximum sensitivity in the green (480–560 nm) and in the red (630–750 nm) spectral ranges. Fluorescence signal is processed and displayed as false-color image in real-time. On those images normal mucosa appears colored in green and neoplastic mucosa appears colored in red [5]. Fluorescence technique is very topical with its practical application in visualization and discrimination of neoplastic tissues during open surgical interventions for tumor excision in lower GIT. This kind of intra-operative, image-guided resection of tumors permits precise tumor excision along with minimal surgery intervention and friendly therapeutic conditions [6,7]. Although several systems have been developed, the existing clinical limitations are one significant technical challenge and initiate a development of new diagnostic modalities based on different spectral and optical techniques. Also the reported specificity is not satisfactory as the rate of false-positive results in differentiating dysplastic from inflamed tissues is one of the main drawbacks. On the way of solving those problems is to find excitation wavelengths that provide fluorescence signal consisting unique spectral characteristic features, correlated with the tissue pathologies and establishing of a robust algorithm that can extract and compare those features of the autofluorescence signal. Therefore different research groups work in the direction of optimization of fluorescence detection that could improve implementation and contribution of the fluorescence techniques in to the clinical diagnostic practice for lower GIT tumour detection.

MATERIALS AND METHODS

In our study, we investigated fluorescence of 8 samples of neoplastic tissue and healthy tissues from 5 patients. Normal and tumour's GIT mucosa samples are received after surgical excision during procedures for a removal of GIT neoplasia lesions. Normal tissue investigated is a part of the safety area around the tumor excised during its removal. Neoplastic tissue in samples has been histological identified in 5 samples as carcinoma, in 2 samples as polyp and in 1 sample as metastatic lymph node. All patients received and signed written informed consent and this research is approved by the ethical committee of University Hospital "Queen Giovanna", Sofia. After surgical removal biological samples are transported in isothermal conditions and safe-keeping solution from the hospital to the spectral laboratory, where their fluorescence is investigated with point-by-point spectroscopy.

For fluorescence measurements we used spectrofluorimeter FluoroLog 3 (HORIBA Jobin Yvon, France). This system allows performance of steady-state and time-resolved fluorescence measurements with light source xenon lamp with power 300 W and performance range 200 - 650 nm and PMT detector with performance range of 220–850 nm for the fluorescence detection. Our tissue samples cannot be put into a standard cuvette, since they vary in shape and dimensions. Therefore we use additional fiber-optic module of Fluorolog 3 – F-3000, which allows investigation of samples outside of the sample chamber. The measurements of the fluorescence signals are obtained in a regime of so called excitation-emission matrices (EEMs) for all tissues investigated. This three-dimensional fluorescence spectral maps provides information about the fluorescence spectra of biological tissue samples, which is needed for determining excitation wavelengths that gave emission fluorescence spectra containing the most significant diagnostic information for a further clinical diagnostic analysis.

Excitation applied to the samples was in 280–440 nm spectral region. Fluorescence emission was measured in the range of 300 to 800 nm. After the spectroscopic measurement procedure the samples were kept in a formalin solution.

RESULTS AND DISCUSSION

Fluorescence spectroscopy of gastrointestinal tissues ex vivo demonstrated that autofluorescence spectra depend on the applied excitation wavelength and tissue type. Different spectral characteristics of autofluorescence spectra of tumours in comparison with autofluorescence spectra of normal GIT mucosa give information about intrinsic sources of fluorescence, that correlate with the biochemical and morphological changes in the neoplastic tissue.

Autofluorescence of the safe-keeping solution, where the tissue samples are kept during transportation and autofluorescence of the surface where the tissue sample is placed during the measurements are evaluated and signals have been found negligible low in comparison with the fluorescence intensities detected from the tissue samples themselves for all excitation wavelengths applied in our investigations.

In Figs. 1.a and 1.b are presented excitation – emission matrices of normal mucosa and of the tumour, in Figs. 1.c and 1.d are presented the autofluorescence spectra respectively for the normal and carcinoma tissues from a colorectal part of GIT. Several major autofluorescence sources could be addressed in the samples investigated. Those are amino acids – tryptophan and tyrosine, structural proteins – elastin and collagen, and their cross-links and coenzymes NADH and FAD. Their maxima of excitation and emission are presented in Table 2.

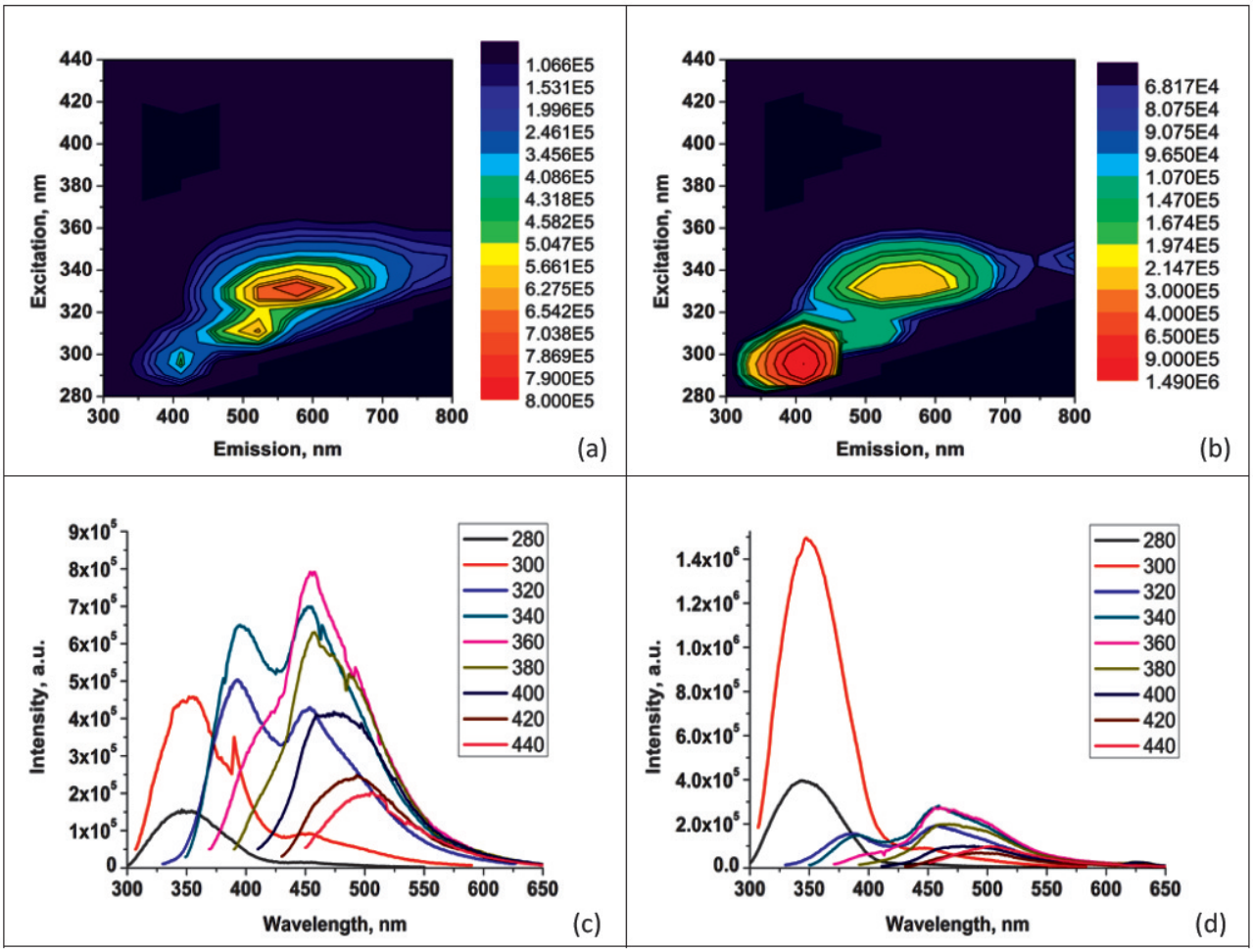


Fig. 1. (a) EEM of normal mucosa; (b) EEM of carcinoma; (c) fluorescence spectra of normal mucosa; (d) fluorescence spectra of carcinoma from the colorectal area of GIT.

Table 2. Endogenous fluorophores identified as main autofluorescence sources in the lower GIT tissues investigated, with their maxima of excitation and emission

Endogenous fluorophores	Maximum of excitation, nm	Maximum of emission, nm
Tryptophan and Tyrosine	280-300	320-360
NADH	340-380	440-480
FAD	340-400	500-530
Collagen and Elastin	320-360	400, 460-500
Protein cross-links	290, 325	340, 400

Coenzymes NADH and FAD are degrading fast in the tissue samples after their surgical excision, therefore the fluorescence arising from those endogenous fluorophores could be detected only in the freshly excised samples. Main difference between autofluorescence of the normal and tumour tissue is in about two times lower intensity of the fluorescence signal from tumour tissue in the spectral range 400 - 600 nm, where the primary source of fluorescence are structural proteins and their cross-links. This could be addressed to decrease of the signal detected in unit volume of the tissue from collagen fibers and collagen cross-links. In the case of tumour lesion, the intercellular matrix is relatively loosened, due to increased tumor cells size and general reduction of collagen and elastin concentration on volume unit. Similar observations of fluorescence signal reduction are reported from different research groups and are proposed to be used as an indication of tumor lesion presence for diagnostic analyses [8,9].

Specific alteration in the metabolic activity in tumour cells causes oxidation of NADH, whose oxidized form NAD+ is non-fluorescent. That lead to significant loss of fluorescence signal in the 450–550 nm region. That is another essential difference between autofluorescence spectra of normal and tumor tissues, which could be applied for differentiation. As a summary the most significant fluorescence spectra differences are observed for the excitation wavelengths applied in the region of 300–360 nm, where NADH and structural proteins have maximum of excitation, because the alterations in their fluorescence spectra are the main difference between autofluorescence spectra of normal and tumour tissue. Excitation wavelengths from this range have been investigated by other research groups as well for the diagnostic meaning of the corresponding fluorescence spectra of normal and neoplastic GIT tissue [9,10]. The results obtained show high sensitivity and specificity for determining cancerous tissues on the basis of the obtained fluorescence spectra.

CONCLUSIONS

Implementing fluorescence techniques into the clinical practice has potential to improve determination of the site, borders and size of the lesions, not only for initial diagnostics but also in real-time monitoring of resection procedures and in the personalization of the patient healthcare. One of the main advantages of fluorescence techniques is that they are patient friendly, not using ionizing radiation and could help for further understanding of tumors nature, which will result in improving patients' lives. Our efforts are directed towards developing a robust algorithm for processing fluorescence spectra, which will result in reliable differentiation between normal and cancerous tissues and to be implemented in practical clinical diagnostics. This requires gaining more significant data base for the main spectral characteristics of lower GI neoplasia.

Aknowledgments. *This work is supported by the National Science Fund of Bulgarian Ministry of Education, Youth and Science under grant # DMU-03-46/2011 "Development and introduction of optical biopsy for early diagnostics of malignant tumours", grant # DO-02-112/2008 "National Center on Biomedical Photonics" and grant # DFNI-B02/9/12.12.2014 "Development of Biophotonics methods as a basis of Oncology Theranostics". E. Borisova would like to thank to UNESCO-L'OREAL International Fellowships Programme for Young Women in Life Sciences for the financial support of this work.*

REFERENCES

[1] A. Jemal, F. Bray, M. Center, J. Ferlay, E. Ward, D. Forman. *CA: A Cancer Journal for Clinicians*, **61(2)**, 69-90 (2011).

[2] J.Q. Brown, K. Vishwanath, G. Palmer and N. Ramanujam. *Current Opinion in Biotechnology*, **20**, 119-131 (2009).

[3] K. Tada, I. Oda, C. Yokoi, T. Taniguchi, T. Sakamoto, H. Suzuki, S. Nonaka, S. Yoshinaga, Y. Saito and T. Gotoda. *Diagnostic and Therapeutic Endoscopy*, (2011)

[4] R. Da Costa, B. Wilson And N. Marcon, *Digestive Endoscopy*, **15**, 153-173 (2003)

[5] S. Wildi and M. Wallace, "Emerging Tech-

niques: Spectroscopy." in "Barrett's Esophagus and Esophageal Adenocarcinoma", edited by P. Sharma, R. Sampliner, John Wiley & Sons, 2008, p. 163.

[6] H. Handgraaf, M. Boonstra, A. Van Erkel, B. Bonsing, H.Putter, C. Van De Velde, A. Vahrmeijer, and J. Mieog, *BioMed Research International*, (2014).

[7] F. Verbeek, J. Vorst, B. Schaafsma, M. Hutteman, B. Bonsing, F. Leeuwen, J. Frangioni, C. van de Velde, R. Swijnenburg, A. Vahrmeijer, *J Hepatobiliary Pancreat Sci*, **19**, 626-637 (2012).

[8] R. Richards-Kortum, R. P. Rava, R. E. Petras, M. Fitzmaurice, M. Sivak and M. S. Feld, *Photochemistry and Photobiology*, **53**, 777-786 (1991).

[9] Liu L, et al., *Photodiagnosis and Photodynamic Therapy*, **10**, 111-119 (2013).

[10] Li BH, Xie SS, *World J Gastroenterol*, **11(25)**, 3931-3934 (2005).

МАТРИЦИ НА ВЪЗБУЖДАНЕ И ФЛУОРЕСЦЕНЦИЯ ЗА ДЕТЕКТИРАНЕ НА КОЛО-РЕКТАЛНИ ТУМОРИ – НАЧАЛНИ ИЗСЛЕДВАНИЯ

Ц. Генова[1], Е. Борисова[1], Л. Ангелова[1], Ал. Желязкова[1], М. Кермедчиев[2], Б. Владимиров[2], Л. Аврамов[1]

[1] *Институт по електроника, Българска академия на науките, бул. "Цариградско шосе" № 72, 1784 София, България*
[2] *Университетска болница "Царица Йоанна" – ИСУЛ, ул. "Бяло море" №8, 1527, София, България*

(Резюме)

Диагностиката на неоплазии в областта на гастроинтестиналния тракт (ГИТ), се извършва със стандартни ендоскопски изследвания, чиито ограничения са предпоставка за търсенето и развитието на нови, по-точни и по-чувствителни диагностични методи. Търсенето на нови диагностични техники, чрез прилагане на спектралните и оптични методи в клиничната практика е обещаващо направление.

Флуоресцентната диагностика е един от най-разпространените оптични методи за диагностика, с добри перспективи за развитие. Методът се прилага за по-точно идентифициране на лезии и по време на операции, осигурявайки минимална намеса в състоянието на оперативното поле и цялостното състояние на пациента. Автофлуоресценцията на биологичните тъкани, дължаща се на излъчването на ендогенн флуорофори, се наблюдава в диапазона 320-550 nm и се получава при възбуждане в диапазона 280-440 nm.

В нашето изследване оценяваме флуоресценцията на in vitro образци от лезии и здрава тъкан на долен ГИТ, за да проучим възможностите за приложение на автофлуоресцентни техники за клинична диагностика на тумори на ГИТ in vivo.

Флуоресценцията на образците in vitro е изследвана чрез системата FluoroLog 3 (HORIBA Jobin Yvon, Франция), която използва като източник мощна ксенонова лампа (300 W., 200-850 nm), два двойни монохроматора, и детектор - ФЕУ с висока чувствителност в областта 220-850 nm. Автофлуоресцентните сигнали са детектирани чрез методиката за определяне на матрици на възбуждане и флуоресценция от образци на здрава тъкан, дисплазия и карцином на дебелото черво. Изследваните образци проявяват специфични спектрални характеристики в зависимост от състоянието на тъканта, като могат да се определят диагностично-значими особености, приложими в клинични алгоритми за диференциация на патологичните изменения.

Автофлуоресцентната техника може да направи диагностичната процедура по- ефективна, неинвазивна и съобразена с индивидуалните особености на пациента. Приложението ѝ може да допринесе за по-доброто разбирането на същността на неопластичните процеси и подобряване на качеството на живот на пациентите. Нашите усилия са насочени в посока на събиране и систематизиране на статистически данни за основните флуоресцентни характеристики на неоплазии на долния ГИТ, които да бъдат използвани за основа за развитие на подходящи алгоритми за разграничаване на здрава от туморна тъкан.

Благодарности: Проектът е финансиран от Фонд Научни Изследвания към Министерство на Образованието и Науката по прокет #DMU-03-46/2011 "Разработка и внедряване на оптична биопсия за ранна диагностика на злокачествени тумори" и проект ДО-02-112/2008 "Национален Център по Биомедицинска Фотоника". Е. Борисова иска да благодари на програмата на ЮНЕСКО/Л'Ореал „За жените в науката" за оказаната ѝ финасова подкрепа в настоящите изследвания.

Bulgarian Chemical Communications, Volume 47, Special Issue B (pp. 469–475) 2015

Synchronous fluorescence spectroscopy for analysis of vegetable oils

Ya. Andreeva, E. Borisova*, Ts. Genova, Al. Zhelyazkova, L. Avramov

[1] *Institute of Electronics, Bulgarian Academy of Sciences, 72 Tsarigradsko Chaussee Blvd., 1784 Sofia, Bulgaria*

Synchronous fluorescence spectroscopy is a well established and proven method for analysis in many disciplines. This research shows the potential of the technique for analysis of vegetable oils. The synchronous fluorescence spectra of two different types of oils - sunflower and extra virgin olive oil, were acquired in the excitation wavelength region 220-800 nm and for wavelength intervals from 0 to 100 nm in 10 nm interval. The study includes the spectra of samples heated for different time intervals - unheated oil, 0 min (oil moved from the oven when just boiled), 5 min boiling and 10 min boiling oil respectively. It's shown that the method gives good results and allows assessment of the quality and constituents of the oils according to the heat treatment applied to samples. Processes such as oxidation may lead to production of potentially toxic compounds for human body. That's way the method is very important and useful.

Key words: synchronous fluorescence spectroscopy, vegetable oils, extra virgin olive oil, sunflower oil, heat treatment, oxidation

INTRODUCTION

Vegetable oils constitute a very large and important group of foods. This is why considerable interest is manifested in the study of their quality and content. The need of rapid method for their quality assessment and detection of deteriorations and adulterations of the products is increasing [1-3]. The reasons are not only of a moral nature. Potentially toxic compounds can be produced during for example a heat treatment of the products or exposure to light - secondary oxidation products [4-7].

Spectroscopic techniques are very widely used and new applications of them are found. They are well established for analysis of multicomponent systems such as oils and allow better differentiation of the compounds of the system than other used techniques. For example NMR spectroscopy [3], FTIR [8,9], nuclear magnetic resonance [10], liquid and gas chromatography techniques [2,6,11-13] are used for oil analysis. Some of these techniques lack sensitivity [9]. Other advantages of the spectroscopic techniques are that there is no need of expensive materials and any pretreatment of the oil samples [6,13]. The standard fluorescence techniques are insufficient for the analysis of vegetable oils because the spectra shows big overlapping of the bands attributed to different constituents [9,13]. That's way synchronous fluorescence spectroscopy is applied for this type of analysis. Furthermore the time for collecting synchronous spectra of one sample is decreased compared with total luminescence spectra [13].

* To whom all correspondence should be sent:
borisova@ie.bas.bg

The technique is based on simultaneously scanning of the excitation and emission wavelength with constant difference between them maintained - wavelength interval $\Delta\lambda$. The idea is more information to be acquired for the complex system by decreasing the overlapping of the spectra and preferentially amplifying strong fluorescence bands by using different wavelength interval [6,9,13,14]. With this method it is possible to distinguish fluorescence bands of tocopherols and phenols for example [15].

Three main groups of fluorophores were observed – vitamin E group, phenols and chlorophylls.

Results are shown by plotting the intensity as combined function of the other two variables – $\Delta\lambda$ and λ_{ex}. We use total synchronous fluorescence spectra (intensity as a function of excitation wavelength) and also contour plots of synchronous spectra ($\Delta\lambda$ as a function of λ_{ex}) where linking points are curves with the same intensity.

Synchronous fluorescence spectroscopy is used for monitoring of other types of foods and nutritional products – brandy [16], milk [17,18], beer [19], energy drinks [20], honey [21] and also petroleum product [22]. The obtained results also give the possibility for monitoring of these products.

METHOD AND MATERIALS

Measurements were made by the Jobin Yvon fluorolog-3 spectrofluorometer. The instrument is fully-computerized and uses a Xenon lamp as a source for excitation. The wavelength range was set at 220-800 nm in excitation and emission. The slits were set at 3 nm and the increment was set at 1 nm for both excitation and emission measurements. For

© 2015 Bulgarian Academy of Sciences, Union of Chemists in Bulgaria

the needs of the synchronous spectra a constant wavelength difference between the excitation and emission wavelengths was maintained – $\Delta\lambda$. The wavelength offset $\Delta\lambda$ was set at the range 0–100 nm in 10 nm intervals. All of the acquired spectra were corrected for the spectral response of the system - photomultiplier, Xenon lamp and excitation/ emission gratings.

The samples were set in quartz cells - 10 mm optical length was used for the measurements.The spectra were collected for 8 samples separated into two groups according to the oil type – sunflower oil and extra virgin olive oil. Each group includes 4 samples depending on the heat treatment applied – unheated oil, 0 min (oil moved from oven when just boiled), oil boiling for 5 min and oil boiling for 10 min.

Synchronous fluorescence spectra are obtained by plotting the intensity as a function of wavelength interval and excitation wavelength. Contour plots of the total synchronous fluorescence spectra are also shown. The shape and the intensity of the bands of the spectra depend on the wavelength interval $\Delta\lambda$.

The results were constructed using the Origin Software Version 8.0.

RESULTS AND DISCUSSION

In synchronous fluorescence spectra usually one fluorophore is presented in one peak [9,23]. Compared with total luminescence spectra significant amplification of signals of particular bands is gained [9]. This is how simplification is obtained.

Synchronous fluorescence spectra are obtained by plotting the intensity as a function of wavelength interval and excitation wavelength. The shape and the intensity of the bands depend on the used wavelength interval. Contour plots of the total synchronous spectra are also shown.

The results obtained for extra virgin olive oil samples are shown in Fig. 1. The fluorescence bands of unheated sample are concentrated in the wavelength regions 300-400 nm and 550-720 nm. The most intensive peak is observed around 675 nm. Just boiled sample gives signals in the wavelength range 300–720 nm and contours are concentrated in the region 300–400 nm and 600–720 nm. Again the peak with maximum intensity is 675 nm but decreasing in the intensity of the band is spotted. Olive oil boiling for 5 minutes shows results at the wavelength region 320–700 nm with maximum at 320-550 nm range in excitation and another one in the range 600–720 nm. Additional decreasing of the intensity of the peak around 675 nm is observed but also and appearing of new bands in the region 400–450 nm in excitation. The last sample, sample boiling for 10 min, shows fluorescence bands concentrated in the region 300–650 nm with maximum in the range 400–425 nm. The intensity of already observed long wavelength band in the region 600-720 nm is significantly decreased and the sample shows very low fluorescence intensity band around 650 nm. We noticed dramatically changes in the constituent of the extra virgin olive oil during the thermal treatment.

In Fig. 2 are shown the results obtained for sunflower oil. The unheated sample shows fluorescence bands in the region 300–550 nm with maximum around 360 nm and gives another maximum in the wavelength region 650–690 nm – 675 nm in excitation. The signals for just boiled sample are registered in wavelength range 300-550 nm with maximum around 360 nm and in the range 650–690 nm – again at 675 nm in excitation. Compared with the unheated sample we can observe decrease in the fluorescence intensity of the maximum around 350 nm and that one at 675 nm. The other two samples give results in the same wavelength ranges but major reduction of the intensity of the maximums is observed. Furthermore the bands with maximum intensity are shifted to longer wavelengths.

The results can be analyzed and conclusions for the nature and changes in the composition of the oils during the process can be made.

Vegetable oils include three main groups of natural fluorophores – tocopherols, chlorophyls and phenols [13].

The group of the phenolic compounds includes oleic acid, linoleic acid, palmitic acid, vanillic acid, syringic acid, gallic acid, p-coumaric acid, caffeic acid and etc. [9,15]. Olive oils are rich of phenolic compounds but the amount of these fluorophores dramatically decreases during refining [15].

The other big group of fluorescent compounds is vitamin E group which contains α-, β-, γ-, δ-Tocopherol and α-, β-, γ-, δ-Tocotrienol. The most recently present fluorophore from the listed is α-Tocopherol [9]. Tocopherols are the most important antioxidants in the oils [11].

Fluorescence properties of tocopherols and phenols are very similar [15]. The short excitation wavelength range 300–400 nm can be attributed to both tocopherols and phenols. As evidence for that the shape and the form of the spectra are similar to those of pure α-tocopherol as reported by [13,15].

The last mentioned group of natural fluorescence constituents of the oils is those of chlorophylls and pheophytins which includes chlorophyll *a*, chlorophyll *b*, pheophytin *a* and pheophytin *b*. These compounds are responsible for the long wavelength bands with maximum at 675 nm [1,2,4,6,9,13,15]. The fluorescence properties of the pigments are very similar and that's way signals in the wide wavelength range 600–720 nm are detected [13]. There is presence of the chlorophyll group in all studied samples. The observed differences in the intensity of the band are explained with their involving in the oxidation process caused by the heat [5-7].

During the heat treatment is observed significantly decreasing in the chlorophylls amount and appearing of new bands attributed to their oxidative forms and particularly from products formed by the reactions between amino-phospholipids and aldehydes [6,15]. Among the primary oxidation products are hydroperoxides which further degrade to secondary products: aldehydes, alcohols, hydrocarbons and ketons as was mentioned by [6]. It's important to notice that the known products formed during oxidation of vitamin E group are all non-fluorescent [15]. Changing in the content of tocopherols and phenols is also detected.

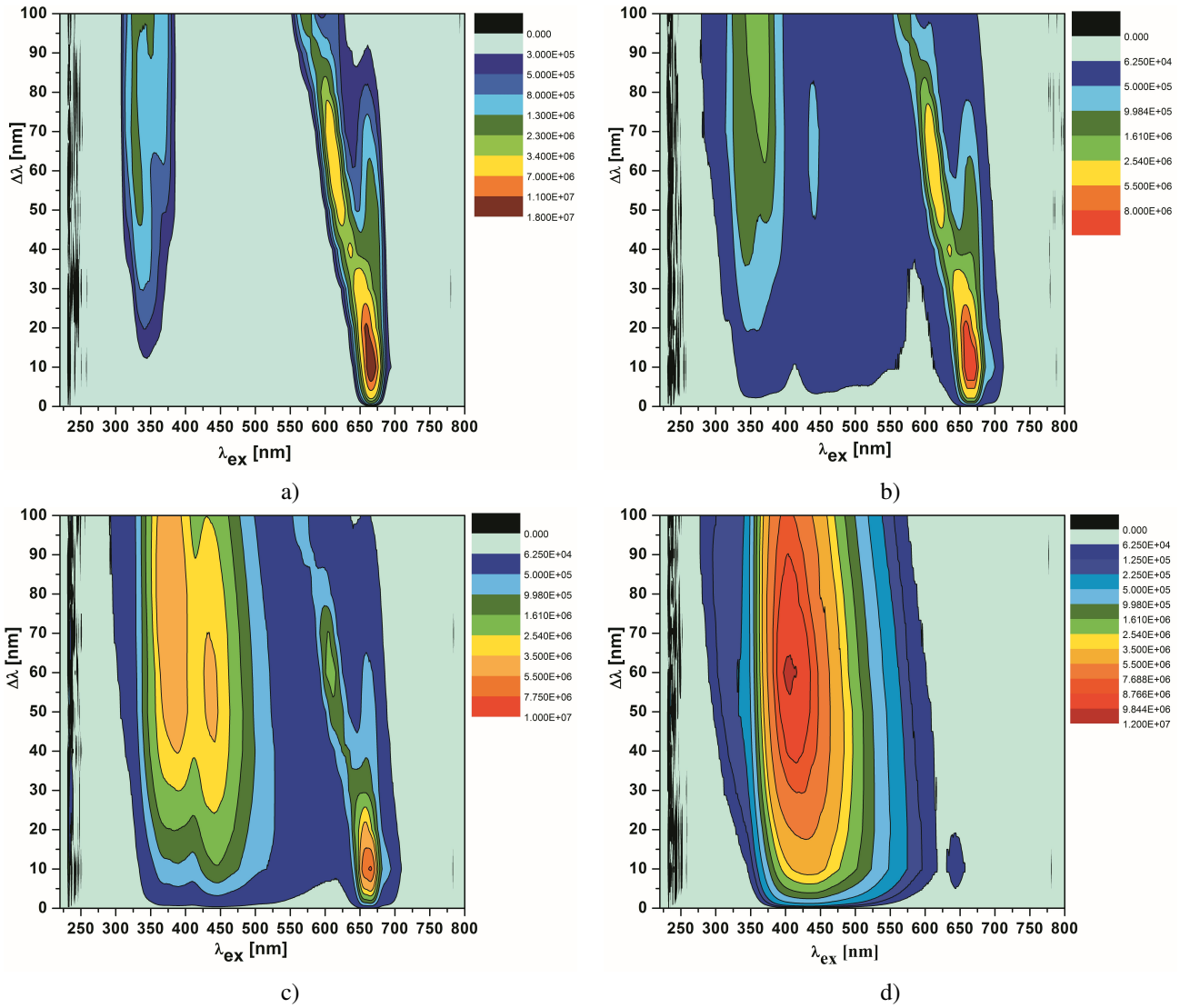


Fig. 1. Contour plots of total synchronous fluorescence spectra of extra virgin olive oil: unheated sample (a), just boiled sample (b), boiling sample for 5 min (c) and boiling sample for 10 min (d).

In Fig. 3 are demonstrate once more the changes in the synchronous spectra of the samples depending on the heat treatment applied. The spectra show that the short wavelength maximum is slowly shifted to longer wavelengths. For extra virgin olive oil the maximum is moved from 350 nm for unheated sample to 450 nm for 10 min boiling sample. The same result is achieved for sunflower oil samples. As it was mentioned the reason is involving of chlorophyls and phenols in the oxidation and formation of oxidative products [7]. The band around 450 nm is ascribed to hydroperoxide producing during the heating process [7].

On the other hand Fig. 3 can be used for comparison of the properties of the two types of oil. The same wavelength interval is applied for the both graphics - 80 nm. Extra virgin olive oils shows splitting of the short wavelength band. This can be used as a fin-

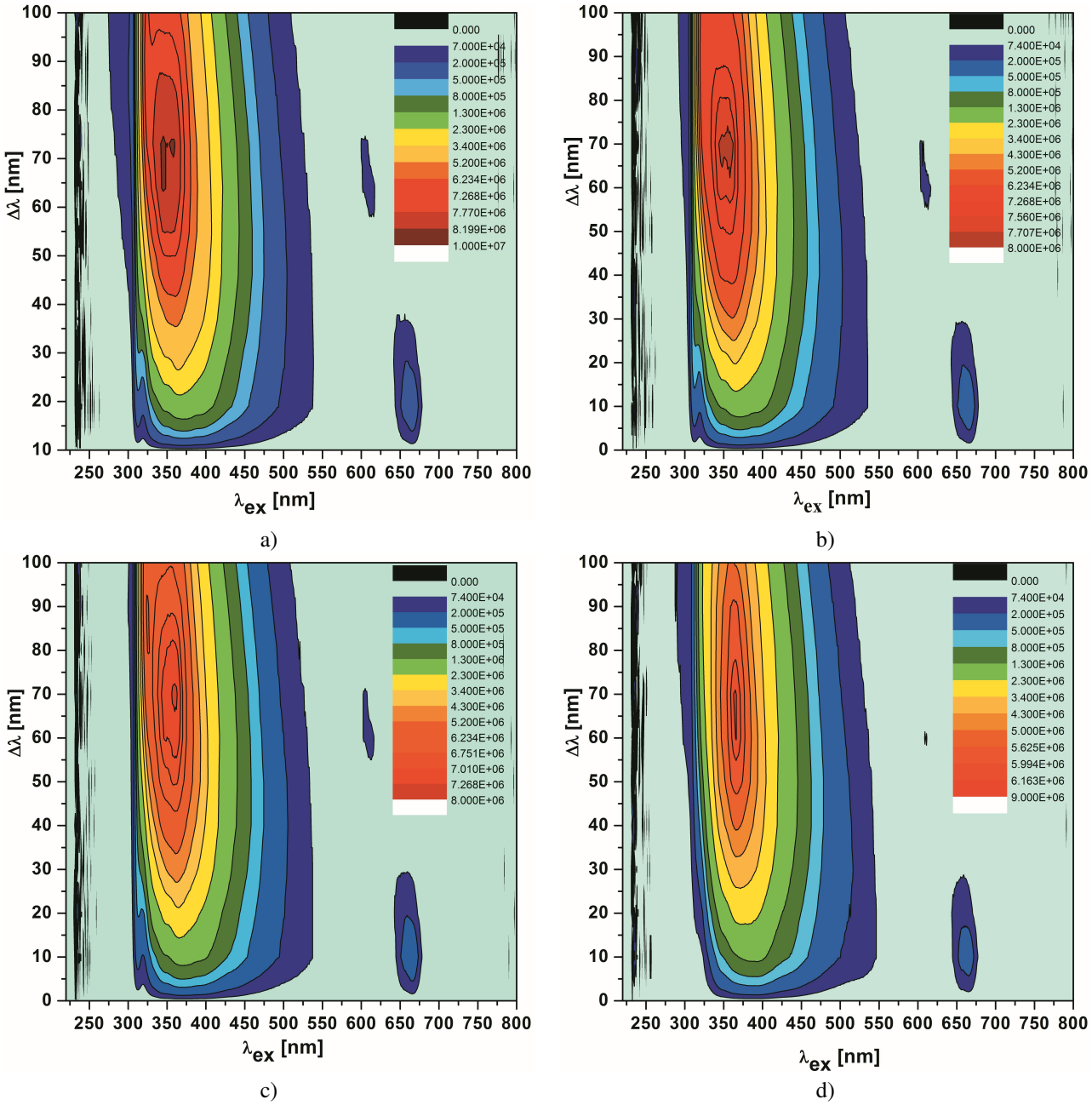


Fig. 2. Contour plots of total synchronous fluorescence spectra of sunflower oil: unheated sample (a), just boiled sample (b), boiling sample for 5 min (c) and boiling sample for 10 min (d).

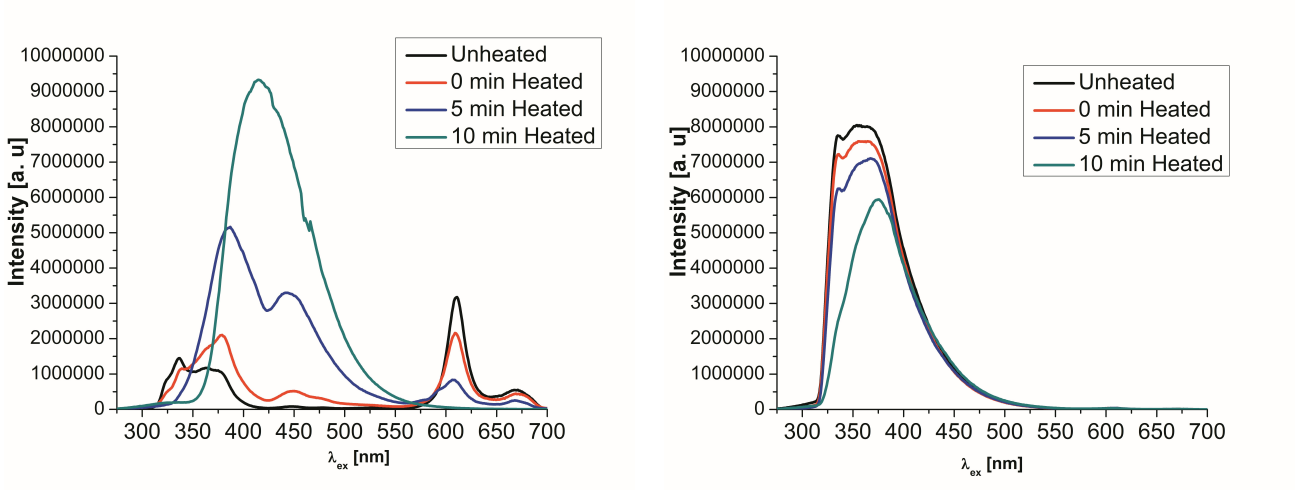


Fig. 3. Synchronous fluorescence spectra of extra virgin olive oil (a) and sunflower oil (b) recorded for wavelength interval $\Delta\lambda$ 80 nm.

gerprint for authentication – refined oils don't give the same splitting [7]. This is possible because oleic acid is presented in extra virgin olive oils in high amounts [1,2]. With increasing of the time of heat treatment the bands are shifted to longer wavelength interval. For sunflower oil only one peak is detected in the short wavelength area attributed to linoleic acid [1,2,9]. Good separation between different types of vegetable oils is achieved with detailed determination of particular bands acquired in the spectra of the products.

The oxidation affects the organoleptic and nutritional properties of the oils. It leads to considerable deterioration of the products such as degradation of their beneficial constituents and consequent producing of toxic compounds [6].

As it was reported by [7] that the oil degradation is controlled not only from the heat but also by the mass transfer which depends on the oil origin.

The same effect, producing of oxidative products, is observed during the storage of oils or exposure to light and the acquired results are similar [4,6,7].

CONCLUSION

Synchronous fluorescence spectroscopy can be successfully applied as a rapid technique in analysis of vegetable oils. Compared with other already used techniques it has advantages in spectra acquisitions, decreasing of the experiment time and lack of prior preparation of the studied samples.

In this research are shown the changes in the constitution of the oil during a heating process. The intensity of the bands attributed to main fluorophores in the vegetable oils - phenols, tocopherols and chlorophylls, is decreasing with increasing of the time of thermal treatment. Producing of potentially toxic compounds because of the degradation of natural antioxidants and formation of secondary oxidation products is detected.

The existence of a threat for the human health makes this issue very important and serious.

Acknowledgments. *This work is supported partially by the National Science Fund of Bulgarian Ministry of Education, Youth and Science under grant #DMU-03-46/2011 "Development and introduction of optical biopsy for early diagnostics of malignant tumours", grant #DO-02-112/2008 "National Center on Biomedical Photonics" and #DFNI-B02/9/12.12.2014 "Development of Biophotonics methods as a basis of Oncology Theranostics".*

REFERENCES

[1] K. I. Poulli, G. A. Mousdis and C. A. Georgiou, *Food Chemistry* **105**, 369–375 (2007).

[2] K. I. Poulli, G. A. Mousdis and C. A. Georgiou, *Anal. Bioanal. Chem.* **386**, 1571–1575 (2006).

[3] D. Šmejkalová and A. Piccolo, *Food Chemistry* **118**, 153–158 (2010).

[4] F. Caponio, M. T. Bilancia, A. Pasqualone, E. Sikorska and T. Gomes, *Eur. Food. Res. Technol.* **221**, 92–98 (2005).

[5] E. Choe and D. B. Min, *Comprehensive Reviews in Food Science and Food Safety* **5**, 169–186 (2006).

[6] K. I. Poulli, G. A. Mousdis and C. A. Georgiou, *Food Chemistry* **117**, 499–503 (2009).

[7] Sh. Naz, R. Siddiqi, H. Sheikh and S. A. Sayeed, *Food Research International* **38**, 127–134 (2005).

[8] J. Lerma-García, G. Ramis-Ramos, J. M. Herrero-Martínez and E. F. Simó-Alfonso, *Food Chemistry* **118**, 78–83 (2010).

[9] K. I. Poulli, G. A. Mousdis and C. A. Georgiou, *Analytica Chimica Acta* **542**, 151–156 (2005).

[10] M. D. Guillen and A. Ruiz, *Food Chemistry* **96**, 665–674 (2006).

[11] A. Cert, W. Moreda and M. C. Perez-Camino, *Journal of Chromatography* **881**, 131–148 (2000).

[12] M. T. Bilancia, F. Caponio, E. Sikorska, A. Pasqualone and C. Summo, *Food Research International* **40**, 855–861 (2007).

[13] E. Sikorska, T. Górecki, I. V. Khmelinskii, M. Sikorski and J. Kozioł, *Food Chemistry* **89**, 217–225 (2005).

[14] D. Patra and A. K. Mishra, *Trac-Trends in Analytical Chemistry* **374**, 304–309 (2002).

[15] E. Sikorska, I. Khmelinskii and M. Sikorski, in *Agricultural and Biological Sciences*, edited by Dr. D. Boskou, InTech, 2012, pp. 67-84.

[16] Jana Sádecká and Jana Tóthová, *Eur. Food Res. Technol.* **230**, 797–802 (2010).

[17] Ch. Tong, X. Zhuo, W. Liu and J. Wu, *Talanta* **82**, 1858–1863 (2010).

[18] Yan-Ni Yi, Gui-Rong Li, Yong-Sheng Wang, Yu-Zhen Zhou and Hui-Min Zhu, *Analytica Chimica Acta* **707**, 128–134 (2011).

[19] E. Sikorska, T. Gorecki, I. V. Khmelinskii, M. Sikorski and D. De Keukeleire, *Food Chemistry* **96**, 632–639 (2006).

[20] L. Ziak, P. Majek, K. Hrobonŏva, F. Căcho and J. Sadecka, *Food Chemistry* **159**, 282–286 (2014).

[21] I. Sergiel, P. Pohl, M. Biesaga and A. Mironczyk, *Food Chemistry* **145**, 319–326 (2014).

[22] D. Patra and A. K. Mishra, *Anal Bioanal Chem* **373**, 304–309 (2002).

[23] T. Vo-Dinh, *Anaytical Chemistry* **50**, 396–401 (1978).

СИНХРОННА ФЛУОРЕСЦЕНТНА СПЕКТРОСКОПИЯ ЗА АНАЛИЗ НА РАСТИТЕЛНИ МАСЛА

Я. Андреева, Е. Борисова, Ц. Генова, Ал. Желязкова, Л. Аврамов

[1] *Институт по електроника, Българска академия на науките, бул. "Цариградско шосе" № 72, 1784 София, България*

(Резюме)

Синхронизираната флуоресцентна спектроскопия (СФС) е доказан и широко използван метод за изследвания и анализ в много дисциплини. През последните години се наблюдава значително увеличение на приложенията на СФС при анализа на храни и хранителни продукти. Флуоресцентните анализи се използват за изследване на различни течности, като вино, бренди, оцветители, растителни масла, мед и други.

Растителните масла, в това число и зехтините, са една от основните групи хранителни продукти, за които флуоресцентният анализ се прилага успешно. Методът използва наличието на естествени флуорофори като фенолни съединения, токофероли, феофитини и техните оксидирани продукти.

Растителните масла са многокомпонентни системи и затова стандартните флуоресцентни техники, базиращи се на снемането на единичен спектър на възбуждане и на излъчване, са недостатъчни за такива проучвания. В такъв случай се прилагат синхронно-флуоресцентни техники за подобряване на аналитичната способност на този тип изследвания.

Направени са измервания на набор от образци на растителни масла, използвайки спектрофлуориметър FluoroLog3 и възбуждане в областта 200-650 nm. Получени са емисионни спектри в областта 220–850 nm и за $\Delta\lambda$ от 10 до 100 nm със стъпка на синхронно сканиране 10 nm.

Показано е разграничаването на рафинираните от нерафинираните масла, както и възможността за детекция на влошаване на качествата на маслата в процеса на рафиниране. Това проучване представя способността за лесен анализ и оценка на качеството на масла. Получените до момента резултати, показват възможността за анализ на растителни масла чрез бърз и надежден метод, основаващ се на синхронизирана флуоресцентна спектроскопия. Предвидени са допълнителни проучвания, включващи по-голяма база данни и приписване на наблюдаваните флуоресцетни максимуми на химичните компоненти на различните типове растителни масла, както и на странични продукти, получени при оксидация или топлинна обработка на продуктите.

Благодарности: Използваната апаратура е закупена по проект на Фонд Научни изследвания към Министерство на Образованието и Науката ДО-02-112/2011 "Национален Център по Биомедицинска Фотоника".

Bulgarian Chemical Communications, Volume 47, Special Issue B (pp. 476–479) 2015

Optical properties of oil extracts of Bulgarian herbs

Kr. Nikolova[1], T. Eftimov[2*], G. Antova[3], Zh. Petkova[3]

[1] *University of Food Technologies, 26 Maritsa Blvd., BG-4002 Plovdiv, Bulgaria*
[2] *Faculty of Physics, Paisii Hilendarski University of Plovdiv, 24 Tsar Asen Str., BG-4000 Plovdiv, Bulgaria*
[3] *Faculty of Chemistry, Paisii Hilendarski University of Plovdiv, 24 Tsar Asen Str., BG-4000 Plovdiv, Bulgaria*

We have studied oil extracts form oregano, thyme and pine cone in sunflower oil in 1:5 ratio (herb extract/sunflower oil). The fluorescence spectra have been obtained by using Light emitting diods (LEDs) working at wavelengths of $\lambda = 370$ nm, $\lambda = 395$ nm, $\lambda = 425$ nm and $\lambda = 450$ nm have been obtained. The oxidation processes have been studied using UV spectroscopy. The content of chlorophyll and β-carotene has been studied with the objective of finding correlation between them and the intensity of the fluorescence peak. It has been shown that the most informative spectra are those obtained for excitation at $\lambda = 425$ nm. They contain three fluorescence maxima related to the oxidation processes ($\lambda = 500$ nm) and chlorophyll ($\lambda = 675$ nm). Linear dependencies between the full content of tocopherols (Y) and absorption at 270 nm (A_{270}) and 232 nm (A_{232}) have been obtained $Y = -717.15A_{232} + 1830$, $R^2 = 0.924$, $Y = -1599A_{270} + 1549$, $R^2 = 0.947$.

Key words: UV-spectroscopy, fluorescence, sunflower oil with herbs, oxidation product, tocopherols

INTRODUCTION

Sunflower oil is a lipid product typical for Bulgaria with large application in cookery and food industry. Its consumer qualities depend mainly on its fatty acid composition, the content of tocopherols (vitamin E), and of the possibilities to be stable during long term storage and thermal treatment. Bulgaria is rich in a great variety of herbs that contain a high percentage of biologically active substances. They are rich in various compounds: alkaloids, glycosides, saponins, polysaccharides, tannins, flavonoids, lignans, coumarins, essential oils, vitamins, trace elements etc. In this regard, it is interesting to carried out investigations on the fluorescence spectra and content of oxidation product of sunflower oil when adding thereto of various kinds of Bulgarian herbs.

The objective of the present work is to establish the relations between the physical and chemical parameters of oil extracts of sunflower oils enriched with Bulgarian herbs in analogy with commercially available the salad olive oils.

MATERIALS AND METHODS

Sunflower oil, production of Pearl Ltd, Veliko Tarnovo, is used for conducting the surveys. The oil extracts were prepared from authors in a ratio of 1:5 (herb / sunflower oil) 40 grams from oregano, thyme and pine cone were added in 200 ml sunflower oil and were kept under refrigerated conditions (0°C-4°C) for 6 months. After that extracts were filtered and their optical properties were investigated.

Analysis of tocopherols

Tocopherols were determined directly in the oil by HPLC on a "Merck-Hitachi" (Merck, Darmstadt, Germany) instrument equipped with 250 mm x 4 mm Nucleosil Si 50-5 column (Merck, Darmstadt, Germany) and fluorescent detector "Merck-Hitachi" F 1000. The operating conditions were as follows: mobile phase of n-hexane: dioxan 96:4 (by volume), flow rate 1.0 ml/min, excitation 295 nm, and emission 330 nm [1] 20 mL 10 g.kg^{-1} solution of oil in hexane were injected. Tocopherols were identified by comparing the retention times with those of authentic individual tocopherols. The tocopherol content was calculated on the basis of tocopherol peak areas in the sample versus tocopherol peak area of standard a-tocopherol solution.

Color parameters

SIELab coordinates have been measured directly with spectrophotometer (Trintometer Lovibond PFX 195, UK). In mentioned colorimetric system L^* is the brightness and it takes values from 0 (black) to 100 (white), a^* is red-green axis, and b^* is yellow-green axis [2]. The chlorophyll and β-carotene are calculated using the transmission spectra in the visible region and values for color parameters by software program developed specially for Lovibond PFX 880 from the producer.

* To whom all correspondence should be sent:
teftimov@abv.bg

© 2015 Bulgarian Academy of Sciences, Union of Chemists in Bulgaria

The sources used to measure the fluorescence spectra are 370 nm, 395 nm, 425 nm LEDs. A fiber optic spectrometer (AvaSpec-2038, Avantes) with sensitivity in the (200-1100) nm range and a resolution of about 8 nm was used to measure the fluorescence spectra. The oil samples were placed in a cuvette 10 mm x 10 mm and irradiated by laser diodes (LDs) or light emitting diodes (LEDs).

RESULTS AND DISCUSSION

The fluorescence spectra were measured at 370 nm, 395 nm, 425 nm. It is evident that the good ratio between excitation and emission intensity there is for wavelength 425 nm and 450 nm. The results are present on the Fig. 1.

Two fluorescence peaks are clearly discernible.

i The first (500-525 nm), is related to oxidation products. Similar fluorescence maxima are observed for extra virgin olive oil between 500 nm and 520 nm [3].

ii The second (680-690 nm) is related to chlorophyll content in the studied oil samples. Similar fluorescence maxima have been observed for other vegetable oils such as rape seed, soy bean etc. [4].

The optical properties of sunflower oil extracts of traditional Bulgarian herbs were investigated similarly to herbs extracts from olive oil because sunflower salad oil is the most widely used in Bulgaria. The addition of herbs leads to a considerable increase of the chlorophyll content of the extract. In Fig. 1 the intensity of the second fluorescence peak related to chlorophyll increases.

Quantitative relations between the intensities of the indicated fluorescence peaks and parameters have been established. A specialized software to the Lovibond PFX 195 (UK) titrometer was used to determine the content of β-carotene by the color parameter data from the samples. The data is presented in Table 1.

The addition of herbs leads to a substantial increase of the content of β-carotene and pigments. The higher content of β-carotene correlates with the absorption in the UV range at 232 nm and 270 nm. Using the latter two parameters the degree of oxidation of the samples was estimated by determining the primary products of the oxidation (peroxides) by the UV absorption spectroscopy of the conjugated dien structures. The addition of herbs leads to a comparatively fast oxidation of the oil extracts which shows that they can be used n salads, dressings and sauces, but are not suitable for heat treatment. Dependencies between the chlorophyll content and that of β-carotene using the intensities of the fluorescence peaks were tested. With the increase of the absorption a 232 nm, the intensity of the fluorescence peak around 500 nm decreases. A linear dependence of the type $I_{676} = 76349.clorolophhyl + 9738.1$ between the chlorophyll and the second fluorescence peak with a high correlation R^2=0.96 is established.

Linear dependencies between the full content of tocopherols (Y), absorption at 270 nm (A_{270}) and absorption at 232 nm (A_{232}) and the have been obtained $Y = -717.15A_{232} + 1830$, $R^2 = 0.924$, $Y = -1599A_{270} + 1549$, $R^2 = 0.947$.

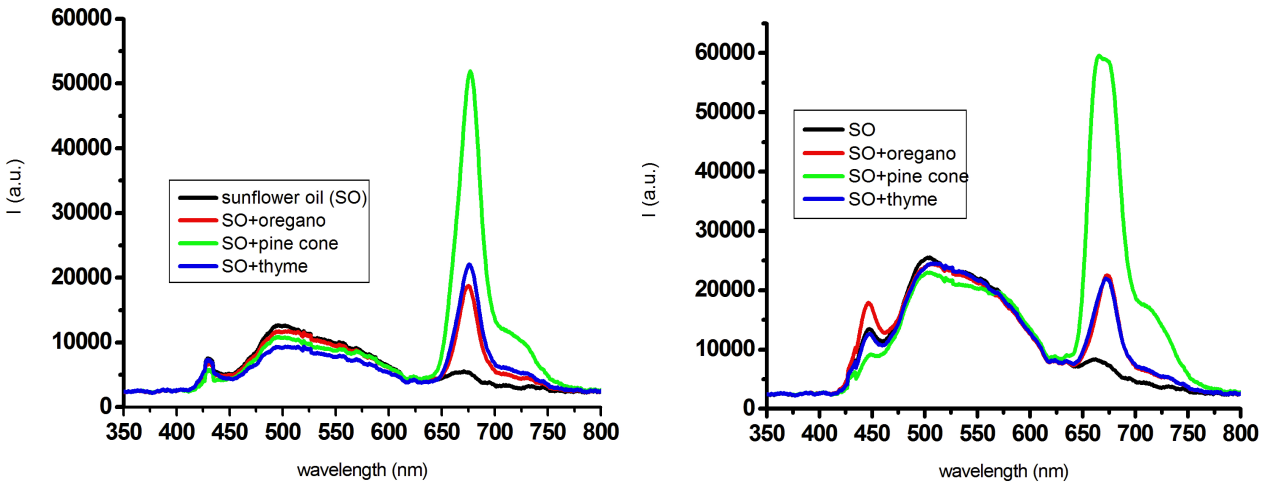


Fig. 1. Fluorescence spectra for sunflower oil extracts with herbs.

Table 1. Data for the absorption in the UV range, chlorophyll, β-carotene and total contetne of tocopherols in oil herb extracts

Type of oil extract	Clorophyll, ppm	β-carotene, ppm	Absorption at 232 nm (A_{232})	Absorption at 270 nm (A_{270})	Total content of tocopherols, mg/kg
Sunflower oil	0.003	2.76	1.554	0.523	721
Oil extract of thyme	0.094	5.57	1.983	0.709	459
Oil extract of oregano	0.117	4.92	1.898	0.661	458
Oil extract of pine cones	0.564	7.09	1.946	0.715	388

CONCLUSIONS

1. The addition of herbs to sunflower enriches it in pigments and vitamins.
2. The oily herbal extracts have a smaller oxidation stability and a lower general solution of tocopherols, which makes them inappropriate for thermal treatment.
3. There is a relation between the chemical parameters and the optical properties – the chlorophyll content and the fluorescence as well as UV absorption, and the general tocopherol content.
4. The combination of optical with chemical methods provides an accurate idea of the properties of modified food products.

Acknowledgments. *The authors thank the University Scientific Project NI13FF003 for the financial support.*

REFERENCES

[1] Animal and vegetable fats and oils. Determination of oxidative stability (Accelerated oxidation test), Method using high-performance liquid chromatography, ISO 9936, p. 17, 2006.

[2] Commission Internationale de I Elairage, 1971. Recommendations on uniform color spaces, color difference equations. psychometric color terms. CIE publication no 15 (F. 1. 3. 1.) 1971. supplement 2. Burean central. de la Commission Internationale de I Eclairage. Vienna. 1978

[3] N. Tena, D. L. García-González and R. Aparicio, *J. Agric. Food Chem.* **57**, 10505–10511 (2009).

[4] N. Dupuy, Y. Le Dréau, D. Ollivier, J. Artaud, C. Pinatel and J. Kistel, *J. Agric. Food Chem.* **53**, 9361–9368 (2005).

ОПТИЧНИ СВОЙСВА НА МАСЛЕНИ ЕКСТРАКТИ ОТ БЪЛГАРСКИ БИЛКИ

Т. Ефтимов[1], Кр. Николова[2], Г. Антова[3], Ж. Петкова[3]

[1] *Физически факултет, Пловдивски университет "Паисий Хилендарски", ул. "Цар Асен" №24, 4000 Пловдив, България*
[2] *Университет по хранителни технологии, бул. "Марица" №26, 4002 Пловдив, България*
[3] *Химически факултет, Пловдивски университет "Паисий Хилендарски", ул. "Цар Асен" №24, 4000 Пловдив, България*

(Резюме)

Изследвани са маслени екстракти от риган, мащерка и борова шишарка в слънчогледово олио в съотношение 1:5 (билка/слънчогледово олио). Получени са спектрите на флуоресценция при дължини на вълните съответно $\lambda = 370$ nm, $\lambda = 395$ nm, $\lambda = 425$ nm и $\lambda = 450$ nm. Проследени са окислителните процеси чрез ултравиолетова спектроскопия. Изследвано е съдържанието на хлорофил и β-каротен с цел откриване на корелация между тях и интензитета на пика на излъчване при флуоресцентните спектри. Показано е, че най-информативни са спектрите при $\lambda = 425$ nm. Те съдържат три флуоресцентни максимума, свързани с окислителните продукти около $\lambda = 500$ nm, с хлорофила около $\lambda = 675$ nm и с β-каротена около $\lambda = 429$ nm. Установени са линейни регресионни зависимости между пълното съдържание на токоферолите и адсорбцията при 270 nm и 232 nm от типа

$$Y = -717,15A_{232} + 1830, \qquad R^2 = 0,924; \qquad Y = -1599A_{270} + 1549, \qquad R^2 = 0,947.$$

където Y е пълното съдържание на токоферолите, а A_{232} и A_{270} са адсорбциите при 232 nm и 270 nm.

Bulgarian Chemical Communications, Volume 47, Special Issue B (pp. 480–486) 2015

On the influence of some factors on the functional properties of electrogalvanic coatings promising for medical applications

D. Kiradzhiyska[1*], R. Mantcheva[1], D. Mileva[2], T. Yovcheva[3], A. Viraneva[3]

[1] *Faculty of Pharmacy, Medical University of Plovdiv, 15A Vasil Aprilov Blvd., BG-4000 Plovdiv, Bulgaria*
[3] *Department of Languages and Specialized Training, Medical University of Plovdiv, 15A Vasil Aprilov Blvd., BG-4000 Plovdiv, Bulgaria*
[3] *Faculty of Physics, Paisii Hilendarski University of Plovdiv, 24 Tsar Asen Str., BG-4000 Plovdiv, Bulgaria*

This work investigates some functional properties of galvanic chromium coatings deposited from a non-standard chloride electrolyte of *Chromispel type*, modified with combined, complexly acting additive containing $CoCl_2.6H_2O$. The influence of various technological factors such as current density, $CoCl_2.6H_2O$ content and stirring, on the properties of the electrolyte and the coatings was studied. The experimental results obtained showed that stirring and higher current density (15-50 $A.dm^{-2}$) make coating smoother, brighter and increase the deposition rate and cathode current efficiency. It was experimentally established that increase in concentration of $CoCl_2.6H_2O$ in the range 1-5 $g.L^{-1}$ results in reduction of reflectance and thickness of layers. For the determination of the surface morphology of the investigated coatings an atomic force microscope was used. Root mean square roughness of the deposited coatings was measured and the average size of grains observed was determined.

Key words: Cr-Co alloy, functional properties, Chromispel electrolyte

INTRODUCTION

Medical implants are products that must meet functionality requirements in human body conditions as a working environment. Ideally, they must have biomechanical properties comparable to those of autogenous tissue, must have no adverse effects and must ensure safe and efficient operation.

There is a huge variety of materials and alloys used for the production of implants. After stainless steel, various binary and ternary cobalt alloys are most widely used. They are characterized as non-magnetic and resistant to corrosion, high temperature and mechanical stress [1]. Their properties are closely related to the crystallographic structure and the ability to form hard carbides, which give strength to implants.

Because of their excellent resistance to degradation in the oral cavity, the main medical applications of Cr-Co alloys are for dental implants.

Various in vivo and in vitro tests give evidence that cobalt alloys have good biocompatibility. That is why they are used for the manufacture of surgical instruments, orthopaedic prostheses, fixtures, knee, hip and shoulder replacement prostheses [2–4].

Cr-Co alloys are also applications for the production of cardiac stents [5].

Sometimes, implants are produced from a combination of various types of materials, e. g. femoral heads manufactured from highly cross-linked polyethylene in combination with ceramic materials or Cr-Co alloy [6].

The difficulties in working with metallurgical Cr-Co alloys are associated with the fact that they are more difficult to process. This problem can be solved by a continuous development of technology and establishment of new, modern methods for specialized casting [7] and selective laser sintering.

The purpose of this study is to develop a technology for electrochemical deposition of cobalt alloys which helps avoiding difficulties in machine processing after metallurgical casting.

In this new technology, a non-standard electrolyte for chromium plating of *Chromispel* type is used. What is typical of it is that it operates at room temperature and has current efficiency several times higher than that of the conventional sulphate electrolyte.

EXPERIMENTAL CONDITIONS

Standard concentrated (250 $g.L^{-1}$ CrO_3) chloride electrolyte of *Chromispel* type modified with combined complexly acting additive was used for deposition of coatings. The basic composition is registered with a copyright license [8].

In the experiments performed the current density varied in the range 15–50 $A.dm^{-2}$. Cathodes were

* To whom all correspondence should be sent:
denica.kiradjiiska@gmail.com

© 2015 Bulgarian Academy of Sciences, Union of Chemists in Bulgaria

copper plates which surface was 0.02 dm^2. Deposition time was 5 minutes. Some of the coatings were obtained in stationary conditions, others - by stirring the electrolyte at a speed of 600-1000 rpm/min.

Cobalt was imported into the galvanic bath by $CoCl_2.6H_2O$ and its concentration in different compositions was within the range from 1 $g.L^{-1}$ to 5 $g.L^{-1}$.

Faraday's laws were used for determining the cathode current efficiency (K_{Cr}).

An important characteristic of each electrolyte is the deposition rate (U_e). It is calculated using the Eq. (1):

$$U_e = 0.047 i_k K_{Cr} \quad (1)$$

Coatings were deposited at operating temperature of $(20\pm2)^oC$, and their thickness (d) was determined by a fluorescence analysis.

The reflectance was measured using a gloss meter of Lange type.

The surface morphology of all samples was investigated by means of Atomic force microscope (NANOSURF Flex AFM). The samples were scanned with a standard silicon cantilever (type Tap 190Al-G) and the measurements were performed in ambient atmosphere, and dynamic operating mode. The applied force was always minimized, not to deform the samples. The surface topographic images of the samples were taken and the diameter of the obtained grains in the plane of the picture was calculated.

EXPERIMENTAL RESULTS AND DISCUSSION

Current efficiency

Deposition of chromium coatings from aqueous solutions of chromic anhydride is not possible without the presence of external anions acting as catalysts for the primary reaction - chromium deposition. In chloride *Chromispel* electrolytes these are Cl^-. Their concentration is determined by the ratio CrO_3:Cl^- = 20:1 and for standard concentration compositions it is approximately 12.5 $g.L^{-1}$.

According to the theory of the chromium plating, at least three partial reactions take place simultaneously on the cathode during electrolysis:

$$Cr^{6+} \rightarrow Cr^0$$
$$2H^+ \rightarrow H_2$$
$$Cr^{6+} \rightarrow Cr^{3+}$$

An important characteristic of each electrolyte is cathode current efficiency (K_{Cr}) i.e. that part of the total amount of electricity which is only consumed for the useful reaction of chromium deposition.

Standard sulphate electrolytes have maximum current yield 10-12%.

Pure chloride electrolytes, i.e. without additive, with concentrations from 500 $g.L^{-1}$ CrO_3 to 750 $g.L^{-1}$ CrO_3, can reach 60%, and modified standard concentration (250 $g.L^{-1}$ CrO_3) chloride *Chromispel* about 40% [9, 10]. According to the obtained experimental results, the higher the operating current density, the better its cathode efficiency - Fig. 1. The same relationship was also observed when stirring the electrolyte. For example, at a density of 25 $A.dm^{-2}$, if the liquid were not mixed, the determined value of $K_{Cr} = 24\%$. After stirring, the yield increased to value of $K_{Cr} = 34.2\%$.

Coatings deposited with operating current densities above 50 $A.dm^{-2}$ are characterized with high internal stresses and are not recommended for practical applications.

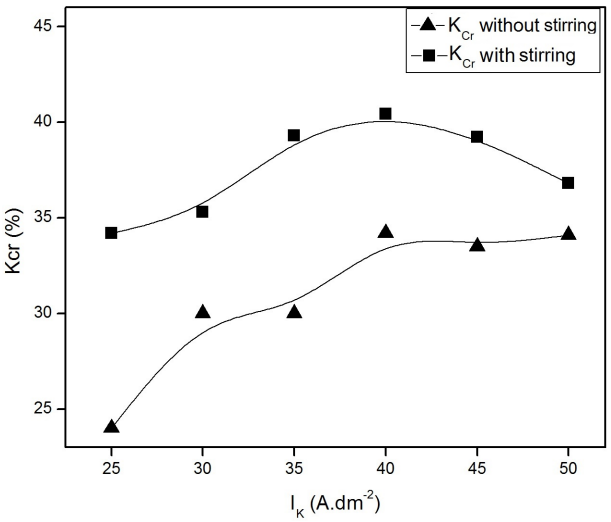


Fig. 1. Dependence of K_{Cr} on both cathode current density and stirring for electrolyte containing 1 $g.L^{-1}$ $CoCl_2.6H_2O$.

Deposition rate and thickness of the coatings

Both of these parameters are a function of the current density and are important for the practical properties of the coatings. Galvanic rate is a particularly important feature when thick coatings need to be deposited. At small rates chromium plating may take several days. In the literature, standard sulphate electrolytes at temperature 50^oC, current density 48 $A.dm^{-2}$ and cathode efficiency 18.8% have deposition rate of 42.3 $\mu m.h^{-1}$ [11]. The dependence of U_e and

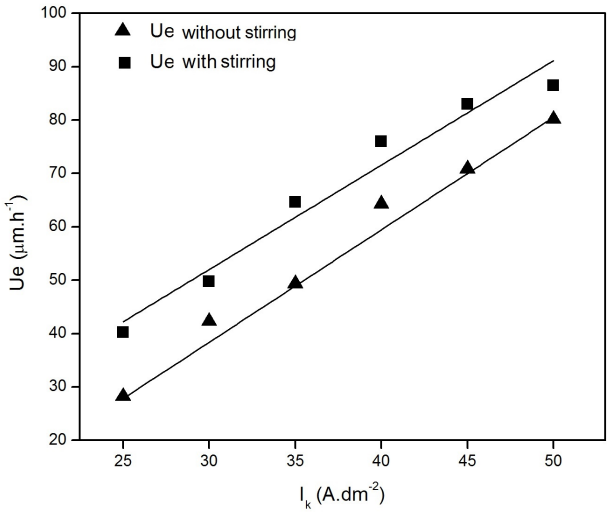


Fig. 2. Influence of cathode density and stirring on deposition rate for electrolyte containing 1 g.L^{-1} $CoCl_2.6H_2O$.

d on the current density is proportional and is illustrated in Fig. 2 and Fig. 3.

According to the data illustrated in Fig. 2 for current densities 45-50 A.dm^{-2} the deposition rate is 70-80 μmh^{-1}, i.e. almost twice as high as that of standard sulphate electrolytes. This fact makes the chloride *Chromispel* electrolytes some of the most highly efficient electrolytes for deposition of chromium coatings.

The stirring influences favourably the coating thickness (Fig. 3). For example, when cathode current density is 40 A.dm^{-2} and the content in the galvanic bath is 1 g.L^{-1} $CoCl_2.6H_2O$, if the electrolyte is not mixed, $d = 2.6$ μm, and if mixed, $d = 3.3$ μm.

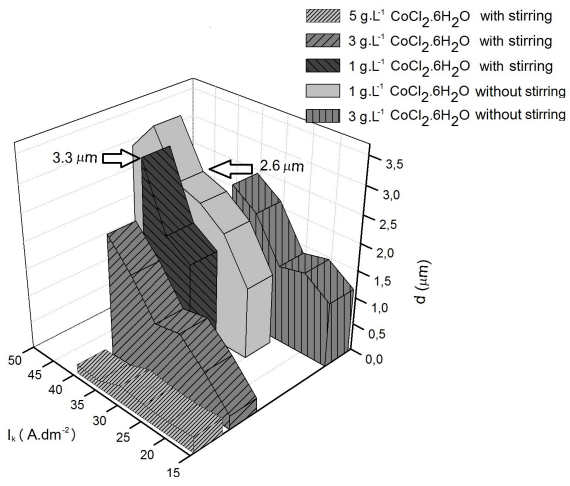


Fig. 3. Thickness of coatings deposited with and without stirring of the electrolyte at different current densities for a period of 5 minutes.

The higher concentration of $CoCl_2.6H_2O$ slows down the electrocrystallization, and under the same conditions of chromium plating, e.g. 40 A.dm^{-2} and stirring of the electrolyte, if the amount of $CoCl_2.6H_2O$ of 1 g.L^{-1} is increased to 5 g.L^{-1} the thickness decreases from 3.3 μm to 0.17 μm, i.e. about 20 times. To make an unbiased interpretation of this fact, it is necessary to examine the kinetics of cathode process in order to determine how the ratio between the rates of the partial cathode reactions.

Surface morphology and reflectance

These properties determine the decorative qualities and the beautiful appearance of chromium coatings.

Today most of the electroplated coatings are deposited glossy directly from the electrogalvanic baths. Thus, the need for additional mechanical polishing of the layers is eliminated.

According to [12], the reflectance does not depend on their texture, so it is not subject to examination in this study.

Surface morphology of the samples investigated by AFM was judged by their root mean square roughness S_q. Figs. 4 and 5 show surface topographic images of the samples.

Line graphs and 3-D images on Fig. 4 and Fig. 5 show that, in general, when increasing the concentration of $CoCl_2.6H_2O$, the crystals of coatings become larger in size. For example, with 1 g.L^{-1} $CoCl_2.6H_2O$ the value of the root mean square roughness is $S_q = 5.84$ nm, and with 5 g.L^{-1} $CoCl_2.6H_2O$, it is $S_q = 10.88$ nm. Such roughening of the layers was also found in case of stirring the electrolyte – Fig. 5. Regardless of whether the electroplating is carried out with or without stirring, the highest root mean square roughness is of coatings obtained from compositions containing 5 g.L^{-1} $CoCl_2.6H_2O$.

Fig. 6 shows the dependence of reflectance on cathode current density and stirring. By increasing the cathode density (due to high plating rate) more small crystal and smooth coatings are deposited, and the reflectance increases. After density of 35 A.dm^{-2}, in case of no stirring, gloss decreases, which can be associated with some concentration restrictions changing the deposition mechanism and properties of coatings, or by impurities in their composition.

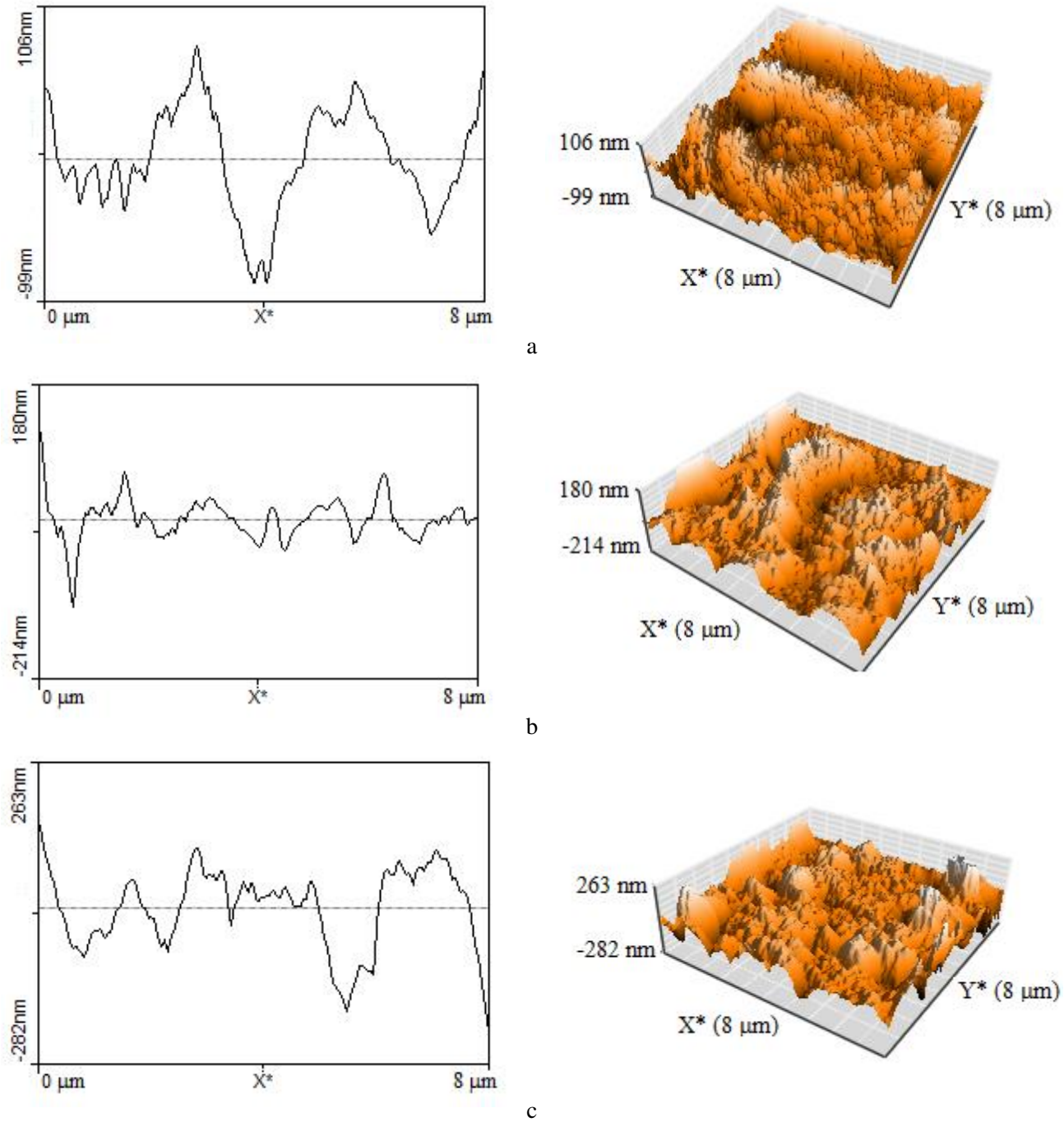


Fig. 4. Values of S_q for coatings deposited at $i_k = 35$ A.dm^{-2} from electrolytes without stirring containing different amounts of $CoCl_2.6H_2O$: a) 1 g.L^{-1} $CoCl_2.6H_2O$; $S_q = 5.84$; b) 3 g.L^{-1} $CoCl_2.6H_2O$; $S_q = 6.80$; c) 5 g.L^{-1} $CoCl_2.6H_2O$; $S_q = 10.88$.

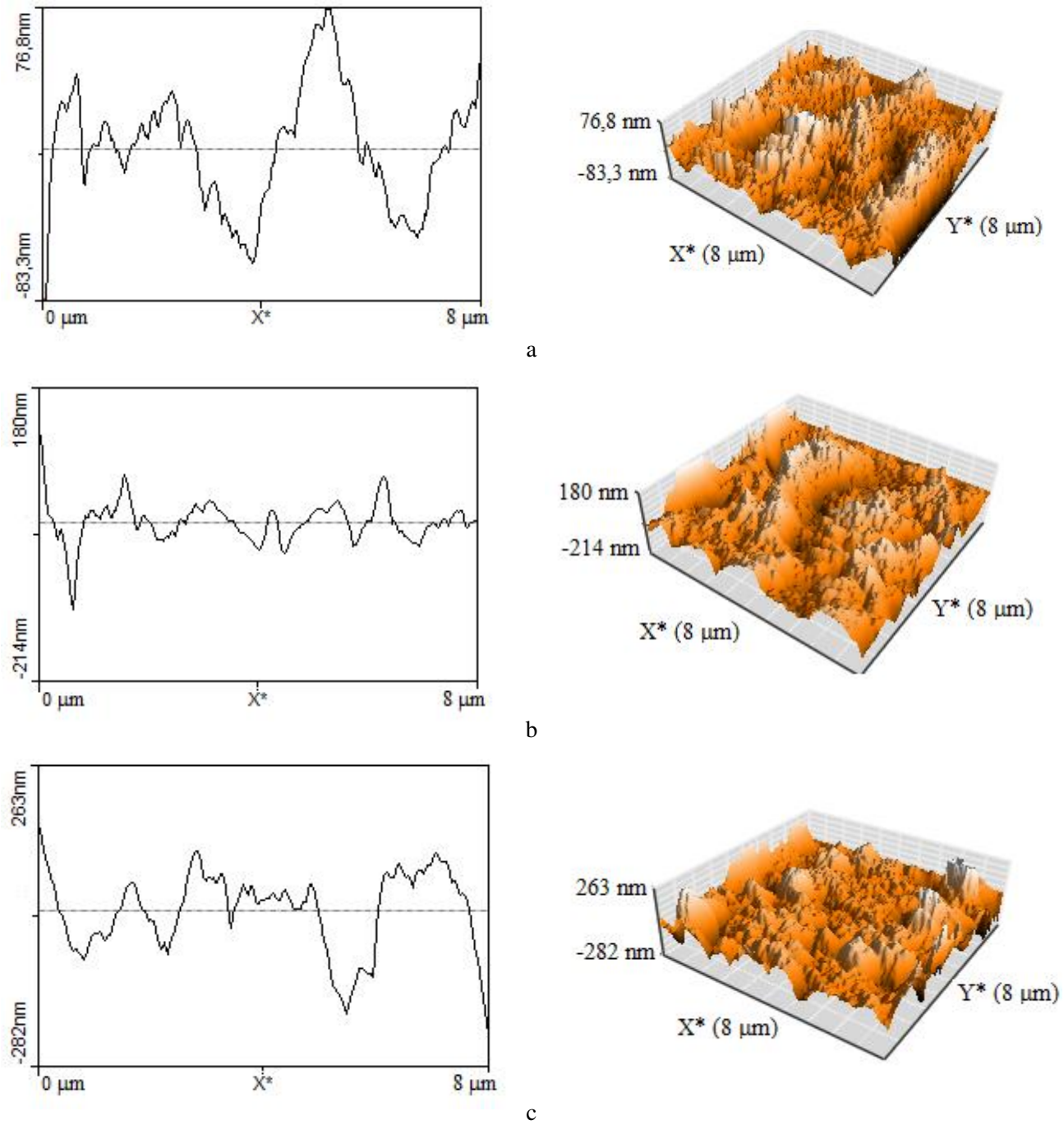


Fig. 5. Values of S_q for coatings deposited at $i_k = 35$ A.dm^{-2} and stirring of electrolytes containing different amounts of $CoCl_2.6H_2O$: a) 1 g.L^{-1} $CoCl_2.6H_2O$; $S_q = 6.11$; a) 3 g.L^{-1} $CoCl_2.6H_2O$; $S_q = 11.35$; c) 5 g.L^{-1} $CoCl_2.6H_2O$; $S_q = 14.61$.

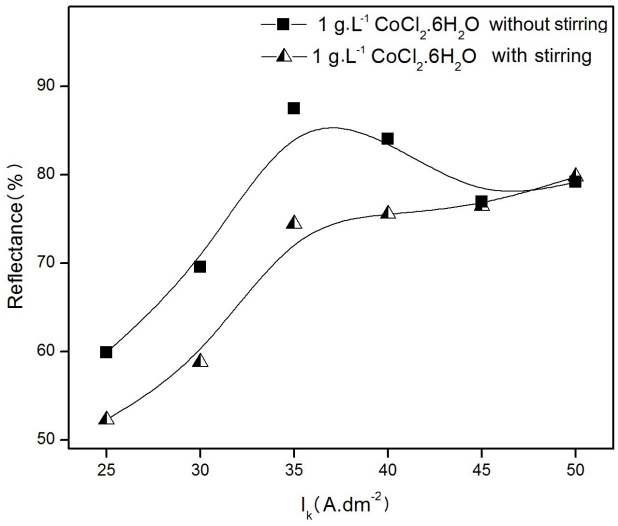


Fig. 6. Dependence of reflectance on cathode current density and electrolyte stirring.

The data presented in Table 1 indicates that higher concentration of $CoCl_2.6H_2O$ and stirring of the electrolyte increase root mean square roughness and reduce reflectance of coatings.

Table 1. Class of roughness and reflectance of coatings deposited for a period of 5 minutes at i_k = 35 A.dm^{-2} and different concentrations of $CoCl_2.6H_2O$

No	$CoCl_2.6H_2O$ g.L^{-1}	S_q nm	Grain size nm	δ %	Note
1	1	5.84	458.60	87.5	without
2	3	6.80	1122.0	76.04	stirring
3	5	10.88	1280.00	25.56	
4	1	6.11	658.20	77.92	with
5	3	11.35	674.60	64.24	stirring
6	5	14.61	1140.00	20.28	

CONCLUSION

Some functional properties of electroplated chromium coatings deposited from non-standard, modified electrolyte of *Cromispel* type were studied. The influence of different technological factors - current density, $CoCl_2.6H_2O$ content and stirring – on the most important characteristics of the electrolyte and the coatings was studied.

It was found that higher cathode current density and stirring may increase current yield to 35%, i.e. almost twice as high as that of conventional sulphate electrolytes. Deposition rate, coating thickness and root mean square roughness were also increased.

It was demonstrated that increasing the content of $CoCl_2.6H_2O$ in the investigated range of 1-5 g.L^{-1} makes the coating rougher and less glossy.

To highlight particular areas of the application of these chromium coatings, it is advisable to determine the content of cobalt in them and to study their biocompatibility.

REFERENCES

[1] J. R. Davids, *Metals Handbook, ASM International*, 944-967 (1998).

[2] P. Sury and M. Semlitsch, *J. Biomed. Mater. Res.* **12**, 723–741 (1978).

[3] K. S. Katti, *Colloid Surface B* **39**, 132-142 (2004).

[4] M. Long and H. J. Rack, *Biomaterials* **19**, 1621–1639 (1998).

[5] P. Agostoni, Van Belle and P. R. Stella, *J. Invasive Cardiol.* **22**, 453–455 (2012).

[6] T. Newson, *Stainless Steel - A Family of Medical Device Materials*, Business briefing: medical device manufacturing & technology, 2002.

[7] R. H. Shetty and W. H. Ottersburg, *Metals in Orthopedic Surgery*, Part B: Applications, edited by D. L. Wise *et al.*, Marcel Dekker Inc., New York NY, 1995, pp. 509-540.

[8] R. Mantcheva, I. Gadshov and Iv. Nenov, Copyright License No 85289, 1988.

[9] R. Mantcheva, I. Nenov and I. Gadshov, *Metalloberfläche* **43**, 262–264 (1989).

[10] I. Nenov, R. Mantcheva and I. Gadshov, *Metalloberfläche* **43**, 305–308 (1989).

[11] M. A. Shluger, *Galyvanicheskie pokritiya v mashinostroyenii*, Vol. 1, Mashinostroyenie, Moscow (1985).

[12] R. Mancheva and D. Mileva, "Influence of additive on complex properties of the chlorides and iodides chromium coatings" in *Jub. Nation. Conf. with Intern. Particip. "THE MAN AND UNIVERSE"*, Smolyan, Oct. 6–8 2011, Scientific Papers, pp. 406–415, ISBN:978-954-397-025-4.

ЗА ВЛИЯНИЕТО НА НЯКОИ ФАКТОРИ ВЪРХУ ФУНКЦИОНАЛНИТЕ СВОЙСТВА НА ГАЛВАНИЧНО ОТЛОЖЕНИ ПОКРИТИЯ, ПЕРСПЕКТИВНИ ЗА МЕДИЦИНСКО ПРИЛОЖЕНИЕ

Д. Кираджийска[1], Р. Манчева[1], Д. Милева[2], Т. Йовчева[3], А. Виранева[3]

[1] *Фармацевтичен Факултет, Медицински университет – Пловдив, бул. "Васил Априлов" №15 А, 4000 Пловдив, България*

[2] *ДЕСО, Медицински университет – Пловдив, бул. "Васил Априлов" №15 А, 4000 Пловдив, България*

[3] *Физически факултет, Пловдивски университет "Паисий Хилендарски", ул. "Цар Асен" №24, 4000 Пловдив, България*

(Резюме)

В настоящата работа са изследвани някои функционални свойства на галванични хромови покрития, отложени от нестандартен хлориден електролит тип "Cromispel", модифициран с комбинирана, комплексно действаща добавка $CoCl_2.6H_2O$.

Изследвано е влиянието на различни технологични фактори като плътност на тока, съдържание на $CoCl_2.6H_2O$ и разбъркване върху свойствата на електролита и покритията. Получените експериментални резултати показват, че прилагането на разбъркване и нарастването на плътността на тока от 15 $A.dm^{-2}$ до 50 $A.dm^{-2}$ правят покритията по-гладки, по-блестящи и повишават скоростта на отлагане и използваемостта на катодния ток. Експериментално е установено, че по-високата концентрация на $CoCl_2.6H_2O$ води до намаляване на отражателната способност и дебелината на слоевете.

За определяне на повърхностната морфология на изследваните покрития е използван атомен силов микроскоп. Измерена е средната квадратична грапавост на изследваните покрития и е определен средният размер на наблюдаваните зърна.

ELECTRONICS, INFORMATION AND EDUCATIONAL TECHNOLOGIES

ЕЛЕКТРОНИКА, ИНФОРМАЦИОННИ И ОБРАЗОВАТЕЛНИ ТЕХНОЛОГИИ

Bulgarian Chemical Communications, Volume 47, Special Issue B (pp. 489–497) 2015

Project-based teaching in physics and its implementation for creating a website

G. Malchev*

Peyo Yavorov High School, 31 Yane Sandanski Str., BG-2850 Petrich, Bulgaria

The report presents a project-based teaching as one of the methods for developing cognitive skills in students in their studies of Physics. What is described is an exemplary application of the method in the 9th grade for building a website dealing with electromagnetic phenomena. There are described all the activities of the students through which a virtual environment has been built, providing access to learning resources and popular science information from the Chapter on Electromagnetic interaction.

Key words: project based teaching in physics, project method, cognitive skills, electromagnetic phenomena, a website, information and communication technologies

CONTEMPORARY DIMENSIONS OF PROJECT-BASED LEARNING ACTIVITIES IN TEACHING PHYSICS

Nature of the project method

Quality teaching is achieved by proper selection of one or another approach, in which students can develop active cognitive skills to learn. Students should be motivated to act as if they were researchers themselves and on their own being able to discover the pathway to knowledge through activities they will conduct – such as reading, thinking, discussing, exploring and so on. That us why a contemporary teaches shold be able to create a proper learning environment, in which they can build up knowledge, skills and attitudes through problem solving, discussions and cooperation amongst students. Such an education environment is created with the help of a project-based instruction through applying various methods and implementing different approaches [1].

The term "project" is in the grounds of project-based teaching. The literal translation of the term comes from Latin and means "thrown forward". It is used in various areas of human life with the meaning of intention or action plan. In didactics the term "project" is understood as research topic in the context of didactic task whose successful development requires theoretical knowledge and practical actions.

The Project Method as part of the interactive approach enables students to develop their cognitive skills. It also simulates their aspiration for a creative self-expression, independent handling of information and critical understanding of reality. Project-based teaching is based both on cooperation among students, and also between them and the teacher. "Here there is an expression of the synergistic idea of cooperative joint action of all parts in the whole unit, as well as about qualitative changes occurring in the system as a result of self-organization processes taking place in it" [2].

In the implementation of the project work students learn:

- to create, consider and adopt ideas;
- to plan tasks and activities to achieve the objective;
- to calculate out learning resources;
- to allocate positions and responsibilities;
- to present and stand up for their ideas to the class, their teacher or parents;
- to put practice the idea of the project;
- to evaluate the process and outcome.

Didactic characteristics of the project learning activities in physics

School project in Physics enable the teacher to organize the circumstances in which students reveal themselves as researchers. Through this method, they look for and find solutions to specific problems on their own, creating an intellectual product of practical importance.

Work on a project begins by a precise definition of the topic. Then the topic is discussed among the participants, who specify the details and plan the activities. The clearer the concept of the value of the final product is, the more interested students are in the project. In practice this learning activity is a challenge for the manifestation of students' own strengths and capacities. In order that this activity becomes of systemic nature and to achieve the desired synergetic effect, the Physics teacher should strike a balance be-

* To whom all correspondence should be sent:
gmalchev@abv.bg

© 2015 Bulgarian Academy of Sciences, Union of Chemists in Bulgaria

tween traditional and innovative elements un teaching.

Planning of the project activity can be done in class, agreed within the school framework of among several schools. The teacher should focus on the individual elements of the project manager, but further on, when difficulties arise, he/she becomes a consultant and facilitator.

According to the didactic theory, the structure of the learning project invikves the following stages:

1. Stage of Searching;
2. Stage of Analysing;
3. Implementation of Planned Activities;
4. Presentation Stage;
5. Evaluation Stage.

The types of projects in Physics are classified according to the following criteria [3]:

- Didactic objectives:
  - to visualize a phenomenon;
  - to consolidate knowledge;
  - for systematization and generalization of knowledge;
  - to develop skills for solving problems;
  - to develop skills for conducting experiments and similar.

Products: computer presentations, virtual demonstration experiments, computer tests, etc.., simulation labs, equipment and learning aids.

- Contents of the syllabus:
  - for developing topics related to applying Physics in sports, medicine, technology, etc..;
  - for developing topics where the studied objects and phenomena are difficult to visualize;
  - for presenting and studying a particular phenomenon or object.

Products: a computer presentation, panels, posters, films, simulation labs, equipment and learning aids, tests, assignments, and others.

- Purpose of using physical knowledge:
  - creating a practical relevant product for the man with tailored properties;
  - evaluating or determining the parameters of properties of objects in a certain state;
  - developing a technology (a method) for achieving a practical relevant result;
  - establishing causes of phenomena and processes.

Products: dynamic model, static model, mechanism.

- Type of results:
  - aimed at creating objects;
  - aimed at aesthetic, emotional or another type of experience;
  - aimed at solving a problem;
  - aimed at acquiring knowledge, skills.

Products: an article, a report, communication, an appliance, a didactic game, a picture.

- Degree of utilization of information and communication technologies in the educational-cognitive activity of students:
  - web reference;
  - web search;
  - web research;
  - e-mail project;
  - cooperation.

Products: a computer presentation, online tests, a report, a poster etc..

The evaluation can be conducted according to several exemplary criteria [3]:

- relevance and significance of the problem in accordance with a given topic, and how much it is linked to the syllabus;
- properly assigned and used research methods and processing of results;
- activity of each participant according to their individual abilities;
- collective decision making;
- team work;
- using knowledge and skills from other subject areas to complete the project;
- argumentation skills, drawing inferences and making conclusions during the presentation of the final product of the project;
- aesthetic finishing of the designed product.

The project method in terms of the class-lesson system in teaching physics

A trend in the global educational theory and practice is the redistribution of the functions of the class-lesson system and self-study activities of the students. The optimum combination and mutual completion of the class-lesson system and the project method leads to an enrichment of tradition and innovation. As a result, teaching Physics gets individualized; knowledge

and skills from different fields of science get updated and applied into practice. Students learn to plan, observe, experiment, analyze and create. This enhances their motivation and makes knowledge, habits and skills more sound, leading to more effective results in teaching Physics. From a practical point of view, an emphasis is placed on the following key points:

- A self-study cognitive activity in teaching Physics is conducted, through which students solve significant personal problems;
- The Physics teacher takes the role of advisor and partner, guiding students in self-study acquisition of physical knowledge;
- "Teacher - student" relationship is developed based on the constant feedback, which timely enables to identify the positive and negative aspects of the activities in the physical project as well as to overcome any encountered difficulties;
- Self-reflection on the individual cognitive activity of students in teaching Physics is made, which itself is a sign of self-governing development in terms of synergetic ideas for self-organization in complex nonlinear structures.

In the process of implementation of the Project Method in teaching Physics, some controversies ought to be overcome. They are caused by the mutual contradiction of the project activity with the proven class-lesson system. When working out on a school project in Physics, the student searches for a solution of a subjectively significant problem by using various resources. However, this cannot be implemented entirely within the class. Since knowledge and resources from a variety of subjects are applied and quite often the information goes beyond the curriculum, the project activity cannot be always organized within the frame of one lesson. Nevertheless, in pedagogical practice the class-lesson system has long been established to be effective for fundamental acquisition of knowledge, skills and habits. Therefore, the Physics teacher needs to find ways to a measured balance. The teacher should conduct a mutual completion of the two pedagogical phenomena in their teaching practice and thus thoroughly reach the educational goals.

Using information and communication technologies in the implementation of the project method

The educational process in Physics is more effective if the project-based learning is integrated with Information and Communication Technologies (ICT). According to the European reference framework this is how a certain level of digital competence is accomplished, including free and critical use of these technologies for extracting, assessing, saving, creating, presenting and exchange of information as well as communication, and participation in collaborative networks [4]. Virtual learning environment is extremely popular and can provide access to a variety of learning resources, even outside the school framework. Such an environment is the educational portal through which the student does informal learning outside the classroom. It will be interesting for students if the contents of the site is entertaining, one that makes them share opinions, comment on problems and propose solutions. Thus, a website can be a powerful tool not only for entertainment but also for sharing knowledge and ideas. Therefore, a project activity linked to any virtual environment is particularly effective. Project-based teaching using ICT stimulates students to learn more efficiently and gain more information within a shorter period of time. "Technologies should be used as a tool through which students, thinking on their own, more quickly and easily can get to resolve issues and solve problems that have been assigned to them" [5].

ICT are at the core of electronic learning (e-learning). It is regarded as "a system of methods, techniques and technologies for organizing and presenting different objects through ICT" [6]. Thus, by using different types of educational information technologies, scientific information is visualized, the learning process is automated, the training is more efficient and interesting for students. What do matters is the quality and selection of contents, as well as the design of the educational product in order to attract and hold the students' attention. Both conditions should be observed in the implementation of the project learning activity for creating of an e-content course or an educational internet site.

APPLICATION OF THE PROJECT METHOD TO CREATE A WEBSITE ABOUT ELECTROMAGNETIC PHENOMENA STUDIED IN 9th GRADE

he Project Method could be an exemplary embodiment in teaching Physics in the 9th grade by students working out a virtual environment to access information from Chapter on Electromagnetic interaction. The website should contain selected learning resources and interesting popular science audio-visual

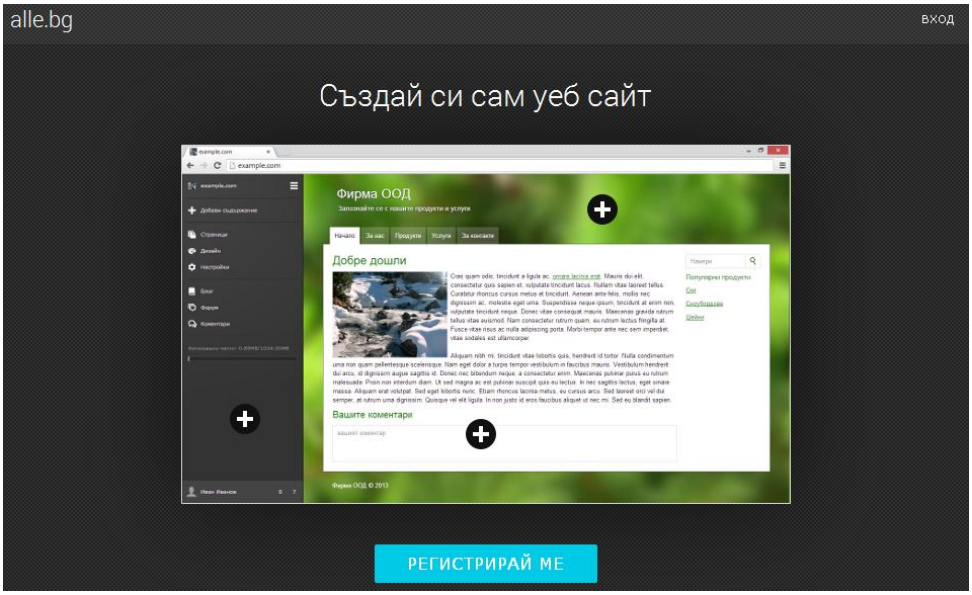


Fig. 1. Exemplary www.alle.bg platform for creating websites.

information about electromagnetic phenomena. Thus, participants in the project from being trainees by teaching their peers turn into trainers. They virtually pass their curiosity to potential web users of the website. Most of them are expected to be peers who are motivated to visit the page, even out of curiosity.

The project objectives are:

- extension and consolidation of students' knowledge on electromagnetism;
- stimulating their creative cognitive activity;
- developing their skills for searching and dealing with information;
- developing their skills for using a computer;
- developing their organizational skills.

Prior to the start of activities, the teacher reports to a chosen by him class the idea of creating a website template on a ready-made platform. The contents of the future virtual environment is subjected to a discussion in class, during which constructive suggestions are noted. Next, the students are informed that the school project will be implemented primarily extracurricular within 3 weeks' time and the website will be promoted in the consolidation section of the lesson. Afterwards, the project will proceed to realization in the following stages:

Stage of searching

According to students' wishes and abilities at the beginning of the first week three groups of 8 people in total are formed to realize the project. Each group elects its leader, and each member undertakes to perform a particular activity: The first group (consists of three people) – editors of information about:

- magnetic field and magnetic induction;
- direct current (DC) electromotor;
- the Northern Lights.

The second group (consists of three people) – editors of information about:

- magnetic properties of substances;
- electromagnetic induction;
- generators and power transformers.

The third group (consists of two people) – administrators responsible for:

- graphic design, selection of photos and videos;
- uploading information.

The groups responsible for the information start searching in textbooks, in books and on the internet for a week. During this time administrators review the available in the global network ready-made platforms on which to build the educational website (Fig. 1). The teams work mainly extracurricular, primarily at home, if necessary some of the computer labs at school can be used. In Physics classes teachers consult each group and ideas are shared with the teacher.

Stage of analyzing

At the beginning of the second week the editorial teams through a discussion analyze the information collected in their portfolio, they offer working thematic sections and discuss what to include in it.

The administrators' group give ideas about the website layout and create a gallery of photos and videos.

At a common meeting of all members the structure, the sample design and the chosen platform of the virtual learning environment are approved, of which the teacher is also informed. Then the activities of the three teams are scheduled until the end of the project.

Implementation of planned actions

At the end of the second week the administrators' group makes a registration on the Internet page, whose server will host the school website. An account is created and a web address is given, at which address the website will be accessible in the global network (Fig. 2). This is how the foundations of the virtual environment are laid, which will be uploaded with information (Fig. 3).

The administrator responsible for the design chooses from the available templates the one that is closer to the pre-approved looks. Then the two groups of editors in stages submit to the administrators the finished text files and audio-visual contents to the website sections (Fig. 4). One administrator uploads information (Fig. 5) and the other selects graphics and videos, and those that are more interesting of them are placed in a gallery (Fig. 6). Furthermore, administrators activate social voting buttons ("like", "do not like") to any material or file including optional comments by readers (most platforms support these features). These features turn the school website into a modern social learning environment.



Fig. 2. Registering a web address.

Presentation stage

At the end of the third week the project is accomplished and the website is completely ready (Fig. 7). Its official presentation is given by all students in a computer lab during the consolidation lesson of the chapter. The authors present their virtual work to the class and explain what it contains. Their peers visit sections in the site out of curiosity, getting to know with the information, looking through the photos and videos, voting for them or commenting on them. As users of the website, they consolidate and extend their knowledge, raise their curiosity and motivation to learn.

Evaluation stage

The teacher comments to the class how the project participants have dealt with the project. He points out the merits and drawbacks of the school website, stimulates original ideas, analyzes the mistakes of some of the groups (if any are made) and sets the assessment. Students do their self-evaluation, also share how they

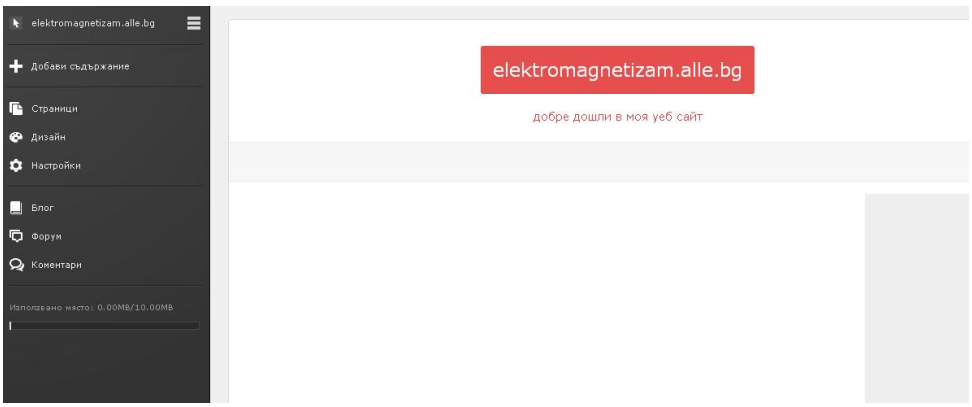


Fig. 3. A blank site with and exemplary title was created: elektromagnetizam.alle.bg

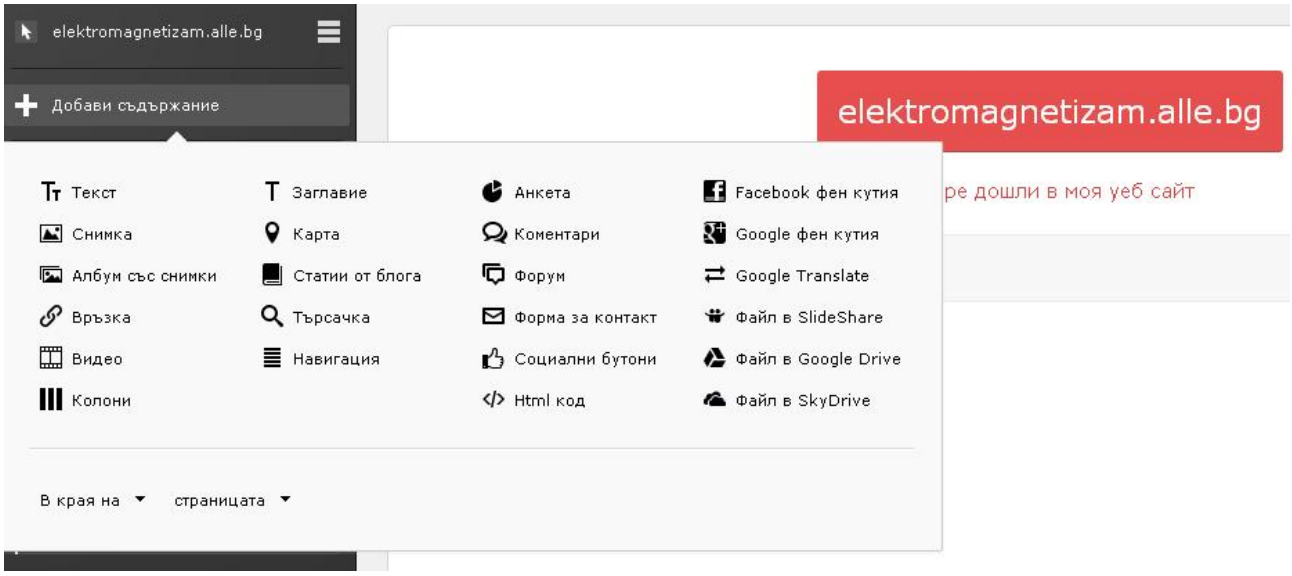


Fig. 4. Menu for uploading contents.

have dealt with encountered difficulties and tell interesting details of the implementation of the learning virtual environment, through which they have attracted the interest of both the other classmates and users in the global network.

SIGNIFICANCE OF PROJECT-BASED TEACHING IN PHYSICS

The school project in Physics is a comprehensive educational and cognitive activity with an objective, a topic, structured actions and a final result. A key role in the implementation of the Project Methods is the independent work of students. Such training provides an opportunity to leapfrog the limitations of authoritarian and reproductive methods. Through it the educational process turns into a personality-centered, interactive and thoughtful combination of methods and tools.

With the help of project-based teaching in Physics students manage to master new knowledge, which is relevant, of practical value and viability. Moreover, they stock their mind with knowledge and consolidate



Fig. 5. Exemplary uploaded information illustrated with a photo.



Fig. 6. Exemplary Gallery of Photos.



Fig. 7. Exemplary view of the ready–made website.

it, develop their skills to seek information and handle it. They learn to plan, analyze and create. Thus, students themselves turn into motivated participants in an effective educational process. Their independent cognitive activity enhances the ambition for further improvement of the individual. The accumulation of information on the project provokes new perspectives and generates new ideas, which can be implemented in new activities and projects.

REFERENCES

[1] P. Dyulgyarova, *Pedagogy* **5**, 695 (2013).

[2] Kr. Marulevska, *Pedagogy* **2**, 4 (2008).

[3] N. Dimitrova, *i–Continuing Education* **18**, 18 (2009).

[4] European Reference Framework, *Communication strategy for joining the Republic of Bulgaria to the European Union* Sofia (2007).

[5] A. Smrikarov, and A. Ivanova, *Concepts for introducing Information Communication Technologies in the school educational system in the next five years* by The Centre of Innovative Educational Technologies "Angel Kanchev" University of Rousse, Rousse, (2011).

[6] V. Dimitrova, Fr. Lustig, *Annual journal of "St. Kliment Ohridski" University of Sofia, Faculty of Physics* **104**, 47–61 (2011).

ПРОЕКТНО-БАЗИРАНОТО ОБУЧЕНИЕ ПО ФИЗИКА И ПРИЛОЖЕНИЕТО МУ ЗА СЪЗДАВАНЕ НА ИНТЕРНЕТ САЙТ

Г. Малчев

Гимназия "П. К. Яворов", ул. "Яне Сандански" №31, 2850 Петрич, България

(Резюме)

Качествено обучение по физика се постига с правилен избор на подход, в който е заложена активната познавателна дейност на учениците. Те трябва да се мотивират да бъдат изследователи и сами да откриват пътя към знанието чрез дейностите, които ще извършват – да четат, да мислят, да дискутират, да изследват [1]. В тази връзка докладът разглежда проектно-базираното обучение като един от методите на интерактивния подход, с който се развиват познавателните умения у учениците в обучението им по физика. Методът на проектите стимулира техния стремеж за творческа изява, самостоятелно боравене с информация и критично осмисляне на действителността [2].

Констатира се, че образователният процес по физика е по-ефективен, ако проектно-базираното обучение е съчетано с информационни и комуникационни технологии [3]. Според Европейската референтна рамка така се постига определено ниво на дигитална компетентност, включваща свободното и критично използване на технологиите за извличане, оценяване, съхранение, създаване, представяне и обмен на информация, както и комуникация и участие в мрежи за съвместна дейност [4].

В доклада е описано примерно приложение на метода на проектите в 9. клас за създаване на интернет сайт, посветен на електромагнитните явления [5]. Разгледани са всички дейности на учениците, с които се изгражда виртуална среда, осигуряваща достъп до учебни ресурси и научнопопулярна информация от раздел "Електромагнитно взаимодействие". Така се стимулира творческата познавателна активност на деветокласниците и те се улесняват при изучаване на електромагнетизма [6].

Прави се изводът, че с проектно-базираното обучение учениците обогатяват и затвърдяват своите знания, развиват уменията си да търсят информация и да боравят с нея, да планират, да анализират и да творят. Това ги превръща в мотивирани участници в ефективен образователен процес по физика.

1. П. Дюлгярова, Проектно-базираното обучение – в търсене на формулата на успеха. *Педагогика*, 5 (2013).
2. Кр. Марулевска, Активизиране на синергетичния потенциал на метода на проектите в условията на класно-урочната система. *Педагогика*, 2 (2008).
3. А. Смрикаров, А. Иванова, *Концепция за въвеждане на информационните и комуникационни технологии в системата на училищното образование в следващите 5 години*, Център за иновационни образователни технологии, РУ „Ангел Кънчев", Русе, 2011, ciot.uni-ruse.bg/static/downloads/Koncepcia-AS.pdf
4. Европейска референтна рамка, *Комуникационна стратегия за присъединяване на Република България към Европейския съюз*, София, 2007, www.eufunds.bg/document/598
5. Н. Димитрова, Учебният проект по физика като основен елемент на проектно-базирано обучение при продължаващото образование на учителите и в средното училище. *i-продължаващо образование*, 18 (2009), http://www.diuu.bg/ispisanie/broi18/18kt/uchebnijat_proekt.pdf
6. В. Димитрова, Фр. Лустиг, Методологични аспекти на електронното обучение по физика. *Годишник на СУ „Св. Климент Охридски", Физически факултет*, 104 (2011) 47-61, www.phys.uni-sofia.bg/annual/archive/104/full/GSU-Fizika-104-05_full.pdf.

Bulgarian Chemical Communications, Volume 47, Special Issue B (pp. 498–503) 2015

Technological and methodological aspects of the acquisition of concepts in the process of physics education

R. I. Vassileva*

Department of Physics, Faculty of Mathematics and Natural Sciences, South-West University, 66 Ivan Mihailov Str., 2700 Blagoevgrad, Bulgaria

The current paper analyzes some aspects of the problem of forming a concept structure in physics education in secondary schools as a key factor for the quality of the knowledge being acquired. Specific ideas which help the solution to this problem are presented. They refer to the different aspects of the technology and methodology of education, they comply with the current educational trends and together with that they accentuate on the ways of increasing the motivation and cognitive development of students.

Key words: physics education, scientific concept, formation of concepts

INTRODUCTION

One of the most significant tasks of modern physics education is for the students to acquire a knowledge system of physics comprising the basic elements of scientific cognition such as concepts, laws, principles, models, theories, and ideas; students are expected to acquire the aforementioned by means of relations and connections which unite them and make them one whole. It is a well-known fact that concepts are the smallest units in the knowledge system of a science. They present the general and significant properties of objects and phenomena in reality. Furthermore, it is namely the process of formation of conceptual structure in a certain school subject training that forms the foundation of the cognitive development of students, viewed from a psychological aspect. Therefore, the successful solution to this problem is a key factor for the quality of students' acquired knowledge.

Striving against the constantly decreasing interest in studying physics, teachers, in their work, search for and apply various methods, ways and means of increasing the cognitive activity of students. However, the result is not always positive. For one reason or another, one of the preconditions for that, is the fact that not enough attention is paid to the problem of concept formation in the course of studying. Consequently, different aspects of formalism may be found in students' knowledge: memorizing without comprehension; inability to use the learned material for explanation of real phenomena; complete break between knowledge and reality.

* To whom all correspondence should be sent:
radostiv@abv.bg

From a pedagogical and psychological viewpoint, the learning process is comprised of "three units:

- The student's knowledge as a product of their education;
- The mental processes by means of which a certain result is achieved;
- The property of the student's reasoning characterizing their cognitive development" [1].

This means that the thing to be sought for in education is the balance between the result and the process of its achievement. Observations, however, show that the emphasis is put on what and how much is acquired, rather than on how it is acquired. The thing that is of great importance is the "correct answer" of the students as a proof of success [2], whereas the issue of what actually happens in their mind, what their personal attitude is towards the experience acquired remains in the background.

It is also important to mention that during the process of knowledge (concept) acquisition, several aspects which are correlative can be categorized, and special attention is to be paid to them in school work:

- Perception (initial comprehension of the material);
- Rationalization;
- Reassertion;
- Mastery (usage of the material in different situations, practical application of the acquired knowledge) [3].

The rational organization of the teaching process makes it necessary for the teacher to search for answers to numerous important questions:

1. What is to be done in order to support the initial acquisition of the new school material and, parallel to that, to facilitate as much as possible

© 2015 Bulgarian Academy of Sciences, Union of Chemists in Bulgaria

its full comprehension in the process of acquisition? Because, "the acquisition of the material taught is always determined by these preconditions which have been formed up to its comprehension and are also formed in the very process of comprehension" [3]. In this sense, the new school material is to be presented, on the one hand, as a part of a certain knowledge system, i.e. to justify the necessity for its acquisition; and on the other hand, its significant items need to be clearly shown as well as the logical connections with the already learned material to be seen. Therefore, the foundations of comprehension and permanent learning of the material are laid precisely at the initial acquaintance of the students with it.

2. What additional work is to be done in order to further reveal the contents of the school material in detail? The result of that is strongly influenced by the features and quality of explanations the teacher gives in the process of studying. These explanations are to be built and analyzed from a psychological viewpoint and the possibilities should be recognized for their remembering. This is how the matter of repetition in the school process arises, with the accent put not on the simple mechanical reproduction, but on such repetition of the material which is related to its recurring, remodeling, understanding and even re-understanding. This is the way to successfully influence not only the comprehension of the school material but also the permanent "engraving" (reassertion) of knowledge in students' minds.
3. What specific work is to be done in order to form the students' ability for practical application of knowledge, namely the ability to operate with the acquired material in various theoretical and practical situations, assigned through concrete cognitive problems? In this case the basic aim is for students to get involved into active, life-motivated activity, where the formation of practical abilities and habits is combined with the acquisition of new aspects, new characteristics of already acquired competences, with the result of these competences to be turned into a means of knowledge.

The analysis of the examined theoretical formulations shows that what is of great importance for the adequate and permanent acquisition of knowledge (concepts) in the process of physics education is not only the way of elaborating the school material but also the characteristics of the cognitive activity which students are involved in. These are basic factors which show to what extent students can master mental processes, such as analysis, synthesis, comparison, systematization, disregard, generalization, concreteness, without which the acquisition of knowledge is impossible. This is so because in order to be acquired knowledge needs to be understood first, and the way scientific information is processed in students' minds lies in the basis of understanding, that is, all in all, understanding is directly connected and dependent on the level of formation of the scrutinized cognitive operations. Therefore, concept acquisition in physics education has inevitably to be a result of purposeful and various cognitive activities of students, whereas the way teachers create the necessary conditions for that depends on their professionalism and their ability to be innovators and creators in school work.

PRACTICAL ASPECTS OF CONCEPT ACQUISION

Teachers can obtain some very useful feedback about how their students acquire concepts if they carefully analyze the mistakes they make in different school situations. One can, for example, assign the following task: A motorcyclist has passed the first half of a certain distance with speed rate of 30 m/s, and the second half – with 15 m/s. Find the average velocity of the motorcyclist. Observations show that a great number of students immediately give the wrong answer, which is 22.5 m/s, without preliminary analyzing the task in advance. What they do is calculate the average velocity, corresponding to the separate distances. This very simple example makes it possible to draw several conclusions. It is obvious that the students do not understand the concept *average velocity*. This is the reason why students cannot distinguish between the above mentioned concept and the concept *arithmetic mean of velocity* and therefore experience difficulty applying it in the new conditions given in the physical situation in the problem. What one can see is a considerable blunder in teachers' work: they have not done the necessary, they have not created the preconditions which contribute to the perception, rationalization, understanding and reassertion of the concept; and, naturally, students cannot operate with it, they have problems with its practical application.

The first step teachers can perform in such a situ-

ation is to ask their students to give a definition of the concept of interest. This includes a concrete verbal formulation of the concept as well as a written definition of the formula. It is appropriate for the analysis to be like a discussion where the whole class participates. This situation will help the teacher to notice the failures of their students because this activity will result in finding those who: give a concrete definition of the concept verbally, but cannot write the formula which defines it; write the definition formula correctly but cannot explain the concept; define the concept impeccably not only verbally, but also using the formula. Naturally, there are cases of students who cannot perform either task. Then, analogically, the basic idea of the concept *arithmetic mean of velocity* is to be clarified and after that to start solving the problem and it is again advisable that each step be discussed with the whole class. It is essential, in the end, that the teacher accentuate on the following: calculating the average velocity as the arithmetic mean of the average velocities, corresponding to different parts of the motion, without any connection with the definitive formula of this physical quantity, means to transfer incorrectly the mathematical concept *arithmetic mean of several numbers* to the context of a particular physical problem.

Therefore, a question arises: What can teachers do in order to restrict the occurrence of such mistakes? Firstly, they should think carefully about the way to introduce each concrete concept. In accordance with [4] for most concepts that are taught at school, it is most useful for a definition to be given fist, followed by several examples and then the definition should be elicited again, showing how the examples characterize the definition. Therefore, in this particular case, the teacher should perform the following actions: substantiating the necessity to introduce the concept *average velocity* as a characteristic of non uniform motion; giving a concrete definition of the concept with words and a definition formula; showing examples of non uniform motion, connected with the calculation of average velocity; going back to the definition and accentuating on the physical sense of the definition formula.

From a psychological viewpoint, it is of great importance for the thoughts of the students to be brought back again to the acquired concept at the later stages of the study process. These phenomena are also known as current and general repetitions. In order to show the current repetitions, the teacher should choose informative problems which require the use (application) of the concept in various physical situations, different from those the concept was initially introduced in. In this way, the redefinition of the studied material is realized, but this happens under new conditions and the necessary prerequisites are met for the detailed understanding and reassertion of knowledge. The general repetitions are related to the systematization of concepts. In this particular case, this means that the relations and inter-dependence between the concept *average velocity* and all other kinematic characteristics of motion are to be shown. Therefore, the above presented problem can be given to students to solve at a later stage of their study process as an element of current repetition. This can be done after teaching the uniformly-variable motions when students already know that with this type of irregular motion the velocity changes with one and the same value for equal intervals and therefore the average velocity can easily be calculated in another way using the definition formula: it is equal to the arithmetic mean of velocity at the beginning and velocity at the end of the considered interval. At that stage it is appropriate for the teacher to check the extent to which students are prone to make the mistake mentioned above.

It is important to point out that the choice of this example is not arbitrary. It directs the attention of the teacher to the opportunity to use comparison as very helpful practice for formation of concepts. What is more, in this specific case, the matter concerns the comparison of concepts from different subject areas – physics and mathematics; and it is well-known that the math preparation of students is of primary importance for physics education. That is why, finding and analyzing the relations and dependence between such concepts has to be a compulsory element in the teaching process.

Other recurrent mistakes may be stated if students are given various problems requiring classification of already studied concepts. This method is very productive for physics education because "classification is what gives our way of thinking strictness and concreteness" [5]. For example, the teacher can prepare a number of concepts and ask students to analyze them in two groups: concepts of physical phenomena and concepts of physical quantities. The result of this activity mostly depends on the extent to which students are ready to answer the question: What is necessary to know about physical phenomena and physical quantities? It is an irrefutable fact that student's

course books do not give a definition to these concepts and teachers do not pay such close attention to them, as they presume that their idea can be clarified only by means of concrete examples. The frequency of students' mistakes, however, shows that this is not enough. How can one help the solution to this problem? Talking from a psychological and methodological viewpoint, it is helpful for the teacher to use general didactic models in the teaching process. These models reflect the specific logical structure of the activity employed in acquiring each of the examined elements of the scientific knowledge and play a vital role as an outer support in the formation of the inner mental processes of students. For example, the summary of a physical phenomenon studies shows the structure typical of phenomena studies in science, and it consists of the following steps [5]:

1. Finding the external characteristics of a phenomenon.
2. Clarifying the conditions under which it occurs.
3. Analyzing the phenomenon in laboratory environment (if possible) or getting acquainted with the results of such analysis.
4. Defining the physical quantities which characterize the phenomenon and presenting the connections between them (by means of formulas, graphs, etc.).
5. Defining the phenomenon (clarification of the essence of the phenomenon, its inner course on the basis of popular physical theories).
6. Clarifying the connections between a given phenomenon and others.
7. Scrutinizing the most important uses of the phenomenon in practice.

The summary of quantity characteristics of physical objects studies, which is physical quantities, consists of the following steps [5]:

1. Clarifying what property of the physical object characterizes a given quantity.
2. Giving the definition of the term quantity.
3. Writing of the definition (definite) formula. Finding out whether the quantity is basic or derivative, whether it is a vector or scalar quantity.
4. Revealing the physical sense of the quantity.
5. Defining the measurement units.
6. Clarifying the ways of measurement (measurement procedures).

Importantly, it is not enough for these general schemes to be merely explained to the students. It is necessary for the teacher to show how the schemes are applied in practice, i.e. to present the activity of concept acquisition of concrete physical phenomena and quantities. The method of teaching is also of great importance; the way it comes to realize the separate logical steps in the school process in accordance with their specific traits, enabling students to apply the examined models on their own, using them as a point of orientation when acquiring new concepts; teachers can use these models to check how detailed students' knowledge about a certain phenomenon or quantity is. This is the way to form the necessary preconditions for appropriate grouping of each concrete physical concept into one of the two categories. In the language of logic this means the following: suitably realized operation of categorization of concepts in which the range of the generic concept (the number of objects included in a given generic concept) is sub-divided into specific concepts.

Apart from comparison, systematization and classification, teachers can use another helpful method of concepts acquisition: put the students in a situation where they have to determine the difference between similar concepts [6]. What does that mean? It is frequent practice for teachers to ask the same questions at different stages of education, aiming at reassertion of students' knowledge. An example of this is: Which process do we call heat transfer? In this situation, the way the question is asked presupposes an answer which requires recollection of material taught and in this case what comes to be examined is the memory of students. Therefore, even if the answer is correct, it does not necessarily mean that the concept is understood. However, the situation would be completely different if the teacher asked the question: What is the difference between heat transfer and thermal conductivity? In this case the student's answer is the result of specific cognitive activity.

This example shows that it is of primary importance for the teacher to ask questions which urge students to think about the concepts. Furthermore, teachers should stimulate their students to perform this action on their own, i.e. students are to generate similar questions to themselves and to their classmates.

There are exercises, which are interesting and innovative, related to the concretization and generalization of concepts [6]. These are logical operations of transition from a generic to a specific concept and vice versa. Let us say, for example, that the following concepts are given: heat transfer; physical phe-

nomenon; heat phenomena with solid bodies; thermal conductivity; heat phenomenon. In order for the operation of concretization of concepts to be performed, they are to be arranged in the following logical succession: physical phenomenon; heat phenomenon; heat phenomena with solid bodies; heat transfer; thermal conductivity. The generalization of the concepts requires that they be arranged in exactly the opposite succession.

CONCLUSION

It is an unarguable fact that the problem of concepts formation in physics education is extremely complicated and always of present interest. In order to solve it, teachers should find the answer to the fundamental question: How, or so to say, in what way are students to acquire systems of scientific concepts in the school process? This question does not have an unambiguous answer. It urges teachers to perform two important tasks: 1) to develop and improve their knowledge about the problem by getting acquainted with some basic as well as general theoretical formulations in the field of psychology, logic, pedagogy, etc. and 2) to search for adequate practical realization of these formulations in school work, while having in mind the age peculiarities of students and the features of the educational content. In this way, teachers find themselves in a very complicated situation because, on the one hand, the theoretical views upon the subject are diverse and numerous and teachers cannot easily find their way; and on the other hand, the solution to the second task makes teachers ask many additional questions connected with the organization of the teaching process, the methods of presenting the school material, the choice of cognitive problems. Due to the abovementioned issues, teachers cannot always create favorable circumstances which will contribute to a detailed and permanent concept acquisition. As a result, they are faced with the respective negative consequences. Concept acquisition for some students turns into memorizing words. They do not understand the essence of concepts, they find it difficult to see the connections and dependence between them and, in the end, students cannot see concepts as structural elements of a given system. Consequently, such students are unable to use the systems of concepts when acquiring new knowledge. This is the path which leads to loss of interest and motivation for school work and alienation from the school process.

What should teachers accentuate on in the organization of this complex cognitive activity? They have to create the necessary environment for multi-faceted adaptation of the scientific information students obtain during their study process. This means that the new knowledge (concepts) has to be presented in such a way that its acquisition demands as much active reasoning on part of the students as possible. This is an effective way of improving the quality of students' knowledge. On the other hand, during the acquisition process the change of knowledge is accompanied by a change in the structure of the mental processes by means of which these competences are realized. Thus, teachers can develop the theoretical thinking of their students.

REFERENCES

[1] B. P. Barhaev, *Pedagogical Psychology*, Piter, Moscow, 2007, pp. 67–77 (in Russian).

[2] J. Dewey, *Psychology and Pedagogy of Thinking*, Labirint, Moscow, 1999, p. 46 (in Russian).

[3] S. L. Rubinstein, *Foundations of General Psychology*, vol. II, Pedagogica, Moscow, 1989, pp. 84–93 (in Russian).

[4] R. E. Slavin, *Pedagogical Psychology*, Nauka i izkustvo, Sofia, 2004, 291–296 (in Bulgarian).

[5] M. S. Kyuldzhieva, *Didactics of Physics in High Schools*, Episkop Konstantin Preslavski UP, Shumen, 1997, pp. 37-38 (in Bulgarian).

[6] A. I. Slavenkov, *Psychological Foundations of the Research Approach to Education*, Os-89, Moscow, 2006, pp. 309-328 (in Russian).

ТЕХНОЛОГИЧНИ И МЕТОДИЧЕСКИ АСПЕКТИ НА УСВОЯВАНЕТО НА ПОНЯТИЯ В ОБУЧЕНИЕТО ПО ФИЗИКА

Р. Василева

Природо-математически факултет, Югозападен университет "Неофит Рилски",
ул. "Иван Михайлов" №66, 2700 Благоевград, България

(Резюме)

В доклада се анализират някои страни на проблема за изграждането на понятийната структура в обучението по физика в средното училище като ключов фактор за качеството на усвояваните знания. Предлагат се конкретни идеи, подпомагащи решаването на този проблем. Те касаят отделни аспекти на технологията и методиката на обучение, съобразени са със съвременните образователни тенденции и поставят акцент върху възможностите за повишаване мотивацията и развиване мисленето на учениците.

Bulgarian Chemical Communications, Volume 47, Special Issue B (pp. 504–507) 2015

Innovative practices and technologies in educational projects of European Schoolnet and the project "Scientix"

Ts. Ts. Hristova*

PG po KTS, Pravets, affiliated to Technical University of Sofia, 4 Perusha Str., 2161 Pravets Bulgaria

European Schoolnet (EUN) was established in 1997 as a non-governmental organization of 31 Ministries of Education in Europe, which provides major European education portals for teaching, learning and collaboration. European Schoolnet (EUN) provides major European education portals for teaching, learning and collaborating and leads the way in bringing about change in schooling through the use of new technologies and innovative teaching methods. EUN has been tackling the reasons for that lack of interest in MST education, especially developing and extending the ways in which science is taught. To help implement innovative methods and teaching practices, effective use of ICT and the latest trends in education, European Schoolnet create guidelines for best practices in various aspects of teaching, including the training of teachers. The guidelines are based on scientific reports, studies and distribution through pilot schools performed within its projects or with ministries of education or with partners from industry.

To ensure regular dissemination and sharing of progress, know-how and best practices in science education and to provide a feedback mechanism the European Commission launched a project Scientix, managed by European Schoolnet (EUN) on behalf of DG "Research" and funded by the 7th Framework Programme.

Scientix portal http://scientix.eu is available in six European languages. Main user groups are teachers, but the audience is much wider – from scientists and researchers to students, parents and politicians and all stakeholders.

The project offers a resource repository of hundreds of educational materials from European projects, research reports, and opportunities for access to documents; options for filing an application for transfer of learning materials in the 23 languages of the European Union. Online platform offers communication, including forum and chat rooms, online news including international scientific topics related to education and a calendar of upcoming events. A valuable asset is the ability to online training and regularly receive a monthly newsletter to registered users. The platform is dynamic and focused on consumers.

In the first phase (2009-2012), was created as an online portal repository projects in science, mathematics and technology (STEM) and began spreading the project. The main initiative of SCIENTIX conference was held in May 2011 in Brussels.

The aim of the second phase (2013–2015) is the distribution at the national level to reach a wider audience and teaching contribute to the uptake of innovative practices and new methods of training in education.

Key words: innovative practices and technologies, european schoolnet, project "Scientix", ingenius project, european schoolnet academy, virtual labs and remote labs

INNOVATIVE PRACTICES IN THE PROJECTS OF EUROPEAN SCHOOLNET

In recent years there has been an alarming decline in interest among young people for the study of natural and engineering sciences and mathematics, both in our country and in Europe. Moreover, among the general population, threatening reduces the acquisition of basic skills that are important in all areas of life in the community. Teachers, professors and researchers from universities should to have quick access to all initiatives, know-how and best practices, as well as changes in terms of training, which can increase the interest of young people to science and research.

One of the projects of European Schoolnet using innovative practices is the project InGenius. It is a joint initiative launched by European Schoolnet and the European Round Table of Industrialists (ERT) in order to increase the interest of young Europeans in science education and careers and thus to meet the expected future skills gaps within the European Union.



Fig. 1. European Schoolnet projects.

Through strategic partnerships between key industries and ministries of education project involves

* To whom all correspondence should be sent:
tzetza@gmail.com

© 2015 Bulgarian Academy of Sciences, Union of Chemists in Bulgaria

1,000 schools across Europe. The project involved 42 partners from 20 countries, including seven major industries.

During the project as a pilot school had the opportunity to test a variety of resources related to STEM education, to participate in a web binary, discussions related to various best practices, discuss problems in education and to suggest ways to overcome them, to participate in various activities related to the industry as a visiting factories and companies and discussions with their managers, visiting research laboratories and museums, and participate in competitions. Was very useful guide for visiting the companies that can be used in industrial practice: http://www.ingenious-science.eu/web/guest/ingenious-code

Testing the various resources associated with completing questionnaires from both teachers and students who submit opinions to the appropriate resources and suggestions for improvement. As in the beginning of the school year and at the end of filling questionnaires sharpening students' attention on the relationship between science education and industry and their success in life.

Interesting resources for a football game that can be used to improve scientific knowledge and those in mathematics, by energy, energy efficiency and ecology and the relationship of science and technology with industry project has InGenius: http://www.ingenious-science.eu/web/guest

During the chats students have the opportunity to communicate and ask questions of professionals from various fields, which they had previously prepared using different sources. During testing, the teachers and students had the opportunity to adapt the practices. An example of such adaptation is testing the resource Volvo's poster "Mathematic practice": http://www.ingenious-science.eu/c/document_library/get_file?folderId=199356&name=DLFE-4048.pdf

There were organized different competitions, which joined teachers from Bulgaria too: http://www.ingenious-science.eu/web/guest/competition-for-schools

After discussions of best practices was a summary of the discussions. For example, after the discussion on "Using Astronomy as an aid to teaching STEM" its results were published on: http://www.ingenious-science.eu/web/cop9/conclusion

One major initiative InGenius project training courses for Future classroom and Innovative teaching practices - European Schoolnet Academy. After the successful first phase of the project started the second phase of these training courses. During the course of innovative practices was demonstrated using web binary videoconferencing virtual laboratories and remote laboratories. The past is important for science education of young people. Studies show that the use of learning methods to study more likely to understand and remember this phenomenon or process. Two-day workshops and five-day courses on different topics will be organised at the Future Classroom Lab in Brussels. More information about training programme here: http://www.eun.org/teaching/teacher-training

The role of the teacher in the preliminary preparation for learning through research is leading. He led the study indicating preliminary information about the study plan of the study, assisted students in designing hypotheses set tasks to be performed during the experiment and requires summarizing their respective protocols. Before making remote experiment in advance should contact the research center and the state during the experiment, assigns students to be studied phenomenon will experiment and prepare questions for researchers.

One of the problems that can arise are technical - problems with internet connection, webcam, headset or need to communicate in a foreign language, which may be different from English. It is necessary to have installed the appropriate platform for video:

- Webex – http://www.webex.com/
- Google Hangouts – http://www.google.com/hangouts
- MashMe.tv – www.mashme.tv

Are effective simulation / online labs?

If well planned, including instructions, learning to study through online labs and simulations superiority over awareness lessons. Students in online laboratories obtain the same level of knowledge or advanced level of knowledge of students who learn in a real laboratory.

In educational platform "Scientix" uploaded a lot of resources and projects involving innovative educational practices and technologies that are useful for improving the quality of education physics and astronomy as: EU-HOU, Global excursion, Go lab, InGenius project, Nanopinium, Spice, Establish, GenisLab, Items etc.. The platform itself provides opportunities for online communication, free use of uploaded resources for doing videoconferencing and training of Moodle.

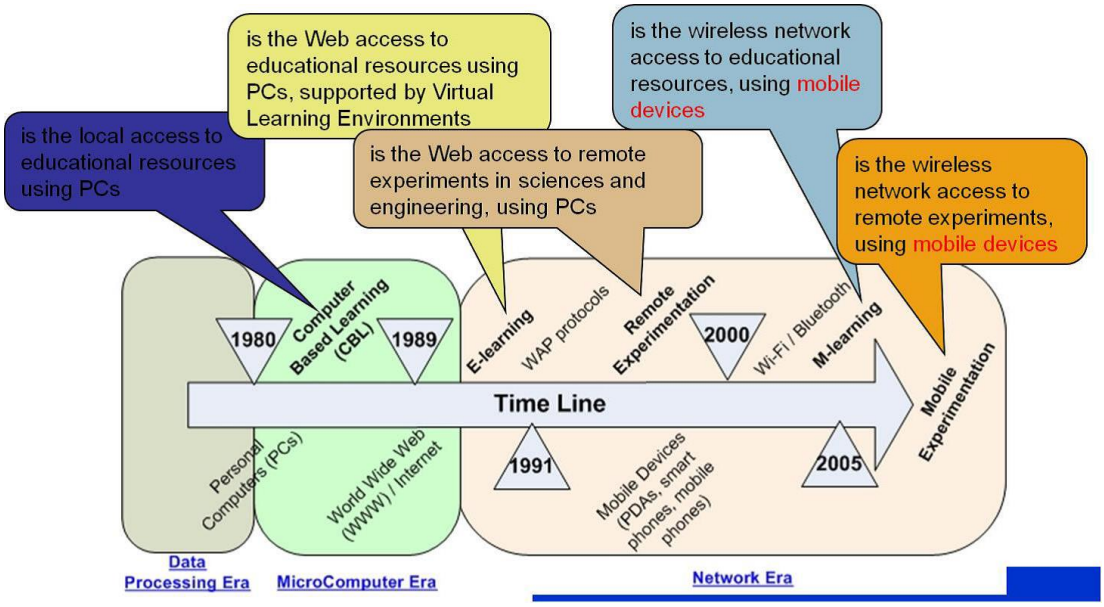


Fig. 2. Development of remote experiments with the development of Internet and computer technology.

Upcoming initiative Scientix 2 conference from 24 to 26 October 2014 in Brussels. Project details can be found on the website of the project: www.scientix.eu and presentations uploaded to my blog: http://ceca-scientix.blogspot.com/

Part of the Global excursion is Virtual Science hub – ViSH (www.vishub.org), which includes a variety of features and options to make presentations by flash cards, google maps, images from the Internet, movies from you tube, use chat, rating resources, sharing of resources, use of other resources uploaded online in your presentation, and the possibility of videoconferencing as MashMeTV.

Example of Remote experiments:
Robotic tuna:

http://www.youtube.com/watch?v=pDitxrXeYnA
Curiosity rover-Mars Science Laboratory:

http://www.youtube.com/watch?v=P4boyXQuUIw
Other virtual laboratories:
http://www.simquest.nl/SQsims.jsp
http://phet.colorado.edu
http://home.web.cern.ch/
http://www.donanareservas.com/entorno_en.php
http://www.projectolynx.com/ao-vivo/
http://socientize.eu/?q=pt-pt/node/382
http://cellspotting.socientize.eu
http://www.go-lab-project.eu/lab/sun4all
http://cosmoquest.org/projects/moon_mappers/
https://www.zooniverse.org/
http://boinc.berkeley.edu/projects.php
https://www.mindpaths.socientize.eu
http://rrlab.bifi.es/home
http://www.bifi.es/en/infrastructures/edificio-id/laboratories/2103-supercomputing-lab

The high cost of equipment brings us to the first barrier in practice using traditional laboratories. Online labs allow the implementation of real Experiment, regardless of time and distance, reducing the cost of equipment, personnel and maintenance of laboratory demonstrate in class specific thematic experiments without using laboratory equipment. These labs are available seven days a week for 24 hours, allowing the students to coordinate laboratory practice with their own agenda and are free. Remote laboratory can be used to improve laboratory work students with engineering or physics or seek new and effective forms of education.

Innovative practices and new methodologies in the projects of European Schoolnet and the project "Scientix" are interesting, attractive, new technologies have applications for handheld computers, laptops, tablets, online phones. Knowledge and the use of a guarantee for quality science education.

Acknowledgments. *This paper was published with the financial support of Scientix project, as an initiative of the European Commission, Scientix is managed by European Schoolnet (EUN) under the European Union's 7thFramework Programme.*

REFERENCES

[1] www.scientix.eu

[2] SCIENTIX: The new Internet- based community for science edication in Europe, E. Gerard, Á. Gras-Velázquez

[3] http://www.ingenious-science.eu/web/guest/partner-description

[4] http://www.ingenious-science.eu/web/guest/ingenious-code

[5] http://www.ingenious-science.eu/web/guest

[6] http://www.europeanschoolnetacademy.eu/web/general-navigation/courses

[7] www.vishub.org/

ТЕХНОЛОГИЧНИ И МЕТОДИЧЕСКИ АСПЕКТИ НА УСВОЯВАНЕТО НА ПОНЯТИЯ В ОБУЧЕНИЕТО ПО ФИЗИКА

Ц. Христова

ПГ по КТС, Технически Университет – София, ул. "Перуша" № 4, 2161 Правец, България

(Резюме)

През последните години се наблюдава тревожен спад на интерес сред младите хора за изучаване на природни и инженерни науки и математика, както в нашата страна, така и в Европа. Освен това, сред населението като цяло, заплашително намалява придобиването на основните умения, които са от важно значение във всички области на живота в обществото.

Би трябвало учители, преподаватели от университети и изследователи да имат бърз достъп до всички инициативи, ноу-хау и добри практики, както и до промените по отношение на обучението, което може да доведе до увеличаване на интереса на младите хора към природни науки и научни изследвания.

За да отговори на тези изисквания от декември 2009 г. стартира нова, уеб базирана информационна платформа "Scientix", управлявана от Европейската Училищна Мрежа от името на ГД "Изследвания" на Европейската комисия [1-3].

Европейска училищна мрежа (EUN) е създадена през 1997 година като неправителствена организация от 30 министерства на образованието в Европа, която предвижда големи европейски образователни портали за обучение, преподаване и съвместна работа. Има водеща роля в постигането на промяна в образованието чрез използването на нови технологии.

Едни от интересните инициативи на EUN са онлине курсовете, които са достъпни за всички, като иновативните практики за подпомагане на обучението по природни науки и класната стая на бъдещето.

В образователната платформа "Scientix" са качени много ресурси и проекти, които са полезни за подобряване качеството на образованието физика и астрономия, на които ще се спра подробно: EU-HOU, Global excursion, Go lab, InGenius project, Nanopinium, Spice, Items и др.

Европейската комисия възнамерява да инвестира повече в образованието и изследователските проекти, което ще доведе до стабилно обществено развитие в бъдеще.

1. http://www.scientix.eu/web/guest

2. http://www.europeanschoolnetacademy.eu/web/innovative-practices-for-engaging-stem-teaching
item SCIENTIX: The new Internet-based community for science edication in Europe, E. Gerard, À. Gras-Velázquez

Bulgarian Chemical Communications, Volume 47, Special Issue B (pp. 508–513) 2015

Possibilities of the inquiry based approach to built motivation for studying sciences

Zh. Raykova*

Faculty of Physics, Paisii Hilendarski University of Plovdiv, 24 Tsar Asen Str., BG-4000 Plovdiv, Bulgaria

This work is considered the place and role of the Inquiry Based Science Education (IBSE) and tries to describe the opportunities for the formation of different types of motivation. A result of the training using IBSE in five Plovdiv schools and of the survey of the students is described. Conclusions are made, which identified and orient us in opportunities of IBSE approach in building motivation for study science.

Key words: inquiry based science education

ACTUALITY, OBJECTIVE AND TASKS

Inquiry based education is an important approach in the process of natural sciences teaching, which involves the students in exploration and use of data as proof for the answer to the questions asked [1]. It is considered that the inquiry based approach contributes for the formation of scientific literacy and it has the potential to improve the understanding of the educational content of natural sciences, to encourage interest in science and participation in its studying in the classroom, and it is a powerful motivational means.

In this study the main features of the inquiry based approach are reviewed, and an attempt is made on the grounds of the conducted natural sciences education process, to describe its significance and ability to create motivation in students.

This approach was first formulated in the studies of John Dewey in the beginning of 20-th century. His ideas about natural sciences education based on a model, in which the role of the teacher is to encourage the activities of the students, later have been adapted and used as a basis of the educational programme of the USA for the year 1937. In the year 1960 Joseph Schwab introduces the term "inquiry based science education (IBSE)". In 1996 the educational standards of the USA define IBSE as an important approach (but not the only) in natural science teaching.

Being a pedagogical approach the inquiry based education has its scientific and theoretical roots in the theories of Dewey and Jean Piaget in the constructivist educational paradigm. According to constructivism learning is an active process, of social nature and it allows the students to construct their own knowledge about the different phenomena and about the path towards scientific knowledge by means of active work, discussion of questions and cooperation between classmates, teachers, scientists, resources and educational environment [2].

The inquiry based education (exploratory approach, heuristic approach, IBSE) uses methods that focus on the student's motivation and that are the driving force in the learning process. The teaching process is organized by means of questions and problem solving in a student focused inquiry process. The teaching methods, in line with this approach, play a central role in establishing motivation in the students and in the development of their scientific literacy.

WHAT DOES THE APPROACH "INQUIRY BASED EDUCATION" MEAN?

Inquiry based education is an approach applicable to all levels of the educational system: from primary school to university education, and it can be conducted both in class and in out of class educational forms. It includes a system of teaching and learning methods in which the students learn by making an inquiry and discovering themselves certain knowledge. Often students make inquiries in order to answer to problems formulated by them and which are related to a certain educational subject. In the course of the inquiry they use the same methods which the respective science uses.

The inquiry based education allows not only to organize effectively the education in the separate educational subjects, but also to form in students important intellectual qualities and practical skills. The success of this approach is achieved by purposeful involvement of the students with suitable questions and tasks in a stimulating and supportive educational environment.

* To whom all correspondence should be sent:
janeraikova@abv.bg

© 2015 Bulgarian Academy of Sciences, Union of Chemists in Bulgaria

It can be applied to all educational subjects, but presently it is most widely researched and applied in the natural sciences education.

The student's inquiries can be small or large scaled, including the entire cycle of scientific knowledge or only separate elements of it. They can include the use of digital resources or appropriate equipment, they can be real-time or on-line, or a combination of both.

Inquiry based education can be reviewed as a variant of the active education, in which the students perform scientific inquiries and so they form new knowledge and skills [Levy and Petrulis 2011].

This approach includes problem-based learning (PBL), and it can be reviewed as a form of project-based learning. Very often the inquiry based education and problem-based education are used as synonyms, but difference between them does exist, taking into account the different forms the problem-based learning can assume. Inquiry based education can be seen as a broader and more flexible concept where the problem-oriented learning can viewed as its subset. For example, while in the problem-based learning the search is made according to a predetermined scenario which the students follow, the inquiry based education includes numerous conditions for study (phenomena or objects), which students independently choose and they have more freedom, to determine the course of the inquiry by being encouraged to ask questions and to observe less instructions in the inquiry process.

There are several characteristic features typical for the inquiry approach and which discern it from the others. They are: appropriately formulated questions, problems or scientific scenario subject to inquiry (often formulated by the students themselves), conducting of inquiries in scientific laboratories or on a terrain, as well as involvement in different kinds of research projects. In this approach the discovery of knowledge is the first priority, while everything else - educational tasks, assessment, resources, educational environment and educational strategies, are intended to support the education through the processes of inquiry and discovery.

The main characteristics of the inquiry based education can be summarized in the following statements:

- The educational process is organized as inquiry and search for answers to questions or solutions to problems, which is implemented in cooperation with the other students and with the help of ICT (Information and Communication technologies);
- It applies the principles and regularities of the scientific inquiry;
- It can be related to questions and problems which answers and solutions are of open nature;
- The knowledge is gained by the student's activity, critical and creative thinking;
- It attributes new meaning to the learned knowledge and raises the level of the knowledge depth;
- It forms practical skills and knowledge about the methods of scientific learning. It forms scientific literacy, skills for teamwork and reflection skills;
- It helps to build social skills for sharing the results from the inquiry with contemporaries and with the broader audience.
- It is a key to the formation of stable motivation for learning [2,3,4].

METHODOLOGY OF THE STUDY

The implementation of the inquiry based science education was organized within the framework of the project "Chain Reaction: A Sustainable approach to Inquiry Based Science Education" (FP7), in which Bulgaria is involved as a partner. This education was implemented during the educational year 2013 and 2014 in five schools in the city of Plovdiv, where participants were students at the age of $15-16$ years. The education was organized according to the requirements towards the implementation of this approach and was aimed at fulfilling the project tasks. The Bulgarian team set an additional task to itself to monitor the changes in the motivation of students to study scientific sciences (physics, chemistry and biology).

The initial state of their motivation was determined by two indicators: grades of the students in the respective educational subject and their desire to be involved in the enquiry based education in this subject, declared in the application for participation. At the conclusion of the conducted education two methods were applied for diagnostics of their learning motivation: questionnaire filled by all participants and interview with the teachers.

ABOUT THE PROJECT

The Project "Chain Reaction" is sponsored by the European Commission and it is aimed at training science teachers to apply the approach "inquiry based education", in which the students are involved in "research work". It provides interactive training to teachers about the "inquiry based education approach" (IBSE), which contributes to their professional development. The main objective of the project is to organize the science education of students by using applied and practically tested scientific resources related to this approach. Ten teachers, acquainted with the inquiry based approach and with the educational resources provided by the project organized a series of lessons (student focused), in which the students independently researched the suggested topics. The students worked together on the suggested scenarios and thematic reference resources, based on scientific facts, by applying critical thinking and problem solving skills [5,6].

The suggested topics for study are from sectors from the three educational subjects: Physics (Science about Mars, Green light, Space Collisions, Extraterrestrials), Chemistry (Ozone conference, To feed the world), Biology (Plants in cosmos, Science about Mars). The education continued for three months where parts of the lessons were carried out in the laboratories of Plovdiv University.

The choice of topics for study was made by the students themselves based on the interest shown by them. Thus the constructivist principle was observed regarding the right of the student to be involved in the planning of the educational process. Later on the work continued with the organization of meetings for clarification of the key points of the final product of the study and for deciding on the necessity to conduct experiments in different laboratories. The teachers provided instructions for this type of educational process. These instructions were in line with the constructivist principle not to impose ready ideas and solutions, to give only answers to the questions asked by the students and to assist the students only if they need or seek help.

In the educational process lessons were conducted in the laboratories of Optics, Inorganic chemistry and Botany, and Molecular physics of Plovdiv University. The work of the students in these laboratories was conducted in actual scientific environment and the teachers assessed it as very beneficial.

For each separate topic the inquiry results of the students were formed as reports, articles, or as an apparatus constructed by them, or as a brochure, and they were presented at the National student conference "Express yourself" in April 2014 carried out in Plovdiv University.

SOME RESULTS AND CONCLUSIONS FROM THE STUDY

In order to summarize the results and to find the effect of this type of education a questionnaire was filled in by the participants, as well as interview with the teachers who organized the education.

The questionnaire (Fig. 1) was filled in by 78 students who have participated in or attended the National Student Conference. The answers of 76 students (97%) to questions no. 1, no. 2, no. 6, no. 7 and no. 8 are "I agree completely" whereas only two students replied with "I agree". A little less is the percentage of the replies "I agree completely" (80%), to questions no. 3, no. 4 and no. 5, while the remaining 20% reply positively, but in the more moderate scale.

The analysis of the obtained results showed not only the situation about the project work, but also the self-assessment of the students about the benefits from the conducted education. They share that they have felt responsible in finding the solution to the assigned task, they have learned to work in a team, they have understood in a better way how science is made. They have been interested in the different scientists who have visited their school and they have enjoyed the making of different scientific inquiries. Again positive, but not so definite positive assessment they give to their confidence of presentation at the conference.

In the interview with the teachers, they share that they have been pleasantly surprised by the interest and active involvement of the students which show a good motivation for learning. According to them, education organized in such a way encourages the expression of the best personal qualities of the students, which develops their self-confidence. The opportunity to learn in an environment different from the school, to visit libraries and laboratories, to search information in Internet, is accepted with joy by the students and they willingly participate in the independent solution of the assigned tasks. Thus a feeling of importance and usefulness of the learned knowledge is built, which is an important motivation factor. All teachers who worked on the project and applied this



Chain Reaction: questions to the students at the end of the National Conference

Researchers from the Sheffield Hallam University (the UK) have a request to the students who participated in the National Conference *Express Yourself* to share their experience, to help the people running it learn how well it has gone. Your answers will be kept carefully and your personal information will not be used in our reports.

1. Student's information:

Age:_____ Gender? _____

School name:_____

Country:_____

Conference participation:

What did you take part with in the conference?

- poster ☐
- presentation ☐
- both ☐

Please, answer to the following questions to what extend do you agree or disagree with the statements about the National Conference

	Totally agree	Agree	No opinion	Disagree	Totally Disagree
I generally like *Express Yourself*					
I generally learnt a lot from *Express Yourself*					
I learnt a lot about team work in the project *Express Yourself*					
I felt that my team was responsible for the work that was presented in the conference *Express Yourself*					
I enjoyed making scientific research/ experiments which were presented at the conference					
I felt confident at presenting my work at the conference *Express Yourself*					
While preparing for the conference, I better realized how science is made					
I was happy to be visited by a real scientist at school e					

Fig. 1. The questionnaire filled in by the students after the National Student Conference.

approach find desire and enthusiasm for work in the students, which rarely can be found during the traditional lessons in the classroom.

The inquiry based science education solves also a number of disciplinary tasks. Students learn to be disciplined due to the requirement to observe the deadlines and to follow certain rules. The application of the newest ICT (Skype, Facebook) in the educational process allowed the teachers and scientists to be allowed into the world of teenagers and consolidated and formed in them specific communicative skills and knowledge about the newest information technologies.

The implementation of this approach stimulated the students to be involved in new educational activities, different from those in the conventional educational environment - they express ideas, ask questions, accept other's opinions, comply with the re-

quirements, transform their initial concepts, organize meetings, use scientific literature and learn to quote it and to present results. All these activities contribute for the establishment of the separate elements of scientific literacy.

Interesting and unexpected result from the so conducted education is the increased interaction between parent - student and parent - teacher. The information about the work under the project was spread rapidly among colleague teachers and parents too. The teachers share their surprise from the activeness and support provided by the parents during the education and from their involvement during the entire time. They not only supported the conducting of this type of education, but they shared their observation that the work on the assigned tasks make their children more responsible and inventive.

In the inquiry based education there are involved students with different academic achievements, which is a confirmation of the broad social functions of this approach. In a situation of informal communication the teachers and students got to know each other in a better way and increased the trust in the teacher, while the students themselves got to know each other better and created skills for teamwork.

Along with this, the teachers share their feeling about a change in their role in the educational process. Their role as information intermediary and leader is transformed into that of a counselor and assistant.

The described results from the conducted inquiry based science education in several schools in Plovdiv allowed us to draw many conclusions about the benefits of its application. Not only did it encourage the independent work and thinking of the students, developed and consolidated their ability to analyze and explore, created skills for independent learning, but it also built a positive attitude towards learning and motivated them to study natural sciences.

REFERENCES

[1] B. A. Crawford, *Journal of research in Science education* **37 (9)**, 916–937 (2000).

[2] http://www.pathwayuk.org.uk/what-is-ibse.html

[3] NRC–National Research Council guide, USA, 2000, see http://www.nationalacademies.org/nrc/index.html.

[4] P. Levy, S. Little, P. McKinney, A. Nibbs, and J. Wood, The Sheffield Companion To Inquiry-based Learning, UK, see http://www.shef.ac.uk/polopoly_fs/1.122757!/file/Sheffield_IBL_Companion.pdf

[5] http://chainreact.dipseil.net/

[6] http://www.chreact.eu/?q=node/10

[7] http://cft.vanderbilt.edu/guides-sub-pages/motivating-students/

[8] G. Lecheva, in *Research studies* (University of Ruse, Ruse, 2009), p. 4

ВЪЗМОЖНОСТИТЕ НА ИЗСЛЕДОВАТЕЛСКИЯ ПОДХОД ЗА ИЗГРАЖДАНЕ НА МОТИВАЦИЯ ЗА УЧЕНЕ ПО ФИЗИКА

Ж. Райкова

Физически факултет, Пловдивски университет "Паисий Хилендарски", ул. "Цар Асен" №24, 4000 Пловдив, България

(Резюме)

Ученето чрез изследване е важен подход в преподаването на природните науки, който въвлича учениците в изследване на теми и в използване на данни като доказателство за отговор на поставени въпроси [1]. Смята се, че изследователският подход допринася за формиране на научна грамотност и има потенциал да подобрява разбирането на учебното съдържание по природните науки, да провокира интерес към науката и участие в изучаването ѝ в класната стая и е мощно мотивационно средство [2-5].

Обучаването на учениците да правят научни изследвания всъщност представлява въвличане на учениците от учителите в практикуването на наука. Това включва различни дейности и процеси, за да се отговори на въпроси и да се направят обяснения и модели, като се използва логическо и критично мислене. Включвайки се в научния процес, подобно на учените, учениците използват наблюдения и експерименти, правят заключения, за да дадат обяснения, базирани на доказателства.

Едно от основните предимства на този подход на обучение е, че стимулира самостоятелната работа и мислене на учениците, развива и укрепва способността им да анализират и изследват, създава умение за самостоятелно учене през целия живот, изгражда мотивация за учене и за правене на наука.

В настоящата работата се разглеждат мястото и ролята на изследователския подход в обучението по физика като се прави опит да се опишат значението и възможностите му за формирането на различни видове мотивация.

Описан е резултат от проведено обучението по физика с използването на изследователски подход в четири пловдивски училища и на базата на наблюдение и проведени анкети с учениците са направени изводи, които ориентират и конкретизират възможностите на изследователския подход при изграждане на мотиви за изучаване на физика [3,4].

1. Crawford, B. A. (2000) Embracing the essence of inquiry: new roles for science teachers. Journal of research in Science education, 37 (9), p. 916 – 937
2. http://chainreact.dipseil.net/
3. http://www.chreact.eu/?q=node/10
4. http://cft.vanderbilt.edu/guides-sub-pages/motivating-students/
5. Лечева, Г. Мотивацията – гаранция за позитивно отношение към учебния процес, НТ на Русенския университет, 2009, т.4, с.10

Bulgarian Chemical Communications, Volume 47, Special Issue B (pp. 514–518) 2015

Formation of meta-subject knowledge and skills in the process of training in physics in the secondary school

Hr. Petrova*

Paisiy Hilendarski University of Plovdiv, Department Methods of Physics Teaching, 24 Tsar Asen Str., BG-4000 Plovdiv, Bulgaria

The meta-subject approach implies translation of the educational content not as information to remember, but as knowledge ready for application. Through it basic skills in students are developed: thinking, imagination, goal setting, understanding, action [1–3].

A technological model is presented, based on the application of the meta subject approach in the physics training in the secondary school. The practical value of the model is that the theory and practice of the training in physics are enriched with new ideas for the formation of meta subject knowledge, and respectively skills of the students.

The technology we offer can be used for studying in all the sections of physics in the secondary school.

Its implementation would allow a real increase in the quality of the learning process in physics through work with the students' abilities.

Key words: meta-subject, physics, an activity approach, systematization

INTRODUCTION

The objectives of modern education are related to training, development and education of free humane individuals, enriched with scientific knowledge of nature and humans, capable of and ready for creative activity and moral behaviour. In view of achieving these objectives, the results of education may be considered in three aspects: subject, metasubject and personal. The metasubject results involve students' acquisition of universal educational activities (UEA), applicable both within the educational process and in real-life situations. UEA may include educational motives (personal UEA); educational purposes (regulatory UEA); learning tasks (cognitive UEA); educational activities and operations (regulatory and communicative UEA). Mastery of the UEA system appears to be a necessary basis for the overall subsequent development of learners.

In physics laws and natural phenomena are studied, which provide great opportunities for transfer into real-life situations. That is why the teaching of physics is a favourable field for the application of the meta-subject approach.

Application of the meta-subject approach in the training of physics involves work with the students' abilities, namely: ability to work with concepts. ability to systematise; ability for graphic representation of study information. ability to understand and schematise the condition of a task, modelling the object of the task, design of ways for solving it, etc.

DESCRIPTION OF THE TECHNOLOGY

Our main objective is to construct a technology model, based on the idea for the realization of the meta-subject approach in physics training.

We consider the expected results in view of the formation of meta-subject knowledge, respectively skills which, in turn, is connected with qualitative and thorough absorption of physical knowledge. Meta-subject knowledge are about:

- planning an educational-cognitive activity for studying a physics section;
- summarised plans for studying a physical law, physical phenomenon, physical quantity, physical device;
- an algorithm for carrying out observations and experiments in the course of individual activity;
- work in a team;
- self - assessment of self activity.

An essential component in the proposed by us technology is the planning of the educational-cognitive activities by both the teacher and the students. This approach places students in an active role. Originally, they are trained to analyse an unknown topic by a certain plan. Then they proceed to planning an in-depth study of the topic. The teacher discusses with students the way of formation of new knowledge, of synthesis and systematization of knowledge, control, self-diagnosis. Then follows compilation of questions on the topic and the allocation of tasks be-

* To whom all correspondence should be sent:
hrpetrova@yahoo.com

© 2015 Bulgarian Academy of Sciences, Union of Chemists in Bulgaria

tween students in project activity. The students in groups are also allocated tasks for systematising of the learning material. Students also carry out observations and experiments by a specified algorithm in the course of individual activity.

Students are trained to analyse a forthcoming section by the following plan:

1. Determination of the objects for studying - physical quantities, physical processes, physical phenomena.
2. Determination of the means for description of the objects of study - laws, theories, models.
3. Determination of the objects for application of physical knowledge - machines, appliances, equipment, generators, motors, etc.
4. Determination of classifications existing in the topic, indicating classification characteristics.

We offer a definite example of this plan in the study of section "Heat phenomena" in the eighth grade.

Objects for study

- Physical quantities – internal energy of an ideal gas, temperature, amount of heat, work done on a gas or by a gas.
- Physical phenomena – heat exchange, melting, solidification. evaporation, condensation.
- Physical processes – isothermal process, isobaric process, isochoric process.
- Physical principles – first law of Thermodinamics, second law of Thermodinamics.

Means for description the objects

- Physical laws - the law of Boyle and Mariotte, Gay - Lussac' s law, Charle' s law.
- Physical theories - kinetic theory, thermodynamic theory
- Physical models - ideal gas, model for structure of substance in solid state, liquid state and gas state.

Classifications

Isothermal process $T = const$; Isobaric process $p = const$; Isochoric process $V = const$.

For the organization of the study information systematization it is necessary that the students know and apply the summarised plans for studying the physical quantity, physical law, physical phenomenon, physical theory, physical device [4]. We present this information follows:

Summary plan for physical quantity

1. Name and symbol.
2. Physical meaning.
3. Formula.
4. Units for measurement.

Summary plan for physical phenomenon

1. External characteristics of the phenomenon.
2. Descriptive definition based on the external characteristics.
3. Conditions for emergence.
4. Examples for observation of the phenomenon.
5. Experiments for demonstration of the phenomenon.
6. Quantities, concepts and laws wich describe the phenomenon.
7. Models for research.
8. Explanation of the phenomenon based on modern scientific theories.
9. Application of the phenomenon in the practice.

Summary plan for physical law

1. Physical phenomena wich characterized the law and relation between physical quantities wich concider the law.
2. Conditions for validity of the law.
3. Limits of the applicability of the law.
4. Presentation of the law – with words, with formula, with table, with graphics.
5. Presentation of the physical meaning of the law.
6. Examples for application of the law in the practice.

Summary plan for physical theory

1. Basic facts for creation of the theory.
2. Areas of the applicability.
3. Basics of the theory.
4. Phenomena, facts and laws wich the theory explains.
5. Phenomena, facts and laws wich the theory predicts.
6. Historical information for creation and developing of the theory.

Summary plan for physical device

1. Name and use.
2. Appearance and characteristics.
3. Marking scheme.
4. Principle of operation.
5. Main parts and their use.
6. The rules for work with device.
7. Application in the science, technics and practice.

Table 1. Physical quantities in the section "Heat phenomena"

Physical quantity	**Denotation**	**Physical sense**	**Definition**	**Formula**	**Units of measurement**	**Means and devices for measurement**
Temperature	T	Characterizes the property of heatedness	A scalar physical quantity characterizing a given thermodynamic state under certain outside conditions	Thermodynamic approach: $pV = \frac{m}{\mu}RT$ $\frac{p_1}{p_2} = \frac{T_1}{T_2}$ Statistical approach: $T = \overline{E_K}\frac{2}{3k}$	K	Thermometer, thermo-couple, thermistor, gas thermometer, etc.
Work done on a gas or by a gas	A	Characterizes the change of volume under the action of forces; the change of energy of the gas or other bodies	A scalar physical quantity whose magnitude at fixed pressure is defined as the product of the pressure and the change of volume of the gas	Work by outside forces to contract the gas: $A = p\Delta V$ Work by outside forces to expand the gas: $A = -p\Delta V$	J	Indirectly by measuring the pressure and volume
Internal energy of an ideal gas	U	Characterizes the movement and interaction between the molecules of the gas	A scalar physical quantity whose magnitude is defined as a sum of the kinetic energy of the chaotic movement of the particles and the potential energy of the interaction between them	Statistical approach: $U = N\frac{3}{2}kT$	J	Indirectly, by measuring T $U = N\frac{3}{2}kT$
Amount of heat	Q	Quantitatively characterizes the process of heat exchange	The energy that a body receives or gives away during heat exchange with its surroundings	$Q_{giv.} = cm(t_1 - t_2)$ $Q_{rec.} = cm(t_2 - t_1)$	J, cal 1 cal = 4.18 J	Calorimeter

We present definite example of the summary plan for physical quantities in the section "Heat phenomena" (Table 1).

Knowledge of summarised plans allows students to ask individual questions, and the teacher to organize communicative, reflexive and cognitive activity, in the process of which the students systematise knowledge.

During individual observations and experiments students follow the algorithm:

1. Select the necessary equipment/materials/.
2. Install set of experiment.
3. Demonstrate experiment and comment by the following plan:
    - What hypothesis is verified with the experiment.
    - What equipment is selected and why;
    - What is observed in conducting the experiment;
    - What can be deducted from the results of the experiment.

The teacher organizes assimilation of metasubject knowledge during the lessons in physics using work in groups, work in pairs, didactic games, etc.

Meta-subject knowledge appears to be a matter of control by the teacher and self-control by the students. Acquiring metasubject knowledge, students compile control questions on the topic. In the process of reflexive activity they formulate difficulties, which are then successfully overcome in the process of training.

CONCLUSION

Formation of meta-subject knowledge and skills is an extremely important process for the training in each school subject. They are necessary for the organization of all types of school activities: cognitive, communicative and reflexive. The Importance of the meta-subject approach in education also consists in this, it allows you to store and maintain the culture of thinking and the culture if formation of the scientific worldview of the students.

REFERENCES

[1] A. V. Hutorski, *Didactic heuristics. Theory and technology of the creation training.*, MSU, Moscow, 2012.

[2] E. E. Malakhova, *Digital Scientific Journal* **1**, 1–9 (2013).

[3] I. S. Kalechkin, "Intersubject concepts in keeping with meta-subgect approach" in *XXXII International scientific and practical conference*, Novosibirsk, 2012.

[4] S. A. Nikolov, R. Mavrova, *Methods of scientific knowledge*, Macros 2000, Plovdiv, 1993.

ФОРМИРАНЕ НА МЕТАПРЕДМЕТНИ ЗНАНИЯ И УМЕНИЯ В ПРОЦЕСА НА ОБУЧЕНИЕ ПО ФИЗИКА В СРЕДНОТО УЧИЛИЩЕ

Хр. Петрова

Физически факултет, Пловдивски университет "Паисий Хилендарски", ул. "Цар Асен" №24, 4000 Пловдив, България

(Резюме)

Метапредметният подход в обучението предполага транслиране на учебното съдържание не като сведения за запомняне, а като знания за осмислено прилагане. Чрез него се развиват базови способности у учениците като мислене, въображение, целеполагане, разбиране, действие [1-3].

Представен е технологичен модел, основан на прилагането на метапредметния подход в обучението по физика в средното училище. Практическата ценност на модела се състои в това, че теорията и практиката на обучението по физика се обогатяват с нови идеи за формиране на метапредметните знания, респективно умения на учениците.

Технологията, която предлагаме може да се използва при изучаване на всички раздели на физиката в средното училище.

Прилагането ѝ би позволило реално да се повиши качеството на учебния процес по физика чрез работа със способностите на учениците.

1. Хуторский, А.В., Дидактическая эвристика. Теория и технология креативного обучения. МГУ, Москва, 2012.
2. Malakhova, E.E., Formation methods and techniques of analytical and synthetic activity as a component of meta-subgect content of education, *Modern problems of science and education / Digital Scientific Journal,* **1**, (2013).
3. Калечкин, И. С., Середа Е. В., Intersubject concepts in keeping with meta-subgect approach. XXXII Международная научно-практическая конференция, Новосибирск, 2012.

Bulgarian Chemical Communications, Volume 47, Special Issue B (pp. 519–527) 2015

Innovative heat transfer analysis of LED modules by thermal simulations

N. Vakrilov[1*], A. Andonova[2]

[1] *Paisii Hilendarski University of Plovdiv, Department of EKIT, 24 Tzar Asen Str., BG-4000 Plovdiv, Bulgaria*
[2] *Department of Microelectronics, Technical University of Sofia, 8 Kl. Ohridski Blvd., BG-1797 Sofia, Bulgaria*

A critical analysis of the heat transfer processes in LED module via 3D CFD thermal modeling is made in the current work. A 3D thermal model of LED matrix is created and its thermal efficiency is investigated. The thermal stresses in the structure are derived from the thermal simulations and approaches for optimization of the design and increase of the reliability are proposed. For this purpose digital models of structures of the printed circuit board with various configurations of thermal vias were created. An analysis of FR4 PCB with 4, 5 and 9 thermal vias is made and the effect of different filling materials - air, copper and SnAgCu is made, in order to clarify the complex interrelationships of heat transfer in the structure.

Key words: heat transfer, LED modules, CFD simulations, thermal management, thermal via, reliability

INTRODUCTION

Despite its high efficiency power LEDs produce large amounts of heat during operation. The large amount of heat, together with the small dimensions of the LED chips results in an increase of the operating temperature. Prolonged operation at high temperature has a negative impact on the reliability and lifetime. The operating temperature should not exceed the maximum allowable temperature of the junction T_j of the chip. Heat dissipation from the LED structure to the environment is a task in which there are many complex connections between the components [1, 2]. This requires the use of innovative techniques for the analysis of heat transfer in order to optimize the structure and improve the reliability. This paper deals with some innovative techniques for fast and reliable study of heat transfer processes in the LED modules to optimize the design and increase reliability.

This article addresses some innovative techniques for fast and reliable study of heat transfer processes in the LED modules for optimization of the design and increasing of the reliability.

For the heat transfer analysis a CFD (Computational Fluid Dynamics) software FloTherm, by Mentor Graphics is used. 3D models of LED matrix, consisting of 3×4 (12) white LEDs mounted on a printed circuit board are created in the software. To create the reference 3D model of the LED matrix a LED matrix with known electrical parameters and physical dimensions of the LED chip is used, as well as the circuit board on which they are mounted. The internal structure of the circuit board is knows, as well as the materials of the constituent layers and their size (width, length and thickness).

The thermal stresses in the structure of the reference model are detected by the conducted CFD thermal simulations and approaches to improve heat transfer are proposed. For that purpose 3D models are generated, which include variations of the circuit board structure of the circuit board with thermal vias.

PCB structures with different configurations of thermal vias (4, 5 and 9 respectively) in the insulating FR4 material of the PCB and also in the FR4 bilateral copper foil are tested. An analysis of the impact of different filling materials for the thermal via (air, copper and SnAgCu) on the structure heat transfer is made.

Data, obtained from the simulations is summarized and can be used by engineers, dealing with the problems of thermal design.

DESIGN OF THE REFERENCE LED MATRIX

The LED matrix, which we will use to create a reference digital model represents an array of 3×4 (total 12) white SMD LEDs located on a FR4 PCB.

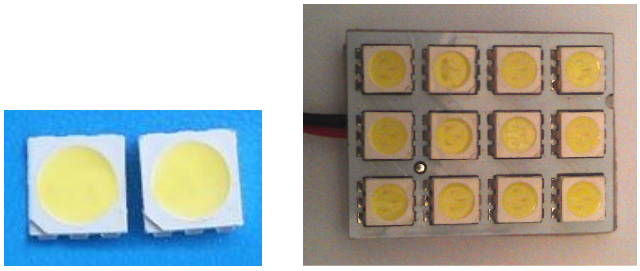
The LEDs are model PLCC6 (5050) with three chips in one case and have the following dimensions: $5 \times 5 \times 1.6$ mm. Fig. 1a shows what the LED looks like (PLCC6 (5050)), and Fig. 1b shows the entire LED matrix.

Some technical features of the LEDs in the matrix are shown in Table 1.

The PCB, on which the LEDs of the LED array are mounted, has the dimensions $220 \times 290 \times 1.07$ mm.

* To whom all correspondence should be sent:
n_vakrilov@abv.bg

© 2015 Bulgarian Academy of Sciences, Union of Chemists in Bulgaria



(a) **(b)**

Fig. 1. (a) SMD LED (5050); (b) LED matrix.

Table 1. Specifications of SMD LED series PLCC6 (5050)

Parameters	**Value**
Materials of the LED	InGaN
Viewing angle	120°
Forwarding voltage	3.2 V
Forward current (typ/max)	3 x 20 mA / 3 x 25 mA
Power dissipation	0.3 W
Operating temperature range	-40°C ∼ 100°C
Storage temperature	-40°C ∼ 100°C
Soldier temperature range	260°C (3 sec.)

The basic material, from which the board is made is FR4, and has a thickness of 1 mm. The FR4 insulating material on the top and bottom plate is covered with a copper foil, which has a thickness of 35 μm.

The adhesive for soldering the LEDs on the board is H2OS and has a thickness of about 50 μm. Fig. 2 shows a cross-sectional view of the entire structure (PCB and LEDs).

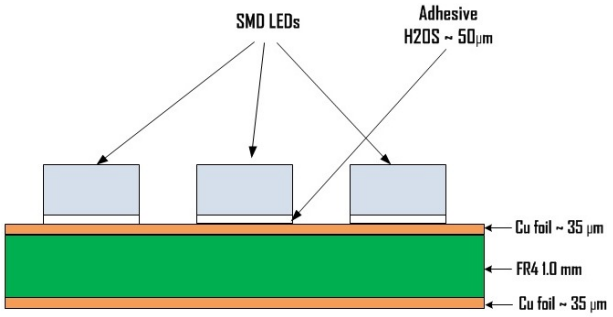


Fig. 2. Cross-section of the circuit board and LEDs - PCB base of FR4, which is bilateral copper foiled, H2OS glue to attach the LEDs, the material of each LED chip is InGaN.

ANALYSIS OF HEAT TRANSFER OF THE REFERENCE LED MATRIX

To create the digital 3D model a for thermal simulation software FloTherm, by Mentor Graphics is

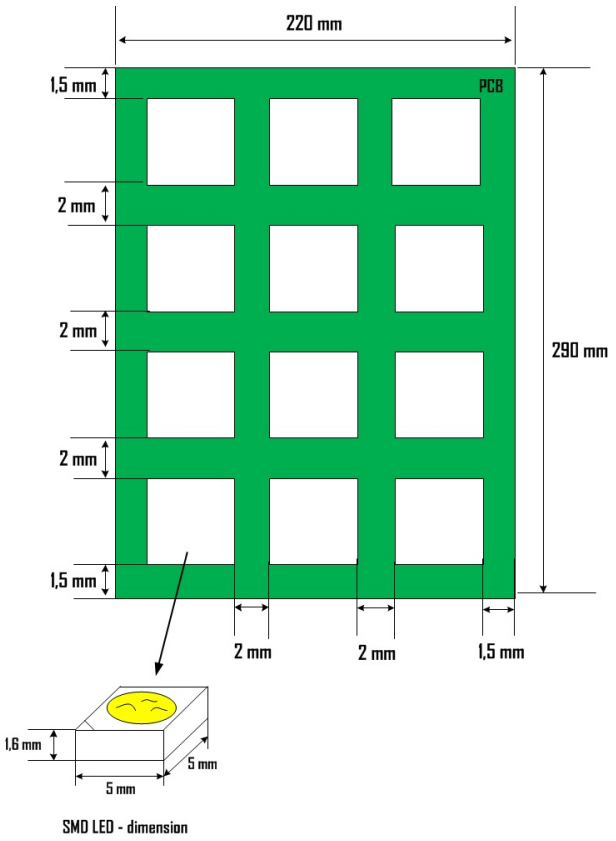


Fig. 3. Geometry of the LED array, which will be used to create a digital 3D model.

used. Flotherm is a powerful CFD tool with the help of which airflow, temperature, and heat transmission of electronic components and whole systems can be predicted [3].

Fig. 3 shows the geometry of the reference LED matrix that is used to create the digital model. The digital model is a simplified model of the LED matrix structure, with the help of which its thermal behavior is examined.

Each LED is modeled as a separate heat source and dissipates power of 0.13W. Due to the complex structure of the LEDs, they are presented as cubes with their real sizes. As it is known the heat, released by the junction of the LED chip is dissipated mainly through the PCB by conduction and from the free surfaces to the environment by radiation and convection [4].

It is therefore of extreme importance the correct modeling of the circuit board for the analysis of heat transfer processes in the LED array.

Table 2 shows the thermal characteristics of the materials, making up the PCB, which are used in the digital simulation.

Table 2. Characteristics of the PCB materials.

Layer Layer	**Material** Material	**Thickness** (μm)	**Thermal conductivity** (W/m.k)
Adhesive	H2OS	50	3.25
Top-layer foil	Cu	35	400
Dielectric layer	FR4	1000	0.8
Bottom-layer foil	Cu	35	400

Results of the thermal simulations made by FloTherm, via the instrument Visual Editor are shown in Fig. 4 and Fig. 5.

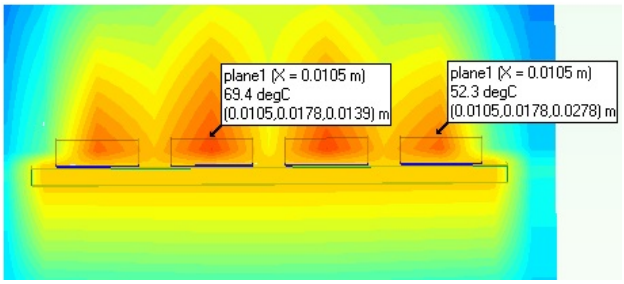


Fig. 4. Distribution of heat in the structure of the LED matrix.

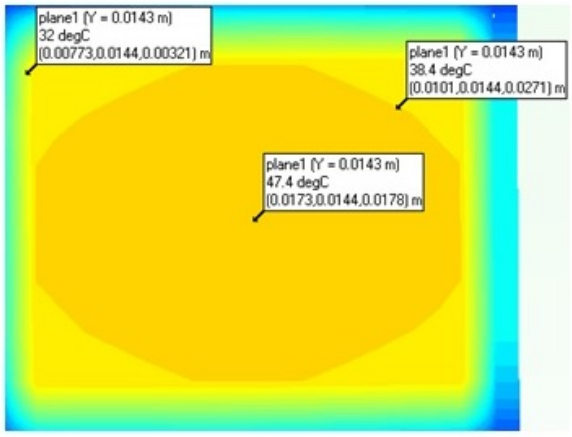


Fig. 5. Distribution of heat on the underside of the circuit board.

For the simulation the thermal behavior of LED matrix at a supply voltage of 12 V and current of 130 mA is studied. The maximum power P_D of a LED is a product of the multiplication of the forward voltage U_F and the current I_F. Thus by substituting the appropriate values for voltage and current, the power P_D of the LED matrix is

$$P_D = U_F I_F = 12\ \text{V} \times 0.130\ \text{A} = 1.56\ \text{W} \qquad (1)$$

Simulations are made at an ambient temperature of 25°C. They show that the temperature of LEDs, which are located closer to the center of the PCB is 69.4°C, and the temperature of LEDs at the periphery of the PCB is 52.3°C. The high temperature of the LEDs in the center is due to their great proximity to one another, a relatively high power, which is dissipated, compared to the size of the PCB, and the poor thermal conductivity of the PCB.

The distribution of heat on the bottom of the circuit board shown in Fig. 5 demonstrates the thermal load around the center of the board. It is seen that the temperature in the center is 47.4°C, by increasing the distance from the center temperature rapidly decreases to 38.4°C, and at the very end of the PCB, where there is more space, the PCB temperature is 32°C.

From the conducted simulations and the analysis of the results it can be concluded that despite the small power of the LED matrix it releases large amounts of heat, which may have negative impact on its reliability. Therefore an optimization needs to be done, in order to improve the heat exchange in the matrix structure.

In the next section methods to improve the heat transfer of the LED matrix by using thermal vias in the PCB are proposed.

OPTIMIZATION OF THE REFERENCE LED MATRIX MODEL

The simulations in the previous section show that FR4 circuit boards have very low thermal conductivity and cannot dissipate heat efficiently. One method for improving heat transfer of FR4 boards is by adding thermal vias in the PCB layers. Using thermal vias is common in thermal design, but still there is no exact method of where to place them or what their configuration must be [5].

In this point there are studied various structural modifications of the already created digital model of LED matrix. The studies include various configurations of PCBs with various locations of the thermal vias, which are most commonly used. The effect of thermal vias on the heat transfer on the board at configuration with 4, 5 and 9 vias, located beneath each of the LEDs, and different filling material are analyzed [6, 7]. In all simulations the thermal vias have a diameter of 0.5 mm.

Fig. 6 show various configurations of the thermal vias and the distance between them.

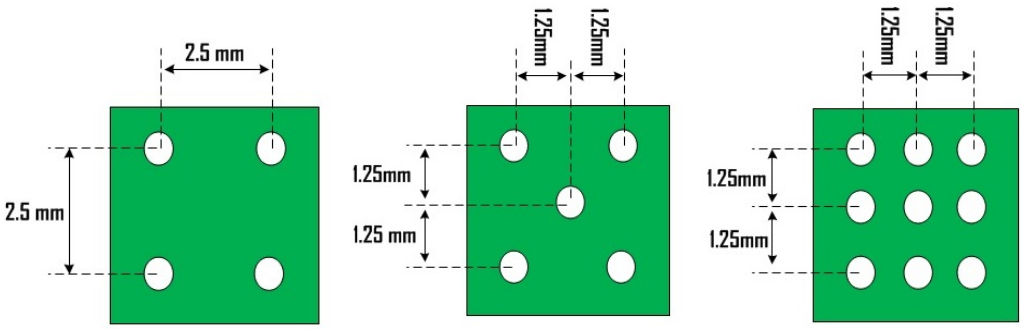


Fig. 6. a) 4 vias configuration; b) 5 vias configuration; c) 9 vias configuration.

Different configurations and parameters for CFD simulations are shown in Table 3.

Table 3. Parameters for thermal simulations.

PCB parameters			
PCB dimensions: 22×29 mm; Thickness: 1.07 mm			
LED parameters			
LED dimensions: 5×5 mm; Thickness: 1.6mm			
Power dissipated per a LED: 0.13 W			
PCB via configuration			
Diameter of the via,mm		0.5	
Via configuration	4	5	9
	Air	Air	Air
Filled via (Material)	Cu	Cu	Cu
	SnAgCu	SnAgCu	SnAgCu
Thermal conductivity of the via, (W/m.k)			
	Air		0.0261
Material of the via	Cu		400
	SnAgCu		58

The geometry of the PCB and the location of the LEDs remain the same as the reference LED matrix model. The physical dimensions and properties of the PCB materials and LEDs also remain unchanged.

The results of the conducted thermal simulations of the created LED matrix model with configuration of 4 thermal vias at a different filling material are shown on Fig. 7.

The geometry of the PCB and the location of the LEDs remain the same as the reference LED matrix model. The physical dimensions and properties of the PCB materials and LEDs also remain unchanged.

The results of the conducted thermal simulations of the created LED matrix model with configuration of 4 thermal vias at a different filling material are shown on Fig. 7

From the simulation of the 4 thermal via model it is obvious that the temperature of the LED close to the center of the PCB is the highest when the thermal vias are filled with air - 59.5°C. In the first case, in spite of the presence of thermal vias in the structure of the LED matrix the heat cannot be dissipated effectively due to the low thermal conductivity of the air ($K_{\text{air}} = 0.0261$ W/m.k). However, the dissipation of heat from the structure of the 4 thermal via model, filled with air is significantly better than the reference model without thermal vias. This can be seen from the temperature markers, placed on the LEDs of the simulated models on Fig. 4 and Fig. 7.

As expected, the temperature of the copper filled vias model is the lowest - 57.8°C and the heat dissipation throughout the structure of the circuit board is most effective. This is confirmed by the markers, placed at the same places on the circuit board in the three examined cases. There it is clearly seen that the PCB with copper filled vias is the coldest. This is due to the good thermal conductivity of the copper ($K_{\text{copper}} = 400$ W/m.k), which effectively channels the heat from the source through the PCB to the surrounding area.

In the case of 4 thermal vias, filled with soldering paste SnAgCu the temperature of the LEDs and the bottom side of the board is close to those, filled with copper. The difference in the temperatures of the LEDs near the center of the structure is $\Delta T_d = T_{d_{\text{SnAgCu}}} - T_{d\_\text{Cu}} = 58.6 - 57.8 = 0.8$°C, and the temperature on the bottom side of the circuit board is in the center $\Delta T_{\text{pcb}} = T_{\text{pcb}_{\text{SnAgCu}}} - T_{\text{pcb}_{\text{Cu}}} = 40.9 - 40 = 0.9$°C. These results show that the temperature distribution in the structures of the two examined models is with a very similar behavior.

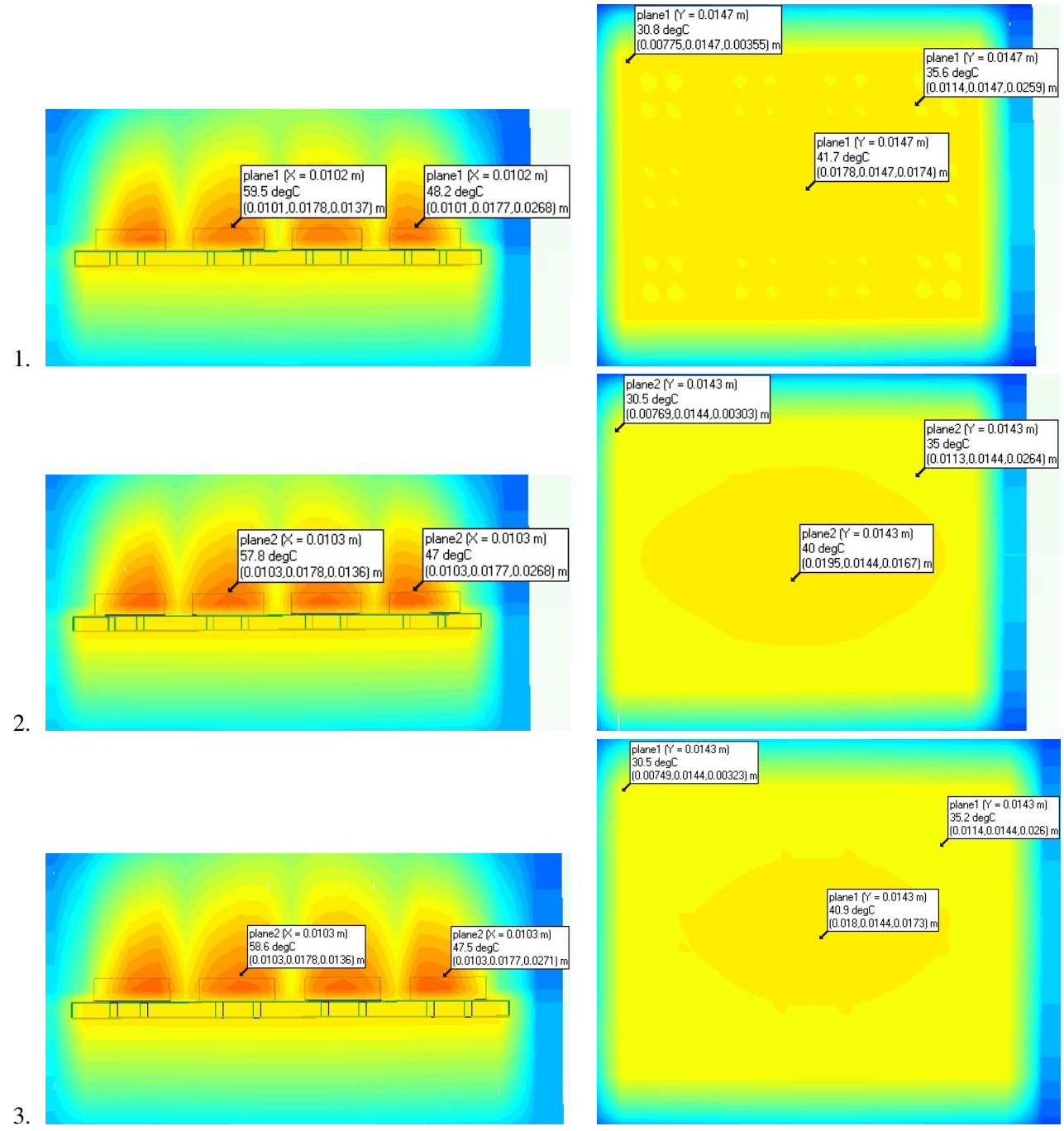


Fig. 7. Simulations with 4 thermal vias filled with different material: 1) filled with air; 2) filled with Cu; 3) filled with SnAgCu.

The simulation results from a configuration with 5 thermal vias, filled with different filling materials are shown in Fig. 8.

The simulation shows that the temperatures of the LEDs and the circuit board of each of the models with 5 thermal vias drops by a few degrees. Again the temperatures of the models with vias, filled with copper and those filled with SnAgCu paste are very

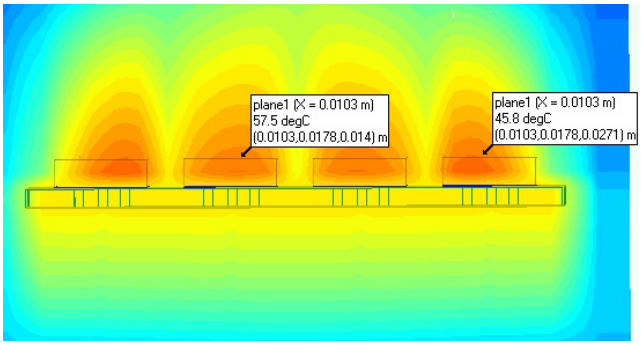
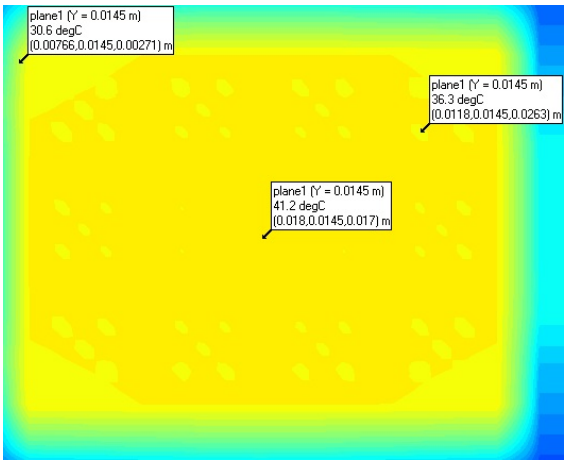
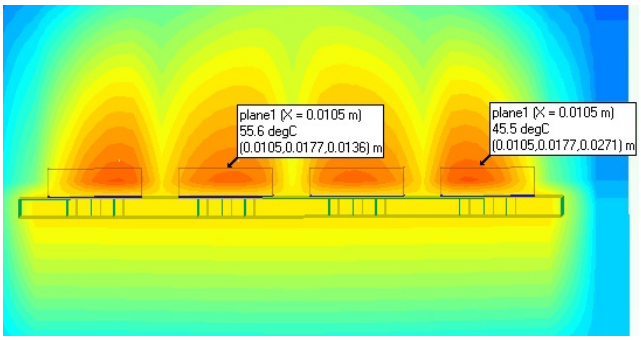
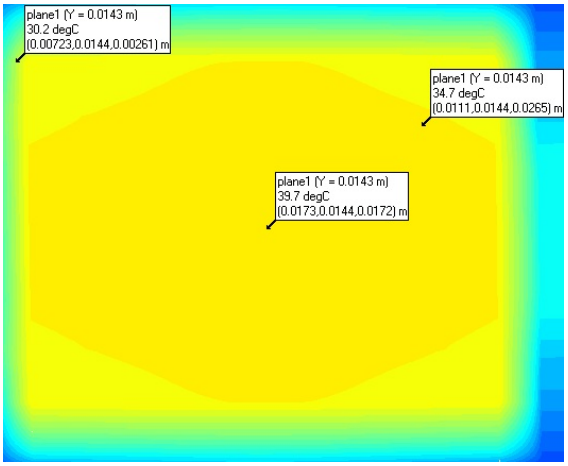
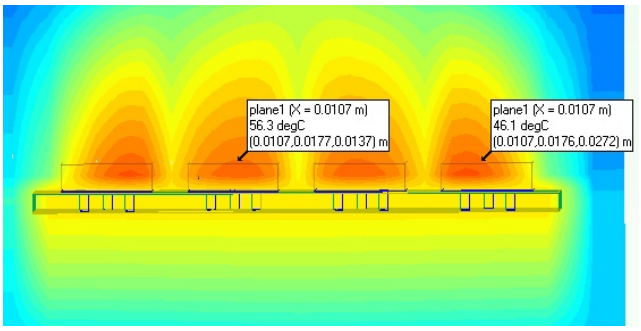
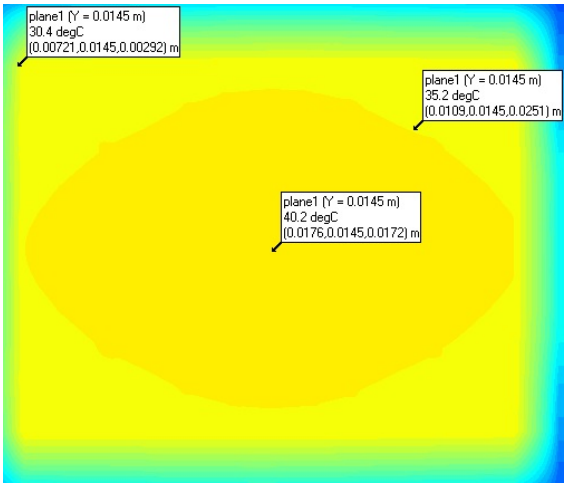
No.	Thermal simulation by Flotherm of the whole structure of the LED matrix	Temperature distribution on the underside of the circuit board
1.		
2.		
3.		

Fig. 8. Simulations with 5 thermal vias filled with different material: 1) filled with air; 2) filled with Cu; 3) filled with SnAgCu.

close, while the temperature of the model with thermal vias, filled with air remains significantly higher in the whole structure.

The results of the simulations for the 9 thermal vias configuration are shown in Fig. 9

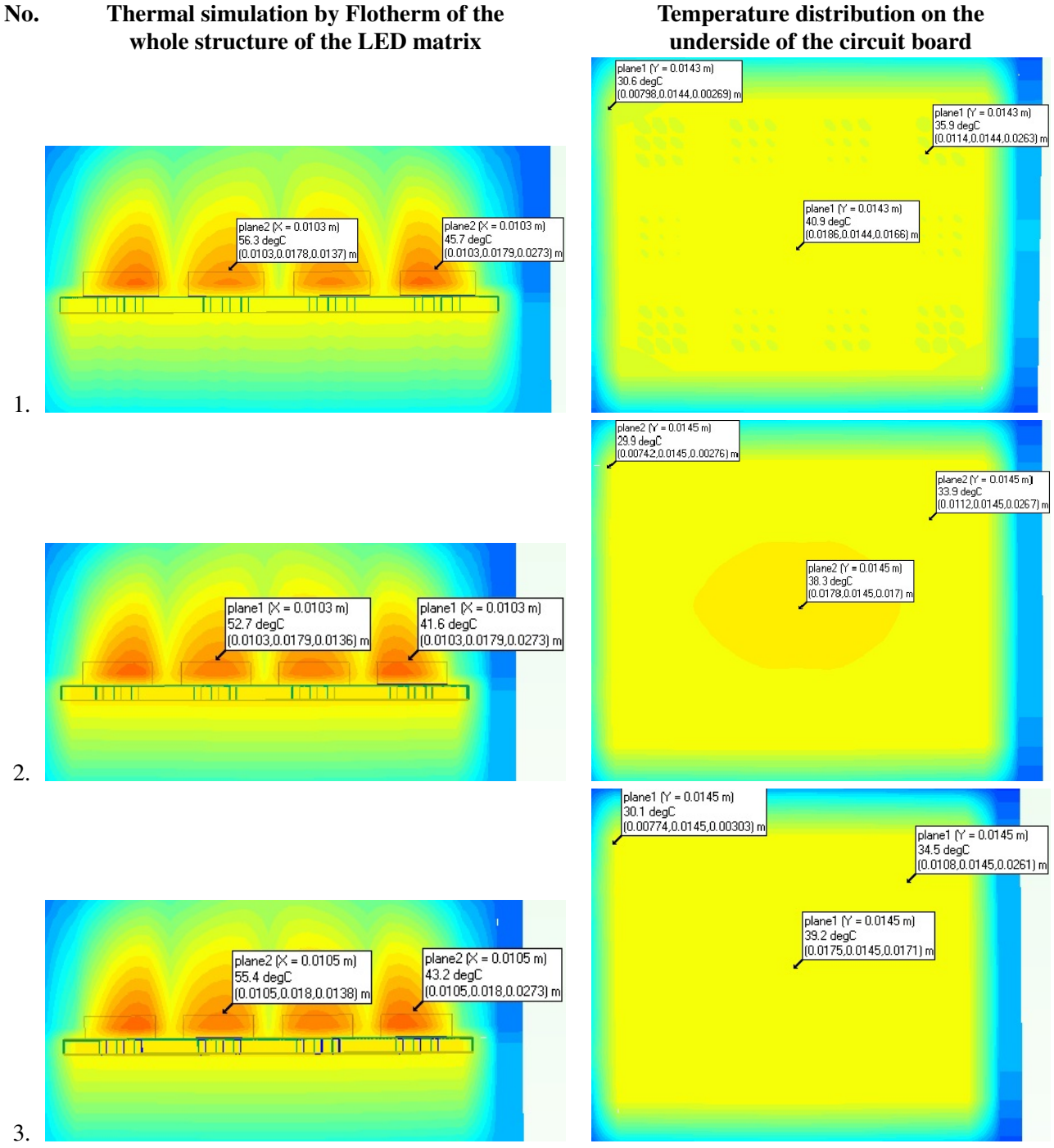


Fig. 9. Simulations with 9 thermal vias filled with different material: 1) filled with air; 2) filled with Cu; 3) filled with SnAgCu.

Table 4 summarizes the temperature results for simulations with 4, 5 and 9 thermal vias. In the table, T_d is the temperature of the LED, near the center of the structure, and T_{pcb} is the temperature at the center of the underside of the circuit board.

A graphical representation of the temperature profiles for the various via configurations and filling materials are presented in Fig. 10 and Fig. 11.

Table 4. Temperatures, generated by the thermal simulations with various thermal via configurations and different filling material

Thermal vias configuration	Thermal vias filled with air		Thermal vias filled with Cu		Thermal vias filled with SnAgCu	
	T_d (°C)	T_{pcb} (°C)	T_d (°C)	T_{pcb} (°C)	T_d (°C)	T_{pcb} (°C)
4	59.5	41.7	57.5	40	58.6	40.9
5	57.5	41.2	55.6	39.7	56.3	40.2
9	56.3	40.9	52.7	38.3	55.4	39.2

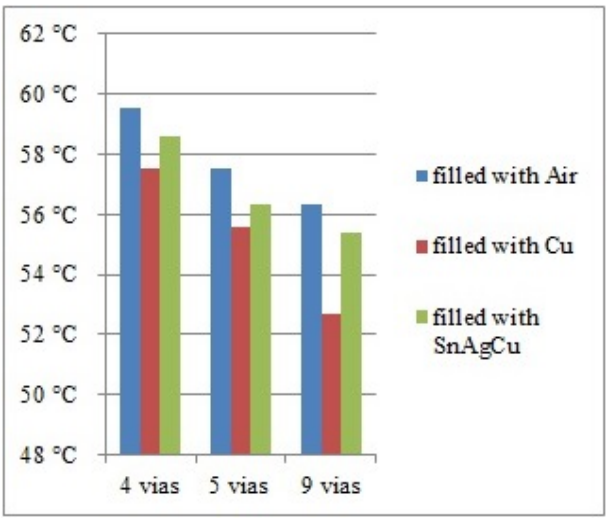


Fig. 10. Temperature of the LED close to the center of the circuit board.

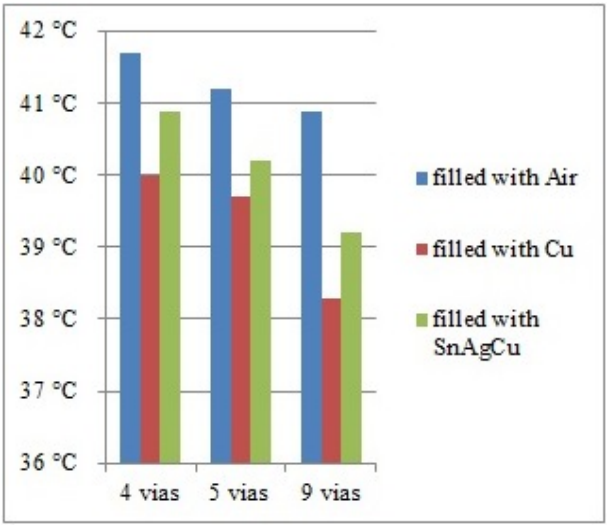


Fig. 11. Temperature at the center of the circuit board.

When comparing the results of Fig. 10 and 11 it can be seen that by increasing the number of vias the LEDs and the circuit board temperatures are reduced in each of the examined cases. The temperature difference of the LEDs near the center in the configurations with 4 and 9 thermal vias, filled with air is $\Delta T_{d_{\text{air}}} = T_{d_{4\text{vias\_air}}} - T_{d_{9\text{vias\_air}}} = 59.5 - 56.3 = 3.2°\text{C}$. In the configurations with 4 and 9 thermal vias, filled with copper the difference is $\Delta T_{d_{\text{Cu}}} = T_{d_{4\text{vias\_Cu}}} - T_{d_{9\text{vias\_Cu}}} = 57.5 - 52.7 = 4.8°\text{C}$. Lower temperature decrease of the LEDs is observed in the case of vias filled with paste SnAgCu paste, respectively $\Delta T_{d_{\text{SnAgCu}}} = T_{d_{4\text{vias\_SnAgCu}}} - T_{d_{9\text{vias\_SnAgCu}}} = 58.6 - 55.4 = 3.2°\text{C}$.

The temperature differences on the bottom side of the PCB are much smaller, for example in configurations with 4 and 5 thermal vias, filled with air it is $\Delta T_{\text{pcb}_{\text{air}}} = T_{\text{pcb}_{4\text{vias\_air}}} - T_{\text{pcb}_{5\text{vias\_air}}} = 41.7 - 41.2 = 0.5°\text{C}$, between those with 4 and 9 vias it is $\Delta T_{\text{pcb}_{\text{air}}} = T_{\text{pcb}_{4\text{vias\_air}}} - T_{\text{pcb}_{9\text{vias\_air}}} = 41.7 - 40.9 = 0.8°\text{C}$. In the other cases with 4 and 5 vias, filled with copper the difference is $T_{\text{pcb}_{4\text{vias\_Cu}}} - T_{\text{pcb}_{5\text{vias\_Cu}}} = 41.7 - 41.2 = 0.5°\text{C}$, and between 4 and 9 vias the difference is $T_{\text{pcb}_{4\text{vias\_Cu}}} - T_{\text{pcb}_{9\text{vias\_Cu}}} = 41.7 - 40 = 1.7°\text{C}$. The results for vias, filled with SnAgCu paste are similar.

SUMMARY OF THE OBTAINED RESULTS

From the obtained results it can be concluded that by increasing in the number of thermal vias the heat transfer in the test structure in each examined case is significantly improved. By increasing the number of thermal vias, the thermal conductivity of the circuit board is increased, which significantly improves the heat transfer. While increasing the number of vias it is very important to take into account the temperature changes and the temperature gradients, in order to find the optimal solution for the specific needs.

Simulations show that when the thermal vias are filled with a material, having a high thermal conductivity, the heat is transferred substantially more efficient trough the circuit board because of the lower thermal resistance. Thermal vias, filled copper provide the lowest thermal resistance and thus dissipate the heat better. They are suitable for high-power LED

applications. Thermal vias, filled with SnAgCu are cheaper than copper and, although having a smaller thermal conductivity convey heat well and are suitable for low-power LED applications. Thermal vias, filled with air improve heat transfer, but to a smaller extent. They have a large thermal resistance and heat cannot be channeled well from the source through the PCB to be dissipated in the surrounding area.

In conclusion from the obtained results we can say that the proposed method for improving the heat transfer of the reference LED structure leads to a considerable temperature decrease in the structure, especially in the case with 9 copper filled thermal vias. The reduced temperature of the LED matrix reduces the thermal stress and increases the reliability.

Acknowledgments. *This paper was published with the financial support of project No.142PD0057-03, "3D thermal simulations to optimize the efficiency of the LED modules by multifactorial study of the influence of different effects", programme "Research projects to support PhD" - TU - Sofia and the project No. NIS14-KS-006/25.03.2014, "BUILDING of complex laboratory equipment for automation and research of processes for automotive engineering and telecommunications", PROJECT BG051PO001-3.1.07-0002, "Project-based Adaptive Learning Curriculumfor the Needs of Business and Employment - PAUP" PROJECT BG051PO001-3.1.07-0002..*

REFERENCES

[1] H. Fengze, Y. Daoguo and Z. Guogi, *Journal of Semiconductors* **32**, 014006(1)–014006(3) (2011).

[2] Cree®XLamp®LED Thermal Management.pdf available at http://www.leds.de/out/media/W_rmemanagement.be4e8996.pdf

[3] http://s3.mentor.com/public_documents/datasheet/products/mechanical/products/flotherm.pdf

[4] N. Kafadarova and A. Andonova, "Thermal Design of RGB LED Modules" in *Proc. of ICEP2009*, 14–16 April, Kyoto, Japan, 2009, pp. 508–512.

[5] A. V. Andonova, N. M. Kafadarova, V. H. Videkov and S. K. Andreev, "Investigation of Thermal Conductivity of PCB" in *Proc. of ISSE2009*, 13-17 May, 2009, Brno, Czech Republic, pp. 321–325.

[6] E. Juntunen, O. Tapaninen, A. Sitomaniemi, M. Jämsä, V. Heikkinen, M. Karppinen and Pentti Karioja, *IEEE Transactions* **29**, 1410–1417 (2014).

[7] Optimizing PCB Thermal Performance for Cree®XLamp®LEDs.pdf available at http://www.cree.com/~/media/Files/Cree/LED%20Components%20and%20Modules/XLamp/XLamp%20Application%20Notes/PCB_Thermal_XQ_XH.pdf

ИНОВАТИВНО ИЗСЛЕДВАНЕ НА ТОПЛООБМЕНА В СВЕТОДИОДНИ МОДУЛИ ЧРЕЗ ТОПЛИННИ СИМУЛАЦИИ

Н. Вакрилов[1], А. Андонова[2]

[1] *Физически факултет, Пловдивски университет "Паисий Хилендарски", ул. "Цар Асен" №24, 4000 Пловдив, България*
[2] *Факултет по електронна техника и технологии, ТУ–София, бул. "Климент Охридски", 1000 София, България*

(Резюме)

В настоящата работа е направен критичен анализ на топлообменните процеси в светодиоден модул чрез 3D CFD топлинно моделиране. Създаден е топлинен 3D модел на светодиодна матрица и е изследвана неговата топлинна ефектиност. От направените топлинни симулации са намерени топлинните напрежения в структурата и са предложени подходи за оптимизация на конструкцията и повишаване на надеждността. За тази цел са създавани цифрови модели на конструкции на печатната платка с различни конфигурации топлинни отвори. Направен е анализ на FR4 печатна платка с 4, 5 и 9 топлинни отвора и е изследвано въздействието на различни запълващи материали – въздух, мед и SnAgCu, за да се изяснят комплексните взаимовръзки на топлоотвеждането в структурата.

Bulgarian Chemical Communications, Volume 47, Special Issue B (pp. 528–531) 2015

Application of the scientific research approach in science education in Language School "Plovdiv", Plovdiv

K. Katsarova*, R. Kaleva-Levi

Plovdiv Language School, 123 Bulgaria Blvd., 4003 Plovdiv, Bulgaria

In this article two science teachers from one Bulgarian high school share their experience with teaching science using inquiry based science education approach (IBSE). They describe their point of view for the importance of the IBSE and its impact on the effectiveness of teaching.

Key words: inquiry based science education

The important thing about science is not so much the discovery of new facts as the discovery of new approaches for their explanation.
Sir William Henry Bragg

The National Program for the development of secondary education and the educational training in schools (2006-2015 year) mark as the first major problem the "orientation of the system towards memorizing and citing, and not to provoke critical thinking, independence and formation of skills" [8].

Studies conducted in the country by the Institute for Population and Human show that "80 % of teenagers explore the world by using emotions for what they do and this style is the exact opposite from the elder's style, which is dominated by logic and structure." Ass. Prof. Antoaneta Hristova, who conducted the study, believes that "in order to overcome the negative effects, it is necessary to introduce the research approach in education, in order to change priorities in teaching" [9].

We support this view, because if such an approach is used, then the teaching will be more based on "studying" the problem or the phenomenon. The end goal is the self-discovery of the facts and the connections between them. This can develop critical thinking, which is only characteristic to humans.

Today dynamic life requires changes in the educational policies, in order a modern educational system, which allows for expression of each student, to be build. There is a real need for rationalization of the leisure time of young people through activities, which develop their creative interests and abilities.

A review of the educational reforms worldwide, highlights a general trend towards the main aim of natural-school education – the formation of natural science literacy (Hurd, 2000; Bartholomew et al., 2004; Hodson, 2006, 2008; Osborne & Dillon, 2008; Dillon, 2009).

Besides the specific characteristics of educational reforms in the different countries, a general trends and problems are being observed. Their discussion and coordination is in the focus of the work of international organizations involved in educational activities. Such an international project, sponsored by the European Commission with a duration of 3 years is "Chain Reaction". Its purpose is to train science teachers to use an approach in which the students are performing real research ("learning by research" (IBSE)) [10].

This is completely understandable In light of the new strategy of the European countries, called "2020", which focuses on the key areas of knowledge and innovation to achieve more sustainable economy and higher employment. It is guaranteed by the EU, which targets to be implemented at national level.

EG "Plovdiv", which include the project in 2013 by PW "P. Hilendarski", have traditions and continuity in terms of science education, held by qualified teachers, graduates of language schools. (It is among the few schools in the country associated with UNESCO by Decree of the State Council of the People's Republic 1517 / 19.05.1983, the school was awarded with medal "Cyril and Methodius" - first grade for high achievements in educational activity. On 10.07.1988 year, the Presidium of the League of friendship between peoples in Berlin, awarded the school with medal for friendship between peoples, and on 19.05.2001 The Ministry of Education has

* To whom all correspondence should be sent:
sigen_consult@abv.bg

© 2015 Bulgarian Academy of Sciences, Union of Chemists in Bulgaria

recognized the school with an honorary award "Neophyte Rilski", for a comprehensive and highly professional activity in the system of public education. Decision of the municipal council, from the city of Plovdiv, on 15.05.2003, gave the high school the proud name "Plovdiv", as the highest honorary award from the city, for the significant contribution to the development of the city and its contributions to the citizens).

Our extracurricular activities, which accompanies and support the learning process, have a significant role in enhancing students' interest to the education. They contribute to the formation of civic personalities, associated with the values of a democratic society and are a form of prevention of risky behaviors and health promotion through health and civic education. They provide ample opportunities for the involvement of various stakeholders, partners and supporting structures - parents, NGOs, the media, civil society in education.

Over 95 % of graduates of EV "Plovdiv" continue their education in high schools in the first year after graduation, thanks to the exceptional performance of internationally recognized exams such as: SAT, TOEFL, DSD, Test DAF and others. Currently, about 180 alumnus are working in world universities in USA, UK, Germany, France, Canada and Japan.

Project "Chain Reaction" offers an interactive and entertaining training methods "learning through research" (IBSE), which is contributing to the professional development of science teachers from each participating countries. The teacher can organize a series of lessons in which students independently examine the proposed topics, in series of materials using applied resources and practical tests as scientific resources.

The seriousness of the phenomenon "free time" among the youth, objectively necessitates a concerted action to create a multipurpose model to attract young people and engage them in various activities carried out in school environments. The lack of these features among the younger generation puts the issue of missed educational impacts. N. Boyadjieva states that "much of the phenomenon free time" is riddled with extremely neuralgic points "in the education and socialization of todays young generation in the country" [1].

Overcoming these weaknesses is training and educating, which gradually is becoming a priority. It is the school, which has to become a desirable area for exhibiting knowledge, skills and competencies of adolescents.

Project "Chain Reaction" is a good opportunity for students aged 14-16 years to have meaningful leisure time and work together on the proposed scenarios, forming their critical thinking skills and problem solving.

In their writings writers M. Andreev, D. Tsvetkov, Pl. Radev and others are describing the multiples "extra-organizational forms", "extracurricular non educational, organizational systems" or "external forms of education" [1,3,5] P. Petrov also pay attention summarizes that "in the system of organizational forms of training, extracurricular activities at school play prominent role" [2].

Generally, extracurricular activities, are targeted activities performed outside of school hours, but organized with the funds and resources of the school or the university. They also are targeted activities outside of school hours, which are organized by various educational institutions and NGOs, without using resources of the school in which they are trained [1-4].

E. Feldman and J. Matyasko bring concrete evidence that the involvement of students in extracurricular activities has a positive impact on their personal development. They pay special attention to the details of the extracurricular environment. They are certain that under these conditions youths develop number of specific skills, that are essential for their development (coping skills in atypical situations, communication with a wide range of people with similar interests, a sense of collective responsibility etc.), which cannot be utilized in the classroom. Young people get to know, prove and define themselves in a characteristic environment. Relationships change in the direction of cohesion and understanding in atypical conditions, which is a good opportunity to show students and others how to develop their skills. Particularly sensitive is the change of the communication and implementation of joint tasks. Gradually young people acquire the skills to complement each other's work and to flexibly allocate tasks, which leads to increased enthusiasm and motivation for new activities [7].

Our observations in the course of the implementation of the main tasks, during the execution of the project, have confirmed this. Despite the time constraints, insufficient information, etc., participants found ample opportunities for creative expression. The demand for and the use of additional sources of knowledge – Internet, encyclopedias, movies, dictio-

Table 1. Stages of the research process

Preliminary stage (What is this?)							
Subject			Goal				
Subject	Object	Expected Product	Task of the study				
Research stage (What?)							
Hypothesis			**Proof Of Hypothesis**				
State of the object and the subject of study in the theory	Status in the subject viewed in practice	Summary of hypothesis	Theoretical proof of concept	Experimental proof	Description of facts, processes	Experimental evidence	Conclusion
Final Stage (What is next?)							
Evaluation of the results, including and final verification of the hypothesis			Opportunities for the implementation of the results in practice			Guidelines for new research	
REPRESENTATIVE (formal) stages ("The Shell"!)							
Shaping	Binding	Reviews	Autoreference (summary, annotation) of the study (printing)			Protection of development (presentation and sale of research products)	

naries, books and others, not only confirmed and enriched the learning process for them, but they also unleashed their personal, emotional and intellectual potential. In their joint activity they showed an exceptionally high degree of motivation.

The summary of the main stages of research process is presented in Table 1 (1).

Project participants saw the result of their activity – the fruit of their joint efforts. The team of young scientists – physicists, were ranked first.

Research in recent decades from scientists, educators and psychologists definitely prove that "the formation of the whole person is done best in terms of its activity" [1,7,8]. The systems of The "research approach" is well distributed in highly developed countries, says noted academician. D. Damianov – Deputy Chairman of the BAS.

The world has changed and the education system, which is conservative, cannot react as fast in order to incorporate all innovations in it, said Academician. Kenderov Peter, who also noted that "lifelong learning" takes on a new meaning and is backing the research approach that does not force knowledge and learning, but instead motivates young people to experiment. According to him, this approach has already entered the Bulgarian educations system through European projects [8].

We are proud that EG "Plovdiv", which has celebrates its 55th anniversary, has more than 7,000 alumni who assert and develop the best, which they have learned from it.

REFERENCES

[1] P. Lulanski, *Economic Alternatives* **1 (EN)**, (2005).

[2] P. Petrov, *Didactics. S.*, (2001).

[3] P. Radev, *General school didactics. P.*, (2005).

[4] E. Rangelova, *Methods of educational activities. G.*, (2005).

[5] D. Tsvetkov, *General Education. Philosophy of education. S.*, (1994).

[6] B. Tsvetkov, Forms for extracurricular activities and izvanuchilishni youth program "Youth in Action".

[7] A. Feldman, and J. Matjasko, *Educational Research* **75 (2)**, 159–210 (2005).

[8] National program for development of secondary education - 2005/2010.

[9] www.investor.bg/.../ban-predlaga-izsledovatelski-podhod-v-obrazovanieto

[10] http://chainreact.dipseil.net/

[11] http://www.chreact.eu/?q=node/10

ПРИЛОЖЕНИЕ НА НАУЧНО-ИЗСЛЕДОВАТЕЛСКИЯ ПОДХОД В ОБУЧЕНИЕТО ПО ПРИРОДНИ НАУКИ В ЕЗИКОВА ГИМНАЗИЯ "ПЛОВДИВ", ГРАД ПЛОВДИВ

К. Кацарова, Р. Калева-Леви

ЕГ "Пловдив" гр. Пловдив, бул. "България" №123 4003 Пловдив, България

(Резюме)

"*Важното за науката не е толкова откриването на нови факти,*
а откриването на нови подходи за тяхното обяснение."
Sir William Henry Bragg

Националната програма за развитие на средното образование и пред училищна подготовка (2006-2015 година) отчита като първи основен проблем "*ориентираност на системата към запаметяване и възпроизвеждане, а не към провокиране на мислене, самостоятелност и формиране на умения*" [1].

Динамиката на съвременността налага промяна в образователната политика и изграждане на модерна образователна система, която да даде възможност за изява на всеки ученик. Наред със специфичните характеристики на образованието в различните държави, се открояват и общи тенденции и въпроси за решаване. Тяхното обсъждане и съгласуването им е във фокуса на работата на международни организации, ангажирани с активни образователни дейности. Един такъв международен проект, спонсориран от Европейската комисия с продължителност 3 години, е "Chain Reaction". Неговата цел е да обучи учители по природни науки в използването на подход, при който учениците да се включват в изследователска дейност ("учене чрез изследване" (IBSE)) [3].

Проектът "Chain Reaction" предлага интерактивно и занимателно обучение по метода "учене чрез изследване" (IBSE), което е и принос към професионално развитие на учители по природни науки от всяка една от участващите страни. Обучаващият може да организира серия от уроци, в които учениците самостоятелно да разглеждат предложените в материалите теми, използвайки прилагани и тествани в практиката научни ресурси [2].

В статията се описва работата и резултатите от нея на учителите Р. Калева - Леви (биология) и К. Кацарова (физика) от ЕГ "Пловдив", гр. Пловдив, която се включи в проекта през 2013 година чрез ПУ "П. Хилендарски".

Темите, по които е работено по време на организираното по този метод обучение са: Зелена светлина и Животоподдържаща система в Космоса. В предложената работа се описват наблюденията на учителите по отношение на резултатите от използването на изследователския метод в обучението по природни науки по отношение на дейността на учениците, тяхната активност, мотивираност и личностна ангажираност, както и постигнатите учебни резултати.

Смятаме че, тя представлява интерес, както за учители по природни науки така и за изследователи в областта на педагогическите науки.

1. Националната програма за развитие на средното образование – 2005/2010
2. http://www.chreact.eu/?q=node/10
3. http://chainreact.dipseil.net/

Bulgarian Chemical Communications, Volume 47, Special Issue B (pp. 532–536) 2015

Enhancing elementary student learning in natural sciences through mobile augmented reality technology

D. Stoyanova*, N. Kafadarova, S. Stoyanova-Petrova

Faculty of Physics, Paisii Hilendarski University of Plovdiv, 24 Tsar Asen Str., BG-4000 Plovdiv, Bulgaria

The main aim of the presented paper is to describe the implementation of Mobile Augmented Reality (MAR) applications in teaching practice as an innovative way to transfer knowledge in education. It has been envisioned to revolutionize the way in which information is accessed and presented to students and thus enhance their perceptions. Although MAR technology is not new, its potential in education is relatively unexplored. This was the reason the "Research&Development" Division of Plovdiv University to start a research project dealing with the usage of augmented reality technology with mobile devices in the learning process. The aim is to design, develop, implement and evaluate innovative mobile services using augmented reality technology in the natural science education in elementary school. The project started in 2013 and its duration is 2 years.

The hypothesis of the study is that mobile augmented reality technology can be successfully applied in Bulgarian elementary schools and has didactical value. In order to confirm or reject this hypothesis, a pedagogical study was conducted by developing a system of mobile augmented reality applications and usage of adequate diagnostic tools. The system of MAR applications developed within the project includes the following components:

- A mobile application in which multimedia models of objects from the "Man and Nature" textbook are visualized by using augmented reality technology. They can be seen on the screen of a smartphone or tablet.
- An adapted mobile application with augmented reality in astronomy for the needs of students in Bulgarian primary school.

The implementation of these MAR applications in teaching practice is organized as a pilot experiment. Teachers and 4th grade students from several elementary schools has participated in the experiment. The data obtained from the study is evaluated using Microsoft Excel. The results clearly demonstrate the potential benefits of using MAR in the learning process.

Key words: augmented reality, mobile learning, educational technology

INTRODUCTION

Augmented Reality (AR) is considered to be one of the most promising technologies likely to impact the way we teach and learn [1]. The potential power of AR as a learning tool is its ability "to enable students to see the world around them in new ways and engage with realistic issues in a context with which the students are already connected" [2].

In this paper we describe our experience in applying this technology to enhance elementary student learning in natural sciences. The pilot study is within a research project entitled "Usage of Augmented Reality Technology with Mobile Devices in the Learning Process", within the research project competition of the "Research &Development" Division of Plovdiv University "Paisii Hilendarski". The project started in 2013 and its duration is two years.

THE MAR PACKAGE

The project aim is to design, develop, implement and evaluate innovative mobile services using augmented reality technology in the natural science education in primary school [3].

The achievement of this aim involves completing of the following tasks:

1. Developing didactic models of using "augmented reality" technology and mobile technologies in the context of natural science education in elementary school.
2. Designing and developing a SYSTEM with mobile "augmented reality" applications for natural science education in elementary school.
3. Preparing audio visual and multimedia learning resources for mobile devices in accordance with the characteristics of natural science education in primary school.
4. Integrating the learning resources in the developed System of mobile applications and their implementation in education - MAR package (Mobile Augmented Reality).
5. Conducting an experimental study of the pedagogical efficiency of the use of "augmented reality" technology through the use of mobile devices in natural sciences teaching at primary schools.
6. Analyzing the results.

* To whom all correspondence should be sent:
di_vest@yahoo.com

© 2015 Bulgarian Academy of Sciences, Union of Chemists in Bulgaria

The development of didactic models using "augmented reality" technology and mobile technologies in the context of natural science education in elementary school is done according to the following predefined conditions:

- consistency with the requirements of the state educational curriculum documents and teaching textbooks available;
- consistency with the requirements of the target group of users - students and teachers in primary education;
- specific features of mobile platforms;
- characteristics of the digital objects presentation and accessing them by mobile devices in all popular formats: text, images, video, audio;
- possibilities of "augmented reality" technology.

Based on the didactic model a SYSTEM with mobile "augmented reality" applications for natural science education in elementary school is developed in the following variants:

- visualization of multimedia object models from the "Man and Nature" textbook which can be seen on the screen of a smartphone or tablet (Fig. 1);
- adapted mobile application with augmented reality in astronomy for the needs of students in Bulgarian primary school (Fig. 2).

Audio visual and multimedia learning resources for mobile devices are created in accordance with the characteristics of natural science education in primary school.

The final result of the integration of teaching materials in the developed system with mobile applications and their implementation in education on the basis of the established teaching model we called "The MAR package".

IMPLEMENTATION OF THE MAR PACKAGE IN TEACHING PRACTICE

Methodology of the study

The organization of the pilot study aims confirmation of the project hypothesis, which is: mobile augmented reality technology can be successfully applied in Bulgarian elementary schools and has a didactical value.

Objects of our study are:

- The quality of the developed digital learning resources
- Students' and teachers' attitude toward the MAR package

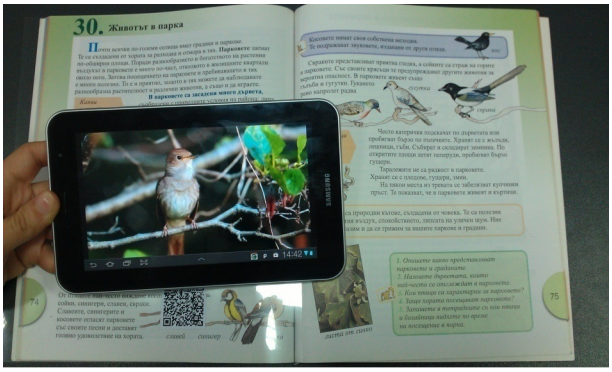


Fig. 1. Multimedia educational material started after scanning the relevant QR code.

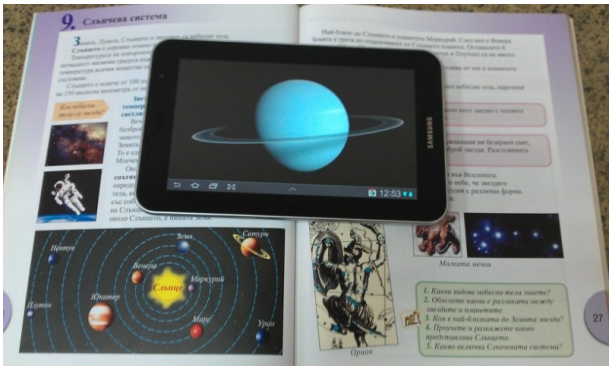


Fig. 2. Developed application for viewing sky objects by using Google SkyMap.

The following diagnostic methods are used:

- Expert assessment- for analyzing the quality of the developed digital learning resources for mobile devices
- Classroom observation
- Interview Face-to-face interviews with students in order to understand their perception of using the mobile "augmented reality" technology in education
- Completion of a questionnaire by the students participating in the study
- Video Analysis- analyzing videos captured during classes, in order to obtain more reliable information.

The implementation of the MAR package in the teaching practice is organized as a pilot experiment with the 4th grade students from two Plovdiv schools (Fig. 3, Fig. 4). The total number of participating students is 92 (52% of them are girls and 48% are boys).

The experiment involves an use of the mobile "augmented reality" technology in the "Solar system", "Life in the Park", "Life in the marshes" lessons from the "Man and Nature" textbook for 4th grade.



Fig. 3. Pilot experiment.



Fig. 4. Pilot experiment.

For this purpose, we selected three video clips presenting in an attractive way: the Sun and the planets of the Solar system, a singing nightingale (Life in the park) and a great diving beetle (Life in the marshes). Each of the videos supplements and expands the learning content in the textbook.

Teachers, involved in the experiment, were pretrained how to work with the MAR package. These teachers together with team members prepared plan scenarios of lessons in which "augmented reality" technology and mobile technology are embodied by using the MAR package. The location of each generated QR code on the transparencies was also pre-set.

Members of the team project attended the lessons in order to observe the learning process. All lessons were recorded by video camera which allowed us to conduct a subsequent analysis.

Before the beginning of each lesson, students and teachers were handed tablets and transparencies with the corresponding QR code. All tablets were purchased with project funds. The teacher instructed students how to work with tablets wright before the first scanning of a QR code.

After each lesson a face -to -face interview with two randomly selected children from a class (a girl and a boy) was conducted. All questions in the interview are open-ended.

At the end of the experiment, students were asked to complete a questionnaire with 7 questions. All questions are closed-ended.

Results analysis

Our observations during lessons show that:

1. Students did not encounter any difficulties in working with tablets. The teacher gave instructions to students only one time, just before the very first scanning of a QR code and then the children worked entirely alone. This shows that mobile devices are a suitable tool for education, because there is no need of preliminary training of students in using them.
2. All our fears that mobile devices can be distracting to students proved completely unfounded. Children worked with tablets only when teachers allowed this. We noticed only one child who was playing with the tablet during the lesson.
3. There was some slowdown in the learning process during the lesson "Solar system". The slow Internet connection and the relatively large file size of the video clip (about 18MB) delayed the opening of the video, which is a potential risk for the discipline in the classroom. The other two videos were small in size and opened almost immediately. This indicates that digital resources should be with a file size less than 10 MB.
4. The students easily answered most of the questions concerning the observed digital resources. Even in the lesson "Solar System", it was observed that many children used in their answers words and phrased from the video. This is certain evidence that the technology "augmented reality" stimulates their cognitive activity.
5. Students were very excited to work with tablets but this doesn't hinder the lesson. On the con-

trary, we can say that mobile devices stimulate their interest and they actively participated in all class games and tasks. After lessons many children asked us such questions like: "When will we use tablets again?"; "Where can we download these clips from?". This clearly and doubtlessly proves their interest.

At the end of the experiment, students completed a questionnaire. The purpose of the survey was to examine their attitude towards the use of mobile "augmented reality" technology in the learning process.

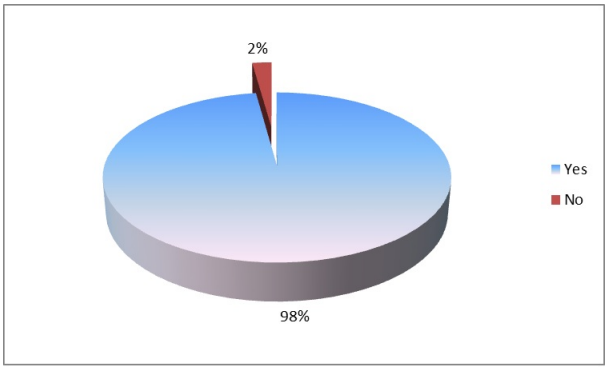


Fig. 5. Did you receive enough information from the videos about the Solar system / A singing nightingale / The great diving beetle?.

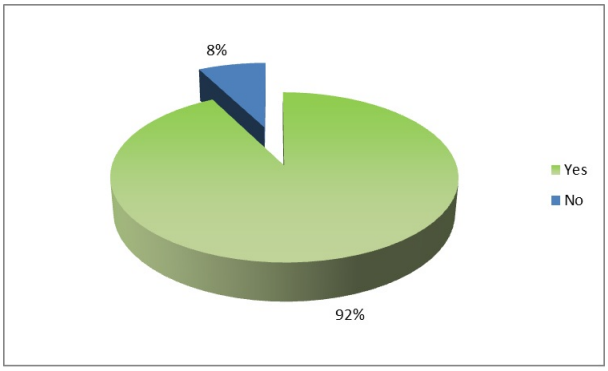


Fig. 6. Would you like to watch these videos at home?

All students answered "Yes" to the question "Was it interesting to use tablets during the lesson?". 98% of children give a positive response to the second question, "Did you receive enough information from the videos about the Solar system / A singing nightingale / The great diving beetle?" (Fig. 5). 92% of students would like to watch these videos at home (Fig. 6). Furthermore, 99% believe that this technology has helped them to learn more easily (Fig. 7), and all would like this technology to be used in other

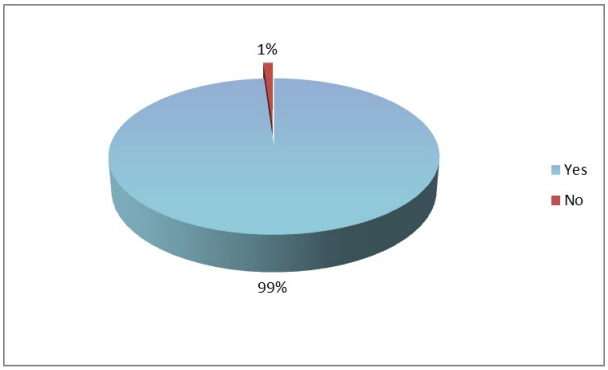


Fig. 7. Do you think that this technology has helped you to learn more easily the lesson?

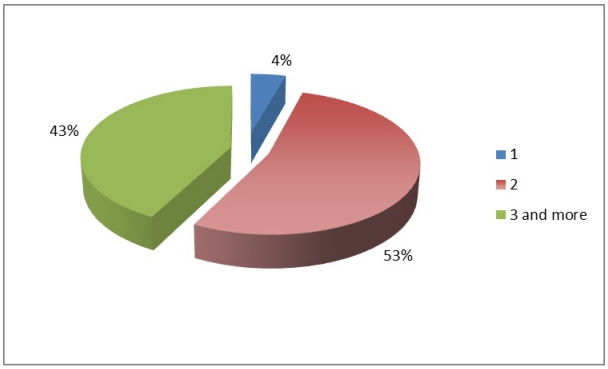


Fig. 8. How many times have you observed the videos?

lessons from "Man and Nature". To the question "How many times have you observed the videos?" 4.3% answered 1 time, 53.3% – 2 times and 42.4 percent – three times or more (Fig. 8). Variation in responses to this question is due to the fact that on each tablet video files have been downloaded with different speed and that automatically affects the number of observations. 95% give a positive response to the question "Would you like to show these videos to someone else?".

CONCLUSIONS

Results from the pilot study doubtlessly reveal that the mobile "augmented reality" technology is positively accepted by all students. We observe that the usage of tablets in the classroom does not distract students. Moreover, we can conclude that mobile devices are a suitable tool for education, because there is no need of preliminary training of children how to use them. The collected data show that mobile "augmented reality" technology stimulates students' interest in learning content and encourage their cognitive activity. It makes learning more attractive and fun,

which is essential for achieving educational effectiveness.

Acknowledgments. *The authors would like to acknowledge the support of the projects ID13 FF/005 and NIS14-FFIT-009 of the "Research & Development" division of Plovdiv University and the project "Project-based Adaptive Learning Curriculum for the Needs of Business and Employment - PAUP" PROJECT BG051PO001-3.1.07-0002.*

REFERENCES

[1] S. Martin, G. L. Diaz, E. Sancristobal, R. Gil, M. Castro and J. Peire, *Computers & Education* **57** (3), 1893–1906 (2011).

[2] E. Klopfer and J. Sheldon, *New Directions for Youth Development* **28**, 85–94, (2010).

[3] S. Stoyanova-Petrova, N. Kafadarova and D. Stoyanova, "Using the Potential of Mobile Augmented Reality for Teaching/Learning Elementary School Natural Sciences" in *Proceedings of International Conference of Education, Research and Innovation (ICERI2013)*, 18-20 November 2013, Seville Spain, pp. 1721–1726.

ПОДОБРЯВАНЕ НА РЕЗУЛТАТИТЕ ОТ ОБУЧЕНИЕТО ПО ПРИРОДНИ НАУКИ В НАЧАЛНОТО УЧИЛИЩЕ ЧРЕЗ ИЗПОЛЗВАНЕ НА ТЕХНОЛОГИЯТА "ДОБАВЕНА РЕАЛНОСТ" С МОБИЛНИ УСТРОЙСТВА

Д. Стоянова, Н. Кафадарова, С. Стоянова-Петрова

Физически факултет, Пловдивски университет "Паисий Хилендарски",
ул. "Цар Асен" №24, 4000 Пловдив, България

(Резюме)

Основната цел на статията е да се опише използването на технологията "добавена реалност" с мобилни устройства и съответните приложения в преподавателската практика като иновативен начин за предаване на знания в областта на образованието. Посредством тази иновативна технология съществено може да се промени начина, по който информацията е достъпна и се представя на учениците, което ще подобри техните възприятия. Въпреки че, технологията "добавена реалност" не е нова, нейният потенциал в областта на образованието е сравнително неизследван. Това е причината, поради която поделение "Научна и приложна дейност" на Пловдивския университет финансира проект, който изследва използването на технологията "добавена реалност" с мобилни устройства в процеса на обучение. Целта е да се проектират, разработят, внедрят и оценят иновативни мобилни услуги чрез използване на технологията "добавена реалност" (augmented reality) в обучението по природни науки в началното училище. Проектът стартира през 2013 г. и е с продължителност две години.

Изследването е подчинено на хипотезата, че използваната иновативна технология "добавена реалност" с използване на мобилни устройства е успешно приложима в началното образование в българското училище и има дидактическа стойност. За потвърждаване или отхвърляне на тази хипотеза, е проведено педагогическо изследване, като са разработени подходящи мобилни приложения с добавена реалност и е използван адекватен диагностичен инструментариум.

Системата от приложения MAR, разработена в рамките на проекта включва:

- Мобилно приложение за визуализиране на мултимедийни модели на обекти от съответния използван учебник по "Човекът и природата", които могат да бъдат визуализирани на дисплей на смартфон или таблет;
- Адаптирано мобилно приложение с добавена реалност по астрономия за нуждите на учениците в българското начално училище.

Внедряването на тези мобилни приложения в преподавателска практика бе организирано като пилотен експеримент. В експеримента участваха четвъртокласници от две пловдивски училища. Резултатите от пилотния експеримент несъмнено показват, че технология "добавена реалност" с мобилни устройства се възприема положително от всички ученици. Използването на таблети в класната стая не отвлича вниманието на учениците. Освен това, можем да заключим, че мобилните устройства са подходящ инструмент за обучение, тъй като не изисква от децата предварителна подготовка за работа с тях. Анализът на получените резултати показва, че технологията "добавена реалност" с мобилни устройства стимулира интереса на учениците към учебното съдържание и насърчават тяхната познавателно дейност. Това прави ученето по-привлекателно и забавно, което е от съществено значение за постигането на образователна ефективност.

BULGARIAN CHEMICAL COMMUNICATIONS

Instructions about Preparation of Manuscripts

General remarks: Manuscripts are submitted in English by e-mail or by mail (in duplicate). The text must be typed double-spaced, on A4 format paper using Times New Roman font size 12, normal character spacing. The manuscript should not exceed 15 pages (about 3500 words), including photographs, tables, drawings, formulae, etc. Authors are requested to use margins of 3 cm on all sides. For mail submission hard copies, made by a clearly legible duplication process, are requested. Manuscripts should be subdivided into labelled sections, e.g. **Introduction, Experimental, Results and Discussion**, *etc*.

The title page comprises headline, author's names and affiliations, abstract and key words.

Attention is drawn to the following:

a) **The title** of the manuscript should reflect concisely the purpose and findings of the work. Abbreviations, symbols, chemical formulas, references and footnotes should be avoided. If indispensable, abbreviations and formulas should be given in parentheses immediately after the respective full form.

b) **The author**'s first and middle name initials, and family name in full should be given, followed by the address (or addresses) of the contributing laboratory (laboratories). **The affiliation** of the author(s) should be listed in detail (no abbreviations!). The author to whom correspondence and/or inquiries should be sent should be indicated by asterisk (*).

The abstract should be self-explanatory and intelligible without any references to the text and containing not more than 250 words. It should be followed by key words (not more than six).

References should be numbered sequentially in the order, in which they are cited in the text. The numbers in the text should be enclosed in brackets [2], [5, 6], [9–12], etc., set on the text line. References, typed with double spacing, are to be listed in numerical order on a separate sheet. All references are to be given in Latin letters. The names of the authors are given without inversion. Titles of journals must be abbreviated according to Chemical Abstracts and given in italics, the volume is typed in bold, the initial page is given and the year in parentheses. Attention is drawn to the following conventions:

a) The names of all authors of a certain publications should be given. The use of "*et al*." in the list of references is not acceptable.

b) Only the initials of the first and middle names should be given.

In the manuscripts, the reference to author(s) of cited works should be made without giving initials, e.g. "Bush and Smith [7] pioneered...". If the reference carries the names of three or more authors it should be quoted as "Bush *et al*. [7]", if Bush is the first author, or as "Bush and co-workers [7]", if Bush is the senior author.

Footnotes should be reduced to a minimum. Each footnote should be typed double-spaced at the bottom of the page, on which its subject is first mentioned.

Tables are numbered with Arabic numerals on the left-hand top. Each table should be referred to in the text. Column headings should be as short as possible but they must define units unambiguously. The units are to be separated from the preceding symbols by a comma or brackets.

Note: The following format should be used when figures, equations, *etc*. are referred to the text (followed by the respective numbers): Fig., Eqns., Table, Scheme.

Schemes and figures. Each manuscript (hard copy) should contain or be accompanied by the respective illustrative material as well as by the respective figure captions in a separate file (sheet). As far as presentation of units is concerned, SI units are to be used. However, some non-SI units are also acceptable, such as °C, ml, l, etc.

The author(s) name(s), the title of the manuscript, the number of drawings, photographs, diagrams, etc., should be written in black pencil on the back of the illustrative material (hard copies) in accordance with the list enclosed. Avoid using more than 6 (12 for reviews, respectively) figures in the manuscript. Since most of the illustrative materials are to be presented as 8-cm wide pictures, attention should be paid that all axis titles, numerals, legend(s) and texts are legible.

The authors are asked to submit **the final text** (after the manuscript has been accepted for publication) in electronic form either by e-mail or mail on a 3.5'' diskette (CD) using a PC Word-processor. The main text, list of references, tables and figure captions should be saved in separate files (as *.rtf or *.doc) with clearly identifiable file names. It is essential that the name and version of the word-processing program and the format of the

text files is clearly indicated. It is recommended that the pictures are presented in *.tif, *.jpg, *.cdr or *.bmp format, the equations are written using "Equation Editor" and chemical reaction schemes are written using ISIS Draw or ChemDraw programme. The authors are asked to submit the final text with a list of three potential reviewers. The Editorial Board of the journal is not obliged to accept these proposals.

EXAMPLES FOR PRESENTATION OF REFERENCES

REFERENCES

1. D. S. Newsome, *Catal. Rev.–Sci. Eng.*, **21**, 275 (1980).
2. C.-H. Lin, C.-Y. Hsu, *J. Chem. Soc. Chem. Commun*., 1479 (1992).
3. R. G. Parr, W. Yang, Density Functional Theory of Atoms and Molecules, Oxford Univ. Press, New York, 1989.
4. V. Ponec, G. C. Bond, Catalysis by Metals and Alloys (Stud. Surf. Sci. Catal., vol. 95), Elsevier, Amsterdam, 1995.
5. G. Kadinov, S. Todorova, A. Palazov, in: New Frontiers in Catalysis (Proc. 10th Int. Congr. Catal., Budapest, 1992), L. Guczi, F. Solymosi, P. Tetenyi (eds.), Akademiai Kiado, Budapest, 1993, Part C, p. 2817.
6. G. L. C. Maire, F. Garin, in: Catalysis. Science and Technology, J. R. Anderson, M. Boudart (eds), vol. 6, Springer-Verlag, Berlin, 1984, p. 161.
7. D. Pocknell, *GB Patent* 2 207 355 (1949).
8. G. Angelov, PhD Thesis, UCTM, Sofia, 2001.
9. JCPDS International Center for Diffraction Data, Power Diffraction File, Swarthmore, PA, 1991.
10. CA **127**, 184 762q (1998).
11. P. Hou, H. Wise, *J. Catal.*, in press.
12. M. Sinev, private communication.
13. http://www.chemweb.com/alchem/articles/1051611477211.html.

CONTENTS

PHOTONICS AND TELECOMMUNICATIONS

T. Pashova, I. Kostova, T. Eftimov, D. Tonchev, Analysis of fluorescence spectra of oxyfluoride compositions doped with samarium oxide (Sm_2O_3) and samarium fluoride (SmF_3) 9

V. Plachkova, P. Balzhiev, G. Dyankov, T. Eftimov, P. Petrov, Research of 16-channel fiber-optic (FO) system for measuring long period sensor networks (LPSN) 15

E. Karakoleva, B. Zafirova, A. Andreev, Calculations of photonic crystal fibers by the Galerkin method with sine functions without a refractive index approximation 21

A. Lalova, R. Todorov, Optical properties of thin PMMA films for sensor application 29

E. V. Penchev, W. J. Bock, T. A. Eftimov, P. Mikulic, Using double resonance long period gratings to measure refractive index of milk of varying fat content 35

R. Todorov, A. Lalova, V. Lozanova, Optical properties of thin Ag/As-S-Ge films 40

S. Kasarova, N. Sultanova, I. Nikolov, Polymer materials in optical design 44

V. Lozanova, R. Todorov, Microstructure and optical properties of thermally evaporated very thin silver films 55

CONDENSED MATTER PHYSICS

S. Alexandrova, A. Szekeres, E. Valcheva, Silicon surface modified by H^+ ion plasma immersion implantation and thermal oxidation 63

M. Milanova, P. Vitanov, P. Terziyska, G. Koleva, C. Barthou, B. Clerjaud, Study of LPE grown dilute nitride GaInAsN layers with small concentration of Nitrogen by PL and Hall effect measurements 71

L. Bedikyan, S. Zakhariev, M. Zakharieva, UV selective photodetector based on nanosized TiO_2 layers . 76

A. Hristova, T. Dimov, I. Iliev, Impurity absorption in uniaxial gyrotropic crystals of magnesium sulfite hexahydrate 80

G. S. Valchev, V. M. Vassilev, P. A. Djondjorov, On different models describing the equilibrium shape of erythrocyte 84

I. Petrova, E. Ivanov, R. Kotsilkova, Structure and properties of polypropylene containing organo-clay and carbon nanotubes as fillers 95

A. Guzhova, M. Galikhanov, Charge depth in polylactic acid electret filled with fine filler 103

V. Dryakhalov, T. Shaikhiev, I. Shaikhiev, I. Zagidullina, B. Bonev, V. Nenov, Intensification of breaking of water-in-oil emulsions by membranes treated in the area of corona discharge or in the plasma flow 109

A. Guzhova, T. Yovcheva, A. Viraneva, Study of polylactic acid corona electrets 115

A. Viraneva, T. Yovcheva, K. Krezhov, S. Sotirov, Electret stability of gamma irradiated PP and PET films 121

M. Marudova, E. Delcheva, G. Zsivanovits, Mechanical properties of composite films based on chitosan and poly(L-lactic acid) 127

P. Petkova, P. Vasilev, M. Mustafa, V. Nedkov, J. Tacheva, Y. Tzoukrovsky, Optical spectra of the complexes $[M(H_2O)_6]^{2+}$ and MSO_3–$(H_2O)_2$ ($M = Ni^{2+}$) 135

D. L. Lyutov, G. G. Tsutsumanova, S. C. Russev, Ellipsometry of micro-objects and structures 140

© 2015 Bulgarian Academy of Sciences, Union of Chemists in Bulgaria

CONTENTS

S. A. Hadjiiski, D. L. Lyutov, K. M. Kirilov, K. V. Genkov, G. G. Tsutsumanova, A. N. Tzonev, S. C. Russev, Ellipsometric detection of optically and electron-beam induced changes in the optical properties of materials 147

K. V. Genkov, G. G. Tsutsumanova, S. A. Hadjiiski, A. N. Tzonev, D. L. Lyutov, S. C. Russev, Electron-beam annealing of micro-sized objects and structures in SEM 155

Ts. Mihailova, S. Nedev, E. Toshkov, A. Stoyanov, Structural and electro-physical parameters of n-GaAs 162

E. Valcheva, G. Yordanov, Low temperature photoluminescence studies of colloidal CdSe nanocrystals . 168

V. Jelev, P. Petkov, Iv. Markova, T. Petrov, Thin films of metal oxides for preparing of a position sensitive photodetector 173

N. Petkov, Predicting the erosion of the cathode material in PVD systems 177

ATOMIC AND NUCLEAR PHYSICS

M. Shopova, M. S. Kim, Y. Ban, J. Cai, Q. Li, S. Liu, S. Qian, D. Wang, Z. Xu, F. Zhang, Y. Choi, D. Kim, J. Goh, S. Choi, B. Hong, J. W. Kang, M. Kang, J. H. Kwon, K. S. Lee, S. K. Lee, S. K. Park, L. M. Pant, A. K. Mohanty, R. Chudasama, J. B. Singh, V. Bhatnagar, A. Mehta, R. Kumar, S. Cauwenbergh, S. Costantini, A. Cimmino, S. Crucy, A. Fagot, G. Garcia, A. Ocampo, D. Poyraz, S. Salva, F. Thyssen, M. Tytgat, N. Zaganidis, W. V. Doninck, L. Chaparro, A. Cabrera, J. P. Gomez, B. Gomez, J. C. Sanabria, C. Avila, A. Ahmad, S. Muhammad, M. Shoaib, H. Hoorani, I. Awan, I. Ali, W. Ahmed, M. I. Asghar, H. Shahzad, A. Sayed, A. Ibrahim, S. Aly, Y. Assran, A. Radi, T. Elkafrawy, A. Sharma, S. Colafranceschi, M. Abbrescia, C. Calabria, A. Colaleo, G. Iaselli, F. Loddo, M. Maggi, S. Nuzzo, G. Pugliese, R. Radogna, R. Venditti, P. Verwillingen, L. Benussi, S. Bianco, D. Piccolo, P. Paolucci, S. Buontempo, N. Cavallo, M. Merola, F. Fabozzi, O. M. Iorio, A. Braghieri, P. Montagna, C. Riccardi, P. Salvini, P. Vitulo, I. Vai, A. Magnani, A. Dimitrov, L. Litov, B. Pavlov, P. Petkov, A. Aleksandrov, V. Genchev, P. Iaydjiev, M. Rodozov, G. Sultanov, S. Stoykova, R. Hadjiiska, H. S. Ibargüen, M. I. P. Morales, S. C. Bernardino, I. Bagaturia, Z. Tsamalaidze, I. Crotty, Resistive plate chambers for the LS1 muon upgrade in CMS experiment at LHC 185

E. Popov, T. Troev, L. Petrov, K. Berovski, S. Peneva, B. Kolev, Model calculations of positron interaction in materials for ITER 192

D. Suvarieva, M. Ilieva, V. Kolesnikov, V. Vasendina, A. Zinchenko, A feasibility study of hyperon measurements in Au-Au collisions at NICA/MPD 200

L. S. Yordanova for the MPD Collaboration, Feasibility study of $\phi(1020)$ production at NICA/MPD . . . 208

V. Babkin, S. Bazylev, O. Batenkov, P. Dulov, V. Golovatyuk, S. Lobastov, V. Petrov, M. Rumyantsev, A. Schipunov, A. Shutov, I. Slepnyov, V. Slepnyov, A. Veschikov, S. Volgin, V. Yurevich, Fast detectors for the MPD/NICA time-of-flight system 215

M. S. Yavahchova, D. Tonev, N. Goutev, G. de Angelis, P. Petkov, R. K. Bhowmik, R. P. Singh, S. Muralithar, N. Madhavan, R. Kumar, M. Kumar Raju, J. Kaur, G. Mohanto, A. Singh, N. Kaur, R. Garg, A. Sukla, Ts. K. Marinov, S. Brant, Does chirality exist in nuclei? The case of ^{102}Rh 222

Ts. Lazarova, D. Kovacheva, T. Ruskov, S. Atanasova-Vladimirova, P. Krastev, N. Tanev, Composite thin films of nanosized $CoFe_2O_4$ in polymer matrix 227

M. Ilieva, V. Kolesnikov, D. Suvarieva, V. Vasendina, A. Zinchenko, Hypernuclei reconstruction at NICA/MPD: a feasibility study 232

N. S. Geraksiev for the MPD collaboration, Feasibility of flow studies at NICA/MPD 239

B. Marinova, N. Javadov, I. Tyapkin, Monte Carlo study of the electromagnetic calorimeter optimization for MPD/NICA 247

CONTENTS

THEORETICAL AND MATHEMATICAL PHYSICS

V. Filev, R. C. Rashkov, T. Vetsov, Holographic mesons in Pilch-Warner geometry 253

B. G. Dimitrov, Manoff's generalized deviation equation and its possible applications in celestial mechanics and relativistic astrometry 262

E. S. Pisanova, S. I. Ivanov, Non-universal critical properties of the ferromagnetic mean spherical model with long-range interaction 269

A. Angelow, E. Stoyanova, Fundamental quantum limit in Mach-Zehnder interferometer 275

R. S. Kamburova, M. T. Primatarowa, Scattering of solitons from point defects in two coupled Ablowitz-Ladik chains 282

I. K. Ivanov, Application of finite-difference method for numerical investigation of eigenmodes of anisotropic optical waveguides with an arbitrary tensor 287

PHYSICS OF EARTH, ATMOSPHERE AND SPACE. OCEANOLOGY

N. Dobrev, E. Botev, V. Protopopova, I. Georgiev, D. Dimitrov, Seismicity and nowadays movements along some active faults in SW Bulgaria 299

D. Solakov, Biased magnitude estimates – impact on the magnitude-frequency distribution assessment . 309

D. Gospodinov, RETAS model software to identify the best fit model version of aftershock temporal decay 314

G. D. Georgieva, Crustal and upper mantle structure in the southen part of the Moesian platform obtained by data from seismic stations MPE, PVL and SZH 323

J. S. Stoyanova, I. A. Zamfirov, Land surface state anomalies and related severe meteorological phenomena 331

A. I. Ivanov, Harmonic analysis of tide gauge data 2013-2014 in Bulgaria 343

N. Nikolov, A. L. Pandelova, Calculation of oxygen concentration in the Black Sea using data from Argo automatic profiling floats 349

D. Krezhova, S. Maneva, I. Moskova, K. Krezhov, Hyperspectral remote sensing applications for early stress detection of young plants 355

P. L. Nedialkov, Extinction and massive stellar population in Andromeda galaxy 364

T. M. Mishonov, N. I. Zahariev, R. V. Topchiyska, B. V. Lazov, S. B. Mladenov, Heating of the solar corona by Alfvén waves – self-induced opacity 368

E. Marekova, Temporal variations of the fractal properties of seismicity 380

L. Dimitrova, D. Solakov, S. Simeonova, I. Aleksandrova, System of Earthquakes Alert (SEA) in the Romania-Bulgaria cross border region 390

S. Simeonova, D. Solakov, I. Aleksandrova, P. Raykova, V. Protopopova, The 2012 M_w5.6 earthquake in Sofia seismic zone and some characteristics of the aftershock sequence 397

L. Bocheva, I. Gospodinov, Tornado climatology for Bulgaria (2001-2010) 405

R. I. Penchev, E. L. Peneva, Use of the numerical simulations with weather forecast model WRF as a proxy to atmospheric soundings 412

CONTENTS

INTERDISCIPLINARY PHYSICS

S. Nikolov, H. Fabritius, M. Friák, D. Raabe, Integrated multiscale modeling approach for hierarchical biological nanocomposites applied to lobster cuticle 423

G. Zamfirova, S. Cherneva, V. Gaydarov, T. Vladkova, Influence of crosslinking on micromechanical characteristics of liquid silicone rubber. Numerical simulations of microindentation process 433

Y. Ivanova, V. Vassilev, P. Djondjorov, S. Djoumaliisky, Experimental-theoretical approach to the identification of effective sound attenuation panels from recycled materials 442

L. Lazov, H. Deneva, Investigation on the influence of the process parameters power and velocity to laser cutting of lamellae 450

Ya. Gluhcheva, T. L. Dimitrova, R. Dukova, N. Zheleva, I. Koleva, E. Encheva, Dosimetry acceptance test of linear accelerator Varian Clinac iX 458

Ts. Genova, E. Borisova, L. Angelova, Al. Zhelyazkova, M. Keremedchiev, N. Penkov, B. Vladimirov, L. Avramov, Excitation-emission matrices for detection of colorectal tumors – initial investigations 464

Ya. Andreeva, E. Borisova, Ts. Genova, Al. Zhelyazkova, L. Avramov, Synchronous fluorescence spectroscopy for analysis of vegetable oils 469

Kr. Nikolova, T. Eftimov, G. Antova, Zh. Petkova, Optical properties of oil extracts of Bulgarian herbs .. 476

D. Kiradzhiyska, R. Mantcheva, D. Mileva, T. Yovcheva, A. Viraneva, On the influence of some factors on the functional properties of electrogalvanic coatings promising for medical applications 480

ELECTRONICS, INFORMATION AND EDUCATIONAL TECHNOLOGIES

G. Malchev, Project-based teaching in physics and its implementation for creating a website 489

R. I. Vassileva, Technological and methodological aspects of the acquisition of concepts in the process of physics education 498

Ts. Ts. Hristova, Innovative practices and technologies in educational projects of European Schoolnet and the project "Scientix" 504

Zh. Raykova, Possibilities of the inquiry based approach to built motivation for studying sciences 508

Hr. Petrova, Formation of meta-subject knowledge and skills in the process of training in physics in the secondary school 514

N. Vakrilov, A. Andonova, Innovative heat transfer analysis of LED modules by thermal simulations 519

K. Katsarova, R. Kaleva-Levi, Application of the scientific research approach in science education in Language School "Plovdiv" 528

D. Stoyanova, N. Kafadarova, S. Stoyanova-Petrova, Enhancing student learning in natural sciences through mobile augmented reality technology 532

INSTRUCTION TO THE AUTHORS 537

СЪДЪРЖАНИЕ

ФОТОННИ И ТЕЛЕКОМУНИКАЦИОННИ ТЕХНОЛОГИИ

Т. Пашова, И. Костова, Т. Ефтимов, Д. Тончев, Анализ на флуоресцентни спектри на оксифлуоридни композиции, легирани със самариев окис (Sm_2O_3) и самариев флуорид (SmF_3) 9

В. Плачкова, Пл. Балджиев, Г. Дянков, Т. Ефтимов, Изследване на 16-канална влакнесто-оптична (ВО) система за измерване на дългопериодични (ДПР) сензорни мрежи 15

Е. Караколева, Бл. Зафирова, А. Андреев, Пресмятане на фотонно-кристални влакна с метода на Галеркин с разложение по синусови функции без апроксимация на показателя на пречупване 21

А. Лалова, Р. Тодоров, Изследване на оптичните свойства на тънки PMMA слоеве за приложението им като сензори 29

Е. Пенчев, В. Бок, Т. Ефтимов, П. Микулич, Използване на дълго-периодична решетка с двоен резонанс за измерване показателя на пречупване на млека с различно съдържание на мазнини. 35

Р. Тодоров, А. Лалова, В. Лозанова, Оптични свойства на тънки Ag/As-S-Ge слоеве 40

Ст. Касърова, Н. Султанова, Ив. Николов, Полимерни материали за оптичен дизайн 44

В. Лозанова, Р. Тодоров, Микроструктура и оптични свойства на много тънки сребърни слоеве, отложени чрез термично изпарение 55

ФИЗИКА НА КОНДЕНЗИРАНАТА МАТЕРИЯ

С. Александрова, А. Секереш, Е. Вълчева, Модифициране на Si повърхност чрез плазмена йонна имплантация на H^+ и термично окисление 63

М. Миланова, П. Терзийска, П. Витанов, Г. Колева, К. Барту, Б. Клерио, Нови материали за приложение в многопреходни слънчеви елементи на основата на A^3B^5 хетероструктури 71

Л. Бедикян, Ст. Захариев, М. Захариева, UV сензори на основата на TiO_2 76

А. Христова, Т. Димов, И. Илиев, Поглъщане и оптична активност в едноосни жиротропни кристали от магнезиев сулфид хексахидрат 80

Г. Вълчев, В. Василев, П. Джонджоров, Върху различните модели, описващи равновесната форма на еритроцит 84

Ив. Петрова, Е. Иванов, Р. Коцилкова, Структура и свойства на полипропилен, съдържащ органична глина и въглеродни нанотръбички като пълнители 95

А. Гуджова, М. Галиханов, Разпределение на зарядите в електрети от ПМК с фин напълнител 103

В. Дряхлов, Т. Шайхиев, И. Шайхиев, И. Загидулина, Б. Бонев, В. Ненов, Интензификация на разрушаването на емулсии вода-в-масло посредством мембрани, третирани в коронен разряд или в плазмен поток 109

А. Гуджова, Т. Йовчева, А. Виранева, Изследване на короноелектрети от полимлечна киселина 115

А. Виранева, Т. Йовчева, К. Крежов, С. Сотиров, Електретна стабилност на γ-облъчени полимерни филми от полипропилен и полиетилентерефталат 121

М. Марудова, Е. Делчева, Г. Живанович, Реологични свойства на композитни филми на основата на хитозан и биоразградими полиестери 127

П. Петкова, П. Василев, М. Мустафа, В. Недков, Й. Тачева, Ю. Цукровски, Оптични спектри на MSO_3 и $[M(H_2O)_6]^{2+}$ ($M = Ni^{2+}$) 135

© 2015 Bulgarian Academy of Sciences, Union of Chemists in Bulgaria

СЪДЪРЖАНИЕ

Д. Лютов, Г. Цуцуманова, Ст. Русев, Елипсометрия на микрообекти и структури 140

Ст. Хаджийски, Д. Лютов, К. Кирилов, К. Генков, Г. Цуцуманова, А. Цонев, Ст. Русев, Елипсометрична детекция на оптично и електронно-лъчево индуцирано изменение на оптичните свойства на материали и структури 147

К. Генков, Г. Цуцуманова, Ст. Хаджийски, А. Цонев, Д. Лютов, Ст. Русев, Електронно-лъчево отгряване на микрообекти и структури в SEM 155

Цв. Михайлова, Ст. Недев, Е. Тошков, А. Стоянов, Структурни и електрофизични параметри на n-GaAs 162

Е. Вълчева, Г. Йорданов, Ниско-температурни фотолуминесцентни изследвания на CdSe нанокристали 168

В. Желев, Пл. Петков, Ив. Маркова, Т. Петров, Тънки слоеве от метални оксиди за получаване на позиционно чувствителен фотодетектор 173

Н. Петков, Предсказване на ерозията на материала на катода при PVD системи 177

АТОМНА И ЯДРЕНА ФИЗИКА

М. Шопова (от името на CMS колектива), Изработка и тестване на камери със съпротивителна плоскост за обновяване на мюонната система на експеримента CMS 185

Е. Попов, Т. Троев, Л. Петров, К. Беровски, С. Пенева, Б. Колев, Моделни пресмятания на позитронното взаимодействие в материали за ИТЕР 192

Д. Сувариева, М. Илиева, В. Колесников, В. Васендина, Ал. Зинченко, Реконструкция на хиперони в многоцелевия детектор MPD (NICA) 200

Любка Йорданова (от името на MPD колектива), Изучаване на добива на ϕ (1020) в сблъсъци на тежки йони на NICA/MPD 208

П. Дулов, В. Бабкин, М. Румянцев, В. Галватюк, В. Чолаков, Време-прелитна система (TOF) на детектора MPD (NICA) 215

М. Явахчова, Д. Тонев, Н. Гутев, Дж. ди Анжелис, П. Петков, Р. К. Боумик, Р.П. Сингх, С.. Муралитар, Н. Мадхаван, Р. Кумар, М. Кумар Раджу, Дж. Каур, Г. Моханто, А. Сингх, Н. Каур, Р. Гарг, А. Сукла, Цв. К. Маринов, Ц. Брант, Съществува ли хирална симетрия в ядрото ^{102}Rh? 222

Цв. Лазарова, Д. Ковачева, Т. Русков, С. Атанасова-Владимирова, П. Кръстев, Н. Танев, Композитни тънки слоеве от наноразмерен $CoFe_2O_4$ в полимерна матрица 227

М. Илиева, В. Колесников, Д. Сувариева, В. Васендина, Ал. Зинченко, Изучаване и реконструкция на хиперядра към проекта NICA/MPD 232

Н. Гераксиев (от името на MPD колектива), Разработка на методи за анализ на анизотропичен поток на частици към експеримента MPD/NICA 239

Б. Маринова, Н. Джавадов, И. Тяпкин, Моделиране на електромагнитния калориметър към NICA/MPD 247

ТЕОРЕТИЧНА И МАТЕМАТИЧЕСКА ФИЗИКА

В. Филев, Р. Рашков, Цв. Вецов, Холографски мезони в геометрия на Пилч-Уорнър 253

Б. Димитров, Обобщено уравнение на девиацията на С. Манов и възможните му приложения в небесната механика и релативистката астрометрия 262

Е. Писанова, С. Иванов, Неуниверсални критични свойства на средносферичния модел на феромагнетик с далекодействие 269

СЪДЪРЖАНИЕ

А. Ангелов, Е. Стоянова, Фундаментално квантово ограничение в Мах–Цендер интерферометър .. 275

Р. Камбурова, М. Приматарова, Разсейване на солитони от точкови дефекти в система от две свързани верижки на Абловиц–Ладик 282

Ив. Иванов, Приложение на метода на крайните разлики за намиране на собствените стойности и вектори на многослойни анизотропни оптични вълноводи 287

ФИЗИКА НА ЗЕМЯТА, АТМОСФЕРАТА И КОСМОСА. ОКЕАНОЛОГИЯ

Н. Добрев, Е. Ботев, В. Протопопова, Ив. Георгиев, Д. Димитров, Сеизмичност и съвременни движения по активни разломи в Югозападна България 299

Д. Солаков, Отместване на магнитудните оценки – влияние върху оценката на магнитудно-честотното разпределение 309

Др. Господинов, Софтуерна програма за идентифициране на най-добрата версия на RETAS модела за представяне затихването на афтершоковата активност във времето 314

Г. Георгиева, Структура на земната кора и горната мантия в южната част на Мизийската платформа по данни от CC MPE, PVL и SZH 323

Ю. Стоянова, И. Замфиров, Аномалии в състоянието на земната повърхност и свързани с това опасни метеорологични явления 331

А. Иванов, Хармоничен анализ на мареографни данни 2013–2014 г. 343

Н. Николов, А. Панделова, Изчисляване на концентрацията на кислород в Черно море по данни от Арго автоматични профилиращи сонди 349

Д. Крежова, Св. Манева, И. Москова, К. Крежов, Приложение на хиперспектралните дистанционни изследвания за ранно откриване на стрес в млади растения 355

П. Недялков, Екстинкция и масивно звездно население в галактиката Андромеда 364

Т. Мишонов, Н. Захариев, Р. Топчийска, Б. Лазов, Ст. Младенов, Нагряване на слънчевата корона чрез Алфвенови вълни – самоиндуцирана непрозрачност 368

Е. Марекова, Времеви вариации на фракталните свойства на сеизмичността 380

Л. Димитрова, Д. Солаков, С. Симеонова, И. Александрова, Система за ранно оповестяване на земетресения в транс-граничния район Румъния–България 390

С. Симеонова, Д. Солаков, И. Александрова, П. Райкова, В. Протопопова, Земетресението (M_W5.6) от 2012 година, реализирано в Софийска сеизмична зона и последвалата го афтършокова активност 397

Л. Бочева, Ил. Господинов, Климатично изследване на торнадо (смерч) в България 405

Р. Пенчев, Е. Пенева, Числена апроксимация на профили от аерологични сондажи с помощта на числения модел за прогноза на времето WRF 412

ИНТЕРДИСЦИПЛИНАРНА ФИЗИКА

Св. Николов, Х. Фабрициус, М. Фриак, Д. Раабе, Конструктивни принципи и механични свойства на биологични нанокомпозити с йерархична структура: многомащабно моделиране на черупката на омара Homarus americanus 423

Г. Замфирова, С. Чернева, В. Гайдаров, Т. Владкова, Влияние на степента на омрежване върху микромеханичните характеристики. Симулация на микроиндентационния процес 433

Й. Иванова, В. Василев, П. Джонджоров, Стр. Джумалийски, Експериментално-теоретичен подход за идентификация на ефективното шумозаглушаване на панели от рециклирани материали .. 442

СЪДЪРЖАНИЕ

Л. Лазов, Хр. Денева, Изследване на влиянието на технологичните параметри мощност и скорост при лазерно рязане на ламели 450

Я. Глухчева, Т. Димитрова, Р. Дукова, Н. Желева, И. Колева, Е. Енчева, Дозиметрични предварителни приемни изпитвания на линеен ускорител Clinac iX, Varian 458

Ц. Генова, Е. Борисова, Л. Ангелова, Ал. Желязкова, М. Кермедчиев, Б. Владимиров, Л. Аврамов, Матрици на възбуждане и флуоресценция за детектиране на коло-ректални тумори – начални изследвания 464

Я. Андреева, Е. Борисова, Ц. Генова, Ал. Желязкова, Л. Аврамов, Синхронна флуоресцентна спектроскопия за анализ на растителни масла 469

Кр. Николова, Т. Ефтимов, Г. Антова, Ж. Петкова, Оптични свойсва на маслени екстракти от български билки 476

Д. Кираджийска, Р. Манчева, Д. Милева, Т. Йовчева, А. Виранева, За влиянието на някои фактори върху функционалните свойства на галванично отложени покрития, перспективни за медицинско приложение 480

ЕЛЕКТРОНИКА, ИНФОРМАЦИОННИ И ОБРАЗОВАТЕЛНИ ТЕХНОЛОГИИ

Г. Малчев, Проектно-базираното обучение по физика и приложението му за създаване на интернет сайт 489

Р. Василева, Технологични и методически аспекти на усвояването на понятия в обучението по физика 498

Ц. Христова, Технологични и методически аспекти на усвояването на понятия в обучението по физика 504

Ж. Райкова, Възможностите на изследователския подход за изграждане на мотивация за учене по физика 508

Хр. Петрова, Формиране на метапредметни знания и умения в процеса на обучение по физика в средното училище 514

Н. Вакрилов, А. Андонова, Иновативно изследване на топлообмена в светодиодни модули чрез топлинни симулации 519

К. Кацарова, Р. Калева-Леви, Приложение на научно-изследователския подход в обучението по природни науки в Езикова гимназия “Пловдив”, град Пловдив 528

Д. Стоянова, Н. Кафадарова, С. Стоянова-Петрова, Подобряване на резултатите от обучението по природни науки в началното училище чрез използване на технологията “добавена реалност” с мобилни устройства 532

ИНСТРУКЦИЯ ЗА АВТОРИТЕ 537